

University of Nevada, Reno

**Seismic Performance of Circular and Interlocking Spirals RC Bridge  
Columns under Bidirectional Shake Table Loading**

A dissertation submitted in partial fulfillment of the  
requirements for the degree of Doctor of Philosophy in  
Civil Engineering

by  
Juan Guillermo Arias Acosta

Dr. David. H. Sanders/Dissertation Advisor

August, 2011

Copyright by Juan G. Arias Acosta 2011

All Rights Reserved



University of Nevada, Reno  
Statewide • Worldwide

THE GRADUATE SCHOOL

We recommend that the dissertation  
prepared under our supervision by

**JUAN G. ARIAS ACOSTA**

entitled

**Seismic Performance Of Circular And Interlocking Spirals RC Bridge Columns  
Under Bidirectional Shake Table Loading**

be accepted in partial fulfillment of the  
requirements for the degree of

**DOCTOR OF PHILOSOPHY**

Dr. David H. Sanders, Advisor

Dr. Ian Buckle, Committee Member

Dr. Ahmad Itani, Committee Member

Dr. Yanyao Jiang, Committee Member

Dr. John Louie, Graduate School Representative

Marsha H. Read, Ph. D., Dean, Graduate School

August, 2011

## **Abstract**

Under seismic excitations reinforced concrete bridge columns (RCC) are subjected to combinations of forces and deformations. These complex actions are caused by spatially-complex variation of earthquake ground motions, the bridge structural configuration, and the interactions between input and response characteristics. The seismic behavior of RCC may be seriously affected by these complex actions, and that in turn influences the performance of bridges as essential components of transportation systems

To study the impact of bidirectional ground acceleration on the seismic performance of circular and oblong sections (double interlocking spirals), four large-scale cantilever-type RCC specimens were designed and tested on the bidirectional shake table facility at the University of Nevada, Reno (UNR). As part of the study, a unique inertial loading system named the Bidirectional Mass Rig (BMR) was developed to allow shake table testing of single RCC under biaxial ground motions. Pairs of circular and interlocking RC specimens were subjected to different levels of biaxial real time earthquake motions. Within each pair, one specimen had asymmetric distribution of masses on the BMR to induce more torsion. The performance of the specimens was assessed in terms of strength, deformation, ductility and failure mode.

The seismic performance of each pair of specimens was similar and was controlled by the biaxial effect of bending with small influence of shear deformations. The RCC exhibited stable and ductile behavior, and without collapse, under repetitions of earthquakes with spectral amplitude equal to or larger than the design and maximum

considered earthquakes in California. For the sections and ground motions used, the biaxial interactions affected mostly the seismic performance of the columns along the direction where the small component of the earthquake was applied, showing reductions in the lateral capacity as predicted by moment-curvature analyses. It was also observed that the asymmetric mass configuration used for specimens C2 and I2 only induced low values of torsion on the columns with measured values of the torque to bending ratio below 20%.

An analytical investigation using OpenSees software was conducted to develop and validate analytical models that can reasonably predict the seismic behavior of RC columns subjected to biaxial earthquake loading. The results show that the modeling of the specimens with a nonlinear beam-column element with fibers (beam-with-hinges element), hysteretic material models with strength degradation (Concrete07 and ReinforcingSteel materials), bond slip and viscous damping (stiffness proportional-only) leads to the best estimation of the measured performance.

In order to investigate the impact of biaxial loading on the seismic response of columns, the analytical models were subjected to the combined effects of axial loads, either unidirectional or bidirectional excitations and P-delta effects. The results indicate that circular and interlocking columns designed according to the Caltrans BDS and SDC generally behave well, even under large levels of biaxial earthquake loading. From the analytical results it was observed that for small amplitude earthquakes (before yielding) no major differences are observed in the response of columns under unidirectional or bidirectional excitations. After yielding the biaxial excitations resulted in a reduction of the capacity of the columns, increase of lateral displacements and more accelerated

stiffness degradation compared to unidirectional excitation. It was also found that for near-fault earthquakes with forward directivity effects, the peak bidirectional displacements are comparable to the peak unidirectional displacements computed using the strong component of the earthquake, and to the component displacement calculated from the individual uniaxial responses combined using the square root of the sum of squares (SRSS) rule.

*To my wife Natalia, Daughter Dana Sofia and my Family*

## Acknowledgements

This research was made possible through the support, guidance and encouragement of many individuals and institutions.

I would like first to express my appreciation and gratitude to my advisor, Dr. David H. Sanders for his dedicated guidance, friendship, support, and encouragement throughout my time at the University of Nevada Reno and during the course of this study.

I would also like to thank my doctoral committee members, Dr. Ian Buckle, Dr. Ahmad Itani, Dr. John Louie and Dr. Yanyao Jiang for their contributions and advice on this project. Their efforts were not just limited to the work presented here, but also many other activities during my time at Nevada.

This research project was financially supported through the CABER NEESR-SG project, Seismic Simulation and Design of Bridge Columns under Combined Actions and Implications on System Response, funded by the National Science Foundation (NSF) under Grant No. EMS-0530737.

Next I would like to express my gratitude to Dr. Patrick Laplace, Mr. Chad and Todd Lyttle, Mr. Robert Nelson, and Mr. Paul Lucas of the UNR Large Scale Structures Laboratory for their advice and dedicated assistance during the course of the shake table experiments. The assistance and support of Dr. Sherif Elfass and Rodney Porter of NEES-UNR are gratefully appreciated. Special thanks also go to fellow students Jeremy Hasselbauer, Mike Levi and Steven Kenny, for their assistance during the construction, testing and data processing of the specimens of this research work. I would also like to

thank Don and Geoffrey Roberts for the construction of the specimens and Bidirectional Mass Rig.

My heartfelt thanks to Carlos Cruz, Eric Monzon, Ashkan Vosooghi, Mohamed Ayoub, Arash Esmaili Zaghi, Sarira Motaref, Camilo Builes, Chunli Wei and many others for the enjoyable and cheerful conversations during the time of our studies at Nevada.

This acknowledgment would not be completed without expressing gratitude to my family. My lovely wife Natalia and daughter Dana Sofia are my inspiration. I am eternally grateful for their confidence, unlimited emotional support and encouragement. Special thanks are expressed to my sister Beatriz and my cousin Merce for their emotional support and encouragement. I would like also to thank my brothers and sister, Jesus, Carlos and Martha Arias; my sisters in-law Nena and Lina, and my nephews and nieces, my family in-law Caridad, Liliana, Juan and Carlos for their love, encouragement and support. Finally, thanks to God for my extraordinary parents: Antonio and Amparo; their life lessons, will never be forgotten, may they rest in peace.



## Table of Contents

<b>Chapter 1. Introduction</b> .....	1
1.1 Introductory Remarks .....	1
1.2 Literature Review .....	2
1.2.1 Quasi-static Tests on Rectangular and Circular Sections under Biaxial Lateral Loading.....	4
1.2.2 Quasi-static Tests on Rectangular and Circular Sections under Combined Lateral Loading and Torsion.....	11
1.2.3 Quasi-static Tests on Double Interlocking Sections.....	14
1.2.4 Pseudo-dynamic Tests on Rectangular and Circular Sections .....	18
1.2.5 Dynamic Tests on Rectangular and Circular Sections subjected to Unidirectional Earthquake Motions .....	21
1.2.6 Dynamic Tests on Rectangular and Circular Sections Subjected to Bidirectional Earthquake Motions.....	29
1.2.7 Dynamic Tests on Interlocking Sections.....	39
1.2.8 Literature Review Summary .....	42
1.3 Design Guidelines for Columns Reinforced with Spirals and Interlocking Spirals .....	44
1.3.1 2006 Caltrans Seismic Design Criteria Overview.....	44
1.3.2 Displacement Ductility.....	45
1.3.3 Maximum and Minimum Longitudinal reinforcement.....	45
1.3.3 Confinement Reinforcement .....	46
1.3.4 Shear Capacity.....	47
1.4. Objectives and Scope.....	50
1.4.1 Overall Project (CABER).....	50
1.4.2 Study at University of Nevada Reno.....	52
1.5. Organization .....	55
<b>Chapter 2. Specimen Design and Preliminary Analysis</b> .....	57
2.1. Introduction.....	57
2.2. Prototype Columns .....	57
2.3. Specimen Design .....	59
2.3.1. Modeling Procedure .....	59
2.3.2. Circular Columns .....	60
2.3.3. Interlocking Columns .....	61

2.3.4. Footing and Top Head.....	61
2.4. Preliminary Analysis .....	63
2.4.1. Moment-Curvature Analysis .....	63
2.4.2. Lateral Force-Displacement Prediction.....	70
2.4.3. Torque-twist Analysis .....	72
<b>Chapter 3. Specimen Details and Experimental Test Setup .....</b>	<b>79</b>
3.1. Introduction.....	79
3.2. Construction of the Specimens .....	79
3.3. Material Properties.....	81
3.3.1. Steel Reinforcement .....	82
3.3.2. Concrete .....	82
3.4. Test Setup: Bidirectional Mass Rig .....	83
3.5. Instrumentation .....	87
3.5.1. Acceleration .....	87
3.5.2. Lateral Force .....	88
3.5.3. Lateral Displacement.....	88
3.5.4. Curvature and Concrete Strains.....	89
3.5.5. Strain Gauges .....	91
<b>Chapter 4. Experimental Results for Circular Columns.....</b>	<b>92</b>
4.1. Introduction.....	92
4.2. Test Procedure .....	92
4.3. Shake Table Performance .....	94
4.4. Observed Column Performance.....	95
4.5. Lateral Force-Displacement Hysteresis.....	97
4.6. Dynamic Properties .....	101
4.7. Lateral Stiffness.....	102
4.8. Curvature .....	104
4.9. Flexural and Shear Deformations .....	105
4.10. Strains .....	106
4.11. Displacement and Curvature Ductility .....	108
4.12. Plastic Hinge Length.....	109
4.13. Torque-Rotation Hysteresis .....	111
<b>Chapter 5. Experimental Results for Interlocking Columns .....</b>	<b>113</b>
5.1. Introduction.....	113
5.2. Test Procedure .....	113
5.3. Shake Table Performance .....	115

5.4. Observed Column Performance.....	116
5.5. Lateral Force-Displacement Hysteresis.....	118
5.6. Dynamic Properties .....	120
5.7. Lateral Stiffness.....	121
5.8. Curvature .....	122
5.9. Bond-slip Rotations .....	123
5.10. Flexural and Shear Deformations .....	125
5.11. Strains .....	126
5.12. Displacement and Curvature Ductility .....	128
5.13. Plastic Hinge Length.....	129
5.14. Torque-Rotation Hysteresis .....	129
<b>Chapter 6. Columns Tested Under Unidirectional Ground Motions.....</b>	<b>131</b>
6.1 Introduction.....	131
6.2 Test Setup for Unidirectional Tested Specimens.....	131
6.3 Circular Columns 9F1 and NF1.....	132
6.4 Interlocking Column ISL1.0.....	134
6.5 Force-Displacement Envelopes .....	135
6.6 Axial Load Variation .....	136
6.7 Measured Dynamic Properties.....	137
6.8 Moment – Curvature Envelopes .....	138
6.9 Concrete Strains.....	139
6.10 Comparisons of Unidirectional and Bidirectional Tests.....	140
6.11.1 Circular Specimens.....	140
6.11.2 Interlocking Specimens .....	143
<b>Chapter 7. Analytical Modeling of Specimens .....</b>	<b>146</b>
7.1. Introduction.....	146
7.2. Strain Rate Effect.....	147
7.3. Moment-Curvature Analysis .....	151
7.4. Calculated Lateral Force-Displacement from Moment-Curvature .....	155
7.5. Bond Slip Deformation and Rotation .....	157
7.5.1 Wehbe Method .....	157
7.5.2 Zhao Method .....	158
7.6. Shear Deformations .....	161
7.7. OpenSees Software.....	163
7.7.1 Modeling Strategies.....	164
7.7.2 Material Models .....	166
7.7.3 Pushover Analyses for Unidirectionally Tested Specimens.....	171
7.7.4 Nonlinear Time History Analyses for Unidirectionally Tested Specimens .....	173

7.7.5 Nonlinear Time History Analyses for Bidirectionally Tested Specimens .....	180
<b>Chapter 8. Analytical Investigation of the Seismic Performance of RC Bridge Columns under One and Two Earthquake Components .....</b>	<b>186</b>
8.1 Introduction.....	186
8.2 Analytical Models.....	186
8.3 Ground Motions.....	188
8.4 Unidirectional vs. Bidirectional Response.....	189
<b>Chapter 9. Summary and Conclusions .....</b>	<b>194</b>
9.1 Summary.....	194
9.2 Conclusions.....	197
9.2.1 Experimental Investigation .....	197
9.2.2 Analytical Investigation.....	201
9.3 Phase II of the Experimental Program at the University of Nevada, Reno .....	204
9.4 Future Research .....	206
<b>Appendix A: Database of Columns Tested under Bidirectional Loading.....</b>	<b>633</b>
<b>Appendix B: Columns Design According to the 2006 Caltrans SDC.....</b>	<b>655</b>
<b>Appendix C: Strain Time History.....</b>	<b>665</b>

## List of Tables

### Chapter 1

Table 1-1 Experimental Test Program at University of Nevada, Reno .....	216
---	-----

### Chapter 2

Table 2-1 Similitude Requirements and Scaling Factors .....	217
Table 2-2 Steel Properties Used for Preliminary Moment-Curvature Analysis (Xtract).....	217
Table 2-3 Stress-Strain Properties Used for Preliminary Moment-Curvature Analysis (Xtract).218	
Table 2-4 Idealized Moment-Curvature Results, P=0 kips.....	218
Table 2-5 Idealized Moment-Curvature Results, P=80 kips.....	219
Table 2-6 Force-Displacement Predictions, P=0 kips.....	219
Table 2-7 Force-Displacement Predictions, P=80 kips.....	220
Table 2-8 Torque-twist Predictions, Circular Specimen P=0 kips.....	221
Table 2-9 Torque-twist Predictions, Circular Specimen P=80 kips.....	222
Table 2-10 Torque-twist Predictions, Interlocking Specimen P=0 kips .....	223
Table 2-11 Torque-twist Predictions, Interlocking Specimen P=80 kips .....	224

### Chapter 3

Table 3-1 Steel Properties for the Specimens .....	225
Table 3-2 Concrete Cylinder Test Results for Footings .....	225
Table 3-3 Concrete Cylinder Test Results for Columns .....	225

### Chapter 4

Table 4-1 Test Procedure, Specimen C1.....	226
Table 4-2 Test Procedure, Specimen C2.....	226
Table 4-3 Target and Achieved Peak Table Accelerations for Specimen C1 .....	227
Table 4-4 Target and Achieved Peak Table Accelerations for Specimen C2 .....	228
Table 4-5 Spectral Response at Structural Period, Specimen C1 .....	229
Table 4-6 Spectral Response at Structural Period, Specimen C2 .....	230
Table 4-7 Observed Performance for Specimen C1 .....	231
Table 4-8 Observed Performance for Specimen C2 .....	232
Table 4-9 Peak Force and Corresponding Displacement for Specimen C1.....	233
Table 4-10 Peak Displacement and Corresponding Force for Specimen C1.....	234
Table 4-11 Peak Force and Corresponding Displacement for Specimen C2.....	235
Table 4-12 Peak Displacement and Corresponding Force for Specimen C2.....	236
Table 4-13 Measured Dynamic Properties for Specimen C1.....	237
Table 4-14 Measured Dynamic Properties for Specimen C2.....	238
Table 4-15 Measured Effective Lateral Stiffness (E <sub>l</sub> /E <sub>l</sub> g), Specimen C1 .....	239
Table 4-16 Measured Effective Lateral Stiffness (E <sub>l</sub> /E <sub>l</sub> g), Specimen C2 .....	239
Table 4-17 Measured Strains in Longitudinal Bars at -4 in. from the Top of the Footing, Specimen C1 .....	240

Table 4-18 Measured Strains in Longitudinal bars and Spirals at 0 in. from the Top of the Footing, Specimen C1.....	241
Table 4-19 Measured Strains in Longitudinal bars and Spirals at 8 in. from the Top of the Footing, Specimen C1.....	242
Table 4-20 Measured Strains in Longitudinal bars and Spirals at 16 in. from the Top of the Footing, Specimen C1.....	243
Table 4-21 Measured Strains in Longitudinal bars and Spirals at 24 in. from the Top of the Footing, Specimen C1.....	244
Table 4-22 Measured Strains in Longitudinal Bars at -4 in. from the Top of the Footing, Specimen C2.....	245
Table 4-23 Measured Strains in Longitudinal bars and Spirals at 0 in. from the Top of the Footing, Specimen C2.....	246
Table 4-24 Measured Strains in Longitudinal bars and Spirals at 8 in. from the Top of the Footing, Specimen C2.....	247
Table 4-25 Measured Strains in Longitudinal bars and Spirals at 16 in. from the Top of the Footing, Specimen C2.....	248
Table 4-26 Measured Strains in Longitudinal bars and Spirals at 24 in. from the Top of the Footing, Specimen C2.....	249
Table 4-27 Values for Idealized Force-Displacement and Moment-Curvature.....	250
Table 4-28 Plastic Hinge Lengths.....	250

## Chapter 5

Table 5-1 Test Procedure, Specimen I1.....	251
Table 5-2 Test Procedure, Specimen I2.....	251
Table 5-3 Target and Achieved Peak Table Accelerations for Specimen I1.....	252
Table 5-4 Target and Achieved Peak Table Accelerations for Specimen I2.....	253
Table 5-5 Spectral Response at Structural Period, Specimen I1.....	254
Table 5-6 Spectral Response at Structural Period, Specimen I2.....	255
Table 5-7 Observed Performance for Specimen I1.....	256
Table 5-8 Observed Performance for Specimen I2.....	257
Table 5-9 Peak Force and Corresponding Displacement for Specimen I1.....	258
Table 5-10 Peak Displacement and Corresponding Force for Specimen I1.....	259
Table 5-11 Peak Force and Corresponding Displacement for Specimen I2.....	260
Table 5-12 Peak Displacement and Corresponding Force for Specimen I2.....	261
Table 5-13 Measured Dynamic Properties for Specimen I1.....	262
Table 5-14 Measured Dynamic Properties for Specimen I2.....	263
Table 5-15 Measured Effective Lateral Stiffness (E <sub>l</sub> /E <sub>l</sub> g), Specimen I1.....	264
Table 5-16 Measured Effective Lateral Stiffness (E <sub>l</sub> /E <sub>l</sub> g), Specimen I2.....	264
Table 5-17 Measured Strains in Longitudinal bars and Spirals at -5 in. from the Top of the Footing, Specimen I1.....	265
Table 5-18 Measured Strains in Longitudinal bars and Spirals at 0 in. from the Top of the Footing, Specimen I1.....	266

Table 5-19 Measured Strains in Longitudinal bars and Spirals at 5 in. from the Top of the Footing, Specimen I1 .....	267
Table 5-20 Measured Strains in Longitudinal bars and Spirals at 10 in. from the Top of the Footing, Specimen I1 .....	268
Table 5-21 Measured Strains in Longitudinal bars and Spirals at 15 in. from the Top of the Footing, Specimen I1 .....	269
Table 5-22 Measured Strains in Longitudinal bars and Spirals at 20 in. from the Top of the Footing, Specimen I1 .....	270
Table 5-23 Measured Strains in Longitudinal bars and Spirals at -5 in. from the Top of the Footing, Specimen I2 .....	271
Table 5-24 Measured Strains in Longitudinal bars and Spirals at 0 in. from the Top of the Footing, Specimen I2 .....	272
Table 5-25 Measured Strains in Longitudinal bars and Spirals at 5 in. from the Top of the Footing, Specimen I2 .....	273
Table 5-26 Measured Strains in Longitudinal bars and Spirals at 10 in. from the Top of the Footing, Specimen I2 .....	274
Table 5-27 Measured Strains in Longitudinal bars and Spirals at 15 in. from the Top of the Footing, Specimen I2 .....	275
Table 5-28 Measured Strains in Longitudinal bars and Spirals at 20 in. from the Top of the Footing, Specimen I2 .....	276
Table 5-29 Values for Idealized Force-Displacement and Moment-Curvature .....	277
Table 5-30 Plastic Hinge Lengths .....	277

## **Chapter 6**

Table 6-1 Testing Protocol for Specimens 9F1 .....	278
Table 6-2 Testing Protocol for Specimens NF1 .....	278
Table 6-3 Concrete Compressive Strength .....	279
Table 6-4 Reinforcing Steel Properties .....	279
Table 6-5 Testing Protocol for Specimens ISL1.0 .....	279
Table 6-6 Measured Response for Circular Specimens 9F1 and NF1 .....	280
Table 6-7 Measured Response for Interlocking Specimen ISL1.0 .....	281
Table 6-8 Measured Dynamic Properties .....	282
Table 6-9 Measured Curvature Ductility .....	283
Table 6-10 Measured Concrete Strains at Plastic Hinge, Specimen 9F1 .....	283
Table 6-11 Measured Displacement Ductility .....	284

## **Chapter 7**

Table 7-1 Measured Strain Rate for Longitudinal Reinforcement .....	285
Table 7-2 Measured Strain Rate for Concrete .....	285
Table 7-3 Stress-Strain Properties Modified by Strain Rate, Used for Moment-Curvature Analysis .....	286
Table 7-4 Stress-Strain Properties Modified by Strain Rate and Ultimate Confined Concrete Strain, Used for Moment-Curvature Analysis .....	286

Table 7-5 Influence of Strain Rate on the Idealized Moment-Curvature Properties, Unidirectional Specimens .....	287
Table 7-6 Influence of Strain Rate on the Idealized Moment-Curvature Properties, Bidirectional Specimens .....	287
Table 7- 7 Idealized Force-Displacement Properties for Unidirectional Specimens (Priestley’s Method).....	288
Table 7-8 Idealized Force-Displacement Properties for Bidirectional Specimens (Priestley’s Method).....	288
Table 7-9 Moment-Slip Rotation Properties for Unidirectional Specimens (Wehbe Method)....	289
Table 7-10 Analytical Model in OpenSees for Time History Analysis, Specimen NF1 .....	290
Table 7-11 Analytical vs. Experimental Seismic Performance, Specimen NF1.....	291
Table 7-12 Analytical Model in OpenSees for Time History Analysis, Specimen 9F1 .....	292
Table 7-13 Analytical vs. Experimental Seismic Performance, Specimen 9F1.....	293
Table 7-14 Analytical Model in OpenSees for Time History Analysis, Specimen ISL1.0 .....	294
Table 7-15 Analytical vs. Experimental Seismic Performance, Specimen ISL1.0.....	295
Table 7-16 Analytical Model in OpenSees for Time History Analysis, Specimens C1 and C2..	296
Table 7-17 Analytical vs. Experimental Seismic Performance, Specimen C1-Longitudinal .....	297
Table 7-18 Analytical vs. Experimental Seismic Performance, Specimen C1-Transverse .....	297
Table 7-19 Analytical vs. Experimental Seismic Performance, Specimen C2-Longitudinal .....	298
Table 7-20 Analytical vs. Experimental Seismic Performance, Specimen C2-Transversal .....	298
Table 7-21 Analytical Model in OpenSees for Time History Analysis, Specimen I1 and I2.....	299
Table 7-22 Analytical vs. Experimental Seismic Performance, Specimen I1-Longitudinal .....	300
Table 7-23 Analytical vs. Experimental Seismic Performance, Specimen I1-Longitudinal- Transverse .....	300
Table 7-24 Analytical vs. Experimental Seismic Performance, Specimen I2-Longitudinal .....	301
Table 7-25 Analytical vs. Experimental Seismic Performance, Specimen I2-Transverse.....	301

## Chapter 8

Table 8-1 Ground Motions used for Analytical Investigation .....	302
Table 8-2 Spectral Acceleration Demands for Each Earthquake.....	302
Table 8-3 Ground Motion Intensity Factors for the Analytical Loading Sequence.....	303
Table 8-4 Maximum Predicted Displacement from Unidirectional, Bidirectional and Components under El Centro .....	303
Table 8-5 Maximum Predicted Displacement from Unidirectional, Bidirectional and Components under Los Gatos (Circular) .....	304
Table 8-6 Maximum Predicted Displacement from Unidirectional, Bidirectional and Components under Los Gatos (Circular) .....	304
Table 8-7 Maximum Predicted Displacement from Unidirectional, Bidirectional and Components under Petrolia (Circular) .....	305
Table 8-8 Maximum Predicted Displacement from Unidirectional, Bidirectional and Components under Rinaldi (Circular).....	305
Table 8-9 Maximum Predicted Displacement from Unidirectional, Bidirectional and Components under Sylmar (Circular) .....	306



Table 8-10 Maximum Predicted Displacement from Unidirectional, Bidirectional and Components under Takatori (Circular).....	306
Table 8-11 Maximum Predicted Displacement from Unidirectional, Bidirectional and Components under El Centro (Interlocking).....	307
Table 8-12 Maximum Predicted Displacement from Unidirectional, Bidirectional and Components under Los Gatos (Interlocking).....	307
Table 8-13 Maximum Predicted Displacement from Unidirectional, Bidirectional and Components under Petrolia (Interlocking).....	308
Table 8-14 Maximum Predicted Displacement from Unidirectional, Bidirectional and Components under Rinaldi (Interlocking).....	308
Table 8-15 Maximum Predicted Displacement from Unidirectional, Bidirectional and Components under Sylmar (Interlocking).....	309
Table 8-16 Maximum Predicted Displacement from Unidirectional, Bidirectional and Components under Takatori (Interlocking).....	309

## **Appendix A**

Table A-1 Summary of RC Columns Tested Using Quasi-static Tests.....	633
Table A-2 Summary of RC Columns Tested Using Quasi-static Tests.....	634
Table A-3 Summary of RC Columns Tested Using Quasi-static Tests.....	635
Table A-4 Summary of RC Columns Tested Using Quasi-static Tests.....	636
Table A-5 Summary of RC Columns Tested Using Quasi-static Tests.....	637
Table A-6 Summary of RC Columns Tested Using Quasi-static Tests.....	638
Table A-7 Summary of RC Columns Tested Using Quasi-static Tests.....	639
Table A-8 Summary of RC Columns Tested Using Quasi-static Tests.....	640
Table A-9 Summary of RC Columns Tested Using Quasi-static Tests under Lateral Loading and Torsion.....	641
Table A-10 Summary of RC Columns Tested Using Quasi-static Tests under Lateral Loading and Torsion.....	642
Table A-11 Summary of RC Columns Tested Using Quasi-static Tests under Lateral Loading and Torsion.....	643
Table A-12 Summary of RC Columns Tested Using Dynamic Testing (Unidirectional Shake Table).....	644
Table A-13 Summary of RC Interlocking Columns Tested Using Quasi-static Tests.....	645
Table A-14 Summary of RC Columns Tested Using Pseudo-dynamic Tests.....	646
Table A-15 Summary of RC Columns Tested Using Dynamic Testing (Unidirectional Shake Table).....	647
Table A-16 Summary of RC Columns Tested Using Dynamic Testing (Unidirectional Shake Table).....	648
Table A-17 Summary of RC Columns Tested Using Dynamic Testing (Unidirectional Shake Table).....	649
Table A-18 Summary of RC Columns Tested Using Dynamic Testing (Unidirectional Shake Table).....	650

Table A-19 Summary of RC Columns Tested Using Dynamic Testing (Bidirectional Shake Table) .....	651
Table A-20 Summary of RC Columns Tested Using Dynamic Testing (Bidirectional Shake Table) .....	652
Table A-21 Summary of RC Columns Tested Using Dynamic Testing (Bidirectional Shake Table) .....	653
Table A-22 Summary of Interlocking Columns Tested Using Dynamic Testing (Shake Table)	654

## List of Figures

### Chapter 2

Figure 2-1 Specimens Cross Section .....	310
Figure 2-2 Circular Columns Steel Detail (N – S Elevation).....	311
Figure 2-3 Circular Columns Steel Detail (E – W Elevation) .....	312
Figure 2-4 Circular Columns Footing and Top Head Details .....	313
Figure 2-5 Interlocking Columns N – S Elevation .....	314
Figure 2-6 Interlocking Columns E – W Elevation .....	315
Figure 2-7 Interlocking Columns Footing and Top Head Details.....	316
Figure 2-8 Stress-Strain Relationship for Unconfined Concrete .....	317
Figure 2-9 Stress-Strain Relationship for Confined Concrete .....	317
Figure 2-10 Stress-strain behavior for Steel .....	318
Figure 2-11 Cross Sections Used in Xtract (Fiber Model) .....	318
Figure 2-12 Moment-Curvature for Circular Column P=0, N.A at 0o .....	319
Figure 2-13 Moment-Curvature for Circular Column P=80 kips, N.A at 45o.....	319
Figure 2-14 Moment-Curvature for Interlocking Column P=0, N.A at 0o .....	320
Figure 2-15 Moment-Curvature for Interlocking Column P=80 kips, N.A at 30o .....	320
Figure 2-16 Capacity Orbits for Ultimate Moments and Curvatures, Circular Section.....	321
Figure 2-17 Capacity Orbits for Ultimate Moments and Curvatures, Interlocking Section .....	322
Figure 2-18 Force-Displacement Idealization (Priestley et al., 2007) .....	323
Figure 2-19 Idealization of Curvature Distribution (Priestley et al., 2007) .....	323
Figure 2-20 Reinforced Concrete Membrane Element Under In-plane Stresses .....	324
Figure 2-21 Flow Chart for Torque-twist Analysis .....	325
Figure 2-22 Torque-twist Relationship for Circular Specimens .....	326
Figure 2-23 Torque-twist Relationship for interlocking Specimens.....	326

### Chapter 3

Figure 3-1 Steel Cage for interlocking Column (view from bottom) .....	327
Figure 3-2 Steel Cage for interlocking Column (view from top).....	327
Figure 3-3 Circular Column Steel Cage Set on the Footing .....	328
Figure 3-4 Interlocking Column Steel Cage Set on the Footing.....	328
Figure 3-5 Circular Column Footing before Pouring the Concrete .....	329
Figure 3-6 Interlocking Column Footing before Pouring the Concrete.....	329
Figure 3-7 Circular Column Footing Concrete Pouring .....	330
Figure 3-8 Interlocking Column Footing Concrete Pouring.....	330
Figure 3-9 Circular Column Formwork .....	331
Figure 3-10 Wood and Steel Sheets Used for Interlocking Column Formwork.....	331
Figure 3-11 Column and top Head Pouring (Circular Specimen).....	332
Figure 3-12 Column and top Head Pouring (Interlocking Specimen) .....	332
Figure 3-13 Circular Columns after Form Removal.....	333
Figure 3-14 Interlocking Columns after Form Removal.....	333

Figure 3-15 Measured Stress-Strain Curves for Grade 60 No.4 Deformed Bars.....	334
Figure 3-16 Measured Stress-Strain Curves for Grade 60 No.3 Deformed Bars.....	334
Figure 3-17 Stress-Strain Curves of Grade 60 W5.0 Galvanized Wire .....	335
Figure 3-18 Stress-Strain Curves of Grade 60 W2.9 Galvanized Wire .....	335
Figure 3-19 Shake Table Testing of Single Cantilever-type Column (Mahin et al., 2004).....	336
Figure 3-20 Unidirectional Mass Rig at UNR (Adapted from Laplace et al., 1999).....	336
Figure 3-21 Bidirectional Mass Rig (3D View).....	337
Figure 3-22 Bidirectional Mass Rig (Elevation).....	337
Figure 3-23 Bidirectional Mass Rig (Supporting Structure Plan View).....	338
Figure 3-24 Bidirectional Mass Rig (Elevation View) .....	339
Figure 3-25 Bidirectional Mass Rig (Platform Plan View) .....	340
Figure 3-26 Bidirectional Mass Rig (Platform Assemblage).....	304
Figure 3-27 Bidirectional Mass Rig (Lead Pallets) .....	342
Figure 3-28 Bidirectional Mass Rig (Safety Arms).....	343
Figure 3-29 Bidirectional Mass Rig (Ball Bearings) .....	344
Figure 3-30 Bidirectional Mass rig (Links Configuration).....	345
Figure 3-31 Bidirectional Mass Rig (Assembling Process).....	346
Figure 3-32 Bidirectional Mass Rig and Specimen(Before Testing).....	347
Figure 3-33 Bidirectional Mass Rig (Link Details) .....	347
Figure 3-34 Bidirectional Mass Rig with Axial Force and P-delta Effects (3D view) .....	348
Figure 3-35 Bidirectional Mass Rig with Axial Force and P-delta Effects (Elevation) .....	348
Figure 3-36 Distribution of Accelerometers and Displacement Transducers.....	349
Figure 3-37 Distribution of Accelerometers and Displacement Transducers.....	350
Figure 3-38 Distribution of Displacement Transducers (Circular Specimens).....	351
Figure 3-39 Distribution of Displacement Transducers (Interlocking Specimens) .....	351
Figure 3-40 Column Strains, Rotations and Curvature.....	352
Figure 3-41 Distribution of Strain Gauges (Circular Specimens).....	353
Figure 3-42 Distribution of Strain Gauges (Interlocking Specimens) .....	354

#### **Chapter 4**

Figure 4-1 Compressed Petrolia Earthquake, (Time History, Spectrum and Orbit).....	355
Figure 4-2 Time History Acceleration used for Specimens C1 and C2 (Long. Direction).....	356
Figure 4-3 Time History Acceleration used for Specimens C1 and C2 (Trans. Direction).....	356
Figure 4-4 Comparison of Target and Achieved Trilogarithmic Response Spectra.....	357
Figure 4-5 Comparison of Target and Achieved Trilogarithmic Response Spectra.....	357
Figure 4-6 Comparison of Target and Achieved Trilogarithmic Response Spectra.....	358
Figure 4-7 Comparison of Target and Achieved Trilogarithmic Response Spectra.....	358
Figure 4-8 Comparison of Target and Achieved Trilogarithmic Response Spectra.....	359
Figure 4-9 Comparison of Target and Achieved Trilogarithmic Response Spectra.....	359
Figure 4-10 Comparison of Target and Achieved Trilogarithmic Response Spectra.....	360
Figure 4-11 Comparison of Target and Achieved Trilogarithmic Response Spectra.....	360
Figure 4-12 Comparison of Target and Achieved Trilogarithmic Response Spectra.....	361
Figure 4-13 Comparison of Target and Achieved Trilogarithmic Response Spectra.....	361

Figure 4-14 Comparison of Target and Achieved Trilogarithmic Response Spectra.....	362
Figure 4-15 Comparison of Target and Achieved Trilogarithmic Response Spectra.....	362
Figure 4-16 Comparison of Target and Achieved Trilogarithmic Response Spectra.....	363
Figure 4-17 Comparison of Target and Achieved Trilogarithmic Response Spectra.....	363
Figure 4-18 Comparison of Target and Achieved Trilogarithmic Response Spectra.....	364
Figure 4-19 Comparison of Target and Achieved Trilogarithmic Response Spectra.....	364
Figure 4-20 Comparison of Target and Achieved Trilogarithmic Response Spectra.....	365
Figure 4-21 Comparison of Target and Achieved Trilogarithmic Response Spectra.....	365
Figure 4-22 Comparison of Target and Achieved Trilogarithmic Response Spectra.....	366
Figure 4-23 Comparison of Target and Achieved Trilogarithmic Response Spectra.....	366
Figure 4-24 Comparison of Target and Achieved Trilogarithmic Response Spectra.....	367
Figure 4-25 Comparison of Target and Achieved Trilogarithmic Response Spectra.....	367
Figure 4-26 Hairline Horizontal Cracks, Specimens C1 and C2 (PETx0.1).....	368
Figure 4-27 Cracks at First Bar Yielding, Specimens C1 and C2 (PETx0.2).....	368
Figure 4-28 First Concrete Spalling Specimens C1 (PETx1.0).....	369
Figure 4-29 First Concrete Spalling Specimens C2 (PETx1.0).....	369
Figure 4-30 Specimen C1, Column Distress (PETx1.2).....	370
Figure 4-31 Specimen C2, Column Distress (PETx1.2).....	370
Figure 4-32 Spiral and Longitudinal. Bars visible, Specimen C1.....	371
Figure 4-33 Spiral and Longitudinal. Bars visible, Specimen C2.....	371
Figure 4-34 Damage at Failure, Specimen C1.....	372
Figure 4-35 Damage at Failure, Specimen C2.....	373
Figure 4-36 Specimens C1 and C2, Damage Pattern After Testing.....	374
Figure 4-37 Base Shear-Displacement Hysteresis, Specimen C1 (0.1xPET).....	375
Figure 4-38 Base Shear-Displacement Hysteresis, Specimen C1 (0.2xPET).....	375
Figure 4-39 Base Shear-Displacement Hysteresis, Specimen C1 (0.4xPET).....	376
Figure 4-40 Base Shear-Displacement Hysteresis, Specimen C1 (0.6xPET).....	376
Figure 4-41 Base Shear-Displacement Hysteresis, Specimen C1 (0.8xPET).....	377
Figure 4-42 Base Shear-Displacement Hysteresis, Specimen C1 (1.0xPET).....	377
Figure 4-43 Base Shear-Displacement Hysteresis, Specimen C1 (1.2xPET).....	378
Figure 4-44 Base Shear-Displacement Hysteresis, Specimen C1 (1.4xPET).....	378
Figure 4-45 Base Shear-Displacement Hysteresis, Specimen C1 (1.6xPET).....	379
Figure 4-46 Base Shear-Displacement Hysteresis, Specimen C1 (1.8xPET).....	379
Figure 4-47 Cumulative Base Shear-Displacement Hysteresis, Specimen C1 (Longitudinal)....	380
Figure 4-48 Cumulative Base Shear-Displacement Hysteresis, Specimen C1 (Transverse).....	380
Figure 4-49 Base Shear-Displacement Hysteresis, Specimen C2 (0.1xPET).....	381
Figure 4-50 Base Shear-Displacement Hysteresis, Specimen C2 (0.2xPET).....	381
Figure 4-51 Base Shear-Displacement Hysteresis, Specimen C2 (0.4xPET).....	382
Figure 4-52 Base Shear-Displacement Hysteresis, Specimen C2 (0.6xPET).....	382
Figure 4-53 Base Shear-Displacement Hysteresis, Specimen C2 (0.8xPET).....	383
Figure 4-54 Base Shear-Displacement Hysteresis, Specimen C2 (1.0xPET).....	383
Figure 4-55 Base Shear-Displacement Hysteresis, Specimen C2 (1.2xPET).....	384
Figure 4-56 Base Shear-Displacement Hysteresis, Specimen C2 (1.4xPET).....	384

Figure 4-57 Base Shear-Displacement Hysteresis, Specimen C2 (1.6xPET).....	385
Figure 4-58 Base Shear-Displacement Hysteresis, Specimen C2 (1.8xPET).....	385
Figure 4-59 Base Shear-Displacement Hysteresis, Specimen C2 (2.0xPET).....	386
Figure 4-60 Cumulative Base Shear-Displacement Hysteresis, Specimen C2 (Longitudinal)....	387
Figure 4-61 Cumulative Base Shear-Displacement Hysteresis, Specimen C2 (Transverse).....	387
Figure 4-62 Envelope of Cumulative Base Shear-Displacement Hysteresis, Specimen C1.....	388
Figure 4-63 Envelope of Cumulative Base Shear-Displacement Hysteresis, Specimen C2.....	388
Figure 4-64 Displacement Interaction Orbit, Specimen C1.....	389
Figure 4-65 Displacement Interaction Orbit, Specimen C2.....	389
Figure 4-66 Moment Interaction Orbit, Specimen C1.....	390
Figure 4-67 Moment Interaction Orbit, Specimen C2.....	390
Figure 4-68 Power Spectral Density and Natural Frequencies, Specimen C1(Longitudinal).....	391
Figure 4-69 Power Spectral Density and Natural Frequencies, Specimen C1(Transverse).....	392
Figure 4-70 Power Spectral Density and Natural Frequencies, Specimen C2(Longitudinal).....	393
Figure 4-71 Power Spectral Density and Natural Frequencies, Specimen C2(Transverse).....	394
Figure 4-72 Variation in the Dynamic Properties Measured using Power Spectrum, C1.....	395
Figure 4-73 Variation in the Dynamic Properties Measured using MIMO, C1.....	395
Figure 4-74 Variation in the Dynamic Properties Measured using Power Spectrum, C2.....	396
Figure 4-75 Variation in the Dynamic Properties Measured using MIMO, C2.....	396
Figure 4-76 Comparison between the Dynamic Properties Measured using Power Spectrum and MIMO, C1 (Longitudinal Direction).....	397
Figure 4-77 Comparison between the Dynamic Properties Measured using Power Spectrum and MIMO, C2 (Longitudinal Direction).....	397
Figure 4-78 Variation in Effective Stiffness, Specimen C1.....	398
Figure 4-79 Variation in Effective Stiffness, Specimen C2.....	398
Figure 4-80 Curvature Profile in Longitudinal Direction, Specimen C1.....	399
Figure 4-81 Curvature Profile in Transverse Direction, Specimen C1.....	399
Figure 4-82 Curvature Profile in Longitudinal Direction, Specimen C2.....	400
Figure 4-83 Curvature Profile in Transverse Direction, Specimen C2.....	400
Figure 4-84 Average Moment-Curvature Hysteresis for Specimen C1, Long. Direction.....	401
Figure 4-85 Average Moment-Curvature Hysteresis for Specimen C1, Trans. Direction.....	401
Figure 4-86 Average Moment-Curvature Hysteresis for Specimen C2, Long. Direction.....	402
Figure 4-87 Average Moment-Curvature Hysteresis for Specimen C2, Trans. Direction.....	402
Figure 4-88 Average Moment-Curvature Envelope for Specimen C1, Long. Direction.....	403
Figure 4-89 Average Moment-Curvature Envelope for Specimen C2, Long. Direction.....	403
Figure 4-90 Flexural Deformation for Specimen C1.....	404
Figure 4-91 Flexural Deformation for Specimen C2.....	404
Figure 4-92 Shear Deformation for Specimen C1.....	405
Figure 4-93 Shear Deformation for Specimen C2.....	405
Figure 4-94 Contribution of Flexural Deformation to Total Deformation, Specimen C1.....	406
Figure 4-95 Contribution of Flexural Deformation to Total Deformation, Specimen C2.....	406
Figure 4-96 Longitudinal Bar Strain Distribution in Circular Specimens, Bar No.1.....	407
Figure 4-97 Longitudinal Bar Strain Distribution in Circular Specimens, Bar No.3.....	407

Figure 4-98 Longitudinal Bar Strain Distribution in Circular Specimens, Bar No.6.....	408
Figure 4-99 Longitudinal Bar Strain Distribution in Circular Specimens, Bar No.8.....	408
Figure 4-100 Longitudinal Bar Strain Distribution in Circular Specimens, Bar No.11.....	409
Figure 4-101 Longitudinal Bar Strain Distribution in Circular Specimens, Bar No.13.....	409
Figure 4-102 Longitudinal Bar Strain Distribution in Circular Specimens, Bar No.16.....	410
Figure 4-103 Longitudinal Bar Strain Distribution in Circular Specimens, Bar No.18.....	410
Figure 4-104 Spiral Strain Distribution in Circular Specimens, West Side.....	411
Figure 4-105 Spiral Strain Distribution in Circular Specimens, North Side.....	411
Figure 4-106 Spiral Strain Distribution in Circular Specimens, East Side .....	412
Figure 4-107 Spiral Strain Distribution in Circular Specimens, South Side.....	412
Figure 4-108 Elasto-Plastic Idealization for Force-Displacement, Specimen C1 (Longitudinal)	413
Figure 4-109 Elasto-Plastic Idealization for Force-Displacement, Specimen C1 (Transverse)..	413
Figure 4-110 Elasto-Plastic Idealization for Moment-Curvature, Specimen C1 (Longitudinal).	414
Figure 4-111 Elasto-Plastic Idealization for Moment-Curvature, Specimen C1 (Transverse)....	414
Figure 4-112 Elasto-Plastic Idealization for Force-Displacement, Specimen C2 (Longitudinal)	415
Figure 4-113 Elasto-Plastic Idealization for Force-Displacement, Specimen C2 (Transverse)..	415
Figure 4-114 Elasto-Plastic Idealization for Moment-Curvature, Specimen C2 (Longitudinal)	416
Figure 4-115 Elasto-Plastic Idealization for Moment-Curvature, Specimen C2 (Transverse)....	416
Figure 4-116 Torque-Rotation Hysteresis, Specimen C1 .....	417
Figure 4-117 Torque-Rotation Hysteresis, Specimen C1 .....	418
Figure 4-118 Torque-Rotation Hysteresis, Specimen C2 .....	419
Figure 4-119 Torque-Rotation Hysteresis, Specimen C2 .....	420
Figure 4-120 Cumulative Torque-Rotation Hysteresis, Specimen C1.....	421
Figure 4-121 Cumulative Torque-Rotation Hysteresis, Specimen C2.....	421
Figure 4-122 Torque-Rotation Hysteresis and Capacity, Specimen C1 .....	422
Figure 4-123 Torque-Rotation Hysteresis and Capacity, Specimen C2 .....	422

## Chapter 5

Figure 5-1 Compressed Sylmar Earthquake (Time History, Spectrum and Orbit).....	423
Figure 5-2 Time History Acceleration used for Specimens I2 (Long. Direction) .....	424
Figure 5-3 Time History Acceleration used for Specimens I2 (Trans. Direction).....	424
Figure 5-4 Comparison of Target and Achieved Trilogarithmic Response Spectra.....	425
Figure 5-5 Comparison of Target and Achieved Trilogarithmic Response Spectra.....	425
Figure 5-6 Comparison of Target and Achieved Trilogarithmic Response Spectra.....	426
Figure 5-7 Comparison of Target and Achieved Trilogarithmic Response Spectra.....	426
Figure 5-8 Comparison of Target and Achieved Trilogarithmic Response Spectra.....	427
Figure 5-9 Comparison of Target and Achieved Trilogarithmic Response Spectra.....	427
Figure 5-10 Comparison of Target and Achieved Trilogarithmic Response Spectra.....	428
Figure 5-11 Comparison of Target and Achieved Trilogarithmic Response Spectra.....	428
Figure 5-12 Comparison of Target and Achieved Trilogarithmic Response Spectra.....	429
Figure 5-13 Comparison of Target and Achieved Trilogarithmic Response Spectra.....	429
Figure 5-14 Comparison of Target and Achieved Trilogarithmic Response Spectra.....	430
Figure 5-15 Comparison of Target and Achieved Trilogarithmic Response Spectra.....	430

Figure 5- 16 Comparison of Target and Achieved Trilogarithmic Response Spectra.....	431
Figure 5-17 Comparison of Target and Achieved Trilogarithmic Response Spectra.....	431
Figure 5-18 Comparison of Target and Achieved Trilogarithmic Response Spectra.....	432
Figure 5-19 Comparison of Target and Achieved Trilogarithmic Response Spectra.....	432
Figure 5-20 Comparison of Target and Achieved Trilogarithmic Response Spectra.....	433
Figure 5-21 Comparison of Target and Achieved Trilogarithmic Response Spectra.....	433
Figure 5-22 Comparison of Target and Achieved Trilogarithmic Response Spectra.....	434
Figure 5-23 Comparison of Target and Achieved Trilogarithmic Response Spectra.....	434
Figure 5-24 Comparison of Target and Achieved Trilogarithmic Response Spectra.....	435
Figure 5-25 Comparison of Target and Achieved Trilogarithmic Response Spectra.....	435
Figure 5-26 Hairline Horizontal Cracks, Specimens I1 and I2 (SYLx0.1).....	436
Figure 5-27 Cracks at First Longitudinal Bar Yielding, Specimens I1 and I2 (SYLx0.2) .....	436
Figure 5-28 First Concrete Spalling Specimens I1 (SYLx1.0).....	437
Figure 5-29 First Concrete Spalling Specimens I2 (SYLx1.0).....	437
Figure 5-30 Specimen I1, Increasing of Cracks and Spalling (SYLx1.2).....	438
Figure 5-31 Specimen I2, Increasing of Cracks and Spalling (SYLx1.2).....	438
Figure 5-32 Spiral and Longitudinal Bars Visible, Specimen I1 .....	439
Figure 5-33 Spiral and Longitudinal Bars Visible, Specimen I2 .....	439
Figure 5-34 Specimen I1, Damage at Failure .....	440
Figure 5-35 Specimen I2, Damage at Failure .....	441
Figure 5-36 Specimens I1 and I2, Damage Pattern after Testing .....	442
Figure 5-37 Base Shear-Displacement Hysteresis, Specimen I1 (0.1xSYL).....	443
Figure 5-38 Base Shear-Displacement Hysteresis, Specimen I1 (0.2xSYL).....	443
Figure 5-39 Base Shear-Displacement Hysteresis, Specimen I1 (0.4xSYL).....	444
Figure 5-40 Base Shear-Displacement Hysteresis, Specimen I1 (0.6xSYL).....	444
Figure 5-41 Base Shear-Displacement Hysteresis, Specimen I1 (0.8xSYL).....	445
Figure 5-42 Base Shear-Displacement Hysteresis, Specimen I1 (1.0xSYL).....	445
Figure 5-43 Base Shear-Displacement Hysteresis, Specimen I1 (1.2xSYL).....	446
Figure 5-44 Base Shear-Displacement Hysteresis, Specimen I1 (1.4xSYL).....	446
Figure 5-45 Base Shear-Displacement Hysteresis, Specimen I1 (1.6xSYL).....	447
Figure 5-46 Base Shear-Displacement Hysteresis, Specimen I1 (1.8xSYL).....	447
Figure 5-47 Base Shear-Displacement Hysteresis, Specimen I1 (1.4*xSYL).....	448
Figure 5-48 Cumulative Base Shear-Displacement Hysteresis, Specimen I1 (Longitudinal) .....	448
Figure 5-49 Cumulative Base Shear-Displacement Hysteresis, Specimen I1 (Transverse) .....	449
Figure 5-50 Base Shear-Displacement Hysteresis, Specimen I2 (0.1xSYL).....	449
Figure 5-51 Base Shear-Displacement Hysteresis, Specimen I2 (0.2xSYL).....	450
Figure 5-52 Base Shear-Displacement Hysteresis, Specimen I2 (0.4xSYL).....	450
Figure 5-53 Base Shear-Displacement Hysteresis, Specimen I2 (0.6xSYL).....	451
Figure 5-54 Base Shear-Displacement Hysteresis, Specimen I2 (0.8xSYL).....	451
Figure 5-55 Base Shear-Displacement Hysteresis, Specimen I2 (1.0xSYL).....	452
Figure 5-56 Base Shear-Displacement Hysteresis, Specimen I2 (1.2xSYL).....	452
Figure 5-57 Base Shear-Displacement Hysteresis, Specimen I2 (1.4xSYL).....	453
Figure 5-58 Base Shear-Displacement Hysteresis, Specimen I2 (1.6xSYL).....	453



Figure 5-59 Base Shear-Displacement Hysteresis, Specimen I2 (1.8xSYL).....	454
Figure 5-60 Base Shear-Displacement Hysteresis, Specimen I2 (1.8*xSYL).....	454
Figure 5-61 Cumulative Base Shear-Displacement Hysteresis, Specimen I2 (Longitudinal) .....	455
Figure 5-62 Cumulative Base Shear-Displacement Hysteresis, Specimen I2 (Transverse) .....	455
Figure 5-63 Envelope of Cumulative Base Shear-Displacement Hysteresis, Specimen I1 .....	456
Figure 5-64 Envelope of Cumulative Base Shear-Displacement Hysteresis, Specimen I2 .....	456
Figure 5-65 Power Spectral Density and Natural Frequencies, Specimen I1 .....	457
Figure 5-66 Power Spectral Density and Natural Frequencies, Specimen I1 .....	458
Figure 5-67 Power Spectral Density and Natural Frequencies, Specimen I2 .....	459
Figure 5-68 Power Spectral density and natural Frequencies, specimen I2 .....	460
Figure 5-69 Variation in the Dynamic Properties Measured using Power Spectrum, Col. I1 .....	461
Figure 5-70 Variation in the Dynamic Properties Measured using MIMO, Col. I1 .....	461
Figure 5-71 Variation in the Dynamic Properties Measured using Power Spectrum, Col. I2 .....	462
Figure 5-72 Variation in the Dynamic Properties Measured using MIMO, Col. I2 .....	462
Figure 5-73 Comparison between the Dynamic Properties Measured using Power Spectrum and MIMO, Specimen I1 (Longitudinal Direction).....	463
Figure 5-74 Comparison between the Dynamic Properties Measured using Power Spectrum and MIMO, Specimen I2 (Longitudinal Direction).....	463
Figure 5-75 Variation in Effective Stiffness, Specimen I1 .....	464
Figure 5-76 Variation in Effective Stiffness, Specimen I2 .....	464
Figure 5-77 Curvature Profile along Longitudinal Direction, Specimen I1 .....	465
Figure 5-78 Curvature Profile along Transverse Direction, Specimen I1 .....	465
Figure 5-79 Curvature Profile along Longitudinal Direction, Specimen I2 .....	466
Figure 5-80 Curvature Profile along Transverse Direction, Specimen I2. ....	466
Figure 5-81 Average Moment-Curvature Hysteresis Measured at 3 in. and 8 in., Specimen I1 (Longitudinal Direction) .....	467
Figure 5-82 Average Moment-Curvature Hysteresis Measured at 3 in. and 8 in., Specimen I1 (Transverse Direction). ....	467
Figure 5-83 Average Moment-Curvature Hysteresis Measured at 3 in. and 8 in., Specimen I2, (Longitudinal Direction) .....	468
Figure 5-84 Average Moment-Curvature Hysteresis Measured at 3 in. and 8 in., Specimen I2, (Transverse. Direction). ....	468
Figure 5-85 Average Moment-Curvature Envelope Measured at 3in. and 8 in., Specimen I1 ....	469
Figure 5-86 Average Moment-Curvature Envelope Measured at 3in. and 8 in., Specimen I2....	469
Figure 5-87 Base Moment – Bond Slip Rotation Hysteresis, I1 (Longitudinal Direction) .....	470
Figure 5-88 Base Moment – Bond Slip Rotation Hysteresis, I1 (Transverse Direction).....	470
Figure 5-89 Base Moment – Bond Slip Hysteresis, I2 (Longitudinal Direction) .....	471
Figure 5-90 Base Moment – Bond Slip Hysteresis, I2 (Longitudinal Direction) .....	471
Figure 5-91 Base Moment – Bond Slip Rotation Backbone Envelope, I1 .....	472
Figure 5-92 Base Moment – Bond Slip Rotation Backbone Envelope, I2 .....	472
Figure 5-93 Shear Deformation for Specimen I1 .....	473
Figure 5-94 Shear Deformation for Specimen I2.....	473
Figure 5-95 Contribution of Flexion to Total Deflexion, Specimen I1 .....	474

Figure 5-96 Contribution of Flexion to Total Deflexion, Specimen I2. ....	474
Figure 5-97 Longitudinal Bar Strain Distribution in Interlocking Specimens, Bar No.1 .....	475
Figure 5-98 Longitudinal Bar Strain Distribution in Interlocking Specimens, Bar No.4. ....	475
Figure 5-99 Longitudinal Bar Strain Distribution in Interlocking Specimens, Bar No.7 .....	476
Figure 5-100 Longitudinal Bar Strain Distribution in Interlocking Specimens, Bar No.13. ....	476
Figure 5-101 Longitudinal Bar Strain Distribution in Interlocking Specimens, Bar No.16 .....	477
Figure 5-102 Longitudinal Bar Strain Distribution in Interlocking Specimens, Bar No.19. ....	477
Figure 5-103 Longitudinal Bar Strain Distribution in Interlocking Specimens, Bar No.21 .....	478
Figure 5-104 Longitudinal Bar Strain Distribution in Interlocking Specimens, Bar No.24. ....	478
Figure 5-105 Longitudinal Bar Strain Distribution in Interlocking Specimens, Bar No.28 .....	479
Figure 5-106 Longitudinal Bar Strain Distribution in Interlocking Specimens, Bar No.30. ....	479
Figure 5-107 Spiral Strain Distribution in Interlocking Specimens, North .....	480
Figure 5-108 Spiral Strain Distribution in Interlocking Specimens, East 1.....	480
Figure 5-109 Spiral Strain Distribution in Interlocking Specimens, East 2.....	481
Figure 5-110 Spiral Strain Distribution in Interlocking Specimens, South .....	481
Figure 5-111 Spiral Strain Distribution in Interlocking Specimens, West 1 .....	482
Figure 5-112 Spiral Strain Distribution in Interlocking Specimens, West 2. ....	482
Figure 5-113 Elasto-Plastic Idealization for Force-Displacement, Specimen I1 (Longitudinal). ....	483
Figure 5-114 Elasto-Plastic Idealization for Force-Displacement, Specimen I1 (Transverse)....	483
Figure 5-115 Elasto-Plastic Idealization for Moment-Curvature, Specimen I1 (Longitudinal) ..	484
Figure 5-116 Elasto-Plastic Idealization for Moment-Curvature, Specimen I1 (Transverse) .....	484
Figure 5-117 Elasto-Plastic Idealization for Force-Displacement, Specimen I2 (Longitudinal). ....	485
Figure 5-118 Elasto-Plastic Idealization for Force-Displacement, Specimen I2 (Transverse)....	485
Figure 5-119 Elasto-Plastic Idealization for Moment-Curvature, Specimen I2 (Longitudinal) ..	486
Figure 5-120 Elasto-Plastic Idealization for Moment-Curvature, Specimen I2 (Transverse) .....	486
Figure 5-121 Torque-Rotation Hysteresis, Specimen I1.....	487
Figure 5-122 Torque-Rotation Hysteresis, Specimen I1.....	488
Figure 5-123 Torque-Rotation Hysteresis, Specimen I2.....	489
Figure 5-124 Torque-Rotation Hysteresis, Specimen I2.....	490
Figure 5-125 Cumulative Torque-Rotation Hysteresis, Specimen I1.....	491
Figure 5-126 Cumulative Torque-Rotation Hysteresis, Specimen I2.....	491
Figure 5-127 Torque-Rotation Hysteresis and Capacity, Specimen I1 .....	492
Figure 5-128 Torque-Rotation Hysteresis and Capacity, Specimen I2 .....	492

## Chapter 6

Figure 6-1 Experimental Test Setup, Circular Specimen 9F1 .....	493
Figure 6-2 Experimental Test Setup, Circular Specimen NF1 .....	493
Figure 6-3 Compressed El Centro Ground Acceleration, Time History and SA Spectrum for Specimen 9F1.....	494
Figure 6-4 Compressed Rinaldi Ground Acceleration, Time History and SA Spectrum for Specimen NF1.....	494
Figure 6-5 Experimental Test Setup, Interlocking Specimen ISL1.0 .....	495
Figure 6-6 Cumulative Hysteresis and Envelope for Circular Specimen 9F1 .....	495

Figure 6-7 Cumulative Hysteresis and Envelope for Circular Specimen NF1 .....	496
Figure 6-8 Cumulative Hysteresis and Envelope for Interlocking Specimen ISL1.0.....	496
Figure 6-9 Axial Load - Displacement Accumulated Hysteresis for Specimen 9F1 .....	497
Figure 6-10 Axial Load – Base Moment Accumulated Hysteresis for Specimen 9F1 .....	497
Figure 6-11 Axial Load - Displacement Accumulated Hysteresis for Specimen NF1 .....	498
Figure 6-12 Axial Load - Displacement Accumulated Hysteresis for Specimen NF1 .....	498
Figure 6-13 Axial Load - Displacement Accumulated Hysteresis for Specimen ISL1.0 .....	499
Figure 6-14 Axial Load – Base Moment Accumulated Hysteresis for Specimen ISL1.0 .....	499
Figure 6-15 Variation in Effective Lateral Stiffness, Circular Specimens .....	500
Figure 6-16 Variation in Effective Lateral Stiffness, Interlocking Specimens .....	500
Figure 6-17 Comparison of Moment-Curvature (M- $\phi$ ) Envelopes, Circular Specimens.....	501
Figure 6-18 Comparison of Moment-Curvature (M- $\phi$ ) Envelopes, Interlocking Specimens .....	501
Figure 6-19 Comparison of Elasto-Plastic Envelopes (M- $\phi$ ), Circular Specimens .....	502
Figure 6-20 Comparison of Elasto-Plastic Envelopes (M- $\phi$ ), interlocking Specimens .....	502
Figure 6-21 Comparison of Base Shear-Displacement Envelopes, Circular Specimens.....	503
Figure 6-22 Comparison of Base Moment-Drift Ratio Envelopes, Circular Specimens .....	503
Figure 6-23 Comparison of Envelopes Base Shear-Displacement, Interlocking Specimens.....	504
Figure 6-24 Comparison of Elasto-Plastic Envelopes (F-D) for Interlocking Specimens .....	504
Figure 6-25 Comparison of Elasto-Plastic Envelopes (BS-D), Circular Specimens .....	505
Figure 6-26 Comparison of Elasto-Plastic Envelopes (M- $\phi$ ), Circular Specimens .....	505
Figure 6-27 Comparison Between Elasto-Plastic Envelopes (BS-D), Interlocking Specimens ..	506
Figure 6-28 Comparison Between Elasto-Plastic Envelopes (M- $\phi$ ), Interlocking Specimens ...	506

## Chapter 7

Figure 7-1 Typical Strain and Strain Rate Histories at First Yielding, Specimen C2.....	507
Figure 7-2 Typical Strain and Strain Rate Histories at First Yielding, Specimen I2 .....	507
Figure 7-3 Measured Strain Rate versus Strain at Yielding, Specimen C1 (Sg 16) .....	508
Figure 7-4 Measured Strain Rate versus Strain at Yielding, Specimen C2 (Sg 12) .....	508
Figure 7-5 Measured Strain Rate versus Strain at Yielding, Specimen I1 (Sg 11).....	509
Figure 7-6 Measured Strain Rate versus Strain at Yielding, Specimen I2 (Sg 11).....	509
Figure 7-7 Measured and Calculated Moment-Curvature, 9F1 .....	510
Figure 7-8 Measured and Calculated Elasto-Plastic M- $\phi$ , 9F1 .....	510
Figure 7-9 Measured and Calculated Moment-Curvature, NF1 .....	511
Figure 7-10 Measured and Calculated Elasto-Plastic M- $\phi$ , NF1 .....	511
Figure 7-11 Measured and Calculated Moment-Curvature, ISL1.0 .....	512
Figure 7-12 Measured and Calculated Elasto-Plastic M- $\phi$ , ISL1.0 .....	512
Figure 7-13 Measured and Calculated Moment-Curvature, C1 and C2 (NA=30°) .....	513
Figure 7-14 Measured and Calculated Elasto-Plastic M- $\phi$ , C1 and C2 (NA=30°) .....	513
Figure 7-15 Measured and Calculated Moment-Curvature, I1 and I2 (NA=45°).....	514
Figure 7-16 Measured and Calculated Elasto-Plastic M- $\phi$ , I1 and I2 (NA=45°).....	514
Figure 7-17 Modified Mander's Model for Confined Concrete, Used for M- $\phi$ Analysis.....	515
Figure 7-18 Modified Mander's Model for Unconfined Concrete, Used for M- $\phi$ Analysis.....	515
Figure 7-19 Measured and Calculated Moment-Curvature, 9F1 (Modified Model) .....	516

Figure 7-20 Measured and Calculated Elasto-Plastic M- $\phi$ , 9F1 (Modified Model) .....	516
Figure 7-21 Measured and Calculated Moment-Curvature, NF1 (Modified Model) .....	517
Figure 7-22 Measured and Calculated Elasto-Plastic M- $\phi$ , NF1 (Modified Model) .....	517
Figure 7-23 Measured and Calculated Moment-Curvature, ISL1.0 (Modified Model).....	518
Figure 7-24 Measured and Calculated Elasto-Plastic M- $\phi$ , ISL1.0 (Modified Model) .....	518
Figure 7-25 Measured and Calculated M- $\phi$ , C1 and C2 (NA=30°) Modified Model) .....	519
Figure 7-26 Measured and Calculated Elasto-Plastic M- $\phi$ , C1 and C2 Modified Model).....	519
Figure 7-27 Measured and Calculated M- $\phi$ , I1 and I2 (NA=45°) Modified Model).....	520
Figure 7-28 Measured and Calculated Elasto-Plastic M- $\phi$ , I1 and I2 Modified Model) .....	520
Figure 7-29 Measured and Calculated Force-Displacement, 9F1 (P=80 kips).....	521
Figure 7-30 Measured and Calculated Force-Displacement, 9F1 (P=115 kips).....	521
Figure 7-31 Measured and Calculated Force-Displacement, NF1 .....	522
Figure 7-32 Measured and Calculated Force-Displacement, ISL1.0 .....	522
Figure 7-33 Measured and Calculated Force-Displacement, C1 and C2 (NA=30°).....	523
Figure 7-34 Measured and Calculated Force-Displacement, I1 and I2 (NA=45°) .....	523
Figure 7-35 Bidirectional Displacement Interaction Orbits, C1 .....	524
Figure 7-36 Bidirectional Displacement Interaction Orbits, C2 .....	524
Figure 7-37 Bidirectional Displacement Interaction Orbits, I1 .....	525
Figure 7-38 Bidirectional Displacement Interaction Orbits, I2 .....	525
Figure 7-39 Bond-Slip Idealization, Wehbe Method.....	526
Figure 7-40 Bond-Slip Monotonic curves .....	526
Figure 7-41 Specimens Idealization Using Nonlinear Beam-Column Fiber Elements .....	527
Figure 7-42 Specimens Idealization Using Beam with Hinges Beam-Column Elements .....	527
Figure 7-43 Fiber Section Discretization in OpenSees, Unidirectionally Tested Specimens .....	528
Figure 7-44 Fiber Section Discretization in OpenSees, Bidirectionally Tested Specimens .....	528
Figure 7-45 Typical Hysteretic Stress-Strain Behavior in Concrete02.....	529
Figure 7-46 Typical Hysteretic Stress-Strain Behavior in Concrete07.....	529
Figure 7-47 Comparison of Hysteretic Stress-Strain for Different Concrete Models.....	530
Figure 7-48 Typical Hysteretic Stress-Strain Behavior in Steel02 Material.....	530
Figure 7-49 Typical Hysteretic Stress-Strain Behavior in ReinforcingSteel Material.....	531
Figure 7-50 Comparison of Tension Stress-Strain Envelopes for Different Reinforcement Models .....	531
Figure 7-51 Comparison of Hysteretic Stress-strain for Different reinforcement Models .....	532
Figure 7-52 OpenSees Analytical Model for Unidirectionally Tested Columns .....	532
Figure 7-53 Measured and Predicted Force-Displacement Envelope, NF1 (WithoutBondslip)..	533
Figure 7-54 Measured and Predicted Force-Displacement Envelope, NF1 (With Bondslip).....	533
Figure 7-55 Measured and Predicted Force-Displacement Envelope, 9F1 (With Bondslip).....	534
Figure 7-56 Measured and Predicted Force-Displacement Envelope, ISL1.0 (With Bondslip)..	534
Figure 7-57 Measured and Calculated Displacement History, NF1-Model C02S02.....	535
Figure 7-58 Measured and Calculated F-D Hysteresis, NF1-Model C02S02.....	535
Figure 7-59 Measured and Calculated Displacement History, NF1-Model BWHC02S02 .....	536
Figure 7-60 Measured and Calculated F-D Hysteresis, NF1-Model BWHC02S02 .....	536
Figure 7-61 Measured and Calculated Displacement History, NF1-Model BWHC07RS.....	537

Figure 7-62 Measured and Calculated F-D Hysteresis, NF1-Model BWHC07RS.....	537
Figure 7-63 Measured and Calculated Displacement History, NF1-Best Model .....	538
Figure 7-64 Measured and Calculated F-D Hysteresis, NF1-Best Model .....	538
Figure 7-65 Measured and Calculated Displacement Hysteresis, NF1 (Runs 1 to 3).....	539
Figure 7-66 Measured and Calculated Displacement Hysteresis, NF1 (Runs 4 to 6).....	540
Figure 7-67 Measured and Calculated Displacement Hysteresis, NF1 (Runs 7 to 9).....	541
Figure 7-68 Measured and Calculated Displacement Hysteresis, NF1 (Runs 10 and 11).....	542
Figure 7-69 Measured and Calculated Displacement History, 9F1-Best Model .....	543
Figure 7-70 Measured and Calculated Displacement Hysteresis, 9F1-Best Model.....	543
Figure 7-71 Measured and Calculated Displacement Hysteresis, 9F1 (Runs 1 to 3).....	544
Figure 7-72 Measured and Calculated Displacement Hysteresis, 9F1 (Runs 4 to 6).....	545
Figure 7-73 Measured and Calculated Displacement Hysteresis, 9F1 (Runs 7 to 9).....	546
Figure 7-74 Measured and Calculated Displacement History, ISL1.0-Best Model.....	547
Figure 7-75 Measured and Calculated Cumulative F-D Hysteresis, ISL1.0-Best Model.....	547
Figure 7-76 Measured and Calculated Displacement and Hysteresis, ISL1.0 (Runs 1 to 3).....	548
Figure 7-77 Measured and Calculated Displacement and Hysteresis, ISL1.0 (Runs 4 to 6).....	549
Figure 7-78 Measured and Calculated Displacement and Hysteresis, ISL1.0 (Runs 7 to 9).....	550
Figure 7-79 OpenSees Analytical Model for Bidirectionally Tested Circular Specimens .....	551
Figure 7-80 Mass Distribution and Mass Centroid for Circular Specimens .....	551
Figure 7-81 Measured and Calculated Displacement History, C1-Long. ....	552
Figure 7-82 Measured and Calculated Cumulative F-D Hysteresis, C1-Long. ....	552
Figure 7-83 Measured and Calculated Displacement History, C1-Trans. ....	553
Figure 7-84 Measured and Calculated Cumulative F-D Hysteresis, C1-Trans.....	553
Figure 7-85 Measured and Calculated Displacement and Hysteresis, C1-Long.....	554
Figure 7-86 Measured and Calculated Displacement and Hysteresis, C1-Long.....	555
Figure 7-87 Measured and Calculated Displacement and Hysteresis, C1-Long.....	556
Figure 7-88 Measured and Calculated Displacement and Hysteresis, C1-Long.....	557
Figure 7-89 Measured and Calculated Displacement and Hysteresis, C1-Trans.....	558
Figure 7-90 Measured and Calculated Displacement and Hysteresis, C1-Trans.....	559
Figure 7-91 Measured and Calculated Displacement and Hysteresis, C1-Trans.....	560
Figure 7-92 Measured and Calculated Displacement and Hysteresis, C1-Trans.....	561
Figure 7-93 Measured and Calculated Displacement History, C2-Long. ....	562
Figure 7-94 Measured and Calculated Cumulative F-D Hysteresis, C2-Long. ....	562
Figure 7-95 Measured and Calculated Displacement History, C2-Trans. ....	563
Figure 7-96 Measured and Calculated Cumulative F-D Hysteresis, C2-Trans.....	563
Figure 7-97 Measured and Calculated Displacement and Hysteresis, C2-Long.....	564
Figure 7-98 Measured and Calculated Displacement and Hysteresis, C2-Long.....	565
Figure 7-99 Measured and Calculated Displacement and Hysteresis, C2-Long.....	566
Figure 7-100 Measured and Calculated Displacement and Hysteresis, C2-Long.....	567
Figure 7-101 Measured and Calculated Displacement and Hysteresis, C2-Trans.....	568
Figure 7-102 Measured and Calculated Displacement and Hysteresis, C2-Trans.....	569
Figure 7-103 Measured and Calculated Displacement and Hysteresis, C2-Trans.....	570
Figure 7-104 Measured and Calculated Displacement and Hysteresis, C2-Trans.....	571

Figure 7-105 OpenSees Analytical Model for Bidirectionally Tested Interlocking Specimens..	572
Figure 7-106 Mass Distribution and Mass Centroid for Interlocking Specimens.....	572
Figure 7-107 Measured and Calculated Displacement History, I1-Long. ....	573
Figure 7-108 Measured and Calculated Cumulative F-D Hysteresis, I1-Long.....	573
Figure 7-109 Measured and Calculated Displacement History, I1-Trans.....	574
Figure 7-110 Measured and Calculated Cumulative F-D Hysteresis, I1-Trans.....	574
Figure 7-111 Measured and Calculated Displacement and Hysteresis, I1-Long. ....	575
Figure 7-112 Measured and Calculated Displacement and Hysteresis, I1-Long.....	576
Figure 7-113 Measured and Calculated Displacement and Hysteresis, I1-Long. ....	577
Figure 7-114 Measured and Calculated Displacement and Hysteresis, I1-Long.....	578
Figure 7-115 Measured and Calculated Displacement and Hysteresis, I1-Trans. ....	579
Figure 7-116 Measured and Calculated Displacement and Hysteresis, I1-Trans. ....	580
Figure 7-117 Measured and Calculated Displacement and Hysteresis, I1-Trans. ....	581
Figure 7-118 Measured and Calculated Displacement and Hysteresis, I1-Trans. ....	582
Figure 7-119 Measured and Calculated Displacement History, I2-Long. ....	583
Figure 7-120 Measured and Calculated Cumulative F-D Hysteresis, I2-Long.....	583
Figure 7-121 Measured and Calculated Displacement History, I2-Trans.....	584
Figure 7-122 Measured and Calculated Cumulative F-D Hysteresis, I2-Trans.....	584
Figure 7-123 Measured and Calculated Displacement and Hysteresis, I2-Long. ....	585
Figure 7-124 Measured and Calculated Displacement and Hysteresis, I2-Long.....	586
Figure 7-125 Measured and Calculated Displacement and Hysteresis, I2-Long.....	587
Figure 7-126 Measured and Calculated Displacement and Hysteresis, I2-Long.....	588
Figure 7-127 Measured and Calculated Displacement and Hysteresis, I2-Trans. ....	589
Figure 7-128 Measured and Calculated Displacement and Hysteresis, I2-Trans. ....	590
Figure 7-129 Measured and Calculated Displacement and Hysteresis, I2-Trans. ....	591
Figure 7-130 Measured and Calculated Displacement and Hysteresis, I2-Trans. (Runs 10 to 12) .....	592

## Chapter 8

Figure 8-1 Acceleration, Spectrum and Orbit of the El Centro Record (Circular Column) .....	593
Figure 8-2 Acceleration, Spectrum and Orbit of Los Gatos record (Circular Column).....	594
Figure 8-3 Acceleration, Spectrum and Orbit of Petrolia Record (Circular Column) .....	595
Figure 8-4 Acceleration, Spectrum and Orbit of Rinaldi (Circular Column) .....	596
Figure 8-5 Acceleration, Spectrum and Orbit of Sylmar Record (Circular Column).....	597
Figure 8-6 Acceleration, Spectrum and Orbit of Takatori Record (Circular Column).....	598
Figure 8-7 Acceleration, Spectrum and Orbit of the El Centro Record (Interlockig Column)....	599
Figure 8-8 Acceleration, Spectrum and Orbit of Los Gatos record (Interlocking Column) .....	600
Figure 8-9 Acceleration, Spectrum and Orbit of Petrolia Record (Interlockig Column).....	601
Figure 8-10 Acceleration, Spectrum and Orbit of Rinaldi (Interlockig Column).....	602
Figure 8-11 Acceleration, Spectrum and Orbit of Sylmar Record (Interlockig Column).....	603
Figure 8-12 Acceleration, Spectrum and Orbit of Takatori Record (Interlockig Column).....	604
Figure 8-13 Unidirectional vs. Bidirectional Displacement History, El Centro (Circular) Longitudinal Direction.....	605

Figure 8-14 Unidirectional vs. Bidirectional Displacement History, El Centro (Circular) Transverse Direction.....	605
Figure 8-15 Unidirectional vs. Bidirectional Displacement History, Los Gatos (Circular) Longitudinal Direction.....	606
Figure 8-16 Unidirectional vs. Bidirectional Displacement History, Los Gatos (Circular) Transverse Direction.....	606
Figure 8-17 Unidirectional vs. Bidirectional Displacement History, Petrolia (Circular) Longitudinal Direction.....	607
Figure 8-18 Unidirectional vs. Bidirectional Displacement History, Petrolia (Circular) .....	607
Figure 8-19 Unidirectional vs. Bidirectional Displacement History, Rinaldi (Circular) Longitudinal Direction.....	608
Figure 8-20 Unidirectional vs. Bidirectional Displacement History, Rinaldi (Circular) .....	608
Figure 8-21 Unidirectional vs. Bidirectional Displacement History, Sylmar (Circular) Longitudinal Direction.....	609
Figure 8-22 Unidirectional vs. Bidirectional Displacement History, Sylmar (Circular) .....	609
Figure 8-23 Unidirectional vs. Bidirectional Displacement History, Takatori (Circular) Longitudinal Direction.....	610
Figure 8-24 Unidirectional vs. Bidirectional Displacement History, Takatori (Circular) .....	610
Figure 8-25 Unidirectional vs. Bidirectional Force-Displacement Hysteresis, El Centro (Circular) .....	611
Figure 8-26 Unidirectional vs. Bidirectional Force-Displacement Hysteresis, Los Gatos (Circular) .....	611
Figure 8-27 Unidirectional vs. Bidirectional Force-Displacement Hysteresis, Petrolia (Circular) .....	612
Figure 8-28 Unidirectional vs. Bidirectional Force-Displacement Hysteresis, Rinaldi (Circular) .....	612
Figure 8-29 Unidirectional vs. Bidirectional Force-Displacement Hysteresis, Sylmar (Circular) .....	613
Figure 8-30 Unidirectional vs. Bidirectional Force-Displacement Hysteresis, Takatori (Circular) .....	613
Figure 8-31 Unidirectional vs. Bidirectional Displacement History, El Centro (Interlocking) Longitudinal Direction.....	614
Figure 8-32 Unidirectional vs. Bidirectional Displacement History, El Centro (Interlocking)...	614
Figure 8-33 Unidirectional vs. Bidirectional Displacement History, Los Gatos (Interlocking) Longitudinal Direction.....	615
Figure 8-34 Unidirectional vs. Bidirectional Displacement History, Los Gatos (Interlocking)..	615
Figure 8-35 Unidirectional vs. Bidirectional Displacement History, Petrolia (Interlocking) Longitudinal Direction.....	616
Figure 8-36 Unidirectional vs. Bidirectional Displacement History, Petrolia (Interlocking).....	616
Figure 8-37 Unidirectional vs. Bidirectional Displacement History, Rinaldi (Interlocking) Longitudinal Direction.....	617
Figure 8-38 Unidirectional vs. Bidirectional Displacement History, Rinaldi (Interlocking).....	617

Figure 8-39 Unidirectional vs. Bidirectional Displacement History, Sylmar (Interlocking) Longitudinal Direction.....	618
Figure 8-40 Unidirectional vs. Bidirectional Displacement History, Sylmar (Interlocking).....	618
Figure 8-41 Unidirectional vs. Bidirectional Displacement History, Takatori (Interlocking) Longitudinal Direction.....	619
Figure 8-42 Unidirectional vs. Bidirectional Displacement History, Takatori (Interlocking).....	619
Figure 8-43 Unidirectional vs. Bidirectional Force-Displacement Hysteresis, El Centro (Interlocking) .....	620
Figure 8-44 Unidirectional vs. Bidirectional Force-Displacement Hysteresis, Los Gatos (Interlocking) .....	620
Figure 8-45 Unidirectional vs. Bidirectional Force-Displacement Hysteresis, Petrolia (Interlocking) .....	621
Figure 8-46 Unidirectional vs. Bidirectional Force-Displacement Hysteresis, Rinaldi (Interlocking) .....	621
Figure 8-47 Unidirectional vs. Bidirectional Force-Displacement Hysteresis, Sylmar (Interlocking) .....	622
Figure 8-48 Unidirectional vs. Bidirectional Force-Displacement Hysteresis, Takatori (Interlocking) .....	622
Figure 8-49 Unidirectional vs. Bidirectional at Maximum Displacement, El Centro(Circular)..	623
Figure 8-50 Unidirectional vs. Bidirectional at Maximum Displacement, Los Gatos (Circular)	624
Figure 8-51 Unidirectional vs. Bidirectional at Maximum Displacement, Petrolia (Circular)....	625
Figure 8-52 Unidirectional vs. Bidirectional at Maximum Displacement, Sylmar (Circular).....	626
Figure 8-53 Unidirectional vs. Bidirectional at Maximum Displacement, Takatori (Circular)...	627
Figure 8-54 Unidirectional vs. Bidirectional at Maximum Displacement, El Centro (Interlocking) .....	628
Figure 8-55 Unidirectional vs. Bidirectional at Maximum Displacement, Los Gatos (Interlocking) .....	629
Figure 8-56 Unidirectional vs. Bidirectional at Maximum Displacement, Petrolia (Interlocking) .....	630
Figure 8-57 Unidirectional vs. Bidirectional at Maximum Displacement, Sylmar (Interlocking) .....	631
Figure 8-58 Unidirectional vs. Bidirectional at Maximum Displacement, Takatori (Interlocking) .....	632

## Appendix C

Figure C-1 Strain History of Gauges 1, 2 and 3 in Specimen C1 .....	665
Figure C-2 Strain History of Gauges 4, 5 and 6 in Specimen C1 .....	666
Figure C-3 Strain History of Gauges 7, 8 and 9 in Specimen C1 .....	667
Figure C-4 Strain History of Gauges 10, 11 and 12 in Specimen C1 .....	668
Figure C-5 Strain History of Gauges 13, 14 and 15 in Specimen C1 .....	669
Figure C-6 Strain History of Gauges 16, 17 and 18 in Specimen C1 .....	670
Figure C-7 Strain History of Gauges 19, 20 and 21 in Specimen C1 .....	671
Figure C-8 Strain History of Gauges 22, 23 and 24 in Specimen C1 .....	672



Figure C-9 Strain History of Gauges 25, 26 and 27 in Specimen C1 .....	673
Figure C-10 Strain History of Gauges 28, 29 and 30 in Specimen C1 .....	674
Figure C-11 Strain History of Gauges 31, 32 and 33 in Specimen C1 .....	675
Figure C-12 Strain History of Gauges 34, 35 and 36 in Specimen C1 .....	676
Figure C-13 Strain History of Gauges 37, 38 and 39 in Specimen C1 .....	677
Figure C-14 Strain History of Gauges 40, 41 and 42 in Specimen C1 .....	678
Figure C-15 Strain History of Gauges 43, 44 and 45 in Specimen C1 .....	679
Figure C-16 Strain History of Gauges 46, 47 and 48 in Specimen C1 .....	680
Figure C-17 Strain History of Gauges 49, 50 and 51 in Specimen C1 .....	681
Figure C-18 Strain History of Gauges 52, 53 and 54 in Specimen C1 .....	682
Figure C-19 Strain History of Gauges 55 and 56 in Specimen C1 .....	683
Figure C-20 Strain History of Gauges 1, 2 and 3 in Specimen C2 .....	684
Figure C-21 Strain History of Gauges 4, 5 and 6 in Specimen C2 .....	685
Figure C-22 Strain History of Gauges 7, 8 and 9 in Specimen C2 .....	686
Figure C-23 Strain History of Gauges 10, 11 and 12 in Specimen C2 .....	687
Figure C-24 Strain History of Gauges 13, 14 and 15 in Specimen C2 .....	688
Figure C-25 Strain History of Gauges 16, 17 and 18 in Specimen C2 .....	689
Figure C-26 Strain History of Gauges 19, 20 and 21 in Specimen C2 .....	690
Figure C-27 Strain History of Gauges 22, 23 and 24 in Specimen C2 .....	691
Figure C-28 Strain History of Gauges 25, 26 and 27 in Specimen C2 .....	692
Figure C-29 Strain History of Gauges 28, 29 and 30 in Specimen C2 .....	693
Figure C-30 Strain History of Gauges 31, 32 and 33 in Specimen C2 .....	694
Figure C-31 Strain History of Gauges 34, 35 and 36 in Specimen C2 .....	695
Figure C-32 Strain History of Gauges 37, 38 and 39 in Specimen C2 .....	696
Figure C-33 Strain History of Gauges 40, 41 and 42 in Specimen C2 .....	697
Figure C-34 Strain History of Gauges 43, 44 and 45 in Specimen C2 .....	698
Figure C-35 Strain History of Gauges 46, 47 and 48 in Specimen C2 .....	699
Figure C-36 Strain History of Gauges 49, 50 and 51 in Specimen C2 .....	700
Figure C-37 Strain History of Gauge 52 in Specimen C2 .....	701
Figure C-38 Strain History of Gauges 1, 2 and 3 in Specimen II .....	702
Figure C-39 Strain History of Gauges 4, 5 and 6 in Specimen II .....	703
Figure C-40 Strain History of Gauges 7, 8 and 9 in Specimen II .....	704
Figure C-41 Strain History of Gauges 10, 11 and 12 in Specimen II .....	705
Figure C-42 Strain History of Gauges 13, 14 and 15 in Specimen II .....	706
Figure C-43 Strain History of Gauges 16, 17 and 18 in Specimen II .....	707
Figure C-44 Strain History of Gauges 19, 20 and 21 in Specimen II .....	708
Figure C-45 Strain History of Gauges 22, 23 and 24 in Specimen II .....	709
Figure C-46 Strain History of Gauges 25, 26 and 27 in Specimen II .....	710
Figure C-47 Strain History of Gauges 28, 29 and 30 in Specimen II .....	711
Figure C-48 Strain History of Gauges 31, 32 and 33 in Specimen II .....	712
Figure C-49 Strain History of Gauges 34, 35 and 36 in Specimen II .....	713
Figure C-50 Strain History of Gauges 37, 38 and 39 in Specimen II .....	714
Figure C-51 Strain History of Gauges 40, 41 and 42 in Specimen II .....	715

Figure C-52 Strain History of Gauges 43, 44 and 45 in Specimen I1 .....	716
Figure C-53 Strain History of Gauges 46, 47 and 48 in Specimen I1 .....	717
Figure C-54 Strain History of Gauges 49, 50 and 51 in Specimen I1 .....	718
Figure C-55 Strain History of Gauges 52, 53 and 54 in Specimen I1 .....	719
Figure C-56 Strain History of Gauges 55, 56 and 57 in Specimen I1 .....	720
Figure C-57 Strain History of Gauges 58, 59 and 60 in Specimen I1 .....	721
Figure C-58 Strain History of Gauges 61, 62 and 63 in Specimen I1 .....	722
Figure C-59 Strain History of Gauges 64, 65 and 66 in Specimen I1 .....	723
Figure C-60 Strain History of Gauges 67, 68 and 69 in Specimen I1 .....	724
Figure C-61 Strain History of Gauges 70, 71 and 72 in Specimen I1 .....	725
Figure C-62 Strain History of Gauges 73, 74 and 75 in Specimen I1 .....	726
Figure C-63 Strain History of Gauges 76 and 77 in Specimen I1 .....	727
Figure C-64 Strain History of Gauges 1, 2 and 3 in Specimen I2 .....	728
Figure C-65 Strain History of Gauges 4, 5 and 6 in Specimen I2 .....	729
Figure C-66 Strain History of Gauges 7, 8 and 9 in Specimen I2 .....	730
Figure C-67 Strain History of Gauges 10, 11 and 12 in Specimen I2 .....	731
Figure C-68 Strain History of Gauges 13, 14 and 15 in Specimen I2 .....	732
Figure C-69 Strain History of Gauges 16, 17 and 18 in Specimen I2 .....	733
Figure C-70 Strain History of Gauges 19, 20 and 21 in Specimen I2 .....	734
Figure C-71 Strain History of Gauges 22, 23 and 24 in Specimen I2 .....	735
Figure C-72 Strain History of Gauges 25, 26 and 27 in Specimen I2 .....	736
Figure C-73 Strain History of Gauges 28, 29 and 30 in Specimen I2 .....	737
Figure C-74 Strain History of Gauges 31, 32 and 33 in Specimen I2 .....	738
Figure C-75 Strain History of Gauges 34, 35 and 36 in Specimen I2 .....	739
Figure C-76 Strain History of Gauges 37, 38 and 39 in Specimen I2 .....	740
Figure C-77 Strain History of Gauges 40, 41 and 42 in Specimen I2 .....	741
Figure C-78 Strain History of Gauges 43, 44 and 45 in Specimen I2 .....	742
Figure C-79 Strain History of Gauges 46, 47 and 48 in Specimen I2 .....	743
Figure C-80 Strain History of Gauges 49, 50 and 51 in Specimen I2 .....	744
Figure C-81 Strain History of Gauges 52, 53 and 54 in Specimen I2 .....	745
Figure C-82 Strain History of Gauges 55, 56 and 57 in Specimen I2 .....	746
Figure C-83 Strain History of Gauges 58, 59 and 60 in Specimen I2 .....	747
Figure C-84 Strain History of Gauges 61, 62 and 63 in Specimen I2 .....	748
Figure C-85 Strain History of Gauges 64, 65 and 66 in Specimen I2 .....	749
Figure C-86 Strain History of Gauges 67, 68 and 69 in Specimen I2 .....	750
Figure C-87 Strain History of Gauges 70, 71 and 72 in Specimen I2 .....	751
Figure C-88 Strain History of Gauges 73, 74 and 75 in Specimen I2 .....	752
Figure C-89 Strain History of Gauge 76 in Specimen I2.....	753

## **Chapter 1. Introduction**

### **1.1 Introductory Remarks**

Bridges are an essential component of transportation systems; as such, any closure or disruption of their functionality may result in elevated economical losses. Reinforced concrete bridges are vulnerable to earthquakes. Earthquakes in the last few decades (1971 San Fernando, 1989 Loma Prieta and 1994 Northridge earthquakes in California, USA; 1995 Kobe earthquake in Japan; 1999 Chi-Chi earthquake in Taiwan; 2008 Wenchuan earthquake in China; 2010 Maule earthquake in Chile; 2011 Christchurch earthquake in New Zealand, and 2011 Tohoku earthquake in Japan), have provided evidence about the susceptibility of concrete substructures to moderate and large ground excitations.

For many years, bridges have been designed to prevent collapse under strong earthquakes. In the past, this objective was met by designing structures using elastic methods (allowable stress design). However the aforementioned earthquakes demonstrated that the use of elastic methods for bridge design, were in most cases inappropriate leading to large damage and even collapse. As a consequence of the huge economical impact of the bridge damage, the loss of functionality and business interruption, it is critical to understand how structures will perform under complex and extreme loading.

Reinforced concrete columns (RCC) are often the most susceptible bridge component to damage. Excessive lateral deformations induced by earthquakes can result in concrete spalling, buckling of longitudinal reinforcement, degradation of stiffness and lateral capacity, bar fracture, and eventually collapse in the presence of axial forces.

Evidence found after earthquakes have shown that RCC are frequently subjected to combinations of actions and deformations, caused by spatially-complex earthquake ground motions, structural configurations and the interaction between input and response characteristics. As a result, the seismic behavior of these components can be seriously affected, and that in turn influences the performance of bridges as essential components of transportation systems.

In order to address the complex behavior of bridge members under combined loadings and its impact on system response, a comprehensive project sponsored by the National Science Foundation was established in 2006. This research project includes researchers from six institutions and was established to developing a fundamental knowledge of the impact of combined actions on the RCC seismic performance and their implications on system response through analytical and experimental research. The research at University of Nevada, Reno is presented in this document; it focused on the seismic behavior of bridges with single column bents. Accordingly, single cantilever-type scaled bridge columns were subjected to different levels of biaxial excitation until failure on a shake table. The experiment design, dynamic simulations, data collection and interpretation, response evaluation and detailed analytical modeling are discussed.

## **1.2 Literature Review**

After the 1971 San Fernando earthquake in California, a significant effort has been undertaken to understand the seismic performance of reinforced concrete columns (RCC), used both in buildings and/or bridges. As a result, experimental and analytical research has been carried out worldwide to study the response of RCC to simulated

seismic loads. The experimental research conducted to date has been based mainly on scale column specimens subjected to unidirectionally or bidirectionally loading, with or without axial loads and through three testing methodologies: quasi-static, pseudo-dynamic and dynamic (shaking table) tests. The member geometry and reinforcement detailing (cross sectional shape, aspect ratio and steel ratios), the material properties (concrete and steel), and the loading protocols have been the most commonly studied variables.

An extensive literature review on the experimental behavior of RCC subjected to bidirectional loads is presented in this section. The experimental results have been categorized based on the three testing methodologies: quasi-static, pseudo-dynamic and dynamic tests. In order to provide a reference for this and future works, a data base with information about specimen geometry, reinforcement detailing, material properties, loading paths and axial load ratio was prepared as part of this study, and it is summarized in Appendix A. Since the focus of the present study is on the behavior of RCC under bidirectional loading, experimental studies conducted using quasi-static or pseudo-dynamic methods under unidirectional loading were not considered here, interested readers are referred to the work of Lehman and Moehle (Lehman and Moehle, 1998), PEER Column database (PEER, 2004) and the Kawashima Earthquake Engineering Laboratory (Tokyo Institute of Technology).

### **1.2.1 Quasi-static Tests on Rectangular and Circular Sections under Biaxial Lateral Loading**

A quasi-static test is a testing method in which displacement or force histories are applied to a specimen at low frequencies ( $f \approx 0.002$  Hz). These histories are applied to a specific point in the model using hydraulic actuators, which can be controlled by load, displacement or a combination of both. Since the histories are applied to the model at large time intervals, it is possible to have a better control of the specimen and its response.

A number of researchers have used quasi-static tests to measure the ultimate capacity, ductility and failure mode of RCC with rectangular or circular cross sections under biaxial loading. Most of the research has been devoted to evaluate the seismic performance of specimens detailed according to seismic design codes. Following is a compilation of the more relevant studies. Details of the columns studied in each project are summarized in Tables A-1 through A-8.

Karlsson *et al.* (1973) tested six half-scale square RCC spirally reinforced, to model the behavior of typical first story columns of the Olive View Medical Center building of California. The seismic response of the columns was studied by subjecting the specimens to lateral load reversal and a constant axial load. They found that the lateral capacity was increased with the level of compressive axial load. It was also observed that the spiral reinforcement was very effective in confining the sections.

Takiguchi *et al.* (1980) conducted an experimental and analytical study to evaluate the bi-directional behavior of columns responding to lateral displacements and under constant axial force. Twelve square specimens with different levels of axial force,

loading paths, and arrangements of longitudinal and transverse reinforcement were studied. Sets of specimens were loaded following either unidirectional or bidirectional (circular or elliptic) cyclic loading paths. The researchers concluded that the close spacing of the transverse reinforcement resulted in stable force-displacement hysteresis under biaxial loading.

Otani *et al.* (1980) tested eight square RCC typical of a first story building. The lateral behavior of four pairs of two identical specimens were assessed by imposing unidirectional or bidirectional loading, without axial force. The test variables included both the amount of lateral and longitudinal reinforcement, and the path of applied loads (uniaxial vs. biaxial). The researchers found that the failure mode and overall hysteretic characteristics of pairs of identical specimens were similar independently of the path of load. They also observed that the loading and resulting damage in one direction of the specimens induced a reduction in the stiffness of the other direction for biaxially loaded columns. In addition, they noted that the inelastic biaxial interaction caused a lower yielding capacity compared to the uniaxially tested specimens.

Maruyama *et al.* (1984) tested eighteen 2/3-scale models of square RCC by subjecting them to different paths of lateral deformation and axial load histories (tension or compression). They observed that the shear capacity of short columns was not significantly affected by bidirectional effects unless the deflection reached in previous loading did not exceed the deflection corresponding to the maximum capacity of specimens under monotonic loading. However a stiffness reduction was observed on the biaxially tested specimens. Furthermore, they found that the level and mode of application of the axial load affected the seismic behavior. Accordingly, compressive

axial force accelerated the capacity degradation and reduced the energy dissipation. In contrast, axial tension reduced the capacity deterioration but also decreased the shear strength; therefore flexural hinging controlled the response.

Umehara and Jirsa (1984) conducted experimental research on twenty  $2/3$ -scale square and rectangular RCC models tested following different loading paths. The specimens were tested under monotonic or cyclic loads along the principal axis as well as diagonal directions, and different levels of axial loads. The authors found that the shear capacity of columns subjected to diagonal loads could be estimated from circular or elliptical interaction diagrams developed from unidirectional loading acting along the principal axis. They also observed that compressive axial loads increased the capacity of columns but at the same time increased the rate of degradation after the maximum shear was reached, with a greater degradation rate in specimens under biaxial cyclic loading. Additionally, they concluded that previous loading in perpendicular directions did not affect the shear strength unless the maximum deflection in any previous loading exceeded the deflection at which the shear capacity under unidirectional loading was reached.

Low and Moehle (1987) evaluated the seismic behavior of rectangular RCC designed to satisfy requirements of U.S building code in regions of high seismicity. In this research, five identically  $1/4$ -scale rectangular columns were subjected to different loading histories, including uniaxial and biaxial lateral loads with constant or variable axial forces. They observed differences in the force-displacement hysteresis of uniaxially loaded specimens compared to those biaxially tested. Accordingly, the visible damage and measured reinforcement strains were larger in biaxially tested columns. The



researchers also noted that the strength and stiffness of biaxially loaded specimens were less than those under monotonic loading.

Li *et al.* (1988) compared the behavior of seven 1/4-scale square columns tested under varying axial and lateral load reversals (unidirectional vs. bidirectional). The specimens tested represented typical interior, exterior and corner columns in the first story of an eight-story building. The researchers concluded that there was a significant degradation in stiffness and lateral capacity in specimens subjected to biaxial lateral loading compared with those subjected to uniaxial lateral loads for the same axial load amplitude. It was also observed that the corner columns subjected to larger variations of axial and lateral loads, deteriorated faster and more severely than other columns.

Zhan *et al.* (1989) investigated the effects of biaxial bending on the strength and ductility characteristics of square RCC by subjecting four large-scale specimens to loads along the section diagonal. By comparing the result of biaxial testing with those of similar columns tested under uniaxial loads, the researcher found that for the same magnitude of axial load and transverse reinforcement ratios there was small influence of the biaxial effects on the flexural capacity and ductility of square sections. They also concluded that the transverse steel ratios specified in seismic codes for rectangular columns and derived from uniaxial bending loading were equally effective for columns under biaxial loading histories.

Saatcioglu and Ozcebe (1989) tested fourteen full-scale square columns under unidirectional and bidirectional (elliptical) loading reversals with and without axial loads, including variable axial tension and compression. The authors found that axial loads have a significant influence on the hysteretic response of columns. For instance, constant axial

compression reduces the ductility and accelerates strength and stiffness degradation, whereas constant axial tension reduced the flexural yielding strength with a significant delay in strength degradation beyond the initial yielding. They also observed that the level of damage in one direction has a significant effect in the second direction if post-yield deformations were experienced. Additionally, it was noted that the ductility of columns under combined axial and bending reversal was improved significantly with the use of a proper confinement configuration.

Bousias *et al.* (1992) studied the behavior of eight square flexure-dominated RCC subjected to different biaxial loading paths and constant axial load. The authors observed a strong coupling between the two directions of bending and the vertical direction, which increased the level of damage (energy dissipation). This coupling affected the rate of strength and stiffness degradation at large displacements levels. They also observed that circular loading paths produced a large degradation of strength and stiffness, compared with linear or square paths.

Ogawa *et al.* (1992) studied the effects of biaxial lateral loading on the strength and damage behavior of square RCC representative of low rise concrete buildings in Japan. Eleven large-scale specimens were subjected to different loading paths including; uniaxial cyclic and biaxial cyclic (principal axis, diagonal, square, circular and elliptical paths). The researchers concluded that the strength degradation and damage were more severe in columns subjected to biaxial loading, with more damage in columns under circular paths than those under linear paths.

Wong *et al.* (1993) evaluated the effects of transverse reinforcement content on the seismic behavior of shear-dominated columns tested under compressive axial force

and different uniaxial and biaxial displacement patterns. Based on the observations of sixteen tested circular RCC, the author found that the hysteresis performance and ductility capacity were improved by increasing the content of transverse reinforcement or by increasing the level of compressive axial load. They also observed that biaxial paths led to a more severe capacity and stiffness degradation than uniaxial paths. It was also noted that the displacement ductility was not sensitive to the type of biaxial loading.

Kuramoto *et al.* (1995) conducted experimental and analytical research to study the influence of axial deformations on the ductility capacity of columns subjected to bidirectional loading combined with axial force. Based on the experimental results of four 1/3-scale square RCC, they found that the ductility was reduced by increasing the compressive axial deformation in the same way as columns subjected to uniaxial bending moment and constant axial load.

Yoshimura and Tsumura (1996) tested four square RCC under compressive axial force and bidirectional lateral loads. The researchers observed that the level of axial force had a significant effect on the lateral capacity of columns after yielding. Accordingly, high values of axial force increased the lateral capacity but simultaneously accelerated the strength degradation and induced P-delta effects.

Qiu *et al.* (2002) investigated the strength and stiffness degradation of square RCC by subjecting seven specimens to constant compressive axial load and different bidirectional loading patterns. The authors stated that the lateral capacity and observed damage of columns tested under biaxial loads differed greatly from those loaded uniaxially, specifically for loading patterns following revolving configurations. For instance, under biaxial loading the deformation interactions caused reduction in the

lateral capacity, ductility and hysteretic energy dissipation compared with those observed in uniaxially tested columns.

Kawashima *et al.* (2006) studied the effects of bilateral excitations on the seismic performance of reinforced concrete bridge columns (RCBC). Five large-scale square specimens were subjected to unilateral or bilateral deformations following diagonal, square, circular or elliptic paths. They concluded that the flexural capacity and ductility of columns were significantly reduced under bilateral loads compared to unilateral loads. They also realized that the loading protocol greatly influenced in the performance of square columns.

From the experimental results review above, it is clear that larger reductions in strength, stiffness and ductility were observed under bidirectional loading compared to unidirectional loading. Nevertheless the extent of the biaxial interactions appeared to be associated with the loading history, rate of loading and number of repetitions used. For instance, revolving loading paths (circular or elliptical) induced more damage on the sections and contributed significantly more capacity reduction than those using linear or simple loading patterns. It was also found that the magnitude and the direction of the axial load (compression or tension) had a significant influence in the seismic performance of columns. Accordingly, large compressive axial loads increased the capacity of the section, but simultaneously reduced the ductility and accelerated the strength and stiffness degradation. Although much effort was expended attempting the biaxial effects on the hysteretic characteristics of the columns, limited research addressed the influence of biaxial interactions on the ultimate force and displacement capacity of well confined RCC with relatively low axial loads, which are typical for bridge columns.

### **1.2.2 Quasi-static Tests on Rectangular and Circular Sections under Combined Lateral Loading and Torsion**

Since the 1995 Kobe earthquake in Japan, several research projects have been established to investigate the seismic performance of bridges with particular configurations such as skewed or curved bridge superstructures and C-type or inverted L-type bent columns. Of particular interest has been the study of seismic performance of RCC subjected to combined loads including biaxial bending, torsion and axial compressive loads. A synopsis of the most relevant studies is discussed in this section. Details of the columns studied in each experimental program are presented in Table A-9 through A-11.

Nguyen and Irawan (2003) investigated experimentally the shear capacity of short rectangular RCC subjected to cyclic lateral loading and torsion. Eight identical specimens were subjected to constant compressive axial force and lateral loading applied at different inclinations with respect to the weak axis of the column ( $0^\circ$ ,  $30^\circ$ ,  $60^\circ$  and  $90^\circ$ ). On four specimens the point of application of the lateral load coincided with the vertical axis of the column, whereas in the other four a small eccentricity was applied. Another specimen was tested under compressive axial force and pure torque. The researchers observed that for short columns the shear capacity was reached without yielding of the longitudinal reinforcement giving place to a brittle shear failure. Columns under bidirectional loads behaved more brittle than under unidirectional loading. They also found that torsion reduced the shear strength, lateral stiffness and ductility. Additionally, the combination of torsion and compressive axial forces accelerated the strength and stiffness degradation after the peak loading. From the specimen subjected to pure torsion, they observed that

severe damage was localized at the midheight of the specimen where the deformations were the highest.

Otsuka *et al.* (2004) evaluated the seismic performance of RCC subjected to compressive axial loads, bending, and torsion. Nine square specimens with two different volumetric steel ratios were experimentally tested under cyclic loading in pure bending, pure torque or a combination of them. They discovered that the tie spacing along the column greatly affected the torsional hysteretic behavior (torque – twist angle), but it was less significant for the flexural hysteresis (lateral load – deflection). They also found that the interactions between torsion and bending moment (T/M) affected the flexural and torsional strength and ductility. Accordingly, for larger values of the T/M ratio the bending capacity and ductility are considerably reduced; the same is observed for the torsional capacity and rotational ductility for low values of T/M. Finally, it was observed that for bending dominated behavior the damage is localized at the base of the column (plastic hinge), whereas it is concentrated at the midheight for torsional dominate behavior.

Tirasit, Kawashima and Watanabe (2006) conducted an experimental investigation to study the effects of combined cyclic flexural and torsional loading on the seismic performance of square RCC designed according to the 1996 Japanese bridge design specifications. Seven large-scale columns were tested under three cyclic loading conditions: uniaxial bending, pure torsion and combined bending and torsion. They observed that the typical plastic hinge at the base (pure bending) was shifted toward the midheight of the column due to the presence of torsion. They also determined that the flexural and torsional hystereses are significantly changed for the combined actions of

bending and torsion. For instance, the flexural capacity and displacement ductility are reduced when the torsion is increased. Similarly, the torsion capacity and ultimate twist rotation are reduced as the bending moment is increased.

Nagata *et al.* (2006) studied the effects of combined bending, torsion and axial force on the seismic behavior of C-bent columns typical of bridges in Japan. Six model columns were subjected to cyclic loads at the column tip; three using uniaxial loading and three with biaxial loading. To induce torsion, the lateral load was applied with eccentricities of 0, 0.5 and 1.0 times the width of the column. The authors found that the eccentricity in the application of the lateral load resulted in rotations of the column around the longitudinal axis under both uniaxial and biaxial loading. The rotation was more significant as the eccentricity was increased, but this effect was less significant for the columns under biaxial loading. They also observed that the failure mode was dominated by the compression resulting from the interaction of axial, bending and torsion on the eccentric compression side of the section.

Belarbi, Qi and Prakash (2009) compared the seismic performance of RCC with circular and square sections under cyclic bending, cyclic torsion and compressive axial loading. Four 1/2-scale circular and four square specimens were subjected to compressive axial loading in combination with pure bending, pure torsion or combinations of them. The researchers observed that for both sections under pure torsion, the failure mode was characterized by large diagonal shear cracks and the development of a torsional plastic hinge at the midheight of the column. For pure bending or low values of torsion a plastic hinge was developed at the column base. They concluded that the ultimate load and displacement capacity were deteriorated with increasing levels of torsion. Similarly, the

torsional moment and ultimate twist capacity were reduced by the increase of bending. They pointed out that the transverse reinforcement in the square columns was as effective as the circular spirals in confining the core concrete under bending and shear forces, but it needed to be further investigated for torsional loading.

From the experimental studies conducted so far on the seismic performance of bridge RCC under combined bending, torsion and axial force, it is evident that the presence of torsion and compressive axial loading affected the flexural strength, ductility, and capacity and stiffness degradation of the columns. These effects were more significant in columns with values of the relationship torque to bending moment ( $T/M$ ) larger than 20%. Another important observation about the magnitude of the  $T/M$  ratio was the distribution of damage and the location of the plastic hinge. For single cantilever columns with large values of the  $T/M$  ratio, the plastic hinge was shifted from the bottom to the midheight of the column. Although some experimental studies have been carried out, there are still issues on the flexural-torsional interaction that need to be clarified; one of them is the performance of bridge columns under dynamic loads including large values of torsion.

### **1.2.3 Quasi-static Tests on Double Interlocking Sections**

Provisions for the seismic design of interlocking columns were first introduced in the standard specifications for highway bridges in the US in 1977 by the American Association of State Highway and Transportations Officials (AASHTO) and by California Department of Transportation (Caltrans) in 1990. Unlike rectangular or circular columns, most of the experimental work in interlocking columns has been



focused on understanding the flexural and shear behavior under uniaxial loads. Since interlocking columns are included in the present study, the results of relevant studies are reviewed here. Table A-12 summarizes the characteristics of the specimens tested in each study.

Tanaka and Park (1993) conducted an experimental research to study the seismic behavior of RCC with double interlocking spirals. Three large scale specimens with oval section were tested under uniaxial loads applied along the strong direction of the section. By comparison a rectangular column reinforced with hoops and cross ties (volumetric steel ratio of almost twice the one in interlocking sections), was also tested. The researchers observed that the force-displacement hysteresis loops were stable with high energy dissipation and low capacity degradation up to the end of the test at displacement ductility values of 10. They also found that for columns with an aspect ratio of 3, the shear deformations contributed around 10% to 30% of the lateral deformation. Finally they recommended that the amount of lateral reinforcement at the plastic hinge zone could be reduced considerably by using interlocking spirals instead of hoops and cross ties.

Buckingham and MacLean (1994) studied experimentally the seismic behavior of bridge RCC with double interlocking spirals. Six 1/5-scale specimens with interlocking spirals and oblong shape were subjected to shear, flexural and torsional loading with constant axial force. By comparison, two rectangular columns with conventional hoops and cross ties were also investigated. The authors observed that the performance of columns with double interlocking spirals was similar to that observed on the rectangular columns that contained 50% more transverse reinforcement. They also found that

specimens loaded to failure in shear with distance between center to center of the spirals equal to 1.2 times the spiral radius underwent less strength degradation than specimens with spacing of 1.5 times the spiral radius. It was also observed that at least four bars of the same size as the main longitudinal reinforcement were required in the interlocking zone to maintain the spiral interlock action.

Tsitotas and Tegos (1996) investigated the seismic behavior of reinforced concrete elements with interlocking spirals and detailing typical of Greece. For this, two 1/8-scale specimens were tested; one under monotonic load and one under cyclic load with constant axial compression. It was found that the force-displacement hysteretic loops were stable and showed high energy dissipation. Additionally the lateral capacity of the specimen was maintained almost constant until the end of the test producing large displacement ductilities.

Benzoni *et al.* (2000) evaluated the seismic behavior of shear-critical rectangular columns reinforced with interlocking spirals. Four 1/4-scale specimens were experimentally tested in double bending and with axial force ratios ( $P/f'_c A_g$ ) of 0.0, 0.35 and -0.1. It was found from the lateral force-displacement hysteresis that the axial compressive forces had a detrimental influence on the shear capacity of the sections. Accordingly, large compressive axial ratios induced brittle shear failure with low ductility. On the contrary, low values of compressive axial loads or alternating tension/compression loads produced more stable hysteresis loops with displacement ductility values up to 6. Based on the experimental results, the authors proposed a method to calculate the shear capacity of columns with interlocking spirals.

Mizugami (2000) examined the performance of RCC with interlocking spirals under flexural and shear loading. Three single cantilever specimens with an aspect ratio of 5 were loaded along the strong axis to study the flexural behavior. Three more specimens with aspect ratio of 1.9 were loaded along the weak axis of the section to investigate the shear behavior. For comparison a rectangular section reinforced with hoops and cross ties was tested along the weak axis. The author observed that the flexural capacity and ductility of the interlocking columns were comparable to that of the rectangular section which was reinforced with 300% higher volumetric ratios than the interlocking spirals. It was also noted for the shear tests specimens that the amount of transverse steel had a big influence on the failure mode of the columns. Finally, it was recommended to use volumetric confinement ratios of at least 0.3% in order to achieve ductile response on interlocking sections.

From the above, it is evident that the behavior of columns with double interlocking spirals subjected to simulated earthquake loads had been satisfactory in terms of flexural and shears strength, ductility and stiffness degradation for low to moderate levels of compressive axial forces. Contrarily, large values of axial compressive force in relatively short columns can induce brittle shear failure. It was also pointed out that the seismic performance of interlocking columns is equal or even better than that of well detailed rectangular sections; despite the reduced amount of transverse steel required to effectively confine the section. However, the distance between the centers of adjacent spirals and the rebar size in the interlocking region need to be appropriately selected to avoid degradation of the column capacity. Although interlocking sections have been widely adopted for highway bridge columns for more than three decades and their good

performance has been demonstrated under uniaxial loads, little is known about the seismic response of these elements under dynamic bidirectional loading.

#### **1.2.4 Pseudo-dynamic Tests on Rectangular and Circular Sections**

The pseudo-dynamic test is essentially a quasi-static test in which an analytical idealization of the specimen, or a part of it, is used to determine the required forces or displacements that the specimen needs to be subjected to in subsequent time steps, based on the measured deformations.

A limited number of studies have been conducted using pseudo-dynamic methods to measure the seismic performance of RCC under biaxial loading; most of them have been devoted to comparing the behavior of specimens tested under uniaxial loads with those tested under biaxial loading, and in most of the cases using rectangular sections. Following is a summary of the more relevant studies. Details of the specimens experimentally tested in each study are shown in Table A-13.

Quadra *et al.* (2000) conducted experiments to evaluate the impact of bidirectional loading on the performance and damage characteristics of RCC subjected to combined compressive axial loads and bidirectional input motions. Three identical large-scale square RCC were subjected to simulated and recorded earthquakes; one specimen tested under unidirectional loading and two more under bidirectional loading. The researchers found that before the yielding load, the behavior and damage of columns were not appreciably influenced by the bidirectional effects. However, once the yielding load was reached, the bidirectional actions affected the capacity and ductility of the columns. For square sections under bidirectional loading, the maximum capacity was

slightly lower than that of the unidirectional columns. In addition, they observed that for the bidirectionally tested specimens the damage was distributed around the surface of the columns with spalling of the corners, therefore, these specimens showed more energy dissipation than the one under unidirectional loading.

Kawashima *et al.* (2006) studied the effects of bilateral excitations on the seismic performance of bridge RCC by testing square cantilever columns using a hybrid loading method. Six large-scale specimens were tested either under unilateral or bilateral loading by subjecting them to fractions of the Kobe and Sylmar records. By comparing the experimental results of hybrid testing with those of quasi-static tests on similar specimens, the authors found that the flexural strength and ductility capacity of square RCC were significantly deteriorated under bilateral excitations. They also observed that the damage of the columns using quasi-static test was more extensive than that on the hybrid test, therefore the loading protocol in quasi-static testing need to be carefully determined to resemble that of pseudo-dynamic tests.

Dhakal *et al.* (2006) compared the seismic performance of ductile highway bridge circular columns under bidirectional earthquake loading. Three 1/3-scale specimens were designed and detailed according to Caltrans, New Zealand and Japanese seismic design specifications, and were experimentally tested by imposing three earthquake ground motions scaled to represent design (DE with  $PGA=0.4g$ ) and maximum considered events (MCE with  $PGA=0.8g$ ) with 50% and 90% confidence. They found that the performance of the three bridge piers was satisfactory with slight to moderate damage under the DE. For the MCE, severe damage was observed for the Caltrans and Japanese

columns, while the New Zealand pier collapsed. Good energy dissipation and ductility capacity under biaxial loading was observed in all specimens.

Chang (2010) evaluated the seismic performance of RCC designed in accordance with the Taiwanese bridge design code and subjected to compressive axial loading and biaxial bending. Six 2/5-scale rectangular identical specimens were subjected to near-fault earthquake ground motions; three specimens under uniaxial loading and three under biaxial loading. By superimposing the force displacement hysteresis plots of specimens tested uniaxially and biaxially, the author observed that the specimens subjected to biaxial ground motions exhibited stiffness and strength degradation and significant pinching effect. These effects were attributed to the biaxial interaction in which the damage due to loading in one direction weakened the lateral stiffness in the orthogonal direction.

From the experimental results of specimens tested using pseudo-dynamic method it is inferred that for rectangular or square cantilever RCC subjected to bidirectional loading the lateral stiffness, flexural strength and ductility are degraded due to the biaxial interactions. Additionally, due to the fact that the damage is distributed uniformly around the perimeter of the section for bidirectionally tested specimens, more energy is dissipated in comparison to unidirectionally loaded columns. Moreover, the large concrete spalling at the corners made the RCC more susceptible to bar buckling. It is worth noting that the former observations are applied only to rectangular columns. Due to the limited number of experimental studies, little is known about the biaxial interactions in circular or interlocking sections tested using pseudo-dynamic methods.

### **1.2.5 Dynamic Tests on Rectangular and Circular Sections subjected to Unidirectional Earthquake Motions**

The dynamic testing of structures is an experimental method in which the base of a structural model is subjected to displacement histories applied at high frequencies ( $f \approx 20$  Hz) using a shake table system. This system has the advantage of reproduce the recorded accelerations of a real earthquake with high reliability, and it has also the ability to reproduce inertial effects that cannot be correctly modeled on the quasi-static or pseudo-dynamic tests. Despite of the advantages of the shake table systems to accurately represent the earthquake response of structures, limitations of testing facilities and the large scale required to model bridges or buildings, have made the dynamic testing of components, the most popular technique to address the seismic performance of structures.

The majority of dynamic experiments on RCC have been focused to quantify limit states of the response and to study the failure mechanics under earthquake excitation. Since most of the experimental studies have been conducted on shake table under unidirectional excitations, they are first presented. Following is a compilation of the more relevant studies. Details of the specimens investigated in each research program are summarized in Tables A-14 through A-17.

Shiying and Zhenchang (1990) conducted experiments to study the damage progression, strength and deformation capacity of RCC under dynamic vibrations. Two single cantilever columns and six two-column bents with rectangular sections were tested on a shake table under harmonic vibrations. By comparison two identical single columns were tested using pseudo-dynamic methods. The authors observed that the initiation and propagation of cracking was different on the shake table tests compared with the pseudo-

dynamic tests. They also found that the initial stiffness on dynamic tests was less than the one observed on static tests. In addition, they observed that the failure mode of single cantilever columns was dominated by flexure deformations whereas that for the two-column bents was dominated by shear deformations.

Kogoma *et al.* (1992) compared the dynamic behavior and collapse mechanism of square columns tested using shake table and static tests. Four 1/3-scale columns with different transverse steel ratios were tested under uniaxial accelerations. In addition two similar specimens were tested under cyclic loading. The researchers found that the maximum strength and deformation capacities measured in the dynamic test were similar to the one measured on the static test. However the shear failure and the pattern of damage were influenced by the transverse steel ratio and type of testing. The failure mechanism was characterized by the development of plastic hinges at the bottom and top of the specimens, typical of elements tested in double curvature. The displacement ductility was observed to increase with the increase in volumetric steel ratio.

Dodd and Cooke (2000) carried out a research project aimed to understand the seismic performance of circular columns subjected to dynamic excitations and to evaluate the applicability of design provisions and analytical modeling in predicting the strength and displacement capacity of these columns. Fourteen 1/6-scale single cantilever RCC with different aspect ratios (4, 7 and 10) and two axial load ratios (5% and 40%  $A_g f'_c$ ), were tested on the shake table at the University of Canterbury, New Zealand. The specimens were subjected to uniaxial excitations consisting of either the 1940 El Centro earthquake or sinusoidal base motions. A massive block attached to the top of the specimens was used to induce both inertial forces and axial loads. In addition a post-



tensioning system was employed to apply large values of axial force. The authors found that the behavior of the columns was dominated by flexural deformations with a failure mode due to the development of a plastic hinge at the column base. Likewise, they observed that the columns with high axial load typically failed due to rupture of the spirals, while the longitudinal bars fractured in columns with low axial loads. Adequate spiral content is required to prevent premature buckling of the longitudinal reinforcement. In addition, they also realized that the flexural capacity of the specimens was underestimated by nearly 20% using analytical predictions developed from quasi-static tests. They attributed this increase to the high strain rate in dynamic tests.

MacRae *et al.* (1994) simulated the seismic response of two-column bents typical of bridges in route 5/405 in California by testing model structures on a shake table. One as-built and one retrofitted 1/6-scale RC two-column bents with rectangular sections were subjected to unidirectional ground accelerations on the shake table using the 1940 El Centro earthquake at University of California, San Diego. A massive concrete block and a post-tensioning system were used to simulate the mass and axial load in the columns. The failure mode of the as-built bent consisted of shear failure followed by a reduction in the axial capacity resembling the behavior of a number of column-bents during the 1971 San Fernando earthquake. The second model, retrofitted with steel jacketing showed great improvement in the seismic performance during the experimental tests, with considerable increase in the lateral capacity and ductility as compared with the as-built model.

Laplace *et al.* (1999) studied the seismic performance of flexure dominated RCC designed according to 1992 Caltrans seismic design specifications. Two 1/3-scale circular

single cantilever columns were tested on a shake table using the 1940 El Centro earthquake at University of Nevada, Reno. The first column was tested under 9 consecutive runs of increase amplitude from 1/3 to 4 times El Centro, whereas the second specimen was tested under 3 repetitions at 3.5 El Centro. A sophisticated inertial loading system was designed for this study, in which the mass was located away from the shake table and the inertial forces were transferred to the RC specimen through a swiveled rigid link. The authors observed that the seismic performance was satisfactory, with the column subjected to large amplitude excitations exhibiting higher capacity than the column subjected to increased amplitude accelerations. By comparing the seismic performance with columns tested using quasi-static methods, they found an increase in the capacity and ductility due to dynamic effects (strain rate). The first columns failed once a plastic hinge was developed at the base of the column and then collapsed due to lateral instability (P-delta effects). The second column did not fail and was used in a different study to investigate retrofitting methods.

Kowalski *et al.* (2000) assessed the effects of dynamic response of bridge RCC constructed with lightweight concrete. Two 1/6-scale two column-bents with circular columns were tested on the shake table at University of California, San Diego and were subjected to various levels of excitation of the strong component of the 1978 Tabas earthquake. A massive concrete block was used to simulate the mass and axial load in the columns. The authors observed that the specimen with lightweight concrete behaved as well as structures with normal weight concrete. A third specimen was defined by retrofitting the columns with steel jacketing at the plastic hinge zones. After several runs of large amplitude accelerations, the frame failed showing high ductility and energy

dissipation. The researchers concluded that good detailed lightweight concrete structures can be used in highly seismic regions, with the benefit of reduction of the structure inertial mass.

Inoue *et al.* (2000) investigated the influence of ground motion time duration on the inelastic dynamic behavior of RCC. Three large scale two-column bents with rectangular sections were tested either under static loading or dynamic excitations (shake table tests) at the University of Tohoku, Japan. Two synthetic ground motions with different duration and selected to match the same spectrum, were used as the input accelerations for the shake table. To induce inertial and axial forces on the columns, series of steel plates were attached to the bent cap. By comparing the results of both testing method it was found that the lateral capacity of the specimens under dynamic excitation was 10% to 20% larger than the one on static test. However the damage pattern was similar in all the specimens. It was also found that the occurrence of the peak displacement coincided with the instant of maximum input energy of the acceleration records.

Laplace *et al.* (2001) evaluated the seismic performance of as-built and retrofitted RCC designed according to the 1971 Caltrans seismic design specifications. Four 1/3-scale flexural-dominated single cantilever circular columns were tested on the shake table at University of Nevada, Reno; one as-built column served as a benchmark, two were retrofitted with steel jacketing and the fourth one using carbon fiber wraps (FRP). In addition, two shear-dominated columns with circulars section were tested in double curvature on a shake table. Increased amplitudes of the 1940 El Centro earthquake were used as the input ground motion. The inertial mass structure developed by Laplace *et al.*

(1999) was used to apply inertial forces to the specimens. They observed that for the flexural dominated columns, the as-built column and two more retrofitted with steel jacketing failed due to lap-splice with low ductility and without developing the flexural capacity. Nevertheless the column retrofitted with FRP provided a better ductility and delayed the lap-splice failure. The two shear-dominated columns failed due to severe shear deformations followed by the collapse of the specimens. They found that the shear capacity calculated based on Caltrans method was close to the test values.

Park *et al.* (2003) compared the seismic performance of bridge RCC designed according to US and Japan seismic design codes. Three 1/6-scale circular columns were tested on the shake table at the Public Works Research Institute of Japan; one column was designed based on ductility design according to the 1995 AASHTO specification, while the other two were designed based on working stress design according to 1996 Japan Road Association (JRA) specifications. All columns had the same height, but different diameter and reinforcement detailing (hoops for JRA columns and spirals for US AASHTO column). A setup was constructed to simulate a two-span bridge superstructure, with the model column set on the shake table with two abutments off the table. The 1990 Kaihoku-bashi spectrum was used to generate ground accelerations of different intensities to be applied in the longitudinal direction of the structure. The authors observed that all the specimens performed well under the design level excitation; however the US specimen experienced less damage for all levels of accelerations. The Japanese specimens, which were stiffer, attracted larger seismic forces and were vulnerable to bar buckling as compared to the US column.

Mostafa *et al.* (2004) tested on a shake table RC two-column bents designed according to the 1999 Caltrans seismic design criteria. Three 1/3-scale specimens with circular columns and different aspect ratios (2.5, 4.5 and 6.64) were subjected to increasing amplitude accelerations of the 1994 Northridge earthquake (Sylmar station) on the shake table at University of Nevada, Reno. While the connection between the beam and columns was monolithic, dowel hinges were used to connect the columns to the footings. In order to induce inertial and axial loads in the columns, lead blocks were attached to the bent cap; in addition, a safety structure was built around the specimen to capture the mass in case of specimen collapse. It was observed that the three frames behaved very well, even under high levels of excitation. In the two taller specimens the behavior was dominated by flexural deformations with high levels of drift and ductility; the failure was preceded by the development of plastic hinges at the top and bottom of the columns. Nevertheless the short specimen had a flexural/shear behavior with lower levels of ductility and deformation; failure was due to column sliding along the hinge at the column-footing interface.

Phan *et al.* (2005) conducted an experimental and analytical study to evaluate the effects of near-fault earthquakes on the performance of bridge RCC. Two 1/3-scale single cantilever circular columns were tested on the shake table at the University of Nevada, Reno. The specimens were subjected to the 1994 Northridge earthquake (Rinaldi station) and using the inertial mass system developed by Laplace *et al.* (1999). One column was designed according to the 2004 Caltrans seismic design criteria, and the other was designed based upon the 2002 AASHTO-LRFD bridge design. The researchers observed that both columns performed very well with the AASHTO column showing a

slightly larger capacity and less ductility than the Caltrans column. They also found that near-fault earthquakes induced an asymmetrical high-amplitude velocity pulse, which produced large displacements (maximum and residual) in one direction. This biased displacement response led to higher ductility capacities than symmetrical responses, with the damage occurring mainly on side of the column. However the measured strain rate and plastic hinge length were comparable to those observed on columns tested under far-field earthquakes.

Choi *et al.* (2007) studied the effects of near-fault earthquakes on the seismic performance of single columns and a bridge structure designed according to the 2004 Caltrans seismic design criteria. Four 1/3-scale circular single cantilever bridge RCC were tested on the shake table at University of Nevada, Reno and under series of the 1994 Northridge earthquake (Rinaldi station), with an increased level of acceleration in consecutive runs. Dynamic inertial forces were applied to the top of the specimens using the inertial mass rig developed by Laplace *et al.* (1999). The variables studied were the aspect ratio (4.5 and 7.75) and the detailing of the longitudinal reinforcement. Ductile behavior of the columns was observed even under large acceleration amplitudes. The failure was due to the development of a plastic hinge at the column base followed by the concrete deterioration and buckling of the longitudinal reinforcement. Large residual displacements were observed for all the tests and were attributed to the forward directivity effect of the near-fault motions. It was also observed that the length of the plastic hinge and magnitude of the strain rate effects were comparable to the ones measured in previous studies using far-field earthquakes. The researchers concluded that the addition of more longitudinal reinforcement required to satisfy the new spectral

acceleration for near-fault earthquake provisions was not sufficient to control the magnitude of the residual displacements.

The results of the unidirectional shake table testing of RCC to date suggest that the high strain rate in dynamic tests led to a difference in the initial lateral stiffness, lateral capacity, and damage propagation compared to quasi-static or pseudo-dynamic tests. It was also found that high values of compressive axial force, acting together with inertial lateral forces, produced an increase in the lateral capacity and a reduction in the ductility. Additionally, more stiffness and strength degradation was observed in columns with large values of axial force and/or low transverse reinforcement ratios. It was also observed that the characteristics of the input ground motion may influence the performance of the specimens. For instance, near-fault earthquakes with forward directivity effects leads to large one-sided residual displacements compared to far-field ground motions. Although valuable data is obtained from unidirectional shake table testing, the seismic performance of the columns can be modified as a consequence of bidirectional loading interactions.

### **1.2.6 Dynamic Tests on Rectangular and Circular Sections Subjected to Bidirectional Earthquake Motions**

The first bidirectional shake table tests of RCC were performed 20 years ago on small-scale square specimens, and were intended to study the effects of loading interactions in the seismic response and failure mechanism of columns. Since these pioneer studies, several investigations have been undertaken to study not only the behavior of large scale bridge columns under bidirectional loads, but the seismic

performance of large-scale bridge structures with multiple columns and complex loading protocols. Some of the test programs are describe here. Tables A-18 through A-20 present the main characteristic of the column specimens tested on each research program.

Kitajima *et al.* (1990) investigated the response characteristics of RCC subjected to unidirectional and bidirectional excitations using a shake table and a sophisticated mass setup. Six identical 1/9-scale square specimens were subjected to constant axial load and ground accelerations based on the 1968 Tokachi-Oki earthquake to investigate the elastic and elasto-plastic behavior. The researchers noticed slight differences between the seismic behavior of the columns under unidirectional and bidirectional excitations for the elastic level. However after the yielding point, they observed a significant reduction in the lateral stiffness of the columns tested bidirectionally. As a result, larger displacements (maximum and residual) were observed on the bidirectional tested columns. They also found that although the capacity was comparable between the unidirectional and bidirectional tests, more energy was dissipated on the bidirectional tested columns due to the extensive cracking. The failure mode for both types of tests was due to the development of plastic hinges at the top and bottom of the specimens.

Kitajima *et al.* (1996) compared the experimental results of RCC tested under unidirectional and bidirectional accelerations on a shake table. Two 1/9-scale square model columns were subjected to a constant axial load and ground accelerations based on the 1968 Tokachi-Oki earthquake to study the inelastic behavior. By comparing the lateral force-displacement hysteresis curves for the uniaxial and biaxial tests, it was seen that the strength and stiffness under bidirectional excitation were smaller than hose under unidirectional excitations. Additionally, it was observed that the maximum displacement



and energy dissipated under bidirectional excitation were larger than those under unidirectional excitation. Based on analytical results they found that shear deformations and bond slip effects need to be included to better predict the response.

Takashi *et al.* (1996) examined the bidirectional effects on the seismic performance of RCC by testing on a shake table two single story structures under uniaxial and biaxial accelerations. Each story was composed of five square columns whose top was connected to a rigid steel plate. Artificial earthquake motions with low and high levels of acceleration were used. From the tests it was evident that up to the yielding point, the force-displacement behavior of both structures was almost the same. Nevertheless, the inelastic behavior was remarkable different on each test, with a lower capacity and more degradation on the structure under bidirectional shaking compared to the structure tested under unidirectional excitations. In fact, the lateral capacity of the structure was lost after an acceleration of 0.35g for the bidirectional test, whereas the structure under unidirectional excitations withstood an acceleration of 0.48g.

Hachem *et al.* (2003) studied the seismic performance of RCC subjected to multidirectional actions by testing circular columns on a shake table. Four 2/9-scale single cantilever columns designed according to 1990 Caltrans design specification were subjected to one or two components of either the 1994 Northridge earthquake or the 1985 Llolele earthquake. Series of tests of increasing acceleration amplitudes were imposed to the specimens to study different performance levels. Massive concrete blocks were set at the top of the columns to induce inertial and axial forces. It was confirmed from the test that columns designed according to recent seismic design provisions behave satisfactorily well with ductile behavior and minor damage under high level excitations (maximum

credible earthquakes, MCE). After several repetitions of the MCE's, the columns failed due to the formation of a plastic hinge and then fracture of longitudinal or spiral reinforcement. By comparing the response along the strong component (longitudinal) of the excitation, the authors observed that the bidirectionally columns behaved similarly to the unidirectionally tested columns without any deterioration of the response. In fact, the bidirectionally columns resisted more runs before failure than the unidirectionally tested columns. However the biaxial interactions affected the behavior along the transverse direction of the bidirectionally loaded specimens. It was further observed that the concrete blocks introduced second mode effects into the response, and made the column more susceptible to shear deformations, not expected in single cantilever columns with flexural dominated behavior.

Nishida and Unjoh (2004) conducted experimental and analytical research intended to compare the seismic behavior of RCC with different cross sections and subjected to bilateral excitations of a near-field earthquake. Three 1/4-scale bridge RCC with square, circular and rectangular sections were tested on a shake table under the 1995 Kobe earthquake (Takatori). Two excitation levels were studied; one for elastic demands corresponding to 20% of the earthquake (Run 1) and other for inelastic demands (Run 2) of 100% the earthquake. Steel plates were set at the top of the columns to produce both inertial and axial forces in the columns; in addition, a safety structure was built around the specimen to capture the mass in case of specimen collapse. The authors found that after Run 1 the specimens behaved elastically without any noticeable damage and without yielding of the longitudinal reinforcement. However after Run 2 a plastic hinge was fully developed at the column base and the failure occurred after concrete spalling and

buckling of the longitudinal reinforcement. From the analysis of the interaction displacement and acceleration orbits, it was observed that after Run 1 the acceleration and displacement orbits followed the same path; however, after Run 2 these orbits were different. For circular and square sections the accelerations orbits followed approximately a  $45^\circ$  direction, while the displacement orbits followed a line of  $30^\circ$ . For the rectangular column the acceleration orbits followed a  $0^\circ$  direction (large acceleration along the short side of the column), whereas the displacements followed a less obvious tendency. Analytical models based on fibers showed good agreement with experimental results up to the bar buckling, after this point, the model underestimated the response. They concluded that the stiffness interaction for orthogonal axes is significant especially after deterioration of the column.

Sakai *et al.* (2006) evaluated the use of unbonded post-tensioning tendons to reduce residual displacements in bridge RCC after earthquakes. Six 2/9-scale circular RC cantilever columns were tested on the shake table at university of California, Berkeley. The first specimen was a conventional RCC, the next two columns were a variant of the first one in which the longitudinal steel ratio was reduced to half and an unbonded post-tensioned tendon was placed at the center, the next two columns were variations in which the longitudinal reinforcement was unbonded in the plastic hinge; the last column, was the same as before but included steel jacketing. The two horizontal components of the 1989 Loma Prieta earthquake (Los Gatos station) were scaled to study different performance levels. From the test it was observed that the specimen performed remarkably well. While the peak displacements were almost the same, the residual displacements were reduced to more than 50% at maximum excitation level. It was also

observed that by unbonding some longitudinal bars at the plastic hinge, the peak and residual displacements were slightly increased; however, this increase was reduced by increasing the postensioning force. Steel jacketing was incorporated to prevent the concrete degradation and the buckling of the unbonded bars. From the test it was found that this technique reduced the residual displacements and damage of the section even for repetitions of the maximum level acceleration.

Sakai and Unjoh (2006) investigated the seismic performance of bridge RCC typical of Japan under multidirectional seismic excitations. One 1/4-scale circular column was tested on a shake table under the vertical and 2 horizontal components of an earthquake with long duration and several strong pulses (1983 Nihonkai Chubu). Elastic demands were studied by scaling the record 20% (Run 1), while inelastic demands were considered by scaling the record by 400% (Run 2). After Run 1 it was observed minor cracking at the bottom of the specimen. However, during Run 2 significant cracking, spalling, bar buckling and rupture were associated with the ground motion pulses. The failure was characterized by the development of a plastic hinge. Despite the considerable damage at the column base, the specimen did not lose its stability and showed minor residual displacements. The authors found that the measured flexural capacity was smaller than the calculated one due to biaxial interactions. They also observed that the vertical inertial forces did not affect the lateral response because the maximum values in each direction did not occur at the same time. Analytical modeling based on section fibers and viscous damping showed good agreement with experimental results up to the bar buckling, after this point the model underestimated the response.

Johnson *et al.* (2006) conducted experimental and analytical research to evaluate the seismic performance of straight bridges. A  $\frac{1}{4}$ -scale two-span RC bridge containing three two-column bents was tested on three shake tables at the University of Nevada, Reno. The bents had circular sections with the same diameter (12 in.) and different aspect ratios ( $H/d=5, 7.5$  and  $6$ ); the tallest bent was at the middle and the other two at each end of the bridge. Two horizontal acceleration components derived from the 1994 Northridge earthquake (Century City station) were applied to the bridge on successive runs of increasing amplitude. Low and high amplitude coherent accelerations were applied at each bent (shake table) to study the elastic and inelastic response. The superstructure was a solid slab, composed of six beams post-tensioned in the longitudinal and transverse directions. Additional masses were set at the superstructure to account for live-load and scaling effects. From the experimental results it was observed that the bridge performed very well, satisfying the code specified performance for life safety, even under high level of excitation with displacement ductilities as high as 9. It was observed that due to the asymmetric distribution of stiffness (columns with different aspect ratios), the lateral accelerations induced in-plane rotations of the system. As a result, the failure of the bridge occurred when one of the end bents failed in flexure (double curvature) without any signs of shear distress. Additional tests of small amplitude were performed to evaluate the strength redistribution after failure of one bent.

Choi *et al.* (2007) studied the effects of near-fault earthquakes on the seismic performance of a bridge structure designed according to the 2004 Caltrans seismic design criteria. A  $\frac{1}{4}$ -scale RC bridge with the same configuration of that tested by Johnson *et al.* (2006) was subjected to near-fault incoherent accelerations to simulate fault rupture. In

total, six runs of increased acceleration level were used to study the elastic and inelastic behavior of the bridge. Synthetic ground motions with directivity pulses and permanent ground displacements, representative of fault rupture zones, were applied to each shake table. It was observed that incoherent ground accelerations induced in-plane rotations in the bridge, but the failure mechanism was completely different to that in the bridge under uniform excitations. The failure of the bridge occurred when the columns of the middle bent developed plastic hinges at the top and bottom, with large concrete spalling and bar buckling. In addition inclined cracking due to torsion was observed at the midheight of the middle bent.

Nelson *et al.* (2007) investigated the seismic performance of a contemporarily designed straight bridge typical of California subjected to biaxial ground accelerations. A 1/4-scale four-span RC bridge containing three two-column bents and abutment interaction was tested on the three shake table system at the University of Nevada, Reno. The columns at each bent had a circular section with a diameter of 12 in. and different aspect ratios ( $H/d=6, 7$  and  $5$  in bent 1, 2 and 3); the tallest bent was at the middle and the other two at each end of the bridge. Abutment seats driven by hydraulic actuator were designed at each end of the bridge to simulate abutment-soil interaction. The superstructure was composed by twelve beams post-tensioned in the longitudinal and transverse directions. Additional masses were set at the superstructure to account for live-load and scaling effects. The bridge structure was designed in accordance with the provisions of the National Cooperative Highway Research Program (NCHRP) document 12-49. The two horizontal acceleration components from the 1994 Northridge earthquake (Century City station) were applied to the longitudinal and transverse directions of the bridge in seven

successive runs of increased amplitude until failure. It was observed that the bridge performed very well, satisfying the code performance level of life safety, even under rare design earthquakes. As a result of the asymmetry in the lateral stiffness (columns with different aspect ratios), the biaxial accelerations induced in-plane rotations of the bridge. The failure was ductile and occurred when plastic hinges were fully developed in the columns of the shortest bent. While bar buckling, reinforcement rupture and concrete crushing was observed at bent 3, only concrete spalling occurred at bents 1 and 2 at the time of failure. Biaxial bending dominated the behavior of the columns; signs of shear deformations due to torsion were observed at the failure.

Kawashima *et al.* (2009) conducted experimental research to clarify the failure mechanism of bridge RCC designed according to old and new Japanese seismic design specifications. Three real-size circular RCC were tested on a shake table; one column with flexural-dominated behavior typical of 1970s code (C1-2), one column with shear-dominated behavior typical of 1970s practice (C1-1), and a typical column designed according to the current seismic code (C1-5). C1-1 and C2-2 were representative of columns which failed during the 1995 Kobe earthquake. Additional mass was placed on a deck, which was simply supported by the specimen and on rollers at the top of two steel supporting structures. A safety system was also designed to avoid the specimen collapse. All columns had the same height and diameter, but in column C1-2 some of the longitudinal bars were cut-off at midheight following Japanese construction practice prior to 1980. Transverse reinforcement in C1-1 and C1-2 consisted of circular hoops joined using lap-splices, while those of C1-5 used hooks at  $135^\circ$ . A near-field ground motion was used as the input acceleration (1995 Kobe at Takatori station); 80% of the

real earthquake was used in C1-1 and C1-2, while it was scaled to 125% in C1-5. Column C1-1 was subjected to two repetitions of the earthquake; on the first, extensive spalling was observed at the bottom plastic hinge, however during the second motion the lateral capacity was suddenly lost due to the separation of the hoop at lap-splices and buckling of the longitudinal bars. C1-5 resisted four repetitions of the motion; for the first, minor cracking was observed, for the next two motions extensive spalling was observed, but at the last motion the core concrete crushed due compression and pieces of concrete were spilled out of the section, followed by bar buckling. C1-2 failed in shear once the circular hoops yielded at the cut-off zone, several horizontal and inclined cracks were developed until the concrete crushed and the longitudinal bars were moved out of the section. Analytical models using fiber elements and almost zero viscous damping agreed well with the experimental results up to the point of buckling, after this point, the model underestimate the measured response.

From the results of square single columns bidirectionally tested on a shake table, it is noted that for small amplitude acceleration (elastic behavior), the seismic response was almost the same as unidirectionally tested columns; nevertheless, significant reduction in the lateral stiffness and strength was observed for bidirectionally tested columns at large levels of deformation. In addition, more damage and energy dissipation was observed for columns under bidirectional loading. It was also observed that unbonded prestressed tendons inside the RCC were an effective method to reduce residual displacements and control damage at large levels of biaxial acceleration. For the three large-scale bridge models studied it was observed that bridges with straight alignment but with unsymmetrical distribution of lateral stiffness underwent significant



rotations in addition to bilateral loading. These rotations combined with biaxial flexural deformations increased the stiffness degradation. The failure mode was highly dependent of the ground excitation. Near-field ground accelerations with a high velocity pulse can be more severe and resulted in larger residual displacements than far-field uniform excitations. Although the shake table testing of large-scale multi-span bridges is considered the best approximation to the real bridge seismic performance and invaluable data can be obtained from these experiments, the cost and time required to fabricate and test a complete structure is too large for most situations.

### **1.2.7 Dynamic Tests on Interlocking Sections**

Unlike columns with circular, square or rectangular cross sections, columns with double interlocking spirals have been less studied. At the time of this study, only the results of two research programs have been published about the seismic performance of bridge RCC with interlocking spirals tested on shake table; one was undertaken under unidirectional accelerations, while the other was under bidirectional excitations. A brief overview of these studies is presented here. A summary of the characteristics of the columns investigated in each study is presented in Table A-21.

Correal *et al.* (2004) studied the effects of the level of shear stress and the distance between the centers of spirals on the seismic behavior of columns with double interlocking spirals. Two 1/4-scale single RCC with low levels of shear stress and four 1/5-scale with high levels of shear stress, were tested uniaxially on the shake table at the University of Nevada, Reno. The six columns were designed according to the 1999 Caltrans seismic design criteria and were subjected to the 1994 Northridge earthquake

(Sylmar station) in successive runs of increasing amplitudes until failure. Inertial forces were applied using the mass system developed by Laplace *et al.* (1999). Columns with low shear stress were tested in single curvature, whereas those with high shear stress were tested in double curvature. It was observed that the performance of the columns subjected to low shear stresses was similar and satisfactory, with large displacement ductilities; the distance between spirals of 1.5 times the spiral radius ( $d_i=1.5R$ ) did not suffer significant shear distress. Similarly, the columns with  $d_i=1.0R$  and  $d_i=1.25R$  subjected to high shear performed well, however the column with  $d_i=1.5R$  did not achieve the target ductility and vertical cracks were developed on the interlocking area, even for small amplitude motions. Another specimen built with the same section but including cross ties showed a similar behavior but the vertical cracking was controlled. The authors concluded that the Caltrans upper spacing limit of  $d_i=1.5R$  is satisfactory even under high shear, but supplementary cross ties are required to prevent premature vertical shear cracking.

Matsumoto *et al.* (2010) conducted an experimental research aimed to compare the seismic performance of bridge RCC with rectangular and double interlocking sections and subjected to biaxial accelerations typical of near-field earthquakes. Four 1/6-scale single cantilever columns were tested on the shake table at the University of California, Berkeley; two rectangular columns and two with interlocking spirals. The section of the interlocking columns was the same as rectangular, but with the four corners chamfered. All the specimens were designed using both 2002 JRA and 2004 Caltrans seismic design specifications. The 3 components of the 1995 Kobe earthquake (JR Takatori station) were scaled and applied in successive runs of increased amplitude to study different

performance levels. Massive concrete blocks were attached to the top of the column to induce inertial and axial forces in the columns. From the experimental results it was found that the seismic performance of the four columns was satisfactory with minor spalling under the design and ultimate level excitations. After several repetitions of the design earthquake, plastic hinges were developed at the base of the columns, followed by the concrete degradation and bar buckling. The progress of damage was larger in the rectangular columns compared to the interlocking columns mainly due to the concrete spalling at the corners. However the response of the rectangular columns was stable during the complete test protocol. Inelastic time history analyses were conducted using fiber elements, and it was concluded that the analytical response was well simulated until the strength deterioration due to bar buckling.

From the above, it was confirmed that flexure-dominated columns with interlocking spirals designed according to recent seismic design codes behaved satisfactorily well with high level of ductility and energy dissipation when subjected to large accelerations. In addition it was observed that the use of double interlocking spirals was an economic and effective method to provide confinement to rectangular or oblong RC columns subjected to uniaxial or biaxial earthquakes. Even though valuable data has been obtained from the few shake table tests conducted to date, more experimental studies are required to clarify the seismic behavior of this kind of columns under complex loading conditions. The results of these experiments will help in the development of more accurate analytical tools.

### 1.2.8 Literature Review Summary

A general overview of the experimental results on the seismic behavior of RCC under bidirectional loading indicates that shake table testing can simulate realistically dynamic features that cannot be identified in quasi-static or pseudo-dynamic tests. When bidirectional effects are important, poor detailing and large values of axial loads can increase the susceptibility of columns to undergo loading interactions. As a result, significant stiffness and strength degradation can be observed, which at large levels of deformation can lead to a loss of the column capacity and its lateral stability.

Experimental results have shown that the use of circular spirals or double interlocking spirals is an economical and efficient method to confine the core concrete at plastic zones, even at large deformations when the bar buckling may occur. The ability of the spiral configuration to restrain the lateral deformation of the longitudinal reinforcement leads to large displacement ductilities. To get similar confinement properties a considerable amount of hoops and cross ties will be required.

Studies of bridge RCC under combined bending, torsion and axial force have shown that the magnitude of torsion and compressive axial loading can adversely affect the flexural capacity, ductility, and strength and stiffness degradation of the columns. Values of the torque to bending ratio ( $T/M$ ) larger than 20% lead to a considerable reduction in the flexural capacity and ductility of the columns, and shifted the plastic hinge from the bottom to the midheight of the column.

The results of shake table tests on multi-span bridges with straight alignment and column-bents with different aspect ratios showed that bridges can undergo significant rotations in addition to the bilateral loading, as a consequence of the unsymmetrical

distribution of lateral stiffness and strength of the columns. It was also observed that the characteristics of the ground acceleration have a significant influence in the failure mode. Near-fault ground accelerations with forward directivity effects (high asymmetric velocity pulse) can be more severe and result in large residual displacements than far-field uniform excitations.

Analytical models developed and calibrated with experimental results have shown that inelastic models using fiber elements provide a good approximation to the nonlinear behavior of columns. However bidirectional loading, confined concrete degradation and bar buckling result in underestimations of the strength and displacement capacity.

During the last few decades the experimental methods to study the seismic performance of bridge columns have evolved dramatically from quasi-static uniaxial testing of single cantilever small-scale columns to shake table testing of large-scale bridge structures subjected to complex loading and systems interactions. Although the later experimental method represents the best approximation to the real bridge seismic performance, the cost and time required to build, test and analyze the recorded data for a complete structure is too large. In addition, the complex system interactions and limitations of the instrumentation make difficult capturing the bridge column response. Therefore, shake table testing of single cantilever columns subjected to different levels of biaxial bending, axial force and torsion are required to validate analytical models and design methods. In previous experimental studies of single columns subjected to biaxial loads, large concrete blocks were used to induce axial and inertial forces. As a result, the lateral deformations were affected by second mode contributions, and made the column more susceptible to shear deformations. Therefore, a test setup is needed with the

capability to induce the abovementioned load combinations with the adverse effects to characterize the seismic response of bridge column.

### **1.3 Design Guidelines for Columns Reinforced with Spirals and Interlocking Spirals**

The preferred mode of failure of bridges with single-column bents under seismic loads is flexure. Therefore RC columns need to be designed in such way that the earthquake loads are resisted through ductile inelastic deformations and premature failure, like shear, slippage or anchorage be avoided. In order to withstand these ductility levels, special reinforcement details need to be followed to ensure an effective confinement of the columns at the regions of high inelastic deformations (plastic hinges). Since at the time of design of the columns of this study, Caltrans was the only code in the United States that had provisions for both single spirals and double interlocking spirals, their documents: Seismic Design Criteria (SDC, 2006) and Bridge Design Specifications (BDS, 2006) are described here.

#### **1.3.1 2006 Caltrans Seismic Design Criteria Overview**

The 2006 Caltrans Seismic Design Criteria (SDC) version 1.4, is a design methodology based on displacements. Accordingly, the displacement capacity of the sections (columns) needs to be checked against the expected displacement demand obtained from mean spectral accelerations. These spectral accelerations can be determined from acceleration response spectrum (ARS) curves specified for different soil profiles and earthquake magnitudes typical of California. To account for the near-fault earthquakes, SDC recommends amplification factor of up 20% of the demands of the

ARS curves for structures with vibration periods between 0.5 and 1 seconds. Columns need to be designed to resist a minimum lateral force of 10% the tributary dead load ( $0.1P_{DL}$ ). P-delta effects need to be considered in the analysis, if the base moment induced by these effects exceeds 20% of the plastic moment capacity of the column.

### **1.3.2 Displacement Ductility**

Displacement ductility is a measure of the post-elastic deformation of a member. In order to insure ductile behavior SDC section 2.2.4 specifies minimum target ductility ( $\mu_d$ ) of 4 for single column bents supported on fix foundation.

### **1.3.3 Maximum and Minimum Longitudinal reinforcement**

The area of longitudinal reinforcement for compression members in the SDC is specified in section 3.7 by imposing minimum and maximum values of  $0.01A_g$  and  $0.04A_g$ , where  $A_g$  is the gross area of the section. Moreover, BDS in 8.18.1.2 specifies a minimum number of longitudinal bars of 6 and 4 for circular and rectangular arrangement, respectively, and with a minimum bar size of No.5. For interlocking columns, BDS section 8.18.1.4, specifies that the spacing center to center of the spirals be less than 1.5 times the diameter of each cage, and be interlocked by a minimum of four bars. In addition, SDC section 3.6.5.3, specifies that the maximum lateral spacing of longitudinal bars in the interlocking portion is limited to 8 in. The size of the bars in the interlocking portion depends on the size of the bars outside the interlocking portion.

### 1.3.3 Confinement Reinforcement

In order to fulfill the displacement ductility requirement and increase the shear capacity of the section, a minimum amount of spiral reinforcement or welded circular hoops needs to be provided inside the plastic hinge length of a column. SDC section 3.8.1, defines the minimum amount of lateral reinforcement for columns with circular or interlocking core sections in terms of a volumetric spiral reinforcement ratio, which is given by:

$$\rho_s = \frac{V_{spiral}}{V_{core}} = \frac{4 A_b}{D_c S} \quad (1-1)$$

Section 8.18.2.2 of BDS, requires that the volumetric spiral ratio inside the plastic hinge zone for columns with a diameter less than 3 ft., be larger than:

$$0.45 \left( \frac{A_g}{A_c} - 1 \right) \frac{f'_c}{f_{yh}} \left( 0.5 + \frac{1.25 P_e}{f'_c A_g} \right) \quad (1-2)$$

Or for column with diameter larger than 3 ft, larger than:

$$0.12 \frac{f'_c}{f_{yh}} \left( 0.5 + \frac{1.25 P_e}{f'_c A_g} \right) \quad (1-3)$$

But not less than:

$$0.45 \left( \frac{A_g}{A_c} - 1 \right) \frac{f'_c}{f_{yh}} \quad (1-4)$$

Where:

$V_{spiral}$  = volume of the spiral or interlocking spiral

$V_{core}$  = volume of the core



$A_b$  = area of the spiral or hoop

$D_c$  = confined concrete core area, measured between the centerline of spirals

$s$  = spacing of spiral or hoop along the height of the column

$A_g$  = area of the gross section

$A_c$  = area of core section, measured at the outside diameter of the spiral

$f'_c$  = concrete compressive strength

$f_{yh}$  = specified yielding strength of hoops or spirals

$P_e$  = design axial load due to gravity and seismic loading combination

In addition, SDC section 8.2.5, specifies that the maximum spacing of transverse reinforcement in the plastic hinge zone need to be the less of:

- 1/5 of the least dimension of the cross section for a column and 1/2 of the least dimension of the cross section for a pier
- Six times the nominal diameter of the longitudinal reinforcement
- 8 in

#### 1.3.4 Shear Capacity

In order to prevent premature failure due to shear stresses, the shear capacity shall be larger than the maximum probable shear in the section when the plastic moment is developed in the column. Therefore:

$$\phi V_n \geq V_o \quad (1-5)$$

Where:

$V_o$ = plastic shear associated with the overstrength moment,  $M_o=1.2 M_p$

$\phi$  = strength reduction factor (0.85)

$V_n$ = nominal shear strength,  $V_n=V_c+V_s$

$V_c$ = shear capacity provided by concrete

$V_s$ = shear capacity provided by reinforcement

According to SDC section 3.6.2 the shear capacity provided by the concrete is calculated as:

$$V_c \geq v_c A_e \quad (1-6)$$

inside the plastic hinge  $v_c = F1xF2x\sqrt{f'_c} \leq 0.33\sqrt{f'_c}$  (1-7)

outside the plastic hinge  $v_c = 3F2x\sqrt{f'_c} \leq 4\sqrt{f'_c}$  (1-8)

$$F1 = 0.3 \geq \frac{\rho_s f_{yh}}{0.150} + 3.67 - \mu_d < 3 \quad (1-9)$$

$$F2 = 1 + \frac{P_c}{2000 A_g} < 1.5 \quad (1-10)$$

Where:

$v_c$ = permissible shear stress contributed by concrete, ( $v_c=0$  if tension axial load)

$A_e$ = effective shear area (0.8  $A_g$ )

$A_g$ = gross area of the section (in<sup>2</sup>)

$f'_c$ = concrete compressive strength (psi)

$\rho_s$ = volumetric spiral ratio

$f_{yh}$ = nominal yielding strength of spirals (ksi)

$\mu_d$ = displacement ductility demand

$P_c$ = axial force in the columns (lb)

According to SDC section 3.6.3 the shear capacity provided by the transverse reinforcement is calculated as:

$$V_s = \frac{A_v f_{yh} D_c}{s} \quad (1-11)$$

$$A_v = n \left( \frac{\pi}{2} \right) A_b \quad (1-12)$$

$$A_v \leq 8 \sqrt{f'_c} A_e \quad (1-13)$$

For interlocking spirals  $A_v \geq 0.025 \frac{D_c s}{f_{yh}}$  (1-14)

Where:

$A_v$ = total area of shear reinforcement

$n$ = number of interlocking spirals core sections

## **1.4. Objectives and Scope**

The main objective of the research presented in this document was to investigate the seismic performance of RC single-column bents subjected to biaxial ground excitations through an experimental study on a shake table and analytical verification. This project was a component of a collaborative multi-university research sponsored by the National Science Foundation, and uses the Network for Earthquake Engineering Simulation (NEES). Information about the objectives and scope of the overall project as well as the specific study presented in this document, are presented in this section.

### **1.4.1 Overall Project (CABER)**

In an effort to understand the complex behavior of bridge members under combined earthquake actions and its impact on system response, a collaborative project integrating analytical and experimental research at multiple universities across the United States was established in 2006. The goals of the project include: (a) investigate experimentally bridge columns with different sections under various load conditions including constant and variable axial load, bidirectional motions and torsion, by using quasi-static, pseudo-dynamic and dynamic testing methods; (b) examine bridge configurations to determine their susceptibility to load combinations; (c) development of analytical tools to be used by researchers and designers to accurately account for load combinations; (d) development of refined behavioral model and simplified analysis procedures to account for load combinations; (e) distributing research results to engineering and non-engineering communities through educational modules.

Experimental studies were conducted at three US institutions: (1) quasi-static tests on large-scale single cantilever columns with circular and noncircular sections at Missouri University of Science and Technology (MS&T) to determine the direct interaction of bending, shear and torsion under constant axial loading; (2) real time dynamic shake table tests on large-scale specimen with circular and oval sections subjected to different levels of biaxial ground acceleration, torsion and axial load at University of Nevada, Reno to examine the effects of combined dynamic loading on the performance of columns; (3) pseudo-dynamic tests on large and small scale columns subjected to different level of axial and lateral loads using the loading and boundary condition boxes (LBCB) at University of Illinois at Urbana-Champaign (UIUC) to study the impact of varying axial load on flexural-shear-axial interaction; (4) pseudo-dynamic tests of a 4-span curve bridge at UIUC in a joint effort between researchers at George Washington University and University of Illinois at Urbana-Champaign to verify local and global analytical models developed in the course of the project. Prototype columns were designed and constructed following bridge design specifications for structures in regions of high seismicity.

Analytical studies were conducted at three US universities: (I) study of bridge configurations and definition of ground excitations, as well as constitutive material modeling to combine flexural, shear and axial deformation in lump-plasticity elements at University of California, Los Angeles (UCLA); (II) constitutive material models to account for combined axial/bending/shear and torsional actions in nonlinear fiber elements with distributed plasticity at University of Houston (UH); (III) development of

nonlinear time history analyses of bridge structures subjected to the two horizontal and one vertical component of earthquakes at UIUC.

By combining experimental and analytical results, the project will have an impact on the engineering community by developing new design methodologies to account for the effects of combined loads in components and system response. In addition, code changes will be proposed to account for experimentally validated load combination interaction curves.

The team name for the project was CABER, which stood for Combined Actions on Bridge Earthquake Research.

#### **1.4.2 Study at University of Nevada Reno**

In order to examine the effects of the two horizontal component of the ground acceleration, the level of axial force, as well as in-plane rotation of the superstructure (torsional effects), single cantilever columns reinforced with circular and interlocking spirals were dynamically tested.

To achieve this objective a unique inertial loading system: Bidirectional Mass Rig (BMR) was developed to test single cantilever-type columns on a biaxial shake table at University of Nevada, Reno. This system was designed to provide a supporting structure which safely carried the vertical component of the inertial mass (superstructure weight) but allowed transferring bidirectional inertial forces from that structure to the specimen. The system also has the ability to induce torsional effects in the column specimen by placing the inertial masses in an unsymmetrical configuration. The axial force is applied to the specimen through a ram equipped with a servo-valve, which is connected to the

specimens through an unbonded prestressed bar placed in an ungrouted conduit at the middle of the column and anchored at the footing. Since the BMR does not induce secondary moments (P-delta effects) in the specimen and the unbonded prestressed bar inside the column would generate restoring lateral forces, additional dynamic actuators are used at the top of the specimen to induce the equivalent force to the P-delta effects and for the restoring force.

Due to the complexity of the system in terms of the active control of dynamic actuators, the experimental program was divided in two phases. At the beginning a set of two circular and two interlocking columns were tested without any axial load or P-delta effects. A second phase will incorporate all the effects. Table 1-1 outlines the test matrix for the entire research project.

The first phase of the experimental program is the goal of the present study and was aimed to:

- 1) Develop and experimentally validate the effectiveness of the Bidirectional Mass Rig for testing single cantilever columns under real time biaxial earthquakes;
- 2) Studying the impact of biaxial ground acceleration on the seismic performance of circular and interlocking columns designed according to Caltrans specifications;
- 3) Investigate the effects of combined torsion and biaxial bending on the seismic response of columns tested without axial force;
- 4) Compare experimental results of similar RCC tested on a shake table under unidirectional and bidirectional ground excitations;
- 5) Examine the ability of analytical models to predict the measured response; and

- 6) Evaluate analytically the seismic response of circular and interlocking bridge columns subjected to different load conditions.

In order to satisfy these objectives, four large-scale single cantilever-type columns were constructed using materials and current design details typical of bridges in California in accordance with the 2006 Caltrans seismic design criteria. The structural configuration was similar to previous columns tested unidirectionally at Nevada with flexural-dominated behavior (Laplace *et al.*, 1999 and Correal *et al.*, 2004). Two of the specimens were 1/3-scale circular columns with an aspect ratio of 4.5 and were subjected to the two horizontal components of the 1992 Petrolia earthquake at Mendocino, California. Likewise, two 1/4-scale oval specimens with interlocking spirals were subjected to the two horizontal components of the 1994 Northridge earthquake recorded at the Sylmar station. All the specimens had the same height (72 in) and were subjected to successive runs of increasing acceleration amplitude until failure, and without applying any axial load. They were also designed to fail in a ductile mode (flexure-dominated behavior). The only difference, between the two identical columns, was the way in which the mass was distributed on the BMR; for one circular and one interlocking column a symmetric distribution of masses was used, while it was asymmetric for the other two columns, hence, more torsion was expected. The seismic performance of the specimens was assessed in terms of hysteretic response (strength and deformation), strain rate, plastic hinge length and failure mode

In order to validate the effectivity of analytical methods in capturing performance characteristics of conventional RC bridge columns, different approaches were



implemented in OpenSees (PEER, 2006) in attempt to reproduce the measured response of the tested specimens.

## **1.5. Organization**

Chapter 1 presents the introductory remarks with an overview of the project, as well as an extensive literature review of experimental research on columns under bidirectional loading. The similitude requirements, the design of the specimens and preliminary analysis are described in Chapter 2. The specimen details and test setup, instrumentation and input ground accelerations are presented in Chapter 3. The observed behavior and experimental results for circular columns and interlocking columns are described in Chapters 4 and 5, respectively. Chapter 6 summarizes the experimental results of previous columns tested at University of Nevada, Reno under uniaxial ground accelerations, along with comparisons of the seismic performance of columns under unidirectional and bidirectional loading. Different analytical approaches to attempt to reproduce the measured responses are described in Chapter 7. Chapter 8 presents the results of analytical models of the columns subjected to one or two components of different earthquakes. Finally, conclusions and recommendations are presented in Chapter 9. In addition three appendices were included to provide further information about different aspects of the study. Appendix A, present a database of the main characteristics of the columns experimentally tested in previous studies and discussed in the literature review. The flexural and shear capacity of the specimens are evaluated according to the 2006 Caltrans SDC and 2004 Caltrans BDS in Appendix B. Appendix C

presents, for each specimen, plots of the cumulative strains recorded by different strain gauges during the complete test protocol.

## **Chapter 2. Specimen Design and Preliminary Analysis**

### **2.1. Introduction**

The research program at the University of Nevada, Reno was focused on studying the seismic performance of reinforced concrete bridge columns of both circular and non-circular sections (double interlocking spirals) subjected to different levels of biaxial bending, torsion and vertical loads through real time earthquake motions. For this purpose, four scaled single columns were subjected to bidirectional excitations on a shake table system. Two 1/3-scale circular columns and two 1/4-scale double interlocking spirals were constructed, instrumented and tested at the University of Nevada, Reno Large Scale Structures Laboratory. A new inertial loading system, termed Bidirectional Mass Rig was developed as part of the study to test on shake table single cantilever-type columns under bidirectional dynamic actions.

This chapter describes the prototype selection, the specimens design criteria, the modeling procedure and preliminary analysis performed for the reinforced concrete (RC) specimens.

### **2.2. Prototype Columns**

For comparison purpose, the selection of the circular and double interlocking specimens was based on previous unidirectional shake table tests developed at UNR. The circular column configuration was identical to the specimens 9F1, tested by Laplace *et al.* (1999) and NF1 tested by Phan *et al.* (2005), while the interlocking columns were based on the specimen ISL1.0 tested by Correal *et al.* (2004). In all cases, the test specimens

were designed using details typical of bridges in California and in accordance with the *Seismic Design Criteria* (CALTRANS, 1992, 2001); those specimens were designed to have a flexure dominated behavior under unidirectional ground motions.

According to Laplace *et al.* (1999), the RC circular column prototype was a 48 in. diameter and 18 ft. tall column with aspect ratio of 4.5. The column had an axial load of  $0.1A_gf'_c$ , where  $A_g$  is the gross section of the column and  $f'_c$  is the nominal compressive strength of the concrete, specified as 4000 psi. The longitudinal and transverse steel ratios were specified to be 2% and 0.95%, respectively.

The double interlocking spiral prototype column was designed to have two identical circular steel cages interlocked on a distance equivalent to one time the radius of the circular cage in an oval configuration. Thus, the dimensions were 70 in. on the long side and 48 in. on the short side, while the height was specified as 19.3 ft. Since the model column was designed to be tested parallel to the long side, the aspect ratio was 3.3. The column axial load was specified to be  $0.1A_gf'_c$  based on a nominal strength of the concrete of 5000 psi. A longitudinal steel ratio of 2% and transverse volumetric steel ratio of 1.1% were chosen to be typical of design according to *Caltrans* provisions.

Both prototype columns were designed as cantilever-type columns with a fixed end condition at the footing and pinned at the top. Additionally, the inertial mass tributary to the column was specified as the axial load supported by the column divided by the gravity. This mass was considered only to excite the lateral inertial forces without any rotational effect.

### **2.3. Specimen Design**

Limitations in space, as well as on the testing equipment and the cost associated with the fabrication and testing prohibits the use of full scale prototypes for experimentation, therefore reduced scale models were used. This is especially true for the shake table facility at University of Nevada, Reno, where the physical dimension of the shake tables, as well as the maximum displacement, acceleration, velocity and weight of the specimens allow the use of scaled models in the range of  $\frac{1}{4}$  to  $\frac{1}{2}$ . Reinforced concrete specimens tested using these scale factors are considered large enough to resemble the dynamic behavior of the prototype structures. As a result of these considerations, the dimension of the prototype columns were scaled down using a factor of  $\frac{1}{3}$  and  $\frac{1}{4}$  for the circular and interlocking specimens, respectively.

#### **2.3.1. Modeling Procedure**

The theory of modeling establishes the relationships in geometry, material properties, loads and boundary conditions between the model and prototype. These relationships called scale factors are determined through dimensional analysis. For the case of statically or quasi-statically loaded specimens, those scaled factors are calculated in a relatively straightforward way. However for the case of dynamic loads, time and time-dependant parameters such as acceleration, velocity and strain rate effects must also be considered in the dimensional analysis.

According to Tomazevic *et al.* (1992) two extreme cases of modeling similitude can be established: complete and simple model similarity. In the first case, all requirements of a dimensional analysis are satisfied, it implies that special model material

will be manufactured to have their stress-strain properties scaled with respect to the prototype, at the same time the specific weight, Poisson's ratio and damping properties are required to be the same as in the prototype. In the simple model some similitude requirements are relaxed and it is possible to use the same materials in the model as in the prototype.

The specimens built and tested as part of this study, were designed using simple similitude models, in which, real concrete and steel materials were used. In addition, it was specified that the accelerations in the model and the prototype would be identical to ensure that the stresses and strains in the model would be the same as in the prototype. Table 2.1 summarizes the dimensional similitude requirements used in this study.

### **2.3.2. Circular Columns**

The dimensions of circular columns were based on a 1/3-scale of the prototype. Therefore, the diameter of the specimens was 16 in., and the height was 72 in. providing an aspect ratio of 4.5; which allows for flexural dominated behavior. The height was taken as the distance from the top of the footing to the centerline of the column head where the inertial load was applied. The columns were reinforced with 20 No.4 deformed longitudinal bars, distributed uniformly around the perimeter and fully developed with 90 degree hooks in the footing. This resulted in a longitudinal reinforcement ratio of 2%. The confinement consisted of a continuous spiral made from galvanized smooth steel wire with a diameter of 0.25 in. (W5.0) and a pitch of 1.5 in. The concrete clear cover was set to 0.75 in., and the resulting volumetric ratio of the spiral reinforcement was 0.92% (see Fig. 2-1). The nominal concrete strength was set as 4500 psi. Details of the

circular specimens are shown in Figs. 2.2 and 2.3. The bending and shear capacity of the columns were verified following the 2006 Caltrans Seismic Design Criteria (SDC) and 2000 Caltrans Bridge Design Specifications (BDS) as can be seen in Appendix B.

### **2.3.3. Interlocking Columns**

A scale factor of 1/4 was used for double interlocking columns. Consequently, the height was 72 in., and the diameter in the short side was 12 in., and 17.5 in. in the large side. The longitudinal reinforcement consisted of 32 No.3 deformed bars, spaced evenly in two circular patterns and fully developed with 90 degree hooks inside the footing. The resulting reinforcement ratio was approximately 2%. The confinement for each of the circular patterns consisted of a continuous spiral made from galvanized steel wire with a diameter of 0.192 in. (W2.9) and a pitch of 1.0 in. The clear cover was set to 0.5 inches and the resulting volumetric ratio of the spiral reinforcement was 1.05% (see Fig. 2-1). The nominal concrete strength was specified to be 4500 psi. Details of interlocking specimens are shown in Figs. 2.5 and 2.6. Appendix B presents the bending and shear capacity of the columns, calculated following the 2006 Caltrans Seismic Design Criteria (SDC) and 2000 Caltrans Bridge Design Specifications (BDS).

### **2.3.4. Footing and Top Head**

Strong footings were used to attach the specimens to the shake table. Since all the specimens were planned to behave as cantilever members, the dimensions and reinforcement of the footings were designed in such way that the plastic moment capacity of the column at the base were resisted elastically and without any damage. In addition, the footing was designed to not exceed the capacity of the tie down points in the shake

table, and to prevent uplift. Thus the dimensions of the footing were selected as 64 in. x 64 in., while the height was 28 in. The height of the footing was selected in such way that the top of the column could be properly connected to the inertial loading system and to provide enough anchorage length for the longitudinal bars. Sixteen 3-in. diameter PVC ducts were cast in the footing to allow the coupling and pretension of the specimen to the shake table deck. The specimens were fully anchored to the table deck using a system of sixteen 1 ¼ in. Dywidag bars prestressed to a maximum force of 30 kips.

For the circular columns the footing reinforcement consisted of two top and bottom mats of 8 No. 4 deformed bars in each direction. Similar top and bottom mats were used for the interlocking columns with the same configuration but made with No.5 deformed bars. In addition, No. 3 cross ties were used at each joint to connect the top and bottom mats. The lateral concrete cover was set as 1 in., while the top and bottom was 1.5 and 2.0 in, respectively. Additionally, four No.10 lift hooks were included in each footing for transportation purposes. Details for the footings in the circular and interlocking specimens are shown in Figs. 2.4 and 2.7, respectively.

A concrete loading top head was designed to connect the inertial mass system to the specimens. Since a low stress level was expected at the point of connection, the dimensions and reinforcement were selected to have elastic behavior. Dimension of the loading head were 24 in. x 24 in. x 22 in., in length, width and height. Four vertical No.4 bars at each corner and 4 No.4 ties were used to confine the concrete. Four 2 in. diameter PVC ducts were cast in two perpendicular faces of the columns to provide holes for the bolts in order to attach the specimen to the loading system in the two horizontal directions. The longitudinal bars were bent at the top of the column in the head region to



allow space for the PVC ducts. The concrete cover was set as 1 in. on all sides of the top loading head. Details of the loading top heads are shown in Figs. 2.4 and 2.7.

The nominal strength of the concrete for the footings was set as 5000 psi, whereas that for the top loading heads was the same as the columns, 4500 psi. These nominal concrete strengths were chosen to be typical of bridge design according to the *Seismic Design Criteria* (CALTRANS, 2006).

## **2.4. Preliminary Analysis**

In order to design and anticipate the seismic performance of the specimens, different analytical approaches were used. Initially, nonlinear cross sectional analyses were developed to determine the moment-curvature ( $M-\phi$ ) curves for the specimens. Once the  $M-\phi$  curves were calculated, the lateral load and displacement capacities of the specimens were estimated from idealized moment-curvature relationships at discrete points (cracking, yielding, ultimate). Once the capacity was estimated and the maximum displacement ductility defined, inelastic pushover analyses were conducted to determine the force-displacement relationships.

### **2.4.1. Moment-Curvature Analysis**

The nonlinear cross sectional analyses of the specimens were developed using the program XTRACT (TRC/Imbsen, 2007). In this software the cross section geometry is modeled using refined meshes of fibers, each of which it is characterized by a uniaxial constitutive model for the material it represents. The model assumes Navier-Bernoulli hypothesis of plane sections and strain compatibility. The moment-curvature ( $M-\phi$ ) curve

is obtained by calculating the section moment corresponding to a certain imposed curvature and axial load. This is achieved by iteratively solving for a neutral axis depth that satisfied axial load equilibrium.

For the sections analyzed, three different types of materials were used: unconfined concrete for the concrete cover, confined concrete for the core concrete and steel bars for the longitudinal reinforcement. The stress-strain relationship for the concrete was represented using Mander's model (Mander et al., 1988), while the reinforcement was modeled as steel with a parabolic strain hardening.

The stress-strain relationship for cover concrete was modeled using the unconfined properties for Mander's model. As can be seen in Fig. 2-8, this model consists of two segments. The first segment is a parabolic curve representing the behavior from zero up to the crushing strain, and its strength is given by:

$$f_c = \frac{f'_c x r}{r - 1 + x^r} \quad (2-1)$$

Where:

$$f_c = \text{concrete stress}$$

$$f'_c = \text{nominal compressive strength at 28 days}$$

$$x = \frac{\varepsilon_c}{\varepsilon_{cc}}$$

$$r = \frac{E_c}{E_c - E_{sec}}$$

$$E_c = 57,000\sqrt{f'_c} \text{ [psi]}$$

$$E_{sec} = \frac{f'_c}{\varepsilon_{cc}}$$

$\varepsilon_c$  = concrete strain

$\varepsilon_{cc}$  = strain at peak stress (0.002)

$E_c$  = elastic modulus

$E_{sec}$  = secant modulus

The second segment represents the strength degradation in the crushed concrete. The behavior of the concrete in this segment is modeled by a descending straight line connecting the points at crushing and spalling strains. The stress in this region is given by:

$$f_c = f_{cu} + (f_{cp} + f_{cu}) \frac{(\varepsilon - \varepsilon_{cu})}{(\varepsilon_{sp} - \varepsilon_{cu})} \quad (2-2)$$

Where:

$\varepsilon_{cu}$  = ultimate or crushing concrete strain (0.004)

$f_{cu}$  = stress at  $\varepsilon_{cu}$

$f_{cp}$  = post spalling strength

$\varepsilon_{sp}$  = spalling strain (0.006)

For the core concrete, the stress-strain relationship was represented using Mander's model for confined concrete (Mander et al., 1988). This model consist of a parabolic curve representing the concrete behavior up to the crushing strain; once this strain is reached, the section is assumed to have failed and analysis will cease (see Fig. 2-9). The stress-strain curve can be described by the expression:

$$f_c = \frac{f'_{cc} x r}{r - 1 + x^r} \quad (2-3)$$

Where:

$f_c$  = concrete stress

$f'_{cc}$  = confined concrete compressive strength

$$x = \frac{\epsilon_c}{\epsilon'_{cc}}$$

$$r = \frac{E_c}{E_c - E_{sec}}$$

$$E_c = 57,000\sqrt{f'_c} \text{ [psi]}$$

$$E_{sec} = \frac{f'_{cc}}{\epsilon'_{cc}}$$

$\epsilon_c$  = concrete strain

$\epsilon'_{cc}$  = strain at concrete compressive strength

$E_c$  = elastic modulus

$E_{sec}$  = secant modulus

The compression strength of the confined concrete,  $f'_{cc}$ , is related to the unconfined compression strength and the effective lateral confining pressure by:

$$f'_{cc} = f'_c \left( 2.254 \sqrt{1 + \frac{7.94 f_l}{f'_c}} - 2 \frac{f_l}{f'_c} - 1.254 \right) \quad (2-4)$$

For circular and double interlocking sections, the effective lateral confining stress,  $f_l$ , is given by:

$$f_l = \frac{2 A_{sh} f_{yh}}{d_s s_h} \quad (2-5)$$

Where:

$A_{sh}$  = spiral or hoop cross-sectional area

$f_{yh}$  = spiral or hoop yielding strength

$d_s$  = diameter of the confined core

$s_h$  = spacing of the spiral or hoop along the column

The confined concrete compressive strain,  $\epsilon_{cc}$ , and the ultimate compressive strain,  $\epsilon_{cu}$ , are defined by:

$$\epsilon_{cc} = 0.002 \left[ 1 + 5 \left( \frac{f'_{cc}}{f'_c} - 1 \right) \right] \quad (2-6)$$

$$\epsilon_{cu} = 0.004 + \frac{1.4 \rho_s f_{yh} \epsilon_{su}}{f'_{cc}} \quad (2-7)$$

Where:

$$\rho_s = \frac{4 A_{sh}}{d_s s_h}$$

$\rho_s$  = volumetric transversal steel ratio

$\epsilon_{su}$  = steel strain at maximum tensile stress

The concrete tension strength was ignored since its contribution to flexural strength is normally negligible.

The monotonic stress-strain response of the longitudinal reinforcement was represented using a three segments model (see Fig. 2-10). The first segment represents the elastic range, where the stresses are linearly proportional to the strains and where the slope is the steel elastic modulus,  $E_s$ . The second portion represents the yield plateau where the strain increases with no noticeable increase in stress. The third segment represents the parabolic hardening, where the material experiences an increased resistance to further deformation. The behavior of the steel can be represented by the following expressions:

$$\text{Elastic} \quad 0 \leq \varepsilon_s \leq \varepsilon_y \quad f_s = E_s \varepsilon_s \leq f_y \quad (2-8)$$

$$\text{Yield plateau} \quad \varepsilon_y \leq \varepsilon_s \leq \varepsilon_{sh} \quad f_s = f_y \quad (2-9)$$

$$\text{Strain hardening} \quad \varepsilon_{sh} \leq \varepsilon_s \leq \varepsilon_{su} \quad f_s = f_u \left[ 1 - (f_u - f_y) \left( \frac{\varepsilon_{su} - \varepsilon_s}{\varepsilon_{su} - \varepsilon_{sh}} \right)^2 \right] \quad (2-10)$$

Where:

$f_s$  = steel stress

$f_y$  = yielding stress

$E_s$  = steel elastic modulus

$\varepsilon_s$  = steel strain

$\varepsilon_y$  = yielding strain

$\varepsilon_{sh}$  = strain at beginning of strain hardening

$\varepsilon_{su}$  = ultimate tensile strain

The material properties used for the preliminary  $M-\phi$  analysis were based on cylinders and coupons tested on previous studies at UNR (Laplace *et al.*, 1999 and Correal *et al.*, 2004), and are summarized in Table 2-2. Using these properties and the geometry of the sections, the concrete and steel stress-strain properties were determined as shown in Table 2-3. The cross sectional geometries were modeled using the drawing and discretizer options in XTRACT (see Fig. 2-11). For that, meshes of 1726 and 1264 fibers were implemented for the circular and interlocking sections, respectively.

Two extreme cases for the axial load were studied: columns without axial force and columns with an axial load equivalent to  $0.1f'_cA_g$ , which for the scaled specimens and nominal concrete strengths was calculated to be 80 kips. Biaxial effects were included in the moment-curvature analysis by applying curvatures around the neutral axis, which is inclined with respect to the horizontal. Since the circular sections have radial symmetry (the  $M-\phi$  capacity is the same around any inclined axis), only analyses at  $0^\circ$  and  $45^\circ$  were conducted for this section (See Figs. 2-12 and 2-13). The interlocking sections moment-curvature analyses were performed for inclination of the N.A from  $0^\circ$  through  $90^\circ$  with  $15^\circ$  increments. Typical  $M-\phi$  curves for interlocking sections are shown in Figs. 2-14 and 2-15. As can be seen in Figs. 2-12 through 2-15, the moment-curvature curves were idealized as bilinear models containing a primary and secondary slope of the cross sectional stiffness. The secondary slope was found in such a way that both the ultimate curvature and the ultimate moment of the bilinearization match the values for the calculated curve and by balancing the areas between the actual and the idealized  $M-\phi$  curves beyond the first reinforcing bar yield point. Tables 2-4 and 2-5 summarize the

values calculated for the idealized M- $\phi$  curves for different inclinations of the N.A. The curvature ductility was calculated as:

$$\mu_{\phi} = \frac{\phi_u}{\phi_y} \quad (2-11)$$

Where:

$\phi_y$  = yielding curvature

$\phi_u$  = ultimate curvature

In addition to biaxial moment-curvature analysis, a moment-moment interaction analysis (capacity orbit) was conducted. The capacity orbit is essentially a graph that shows the interaction between moments applied at varying inclinations of the N.A., and is found by cutting the three dimensional axial force-moment interaction surface at a specific axial load level. XTRACT was used to calculate the moments (and curvatures) corresponding to the failure strain. Figs. 2-16 and 2-17, show the capacity orbits (moments and curvatures) for the circular and interlocking sections for different levels of axial load

#### **2.4.2. Lateral Force-Displacement Prediction**

For single cantilever type columns the relationship between curvature and displacements can be simply found by integrating the curvature distribution along the height of the member and using the plastic hinge concept. The plastic hinge is defined as the region of a member over which strain and curvatures are considered to be equal to the maximum. The main parameter defining the plastic hinge region is its extension over the length of the column or plastic hinge length ( $L_p$ ). Theoretical values for  $L_p$  have been



proposed based on experimental test results; one of the most widely used is the Priestley's model (Priestley *et al.*, 2007). Priestley's model allows determining the ultimate displacement at the tip of the cantilever column as the summation of the yielding and plastic displacements (Fig. 2-18). The curvature distribution above the plastic hinge is idealized as linear (Fig. 2-19). The inelastic behavior is then defined by the following expressions:

$$\Delta_u = \Delta_y + \Delta_p \quad (2-12)$$

Where:

$$\Delta_y = \phi_y \frac{(L_c + L_{sp})^2}{3}$$

$$\Delta_p = \phi_p L_p L_c = (\phi_u - \phi_y) L_p (L_c - 0.5 L_p)$$

$\Delta_y$  = yielding lateral displacement

$\Delta_p$  = plastic lateral displacement

$\Delta_u$  = ultimate lateral displacement

$\phi_y$  = yielding curvature

$\phi_p$  = plastic curvature

$\phi_u$  = ultimate curvature

$L_{sp}$  = strain penetration length

$L_p$  = plastic hinge length

$L_c$  = distance from point of maximum moment to the point of contra-flexure

The plastic hinge length is given by the expression:

$$L_p = k L_c + L_{sp} \geq 2L_{sp} \quad (2-13)$$

Where:

$$k = 0.2 \left( \frac{f_u}{f_y} - 1 \right) \leq 0.08$$

$$L_{sp} = 0.15 f_y d_{bl}$$

$f_u$  = ultimate strength of the longitudinal bars [ksi]

$f_y$  = yielding strength of the longitudinal bars [ksi]

$d_{bl}$  = diameter of the longitudinal bars [in<sup>2</sup>]

The displacement ductility was calculated as:

$$\mu_{\Delta} = \frac{\Delta_u}{\Delta_y} \quad (2-14)$$

Tables 2-6 and 2-7 summarize the values calculated for the sections under study. The calculations used the idealized bilinear M- $\phi$  curves for different inclinations of the neutral axis.

### 2.4.3. Torque-twist Analysis

The torsional moment-twist properties of the specimens were investigated using the Softened Truss Model (Hsu, 1993). This model is based on the assumption that a solid reinforced concrete member subjected to torsion develops high shear and normal stresses near the outer perimeter of the section to resist the torsional moment, therefore the cross section could be represented by an equivalent thin-walled tube subjected to a

shear flow along the periphery of the cross-section. The thin-walled tube is then represented by an assemblage of two-dimensional membrane elements treated as trusses in which the shear and normal stresses induced by the torsion are resisted by concrete struts working in compression and the longitudinal and transverse reinforcing acting as ties in tension. The compression struts are oriented following the direction of the principal stresses and strains (direction  $d$  and  $r$ ), which are oriented with an angle  $\alpha$  with respect to the direction of longitudinal and transverse reinforcing ( $l$  and  $t$ ) as it is shown in Fig. 2-20. From the in-plane equilibrium it is possible to relate the internal stresses in the concrete ( $\sigma_d$  and  $\sigma_r$ ) and in the reinforcing steel ( $f_l$  and  $f_t$ ) to the applied stresses ( $\sigma_l$ ,  $\sigma_t$  and  $\tau_{lt}$ ) as:

$$\sigma_l = \sigma_d \cos^2 \alpha + \sigma_r \sin^2 \alpha + \rho_l f_l \quad (2-15)$$

$$\sigma_t = \sigma_d \sin^2 \alpha + \sigma_r \cos^2 \alpha + \rho_t f_t \quad (2-16)$$

$$\tau_{lt} = (-\sigma_d + \sigma_r) \sin \alpha \cos \alpha \quad (2-17)$$

$$T = \tau_{lt} (2A_o t_d) \quad (2-18)$$

Where  $A_o$  and  $p_o$  are the equivalent area and perimeter of the thin-walled equivalent section of thickness  $t_d$ , and  $\rho_l$  and  $\rho_t$  are the reinforcing steel ratios in the longitudinal and transverse directions, given by:

$$\rho_l = \frac{A_l}{p_o t_d} \quad \text{and} \quad \rho_t = \frac{A_t}{s t_d} \quad (2-18a)$$

Where  $A_l$  and  $A_t$  are the total area of longitudinal and transverse steel, and  $s$  is the spiral pitch.

From the compatibility it is possible to relate the strains in the principal direction ( $\epsilon_d$  and  $\epsilon_r$ ) to the l-t direction ( $\epsilon_l$ ,  $\epsilon_t$  and  $\gamma_{lt}$ ) using transformation equations given by:

$$\epsilon_l = \epsilon_d \cos^2 \alpha + \epsilon_r \sin^2 \alpha \quad (2-19)$$

$$\epsilon_t = \epsilon_d \sin^2 \alpha + \epsilon_r \cos^2 \alpha \quad (2-20)$$

$$\gamma_{lt} = (-\epsilon_d + \epsilon_r) \sin \alpha \cos \alpha \quad (2-21)$$

Additional compatibility equations are required to account for the out of plane warping effects, and for the distribution of strains in the concrete struts affected by warping

$$\theta = \frac{p_o}{2A_o} \gamma_{lt} \quad (2-22)$$

$$\psi = \theta \sin 2\alpha \quad (2-23)$$

$$t_d = \frac{\epsilon_{ds}}{\psi} \quad (2-24)$$

$$\epsilon_d = \epsilon_{ds} / 2 \quad (2-25)$$

Where  $\theta$  is the angle of twist,  $\psi$  is the curvature of the concrete struts, and  $\epsilon_{ds}$  is the strain in the concrete struts on the outer face.

The constitutive relationships of the concrete under uniaxial loading of compression and tension are given by the following expressions (You and Belarbi, 2008):

$$\xi = \frac{2.21}{\sqrt{f'_c \text{ (ksi)}}} \frac{1}{\sqrt{1 + 400\varepsilon_r}} \leq 0.9 \quad (2-26)$$

$$\sigma_d = \xi f'_c \left[ 2 \left( \frac{\varepsilon_d}{\xi \varepsilon_o} \right) - \left( \frac{\varepsilon_d}{\xi \varepsilon_o} \right)^2 \right]; \text{ when } \left( \frac{\varepsilon_d}{\xi \varepsilon_o} \right) \leq 1 \quad (2-27a)$$

$$\sigma_d = \xi f'_c \left[ 1 - \left( \frac{\varepsilon_d/\xi \varepsilon_o - 1}{4/\xi - 1} \right)^2 \right]; \text{ when } \left( \frac{\varepsilon_d}{\xi \varepsilon_o} \right) > 1 \quad (2-27b)$$

$$\sigma_r = E_c \varepsilon_r; \text{ when } \varepsilon_r \leq \varepsilon_{cr} \quad (2-28a)$$

$$\sigma_r = f_{cr} e^{-380(\varepsilon_r - \varepsilon_{cr})}; \text{ when } \varepsilon_r > \varepsilon_{cr} \quad (2-28b)$$

$$f_{cr} = 4\sqrt{f'_c \text{ (psi)}} \quad (2-28c)$$

Where  $\xi$  is the coefficient to take into account the softening of the concrete struts,  $\varepsilon_o$  is the compression strain at maximum concrete stress (0.002 in/in),  $\varepsilon_{cr}$  is the concrete strain at cracking (0.0001 in/in),  $E_c$  is the elastic modulus of the concrete and  $f_{cr}$  is the concrete tensile cracking stress.

The stress-strain behavior of the longitudinal and transverse reinforcing steel is modeled using elasto-plastic models:

$$f_l = E_s \varepsilon_l; \text{ when } \varepsilon_l \leq \varepsilon_{ly} \quad (2-29a)$$

$$f_l = f_{yl}; \text{ when } \varepsilon_l > \varepsilon_{ly} \quad (2-29b)$$

$$f_t = E_s \varepsilon_t; \text{ when } \varepsilon_t \leq \varepsilon_{ty} \quad (2-30a)$$

$$f_t = f_{yt}; \text{ when } \varepsilon_t > \varepsilon_{ty} \quad (2-30b)$$

Where the subscripts  $l$  and  $t$  refer to the longitudinal and transverse reinforcing steel,  $f_y$  is the yielding stress and  $E_s$  is the elastic modulus of the steel (29,000 ksi).

From the equilibrium, compatibility and constitutive laws, it is clear that the problem of a member subjected to torsion involves the solution of 16 equations in terms of 18 variables. Since the out of plane warping effects in round sections are minimum, it is possible to ignore these effect by eliminate the variables ( $\psi$  and  $\varepsilon_{ds}$ ) and transform the problem into one with 16 equations and 16 unknowns. In addition, it is possible to combine and manipulate the system of equations to facilitate the solution process. The thickness of the shear flow zone  $t_d$  can be expressed in terms of strains using the compatibility equations, resulting in:

$$t_d = \frac{A_o}{p_o} \left[ \frac{(-\varepsilon_d)(\varepsilon_r - \varepsilon_d)}{(\varepsilon_l - \varepsilon_d)(\varepsilon_{tl} - \varepsilon_d)} \right] \quad (2-31)$$

The strains in the longitudinal and transverse steel ( $\varepsilon_l$ ,  $\varepsilon_t$ ) can be related to the stresses  $f_l$  and  $f_t$  by eliminating the angle  $\alpha$  from the equilibrium equations, resulting in:

$$\varepsilon_l = \varepsilon_d + \frac{A_o(-\varepsilon_d)(-\sigma_d + \sigma_r)}{[-p_o t_d(\sigma_l - \sigma_r) + A_l f_l]} \quad (2-32)$$

$$\varepsilon_t = \varepsilon_d + \frac{A_o s(-\varepsilon_d)(-\sigma_d + \sigma_r)}{p_o[-s t_d(\sigma_t - \sigma_r) + A_t f_t]} \quad (2-33)$$

The area and perimeter of the equivalent thin-walled section ( $A_o$ ,  $p_o$ ) can be expressed as function of the thickness  $t_d$ , as:

$$A_o = A_c - \frac{1}{2} p_c t_d + t_d^2 \quad (2-34)$$

$$p_o = p_c - 4t_d \quad (2-35)$$

By compatibility of strain in different directions it is possible to write:

$$\varepsilon_r = \varepsilon_l + \varepsilon_t - \varepsilon_d \quad (2-36)$$

$$\alpha = \arctan \sqrt{\frac{\varepsilon_l - \varepsilon_d}{\varepsilon_t - \varepsilon_d}} \quad (2-37)$$

For a member subjected to torsion the normal stress  $\sigma_l$  is equal to the applied axial stress or zero in the case of pure torsion; while  $\sigma_t$  is equal to zero in the shear flow zone. If the strain in the concrete struts  $\varepsilon_d$  is selected as the third variable, a solution could be found if the values of strain  $\varepsilon_r$  and thickness  $t_d$  are iteratively calculated by a trial and error process until the equilibrium, compatibility and stress-strain relationships are satisfied. With this process one point is found in the torque-twist curve. Additional points in the torque-twist curve can be found by varying the compression strain  $\varepsilon_d$  from a near

zero value to a maximum value when the peak torque is reached or when the strains in the longitudinal or transverse steel begin to decrease. A flow chart describing the solution procedure is shown in Fig. 2-21.

Using the described procedure an Excel spreadsheet using Macros was developed to compute the Torque-twist curves for the specimens under study. As in the case of bending, two cases of axial load were considered  $P=0$  and  $P=80$  kips. A summary of the calculations are included in Tables 2-8 and 2-9 for circular columns, and in Tables 2-10 and 2-11 for the interlocking sections. Also, Figs. 2-22 and 2-23 show the Torque-twist curves for the circular and interlocking specimens, respectively. From the figures, it is evident that the presence of axial compression increases the torsional capacity of the sections. This effect is the result of a stress balance in the reinforcing steel, in which the tension stresses in the longitudinal steel induced by torsion are reduced by the presence of axial compression.



## **Chapter 3. Specimen Details and Experimental Test Setup**

### **3.1. Introduction**

To study the seismic performance of bridge reinforced concrete columns, four single cantilever-type specimens were subjected to biaxial earthquake excitation on a shake table. Two 1/3 scale circular and two 1/4 scale interlocking spirals columns were built, instrumented and tested at the University of Nevada Reno Large Scale Structural Laboratory. The specimen design procedures, geometry and reinforcement details were discussed in Chapter 2. This chapter describes the construction procedure, material properties and the instrumentation. Furthermore, the development of the new inertial loading system, termed Biaxial Mass Rig is presented in this chapter.

### **3.2. Construction of the Specimens**

All the specimens were built at the fabrication yard of the Rogers and Wiener Large Scale Structures Laboratory at the University of Nevada, Reno. The specimens were constructed in pairs; two specimens with circular section were constructed first and then, four months later, specimens with double interlocking spirals. The construction procedure was the same for all the specimens. First, the site was cleaned and leveled to guarantee a uniform and horizontal surface, subsequently; wood forms were set up for the specimen footings. After that, the bottom steel mats for the footings as well as the PVC ducts were placed in the forms.

The rebar cages for the columns were assembled separately to facilitate their instrumentation with strain gauges and sensors to measure strains in the concrete (smart

aggregator sensors). For the circular columns, the 20 No.4 longitudinal bars forming the cage were assembled first by welding steel circular hoops at the top and bottom of the cage. The continuous spiral was then tied around the cage with a spacing of 1.5 in. Moreover, for the interlocking specimens, each circular spiral cage was fabricated separately using 14 No.3 bars and a continuous spiral with 1 in. pitch along the circular cage. The circular spirals were then interlocked to each other and the remaining 4 No.3 bars were placed to form the cage of the column. Oblong steel hoops were welded to the cage to maintain the lateral spacing between bars and to avoid twisting of the column cage (Figs. 3.1 and 3.2). Once the steel cages were assembled, strain gauges were attached to the longitudinal bars and spirals. Plastic shrink tubes were used to protect the strain gauges wires during casting of the concrete.

Those cages were then installed in the middle of the footing, and tied down to the bottom mats of the footing (Figs. 3.3 and 3.4). The footing top steel mats, the cross ties and lifting bars were positioned (Figs 3.5 and 3.6), and the concrete was poured (Figs 3.7 and 3.8). Formwork for the column and top heads was then put in place followed by the installation of PVC ducts and the steel for the top head. The formwork for the circular specimen consisted of a 16 in. diameter sonotube (Fig 3.9), while that for the interlocking columns was made by attaching steel sheets to a wood forms to ensure the oblong shape of the column (Fig. 3-10). Finally, a scaffolding system was built to support the top head formwork, and to facilitate the pouring of the concrete.

The columns and top heads were then cast monolithically (Figs. 3-11 and 3-12). Since the concrete cover in the columns was relatively small, aggregate with a maximum size of 3/8" was used. Additionally, superplasticizer (DARACEM 19) was added to the

concrete in order to improve the workability of the mix; a slump of 3 in. of the original concrete was increased to 5 in. by the inclusion of superplasticizers. Once, the concrete in the columns was poured, 5/16 in. threaded bars were inserted through the column form. These would be used during the test to attach displacement transducers to measure the distribution of curvature along the height of the column, especially in the plastic hinge region. The specimens were then cured for 8 days before the formwork was removed (Figs. 3-13 and 3-14).

Concrete cylinders were cast for each of the concrete mixes used during the construction. The cylinders had a length to diameter ration of 2:1, with 12 in. length. Those cylinders were cured in the same way as the column specimens

### **3.3. Material Properties**

The stress-strain properties and dimensions for the concrete and reinforcing steel were selected to meet the requirements of the similitude model and scale factor. Since for the simple similitude model the stress-strain properties are kept unaltered, only the dimensions were reduced to meet the scale. Therefore, No.4 and No.3 deformed longitudinal bars and W5.0 and W2.9 galvanized plain wire were used for the circular and interlocking specimens, respectively. Normal weight concrete with maximum aggregate size of 3/8" was specified for the columns.

The longitudinal reinforcement and concrete were supplied by local companies in Nevada, whereas, the galvanized wire was purchased from Western Steel & Wire in San Francisco, CA. The concrete was designed and distributed by Reno-Sparks Ready Mix,

while, deformed steel bars were supplied by A-1 Steel Inc., Sparks, Nevada. Spiral fabrication was made by Camblin Steel Service Inc., Sacramento, CA.

### **3.3.1. Steel Reinforcement**

The column longitudinal reinforcement was specified as ASTM A615 grade 60 steel. Three samples of each size were tested in a Tinius Olson machine using standard methods. Figs. 3-15 and 3-16 show typical stress-strain curves for the No.4 and No.3 coupons tested. Average values of the yielding strength, strain at beginning of hardening, and ultimate strength and strain are summarized in Table 3-1. The main reinforcement in the footings was specified as No.5 and No.6 grade 60 for the circular and interlocking specimens, respectively.

For the spirals, W2.9 and W5.0 plain galvanized wire grade 60 ASTM A641 was specified. The same testing procedure used for deformed steel was used for wires. Because the stress-strain relationship for the wire did not show a clear yielding point, the 0.2% offset method described in ASTM A370 was used to determine the effective yielding strength (Figs. 3-17 and 3-18). Average values of the effective yielding strength and ultimate strength and strain are included in Table 3-1.

### **3.3.2. Concrete**

The concrete was specified as normal weight with a 28-day design strength of 4500 psi and 3/8" maximum aggregate size. For each pair of columns, the concrete was poured in two stages and using different batches: one for the footing, and another for the column and top head. The ultimate compressive strength of the concrete was determined by testing series of three concrete cylinders at ages of 7 days, 14 days, 28 days and the

day of the column test. Compressive strength results for the footings and columns are listed in Tables 3-2 and 3-3. The concrete cylinders were tested on a SATEK-MKIII\_C machine using standard testing methods.

#### **3.4. Test Setup: Bidirectional Mass Rig**

In many shake table tests of single cantilever-type columns, the mass is placed directly on the specimens, using large concrete blocks. As a result, a supporting or restraining structure must be included to prevent damage to the shake table system and instrumentation in the event of specimen collapse (Fig. 3-19). A mass rig is a supporting structure that carries safely the vertical component of the inertial mass (bridge superstructure weight) but allows transfer of the inertial forces from the structure to the specimen, when the shake table and specimen move. A mass rig that allows unidirectional shake table testing of single columns and column bents was developed at University of Nevada, Reno in 1999 (Laplace *et al.*, 1999). As can be seen in Fig. 3-20, the unidirectional mass rig is an eight pin steel frame, located away from the shake table that transfers the inertial forces to the specimen via a rigid link. The axial load on the specimens is applied through a hydraulic ram on top of the columns.

Following the same principle of the unidirectional mass rig of having a structure supporting the mass (vertical component), a new structure named Bidirectional Mass Rig (BMR) was developed as part of this study, to enable the shake table testing of single cantilever-type reinforced concrete columns subjected to biaxial earthquake excitations. The new system is composed of a supporting frame and a platform that sits on ball bearings located at the top of the frame columns. The platform is connected to the specimen through

three links, two placed in one direction and another in the orthogonal direction, which allow transferring of the shear and torsion but not vertical axial forces (Figs. 3-21 and 3-22). Additional mass is placed on the platform to simulate a portion of the bridge superstructure weight, and this can be placed in a symmetric or asymmetric configuration to induce different levels of torsion.

The supporting structure consisted of a steel frame with four columns and bolted beams, designed to carry the vertical load (additional mass) and the moments originated at the top of the columns due to the motion of the platform (Figs. 3-23 and 3-24); each of the columns was fixed to the shake table using high strength bolts. A 1.5 in. thickness and 45 in. diameter circular plate was welded at the top of each supporting column to provide a smooth surface for the ball bearings. The platform was composed of a grid of hollow steel structural sections (HSS 8x8x5/16") welded together using fillet welds (Figs. 3-25). To allow the storage and facilitate the lifting operations inside the laboratory, the platform structure was divided into two sections, which were joined together by means of high strength bolts (see Figs. 3-25 and 3-26). The geometry of the platform was designed to carry the additional masses with minimum deflection and to allow the placement and replacement of the RC specimen on the shake table using the lab cranes without removal of the BMR. For specimen removal, a 64x64 in. opening was provided in the center of the platform structure (Figs. 3-25 and 3-26). The BMR structure was fabricated by Remarc Manufacturing Inc, Reno.

Additional mass was incorporated into the system by using lead pallets, each one with an approximate weight of 8,000 lb. In total 8 pallets were used for this study (See Fig. 3-27). It is worth noting that the platform was designed for a maximum additional weight

of 90 kips. A grid of holes (2 in. diameter) spaced every 2 ft. on the platform was incorporated to allow the positioning of the lead pallets in a wide range of configurations (Fig. 3-25 and 3-27).

A safety system was designed to catch the platform in the event of large displacements or specimen collapse. This system was formed by a series of “L” shape safety arms, located on each of the four sides of the platform as is shown in Fig. 3-25. The safety arms were made from HSS steel and were connected to the platform using high strength bolts (See Fig. 3-28). The motion on the platform in any of the orthogonal directions is stopped when the safety arms impact against the beams of the supporting frame. A maximum drift of 15 in. is allowed by the safety system in any direction.

In order to allow the free displacement of the platform in any direction, a ball bearing device was developed as part of this study. The bearing was composed by 37, 1.5 in diameter, high strength steel balls mounted between two circular steel plates. Each plate was machined with recesses to accommodate each ball, in order to minimize rolling resistance with minimum sliding of the entire device (See Fig. 3-29). The diameter of each ball bearing device was 15 in., and the number of balls was selected to minimize the stress concentration on the bearing plates.

The links were designed to transfers the inertial forces created on the mass rig platform to the specimen without imposing any constraint. For that, universal joints were added at the ends of round structural sections (HSS6x0.5”). Universal joints have the ability to swivel in any direction. In addition, a thrust bearing was included at one end of the links to allow rotations around the longitudinal axis of the links. Load cells were also

mounted in the links to measure the lateral force transferred to the specimen. Fig. 3-30 shows all the components used for the links.

Since the BMR was fabricated with bolted steel components, the assembling and disassembling process of the structure can be completed in a short time. As is illustrated in Fig. 3-31, the process of assembling the BMR includes the following steps: a) assemblage of the supporting structure (columns and beams) and attachment of the columns to the shake table; b) setting the RC specimen on the shake table; c) assembling the two components of the platform and placing it on the ball bearing, which rest on the supporting structure; d) connecting the links between the platform and the head of the RC specimen; e) placing the additional mass on the platform; and f) attaching the safety arms to the platform. Fig. 3-32 shows the assembled BMR with a RC specimen before testing, while Fig. 3-33 shows details of the connecting links at the top of the RC specimen.

For the case of columns with axial loading, the required axial force can be applied directly to the specimen through a center-hole ram equipped with a servo-valve. The ram would be connected to the specimens through an unbonded prestressed bar placed in an ungrouted conduit in the middle of the column and anchored in the footing. It is important to note that the main purpose of the prestressed bar is to induce the required level of axial load in the columns rather than increase its displacement capacity as has been found in other studies (Sakai *et al.*, 2006).

Since the BMR does not induce secondary moments in the specimens (P-delta effects), and the unbonded prestressed bar inside the column would generate restoring lateral forces, additional dynamic actuators must be located at the top of the specimen to induce the equivalent force to have P-delta effects and to compensate the restoring force.



The motion of the dynamic actuators and the shake table will be controlled throughout hybrid simulation. Figures 3-34 and 3-35 show the configuration of the BMR for a specimen test including axial force and P-delta effects. This configuration will be used in the testing of four columns that will be documented in a future report.

The BMR was designed specifically for the RC specimens discussed in this study. As can be seen in Fig. 3-24 specimens with footing height of 28 in., and a 72 in. height to the links were initially tested using the BMR. Nevertheless, some minor modifications on the specimen dimensions or BMR could allow the use of higher specimens.

### **3.5. Instrumentation**

The specimens were extensively instrumented to monitor the local and global response. Transducers were used at selected locations to measure acceleration, lateral force and displacement, torsion, and curvature. Also, strain gauges were attached to the longitudinal and transverse steel to measure local deformations. Furthermore, the acceleration, velocity and displacements of the shake table were recorded using accelerometers and displacement transducers integrated to the platform system. The instrumentation scheme used in the test specimens is described in the following subsections.

#### **3.5.1. Acceleration**

To measure the two horizontal components of the acceleration in the specimens, two biaxial accelerometers (Analog Devices ADXL-320  $\pm$  5g Micro MEM) were mounted at the opposite corners of the column head. Similarly, the same accelerometers were mounted at the opposite corners of the BMR. The configuration of the

accelerometers was selected to measure the acceleration in the longitudinal (X) and transverse (Y) directions, and to calculate from those the rotational acceleration of the specimens and BMR. In total four sensors were used to measure all the acceleration as can be seen in Figs. 3-36 and 3-37 for circular and interlocking columns, respectively. In addition, the input accelerations at the base of the column were measured using the accelerometers incorporated into the shake table platform.

### **3.5.2. Lateral Force**

The inertial lateral forces transferred to the specimens were measured using load cells integrated in the links. Two 150-kip Lebow load cells were used in the two parallel links (see Figs. 3-33 and 3-37) whereas, a 200-kip load cell designed and instrumented by the UNR laboratory staff was used in the perpendicular link. The torque induced in the specimen was calculated using the difference in force measured by the two parallel links at each step of time, and the distance between them. The location of the load cells is shown in Figs. 3-36 and 3-37 (LC1, LC2 and LC3).

### **3.5.3. Lateral Displacement**

The absolute displacements in the two horizontal components (X, Y) of the specimen and BMR were measured by means of String Potentiometers (UniMeasure PA series with 40 and 60 in. in stroke) displacement transducers. The displacements in the RC specimens were measured using two parallel transducers located in two perpendicular faces of the column top head. These transducers were located off the shake table on the lab wall in the EW and attached to a metal structure in the NS directions, respectively. The absolute displacements in the longitudinal and transverse directions were calculated

as the average of the two transducers. In addition, the twist angle of the RC specimens was calculated using the difference in displacements measured by the two parallel transducers, and the distance between them. Furthermore, the absolute displacement of the shake table was also measured using transducers incorporated into the shake table actuators. The relative displacements were calculated as the difference between the values measured by the String Potentiometers and the transducers of the shake table actuators. A similar process was used to measure the lateral displacements and rotations of the BMR platform. Figs. 3-36 and 3-37 show the location of the displacement transducers for circular and interlocking columns, respectively.

#### **3.5.4. Curvature and Concrete Strains**

To measure the average curvature in the potential plastic hinge region of the specimens, Novoteknik TR-75 displacement transducers were used. These instruments were mounted on 5/16 in. threaded rods on the four opposite sides of the columns. These rods were inserted into the columns during the pouring of the concrete; an anchorage length of 4 in. was specified. The transducers were distributed over a height of 20 in. measured from the top of the footing, and were spaced every 4 in. Figs. 3-38 and 3-39 show the locations of the curvature transducers.

The average curvature in each direction was calculated from the average strain recorded at each location of the transducers, the geometry of the sections and the gauge length as it is shown in Fig. 3-40. The average strain was calculated from vertical measurements recorded by every transducer and the geometry of the section as follows:

$$\phi_i = \frac{\varepsilon_{1i} - \varepsilon_{2i}}{x_{1i} + D + x_{2i}} \quad (3-1)$$

Where:

$\varepsilon_{1i}$  = strain at side 1 along the gauge length  $i$

$\varepsilon_{2i}$  = strain at side 2 (opposite to side 1) along the gauge length  $i$

$x_{1i}$  = distance from the column face to the centroid of the transducer at side 1 for length  $i$

$x_{2i}$  = distance from the column face to the centroid of the transducer at side 2 for length  $i$

$D$  = column depth on the direction of analysis

Average strains at the surface of the concrete (unconfined concrete) are given by:

$$\varepsilon_{uc1i} = \varepsilon_{1i} - x_{1i}\phi_i, \quad \varepsilon_{uc2i} = \varepsilon_{2i} - x_{2i}\phi_i \quad (3-2)$$

And the strains at the level of the longitudinal reinforcement (confined concrete) are calculated by:

$$\varepsilon_{cc1i} = \varepsilon_{1i} - (x_{1i} + c)\phi_i, \quad \varepsilon_{cc2i} = \varepsilon_{2i} - (x_{2i} + c)\phi_i \quad (3-3)$$

Where:

$\phi_i$  = average curvature of the section at the gauge length  $i$

$\varepsilon_{uc1i}$  = unconfined concrete strain at side 1 and gauge length  $i$

$\epsilon_{uc2_i}$  = unconfined concrete strain at side 2 (opposite to side 1) and gauge length  $i$

$\epsilon_{cc1_i}$  = confined concrete strain at side 1 and gauge length  $i$

$\epsilon_{cc2_i}$  = confined concrete strain at side 2 (opposite to side 1) and gauge length  $i$

$c$  = distance from the concrete surface to the centroid of the longitudinal bar

### 3.5.5. Strain Gauges

Strain gauges were attached to the spirals and longitudinal reinforcement along the potential plastic hinge zone and distributed over the four faces of the specimens; these sensors were adhered to the surface of the reinforcement facing outward. Six sections along the height of the interlocking specimen were instrumented, while only five were instrumented for the circular column; for both specimens the first section was located inside the footing. Strain gauge YFLA-2-5L, distributed by Texas Measurements was used to measure large strains up to 20%. Adhesive CN-Y was used to install the gauges as recommended by Texas Measurements. To provide a clean and smooth surface to attach the gauges, the reinforcement surface was sanded to eliminate the threads and was also cleaned to eliminate dust and grease. Once the sensors were attached with the adhesive, the gauges were covered with a piece of rubber mastic tape and were also draped with two layers of electric tape to avoid damage to the gauges during the construction process. Furthermore, to avoid damage of the gauge electric wires, these were encased using heat shrink plastic tubing of different diameters and were tied to the reinforcement using zip ties. Fig. 3-41 and 3-42 show the distribution of the strain gauges on the circular and interlocking specimens, respectively.

## **Chapter 4. Experimental Results for Circular Columns**

### **4.1. Introduction**

The seismic performance of bridge reinforced concrete circular columns under combined loads was investigated through shake table testing. Two identical 1/3-scale circular specimens (C1 and C2) were tested under the two horizontal components of the 1992 Cape Mendocino Earthquake recorded at Petrolia station; C1 used a symmetric distribution of mass on the mass rig, while in C2 an unsymmetrical configuration was used. Ground accelerations with increasing amplitude were applied in successive runs until failure and without applying any axial load. Failure was defined as the rupture of either the longitudinal or transverse steel or the point when the shake table or mass rig physical limits were reached and a higher amplitude motion could not be applied. The measured response both global (relative displacements, base shear and overturning moments) and local (strains and curvature) as well as the visual damage progression is discussed in this chapter. In this chapter is also presented calculations of the plastic hinge and a bilinearization of the force-displacement envelopes based on effective yielding force and displacement.

### **4.2. Test Procedure**

The two horizontal components of the 1992 Cape Mendocino earthquake ( $M=7.0$ ) recorded at Petrolia station in California (PEER, 2000), were used as the input motions for specimens C1 and C2 for two reasons. First, this ground record was used by another member in the NEES-CABER team conducting inelastic seismic analysis of bridge

structures with hazard level of 2% of exceedence in 50 years (Zhang et al., 2008). Second, based on preliminary analysis this record induces moderate values of torque to overturning moment (T/M) on the column before failure for the specimen with an asymmetric mass configuration (C2). Following the requirements of the similitude model with a scale factor of one third, a factor of 0.58 was used to compress the time scale of the records, while the base accelerations were not changed. Fig 4-1 shows the time history accelerations, the pseudoacceleration spectrum and the acceleration interaction orbits for the two horizontal components of the Petrolia record. In order to minimize the differences between the target and achieved table accelerations and compensate for the mass on the shake platform, random vibrations were applied to the system prior to tune the table. Once calibrated, the specimens were subjected to series of motions, increasing the amplitude of the original record in subsequent runs. The testing sequence for each specimen is summarized in Tables 4-1 and 4-2, also the series of accelerograms is shown in Figs. 4-2 and 4-3 for the longitudinal and transverse directions. The test protocol was defined based on preliminary analysis performed in OpenSees (Mazzoni et al., 2006) for the specimens including the test setup. Small increments (10% to 20% of the earthquake) were initially applied to determine elastic properties and the effective yielding point. Once the elastic properties were determined, the amplitude of the records was successively increased until failure. The strongest component of the ground motions was applied on the longitudinal direction (X) of the columns (North-South direction of the shake table), while the orthogonal horizontal component was applied on the transverse direction (Y) or East-West direction of the shake table. Signals of white noise were

independently applied in each direction between each run to measure changes in the specimen effective period and damping ratio between runs.

### **4.3. Shake Table Performance**

The performance of shake table systems is defined as the ability of these systems to accurately reproduce the input signals. Although periodic calibrations and special software is used to reproduce very accurate ground motions, sometimes small differences between the input and achieved signals are detected. For the case of the shake table used for the circular columns tested, small differences between the target and achieved accelerations reproduced by the shake table and the specimens were observed despite the fine-tuning applied to the system. To determine the accuracy of the reproduced signals, the time history accelerations recorded from the shake table were compared with the input acceleration at each run. Tables 4-3 and 4-4 show the differences between the target and achieved peak table acceleration (PGA) and the ratio between them for specimens C1 and C2, respectively. The ratio between target and achieved PGA was almost constant for all the runs with average values of 1.18 and 0.98 for C1 in the longitudinal and transverse direction, respectively. Those values were 1.03 and 0.90 for C2. In addition to the PGA comparison, tri logarithmic elastic spectrums were calculated from the target and achieved acceleration signals for each run. An Excel spreadsheet using Macros was developed to compute the displacement, velocity and accelerations response spectrums using the Newmark-beta time step method (Chopra, 2001). Since the elastic response of the shake table system was investigated rather than that from the specimens, a damping coefficient of 0% of the critical was used for all the calculations. Comparisons between the spectral



responses for target and achieved motions during each run are shown in Figs. 4-4 through 4-14 for C1 on the longitudinal and transverse directions and in Figs. 4-15 through 4-25 for C2. Also, it is shown in the same figures the measured elastic period of the specimens during each run; details of the calculations of this parameter will be presented in section 4.6. The spectral response parameters at the measured period of the specimens are summarized in Table 4-5 for C1 and in Table 4-6 for C2. Although there are variations in the target and achieved elastic responses (displacement, velocity and acceleration) for all the motions, these discrepancies are more important at the low period portion of the spectrum. The impact of these discrepancies is not significant since the potential specimens response is at higher periods as it is shown in the trilogarithmic spectrums. Therefore the table performance is judged as acceptable for the period range of interest.

#### **4.4. Observed Column Performance**

To characterize the damage progression during the test sequence, the specimens were white painted and markers of different colors were used to delineate the trajectory of the cracks after each run. In general, the behavior of specimens C1 and C2 was controlled by the biaxial effect of bending, with horizontal cracks distributed over the specimen height, as well as some inclined cracks at the plastic hinge region near the column base. The ratio between the column relative displacement and the height of the column; drift ratio ( $\delta=\Delta/H$ ), was selected as the performance parameter for the tested specimens. For small amplitude runs (Tuning and 0.1xPET) horizontal hairline cracks were observed on the lower half of the columns and were distributed around the perimeter of the specimens. Drift ratios in the longitudinal and transverse directions,

$\delta_L=0.43\%$  and  $\delta_T=0.29\%$  were recorded for C1 and  $\delta_L=0.28\%$  and  $\delta_T=0.17\%$  for C2. Fig. 4-26 shows the distribution of horizontal flexural cracks for C1 and C2, respectively. The first bar yielding was detected at 0.2xPET for both specimens;  $\delta_L=0.7\%$  and  $\delta_T=0.48\%$  for C1 and  $\delta_L=0.55\%$  and  $\delta_T=0.27\%$  for C2. The damage at this stage was characterized by an increase in the horizontal cracking and the presence of a few inclined cracks in the lower third of the column. The pattern of cracks at this stage is shown in Fig. 4-27 for both specimens. The first concrete spalling occurred at 1.0xPET for both specimens ( $\delta_L=4.5\%$  and  $\delta_T=2.3\%$  in C1 and  $\delta_L=3.8\%$  and  $\delta_T=1.7\%$  in C2); it was located on the S-W face of the columns and was extended about 4 in. from the column footing interface. As it is shown in Figs. 4-28 and 4-29, a large number of horizontal and inclined cracks were observed on the lower half of the columns. Considerable distress was experienced after 1.2xPET ( $\delta_L=6.6\%$  and  $\delta_T=3.44\%$  in C1 and  $\delta_L=5.7\%$  and  $\delta_T=2.5\%$  in C2). At this point, extensive spalling at the base of the columns, as well as propagation of the flexural and shear cracking was observed (Figs. 4-30 and 4-31).

The spirals and longitudinal bars were clearly visible after 1.4xPET for both specimens ( $\delta_L=9.0\%$  and  $\delta_T=3.8\%$  in C1 and  $\delta_L=7.9\%$  and  $\delta_T=3.3\%$  in C2). Figs. 4-32 and 4-33 show the extent of the damage at this stage. The failure in C1 was observed during 1.8xPET ( $\delta_L=14.6\%$  and  $\delta_T=7.0\%$ ); at this stage a number of the longitudinal bars buckled and some degradation of the concrete core was observed. In C2 the failure occurred during 2.0xPET ( $\delta_L=14.5\%$  and  $\delta_T=8.1\%$ ), and it was due to torsional buckling and rupture of the longitudinal bars and spiral fracture in the plastic hinge zone. Figs. 4-34 and 4-35 show the final damage state for both columns. Fig. 4-36 compares the

damage pattern for the circular specimens after testing. From the figure, it is evident the large residual displacement experienced by both models at high amplitude runs. The observed performance for C1 is summarized in Table 4-7 and in Table 4-8 for C2.

#### **4.5. Lateral Force-Displacement Hysteresis**

The total lateral forces induced in each direction of the column were calculated as the summation of those measured by the load cells attached to the links connecting the mass rig and the column, and the inertial forces due to the tributary mass of the specimen. The tributary mass included: the portion of the links between the load cell and the specimen, the steel connecting plates and the self weight of the specimen (top head and the upper half height of the column). The inertial forces due to the mass of the specimen were then calculated as the tributary mass times the acceleration recorded at the top of specimen. The base shear was assumed to be equal to the total lateral forces, while the base moment was defined as the product of the base shear and the distance between the top of the footing and the point of connection of the links at the column head (72 in).

Top specimen total displacements were calculated as the average of the readings of the two displacement transducers attached to the column tip in each direction, as described in section 3.5.3. (See Figs. 3-37 and 3-38). The lateral relative displacements in each direction were calculated as the difference between the total displacement measured at the top of the column and those measured by the shake table instrumentation. Additionally, the displacement drift ratio ( $\delta$ ) was computed as the quotient between the top relative displacement and the distance from the top of the footing until the point of connection of the displacement transducers (83 in).

The measured lateral force-displacement hysteretic curves for C1 are shown in Figs. 4-37 through 4-46 and in Figs. 4-49 through 4-59 for C2. Additionally the hysteresis accumulated during all the runs of C1 is shown in Fig. 4-47 for the longitudinal direction and in Fig. 4-48 for the transverse direction, and in Figs. 4-60 and 4-61 for C2. From the figures, it is evident that in the first runs the specimens behaved elastically with low hysteresis and without stiffness degradation. After the first bar yielding, the behavior of both specimens was characterized by hysteresis and stiffness degradation with the curves clearly biased in one direction and becoming more prevalent after each subsequent run. This behavior is a consequence of the large residual displacements experienced in one direction by the specimens, and is attributed to the characteristics of the 1994 Petrolia at Mendocino ground motion (strike slip earthquake recorded near to the fault rupture). This ground motion is characterized by having a single asymmetric acceleration pulse of short duration where most of the earthquake energy is concentrated. As a result, the specimens subjected to this record did not undergo full displacement reversals. Similar behavior was observed in previous columns tested at UNR under near fault ground motions (Phan *et al.*, 2005 and Choi, 2007). The maximum peak lateral force was recorded during the run at 1.6xPET for both specimens. After this point, the specimens underwent some degradation in the stiffness and lateral force capacity. At the last run, 1.8xPET for C1 and 2.0xPET for C2, the development of plastic hinges at the base of the specimens caused the vibration period of the columns to shift-out from the higher energy portion of the spectrum, isolating the upper part of the column from strong response, and making the columns more sensitive to lateral instability. Tables 4-9 and 4-10 summarize the values of the peak lateral force with the corresponding displacement and the peak

displacement with the corresponding force for each run of the specimen C1. The same values for specimen C2 are shown in Tables 4-11 and 4-12.

A lateral force-displacement envelope curve was calculated from the cumulative hysteresis curves of each column using the peak forces with corresponding displacements for each run until failure. Since large values were calculated for the positive envelopes, these values are only reported here. The force displacement envelopes for each direction of the specimens are shown in Fig. 4-62 for specimen C1 and in Fig. 4-63 for specimen C2. The failure point in the envelopes was defined either as the peak displacement and corresponding force or the peak displacement corresponding to a dropping of 20% in the peak lateral force, whichever displacement was less. In the case of specimen C1, the load did not drop below 80% of the maximum load.

The biaxial effects were studied by means of the displacements and moments interaction orbits. For that, the accumulated values measured in the longitudinal direction of motion versus those in the transverse direction were plotted. Figs. 4-64 and 4-65 show the displacement interaction orbits for both specimens, and Figs. 4-66 and 4-67 present the moment interactions curves. For comparison, the interaction orbits for yielding and ultimate points calculated from the moment-curvature predictions in section 2.4.1, have been included in the same figures.

From the displacement interaction orbits, it is clear that for both specimens, the resultant displacement followed an angle of approximately  $25^\circ$  with respect to the longitudinal direction of motion. This behavior was in agreement with the location of the first concrete spalling observed in both specimens (Figs. 4-28 and 4-29). On the other hand, by comparing the trilogarithmic response spectrums (Figs. 4-4 through 4-14 for C1,

and 4-15 through 4-25 for C2) it is noted that the spectral demands (acceleration, velocity and displacement) along the transverse direction were always smaller than those on the longitudinal direction. Moreover, the average displacements in the transverse direction were about 50% of those measured in the longitudinal direction (Figs. 4-62 and 4-63), indicating that less energy was applied to the specimens in that direction; which caused the specimen's response were dominated mainly by the demands imposed in the longitudinal direction.

Comparing Figs. 4-62 with 4-66 for C1, and 4-63 with 4-67 for C2 it is evident, as in the case of the displacement interaction orbits, that the specimen behavior was dominated by the demands in the longitudinal direction. It is also noted that the capacity in the transverse direction was significantly less than that in the longitudinal direction during all the runs, even though, the peak base moment capacity in the transverse direction did not exceed the calculated yielding moment ( $M_y$ ). This effect is attributed to the biaxial interaction, in which the movement and associate damage in the longitudinal direction affected the capacity in the transverse direction. In fact, as the specimen yielded and deteriorated in the longitudinal direction, the capacity was simultaneously reduced in the transverse direction. By contrast, the moment capacity in the longitudinal direction did not show considerable reduction due to the effects in the transverse direction; as it can be observed in Figs. 4-66 and 4-67, the peak measured biaxial moment capacity was larger than the predicted moment capacity of the specimen under unidirectional excitation (neutral axis at  $0^\circ$ , Table 2-4).

From the plots showing the seismic performance of the two specimens (Figs. 4-62 through 4-67), it is clear that the behavior of C2 did not vary considerably with respect to

C1; which indicates that the asymmetric distribution of the mass used in C2 did not induce large torsional effects that influenced appreciably the biaxial performance of the specimen.

#### **4.6. Dynamic Properties**

The white noise signals applied after each run were used to estimate the vibration period and damping in each direction of the specimens. As a first approach, a power spectrum density was calculated using the transfer function between the accelerations measured at the top of the specimen and the shake table (Clough and Penzien, 1993). In this approach, the natural frequency is defined by the peak value of the spectral density, and the damping is approximated by the inverse of twice the peak spectral density. Figs. 4-68 through 4-71 show the power spectrums and the calculated frequencies after each run of the specimens. Secondly, the free vibration portion of the accelerograms recorded at the top of the specimens was investigated to determine the viscous damping via the logarithmic decrement method (Chopra, 2001). However, reliable values could not be calculated because the free vibration portion of the signals was either too short or very noisy. As an alternative to determine the dynamic properties of the specimens, a multiple input – multiple output (MIMO) for system identification procedure (Li and Mau, 1991) was applied for each run of white noise. In this method, the vibration properties are determined by calculating the response of a linear multiple degree of freedom system with classic damping, in which the measured input and output acceleration signals are known. The system response is then obtained iteratively through a modal synthesis with the vibration properties adjusted until the calculated output response is close enough to

the measured output. The time varying behavior of the structure is studied using a time window approach. A computer routine developed at the University of Houston (Li and Mau, 1990) and modified at the National University of Mexico (Cruz-Noguez *et al.*, 2006) was used to calculate the modal natural frequencies and damping properties of the specimens. The obtained period and damping for the circular specimens are summarized in Tables 4-13 and 4-14. The variation in the dynamic properties with the test progression and measured using different methods is shown in Figs. 4-72 and 4-73 for specimen C1 and in Figs. 4-74 and 4-75 for specimen C2.

From the results, it is clear that the natural period gradually increased with the progression of the test from a value of about 0.60 seconds at the undamaged state to an average value of 1.3 seconds at the ultimate stage. In contrast, the variation in damping followed a less evident trend, but in general it increased with the progression of the damage with values ranging between 3% and 9% for C1 and between 4% and 6% for C2. Good agreement was observed in the values and trends of the dynamic properties measured using the power spectrum and MIMO, as it is illustrated in Figs. 4-76 and 4-77 for the longitudinal direction of the tested columns.

#### **4.7. Lateral Stiffness**

For a single cantilever-type column under dynamic loads, the natural period and lateral stiffness are given by the following expressions:

$$T_n = 2\pi \sqrt{\frac{M}{K}} \quad (4-1)$$



$$K = \frac{3 EI_e}{H^3} \quad (4-2)$$

$$EI_e = \frac{4 \pi^2 M H^3}{3 T_n^2} \quad (4-3)$$

Where

$T_n$  = the natural period of the column

$K$  = lateral stiffness

$M$  = the total lateral mass (column plus additional mass)

$EI_e$  = effective stiffness of the column

$H$  = column height until the center of mass

Using the estimated periods, and by applying equation 4-3 with the properties of the specimens, [mass ( $M=83$  kips) and the column height measured from the top of the footing until the point of connection of the links ( $h=72$  in)], it was possible to estimate the effective lateral stiffness of the specimens after each run of the test protocol as is shown in Tables 4-15 and 4-16. The values of the effective lateral stiffness were also plotted as they change with the progression of the test, as is shown in Figs. 4-78 and 4-79. From the results, it is clear that the effective lateral stiffness ( $EI_e$ ) of the specimens at the undamaged stage was on average about 25% of the gross stiffness ( $EI_g$ ); it was reduced to about 20% of the gross stiffness with the bar yielding; and it was reduced with the progression of the test following a linear trend reaching a minimum value of about  $0.05EI_g$  at the end of the test protocol.

#### 4.8. Curvature

The average curvature in the potential plastic hinge region was calculated based on the deformation measured by the Novoteknik transducers attached to the lower part of the specimens where the plastic behavior was expected to occur. Based on Bernoulli's principle of plane sections, the average strain on opposite sides of the column was calculated as the vertical displacement measured by the transducers divided by the gauge length. The average curvature was computed as the difference in strains on two opposite sides of the column, divided by the total horizontal distance between instruments. In total, four segments were used to measure curvature; details of the instrumentation and calculation procedure were presented in section 3.5.4.

The curvature profiles for C1 and C2 are shown in Figs. 4-80 through 4-83. The points in the curvature profiles represent the curvature measured at the specific location and in correspondence to the maximum and minimum peak values of lateral force. The curvature profiles in each direction were asymmetric, with relatively high measured values when the peak lateral forces were maximum, resembling the asymmetry of the Petrolia ground motion. Also, as it was expected for columns tested on single curvature, large curvature values were measured at the base of the specimens, where the moments were larger and induced extensive nonlinear deformation. This behavior is in agreement with the locations where visible damage occurred (concrete cracks and spalling).

In order to measure the curvature ductility of the specimens, the accumulated average moment-curvature hysteretic curves were calculated. Moment was computed as the product of the lateral force at the top of the specimen and the distance from the top of the column to the relevant segment where curvature was measured. The moment-

curvature for each specimen was defined as the average of the values calculated for the two lowest segments, which approximately correspond to the predicted plastic hinge length. The accumulated average moment-curvatures curves are shown in Figs. 4-84 and 4-85 for C1 and in Figs. 4-86 and 4-87 for C2. Also for the predominant direction of motion of the specimens (longitudinal), an envelope curve was developed based on the peak moments and corresponding curvatures for all the runs before failure. Figs. 4-88 and 4-89 show the positive envelopes of accumulated moment-curvature for the longitudinal direction of motion of the circular specimens.

#### **4.9. Flexural and Shear Deformations**

In order to calculate the contribution of the flexural and shear deformations to the total displacement, the computed moment-curvature profiles were integrated on the height of the specimen. Since Novoteknik transducers were used only to cover a length of 28 in. from the top of the footing, a straight line was used to connect the curvature measured at 28 in. and the zero curvature at the top of the column. As was mentioned before, the curvatures were assumed to be constant over the gauge length and the profiles were calculated for the peak lateral force. The moment-area method was applied to calculate the peak flexural deformations for each run. An envelope curve was plotted based on the peak lateral force and corresponding flexural deformation to show the performance during the test protocol, as it is shown in Figs. 4-90 and 4-91 for specimens C1 and C2, respectively.

Once the flexural deformations were estimated by integrating the curvature profiles, the shear deformations were calculated by subtracting the flexural deformations

from the total displacements measured at the top of the specimens. The shear deformations were computed in each direction only for the predominant component of lateral deformation. A lateral force versus shear deformation envelope was calculated for each specimen during the test protocol as is illustrated in Figs. 4-92 and 4-93. The maximum measured shear deformations in specimen C1 were 30% and 25% of the total deformation on the longitudinal and transverse directions, respectively. For specimen C2, the peak shear deformations were 20% on the longitudinal and 30% on the transverse directions. In addition, Figs. 4-94 and 4-95 show the contribution of the flexural deformation to the total deformation measured at the top of the specimens for the longitudinal direction. From the figures it is apparent that the seismic performance of the specimens was dominated by the flexural deformations.

Since none transducer was used to measure the bar slip at the bottom of the specimens, the calculated values of curvature and therefore flexural deformation, includes the contribution of this effect.

#### **4.10. Strains**

The distribution of strains in the plastic hinge region of the specimens was studied using the strain gauges attached to the longitudinal and transverse reinforcement; the location of the strain gauges was discussed in section 3.5.5. (See Fig. 3-42). For a better interpretation of the strain distribution, five sections were considered at the column base: 4 in. below the top of the footing, at the footing-column interface and then 8 in., 16 in. and 24 in. above the footing. The peak values of the strain (maximum and minimum) in the reinforcement at each section and for each run are summarized in Tables 4-17 through

4-21 for specimen C1 and in Tables 4-22 through 4-26 for specimen C2. In the tables, positive values correspond to tensile strains, while negative values correspond to compressive strains. Although a carefully procedure was implemented to adhere and protect the strain gauges, data from some gauges was lost during the tests due to either failure or unreliable measurements caused by high localized strains; the maximum reliable strain for the gauges used in this study is about 100,000 micro-strains ( $\mu\epsilon$ ). Malfunctioning sensors includes Sg.19, 25, 31 and 51 for C1, and Sg. 2, 14, 25, 28, 34 and 44 for C2. Data from malfunctioning gauges are either not reported in the tables or show erratic trends. The yielding strains for the longitudinal bars and the spirals were calculated as the ratios between the yielding stresses reported in Table 3.1 and the modulus of elasticity of the steel (29,000 ksi). Average yielding strains of 2240 $\mu\epsilon$  and 2000 $\mu\epsilon$  were then calculated for the longitudinal (No.4 bars) and transverse (W5.0) reinforcement, respectively. Values of strain equal or larger than the yielding point are marked with bold characters in the strain summary tables.

For both specimens, the yielding strain in the longitudinal reinforcement was recorded at 0.2xPET (run 2); during this run, 18 bars in C1 and 8 bars in C2, showed strain values in excess of the calculated yielding. Strain gauges attached to the bars 4 in. below the top of the footing showed yielding after 0.2xPET and 0.4xPET for C2 and C1, respectively. After 0.2xPET, the yielding was distributed along the plastic hinge region. Figs. 4-96 through 4-103 show the variation of measured longitudinal strains along the height of the specimens with the level of excitation. These figures show that higher strains were recorded in the proximity of the column base (from 0 to 8 in.) compared with other locations along the height. Also, note that values of strain in excess to the yielding

were recorded at an elevation of 24 in. from the top of the footing which suggested that yielding extended beyond the plastic hinge zone for large levels of excitation.

The distribution of spiral strains along the height of the specimens with the level of excitation is shown in Figs. 4-104 through 4-107. These figures show that for the elevations considered on the four sides of the columns, most of the measured spiral strains were under the yielding point until the last runs, when large strains were a consequence of longitudinal bar buckling or spiral rupture. Also note that higher strains were recorded in the proximity of the column base, similar to the longitudinal reinforcement, but with strain profiles that were more uniform along the height of the plastic hinge zone. The accumulated strain history recorded by each gauge during the test protocol is shown in Appendix C.

Although, the reinforcement strain profiles (longitudinal and spirals) for both specimens followed similar trends, slightly higher strains were measured in C2 particularly toward the end of the test (run at 1.8xPET). This behavior is in agreement with the visible damage observed in C2, which was characterized by slightly more inclined cracks as compared with C1.

#### **4.11. Displacement and Curvature Ductility**

To quantify the ductility capacity of the specimens, the measured load-deflection and moment-curvature envelopes for each direction of the motion were idealized using elasto-perfectly plastic curves. In the load-deflection idealization, failure was defined as the point when either the peak displacement and corresponding force were reached or as the displacement corresponding to a dropping of 20% in the peak recorded lateral force.

The elastic portion of the idealized curve was represented by a secant line passing through the point in the envelope corresponding to the first longitudinal bar yielding. The effective yielding point was found in such way that both the ultimate displacement and the ultimate load of the idealization match the values for the envelope curve and by balancing the areas between the envelope and the idealized curves beyond the first yielding point. The same procedure was used to determine the elasto-plastic moment-curvature idealization.

The ultimate ductility was defined as the ratio between the failure (ultimate) and the effective yielding points in the idealized curves. Table 4-27 summarizes the calculated parameters required to determine the displacement and curvature ductilities for specimens C1 and C2. The idealized elasto-plastic curves are presented in Figs. 4-108 through 4-111 for specimen C1 and in Figs. 4-112 through 4-115 for specimen C2, respectively.

#### **4.12. Plastic Hinge Length**

The plastic hinge zone is defined as the region of a structural member over which strain and curvatures are largest. For single cantilever type columns the ultimate displacement at the tip of the column can be related to the effective yield and plastic displacements by the expression:

$$\Delta_u = \Delta_y + \Delta_p \quad (4-4)$$

If the plastic rotation is assumed to occur at the midheight of the plastic hinge zone, it is possible to find the plastic displacement by applying the moment area method, therefore:

$$\Delta_p = \phi_p L_p H_c = (\phi_u - \phi_y) L_p (H_c - 0.5 L_p) \quad (4-5)$$

Where:

$\Delta_u$  = ultimate lateral displacement

$\Delta_y$  = lateral displacement at the effective yielding point

$\Delta_p$  = plastic lateral displacement

$\phi_y$  = idealized yielding curvature

$\phi_p$  = plastic curvature

$\phi_u$  = ultimate curvature

$L_p$  = plastic hinge length

$H_c$  = distance from point of maximum moment to the point of contra-flexure

Estimations of the plastic hinge lengths were then made by solving simultaneously equations (4-4) and (4-5) using the calculated values of the idealized elasto-plastic force-displacement and moment-curvature curves. Values of the plastic hinge lengths for the tested specimens are reported in Table 4-28. For comparison, the plastic hinge lengths were also calculated by applying the empirical formulas in section 2.4.1 based on the Priestley's model (Priestley et al., 2007). Results show that the measured plastic hinge lengths were larger than the calculated values. An explanation for



this is that the equation proposed by Priestley is based on experimental result of columns tested under cyclic loads with low strain rates.

#### **4.13. Torque-Rotation Hysteresis**

The torque was calculated by taking moments around the geometric centroid of the column. Accordingly, the forces measured by the load cells attached to the links connecting the mass rig and the column, were multiplied by the relative position of the column (at each time instant) with respect to the centroid. The rotations at the top of the column were calculated by taking the difference of the readings of the two displacement transducers attached to the column tip (Fig. 3-37), and dividing by the horizontal distance between them. The measured torque-rotation hysteretic curves for each run of C1 are shown in Figs. 4-116 and 4-117 and in Figs. 4-118 and 4-119 for C2. Additionally, the hysteresis accumulated during all the runs of C1 is shown in Fig. 4-120 and in Fig. 4-121 for C2. From the figures, it is noted that during the first three runs the torque-rotation followed approximately a linear elastic trajectory with low hysteresis and without noticeable stiffness degradation. After the first longitudinal bar yielding, the torque-rotation curves showed energy dissipation but they did not follow a uniform trajectory as in the case of the force-displacement curves. The hystereses showed a distinctive loop and were clearly biased in one direction and becoming more prevalent after each subsequent run. The peak torque was recorded at 1.8xPET for C1 and 2.0xPET for C2, respectively. At this point, residual rotations were observed for both specimens.

In order to evaluate the magnitude of the measured torque and rotation, the accumulated hysteresis curves were compared with the torque-rotation capacity curve

calculated using the Softened Truss Model (Hsu, 1993) described in section 2.4.3 (See Figs. 4-122 and 4-123). From the figures, it is evident that the peak values of torque and rotation measured during the entire test sequence were smaller than the corresponding values at the yielding point for pure torque. This behavior is explained, because flexural deformation dominated the response of the columns. Consequently, softening of the torsional stiffness due to the development of a plastic hinge at the base of the column limited the development of the torsion. Similar behavior was observed by Belarbi *et al.* (2009), for circular columns tested using quasi-static methods under combined bending, torsion and axial load; in which the torque to bending ratio was below of 20%.

## **Chapter 5. Experimental Results for Interlocking Columns**

### **5.1. Introduction**

The preceding chapter described the seismic performance of two bridge reinforced concrete columns with circular sections tested under combined loads on a shake table. In this chapter the experimental results of two reinforced concrete specimens with double interlocking sections are presented. The two specimens were identical, with 1/4-scale double interlocking sections (I1 and I2), and were tested under the two horizontal components of the 1994 Northridge Earthquake recorded at Sylmar. The distribution of masses on the mass rig platform for specimen I1 was symmetric, while that for specimen I2 was unsymmetrical. Ground accelerations were applied in successive runs with increasing amplitude until the failure stage and without applying any axial load. This chapter describes the measured global responses (relative displacements, base shear and overturning moments) and local responses (strains and curvature) as well as the visual damage progression. Also presented are the calculations of the plastic hinge length and a bilinearization of the force-displacement and moment curvature envelopes based on effective yielding force and displacement.

### **5.2. Test Procedure**

The two horizontal components of the 1994 Northridge earthquake ( $M=7.0$ ) at Sylmar, California (PEER, 2000) were used as the input motions for specimens I1 and I2. The main reason to select this record was because it was used in a previous experimental study conducted at Nevada on double interlocking columns tested under unidirectional acceleration on a shake table (Correal *et al.*, 2006). Also because from preliminary

analysis it was found this record induced the highest value of torque to overturning moment (T/M) before failure for the specimen with asymmetric mass configuration (I2). By applying the similitude requirements and a scale factor of 1/4, the ground motion records were modified using a factor of 0.50 for time and 1.0 for the accelerations. Fig 5-1 shows the time history accelerations, the pseudoacceleration spectrum and the acceleration interaction orbits for the two horizontal components of the Sylmar record. The test protocol started with the calibration of the shake table by imposing small amplitude random vibration (tuning), followed by the application of low increments of the Sylmar record (10% to 20%) with the aim of determining the specimen's elastic properties and effective yielding. Once the elastic properties were determined, the specimens were subjected to successive runs of increasing amplitude until failure. Based on preliminary analysis, the maximum earthquake level was 1.8 times Sylmar, however repetitions of the runs at 1.4xSYL and 1.8xSYL for I1 and I2, respectively were required to fracture the reinforcement. These motions reflect the effect of a major aftershock on a bridge that has been previously subjected to a strong ground motion.

Signals of white noise were also applied in each direction to determine the changes in the dynamic properties (period and damping) between runs. The testing protocol for I1 and I2 is described in Tables 5-1 and 5-2, respectively. The input time history accelerograms are shown in Figs. 5-2 and 5-3 for the longitudinal and transverse direction of specimen I2. The large horizontal component of the Sylmar record was applied parallel to the long side of the specimens, longitudinal (X) direction of the columns (North-South directions of the shake table), and the small component was

applied parallel to the short side (transverse direction, Y) or East-West direction of the shake table.

### **5.3. Shake Table Performance**

The same procedure applied in the circular specimens, to verify the accuracy of the shake table in reproducing the input acceleration, was used for the double interlocking specimens. A comparison between the achieved and target acceleration for each direction of the interlocking specimens for all the runs is shown in Tables 5-3 and 5-4. For I1 the ratio between achieved and input PGA was approximately constant for each direction of motion, with averages values of 0.95 and 0.99 in the longitudinal and transverse directions. A similar trend was observed for I2, where the average values for all the runs were 1.02 and 0.99 in the longitudinal and transverse direction. An additional comparison to evaluate the accuracy of the shake table was made by calculating the acceleration, velocity and displacement response spectrums for the input and achieved accelerations. Instead of comparing each response alone, a trilogarithmic spectrum was calculated for each run and for each direction of motion. The trilogarithmic response spectrums were calculated for a range of periods of 0.02 and 3 seconds and for a damping coefficient of 0%. Comparisons between the spectral responses for the target and achieved motions during each run are shown in Fig. 5-4 through 5-14 for I1 on the longitudinal and transverse directions, and in Figs. 5-15 through 5-25 for both directions of I2. Particularly important is the comparison between the input and achieved response at the period of the specimen during each run (details of the calculation of the period is presented in section 5.6). The ratio between the achieved and input spectral parameters at the measured period

of the specimens is summarized in Table 5-5 for I1 and in Table 5-6 for I2. Average values of the ratio (displacement, velocity and acceleration) for all the runs were around 0.97 and 0.87 in the longitudinal and transverse directions for I1 and around 0.99 and 0.90 for the same directions of I2. Although there were some discrepancies between the target and achieved elastic responses for the transverse direction of motion, the performance of the shake table was acceptable for all the motions used in the test protocol.

#### **5.4. Observed Column Performance**

To facilitate the crack detection and characterize the damage after each run of the test protocol, white paint was applied to the surface of the specimens and markers of different colors were used to outline the trajectory of the cracks; each color was associated with a specific run. For specimens I1 and I2 the overall behavior was dominated by the effect of biaxial bending. The damage was characterized by the presence of horizontal cracks distributed both around and along the specimens' surface, and by inclined cracks located on the lower third of the column height. During the last runs of the test protocol, a plastic hinge was completely formed at the bottom of the specimens.

After the tuning and  $0.1 \times \text{SYL}$ , hairline horizontal fissures were detected around the perimeter of the specimen; most of them in the lower half of the column height. Maximum drift ratios in the longitudinal and transverse directions,  $\delta_L=0.34\%$  and  $\delta_T=0.24\%$  were measured for I1 and  $\delta_L=0.29\%$  and  $\delta_T=0.27\%$  for I2. Fig. 5-26 shows the extent of damage for I1 and I2 after these small amplitude runs. The first longitudinal bar

yielding was recorded at 0.2xSYL in both specimens; drift ratios of  $\delta_L=0.78\%$  and  $\delta_T=0.55\%$  for I1 and  $\delta_L=0.85\%$  and  $\delta_T=0.50\%$  for I2 were measured at this stage. As is illustrated in Fig. 5-27, the damage was characterized by an extension in the horizontal cracking and the presence of some inclined cracks concentrated on the lower third of the column. Some cracking was also observed at the surface of the footing. The cover concrete started to spall at the base of the columns during 1.0xSYL for both specimens ( $\delta_L=5.2\%$  and  $\delta_T=4.0\%$  for I1 and  $\delta_L=5.2\%$  and  $\delta_T=3.4\%$  in I2). Until this point of the experiments, a considerable number of horizontal and inclined cracks were observed, most of them concentrated on the lower half of the columns height. (Figs. 5-28 and 5-29). After 1.2xSYL ( $\delta_L=6.02\%$  and  $\delta_T=4.96\%$  in I1 and  $\delta_L=6.0\%$  and  $\delta_T=4.2\%$  in I2) extension of the spalled area at the base of the columns, as well as propagation of the flexural and shear cracking was observed (Figs. 5-30 and 5-31). For both specimens spiral reinforcement was clearly exposed at 1.4xSYL ( $\delta_L=6.8\%$  and  $\delta_T=6.1\%$  in I1 and  $\delta_L=6.7\%$  and  $\delta_T=5.14\%$  in I2) and longitudinal bars were visible at 1.6xSYL ( $\delta_L=8.6\%$  and  $\delta_T=7.32\%$  in I1 and  $\delta_L=7.3\%$  and  $\delta_T=6.0\%$  in I2). Figs. 5-32 and 5-33 show the damage accumulated in the specimens up to this stage. Specimens failed after 1.8xSYL when repetitions of the runs at 1.4xSYL for I1 and 1.8xSYL for I2 were imposed to the columns ( $\delta_L=7.9\%$  and  $\delta_T=9.47\%$  in I1 and ( $\delta_L=7.7\%$  and  $\delta_T=9.39\%$  in I2). At the failure, several longitudinal bars ruptured and other were buckled, and damage penetrated the concrete core in the plastic hinge region. Figs. 5-34 and 5-35 show the damage state at the last run of columns I1 and I2, respectively. Fig. 5-36 compares the damage pattern for

the double interlocking specimens after testing. The observed performance for specimen I1 is summarized in Table 5-7, while this is presented in Table 5-8 for specimen I2.

### **5.5. Lateral Force-Displacement Hysteresis**

Due to the fact that the load cells attached to the links only recorded the forces transmitted from the mass rig to the specimens, additional forces were calculated to account for the dynamic vibration of the columns under the shake table acceleration. These forces were calculated following the same procedure applied in section 4.5 for circular columns. The total lateral forces induced in each direction at the specimens' tip, were then calculated as the summation of the forces measured by the load cells and the inertial forces due to the mass of the specimen. The base shear was defined to be equal to the total lateral force, and the base moment as the product of the base shear and the distance between the top of the footing and the point of connection of the links at the column head (72 in).

The specimen displacements in each direction relative to the footing were calculated by subtracting the total displacements measured at the top of the columns from the shake table displacements. Top column displacements were calculated as the average of the readings of the two displacement transducers attached to the column head in each direction. In addition, the displacement drift ratio ( $\delta$ ) was calculated as the quotient between the top relative displacement and the distance between the column base and the point of connection of the displacement transducer (83 in).

The measured lateral force-displacement hysteresis curves for the longitudinal and transverse directions of motion in specimen I1 are shown in Figs. 5-37 through 5-47



and in Figs. 5-50 through 5-60 for specimen I2. The cumulative force-displacement hysteresis curves for the longitudinal and transverse directions are shown in Figs. 5-48 and 5-49 for specimen I1 and in Figs. 5-61 and 5-62 for specimen I2.

For small amplitude runs, the specimens responded elastically with low hysteresis and without noticeable lateral stiffness degradation. Once the longitudinal bars started to yield, some degradation in the lateral stiffness was observed. At this stage the specimens dissipated more energy; wider hysteresis loops were observed after yielding and the area enclosed by the loops increases with the ground motion amplitude.

The maximum peak lateral force in the longitudinal direction was recorded during the run at 1.4xSYL for both specimens, while it was reached at 1.6xSYL for the transverse direction. Once the specimens reached their maximum capacity (peak resisting force), the response was characterized by a considerable stiffness degradation and a progressive reduction in the lateral force capacity with successive runs until failure. At the last run; 1.4\*xSYL for I1 and 1.8\*xSYL for I2, a plastic hinge was completely developed at the base of the columns causing significant loss in the lateral force capacity, and making the specimens more sensitive to collapse due to lateral instability. A summary of the measured peak lateral force with the corresponding displacement and the peak displacement with the corresponding force is presented in Tables 5-9 and 5-10 for I1, and in Tables 5-11 and 5-12 for I2.

A backbone envelope curve was plotted for each direction of the specimens based on the measured peak lateral forces and the corresponding displacements reached in each run until failure. The failure point for the envelope was defined either as the peak displacement and corresponding force or the displacement corresponding to a drop of

20% in the lateral force capacity. Figs. 5-63 and 5-64 show the calculated envelopes of lateral force-displacement for the longitudinal and transverse directions of motion in specimens I1 and I2, respectively.

## **5.6. Dynamic Properties**

In order to calculate the dynamic properties of the specimens (period and damping), two procedures were applied: the power spectrum density (Clough and Penzien, 1993) and the multiple input - multiple output (MIMO) for system identification (Li and Mau, 1991). Both of them were explained in detail in section 5-6. These properties were determined from the low level white noise signals applied to the specimens before and after each run. Figs. 5-65 through 5-68 show the power spectrums and the calculated frequencies, for each direction of the specimens after each motion of the test protocol. A summary of the computed period and damping for each direction of the double interlocking specimens are presented in Tables 5-13 and 5-14. The variation in the dynamic properties with the test progression, measured using the two different methods, is shown in Figs. 5-69 and 5-70 for I1, and in Figs. 5-71 and 5-72 for I2.

The measured periods for each direction of the specimens were gradually elongated with the level of excitation, as a consequence of the stiffness degradation. At the low level excitation (0.1xSYL) average values of about 0.55 sec. and 0.78 sec. were measured along the longitudinal and transverse direction of the specimens, respectively. These periods were shifted to values of about 1.40 sec. and 1.35 sec. for the same directions during the last run.

Damping coefficients were, in general, increased with the progression of the testing; however, a less evident tendency was observed for the measured values within successive runs. Values in the range of 3% and 10% were measured for I1, and between 3.5% and 10% for I2. Figs.6-73 and 5-74 show a comparison between the variations in the dynamic properties with the test sequence for the longitudinal direction of the specimens and calculated using the different methods. Good agreement was observed in the values and trends of the calculated properties using the power spectrum and MIMO.

### **5.7. Lateral Stiffness**

The effective lateral stiffness ( $EI_e$ ) of the specimens after each run of the test sequence was calculated from the measured periods, the total mass in the system (85 kips) and the geometry of columns; following the procedure described in section 4.7 for single cantilever-type columns. A summary of the measured values for each direction of the columns is shown in Tables 5-15 and 5-16 for specimens I1 and I2, respectively. In order to compare the measured lateral stiffness with respect to the gross stiffness ( $EI_g$ ), the former values were normalized with respect to the latter. Figs. 5-75 and 5-76 show the variation in the values of the effective lateral stiffness as they change with the level of excitation. At the undamaged stage, the measured values were in average 20% and 25% of the gross stiffness on the longitudinal and transverse directions of the specimens; these were reduced to about 18% and 20% of the gross stiffness at yielding; and they were gradually reduced with the progression of the testing reaching a minimum value of 5% during the final runs.

## 5.8. Curvature

The Novoteknik displacement transducers were used to determine the specimens' average curvature in the potential plastic hinge region for each run of the testing sequence. In total, four segments were used to measure curvature; details of the instrumentation and calculation procedure were presented in section 3.5.4.

The curvature distributions along the height of the columns, and for the two perpendicular directions of the excitation are shown in Fig. 5-77 and 5-78 for I1, and in Figs. 5-79 and 5-80 for I2. The points in the curvature profiles represent the curvature measured at the specific location and in correspondence to the maximum and minimum peak values of lateral force reached during each run of the test sequence. The curvature profiles for low level excitations followed a linear distribution along the height of the specimens. Once the first yielding was reached, the curvature profiles showed a nonlinear distribution, with high curvatures measured near the base of the columns and with a reduction in the magnitude with the column height.

The profiles of peak curvatures (maximum and minimum) were approximately symmetric along the longitudinal direction and asymmetric on the transverse direction of the specimens. This behavior is explained in part, by the larger asymmetry in the acceleration pulses (positive and negative) of the record SYL090 (PEER, 2000) used as the acceleration excitation in the transverse direction of the specimens (Figs. 5-1 and 5-3).

Moment-curvature hysteresis curves were calculated in order to estimate the curvature ductility experienced by the specimens during each run of the test protocol. Moment was calculated as the product of the lateral force at the top of the column and the

distance from the top of the column to the relevant segment where curvature was measured. The moment-curvature for each specimen was defined as the average of the values calculated for the two lower segments ( $H=3$  in. and  $H=8$  in). The accumulated average moment-curvatures curves for each direction of the columns are shown in Figs. 5-81 and 5-82 for I1, and in Figs. 5-83 and 5-84 for I2, respectively. A backbone envelope curve was developed based on the peak moment with corresponding curvature for all the motions until failure. Figs. 5-85 and 5-86 show the average moment-curvature envelopes for the double interlocking specimens.

### **5.9. Bond-slip Rotations**

For a single cantilever reinforced concrete column under seismic loading, large stresses and strain demands are expected to occur at the point of connection between the column and the footing, which need to be transferred from one member to the other by bond stresses between the steel bars and the surrounding concrete. To effectively transfer the bond stress and prevent bar pull out, the steel bars need to be properly anchored inside the concrete by a minimum distance known as development length or hooked to provide the required anchorage. When the bars are properly anchored in the concrete, the strains induced along the development length create elongation of the tensile reinforcement at the connection interface; this effect is known as bond slip. When the bar slip occurs at the column-footing contact surface, relative rotations are developed between these two members. These additional rotations induce lateral deflection, which in turn affect the strain and curvature distribution in the critical region, as well as the lateral stiffness of a flexural member.

Bond slip rotations were calculated using the Novoteknik displacements transducers mounted on threaded bars at 4 in. and 1 in. from the footing surface (Figs. 3-39 and 3-40). Rotation along the longitudinal and transverse directions, were calculated as:

$$\theta_{slip} = \frac{\Delta_{i,3} - \Delta_{i,4}}{d_{3-4}} - \frac{\Delta_{i,1} - \Delta_{i,2}}{d_{1-2}} \quad (5-1)$$

Where:

$\Delta_{i,1,2}$  = displacements measured by transducers 1 and 2.

$\Delta_{i,3,4}$  = displacements measured by transducers 3 and 4.

$d_{1-2}$  = horizontal distance between transducers 1 and 2

$d_{3-4}$  = horizontal distance between transducers 3 and 4

The accumulated base moment vs. bond-slip rotation hysteresis curves are shown in Figs. 5-87 and 5-88 for the longitudinal and transverse directions of I1, and in Figs. 5-89 and 5-90 for I2. Backbone envelope curves were also calculated based on the peak base moment with corresponding bond-slip rotation for all the motions until failure, as it is shown in Figs. 5-91 and 5-92 for I1 and I2, respectively. From the figures, it is clear that the calculated envelopes for each specimen are comparable, but specimen I1 showed larger bond-slip rotations than I2. This is because it was not possible to calculate rotations at the last runs of I2, due to the inaccurate readings of the Novoteknik displacement transducers. Average bond-slip rotations of 0.0015 rad., 0.01 rad. and about

0.03 rad. were measured at yielding, peak base-moment and ultimate point along the long side of the specimens. These values were about 0.0015 rad., 0.02 rad. and 0.03 rad. along the short side of the specimens.

### **5.10. Flexural and Shear Deformations**

The contributions of the flexural deformations to the total displacements were calculated by integrating along the height of the columns, the curvature profiles calculated in section 5.8. The moment-area method was applied to calculate the peak flexural deformations for each run. The curvatures were assumed to be constant over the gauge length of the Novoteknik transducers, and a straight line was used to connect the curvature measured at 28 in. (height of the top Novoteknik transducer) and the zero curvature at the top of the specimens. A backbone envelope curve was constructed based on the calculated flexural deformation and the peak lateral force reached at each run of the test sequence. Figs. 5-90 and 5-92 show the lateral force versus flexural deformations for I1 and I2, respectively.

Once the flexural deformations were estimated by integrating the curvature profiles, the shear deformations were calculated by subtracting the flexural deformations from the total displacements measured at the top of the specimens. Shear deformation was calculated only for the predominant component of lateral deformation (negative envelope on the longitudinal direction and positive envelope along the short direction). An envelope curve was developed based on the calculated shear deformation and the peak lateral force reached at each run. Figs. 5-93 and 5-94 show the lateral force versus shear deformation for the longitudinal and transverse directions of I1 and I2, respectively.

The maximum measured shear deformations in specimen I1 were 30% and 20% of the total deformation on the longitudinal and transverse directions, respectively. For specimen I2, these values were 35% on the longitudinal and 15% on the transverse directions. In addition, Figs. 5-95 and 5-96 show the contribution of the flexural deformation to the total deformation measured at the top of the specimens, for the longitudinal direction. From the figures it is apparent that the seismic performance of the specimens was dominated by the flexural deformations

### **5.11. Strains**

The strain gauges attached to the longitudinal and spiral reinforcement were used to study the distribution of strains along the potential plastic hinge zone. As is shown in Fig. 3-42, six sections were used at the base of the columns to study the strain distribution: 5 in. below the top of the footing, footing-column interface and at 5 in., 10 in., 15 in. and 20 in., above the footing.

The peak maximum and minimum strains of the reinforcement at every section are presented in Tables 5-17 through 5-22 for specimen I1 and in Tables 5-23 through 5-28 for specimen I2. Positive values refer to tensile strains, while negative values correspond to compressive strains. Data from malfunctioning gauges are not reported in the tables. The yielding strains for the reinforcement were calculated as the quotient between the yielding stresses reported in Table 4.1 and the modulus of elasticity of the steel (29,000 ksi). Average yielding strains of  $2170\mu\epsilon$  and  $2000\mu\epsilon$  were calculated for the longitudinal (No.3 bars) and transverse (W2.9) spirals, respectively. Values marked with



bold characters on the summary tables refer to deformations larger than or equal to the yielding point.

Yielding in the longitudinal bars was first observed during the second run at  $0.2xSYL$  for both specimens. In total 15 bars in I1 and 23 in I2 recorded strains larger than the calculated yielding point. Strain gauges at the section below the footing (-5 in.) experienced yielding after the motion at  $0.4xSYL$  for both specimens. Once the first longitudinal bars yielded, high strain deformations were observed along the plastic hinge region for successive runs until failure.

In order to study the variation in the measured longitudinal strains along the height of the specimens with respect to the level of excitation, the strain recorded at different locations along a specific bar were plotted as it is illustrated in Figs. 5-94 through 5-103. To facilitate the bars identification, bars on the perimeter were numbered sequentially from the North side of the columns. As was expected, higher strains were observed near the column base (from 0 to 10 in.) as compared with other locations along the column height. Similarly to the circular specimen tested, strains larger than the yielding point were recorded outside the instrumented section (20 in. above the footing), which showed that yielding extended beyond the plastic hinge zone under high levels of excitation.

The first yielding in the spirals was observed after  $0.2xSYL$  and  $0.4xSYL$  for I1 and I2. After the first yielding, the strains gradually increased with the level of excitation. At the end of the test, extremely high strains were recorded in the spirals as a consequence of the longitudinal bar buckling or spiral fracture. Figs. 5-104 through 5-109 show the spiral strain profiles along the instrumented height of the specimens. Higher

values of strains were recorded on the section at 5 in. and 10 in. above the footing, which correspond to the section where large deformations were recorded in the longitudinal bars. Also, a more uniform distribution of strains was observed in the spirals as compared to the longitudinal bars.

The strain distribution along the instrumented height of the specimens followed similar trends for the longitudinal and spiral reinforcement. However, slightly higher strains were measured in I1 compared to I2 for the same level of excitation. This behavior is in agreement with the visible damage observed in specimen I1, which was characterized by a slightly more inclined cracks, compared with column I2.

### **5.12. Displacement and Curvature Ductility**

The measured load-deflection and moment-curvature backbone envelopes were used in order to calculate the ductility capacity and length of the plastic hinge of the specimens. This was accomplished by simplifying each envelope using an elasto-plastic idealization. The procedure described in section 4.11. was followed to determine the effective yielding and ultimate points in the idealized curves.

The ductility was defined as the quotient between the measured displacement or curvature and the values corresponding to the effective yielding point in the idealized curves. A summary of the parameters required to calculate the displacement and curvature ductilities for both specimens is shown in Table 5-29. The idealized elasto-plastic curves are presented in Figs. 5-110 through 5-113 for I1 and in Figs. 5-114 through 5-117 for I2, respectively.

### **5.13. Plastic Hinge Length**

The plastic hinge lengths for both specimens were determined by the moment – area method using the idealized elasto-plastic curves (force-displacement and moment-curvature) and by applying the procedure described in section 4.12. Values of the plastic hinge lengths for the tested specimens are reported in Table 5-30. For comparison, the plastic hinge lengths were also calculated by applying the empirical model developed by Priestley (Priestley et al., 2007) and presented in section 2.4.1. Similar to the case of circular specimens, the measured plastic hinge lengths were larger than those calculated using Priestley’s model. The explanation for this is that the equation proposed by Priestley is based on experimental results of columns tested under cyclic loads with low strain rates.

### **5.14. Torque-Rotation Hysteresis**

The torque and rotations were calculated using the procedure described in section 4.13 for circular columns. The measured torque-rotation hysteretic curves for each run of I1 are shown in Figs. 5-118 and 5-119 and in Figs. 5-120 and 5-121 for I2. Additionally the hysteresis accumulated during all the runs of I1 is shown in Fig. 5-122 and in Figs. 5-123 for I2. From the figures, it is noted that during the first three runs, the torque-rotation followed approximately a linear elastic trajectory with low hysteresis and without noticeable stiffness degradation. After the first longitudinal bar yielding, the torque-rotation curves showed energy dissipation but did not follow a uniform trajectory as in the case of the force-displacement curves. The hystereses showed a distinctive loop and were clearly biased in one direction and becoming more prevalent after each subsequent

run. The peak torque was recorded at 2.0xSYL for I1 and 1.6xPET for I2, respectively. At this point, residual rotations were observed for both specimens.

In order to evaluate the magnitude of the measured torque and rotation, the accumulated hysteresis curves were compared with the torque-rotation capacity curve calculated using the Softened Truss Model (Hsu, 1993) described in section 2.4.3 (See Figs. 5-124 and 5-125). From the figures, it is evident that the peak values of torque and rotation measured during the entire test sequence were smaller than the corresponding values at the yielding point for pure torque. The explanation of this behavior is that flexural deformation dominated the response of the columns. Consequently, softening of the torsional stiffness due to the development of a plastic hinge at the base of the column, limited the development of torsion.

## Chapter 6. Columns Tested Under Unidirectional Ground Motions

### 6.1 Introduction

Since the main objective of this research was to study the effects of combined loading (including biaxial bending and torsion, without axial force) on the seismic performance of RC bridge columns, the experimental results were compared with those obtained in previous studies conducted at the University of Nevada Reno on similar columns tested on a shake table, but using unidirectional acceleration and axial force.

### 6.2 Test Setup for Unidirectional Tested Specimens

To apply the inertial lateral forces to the top of the specimens, the Unidirectional Mass Rig (MR) developed at the University of Nevada Reno by Laplace *et al.* (Laplace *et al.*, 1999) was used. The MR is basically a 3D steel frame with four supporting columns and a deck connected to the columns by two beams (Fig. 6-1). Eight pins, (one at the base of each column and one at the column-beam connection) allow the system to laterally move the mass and transfer the uniaxial inertial forces into the specimen through a rigid swiveled link; the system without the specimen and link is unstable. The deck allows the placing of concrete blocks or lead bricks to provide inertial mass, which added to the self weight of the MR structure, compose the total inertial mass. The total lateral forces transferred from the MR structure to the specimen is a combination of inertial forces due to the driving mass and an additional component induced by secondary moments due to the rotation of the MR and the lateral movement of the mass (P-delta effects). Restrainer cables were incorporated into the system to limit the translation of the mass system and

prevent the total collapse in the event of specimen's failure. For the circular specimens, the total inertial mass used was 80 kips., 60kips. from three concrete blocks (each of 20 kips.) plus 20 kips from the MR. The interlocking specimen used four concrete blocks; thus the total inertial mass was 100 kips.

In order to apply the axial load to the columns, a steel spreader beam was bolted on the top of the specimens. This beam transferred the axial load that was applied through two center-hole hydraulic rams connected to an accumulator (Figs. 6-1 and 6-2). Two external high strength rods were prestressed between the rams and the footing to create a constant axial force, which was kept almost constant during the test sequence because of the accumulator. The axial load transferred to the columns was monitored using load cells between the rams and the spreader beam. Target values of axial load of 80 kips and 90 kips were used for the circular and interlocking specimens, respectively.

### **6.3 Circular Columns 9F1 and NF1**

As it was mentioned in section 2, circular specimens C1 and C2 where designed and constructed using the same scale, dimensions and reinforcement steel ratios as columns 9F1 (Lapace *et al.*, 1999) and NF1 (Phan *et al.*, 2005). Although specimens 9F1 and NF1 were almost identical and tested using the unidirectional MR, they were tested under different earthquakes. 9F1 was tested under series of the 1940 Imperial Valley earthquake at El Centro, while NF1 was tested under the 1994 Northridge earthquake recorded at the Rinaldi station; in both cases increasing amplitude motions were applied in successive runs until specimen failure. According to Phan (Phan *et al.*, 2005), the record at Rinaldi is considered as a near fault ground motion with forward directivity and

the El Centro is not. Figs. 6-3 and 6-4 show the compressed time history acceleration and pseudoacceleration spectrum for El Centro and Rinaldi ground accelerations. Other differences between these specimens include the axial load attained during the test protocol and the way in which the lateral forces were transferred from the MR to the column. For column 9F1 the rigid link transferring the inertial forces from the MR was connected to a steel spreader beam bolted at the top of the column, while in specimen NF1 the link was directly connected to a concrete head monolithically constructed at the top of the column. Nevertheless, the point of connection of the rigid link to the specimens was located at 72 in. from the top of the footing. Details of the instrumentation used in each test can be found in Laplace *et al.* (Laplace *et al.*, 1999) and Phan *et al.* (Phan *et al.*, 2005). A total of 9 runs were required to fail specimen 9F1, whereas 11 runs were required to fail specimen NF1. Tables 6.1 and 6.2 summarize the test sequence followed for columns 9F1 and NF1, respectively. It is important to note, that the first run of 9F1 was repeated five times to insure a good agreement between the input and achieved acceleration on the shake table. Tables 6.3 presents the concrete compressive strength measured from cylinders for each specimen on the test day, while Table 6.4 summarizes the reinforcing steel properties measured from reinforcement samples.

For both tested specimens, the damage progression was controlled by bending, with longitudinal and inclined cracks located on the extreme sides of the columns (E-W for 9F1, and N-S for NF1), which increased with the testing sequence until the formation of a plastic hinge at the base of the specimens. For small amplitude runs, the behavior was elastic with minor cracks visible on the columns. The first longitudinal bar yielding was observed during run 2 for 9F1 (Drift ratio  $\delta=1.62\%$ ) and during Run 3 for NF1

( $\delta=1.11\%$ ). For both specimens, the first concrete spalling was observed at the base of the columns during run 5 ( $\delta=3.78\%$  in 9F1 and  $\delta=3.70\%$  in NF1). Extensive spalling at the base of the columns, as well as propagation of the flexural and shear cracks, was experienced after run 6 for columns NF1 ( $\delta=6.0\%$ ) and after run 7 in 9F1 ( $\delta=6.80\%$ ). The spirals and longitudinal bars were clearly visible at the end of run 8 ( $\delta=8.24\%$  in 9F1 and  $\delta=10.0\%$  in NF1). Finally, the failure of the specimens was observed after run 9 for 9F1 ( $\delta=12.13\%$ ) and after run 11 for NF1 ( $\delta=16.44\%$ ). The failure was characterized by the following events: longitudinal bar buckling, longitudinal bar fracture, spiral rupture and core concrete damage. At the point of failure, specimen NF1 showed large residual displacements, but column 9F1 completely collapsed due to lateral instability induced by secondary moments (P-delta effects).

#### **6.4 Interlocking Column ISL1.0**

Double Interlocking columns I1 and I2 were designed and constructed using the same section and reinforcement as the interlocking column ISL1.0 tested at UNR by Correal *et al.* (Correal *et al.*, 2004), but with a total height of 72 in. instead of 58 in. which was used in ISL1.0. This specimen was tested on the shake table under a series of increasing amplitude motions based on the 1994 Northridge earthquake recorded at Sylmar. The specimen was tested as a single cantilever column using the MR developed by Laplace *et al.* (Laplace *et al.*, 1999), with the inertial forces exciting the specimen about the strong axis of the section. Fig. 6-5 shows details of the specimen and test setup used for the column testing. Tables 6.3 and 6.4 summarize the material properties



measured on test day, based on concrete cylinders and reinforcement samples. The specimen failed after 10 runs of the applied earthquake as shown in Table 6.5.

The seismic performance of the column, similar to the case of the circular specimens 9F1 and NF1, was dominated by flexural deformations. The damage was characterized by the development and extension of longitudinal and inclined cracks distributed on the lower half of the column until a plastic hinge was completely developed at the base. For small amplitude runs, the behavior was essentially elastic with minor horizontal cracks visible. The first longitudinal bar yielding was recorded during run 3 (Drift ratio  $\delta=0.93\%$ ). The first concrete spalling and inclined cracks were observed during run 4 ( $\delta=1.72\%$ ). Considerable spalling, in addition to propagation of flexural and shear cracks was observed after run 6 ( $\delta=2.26\%$ ). The reinforcement (spirals and longitudinal) was clearly visible at run 8 ( $\delta=4.74\%$ ). The failure of the specimen occurred during run 10 ( $\delta=9.34\%$ ), and it was due to the rupture of the spirals and compression buckling of the longitudinal bars in the plastic hinge zone.

## **6.5 Force-Displacement Envelopes**

The lateral force in all the specimens was calculated as the summation of the force measured by the load cell attached to the rig swiveled link, and the inertial force due to the tributary mass of each specimen. The inertial mass on the MR for the circular specimens was set as 80 kips, an approximately 100 kips for the interlocking specimen. The displacement at the top of the column relative to the footing was calculated as the difference between the recorded values at the specimen tip and the displacement of the shake table. Figs. 6-6 through 6-8 show the cumulative lateral force-displacement

hysteresis for all the runs in specimens 9F1, NF1 and ISL1.0, respectively. The figures also show a backbone envelope curve formed by the peak force attained in each run and the corresponding displacement. The failure point in the envelopes was assumed to be either the peak displacement with the corresponding force, or the displacement corresponding to a force equal to 80% of the peak force, whichever occurred first. Once the lateral force and relative displacement were calculated, it was possible to compute the base shear, the base moment and the column drift ratio. The base shear was assumed to be the same as the lateral force, the base moment was computed as the product of the base shear and the bending arm (distance between the top of the footing and the point of connection of the links at the column head), while the drift ratio was calculated as the quotient between the specimen's relative displacement and the bending arm. Tables 6-6 and 6-7 list the peak measured responses parameters for circular and interlocking specimens, respectively. For the circular specimens only the peak maxima response is presented.

## **6.6 Axial Load Variation**

Although the experiments were designed to keep the same level of axial force during the test sequence, some variations were observed in between runs. The peak values of axial load are reported in Table 6-6 for circular columns and in Table 6-7 for the interlocking specimen. From the results, it is clear that deviations larger than 40% between the target and peak values were observed for column 9F1. According to Laplace *et al.* (Laplace *et al.*, 1999) variations of the axial load were due to a malfunction of the hydraulic system during the test. These deviations were only 4% for column NF1 and 6%

for ISL1.0. As pointed out by Phan *et al.* (Phan *et al.*, 2005) the fluctuations in the axial load system for column NF1 were due mainly to a time lag in the control system for the accumulators.

In order to visualize the variations of axial load and its influence on the seismic performance of the columns, the axial load versus top displacement and axial load versus base moment cumulative hystereses are plotted in Figs. 6-9 through 6-14. Column 9F1 showed large hysteresis loops compared with NF1 and ISL1.0, where the axial load was almost constant. For all the specimens, the maximum axial load recorded during the tests coincided with the maximum base moment. By comparing Figs. 6-6 and 6-7, it is clear that the increase in the lateral capacity of 9F1 with respect to NF1 is attributed to the large variation in axial load.

## **6.7 Measured Dynamic Properties**

The accelerations recorded during each run were used to calculate the lateral stiffness and period of the specimens. The period was calculated by using the transfer function between the acceleration recorded at the top of the column and the shake table; whereas the lateral stiffness was calculated following the procedure described in section 4.7 (Eqs. 4-1 through 4-3). The column height used in Eqs. 4-2 and 4-3 was assumed to be the height of the specimens to the link connection; 58 in. for ISL1.0 and 72 in. for circular specimens. Table 6-8 lists the calculated dynamic properties for all the specimens including the longitudinal direction of the bidirectional tested columns C1, C2, I1 and I2. Figs. 6-15 and 6-16 show the variation in the effective lateral stiffness ( $EI_e$ ) with the progression of the test for circular and interlocking columns, respectively. From the

result, it is clear that the specimen period gradually increased as the lateral stiffness was degraded with the damage progression.

## **6.8 Moment – Curvature Envelopes**

In order to estimate the moment and curvature capacity of each of the specimens tested, a backbone envelope curve was plotted based on the moment-curvature hysteresis measured during each run. Moment was calculated as the product of the lateral force measured at the point of connection of the link and the distance from that point to the relevant segment where curvature was measured. The curvature was calculated from the vertical displacement transducers attached to the specimens along the potential plastic hinge zone, following the procedure described in section 4.8. The moment-curvature envelope curve for the unidirectionally tested specimens was defined as the average of the values measured at the three lower instrumented segments (2 in., 6 in. and 8 in. from the top of the footing). Figs. 6-17 and 6-18 show the computed moment-curvature envelopes for the circular and interlocking specimens, respectively. The moment curvature envelope for the longitudinal direction was used for the specimens tested under bidirectional shaking. For these specimens, moments and curvatures were computed as the average of the values measured at the lower two segments (2 in. and 8 in. above the footing).

With the aim of estimating the curvature ductility, the moment-curvature backbone envelope for each specimen was idealized by elasto perfectly plastic curves following the procedure described in section 4.11. The idealized elasto-plastic curves for the circular and interlocking specimens are presented in Figs. 6-19 and 6-20, respectively.

The curvature ductility was defined as the quotient between curvatures at the ultimate and effective yielding points on the idealized curves. Table 6-9 summarizes the calculated parameters required to determine the curvature ductilities for all the specimens tested.

## **6.9 Concrete Strains**

In order to compare the measured concrete strain with those calculated from analytical models, the unconfined and confined concrete strains at the plastic hinge region were calculated for specimen 9F1. Unconfined concrete strain was defined as the average strain at the column surface, while the confined strain was defined as the strain at the level of the longitudinal reinforcement assuming a perfect bond between the concrete and the steel. The concrete strains were calculated from the vertical displacement transducers attached to the specimens along the potential plastic hinge zone using the procedure described in section 3.5.4 and based on the assumption that the column sections remained plane. Concrete strains were computed as the average of the values measured at the lower two segments (2 in. and 6 in. above the footing). Table 6-10 summarizes the calculated concrete strains for 9F1. It is worth noting that the large compressive strains observed at the last runs of the test protocol are associated with the longitudinal bar buckling, bar and spiral rupture, and core damage. By comparing the results in Table 6-10 with those in Table 2-3, it is clear that the calculated values of ultimate confined concrete strain using Mander's model (Mander *et al.*, 1988) are conservative with respect to the measured strains at the last two runs of the testing protocol. It implies that the specimen's failure displacement occurred considerably later than that predicted from the results using Mander's model for confined concrete; in

which the failure is associated with the crushing of the confined concrete. Similar results were observed by Johnson *et al.* based on a shake table test of a two span RC bridge system at University of Nevada Reno (Johnson *et al.*, 2006).

## **6.10 Comparisons of Unidirectional and Bidirectional Tests**

In order to compare the seismic performance of the specimens tested under biaxial bending with those under uniaxial bending plus axial force, the base shear vs. displacement and base moment vs. drift ratio backbone envelope curves were plotted. Figs. 6-21 and 6-22 compare the seismic performance of the circular columns 9F1, NF1, C1 and C2. Similarly Figs. 6-23 and 6-24 show the comparisons for the interlocking specimens ISL1.0, I1 and I2. An idealized elastic perfectly plastic envelope was calculated for each specimen backbone envelope following the procedure described in section 4.11. Figs. 6-25 through 6-28 present the elasto-plastic idealizations for circular and interlocking specimens. For the cases of biaxial bending, the predominant direction of motion (longitudinal direction) of the specimens was used. Once the elastic perfectly plastic envelopes were calculated, the displacement ductility experienced by the specimens during each run was calculated as the quotient between the measured displacement and the displacement corresponding to the effective yielding point. The parameters required to calculate the ultimate displacement ductilities for all the specimens are summarized in Table 6-11.

### **6.11.1 Circular Specimens**

By comparing the base shear-displacement and base moment-drift ratio envelopes for specimens 9F1 and NF1 (Figs. 6-21 and 6-22), it is clear that the large variations in

the axial load (44%) experienced by 9F1 influenced significantly the seismic performance of the specimen. For this specimen, the maximum base shear was about 10% larger, and the drift ratio at failure was 22% less than the same values recorded for NF1. Moreover the large variation in axial force in 9F1 resulted in more significant secondary moment effects (P-delta). Although the variations in axial force played a significant role on the column performance, the near field ground motion used in NF1 also affected the column performance. As pointed out by Phan *et al.* (Phan *et al.*, 2005), the displacement ductility capacity of NF1 was influenced by the biased, one-sided response, in which the specimen's damage was concentrated in one side of the column leading to higher ductility capacities than in the case of a symmetrical response. For symmetrical response, as in the case of 9F1, similar damage occurred on both sides of the specimen resulting in higher rate of degradation and lower ultimate displacement.

When comparing the performance of the specimens tested under unidirectional motions with those subjected to biaxial motions, some similarities and differences were observed in the base shear-displacement envelopes. First, the resisting capacity of the unidirectional specimens (9F1 and NF1), immediately after yielding, was larger than that registered in C1 and C2. This effect is attributed to the axial force applied to the unidirectional specimens, where the moment-axial load relationship was affected by the variation in the applied compressive axial load. Second, the behavior of the unidirectionally tested specimens, once the maximum capacity was reached, was influenced by the P-delta effects induced by the axial force in the specimens and the additional mass in the MR structure. As a consequence, a rapid degradation in strength and displacement capacity was observed after the maximum recorded base shear due to

the lateral instability of the columns (P-delta effects). Although P-delta effects were observed in both 9F1 and NF1, they were more severe in 9F1. Finally, the performance of the specimens tested under bidirectional shaking did not seem to be affected by the biaxial effects. Indeed, for C1 and C2 the base shear-displacement envelopes measured in the longitudinal direction (strongest component of the earthquake), were very similar to that measured in NF1 (in terms of capacity and ductility), even though no axial force was applied (Fig. 6-19).

Since all the specimens had the same geometry (transverse section) and reinforcement, the calculated moment-curvature backbone envelope curves followed similar trends (Fig. 6-17 and 6-19); differences in the curves were attributed to the effect of the axial load and the material properties used in each specimen. As a consequence of the compressive axial load applied to the specimens tested under unidirectional accelerations, a slightly higher moment capacity and a lower ultimate curvature was observed in the backbone envelopes. Although the estimated curvature ductility (Table 6-9) was similar in all the specimens, a small value was computed in 9F1 due to malfunction of the displacement transducer at the last run of the test sequence.

The period and effective lateral stiffness measured with the progression of the tests were comparable for all the specimens (Table 6-8). The large values of effective lateral stiffness (low periods) observed in NF1 at initial stages (Fig. 6-15), were attributed to the one-sided distribution of the damage experienced by this specimen. Nevertheless, once the longitudinal steel yielded and the first spalling occurred, the stiffness degradation followed the same trend as in the other specimens. Towards the end of the tests, the measured periods were larger for specimens tested under bidirectional shaking.



This was attributed to the distribution of the damage, which was uniformly spread around the columns as a result of the biaxial bending.

### **6.11.2 Interlocking Specimens**

When comparing the performance of the specimens tested under unidirectional motions plus axial force (ISL1.0) with those subjected to biaxial accelerations (I1 and I2), some differences were observed in the base shear-displacement envelopes (Fig. 6-23). While the lateral force capacity for specimen ISL1.0 was approximately 35% larger than that recorded in the longitudinal direction of I1 and I2, the measured peak lateral displacement was comparable for all the specimens. Furthermore, the elastic lateral stiffness was substantially larger in ISL1.0, compared with that in I1 and I2. These differences were mainly due to the difference in specimen's height and the applied axial force in ISL1.0. While the height was 72 in. for I1 and I2, it was only 58 in. for ISL1.0. Additionally, the location of the displacement transducers was 83 in. from the top of the footing for I1 and I2, and 58 in. for ISL1.0.

A better correlation in the seismic performance among the specimens was found by comparing the base moment vs. drift ratio. From Fig. 6-24 it is clear that the peak moment capacity of specimen ISL1.0 was about 12% larger than that observed in I1 and I2. This effect, as in the case of the circular columns 9F1 and NF1, was attributed to the applied axial force. It is also noted, from the same figure, that the ultimate drift ratio in ISL1.0 was larger than the values measured in the specimens tested under bidirectional excitations. A plausible reason to explain these differences was the P-delta effects

experienced by specimen ISL1.0, in which a marked capacity degradation and large displacements ductilities were observed once the column reached its maximum capacity.

The calculated moment-curvature backbone envelope curves were similar in between specimens (Figs. 6-18 and 6-23); small differences in the curves were due to the effect of the axial load and the mechanical properties of the concrete and steel used in each specimen. In fact, due to the compressive axial load applied in ISL1.0 a slightly higher moment capacity was observed on the backbone envelopes. Although the estimated curvature ductility (Table 6-9) was comparable between specimens, a large ductility value was computed in ISL1.0. This effect, as in the case of the moment-drift ratio relationships, was attributed to the secondary moments effects (P-delta) experienced for this specimen.

The dynamic properties: period and effective lateral stiffness, measured with the progression of the tests, were larger in ISL1.0 (Table 6-8). These variations were due to the difference in the aspect ratio of the specimens; the aspect ratio was defined as the quotient between the column height and the long side of the section. Since ISL1.0 had a smaller aspect ratio compared with that in I1 and I2 (3.3 vs. 4), its vibration period was shorter making the specimen more rigid. Despite the differences in the values of the dynamic properties, the degradation in the effective stiffness followed a similar trend for all the specimens (Fig. 6-16).

Although comparisons about the seismic performance were established between the specimens tested under uniaxial and biaxial ground accelerations, it is worth noting that the specimens were tested under different load conditions. Specimens 9F1, NF1 and ISL1.0 were simultaneously subjected to uniaxial shaking, compressive axial load and P-

delta effects. As a result, the lateral force and displacement capacities of these specimens were influenced by the combination of these effects. Conversely, the near fault characteristics of the ground motion used in NF1 affected notably the displacement capacity of the specimen, causing large residual deformations. The smaller aspect ratio used in ISL1.0 made the specimen stiffer and therefore more resistant to lateral force and more susceptible to shear deformations. Therefore, the observation on the seismic performance of columns tested under uniaxial and biaxial input accelerations, need to be compared against analytical models that resemble the characteristics of the specimens C1, C2, I1 and I2 but subjected to uniaxial ground accelerations. This topic will be addressed in chapter 8.

## **Chapter 7. Analytical Modeling of Specimens**

### **7.1. Introduction**

In order to validate the adequacy of analytical models in predicting the seismic performance of bridge columns under combined loadings, detailed modeling techniques were implemented and compared with the results of the experimental results. The OpenSees software (Open System for Earthquake Engineering Simulation) was used to create the analytical models and then perform nonlinear static and dynamic analyses. OpenSees is an open-source software framework for developing applications to simulate the performance of structural and geotechnical systems subjected to earthquakes created at the Pacific Earthquake Engineering Research Center (OpenSees, 2006). This software possess advanced capabilities for modeling and analyzing the linear and nonlinear behavior of structural systems using a variety of constitutive material models, elements and solution algorithms

This chapter describes the analytical approaches that were developed, and then evaluated to determine their accuracy, in simulating the seismic response of the unidirectionally and bidirectionally tested specimens. First, moment curvature analyses were conducted to evaluate the capacity of the sections. Next, the nonlinear static pushover procedure was applied to study the capacity of the specimens. Finally, nonlinear time history dynamic analysis was implemented to compare the capacity and hysteresis characteristics of the tested specimens. Results of the analytical models were compared with the shake table experimental results. For this different modeling strategies were

implemented to resemble closely the conditions of the specimens tested on the shake table.

## 7.2. Strain Rate Effect

Under seismic excitations, a high rate of loading is experienced for the reinforced concrete columns. As a consequence, the stress-strain properties of the component materials (concrete and reinforcing steel) can be altered due to the rate of straining. Several studies have shown that at high strain rates, the compressive strength of concrete and the yielding and ultimate stresses of reinforcing steel, exhibit a significant increase compared with the values obtained from slow monotonic tests (Staffier and Sozen, 1975; Mahin and Bertero, 1983; Kulkarni and Shah, 1988; Mander et al., 1988; Zadeh and Saiidi, 2007). However, the elastic modulus is not considerably influenced by the rate of loading.

In order to estimate the strain-rate effects in reinforcement for the bidirectionally tested specimens, the method developed by Zadeh and Saiidi (Zadeh and Saiidi, 2007) was applied. According to the authors, the dynamic yielding and ultimate stresses are given by the following expressions:

$$f_y' = \left( \frac{SRI}{10^{-4}} \right)^\alpha f_y \quad (7-1)$$

$$f_u' = \left( \frac{SRI}{10^{-4}} \right)^{\frac{2}{3}\alpha} f_u \quad (7-2)$$

$$SRI = K \dot{\epsilon}_{ave} \quad (7-3)$$

$$K = \frac{\dot{\epsilon}_y}{\dot{\epsilon}_{0.5y}} \quad (7-4)$$

$$\alpha = 0.022 \left( \frac{\phi}{\phi_8} \right)^{0.15} - 0.066 \left( \frac{f_y}{60} \right) \quad (7-5)$$

Where:

$f_y, f_y'$  = static and dynamic yield stress in reinforcement (ksi);

$f_u, f_u'$  = static and dynamic ultimate stress in reinforcement (ksi);

$\dot{\epsilon}_y, \dot{\epsilon}_{0.5y}$  = strain-rate at yielding and at half yielding (in/in);

$\dot{\epsilon}_{ave}$  = average strain rate between half yielding and yielding (in/in);

$SRI$  = strain rate index;

$\phi, \phi_8$  = diameter of the reinforcement and diameter of a No.8 bar (in).

Strain rate was calculated for the extreme longitudinal bars at the interface between the column and footing, and for the run at which the first yielding was recorded (Run 2). Recorded strains in strain gauges: Sg16, Sg12 and Sg11 were used for the specimens C1, C2, I1 and I2, respectively. The measured strain rate was determined from the strain history as:

$$\dot{\epsilon} = \frac{\epsilon_{i+1} - \epsilon_i}{\Delta t} \quad (7-6)$$

Where:

$\dot{\epsilon}$  = measured strain rate (in/in/sec);

$\epsilon$  = measured strain at time  $i^{\text{th}}$  (in/in);

$\Delta t$  = time step (sec).

Table 7-1 summarizes the strain-rate factors for yielding and ultimate stages of the longitudinal steel in the bidirectionally tested specimens. Average increasing factors for the yielding stress were found to be 6.5% in C1 and C2, 6.9% in I1 and 6.4% in I2. These values at ultimate stress were computed to be 4.5% and 4.6% for C1 and C2, and 4.6% and 4.3% for specimens I1 and I2, respectively. Typical strain-rate histories at the run where the first longitudinal bar yields are shown in Fig. 7-1 and 7-2 for the circular and interlocking columns, respectively. Also, strain rate versus strain orbits for the tested specimens are shown in Fig. 7-3 through 7-6. The strain-rate histories and orbits clearly show that strain rate for a specific bar is not constant during a ground motions; it varies with time and the level of strain. Moreover, it was observed that the rate of straining increases when the strain approaches the peak values in a load cycle.

For the unidirectionally tested specimens (9F1, NF1 and ISL1.0) the equations developed by Kulkarni and Shah (Kulkarni and Shah, 1988) were used to determine the strain rate effects at yielding strength in the longitudinal reinforcement. In this method, the increasing factor for the yielding strength is given by:

$$R_{f_y} = 0.0328 \ln \left( \frac{\dot{\epsilon}_{dyn}}{\dot{\epsilon}_{stat}} \right) + 0.9873, \quad \text{For } f_y=45 \text{ ksi} \quad (7-7)$$

$$R_{f_y} = 0.0124 \ln\left(\frac{\dot{\epsilon}_{dyn}}{\dot{\epsilon}_{stat}}\right) + 0.9832, \quad \text{For } f_y=75.4 \text{ ksi} \quad (7-8)$$

Where:

$$\frac{\dot{\epsilon}_{dyn}}{\dot{\epsilon}_{stat}} = \text{relative strain rate (dynamic strain rate/static strain rate)}$$

The strain-rate factors at yield stress in the longitudinal reinforcement are summarized in Table 7-1. Average increasing factors were found to be 9% in 9F1, 8% in NF1 (Phan *et al.*, 2005) and 5% in ISL1.0 (Correal *et al.*, 2004). Since the strain rate equations proposed by Kulkarni and Shah were developed only for yielding stress, strain factors for ultimate stress were estimated to be 98% of the values at yielding. This was based on the calculations for the bidirectionally tested columns.

The strain rate effect in the concrete was studied following the method developed by Kulkarni and Shah (Kulkarni and Shah, 1988). In this method, the increasing factor for the compressive strength is given by:

$$R_c = 0.022 \ln\left(\frac{\dot{\epsilon}_{dyn}}{\dot{\epsilon}_{stat}}\right) + 0.9973 \quad (7-9)$$

Where:

$$\frac{\dot{\epsilon}_{dyn}}{\dot{\epsilon}_{stat}} = \text{relative strain rate (dynamic strain rate/static strain rate)}$$

The dynamic strain rate in the concrete was determined from the extreme longitudinal bars yielding in compression. This procedure is valid if a perfect bond



between the concrete and the longitudinal bars before yielding is assumed; if strain compatibility is satisfied, the strains in the longitudinal bars will be the same as those in the concrete. Therefore, the peak compression strain rate in the concrete is equivalent to a compression yielding strain in the reinforcement of 0.002. The same procedure followed to determine the dynamic strain rate of the reinforcement yielding in tension was used for the concrete. The first compression yielding was recorded at run 3 for all the specimens (0.4xPET and 0.4xSYL). Table 7-2 summarizes the strain rate factors found for the concrete compression strength of the tested specimens. According to Kulkarni and Shah (Kulkarni and Shah, 1988) an approximate value of  $100 \mu\epsilon$  is used for the static strain rate of the concrete. An average increasing factor of 12% was found for all the bidirectionally tested specimens. For the unidirectionally circular columns Phan *et al.* (Phan *et al.*, 2005) reported increasing factors of 11% for specimens 9F1 and NF1, respectively. Similarly, for the interlocking specimen ISL1.0, Correal *et al.* (Correal *et al.*, 2004) found this value to be 5%.

### **7.3. Moment-Curvature Analysis**

In order to predict the moment curvature characteristics of the tested specimens, a series of nonlinear cross sectional analyses were conducted using the program XTRACT (TRC/Imbsen, 2007). The program characteristics, material models and input and output parameters were discussed in section 2.4. The measured material properties for reinforcement and concrete described in sections 3.3, 6.3 and 6.4 were modified to take into account the strain rate effects as described in the previous section. Table 7-3 summarizes the stress-strain properties for steel and concrete modified by strain rate

factors. The stress-strain relationships for the unconfined and confined concrete were represented using Mander's model (Mander *et al.*, 1988), while the longitudinal reinforcement was modeled as steel with a parabolic strain hardening. The fiber discretization of the sections was discussed in section 2.4.1 for bidirectionally tested specimens. For unidirectionally tested specimens a similar pattern of fibers was used, except that the sections were modeled without a hole in the middle.

For the unidirectionally tested specimens, average values of axial compressive force of 80 kips. and 90 kips. were used for NF1 and ISL1.0, respectively. For the case of 9F1, to account for the large variations in axial force, two levels of compressive force were considered: 80 kips. and 115 kips. These two cases represent the target and maximum values achieved during the test. The calculated moment curvature relationships were idealized using an elastic-perfectly plastic curve. This was achieved by balancing the areas between the actual and the idealized curves. Figs. 7-7 through 7-12 show comparisons between measured and calculated moment curvature curves for 9F1, NF1 and ISL1.0.

For the case of the bidirectionally tested specimens, no axial force was included in the sectional analyses. To account for the biaxial effects, an inclination of the neutral axis (NA) of  $30^\circ$  with respect to the longitudinal direction was considered for circular specimens, whereas a value of  $45^\circ$  was used for the interlocking specimens. It is worth noting that the inclination of the NA was not constant during the test sequence, therefore the values selected represent an average value determined from the displacement interaction orbits and the damage observed at the end of the tests. To compare the predicted moment and curvature values with those experimentally measured, the

components along the longitudinal (X) and transverse directions (Y) of the specimens were reported. Additionally, each moment-curvature curve was simplified into bilinear idealizations. Figs. 7-13 through 7-16 show comparisons between the measured and calculated moment curvature relationships for C1, C2, I1 and I2, respectively.

From Figs. 7-7 through 7-16, it is noted that the values of the predicted moment capacity were comparable with those measured, however, the ultimate predicted curvatures were significantly less than those measured. This is explained by the fact that the ultimate confined concrete compression or crushing strain ( $\epsilon_{cu}$ ), used in Mander's model is by approximately a factor of two. The useful limit of compression strain ( $\epsilon_{cu}$  in Eq. 2-7), was based on experimental research of pure axially compressed columns, and was defined as the strain in the concrete associated with the fracture of the confining reinforcement (Mander *et al.*, 1988). According to Priestley *et al.* (Priestley *et al.*, 2007), the conservatism in the prediction of the ultimate confined concrete compression strain ( $\epsilon_{cu}$ ) is mainly due to two factors. First, low estimates of  $\epsilon_{cu}$  could be found in columns tested under pure bending or combined bending and axial compressive force, and second, additional confining pressure is added to the confined concrete at the plastic hinge region of the column due to the restriction in deformation imposed by the footing.

In order to improve the predictions at the ultimate curvature from sectional analysis a modification of the Mander's confined concrete model was implemented in XTRACT (TRC/Imbsen, 2007), to resemble the damage characteristics of the tested specimens. The proposed modification consisted of the addition of two straight lines after the crushing strain was reached. The first line represents the strength degradation in the concrete between the calculated strength at crushing strain ( $\epsilon_{cu}$  in Eq. 2-7) and zero

strength ( $f_{cu}^*$ ) at a strain of twice the calculated crushing strain ( $\epsilon_{cu}^*$ ). The second line, represents the compression failure of the confined concrete, and it is modeled by a line with zero slope between the strains at 2 and 2.5 times the crushing strain. Fig. 7-17 show details of the proposed model. The stress-strain characteristics of unconfined concrete were also modified to account for the damage in the concrete cover at high levels of deformation; in this case a strain line with zero slope was added between the spalling strain and a strain equivalent to 1.0 in/in., as is shown in Fig. 7-18. Modified values of the ultimate confined concrete strain for the all the specimens are presented in Table 7-4. Figs. 7-19 through 7-28 show comparisons between the measured and calculated moment curvature relationships and bilinear idealizations using the modified concrete stress-strain characteristics for all the specimens studied. From the results, it is clear that the predicted moment-curvature relationships resemble reasonably well the observed behavior of the tested specimens especially at the ultimate stage, where the damage in the unconfined and confined concrete, the longitudinal bar buckling and the reinforcement rupture cause a gradual reduction of the moment capacity of the section prior to the failure. It is worth noting that the ultimate curvature obtained from XTRACT was obtained when either the confined concrete or reinforcement reached the ultimate strain, whichever occurred first.

The calculated elasto-perfectly plastic moment-curvature envelopes were used to evaluate the effects of the inclusion of the strain-rate factors in the stress-strain characteristics of the concrete and reinforcement on the plastic capacity of the specimens. Tables 7-5 and 7-6 summarizes the effect of the strain rate on the idealized moment-curvature curves for the unidirectionally and bidirectionally tested specimens, respectively. From the results, it is clear that by including the strain-rate factors for the

concrete and reinforcement, the plastic moment capacity and effective yielding curvature were increased an average of 5%, the ultimate curvature was reduced by nearly 4%, while the effective stiffness remained almost unaltered. In addition, when comparing the result for ultimate curvature using the modified confined concrete model, no significant influence was observed due to strain rating.

#### **7.4. Calculated Lateral Force-Displacement from Moment-Curvature**

The plastic and ultimate lateral force and top displacements for the tested specimens were calculated using Priestley's method (Priestley *et al.*, 2007), explained in section 2.4.2. The displacements were computed by integrating the calculated curvatures at the plastic hinge location, whereas the lateral force was calculated by dividing the moments by the distance from the top of the footing to the point of contra-flexure (58 in. for ISL1.0 and 72 in. for the rest of the specimens). The elastic-perfectly plastic idealized moment-curvature curves computed from the modified Mander's model for unconfined and confined concrete and strain-rate effects were used as the input parameters for the calculations. Comparisons between the measured and calculated force-displacement curves for 9F1, NF1 and ISL1.0 are shown in Figs. 7-29 through 7-32. Table 7-7 presents the idealized force-displacement properties for the unidirectionally tested specimens and for the two considered levels of confined concrete ultimate strain.

For the case of the bidirectionally tested specimens, the force-displacement curves were calculated based on inclinations of the neutral axes of 30° for C1 and C2, and 45° for I1 and I2, respectively. To compare the calculated and measured values, the elastic-perfectly plastic idealized moment-curvatures along the longitudinal (X) and transverse

(Y) directions were used to determine the plastic and ultimate force and displacement values. Figs. 7-33 and 7-34 show comparisons between the measured and calculated force-displacement curves for C1 and C2, and I1 and I2, respectively. Table 7-8 presents the idealized force-displacement properties for the bidirectionally tested specimens and for the two considered levels of confined concrete ultimate strain. In this case, the results along the principal axis and the two horizontal components (X and Y) were calculated.

To account for the change in the position of the neutral axis during the test sequence, bidirectional displacement interaction orbits were calculated by computing the ultimate displacements along the longitudinal and transverse directions associated with different inclinations of the neutral axis. Figs. 7-35 through 7-38 show comparisons between the measured and calculated bidirectional displacement interaction orbits for circular and interlocking specimens. From the figures, it is noted that by changing the ultimate concrete strain to resemble the level of deformation observed on the tested specimens, as explained in the previous section, the calculated ultimate displacement using Priestley's method (Priestley *et al.*, 2007) was nearly doubled. Although the values of measured and calculated lateral force were comparable, the calculated ultimate displacements underestimated the measure response for all the specimens. This effect is explained in part, because the shear deformations, bond-slip rotations and P-delta effects were not taken in consideration in the sectional analysis (moment-curvature) and therefore were ignored in the force-displacement predictions.

## 7.5. Bond Slip Deformation and Rotation

In order to estimate the bond slip effects and the associated column rotations, two procedures were applied: Wehbe's method (Wehbe *et al.*, 1997) and Zhao's method (Zhao and Sritharan, 2007).

### 7.5.1 Wehbe Method

In this procedure the rotation due to bond slip is assumed to occur about the neutral axis of the column cross section at the column-footing interface, and it is calculated as the quotient between the additional extension ( $\delta l$ ) of the longitudinal outermost tensile bar and the distance from that bar to the neutral axis. If the stress-strain relationship of the longitudinal bars is represented by a bilinear model, two strain profiles are defined; one for the elastic and one for the inelastic range of strains as is illustrated in Fig. 7-39. The bar elongation due to bond slip ( $\delta l$ ) is then calculated by integrating the axial strain profile along the embedment length of the bar, and is given by the following expressions for each strain profile:

$$\varepsilon_s \leq \varepsilon_y ; \delta l = \frac{d_b f_s^2}{8 E_s u} \quad (7-10)$$

$$\varepsilon_s > \varepsilon_y ; \delta l = \frac{d_b}{8 u} (\varepsilon_s f_s - \varepsilon_s f_y + \varepsilon_y f_s) \quad (7-11)$$

$$u = \frac{5.5 \sqrt{f'_c}}{d_b} \leq 800 \quad (7-12)$$

Where:

$\varepsilon_s$ = calculated steel strain;

$\varepsilon_y$ = yielding steel strain;

$d_s$ = bar diameter (in);

$f_s$ = calculated stress in the longitudinal bar (psi);

$E_s$ = steel modulus of elasticity (psi);

$u$ = basic bond strength (psi);

$f_c$ = concrete compressive strength (psi).

The location of the section neutral axis, as well as the value of strain in the outermost longitudinal bar for the desired level of lateral load (performance levels), are determined from moment-curvature relationship of the cross sections. For the tested specimens, the measured material properties modified by strain rate and the modified unconfined and confined concrete models were used in the calculation. A monotonic backbone envelope curve (moment vs. slip rotation) was then calculated by defining three performance levels: concrete cracking, first longitudinal bar yielding and ultimate capacity (See Fig. 7-40a). The values of slip-rotation and corresponding moments at the considered performance levels for specimens 9F1, NF1 and ISL1.0 are presented in Table 7-9.

### **7.5.2 Zhao Method**

Based on experimental results of steel reinforcing bars anchored in concrete with a sufficient embedment length, Zhao and Sritharan (Zhao and Sritharan, 2007) found relationships between the bar stress and the slip. According to the authors, a monotonic



envelope curve represents the stress vs. slip of each bar of a RC member. The envelope curve is characterized by two segments; one linear from zero to yielding stress and one curvilinear for the post-yielding region, as can be seen in Fig. 7.40 b. The relationship between stress ( $\sigma$ ) and slip ( $s$ ) is given by the following expressions:

$$\sigma \leq \sigma_y ; \sigma = K s \quad (7-13)$$

$$\sigma > \sigma_y ; \sigma = \tilde{\sigma} (\sigma_u - \sigma_y) + \sigma_y \quad (7-14)$$

$$\tilde{\sigma} = \frac{\frac{\tilde{s}}{(\mu - \tilde{s})}}{\left[ \left( \frac{1}{\mu \cdot b} \right)^{Re} + \left( \frac{\tilde{s}}{(\mu - \tilde{s})} \right)^{Re} \right]^{\frac{1}{Re}}} \quad (7-15)$$

$$\tilde{s} = \frac{(s - s_y)}{s_y} \quad (7-16)$$

$$\mu = \frac{(s_u - s_y)}{s_y} \quad (7-17)$$

Where:

$\sigma$ = bar stress (ksi);

$s$ = bar slip (in);

$\tilde{\sigma}$  = normalized bar stress (ksi);

$\tilde{s}$  = normalized bar slip (in);

$\mu$ = ductility coefficient;

$K$ =initial stiffness (ksi);

$b$ = stiffness reduction factor after yielding (value between 0.3 and 0.5);

$f_y$ = yielding strength (psi);

$f_u$ = ultimate strength (psi);

$s_y$ = slip at the bar yielding stress (in);

$s_u$ = slip at the bar ultimate stress (in);

$R_e$ = factor equal to 1.01.

Based on regression analysis of experimental data, the following expressions were found for the yielding and ultimate slip

$$s_y(\text{in}) = 0.1 \left[ \frac{d_b f_y}{4000 \sqrt{f_c'}} (2\alpha + 1) \right]^{(1/\alpha)} + 0.013 \quad (7-18)$$

$$s_u = (30 \sim 40)s_y \quad (7-19)$$

Where:

$d_b$ = bar diameter (in);

$f_c$ = concrete compressive strength (psi).

$\alpha$ = parameter equal to 0.4.

Based on the proposed method, the slip at yielding stress was calculated as 0.0151 in. and 0.0141 in. for the circular and interlocking specimens, respectively. The slip at ultimate stress was found to be 0.604 in. and 0.564 in. for the circular and interlocking specimens, respectively.

## 7.6. Shear Deformations

Although the effect of shear deformations on the lateral deflection of relatively slender columns (aspect ratio larger than 4) are expected to be negligible, past research at the University of Nevada, Reno (Correal *et al.*, 2004) have shown that the inclusion of the lateral shear stiffness on the analytical models can improve the prediction of the force-displacement capacity of reinforced concrete columns. In order to estimate the lateral shear stiffness at the uncracked and cracked stages, the expressions proposed by Park and Paulay (Park and Paulay, 1975) were applied. Based on the elastic theory, the authors proposed that the uncracked lateral stiffness of a reinforced concrete member of unit length and rectangular section is given by:

$$K'_v = \frac{E_c b_w d}{3} \quad (7-20)$$

Where:

$K'_v$  = uncracked lateral shear stiffness per unit length;

$E_c$  = elastic modulus of the concrete,  $57000\sqrt{f'_c}$  (psi);

$b_w$  = section width perpendicular to the applied shear (in);

$d$  = effective depth of the section, parallel to the applied shear (in);

For the cracked lateral shear stiffness the authors developed the following expression, based on the truss theory with cracks inclined  $45^\circ$ :

$$K_{v,45} = \frac{\rho_v}{1 + 4 \frac{E_s}{E_c} \rho_v} E_s b_w d \quad (7-21)$$

Where:

$K_{v,45}$  = cracked lateral shear stiffness per unit length;

$\rho_v$  = volumetric steel ratio of the spiral,  $A_v/sb_w$ ;

$E_s$  = elastic modulus of the steel (psi);

$A_v$  = area of the shear reinforcement (in<sup>2</sup>);

$s$  = spacing of the shear reinforcement, pitch (in);

$b_w d$  = shear area of the section (in<sup>2</sup>).

Based on shake table testing of double interlocking columns in single and double curvature, Correal (Correal *et al.*, 2004), observed that the shear deformation mainly occurs on the plastic hinge regions; therefore, the cracked shear stiffness of a single curvature RC element could be calculated in terms of the plastic hinge length ( $L_p$ ) as:

$$K_{v,cr} = \frac{K_{v,45}}{L_p} \quad (7-22)$$

For the specimens studied here, the shear stiffness was assumed to be the value at cracking. For circular sections the shear area ( $b_w d$ ) was assumed to be 80% of the gross area, whereas for the interlocking specimens ( $b_w d$ ) was calculated to be that of an equivalent rectangular section with the same effective depth ( $d$ ) as the interlocking section, and an effective width ( $b_w$ ) such that the area enclosed by the interlocking section be the same as the rectangular section. The plastic hinge length was defined as the section

diameter for circular columns, and as the long side dimension of the interlocking sections. Values of the cracked shear stiffness of 2370 k/in., 2393 k/in., 1396 k/in., 2337 k/in., and 1354 k/in. were calculated for 9F1, NF1, ISL1.0, C1-C2, and I1-I2 specimens, respectively.

### **7.7. OpenSees Software**

In order to accurately predict the seismic performance of the studied specimens, different analytical approaches as well as constitutive material models were implemented and evaluated using OpenSees software. OpenSees is an open-source software framework for developing applications to simulate the performance of structural and geotechnical systems subjected to earthquakes created at the Pacific Earthquake Engineering Research Center (OpenSees, 2006). This software possesses advanced capabilities for modeling and analyzing the linear and nonlinear behavior of structural components and systems using a variety of constitutive material models, elements and solution algorithms. The open source nature of this software allows researchers to develop and enhance the element models, material formulation and solving algorithms.

OpenSees is comprised of four modules to allow the user to implement and analyze a specific problem. The first module allows the creation of the finite element model by defining the element geometry, the connectivity, and the assignment of the material, loads and constraints. A second module allows the definition of analysis parameters and procedures. The third module combines the previous two modules to perform the time-history analysis. Finally, the results of the analysis are written in the recorder module to be post processed by the user. A detailed description of each module

can be found in documentation available at the OpenSees web site: (<http://opensees.berkeley.edu>).

### 7.7.1 Modeling Strategies

Two modeling strategies were used to estimate the nonlinear seismic response of the specimens: Pushover and time-history analyses. The static nonlinear analysis (Pushover) was examined first with the aim of comparing the results with those of simplified methods based on the integration of the moment curvature relationship (section 7-4), and those of the idealized elasto-plastic lateral force-displacements curves measured during the tests. Later on, a more refined modeling strategy was implemented using nonlinear time history analysis to compare the results of different performance parameters with those measured.

To account for the bidirectional bending and axial force interaction, the studied specimens were modeled using nonlinear beam-column elements discretized using fiber sections. In fiber sections, the cross section of a RC member was divided into a finite number of subsections or fiber representing the uniaxial characteristics of the concrete and reinforcing steel. The total length of the element was divided into a number of segments or integration points, where the force-displacement state of the segment can be determined by integrating the stress-strain characteristics of the fiber at that specific point. Finally, the element response can be obtained by integration of the segment deformations along the length of the member. OpenSees uses the flexibility-based formulation developed by Spacone *et al.* (Taucer *et al.*, 1991), in which force interpolation functions are assumed along the length of the element, and where the

deformations are calculated based on the equilibrium between the fiber force and the external applied forces, and the compatibility among fibers. This formulation was established based on Navier-Bernoulli approximation that a plane section remains plane and perpendicular to the longitudinal axis of the element. Fig. 7-41 illustrates models of the tested specimens using fiber sections and multiple integration points. At the present time, the nonlinear beam-column element in OpenSees does not account for initial cracking, shear deformations or bond-slip rotations; these effects can be added to the RC element using springs.

A simplification of the nonlinear beam-column element with fibers and multiple integration points that allows taking into consideration the initial cracking is the beam with hinges element. In this element, the inelastic behavior is specified to occur only at specific regions of the element where the plastic deformations are important (plastic hinges). Outside of the plastic hinge regions the element behaves as linear elastic. The length of the plastic hinge region is specified by the user and is modeled in OpenSees using fibers with two integration points; one at each edge of the plastic hinge. The properties of the elastic portion of the element can be specified in such way that the initial stiffness is adequately modeled. Details of the element formulation and solution strategies implemented in OpenSees can be found in Scott and Fenves (Scott and Fenves, 2006). Idealizations of the tested specimens using beam with hinge elements is shown in Fig. 7-42.

To calculate the beam-column deformations six integrations points were defined along the length of the specimens. The fiber sections were composed of reinforcing steel fibers and concrete fiber with different properties to represent the characteristics of

confined and unconfined concrete. Although the pattern of fibers generated in XTRACT for moment curvature analyses (section 7-3) can be imported into OpenSees, a simplified configuration with a reduced number of fibers was implemented in OpenSees by modeling the sections using circumferential and rectangular paths. The reduction in the number of fibers was established with the purpose of reducing the computational time required for the nonlinear time history analysis. A total of 236 fibers were used to modeling specimens 9F1 and NF1 (36 for the unconfined concrete, 180 for confined concrete and 20 for the longitudinal steel). For ISL1.0 the interlocking section was discretized using 492 fibers (92 for the unconfined concrete, 368 for confined concrete and 32 for the longitudinal steel). The sections for the bidirectional tested columns (C1, C2, I1 and I2) were discretized into a number of fibers similar to those used for the unidirectional tested columns, except that some confined concrete fibers were removed at the center of the specimen to represent the PVC pipe. Figs. 7-43 and 7-44 show details of the fiber discretization for the unidirectionally and bidirectionally tested specimens, respectively.

### **7.7.2 Material Models**

The analytical prediction of the seismic performance of RC members requires an adequate modeling of the stress-strain or force-deformation characteristics of the component materials and its hysteretic behavior. Since the uniaxial or biaxial bending is translated into axial forces and deformation along the longitudinal fibers and can be combined with variable axial forces, uniaxial materials were used to represent the static and dynamic behavior of concrete and reinforcement. Rotational or linear springs need to



be added to the element to represent the torsional or shear deformations. A brief description of the uniaxial material models used in this study is discussed next.

### 7.7.2.1 Concrete Models

Two different material models were evaluated to represent the stress-strain characteristics of the confined and unconfined concrete used in the tested specimens: Concrete02 and Concrete07. Each concrete material uses different approaches to represent the tension-compression properties of concrete.

The Concrete02 allows the representation of the tension-compression stress-strain characteristic of the concrete. The compressive stress-strain envelope is modeled using the Kent and Park model (Kent and Park, 1971), whereas for tension it is represented by straight lines. The hysteresis behavior follows the model by Karsan and Jirsa (Karsan and Jirsa, 1969), in which the loading/unloading follow linear patterns with degrading stiffness. Seven parameters are required in the model material: stress and strain at compressive strength, stress and strain at crushing strength, tension strength and tension softening stiffness and a factor to define the stiffness degradation. Beyond the ultimate or crushing strain, the compressive strength is modeled as constant for large deformations. Fig. 7-45 shows a typical hysteretic stress-strain relationship for confined concrete modeled as Concrete02.

For the Concrete07 material, the tension and compression stress-strain envelope is modeled using the Chang and Mander model (Chang and Mander, 1994). The hysteresis behavior is represented by tri-linear paths for unloading and reloading following the recommendations of the same authors. Eight input parameters are required to define the

monotonic envelope: stress and strain at compressive strength, initial elastic modulus, tension strength and strain, two parameters to define the ultimate strain in tension and compression, and a term that controls the nonlinear descending branch beyond the compressive strength. Beyond the ultimate strain, the tensile and compressive strengths are gradually reduced to zero using linear functions. Fig. 7-46 illustrates the hysteretic stress-strain behavior of a confined concrete elements using the Concrete07 material.

The compressive stress-strain characteristics of the confined concrete were modeled following Mander's model (Mander *et al.*, 1988), except that the ultimate or crushing strain was assumed to occur at larger values of deformation (two times the strain corresponding to compressive strength). Fig. 7-47 presents a comparison of the two concrete models subjected to the same strain history.

### **7.7.2.1 Reinforcing Steel Models**

Two material models representing the uniaxial stress-strain behavior of the longitudinal reinforcement were investigated: Steel02 and ReinforcingSteel.

The Steel02 material uses a bilinear stress-strain backbone to represent the uniaxial behavior of reinforcing steel following the rules of Giuffre-Manegoto-Pinto model (Taucer *et al.*, 1991). The post yielding envelope is modeled by a straight line connecting the yielding and ultimate points and whose slope is defined as a factor of the steel initial elastic modulus (29000 ksi). The hysteretic behavior is characterized by linear trajectories and with stiffness degradation to account for the Bauschinger effect. This material also has the option to model isotropic hardening in tension or compression. Ten key parameters are required to fully represent the steel behavior: Yielding strength, initial

elastic modulus, strain hardening ratio, three parameters to describe the transition from elastic to plastic branches, and four parameters to include the isotropic hardening. Fig. 7-48 illustrates typical stress-strain hysteresis curves for the Steel02 material. From the figure, it is evident that the yielding plateau or strength degradation due to bar buckling is not considered in this model.

In the ReinforcingSteel model, the uniaxial stress-strain backbone envelope curve and the hysteresis behavior are based on the Chang and Mander model (Chang and Mander, 2004). To account for the reduction in area as the bar is stressed, the backbone curve is transformed from engineering stress space to natural stress space. In addition, isotropic hardening, low cycle fatigue as well as buckling effects can be directly represented in the material model. Six parameters are required to define the monotonic stress-strain envelope: yield and ultimate stresses in tension, initial elastic modulus, the slope at strain hardening, strain at the beginning of strain hardening and strain at peak stress (ultimate strain). Although additional parameters are required to model buckling and low cycle fatigue effects, these effects were not included in this study because they are still under development. Fig. 7-49 shows a typical hysteretic stress-strain response of a reinforcing bar modeled with this material.

Results obtained from reinforcement bar samples (Tables 4-1 and 6-5), tested monotonically in tension until failure and including strain rate effects were used as the input parameters for both models. Fig. 7-50 shows a comparison of the monotonic tension stress-strain behavior of the two material models and the measured data of a No.4 bar sample. The stress-strain hysteretic behavior modeled by the two steel materials, when they were subjected to the same strain history, is shown in Fig. 7-51. From the

figures, it is noted that although Steel02 predicts reasonably well the monotonic stress-strain characteristics of steel bars, it does not account for the yield plateau and stiffness degradation due to buckling. The latter effect could result in an overestimation of the reinforcement stress beyond the specified ultimate strain.

### **7.7.2.3 Bond-Slip Models**

To account for the flexibility in the lateral response of the specimens induced by the reinforcement slip rotations at the column-footing interface, two approaches were investigated: Hysteretic material and Bond\_SP01 material.

The Hysteretic material allows the modeling of the uniaxial stress-strain behavior by using a tri-linear monotonic envelope and hysteretic rules that account for pinching of force and deformation, stiffness degradation based on ductility and damage due to ductility and energy dissipation. The parameters required to define the material model include: three points for the tri-linear stress-strain envelope, and four optional values to include pinching and damage in the hysteresis model. The bond-slip moment-rotation relationships obtained by applying Wehbe's method (section 7.5.1) to the moment-curvature curves (Table 7-9), were used as the input parameters of the tri-linear envelopes. The hysteretic material was then assigned to a rotational spring located at the first joint of a beam-column element. Springs in OpenSees are modeled using zero length elements, which allow assigning a force-deformation relationship to a beam-column element by defining a fictitious element connecting two coincident nodes.

The Bond\_SP01 material is used to represent the force-slip response of a reinforcing bar anchored in a beam-column joint. The monotonic envelope followed the

stress-slip model proposed by Zhao and Sritharan (Zhao and Sritharan, 2007) and explained in section 7.5.2, while the hysteretic behavior was modeled using rules to account for pinching and stiffness degradations proposed for the same authors. The material is defined by six input values: yielding strength, rebar slip under yielding stress, ultimate strength, rebar slip under ultimate stress, slope at beginning of slip hardening of the monotonic stress-slip relationship, and a factor to represent pinching due to slip deformations. The material properties are assigned directly to a section of the beam-column elements by using zero length sections. A zero length section element is a fictitious element connecting two coincident nodes with the element representing the force-deformation properties of the section. Since the element has a unit length, the element deformation (rotation) is equal to the section deformation (curvature).

### **7.7.3 Pushover Analyses for Unidirectionally Tested Specimens**

Nonlinear static pushover analyses were implemented in OpenSees using the geometry, measured material properties and boundary conditions of the tested columns. The specimens were idealized by 2 beam-columns elements. The first, representing the footing, was modeled using an elastic beam-column element fix for translation and rotations at the initial joint. The second, representing the cantilever column, was idealized using nonlinear beam-column elements with rotational springs assigned to the first joint (column-footing interface) to represent bond-slip and shear deformations. The measured average value of axial force was applied at the column's tip and was maintained constant for the analysis.

According to Laplace (Laplace *et al.*, 2001), in addition to the inertial forces induced by the total mass on the mass rig (MR), significant lateral forces were transmitted to the specimens due to secondary moments (P-delta effects) on the MR. These additional lateral forces resulted from the overturning moment of the system, which is equivalent to the vertical force times the lateral drift. As it was also pointed out by Laplace, no considerable secondary moments were generated in the specimen column due to the axial force system. In order to represent the additional forces transferred to the specimens, the MR was modeled in OpenSees using an equivalent elastic beam-column element with a pin support and a total height equal to the vertical distance pin-to-pin of the MR (98 in). Additionally, a truss element was used to represent the rigid link connecting the MR and the specimen. The option of corrotational transformations was assigned to the beam-column representing the MR to capture the P-delta effects. Fig. 7-52 illustrates the analytical model used for unidirectionally tested specimens.

Since the pushover curve is a representation of the monotonic behavior of the element, the Concrete02 and the ReinforcingSteel materials were selected to represent the concrete and steel fibers of the specimens. This is because of their simplicity and the numerical stability of the solutions. P-delta effects in the MR were considered by using geometric transformation for the equivalent elastic beam-column element representing the MR. It is worth noting that the impact of the P-delta effects in the MR, is reflected by a reduction in the lateral stiffness of the specimen. These effects are more significant once the longitudinal reinforcement in the specimen has yielded. Fig 7-53 shows a comparison between the measured force-displacement envelope for NF1 and the prediction with and without P-delta effects, and without including shear and bond-slip

deformations. The effects of P-delta in the specimen were calculated by subtracting the force-deformation measured in the MR from that measured in the column.

In order to improve the prediction of the force-displacement envelopes, linear and rotational springs were incorporated at the column-footing interface to simulate shear deformation and bond-slip rotation. Uniaxial materials Hysteretic and Bond\_SP01 were evaluated to represent bond-slip deformations. A comparison between the measured force-displacement envelope and the predictions using Hysteretic and Bond\_SP01 materials for specimen NF1 is presented in Fig. 7-54. From the figure, it is clear that some flexibility is incorporated into the model by including bond-slip and shear deformations. It is also observed that although both material models improve the predictions, the Bond\_SP01 material followed closely the measured data. The force-displacement curves for specimens 9F1 and ISL1.0 are shown in Figs. 7-55 and 7-56, respectively. For all the analyses, the ultimate point in the calculated envelope was reached when either the confined concrete or the longitudinal steel exceeded the ultimate strain, whichever occurred first.

#### **7.7.4 Nonlinear Time History Analyses for Unidirectionally Tested Specimens**

Nonlinear time history analyses were implemented in OpenSees using the same analytical model for the specimen and MR described in the section 7.7.3. A parametric study was developed to evaluate the effectiveness of different analytical approaches in predicting the measured force-displacement characteristics of the specimens. Analyses were first implemented for specimen NF1 and the most suitable model was used to simulate the behavior of specimens 9F1 and ISL1.0.

In order to replicate the measured behavior of the specimens, the acceleration histories recorded by the shake table at each run of the test protocol were used as the input ground motion. To account for the progressive damage, the recorded acceleration signals at each run were concatenated into a single record. An interval of non excitation in between consecutive runs was incorporated to account for the breaks between runs. Similarly, the recorded history of compressive axial load was applied at the top of the beam-column model.

Damping characteristics in OpenSees are modeled using linear viscous damping following the Rayleigh model, in which the damping matrix at each time step is calculated as the linear combination of the mass ( $M$ ) and stiffness ( $K$ ) matrices. According to Charney (Charney, 2008), the damping matrix for nonlinear analysis can be selected in three different ways: stiffness-only proportional, mass-only proportional and mass and stiffness proportional. The stiffness matrix is also a linear combination of the initial ( $K_I$ ) and the tangent ( $K_t$ ) stiffness matrices, therefore the damping matrix is given by:

$$C = \alpha M + \beta K_I + \gamma K_t \quad (7-23)$$

Where  $M$  and  $K$  are the mass and stiffness matrices and  $\alpha$ ,  $\beta$ , and  $\gamma$  are scalar proportional coefficients.

#### 7.7.4.1 Specimen NF1

The first considered analytical model (C02S02), was intended to evaluate the effectiveness of the material models used for the pushover analyses (Concrete02 and



Steel02), in predicting the measured force-displacement characteristics of the specimen. For these analyses, the column was modeled using a nonlinear beam-column element with fibers and six integration points, bond-slip using Bond\_SP01 material, and P-delta effects on the MR. Masses of 80 kips. and 3.6 kips. were lumped on the MR and top of the column, respectively. The damping matrix was established as the linear combination of the mass and stiffness matrices and a damping coefficient of 5% was used to calculate the coefficients in equation 7-23. Figs 7-57 and 7-58 show comparisons between the measured and calculated cumulative displacement histories and force-displacement hysteresis using these materials. From the figures, it is evident that the model is adequate to represent the dynamic characteristics of the specimen up to the effective yielding point, after that point the predicted deformations were less than the measured. In addition, from Fig. 7-56, it is clear that the initial stiffness of the analytical model was larger than that measured. These differences in the initial lateral stiffness are attributed to the fiber model, where the stiffness matrix of each fiber is calculated directly from the concrete and steel material models, which are based on the gross properties ( $EI_g$ ).

In order to simulate adequately the specimen's initial lateral stiffness and its degradation, a beam with hinges element was used to model the RC cantilever column. For specimen NF1 the inelastic behavior was assigned to occur only at the plastic hinge region at the base of the columns. The plastic hinge length was calculated using the model proposed by Priestley (Priestley et al., 2007) and was found to be approximately 70% of the column diameter. An effective lateral stiffness ( $EI_{eff}$ ) of 45% of the gross value ( $EI_g$ ) was selected for the elastic portion of the element to resemble the measured values of the lateral stiffness at the beginning of the test (see section 7.7). The material

models and other modeling parameters remained unaltered from the previous model. The measured and calculated cumulative displacement histories and force-displacement hysteresis for this model (BWHC02S02) are shown in Figs. 7-59 and 7-60, respectively. As can be seen from the figures, the displacement history does not change much compared with the previous model, but a better agreement was observed for the initial lateral stiffness.

To improve the lateral displacement prediction after the yielding point, a new model was proposed (BWHC07RS). In this, the concrete fibers were modeled using the Concrete07 material, while the longitudinal steel fibers were simulated using the ReinforcingSteel material. The other modeling parameters were kept the same as in the previous model. Figs. 7-61 and 7-62 show comparisons between the measured and calculated displacement histories and force-displacement hysteresis. From the figures, it is evident the improvement in the displacement predictions by using this combination of materials.

Several studies have shown that for nonlinear time history analysis, the simulation of the viscous damping as the linear combination of the mass and initial stiffness matrices following Rayleigh method, results in underestimations of the structure displacements at high levels of deformation, when the hysteretic energy dissipation is low (Sakai and Unjoh, 2006; Petrini *et al*, 2008; Jeong *et al*, 2008; Charney, 2008). Instead, tangent stiffness-proportional viscous damping appears to be more appropriate for the nonlinear time history analysis and results in increased displacements at high ductility demands. Therefore, equation 7.23 can be simplified into:

$$C = \gamma K_t \quad (7-24)$$

$$\gamma = \frac{2\xi}{\omega_i} \quad (7-25)$$

Where:

$K_t$ : tangent stiffness matrix;

$\gamma$ : stiffness coefficient;

$\xi$ : damping ratio;

$\omega_i$ : circular frequency of the elastic system.

Accordingly, a further refinement in the computational model was made by using a tangent stiffness-only proportional viscous damping with a damping coefficient of 2.5% for the first natural frequency of the system.

All the parameters required for the definition of the analytical models (best model) are summarized in Table 7-10. The measured and calculated cumulative displacement histories and force-displacement hysteresis for this model are shown in Figs. 7-63 and 7-64, respectively. Figs. 7-65 through 7-68 compare the measured and calculated displacement histories and force-displacement hysteresis at each run of the testing protocol. The close match between the analytical model and measured response up to the maximum capacity of the specimen is apparent. For the first two runs, the analytical model followed closely the experimental lateral stiffness, displacements and force histories, showing the accuracy of the analytical model in predicting the elastic response of the system. After that, the analytical model showed larger stiffness than the

experimental results. Table 7-11 shows comparisons between the maximum values of displacement (peak and residual) and lateral force at each run of the test sequence. From the result, it is evident that for most of the runs the differences between analytical and experimental values were within 20%. It is worth noting that although the ratio between residual displacements was high, the maximum difference between analytical and experimental results was around 0.5 in. At the last run, when the bar buckling, concrete core degradation and the bar rupture took place, the analytical model underestimated the response because these effects were not directly considered in the constitutive material models. The analytical results proved that the applied analytical model was adequate in resembling the experimentally measured nonlinear response of the specimen.

#### **7.7.4.2 Specimen 9F1**

The best model found to resemble the seismic performance of specimen NF1 was used to predict the behavior of 9F1. The measured material properties and the accumulated histories of acceleration recorded by the shake table were used as the input ground motions. The history of compressive axial load recorded by load cells on top of the column during the test was applied to the model specimen. A value of  $0.2 EI_g$  was used to resemble the natural period measured at low amplitude runs and replicate the measured initial stiffness. Table 7-12 summarize all the parameters required in the definition of the analytical model in OpenSees. Figs. 7-69 and 7-70 illustrate the measured and calculated seismic performance in terms of displacement histories and force-displacement hysteresis accumulated during the entire test protocol. The corresponding plots at each run of the testing sequence are shown in Figs. 7-71 through

7-73. From the results, it is noted that in general the analytical model replicated the stiffness, strength and displacement characteristics of the tested specimen reasonably well for all the test sequence. As can be seen in Table 7-13, the maximum differences between the analytical and experimental results were within 20% except at run 9, when the analytical model underestimated the displacements associated with the specimen failure.

#### **7.7.4.3 Specimen ISL1.0**

The analytical prediction of the seismic performance of specimen ISL1.0 was based on the best analytical model developed for specimen NF1. The cantilever column was modeled using a beam with hinges element. The plastic hinge length was defined as 14 in. based on Priestley plastic hinge length (Priestley *et al.*, 2006), while a value of  $0.25 EI_g$  was used to simulate the measured period at low amplitude accelerations. The bond-slip effect was modeled by adding a spring at the column-footing interface with the properties determined from the Bond\_SP01 material. The MR was modeled as a single cantilever elastic element with a pin support, while the link was simulated using a truss element connecting the MR and the specimen. Corrotational transformations were assigned to the MR element to consider P-delta effects, as can be seen in Fig. 7-52. The Concrete07 material was used to model the unconfined and confined concrete fibers, whereas the ReinforcingSteel material was used to model the reinforcement fibers. The measured material properties were used as the input parameters of the selected material models. The input ground motion was applied parallel to the long side of the section and corresponded to the accumulated histories of accelerations recorded by the shake table. Since no significant variation in the axial force was observed during the test sequence, a

constant value of 90 kips was applied at the top of the specimen to model the compressive axial load. Lumped masses of 93 kips and 3.6 kips were assigned to the top nodes of the specimen and MR elements, respectively. Damping properties were simulated using Rayleigh equation with stiffness-only proportional values and a damping coefficient of 2.5%. Table 7-14 presents further details of the parameters required in the definition of the OpenSees analytical model. Comparisons between the calculated and measured cumulative displacement histories and force-displacement hysteresis are illustrated in Figs. 7-74 and 7-75. The same plots but at each run of the testing protocol are shown in Figs. 7-76 through 7-78. Additionally, Table 7-15 presents comparisons between the analytical and experimental results. In general, the analytical predictions simulated the measured performance of the specimen reasonably well with differences within 20%.

#### **7.7.5 Nonlinear Time History Analyses for Bidirectionally Tested Specimens**

The analytical model for the bidirectionally tested specimens was created based on the more suitable model found for the unidirectionally tested specimens. The RC specimens were idealized as single cantilever columns using beam with hinges elements, whereas, the bidirectional mass rig (BMR) platform was represented by a grid of elastic elements set on rollers at the top of the supporting structure. The links connecting the mass rig and the specimen along the X and Y directions were modeled using corrotational truss elements. The additional mass attached to the BMR representing the bridge superstructure weight, was assumed to be lumped on the corners of the BMR platform. Based on the actual distribution of masses on the platform, the coordinates of the center

of mass were calculated. Once these coordinates were calculated, they were used to define a master joint to control the displacement of the platform following a rigid diaphragm. For dynamic analysis, the total lateral mass in each direction, as well as the rotational mass, were assigned to the master joint. The ball bearings were modeled using zero length elements; their properties were defined to reflect the low friction between the steel balls and the supporting plates. Fig. 7-79 illustrates the analytical model used for the bidirectionally tested specimens. The longitudinal and transverse accelerations recorded by the shake table during each run of the test protocol were used as the input excitations. For each direction, a single record with the accumulated acceleration measured during the test protocol was applied to the base of the model.

#### **7.7.5.1 Circular Specimens C1 and C2**

The reinforced concrete cantilever columns were modeled using the beam with hinges element with appropriate effective stiffness. The length of the plastic hinge region was defined as 12 in. measured from the column-footing interface, and derived from Priestley plastic hinge model (Priestley *et al.*, 2006). The section at this location was discretized into a total of 200 fibers; 36 for the unconfined concrete, 144 for confined concrete and 20 for the longitudinal reinforcement, as can be seen in Fig. 7-44. The effective lateral stiffness of the linear elastic portion of the element was set as 20% of the gross stiffness ( $EI_g$ ) for both X and Y directions; these values were selected to mimic the measured natural periods of the specimens. The torsional effective stiffness was defined as 0.2 JG according to Caltrans Seismic Design Criteria (Caltrans, 2006b). The bond-slip effects were simulated by adding a zero length fiber section element at the column-

footing interface with the fiber properties determined from the Bond\_SP01 material. The uniaxial stress-strain characteristics of the confined and unconfined concrete fibers were simulated using the Concrete07 material, while the longitudinal steel bars were modeled using the ReinforcingSteel material.

The coordinates of the center of mass were calculated from the location and magnitude of the attached masses (lead palettes) on the BMR platform, by taking moments with respect to an arbitrary point in the system (longitudinal axis of the RC column). These coordinates were found to coincide with the longitudinal axis of the RC column for specimen C1, whereas these were out of the axis of the column by 12 in. for specimen C2. Translational and rotational masses were lumped on the master joint (center of mass) of the BMR platform. The translational mass was the same for the X and Y directions and had a magnitude of  $0.207 \text{ k-s}^2/\text{in}$ . The rotational masses calculated with respect to the mass centroid of the platform were  $1775 \text{ k-in-s}^2$  and  $1716 \text{ k-in-s}^2$  for C1 and C2, respectively. Fig. 7-80 illustrates the distribution of masses and the location of the center of mass for C1 and C2, respectively. Damping was simulated using the Rayleigh equation with tangent stiffness-only proportional and a damping coefficient of 2.5% for the first translational frequency of the system. Details of the modeling parameters are summarized in Table 7-16.

Comparisons between the calculated and measured accumulated displacement histories and force-displacement hysteresis are presented in Figs. 7-81 through 7-84 for the longitudinal and transverse directions of specimen C1. The same plots, but at each run of the testing protocol are shown in Figs. 7-85 through 7-92. Tables 7-17 and 7-18 show comparisons between the analytical and experimental seismic performance of the



specimen in terms of displacements (peak and residual) and lateral force for the longitudinal and transverse directions, respectively. For C2 the same comparative plots and tables are shown in Figs. 7-93 through 7-104 and in Tables 7-19 and 7-20. In general, the analytical predictions simulated the measured performance of the specimens accurately well, with differences between the analytical and experimental results within 15% for the longitudinal direction of analysis. For the transverse direction of analysis, the analytical model simulated reasonably well the seismic performance up to the maximum lateral capacity was reached. Once this capacity was exceeded, the analytical results showed greater stiffness and, consequently, less residual displacements compared to the experimental results. The good correlation between the analytical and experimental results, especially those along the longitudinal direction of analysis, shows the adequacy of the analytical model in resembling the elastic and inelastic seismic performance of the experimentally tested circular specimens.

#### **7.7.5.2 Interlocking Specimens I1 and I2**

A beam with hinges element was also used to represent the cantilever interlocking specimens (See Fig. 7-105). The plastic hinge zone at the bottom of the column had a length of 14 in., and it was discretized into a total of 468 fibers; 92 for the unconfined concrete, 344 for confined concrete and 32 for the longitudinal steel, as can be seen in Fig. 7-44. The elastic properties of the linear elastic portion of the element were characterized to resemble the measured period of the specimen. Accordingly, values of the effective lateral stiffness of  $0.20 EI_g$  were used for the longitudinal and transverse directions, also an effective torsional stiffness of  $0.2 JG$  was assigned to the element. The

uniaxial stress-strain characteristics of the fibers section at the plastic hinge region were represented by the Concrete07, ReinforcingSteel and Bond\_SP01 materials simulating concrete, longitudinal bars and bond slip effects.

For dynamic analyses, the masses were considered lumped at the center of mass of the BMR platform. The translational mass was the same for both specimens and was calculated as 0.207 k-s<sup>2</sup>/in, whereas the rotational mass was computed as 1774 k-in-s<sup>2</sup> and 1718 k-in-s<sup>2</sup> for I1 and I2, respectively. Fig. 7-106 shows the distribution of masses and the location of the center of mass for I1 and I2, respectively. For specimen I1 the mass centroid coincided with the longitudinal axis of the RC column, whereas for I2 the mass centroid was out of this axis by 12 in. The center of mass was calculated by taking moments with respect to the geometric centroid of the platform, which coincided with the longitudinal axis of the RC column. Damping was modeled as viscous and was simulated using Rayleigh's equation with tangent stiffness-only proportional and a damping coefficient of 2.5% for the first translational frequency of the system. All the parameters required for the definition of the analytical models are summarized in Table 7-21.

Figs. 7-107 through 7-110 present comparisons between the analytical and experimental results in terms of the cumulative displacement histories and the force-displacement hysteresis along the longitudinal and transverse directions of specimen I1. The same plots, but at each run of the testing protocol, are shown in Figs. 7-111 through 7-118. Comparisons of the calculated and measured seismic performance along the longitudinal and transverse directions of analysis are summarized in Tables 7-22 and 7-23, respectively. The same comparative plots and tables for specimen I2 are shown in Figs. 7-119 through 7-130 and in Tables 7-24 and 7-25. In general, the analytical

predictions in terms of stiffness, displacements (peak and residual), lateral capacity and post failure strength were represented reasonably well for the longitudinal direction of analysis, where the differences between the analytical model and experimental results were within 15%. For the transverse direction of analysis, the analytical model could capture most of the characteristics of the measured result up to the maximum capacity. Beyond this point the model showed larger lateral stiffness and less residual displacements than the experimental values. This is a consequence of the inability of the used constitutive material models in capturing the bar buckling, concrete core degradation and the bar rupture observed at the last runs of the experimental tests. Besides these differences at the failure point, the good correlation between the analytical and experimental results, especially those along the longitudinal direction of analysis, proves the accuracy of the analytical model in simulating the linear and nonlinear response of the experimentally tested interlocking specimens.

## **Chapter 8. Analytical Investigation of the Seismic Performance of RC Bridge Columns under One and Two Earthquake Components**

### **8.1 Introduction**

One of the main objectives of this study was to investigate the impact of biaxial ground accelerations on the seismic performance of bridge reinforced concrete columns (RCC). To fulfill this objective, the experimental results of shake table testing of columns subjected to bidirectional and unidirectional ground accelerations were compared in Chapter 6. Although some qualitative comparisons were made, the impact of the axial force, P-delta effects and the differences in the ground excitations used in each test preclude the establishment of quantitative comparisons. In Chapter 7 analytical models for each tests configuration were developed and validated with the experimental results. By using these models, this chapter presents an analytical investigation of the seismic performance of the columns subjected to one or two horizontal components of different ground motions, and including axial force and P-delta effects.

### **8.2 Analytical Models**

Nonlinear time history analyses were performed in OpenSees (PEER, 2006) to investigate the seismic performance of single cantilever columns subjected to unidirectional and bidirectional ground accelerations. Single column elements with the same geometry and reinforcement details of those experimentally tested specimens were modeled using a beam with hinges nonlinear element to represent the inelastic behavior of the columns. The plastic hinge length was defined as 12 in. for both the circular and

interlocking columns, and it was derived from the Priestley plastic hinge model (Priestley *et al.*, 2006). At this location the sections were discretized into fibers to represent the inelastic behavior of concrete and longitudinal reinforcement at the plastic hinge regions. The sections were discretized into 236 and 368 fibers for the circular and interlocking columns, respectively. To account for cracking of reinforced concrete members, the effective lateral stiffness of the linear elastic portion of the element was set as 30% of the gross stiffness ( $EI_g$ ) for both longitudinal and transverse directions; similarly, a value of 0.2 JG was defined for the torsional effective stiffness. These values were calculated according to section 5.6 of Caltrans SDC (Caltrans, 2006).

The uniaxial stress-strain characteristics of the confined and unconfined concrete fibers were simulated using the Concrete07 material, while the longitudinal reinforcement bars were modeled using the ReinforcingSteel material. The measured properties of the concrete and reinforcement described in section 3.3 were used as the input parameter of the uniaxial material models. The bond-slip effects were simulated by adding a zero length fiber section element at the column-footing interface with the fiber properties determined from the Bond\_SP01 material.

The axial load in the column was set as 80 kips, which is equivalent to an axial load ratio capacity ( $f'_c A_g$ ) of 8%. Neither the unidirectional or bidirectional mass rig structures were modeled, instead a translational mass of 0.207 k-s<sup>2</sup>/in (80/g) was lumped at the top of the column. Damping was simulated using Rayleigh's equation with tangent stiffness-only proportional and a damping coefficient of 2.5% for the first translational frequency of the system.

### 8.3 Ground Motions

In order to evaluate columns' response under earthquakes with different characteristics (peak ground accelerations (PGA), frequency content and duration), the columns were subjected to two horizontal components of the records of five historical earthquakes: the 1940 Imperial Valley earthquake at El Centro, the 1989 Loma Prieta at Los Gatos, the 1992 Cape Mendocino earthquake at Petrolia, the 1994 Northridge earthquake at Rinaldi and Sylmar, and the 1995 Kobe earthquake at Takatori (PEER, 2000). These earthquakes were selected for two reasons; first because some of them were used in the experimental program of this research and in previous studies conducted at Nevada, and second because all of them are representative of near-fault ground acceleration typical of seismic conditions in California. The Takatori record was selected because it is representative of near-fault ground motions in Japan, and because it has almost the same peak ground acceleration (PGA), velocity (PGV) and displacements (PFD) in both horizontal components. The main characteristics of these earthquakes are summarized in Table 8-1. To account for the scale of the columns ( $1/3$  for circular and  $1/4$  for interlocking), the time of the records was compressed using factors of 0.58 and 0.5 for the circular and interlocking columns, respectively. Figs. 8-1 through 8-6 show the two horizontal components of the acceleration records, and the corresponding pseudo-acceleration spectrums and acceleration orbits for circular columns. The same plots for interlocking columns are presented in Figs. 8-7 through 8-12.

Based on the experimental results of low amplitude acceleration, the calculated natural periods in the longitudinal and transverse direction of the circular column were estimated to be about 0.6 seconds; whereas the interlocking columns had periods of about

0.5 and 0.7 seconds for the long and short side, respectively. Spectral acceleration demands were estimated for each ground motion using the natural vibration periods, and are summarized in Table 8-2.

In order to replicate the test sequence used during the experimental program and to study the seismic response of the columns under different levels of excitation, the time histories records were scaled in multiple amplitudes of increasing intensity (runs) and combined in a single cumulative record. The scale factors for each ground motion were selected to evaluate the behavior of the columns from the elastic range to failure. From the geometry, material properties and axial load, the yielding was estimated to occur at spectral accelerations of 0.35g for the circular column and at 0.32g for the interlocking column. Accordingly, factors of 0.8, 0.35, 0.3, 0.2, 0.4 and 0.20 were applied to the El Centro, Los Gatos, Petrolia, Rinaldi, Sylmar and Takatori records to induce yielding in the columns. Table 8-3 summarizes the scale factors used for each run of the analytical loading sequence. For the bidirectional input excitations, the same scale factors were used for both horizontal components.

#### **8.4 Unidirectional vs. Bidirectional Response**

In order to evaluate the impact of bidirectional loading on the seismic performance of the columns, the analytical model was subjected to either one or two horizontal components of the selected earthquakes. For the unidirectional case the two components of the earthquakes were applied individually along the longitudinal (X) and transverse (Y) direction of the section. The strong component was applied along X, while the weak one was applied along Y; for the interlocking column, the longitudinal direction

was defined parallel to the long side of the section. Likewise the two horizontal components were applied simultaneously for the bidirectional case of analysis; the components were applied following the same convention as previously mentioned. The time history of base shear and top column displacement were monitored, as well as the residual displacement at the end of the each earthquake intensity (scale factor).

Figs. 8-13 through 8-24 present comparisons of the simulated displacement histories along the longitudinal and transverse directions of the circular column, for the unidirectional and bidirectional analysis, when subjected to the selected earthquakes. The lateral force-displacement hysteresis curves are shown in Figs. 8-25 through 8-30. The corresponding plots for the interlocking columns are shown in Fig. 8-31 through 8-42 for displacement histories, and in Fig. 8-43 through 8-48 for force-displacement hysteresis. From the figures, it is evident that at small earthquake amplitudes (up to yielding), the responses of the column under bidirectional and unidirectional loading are very similar. Once the longitudinal reinforcement has yielded, smaller lateral forces and larger displacements (maximum and residual) were observed in the bidirectional case. These differences become larger with increasing earthquake amplitude. For most of the selected earthquakes, analytical failure of the columns under bidirectional excitation occurred at earthquake amplitudes lower than those of the unidirectional analysis. Failure was defined as the stage when either the strain in the longitudinal reinforcement fibers exceeded the ultimate strain, or when the strains in the confined concrete fibers exceeded the crushing strain, leading to a large displacement and numerical instability. It was also observed from the analytical results that the differences between the response of the columns subjected to unidirectional and bidirectional excitations were large along the



transverse direction of the column where the small component of the earthquake was applied. These differences were attributed to the softening of the specimens, which was more pronounced in the transverse direction of the columns under biaxial motions. This observation was in agreement with the behavior of the bidirectionally tested columns, which showed a more accelerated stiffness degradation along the transverse (Y) direction compared to the longitudinal (X) direction. Therefore, it is noted that the effects of bidirectional interactions are more significant in the direction where the small component of the earthquake is applied.

In order to evaluate the effects of bidirectional excitation on the displacement response of the columns under the selected records, the maximum displacement obtained at each intensity level (scale factor) along the principal directions of the columns, as well as the vector component, were compared. The vector component was calculated using the following equation:

$$D_{vector} = \sqrt{(D_{x-bid}^2 + D_{y-bid}^2)} \quad (8-1)$$

Additionally, the combined response obtained from the individual uniaxial responses was calculated using the square root of the squares (SRSS) rule:

$$D_{SRSS} = \sqrt{(D_{x-unid}^2 + D_{y-unid}^2)} \quad (8-2)$$

Where:

$D_{x\_bid}$  = displacements in the longitudinal direction of the column from biaxial motions;

$D_{y,bid}$  = displacements in the transverse direction of the column from biaxial motions;

$D_{x,unid}$  = displacements in the longitudinal direction of the column from uniaxial motions;

$D_{y,unid}$  = displacements in the transverse direction of the column from uniaxial motions;

Tables 8-4 through 8-10 summarize the numerical results obtained for the circular columns subjected to each intensity (run) of the selected earthquakes. Figs. 8-49 through 8-54 show comparisons of the maximum displacement in each direction, the combined or vector displacement and ratios between bidirectional and uniaxial response for circular columns. From the figures, it is confirmed that the biaxial excitations resulted in larger displacements than unidirectional excitation. These figures also show that for earthquake intensities representing the design earthquakes (DE), the peak bidirectional vector displacement is comparable to the peak unidirectional displacement in the longitudinal (X) direction, and to the component displacement calculated from the individual uniaxial responses combined using the SRSS rule. Better correlations were found for Los Gatos, Petrolia and Sylmar earthquakes, in which the ratio of the peak ground velocity (PGV) of the strong and weak components is around 2.

For the interlocking columns, the calculated maximum displacements at each intensity level are presented in Tables 8-11 through 8-16. Figs. 8-55 through 8-58 present comparisons of the maximum displacement in each direction, the combined or vector displacement and ratios between bidirectional and uniaxial response. Similarly to the circular columns, it is noted from the figures that the biaxial excitations produced larger displacements than the unidirectional excitations. From the figures, it is also noted that the peak bidirectional vector displacement is comparable to the peak unidirectional

displacement in the longitudinal (X) only for the Los Gatos, Petrolia and Sylmar earthquakes. However, the bidirectional responses can be computed from the component displacement of the individual uniaxial responses using the square root of the sum of the squares (SRSS) rule.

## Chapter 9. Summary and Conclusions

### 9.1 Summary

The seismic performance of columns reinforced with circular and double interlocking spirals was investigated by testing large-scale specimens under bidirectional ground excitations with the shake table facility at the University of Nevada, Reno. The specimens represent prototype columns with design details of bridges with single column-bents in California. The main objective of the study was to investigate the effects of combined biaxial bending and torsion on the seismic response of columns without axial force, and evaluate the ability of analytical models to predict the seismic behavior.

Four large-scale single cantilever-type columns were constructed using materials and current design details typical of bridges in California in accordance with the 2006 Caltrans provisions. The structural configuration was similar to previous columns with flexural-dominated behavior tested unidirectionally at Nevada. As part of the research project a unique inertial loading system; the Bidirectional Mass Rig (BMR), was developed to test single cantilever-type columns with a biaxial shake table. The system is composed of a 3D frame structure which safely carries the vertical component of the inertial mass (superstructure weight), and a platform that sits on ball bearings on the frame structure. The platform is connected to the RCC specimen through links in two perpendicular directions, which allows the transferring of shear and torsion through the specimen, but not axial load. The system also has the ability to induce torsional effects in the specimen by placing the inertial masses in an unsymmetrical configuration.

Two of the specimens were 1/3-scale circular columns with a diameter of 16 in., aspect ratio of 4.5 and reinforced using longitudinal and transverse steel ratios of 1.98% and 0.95%, respectively. These specimens were subjected to the two horizontal components of the 1992 Mendocino earthquake at Petrolia, California. Similarly, two 1/4-scale columns with an oblong section and reinforced with interlocking spirals were subjected to the two horizontal components of the 1994 Northridge earthquake recorded at the Sylmar station. The cross sections of these columns have dimensions of 12 in. and 17.5 in. in the short and long side, and with longitudinal and transverse steel ratios of 2% and 1.1%, respectively. All the specimens had the same height (72 in) and were subjected to successive input motions of increasing acceleration intensity until failure. No axial load was applied. The superstructure mass was defined as 80 kips, which is equivalent to an axial load ratio of 8%  $A_g f_c$ .

The only difference between the two identical columns, was the way in which the mass was distributed on the BMR. For one circular and one interlocking column a symmetric distribution of masses was used, while it was asymmetric for the other two columns, hence, more torsion was expected. The specimens were instrumented to measure lateral force, lateral displacement, curvature, strains and accelerations. The seismic performance of the specimens was assessed in terms of hysteretic response (strength and deformation), strain rate, plastic hinge length and failure mode. After each run of the test protocol, the damage was documented by marking cracks and taking a number of pictures.

The behavior of each pair of specimens was similar and was controlled by the biaxial effect of bending. Horizontal cracks were distributed over the specimen height,

including some inclined cracks near the column base. The columns failed after a plastic hinge was fully developed at the column base; the failure mechanism was initiated by buckling of longitudinal bars, followed by reinforcement rupture and degradation of the concrete core.

Measured specimen responses such as lateral force-displacement and moment-curvature (hysteresis and envelopes), torque-rotation, ductility, plastic hinge length and dynamics properties were assessed and compared between each pair of specimens and with similar specimens unidirectionally tested on a shake table as part of previous research projects at the University of Nevada, Reno.

Different analytical approaches were conducted to reproduce the experimentally observed behavior of the specimens. Sectional analyses were completed to investigate the moment curvature characteristics of the sections, and its variation with changes in the orientation of the neutral axis to account for biaxial bending. Nonlinear static analyses (pushover) were conducted in OpenSees to evaluate the force-deformation characteristics of the specimens under monotonic loading. Good agreement between the measured and predicted values was found when strain rate, flexure and shear deformation, and bond slip were included in the analytical models. Nonlinear time history analyses were implemented in OpenSees. Different modeling alternatives were evaluated and validated to reproduce the measured dynamic performance of the specimens when subjected to the same excitation sequence that was applied experimentally.

Based on the validated model, an analytical investigation was conducted to evaluate the performance of a model of the columns subjected to axial load and different intensities of 6 historic ground accelerations. In order to evaluate the impact of bidirectional loading

the horizontal components of the selected earthquakes were applied either simultaneously to simulate biaxial excitation or unidirectionally using the largest of the components. In addition, different combination rules were compared to evaluate their effectiveness in predicting the biaxial behavior of the columns.

## **9.2 Conclusions**

Based on the experimental and analytical investigation performed as part of this research on the seismic performance of bridge columns reinforced with single and double interlocking spirals, and subjected to biaxial ground acceleration without axial force, the following observations and conclusions were established.

### **9.2.1 Experimental Investigation**

1. The inertial loading system: Bidirectional Mass Rig designed and constructed as part of this study, performed as expected providing a reliable and safe tool for testing on a shake table, single cantilever-type large-scale columns subjected to bidirectional ground excitations. One of the main advantages of this system is the ability of placing additional masses in a number of symmetrical or asymmetrical configurations to induce different levels of inertial lateral loads and torsion with or without axial force. Furthermore, the low-friction ball bearings allow transferring of inertial forces, even under low level of lateral excitations.
2. The seismic performance of the circular and interlocking specimens designed according to the 2006 Caltrans BDS and SDC was satisfactory. It was controlled by the biaxial effect of bending with small influence of shear deformations. The columns resisted several repetitions of earthquakes with spectral amplitude equal to or larger

than the maximum considered earthquake with sufficient drift and displacement ductility capacity. Average displacement ductilities of 10 and 6 were observed for the circular and interlocking columns, respectively.

3. The behavior between pairs of specimen was similar; it was characterized by good energy dissipation and high levels of deformation without collapse. At low amplitude earthquakes, the specimens remained essentially elastic, the concrete cover was spalled at a scale factor of 1.2 times Petrolia or Sylmar for the circular and interlocking columns, respectively; which represents design level earthquakes (DE) in California. Application of accelerations of increasing amplitude and larger than the DE, progressively deteriorated the section until the failure. This was initiated by the longitudinal bar buckling, and posterior rupture of longitudinal and/or spiral reinforcement, accompanied by core concrete degradation.
4. For all the specimens, the hysteresis loops were stable and showed good energy dissipation. For each earthquake intensity, most of the energy was dissipated during one cycle (distinctive loop). This behavior is typical of near fault earthquakes, in which most of the energy is concentrated in a short duration high amplitude velocity pulse. When this pulse is asymmetric, as in the case of earthquakes with forward directivity effect, the RC column did not undergo fully displacement reversals leading to large displacements in one direction. This was the case of the circular specimens C1 and C2, where the asymmetric velocity pulse of the strong component of the record induced large residual displacements and ductilities in a predominant direction.



5. For all the specimens, it was observed that after yielding, the maximum lateral capacity remained almost constant for increasing earthquake intensities until the longitudinal bar buckling occurred. After this point the response was characterized by a pronounced stiffness and capacity degradation, leading to failure. Similar behavior was observed for a column subjected to unidirectional excitations and constant axial load tested at the University of Nevada, Reno. Nevertheless, for a similar column tested under unidirectional excitations and variable axial load, the lateral capacity was not constant and it was notably affected by stiffness degradations and P-delta effects. Large variation in the axial load made the column more susceptible to lateral instability as a consequence of P-delta effects.
6. For the sections and ground motions used in this study, the biaxial interactions affected mostly the seismic performance of the columns along the direction where the small component of the earthquake was applied (transverse direction). It was observed that the lateral capacity along the transverse direction was reduced in comparison to the values calculated from moment-curvature analysis. For the longitudinal direction the measured capacity was in good agreement with the calculated values from moment-curvature, indicating that the seismic response in this direction was only slightly affected by the behavior on the transverse direction.
7. The asymmetric mass configuration used for specimens C2 and I2 only induced low values of torsion on the columns. Measured values of the torque to bending ratio were below 20%. The softening of the column's torsional stiffness due to the formation of the plastic hinge limited the development of the torsion.

8. Although the behavior of pairs of specimens was comparable, slightly less capacity was observed after the first yielding on the lateral force-displacement envelope curves of the specimens with larger mass eccentricities (C2 and I2). This behavior might be explained by the combination of torsion and bending deformations. This effect was significant at high intensity earthquakes and played a role in the failure mechanism of the specimens. The buckling mode of the longitudinal reinforcement was inward of the spirals and was accompanied by twisting.
9. The measured dynamic properties of the columns (periods and damping) changed with the damage progression. The periods gradually lengthened with increasing levels of excitation as a consequence of the stiffness degradation. In contrast, the variation in damping followed a less evident trend, but in general, it increased within successive runs. For circular columns the period changed from a value of about 0.60 sec. at the undamaged state to an average value of 1.3 sec. at the last run, whereas the values of viscous damping ranged from 3% to 9%. For interlocking specimens the period changed from 0.55 sec. and 0.78 sec. to 1.40 sec and 1.35 sec. along the longitudinal and transverse directions of the section, respectively. Values of damping ranged from 3% and 10%. The dynamic properties (periods and damping) were estimated using spectral density functions and system identifications algorithms with multiple input-multiple output (MIMO). Comparisons between the two methods showed good agreement in the values and trends estimated using each method.
10. The effective lateral stiffness of the specimens at the undamaged state was on average 30% of the gross stiffness ( $EI_g$ ). It was reduced to about 25%  $EI_g$  with longitudinal bar yielding. It continued to reduce with the progression of the test,

following a linear trend, reaching a minimum value of 10%  $EI_g$  at the end of the test protocol. This suggests that the values in section 5.6 of Caltrans SDC (2006) are also applicable to columns under biaxial bending without axial load.

11. The measured strain-rate and plastic hinge length were comparable to those measured in columns tested unidirectionally and with constant or variable axial load. Biaxial effects or the characteristics of ground acceleration (near-fault earthquakes) did not influence these parameters.

### **9.2.2 Analytical Investigation**

1. For sectional analysis it was found that the stress-strain characteristics of the concrete and reinforcement using Mander's model and using the measured material properties modified by strain rate leads to a good estimation of the moment capacity of the specimens. The ultimate curvature however, was significantly less than the measured values. This is explained by the fact that the maximum confined concrete strain (crushing strain) used in Mander's model is conservative by a factor of approximately two. A modification of the Mander's model for confined concrete to account for the strength degradation, improved considerably the ultimate curvature prediction. The modification consisted of the addition of a straight line connecting the points of crushing strain and corresponding strength with a strain of two times the crushing strain and zero strength.
2. The available elements and material models for concrete and reinforcement in OpenSees were successful in predicting the nonlinear behavior of the columns studied. It was found that the modeling of the specimens with a nonlinear beam-

column element with fibers, hysteretic material model with strength degradation, bond slip and viscous damping leads to the best estimation of the measured performance.

3. In order to model the plastic hinging and take into consideration the reduction in lateral stiffness due to initial cracking, a beam-with-hinges nonlinear element in OpenSees was found to be the best representation of the RC columns. The plastic hinge length and effective lateral and torsional stiffness calculated from the Caltrans SDC provisions were sufficient to capture the nonlinear behavior of the specimens.
4. A representation of the mass rig for the columns tested under unidirectional excitations and axial loading was required to correctly model the additional forces transferred from the mass rig to the specimen due to the P-delta effects at large levels of deformation. A single elastic element with hinge support and connected to the specimen using a truss element was sufficient to induce inertial and P-delta forces in each column. For the analytical model of the bidirectionally tested columns, the bidirectional mass rig structure needed to be included to correctly represent the eccentricities due to the location of masses and the forces transferred from this structure to the column.
5. A combination of the Concrete07 and the ReinforcingSteel materials in OpenSees was the best option to reproduce the measured performance. The Concrete07 material has the ability to model the stress-strain characteristics of the confined concrete at large levels of strain and the hysteresis rules used are able to capture the concrete degradation at those levels of strain. The ReinforcingSteel material, can capture closely the measured monotonic stress-strain characteristics of coupons by

using engineering stress space (rather than natural stress space), and by modeling the yielding plateau and parabolic strain hardening of the longitudinal rebar.

6. Explicit modeling of bond slip was required to represent the flexibility in the lateral response of the specimens due to slip rotations at the column-footing interface. From the two models studied, the Bond\_SP01 material in OpenSees was preferred because of its simplicity and because it considers the actual slipping of individual bars, which is an advantage when a time history analysis of biaxial bending is considered. The Hysteretic material determined using the Wehbe method requires calculations of the moment-rotation of the section, which may be inappropriate for dynamic biaxial bending, due to the uncertainty in determining the orientation of the neutral axis. Both methods showed similar results for columns under unidirectional excitation.
7. Viscous damping of the RC columns calculated using the Rayleigh equation with tangent stiffness-only proportional, and a damping coefficient lower than 3% for the first translational frequency, resulted in adequate displacement predictions at high ductility demands. Larger values of the damping coefficient may result in underestimations of the displacement at high levels of deformation because hysteretic damping is implicitly considered in the material models.
8. From the analytical investigation of the columns subjected to the seismic excitation of 6 earthquakes, it was observed that for small amplitude earthquakes (before yielding) no major differences are observed in the response of columns under unidirectional or bidirectional excitations. However after yielding the biaxial excitations resulted in a reduction of the capacity of the columns, increase of lateral

displacements and more accelerated stiffness degradation compared to unidirectional excitation.

9. For earthquakes in which the ratio of the peak ground velocity (PGV) of the strong and weak components is around 2, as in the case of the Los Gatos, Petrolia and Sylmar, the peak bidirectional vector displacement is comparable to the peak unidirectional displacement in the longitudinal (X) direction, and to the component displacement calculated from the individual uniaxial responses combined using the SRSS rule.

### **9.3 Phase II of the Experimental Program at the University of Nevada, Reno**

During the spring of 2011, the shake table testing of the columns corresponding to the second phase of the experimental program at Nevada were conducted. Two circular (C1-P and C2-P) and two interlocking (I1-P and I2-P) columns with the same geometry, reinforcement ratios, materials properties and instrumentation as the columns tested in phase I, were subjected to real time biaxial accelerations on a shake table. In addition to the ground accelerations of phase I, dynamic actuators were used in phase II to apply the axial load and biaxial lateral forces to simulate P-delta effects.

A center-hole ram controlled by a servo-valve was placed on the column head to apply the axial load. This ram was connected to the specimen through an unbonded prestressed bar placed in an ungrouted conduit located in the middle of the column and anchored in the footing. Likewise, high speed dynamic actuators were connected in two horizontal orthogonal directions at the specimen head to apply the equivalent dynamic forces to induce P-delta effects and to compensate for the restoring force induced by the

prestressed bar of the axial load system. A sophisticated control procedure was developed to drive simultaneously the shake table and the dynamic actuators through hybrid simulation. In this procedure, the dynamic actuators were accurately controlled by force using active feedback and actuator compliance, as well as a calibrated spring-pack between the actuator and the column head.

Each column was subjected to the same horizontal earthquake components used in phase I, increasing the amplitude in successive runs until failure. The circular specimens, C1-P and C2-P, were tested using the Petrolia record of the 1992 Cape Mendocino earthquake, whereas the interlocking specimens, I1-P and I2-P, were subjected to the 1994 Northridge earthquake at Sylmar.

The specimens were extensively instrumented to monitor the local and global response. Electrical transducers were used at selected locations to measure acceleration, lateral force and displacement, torsion, and curvature. In addition, an optical 3D measurement coordinate system (Krypton system) was used to measure the displacements of the specimens in a 3D space. Furthermore, strain gauges were attached to the longitudinal and transverse reinforcement to measure local deformations. The seismic performance of the specimens was assessed in terms of strength, deformation, and failure mode. Details of the testing procedure, data processing and reduction, response evaluation and analytical studies will be presented in a future research report.

#### 9.4 Future Research

A limited number of bidirectional shake table tests have been performed on bridge reinforced concrete columns to date. Although worthy information has been obtained from these tests, there are still issues that require clarification or further investigation, including:

1. The impact of axial load and P-delta effects on the seismic performance of single cantilever-type RC columns subjected to bidirectional ground excitations and torsion. Experimental data from the second phase of the research program at University of Nevada will contribute to understand the behavior of columns under these complex loading combinations.
2. The influence of large values of torsion on the dynamic behavior of flexural-dominated columns. The current work has only had low values of torsion. This issue can be addressed by imposing larger eccentricities either of the mass distribution on the Bidirectional Mass Rig (BMR), or by locating the columns outside of the geometric centroid of the mass setup.
3. The effects of combined loading (bending, axial and torsion) on the seismic behavior of columns with non-circular cross-section and reinforced with hoops and ties.
4. Seismic behavior of substandard columns under combined loads. Of particular interest will be the seismic behavior of columns with insufficient lap-splice on both longitudinal and transverse reinforcement.
5. The influence of different ground motions on the performance of bridge columns. Of interest could be the study of long duration records representative of large magnitude events recorded at moderate distances from the fault or ground motions that have similar intensities in both directions.



6. The effects of the loading history on the bidirectional performance of bridge RCC. Columns subjected to high initial amplitude motions followed by few aftershocks would reveal differences on the seismic behavior of columns.
7. The effects of the slenderness on the bidirectional response of RC bridge columns. A limitation of the current study is due to the fact that only one aspect ratio was considered. A minor modification of the BMR can allow the experimental testing of higher specimens on single curvature, or shorter columns tested in double curvature.
8. The performance of systems of more than one column under biaxial earthquake excitations. Of interest is the behavior of two-column bents with the individual columns having oblong section (interlocking spirals).

From the point of view of analytical models, the following areas need further investigation:

1. Analytical models for uniaxial fiber elements need to be modified to include the softening or degradation in the lateral stiffness due to the biaxial loading interactions.
2. For cases where the behavior of the columns is not flexural-dominated, a different nonlinear element that accounts for the coupling effect of axial, bending, shear and torsion need to be used.
3. Parametric studies need to investigate the influence of different design parameter on the seismic performance of columns under combined loads. Some of them include: column height, column diameter, aspect ratio, longitudinal and transverse steel ratios and concrete and reinforcement steel properties.

4. Different load combinations rules need to be studied to determine the adequacy of seismic code provisions and determine critical loading scenarios for design guidelines.
5. The prediction of residual displacements from time history nonlinear analyses is generally difficult; the results are strongly dependent of the selected material models and damping modeling. Although some parameters were studied in this research to correlate well with the experimental result, further research is required to study the effects of the degradation in the material behavior. Special attention needs to be directed to bar buckling and reinforcement rupture in the ultimate behavior of ductile columns.

## References

- ACI Committee 318** (2008), "Building Code Requirements for Structural Concrete (ACI 318-08) and Commentary." American Concrete Institute, Farmington Hills, Michigan, USA, 465 pp.
- Belarbi, A., Li, Q. and Prakash, S.** (2009) "Torsional effects on Seismic Performance of Square vs. Circular RC Bridge Columns", Proceedings of the 25<sup>th</sup> US-Japan Bridge Engineering Workshop, Tsukuba, Japan.
- Benzoni, G., Priestley, N.M.J and Seible, F.** (2000) "Seismic shear Strength of Columns with Interlocking Spiral Reinforcement" Proceedings of 12<sup>th</sup> World Conference on Earthquake Engineering, Auckland, New Zealand, Paper 1562.
- Bousias, S.N., Verzeletti, G., Magonette, G. and Fardis, M.N.** (1992) "RC Columns in Cyclic Biaxial Bending and Axial Load" Proceedings of Tenth World Conference on Earthquake Engineering, Madrid, Spain, Vol. V, 3041-3046.
- California Department of Transportation.** (2006) "Bridge Design Specifications." Engineering Service Center, Earthquake Engineering Branch, California, USA, 250 pp.
- California Department of Transportation.** (2006b) "Seismic Design Criteria." Engineering Service Center, Earthquake Engineering Branch, Version 1.4, California, USA.
- Chang, G. and Mander, J.** (1994). "Seismic Energy Based Fatigue Damage Analysis of Bridge Columns: Part I – Evaluation of Seismic capacity." NCEER Technical Report 94-0006.
- Chang, S.Y.** (2008). "Experimental Studies of Reinforced Concrete Bridge Columns under Axial Load plus Biaxial Bending." ASCE Journal of Structural Engineering, Vol. 136 No. 1, pp 12 – 25.
- Charney, F.A.** (2008). "Unintended Consequences of Modeling Damping in Structures." ASCE Journal of Structural Engineering, Vol. 134 No. 4, pp 581 – 592.
- Choi, H., Saiidi, M.S., and Somerville, P.** (2007). "Effects of Near-Fault Ground Motion and Fault-Rupture on the Seismic Response of Reinforced Concrete Bridges." Report No. CCEER-07-06, Center for Civil Engineering Earthquake Research, Department of Civil Engineering, University of Nevada-Reno, USA, 531 pp.
- Chopra, A. K.** (2001). "Dynamic of Structures: Theory and Applications to Earthquake Engineering". Second Edition, Prentice Hall, New Jersey, USA.
- Clough, R. W. and Penzien, J.** (1993). "Dynamic of Structures". Second Edition, McGraw-Hill, New York, USA.
- Correal, J.F., Saiidi, M.S., and Sanders, D.H.** (2004). "Seismic Performance of RC Bridge Columns Reinforced with Interlocking Spirals." Report No. CCEER-04-6, Center for Civil

Engineering Earthquake Research, Department of Civil Engineering, University of Nevada-Reno, USA, 438 pp.

**Cruz-Noguez, C.A., Muria-Vila, D. and Camargo, J.** (2007). "Modification to the Computer Program MIMO, for Multiple Input – Multiple Output for System Identification." Engineering Institute, National University of Mexico.

**Choi, H., Saiidi, M.S., and Somerville** (2007). "Effects of Near-Fault Ground Motion and Fault Rupture on the Seismic Response of Reinforced Concrete Bridges." Report No. CCEER-07-06, Center for Civil Engineering Earthquake Research, Department of Civil Engineering, University of Nevada-Reno, USA, 531 pp.

**Dodd, L.L. and Cooke, N.** (1992) "Dynamic Response of Circular Bridge Piers" Proceedings of Tenth World Conference on Earthquake Engineering, Madrid, Spain, Vol. V, 3035-3039.

**Hachem, M.M., Mahin, S.A. and Moehle, J.P.** (2003) "Performance of Circular Reinforced Concrete Bridge Columns under Bidirectional earthquake Loading". Report PEER2003/06, Pacific Earthquake Engineering Research Center, University of California, Berkeley, California, USA.

**Hsu, T.T.C.** (1993). "Unified Theory of Reinforced Concrete". CRC Press, Florida, USA.

**Inoue, N., Wenliuhan, H., Kanno, H., Hori, N. and Ogawa, J.** (2000). "Shaking Table Tests of Reinforced Concrete Columns Subjected to Simulated Input Motions with Different Time Duration". Proceedings of the 12<sup>th</sup> World Conference on Earthquake Engineering, Auckland, New Zealand, Paper No. 1734.

**Jeong, H.I., Sakai, J. and Mahin, S.** (2008). "Shaking Table Test and Numerical Investigation of Self-Centering Reinforced Concrete Bridge Columns". Report PEER2008/06, Pacific Earthquake Engineering Research Center, University of California, Berkeley, California, USA.

**Johnson, N., Saiidi, M.S., and Sanders, D.H.** (2006). "Large-Scale Experimental and Analytical Seismic Studies of a Two- Span Reinforced Concrete Bridge System." Report No. CCEER-06-02, Center for Civil Engineering Earthquake Research, Department of Civil Engineering, University of Nevada-Reno, USA, 688 pp.

**Kawashima, K., Ogimoto, H., Hayakaga, R. and Watanabe, G.** (2006) "Effect of Bilateral Excitation on the Seismic Performance of Reinforced Concrete Bridge Columns", Proceedings of the Eighth US Conference on Earthquake Engineering, San Francisco, California, USA, Paper 567.

**Kawashima, K., Sasaki, T. and Kojiwara, K.** (2009) "Experimental study on the Seismic Response of Bridge Columns using E-Defense", Proceedings of the 25<sup>th</sup> US-Japan Bridge Engineering Workshop, Tsukuba, Japan.

**Karlsson, B. I., Aoyama, H. and Sozen, M. A.** (1973) "Spirally Reinforced Concrete Columns Subjected to Loading Reversals Simulating Earthquake Effects", Proceedings of the Fifth World Conference on Earthquake Engineering, Rome, Italy, Vol.1, 803 – 806.

**Karsan, I.D. and Jirsa, J.O.** (1969). "Behavior of Concrete under Compressive Loads". Journal of the Structural Division ASCE, 95 (ST 12).

**Kitajima, K., Koizumi, T., Akiyama, H., Kanda, M., Nakanishi, M. and Adachi, H.** (1992) "Response Characteristics of Reinforced Concrete Columns under Bi-directional Earthquake Motions", Proceedings of the tenth World Conference on Earthquake Engineering, Madrid, Spain, pp 3019-3024.

**Kitajima, K., Adachi, H. and Nakanishi, M.** (1996) "Response Characteristics of Reinforced Concrete Structures under Bi-directional Earthquake Motions", Proceedings of the 11<sup>th</sup> World Conference on Earthquake Engineering, Mexico, Mexico, Paper No. 566.

**Kogoma, I., Hayashida, T. and Minowa, C.** (1992) "Experimental Studies on the Collapse of RC Columns during Strong earthquake Motions", Proceedings of the tenth World Conference on Earthquake Engineering, Madrid, Spain, pp 3013-3017.

**Kowalsky, M., Priestley, M.J.N., Seible, F.** (2000) "Dynamic Behavior of Lightweight Concrete Bridges", ACI Structural Journal, V97, No.4, 602 – 618.

**Kulkarni, S.M. and Shah, S.P.** (1998). "Response of Reinforced Concrete Beams at High Strain Rates." ACI Structural Journal. Vol. 95 No.6, pp 705-715.

**Kuramoto, H., Kabeyasawa, T. and Shen, F. H.** (1995) "Influence of Axial Deformation on ductility of High-Strength Reinforced Concrete Columns under Varying Triaxial Forces", ACI Structural Journal, V92, No.5, 610 – 618.

**Laplace, P., Sanders, D.H., and Saiidi, M.S.** (1999). "Shake Table Testing of Flexure Dominated Reinforced Concrete Bridge Columns." Report No. CCEER-99-13, Center for Civil Engineering Earthquake Research, Department of Civil Engineering, University of Nevada-Reno, USA, 438 pp.

**Laplace, P., Sanders, D.H., and Saiidi, M.S.** (1999). "Experimental Study and Analysis of Retrofitted Flexure and Shear Dominated Circular Reinforced Concrete Bridge Columns Subjected to Shake Table Excitation." Report No. CCEER-01-6, Center for Civil Engineering Earthquake Research, Department of Civil Engineering, University of Nevada-Reno, USA, 438 pp.

**Lehman, D.E. and Moehle, J.P.** (1998) "Seismic Performance of Well-Confined Concrete Bridge Columns". Report PEER1998/01, Pacific Earthquake Engineering Research Center, University of California, Berkeley, California, USA.

**Li, K. N, Aoyama, H. and Otani, S.** (1988) "Reinforced Concrete Columns Under Varying Axial Load and Bi-directional Lateral load Reversals", Proceedings of Ninth World Conference on Earthquake Engineering, Tokyo, Japan, Vol. VIII, SF-5, 537-542.

**Li, Y. and Mau, S.T.** (1990). "A Computer Program for Multiple Input – Multiple Output System identification Using Building Records." Research report UHCEE 90-07, Department of Civil and Environmental Engineering, University of Houston.

- Li, Y. and Mau, S.T.** (1991). "A Case of study of MIMO System Identification Applied to Building Seismic Records. Earthquake Engineering and Structural Dynamics, Vol 20, pp 1045-1064.
- Low, S. S. and Moehle, J. P.** (1987) "Experimental Study of Reinforced Concrete Columns subjected to Multi-axial Cyclic Loadings", Earthquake Engineering Research Center, Report UCB/EERC-87/14, University of California, Berkeley.
- MacRae, G. A., Hodge, C., Priestley, M.J.N. and Seible, F.** (1994) "Shake Table Tests of As-built and Retrofitted Configuration, Route 5/405 Separation", Structural System Research, Report SSRP-94/18, University of California, San Diego.
- Mahin, S. and Sakai, J.** (2004). "Re-centering RC Columns". Earthquake Engineering Research Center, University of California, Berkeley, California, USA.  
<http://library.eerc.berkeley.edu/archives/sakai/ucb2.html>.
- Mander J.B., Priestley, M.J.N. and Park, R.** (1988). "Theoretical Stress-Strain Model for Confined Concrete." Journal of Structural Eng. 114 (8), pp 1804-1826.
- Maruyama, K., Ramirez, H. and Jirsa, J. O.** (1984) "Short RC Columns under Bilateral Load Histories", Journal of Structural Engineering, V110, No.1, 120 -137.
- Matsumoto, E., Okstad, E., Kawashima, K. and Mahin, S.** (2010) "Seismic Performance of rectangular Columns and Interlocking Spiral Columns" Proceedings of 14<sup>th</sup> World Conference on Earthquake Engineering, Beijing, China.
- Mazzoni, S., McKenna, F., Scott, M., and Fenves, G.L.** (2006). "Open System for Earthquake Engineering Simulation (OpenSees)." User manual, version 1.7.3, Pacific Earthquake Engineering Research Center, University of California, Berkeley, California, USA.  
<http://opensees.berkeley.edu/OpenSees/manuals/usermanual/index.html>.
- Mizugami, Y.** (2000). "Efficiency of Lateral Reinforcement in Interlocking Spirals Rebar". Proceedings of the 16<sup>th</sup> US-Japan Bridge Engineering Workshop, Lake Tahoe, Nevada, USA, pp 289-299.
- Mullapudi, T.R., Ayoub, S. and Belarbi, A.** (2008). "Effect of Coupled Shear-Bending Deformations on the Behavior of RC Highway Structures Subjected to Extreme Seismic Loading." Proceedings of the 6<sup>th</sup> National Seismic Conference on Bridges & Highways, Paper No. P19, Charleston, South Carolina, USA.
- Mostafa, K.F.M., Sanders, D.H., and Saiidi, M.S.** (2004). "Impact of Aspect Ratio on Two-Column Bent Seismic Performance." Report No. CCEER-04-04, Center for Civil Engineering Earthquake Research, Department of Civil Engineering, University of Nevada-Reno, USA.
- Nguyen, X.H. and Irawan, P.** (2003). "Experimental Study on Shear Capacity of RC Short Columns under Multi-directional Loading." Proceedings of the FIB Symposium on Concrete structures in Seismic regions, Athens, Greece.

- Nishida, H. and Unjoh, S.** (2004) "Dynamic Response Characteristic of Reinforced Concrete Column Subjected to Bilateral Earthquake Ground Motions", Proceedings of the 13<sup>th</sup> World Conference on Earthquake Engineering, Vancouver, Canada, Paper No. 576.
- Oani, S., Cheung, V. W. and Lai, S. S.** (1980) "Reinforced Concrete Columns Subjected to Biaxial Lateral Load Reversals", Proceedings of the Seventh World Conference on Earthquake Engineering, Istanbul, Turkey, Vol. 6, 525 - 532.
- Ogawa, J., Shibuya, J. and Hoshi, M.** (1992) "Earthquake Damage Evaluation of RC Columns" Proceedings of Tenth World Conference on Earthquake Engineering, Madrid, Spain, Vol. V, 3053-3058.
- Otsuka, H., Takeshita, E., Yabuki, W., Wang, Y., Yoshimura, T. and Tsunomoto, M.** (2004). "Study on the Seismic Performance of Reinforced Concrete Columns subjected to Torsional Moment, Bending Moment and Axial Force" Proceedings of 13<sup>th</sup> World Conference on Earthquake Engineering, Vancouver, Canada, Paper No.393.
- Pacific Earthquake Engineering Research Center, Peer** (2000). "Strong Motion Database". University of California, California, USA.
- Pacific Earthquake Engineering Research Center, Peer** (2004). "Structural Performance Database". University of California, California, USA.
- Park, S.W., Yen, W.P., Cooper, J.D., Unjoh, S., Terayana, T. and Otsuka, H.** (2003). "A Comparative Study of US-Japan Seismic Design of Highway Bridges: II. Shake-Table Model Test" Earthquake Spectra, Vol. 19 No.4, pp 933-958.
- Phan, V.T., Saïidi, M.S. and Anderson, J.G.** (2005). "Near Fault (Near Field) Ground Motion Effects on reinforced Concrete Bridge Columns". Report No. CCEER-05-7, Center for Civil Engineering Earthquake Research, Department of Civil Engineering, University of Nevada-Reno, USA, 241 pp.
- Petrini, L., Maggi, C., Priestley, M.J.N. and Calvi, G.M.** (2008). "Experimental Verification of Viscous Damping Modeling for Inelastic Time History Analyzes" Journal of Earthquake Engineering, Vol. 12 No.1, pp 125-145.
- Popovic, S.** (1973). "A numerical Approach to the Complete Stress Strain Curve for Concrete". Cement and Concrete Research, 3(5), pp 583-599.
- Priestley, M.J.N., Calvi, G.M. and Kowalsky, M.J.** (2007). "Displacement-Based Seismic design of Structures". IUSS Press, Pavia, Italy.
- Qiu, F., Li, W., Pan, P. and Qian, J.** (2002). "Experimental Test on Reinforced Concrete Columns Under Biaxial Quasi-static Loading." Engineering Structures, Vol. 24, pp 419-428.
- Sakai, J., Jeong H. and Mahin, S.A.** (2006). "Reinforced Concrete Bridge Columns that Re-Center Following Earthquakes." Proceedings of the 8<sup>th</sup> U.S. National Conference on Earthquake Engineering, Paper No. 1421, San Francisco, California, USA.

**Sakai, J., and Unjoh, S.** (2006). "Earthquake Simulation Test of Circular Reinforced Concrete Bridge Columns under Multidirectional Seismic Excitations." *Earthquake Engineering and Engineering Vibrations*, Vol. 5, No. 1, pp 103-110.

**Saatcioglu, M. and Ozebe, G.** (1989) "Response of Reinforced Concrete Columns to Simulated Seismic Loading", *ACI Structural Journal*, V86, No.1, 3 – 12.

**Scott, B.D., Park, R. and Priestley, M.J.N.** (1982). "Stress-strain Behavior of Concrete Confined by Overlapping Hoops at Low and High Strain Rates". *Journal of the American Concrete Institute*, Vol. 79, No.1, pp 13 – 27.

**Scott, M.H. and Fenves, G.L.** (2006). "Plastic Hinge Integration Methods for Force-based Beam Column Elements". *ASCE Journal of Structural Engineering*, Vol. 132 No. 2, pp 244 – 252.

**Shiyng, W and Zhenchang, L.** (1990). "A Study on the Sudden-Crack-Change of R/C Columns under Dynamic Vibration – Strength and Deformation." *Proceedings of the 4<sup>th</sup> U.S. National Conference on Earthquake Engineering*, Palm Springs, California, USA, pp 717-725.

**Takashi, N., Igarashi, K., Maruta, M., Takahashi, M., Nakashima, T. and Suzuki, N.** (1996) "Shaking Table tests of Reinforced Concrete Structures under Bidirectional Earthquake Motions", *Proceedings of the 11<sup>th</sup> World Conference on Earthquake Engineering*, Mexico, Mexico, Paper No. 1001.

**Takiguchi, K., Kokusho, S., Kobayashi, K. and Kimura, M.** (1980) "Response of RC Columns to Horizontal Bi-directional Deflection History", *Proceedings of the Seventh World Conference on Earthquake Engineering*, Istanbul, Turkey, Vol. 6, 403 - 410.

**Tanaka, H. and Park, R.** (1993) "Seismic Design and Behavior of Reinforced Concrete Columns with Interlocking Spirals", *ACI Structural Journal*, V9, No.2, 192 – 203.

**Taucer, F., Spacone, E and Filippou, F.C.** (1991). "A Fiber Beam-Column Element for the Seismic Response Analysis of Reinforced Concrete Structures". Report UCB/EERC-91/17, *Earthquake Engineering Research Center*, University of California, Berkeley, California, USA.

**Tirasit, P., Kawashima, K. and Watanabe, G.** (2006) "Effect of Combined Cyclic Flexural-Torsional Loading on the Seismic Performance of RC Columns", *Proceedings of 8<sup>th</sup> US National Conference on Earthquake Engineering*, San Francisco, USA, Paper No.431.

**Tokyo Institute of Technology.** "Kawashima Earthquake Engineering Laboratory". <http://seismic.cv.titech.ac.jp/>

**Tomazevic, M. and Velechovsky, T.** (1992). "Some Aspects of Testing Small-Scale Masonry Building Models on Simple Earthquake Simulators". *Earthquake Engineering and Structural Dynamics*, Vol 21, pp 945-963.

**Tsitotas, M.A., Tegos, I.A.** (1996) "Seismic Behavior of R/C Columns and Beams with Interlocking Spirals", *Proceedings of Advances in Earthquake Engineering: Earthquake Resistant Engineering Structures*, Greece, Vol. 2, 449 - 461.



**Umehara, H. and Jirsa, J.O.** (1984). "Short Rectangular RC Columns under Bidirectional Loadings", *Journal of Structural Engineering*, V110, No.3, 605 - 618.

**Wehbe, N.I., Saiidi, M.S. and Sanders, D.H.** (1998). "Effects of Confinement and Flares on the Seismic Performance of reinforced Concrete Bridge Columns". Report No. CCEER-97-2, Center for Civil Engineering Earthquake Research, Department of Civil Engineering, University of Nevada-Reno, USA, 407 pp.

**Wong, Y.L., Paulay, T and Priestley, M.J.N.** (1993) "Response of Circular RC Columns to Multi-Directional Seismic Attacks", *ACI Structural Journal*, V90, No.2, 180 – 191.

**Yoshimura, M. and Tsumura, K.** (1996). "Deformation Interaction of RC Columns Subjected to Two-dimensional Lateral Loading ". *Proceedings of the 12<sup>th</sup> World Conference on Earthquake Engineering*, Mexico, Mexico.

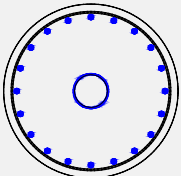
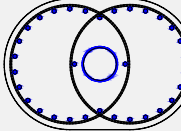
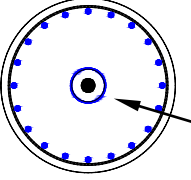
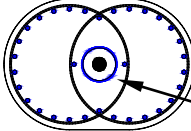
**You, Y.M. and Belarbi, A.** (2008). "An Analytical Model for RC Columns Subjected to Combined Loading Including Torsion". *Proceedings of the 14<sup>th</sup> World Conference on Earthquake Engineering*, Beijing, China.

**Zadeh, M.S. and Saiidi, M.S.** (2007). "Effects of Strain Rate on Stress-Strain Properties and Yield Propagation in Steel Reinforcing Bars". Report No. CCEER-07-2, Center for Civil Engineering Earthquake Research, Department of Civil Engineering, University of Nevada-Reno, USA, 70 pp.

**Zahn, F.A, Park, R. and Priestley, M.J.N.** (1989) "Strength and Ductility of Square Reinforced Concrete Sections Subjected to Biaxial Bending", *ACI Structural Journal*, V56, No.2, 123 – 130.

**Zhang, J. and Xu, S.Y.** (2008) "Seismic Response Simulations of Bridges Considering Shear-Flexural Interaction of Columns. " *Proceedings of the 6<sup>th</sup> National Seismic Conference on Bridges & Highways*, Paper No. P29, Charleston, South Carolina, USA.

**Table 1-1 Experimental Test Program at University of Nevada, Reno**

Test	Shape Diameter (in)	Dimensions (in)	Scale	Ht (in)	Biaxial Bending	Mass Distribution on BMR (Torsion)	Axial and P-delta effects
Phase I	 <p><math>\rho_l=2\%</math> <math>\rho_v=0.95\%</math></p>	16	1:3	72	✓	Symmetric	Not included
		16	1:3	72	✓	Asymmetric	Not included
	 <p><math>\rho_l=2\%</math> <math>\rho_v=1.1\%</math></p>	12x17.5	1:4	72	✓	Symmetric	Not included
		12x17.5	1:4	72	✓	Asymmetric	Not included
Phase II	 <p><math>\rho_l=2\%</math> <math>\rho_v=0.95\%</math> Tendon</p>	16	1:3	72	✓	Symmetric	Included
		16	1:3	72	✓	Asymmetric	Included
	 <p><math>\rho_l=2\%</math> <math>\rho_v=1.1\%</math> Tendon</p>	12x17.5	1:4	72	✓	Symmetric	Included
		12x17.5	1:4	72	✓	Asymmetric	Included

**Table 2-1 Similitude Requirements and Scaling Factors**

Quantity	General equation	Scales factor used
Length	$S_L=L_p/L_M$	$S_L$
Stress	$S_\sigma=\sigma_p/\sigma_M$	1.0
Strain	$S_\varepsilon=\varepsilon_p/\varepsilon_M$	1.0
Modulus of Elasticity	$S_E=S_\sigma/S_\varepsilon$	1.0
Acceleration	$S_A=A_p/A_M$	1.0
Mass Density	$S_\rho=S_E/S_A S_L$	$1/S_L$
Mass	$S_m=S_\rho S_L^3$	$S_L^2$
Force	$S_F=S_\sigma S_L^2$	$S_L^2$
Time	$S_t=S_L(S_\rho/S_E)^{1/2}$	$S_L^{1/2}$
Frequency	$S_w=1/S_t$	$S_L^{-1/2}$
Displacement	$S_d=L_d/L_d$	$S_L$
Velocity	$S_v=S_\varepsilon(S_\sigma/S_\rho)^{1/2}$	$S_L^{1/2}$
Moment	$S_M=S_F S_L$	$S_L^3$
Energy	$S_M=S_F S_L$	$S_L^3$

**Table 2-2 Steel Properties Used for Preliminary Moment-Curvature Analysis (Xtract)**

Steel Properties	¼" Spiral (W5.0)	Spiral (W2.9)	#3 bar	#4 bar
Yield Stress (ksi)	57.64	65	63	65
Yield Strain	0.0024	0.0022	0.0022	0.0022
Strain at hardening	Without plateau	Without plateau	0.008	0.008
Peak Stress (ksi)	70.9	77	99	104.3
Strain at Peak	0.114	Not measured	0.12	0.11
Fracture Strain	0.17	Not measured	0.16	0.19
Fracture Stress (ksi)	40.6	Not measured	94	86.7

**Table 2-3 Stress-Strain Properties Used for Preliminary Moment-Curvature Analysis  
(Xtract)**

Material	Properties	Circular Specimens	Interlocking Specimens
Unconfined Concrete	$f'_c$ (ksi)	4.5	4.5
	$\epsilon_o$	0.002	0.002
	$\epsilon_{cu}$	0.004	0.004
	$\epsilon_{ps}$	0.006	0.006
Confined Concrete	Ke	1.0	0.9
	$f'_{cc}$ (ksi)	6.2	6.02
	$\epsilon_{cc}$	0.0057	0.0054
	$f_{cu}$ (ksi)	5.05	4.76
	$\epsilon_{cu}$	0.0183	0.0186
	x	3.2	3.46
	r	1.39	1.41
Steel Bars	$f_y$ (ksi)	63	63
	$E_s$ (ksi)	29000	29000
	$\epsilon_y$	0.0022	0.0022
	$\epsilon_{sh}$	0.008	0.008
	$f_{su}$ (ksi)	104	99
	$\epsilon_{su}$	0.11	0.16
Steel Spirals	$f_y$ (ksi)	60	65
	$\epsilon_y$	0.0024	0.0022

**Table 2-4 Idealized Moment-Curvature Results, P=0 kips**

Parameter	Specimens								
	Circular		Interlocking						
N.A angle	0°	45°	0°	15°	30°	45°	60°	75°	90°
$M_y$ [kip-in]	1467	1463	1065	1078	1186	1313	1420	1484	1508
$M_u$ [kip-in]	1889	1896	1406	1389	1484	1678	1824	1928	1968
$\phi_y$ [rad/in]	0.00032	0.00032	0.00038	0.00037	0.00034	0.00032	0.00031	0.00029	0.00028
$\phi_u$ [rad/in]	0.0058	0.0057	0.01073	0.00778	0.00637	0.00620	0.00593	0.00585	0.00588
$\mu_\phi$	18.12	17.84	28.24	21.03	18.74	19.38	19.13	20.17	21.00

**Table 2-5 Idealized Moment-Curvature Results, P=80 kips**

Parameter	Specimens								
	Circular		Interlocking						
N.A angle	0°	45°	0°	15°	30°	45°	60°	75°	90°
$M_y$ [kip-in]	1787	1789	1311	1351	1476	1636	1769	1857	1891
$M_u$ [k-in]	2105	2075	1561	1565	1691	1883	2063	2182	2220
$\phi_y$ [rad/in]	0.00032	0.00032	0.00039	0.00038	0.00035	0.00033	0.00031	0.00029	0.00029
$\phi_u$ [rad/in]	0.00489	0.00464	0.00787	0.00624	0.00533	0.00495	0.00479	0.00477	0.00477
$\mu_\phi$	15.06	14.5	20.18	16.42	15.23	15.00	15.45	16.45	16.45

**Table 2-6 Force-Displacement Predictions, P=0 kips**

Parameter	Specimens								
	Circular		Interlocking						
N.A angle	0°	45°	0°	15°	30°	45°	60°	75°	90°
$F_y$ [kips]	20.38	20.32	14.79	14.97	16.47	18.24	19.72	20.61	20.94
$F_u$ [kips]	26.24	26.33	19.53	19.29	20.61	23.31	25.33	26.78	27.33
$\Delta_y$ [rad/in]	0.63	0.61	0.73	0.71	0.65	0.61	0.59	0.55	0.53
$\Delta_p$ [rad/in]	3.85	3.84	6.56	4.70	3.82	3.73	3.56	3.52	3.55
$\Delta_u$ [rad/in]	4.48	4.45	7.28	5.40	4.47	4.34	4.15	4.08	4.08
$\mu_\Delta$	7.15	7.32	10.05	7.65	6.89	7.10	7.02	7.37	7.64

**Table 2-7 Force-Displacement Predictions, P=80 kips**

Parameter	Specimens								
	Circular		Interlocking						
N.A angle	0°	45°	0°	15°	30°	45°	60°	75°	90°
$F_y$ [kips]	24.82	24.85	18.21	18.76	20.50	22.72	24.57	25.79	26.26
$F_u$ [kips]	29.24	28.82	21.68	21.74	23.49	26.15	28.65	30.31	30.83
$\Delta_y$ [rad/in]	0.64	0.63	0.77	0.75	0.69	0.65	0.61	0.57	0.57
$\Delta_p$ [rad/in]	3.2	3.14	5.30	4.16	3.53	3.28	3.18	3.18	3.18
$\Delta_u$ [rad/in]	3.83	3.77	6.07	4.90	4.22	3.93	3.79	3.75	3.75
$\mu_\Delta$	6.02	6.01	7.90	6.55	6.12	6.04	6.20	6.56	6.56

**Table 2-8 Torque-twist Predictions, Circular Specimen P=0 kips**

$\epsilon_d$	-0.00035	-0.00050	-0.00075	-0.00100	-0.00125	-0.00150	-0.00180
$\sigma_l$ [ksi]	0.0000	0.0000	0.0000	0.0000	0.0000	0.0000	0.0000
$\sigma_t$ [ksi]	0.0000	0.0000	0.0000	0.0000	0.0000	0.0000	0.0000
$\epsilon_r$	0.00206	0.00292	0.00427	0.00582	0.00677	0.00756	0.00842
$\zeta$	0.771	0.708	0.633	0.571	0.541	0.519	0.499
$\epsilon_d/\zeta\epsilon_0$	0.227	0.353	0.593	0.876	1.155	1.444	1.805
$\sigma_r$ [ksi]	0.1274	0.0921	0.0550	0.0306	0.0213	0.0158	0.0114
$\sigma_d$ [ksi]	-1.396	-1.853	-2.375	-2.530	-2.433	-2.327	-2.214
$t_d$ [in]	2.19	2.22	2.29	2.34	2.52	2.69	2.87
$A_0$ [in <sup>2</sup> ]	151	150	149	148	144	141	137
$p_0$ [in]	41.5	41.4	41.1	40.9	40.2	39.5	38.8
$\epsilon_l$	0.00062	0.00086	0.00117	0.00136	0.00141	0.00144	0.00145
$\epsilon_t$	0.00110	0.00156	0.00235	0.00346	0.00411	0.00463	0.00517
$\alpha$ [rad]	0.685	0.682	0.667	0.628	0.614	0.606	0.599
$\tau_{tl}$	0.6842	0.9064	1.1543	1.2032	1.1459	1.0888	1.0310
$T$ [k-in]	452.60	604.30	785.71	832.01	832.10	824.37	812.35
$\delta_{tl}$	0.00237	0.00334	0.00488	0.00649	0.00755	0.00848	0.00951
$\theta$ [rad/in]	0.00033	0.00046	0.00067	0.00090	0.00105	0.00119	0.00135
$\theta$ [Deg]	1.34	1.90	2.78	3.71	4.35	4.91	5.55
$f_l$ [ksi]	17.89	24.82	33.99	39.37	40.97	41.66	41.97
$f_t$ [ksi]	31.80	45.25	60.00	60.00	60.00	60.00	60.00

**Table 2-9 Torque-twist Predictions, Circular Specimen P=80 kips**

$\epsilon_d$	-0.00035	-0.00050	-0.00075	-0.00100	-0.00125	-0.00150	-0.00180
$\sigma_r$ [ksi]	-0.3979	-0.3979	-0.3979	-0.3979	-0.3979	-0.3979	-0.3979
$\sigma_t$ [ksi]	0	0	0	0	0	0	0
$\epsilon_r$	0.00181	0.00268	0.00404	0.00560	0.00655	0.00733	0.00816
$\zeta$	0.793	0.724	0.644	0.579	0.548	0.525	0.504
$\epsilon_d/\zeta\epsilon_0$	0.221	0.346	0.582	0.864	1.141	1.427	1.784
$\sigma_r$ [ksi]	0.1401	0.1006	0.0602	0.0332	0.0232	0.0173	0.0126
$\sigma_d$ [ksi]	-1.401	-1.861	-2.393	-2.556	-2.463	-2.355	-2.241
$t_d$ [in]	2.55	2.45	2.45	2.48	2.67	2.85	3.04
$A_0$ [in <sup>2</sup> ]	144	145	145	145	141	138	134
$p_0$ [in]	40.1	40.5	40.4	40.3	39.6	38.9	38.1
$\epsilon_l$	0.00041	0.00065	0.00096	0.00114	0.00118	0.00118	0.00117
$\epsilon_t$	0.00105	0.00154	0.00233	0.00346	0.00412	0.00465	0.00519
$\alpha$ [rad]	0.634	0.644	0.640	0.605	0.592	0.584	0.577
$\tau_{tl}$	0.6686	0.8935	1.1463	1.1961	1.1402	1.0828	1.0249
$T$ [k-in]	488.86	637.07	818.04	860.21	858.24	848.15	833.68
$\delta_{tl}$	0.00206	0.00306	0.00459	0.00618	0.00722	0.00812	0.00911
$\theta$ [rad/in]	0.00029	0.00043	0.00064	0.00086	0.00101	0.00115	0.00130
$\theta$ [Deg]	1.19	1.75	2.63	3.55	4.18	4.73	5.35
$f_l$ [ksi]	11.82	18.76	27.79	33.03	34.10	34.21	33.89
$f_t$ [ksi]	30.57	44.56	60.00	60.00	60.00	60.00	60.00



**Table 2-10 Torque-twist Predictions, Interlocking Specimen P=0 kips**

$\epsilon_d$	-0.00035	-0.00050	-0.00075	-0.00100	-0.00125	-0.00150	-0.00180
$\sigma_l$ [ksi]	0.0000	0.0000	0.0000	0.0000	0.0000	0.0000	0.0000
$\sigma_t$ [ksi]	0	0	0	0	0	0	0
$\epsilon_r$	0.00213	0.00301	0.00447	0.00606	0.00702	0.00783	0.00870
$\zeta$	0.766	0.702	0.624	0.563	0.534	0.512	0.492
$\epsilon_d/\zeta\epsilon_0$	0.229	0.356	0.601	0.888	1.171	1.464	1.829
$\sigma_r$ [ksi]	0.1242	0.0891	0.0510	0.0280	0.0194	0.0143	0.0102
$\sigma_d$ [ksi]	-1.395	-1.849	-2.361	-2.502	-2.401	-2.295	-2.185
$t_d$ [in]	1.94	1.97	2.01	2.07	2.23	2.38	2.54
$A_0$ [in <sup>2</sup> ]	136	135	134	133	130	127	124
$p_0$ [in]	40.9	40.8	40.7	40.4	39.8	39.2	38.5
$\epsilon_l$	0.00065	0.00090	0.00123	0.00143	0.00148	0.00151	0.00152
$\epsilon_t$	0.00113	0.00160	0.00249	0.00363	0.00429	0.00482	0.00538
$\alpha$ [rad]	0.688	0.685	0.664	0.626	0.613	0.604	0.598
$\tau_{tl}$	0.6844	0.9059	1.1457	1.1884	1.1295	1.0731	1.0161
$T$ [k-in]	360.53	481.29	618.37	653.65	653.47	647.82	638.83
$\delta_{tl}$	0.00243	0.00343	0.00507	0.00670	0.00778	0.00872	0.00977
$\theta$ [rad/in]	0.00037	0.00052	0.00077	0.00102	0.00119	0.00135	0.00152
$\theta$ [Deg]	1.51	2.14	3.17	4.20	4.92	5.56	6.28
$f_l$ [ksi]	18.85	26.14	35.79	41.34	43.01	43.81	44.22
$f_t$ [ksi]	32.74	46.51	60.00	60.00	60.00	60.00	60.00

**Table 2-11 Torque-twist Predictions, Interlocking Specimen P=80 kips**

$\epsilon_d$	-0.00035	-0.00050	-0.00075	-0.00100	-0.00125	-0.00150	-0.00180
$\sigma_l$ [ksi]	-0.4467	-0.4467	-0.4467	-0.4467	-0.4467	-0.4467	-0.4467
$\sigma_t$ [ksi]	0	0	0	0	0	0	0
$\epsilon_r$	0.00183	0.00273	0.00419	0.00580	0.00675	0.00755	0.00840
$\zeta$	0.792	0.720	0.637	0.572	0.542	0.520	0.499
$\epsilon_d/\zeta\epsilon_0$	0.221	0.347	0.589	0.874	1.154	1.443	1.804
$\sigma_r$ [ksi]	0.1392	0.0989	0.0568	0.0309	0.0215	0.0159	0.0115
$\sigma_d$ [ksi]	-1.401	-1.860	-2.381	-2.533	-2.435	-2.328	-2.216
$t_d$ [in]	2.31	2.20	2.18	2.21	2.38	2.54	2.71
$A_0$ [in <sup>2</sup> ]	128	130	131	130	127	124	120
$p_0$ [in]	39.5	39.9	40.0	39.9	39.2	38.5	37.9
$\epsilon_l$	0.00040	0.00065	0.00098	0.00117	0.00120	0.00121	0.00119
$\epsilon_t$	0.00108	0.00157	0.00246	0.00363	0.00430	0.00484	0.00540
$\alpha$ [rad]	0.628	0.641	0.634	0.600	0.587	0.579	0.573
$\tau_{tl}$	0.6660	0.8912	1.1363	1.1804	1.1228	1.0662	1.0092
$T$ [k-in]	394.25	511.61	647.83	679.45	677.45	669.71	658.56
$\delta_{tl}$	0.00207	0.00309	0.00472	0.00634	0.00738	0.00829	0.00929
$\theta$ [rad/in]	0.00032	0.00047	0.00072	0.00097	0.00114	0.00129	0.00146
$\theta$ [rad]	1.32	1.95	2.97	4.00	4.70	5.32	6.02
$f_l$ [ksi]	11.67	18.98	28.51	33.87	34.89	34.99	34.65
$f_t$ [ksi]	31.24	45.66	60.00	60.00	60.00	60.00	60.00

**Table 3-1 Steel Properties for the Specimens**

<b>Steel Properties</b>	<b>No.3 bar</b>	<b>No.4 bars</b>	<b>Spiral (W5.0)</b>	<b>Spiral (W2.9)</b>
Yield Stress (ksi)	61.4	65	58	58
Yield Strain	0.0022	0.0023	0.0024	0.0024
Strain at hardening	0.012	0.0075	Without plateau	Without plateau
Peak Stress (ksi)	94.74	103.30	78.50	78.50
Strain at Peak	0.1240	0.1146	0.1260	0.1153
Fracture Strain	81.41	99.66	70.26	78.00
Fracture Stress (ksi)	0.1952	0.1507	0.1378	0.1536

**Table 3-2 Concrete Cylinder Test Results for Footings**

<b>Day</b>	<b>C1 (psi)</b>	<b>C2 (psi)</b>	<b>I1 (psi)</b>	<b>I2 (psi)</b>
7	4140		2645	
14	4244		4053	
28	4818		5184	
279 Test (C1)	5700	-	-	-
313 Test (C2)		5967	-	-
213 Test (I1)			6142	-
249 Test (I2)				6172
Test Average	5834		6157	

**Table 3-3 Concrete Cylinder Test Results for Columns**

<b>Day</b>	<b>C1 (psi)</b>	<b>C2 (psi)</b>	<b>I1 (psi)</b>	<b>I2 (psi)</b>
7	2914		1570	
14	3607		2598	
28	4041		3918	
279 Test (C1)	4651	-	-	-
313 Test (C2)		4661	-	-
213 Test (I1)			4419	-
249 Test (I2)				4442
Test Average	4656		4431	

**Table 4-1 Test Procedure, Specimen C1**

Run No	Times Petrolia	Max. acceleration (g)		Min. acceleration (g)	
		Long.	Trans.	Long.	Trans.
Tuning	-	-	-	-	-
1	0.1	0.066	0.059	-0.066	-0.059
2	0.2	0.132	0.117	-0.131	-0.118
3	0.4	0.265	0.234	-0.262	-0.236
4	0.6	0.397	0.351	-0.393	-0.354
5	0.8	0.530	0.469	-0.524	-0.472
6	1.0	0.662	0.586	-0.655	-0.590
7	1.2	0.795	0.700	-0.786	-0.707
8	1.4	0.927	0.820	-0.917	-0.827
9	1.6	1.059	0.938	-1.048	-0.944
10	1.8	1.192	1.055	-1.179	-1.062

**Table 4-2 Test Procedure, Specimen C2**

Run No	Times Petrolia	Max. acceleration (g)		Min. acceleration (g)	
		Long.	Trans.	Long.	Trans.
Tuning	-	-	-	-	-
1	0.1	0.074	0.055	-0.072	-0.047
2	0.2	0.141	0.094	-0.152	-0.090
3	0.4	0.274	0.184	-0.240	-0.186
4	0.6	0.435	0.283	-0.540	-0.299
5	0.8	0.568	0.427	-0.680	-0.405
6	1.0	0.674	0.553	-0.776	-0.509
7	1.2	0.782	0.689	-0.817	-0.626
8	1.4	0.878	0.849	-0.859	-0.734
9	1.6	0.954	0.989	-0.906	-0.841
10	1.8	1.068	1.137	-0.960	-0.941
11	2.0	1.345	1.353	-1.100	-1.053

Table 4-3 Target and Achieved Peak Table Accelerations for Specimen C1

Run No	Times Petrolia		Longitudinal Direction			Transverse Direction		
			Target (g)	Achieved (g)	Achieved/Target	Target (g)	Achieved (g)	Achieved/Target
1	0.1	Max	0.07	0.11	1.59	0.06	0.05	0.85
		Min	-0.07	-0.09	1.32	-0.06	-0.05	0.83
2	0.2	Max	0.13	0.19	1.44	0.12	0.11	0.91
		Min	-0.13	-0.18	1.41	-0.12	-0.10	0.88
3	0.4	Max	0.26	0.36	1.37	0.23	0.26	1.09
		Min	-0.26	-0.44	1.69	-0.24	-0.24	1.01
4	0.6	Max	0.40	0.45	1.14	0.35	0.34	0.96
		Min	-0.39	-0.59	1.50	-0.35	-0.38	1.08
5	0.8	Max	0.53	0.59	1.11	0.47	0.47	0.99
		Min	-0.52	-0.67	1.27	-0.47	-0.46	0.97
6	1.0	Max	0.66	0.69	1.05	0.59	0.61	1.04
		Min	-0.65	-0.74	1.12	-0.59	-0.57	0.97
7	1.2	Max	0.79	0.81	1.01	0.70	0.75	1.07
		Min	-0.79	-0.81	1.03	-0.71	-0.66	0.93
8	1.4	Max	0.93	0.89	0.96	0.82	0.86	1.05
		Min	-0.92	-0.87	0.95	-0.83	-0.76	0.92
9	1.6	Max	1.06	0.98	0.93	0.94	1.04	1.11
		Min	-1.05	-0.94	0.90	-0.94	-0.88	0.93
10	1.8	Max	1.19	1.10	0.92	1.05	1.18	1.11
		Min	-1.18	-0.99	0.84	-1.06	-0.96	0.91
<b>Average</b>					<b>1.18</b>			<b>0.98</b>

Table 4-4 Target and Achieved Peak Table Accelerations for Specimen C2

Run No	Times Petrolia		Longitudinal Direction			Transverse Direction		
			Target (g)	Achieved (g)	Achieved/Target	Target (g)	Achieved (g)	Achieved/Target
1	0.1	Max	0.07	0.07	1.11	0.06	0.05	0.93
		Min	-0.07	-0.07	1.10	-0.06	-0.05	0.79
2	0.2	Max	0.13	0.14	1.06	0.12	0.09	0.81
		Min	-0.13	-0.15	1.16	-0.12	-0.09	0.76
3	0.4	Max	0.26	0.27	1.04	0.23	0.18	0.78
		Min	-0.26	-0.24	0.92	-0.24	-0.19	0.79
4	0.6	Max	0.40	0.43	1.09	0.35	0.28	0.80
		Min	-0.39	-0.54	1.37	-0.35	-0.30	0.84
5	0.8	Max	0.53	0.57	1.07	0.47	0.43	0.91
		Min	-0.52	-0.68	1.30	-0.47	-0.41	0.86
6	1.0	Max	0.66	0.67	1.02	0.59	0.55	0.94
		Min	-0.65	-0.78	1.19	-0.59	-0.51	0.86
7	1.2	Max	0.79	0.78	0.98	0.70	0.69	0.98
		Min	-0.79	-0.82	1.04	-0.71	-0.63	0.88
8	1.4	Max	0.93	0.88	0.95	0.82	0.85	1.03
		Min	-0.92	-0.86	0.94	-0.83	-0.73	0.89
9	1.6	Max	1.06	0.95	0.90	0.94	0.99	1.05
		Min	-1.05	-0.91	0.86	-0.94	-0.84	0.89
10	1.8	Max	1.19	1.07	0.90	1.05	1.14	1.08
		Min	-1.18	-0.96	0.81	-1.06	-0.94	0.89
11	2.0	Max	1.32	1.34	1.01	1.17	1.35	1.15
		Min	-1.31	-1.10	0.84	-1.18	-1.05	0.89
<b>Average</b>					<b>1.03</b>			<b>0.90</b>

**Table 4-5 Spectral Response at Structural Period, Specimen C1**

Run	Times Petrolia	Longitudinal Direction (Achieved/Target)				Transverse Direction (Achieved/Target)			
		Period (s)	Acceleration	Velocity	Displacement	Period (s)	Acceleration	Velocity	Displacement
1	0.1	0.59	1.14	1.27	1.14	0.57	0.84	0.99	0.84
2	0.2	0.62	1.30	1.33	1.30	0.59	0.80	0.82	0.80
3	0.4	0.67	1.21	1.26	1.21	0.67	1.16	1.15	1.16
4	0.6	0.76	1.02	1.06	1.02	0.73	0.66	0.83	0.66
5	0.8	0.76	0.97	1.00	0.97	0.76	0.85	0.97	0.85
6	1.0	0.84	0.78	0.98	0.78	0.80	0.78	0.98	0.78
7	1.2	0.89	0.81	0.96	0.81	0.89	0.91	0.97	0.91
8	1.4	1.00	0.89	0.94	0.89	0.94	0.89	0.95	0.89
9	1.6	1.00	0.89	0.93	0.89	1.00	0.89	0.95	0.89
10	1.8	1.14	0.84	0.85	0.84	1.00	0.91	0.93	0.91
<b>Average</b>		-	<b>0.99</b>	<b>1.06</b>	<b>0.99</b>	-	<b>0.87</b>	<b>0.95</b>	<b>0.87</b>

**Table 4-6 Spectral Response at Structural Period, Specimen C2**

Run	Times Petrolia	Longitudinal Direction (Achieved/Target)				Transverse Direction (Achieved/Target)			
		Period (s)	Acceleration	Velocity	Displacement	Period (s)	Acceleration	Velocity	Displacement
1	0.1	0.62	0.80	0.76	0.80	0.59	0.53	0.53	0.53
2	0.2	0.64	0.94	0.94	0.94	0.62	0.66	0.67	0.66
3	0.4	0.64	0.90	0.89	0.90	0.64	0.78	0.79	0.78
4	0.6	0.70	0.92	0.95	0.92	0.70	0.60	0.81	0.60
5	0.8	0.76	0.97	0.99	0.97	0.73	0.67	0.77	0.67
6	1.0	0.80	0.88	0.96	0.88	0.73	0.74	0.78	0.74
7	1.2	0.89	0.79	0.94	0.79	0.84	0.81	0.92	0.81
8	1.4	0.94	0.87	0.93	0.87	0.94	0.88	0.90	0.88
9	1.6	0.94	0.88	0.92	0.88	0.94	0.89	0.91	0.89
10	1.8	1.07	0.84	0.85	0.84	1.07	0.93	0.94	0.93
11	2.0	1.14	0.82	0.83	0.82	1.14	0.81	0.83	0.81
<b>Average</b>		-	<b>0.87</b>	<b>0.90</b>	<b>0.87</b>	-	<b>0.77</b>	<b>0.81</b>	<b>0.77</b>



**Table 4-7 Observed Performance for Specimen C1**

Run	Times Petrolia	Longitudinal Direction			Transverse Direction			Performance
		PGA (g)	$\delta_L$ (%) <sup>1</sup>	$\mu_{dL}$ <sup>2</sup>	PGA (g)	$\delta_T$ (%)	$\mu_{dT}$	
1	0.1	0.066	0.43	0.33	0.059	0.29	0.35	Horizontal hairline cracks
2	0.2	0.132	0.70	0.53	0.117	0.48	0.58	First longitudinal bar yielding
3 - 5	0.4 - 0.8	0.265 - 0.530	1.7 - 2.9	1.3 - 2.28	0.234 - 0.469	1.01 - 1.5	1.23 - 1.85	Extension of horizontal cracks and first inclined
6	1.0	0.662	4.5	3.4	0.586	2.3	2.7	First concrete spalling
7	1.2	0.795	6.6	5.0	0.700	2.9	3.44	Extension of cracks and spalling
8	1.4	0.927	9.0	6.88	0.820	3.8	4.6	Spirals and longitudinal bars visible
9	1.6	1.059	11.7	8.96	0.938	5.1	6.13	Extension of cracks and spalling
10	1.8	1.192	14.6	11.2	1.055	7.0	8.5	Flexural failure: Longitudinal bar buckling and concrete degradation

<sup>1</sup> Drift ratio<sup>2</sup> Displacement ductility

Table 4-8 Observed Performance for Specimen C2

Run	Times Petrolia	Longitudinal Direction			Transverse Direction			Performance
		PGA (g)	$\delta_L$ (%) <sup>1</sup>	$\mu_{dL}$ <sup>2</sup>	PGA (g)	$\delta_T$ (%)	$\mu_{dT}$	
1	0.1	0.074	0.28	0.21	0.055	0.17	0.22	Horizontal hairline cracks
2	0.2	0.141	0.55	0.39	0.094	0.27	0.36	First longitudinal bar yielding
3 - 5	0.4 - 0.8	0.274 - 0.568	1.0 - 2.48	0.74 - 1.75	0.184 - 0.427	0.5 - 1.1	0.71 - 1.4	Extension of horizontal cracks and first inclined
6	1.0	0.674	3.8	2.74	0.553	1.7	2.3	First concrete spalling
7	1.2	0.782	5.7	4.04	0.689	2.5	3.23	Extension of cracks and spalling
8	1.4	0.878	7.9	5.7	0.849	3.3	4.34	Spirals and longitudinal bars visible
9 - 10	1.6 - 1.8	0.954 - 1.068	10 - 12.6	7.3 - 9.1	0.989 - 1.137	4.5 - 6.1	5.9 - 7.95	Extension of cracks and spalling; bar buckling
10	2.0	1.345	14.5	10.5	1.353	8.11	10.66	Flexural failure: reinforcement rupture (long. Bars and spirals); concrete degradation

<sup>1</sup> Drift ratio<sup>2</sup> Displacement ductility

**Table 4-9 Peak Force and Corresponding Displacement for Specimen C1**

Run No	Times Petrolia		Longitudinal Direction		Transverse Direction	
			Force (kips)	Displacement (in)	Force (kips)	Displacement (in)
1	0.1	Max	9.5	0.36	5.8	0.24
		Min	-12.2	-0.46	-6.0	-0.28
2	0.2	Max	15.6	0.58	9.3	0.40
		Min	-22.6	-1.01	-11.0	-0.58
3	0.4	Max	23.8	1.40	13.4	0.84
		Min	-28.0	-1.87	-13.4	-0.96
4	0.6	Max	22.0	1.52	11.3	0.84
		Min	-24.5	-1.74	-12.0	-0.83
5	0.8	Max	26.9	2.46	13.0	1.27
		Min	-20.1	-1.34	-11.6	-0.80
6	1.0	Max	29.5	3.71	14.9	1.87
		Min	-16.3	-0.43	-12.0	-0.62
7	1.2	Max	30.3	5.47	16.3	2.36
		Min	-16.4	-0.59	-11.1	-0.24
8	1.4	Max	30.8	7.45	17.1	3.15
		Min	-16.0	0.55	-11.0	-0.06
9	1.6	Max	31.1	9.70	17.3	4.21
		Min	-16.5	1.98	-11.3	1.52
10	1.8	Max	30.2	12.11	18.1	5.82
		Min	-17.9	3.55	-12.6	2.73

**Table 4-10 Peak Displacement and Corresponding Force for Specimen C1**

Run No	Times Petrolia		Longitudinal Direction		Transverse Direction	
			Force (kips)	Displacement (in)	Force (kips)	Displacement (in)
1	0.1	Max	7.4	0.39	5.8	0.24
		Min	-12.1	-0.46	-6.0	-0.28
2	0.2	Max	14.8	0.75	8.1	0.41
		Min	-22.6	-1.01	-11.0	-0.58
3	0.4	Max	23.8	1.40	13.4	0.84
		Min	-27.7	-1.89	-13.4	-0.96
4	0.6	Max	22.0	1.52	11.3	0.85
		Min	-24.4	-1.74	-11.9	-0.84
5	0.8	Max	26.8	2.47	13.0	1.27
		Min	-9.6	-1.49	-11.5	-0.81
6	1.0	Max	28.8	3.79	14.9	1.87
		Min	-15.6	-1.51	-11.8	-0.64
7	1.2	Max	29.5	5.62	15.9	2.60
		Min	-15.9	-0.73	-10.4	-0.40
8	1.4	Max	29.9	7.59	16.6	3.42
		Min	-8.8	0.46	-6.7	-0.11
9	1.6	Max	30.4	9.85	16.7	4.39
		Min	-10.8	1.20	-7.4	0.28
10	1.8	Max	29.3	12.36	18.1	5.82
		Min	-12.1	2.28	-7.5	1.14

**Table 4-11 Peak Force and Corresponding Displacement for Specimen C2**

Run No	Times Petrolia		Longitudinal Direction		Transverse Direction	
			Force (kips)	Displacement (in)	Force (kips)	Displacement (in)
1	0.1	Max	5.1	0.24	3.1	0.14
		Min	-6.8	-0.28	-3.2	-0.14
2	0.2	Max	11.7	0.45	5.5	0.23
		Min	-16.5	-0.71	-6.2	-0.30
3	0.4	Max	19.0	0.86	9.2	0.45
		Min	-25.6	-1.50	-10.4	-0.68
4	0.6	Max	23.5	1.29	10.6	0.65
		Min	-26.7	-2.05	-11.1	-0.84
5	0.8	Max	25.7	2.02	11.3	0.89
		Min	-21.4	-1.79	-11.1	-0.88
6	1.0	Max	29.1	3.16	13.6	1.43
		Min	-16.7	-0.85	-10.3	-0.64
7	1.2	Max	30.4	4.70	15.4	2.04
		Min	-16.9	-0.67	-10.7	-0.40
8	1.4	Max	31.3	6.52	16.3	2.74
		Min	-17.0	0.37	-10.4	-0.22
9	1.6	Max	31.7	8.44	16.8	3.71
		Min	-17.3	1.51	-11.2	0.78
10	1.8	Max	31.0	10.44	16.9	5.02
		Min	-18.5	2.96	-12.7	1.75
11	2.0	Max	27.4	12.04	13.7	6.73
		Min	-13.5	3.35	-12.7	3.71

**Table 4-12 Peak Displacement and Corresponding Force for Specimen C2**

Run No	Times Petrolia		Longitudinal Direction		Transverse Direction	
			Force (kips)	Displacement (in)	Force (kips)	Displacement (in)
1	0.1	Max	5.1	0.24	3.1	0.23
		Min	-6.8	-0.28	-3.1	-0.30
2	0.2	Max	10.9	0.47	5.5	0.45
		Min	-16.5	-0.71	-6.1	-0.69
3	0.4	Max	19.0	0.86	9.1	0.66
		Min	-24.7	-1.55	-10.1	-0.85
4	0.6	Max	23.2	1.31	10.4	0.92
		Min	-25.7	-2.13	-10.9	-0.89
5	0.8	Max	24.8	2.09	10.6	1.49
		Min	-25.7	-2.13	-10.9	-0.76
6	1.0	Max	27.2	3.39	12.9	2.16
		Min	-15.5	-1.37	-9.5	-0.46
7	1.2	Max	27.7	5.04	14.1	2.92
		Min	-16.4	-0.74	-9.7	-0.23
8	1.4	Max	28.4	6.92	15.2	3.84
		Min	-16.3	0.25	-10.4	0.23
9	1.6	Max	28.9	8.90	15.7	5.06
		Min	-16.9	1.45	-10.8	0.90
10	1.8	Max	28.1	11.17	16.3	6.83
		Min	-11.3	2.34	-7.0	1.53
11	2.0	Max	20.9	13.64	13.0	6.83
		Min	-13.5	3.34	-10.1	1.53

**Table 4-13 Measured Dynamic Properties for Specimen C1**

Run No	Power Spectrum		MIMO <sup>1</sup>	
	Period(s)	Damping (%)	Period(s)	Damping (%)
WN1-Long	0.59	3.4	0.6	4.93
WN1-Trans	0.57	2.7	0.61	4.1
WN2-Long	0.62	3.3	0.62	4.5
WN2-Trans	0.59	3.4	0.62	4.1
WN3-Long	0.67	4.8	0.67	4.3
WN3-Trans	0.67	4.2	0.67	4.5
WN4-Long	0.76	3.6	0.75	4.6
WN4-Trans	0.73	3.8	0.75	3.6
WN5-Long	0.76	3.7	0.78	3.6
WN5-Trans	0.76	4.1	0.78	3.2
WN6-Long	0.84	3.4	0.89	3.7
WN6-Trans	0.80	4.5	0.89	5
WN7-Long	0.89	5.7	0.91	4.6
WN7-Trans	0.89	3.8	0.91	4.4
WN8-Long	1.00	5.3	1.00	5
WN8-Trans	0.94	5.5	0.91	4.5
WN9-Long	1.00	5.1	1.06	5.7
WN9-Trans	1.00	5.5	1.01	5.6
WN10-Long	1.14	5.1	1.23	7.8
WN10-Trans	1.00	5.1	1.08	6.7
WN11-Long	1.45	9.7	1.43	8.2
WN11-Trans	1.14	8.5	1.28	8.8

<sup>1</sup> Multiple input - multiple output system identification procedure

**Table 4-14 Measured Dynamic Properties for Specimen C2**

Run No	Power Spectrum		MIMO	
	Period(s)	Damping (%)	Period(s)	Damping (%)
WN1-Long	0.62	4.0	0.61	4.3
WN1-Trans	0.59	4.6	0.61	4.6
WN2-Long	0.64	3.9	0.62	3.5
WN2-Trans	0.62	2.6	0.62	3.5
WN3-Long	0.64	3.1	0.63	3.6
WN3-Trans	0.64	3.1	0.63	4.7
WN4-Long	0.70	2.8	0.71	3
WN4-Trans	0.70	3.8	0.69	4
WN5-Long	0.76	2.5	0.76	3.8
WN5-Trans	0.73	4.5	0.73	5.3
WN6-Long	0.80	4.2	0.81	3.1
WN6-Trans	0.73	3.5	0.78	3.3
WN7-Long	0.89	4.0	0.87	3.6
WN7-Trans	0.84	3.3	0.84	3.7
WN8-Long	0.94	4.8	0.91	4.5
WN8-Trans	0.94	4.9	0.90	5.2
WN9-Long	0.94	3.9	0.94	5.5
WN9-Trans	0.94	3.8	0.93	3.1
WN10-Long	1.07	4.3	1.05	4.6
WN10-Trans	1.07	5.2	1.02	6.3
WN11-Long	1.14	3.5	1.27	8.4
WN11-Trans	1.14	5.6	1.12	7.1



**Table 4-15 Measured Effective Lateral Stiffness ( $EI_e/EI_g$ ), Specimen C1**

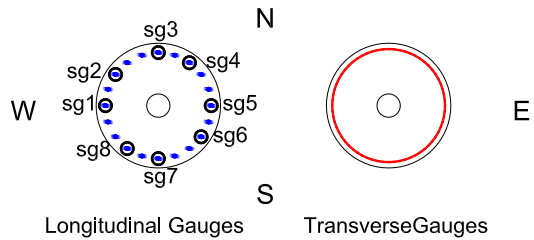
Run No	Power Spectrum		MIMO	
	Longitudinal	Transverse	Longitudinal	Transverse
WN1	0.38	0.41	0.37	0.36
WN2	0.36	0.38	0.35	0.35
WN3	0.30	0.30	0.30	0.30
WN4	0.23	0.25	0.24	0.24
WN5	0.23	0.23	0.22	0.22
WN6	0.19	0.21	0.17	0.17
WN7	0.17	0.17	0.16	0.16
WN8	0.13	0.15	0.13	0.16
WN9	0.13	0.13	0.12	0.13
WN10	0.10	0.13	0.09	0.12
WN11	0.06	0.10	0.07	0.08

**Table 4-16 Measured Effective Lateral Stiffness ( $EI_e/EI_g$ ), Specimen C2**

Run No	Power Spectrum		MIMO	
	Longitudinal	Transverse	Longitudinal	Transverse
WN1	0.36	0.38	0.36	0.36
WN2	0.33	0.36	0.35	0.35
WN3	0.33	0.33	0.34	0.34
WN4	0.28	0.28	0.27	0.28
WN5	0.23	0.25	0.23	0.25
WN6	0.21	0.25	0.21	0.22
WN7	0.17	0.19	0.18	0.19
WN8	0.15	0.15	0.16	0.17
WN9	0.15	0.15	0.15	0.16
WN10	0.12	0.12	0.12	0.13
WN11	0.10	0.10	0.08	0.11

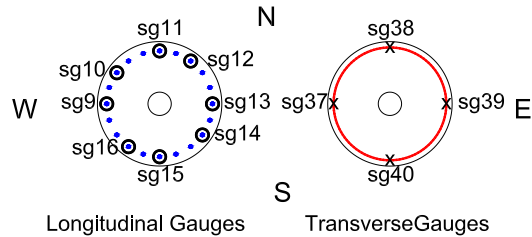
**Table 4-17 Measured Strains in Longitudinal Bars at -4 in. from the Top of the Footing, Specimen C1**

RUN	Gauge	1	2	3	4	5	6	7	8
PETx0.1	MAX	504	471	759	808	400	327	614	479
	MIN	-39	-41	-126	-232	-69	-37	-225	-184
PETx0.2	MAX	1180	1647	1824	1988	1460	907	1783	1115
	MIN	-76	-140	-415	-567	-170	-176	-162	-412
PETx0.4	MAX	1984	<b>2601</b>	<b>2412</b>	<b>2803</b>	<b>2352</b>	1716	<b>2262</b>	1741
	MIN	-113	<b>-4207</b>	-647	-915	-266	-366	-828	-641
PETx0.6	MAX	2178	-1913	<b>2408</b>	<b>2796</b>	<b>2290</b>	1983	<b>2358</b>	1960
	MIN	-309	<b>-4529</b>	-799	-1104	-548	-432	-1040	-677
PETx0.8	MAX	<b>2716</b>	<b>2533</b>	<b>2301</b>	<b>2723</b>	<b>2247</b>	<b>2393</b>	<b>2730</b>	<b>2289</b>
	MIN	-670	-845	-1023	-1361	-581	-667	-1275	-778
PETx1.0	MAX	<b>3536</b>	<b>2812</b>	2205	<b>2637</b>	<b>2345</b>	<b>2797</b>	<b>3278</b>	<b>2714</b>
	MIN	-599	-827	-1125	-1464	-678	-798	-1484	-933
PETx1.2	MAX	<b>11706</b>	<b>3124</b>	<b>2362</b>	<b>2738</b>	<b>2535</b>	<b>3484</b>	<b>18472</b>	<b>6935</b>
	MIN	181	-789	-1198	-1588	-724	-837	-1254	-550
PETx1.4	MAX	<b>15714</b>	<b>3298</b>	<b>2572</b>	<b>2918</b>	<b>2809</b>	<b>3775</b>	<b>27331</b>	<b>11762</b>
	MIN	<b>3570</b>	<b>-2719</b>	-1289	-1727	-825	-991	<b>5750</b>	692
PETx1.6	MAX	<b>19327</b>	<b>7421</b>	<b>2848</b>	<b>3235</b>	<b>3206</b>	<b>10929</b>	<b>34782</b>	<b>8636</b>
	MIN	<b>5592</b>	<b>-4902</b>	-1365	-1806	-928	-732	<b>10108</b>	<b>-4773</b>
PETx1.8	MAX	<b>20477</b>	969	<b>3079</b>	<b>3477</b>	<b>3576</b>	<b>12832</b>	<b>28579</b>	<b>11783</b>
	MIN	<b>9014</b>	<b>-7655</b>	-1365	-1759	-978	1316	<b>11389</b>	-914



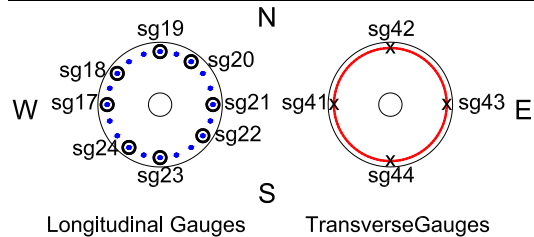
**Table 4-18 Measured Strains in Longitudinal bars and Spirals at 0 in. from the Top of the Footing, Specimen C1**

RUN	Gauge	9	10	11	12	13	14	15	16	37	38	39	40
PETx0.1	MAX	1261	990	1755	2094	1293	790	1440	1728	78	106	45	51
	MIN	-296	-216	-453	-612	-302	-292	-573	-582	59	32	-35	3
PETx0.2	MAX	2141	5315	12599	12714	4937	1944	2344	2635	86	134	49	83
	MIN	-533	-380	-612	-872	-484	-625	-1254	-1261	43	8	-31	-19
PETx0.4	MAX	13410	15572	6097	21149	17442	13322	11450	15810	89	307	79	127
	MIN	-454	1995	2092	532	190	-164	-1365	-278	16	26	12	-116
PETx0.6	MAX	16319	15252	2828	20254	15697	14134	14266	18377	102	404	94	129
	MIN	7442	5657	1115	638	4943	5210	-374	1087	-6	70	5	-55
PETx0.8	MAX	20601	14564	2509	19084	15764	16963	20239	24582	49	306	58	142
	MIN	6921	5151	-205	-358	6157	3794	1813	2706	-70	18	-18	-7
PETx1.0	MAX	24751	15560	1762	16594	15898	21836	28352	32835	82	380	72	249
	MIN	8878	5415	-1201	-1868	5445	6502	6190	8051	-53	29	-12	11
PETx1.2	MAX	28097	18697	1362	16555	17912	29327	39752	45417	173	539	114	486
	MIN	12261	6854	-1720	-7025	6285	9780	13985	16069	-83	32	-6	51
PETx1.4	MAX	29702	23791	1039	15126	20305	36710	52117	46434	275	763	270	8769
	MIN	11585	8028	-6189	-12312	6501	14397	22908	8827	-178	77	-48	134
PETx1.6	MAX	20701	29175	46	15126	18654	26491	53670	17547	236	1507	529	1383
	MIN	5641	9546	-14223	-16038	6372	11869	25010	-6940	-269	143	-77	166
PETx1.8	MAX	35302	34675	609	18206	8889	11660	23678	8704	672	2979	820	141576
	MIN	6517	11536	-21412	-14502	6577	10303	19139	196	-244	218	-69	-19508



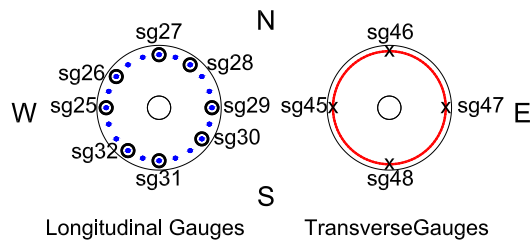
**Table 4-19 Measured Strains in Longitudinal bars and Spirals at 8 in. from the Top of the Footing, Specimen C1**

RUN	Gauge	17	18	19	20	21	22	23	24	41	42	43	44
PETx0.1	MAX	1376	1362	2068	2144	1322	943	1579	1638	53	92	59	96
	MIN	-110	-18	-485	-584	-118	-72	-656	-625	41	53	40	55
PETx0.2	MAX	2185	2837	96249	4164	2782	1817	2491	2451	53	80	70	134
	MIN	-373	-258	-5196	-1093	-352	-432	-1457	-1331	32	18	41	75
PETx0.4	MAX	3743	15061	16617	15402	10233	2994	3164	3047	112	106	81	192
	MIN	-74	-655	-492	-2012	-625	-784	-2255	-1988	37	28	39	92
PETx0.6	MAX	7770	14244	15793	14388	10405	3115	3238	6851	261	180	89	236
	MIN	529	3496	635	-219	1752	-835	-2229	-2608	86	55	36	135
PETx0.8	MAX	16044	13812	14593	13448	10941	4135	18601	17012	270	303	82	393
	MIN	2330	2878	-255	-769	3264	-1373	-1148	-563	78	41	4	101
PETx1.0	MAX	22732	15364	11946	11129	12403	14463	25230	25348	686	743	414	774
	MIN	5551	3234	-1065	-1702	3533	308	3231	4125	123	75	18	165
PETx1.2	MAX	31589	18925	10879	10328	13972	21133	37167	36914	1182	1122	820	1022
	MIN	11164	4909	-4538	-4946	4636	5476	9968	11155	118	102	63	232
PETx1.4	MAX	39822	23992	9510	9015	17048	28348	38594	48596	1350	1385	1110	1344
	MIN	17671	6376	-8456	-8165	6260	9786	11412	19259	162	117	-14	260
PETx1.6	MAX	27053	30020	7375	7344	20213	37070	10595	36216	1397	1706	1378	1609
	MIN	15010	8176	-14378	-12032	7561	14491	9869	18225	178	71	-71	301
PETx1.8	MAX	12889	36757	11616	7244	20708	45468	10056	16695	1695	1787	1700	1775
	MIN	12221	11651	-18220	-9906	5560	20843	9155	15481	-23	25	-266	-356



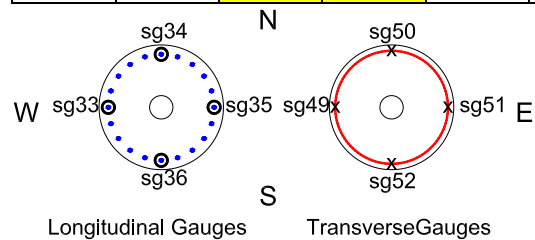
**Table 4-20 Measured Strains in Longitudinal bars and Spirals at 16 in. from the Top of the Footing, Specimen C1**

RUN	Gauge	25	26	27	28	29	30	31	32	45	46	47	48
PETx0.1	MAX		1109	1987	1976	1665	883		1640	98	117	59	146
	MIN		-105	-440	-556	1548	-145		-600	60	73	42	68
PETx0.2	MAX		2104	<b>3506</b>	<b>3151</b>	<b>16641</b>	1652		<b>2383</b>	119	183	79	198
	MIN		-401	-772	-885	<b>-5221</b>	-529		-1141	68	71	47	80
PETx0.4	MAX		<b>3390</b>	<b>12116</b>	<b>9904</b>	<b>22948</b>	<b>2496</b>		<b>3186</b>	139	269	161	233
	MIN		-694	-1143	-1262	<b>-15039</b>	-797		-1452	70	87	52	104
PETx0.6	MAX		<b>3487</b>	<b>11579</b>	<b>9849</b>	<b>20726</b>	<b>2624</b>		<b>3131</b>	157	295	229	251
	MIN		-203	1055	45	<b>2673</b>	-462		-1343	95	108	116	152
PETx0.8	MAX		<b>3247</b>	<b>9811</b>	<b>8823</b>	<b>21174</b>	<b>3099</b>		<b>8434</b>	159	263	217	199
	MIN		-402	95	-659	-350	-564		-981	65	66	105	106
PETx1.0	MAX		<b>4466</b>	<b>7775</b>	<b>7072</b>	<b>22057</b>	<b>12742</b>		<b>15103</b>	451	285	328	252
	MIN		-524	-944	-1045	-556	59		1167	100	100	128	141
PETx1.2	MAX		<b>9994</b>	<b>7630</b>	<b>6941</b>	<b>26145</b>	<b>13096</b>		<b>21381</b>	625	526	1024	539
	MIN		-58	-1233	-1372	-51	<b>4385</b>		<b>4520</b>	149	165	143	173
PETx1.4	MAX		<b>12699</b>	<b>7079</b>	<b>6216</b>	<b>26368</b>	<b>15906</b>		<b>28156</b>	697	799	1707	915
	MIN		<b>2955</b>	-1808	-1898	<b>3294</b>	<b>5444</b>		<b>8265</b>	-285	199	197	171
PETx1.6	MAX		<b>14337</b>	<b>6751</b>	<b>5037</b>	<b>26485</b>	<b>19053</b>		<b>34975</b>	1318	1017	2046	1127
	MIN		<b>3559</b>	<b>-2716</b>	<b>-3128</b>	<b>5121</b>	<b>7099</b>		<b>11793</b>	-270	196	287	192
PETx1.8	MAX		<b>16644</b>	<b>7514</b>	<b>3720</b>	<b>26585</b>	<b>21831</b>		<b>41288</b>	<b>3781</b>	1113	1898	1178
	MIN		<b>4547</b>	<b>-3081</b>	<b>-3946</b>	<b>5807</b>	<b>9470</b>		<b>16823</b>	-4	170	403	242



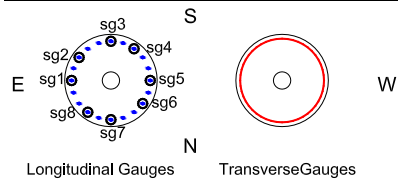
**Table 4-21 Measured Strains in Longitudinal bars and Spirals at 24 in. from the Top of the Footing, Specimen C1**

RUN	Gauge	33	34	35	36	49	50	51	52
PETx0.1	MAX	943	1655	995	1663	50	72		127
	MIN	-64	-347	-70	-414	30	48		81
PETx0.2	MAX	1447	<b>2365</b>	1738	<b>2445</b>	56	114		159
	MIN	-312	-1079	-249	-867	28	51		97
PETx0.4	MAX	2078	<b>6385</b>	<b>2471</b>	<b>5077</b>	98	157		183
	MIN	-293	-603	-460	-337	44	90		105
PETx0.6	MAX	1935	<b>10808</b>	<b>2308</b>	<b>19012</b>	121	171		187
	MIN	-266	-167	-295	70	60	131		117
PETx0.8	MAX	<b>2556</b>	<b>239124</b>	2185	<b>16958</b>	131	151		161
	MIN	-483	<b>-8975</b>	-347	680	21	84		65
PETx1.0	MAX	<b>3310</b>	<b>10069</b>	<b>2429</b>	<b>27760</b>	187	176		189
	MIN	-237	-1102	-467	1617	40	94		80
PETx1.2	MAX	<b>8971</b>	<b>85795</b>	<b>2485</b>	<b>180354</b>	239	201		227
	MIN	264	<b>-6048</b>	-411	<b>-9199</b>	49	108		112
PETx1.4	MAX	<b>12160</b>	<b>145787</b>	<b>2847</b>	<b>195410</b>	360	262		531
	MIN	<b>4299</b>	<b>-14393</b>	-387	<b>-10284</b>	101	131		156
PETx1.6	MAX	<b>12731</b>	<b>32941</b>	<b>3096</b>	<b>198051</b>	458	402		799
	MIN	<b>5726</b>	<b>-6671</b>	-348	<b>-12303</b>	151	160		244
PETx1.8	MAX	<b>13314</b>	<b>42472</b>	<b>3339</b>	<b>222568</b>	496	584		971
	MIN	<b>6393</b>	<b>-7637</b>	-272	1595	162	194		310



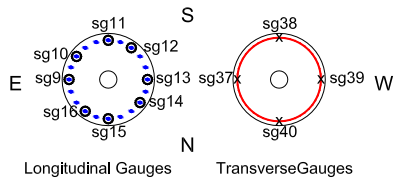
**Table 4-22 Measured Strains in Longitudinal Bars at -4 in. from the Top of the Footing, Specimen C2**

RUN	Gauge	1	2	3	4	5	6	7	8
PETx0.1	MAX	365	204	489	1164	452	245	397	548
	MIN	-107	-85	-180	-444	-197	-122	-360	-356
PETx0.2	MAX	722	568	1472	2856	1134	604	1085	1370
	MIN	-185	-166	-331	-745	-283	-307	-771	-724
PETx0.4	MAX	1229	714	2306	15126	2697	1673	1995	2245
	MIN	-119	-284	-768	-1050	-880	-521	-1396	-1305
PETx0.6	MAX	2100	754	2623	25327	3435	2320	2634	2972
	MIN	-433	-440	-1271	-609	-1020	-716	-1785	-1649
PETx0.8	MAX	2933	713	2569	24362	3499	2903	8947	11659
	MIN	-803	-490	-1615	1425	-1086	-1186	-1001	-659
PETx1.0	MAX	12014	1199	2404	21360	3666	12763	17342	19784
	MIN	-252	-395	-1747	729	-1252	-558	692	1992
PETx1.2	MAX	16206	1754	2621	24415	8735	21304	27509	32095
	MIN	4524	-174	-1792	-315	118	4564	4148	6036
PETx1.4	MAX	26012	2026	2821	26859	13480	59557	41757	49650
	MIN	6741	-165	-1866	-800	2665	7394	10137	13177
PETx1.6	MAX	36248	2159	6457	28986	16212	35796	57295	70182
	MIN	12469	-260	-2085	-1760	4114	16392	18283	22825
PETx1.8	MAX	45959	1415	10159	30421	17846	50547	74606	96299
	MIN	20259	247	-2637	-674	4121	22324	27117	36435
PETx2.0	MAX	52836	866	7419	16802	17551	64389	75855	115284
	MIN	30453	279	-1637	2650	2764	28349	38448	61083



**Table 4-23 Measured Strains in Longitudinal bars and Spirals at 0 in. from the Top of the Footing, Specimen C2**

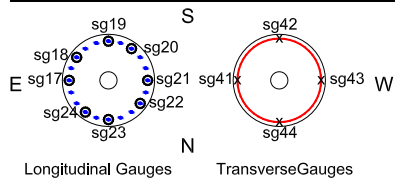
RUN	Gauge	9	10	11	12	13	14	15	16	37	38	39	40
PETx0.1	MAX	526	217	990	978	434	160	714	842	21	-36	-57	8
	MIN	-187	-102	-320	-321	-240	-241	-443	-543	1	-60	-75	-82
PETx0.2	MAX	1121	541	<b>2263</b>	<b>2751</b>	863	385	1648	1766	32	-17	-47	40
	MIN	-328	-141	-601	-661	-333	-370	-1036	-1062	-3	-65	-85	-148
PETx0.4	MAX	1863	<b>8137</b>	<b>16966</b>	<b>19383</b>	<b>6792</b>	510	<b>2841</b>	<b>2797</b>	42	2	-42	48
	MIN	-251	<b>2734</b>	-1301	-1683	-796	-391	-1977	-2054	-15	-87	-92	-269
PETx0.6	MAX	<b>14404</b>	<b>6675</b>	<b>20692</b>	<b>22816</b>	<b>7099</b>	<b>2303</b>	<b>16293</b>	<b>10974</b>	9	-3	-56	176
	MIN	-656	<b>3368</b>	<b>2254</b>	-539	1998	-264	-1738	-458	-88	-159	-136	-209
PETx0.8	MAX	<b>18072</b>	<b>5595</b>	<b>18231</b>	<b>20408</b>	<b>5819</b>	<b>2307</b>	<b>20155</b>	<b>10206</b>	23	49	-8	206
	MIN	<b>5772</b>	<b>2758</b>	1280	15	<b>2385</b>	188	791	1237	-58	-71	-159	-89
PETx1.0	MAX	<b>20084</b>	<b>6243</b>	<b>14890</b>	<b>16159</b>	<b>5416</b>	1483	<b>28408</b>	<b>4622</b>	22	85	-9	230
	MIN	<b>6473</b>	<b>2774</b>	-531	<b>-4488</b>	1784	279	<b>4210</b>	1866	-154	-70	-146	-20
PETx1.2	MAX	<b>17857</b>	<b>7467</b>	<b>16022</b>	<b>16333</b>	<b>5324</b>	1579	<b>39511</b>	<b>4104</b>	23	192	60	359
	MIN	<b>7942</b>	<b>2860</b>	<b>-3805</b>	<b>-10768</b>	1224	186	<b>12348</b>	1979	-229	-38	-137	-48
PETx1.4	MAX	<b>15370</b>	<b>8850</b>	<b>16255</b>	<b>13446</b>	<b>4838</b>	1547	<b>38297</b>	<b>3882</b>	30	321	331	480
	MIN	<b>8456</b>	<b>2491</b>	<b>-6500</b>	<b>-13084</b>	548	319	<b>15500</b>	2046	-263	-67	-105	-64
PETx1.6	MAX	<b>10099</b>	<b>11125</b>	<b>15857</b>	<b>8310</b>	<b>3943</b>	1452	<b>15195</b>	<b>3778</b>	-34	351	797	487
	MIN	<b>7721</b>	<b>2265</b>	<b>-11037</b>	<b>-11407</b>	198	364	<b>13717</b>	1968	-407	-119	-55	-136
PETx1.8	MAX	<b>8616</b>	<b>9477</b>	<b>11676</b>	1412	<b>3616</b>	1249	<b>14234</b>	<b>3189</b>	-79	591	1491	198
	MIN	<b>7490</b>	145	<b>-22459</b>	<b>-5660</b>	291	435	<b>13500</b>	2036	-515	-156	57	-256
PETx2.0	MAX	<b>8221</b>	<b>5526</b>	<b>13410</b>	1328	<b>2834</b>	1093	<b>13651</b>	<b>2412</b>	-120	952	2057	0
	MIN	<b>7287</b>	259	<b>-19309</b>	<b>-5884</b>	-1650	-445	<b>12899</b>	1026	-1264	-296	181	-1309





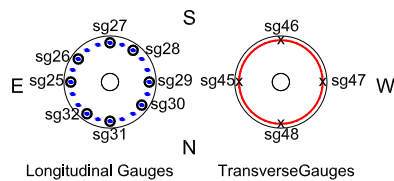
**Table 4-24 Measured Strains in Longitudinal bars and Spirals at 8 in. from the Top of the Footing, Specimen C2**

RUN	Gauge	17	18	19	20	21	22	23	24	41	42	43	44
PETx0.1	MAX	830	697	1409	998	695	729	1794	822	-25	-22	85	
	MIN	-116	6	-364	-492	-167	-65	32	-471	-37	-42	25	
PETx0.2	MAX	1420	1818	<b>3824</b>	1059	1230	1475	<b>2962</b>	1447	-18	3	102	
	MIN	-306	-205	-769	-690	-264	-467	-770	-879	-39	-32	27	
PETx0.4	MAX	2018	<b>12446</b>	<b>18593</b>	<b>6227</b>	<b>7647</b>	<b>2964</b>	<b>4824</b>	2147	-3	44	164	
	MIN	-216	-563	-1150	-402	-689	-949	<b>-4056</b>	-1565	-47	-32	25	
PETx0.6	MAX	<b>10379</b>	<b>15864</b>	<b>21996</b>	<b>4482</b>	<b>8744</b>	<b>17690</b>	1722	<b>10783</b>	32	35	395	
	MIN	-75	<b>3061</b>	-565	702	1900	278	<b>-12064</b>	-1310	-9	-18	27	
PETx0.8	MAX	<b>15045</b>	<b>14806</b>	<b>19777</b>	<b>3208</b>	<b>6993</b>	<b>22720</b>	1147	<b>13840</b>	90	116	408	
	MIN	<b>3899</b>	<b>2805</b>	-1170	645	2197	<b>4863</b>	<b>-11501</b>	-344	25	19	98	
PETx1.0	MAX	<b>21787</b>	<b>15448</b>	<b>15361</b>	2197	<b>6196</b>	<b>29648</b>	-2101	<b>19339</b>	155	260	604	
	MIN	<b>4929</b>	<b>3172</b>	<b>-5005</b>	698	1894	<b>9944</b>	<b>-13506</b>	<b>2551</b>	23	47	123	
PETx1.2	MAX	<b>30599</b>	<b>19498</b>	<b>14337</b>	1703	<b>6301</b>	<b>39736</b>	<b>-5574</b>	<b>26973</b>	247	881	984	
	MIN	<b>10131</b>	<b>5856</b>	<b>-11583</b>	390	1709	<b>15371</b>	<b>-13677</b>	<b>8086</b>	-16	94	107	
PETx1.4	MAX	<b>40881</b>	<b>24812</b>	<b>11310</b>	1596	<b>5968</b>	<b>52512</b>	<b>-8572</b>	<b>34875</b>	532	1601	1264	
	MIN	<b>16712</b>	<b>8496</b>	<b>-20204</b>	69	1710	<b>22901</b>	<b>-14673</b>	<b>13739</b>	-2	62	107	
PETx1.6	MAX	<b>54028</b>	<b>31154</b>	<b>7257</b>	1408	<b>5833</b>	<b>65119</b>	<b>-3380</b>	<b>33695</b>	837	2215	1387	
	MIN	<b>24866</b>	<b>11156</b>	<b>-28631</b>	-688	1419	<b>32342</b>	<b>-9532</b>	<b>13121</b>	-214	87	152	
PETx1.8	MAX	<b>65573</b>	<b>37372</b>	597	1179	<b>5314</b>	<b>58540</b>	<b>-2631</b>	<b>14454</b>	1394	<b>2268</b>	1613	
	MIN	<b>37266</b>	<b>15882</b>	<b>-44493</b>	<b>-4743</b>	842	<b>30943</b>	<b>-8177</b>	<b>11597</b>	-927	243	329	
PETx2.0	MAX	<b>56641</b>	<b>40324</b>	<b>-4974</b>	-245	<b>20293</b>	<b>29391</b>	<b>15406</b>	<b>11750</b>	<b>3350</b>	<b>45368</b>	<b>27974</b>	
	MIN	<b>-251199</b>	<b>17048</b>	<b>-25858</b>	<b>-4979</b>	<b>-248928</b>	<b>27073</b>	<b>-13099</b>	<b>8764</b>	-1189	<b>-255692</b>	-227	



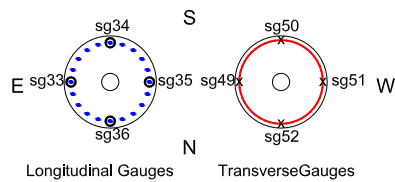
**Table 4-25 Measured Strains in Longitudinal bars and Spirals at 16 in. from the Top of the Footing, Specimen C2**

RUN	Gauge	25	26	27	28	29	30	31	32	45	46	47	48
PETx0.1	MAX		537	1220	203	875	521	1065	1097	29	-25	71	-19
	MIN		-1	-417	-442	-144	-66	-496	-512	-3	-38	45	-41
PETx0.2	MAX		1464	<b>2691</b>	286	1716	1089	2140	2093	58	-7	93	5
	MIN		-200	-840	-443	-253	-383	-1171	-1103	1	-27	46	-37
PETx0.4	MAX		<b>2839</b>	<b>16266</b>	1761	<b>95</b>	1958	<b>3260</b>	<b>2950</b>	87	25	133	38
	MIN		-448	-1300	-683	-504	-748	-1866	-1785	10	-24	66	-17
PETx0.6	MAX		<b>9168</b>	<b>17812</b>	1549	<b>12673</b>	<b>2840</b>	<b>12213</b>	<b>10032</b>	153	40	162	64
	MIN		-704	462	-896	2137	-587	<b>-2429</b>	-1771	48	-8	99	3
PETx0.8	MAX		<b>8927</b>	<b>14877</b>	813	<b>11775</b>	<b>11721</b>	<b>17256</b>	<b>14506</b>	239	89	255	136
	MIN		<b>2498</b>	-87	-796	<b>4953</b>	210	-134	-661	77	18	142	67
PETx1.0	MAX		<b>11707</b>	<b>11265</b>	700	<b>11661</b>	<b>17372</b>	<b>23982</b>	<b>20859</b>	592	304	431	283
	MIN		<b>2757</b>	-1436	-535	<b>6021</b>	<b>5469</b>	<b>2924</b>	<b>2273</b>	199	43	139	95
PETx1.2	MAX		<b>12783</b>	<b>11887</b>	777	<b>12445</b>	<b>22737</b>	<b>34658</b>	<b>29546</b>	<b>66675</b>	698	1018	655
	MIN		<b>4607</b>	<b>-2413</b>	-380	<b>5798</b>	<b>8973</b>	<b>8514</b>	<b>7463</b>	<b>-4348</b>	30	149	114
PETx1.4	MAX		<b>14837</b>	<b>11930</b>	609	<b>12991</b>	<b>26564</b>	<b>44178</b>	<b>38280</b>	503	995	1499	865
	MIN		<b>5200</b>	<b>-3897</b>	-281	<b>5979</b>	<b>12081</b>	<b>15447</b>	<b>13058</b>	-251	-7	142	47
PETx1.6	MAX		<b>17933</b>	<b>12094</b>	627	<b>13627</b>	<b>30896</b>	<b>49864</b>	<b>47052</b>	<b>228805</b>	1031	1873	904
	MIN		<b>5915</b>	<b>-5190</b>	-384	<b>5306</b>	<b>14622</b>	<b>21927</b>	<b>19134</b>	-1232	-211	64	-75
PETx1.8	MAX		<b>21117</b>	<b>12807</b>	679	<b>13902</b>	<b>34259</b>	<b>51282</b>	<b>48969</b>	<b>18881</b>	959	2121	881
	MIN		<b>7902</b>	<b>-6429</b>	-349	<b>4735</b>	<b>18157</b>	<b>27172</b>	<b>25743</b>	-1081	-323	222	-220
PETx2.0	MAX		<b>22922</b>	<b>8616</b>	155	<b>13710</b>	<b>34477</b>	<b>47808</b>	<b>40741</b>	<b>2423</b>	1223	2188	<b>24594</b>
	MIN		<b>10653</b>	<b>-5644</b>	-492	<b>3119</b>	<b>20420</b>	<b>30248</b>	<b>28892</b>	-591	-316	247	<b>-175350</b>



**Table 4-26 Measured Strains in Longitudinal bars and Spirals at 24 in. from the Top of the Footing, Specimen C2**

RUN		33	34	35	36	49	50	51	52
PETx0.1	MAX	760	783	781	656	33	83	91	26
	MIN	-85	-445	-166	-333	-3	53	5	9
PETx0.2	MAX	1233	1217	1471	1302	91	131	134	84
	MIN	-277	-749	-265	-753	6	60	-2	48
PETx0.4	MAX	1665	<b>2924</b>	<b>2407</b>	2075	146	183	196	359
	MIN	-440	-917	-564	-1123	8	78	4	279
PETx0.6	MAX	2219	<b>3987</b>	<b>2636</b>	<b>2638</b>	204	194	207	1238
	MIN	-319	-305	-594	-1112	20	83	29	1110
PETx0.8	MAX	<b>3415</b>	<b>2987</b>	<b>2485</b>	<b>9456</b>	249	210	229	1337
	MIN	4	-304	-581	-339	47	102	60	1166
PETx1.0	MAX	<b>12951</b>	2007	<b>2336</b>	<b>13177</b>	391	214	230	1838
	MIN	516	-922	-548	<b>2691</b>	66	123	71	1192
PETx1.2	MAX	<b>15083</b>	1944	<b>2611</b>	<b>16919</b>	712	296	364	2059
	MIN	<b>5407</b>	-1307	-754	<b>4709</b>	133	122	75	628
PETx1.4	MAX	<b>16964</b>	1562	<b>6030</b>	<b>20745</b>	1189	526	652	1179
	MIN	<b>6984</b>	-1754	-114	<b>7074</b>	166	107	63	436
PETx1.6	MAX	<b>18877</b>	1268	<b>9973</b>	<b>23491</b>	1502	650	798	1832
	MIN	<b>8118</b>	-2140	<b>2278</b>	<b>8688</b>	115	49	1	-136
PETx1.8	MAX	<b>20596</b>	1367	<b>12310</b>	<b>26045</b>	1607	800	977	2043
	MIN	<b>10060</b>	<b>-2322</b>	<b>4689</b>	<b>10343</b>	93	68	-23	-216
PETx2.0	MAX	<b>20480</b>	1156	<b>11580</b>	<b>24663</b>	1455	800	971	<b>19468</b>
	MIN	<b>12691</b>	-1783	<b>5453</b>	<b>11870</b>	152	96	-25	<b>-248814</b>



**Table 4-27 Values for Idealized Force-Displacement and Moment-Curvature**

<b>Specimen</b>	<b>Yielding Displacement (in)</b>	<b>Ultimate Displacement (in)</b>	<b>Yielding Curvature (rad/in)</b>	<b>Ultimate Curvature (rad/in)</b>	<b>Displacement Ductility</b>	<b>Curvature Ductility</b>
C1-Longitudinal	1.1	12.2	0.00066	0.00893	11.0	13.5
C1- Transverse	0.7	5.9	0.00043	0.00469	8.5	10.9
C2-Longitudinal	1.1	12.9	0.00071	0.01213	11.4	17.0
C2- Transverse	0.7	7.2	0.00035	0.00465	10.0	13.3

**Table 4-28 Plastic Hinge Lengths**

<b>Plastic Hinge Lengths (in)</b>	<b>C1</b>	<b>C2</b>
Measured	21.9	16.2
Priestley Equation	11.28	11.28

**Table 5-1 Test Procedure, Specimen I1**

Run No	Times Sylmar	Max. acceleration (g)		Min. acceleration (g)	
		Long.	Trans.	Long.	Trans.
Tuning	-	-	-	-	-
1	0.1	0.094	0.066	-0.073	-0.038
2	0.2	0.165	0.127	-0.113	-0.073
3	0.4	0.359	0.269	-0.214	-0.135
4	0.6	0.552	0.377	-0.282	-0.205
5	0.8	0.760	0.482	-0.353	-0.236
6	1.0	0.962	0.584	-0.427	-0.302
7	1.2	1.108	0.683	-0.483	-0.353
8	1.4	1.261	0.794	-0.506	-0.418
9	1.6	1.410	0.888	-0.607	-0.494
10	1.8	1.740	0.964	-0.745	-0.544
11	1.4*	1.364	0.811	-0.739	-0.424

**Table 5-2 Test Procedure, Specimen I2**

Run No	Times Sylmar	Max. acceleration (g)		Min. acceleration (g)	
		Long.	Trans.	Long.	Trans.
Tuning	-	-	-	-	-
1	0.1	0.118	0.063	-0.084	-0.038
2	0.2	0.188	0.142	-0.136	-0.076
3	0.4	0.368	0.278	-0.236	-0.135
4	0.6	0.556	0.386	-0.335	-0.195
5	0.8	0.758	0.513	-0.436	-0.245
6	1.0	0.979	0.612	-0.475	-0.294
7	1.2	1.169	0.715	-0.499	-0.359
8	1.4	1.331	0.815	-0.532	-0.429
9	1.6	1.508	0.752	-0.746	-0.472
10	1.8	1.650	0.853	-0.749	-0.537
11	1.8*	1.618	0.906	-0.764	-0.550

Table 5-3 Target and Achieved Peak Table Accelerations for Specimen I1

Run No	Times Sylmar		Longitudinal Direction			Transverse Direction		
			Target (g)	Achieved (g)	Achieved/Target	Target (g)	Achieved (g)	Achieved/Target
1	0.1	Max	0.08	0.09	1.11	0.06	0.07	1.09
		Min	-0.06	-0.07	1.23	-0.03	-0.04	1.17
2	0.2	Max	0.17	0.16	0.98	0.12	0.13	1.05
		Min	-0.12	-0.11	0.96	-0.07	-0.07	1.11
3	0.4	Max	0.34	0.36	1.07	0.24	0.27	1.11
		Min	-0.24	-0.21	0.91	-0.13	-0.14	1.04
4	0.6	Max	0.51	0.55	1.09	0.36	0.38	1.04
		Min	-0.35	-0.28	0.80	-0.20	-0.21	1.05
5	0.8	Max	0.67	0.76	1.13	0.48	0.48	1.00
		Min	-0.47	-0.35	0.75	-0.26	-0.24	0.91
6	1.0	Max	0.84	0.96	1.14	0.60	0.58	0.97
		Min	-0.59	-0.43	0.72	-0.33	-0.30	0.93
7	1.2	Max	1.01	1.11	1.09	0.73	0.68	0.94
		Min	-0.71	-0.48	0.68	-0.39	-0.35	0.90
8	1.4	Max	1.18	1.26	1.07	0.85	0.79	0.94
		Min	-0.83	-0.51	0.61	-0.46	-0.42	0.92
9	1.6	Max	1.35	1.41	1.04	0.97	0.89	0.92
		Min	-0.94	-0.61	0.64	-0.52	-0.49	0.95
10	1.8	Max	1.52	1.74	1.15	1.09	0.96	0.89
		Min	-1.06	-0.74	0.70	-0.59	-0.54	0.93
11	1.4	Max	1.18	1.36	1.16	0.85	0.81	0.96
		Min	-0.83	-0.74	0.90	-0.46	-0.42	0.93
<b>Average</b>					<b>0.95</b>			<b>0.99</b>

Table 5-4 Target and Achieved Peak Table Accelerations for Specimen I2

Run No	Times Sylmar		Longitudinal Direction			Transverse Direction		
			Target (g)	Achieved (g)	Achieved/Target	Target (g)	Achieved (g)	Achieved/Target
1	0.1	Max	0.08	0.12	1.40	0.06	0.06	1.05
		Min	-0.06	-0.08	1.42	-0.03	-0.04	1.16
2	0.2	Max	0.17	0.19	1.12	0.12	0.14	1.18
		Min	-0.12	-0.14	1.15	-0.07	-0.08	1.16
3	0.4	Max	0.34	0.37	1.09	0.24	0.28	1.15
		Min	-0.24	-0.24	1.00	-0.13	-0.14	1.04
4	0.6	Max	0.51	0.56	1.10	0.36	0.39	1.06
		Min	-0.35	-0.34	0.95	-0.20	-0.20	1.00
5	0.8	Max	0.67	0.76	1.12	0.48	0.51	1.06
		Min	-0.47	-0.44	0.92	-0.26	-0.25	0.94
6	1.0	Max	0.84	0.98	1.16	0.60	0.61	1.01
		Min	-0.59	-0.47	0.81	-0.33	-0.29	0.90
7	1.2	Max	1.01	1.17	1.16	0.73	0.72	0.99
		Min	-0.71	-0.50	0.71	-0.39	-0.36	0.92
8	1.4	Max	1.18	1.33	1.13	0.85	0.81	0.96
		Min	-0.83	-0.53	0.65	-0.46	-0.43	0.94
9	1.6	Max	1.35	1.51	1.12	0.97	0.75	0.78
		Min	-0.94	-0.75	0.79	-0.52	-0.47	0.90
10	1.8	Max	1.52	1.65	1.09	1.09	0.85	0.78
		Min	-1.06	-0.75	0.71	-0.59	-0.54	0.92
11	1.4	Max	1.52	1.62	1.07	1.09	0.91	0.83
		Min	-1.06	-0.76	0.72	-0.59	-0.55	0.94
<b>Average</b>					<b>1.02</b>			<b>0.99</b>

**Table 5-5 Spectral Response at Structural Period, Specimen I1**

Run	Times Sylmar	Longitudinal Direction (Achieved/Target)				Transverse Direction (Achieved/Target)			
		Period (s)	Acceleration	Velocity	Displacement	Period (s)	Acceleration	Velocity	Displacement
1	0.1	0.59	0.76	0.72	0.76	0.80	0.56	0.55	0.56
2	0.2	0.67	1.16	1.10	1.16	0.84	0.66	0.66	0.66
3	0.4	0.73	0.98	0.96	0.98	0.89	0.89	0.86	0.89
4	0.6	0.8	0.90	0.90	0.90	1	0.92	0.93	0.92
5	0.8	0.84	0.97	0.97	0.97	1	0.91	0.92	0.91
6	1.0	0.84	0.96	0.96	0.96	1.14	0.93	0.94	0.93
7	1.2	0.89	0.98	0.98	0.98	1.07	0.93	0.94	0.93
8	1.4	0.89	0.99	0.99	0.99	1.14	0.94	0.94	0.94
9	1.6	1	0.94	0.96	0.94	1.14	0.94	0.95	0.94
10	1.8	1	0.97	0.99	0.97	1.23	0.93	0.94	0.93
11	1.4*	1.07	1.02	1.02	1.02	1.23	0.96	0.96	0.96
<b>Average</b>		-	<b>0.97</b>	<b>0.96</b>	<b>0.97</b>	-	<b>0.87</b>	<b>0.87</b>	<b>0.87</b>



**Table 5-6 Spectral Response at Structural Period, Specimen I2**

Run	Times Sylmar	Longitudinal Direction (Achieved/Target)				Transverse Direction (Achieved/Target)			
		Period (s)	Acceleration	Velocity	Displacement	Period (s)	Acceleration	Velocity	Displacement
1	0.1	0.53	0.67	0.95	0.96	0.73	0.58	0.88	0.87
2	0.2	0.59	0.88	1.08	1.11	0.73	0.68	0.95	0.96
3	0.4	0.64	1.03	1.04	1.03	0.84	0.75	0.91	0.92
4	0.6	0.67	1.00	0.93	0.93	0.94	0.85	0.95	0.95
5	0.8	0.8	0.94	0.90	0.91	1	0.91	0.89	0.89
6	1.0	0.84	1.01	0.98	0.98	1.07	0.91	1.00	0.99
7	1.2	0.89	1.01	1.02	1.01	1.14	0.93	1.00	1.00
8	1.4	0.89	1.02	1.02	0.98	1.14	0.93	0.95	0.93
9	1.6	0.94	1.00	1.03	1.00	1.14	0.89	0.89	0.88
10	1.8	1.07	1.00	1.00	1.00	1.14	0.91	0.92	0.91
11	1.8*	1.23	0.98	0.99	0.99	1.23	0.92	0.93	0.93
<b>Average</b>		-	<b>0.96</b>	<b>0.99</b>	<b>0.99</b>	-	<b>0.84</b>	<b>0.93</b>	<b>0.93</b>

Table 5-7 Observed Performance for Specimen I1

Run	Times Sylmar	Longitudinal Direction			Transverse Direction			Performance
		PGA (g)	$\delta_L$ (%) <sup>1</sup>	$\mu_{dL}$ <sup>2</sup>	PGA (g)	$\delta_T$ (%)	$\mu_{dT}$	
1	0.1	0.09	0.34	0.24	0.07	0.24	0.16	Horizontal hairline cracks
2	0.2	0.16	0.78	0.56	0.12	0.55	0.36	First longitudinal bar yielding
3 - 5	0.4 - 0.8	0.36 - 0.76	1.8 - 4.2	1.3 - 2.97	0.27 - 0.48	1.41 - 2.8	0.92 - 1.81	Extension of horizontal cracks and first inclined
6	1.0	1.11	5.2	3.73	0.68	4.0	2.61	First concrete spalling
7	1.2	1.01	6.02	4.31	0.73	4.96	3.23	Extension of cracks and spalling
8	1.4	1.26	6.8	4.87	0.79	6.1	3.97	Spirals and longitudinal bars visible
9 - 10	1.6 - 1.8	1.41 - 1.74	8.6 - 8.63	5.34 - 5.35	0.89 - 0.96	7.32 - 9.3	4.77 - 6.08	Extension of cracks and spalling
11	1.4*	1.36	7.9	4.95	0.81	9.47	6.17	Flexural failure: Longitudinal bar buckling and concrete degradation

<sup>1</sup> Drift ratio<sup>2</sup> Displacement ductility

Table 5-8 Observed Performance for Specimen I2

Run	Times Sylmar	Longitudinal Direction			Transverse Direction			Performance
		PGA (g)	$\delta_L$ (%) <sup>1</sup>	$\mu_{dL}$ <sup>2</sup>	PGA (g)	$\delta_T$ (%)	$\mu_{dT}$	
1	0.1	0.12	0.29	0.17	0.06	0.27	0.2	Horizontal hairline cracks
2	0.2	0.19	0.85	0.49	0.14	0.50	0.38	First longitudinal bar yielding
3 - 5	0.4 - 0.8	0.37 - 0.76	1.68 - 4.4	0.97 - 2.57	0.28 - 0.51	1.23 - 2.1	0.93 - 1.61	Extension of horizontal cracks and first inclined
6	1.0	0.98	5.2	3.01	0.61	3.40	2.57	First concrete spalling
7	1.2	1.17	6.0	3.47	0.72	4.20	3.19	Extension of cracks and spalling
8	1.4	1.18	6.7	3.87	0.81	5.14	3.90	Spirals and longitudinal bars visible
9 - 10	1.6 - 1.8	1.35 - 1.52	7.3 - 7.7	4.24 - 4.45	0.75 - 0.85	6.0 - 7.66	4.56 - 5.81	Extension of cracks and spalling; bar buckling
11	1.8*	1.52	4.27	2.47	0.91	9.39	7.12	Flexural failure: reinforcement rupture (long. Bars and spirals); concrete degradation

<sup>1</sup> Drift ratio<sup>2</sup> Displacement ductility

**Table 5-9 Peak Force and Corresponding Displacement for Specimen I1**

Run No	Times Sylmar		Longitudinal Direction		Transverse Direction	
			Force (kips)	Displacement (in)	Force (kips)	Displacement (in)
1	0.1	Max	6.7	0.30	2.0	0.20
		Min	-6.6	-0.28	-1.9	-0.22
2	0.2	Max	14.7	0.64	4.8	0.45
		Min	-15.0	-0.64	-4.6	-0.47
3	0.4	Max	19.5	1.02	9.3	1.17
		Min	-25.0	-1.51	-10.6	-1.33
4	0.6	Max	22.6	1.58	9.8	1.56
		Min	-28.0	-2.75	-14.8	-2.77
5	0.8	Max	24.8	2.51	11.7	2.31
		Min	-27.6	-3.44	-12.9	-2.85
6	1.0	Max	25.5	3.23	13.3	3.32
		Min	-28.1	-4.32	-11.0	-2.44
7	1.2	Max	25.4	4.06	14.1	4.11
		Min	-28.1	-5.00	-10.6	-2.98
8	1.4	Max	24.7	4.64	14.7	5.05
		Min	-28.1	-5.64	-11.5	-3.10
9	1.6	Max	24.3	5.34	15.1	6.07
		Min	-27.9	-6.19	-11.9	-2.93
10	1.8	Max	24.4	6.12	15.2	7.74
		Min	-26.4	-6.20	-11.9	-2.50
11	1.4*	Max	19.8	4.62	11.3	7.86
		Min	-18.8	-5.72	-10.4	-1.07

**Table 5-10 Peak Displacement and Corresponding Force for Specimen I1**

Run No	Times Petrolia		Longitudinal Direction		Transverse Direction	
			Force (kips)	Displacement (in)	Force (kips)	Displacement (in)
1	0.1	Max	6.6	0.30	2.0	0.45
		Min	-6.5	-0.29	-1.9	-0.47
2	0.2	Max	14.6	0.64	4.8	1.20
		Min	-14.9	-0.65	-4.6	-1.34
3	0.4	Max	19.1	1.04	8.9	1.58
		Min	-23.6	-1.60	-10.5	-2.83
4	0.6	Max	22.2	1.60	9.6	2.34
		Min	-26.9	-2.83	-14.3	-2.86
5	0.8	Max	24.0	2.60	11.4	3.36
		Min	-26.3	-3.57	-12.8	-2.95
6	1.0	Max	24.2	3.39	13.1	4.22
		Min	-27.1	-4.43	-7.7	-3.46
7	1.2	Max	23.5	4.28	13.8	5.14
		Min	-27.1	-5.10	-8.8	-3.61
8	1.4	Max	22.8	5.00	14.2	6.20
		Min	-26.2	-5.78	-9.4	-3.46
9	1.6	Max	22.8	5.77	14.7	7.85
		Min	-25.7	-6.44	-10.1	-2.92
10	1.8	Max	22.8	7.05	14.6	8.05
		Min	-22.6	-6.77	-10.4	-1.24
11	1.4*	Max	17.9	5.58	10.3	8.05
		Min	-16.6	-6.11	-9.9	-1.24

**Table 5-11 Peak Force and Corresponding Displacement for Specimen I2**

Run No	Times Petrolia		Longitudinal Direction		Transverse Direction	
			Force (kips)	Displacement (in)	Force (kips)	Displacement (in)
1	0.1	Max	5.8	0.23	2.7	0.22
		Min	-5.9	-0.24	-2.5	-0.23
2	0.2	Max	13.7	0.67	4.9	0.42
		Min	-13.2	-0.71	-4.8	-0.46
3	0.4	Max	20.2	1.07	8.3	1.02
		Min	-23.7	-1.39	-8.9	-1.18
4	0.6	Max	22.6	1.55	9.4	1.34
		Min	-27.6	-2.77	-14.3	-2.74
5	0.8	Max	24.9	2.61	11.1	1.76
		Min	-27.7	-3.68	-13.4	-3.32
6	1.0	Max	26.1	3.76	13.1	2.82
		Min	-26.8	-4.30	-11.3	-3.17
7	1.2	Max	25.6	4.39	14.0	3.49
		Min	-27.4	-4.96	-10.5	-3.57
8	1.4	Max	25.0	5.14	14.5	4.27
		Min	-27.4	-5.54	-11.2	-3.89
9	1.6	Max	24.6	5.84	14.7	4.99
		Min	-27.1	-6.07	-11.6	-3.82
10	1.8	Max	24.5	6.87	13.9	6.36
		Min	-25.3	-6.37	-11.8	-3.67
11	1.8*	Max	19.5	9.00	11.0	7.79
		Min	-13.7	-3.54	-9.3	-1.89

**Table 5-12 Peak Displacement and Corresponding Force for Specimen I2**

Run No	Times Petrolia		Longitudinal Direction		Transverse Direction	
			Force (kips)	Displacement (in)	Force (kips)	Displacement (in)
1	0.1	Max	5.7	0.23	2.6	0.42
		Min	-5.7	-0.25	-2.5	-0.46
2	0.2	Max	13.5	0.68	4.9	1.03
		Min	-13.1	-0.71	-4.8	-1.19
3	0.4	Max	19.7	1.10	8.1	1.38
		Min	-22.4	-1.48	-8.8	-2.81
4	0.6	Max	22.1	1.57	9.3	1.78
		Min	-26.4	-2.93	-13.8	-3.34
5	0.8	Max	23.7	2.67	10.9	2.82
		Min	-26.3	-3.82	-13.3	-3.18
6	1.0	Max	25.1	3.80	13.0	3.57
		Min	-25.8	-4.45	-8.0	-3.87
7	1.2	Max	23.8	4.65	13.6	4.39
		Min	-26.4	-5.08	-9.0	-4.20
8	1.4	Max	23.1	5.55	14.2	5.06
		Min	-25.5	-5.70	-9.9	-4.25
9	1.6	Max	22.6	6.44	14.1	6.57
		Min	-24.6	-6.32	-10.0	-4.04
10	1.8	Max	23.1	7.65	13.4	8.07
		Min	-22.8	-6.79	-10.7	-1.99
11	1.8*	Max	18.8	9.15	10.0	8.07
		Min	-10.1	-4.73	-9.0	-1.99

**Table 5-13 Measured Dynamic Properties for Specimen I1**

Run No	Power Spectrum		MIMO <sup>1</sup>	
	Period(s)	Damping (%)	Period(s)	Damping (%)
WN1-Long	0.59	3.0	0.58	4.2
WN1-Trans	0.80	7.8	0.79	5.8
WN2-Long	0.67	4.6	0.67	4.4
WN2-Trans	0.84	2.4	0.85	3.9
WN3-Long	0.73	5.1	0.72	5.2
WN3-Trans	0.89	2.6	0.90	3.0
WN4-Long	0.80	4.2	0.80	4.9
WN4-Trans	1.00	3.4	0.97	3.3
WN5-Long	0.84	5.4	0.86	5.1
WN5-Trans	1.00	3.5	1.04	3.5
WN6-Long	0.84	3.7	0.84	4.7
WN6-Trans	1.14	5.2	1.08	4.3
WN7-Long	0.89	3.5	0.89	4.7
WN7-Trans	1.07	2.9	1.10	4.6
WN8-Long	0.89	4.0	0.91	5.3
WN8-Trans	1.14	3.3	1.15	4.2
WN9-Long	1.00	3.6	0.96	5.4
WN9-Trans	1.14	6.0	1.19	5.4
WN10-Long	1.00	5.2	0.97	5.5
WN10-Trans	1.23	4.9	1.19	5.7
WN11-Long	1.07	10.4	1.25	8.4
WN11-Trans	1.23	5.9	1.25	8.3
WN12-Long	1.46	8.3	1.33	16.0
WN12-Trans	1.46	12.5	1.22	15.0

<sup>1</sup> Multiple input - multiple output system identification procedure



**Table 5-14 Measured Dynamic Properties for Specimen I2**

Run No	Power Spectrum		MIMO	
	Period(s)	Damping (%)	Period(s)	Damping (%)
WN1-Long	0.53	5.0	0.52	6.9
WN1-Trans	0.73	4.4	0.74	6.7
WN2-Long	0.59	3.9	0.59	3.1
WN2-Trans	0.73	2.5	0.77	3.8
WN3-Long	0.64	3.6	0.65	3.4
WN3-Trans	0.84	3.0	0.83	3.4
WN4-Long	0.67	4.9	0.74	3.7
WN4-Trans	0.94	3.3	0.93	3.8
WN5-Long	0.80	4.0	0.81	4.4
WN5-Trans	1.00	2.1	1.00	3.7
WN6-Long	0.84	3.9	0.89	4.0
WN6-Trans	1.07	3.0	1.04	3.9
WN7-Long	0.89	6.0	0.90	6.3
WN7-Trans	1.14	3.8	1.10	4.1
WN8-Long	0.89	5.7	0.93	7.9
WN8-Trans	1.14	3.0	1.11	4.5
WN9-Long	0.94	4.9	0.94	6.5
WN9-Trans	1.14	4.3	1.12	4.7
WN10-Long	1.07	6.4	1.01	7.7
WN10-Trans	1.14	5.2	1.18	5.1
WN11-Long	1.23	10.0	1.16	12.3
WN11-Trans	1.23	7.4	1.18	12.7
WN12-Long	1.46	7.6	1.43	12.3
WN12-Trans	1.46	9.4	1.19	10.0

**Table 5-15 Measured Effective Lateral Stiffness ( $EI_c/EI_g$ ), Specimen I1**

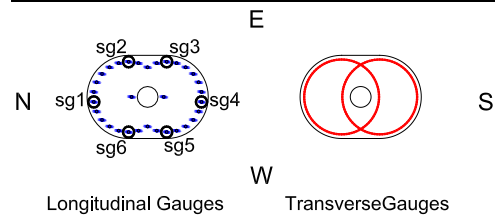
Run No	Power Spectrum		MIMO	
	Longitudinal	Transverse	Longitudinal	Transverse
WN1	0.29	0.32	0.30	0.33
WN2	0.23	0.29	0.23	0.29
WN3	0.19	0.26	0.20	0.25
WN4	0.16	0.20	0.16	0.22
WN5	0.14	0.20	0.14	0.19
WN6	0.14	0.16	0.14	0.17
WN7	0.13	0.18	0.13	0.17
WN8	0.13	0.16	0.12	0.15
WN9	0.10	0.16	0.11	0.15
WN10	0.10	0.14	0.11	0.14
WN11	0.09	0.14	0.07	0.13
WN12	0.05	0.10	0.06	0.14

**Table 5-16 Measured Effective Lateral Stiffness ( $EI_c/EI_g$ ), Specimen I2**

Run No	Power Spectrum		MIMO	
	Longitudinal	Transverse	Longitudinal	Transverse
WN1	0.36	0.39	0.37	0.38
WN2	0.29	0.39	0.29	0.34
WN3	0.25	0.29	0.25	0.30
WN4	0.23	0.23	0.19	0.24
WN5	0.16	0.20	0.16	0.20
WN6	0.14	0.18	0.13	0.19
WN7	0.13	0.16	0.13	0.17
WN8	0.13	0.16	0.12	0.17
WN9	0.12	0.16	0.12	0.16
WN10	0.09	0.16	0.10	0.15
WN11	0.07	0.14	0.08	0.15
WN12	0.05	0.10	0.05	0.14

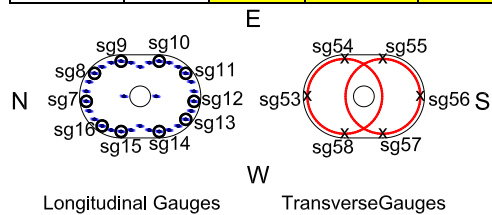
**Table 5-17 Measured Strains in Longitudinal bars and Spirals at -5 in. from the Top of the Footing, Specimen I1**

RUN	Gauge	1	2	3	4	5	6
SYLx0.1	MAX		249	52	319	341	283
	MIN		-213	-31	-293	-222	-259
SYLx0.2	MAX		602	342	1287	709	759
	MIN		-327	262	-479	-247	-389
SYLx0.4	MAX		1718	391	2112	<b>2450</b>	1694
	MIN		-545	273	-707	808	-878
SYLx0.6	MAX		<b>2346</b>	402	<b>2827</b>	<b>7789</b>	2036
	MIN		-730	220	-949	-757	-1104
SYLx0.8	MAX		<b>2523</b>	409	<b>3221</b>	<b>5667</b>	<b>2248</b>
	MIN		-970	-76	-1243	<b>2909</b>	-1288
SYLx1.0	MAX		<b>2531</b>	347	<b>18035</b>	<b>32018</b>	<b>2533</b>
	MIN		-1208	36	-1563	<b>7457</b>	-1499
SYLx1.2	MAX		<b>2806</b>	354	<b>16206</b>	<b>25162</b>	<b>7032</b>
	MIN		-1456	-67	1237	<b>-241843</b>	<b>-2157</b>
SYLx1.4	MAX		<b>7353</b>	135	<b>12251</b>	<b>217854</b>	<b>18323</b>
	MIN		-1308	-46	617	-1366	-583
SYLx1.6	MAX		<b>14682</b>	248	<b>2937</b>	<b>14992</b>	<b>17052</b>
	MIN		113	-66	-1932	757	-995
SYLx1.8	MAX		<b>17855</b>	178	1876	<b>18771</b>	<b>17965</b>
	MIN		<b>2184</b>	-106	<b>-4273</b>	<b>-6464</b>	<b>-2565</b>
SYLx1.4*	MAX		<b>17386</b>	193	1038	<b>31332</b>	<b>6452</b>
	MIN		<b>2760</b>	-91	756	<b>2963</b>	<b>3768</b>



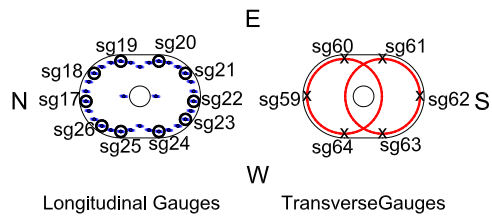
**Table 5-18 Measured Strains in Longitudinal bars and Spirals at 0 in. from the Top of the Footing, Specimen I1**

RUN	Gauge	7	8	9	10	11	12	13	14	15	16	53	54	55	56	57	58
SYLx0.1	MAX	1220	1024	577	853	1273		1291	886	762	1445	79	-1	36	0	16	-15
	MIN	-683	-685	-453	-559	-853		-819	-491	-530	-970	-47	-19	-45	-25	-39	-59
SYLx0.2	MAX	2496	2559	1481	2124	5116		3734	2207	1932	4371	180	23	149	49	84	6
	MIN	-1182	-1141	-777	-942	-1046		-1393	-902	-851	-1662	-44	-22	-33	-16	-30	-87
SYLx0.4	MAX	18640	92869	22343	24048	26165		26481	25476	17770	25403	195	31	236	210	160	32
	MIN	-333	-1107	-856	-1802	-1890		-645	-29	-495	-2650	-66	-29	-58	-38	-24	-185
SYLx0.6	MAX	20102	66866	2844	14337	87373		32485	27584	17085	27189	94	109	274	106	159	19
	MIN	-1955	8779	-2315	3213	-517		2867	2357	-1183	-4149	-158	1	-33	-35	32	-185
SYLx0.8	MAX	27529	44799	1395	9970	90808		42488	37146	19502	30327	222	136	199	183	255	45
	MIN	-1429	8921	-7628	2165	2064		4092	9492	-881	-4037	-94	24	-12	-14	3	-182
SYLx1.0	MAX	34908	91886	2036	7876	46701		52363	47828	22096	27810	302	189	218	207	413	104
	MIN	-690	10835	-9340	7	-12988		7014	12707	1711	-6578	-18	6	-16	-74	-54	-184
SYLx1.2	MAX	44236	94073	4622	5542	54291		61379	54981	18801	23579	384	209	606	301	759	241
	MIN	1597	13813	-10424	-342	-13740		12889	19870	4508	-8359	9	3	-45	-105	-33	-175
SYLx1.4	MAX	50803	93225	7649	3431	58272		75355	48849	7697	9417	531	191	2589	286	1021	383
	MIN	4471	22525	-10487	-2455	-22057		20313	11427	4475	-28976	24	-33	18	-128	-3	-221
SYLx1.6	MAX	59458	101346	10662	3912	55569		93844	19176	5868	5330	769	240	1196	299	1476	584
	MIN	5068	-21135	-10874	-6178	-20701		30406	5596	4635	-48694	3	-6	-123	-151	23	-50
SYLx1.8	MAX	72696	114657	11854	6073	25736		119926	16383	5571	-174	1102	231	1288	1052	1988	1738
	MIN	-3384	-205288	-9240	-32355	2419		43696	3887	4009	-16852	-48	-28	-85	-245	120	116
SYLx2.0	MAX	66000	107245	2912	1178	19214		122863	11061	5303	-792	1527	299	1465	3631	1776	1976
	MIN	29056	-20585	-2673	-14245	18332		74902	8983	-639	-77979	-42	-39	-29	-207	250	723



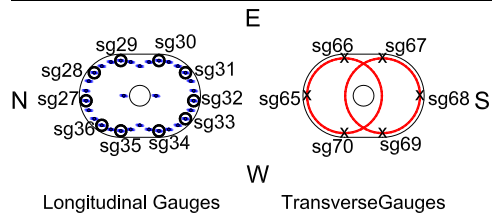
**Table 5-19 Measured Strains in Longitudinal bars and Spirals at 5 in. from the Top of the Footing, Specimen I1**

RUN	Gauge	17	18	19	20	21	22	23	24	25	26	59	60	61	62	63	64
SYLx0.1	MAX	598	827	542	857	1246	947	715	751	912	598	36	11	28	-1	6	2
	MIN	-697	-738	-582	-650	-915	-691	-490	-586	-846	-697	-30	-19	-21	-19	-15	-12
SYLx0.2	MAX	810	2082	1900	2078	5425	2220	1818	1850	1976	810	56	41	120	25	24	30
	MIN	-934	-1266	-649	-1135	-1243	-1334	-932	-973	-1569	-934	-11	-9	-7	-7	-13	0
SYLx0.4	MAX	2775	24745	28259	25495	29941	21969	20959	22054	12315	2775	109	108	160	52	122	123
	MIN	-1847	-1218	-316	-1688	-2490	-991	-4	-2755	-9149	-1847	-20	-13	8	3	-1	11
SYLx0.6	MAX	1903	25214	39072	14049	32063	25022	22308	19859	14175	1903	247	130	205	57	112	180
	MIN	-1167	7294	15789	894	-3385	2107	1505	-2429	-7334	-1167	-34	-2	33	-3	-158	80
SYLx0.8	MAX	2173	28213	37294	3929	38132	32668	27151	24547	21513	2173	410	318	227	145	44	269
	MIN	-1047	5100	8208	367	-5235	2076	7724	-1093	-5158	-1047	23	17	53	-19	-300	112
SYLx1.0	MAX	1783	32219	44431	4001	40153	32731	34671	31272	25863	1783	533	481	200	263	127	402
	MIN	-1303	6437	9246	-799	-7635	5115	10822	2923	-4169	-1303	-20	-20	36	-53	-322	85
SYLx1.2	MAX	1890	36525	39797	3752	39481	30960	41317	26971	25483	1890	718	557	248	351	213	560
	MIN	-1465	9028	15153	-96	-6449	8300	16607	5596	1030	-1465	-149	-50	29	-50	-193	77
SYLx1.4	MAX	2269	37183	16621	3649	39979	15969	47649	20174	14746	2269	973	440	317	377	260	741
	MIN	-1627	12138	13125	94	-5031	7878	24401	7084	2640	-1627	-299	-37	20	-75	-129	69
SYLx1.6	MAX	1900	35412	17209	3842	29520	8055	52959	9237	8881	1900	1058	361	491	644	293	971
	MIN	-3644	14580	12818	815	-152	6838	31430	6688	-6762	-3644	-529	-15	-104	-149	-34	-73
SYLx1.8	MAX	1262	34573	16712	3410	145719	7646	57892	9846	5060	1262	1591	535	1768	1789	518	19060
	MIN	-2521	15602	12585	1459	-262117	6650	39127	7215	3413	-2521	-353	-275	-1727	-108	-104	-236064
SYLx2.0	MAX	707	27679	13644	4590	-218446	7377	57216	7361	4086	707	921	-72	1789	2769	685	-218627
	MIN	-214	13234	11591	1916	-218446	7008	42049	6463	3029	-214	-2	-311	-1968	428	95	-218627



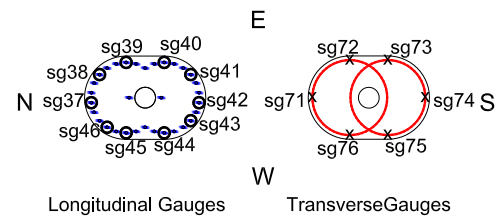
**Table 5-20 Measured Strains in Longitudinal bars and Spirals at 10 in. from the Top of the Footing, Specimen I1**

RUN	Gauge	27	28	29	30	31	32	33	34	35	36	65	66	67	68	69	70
SYLx0.1	MAX	1115	767	367		1085	1106	1006	722		868	47	-23	25	262	32	-1
	MIN	-880	-778	-439		-890	-905	-755	-500		-815	19	-40	-38	205	-300	-16
SYLx0.2	MAX	<b>2466</b>	1830	1300		<b>2417</b>	<b>2391</b>	2106	1701		2031	73	7	58	<b>2452</b>	<b>119766</b>	23
	MIN	-1529	-1339	-421		-1616	-1586	-1393	-969		-1503	30	-35	-39	<b>2306</b>	1897	-10
SYLx0.4	MAX	<b>18815</b>	<b>14728</b>	<b>7214</b>		<b>23065</b>	<b>20587</b>	<b>18212</b>	<b>2712</b>		<b>7656</b>	72	136	177	105	<b>6817</b>	66
	MIN	<b>-5131</b>	-1300	-621		-1999	-1894	-1033	-1479		<b>-8988</b>	-9	-26	-58	-440	340	-7
SYLx0.6	MAX	<b>19123</b>	<b>23704</b>	<b>15527</b>		<b>25539</b>	<b>24860</b>	<b>16560</b>	<b>2930</b>		<b>10207</b>	42	199	156	903	<b>8140</b>	102
	MIN	<b>-3610</b>	<b>4571</b>	<b>2447</b>		-1288	-1546	-540	<b>-2671</b>		<b>-8690</b>	-128	49	-14	113	-1205	13
SYLx0.8	MAX	<b>26943</b>	<b>27398</b>	<b>15462</b>		<b>30876</b>	<b>32855</b>	<b>13906</b>	<b>16730</b>		<b>16598</b>	156	309	240	<b>6605</b>	<b>22864</b>	107
	MIN	-1928	<b>4843</b>	<b>2530</b>		<b>-3582</b>	<b>-4282</b>	<b>-2350</b>	151		<b>-6793</b>	-157	99	60	-714	<b>-3925</b>	37
SYLx1.0	MAX	<b>33847</b>	<b>29885</b>	<b>18271</b>		<b>32461</b>	<b>39443</b>	<b>9394</b>	<b>20655</b>		<b>25318</b>	291	370	237	635	<b>6637</b>	232
	MIN	-924	<b>6325</b>	<b>2591</b>		<b>-5123</b>	<b>-4716</b>	<b>-2665</b>	<b>3151</b>		<b>-7164</b>	-157	76	21	-473	-1032	20
SYLx1.2	MAX	<b>36308</b>	<b>35218</b>	<b>20747</b>		<b>34949</b>	<b>46363</b>	<b>6272</b>	<b>24375</b>		<b>23852</b>	528	578	351	<b>2608</b>	<b>18452</b>	388
	MIN	<b>3608</b>	<b>8779</b>	<b>3327</b>		<b>-3025</b>	<b>-3675</b>	-1537	<b>6033</b>		2090	-391	24	27	-386	<b>-2771</b>	1
SYLx1.4	MAX	<b>8523</b>	<b>39752</b>	<b>22329</b>		<b>39392</b>	<b>53368</b>	<b>3670</b>	<b>27591</b>		<b>7322</b>	636	713	453	1226	<b>6550</b>	499
	MIN	<b>3270</b>	<b>11450</b>	<b>4199</b>		<b>-2294</b>	-1754	48	<b>9710</b>		<b>2573</b>	-270	-31	-17	-596	-1490	-15
SYLx1.6	MAX	<b>7200</b>	<b>43534</b>	<b>23082</b>		<b>42970</b>	<b>60373</b>	<b>3504</b>	<b>26327</b>		<b>7134</b>	1628	815	517	705	<b>94191</b>	706
	MIN	<b>4139</b>	<b>13681</b>	<b>4919</b>		-1632	830	158	<b>12616</b>		<b>3197</b>	-177	-181	-96	-681	<b>-7644</b>	-14
SYLx1.8	MAX	<b>7107</b>	<b>42843</b>	<b>22989</b>		<b>42227</b>	<b>65572</b>	<b>3503</b>	<b>23511</b>		<b>7020</b>	<b>2277</b>	934	<b>122720</b>	<b>15029</b>	<b>31259</b>	1038
	MIN	<b>4272</b>	<b>12052</b>	<b>5267</b>		<b>8092</b>	<b>5442</b>	359	<b>9660</b>		<b>3681</b>	-19	-229	<b>-243890</b>	<b>-2290</b>	<b>-14343</b>	5
SYLx2.0	MAX	<b>6618</b>	<b>21120</b>	<b>19836</b>		<b>34093</b>	<b>248516</b>	<b>3262</b>	<b>10317</b>		<b>6699</b>	<b>2628</b>	1013	<b>92967</b>	<b>75584</b>	<b>48495</b>	887
	MIN	<b>3710</b>	<b>6252</b>	<b>4372</b>		<b>12920</b>	<b>-258615</b>	506	<b>2852</b>		<b>3504</b>	-748	-272	<b>-243888</b>	<b>-31905</b>	<b>-21562</b>	-322



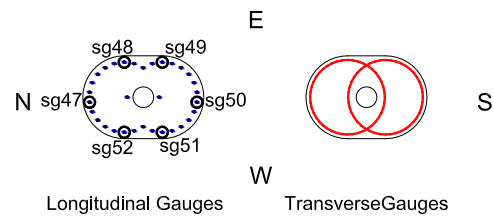
**Table 5-21 Measured Strains in Longitudinal bars and Spirals at 15 in. from the Top of the Footing, Specimen I1**

RUN	Gauge	37	38	39	40	41	42	43	44	45	46	71	72	73	74	75	76
SYLx0.1	MAX	929	826	434	713	898	797	887	700	744	833		-128	1	51	37	-7
	MIN	-788	-879	-476	-647	-722	-653	-629	-450	-607	-731		-143	-14	-3	-47	-21
SYLx0.2	MAX	2088	<b>2131</b>	1191	1830	<b>2209</b>	1972	2072	1686	1803	1938		-46	25	236	107	25
	MIN	-1396	-1511	-867	-1198	-1366	-1287	-1200	-899	-1035	-1377		-110	-7	40	-51	-12
SYLx0.4	MAX	<b>9265</b>	<b>10527</b>	<b>2697</b>	<b>18048</b>	<b>22814</b>	<b>18012</b>	<b>14841</b>	<b>4811</b>	<b>10511</b>	<b>2652</b>		<b>3653</b>	108	276	218	86
	MIN	<b>-2228</b>	-1463	-921	-1163	-1783	-1772	-1148	-800	-2000	<b>-2317</b>		-193	2	126	-65	9
SYLx0.6	MAX	<b>16051</b>	<b>27452</b>	<b>20103</b>	<b>30237</b>	<b>21231</b>	<b>17738</b>	<b>16877</b>	<b>12866</b>	<b>11368</b>	<b>5700</b>		<b>2243</b>	121	443	229	136
	MIN	<b>-3082</b>	<b>2712</b>	-557	<b>3081</b>	1931	864	<b>2473</b>	1859	<b>-3015</b>	<b>-7542</b>		-37	59	229	-76	53
SYLx0.8	MAX	<b>17926</b>	<b>29383</b>	<b>22178</b>	<b>34121</b>	<b>27014</b>	<b>21641</b>	<b>17334</b>	<b>18665</b>	<b>24216</b>	<b>15922</b>		1100	132	784	274	232
	MIN	-1595	<b>8036</b>	<b>4865</b>	<b>3441</b>	-340	-744	1809	<b>6843</b>	603	<b>-4236</b>		-66	8	287	-108	51
SYLx1.0	MAX	<b>22376</b>	<b>27338</b>	<b>25252</b>	<b>33689</b>	<b>32928</b>	<b>27273</b>	<b>22191</b>	<b>20554</b>	<b>27858</b>	<b>17159</b>		1830	296	867	340	237
	MIN	-1367	<b>7082</b>	<b>4125</b>	439	-1874	<b>-2457</b>	586	<b>8099</b>	1974	<b>-4531</b>		-163	36	260	-163	8
SYLx1.2	MAX	<b>27984</b>	<b>20533</b>	<b>29446</b>	<b>30820</b>	<b>36959</b>	<b>31541</b>	<b>26706</b>	<b>22769</b>	<b>32771</b>	<b>22591</b>		<b>2761</b>	330	1202	470	251
	MIN	-731	<b>7105</b>	<b>5441</b>	1938	-1841	<b>-2345</b>	1302	<b>7810</b>	<b>3209</b>	<b>-4747</b>		-177	45	490	-128	-64
SYLx1.4	MAX	<b>32165</b>	<b>18071</b>	<b>31866</b>	<b>31139</b>	<b>41797</b>	<b>35956</b>	<b>30509</b>	<b>25993</b>	<b>40965</b>	<b>26381</b>		<b>2182</b>	362	1176	790	459
	MIN	-69	<b>7429</b>	<b>7311</b>	<b>2220</b>	-1316	-1248	<b>3364</b>	<b>8841</b>	<b>6077</b>	<b>-4840</b>		-86	34	421	18	-102
SYLx1.6	MAX	<b>36550</b>	<b>16804</b>	<b>33475</b>	<b>28550</b>	<b>46299</b>	<b>40250</b>	<b>27829</b>	<b>30189</b>	<b>49250</b>	<b>29094</b>		1778	336	1560	1002	868
	MIN	561	<b>7651</b>	<b>8624</b>	<b>3176</b>	519	616	<b>6045</b>	<b>11161</b>	<b>10311</b>	<b>-5154</b>		69	9	434	75	-81
SYLx1.8	MAX	<b>42134</b>	<b>15834</b>	<b>33866</b>	<b>19483</b>	<b>31308</b>	<b>42732</b>	<b>18110</b>	<b>33024</b>	<b>52828</b>	<b>32099</b>		<b>3527</b>	338	<b>2137</b>	1324	<b>16491</b>
	MIN	<b>2516</b>	<b>7109</b>	<b>8758</b>	<b>4532</b>	<b>-238183</b>	1909	<b>6672</b>	<b>15523</b>	<b>17069</b>	<b>-3600</b>		-20	-59	530	244	<b>-239221</b>
SYLx2.0	MAX	<b>35516</b>	<b>12701</b>	<b>28619</b>	<b>13968</b>	<b>-219917</b>	<b>97116</b>	<b>14990</b>	<b>31018</b>	<b>40001</b>	<b>26068</b>		<b>2874</b>	<b>18090</b>	1658	1570	<b>-218893</b>
	MIN	<b>8009</b>	<b>5131</b>	<b>8935</b>	<b>6091</b>	<b>-219917</b>	<b>20464</b>	<b>6447</b>	<b>18544</b>	<b>20928</b>	<b>6933</b>		-462	<b>-236922</b>	548	299	<b>-218893</b>



**Table 5-22 Measured Strains in Longitudinal bars and Spirals at 20 in. from the Top of the Footing, Specimen I1**

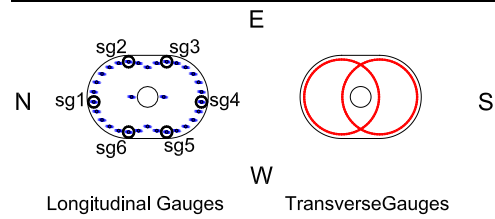
RUN	Gauge	47	48	49	50	51	52
SYLx0.1	MAX	853	446	657	955	949	611
	MIN	-755	-389	-602	-795	-220	-520
SYLx0.2	MAX	1745	2516	1596	2003	1904	1496
	MIN	-1206	648	-1007	-1352	-697	-873
SYLx0.4	MAX	3246	2713	9601	17599	3606	2662
	MIN	-1716	-500	-938	-1783	-1065	-1648
SYLx0.6	MAX	3272	17420	23138	16574	3163	2826
	MIN	-1156	-531	2172	1813	-1717	-2007
SYLx0.8	MAX	2591	16250	26631	16826	17877	5709
	MIN	-277	6140	6227	1030	-606	-1806
SYLx1.0	MAX	2265	21320	25729	20817	22936	17114
	MIN	-486	6629	4482	155	10432	1570
SYLx1.2	MAX	2192	22462	26151	23247	24869	14334
	MIN	-290	6488	2911	201	12892	1868
SYLx1.4	MAX	2051	22669	27346	26020	30322	12593
	MIN	-199	6347	2177	759	15081	1454
SYLx1.6	MAX	2132	23363	27436	29007	28811	13586
	MIN	100	6197	2598	1614	15358	1792
SYLx1.8	MAX	2551	22769	91479	26503	38152	14114
	MIN	280	5821	-245756	3250	18691	2808
SYLx1.4*	MAX	3858	18511	-220289	16732	38509	11757
	MIN	412	7370	-220289	10951	4293	4353





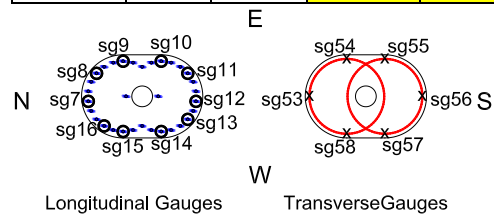
**Table 5-23 Measured Strains in Longitudinal bars and Spirals at -5 in. from the Top of the Footing, Specimen I2**

RUN	Gauge	1	2	3	4	5	6
SYLx0.1	MAX	286	223	277	515	396	377
	MIN	-207	-122	-127	-212	-94	-173
SYLx0.2	MAX	1028	643	807	1375	1023	902
	MIN	-404	-254	-265	-456	-238	-324
SYLx0.4	MAX	1918	1512	1826	<b>2195</b>	1943	2108
	MIN	-1166	-536	-798	-1038	-427	-933
SYLx0.6	MAX	<b>2249</b>	<b>2166</b>	2115	<b>7250</b>	<b>2178</b>	<b>2349</b>
	MIN	-1543	-834	-983	-1345	-948	-1164
SYLx0.8	MAX	<b>2541</b>	<b>2301</b>	<b>2362</b>	<b>7770</b>	<b>2474</b>	<b>2432</b>
	MIN	-1728	-1088	-1143	-1876	-978	-1419
SYLx1.0	MAX	<b>2629</b>	<b>2559</b>	<b>2432</b>	<b>25455</b>	<b>2649</b>	<b>2589</b>
	MIN	-1890	-1204	-1314	<b>-12031</b>	-1092	-1562
SYLx1.2	MAX	<b>18026</b>	<b>2864</b>	<b>2616</b>	<b>16759</b>	<b>7322</b>	<b>3102</b>
	MIN	-900	-1375	-1514	747	-1200	-1823
SYLx1.4	MAX	<b>17473</b>	<b>3233</b>	<b>2807</b>	<b>20053</b>	<b>16869</b>	<b>17997</b>
	MIN	324	-1490	-1719	537	213	-564
SYLx1.6	MAX	<b>22248</b>	<b>4129</b>	<b>2890</b>	<b>23589</b>	<b>15085</b>	<b>21897</b>
	MIN	<b>3527</b>	-1672	-1988	964	<b>4644</b>	1077
SYLx1.8	MAX	<b>27913</b>	<b>6988</b>	<b>6486</b>	<b>26940</b>	<b>10339</b>	<b>22453</b>
	MIN	<b>9889</b>	-1419	<b>-3013</b>	5435	<b>6372</b>	<b>4795</b>
SYLx1.4*	MAX	<b>36292</b>	<b>6483</b>	<b>8859</b>	<b>19900</b>	<b>7155</b>	<b>6842</b>
	MIN	<b>15666</b>	-1449	<b>-3281</b>	<b>15003</b>	<b>5535</b>	<b>6197</b>



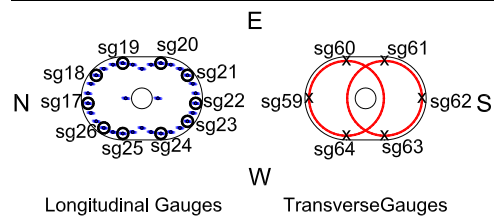
**Table 5-24 Measured Strains in Longitudinal bars and Spirals at 0 in. from the Top of the Footing, Specimen I2**

RUN	Gauge	7	8	9	10	11	12	13	14	15	16	53	54	55	56	57	58
SYLx0.1	MAX	1031	905	2065	1050	1268		1081	858	769	876	30	97	33	104	66	16
	MIN	-456	-516	962	-300	-378		-364	-145	-314	-495	-16	34	-22	24	8	-54
SYLx0.2	MAX	<b>2191</b>	<b>2254</b>	<b>7814</b>	<b>2183</b>	<b>2538</b>		<b>2304</b>	1725	1620	1990	65	127	89	143	126	52
	MIN	-881	-987	-1950	-585	-841		-811	-476	-561	-963	-36	-29	10	4	11	-53
SYLx0.4	MAX	<b>14302</b>	<b>5670</b>	<b>19221</b>	<b>24054</b>	<b>21692</b>		<b>18936</b>	<b>18811</b>	<b>18031</b>	<b>20395</b>	98	190	-31	135	23	159
	MIN	-1724	<b>-3111</b>	<b>-2789</b>	-1103	-1555		-609	190	-805	-1835	-73	-51	-152	-38	-139	-55
SYLx0.6	MAX	<b>12026</b>	291	<b>24744</b>	<b>20369</b>	<b>28812</b>		<b>21864</b>	<b>20014</b>	<b>18301</b>	<b>20275</b>	153	449	806	262	334	200
	MIN	<b>2731</b>	-1937	<b>6986</b>	<b>2663</b>	1009		<b>2767</b>	1724	2034	1704	-74	-64	3	-4	-65	-62
SYLx0.8	MAX	<b>14902</b>	452	<b>23776</b>	<b>21061</b>	<b>31917</b>		<b>25976</b>	<b>22124</b>	<b>20608</b>	<b>46111</b>	177	586	461	275	121	453
	MIN	<b>2766</b>	-1657	<b>-4921</b>	36	-180		<b>4823</b>	<b>6845</b>	1200	<b>5370</b>	-67	-58	-258	22	-110	-20
SYLx1.0	MAX	<b>16562</b>	504	<b>22806</b>	<b>10996</b>	<b>15922</b>		<b>29537</b>	<b>29019</b>	<b>25760</b>	<b>51753</b>	203	549	1280	543	412	<b>37936</b>
	MIN	<b>4856</b>	<b>-2742</b>	<b>-13745</b>	535	-1385		<b>6400</b>	<b>8278</b>	<b>4093</b>	<b>5684</b>	-46	-105	-72	7	-26	-118
SYLx1.2	MAX	<b>15870</b>	-17	<b>11588</b>	<b>5137</b>	<b>8496</b>		<b>20731</b>	<b>34960</b>	<b>12523</b>	<b>7509</b>	197	546	<b>22513</b>	684	354	<b>57681</b>
	MIN	<b>3985</b>	<b>-3651</b>	<b>-33377</b>	1027	<b>-3084</b>		<b>7976</b>	<b>11156</b>	<b>3885</b>	<b>5644</b>	-1	-112	-315	29	42	<b>-4599</b>
SYLx1.4	MAX	<b>9556</b>	<b>2766</b>	<b>19827</b>	<b>5009</b>	<b>8911</b>		<b>9813</b>	<b>35924</b>	<b>7848</b>	<b>34136</b>	321	839	<b>13084</b>	838	<b>3516</b>	158
	MIN	1110	<b>-5860</b>	<b>-86899</b>	597	<b>-7700</b>		<b>6062</b>	<b>17040</b>	<b>3506</b>	<b>3760</b>	-10	-40	287	42	99	-22
SYLx1.6	MAX	<b>6265</b>	866	<b>28376</b>	<b>5323</b>	<b>3381</b>		<b>7412</b>	<b>17694</b>	<b>6582</b>	<b>10036</b>	421	1170	<b>221070</b>	871	640	286
	MIN	403	<b>-20471</b>	<b>-253200</b>	1038	<b>-24089</b>		<b>3275</b>	<b>10160</b>	<b>2653</b>	<b>5221</b>	-293	-47	<b>-5427</b>	-300	-205	-47
SYLx1.8	MAX	<b>5527</b>	-1164	<b>33612</b>	<b>5768</b>	<b>2282</b>		<b>6767</b>	<b>14088</b>	<b>7580</b>	<b>45672</b>	745	1320	<b>-218287</b>	1030	440	<b>14704</b>
	MIN	<b>-5712</b>	<b>-38896</b>	<b>-245398</b>	265	<b>-25617</b>		<b>2417</b>	<b>10510</b>	<b>3034</b>	456	-227	17	<b>-218287</b>	-628	-228	<b>-2598</b>
SYLx2.0	MAX	<b>3888</b>	<b>-2803</b>	<b>11727</b>	<b>5889</b>	<b>2714</b>		<b>5859</b>	<b>11938</b>	<b>5596</b>	<b>22263</b>	661	1294	<b>110030</b>	148	512	<b>8964</b>
	MIN	-1872	<b>-15960</b>	<b>-169955</b>	819	<b>-4601</b>		<b>3103</b>	<b>9436</b>	<b>2785</b>	66	-41	229	<b>-3465</b>	-663	-199	27



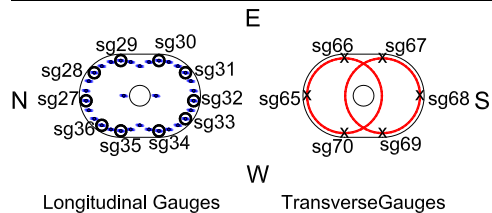
**Table 5-25 Measured Strains in Longitudinal bars and Spirals at 5 in. from the Top of the Footing, Specimen I2**

RUN	Gauge	17	18	19	20	21	22	23	24	25	26	59	60	61	62	63	64
SYLx0.1	MAX	1315	1249	1111	1018	1254	1286	1221	1153	920	1106	115	11	69	139	137	55
	MIN	-397	-395	-123	-171	-208	-320	-174	-61	-175	-325	74	-2	51	68	83	40
SYLx0.2	MAX	<b>2759</b>	<b>2679</b>	1805	2067	<b>2537</b>	<b>2550</b>	<b>2470</b>	<b>2165</b>	1785	<b>2240</b>	155	14	111	224	338	62
	MIN	-1017	-1017	-898	-544	-736	-1005	-682	-486	-572	-975	80	1	80	99	242	47
SYLx0.4	MAX	<b>11313</b>	<b>12163</b>	<b>23746</b>	<b>18555</b>	<b>22417</b>	<b>21040</b>	<b>17321</b>	<b>17288</b>	<b>10473</b>	<b>13480</b>	367	14	217	240	36	194
	MIN	<b>-7760</b>	-1720	-1094	-654	-1127	-1345	-333	400	<b>-2267</b>	<b>-10293</b>	43	3	106	107	-65	101
SYLx0.6	MAX	<b>6576</b>	<b>3141</b>	<b>25163</b>	<b>24229</b>	<b>27327</b>	<b>24979</b>	<b>20322</b>	<b>14778</b>	<b>16326</b>	<b>17775</b>	745	20	331	302	805	419
	MIN	<b>-4171</b>	1753	<b>8879</b>	<b>2603</b>	-154	-645	1977	<b>2244</b>	<b>-7380</b>	<b>-9859</b>	93	7	191	114	262	105
SYLx0.8	MAX	<b>4263</b>	<b>3297</b>	<b>27604</b>	<b>34290</b>	<b>32121</b>	<b>30132</b>	<b>24888</b>	<b>11054</b>	<b>21792</b>	<b>18470</b>	762	23	380	248	<b>40254</b>	500
	MIN	<b>-4363</b>	1753	<b>6343</b>	<b>3661</b>	-974	<b>-3258</b>	<b>3454</b>	<b>4790</b>	<b>-5512</b>	<b>-4453</b>	91	8	188	115	<b>-4981</b>	105
SYLx1.0	MAX	<b>2126</b>	<b>211561</b>	<b>24286</b>	<b>120814</b>	<b>16097</b>	<b>14669</b>	<b>29357</b>	<b>9363</b>	<b>29540</b>	<b>4035</b>	994	46	549	353	<b>35733</b>	504
	MIN	<b>-2453</b>	<b>-216770</b>	<b>6075</b>	<b>-217900</b>	-863	<b>-2686</b>	<b>4923</b>	<b>4606</b>	-680	-1425	150	-26	157	85	157	78
SYLx1.2	MAX	<b>2481</b>	<b>19615</b>	<b>32709</b>	<b>-132476</b>	<b>9096</b>	<b>6589</b>	<b>33809</b>	<b>5133</b>	<b>14544</b>	<b>3165</b>	1181	24	601	441	<b>2751</b>	466
	MIN	<b>-2760</b>	-43	1643	<b>-231037</b>	2055	2089	<b>7492</b>	<b>3784</b>	<b>5138</b>	633	380	10	187	39	-139	44
SYLx1.4	MAX	<b>2558</b>	<b>19408</b>	<b>7168</b>	<b>11047</b>	<b>7191</b>	<b>5815</b>	<b>29327</b>	<b>4448</b>	<b>7150</b>	<b>2765</b>	723	25	661	558	<b>5136</b>	576
	MIN	<b>-3187</b>	-10	<b>4891</b>	<b>6431</b>	<b>4472</b>	<b>2910</b>	<b>11394</b>	<b>3481</b>	<b>5418</b>	1158	-588	13	166	74	-910	-2
SYLx1.6	MAX	<b>2484</b>	<b>27684</b>	<b>6727</b>	<b>20672</b>	<b>6235</b>	<b>5251</b>	<b>11687</b>	<b>4279</b>	<b>6425</b>	<b>2503</b>	<b>17085</b>	16	638	575	<b>21717</b>	806
	MIN	<b>-4055</b>	<b>-189987</b>	<b>4917</b>	<b>-73444</b>	<b>4427</b>	<b>2547</b>	<b>8408</b>	<b>2714</b>	<b>5280</b>	1262	-1225	3	-65	28	<b>-3234</b>	-367
SYLx1.8	MAX	1813	<b>3241</b>	<b>7691</b>	<b>8404</b>	<b>5710</b>	<b>4965</b>	<b>10286</b>	<b>22273</b>	<b>6287</b>	2054	<b>16510</b>	19	1261	1326	<b>3196</b>	1217
	MIN	-694	1653	<b>4784</b>	<b>6862</b>	<b>4874</b>	1690	<b>8027</b>	1027	<b>4927</b>	1142	<b>3352</b>	2	-254	-254	-430	<b>-2152</b>
SYLx2.0	MAX	<b>77963</b>	<b>17674</b>	<b>10814</b>	<b>24355</b>	<b>5448</b>	<b>4432</b>	<b>9431</b>	<b>4982</b>	<b>7747</b>	1902	<b>18859</b>	327	2094	281	<b>5050</b>	<b>4122</b>
	MIN	<b>-111206</b>	898	<b>-28311</b>	<b>-247773</b>	<b>4465</b>	1547	<b>8504</b>	<b>3265</b>	<b>4711</b>	601	<b>-235423</b>	-4	-443	-1668	164	-1814



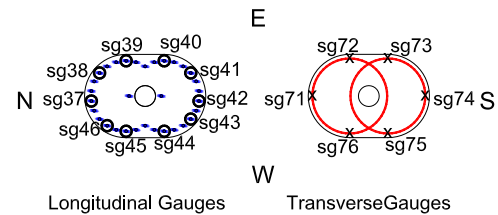
**Table 5-26 Measured Strains in Longitudinal bars and Spirals at 10 in. from the Top of the Footing, Specimen I2**

RUN	Gauge	27	28	29	30	31	32	33	34	35	36	65	66	67	68	69	70
SYLx0.1	MAX	870	960		418	878	1144	993	949	891	941	64	50	64	-270	84	185
	MIN	-412	-333		-532	-698	-356	-211	-60	-116	-340	45	34	43	-493	64	170
SYLx0.2	MAX	<b>2308</b>	<b>2434</b>		<b>-2699</b>	<b>2532</b>	<b>2267</b>	2070	1802	<b>2163</b>	2105	293	108	109	-175	165	9
	MIN	-1013	-994		<b>-4835</b>	-1670	-1019	-761	-468	-188	-934	-18	43	58	-498	96	-14
SYLx0.4	MAX	<b>16654</b>	<b>20099</b>		<b>5924</b>	<b>12342</b>	<b>9154</b>	<b>2768</b>	<b>7009</b>	<b>18233</b>	<b>18438</b>	<b>37474</b>	192	145	<b>42232</b>	290	134
	MIN	<b>-5183</b>	-1548		1571	<b>-4493</b>	<b>-3388</b>	-1522	-446	-1066	<b>-3162</b>	<b>-2620</b>	54	77	<b>-2667</b>	126	-22
SYLx0.6	MAX	<b>13862</b>	<b>22413</b>		<b>33050</b>	<b>19413</b>	<b>17568</b>	<b>10666</b>	<b>18459</b>	<b>122913</b>	<b>17967</b>	1434	369	241	<b>3942</b>	396	273
	MIN	<b>-4671</b>	1491		<b>-7704</b>	<b>-4603</b>	<b>-4668</b>	-1931	1761	1137	<b>-3285</b>	18	14	123	<b>-18991</b>	214	-9
SYLx0.8	MAX	<b>15290</b>	<b>14364</b>		<b>-136736</b>	<b>27088</b>	<b>26516</b>	<b>17828</b>	<b>19098</b>	<b>95044</b>	<b>17057</b>	<b>35717</b>	532	360	<b>79270</b>	370	470
	MIN	<b>-5860</b>	<b>3924</b>		<b>-236304</b>	<b>-6032</b>	<b>-6128</b>	-1169	<b>5367</b>	878	<b>-2529</b>	<b>-131088</b>	-98	101	<b>-14761</b>	174	139
SYLx1.0	MAX	<b>18166</b>	<b>5882</b>		<b>2734</b>	<b>26122</b>	<b>23270</b>	<b>21138</b>	<b>23288</b>	<b>166958</b>	<b>10189</b>	543	765	477	<b>209260</b>	353	700
	MIN	<b>-6301</b>	<b>3840</b>		<b>-3846</b>	<b>-6243</b>	<b>-7672</b>	464	<b>7767</b>	<b>2673</b>	-216	-111	-111	85	<b>-218790</b>	131	150
SYLx1.2	MAX	<b>10661</b>	<b>5284</b>		71	<b>23880</b>	<b>9728</b>	<b>24900</b>	<b>28442</b>	<b>102483</b>	<b>4011</b>	2116	824	524	<b>82464</b>	432	722
	MIN	-1464	<b>4092</b>		<b>-3273</b>	<b>-4854</b>	<b>-3015</b>	<b>2337</b>	<b>10887</b>	-453	1111	-93	-160	119	<b>-6770</b>	107	197
SYLx1.4	MAX	<b>3868</b>	<b>5048</b>		-447	<b>12843</b>	<b>4760</b>	<b>29797</b>	<b>33990</b>	<b>61226</b>	<b>3553</b>	1489	913	565	860	518	837
	MIN	-1146	<b>3833</b>		<b>-2801</b>	368	-503	<b>4640</b>	<b>15828</b>	<b>3319</b>	1387	-74	-398	140	-545	86	139
SYLx1.6	MAX	<b>3361</b>	<b>4888</b>		-492	<b>37249</b>	<b>4068</b>	<b>32455</b>	<b>38483</b>	<b>91485</b>	<b>3262</b>	987	859	558	<b>23741</b>	503	454
	MIN	-1779	<b>3758</b>		<b>-3266</b>	<b>2544</b>	-1141	<b>7275</b>	<b>21397</b>	-700	1567	-110	-530	91	<b>-3106</b>	-29	52
SYLx1.8	MAX	<b>8093</b>	<b>4800</b>		-805	<b>42063</b>	<b>3883</b>	<b>31686</b>	<b>41841</b>	<b>47205</b>	<b>19877</b>	898	799	719	<b>93132</b>	693	<b>17581</b>
	MIN	<b>-47174</b>	<b>3694</b>		<b>-3179</b>	<b>-237140</b>	<b>-3336</b>	9808	<b>25992</b>	<b>-2168</b>	<b>-234263</b>	-280	-576	118	<b>-10812</b>	-31	<b>-236356</b>
SYLx2.0	MAX	<b>14233</b>	<b>63743</b>		276	<b>203554</b>	<b>19611</b>	<b>27356</b>	<b>36626</b>	<b>21853</b>	<b>-217548</b>	<b>16076</b>	142	<b>19570</b>	<b>100613</b>	974	<b>-219131</b>
	MIN	<b>-9128</b>	<b>-242946</b>		<b>-3055</b>	<b>-5998</b>	<b>-236083</b>	<b>13017</b>	<b>27166</b>	-859	<b>-217548</b>	<b>-235814</b>	-703	<b>-239415</b>	<b>-238073</b>	-77	<b>-219131</b>



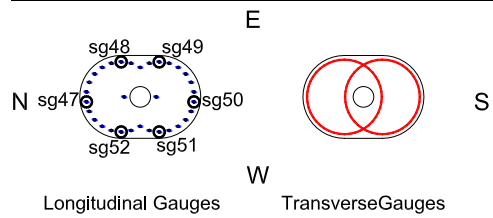
**Table 5-27 Measured Strains in Longitudinal bars and Spirals at 15 in. from the Top of the Footing, Specimen I2**

RUN	Gauge	37	38	39	40	41	42	43	44	45	46	71	72	73	74	75	76
SYLx0.1	MAX	1219	1190		700	903	961	918	833	794	921	76	35	33	68	53	148
	MIN	-360	-291		-85	-152	-263	-157	-22	-153	-351	41	8	11	56	39	92
SYLx0.2	MAX	<b>2314</b>	<b>2304</b>		1432	1926	2051	1974	1606	1594	1867	113	51	51	116	107	233
	MIN	-916	-913		-389	-627	-849	-659	-370	-506	-909	48	4	20	68	60	141
SYLx0.4	MAX	<b>3953</b>	<b>6569</b>		<b>2698</b>	<b>2916</b>	<b>3069</b>	<b>2763</b>	<b>2773</b>	<b>5789</b>	<b>3010</b>	154	616	80	192	230	354
	MIN	-1963	-1444		-1247	-1707	-1628	-1306	-391	-1178	-1933	83	76	17	118	90	185
SYLx0.6	MAX	<b>18610</b>	<b>14201</b>		<b>2957</b>	<b>18731</b>	<b>17926</b>	<b>3320</b>	<b>2853</b>	<b>7889</b>	<b>10142</b>	257	241	121	257	325	408
	MIN	<b>-5743</b>	1043		-1554	-1867	-2044	-1702	-1237	<b>-2309</b>	<b>-5854</b>	97	104	65	189	202	222
SYLx0.8	MAX	<b>18643</b>	<b>11767</b>		<b>16625</b>	<b>23740</b>	<b>22153</b>	<b>18595</b>	<b>3350</b>	<b>15173</b>	<b>17836</b>	287	347	166	323	458	454
	MIN	<b>-2286</b>	733		-1541	-2060	<b>-3774</b>	-1671	-877	-1923	<b>-3179</b>	121	139	108	205	255	253
SYLx1.0	MAX	<b>25023</b>	<b>7759</b>		<b>17208</b>	<b>21956</b>	<b>28484</b>	<b>19710</b>	<b>18610</b>	<b>17813</b>	<b>20091</b>	484	490	<b>209870</b>	497	634	582
	MIN	-889	595		-72	<b>-2445</b>	<b>-3608</b>	1490	849	-889	<b>-2792</b>	144	157	<b>-218639</b>	157	281	216
SYLx1.2	MAX	<b>25364</b>	<b>6063</b>		<b>19214</b>	<b>5599</b>	<b>30778</b>	<b>24151</b>	<b>22230</b>	<b>23408</b>	<b>27281</b>	678	624	237	640	824	535
	MIN	52	1262		-19	247	<b>-2859</b>	<b>3086</b>	<b>8186</b>	208	-1423	190	182	16	194	294	139
SYLx1.4	MAX	<b>20332</b>	<b>4432</b>		<b>20125</b>	<b>3300</b>	<b>25122</b>	<b>29463</b>	<b>26435</b>	<b>24563</b>	<b>30653</b>	743	<b>4570</b>	214	644	977	518
	MIN	292	1976		354	1352	-1268	<b>6136</b>	<b>11109</b>	1465	228	213	-116	-10	174	247	-79
SYLx1.6	MAX	<b>14521</b>	<b>3958</b>		<b>19706</b>	<b>3157</b>	<b>17708</b>	<b>33236</b>	<b>29956</b>	<b>11127</b>	<b>20547</b>	836	<b>3324</b>	375	689	883	<b>16700</b>
	MIN	2088	2058		686	1387	1290	<b>8499</b>	<b>14726</b>	<b>4100</b>	<b>5567</b>	123	-314	-196	79	103	<b>-235222</b>
SYLx1.8	MAX	<b>9718</b>	<b>3690</b>		<b>18832</b>	<b>22860</b>	<b>15057</b>	<b>33823</b>	<b>35158</b>	<b>5748</b>	<b>24664</b>	1123	<b>2281</b>	453	799	926	<b>-218749</b>
	MIN	<b>4406</b>	<b>2132</b>		1081	<b>-227621</b>	<b>3294</b>	<b>11825</b>	<b>18911</b>	<b>4517</b>	<b>-234961</b>	135	-33	-396	143	31	<b>-218749</b>
SYLx2.0	MAX	<b>12100</b>	<b>3664</b>		<b>14936</b>	<b>26969</b>	<b>38804</b>	<b>29398</b>	<b>37529</b>	<b>5288</b>	<b>-217374</b>	721	717	191	<b>19894</b>	742	<b>-218749</b>
	MIN	<b>5036</b>	<b>2341</b>		<b>2120</b>	<b>-248530</b>	<b>-251743</b>	<b>15780</b>	<b>23405</b>	<b>4764</b>	<b>-217374</b>	151	95	-388	<b>-236738</b>	49	<b>-218749</b>



**Table 5-28 Measured Strains in Longitudinal bars and Spirals at 20 in. from the Top of the Footing, Specimen I2**

RUN	Gauge	47	48	49	50	51	52
SYLx0.1	MAX	743	660	918	1272	920	690
	MIN	-304	-133	-120	-306	-6	-126
SYLx0.2	MAX	1821	1452	<b>2168</b>	<b>2403</b>	1768	1374
	MIN	-911	-462	-142	-893	-380	-481
SYLx0.4	MAX	<b>3012</b>	<b>2396</b>	<b>6044</b>	<b>18780</b>	<b>2853</b>	<b>2824</b>
	MIN	-1563	-682	-593	-994	-406	-1155
SYLx0.6	MAX	<b>3315</b>	<b>8015</b>	<b>4864</b>	<b>19662</b>	<b>2790</b>	<b>3013</b>
	MIN	-2009	-530	1860	<b>2366</b>	-1125	-1669
SYLx0.8	MAX	<b>3553</b>	<b>9826</b>	<b>3961</b>	<b>20973</b>	<b>13678</b>	<b>9565</b>
	MIN	<b>-2234</b>	<b>2969</b>	1725	913	-352	-2019
SYLx1.0	MAX	<b>12666</b>	<b>12928</b>	<b>5155</b>	<b>20948</b>	<b>20750</b>	<b>14985</b>
	MIN	-216	<b>3459</b>	1496	608	<b>6943</b>	477
SYLx1.2	MAX	2051	<b>16268</b>	<b>5819</b>	<b>21499</b>	<b>22576</b>	<b>8949</b>
	MIN	931	<b>3652</b>	1430	837	<b>11897</b>	704
SYLx1.4	MAX	1609	<b>18491</b>	<b>22264</b>	<b>18964</b>	<b>25078</b>	<b>5402</b>
	MIN	935	<b>3893</b>	332	1898	<b>12937</b>	1132
SYLx1.6	MAX	1463	<b>18179</b>	<b>8178</b>	<b>6664</b>	<b>27421</b>	<b>4940</b>
	MIN	811	<b>4235</b>	981	<b>2476</b>	<b>15268</b>	1270
SYLx1.8	MAX	<b>2121</b>	<b>18683</b>	<b>177631</b>	<b>230034</b>	<b>30186</b>	<b>4821</b>
	MIN	855	<b>4766</b>	<b>-76956</b>	<b>-266797</b>	<b>17475</b>	1564
SYLx1.4*	MAX	<b>35051</b>	<b>17914</b>	<b>178475</b>	<b>220026</b>	<b>30857</b>	<b>4064</b>
	MIN	<b>-3310</b>	<b>6728</b>	<b>-102525</b>	<b>-244524</b>	<b>18708</b>	1964



**Table 5-29 Values for Idealized Force-Displacement and Moment-Curvature**

Specimen	Yielding Displacement (in)	Ultimate Displacement (in)	Yielding Curvature (rad/in)	Ultimate Curvature (rad/in)	Displacement Ductility	Curvature Ductility
I1-Longitudinal	1.2	6.2	0.00055	0.00525	5.4	9.5
I1- Transverse	1.3	7.9	0.00073	0.00735	6.2	10.0
I2-Longitudinal	1.4	6.4	0.00058	0.00552	4.4	9.5
I2- Transverse	1.1	7.8	0.00068	0.00786	7.1	11.5

**Table 5-30 Plastic Hinge Lengths**

Plastic Hinge Lengths (in)	I1	I2
Measured	16.88	15.57
Priestley Equation	11.28	11.28

**Table 6-1 Testing Protocol for Specimens 9F1**

Run	Input Ground Motion
A	Low level Random
1	El Centro x 1/3
2	El Centro x 2/3
B	Snap back test
3	El Centro x 1.0
4	El Centro x 1.5
5	El Centro x 2.0
C	Snap back test
6	El Centro x 2.5
7	El Centro x 3.0
D	Snap back test
8	El Centro x 3.5
9	El Centro x 4.0

**Table 6-2 Testing Protocol for Specimens NF1**

Run	Input Ground Motion
A	Quick release
1	Rinaldi x 0.05
2	Rinaldi x 0.1
3	Rinaldi x 0.2
4	Rinaldi x 0.3
B	Quick release
5	Rinaldi x 0.45
6	Rinaldi x 0.6
7	Rinaldi x 0.75
C	Quick release
8	Rinaldi x 0.9
9	Rinaldi x 1.05
10	Rinaldi x 1.20
11	Rinaldi x 1.35



**Table 6-3 Concrete Compressive Strength**

Element	9F1 (psi)	NF1 (psi)	ISL1.0 (psi)
Footing	3825	5610	7083
Column	5428	5990	5350

**Table 6-4 Reinforcing Steel Properties**

Specimen	9F1		NF1		ISL1.0	
	Spiral (W5.0)	#4 bar	Spiral (W5.0)	#4 bar	Spiral (W2.9)	#3 bar
Yield Stress (ksi)	57.64	65	57.5	68	65	63
Yield Strain	0.0024	0.00224	0.0022	0.0022	0.00224	0.0022
Strain at hardening	W/O plateau	0.008	W/O plateau	0.0057	W/O plateau	0.008
Peak Stress (ksi)	70.9	104.3	74.05	93.4	77	99
Strain at Peak	0.114	0.11	Not measured	0.10	Not measured	0.16

**Table 6-5 Testing Protocol for Specimens ISL1.0**

Run	Input Ground Motion
A	Free vibration
1	Sylmar x 0.1
2	Sylmar x 0.2
3	Sylmar x 0.3
B	Free vibration
4	Sylmar x 0.5
5	Sylmar x 0.75
6	Sylmar x 1.0
C	Free vibration
7	Sylmar x 1.25
8	Sylmar x 1.50
9	Sylmar x 1.75
10	Sylmar x 2.0

**Table 6-6 Measured Response for Circular Specimens 9F1 and NF1**

Property	Specimen	Run										
		1	2	3	4	5	6	7	8	9	10	11
Earthquake factor	9F1	0.33	0.66	1.0	1.5	2.0	2.5	3.0	3.5	4.0	NA	NA
	NF1	0.05	0.10	0.20	0.30	0.45	0.60	0.75	0.90	1.05	1.20	1.35
Max. Table Displacement (in)	9F1	0.39	0.80	1.31	1.94	2.53	3.15	3.73	4.30	4.84	NA	NA
	NF1	0.17	0.36	0.71	0.93	1.44	2.01	2.58	3.16	3.74	4.31	4.87
Max. Table Acceleration (g)	9F1	0.08	0.17	0.26	0.40	0.66	0.78	1.15	0.89	0.99	NA	NA
	NF1	0.04	0.05	0.10	0.18	0.25	0.32	0.38	0.47	0.54	0.63	0.70
Peak Force (kips) (Base Shear)	9F1	15.56	23.91	30.86	31.95	31.41	32.10	33.09	33.33	26.67	NA	NA
	NF1	7.37	12.29	21.91	28.21	30.81	30.91	30.77	30.61	30.69	29.73	24.73
Base Moment (k-in)	9F1	1120.3	1721.5	2221.9	2300.4	2261.5	2311.2	2382.5	2399.8	1920.2	NA	NA
	NF1	530.6	884.9	1577.5	2031.1	2218.3	2225.5	2215.4	2203.9	2209.7	2140.6	1780.6
Displacement at Peak Force (in)	9F1	0.63	1.16	1.84	2.41	2.72	2.68	4.90	5.93	8.73	NA	NA
	NF1	0.15	0.30	0.80	1.47	2.66	4.32	5.99	7.20	8.43	9.49	10.7
Displacement Ductility	9F1	0.4	0.8	1.2	1.6	1.8	1.7	3.2	3.9	5.7	NA	NA
	NF1	0.1	0.3	0.7	1.3	2.4	3.9	5.5	6.6	7.7	8.7	9.7
Drift ratio (%)	9F1	0.87	1.62	2.55	3.34	3.78	3.73	6.80	8.24	12.13	NA	NA
	NF1	0.21	0.42	1.11	2.04	3.70	6.00	8.31	10.00	11.70	13.18	14.79
Residual Displacement (in)	9F1	0.01	0.23	-0.06	-0.06	-0.09	-0.06	0.21	1.50	15.86	NA	NA
	NF1	0.01	0.02	0.02	0.12	0.46	1.05	2.15	3.00	4.23	6.08	15.07
Residual Drift (%)	9F1	0.014	0.319	-0.083	-0.083	-0.125	-0.083	0.292	2.083	22.028	NA	NA
	NF1	0.011	0.025	0.029	0.167	0.642	1.464	2.988	4.167	5.881	8.441	20.925
Axial Load (kips)	9F1	86.3	90.9	97.2	101.4	103.0	109.1	114.4	115.7	106.6	NA	NA
	NF1	76.9	77.8	78.4	78.9	79.1	79.5	79.4	79.4	79.6	79.3	79.8

**Table 6-7 Measured Response for Interlocking Specimen ISL1.0**

Property	Peak	Run									
		1	2	3	4	5	6	7	8	9	10
Earthquake factor	Sylmar x	0.1	0.2	0.3	0.5	0.75	1.0	1.25	1.5	1.75	2.0
Max. Table Displacement (in)	MAX	0.18	0.38	0.55	0.93	1.38	1.85	2.27	2.76	3.17	3.52
	MIN	-0.19	-0.37	-0.60	-0.92	-1.43	-1.88	-2.39	-2.82	-3.26	-3.72
Max. Table Acceleration (g)	MAX	0.07	0.14	0.22	0.32	0.54	0.73	0.94	1.13	1.33	1.53
	MIN	-0.04	-0.08	-0.12	-0.22	-0.34	-0.45	-0.60	-0.81	-0.97	-1.13
Peak Force (kips) (Base Shear)	MAX	10.3	12.4	25.1	30.1	30.5	31.8	32.1	30.2	27	30.4
	MIN	-11.4	-15.9	-29.9	-35	-31.2	-34.7	-37.1	-38	-38.9	-38.6
Base Moment (k-in)	MAX	597.4	719.2	1455.8	1745.8	1769	1844.4	1861.8	1751.6	1566	1763.2
	MIN	-661.2	-922.2	-1734.2	-2030	-1809.6	-2012.6	-2151.8	-2204	-2256.2	-2238.8
Displacement at Peak Force (in)	MAX	0.11	0.15	0.47	0.81	0.83	1.00	1.25	1.35	1.19	1.51
	MIN	-0.11	-0.23	-0.54	-1.00	-0.96	-1.31	-1.84	-2.75	-3.73	-5.42
Drift ratio (%)	MAX	0.19	0.26	0.81	1.40	1.43	1.72	2.16	2.33	2.05	2.60
	MIN	-0.19	-0.40	-0.93	-1.72	-1.66	-2.26	-3.17	-4.74	-6.43	-9.34
Axial Load (kips)	MAX	89.7	91.3	92.9	92.8	93.0	93.6	94.2	94.8	95.2	95.7
	MIN	89.0	88.9	87.8	88.0	87.3	87.3	87.0	87.1	87.5	87.7
Residual Displacement (in)	MAX	0.001	0.005	0.008	0.006	0.027	0.020	0.035	-0.150	-0.421	-2.092
Residual Drift (%)	MAX	0.002	0.008	0.014	0.010	0.047	0.035	0.060	-0.258	-0.727	-3.607
Displacement Ductility	MAX	0.2	0.3	0.8	1.4	1.4	1.7	2.8	4.3	5.5	9.3

**Table 6-8 Measured Dynamic Properties**

Specimen	Property	Run										
		1	2	3	4	5	6	7	8	9	10	11
<b>9F1</b>	$E_l/E_l^g$ *	0.24	0.21	0.17	0.14	0.13	0.13	0.13	0.12	0.09	NA	NA
	Period (s)	0.57	0.60	0.68	0.74	0.77	0.77	0.78	0.80	0.95	NA	NA
<b>NF1</b>	$E_l/E_l^g$	0.59	0.49	0.35	0.17	0.17	0.15	0.14	0.13	0.06	0.06	0.06
	Period (s)	0.34	0.35	0.42	0.51	0.51	0.55	0.55	0.68	0.69	0.69	0.70
<b>ISL1.0</b>	$E_l/E_l^g$	0.31	0.28	0.20	0.13	0.13	0.12	0.12	0.08	0.07	0.07	NA
	Period (s)	0.31	0.39	0.44	0.55	0.57	0.63	0.72	0.87	1.01	1.22	NA
<b>C1</b>	$E_l/E_l^g$	0.23	0.21	0.16	0.15	0.15	0.14	0.08	0.08	0.07	0.06	NA
	Period (s)	0.60	0.63	0.72	0.75	0.76	0.78	1.03	1.03	1.08	1.22	NA
<b>C2</b>	$E_l/E_l^g$	0.23	0.23	0.17	0.15	0.14	0.13	0.09	0.08	0.08	0.07	0.05
	Period (s)	0.60	0.61	0.71	0.76	0.78	0.82	0.95	1.03	1.03	1.10	1.28
<b>I1</b>	$E_l/E_l^g$	0.17	0.17	0.10	0.09	0.07	0.07	0.06	0.06	0.04	0.03	0.03
	Period (s)	0.62	0.62	0.80	0.86	0.97	0.97	1.06	1.09	1.37	1.43	1.43
<b>I2</b>	$E_l/E_l^g$	0.20	0.18	0.12	0.09	0.07	0.07	0.07	0.06	0.06	0.04	0.03
	Period (s)	0.58	0.61	0.74	0.84	0.95	0.97	0.98	1.09	1.09	1.30	1.43

\* Effective lateral stiffness

**Table 6-9 Measured Curvature Ductility**

<b>Specimen</b>	<b>Effective Yield Ductility (rad/in)</b>	<b>Ultimate Curvature (rad/in)</b>	<b>Effective Yield Moment (k-in)</b>	<b>Curvature Ductility</b>
9F1	0.0010	0.0065	2133	6.5
NF1	0.0005	0.0101	1962	20.2
C1-Longitudinal	0.0007	0.0089	1958	12.7
C2-Longitudinal	0.0007	0.0117	1981	16.7
ISL1.0	0.0005	0.0070	1950	14
I1-Longitudinal	0.0005	0.0052	1767	10.4
I2-Longitudinal	0.0006	0.0055	1761	9.2

**Table 6-10 Measured Concrete Strains at Plastic Hinge, Specimen 9F1**

<b>Run</b>	<b>Average curvature (rad/in)</b>	<b>Concrete Strain (in/in)</b>	
		<b>Unconfined</b>	<b>Confined</b>
1	0.0004	0.0034	0.0029
2	0.0008	0.0063	0.0052
3	0.0016	0.0131	0.0107
4	0.0019	0.0161	0.0132
5	0.0023	0.0206	0.0172
6	0.0029	0.0270	0.0227
7	0.0042	0.0456	0.0396
8	0.0065	0.0702	0.0611
9	Data not available		

**Table 6-11 Measured Displacement Ductility**

<b>Specimen</b>	<b>Effective Yield Displacement (in)</b>	<b>Ultimate Displacement (in)</b>	<b>Effective Yield Moment (k-in)</b>	<b>Ultimate Displacement Ductility</b>
9F1	1.54	8.73	2270	5.66
NF1	1.10	10.65	2164	9.68
C1-Longitudinal	1.1	12.1	2104	11.2
C2-Longitudinal	1.1	12.04	2128	10.5
ISL1.0	0.69	6.42	2157	9.31
I1-Longitudinal	1.16	6.20	1893	4.45
I2-Longitudinal	1.43	6.37	1925	5.35

**Table 7-1 Measured Strain Rate for Longitudinal Reinforcement**

Parameter	C1	C2	I1	I2	9F1	NF1	ISL1.0
$f_y$ (ksi)	65	65	61.4	61.4	65	68	63
$f_u$ (ksi)	103.3	103.3	94.7	94.7	104.3	93.4	99
$\dot{\epsilon}_{0.5y}$ (in/in)	0.0165	0.0213	0.0166	0.0161	-	-	-
$\dot{\epsilon}_y$ (in/in)	0.0083	0.0080	0.0189	0.0106	-	-	-
$\dot{\epsilon}_{avg}$ (in/in)	0.0144	0.0165	0.0182	0.0138	-	-	-
K	0.7562	0.6969	1.0201	0.8781	-	-	-
SRI	0.0109	0.0115	0.0186	0.0121	-	-	-
$\alpha$	0.0133	0.0133	0.0129	0.0129	-	-	-
$f'_y/f_y$	1.065	1.065	1.069	1.064	1.09	1.08	1.05
$f'_u/f_u$	1.045	1.046	1.046	1.043	1.06	1.06	1.03

**Table 7-2 Measured Strain Rate for Concrete**

Parameter	C1	C2	I1	I2	9F1	NF1	ISL1.0
$f_c$ (ksi)	4.65	4.67	4.42	4.44	5.43	5.99	5.35
Strain gauge (Sg)	23	16	16	17	-	-	-
$\dot{\epsilon}_y$ (in/in)	-0.0208	-0.0257	-0.0372	-0.0304	-	-	-
$f'_c/f_{cD}$	1.116	1.121	1.129	1.124	1.11	1.11	1.14

**Table 7-3 Stress-Strain Properties Modified by Strain Rate, Used for Moment-Curvature Analysis**

Material	Properties	9F1	NF1	ISL1.0	C1 and C2	I1 and I2
Unconfined Concrete	$f'_c$ (ksi)	6.03	6.65	6.1	5.22	4.99
	$E_c$ (ksi)	4425	4648	4451	4118	4026
	$\epsilon_o$	0.002	0.002	0.002	0.002	0.002
	$\epsilon_{cu}$	0.004	0.004	0.004	0.004	0.004
	$\epsilon_{ps}$	0.006	0.006	0.006	0.006	0.006
Confined Concrete	$K_e$	1.0	1.0	0.9	1.0	0.9
	$f'_{cc}$ (ksi)	7.75	8.39	8.01	6.87	6.68
	$\epsilon_{cc}$	0.0049	0.0046	0.0051	0.0052	0.0054
	$f_{cu}$ (ksi)	5.80	6.02	5.93	5.23	5.16
	$\epsilon_{cu}$	0.0154	0.0145	0.0172	0.0177	0.0187
	$\alpha$	3.16	3.14	3.35	3.43	3.48
	$r$	1.56	1.64	1.54	1.48	1.44
Steel Bars	$f_y$ (ksi)	70.85	73.44	66.15	69.23	65.48
	$E_s$ (ksi)	29000	29000	29000	29000	29000
	$\epsilon_y$	0.00244	0.00253	0.00228	0.00239	0.00226
	$\epsilon_{sh}$	0.0087	0.0062	0.0084	0.0128	0.008
	$f_{su}$ (ksi)	110.6	100.9	102	108.1	98.96
	$\epsilon_{su}$	0.11	0.10	0.16	0.11	0.12

**Table 7-4 Stress-Strain Properties Modified by Strain Rate and Ultimate Confined Concrete Strain, Used for Moment-Curvature Analysis**

Material	Properties	9F1	NF1	ISL1.0	C1 and C2	I1 and I2
Confined Concrete	$K_e$	1.0	1.0	0.9	1.0	0.9
	$f'_{cc}$ (ksi)	7.75	8.39	8.01	6.87	6.68
	$\epsilon_{cc}$	0.0049	0.0046	0.0051	0.0052	0.0054
	$f_{cu}$ (ksi)	5.80	6.02	5.93	5.23	5.16
	$\epsilon_{cu}$	0.0154	0.0145	0.0172	0.0177	0.0187
	$f_{cu}^*$ (ksi)	0	0	0	0	0
	$\epsilon_{cu}^*$	0.030	0.030	0.030	0.035	0.035



**Table 7-5 Influence of Strain Rate on the Idealized Moment-Curvature Properties, Unidirectional Specimens**

Property	9F1 P=80 kips			9F1 P=115 kips			NF1 P=80 kips			ISL1.0 P=90 kips		
	Without	With	Variation (%)	Without	With	Variation (%)	Without	With	Variation (%)	Without	With	Variation (%)
Mp (k-in)	1984	2106	6.1	2095	2220	6.0	2037	2144	5.3	2185	2270	3.9
EI (10 <sup>3</sup> ksi)	5730	5755	0.4	6263	6305	0.7	5757	5799	0.7	6740	6797	0.8
$\phi_y$ (1/in)	0.000346	0.000366	5.8	0.000335	0.00035	4.5	0.000354	0.00037	4.5	0.000324	0.000334	3.1
$\phi_u$ (1/in)	0.00465	0.0044	5.4	0.00431	0.00413	4.2	0.00458	0.00436	4.8	0.00446	0.00429	3.8
$\phi_u^*$ (1/in)	0.0085	0.0086	1.2	0.0081	0.0082	1.3	0.0090	0.0091	1.1	0.0085	0.0086	1.2

\*Based on modified confined concrete properties to account for ultimate strain ( $\epsilon_{cu}^*$ )

**Table 7-6 Influence of Strain Rate on the Idealized Moment-Curvature Properties, Bidirectional Specimens**

Property	C1 and C2 (Neutral Axis=30°)			I1 and I2 (Neutral Axis=45°)		
	Without	With	Variation (%)	Without	With	Variation (%)
Mp (k-in)	1708	1797	5.2	1392	1473	5.8
EI (10 <sup>3</sup> ksi)	4711	4790	1.5	3964	4013	1.2
$\phi_y$ (1/in)	0.0003625	0.0003753	3.5	0.0003513	0.0003672	4.5
$\phi_u$ (1/in)	0.005985	0.005725	4.3	0.005905	0.005743	2.7
$\phi_u^*$ (1/in)	0.0115	0.0114	0.9	0.01086	0.01078	0.7

\*Based on modified confined concrete properties to account for ultimate strain ( $\epsilon_{cu}^*$ )

**Table 7- 7 Idealized Force-Displacement Properties for Unidirectional Specimens (Priestley’s Method)**

Property	9F1 P=80 kips		9F1 P=115 kips		NF1 P=80 kips		ISL1.0 P=90 kips	
	$\epsilon_{cu}$	0.0154	0.030*	0.0154	0.030*	0.0145	0.030*	0.017
$\Delta y$ (in)	0.73	0.76	0.70	0.72	0.74	0.75	0.43	0.44
$\Delta p$ (in)	2.97	6.03	2.78	5.76	2.93	6.23	1.86	3.67
$\Delta u$ (in)	3.70	6.78	3.48	6.48	3.67	6.99	2.29	4.11
$F_p$ (kips)	29.25	30.43	30.86	31.58	29.93	30.49	38.97	39.29

\*Based on modified confined concrete properties to account for ultimate strain ( $\epsilon_{cu}$ \*)

**Table 7-8 Idealized Force-Displacement Properties for Bidirectional Specimens (Priestley’s Method)**

Property	C1 and C2 (NA=30°)						I1 and I2 (NA=45°)					
	X - Component		Y - Component		Principal Axis		X - Component		Y - Component		Principal Axis	
$\epsilon_{cu}$	0.0177	0.035*	0.0177	0.035*	0.0177	0.035*	0.018	0.035*	0.018	0.035*	0.018	0.035*
$\Delta y$ (in)	0.64	0.69	0.37	0.40	0.97	1.03	0.50	0.54	0.48	0.50	0.73	0.74
$\Delta p$ (in)	3.39	7.00	1.96	4.04	4.88	10.12	2.41	4.70	2.42	4.71	3.36	6.65
$\Delta u$ (in)	4.03	7.68	2.33	4.44	5.85	11.15	2.91	5.23	2.90	5.21	4.09	7.39
$F_p$ (kips)	21.67	23.30	12.51	13.45	21.65	23.34	19.20	20.49	9.79	10.11	21.22	21.64

\*Based on modified confined concrete properties to account for ultimate strain ( $\epsilon_{cu}$ \*)

**Table 7-9 Moment-Slip Rotation Properties for Unidirectional Specimens (Wehbe Method)**

Property	9F1 P=80 kips		9F1 P=115 kips		NF1 P=80 kips		ISL1.0 P=90 kips	
	$\theta$ (rad)	M (k-in)	$\theta$ (rad)	M (k-in)	$\theta$ (rad)	M (k-in)	$\theta$ (rad)	M (k-in)
Cracking	0.00002	398	0.00001	470	0.00002	410	0.00003	521
Yielding	0.00145	1676	0.00150	1676	0.00156	1591	0.00128	1571
Ultimate	0.02633	2146	0.02432	2189	0.01952	2096	0.02138	2145

**Table 7-10 Analytical Model in OpenSees for Time History Analysis, Specimen NF1**

Property	Value	
<b>MR model</b>	One Elastic beam-column with pin support	
<b>Footing model</b>	Elastic	
<b>Column model</b> * Plastic hinge length, $L_p$ (in) * Effective lateral stiffness ( $EI_{eff}$ )	Beam with hinges 11 (at the column base only) $0.45 EI_g$	
<b>Concrete model</b>	Concrete07	
Based on Chang and Mander model	Peak	Crushing
*Unconfined concrete strength, $f'_c$ (ksi)	6.65	0
*Unconfined concrete strain, $e_c$	0.002	0.006
*Confined concrete strength, $f'_{cc}$ (ksi)	8.26	0.0044
*Confined concrete strain, $e_{cc}$	6.21	0.013
Elastic modulus (ksi)	4647	
Descending branch	Linear from crushing to zero strength	
<b>Longitudinal steel model</b>	ReinforcingSteel	
Based on Chang and Mander model	Stress (ksi)	Strain (in/in)
*Yielding (strain rate effect included)	73.44	0.0025
*Ultimate (strain rate effect included)	99.01	0.10
Strain at the beginning of hardening ( $e_{sh}$ )	0.006	
Elastic modulus, $E_s$ (ksi)	29,000	
Tangent at strain hardening, $E_{sh}$ (ksi)	272	
<b>Bond slip model</b>	Bond_SP01 (Zhao and Sritharan model)	
Rebar slip at yielding stress, $s_y$ (in)	0.0144	
Rebar slip at ultimate stress, $s_u$ (in)	0.577	
Hardening ratio, $b$	0.5	
Pinching factor, $R$	0.6	
Axial load on MR, $P_{MR}$ (kips)	80	
Axial load on column, $P_c$ (kips)	80 (constant)	
Translational mass on MR ( $k\text{-s}^2/\text{in}$ )	0.209	
Rotational mass on MR	N.A	
Translational mass on column ( $k\text{-s}^2/\text{in}$ )	0.0083	
Rotational mass on column	N.A	
Damping model	Rayleigh tangent stiffness-only proportional	
Damping ratio	2.5% for the first translational frequency	

**Table 7-11 Analytical vs. Experimental Seismic Performance, Specimen NF1**

Run	Lateral Displacement (in)			Residual Displacement (in)				Lateral Force (kips)		
	Analytical	Experimental	Ratio	Analytical	Experimental	Ratio	Difference	Analytical	Experimental	Ratio
RINx0.05	0.148	0.150	0.99	0.000	0.008	-	0.01	9.065	7.366	1.23
RINx0.1	0.270	0.305	0.89	0.000	0.019	-	0.02	14.239	12.290	1.16
RINx0.2	0.671	0.804	0.83	0.003	0.020	0.13	0.02	26.345	21.906	1.20
RINx0.3	1.315	1.586	0.83	0.140	0.120	1.17	0.02	29.517	28.213	1.05
RINx0.45	2.917	3.182	0.92	0.879	0.462	1.90	0.42	29.677	30.808	0.96
RINx0.6	3.780	4.954	0.76	1.560	1.055	1.48	0.50	29.703	30.911	0.96
RINx0.75	4.740	6.374	0.74	2.384	2.151	1.11	0.23	29.967	30.769	0.97
RINx0.9	5.945	7.368	0.81	3.239	3.001	1.08	0.24	30.232	30.605	0.99
RINx1.05	7.318	8.522	0.86	4.294	4.235	1.01	0.06	30.017	30.685	0.98
RINx1.2	8.869	9.671	0.92	5.305	5.460	0.97	0.15	29.370	29.729	0.99
RINx1.35	10.624	15.559	0.68	8.417	15.068	0.56	6.65	28.817	24.364	1.18

Table 7-12 Analytical Model in OpenSees for Time History Analysis, Specimen 9F1

Property	Value	
<b>MR model</b>	One Elastic beam-column with pin support	
<b>Footing model</b>	Elastic	
<b>Column model</b> * Plastic hinge length, $L_p$ (in) * Effective lateral stiffness ( $EI_{eff}$ )	Beam with hinges 12 (at the column base only) $0.2 EI_g$	
<b>Concrete model</b>	Concrete07	
Based on Chang and Mander model	Peak	Crushing
*Unconfined concrete strength, $f'_c$ (ksi)	6.03	0
*Unconfined concrete strain, $e_c$	0.002	0.006
*Confined concrete strength, $f'_{cc}$ (ksi)	7.61	0.0046
*Confined concrete strain, $e_{cc}$	5.80	0.013
Elastic modulus (ksi)	4425	
Descending branch	Linear from crushing to zero strength	
<b>Longitudinal steel model</b>	ReinforcingSteel	
Based on Chang and Mander model	Stress (ksi)	Strain (in/in)
*Yielding (strain rate effect included)	70.85	0.0024
*Ultimate (strain rate effect included)	110.56	0.114
Strain at the beginning of hardening ( $e_{sh}$ )	0.008	
Elastic modulus, $E_s$ (ksi)	29,000	
Tangent at strain hardening, $E_{sh}$ (ksi)	375	
<b>Bond slip model</b>	Bond_SP01 (Zhao and Sritharan model)	
Rebar slip at yielding stress, $s_y$ (in)	0.0149	
Rebar slip at ultimate stress, $s_u$ (in)	0.596	
Hardening ratio, $b$	0.5	
Pinching factor, $R$	0.6	
Axial load on MR, $P_{MR}$ (kips)	80	
Axial load on column, $P_C$ (kips)	80 (variable)	
Translational mass on MR ( $k\text{-s}^2/\text{in}$ )	0.209	
Rotational mass on MR	N.A	
Translational mass on column ( $k\text{-s}^2/\text{in}$ )	0.0083	
Rotational mass on column	N.A	
Damping model	Rayleigh tangent stiffness-only proportional	
Damping ratio	2.5% for the first translational frequency	

**Table 7-13 Analytical vs. Experimental Seismic Performance, Specimen 9F1**

Run	Lateral Displacement (in)			Residual Displacement (in)				Lateral Force (kips)		
	Analytical	Experimental	Ratio	Analytical	Experimental	Ratio	Difference	Analytical	Experimental	Ratio
CENx0.33	0.616	0.633	0.97	0.001	0.013	0.04	0.012	16.382	15.510	1.06
CENx0.66	0.963	1.187	0.81	-0.025	-0.039	0.64	0.014	23.436	23.836	0.98
CENx1.0	1.680	1.939	0.87	-0.023	-0.059	0.38	0.036	29.991	30.764	0.97
CENx1.5	2.128	2.534	0.84	0.012	-0.061	-0.19	0.072	29.779	31.851	0.93
CENx2.0	2.836	2.801	1.01	0.085	-0.089	-0.95	0.174	30.577	31.319	0.98
CENx2.5	3.869	3.538	1.09	0.367	-0.046	-7.93	0.413	31.777	32.007	0.99
CENx3.0	4.175	5.025	0.83	0.482	0.212	2.27	0.270	32.110	33.006	0.97
CENx3.5	5.082	6.659	0.76	0.895	1.527	0.59	0.632	33.114	33.247	1.00
CENx4.0	6.814	17.462	0.39	2.637	15.891	0.17	13.254	33.495	29.555	1.13

**Table 7-14 Analytical Model in OpenSees for Time History Analysis, Specimen ISL1.0**

Property	Value	
<b>MR model</b>	One Elastic beam-column with pin support	
<b>Footing model</b>	Elastic	
<b>Column model</b>	Beam with hinges	
* Plastic hinge length, $L_p$ (in)	14 (at the column base only)	
* Effective lateral stiffness ( $EI_{eff}$ )	$0.25 EI_g$	
<b>Concrete model</b>	Concrete07	
Based on Chang and Mander model	Peak	Crushing
*Unconfined concrete strength, $f'_c$ (ksi)	6.1	0
*Unconfined concrete strain, $e_c$	0.002	0.006
*Confined concrete strength, $f'_{cc}$ (ksi)	7.984	0.005
*Confined concrete strain, $e_{cc}$	5.93	0.018
Elastic modulus (ksi)	4451	
Descending branch	Linear from crushing to zero strength	
<b>Longitudinal steel model</b>	ReinforcingSteel	
Based on Chang and Mander model	Stress (ksi)	Strain (in/in)
*Yielding (strain rate effect included)	70.35	0.0024
*Ultimate (strain rate effect included)	106.09	0.12
Strain at the beginning of hardening ( $e_{sh}$ )	0.0084	
Elastic modulus, $E_s$ (ksi)	29,000	
Tangent at strain hardening, $E_{sh}$ (ksi)	320	
<b>Bond slip model</b>	Bond_SP01 (Zhao and Sritharan model)	
Rebar slip at yielding stress, $s_y$ (in)	0.0139	
Rebar slip at ultimate stress, $s_u$ (in)	0.486	
Hardening ratio, $b$	0.5	
Pinching factor, $R$	0.6	
Axial load on MR, $P_{MR}$ (kips)	93	
Axial load on column, $P_c$ (kips)	90 (constant)	
Translational mass on MR ( $k\text{-s}^2/\text{in}$ )	0.2403	
Rotational mass on MR	N.A	
Translational mass on column ( $k\text{-s}^2/\text{in}$ )	0.0082	
Rotational mass on column	N.A	
Damping model	Rayleigh tangent stiffness-only proportional	
Damping ratio	2.5% for the first translational frequency	



**Table 7-15 Analytical vs. Experimental Seismic Performance, Specimen ISL1.0**

Run	Lateral Displacement (in)			Residual Displacement (in)				Lateral Force (kips)		
	Analytical	Experimental	Ratio	Analytical	Experimental	Ratio	Difference	Analytical	Experimental	Ratio
SYLX0.1	-0.100	-0.115	0.87	0.001	0.000	-2.38	0.00	-7.319	-11.517	0.64
SYLX0.2	-0.396	-0.229	1.73	0.001	0.001	1.18	0.00	-22.483	-17.464	1.29
SYLX0.3	-0.738	-0.596	1.24	-0.006	0.004	-1.73	0.01	-32.998	-29.936	1.10
SYLX0.5	-0.941	-1.055	0.89	-0.025	0.002	-13.40	0.03	-35.361	-35.141	1.01
SYLX0.75	-1.005	-0.962	1.04	-0.003	0.024	-0.14	0.03	-35.355	-32.345	1.09
SYLX1.0	-1.209	-1.325	0.91	-0.041	0.019	-2.22	0.06	-35.284	-35.017	1.01
SYLX1.25	-1.822	-2.079	0.88	0.011	0.188	0.06	0.18	-36.606	-37.109	0.99
SYLX1.5	-2.662	-3.065	0.87	-0.196	-0.146	1.34	0.05	-37.772	-38.123	0.99
SYLX1.75	-3.697	-4.147	0.89	-0.607	-0.415	1.46	0.19	-39.033	-39.016	1.00
SYLX2.0	-5.410	-6.415	0.84	-2.151	-2.084	1.03	0.07	-40.121	-38.606	1.04

**Table 7-16 Analytical Model in OpenSees for Time History Analysis, Specimens C1 and C2**

Property	Value	
<b>BMR model</b>	Grid of elastic beams on roller supports	
<b>Footing model</b>	Elastic	
<b>Column model</b> * Plastic hinge length, $L_p$ (in) * Effective lateral stiffness ( $EI_{eff}$ )	Beam with hinges 12 (at the column base only) $0.2 EI_g$	
<b>Concrete model</b>	Concrete07	
Based on Chang and Mander model	Peak	Crushing
*Unconfined concrete strength, $f'_c$ (ksi)	5.21	0
*Unconfined concrete strain, $e_c$	0.002	0.006
*Confined concrete strength, $f'_{cc}$ (ksi)	6.84	0.005
*Confined concrete strain, $e_{cc}$	5.23	0.016
Elastic modulus (ksi)	4113	
Descending branch	Linear from crushing to zero strength	
<b>Longitudinal steel model</b>	ReinforcingSteel	
Based on Chang and Mander model	Stress (ksi)	Strain (in/in)
*Yielding (strain rate effect included)	69.25	0.00238
*Ultimate (strain rate effect included)	108.05	0.12
Strain at the beginning of hardening ( $e_{sh}$ )	0.0079	
Elastic modulus, $E_s$ (ksi)	29,000	
Tangent at strain hardening, $E_{sh}$ (ksi)	691	
<b>Bond slip model</b>	Bond_SP01 (Zhao and Sritharan model)	
Rebar slip at yielding stress, $s_y$ (in)	0.0145	
Rebar slip at ultimate stress, $s_u$ (in)	0.582	
Hardening ratio, $b$	0.5	
Pinching factor, $R$	0.6	
Axial load on MR, $P_{BMR}$ (kips)	80	
Axial load on column, $P_c$ (kips)	5	
Translational mass on BMR, ( $k\text{-s}^2/\text{in}$ )	0.207	
Rotational mass on BMR ( $k\text{-in-s}^2$ )	1775 (C1) and 1716 (C2)	
Translational mass on column ( $k\text{-s}^2/\text{in}$ )	0.0082	
Rotational mass on column ( $k\text{-in-s}^2$ )	1.6	
Damping model	Rayleigh tangent stiffness-only proportional	
Damping ratio	2.5% for the first translational frequency	

**Table 7-17 Analytical vs. Experimental Seismic Performance, Specimen C1-Longitudinal**

Run	Lateral Displacement (in)			Residual Displacement (in)				Lateral Force (kips)		
	Analytical	Experimental	Ratio	Analytical	Experimental	Ratio	Difference	Analytical	Experimental	Ratio
PETx0.1	0.450	0.386	1.16	-0.001	-0.002	0.47	0.00	8.914	8.526	1.05
PETx0.2	0.817	0.755	1.08	-0.026	-0.061	0.43	0.03	14.943	14.012	1.07
PETx0.4	1.311	1.404	0.93	-0.564	-0.586	0.96	0.02	21.413	21.285	1.01
PETx0.6	1.296	1.518	0.85	-0.457	-0.544	0.84	0.09	18.007	19.620	0.92
PETx0.8	2.323	2.469	0.94	0.052	0.015	3.61	0.04	22.976	24.564	0.94
PETx1.0	3.609	3.790	0.95	0.863	0.917	0.94	0.05	25.191	26.931	0.94
PETx1.2	5.345	5.617	0.95	1.724	1.870	0.92	0.15	26.918	27.577	0.98
PETx1.4	7.197	7.593	0.95	2.780	3.019	0.92	0.24	28.238	27.826	1.01
PETx1.6	9.304	9.845	0.94	3.949	4.561	0.87	0.61	29.190	27.846	1.05
PETx1.8	11.609	12.359	0.94	5.138	6.142	0.84	1.00	29.687	27.122	1.09

**Table 7-18 Analytical vs. Experimental Seismic Performance, Specimen C1-Transverse**

Run	Lateral Displacement (in)			Residual Displacement (in)				Lateral Force (kips)		
	Analytical	Experimental	Ratio	Analytical	Experimental	Ratio	Difference	Analytical	Experimental	Ratio
PETx0.1	0.281	0.241	1.17	-0.001	-0.005	0.24	0.00	5.665	6.104	0.93
PETx0.2	0.497	0.410	1.21	-0.014	-0.026	0.55	0.01	9.250	9.368	0.99
PETx0.4	0.815	0.844	0.97	-0.213	-0.158	1.34	0.05	13.508	13.239	1.02
PETx0.6	0.808	0.847	0.95	-0.192	-0.154	1.24	0.04	11.183	11.417	0.98
PETx0.8	1.228	1.271	0.97	-0.059	0.054	-1.09	0.11	13.845	12.361	1.12
PETx1.0	1.757	1.868	0.94	0.202	0.433	0.47	0.23	15.638	14.317	1.09
PETx1.2	2.382	2.600	0.92	0.376	0.776	0.48	0.40	17.057	16.033	1.06
PETx1.4	3.014	3.423	0.88	0.680	1.361	0.50	0.68	17.998	16.835	1.07
PETx1.6	3.754	4.391	0.86	1.118	2.387	0.47	1.27	19.121	17.210	1.11
PETx1.8	4.547	5.825	0.78	1.579	3.847	0.41	2.27	19.593	17.721	1.11

**Table 7-19 Analytical vs. Experimental Seismic Performance, Specimen C2-Longitudinal**

Run	Lateral Displacement (in)			Residual Displacement (in)				Lateral Force (kips)		
	Analytical	Experimental	Ratio	Analytical	Experimental	Ratio	Difference	Analytical	Experimental	Ratio
PETx0.1	0.263	0.238	1.11	-0.001	-0.002	0.50	0.00	5.632	4.905	1.15
PETx0.2	0.574	0.471	1.22	-0.001	-0.006	0.12	0.01	10.919	11.341	0.96
PETx0.4	0.900	0.857	1.05	-0.137	-0.223	0.61	0.09	16.333	17.437	0.94
PETx0.6	1.362	1.314	1.04	-0.638	-0.630	1.01	0.01	21.512	21.733	0.99
PETx0.8	2.042	2.090	0.98	-0.226	-0.068	3.34	0.16	22.062	24.014	0.92
PETx1.0	3.346	3.387	0.99	0.714	0.753	0.95	0.04	24.939	27.153	0.92
PETx1.2	5.099	5.042	1.01	1.625	1.668	0.97	0.04	26.849	28.397	0.95
PETx1.4	6.857	6.917	0.99	2.650	2.585	1.03	0.07	28.155	29.193	0.96
PETx1.6	8.990	8.905	1.01	3.806	3.722	1.02	0.08	29.210	30.088	0.97
PETx1.8	11.264	11.168	1.01	5.000	5.236	0.95	0.24	29.747	28.312	1.05
PETx2.0	13.629	13.643	1.00	6.466	6.516	0.99	0.05	29.876	27.840	1.07

**Table 7-20 Analytical vs. Experimental Seismic Performance, Specimen C2-Transversal**

Run	Lateral Displacement (in)			Residual Displacement (in)				Lateral Force (in)		
	Analytical	Experimental	Ratio	Analytical	Experimental	Ratio	Difference	Analytical	Experimental	Ratio
PETx0.1	0.191	0.143	1.33	-0.001	-0.002	0.48	0.00	4.104	3.791	1.08
PETx0.2	0.328	0.229	1.43	-0.001	-0.005	0.22	0.00	6.389	5.963	1.07
PETx0.4	0.499	0.448	1.11	-0.052	-0.062	0.84	0.01	9.373	9.361	1.00
PETx0.6	0.758	0.662	1.15	-0.189	-0.206	0.92	0.02	11.763	11.496	1.02
PETx0.8	1.013	0.916	1.11	-0.126	-0.082	1.53	0.04	12.407	11.040	1.12
PETx1.0	1.522	1.495	1.02	0.123	0.246	0.50	0.12	14.358	13.187	1.09
PETx1.2	2.120	2.164	0.98	0.339	0.629	0.54	0.29	16.191	15.865	1.02
PETx1.4	2.749	2.924	0.94	0.645	1.093	0.59	0.45	17.573	16.454	1.07
PETx1.6	3.480	3.839	0.91	1.070	1.929	0.55	0.86	18.437	16.868	1.09
PETx1.8	4.321	5.063	0.85	1.604	3.232	0.50	1.63	19.400	16.948	1.14
PETx2.0	5.320	6.828	0.78	2.231	4.887	0.46	2.66	20.533	13.663	1.50

**Table 7-21 Analytical Model in OpenSees for Time History Analysis, Specimen I1 and I2**

Property	Value	
<b>BMR model</b>	Grid of elastic beams on roller supports	
<b>Footing model</b>	Elastic	
<b>Column model</b> * Plastic hinge length, $L_p$ (in) * Effective lateral stiffness ( $EI_{eff}$ )	Beam with hinges 12 (at the column base only) $0.2 EI_g$	
<b>Concrete model</b>	Concrete07	
Based on Chang and Mander model	Peak	Crushing
*Unconfined concrete strength, $f'_c$ (ksi)	5.21	0
*Unconfined concrete strain, $e_c$	0.002	0.006
*Confined concrete strength, $f'_{cc}$ (ksi)	6.84	0.005
*Confined concrete strain, $e_{cc}$	5.23	0.016
Elastic modulus (ksi)	4113	
Descending branch	Linear from crushing to zero strength	
<b>Longitudinal steel model</b>	ReinforcingSteel	
Based on Chang and Mander model	Stress (ksi)	Strain (ksi)
*Yielding (strain rate effect included)	69.25	0.0024
*Ultimate (strain rate effect included)	108.05	0.12
Strain at the beginning of hardening ( $e_{sh}$ )	0.0079	
Elastic modulus, $E_s$ (ksi)	29,000	
Tangent at strain hardening, $E_{sh}$ (ksi)	691	
<b>Bond slip model</b>	Bond_SP01 (Zhao and Sritharan model)	
Rebar slip at yielding stress, $s_y$ (in)	0.0145	
Rebar slip at ultimate stress, $s_u$ (in)	0.582	
Hardening ratio, $b$	0.5	
Pinching factor, $R$	0.6	
Axial load on MR, $P_{BMR}$ (kips)	80	
Axial load on column, $P_c$ (kips)	5	
Translational mass on BMR, ( $k\text{-s}^2/\text{in}$ )	0.207	
Rotational mass on BMR ( $k\text{-in-s}^2$ )	1775 (I1) and 1716 (I2)	
Translational mass on column ( $k\text{-s}^2/\text{in}$ )	0.0082	
Rotational mass on column ( $k\text{-in-s}^2$ )	1.6	
Damping model	Rayleigh tangent stiffness-only proportional	
Damping ratio	2.5% for the first translational frequency	

**Table 7-22 Analytical vs. Experimental Seismic Performance, Specimen I1-Longitudinal**

Run	Lateral Displacement (in)			Residual Displacement (in)				Lateral Force (kips)		
	Analytical	Experimental	Ratio	Analytical	Experimental	Ratio	Difference	Analytical	Experimental	Ratio
SYLx0.1	0.194	0.300	0.65	0.001	0.002	0.29	0.00	4.921	5.972	0.82
SYLx0.2	0.490	0.642	0.76	0.001	0.002	0.74	0.00	10.885	12.544	0.87
SYLx0.4	1.138	1.035	1.10	-0.064	-0.109	0.59	0.05	19.998	17.821	1.12
SYLx0.6	1.549	1.604	0.97	0.043	-0.145	-0.30	0.19	20.262	20.723	0.98
SYLx0.8	2.538	2.599	0.98	-0.300	-0.327	0.92	0.03	20.784	22.069	0.94
SYLx1.0	3.186	3.387	0.94	-0.578	-0.663	0.87	0.09	21.293	23.001	0.93
SYLx1.2	3.926	4.276	0.92	-0.854	-1.037	0.82	0.18	22.206	23.317	0.95
SYLx1.4	4.677	5.004	0.93	-1.075	-1.328	0.81	0.25	23.087	21.503	1.07
SYLx1.6	5.450	5.771	0.94	-1.191	-1.475	0.81	0.28	23.964	21.528	1.11
SYLx1.8	6.702	7.049	0.95	-1.186	-1.247	0.95	0.06	25.516	22.849	1.12
SYLx1.4*	4.847	5.583	0.87	-1.485	-1.767	0.84	0.28	19.542	16.966	1.15

**Table 7-23 Analytical vs. Experimental Seismic Performance, Specimen I1-Longitudinal-Transverse**

Run	Lateral Displacement (in)			Residual Displacement (in)				Lateral Force (kips)		
	Analytical	Experimental	Ratio	Analytical	Experimental	Ratio	Difference	Analytical	Experimental	Ratio
SYLx0.1	0.239	0.198	1.21	0.000	0.005	0.07	0.00	3.042	2.373	1.28
SYLx0.2	0.453	0.454	1.00	0.001	0.008	0.12	0.01	5.061	5.224	0.97
SYLx0.4	1.297	1.204	1.08	-0.039	0.073	-0.53	0.11	10.112	12.167	0.83
SYLx0.6	1.214	1.579	0.77	-0.477	-0.150	3.18	0.33	9.021	10.650	0.85
SYLx0.8	1.500	2.342	0.64	-0.536	0.122	-4.40	0.66	10.163	11.191	0.91
SYLx1.0	2.303	3.364	0.68	-0.445	0.390	-1.14	0.83	11.266	13.023	0.87
SYLx1.2	2.959	4.221	0.70	-0.172	0.845	-0.20	1.02	11.783	14.000	0.84
SYLx1.4	3.574	5.140	0.70	0.229	1.466	0.16	1.24	12.062	14.303	0.84
SYLx1.6	4.083	6.200	0.66	0.611	2.209	0.28	1.60	12.330	14.706	0.84
SYLx1.8	4.705	7.855	0.60	1.029	3.429	0.30	2.40	12.291	15.121	0.81
SYLx1.4*	4.094	8.050	0.51	0.632	4.689	0.13	4.06	12.032	10.838	1.11

**Table 7-24 Analytical vs. Experimental Seismic Performance, Specimen I2-Longitudinal**

Run	Lateral Displacement (in)			Residual Displacement (in)				Lateral Force (kips)		
	Analytical	Experimental	Ratio	Analytical	Experimental	Ratio	Difference	Analytical	Experimental	Ratio
SYLx0.1	0.212	0.230	0.92	-0.001	-0.002	0.23	0.00	5.353	5.698	0.94
SYLx0.2	0.516	0.681	0.76	0.001	-0.006	-0.11	0.01	11.374	12.840	0.89
SYLx0.4	1.192	1.097	1.09	-0.042	-0.073	0.57	0.03	20.571	18.653	1.10
SYLx0.6	1.482	1.566	0.95	-0.064	-0.154	0.41	0.09	20.064	20.578	0.97
SYLx0.8	2.566	2.666	0.96	-0.247	-0.316	0.78	0.07	21.123	22.528	0.94
SYLx1.0	3.364	3.799	0.89	-0.200	-0.186	1.07	0.01	21.945	23.451	0.94
SYLx1.2	4.341	4.647	0.93	-0.696	-0.858	0.81	0.16	23.579	22.588	1.04
SYLx1.4	4.958	5.546	0.89	-0.932	-1.159	0.80	0.23	23.706	22.141	1.07
SYLx1.6	5.911	6.437	0.92	-0.981	-1.245	0.79	0.26	24.835	23.926	1.04
SYLx1.8	6.908	7.655	0.90	-1.014	-0.728	1.39	0.29	25.837	21.911	1.18
SYLx1.8*	7.075	7.655	0.92	-0.912	-0.142	6.44	0.77	25.254	18.245	1.38

**Table 7-25 Analytical vs. Experimental Seismic Performance, Specimen I2-Transverse**

Run	Lateral Displacement (in)			Residual Displacement (in)				Lateral Force (kips)		
	Analytical	Experimental	Ratio	Analytical	Experimental	Ratio	Difference	Analytical	Experimental	Ratio
SYLx0.1	0.225	0.221	1.02	-0.001	0.000	-1.56	0.00	2.876	3.812	0.75
SYLx0.2	0.432	0.420	1.03	0.000	-0.002	0.05	0.00	4.842	5.085	0.95
SYLx0.4	1.186	1.034	1.15	-0.039	0.006	-6.36	0.05	9.568	9.156	1.04
SYLx0.6	1.188	1.380	0.86	-0.499	-0.268	1.86	0.23	8.678	10.526	0.82
SYLx0.8	1.121	1.775	0.63	-0.683	-0.215	3.18	0.47	9.299	11.681	0.80
SYLx1.0	1.618	2.819	0.57	-0.583	0.015	-	0.60	10.621	13.959	0.76
SYLx1.2	2.401	3.572	0.67	-0.460	0.299	-1.53	0.76	11.490	14.371	0.80
SYLx1.4	3.036	4.387	0.69	-0.122	0.757	-0.16	0.88	11.878	15.034	0.79
SYLx1.6	3.309	5.060	0.65	0.261	1.197	0.22	0.94	11.869	14.510	0.82
SYLx1.8	4.215	6.570	0.64	0.701	2.588	0.27	1.89	12.147	12.489	0.97
SYLx1.8*	4.398	6.570	0.67	0.917	4.465	0.21	3.55	12.102	9.074	1.33

**Table 8-1 Ground Motions used for Analytical Investigation**

Earthquake	Year	Mw	Station	Closest Distance (km)	Component	PGA (g)	PGV (cm/s)	PGD (cm)
Imperial Valley	1940	7.0	El Centro Array #9	8.8	CEN180	0.313	29.8	13.32
					CEN270	0.215	30.2	23.91
Loma Prieta	1989	6.9	16 Los Gatos Presentation Center	6.4	LGP090	0.605	51.0	11.5
					LGP000	0.563	94.8	41.18
Cape Mendocino	1992	7.1	89156 Petrolia	7.1	PET090	0.662	89.7	29.55
					PET000	0.59	48.4	21.74
Northridge	1994	6.7	77 Rinaldi Receiving Station	9.5	RIN228	0.838	166.1	28.78
					RIN318	0.472	73.0	19.76
Northridge	1994	6.7	24514 Sylmar Olive View Med FF	6.1	SYL360	0.843	129.6	32.68
					SYL090	0.604	78.2	16.05
Kobe	1995	6.9	0 Takatori	0.3	TAK000	0.611	127.1	35.77
					TAK090	0.616	120.7	32.72

**Table 8-2 Spectral Acceleration Demands for Each Earthquake**

Earthquake	Component	Circular SA (g)	Interlocking SA (g)	
			Long Side	Short Side
Imperial Valley El Centro	CEN180	0.46	0.51	0.19
	CEN270	0.28	0.27	0.22
Loma Prieta Los Gatos	LGP090	0.46	0.44	0.47
	LGP000	0.98	0.99	0.86
Cape Mendocino Petrolia	PET090	1.21	0.99	0.51
	PET000	1.02	0.61	0.24
Northridge Rinaldi	RIN228	1.78	1.83	0.77
	RIN318	0.74	1.10	0.51
Northridge Sylmar	SYL360	0.89	0.50	0.87
	SYL090	0.54	0.62	0.87
Kobe Takatori	TAK000	1.38	1.15	1.66
	TAK090	1.51	1.43	1.38



**Table 8-3 Ground Motion Intensity Factors for the Analytical Loading Sequence**

Run	El Centro	Los Gatos	Petrolia	Rinaldi	Sylmar	Takatori
1	0.33	0.1	0.1	0.05	0.1	0.1
2	<b>0.66*</b>	<b>0.2</b>	<b>0.2</b>	<b>0.1</b>	<b>0.2</b>	<b>0.2</b>
3	<b>1</b>	<b>0.4</b>	<b>0.4</b>	<b>0.2</b>	<b>0.4</b>	<b>0.4</b>
4	1.5	0.6	0.6	0.3	0.6	0.6
5	2.0	0.8	0.8	0.45	0.8	0.8
6	2.5	1.15	1.0	0.6	1.0	1.0
7	3.0	1.5	1.2	0.75	1.2	1.2
8	3.5	-	1.4	0.9	1.4	-
9	4.0	-	1.6	1.05	1.6	-
10	-	-	1.8	1.2	1.8	-
11	-	-	-	1.35	-	-

\* Bold values means expected yielding

**Table 8-4 Maximum Predicted Displacement from Unidirectional, Bidirectional and Components under El Centro**

Times El Centro	Unidirectional		Bidirectional		Component	
	Longitudinal (Dx)	Transverse (Dy)	Longitudinal (Dx)	Transverse (Dy)	D <sub>SRSS</sub>	D <sub>vector</sub>
0.33	0.44	0.29	0.49	0.32	0.51	0.57
0.66	1.05	0.61	1.01	0.52	1.12	1.07
1	1.49	0.85	1.48	0.87	1.53	1.66
1.5	2.02	0.88	1.96	1.62	2.15	2.44
2	2.35	1.58	2.41	2.43	2.81	3.21
2.5	2.56	2.54	2.94	3.43	3.43	4.09
3	3.23	3.59	4.25	5.20	4.42	5.57
3.5	4.32	4.83	6.22	10.22	5.58	10.81
4	6.31	6.75	failure	failure	7.39	failure

**Table 8-5 Maximum Predicted Displacement from Unidirectional, Bidirectional and Components under Los Gatos (Circular)**

Times Los Gatos	Unidirectional		Bidirectional		Component	
	Longitudinal Dx (in)	Transverse Dy (in)	Longitudinal Dx (in)	Transverse Dy (in)	D <sub>SRSS</sub> (in)	D <sub>vector</sub> (in)
0.1	0.39	0.22	0.36	0.50	0.50	0.61
0.2	0.63	0.52	0.57	0.48	0.98	0.87
0.4	1.15	0.87	1.14	0.52	1.26	1.22
0.6	1.93	0.81	1.72	0.62	1.99	1.72
0.8	2.77	0.93	2.58	1.20	2.87	2.63
1	5.72	0.95	5.71	2.27	7.59	5.88
1.15	9.80	1.27	9.76	4.04	9.82	10.52
1.3	failure	1.85	failure	failure	failure	failure

**Table 8-6 Maximum Predicted Displacement from Unidirectional, Bidirectional and Components under Los Gatos (Circular)**

Times Los Gatos	Unidirectional		Bidirectional		Component	
	Longitudinal Dx (in)	Transverse Dy (in)	Longitudinal Dx (in)	Transverse Dy (in)	D <sub>SRSS</sub> (in)	D <sub>vector</sub> (in)
0.33	0.44	0.29	0.49	0.32	0.51	0.57
0.66	1.05	0.61	1.01	0.52	1.12	1.07
1	1.49	0.85	1.48	0.87	1.53	1.66
1.5	2.02	0.88	1.96	1.62	2.15	2.44
2	2.35	1.58	2.41	2.43	2.81	3.21
2.5	2.56	2.54	2.94	3.43	3.43	4.09
3	3.23	3.59	4.25	5.20	4.42	5.57
3.5	4.32	4.83	6.22	10.22	5.58	10.81
4	6.31	6.75	failure	failure	7.39	failure

**Table 8-7 Maximum Predicted Displacement from Unidirectional, Bidirectional and Components under Petrolia (Circular)**

Times Petrolia	Unidirectional		Bidirectional		Component	
	Longitudinal Dx (in)	Transverse Dy (in)	Longitudinal Dx (in)	Transverse Dy (in)	D <sub>SRSS</sub> (in)	D <sub>vector</sub> (in)
0.1	0.31	0.30	0.30	0.32	0.39	0.38
0.2	0.64	0.59	0.59	0.56	0.80	0.77
0.4	0.82	0.96	0.71	0.63	1.52	1.54
0.6	1.25	1.37	1.29	0.97	2.22	1.71
0.8	2.19	1.57	2.20	1.39	2.36	2.39
1	3.44	1.58	3.66	1.92	3.63	3.93
1.2	5.39	1.45	5.65	2.59	5.59	6.02
1.4	8.27	1.25	8.68	3.54	8.49	9.19
1.6	12.32	1.28	15.02	5.39	12.56	15.54

**Table 8-8 Maximum Predicted Displacement from Unidirectional, Bidirectional and Components under Rinaldi (Circular)**

Times Rinaldi	Unidirectional		Bidirectional		Component	
	Longitudinal Dx (in)	Transverse Dy (in)	Longitudinal Dx (in)	Transverse Dy (in)	D <sub>SRSS</sub> (in)	D <sub>vector</sub> (in)
0.1	0.35	0.16	0.36	0.17	0.02	0.03
0.2	0.86	0.35	0.89	0.44	0.04	0.00
0.4	2.82	0.89	2.89	1.38	0.29	0.43
0.6	4.58	1.63	4.55	2.23	1.73	1.44
0.8	5.61	2.37	5.62	2.81	2.18	2.09
1	6.93	2.81	6.95	3.34	3.19	3.02
1.2	7.90	3.18	7.94	3.76	3.84	3.91
1.4	8.45	3.52	8.57	4.14	4.35	4.70

**Table 8-9 Maximum Predicted Displacement from Unidirectional, Bidirectional and Components under Sylmar (Circular)**

Times Sylmar	Unidirectional		Bidirectional		Component	
	Longitudinal Dx (in)	Transverse Dy (in)	Longitudinal Dx (in)	Transverse Dy (in)	D <sub>SRSS</sub> (in)	D <sub>vector</sub> (in)
0.1	0.24	0.18	0.24	0.19	0.25	0.25
0.2	0.48	0.60	0.48	0.60	0.62	0.62
0.4	0.97	1.36	1.00	0.99	1.38	1.06
0.6	2.13	1.23	2.38	1.51	2.25	2.54
0.8	3.56	1.55	3.88	2.83	3.58	4.25
1	4.58	2.23	5.16	4.40	4.58	5.77
1.2	5.89	3.81	6.78	7.00	5.89	8.14
1.4	7.79	5.66	15.16	18.29	8.03	failure
1.6	10.57	8.61	failure	failure	12.98	failure

**Table 8-10 Maximum Predicted Displacement from Unidirectional, Bidirectional and Components under Takatori (Circular)**

Times Takatori	Unidirectional		Bidirectional		Component	
	Longitudinal Dx (in)	Transverse Dy (in)	Longitudinal Dx (in)	Transverse Dy (in)	D <sub>SRSS</sub> (in)	D <sub>vector</sub> (in)
0.1	0.32	0.22	0.35	0.22	0.35	0.39
0.2	0.70	0.61	0.70	0.74	0.99	1.09
0.4	2.80	2.07	3.65	2.10	3.19	3.90
0.6	4.81	3.61	5.82	3.48	5.43	6.29
0.8	7.00	4.97	8.30	4.92	7.80	8.99
1	9.22	6.61	failure	failure	10.46	failure
1.2	15.32	8.25	failure	failure	16.02	failure

**Table 8-11 Maximum Predicted Displacement from Unidirectional, Bidirectional and Components under El Centro (Interlocking)**

Times El Centro	Unidirectional		Bidirectional		Component	
	Longitudinal Dx (in)	Transverse Dy (in)	Longitudinal Dx (in)	Transverse Dy (in)	D <sub>SRSS</sub> (in)	D <sub>vector</sub> (in)
0.33	0.31	0.30	0.31	0.41	0.39	0.50
0.66	0.68	0.88	0.66	0.68	1.02	0.89
1	1.08	0.96	1.09	0.96	1.21	1.26
1.5	1.52	1.23	1.36	2.16	1.76	2.16
2	1.61	2.71	1.66	3.17	2.71	3.17
2.5	1.90	4.00	2.54	6.25	4.04	6.26
3	2.62	11.85	15.78	failure	11.86	failure
3.5	3.76	failure	failure	failure	285.08	failure
4	5.32	failure	failure	failure	failure	failure

**Table 8-12 Maximum Predicted Displacement from Unidirectional, Bidirectional and Components under Los Gatos (Interlocking)**

Times Los Gatos	Unidirectional		Bidirectional		Component	
	Longitudinal Dx (in)	Transverse Dy (in)	Longitudinal Dx (in)	Transverse Dy (in)	D <sub>SRSS</sub> (in)	D <sub>vector</sub> (in)
0.1	0.24	0.15	0.26	0.14	0.33	0.31
0.2	0.39	0.30	0.40	0.29	0.50	0.49
0.4	0.91	0.64	0.94	0.90	0.96	1.12
0.6	1.39	1.45	1.15	0.74	1.58	1.56
0.8	2.60	1.89	2.75	1.44	2.68	2.77
1	5.13	1.61	5.34	2.53	5.21	5.48
1.15	7.85	1.43	8.11	4.90	7.89	8.52
1.3	failure	1.35	failure	failure	failure	failure

**Table 8-13 Maximum Predicted Displacement from Unidirectional, Bidirectional and Components under Petrolia (Interlocking)**

Times Petrolia	Unidirectional		Bidirectional		Component	
	Longitudinal Dx (in)	Transverse Dy (in)	Longitudinal Dx (in)	Transverse Dy (in)	D <sub>SRSS</sub> (in)	D <sub>vector</sub> (in)
0.1	0.23	0.12	0.23	0.11	0.27	0.26
0.2	0.44	0.22	0.45	0.21	0.47	0.46
0.4	0.55	0.45	0.56	0.44	1.00	1.00
0.6	1.00	0.65	1.01	0.79	1.38	1.26
0.8	1.78	0.90	1.83	1.11	1.91	1.97
1	2.92	1.19	2.92	1.75	3.07	3.20
1.2	4.34	1.55	4.31	2.59	4.53	4.76
1.4	6.18	2.09	6.26	4.06	6.42	6.99
1.6	8.67	2.37	8.93	7.63	8.92	10.18

**Table 8-14 Maximum Predicted Displacement from Unidirectional, Bidirectional and Components under Rinaldi (Interlocking)**

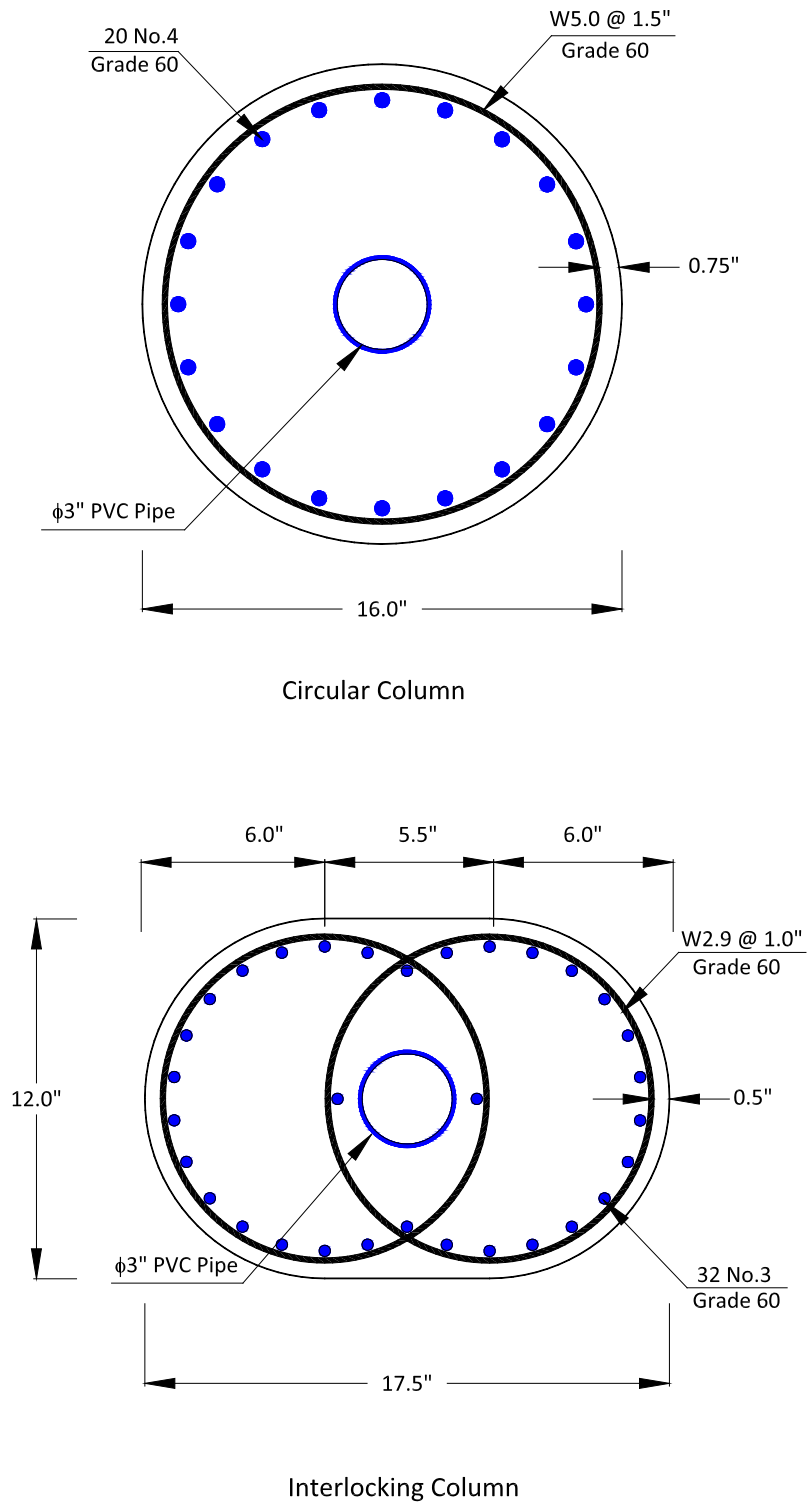
Times Rinaldi	Unidirectional		Bidirectional		Component	
	Longitudinal Dx (in)	Transverse Dy (in)	Longitudinal Dx (in)	Transverse Dy (in)	D <sub>SRSS</sub> (in)	D <sub>vector</sub> (in)
0.1	0.13	0.11	0.29	0.22	0.01	0.00
0.2	0.28	0.22	0.74	0.56	0.02	0.06
0.4	0.74	0.58	2.27	1.24	0.04	0.25
0.6	1.45	1.19	3.52	2.00	0.15	0.46
0.8	2.65	1.38	4.12	3.38	0.31	0.68
1	3.37	1.94	4.46	5.60	0.42	1.78
1.2	3.63	3.32	4.29	8.06	0.86	5.34
1.4	3.90	3.71	20.33	failure	1.39	failure

**Table 8-15 Maximum Predicted Displacement from Unidirectional, Bidirectional and Components under Sylmar (Interlocking)**

Times Sylmar	Unidirectional		Bidirectional		Component	
	Longitudinal Dx (in)	Transverse Dy (in)	Longitudinal Dx (in)	Transverse Dy (in)	D <sub>SRSS</sub> (in)	D <sub>vector</sub> (in)
0.1	0.17	0.12	0.17	0.12	0.17	0.17
0.2	0.35	0.21	0.35	0.25	0.35	0.35
0.4	0.78	0.63	0.82	1.02	0.84	1.05
0.6	1.85	1.55	2.01	2.48	1.97	2.75
0.8	3.17	2.02	3.23	2.93	3.48	3.74
1	4.13	4.55	4.26	3.87	4.79	4.85
1.2	5.17	3.96	5.29	4.97	6.22	6.20
1.4	6.56	3.30	6.29	8.74	7.24	9.90
1.6	8.33	3.35	failure	failure	8.75	failure

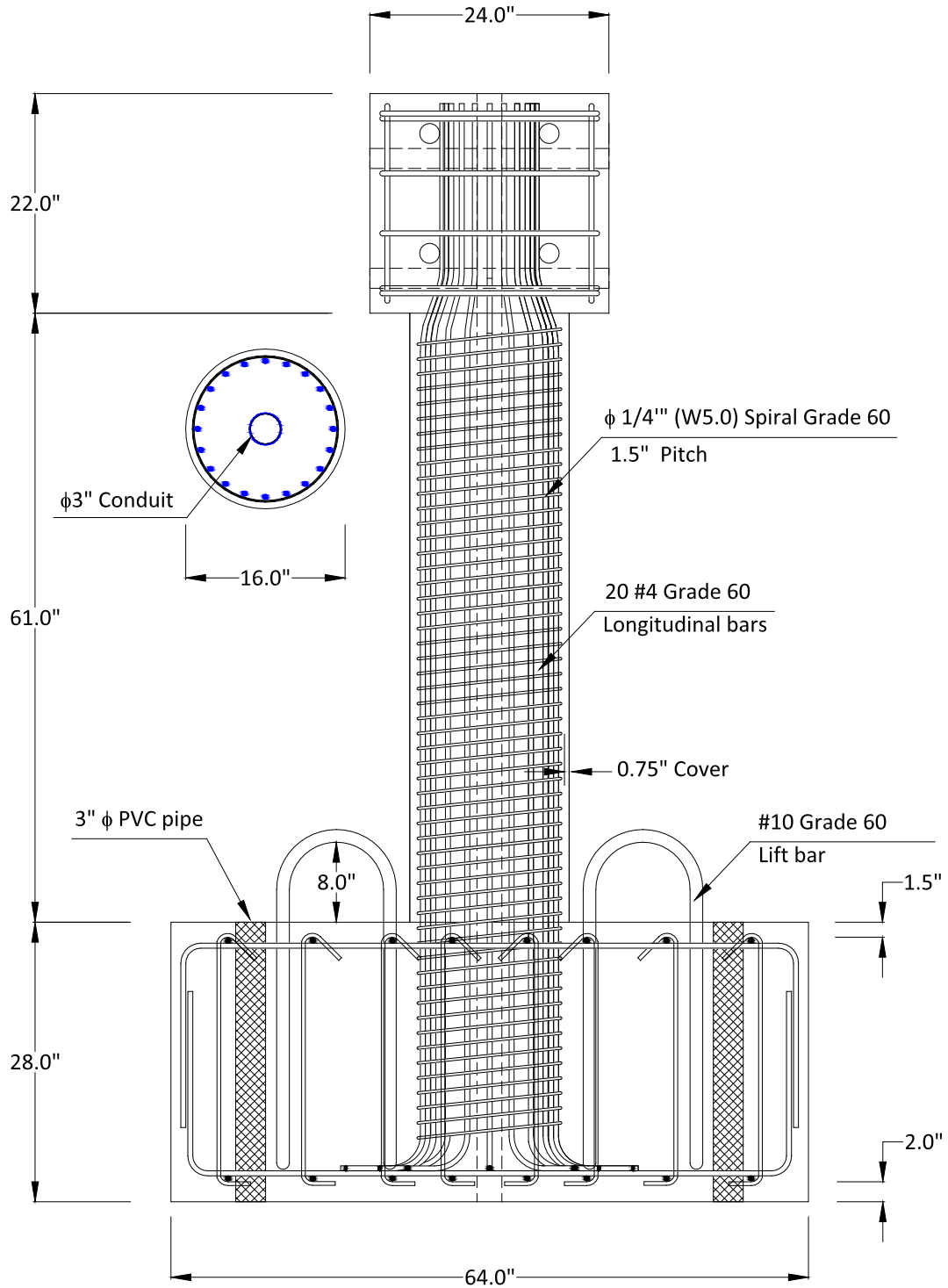
**Table 8-16 Maximum Predicted Displacement from Unidirectional, Bidirectional and Components under Takatori (Interlocking)**

Times Takatori	Unidirectional		Bidirectional		Component	
	Longitudinal Dx (in)	Transverse Dy (in)	Longitudinal Dx (in)	Transverse Dy (in)	D <sub>SRSS</sub> (in)	D <sub>vector</sub> (in)
0.1	0.23	0.81	0.20	0.74	0.89	0.87
0.2	0.53	1.06	0.64	1.26	1.47	1.55
0.4	4.61	1.63	1.81	3.16	3.54	3.17
0.6	3.74	3.66	2.60	5.21	4.81	5.23
0.8	5.15	4.74	3.76	8.02	6.33	8.18
1	6.61	6.58	failure	failure	7.99	failure
1.2	8.02	11.28	failure	failure	11.82	failure



**Figure 2-1 Specimens Cross Section**





**Figure 2-2 Circular Columns Steel Detail (N – S Elevation)**

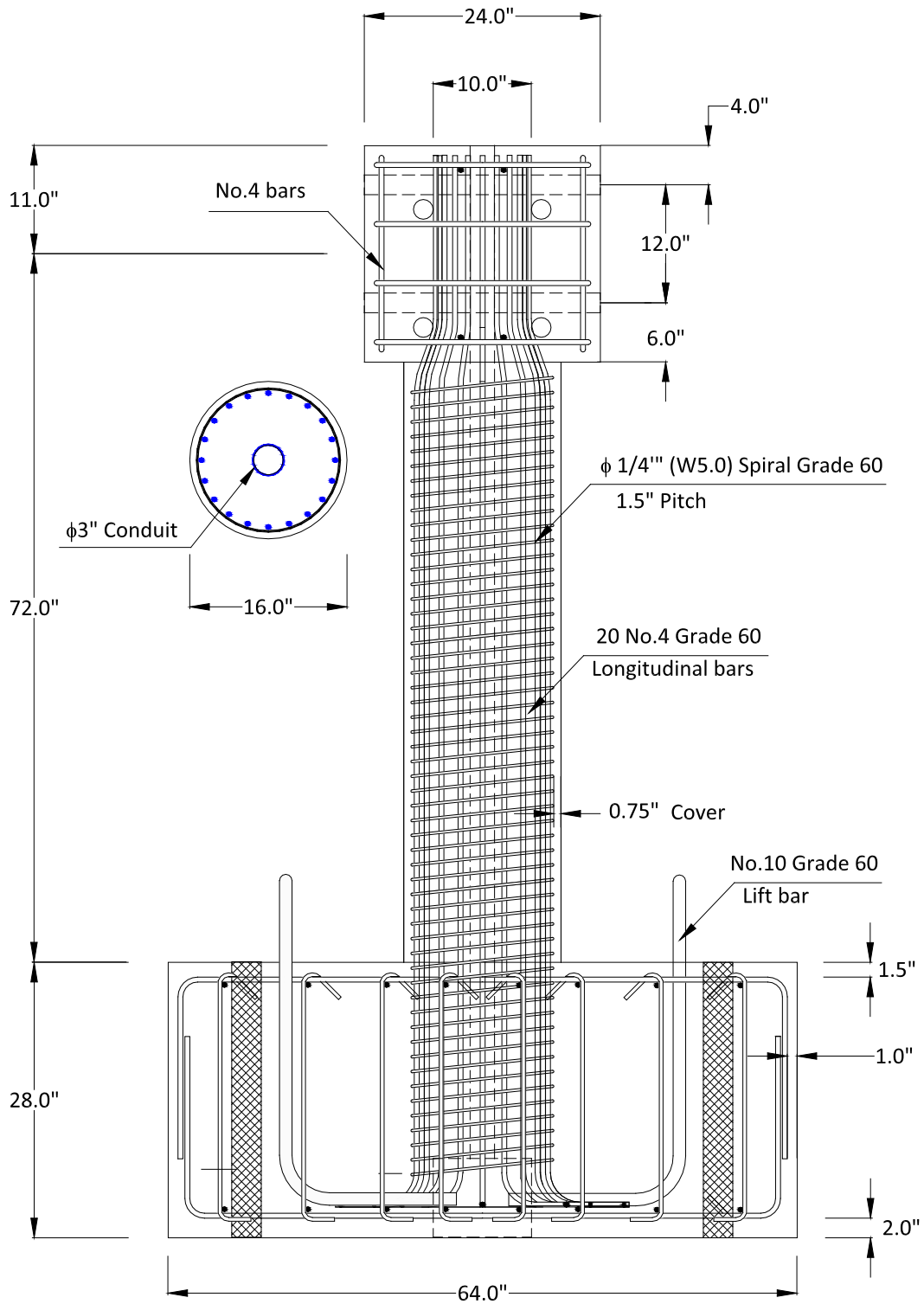
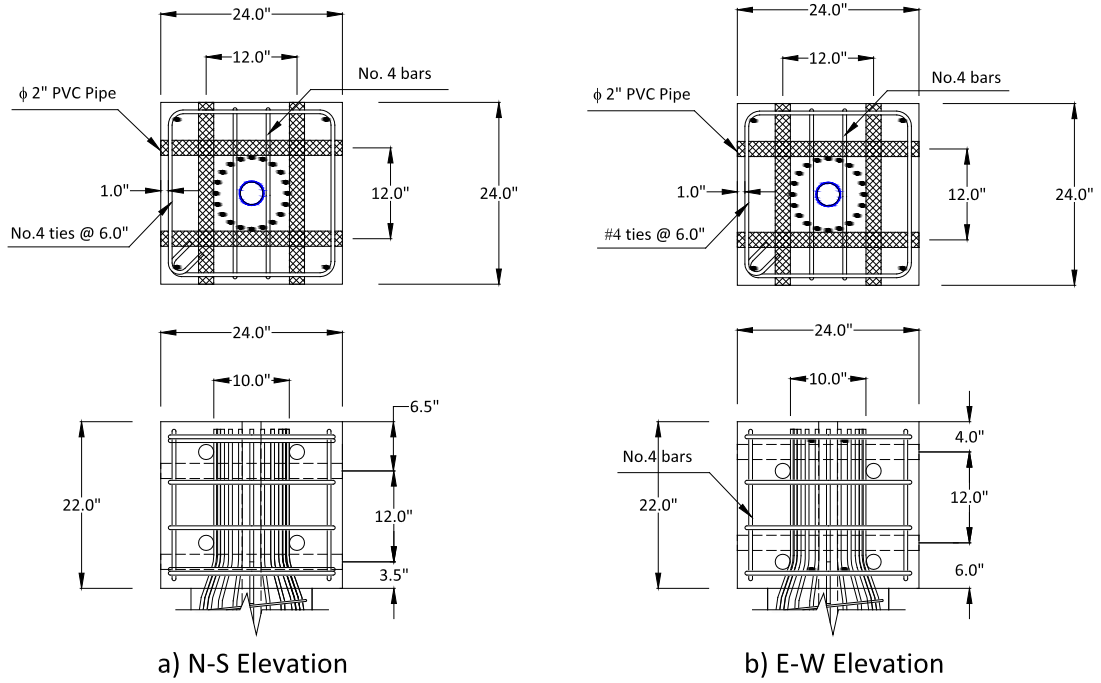
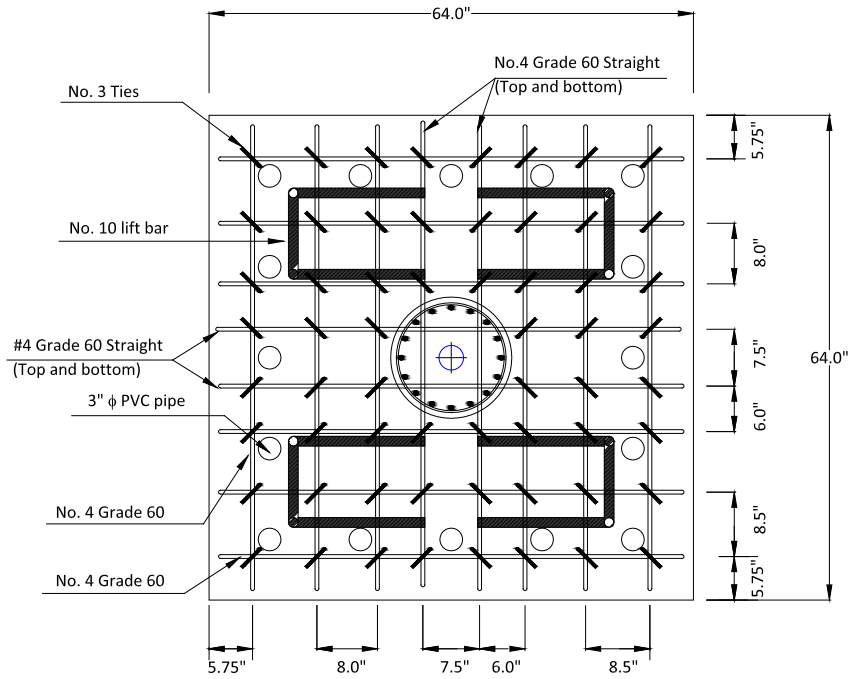


Figure 2-3 Circular Columns Steel Detail (E – W Elevation)

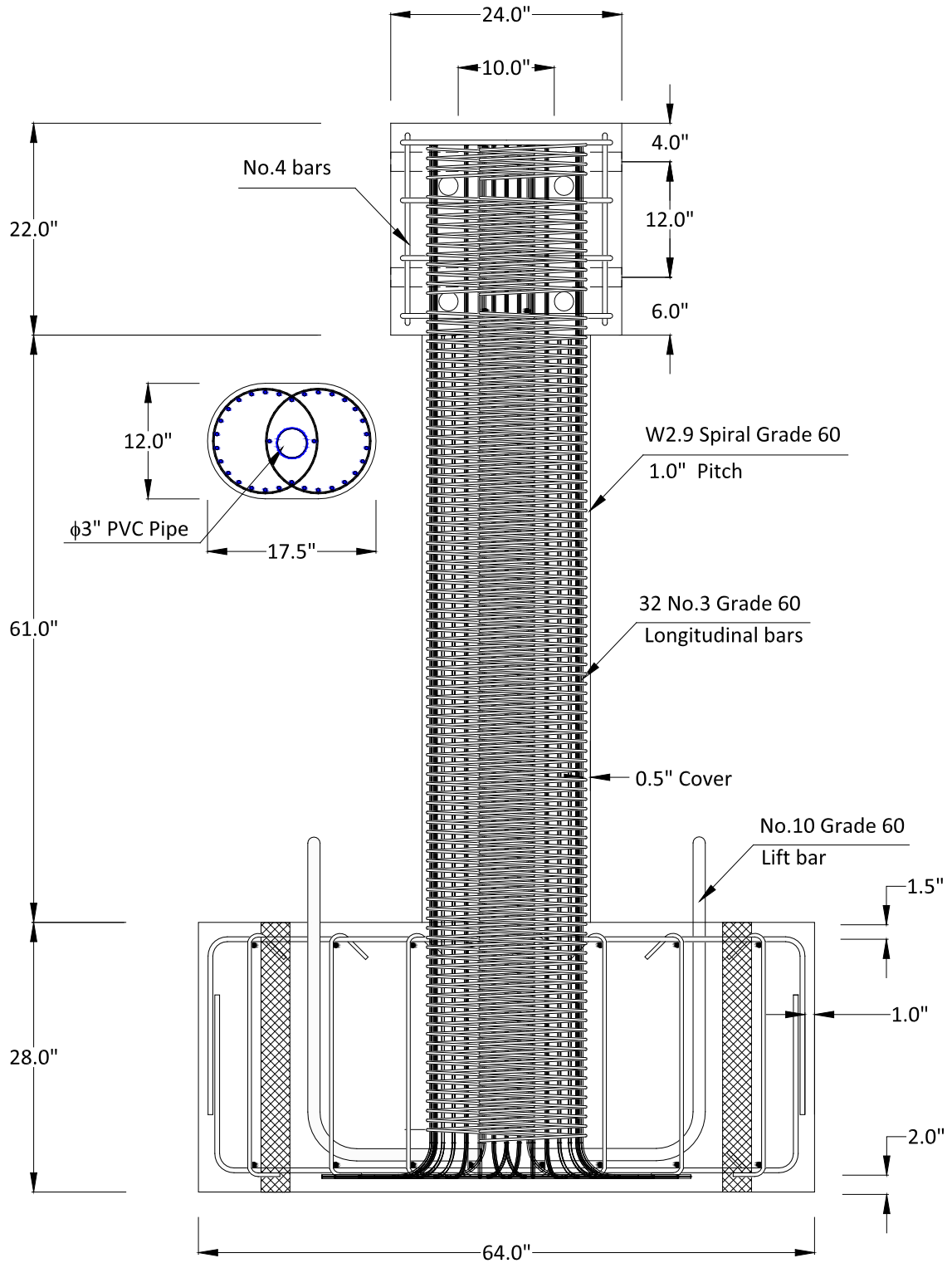


Loading Top Head Details



Footing Details

Figure 2-4 Circular Columns Footing and Top Head Details



**Figure 2-5 Interlocking Columns N – S Elevation**

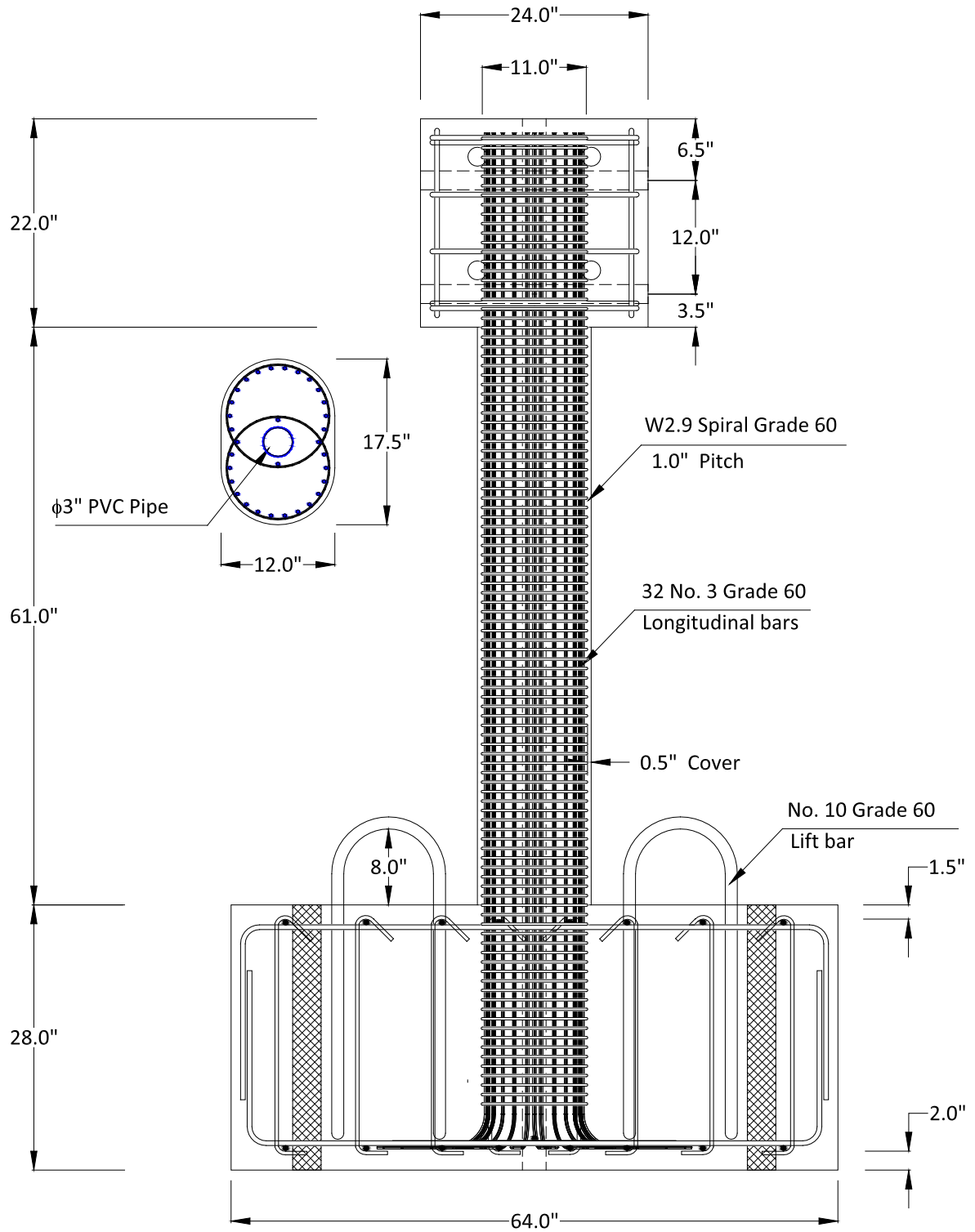
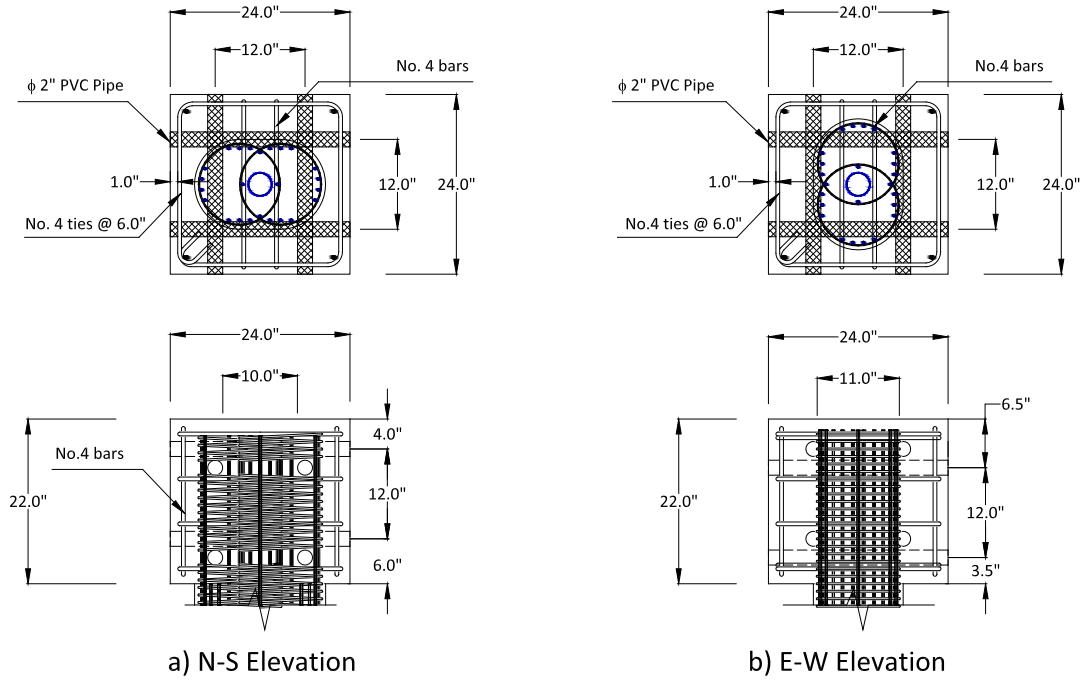


Figure 2-6 Interlocking Columns E – W Elevation



Loading Top Head Details

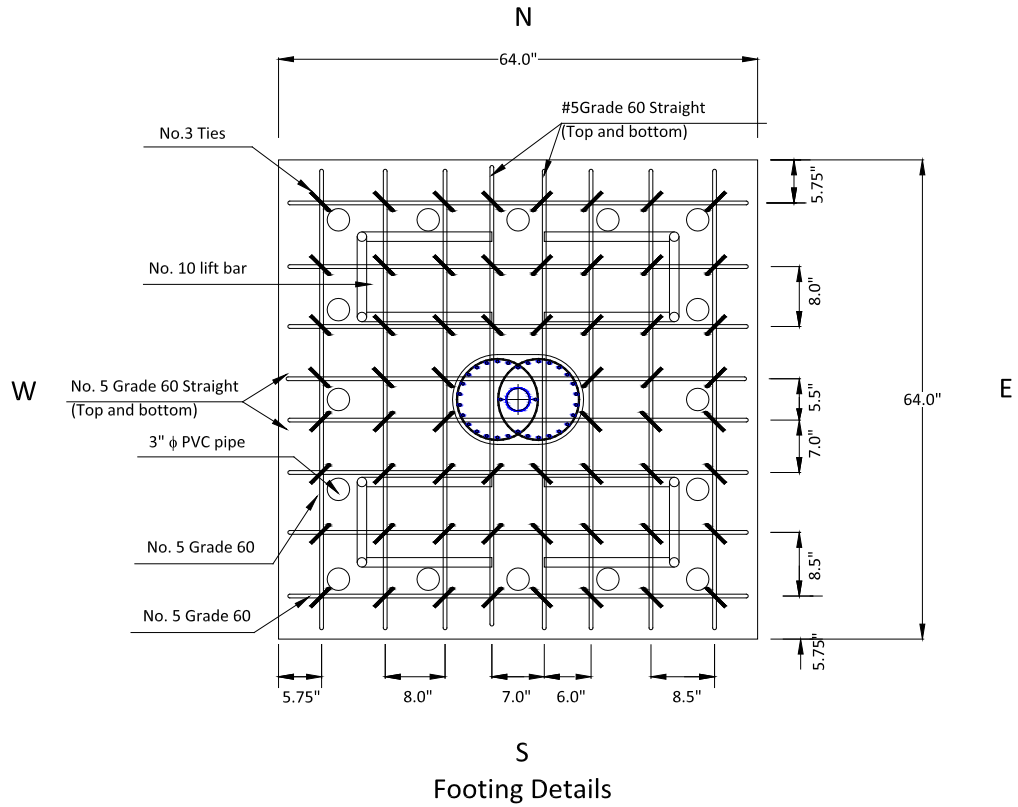


Figure 2-7 Interlocking Columns Footing and Top Head Details

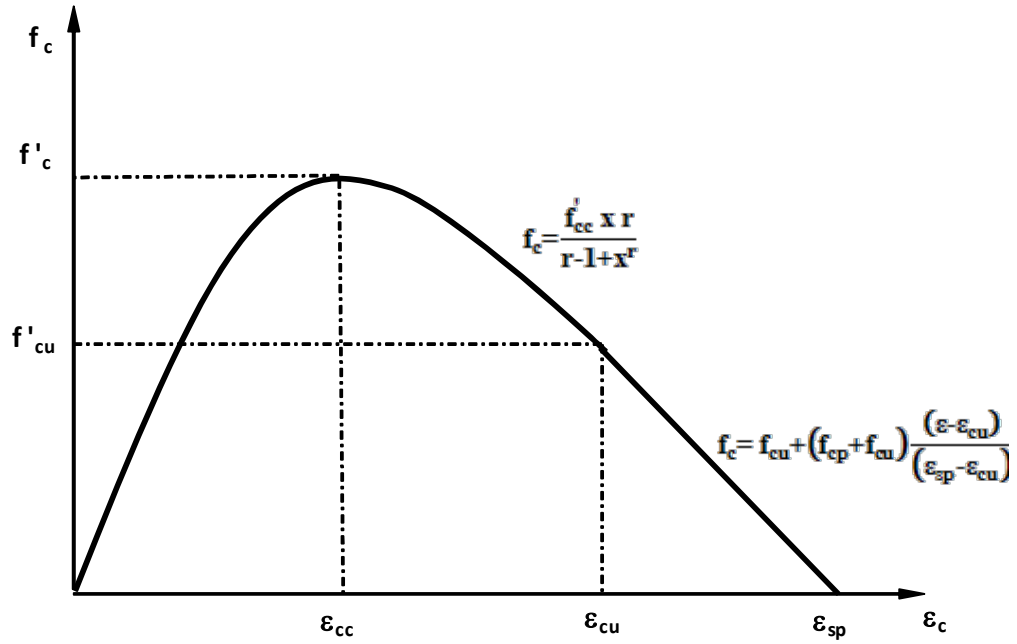


Figure 2-8 Stress-Strain Relationship for Unconfined Concrete

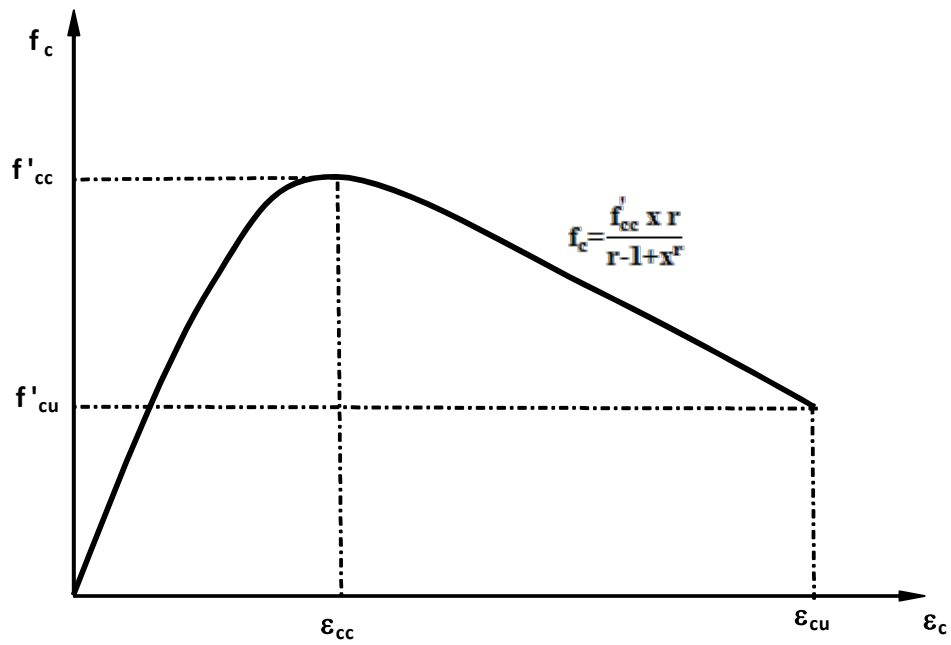


Figure 2-9 Stress-Strain Relationship for Confined Concrete

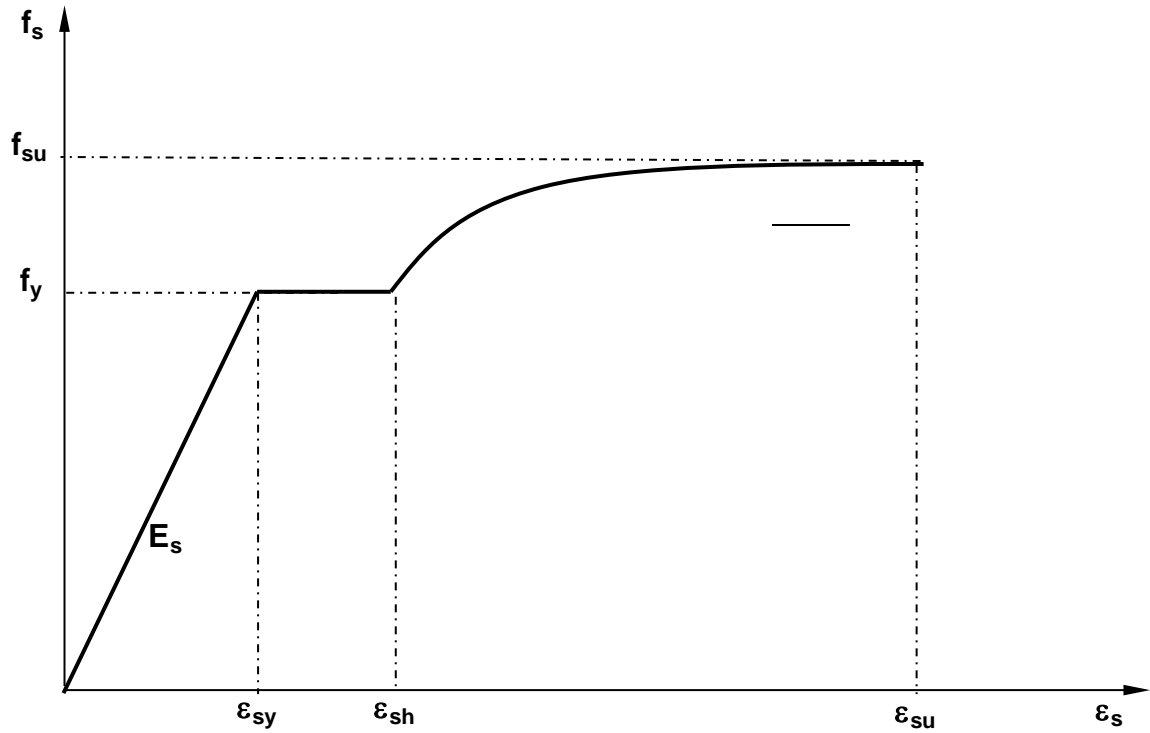


Figure 2-10 Stress-strain behavior for Steel

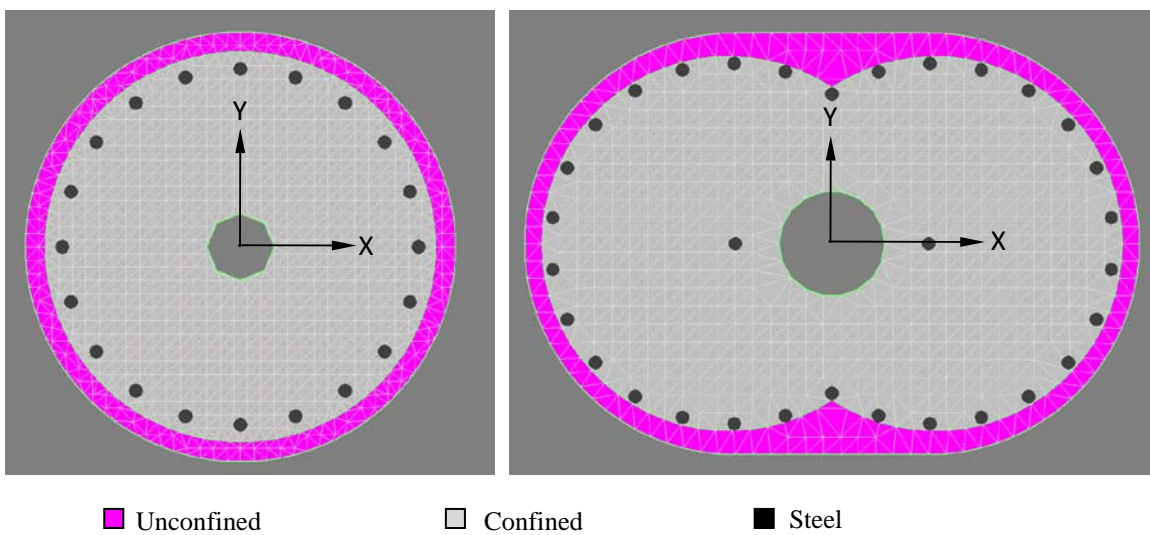


Figure 2-11 Cross Sections Used in Xtract (Fiber Model)



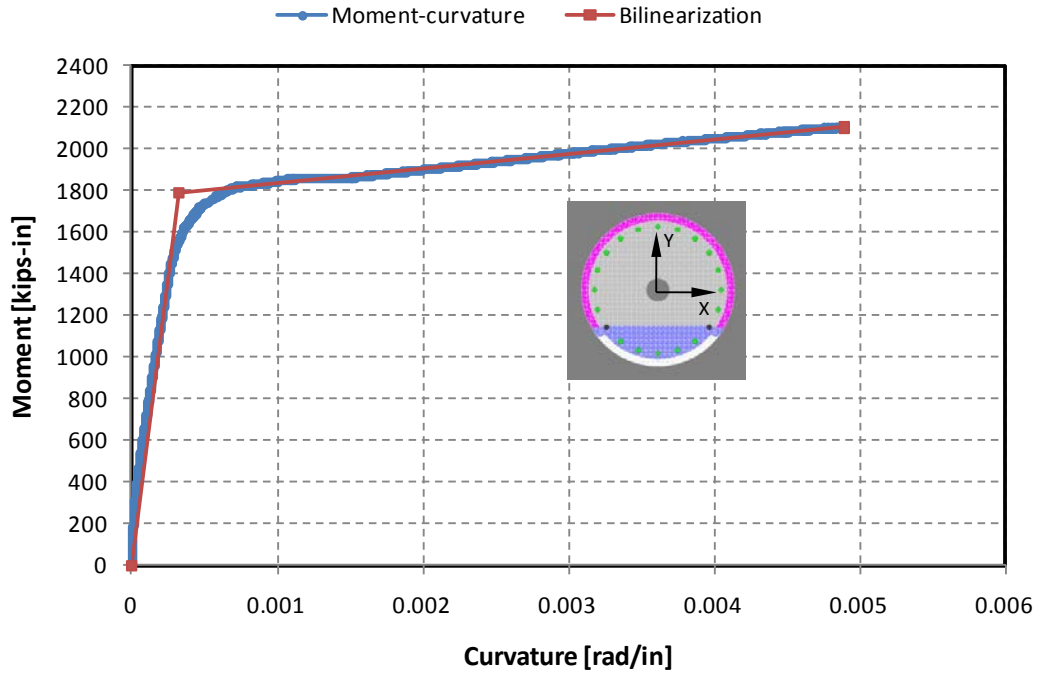


Figure 2-12 Moment-Curvature for Circular Column P=0, N.A at 0°

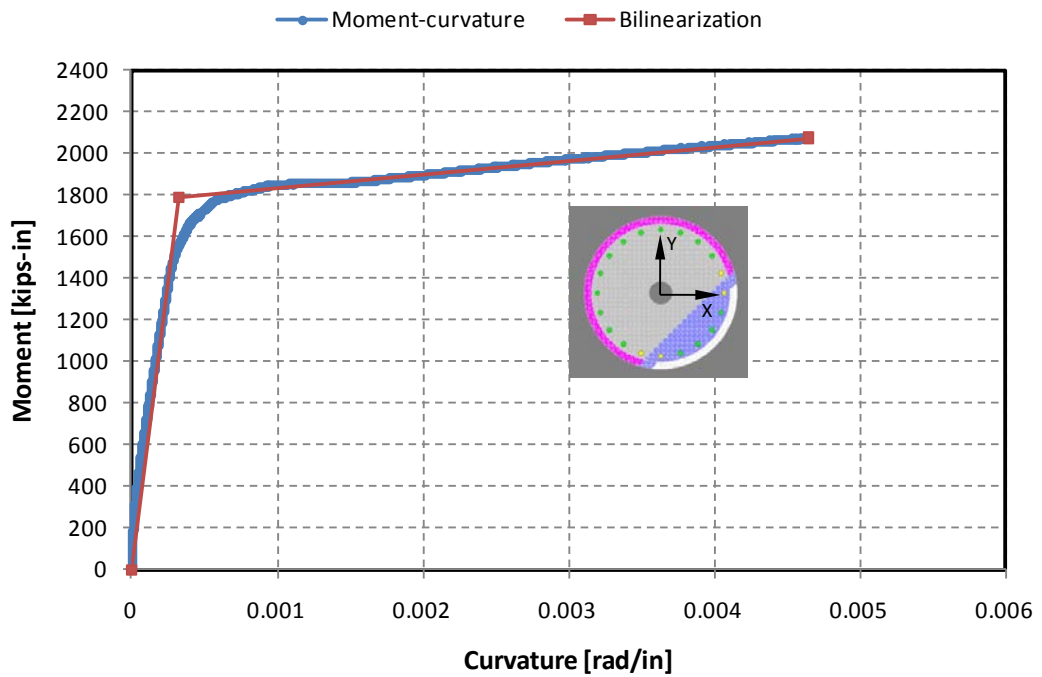


Figure 2-13 Moment-Curvature for Circular Column P=80 kips, N.A at 45°

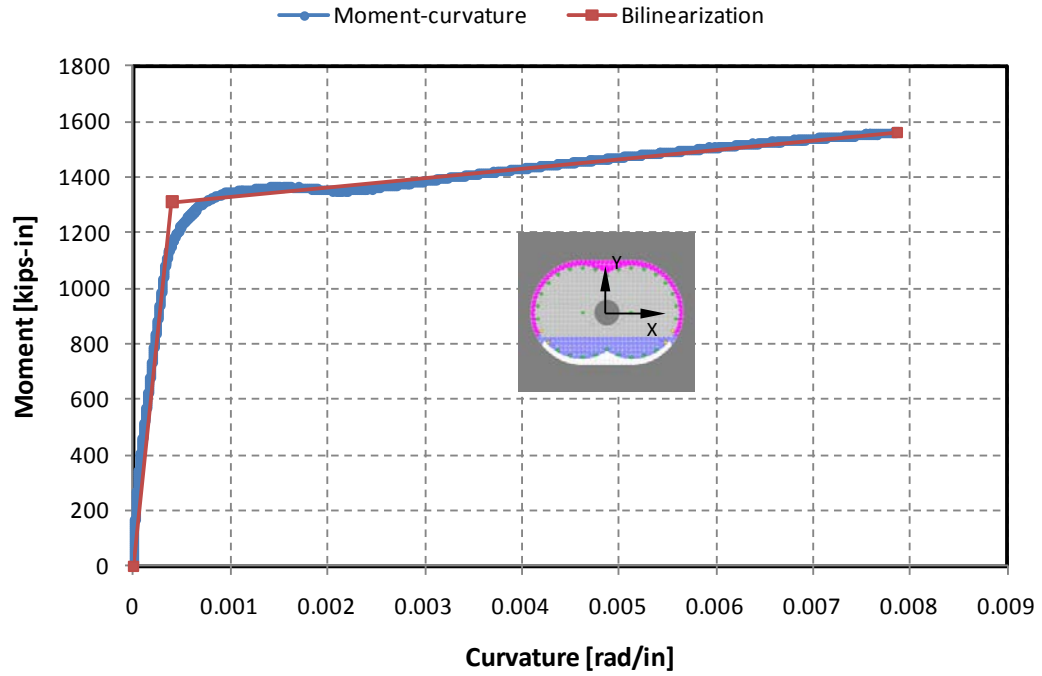


Figure 2-14 Moment-Curvature for Interlocking Column P=0, N.A at 0°

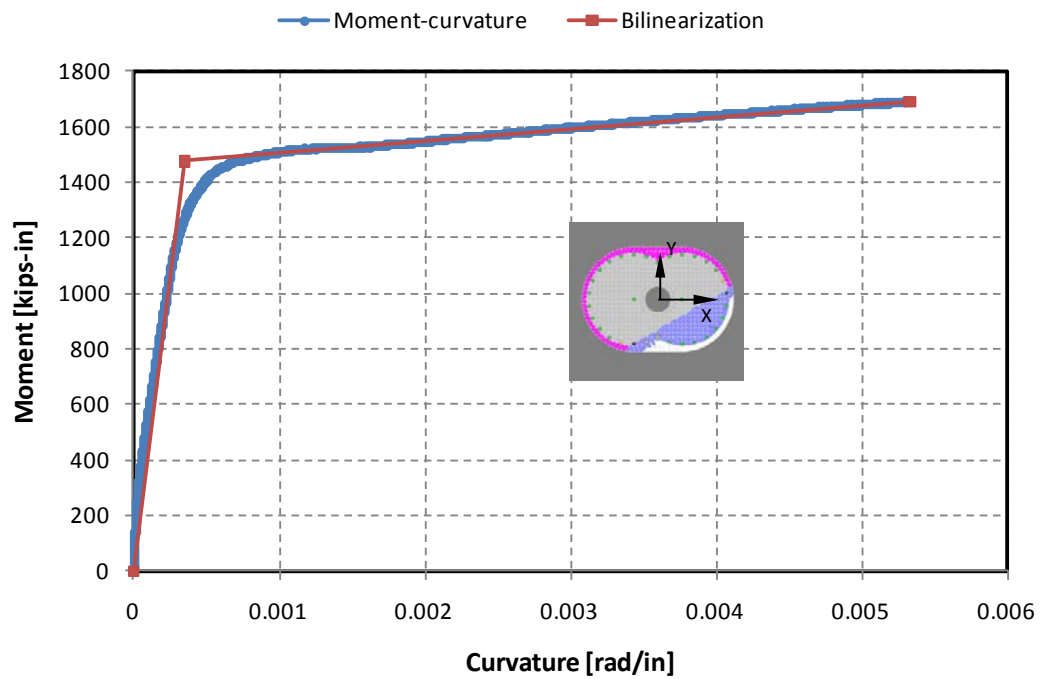


Figure 2-15 Moment-Curvature for Interlocking Column P=80 kips, N.A at 30°

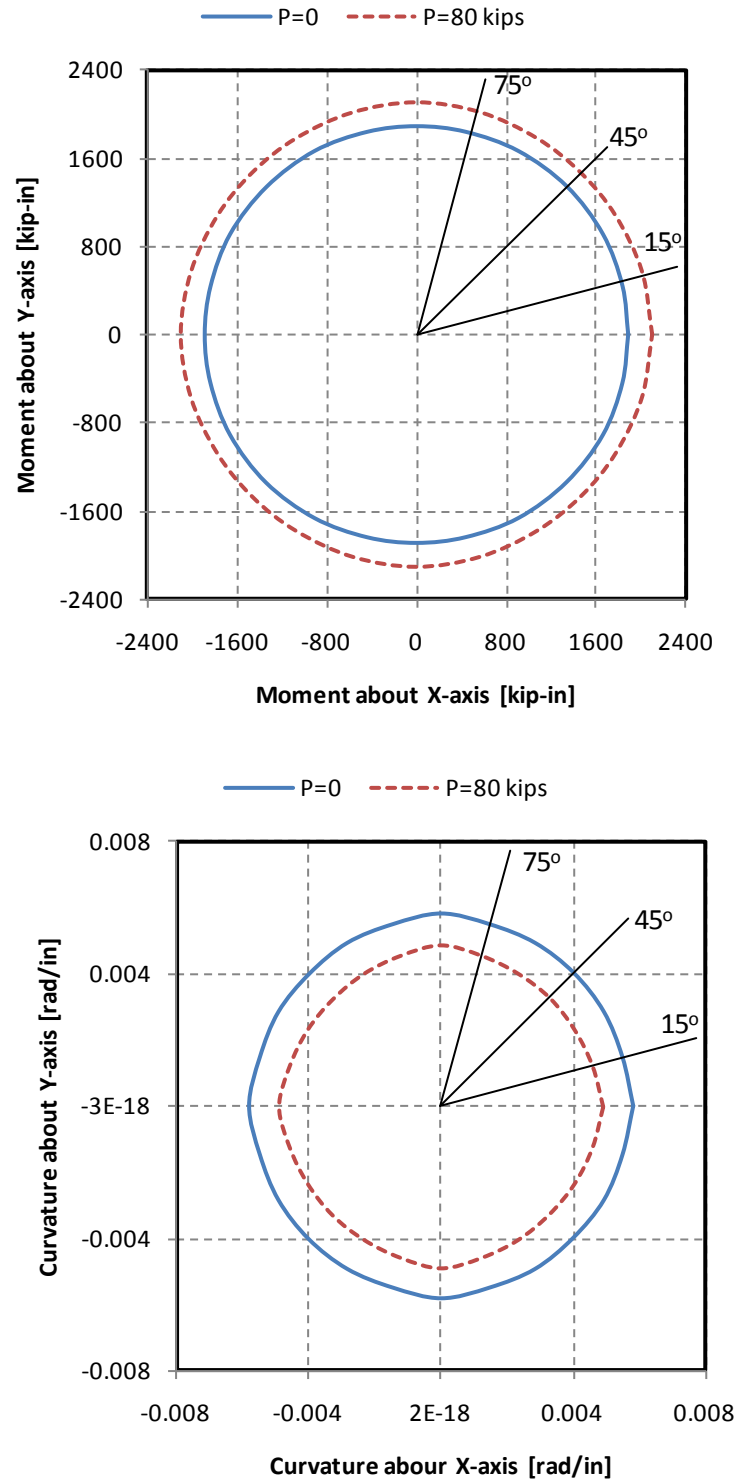


Figure 2-16 Capacity Orbits for Ultimate Moments and Curvatures, Circular Section

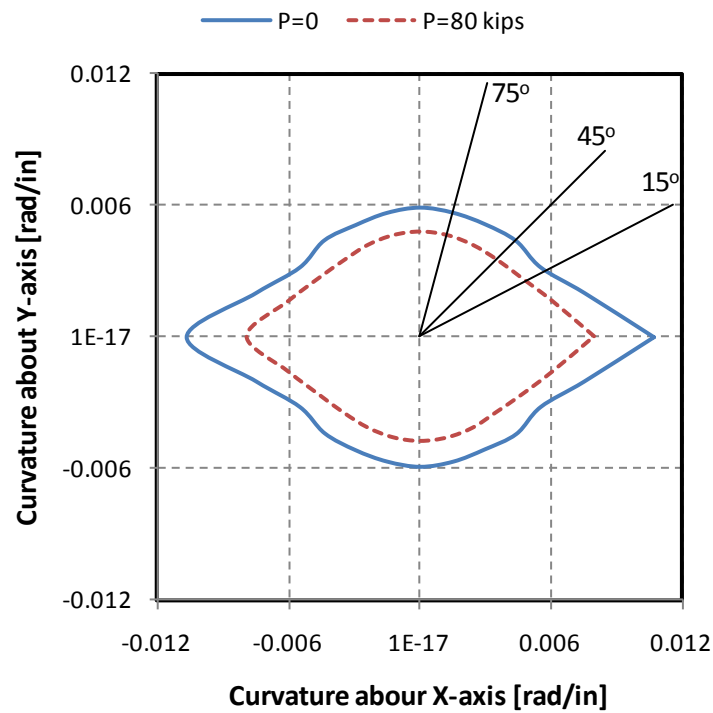
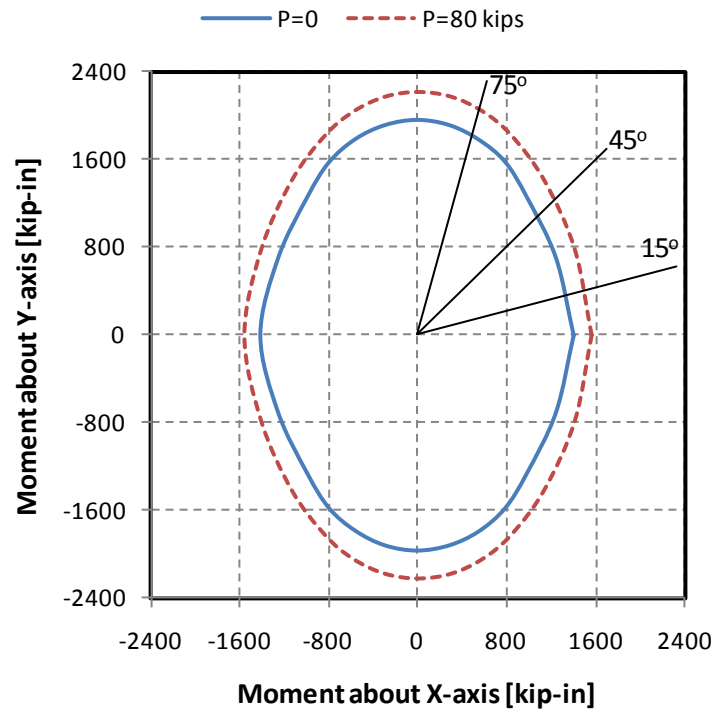


Figure 2-17 Capacity Orbits for Ultimate Moments and Curvatures, Interlocking Section

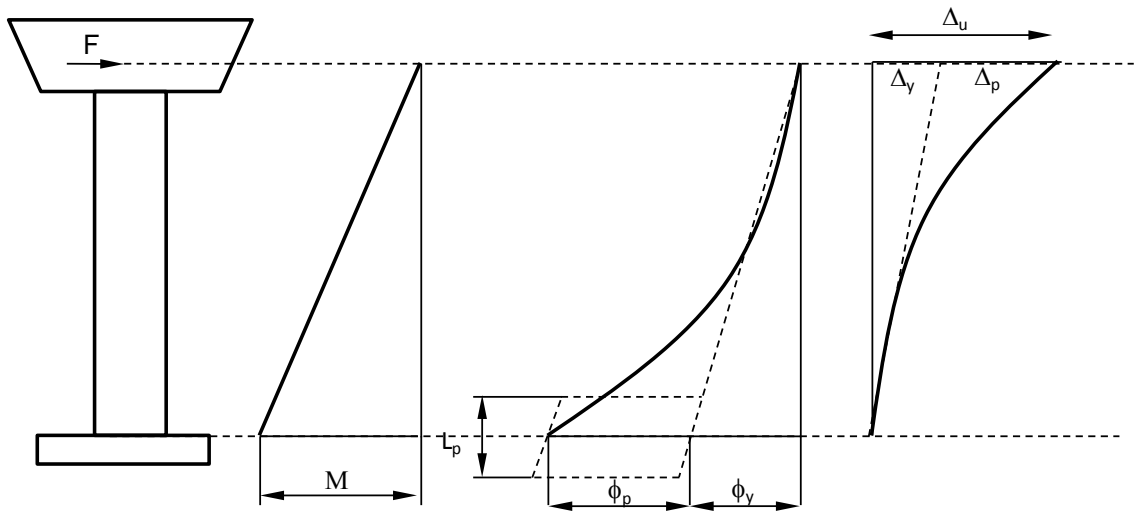


Figure 2-18 Force-Displacement Idealization (Priestley et al., 2007)

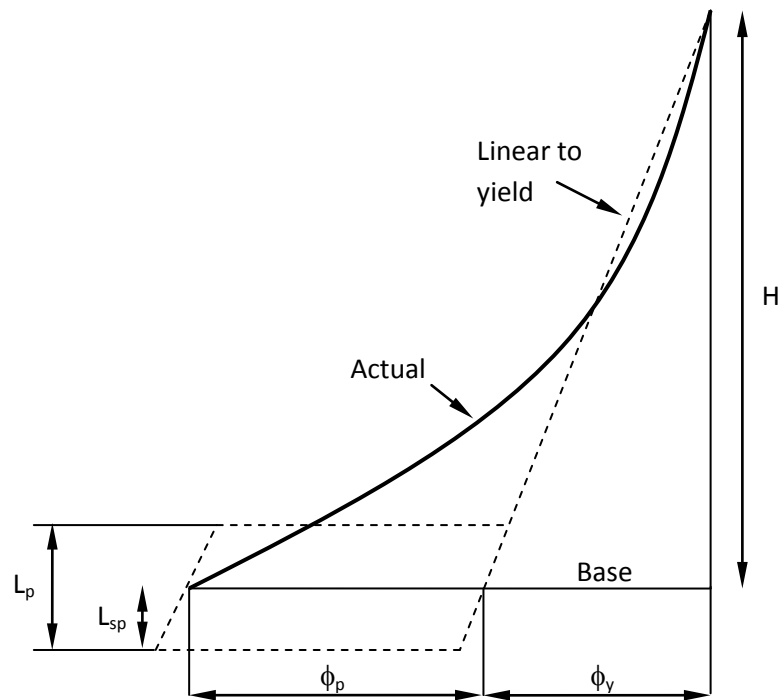
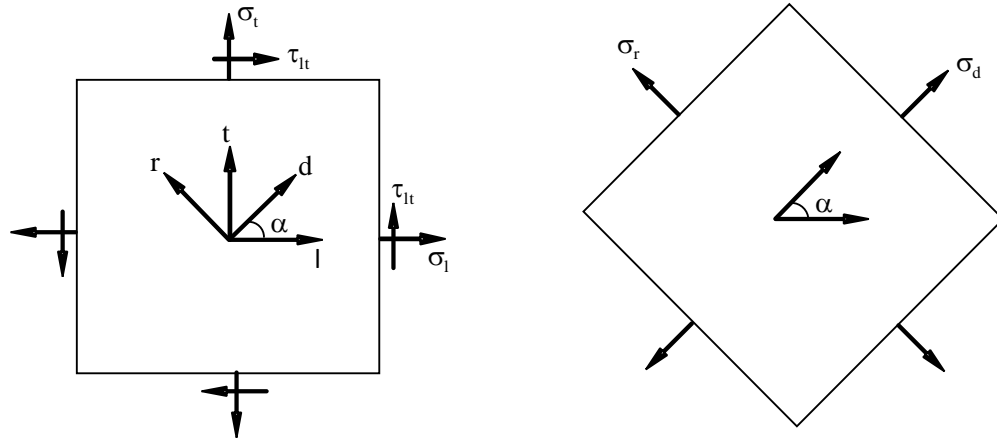
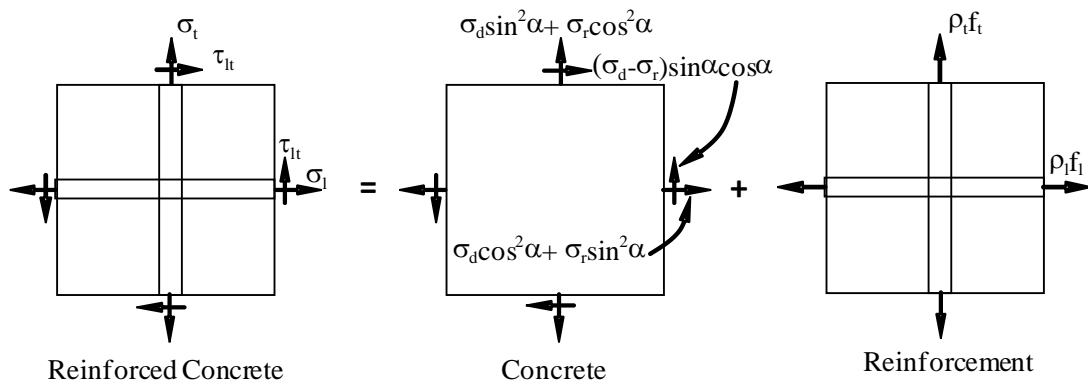


Figure 2-19 Idealization of Curvature Distribution (Priestley et al., 2007)

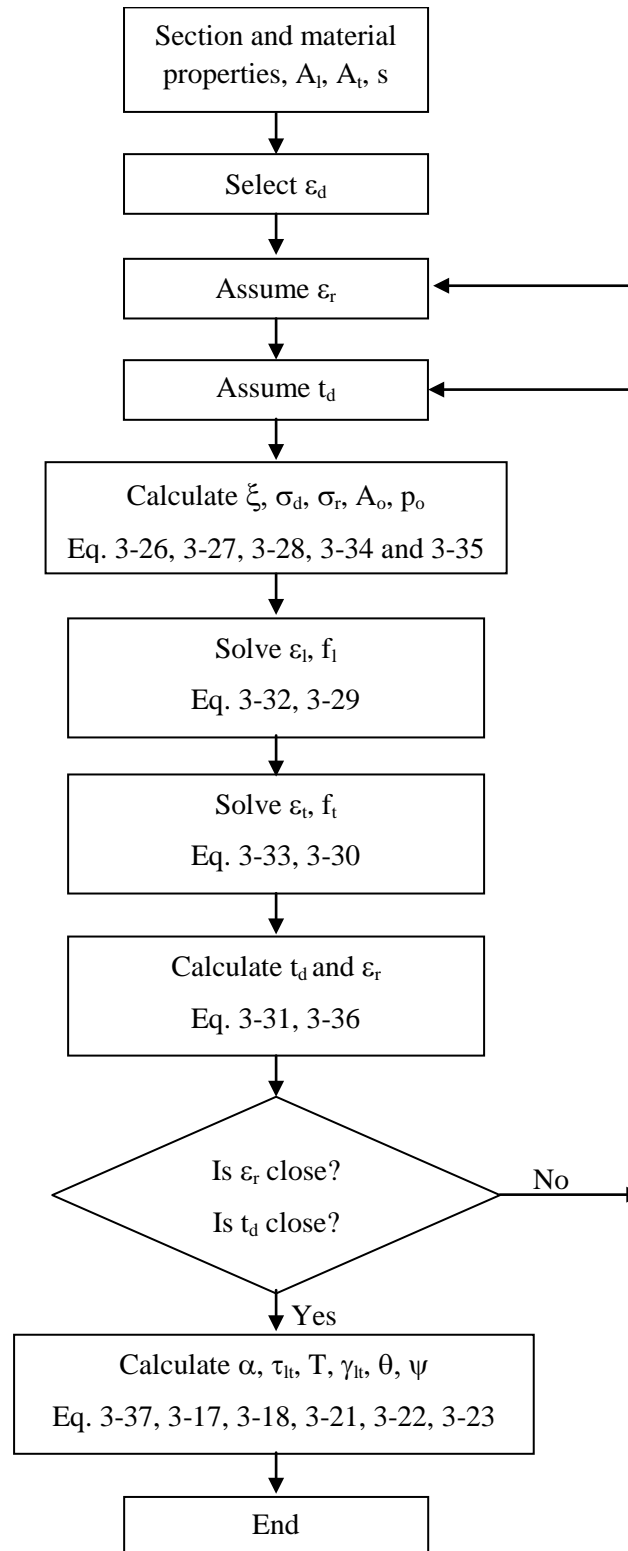


**b) Coordinate System and Definition of Stresses**



**a) Superposition of Stresses in Concrete and Reinforcement**

**Figure 2-20 Reinforced Concrete Membrane Element Under In-plane Stresses**



**Figure 2-21 Flow Chart for Torque-twist Analysis**

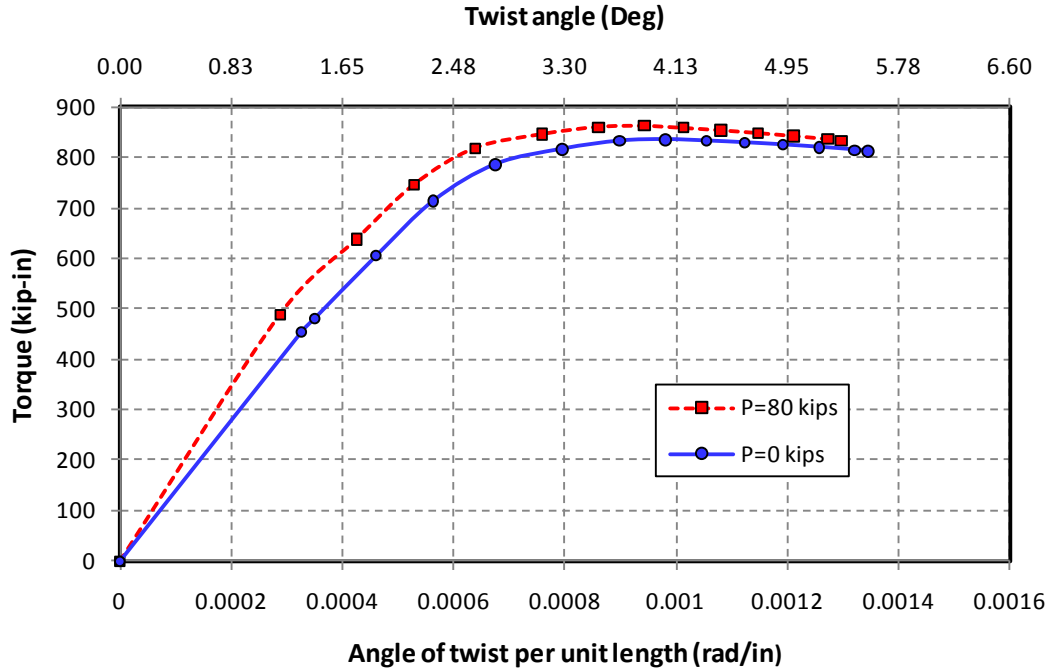


Figure 2-22 Torque-twist Relationship for Circular Specimens

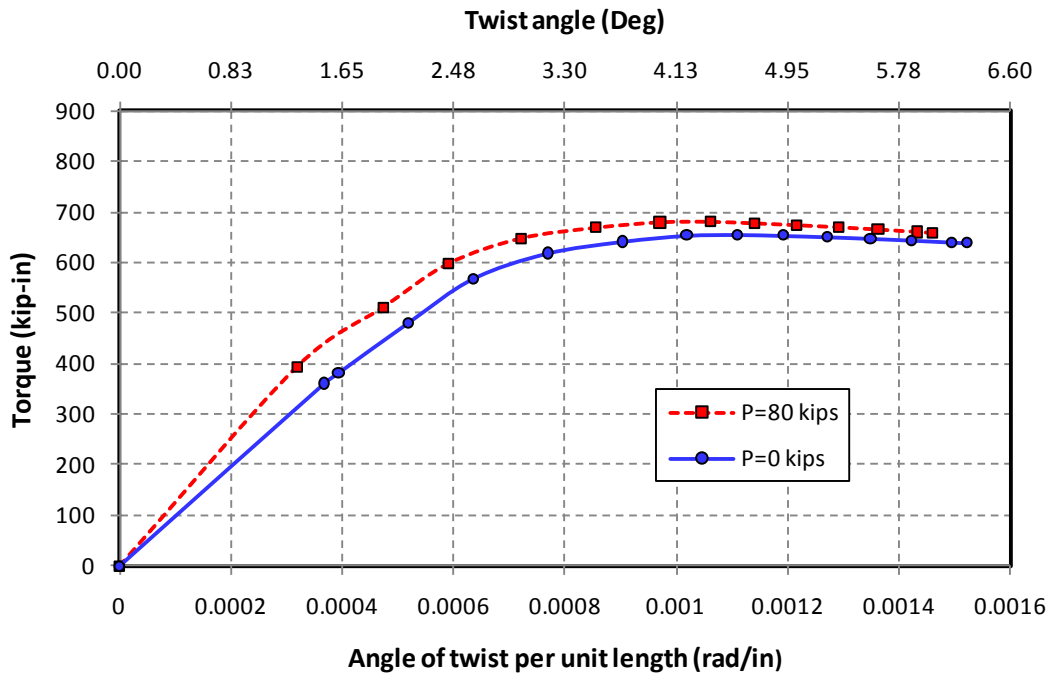


Figure 2-23 Torque-twist Relationship for interlocking Specimens

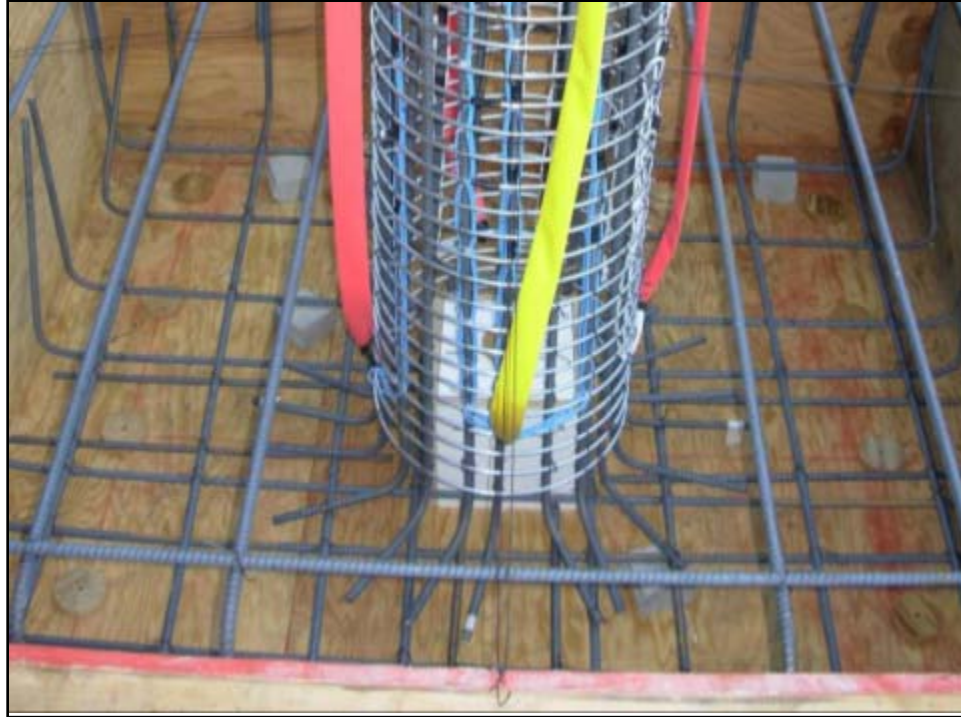




**Figure 3-1 Steel Cage for interlocking Column (view from bottom)**



**Figure 3-2 Steel Cage for interlocking Column (view from top)**



**Figure 3-3 Circular Column Steel Cage Set on the Footing**



**Figure 3-4 Interlocking Column Steel Cage Set on the Footing**



**Figure 3-5 Circular Column Footing before Pouring the Concrete**



**Figure 3-6 Interlocking Column Footing before Pouring the Concrete**



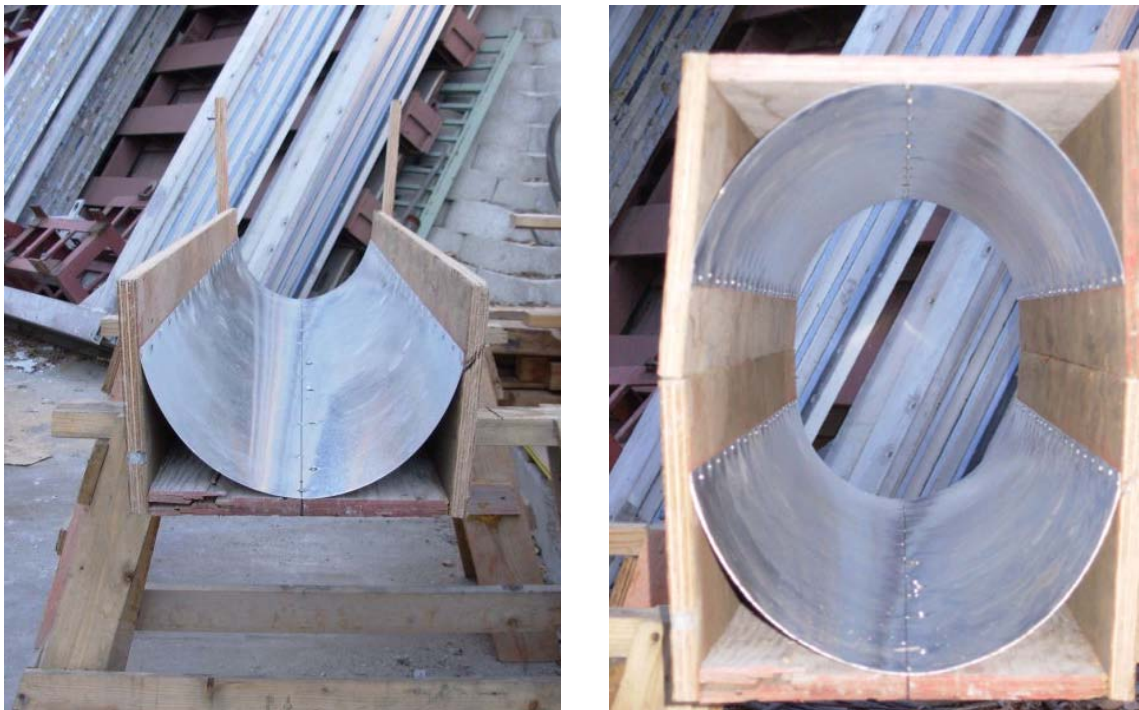
**Figure 3-7 Circular Column Footing Concrete Pouring**



**Figure 3-8 Interlocking Column Footing Concrete Pouring**



**Figure 3-9 Circular Column Formwork**



**Figure 3-10 Wood and Steel Sheets Used for Interlocking Column Formwork**



**Figure 3-11 Column and top Head Pouring (Circular Specimen)**



**Figure 3-12 Column and top Head Pouring (Interlocking Specimen)**



**Figure 3-13 Circular Columns after Form Removal**



**Figure 3-14 Interlocking Columns after Form Removal**

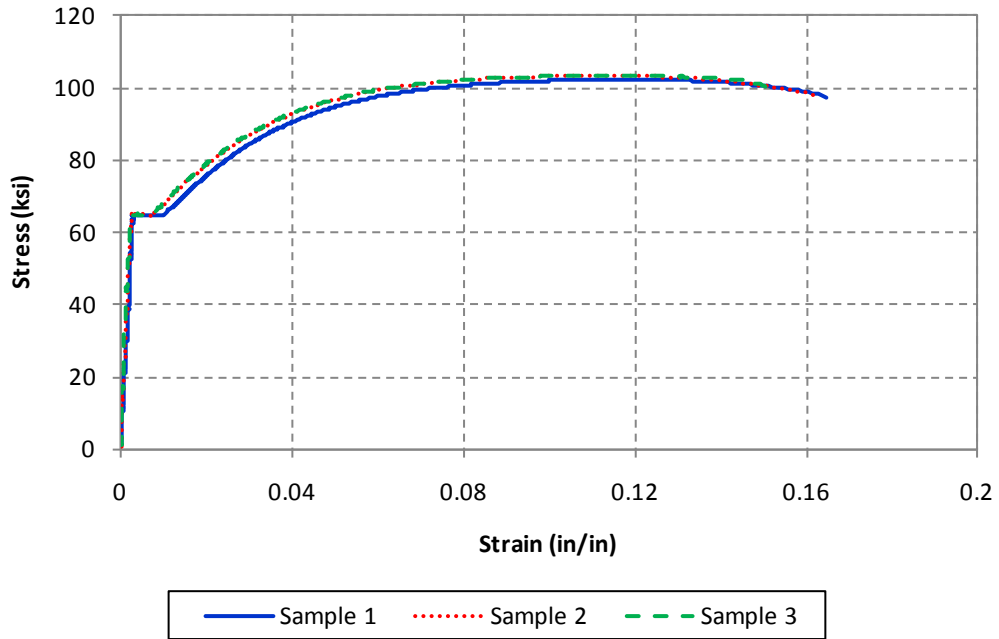


Figure 3-15 Measured Stress-Strain Curves for Grade 60 No.4 Deformed Bars

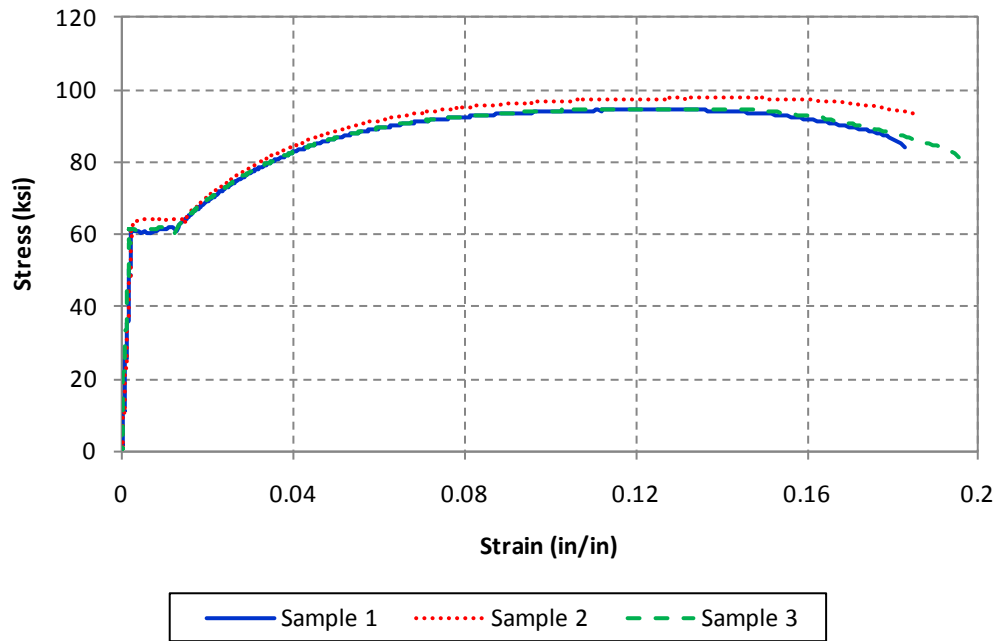
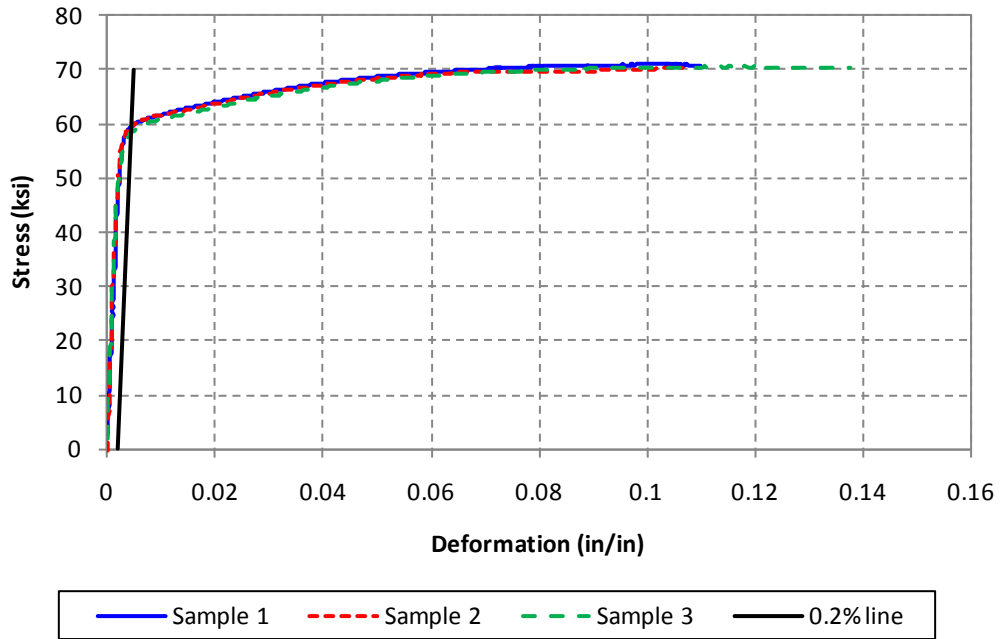
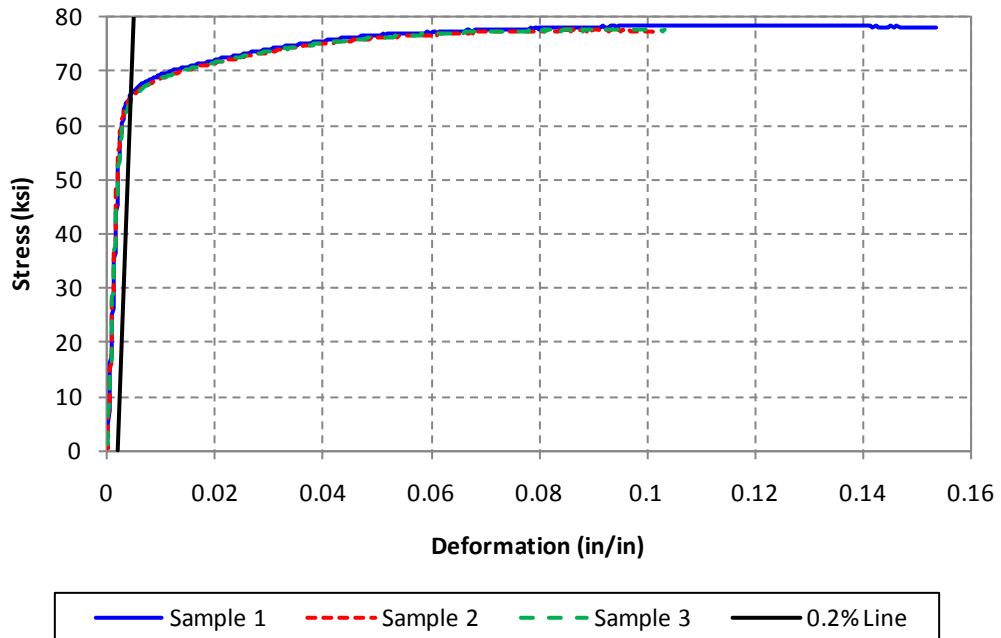


Figure 3-16 Measured Stress-Strain Curves for Grade 60 No.3 Deformed Bars





**Figure 3-17 Stress-Strain Curves of Grade 60 W5.0 Galvanized Wire**



**Figure 3-18 Stress-Strain Curves of Grade 60 W2.9 Galvanized Wire**



Figure 3-19 Shake Table Testing of Single Cantilever-type Column (Mahin *et al.*, 2004)

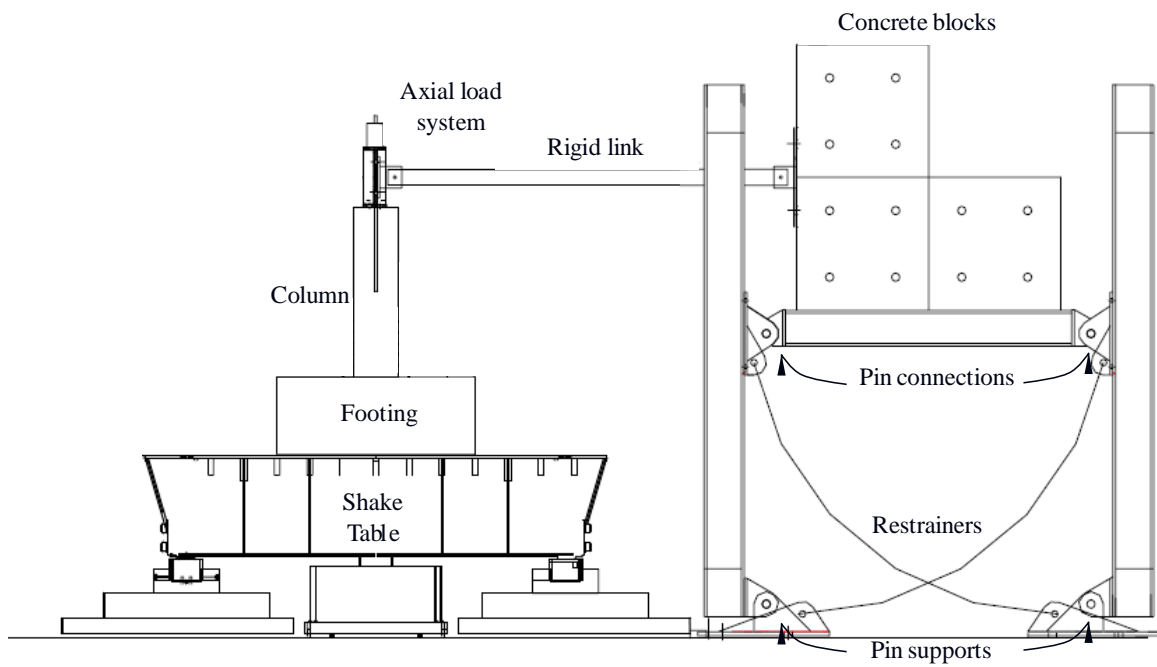


Figure 3-20 Unidirectional Mass Rig at UNR (Adapted from Laplace *et al.*, 1999)

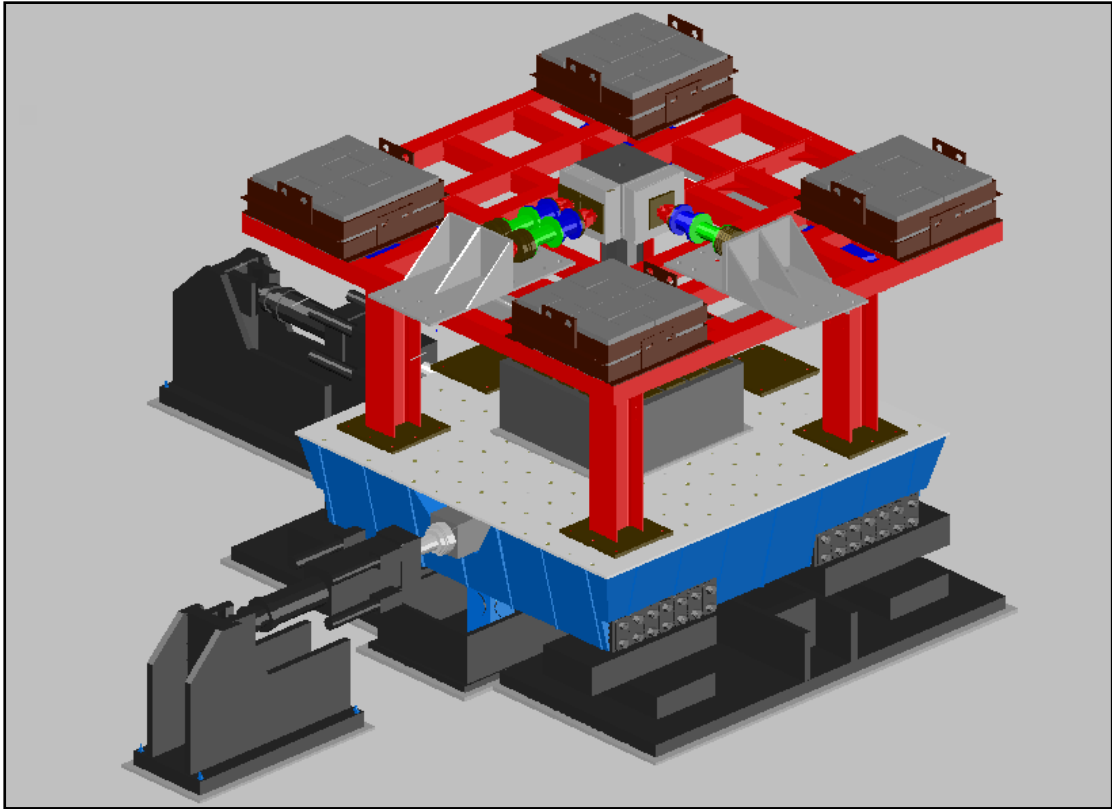


Figure 3-21 Bidirectional Mass Rig (3D View)

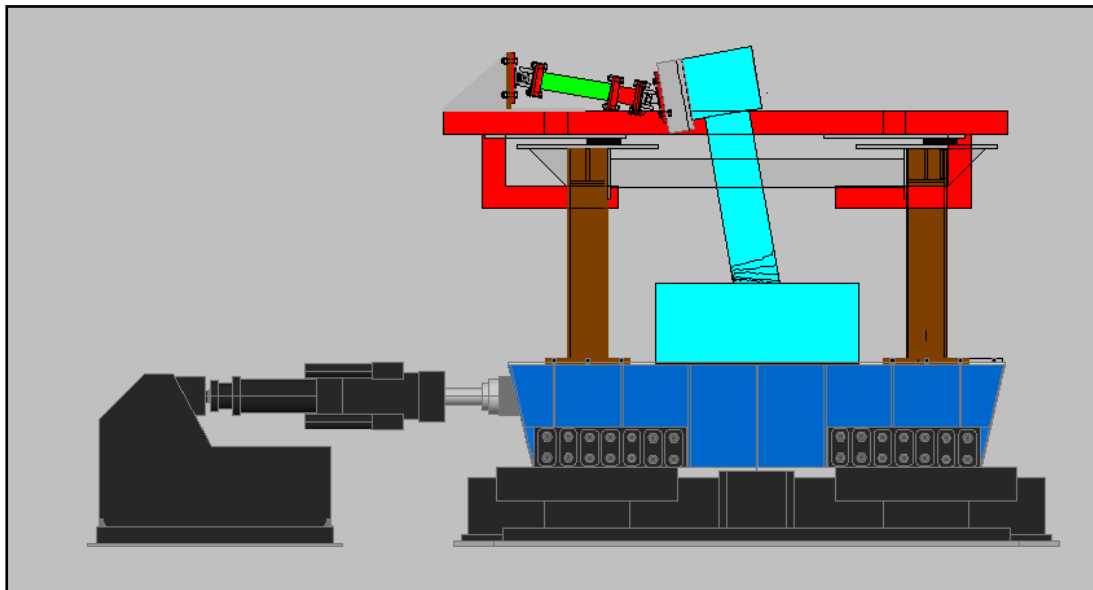
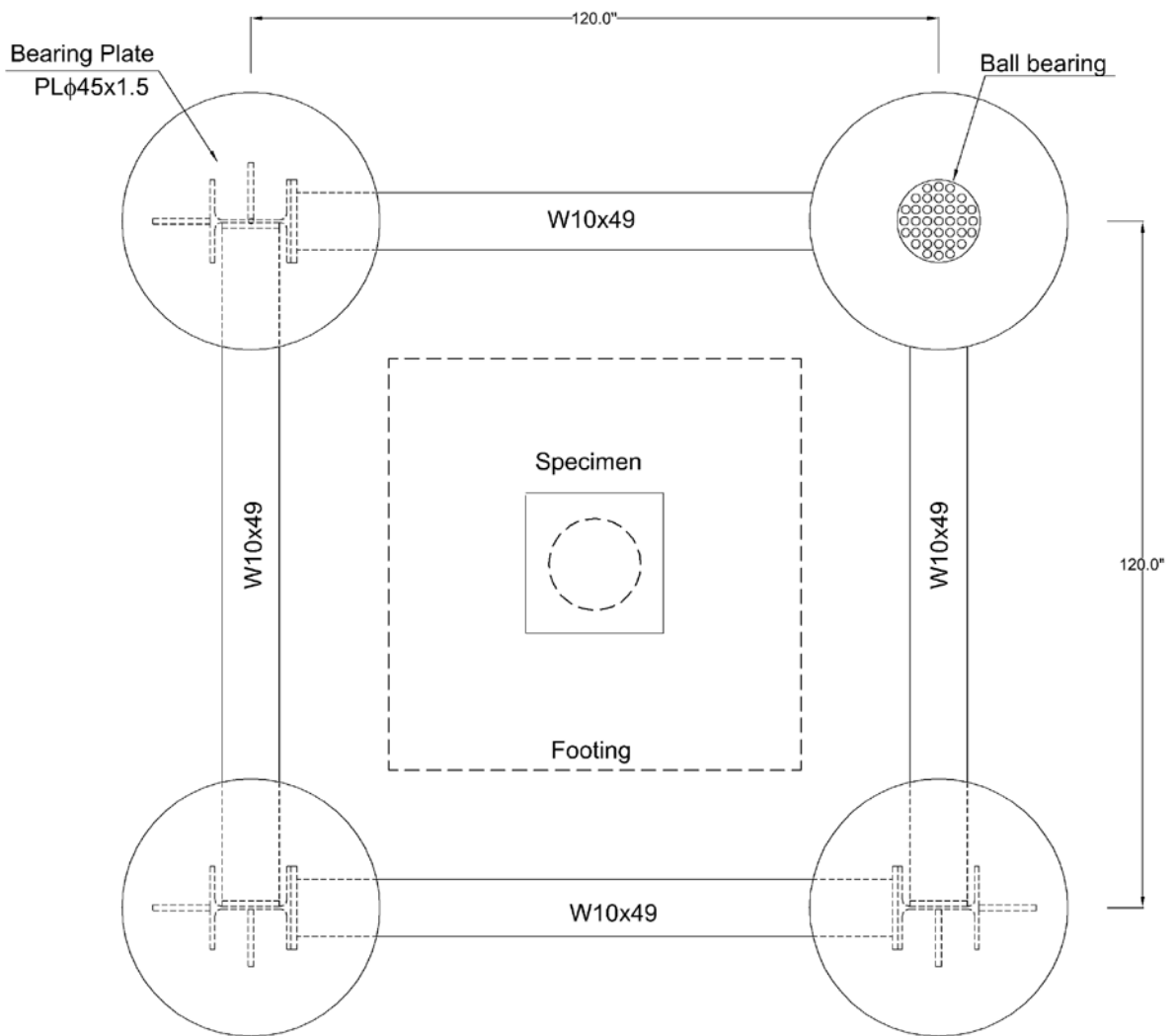


Figure 3-22 Bidirectional Mass Rig (Elevation)



**Figure 3-23 Bidirectional Mass Rig (Supporting Structure Plan View)**

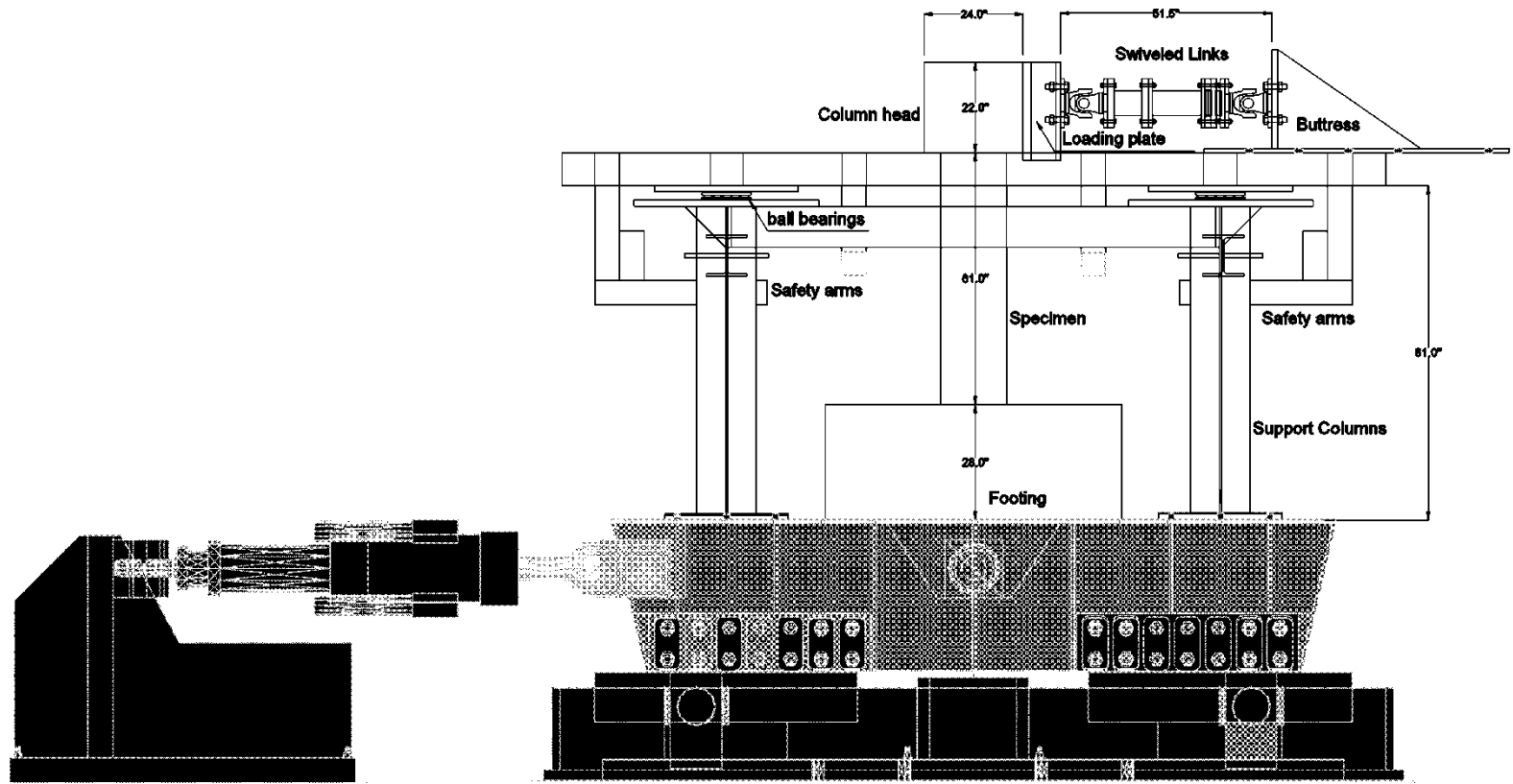


Figure 3-24 Bidirectional Mass Rig (Elevation View)

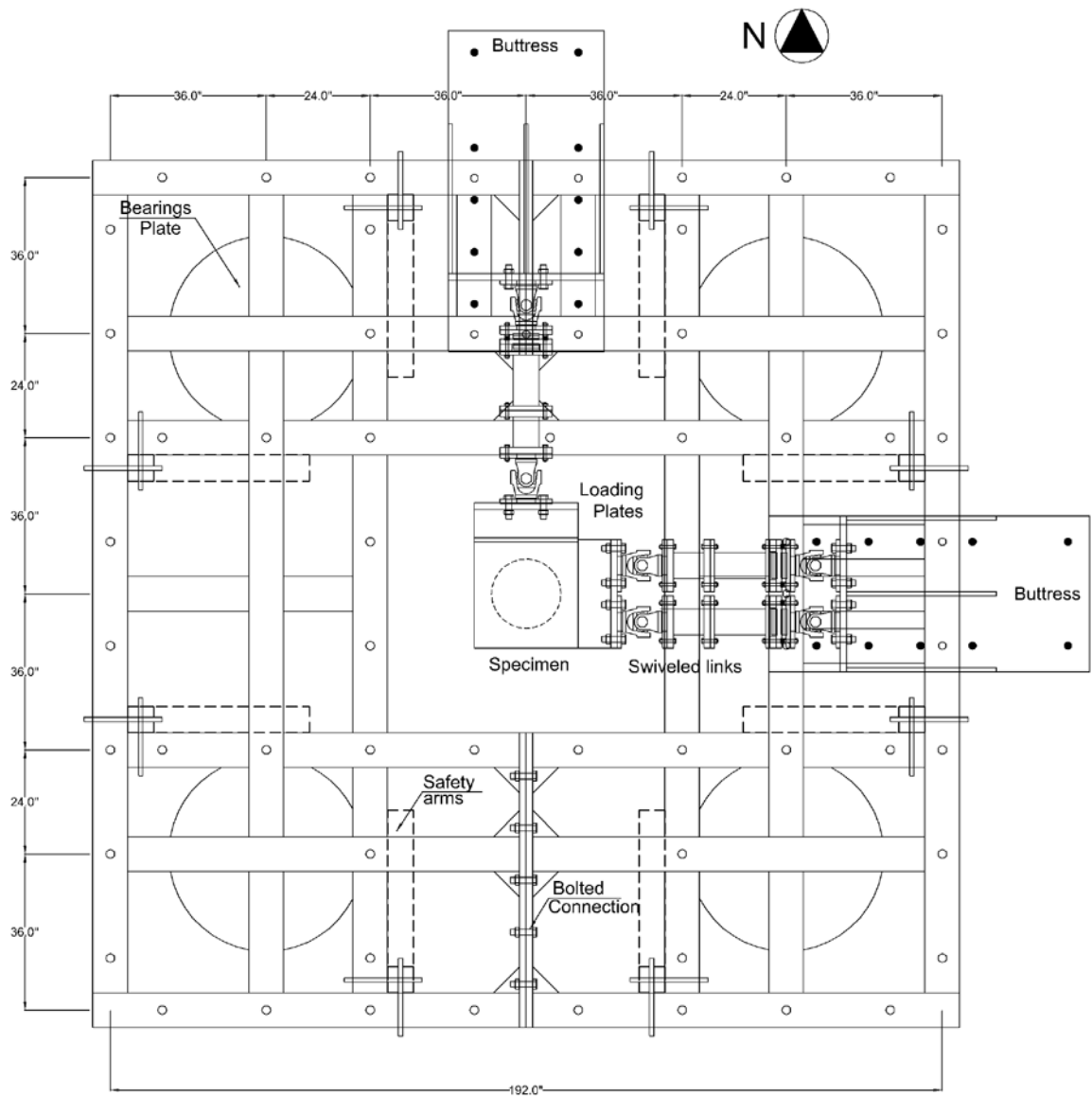


Figure 3-25 Bidirectional Mass Rig (Platform Plan View)

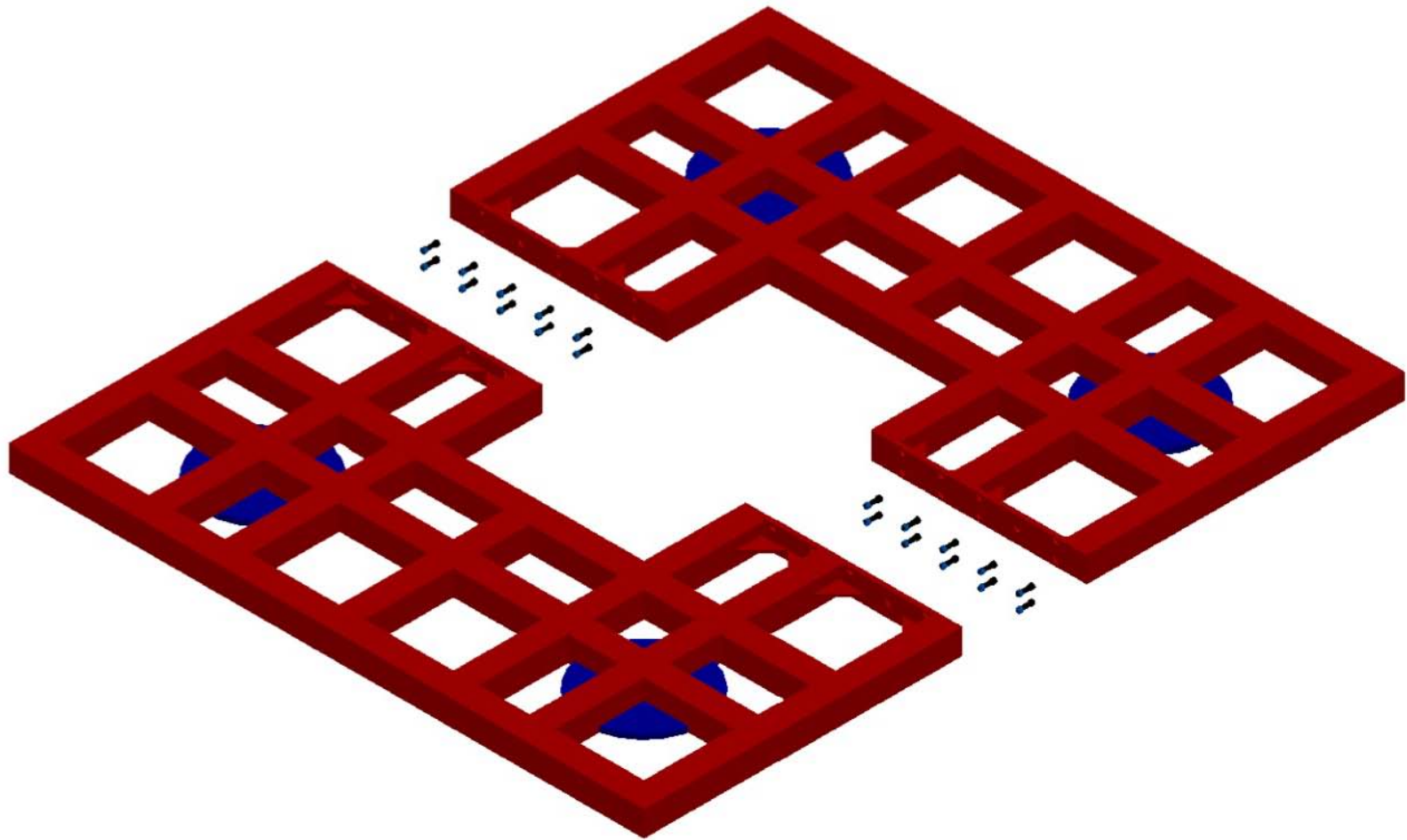
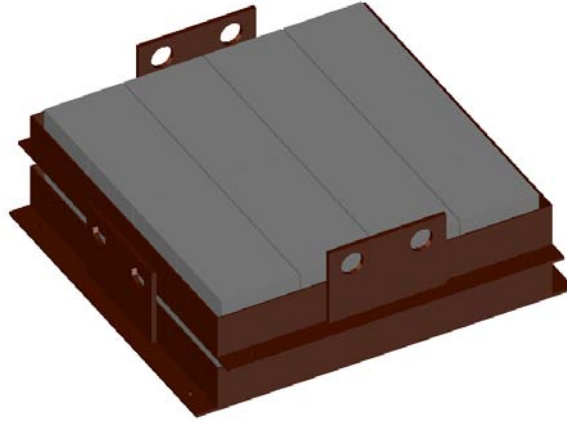
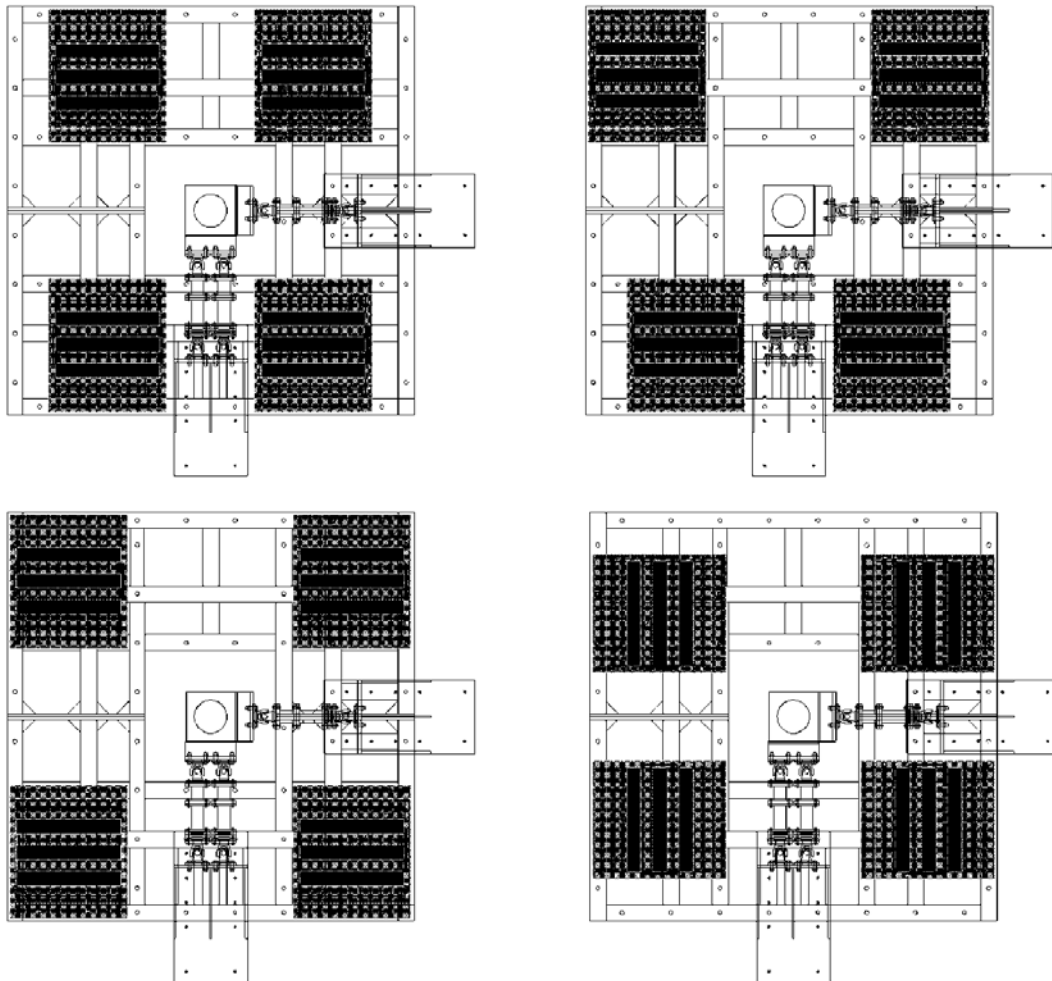


Figure 3-26 Bidirectional Mass Rig (Platform Assemblage)



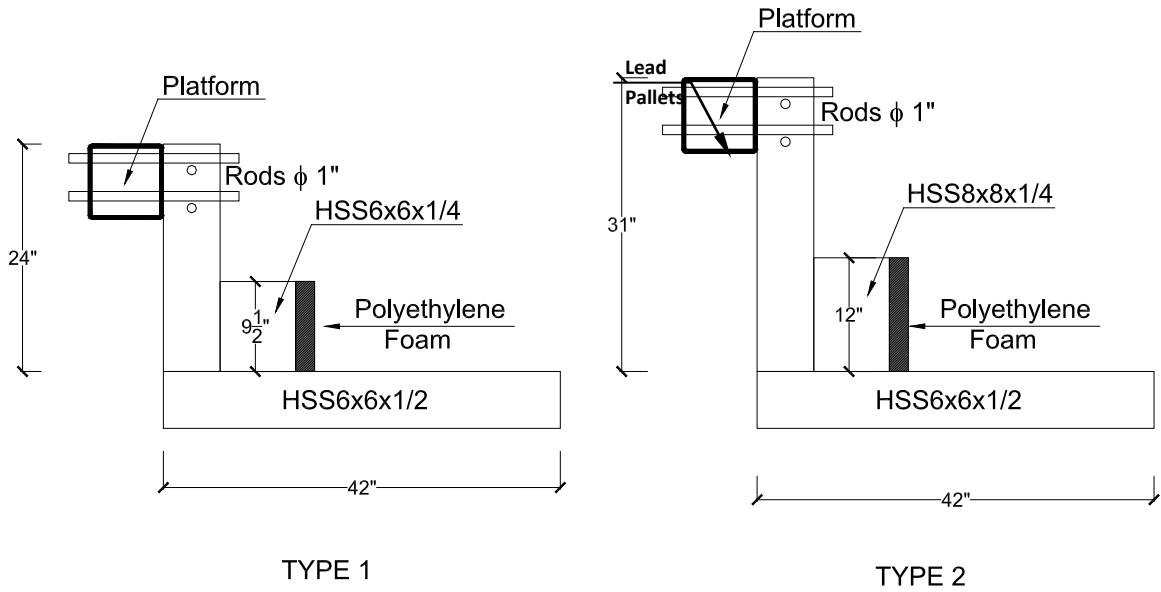
a) Lead Pallets



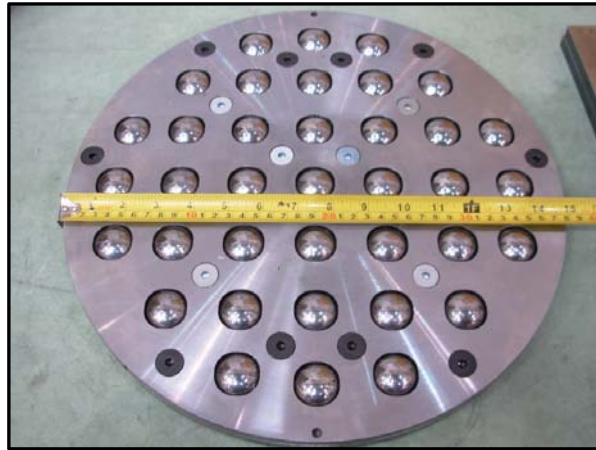
b) Lead Pallets Distribution on BMR

Figure 3-27 Bidirectional Mass Rig (Lead Pallets)





**Figure 3-28 Bidirectional Mass Rig (Safety Arms)**



b) Plan View



c) Elevation View



a) Components

**Figure 3-29 Bidirectional Mass Rig (Ball Bearings)**

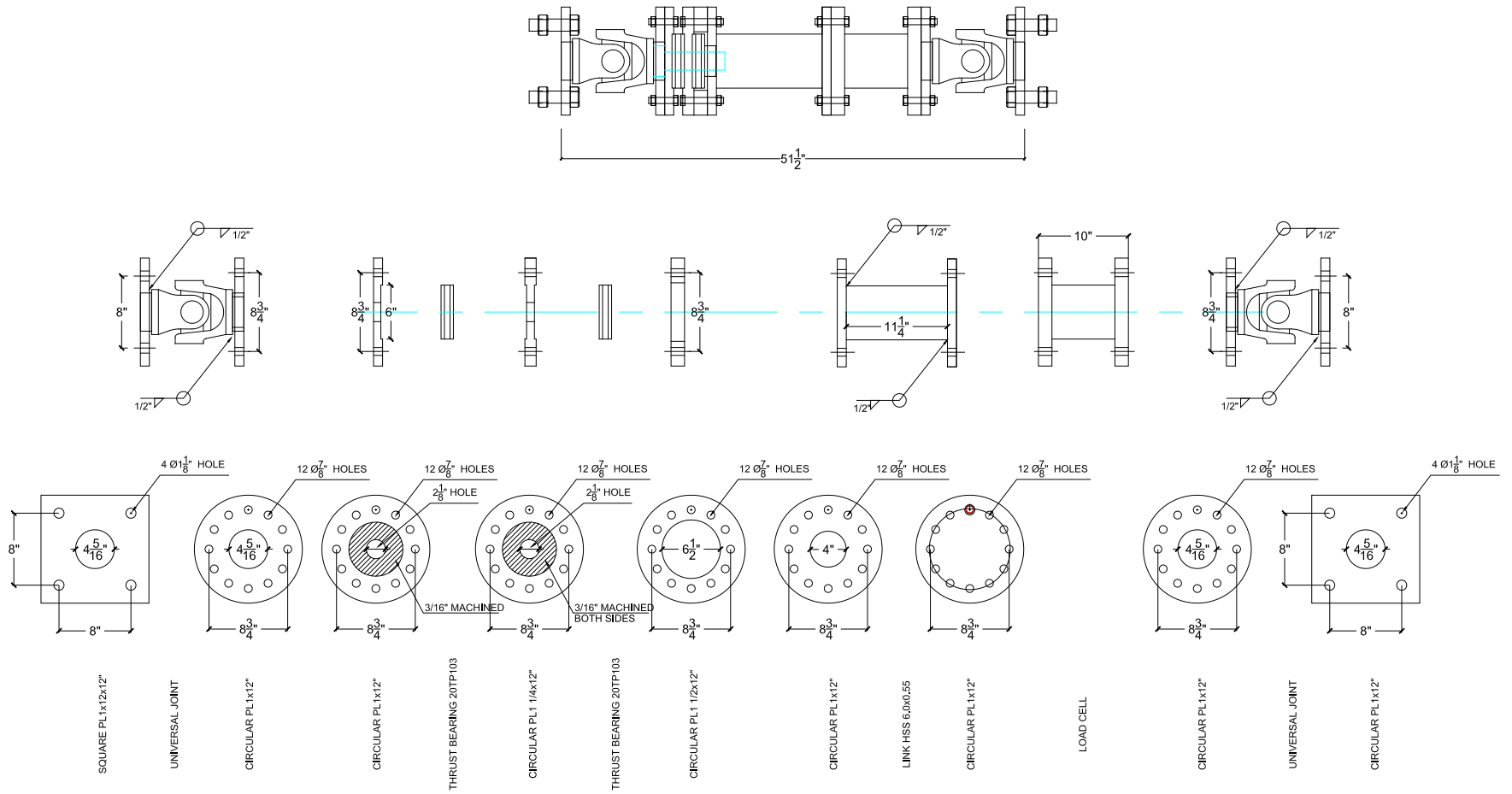


Figure 3-30 Bidirectional Mass rig (Links Configuration)



a) Supporting Structure



b) Setting Specimen



d) Setting Platform



c) Supporting Structure and Platform



e) Connecting Links on Platform

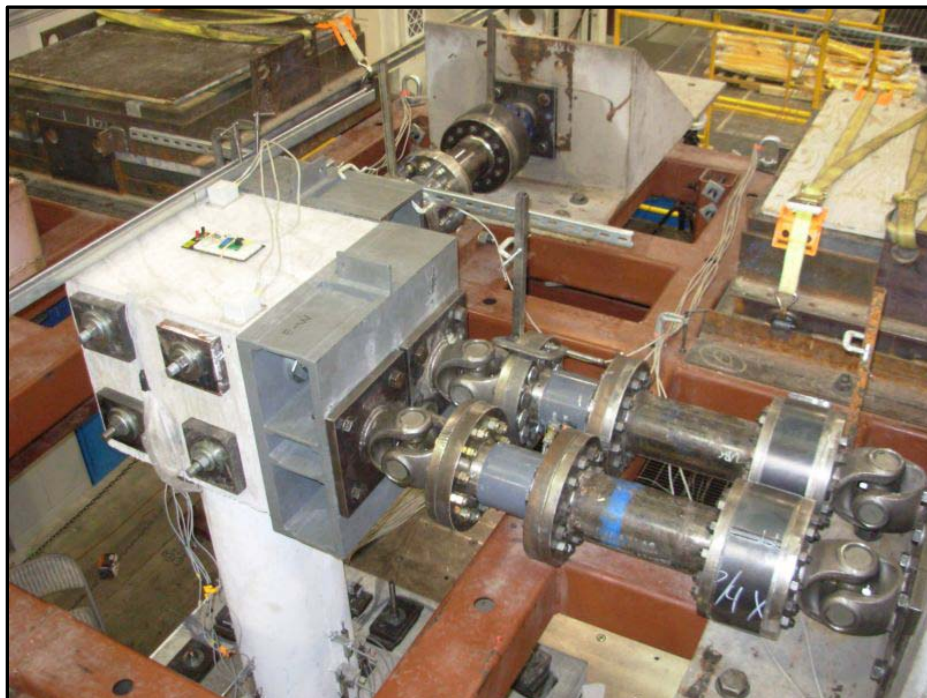


f) BMR Before Test (Top View)

**Figure 3-31 Bidirectional Mass Rig (Assembling Process)**



**Figure 3-32 Bidirectional Mass Rig and Specimen(Before Testing)**



**Figure 3-33 Bidirectional Mass Rig (Link Details)**

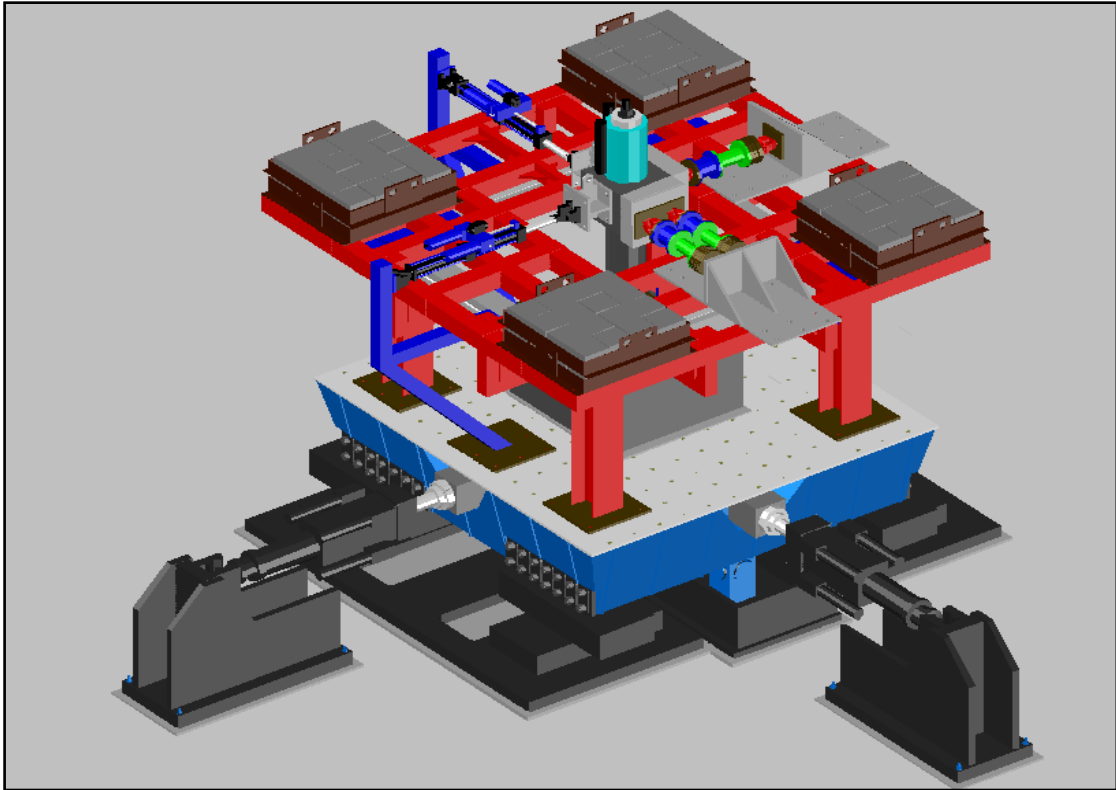


Figure 3-34 Bidirectional Mass Rig with Axial Force and P-delta Effects (3D view)

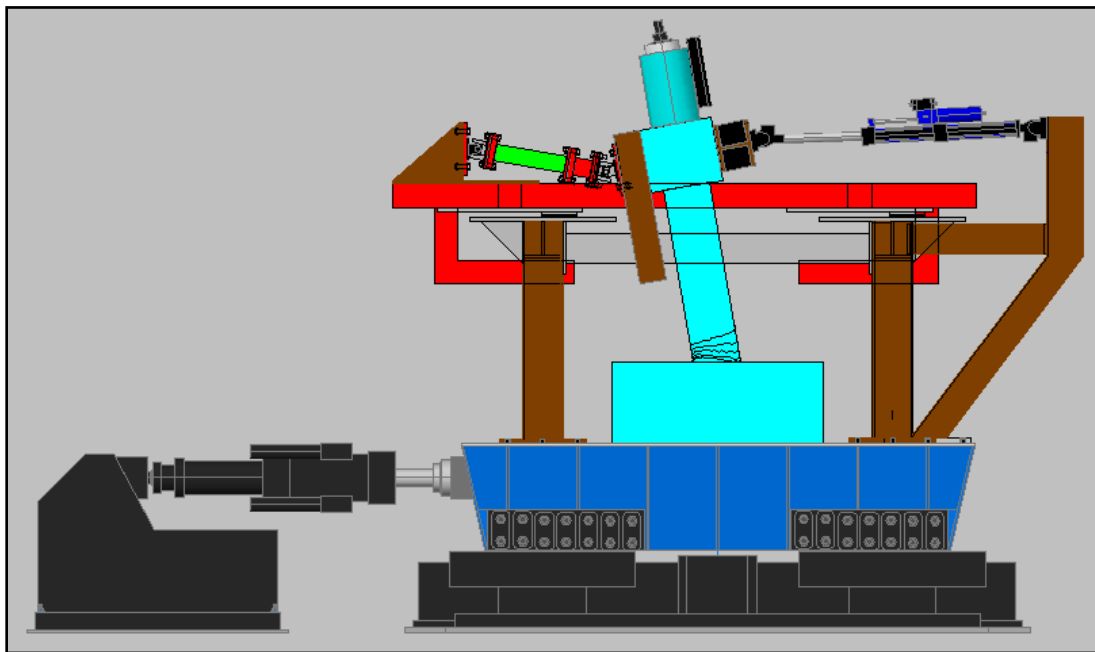
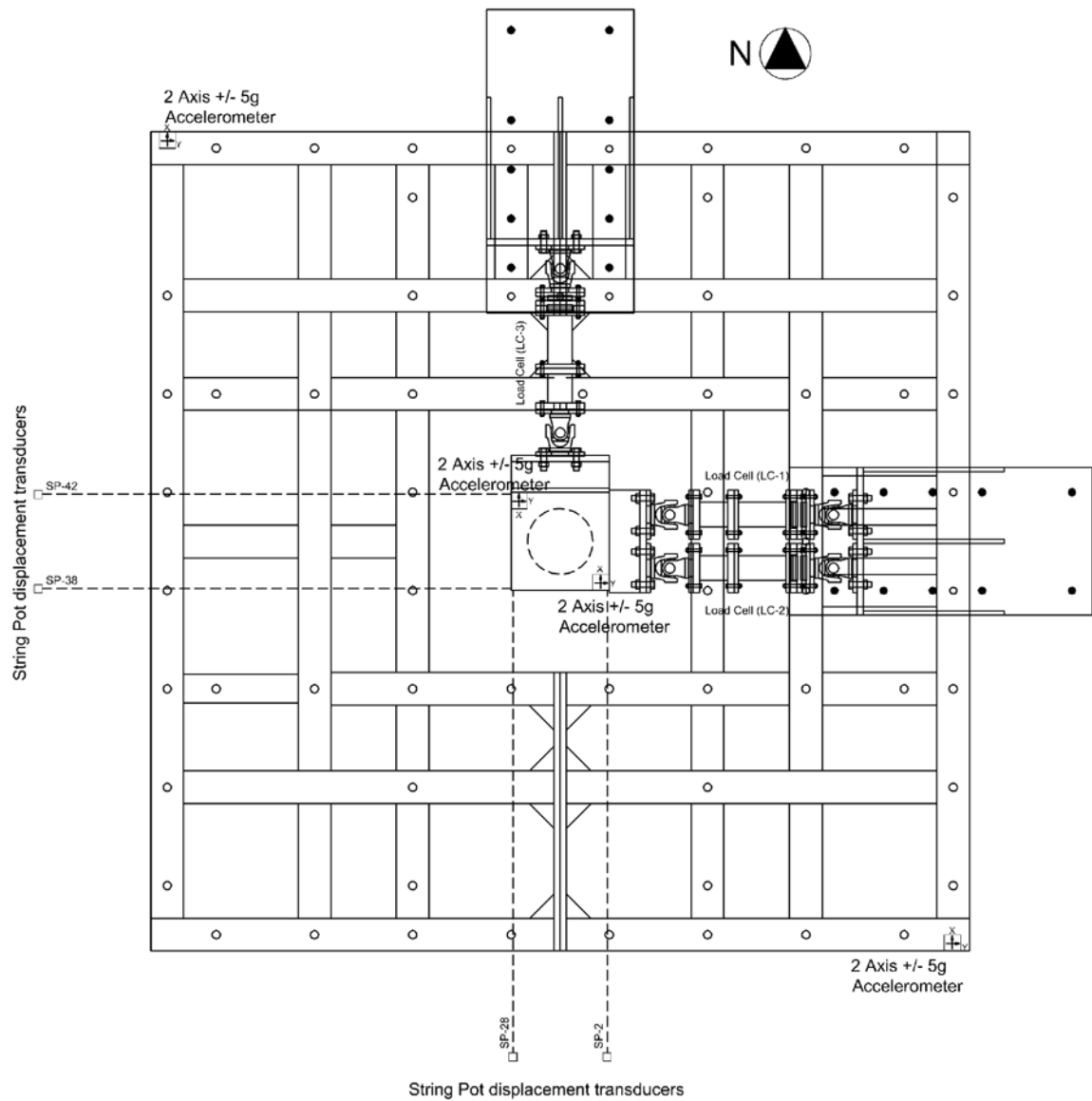
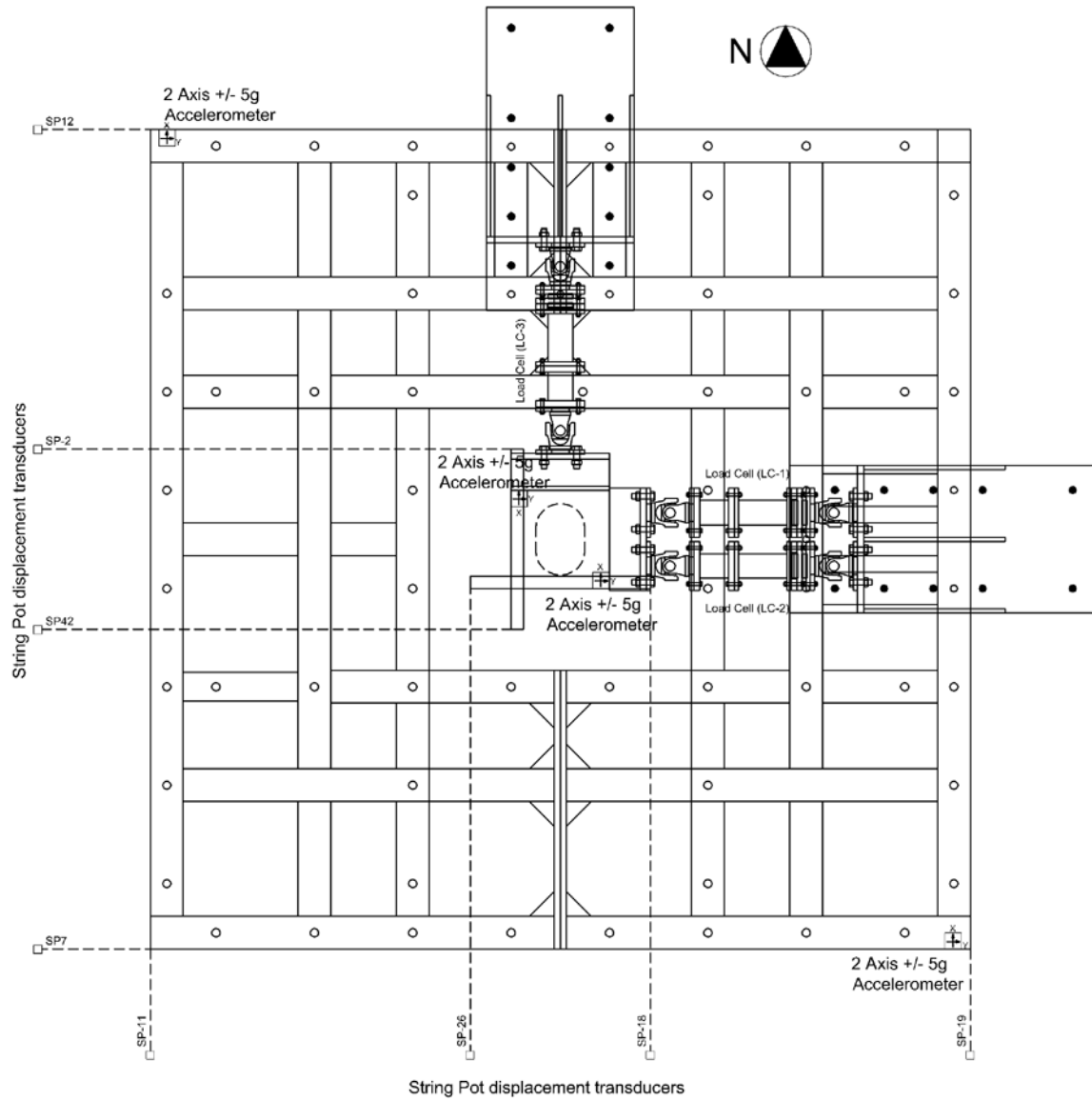


Figure 3-35 Bidirectional Mass Rig with Axial Force and P-delta Effects (Elevation)

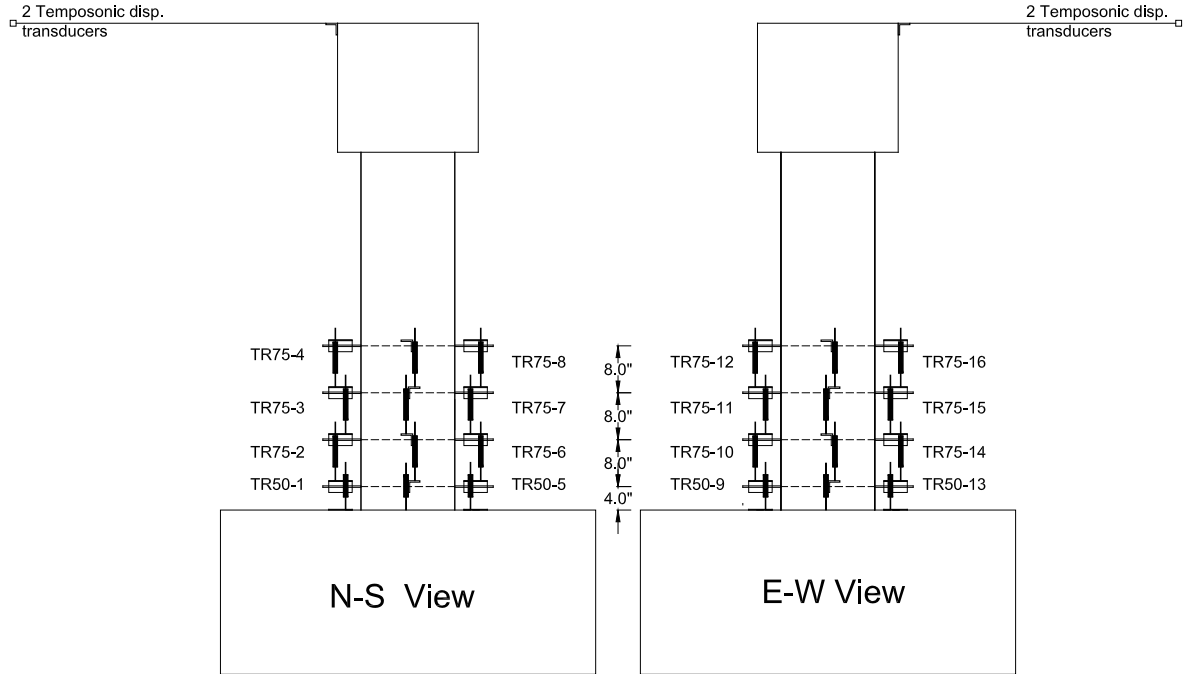


**Figure 3-36 Distribution of Accelerometers and Displacement Transducers  
Circular Specimen and BMR**

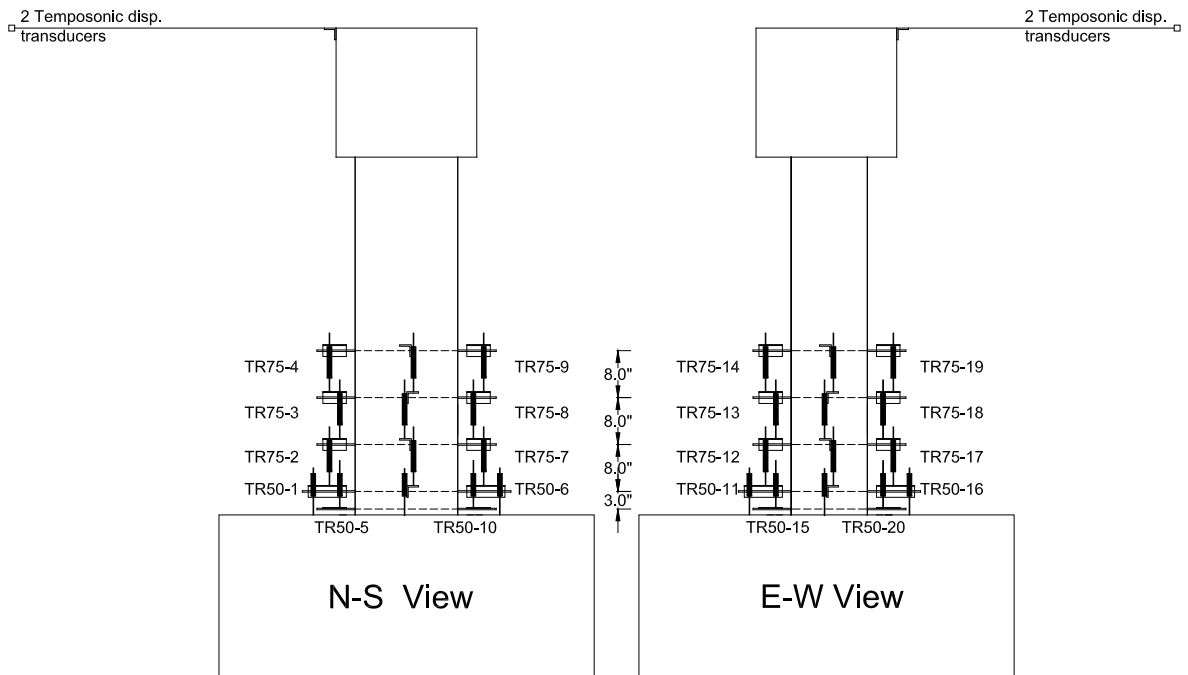


**Figure 3-37 Distribution of Accelerometers and Displacement Transducers Interlocking Specimen and BMR**





**Figure 3-38 Distribution of Displacement Transducers (Circular Specimens)**



**Figure 3-39 Distribution of Displacement Transducers (Interlocking Specimens)**

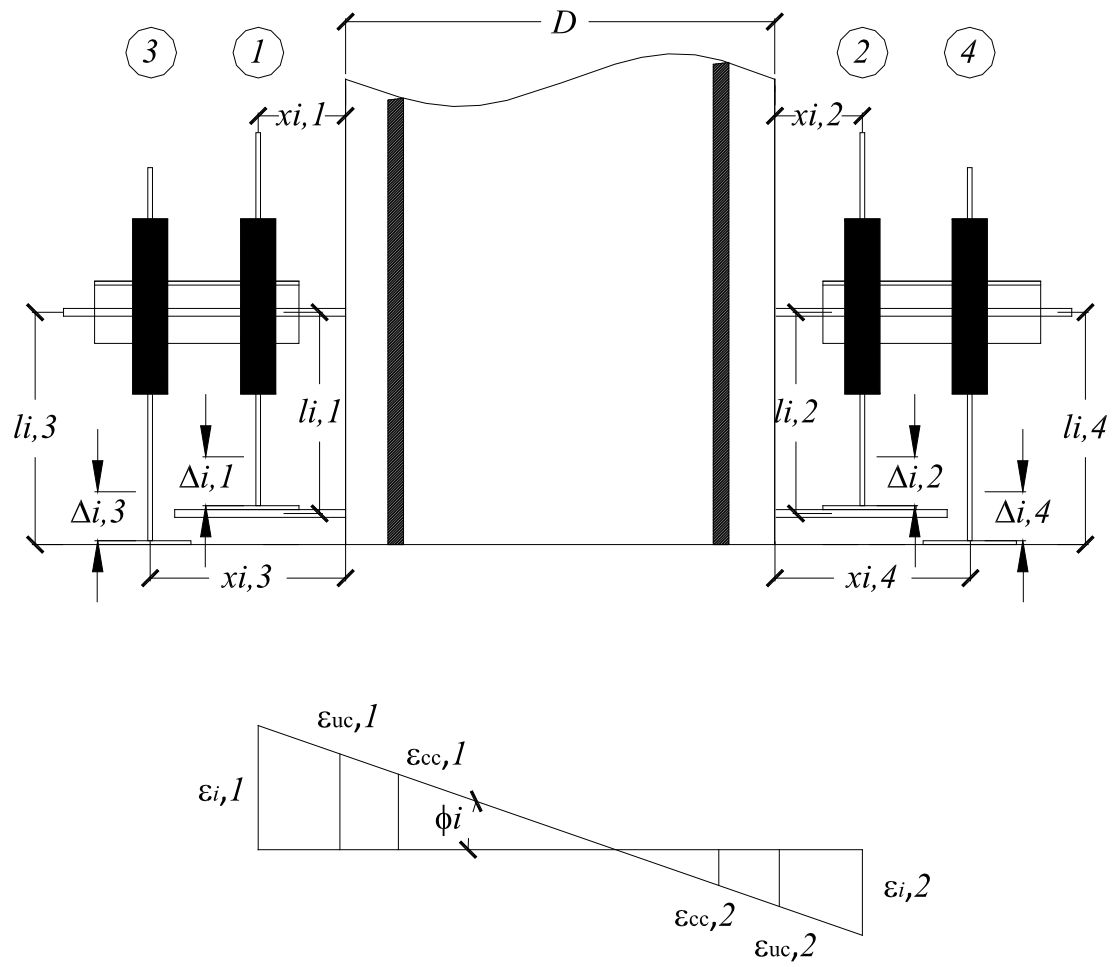
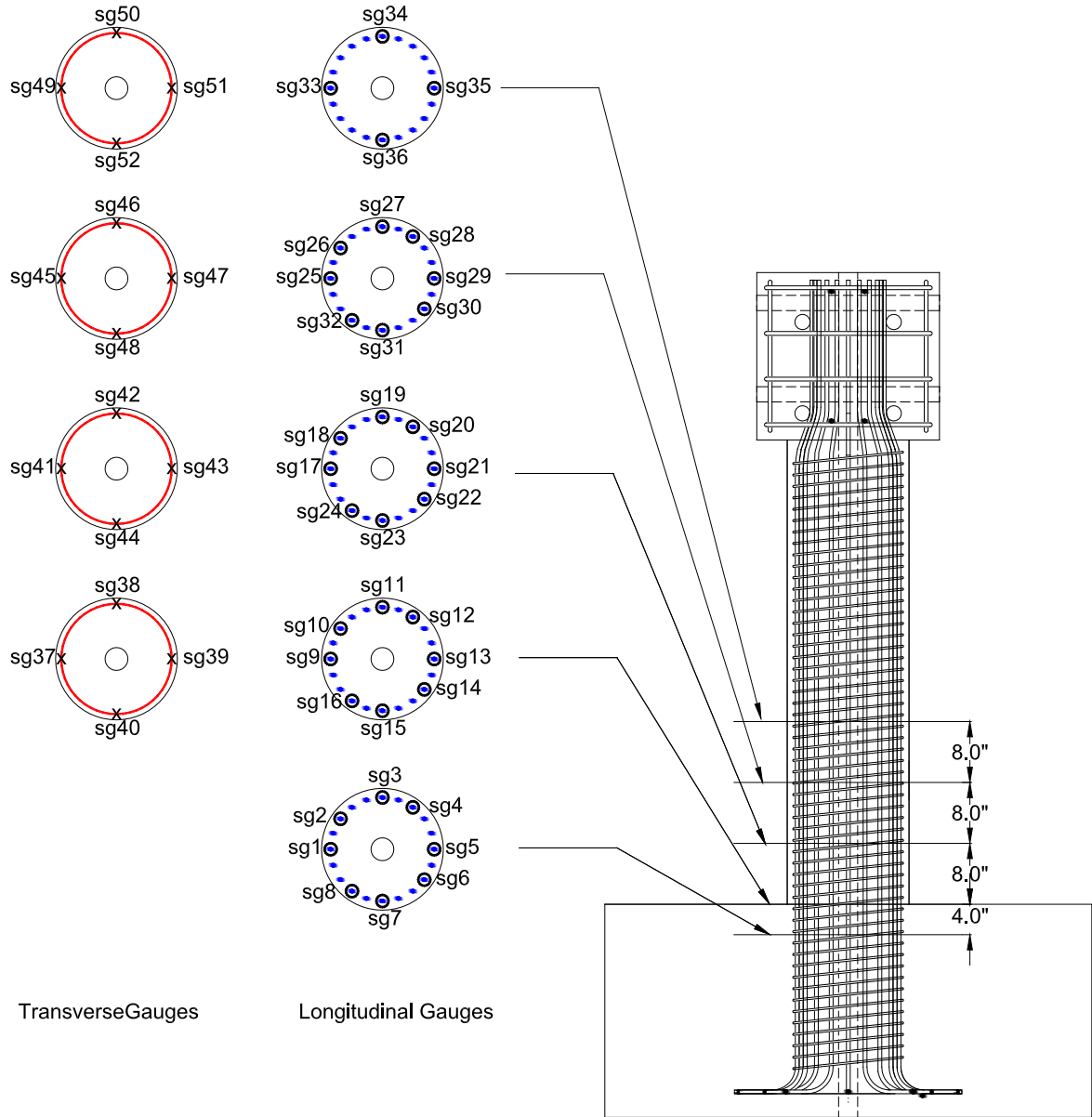


Figure 3-40 Column Strains, Rotations and Curvature



**Figure 3-41 Distribution of Strain Gauges (Circular Specimens)**

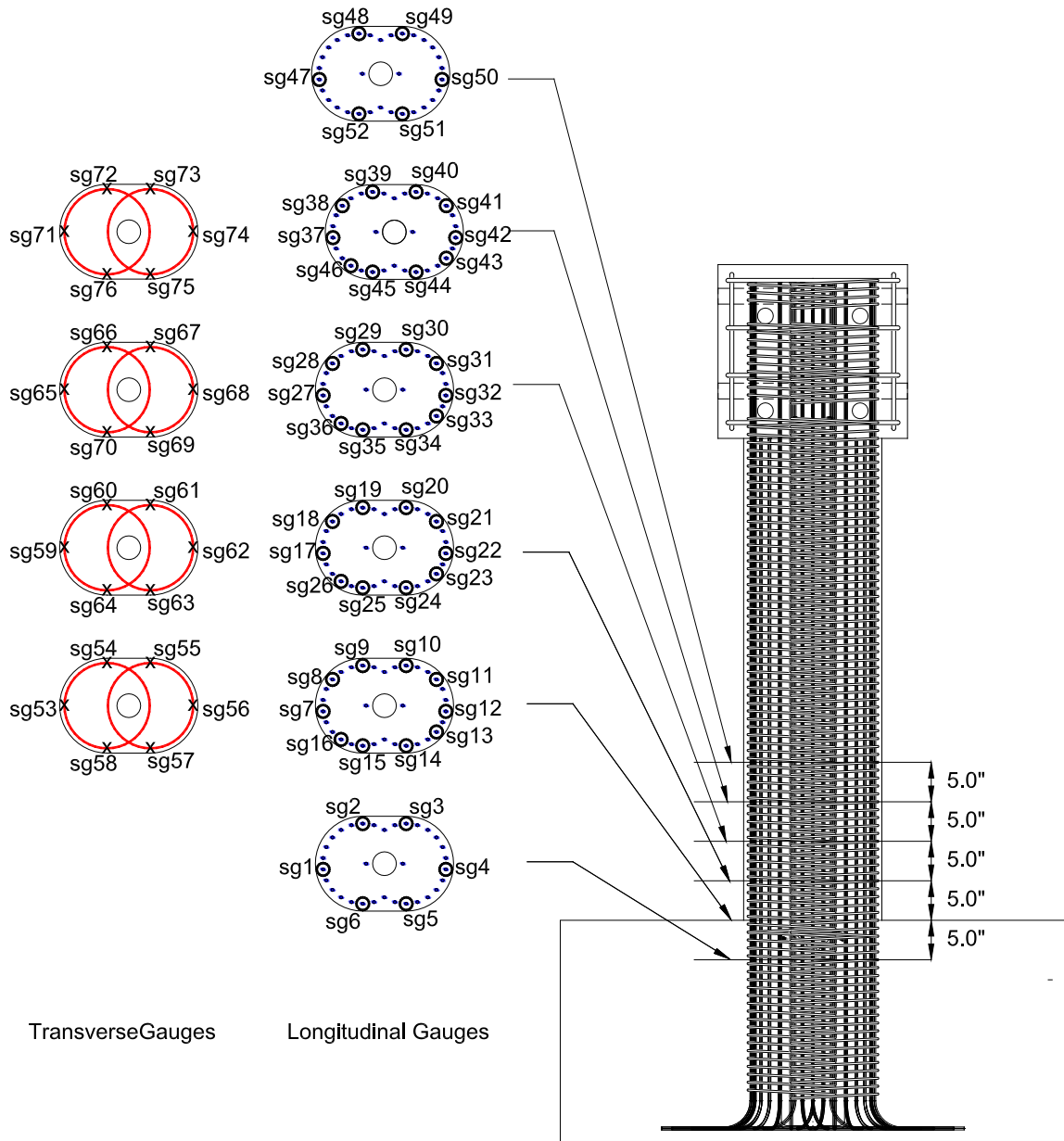
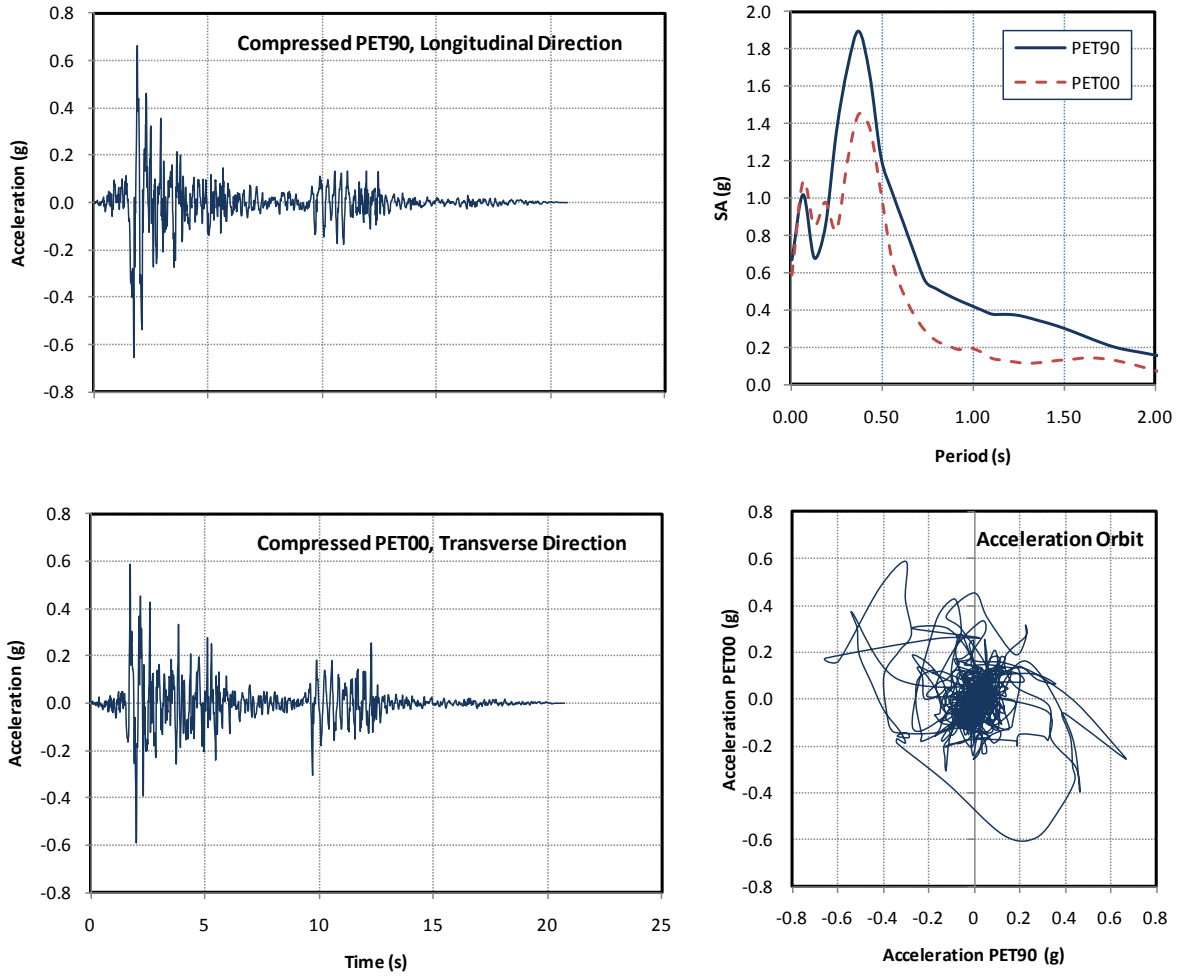
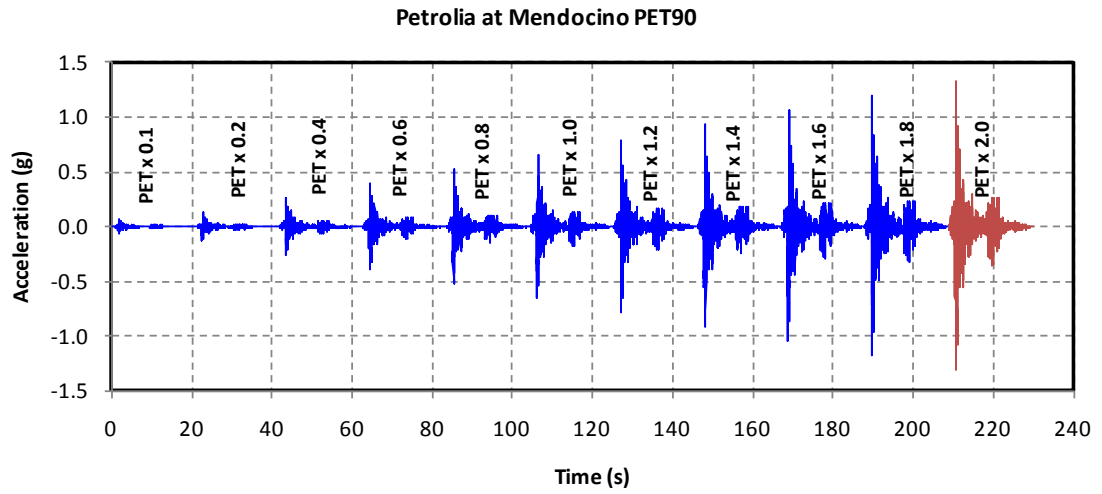


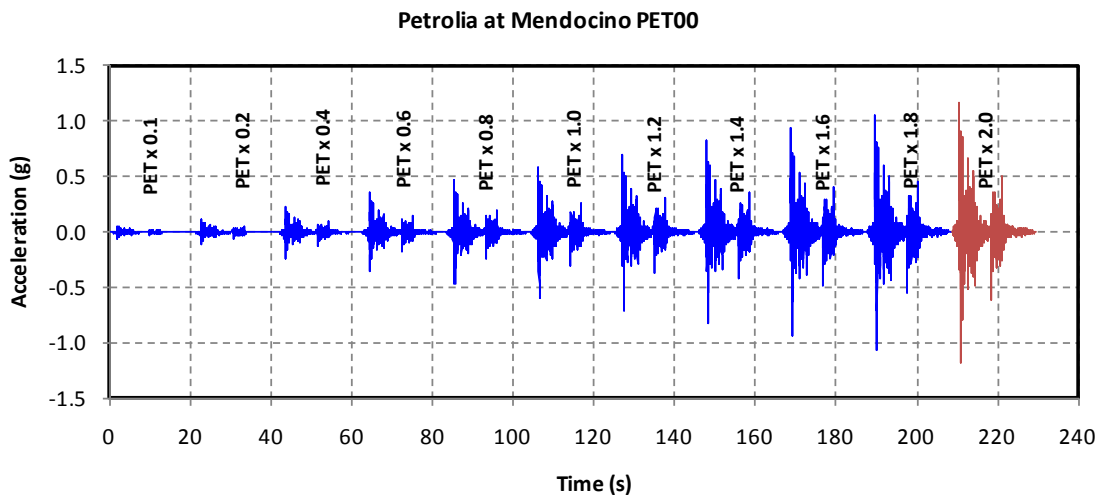
Figure 3-42 Distribution of Strain Gauges (Interlocking Specimens)



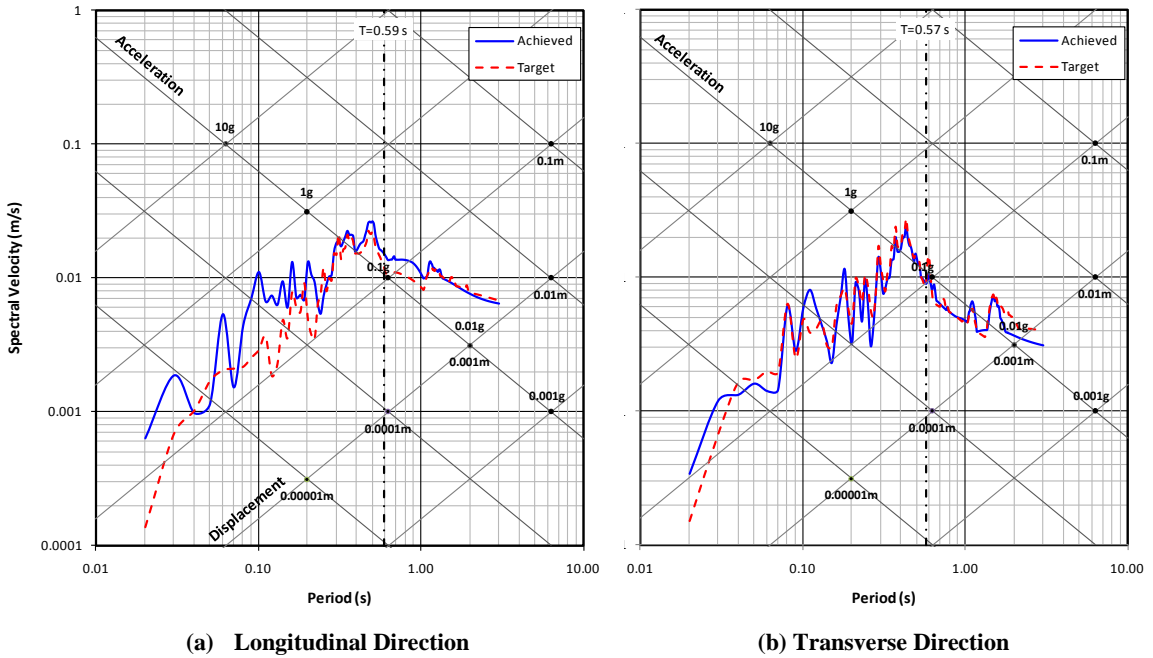
**Figure 4-1 Compressed Petrolia Earthquake, (Time History, Spectrum and Orbit)**



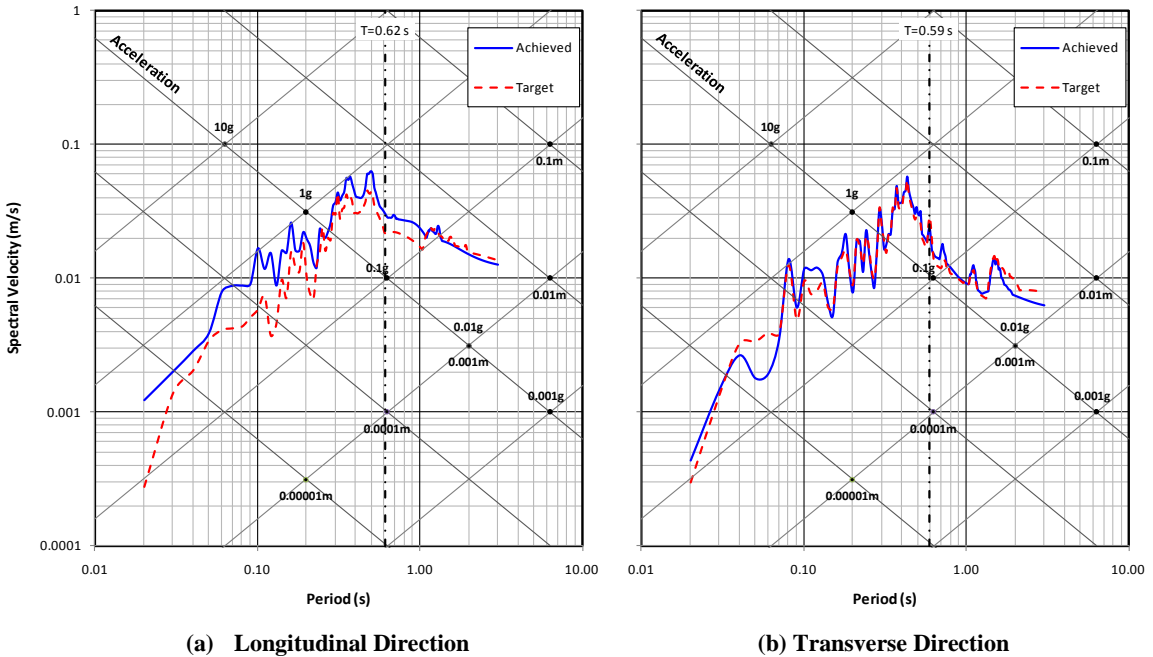
**Figure 4-2 Time History Acceleration used for Specimens C1 and C2 (Long. Direction)**



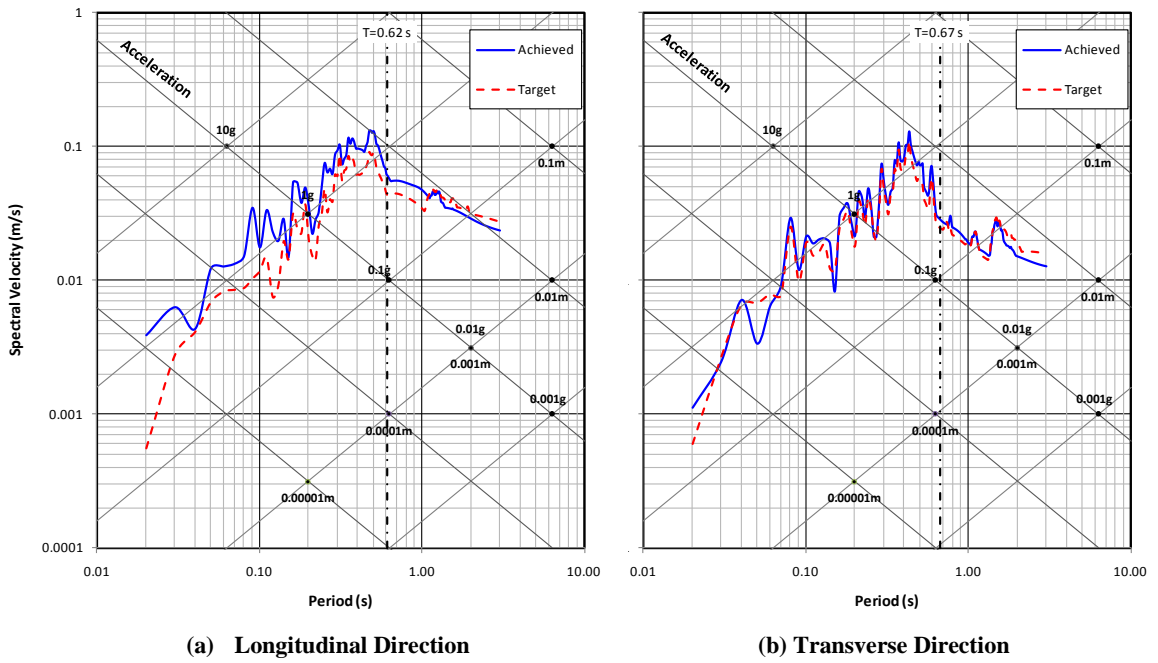
**Figure 4-3 Time History Acceleration used for Specimens C1 and C2 (Trans. Direction)**



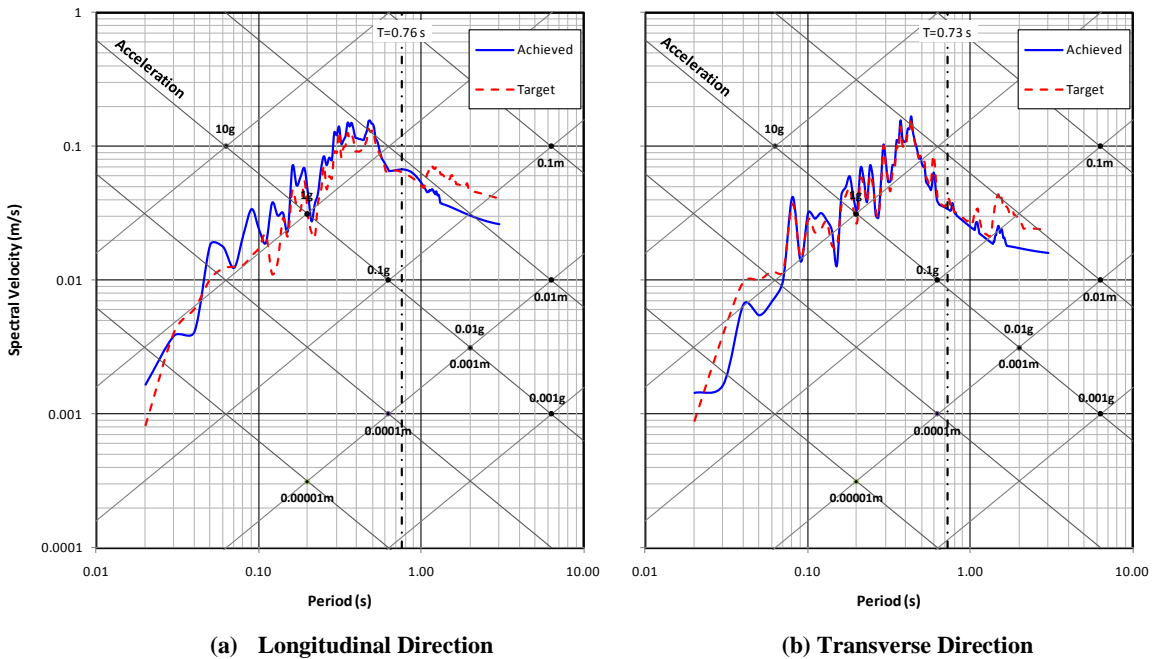
**Figure 4-4 Comparison of Target and Achieved Trilogarithmic Response Spectra  
0.1 x Petrolia Specimen C1**



**Figure 4-5 Comparison of Target and Achieved Trilogarithmic Response Spectra  
0.2 x Petrolia Specimen C1**

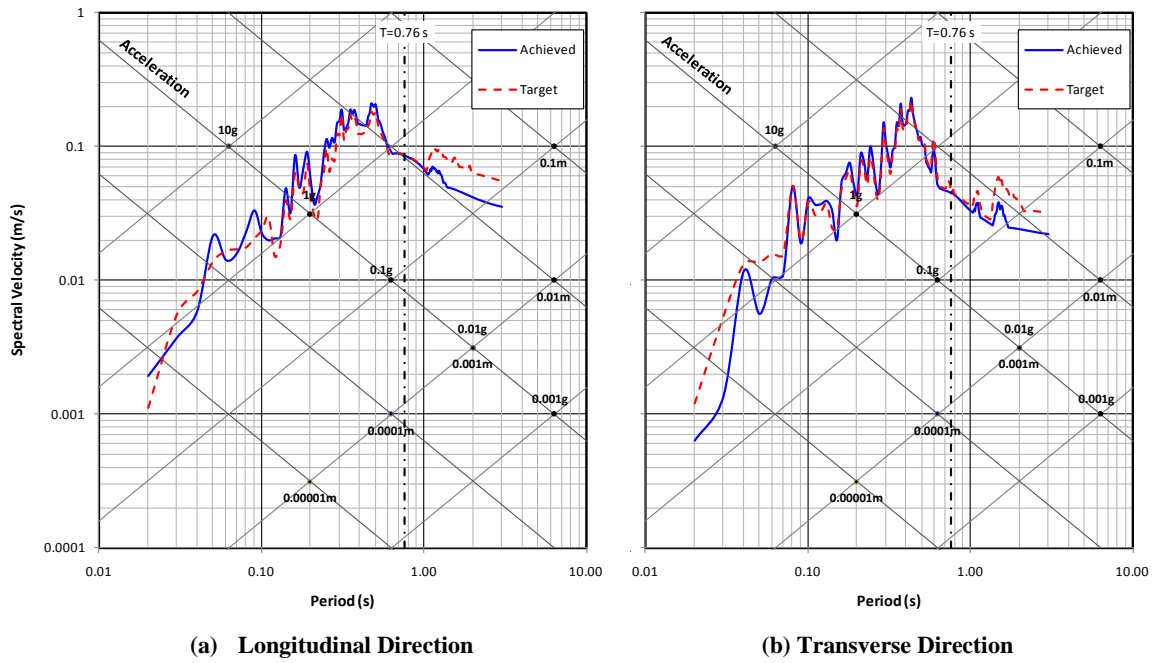


**Figure 4-6 Comparison of Target and Achieved Trilogarithmic Response Spectra  
0.4x Petrolia Specimen C1**

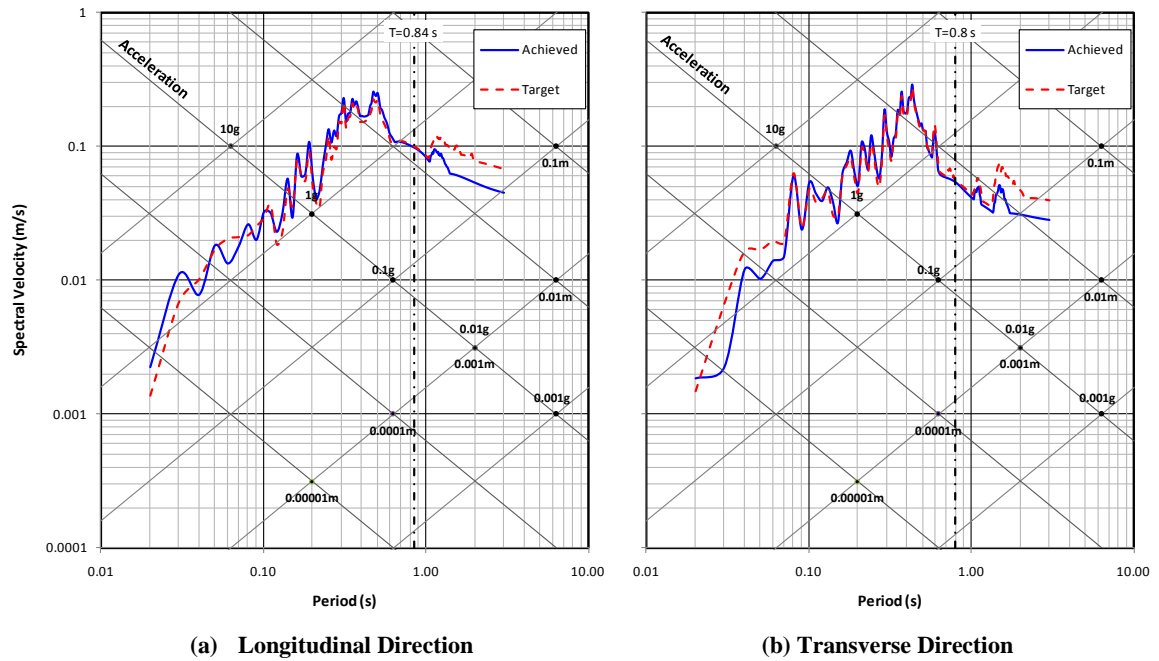


**Figure 4-7 Comparison of Target and Achieved Trilogarithmic Response Spectra  
0.6x Petrolia Specimen C1**

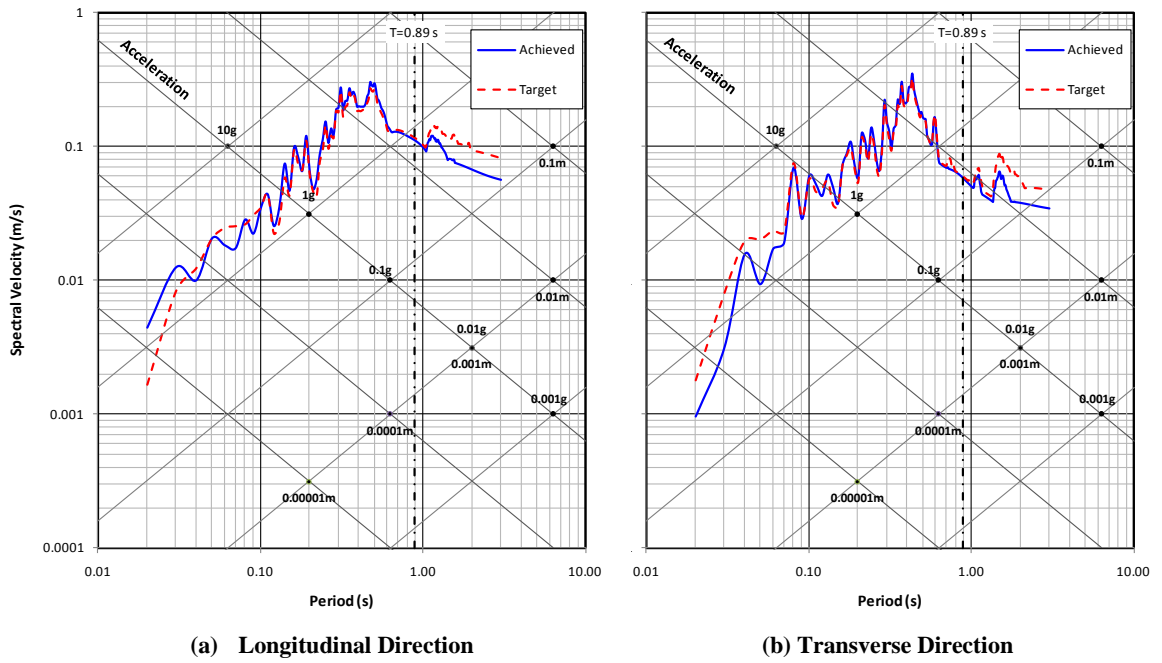




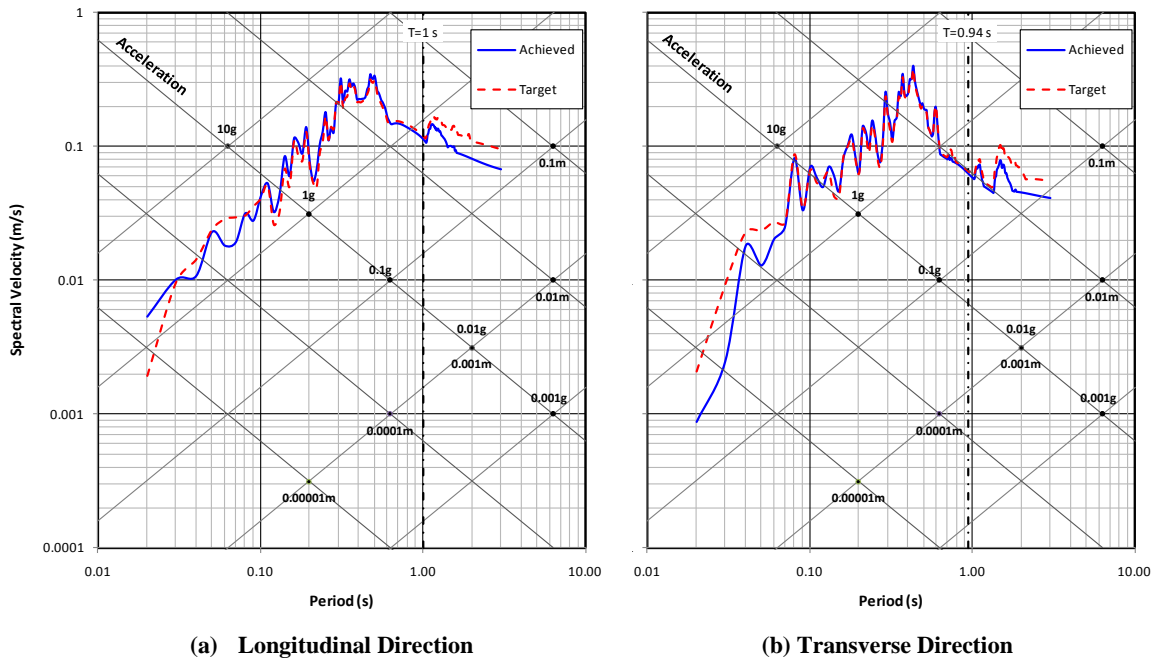
**Figure 4-8 Comparison of Target and Achieved Trilogarithmic Response Spectra  
0.8x Petrolia Specimen C1**



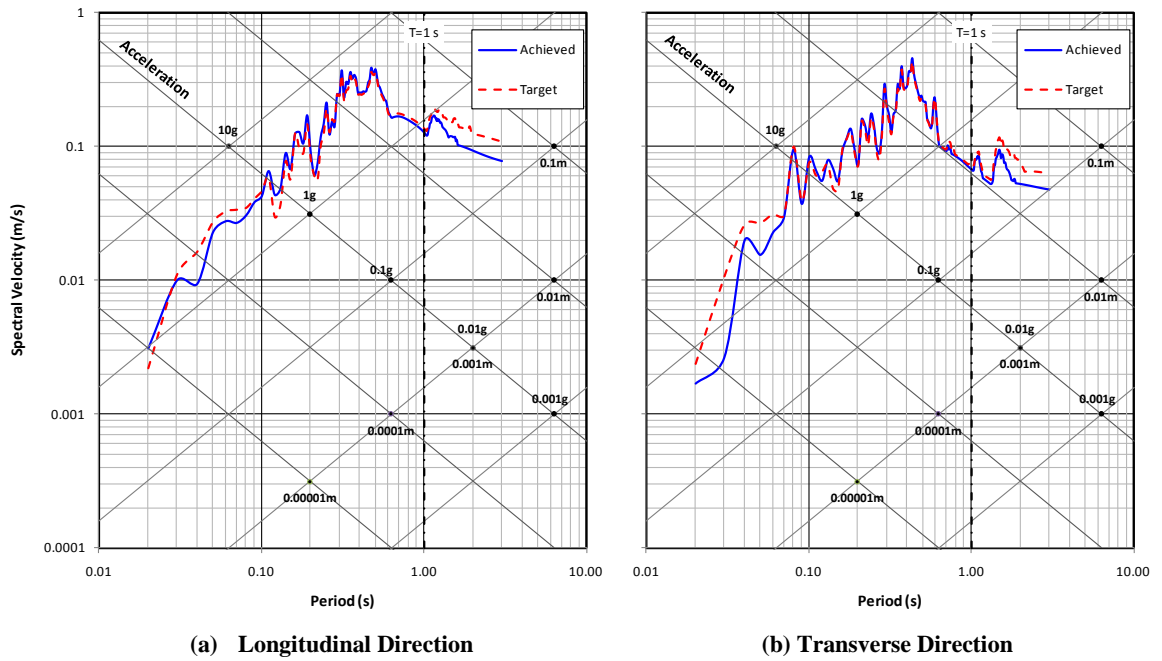
**Figure 4-9 Comparison of Target and Achieved Trilogarithmic Response Spectra  
1.0 x Petrolia Specimen C1**



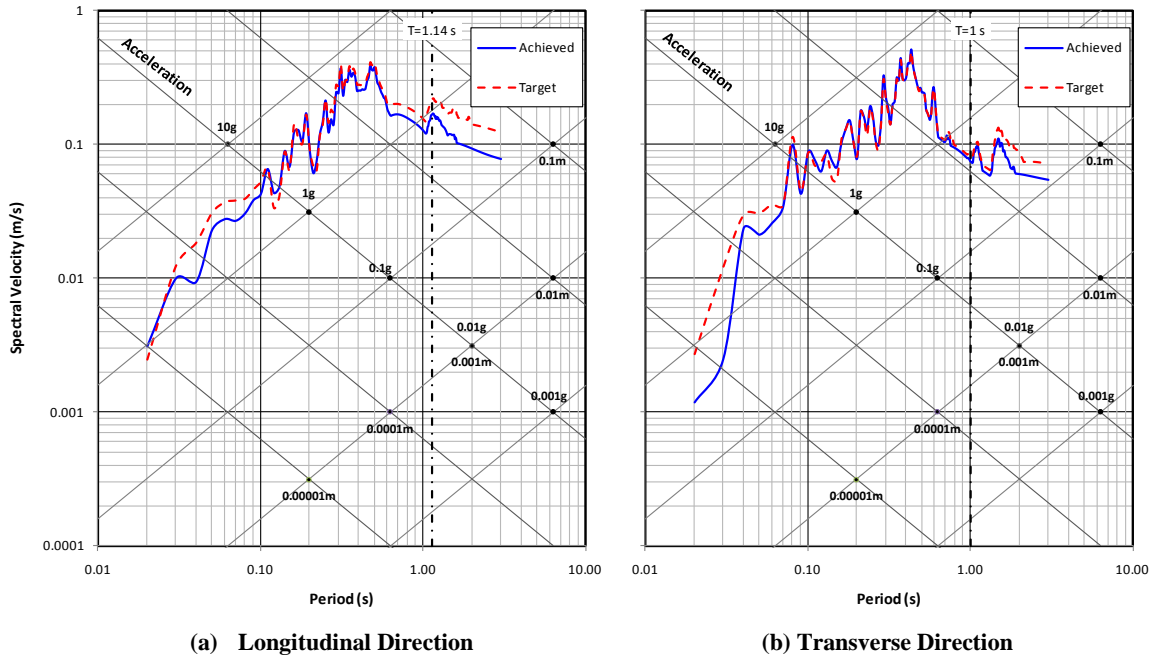
**Figure 4-10 Comparison of Target and Achieved Trilogarithmic Response Spectra  
1.2x Petrolia Specimen C1**



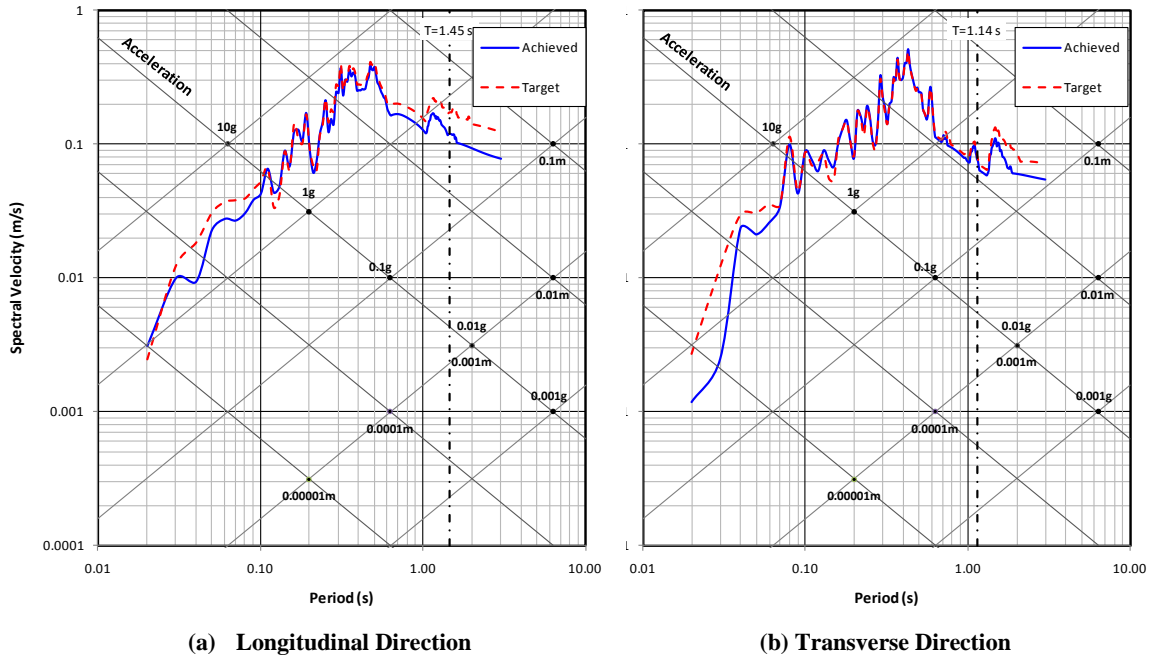
**Figure 4-11 Comparison of Target and Achieved Trilogarithmic Response Spectra  
1.4x Petrolia Specimen C1**



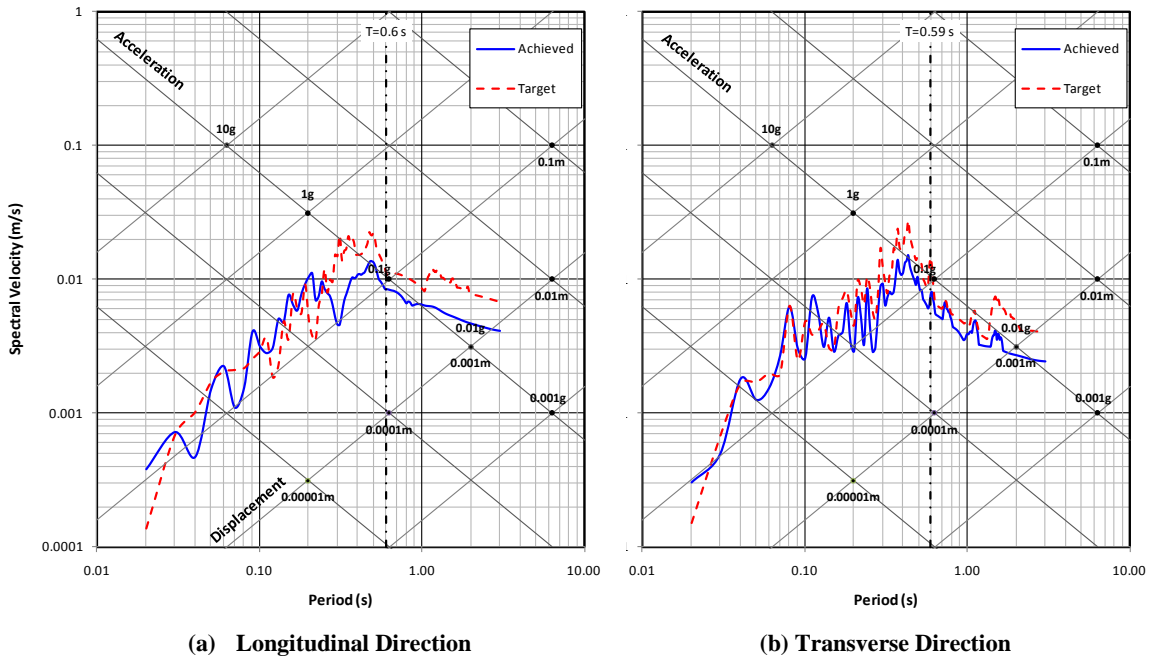
**Figure 4-12 Comparison of Target and Achieved Trilogarithmic Response Spectra  
1.6x Petrolia Specimen C1**



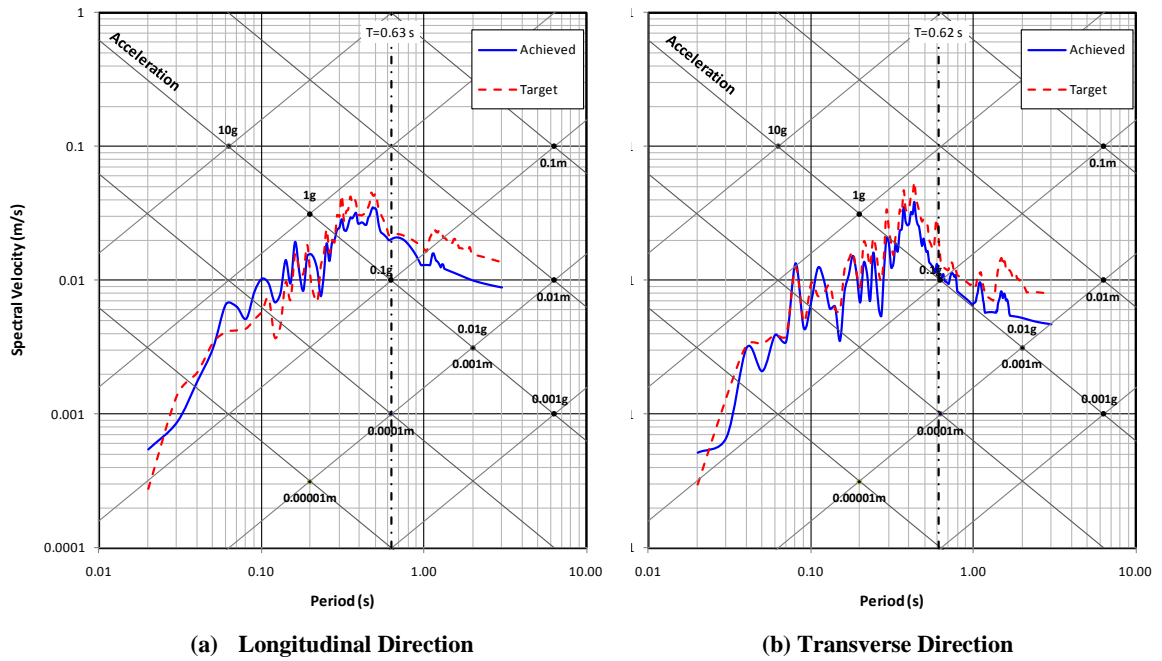
**Figure 4-13 Comparison of Target and Achieved Trilogarithmic Response Spectra  
1.8x Petrolia Specimen C1**



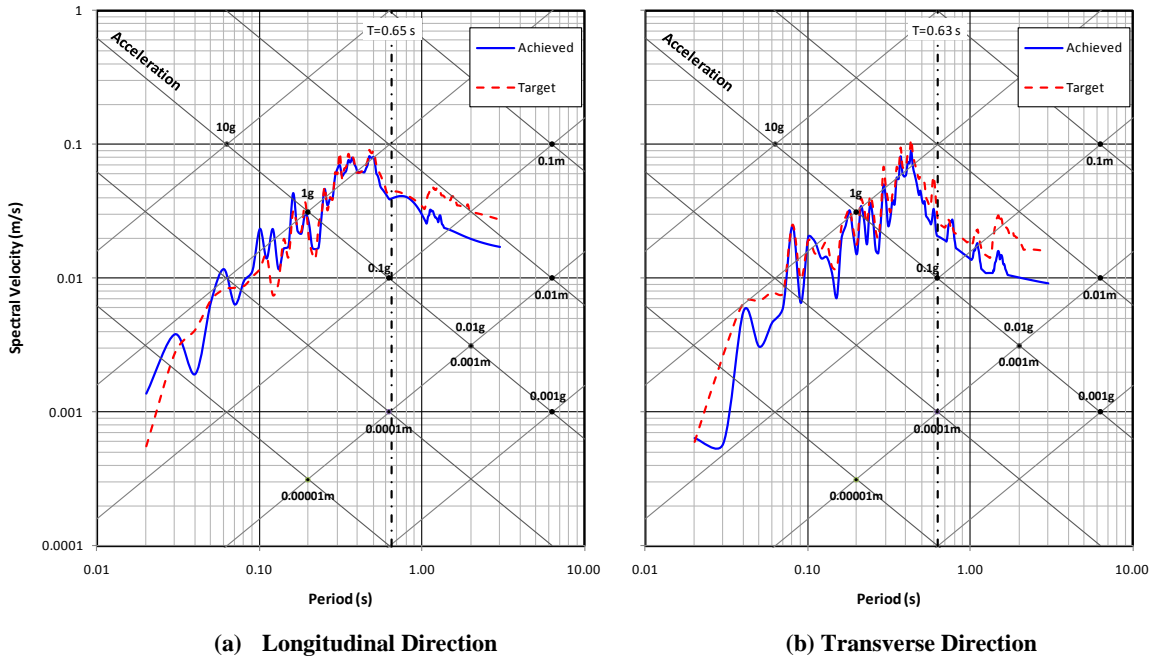
**Figure 4-14 Comparison of Target and Achieved Trilogarithmic Response Spectra  
1.8x Petrolia (After Test) Specimen C1**



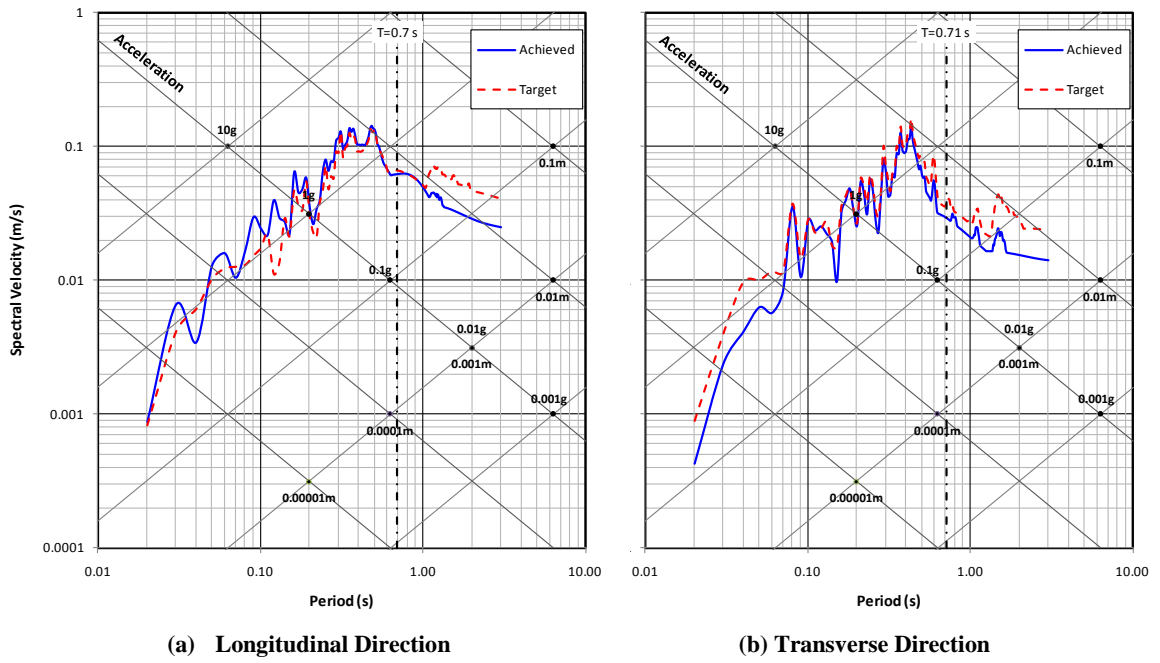
**Figure 4-15 Comparison of Target and Achieved Trilogarithmic Response Spectra  
0.1 x Petrolia Specimen C2**



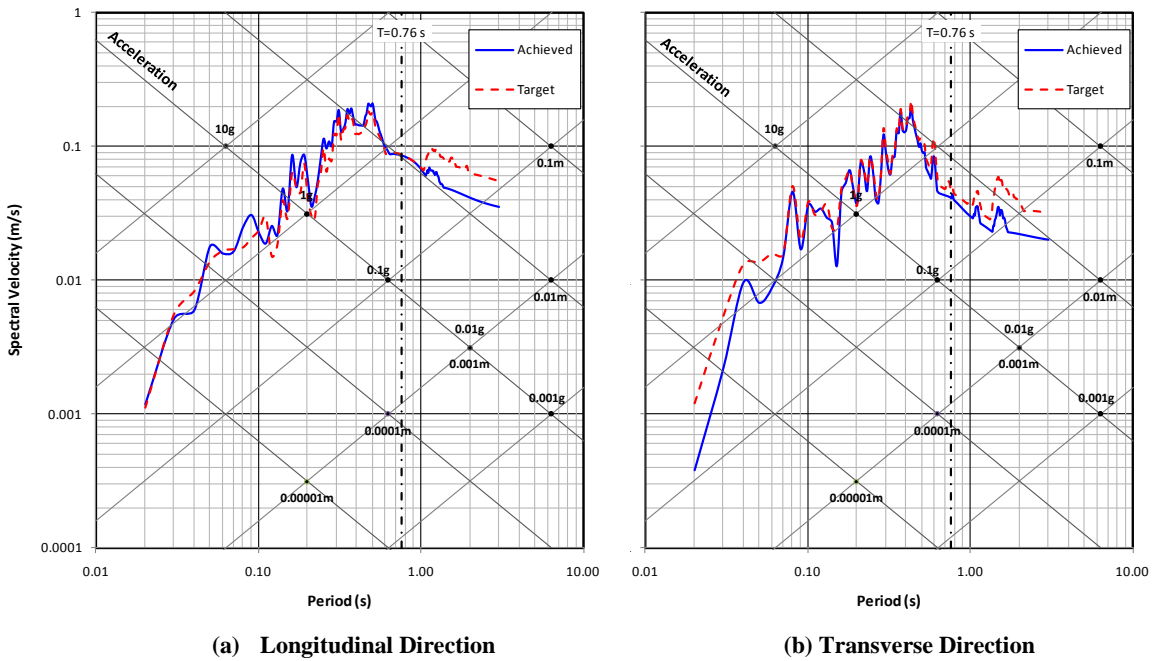
**Figure 4-16 Comparison of Target and Achieved Trilogarithmic Response Spectra  
0.2 x Petrolia Specimen C2**



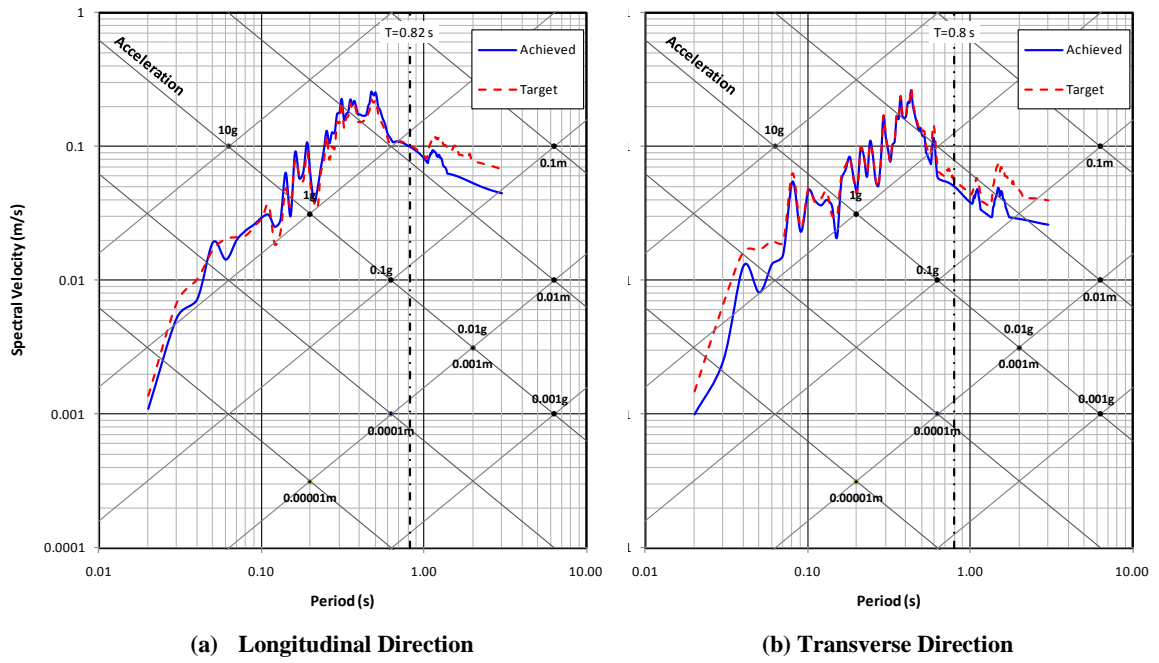
**Figure 4-17 Comparison of Target and Achieved Trilogarithmic Response Spectra  
0.4 x Petrolia Specimen C2**



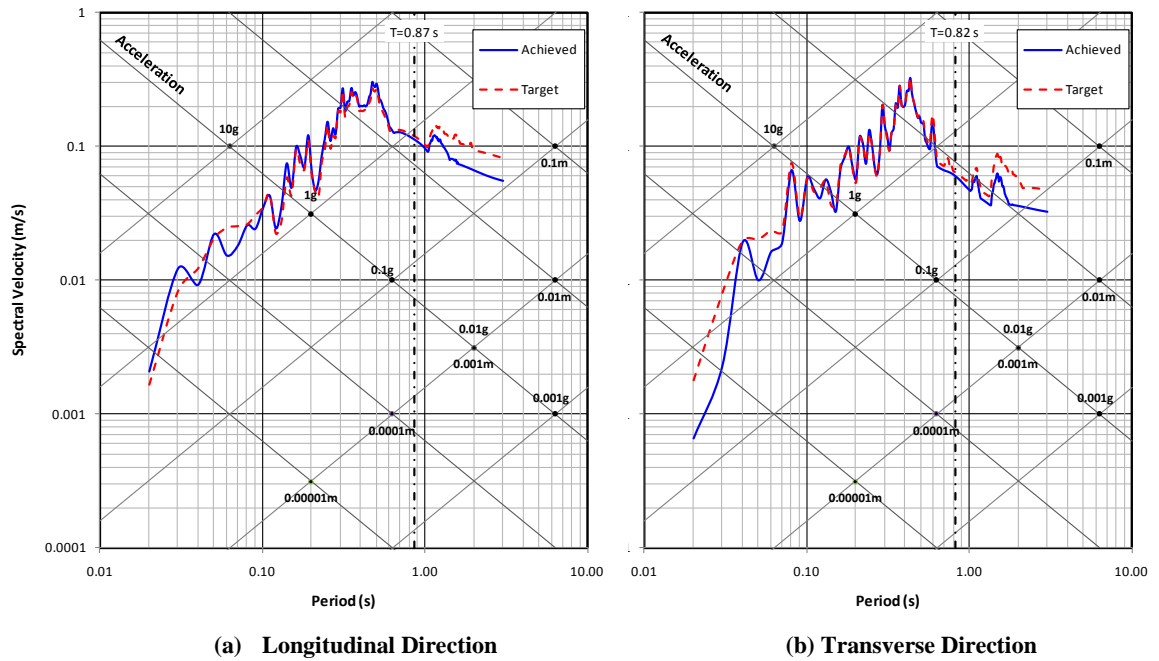
**Figure 4-18 Comparison of Target and Achieved Trilogarithmic Response Spectra  
0.6 x Petrolia Specimen C2**



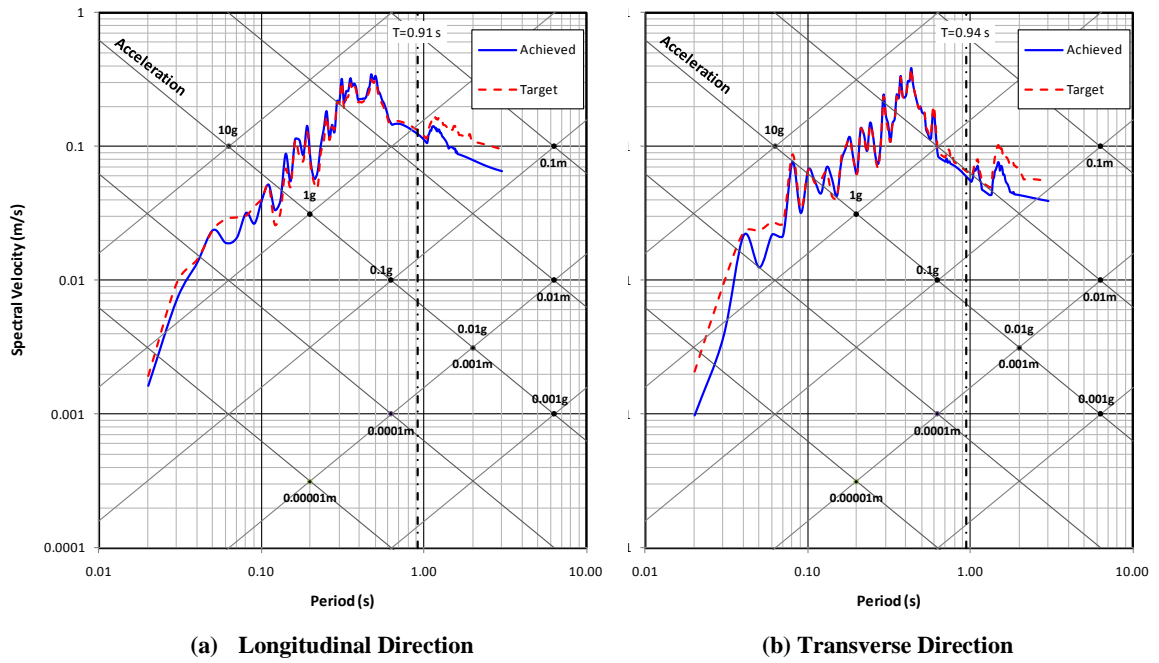
**Figure 4-19 Comparison of Target and Achieved Trilogarithmic Response Spectra  
0.8 x Petrolia Specimen C2**



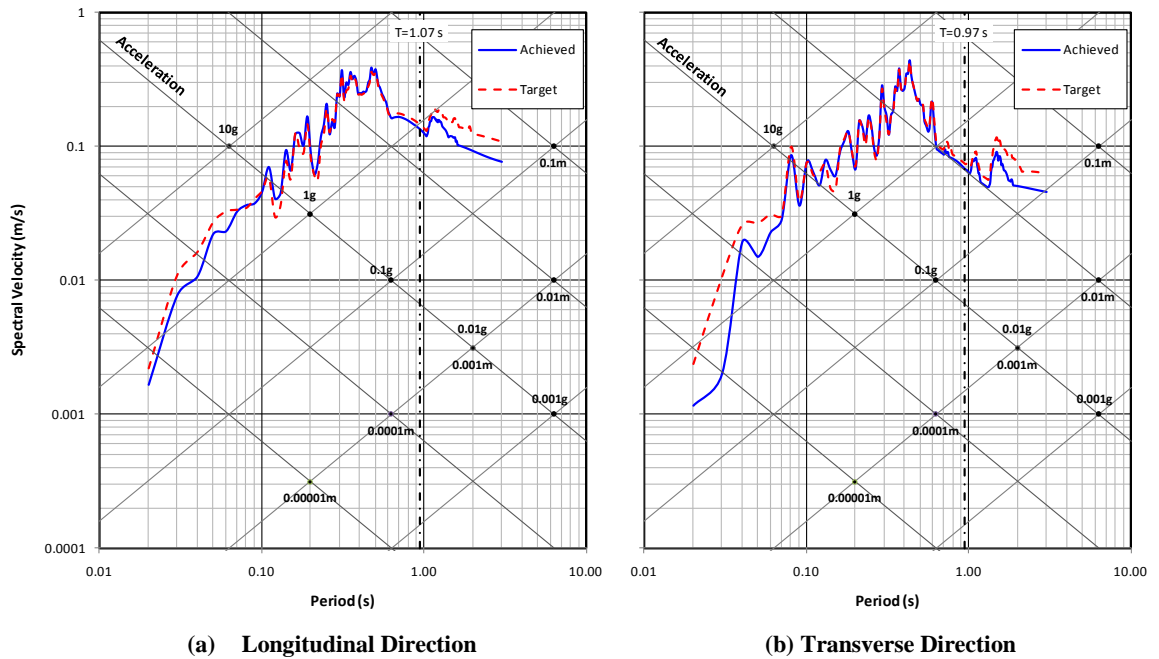
**Figure 4-20 Comparison of Target and Achieved Trilogarithmic Response Spectra  
1.0 x Petrolia Specimen C2**



**Figure 4-21 Comparison of Target and Achieved Trilogarithmic Response Spectra  
1.2 x Petrolia Specimen C2**

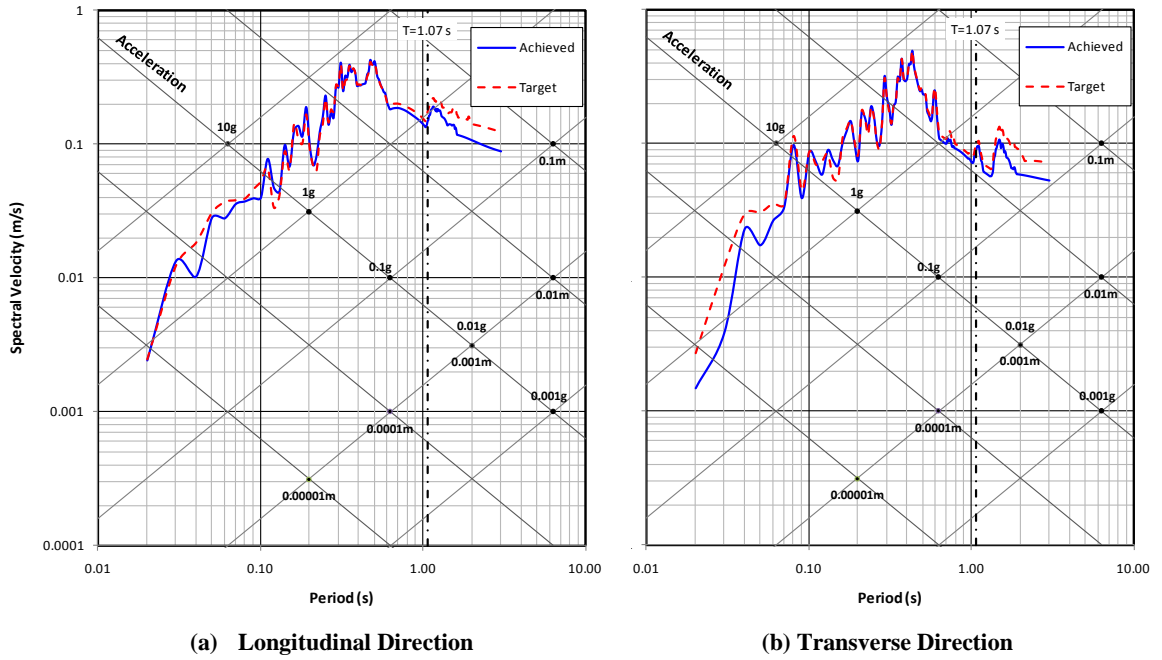


**Figure 4-22 Comparison of Target and Achieved Trilogarithmic Response Spectra  
1.4 x Petrolia Specimen C2**

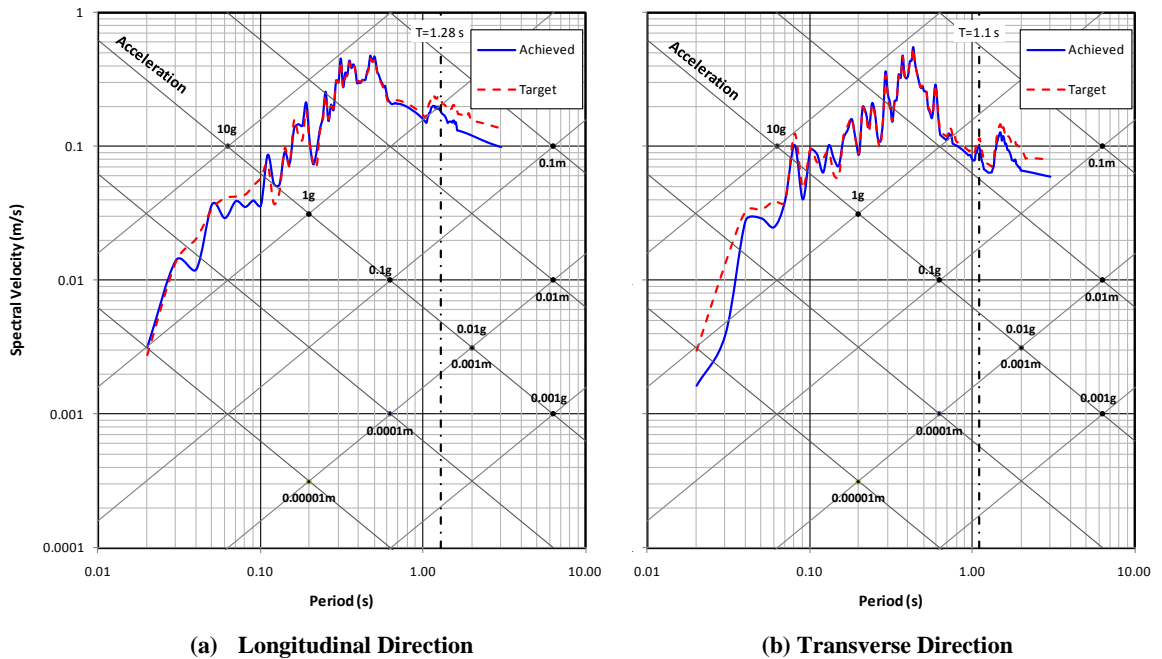


**Figure 4-23 Comparison of Target and Achieved Trilogarithmic Response Spectra  
1.6 x Petrolia Specimen C2**





**Figure 4-24 Comparison of Target and Achieved Trilogarithmic Response Spectra  
1.8 x Petrolia Specimen C2**



**Figure 4-25 Comparison of Target and Achieved Trilogarithmic Response Spectra  
2.0 x Petrolia Specimen C2**

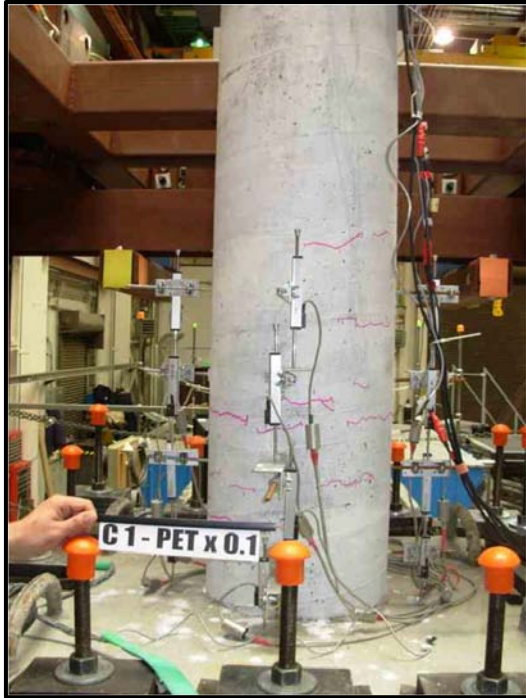


Figure 4-26 Hairline Horizontal Cracks, Specimens C1 and C2 (PETx0.1)

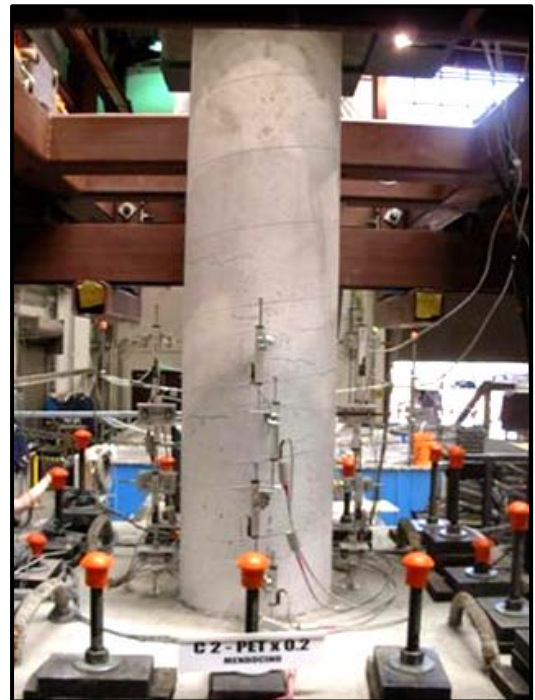


Figure 4-27 Cracks at First Bar Yielding, Specimens C1 and C2 (PETx0.2)

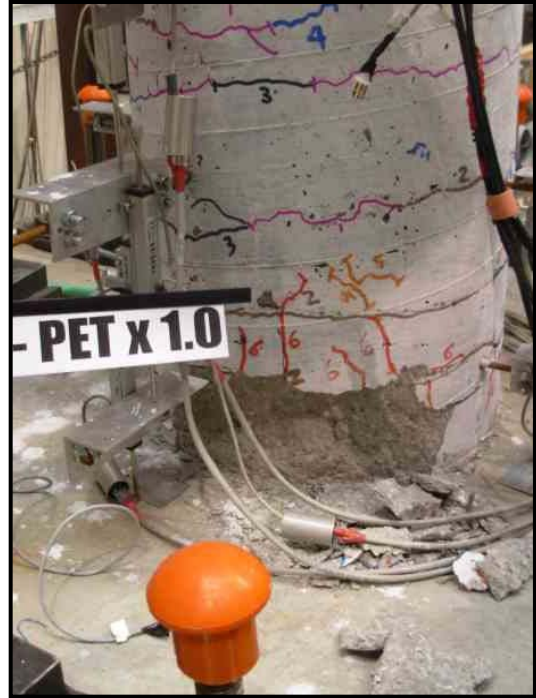


Figure 4-28 First Concrete Spalling Specimens C1 (PETx1.0)

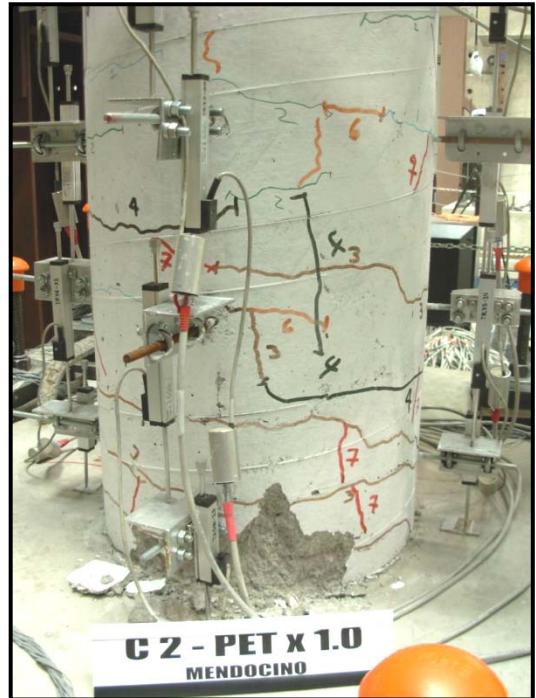


Figure 4-29 First Concrete Spalling Specimens C2 (PETx1.0)

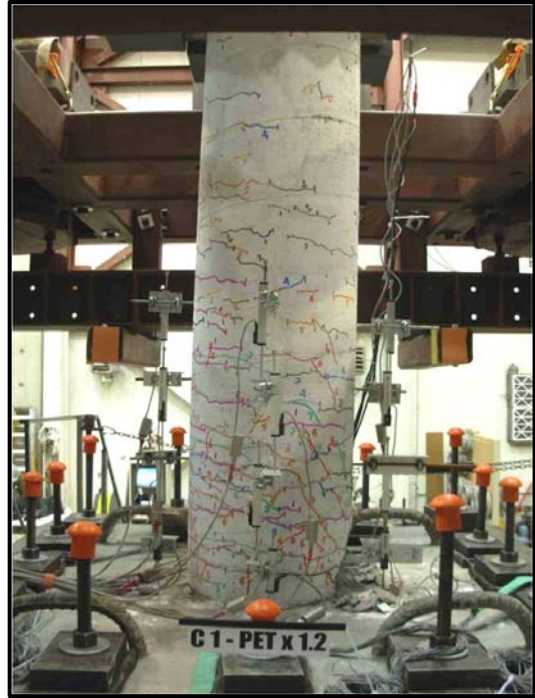
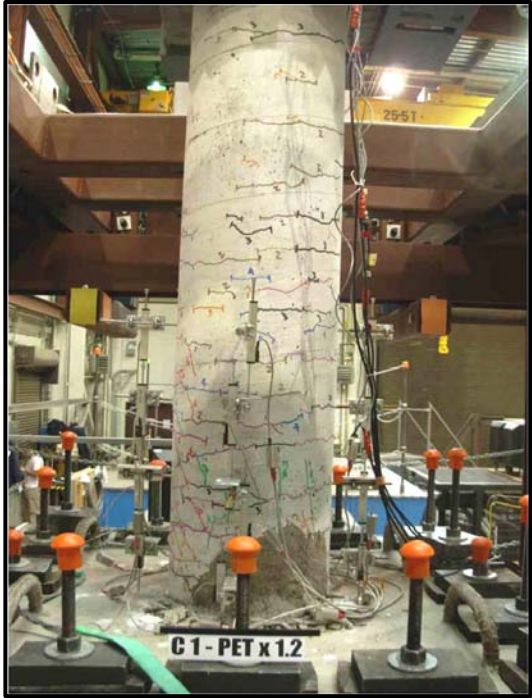


Figure 4-30 Specimen C1, Column Distress (PETx1.2)

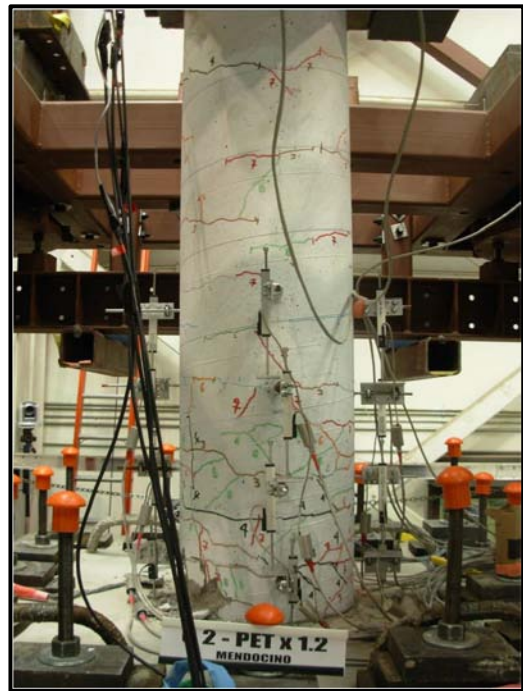
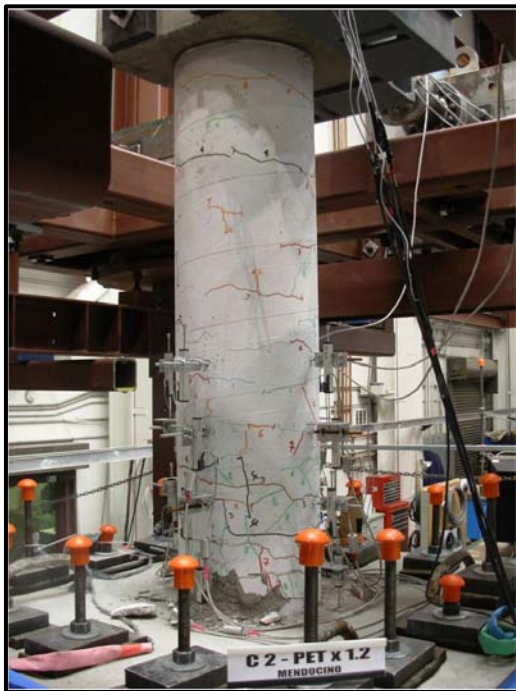


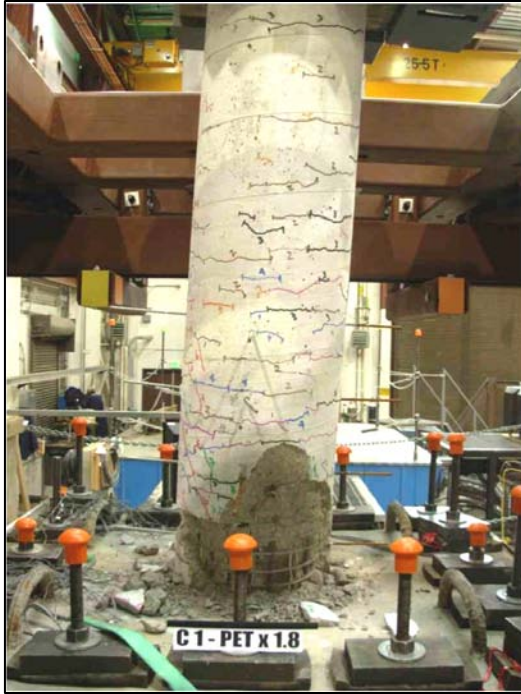
Figure 4-31 Specimen C2, Column Distress (PETx1.2)



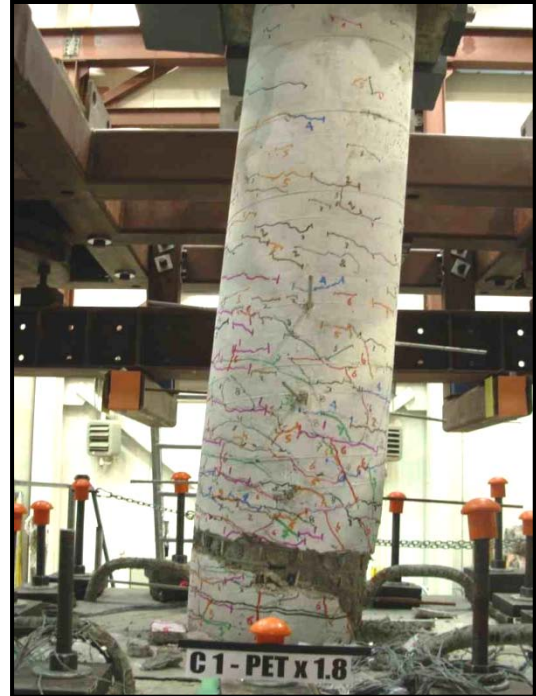
Figure 4-32 Spiral and Longitudinal. Bars visible, Specimen C1



Figure 4-33 Spiral and Longitudinal. Bars visible, Specimen C2



a) E - W View



b) N - S View



c) Plastic Hinge

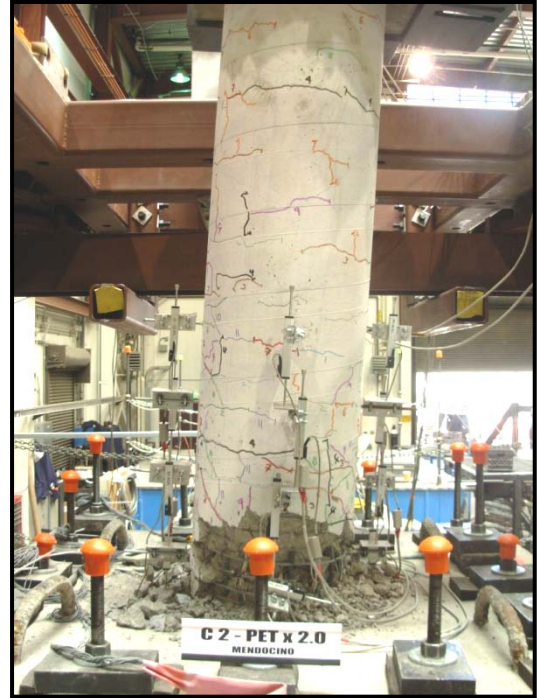


d) Long. Bars Buckling

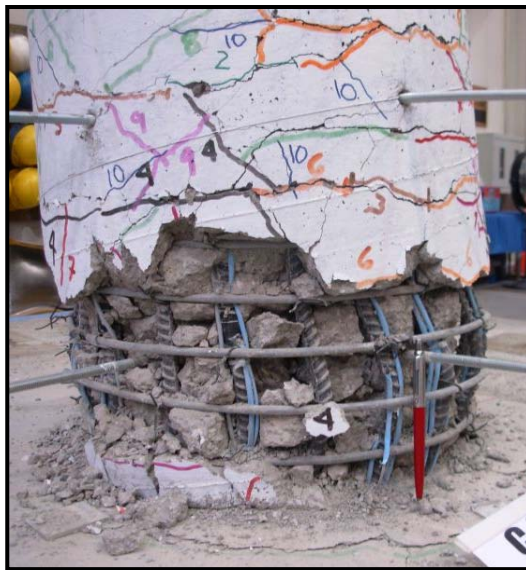
**Figure 4-34 Damage at Failure, Specimen C1**



a) E - W View



b) N - S View



c) Long. Bars Buckling



d) Long. Bars and Spiral Rupture

**Figure 4-35 Damage at Failure, Specimen C2**



a) Specimen C1

b) Specimen C2

**Figure 4-36 Specimens C1 and C2, Damage Pattern After Testing**



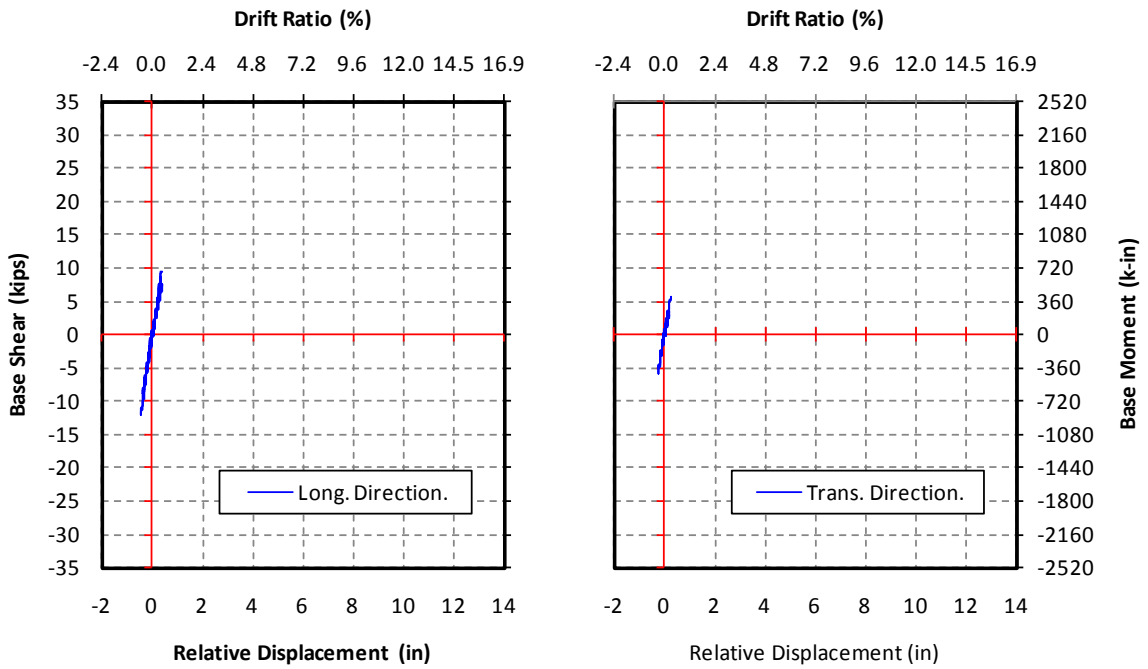


Figure 4-37 Base Shear-Displacement Hysteresis, Specimen C1 (0.1xPET)

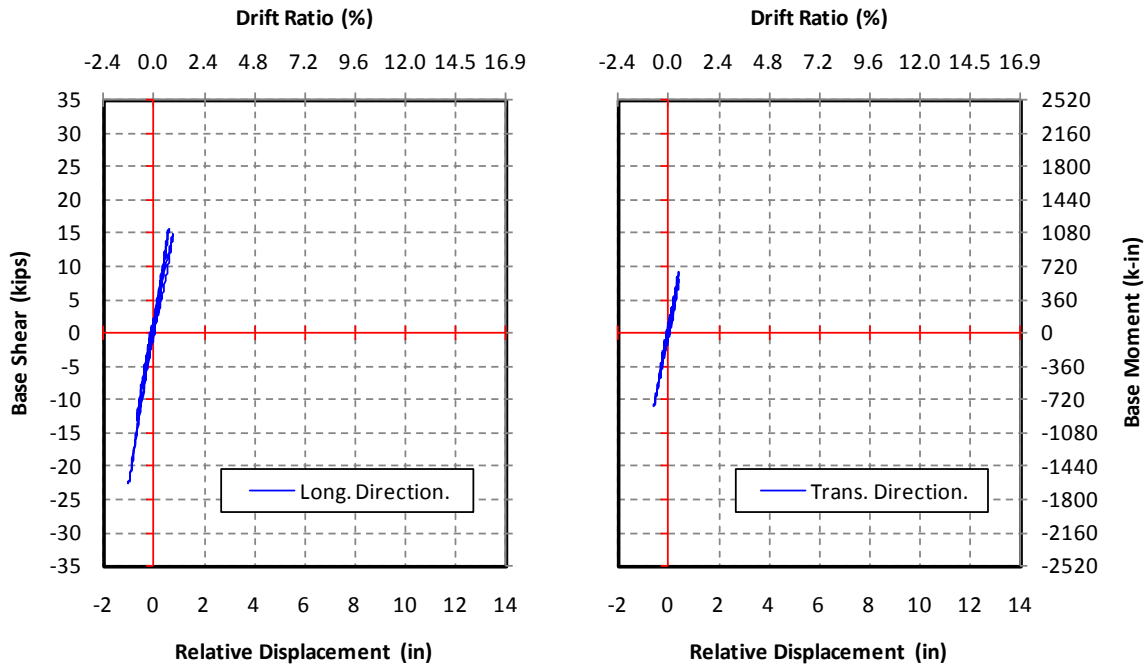


Figure 4-38 Base Shear-Displacement Hysteresis, Specimen C1 (0.2xPET)

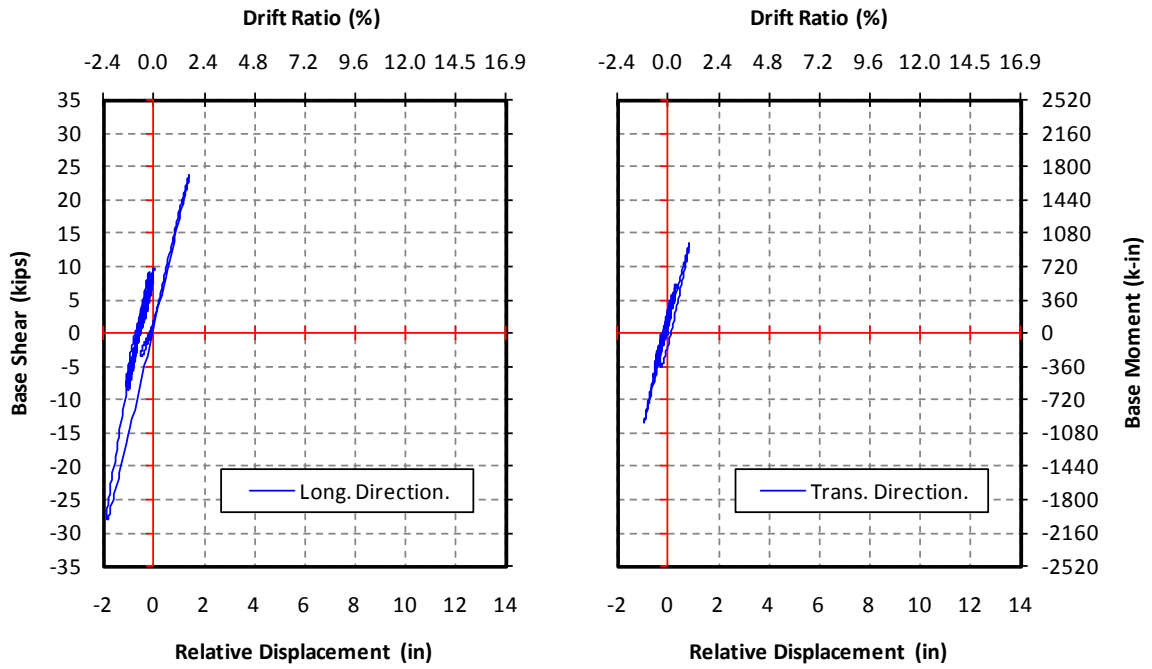


Figure 4-39 Base Shear-Displacement Hysteresis, Specimen C1 (0.4xPET)

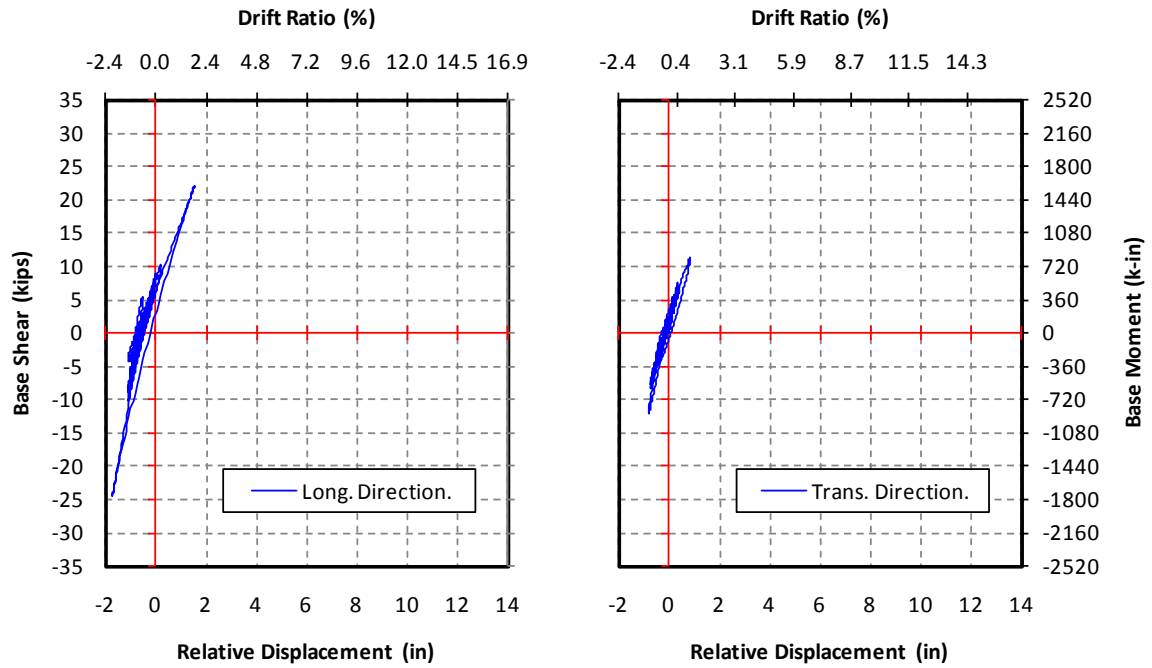


Figure 4-40 Base Shear-Displacement Hysteresis, Specimen C1 (0.6xPET)

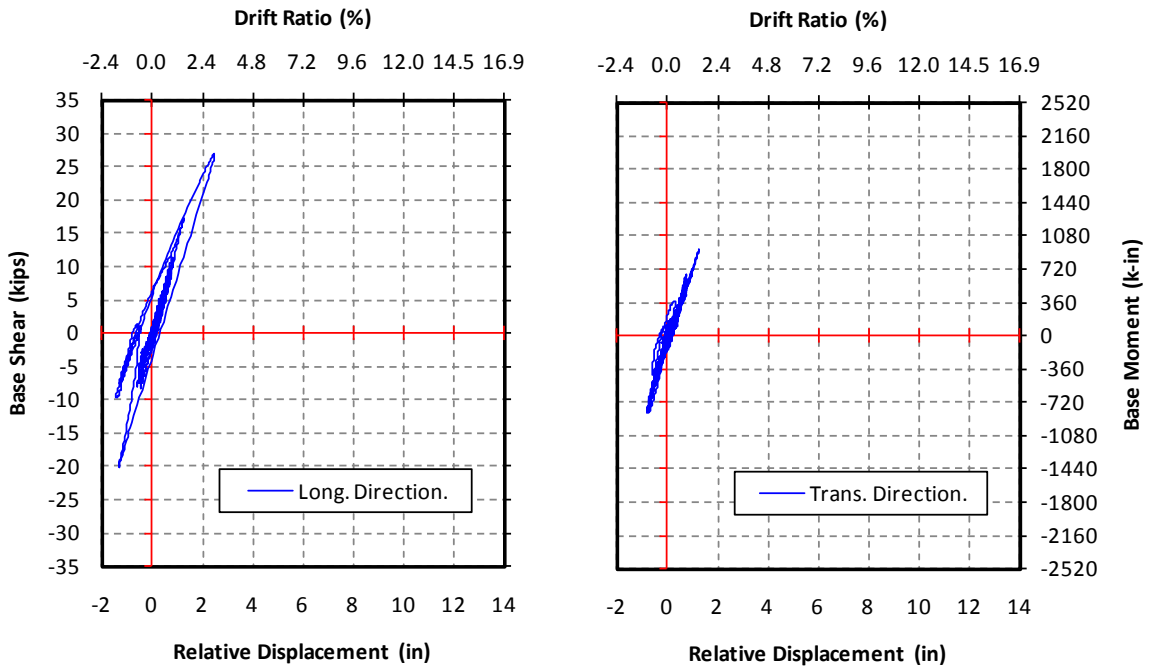


Figure 4-41 Base Shear-Displacement Hysteresis, Specimen C1 (0.8xPET)

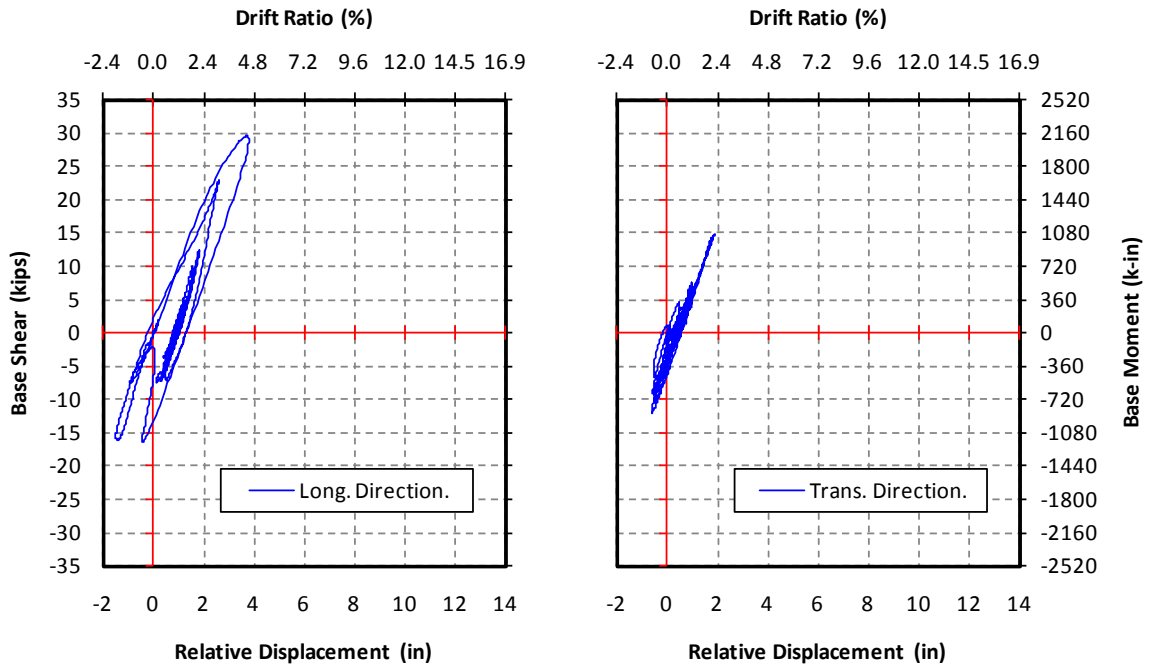


Figure 4-42 Base Shear-Displacement Hysteresis, Specimen C1 (1.0xPET)

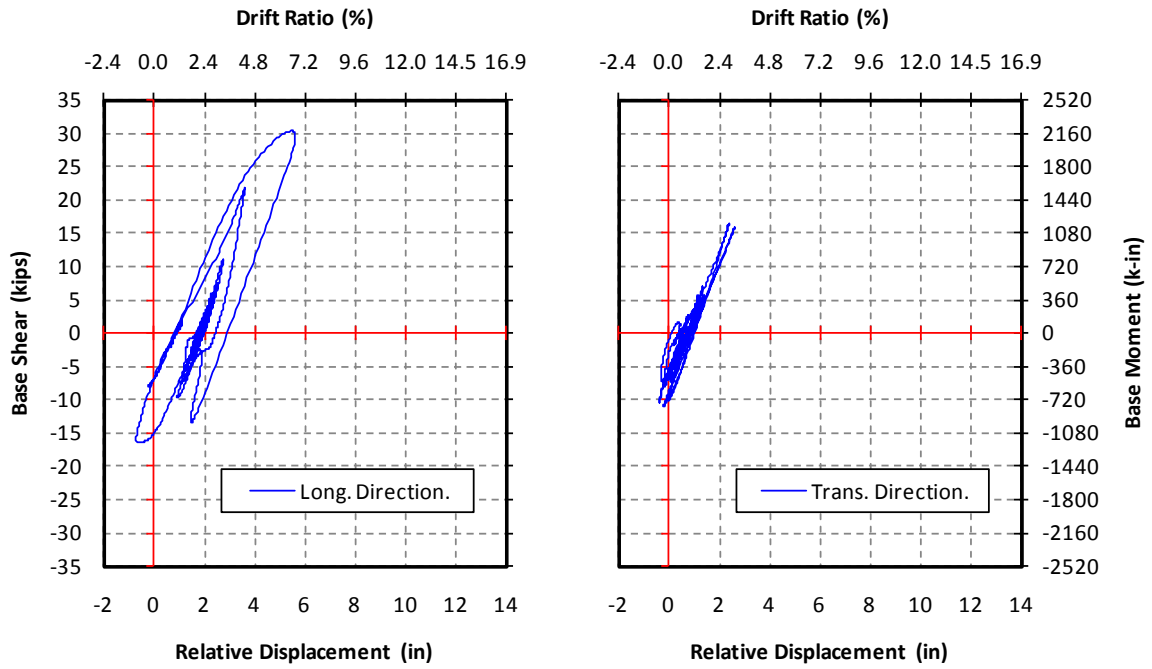


Figure 4-43 Base Shear-Displacement Hysteresis, Specimen C1 (1.2xPET)

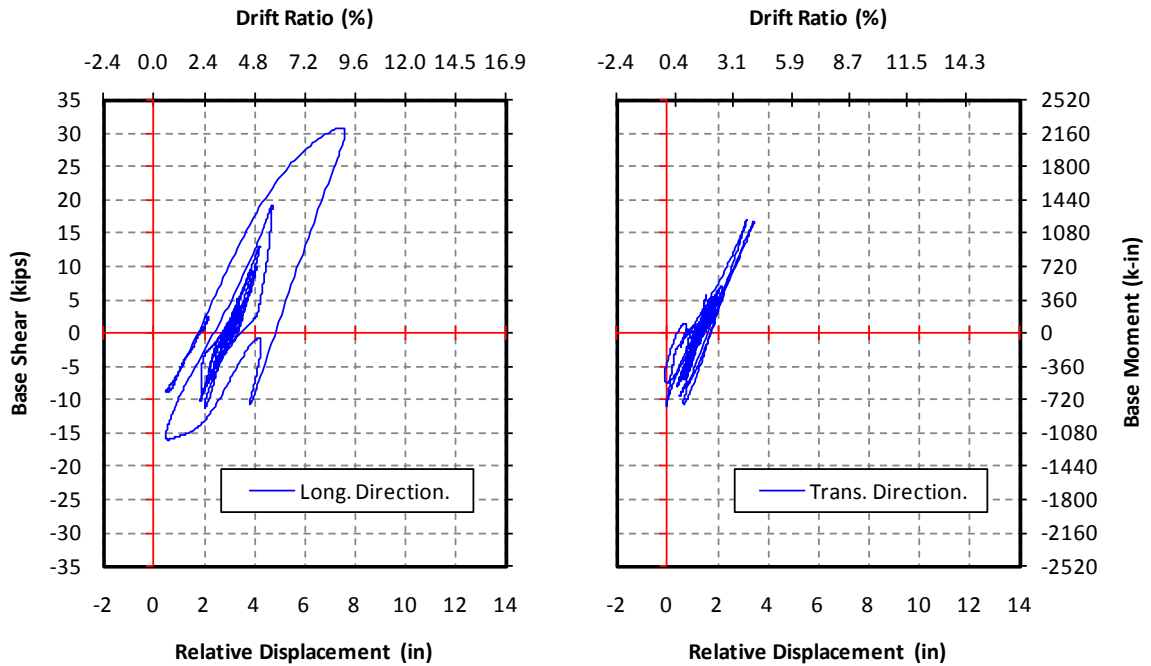


Figure 4-44 Base Shear-Displacement Hysteresis, Specimen C1 (1.4xPET)

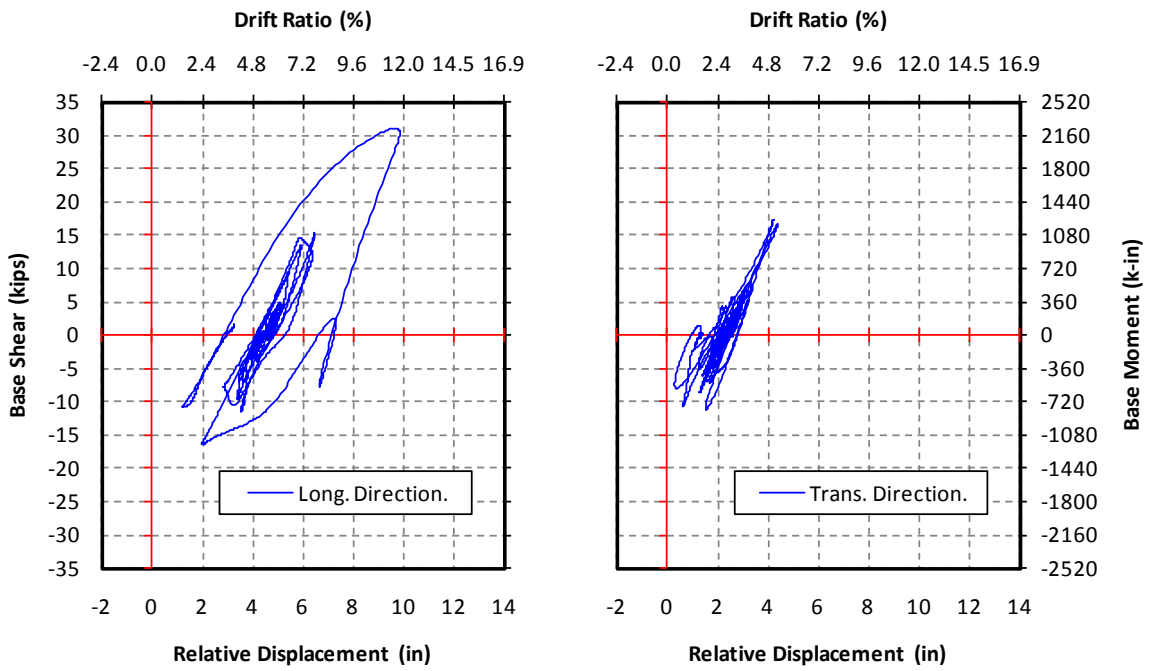


Figure 4-45 Base Shear-Displacement Hysteresis, Specimen C1 (1.6xPET)

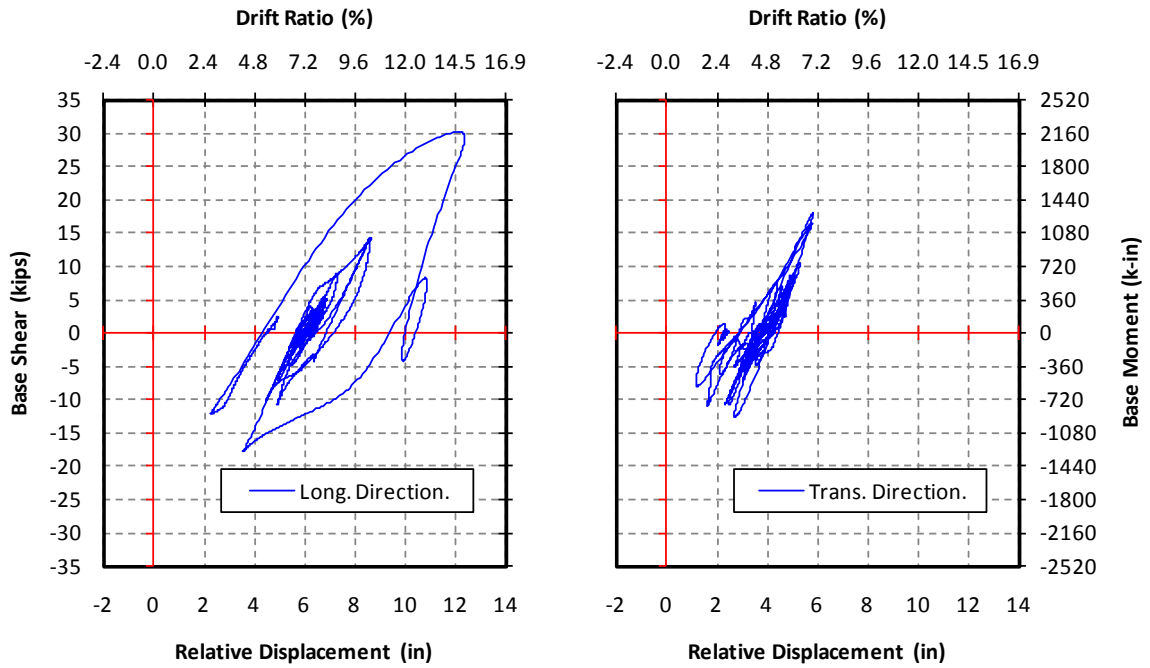


Figure 4-46 Base Shear-Displacement Hysteresis, Specimen C1 (1.8xPET)

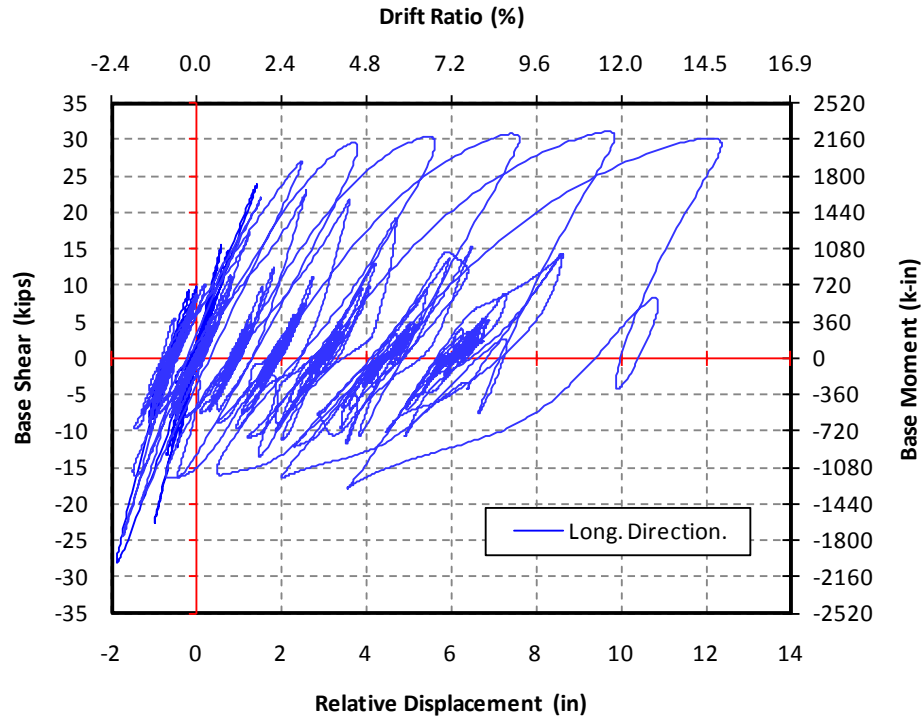


Figure 4-47 Cumulative Base Shear-Displacement Hysteresis, Specimen C1 (Longitudinal)

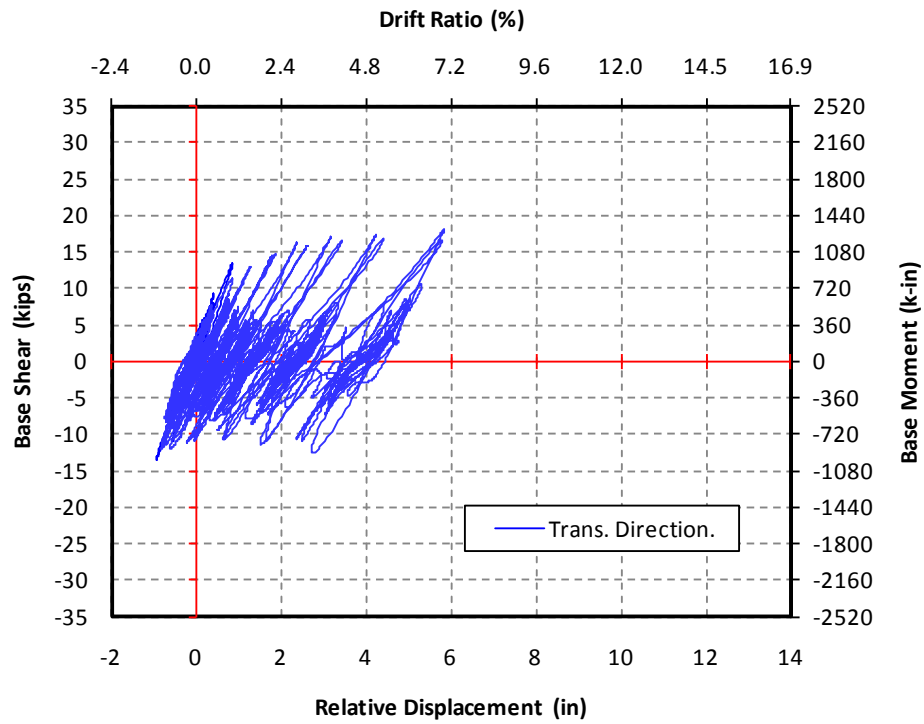
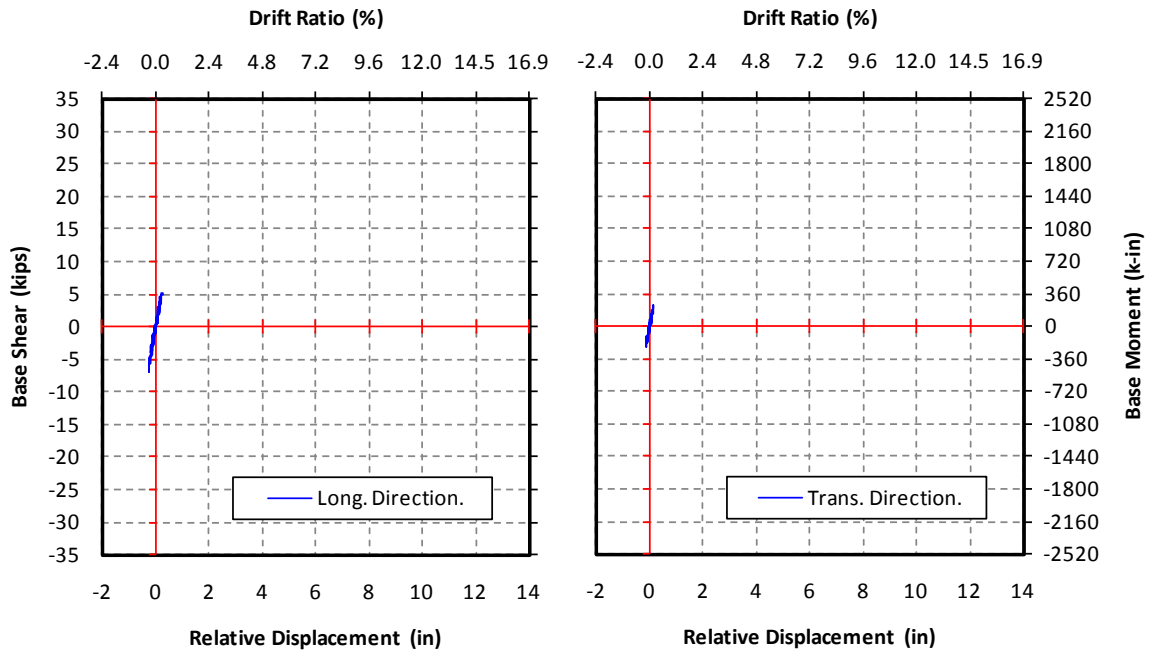
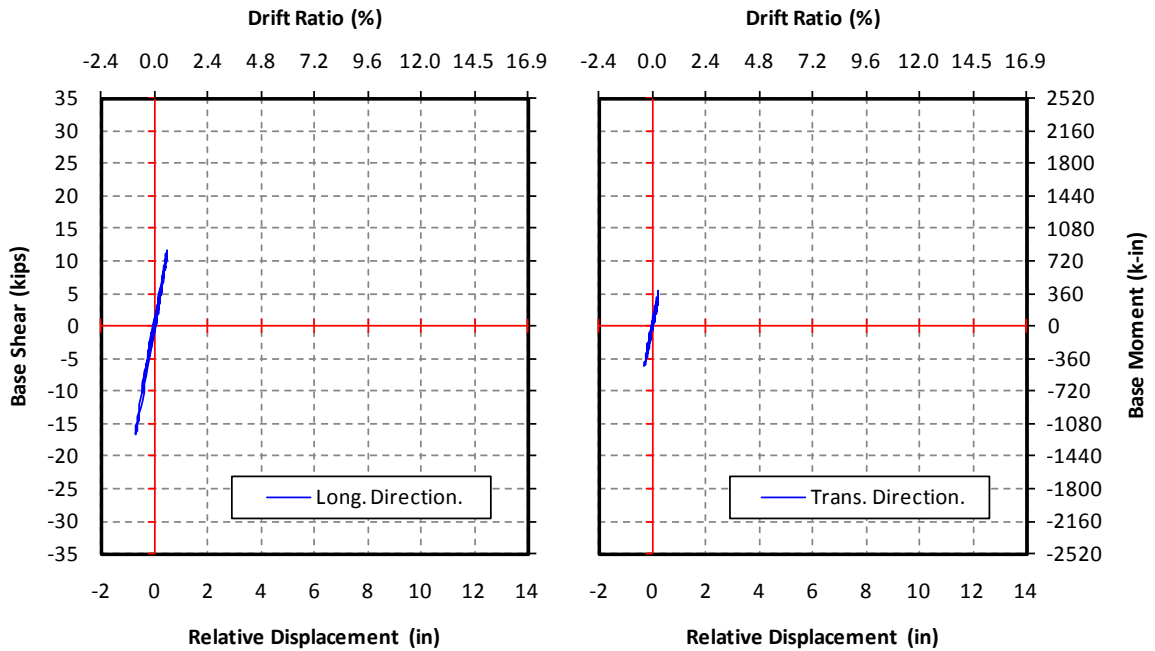


Figure 4-48 Cumulative Base Shear-Displacement Hysteresis, Specimen C1 (Transverse)



**Figure 4-49 Base Shear-Displacement Hysteresis, Specimen C2 (0.1xPET)**



**Figure 4-50 Base Shear-Displacement Hysteresis, Specimen C2 (0.2xPET)**

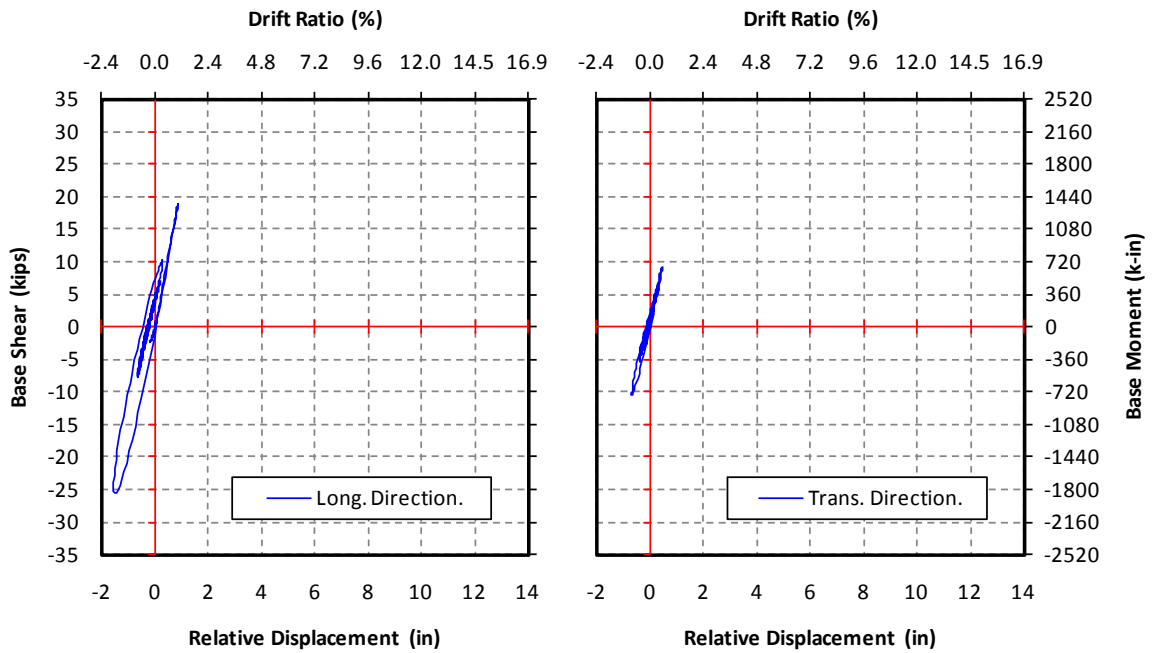


Figure 4-51 Base Shear-Displacement Hysteresis, Specimen C2 (0.4xPET)

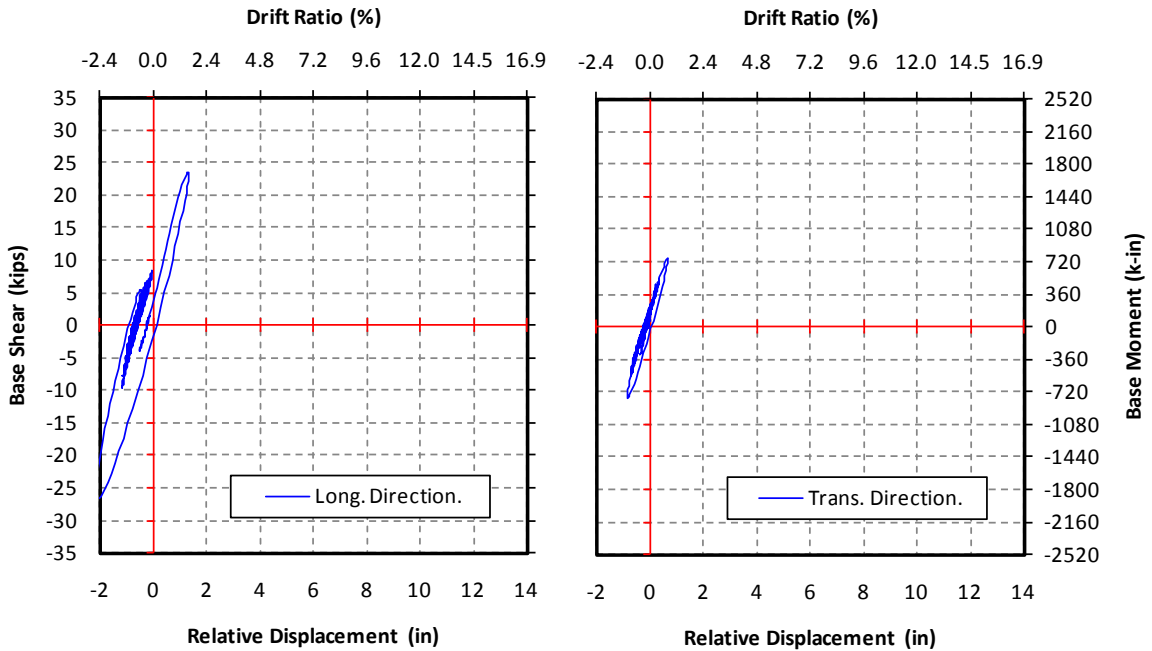


Figure 4-52 Base Shear-Displacement Hysteresis, Specimen C2 (0.6xPET)



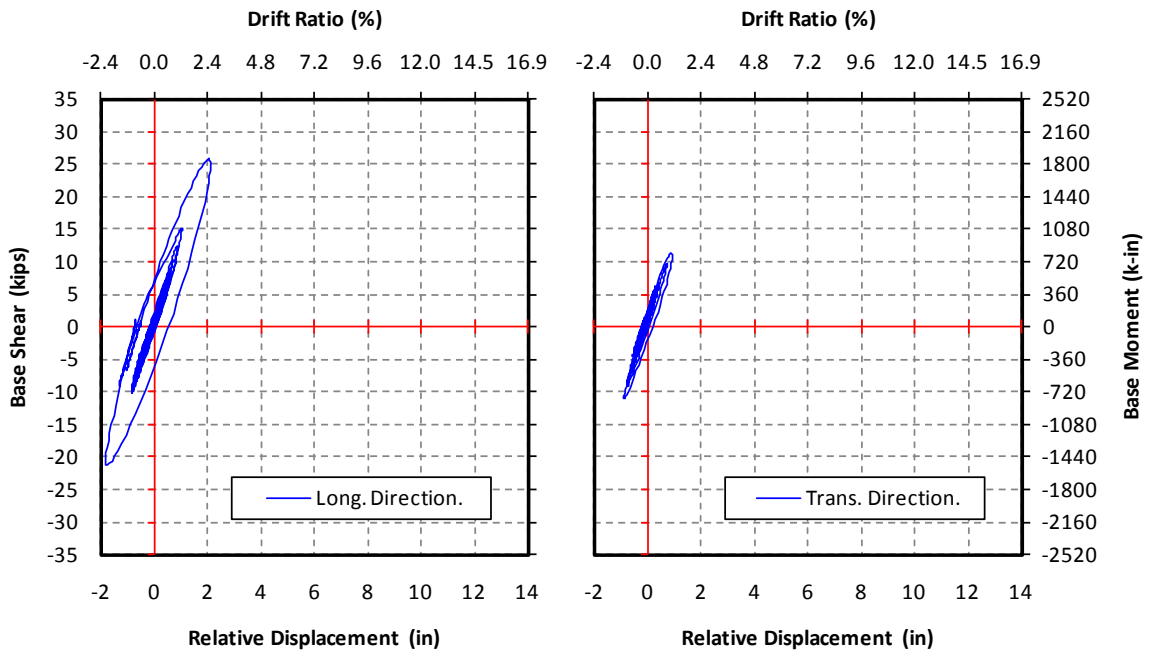


Figure 4-53 Base Shear-Displacement Hysteresis, Specimen C2 (0.8xPET)

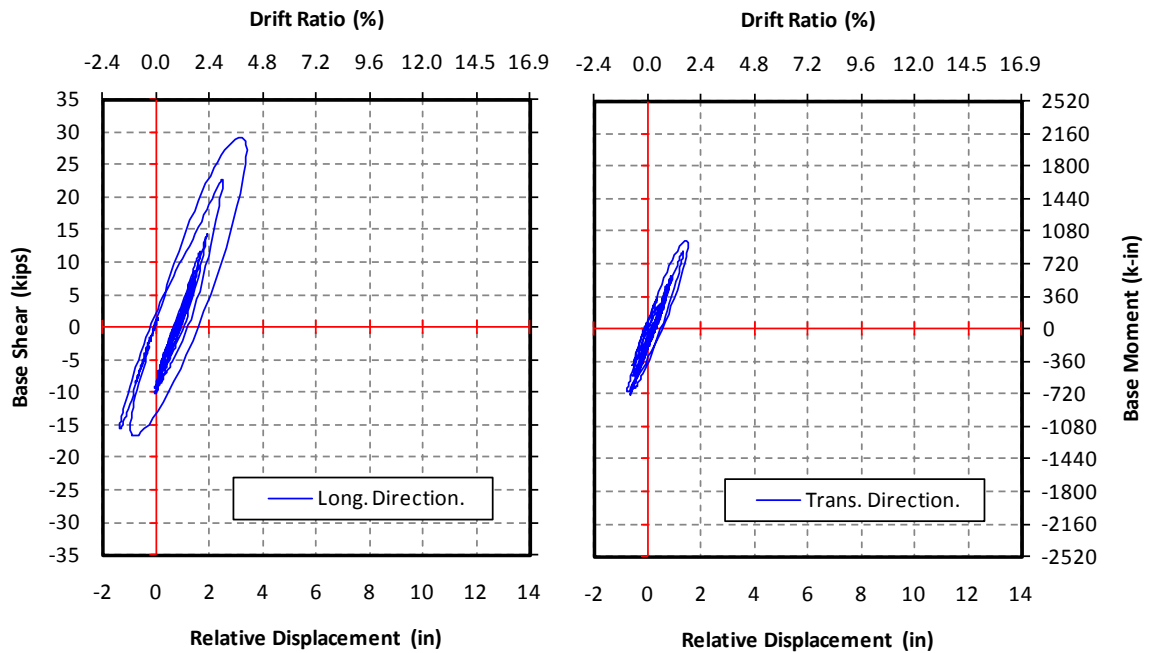


Figure 4-54 Base Shear-Displacement Hysteresis, Specimen C2 (1.0xPET)

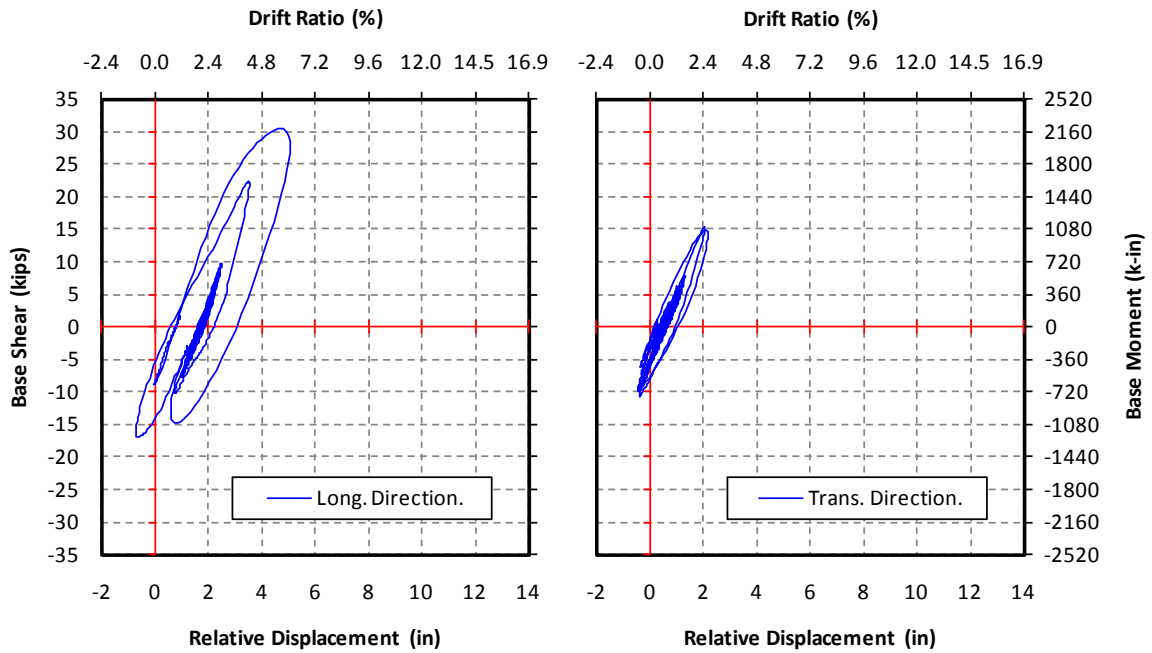


Figure 4-55 Base Shear-Displacement Hysteresis, Specimen C2 (1.2xPET)

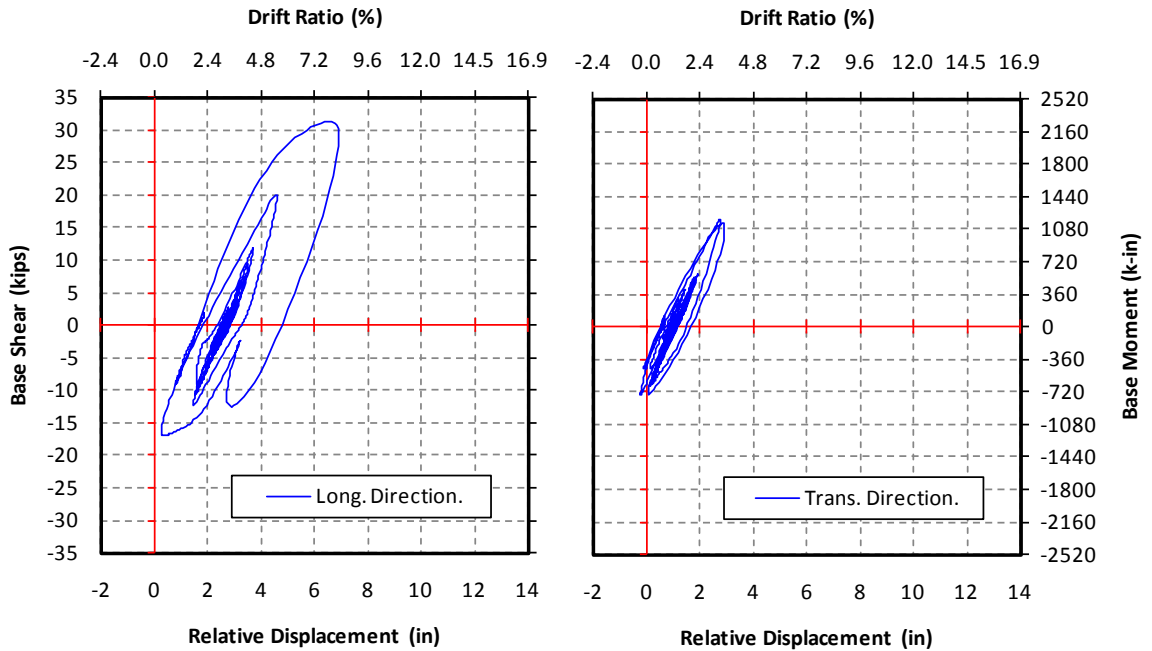


Figure 4-56 Base Shear-Displacement Hysteresis, Specimen C2 (1.4xPET)

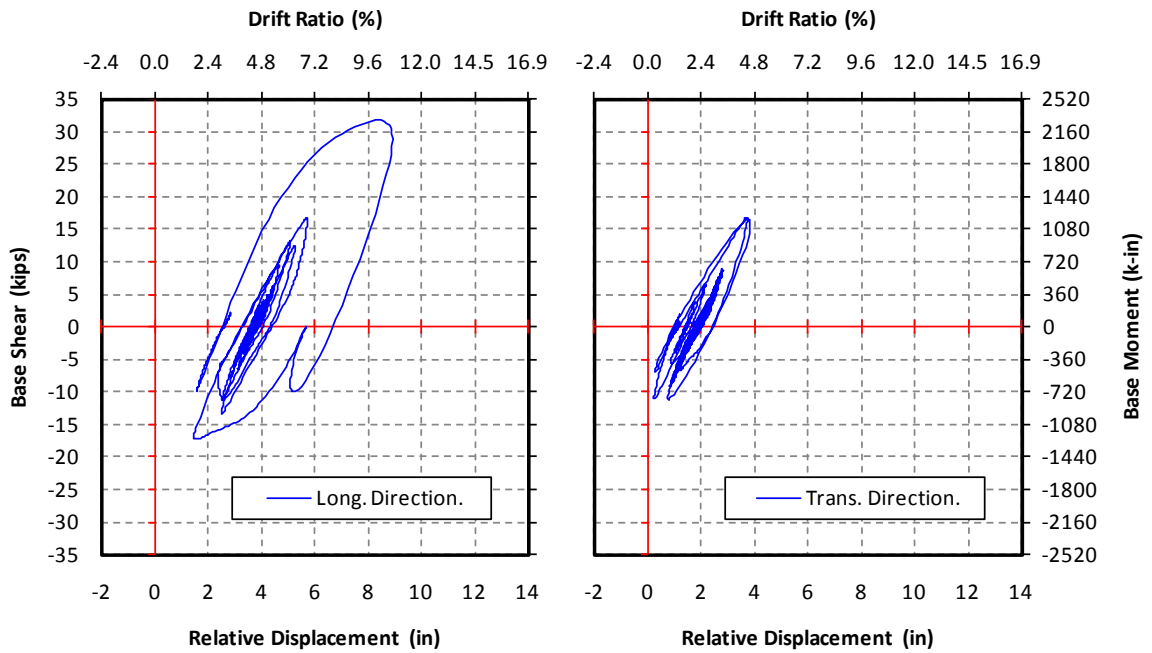


Figure 4-57 Base Shear-Displacement Hysteresis, Specimen C2 (1.6xPET)

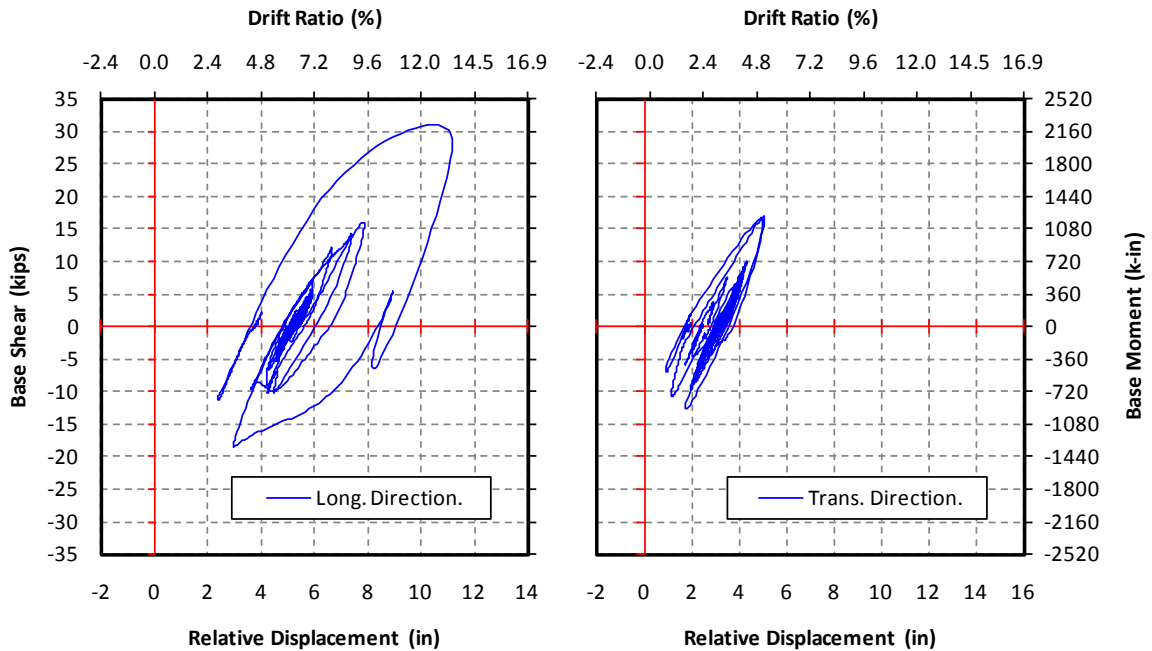
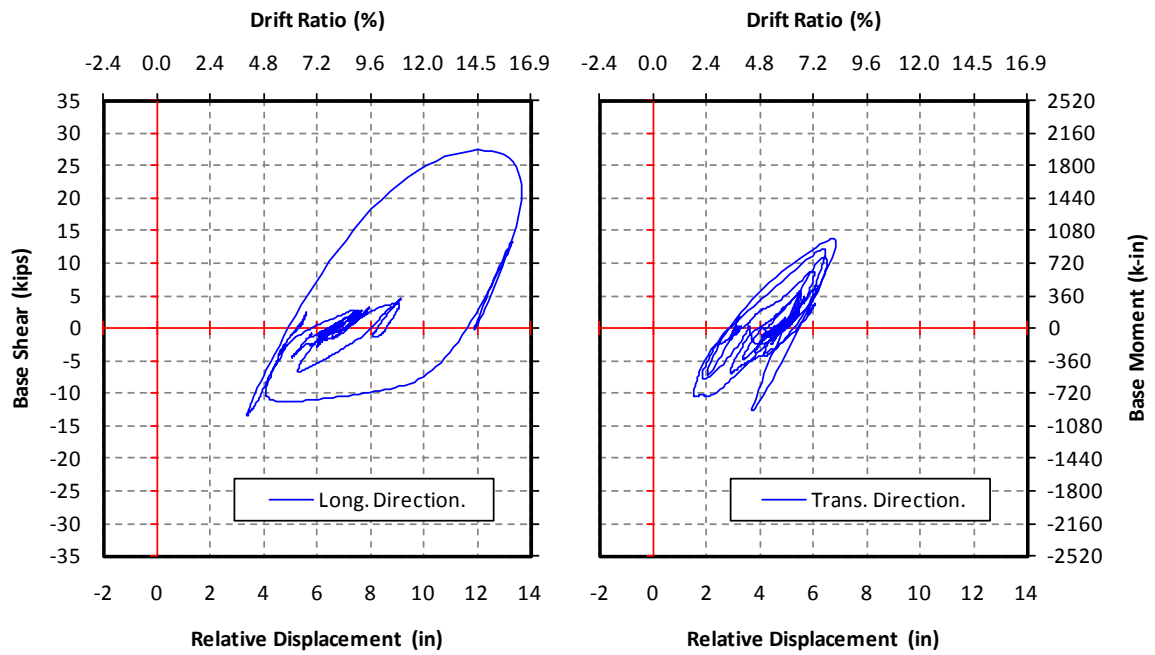


Figure 4-58 Base Shear-Displacement Hysteresis, Specimen C2 (1.8xPET)



**Figure 4-59 Base Shear-Displacement Hysteresis, Specimen C2 (2.0xPET)**

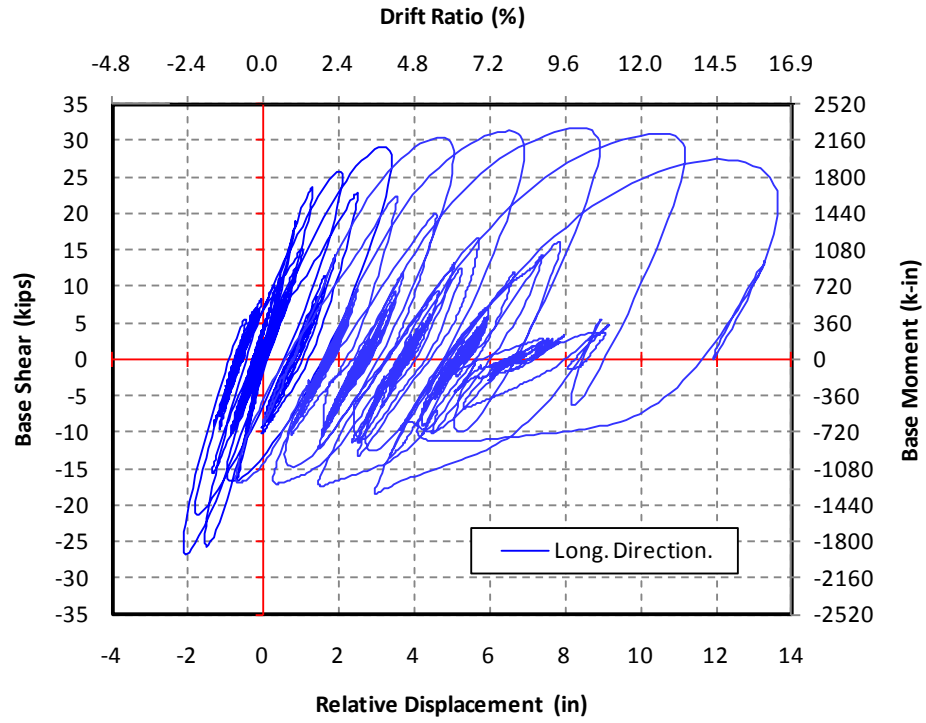


Figure 4-60 Cumulative Base Shear-Displacement Hysteresis, Specimen C2 (Longitudinal)

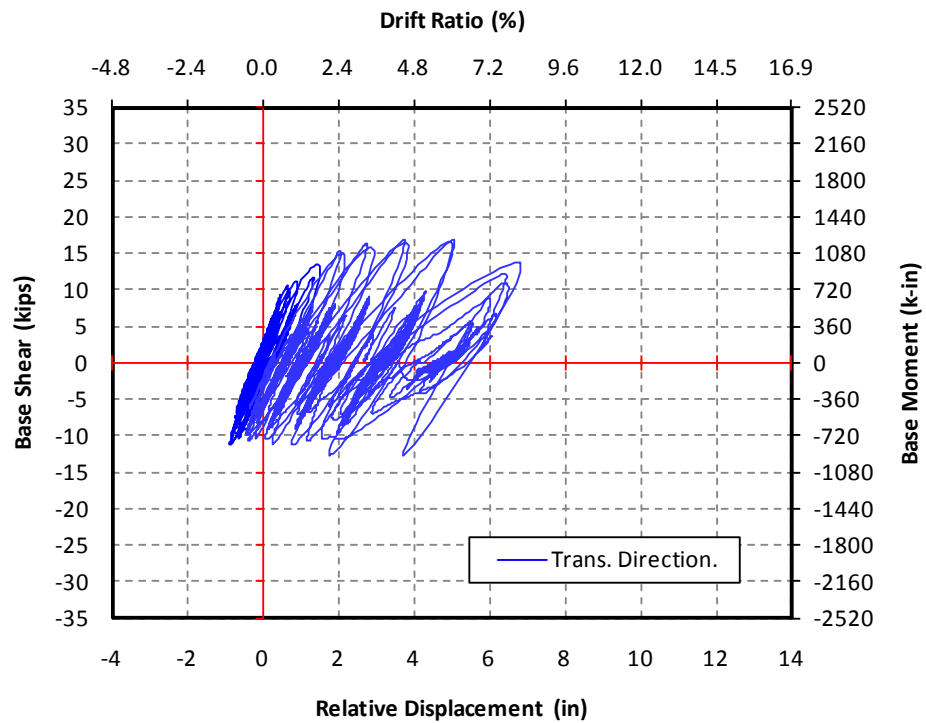


Figure 4-61 Cumulative Base Shear-Displacement Hysteresis, Specimen C2 (Transverse)

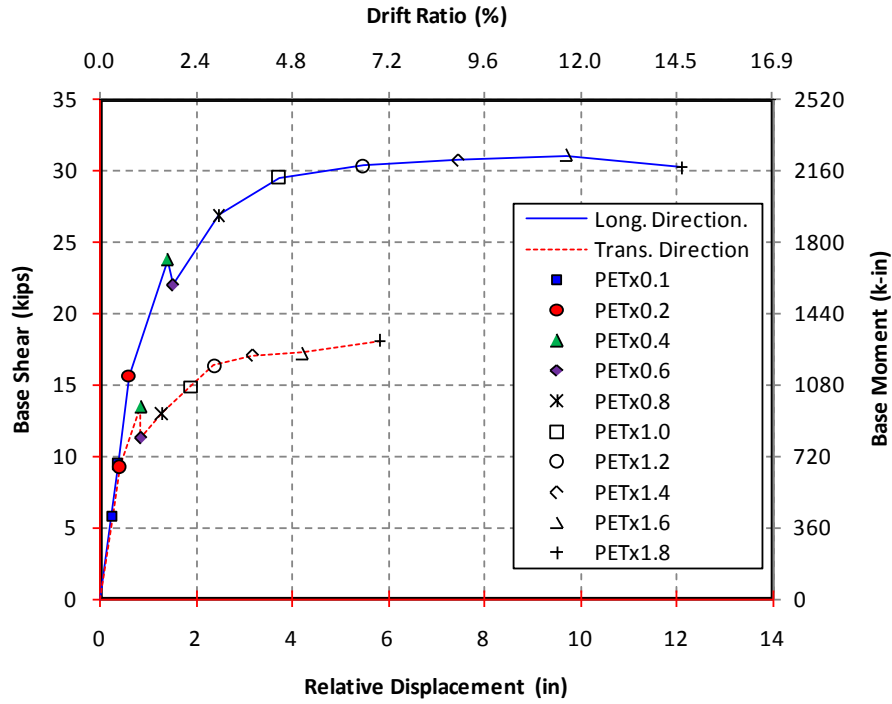


Figure 4-62 Envelope of Cumulative Base Shear-Displacement Hysteresis, Specimen C1

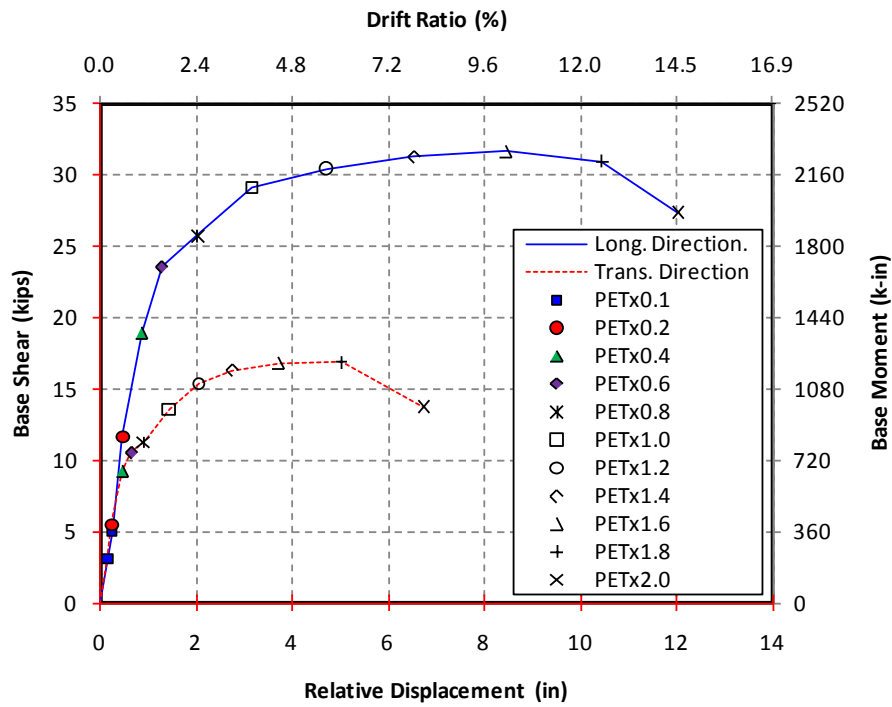
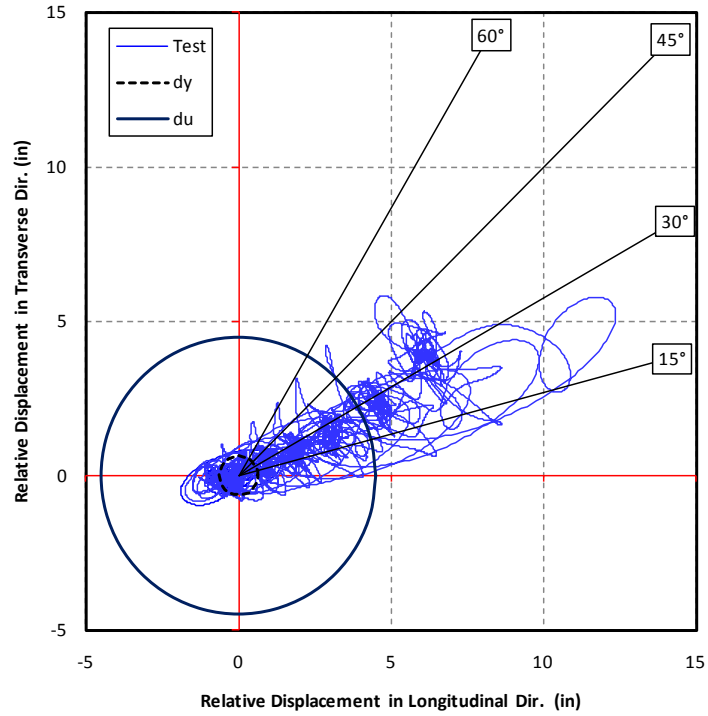
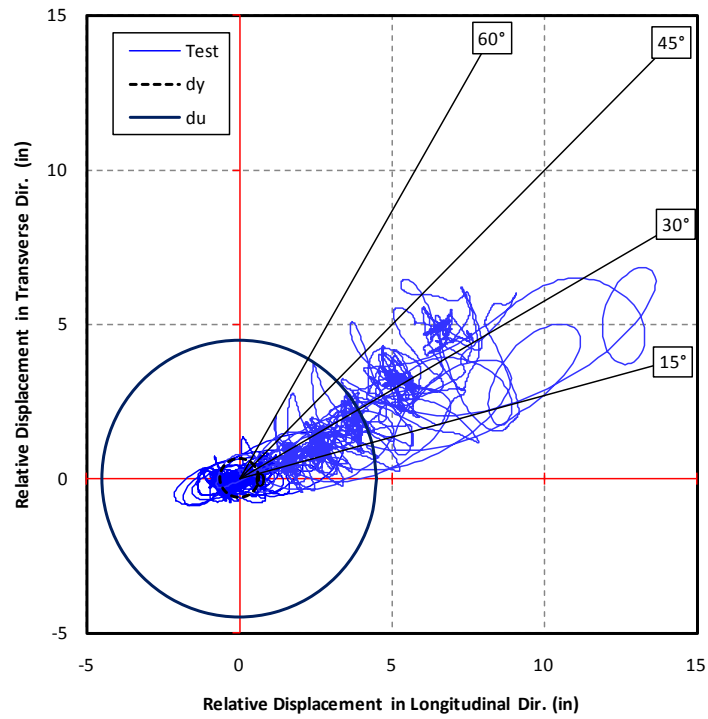


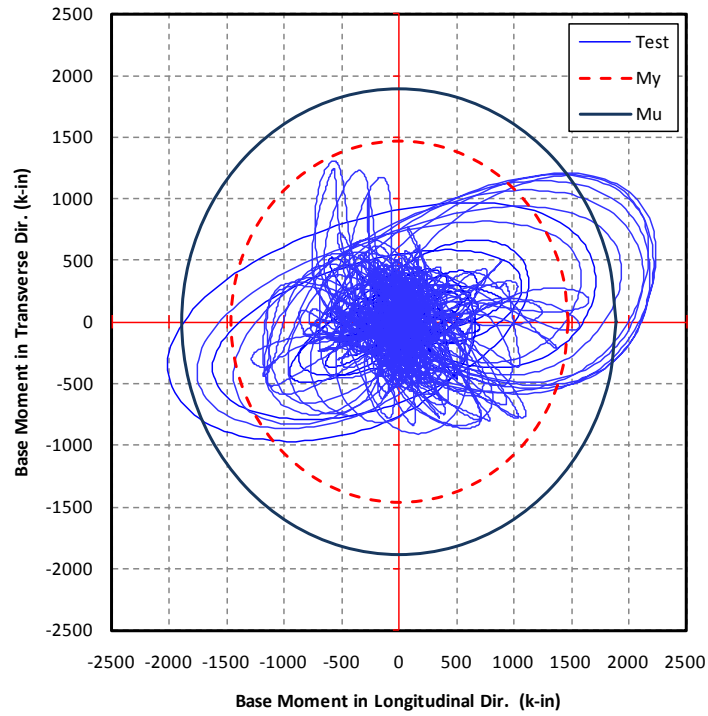
Figure 4-63 Envelope of Cumulative Base Shear-Displacement Hysteresis, Specimen C2



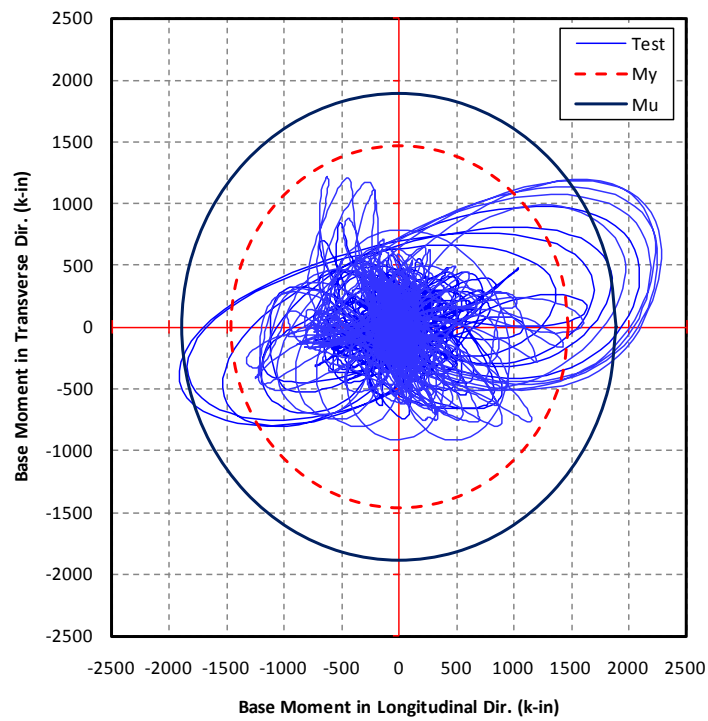
**Figure 4-64 Displacement Interaction Orbit, Specimen C1**



**Figure 4-65 Displacement Interaction Orbit, Specimen C2**



**Figure 4-66 Moment Interaction Orbit, Specimen C1**



**Figure 4-67 Moment Interaction Orbit, Specimen C2**



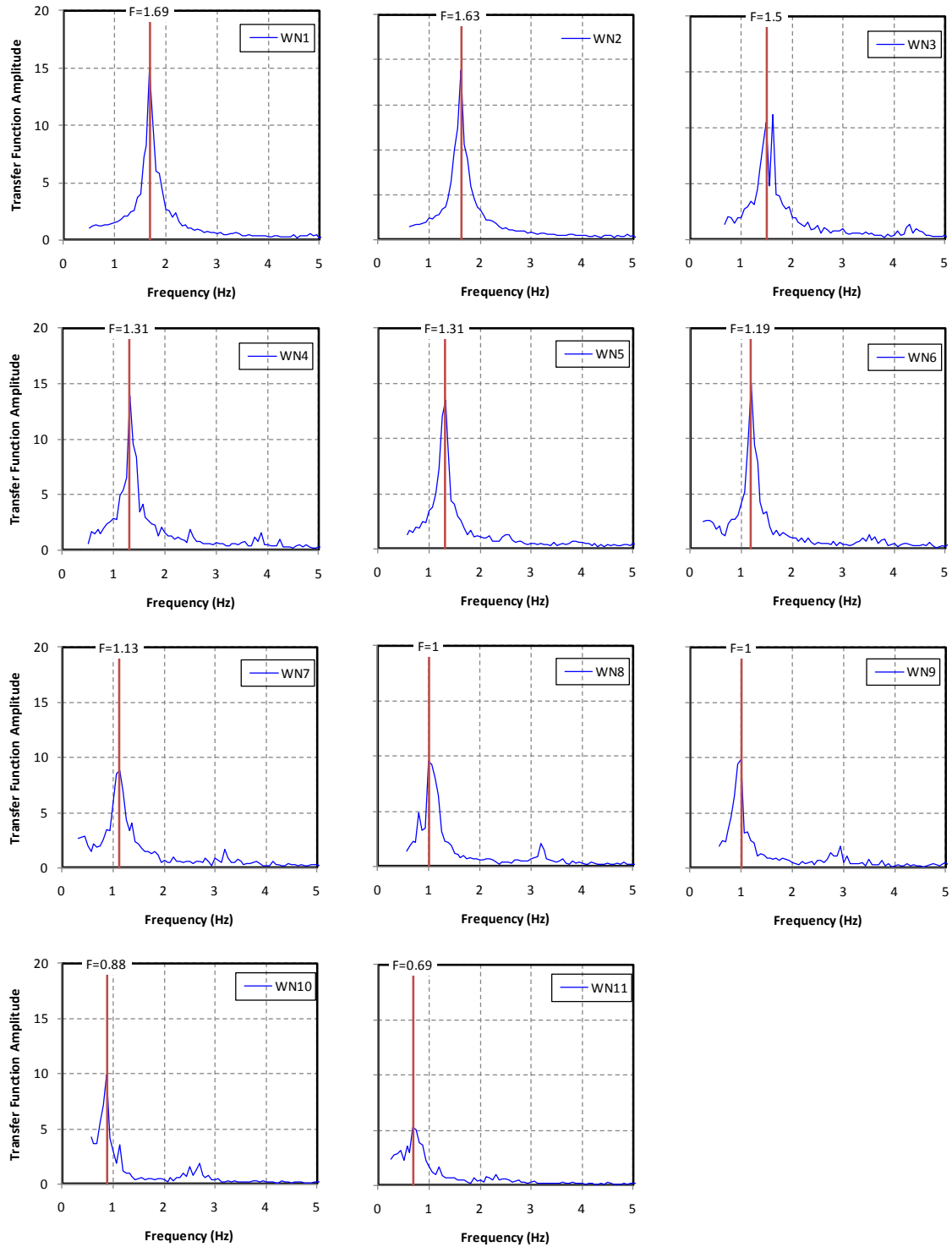
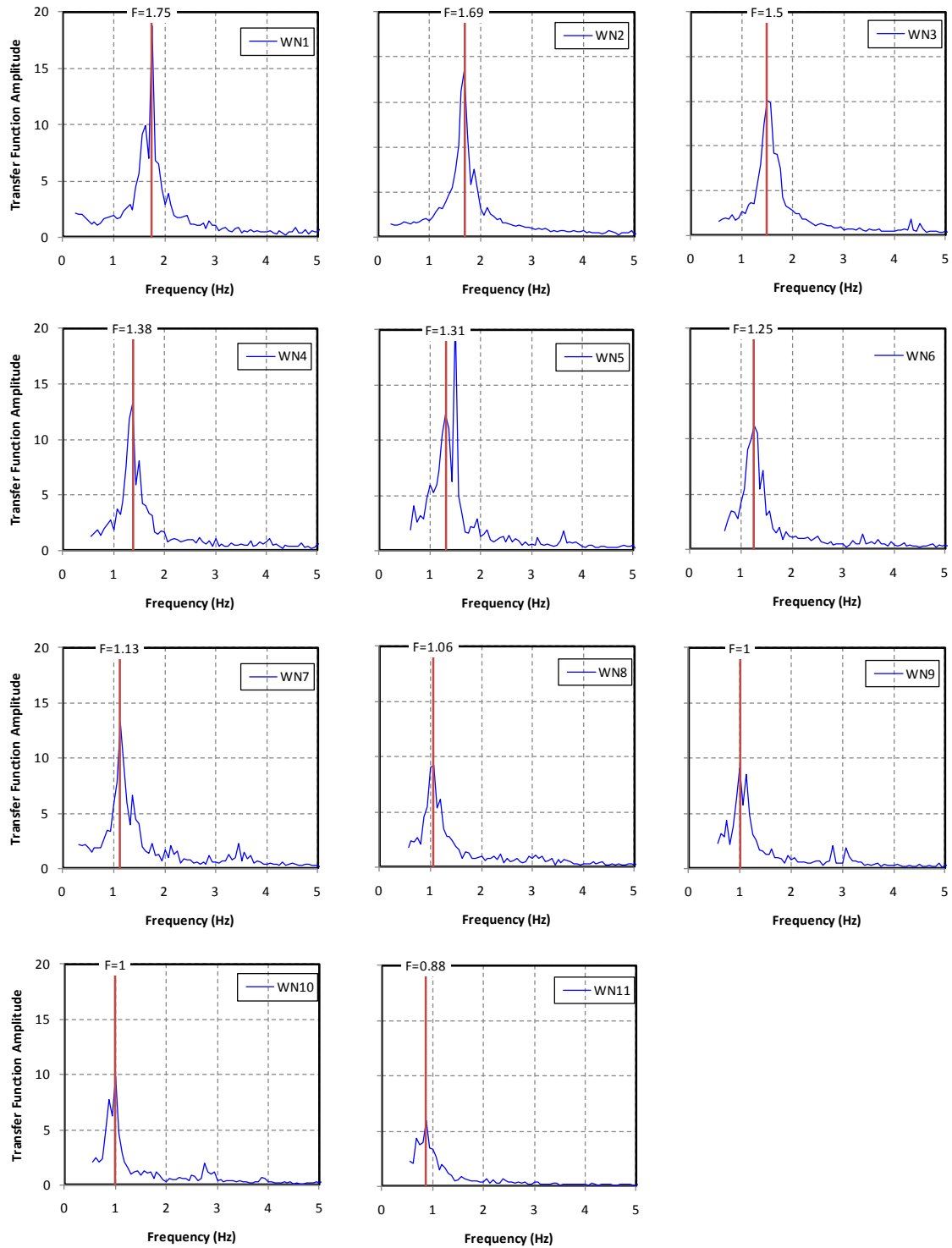


Figure 4-68 Power Spectral Density and Natural Frequencies, Specimen C1(Longitudinal)



**Figure 4-69 Power Spectral Density and Natural Frequencies, Specimen C1(Transverse)**

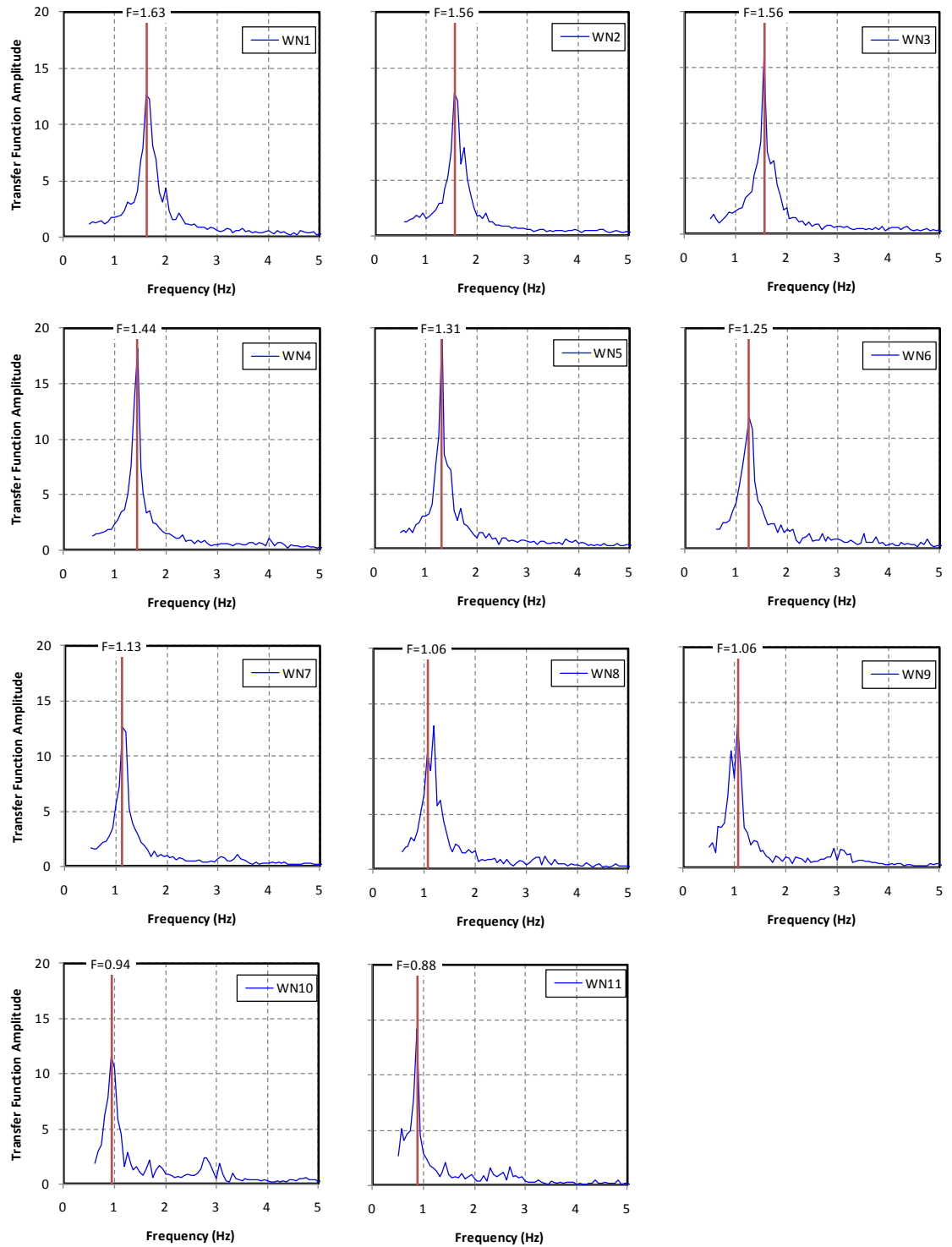
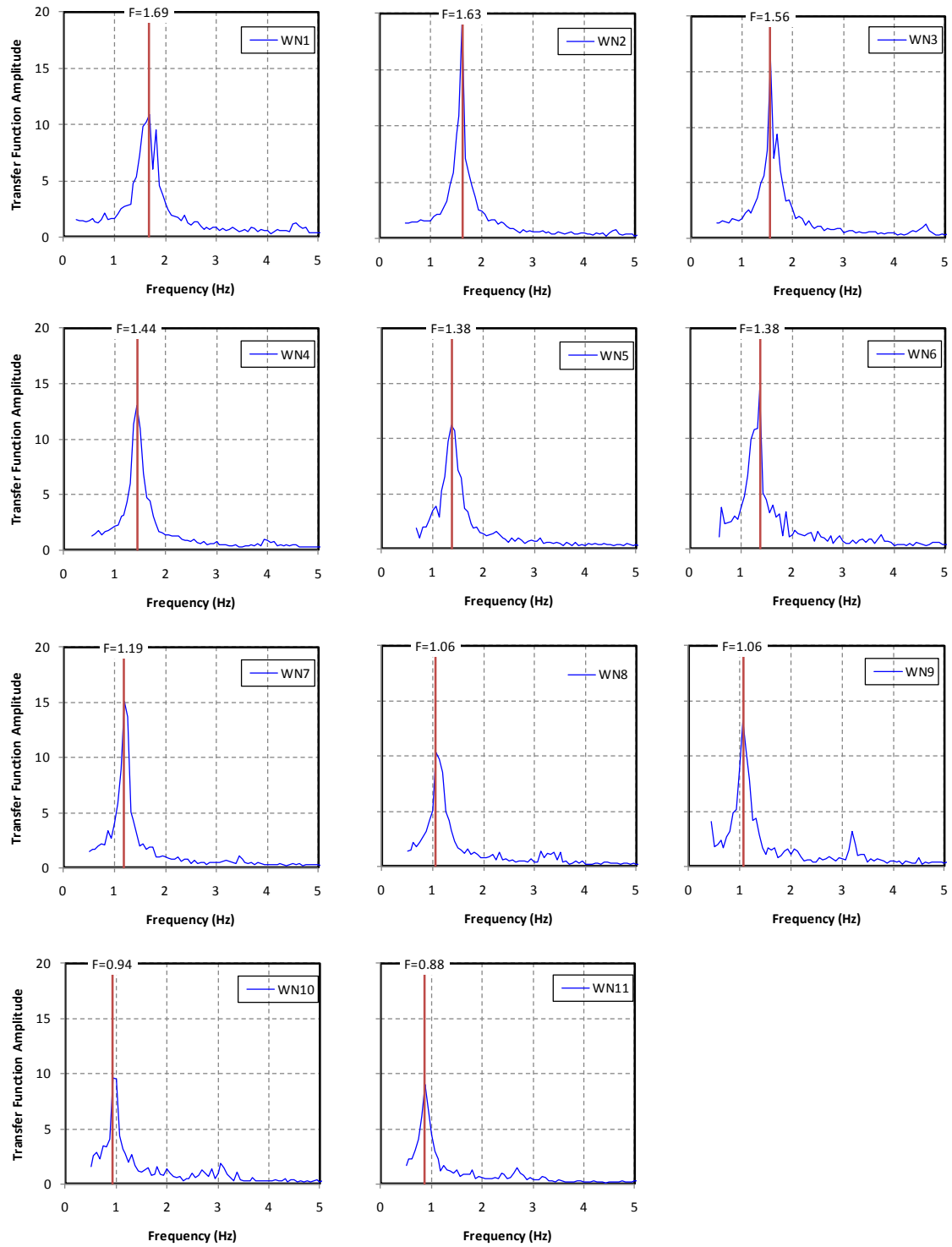


Figure 4-70 Power Spectral Density and Natural Frequencies, Specimen C2(Longitudinal)



**Figure 4-71 Power Spectral Density and Natural Frequencies, Specimen C2(Transverse)**

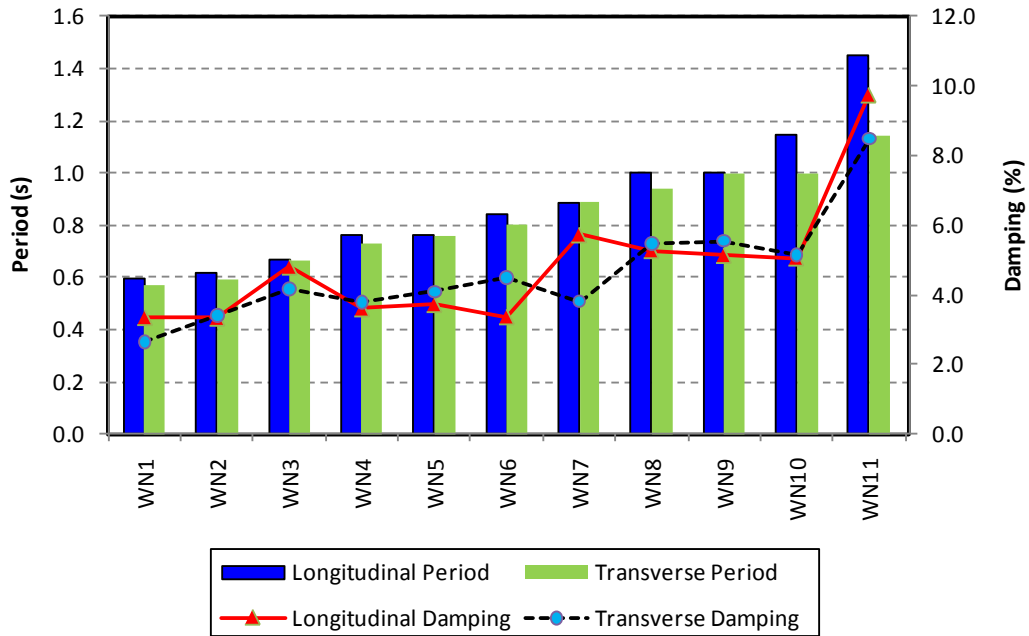


Figure 4-72 Variation in the Dynamic Properties Measured using Power Spectrum, C1

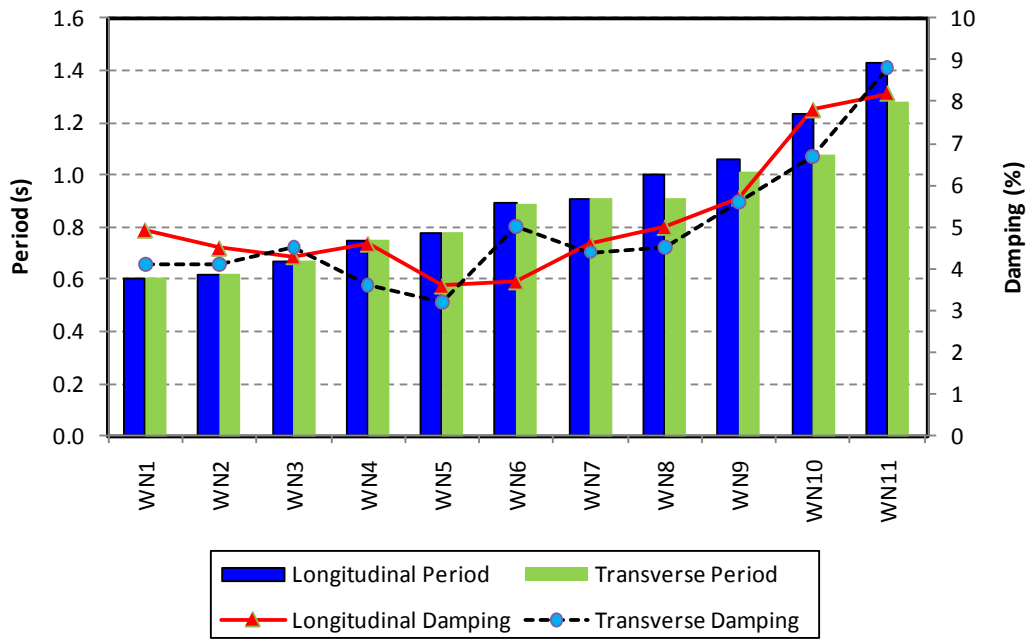


Figure 4-73 Variation in the Dynamic Properties Measured using MIMO, C1

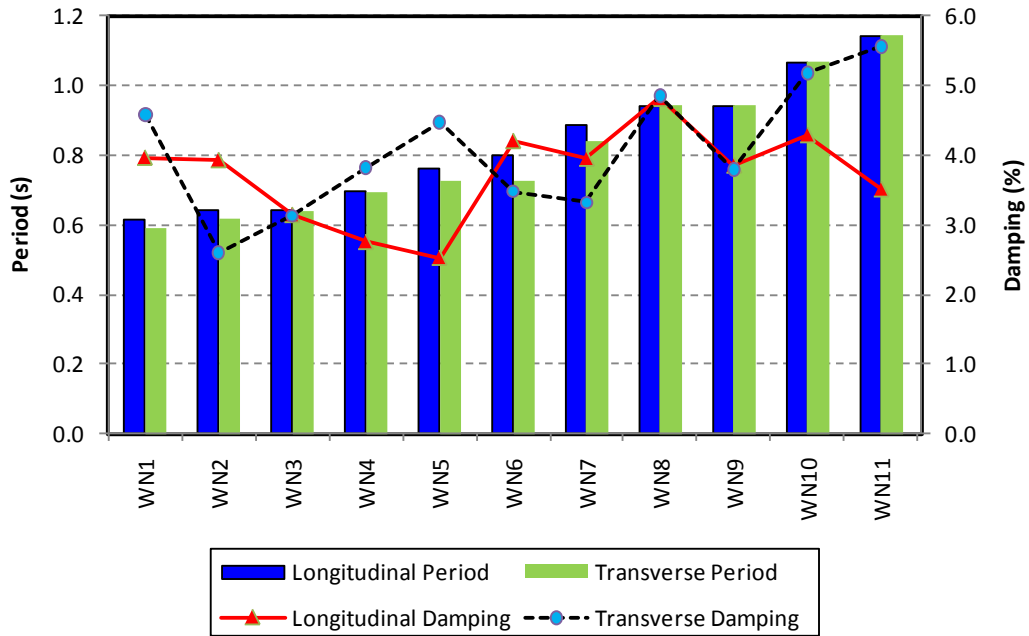


Figure 4-74 Variation in the Dynamic Properties Measured using Power Spectrum, C2

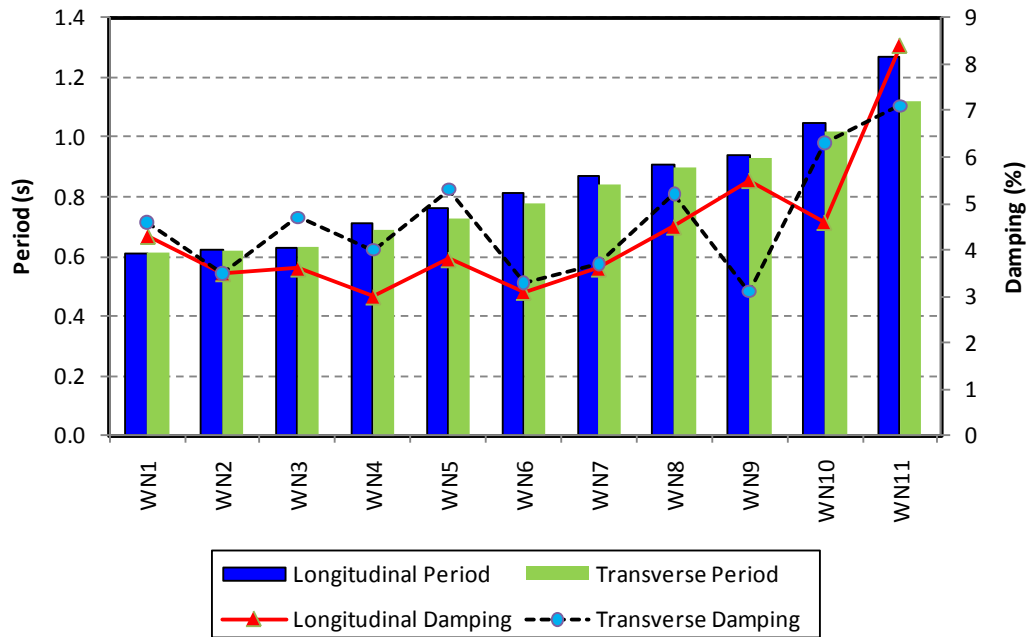


Figure 4-75 Variation in the Dynamic Properties Measured using MIMO, C2

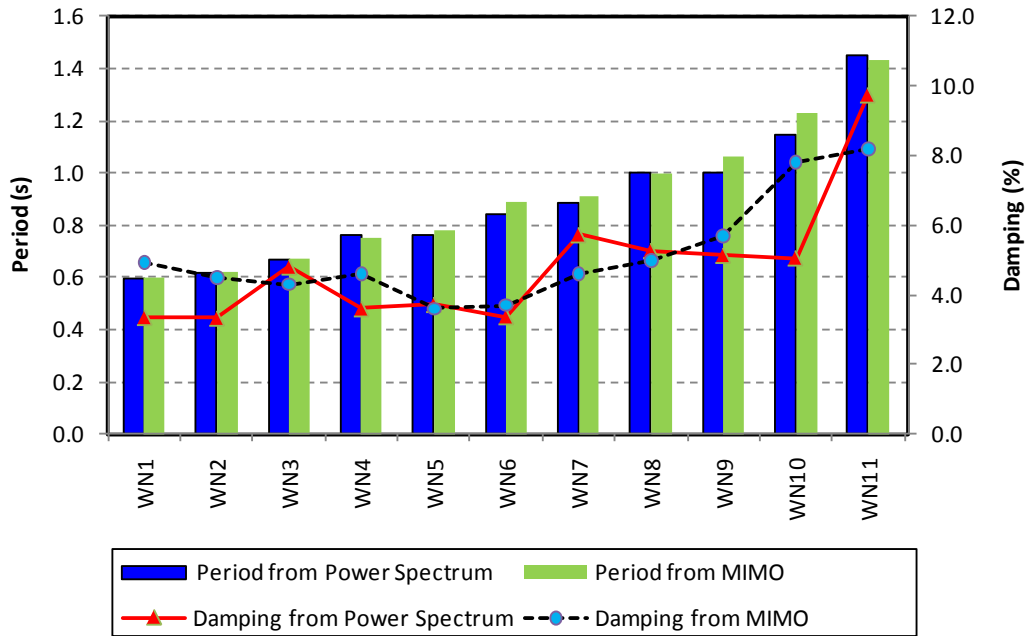


Figure 4-76 Comparison between the Dynamic Properties Measured using Power Spectrum and MIMO, C1 (Longitudinal Direction)

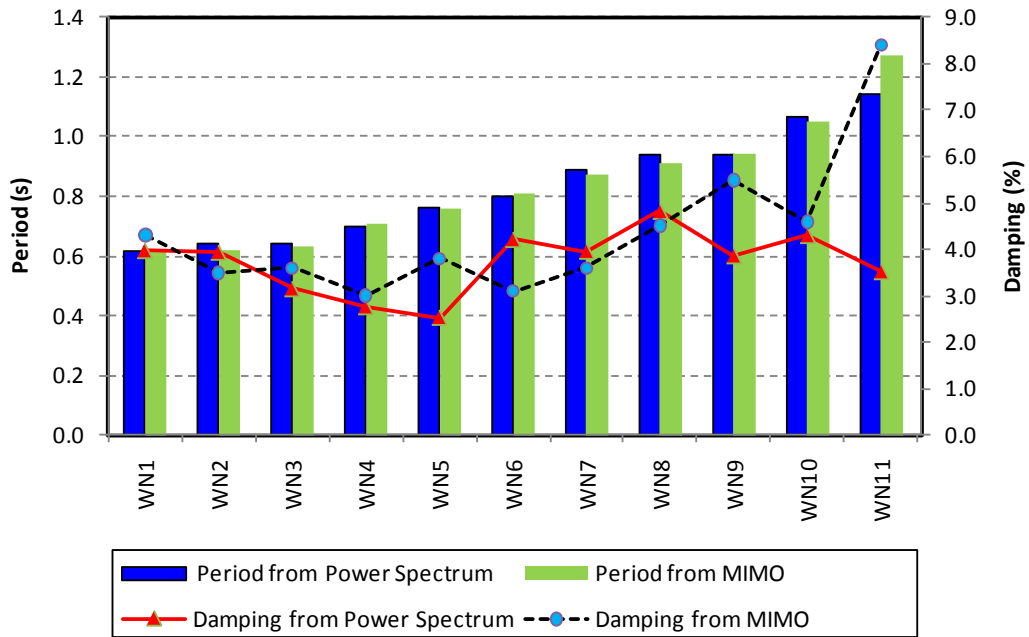


Figure 4-77 Comparison between the Dynamic Properties Measured using Power Spectrum and MIMO, C2 (Longitudinal Direction)

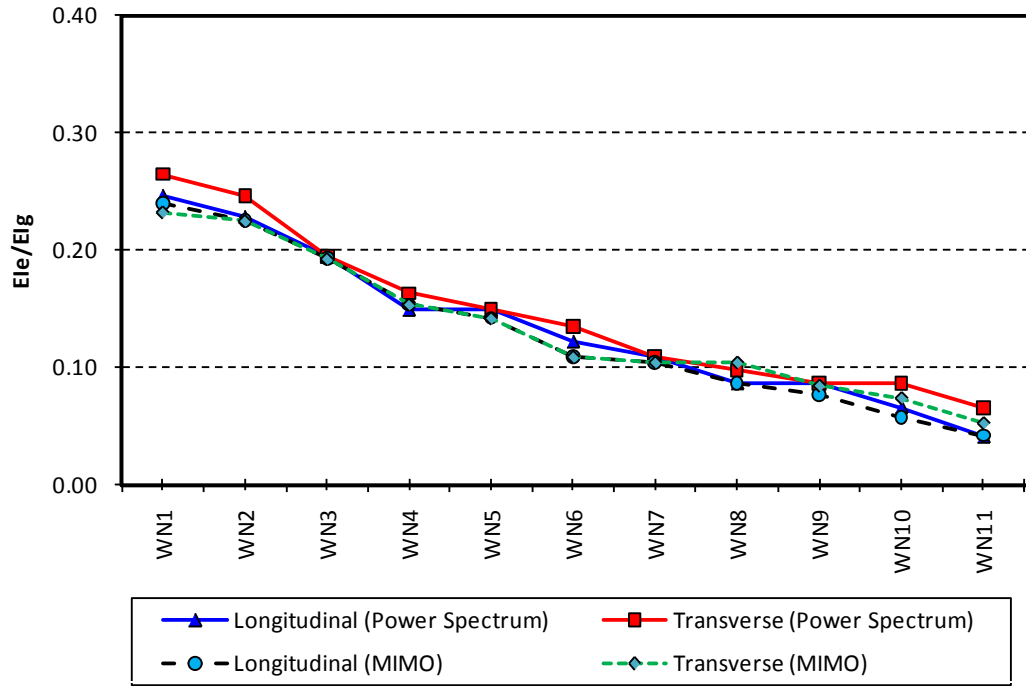


Figure 4-78 Variation in Effective Stiffness, Specimen C1

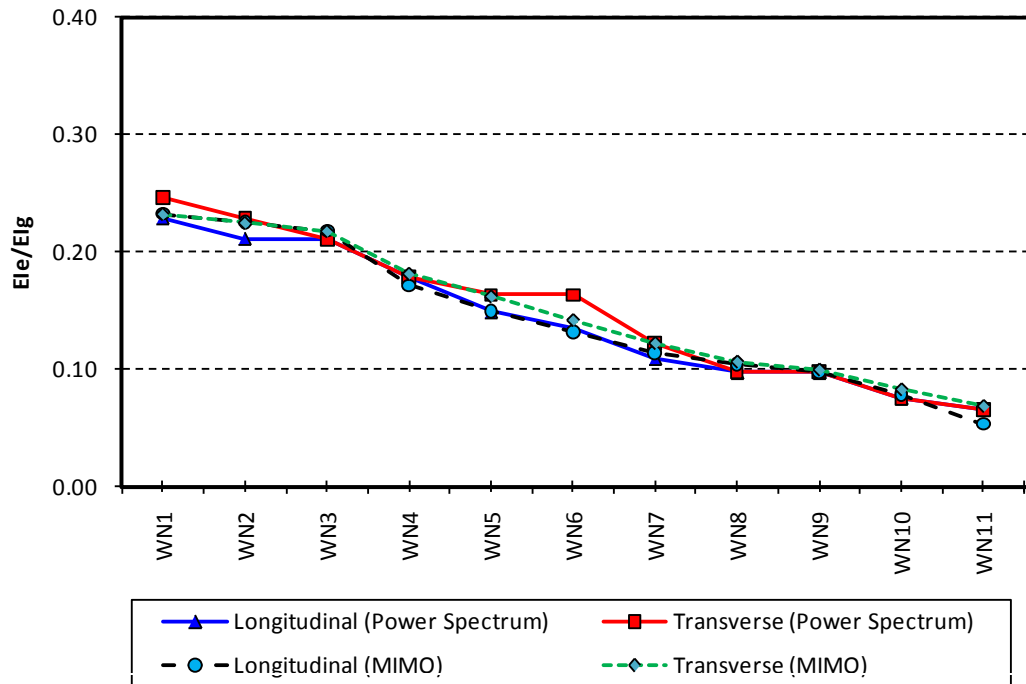


Figure 4-79 Variation in Effective Stiffness, Specimen C2



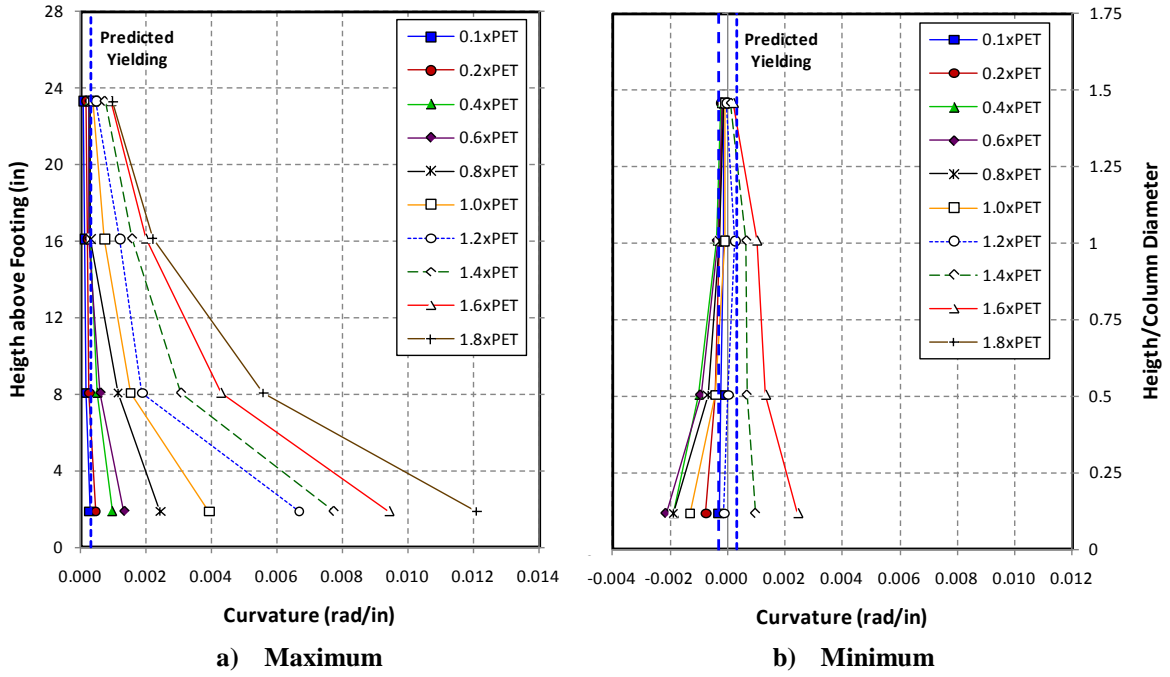


Figure 4-80 Curvature Profile in Longitudinal Direction, Specimen C1

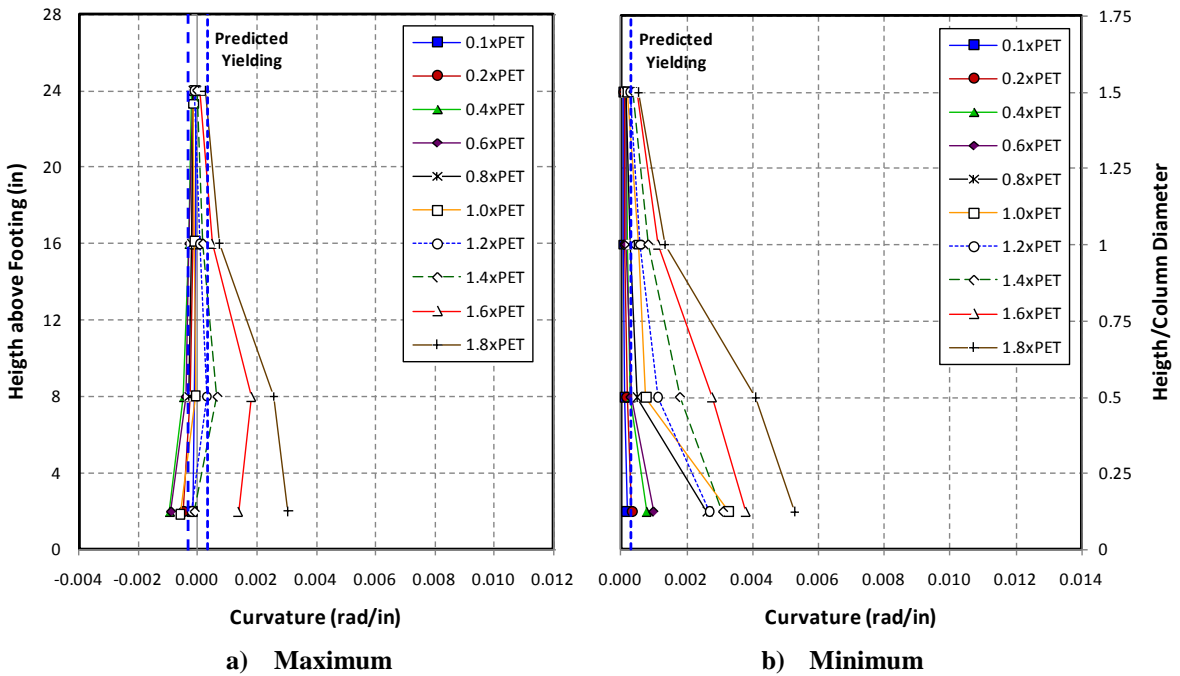


Figure 4-81 Curvature Profile in Transverse Direction, Specimen C1

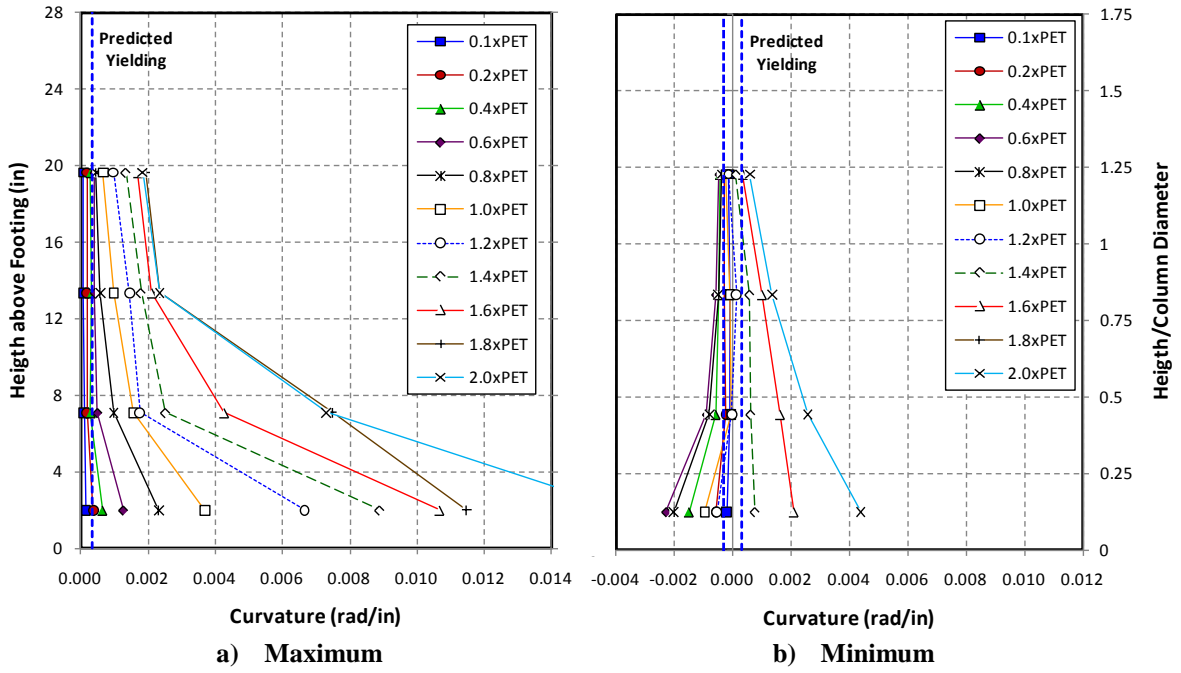


Figure 4-82 Curvature Profile in Longitudinal Direction, Specimen C2

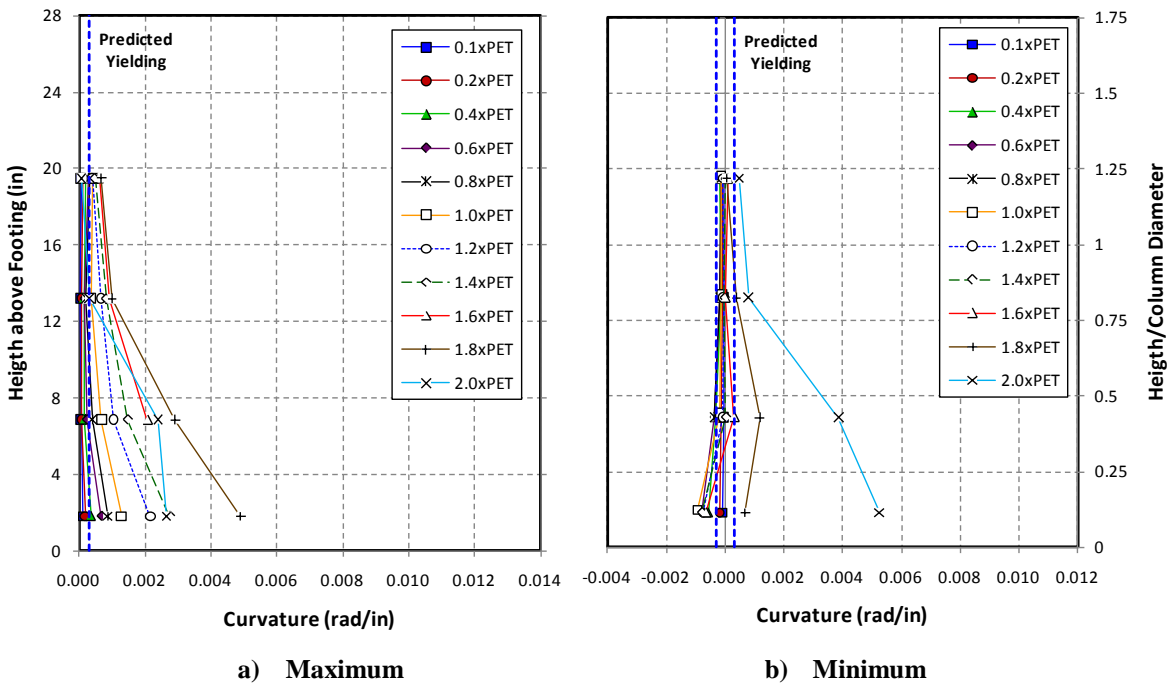
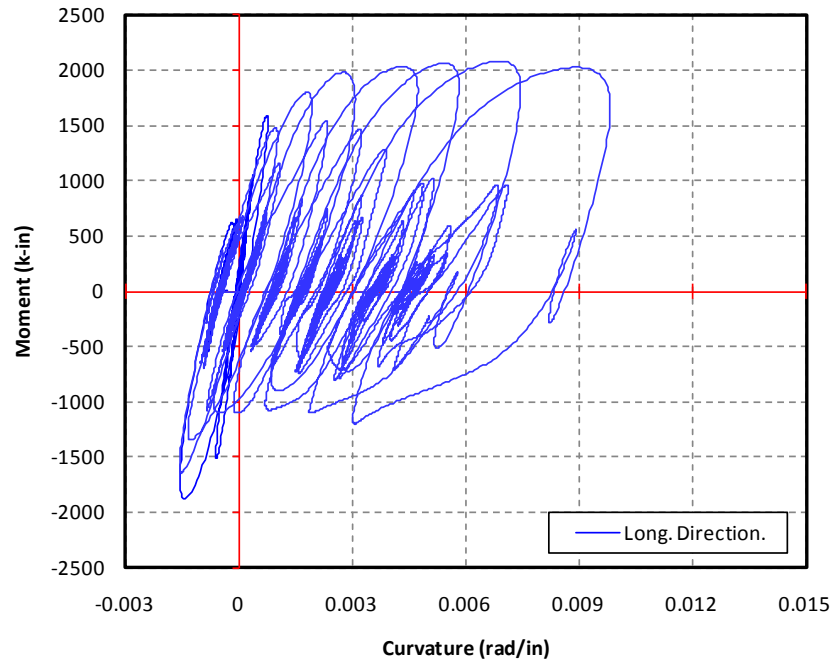
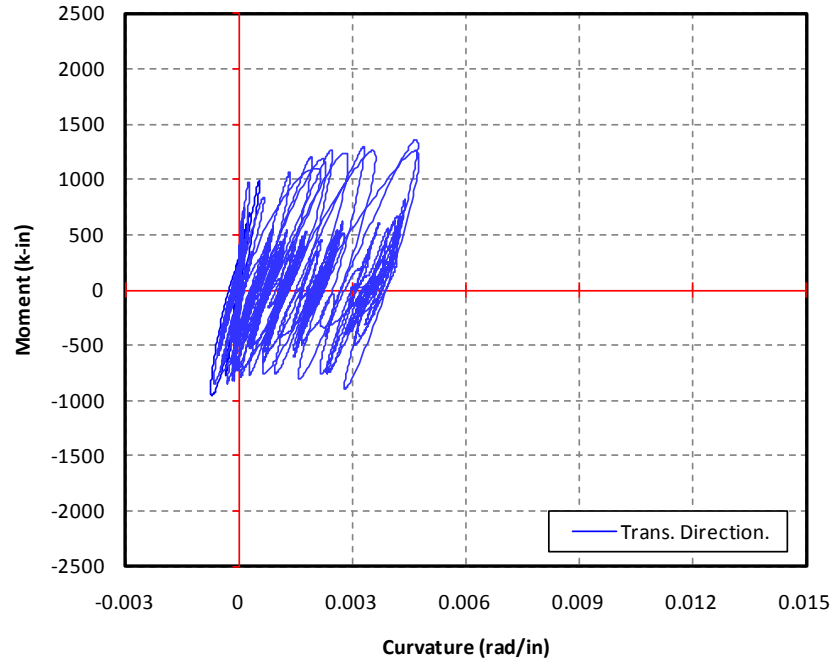


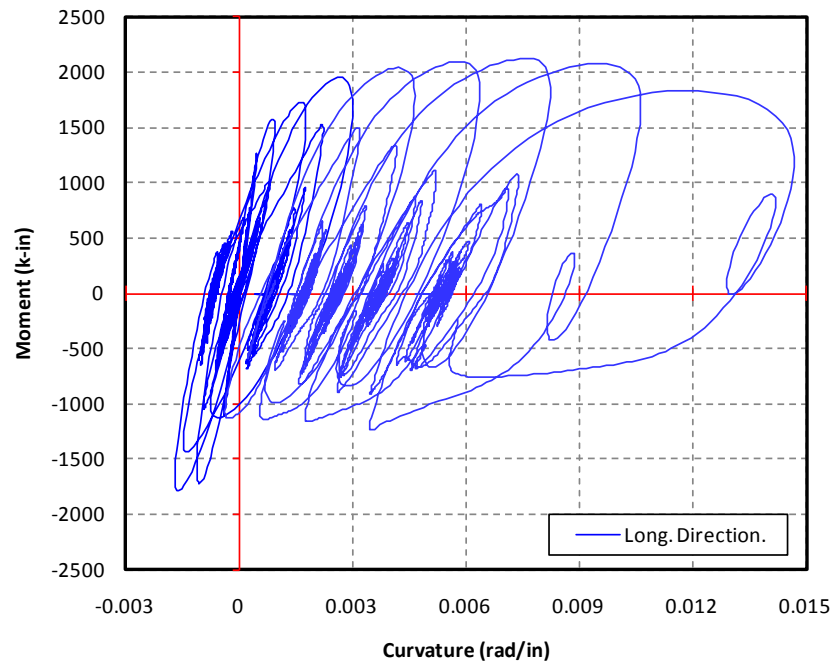
Figure 4-83 Curvature Profile in Transverse Direction, Specimen C2



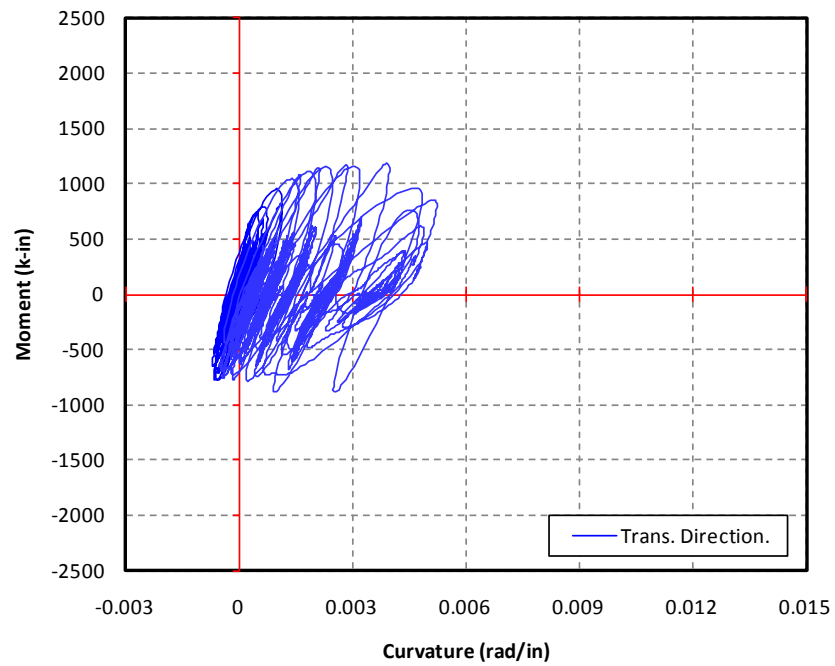
**Figure 4-84 Average Moment-Curvature Hysteresis for Specimen C1, Long. Direction**



**Figure 4-85 Average Moment-Curvature Hysteresis for Specimen C1, Trans. Direction**



**Figure 4-86 Average Moment-Curvature Hysteresis for Specimen C2, Long. Direction**



**Figure 4-87 Average Moment-Curvature Hysteresis for Specimen C2, Trans. Direction**

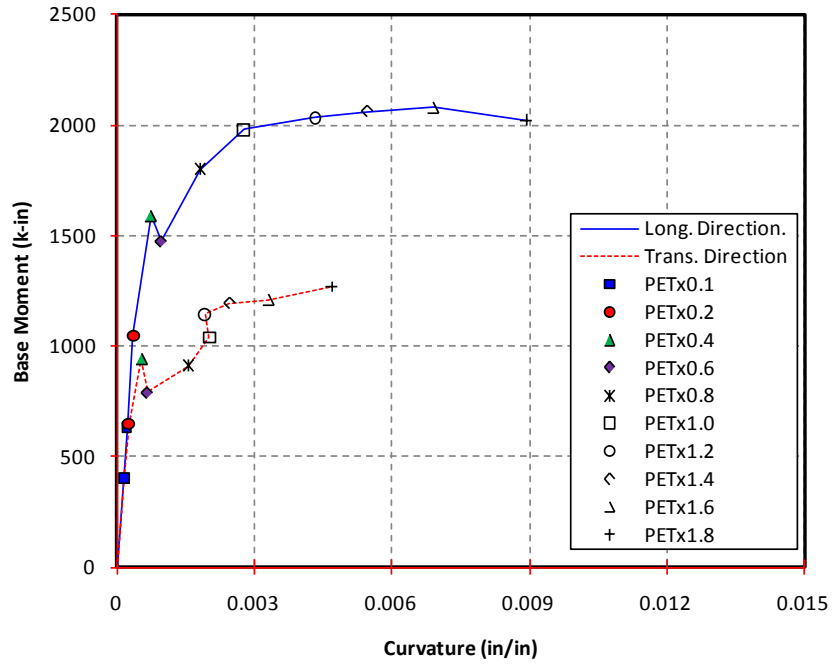


Figure 4-88 Average Moment-Curvature Envelope for Specimen C1, Long. Direction

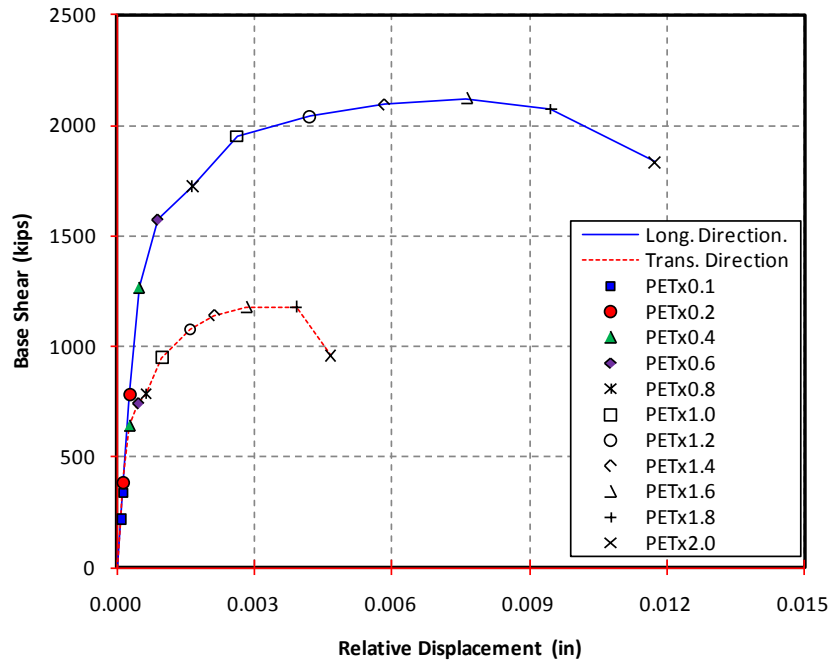
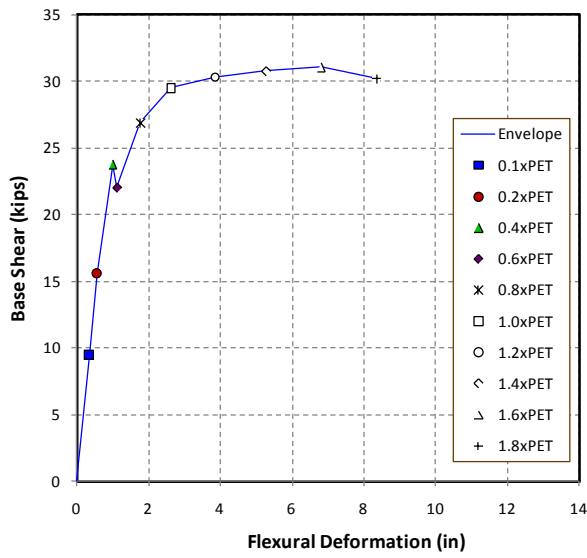
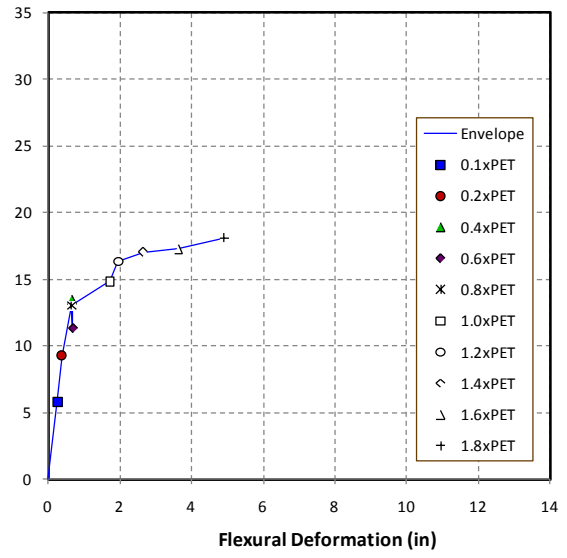


Figure 4-89 Average Moment-Curvature Envelope for Specimen C2, Long. Direction

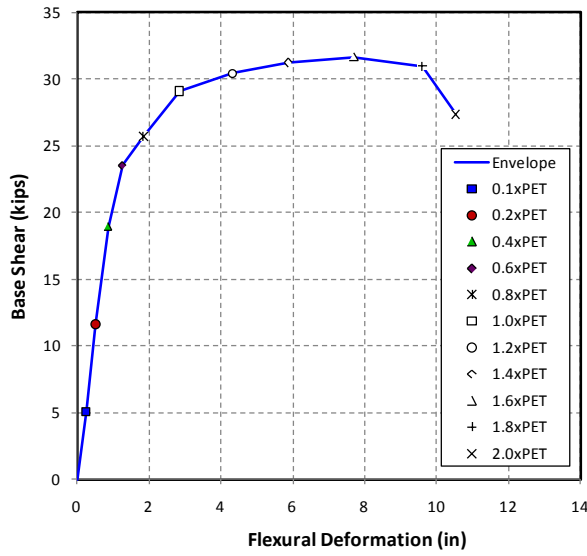


a) Longitudinal Direction

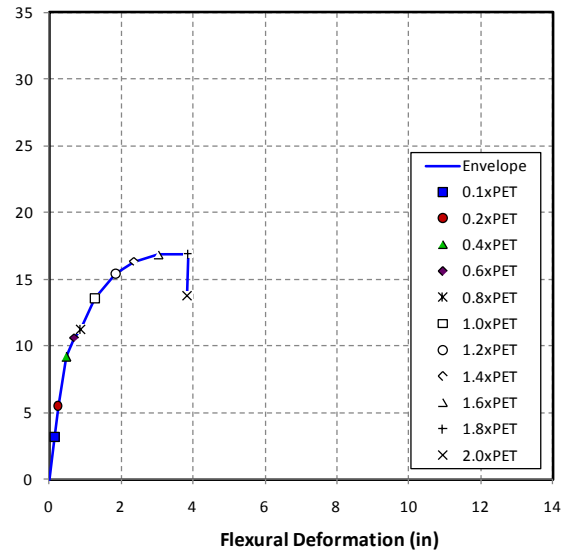


b) Transverse Direction

Figure 4-90 Flexural Deformation for Specimen C1

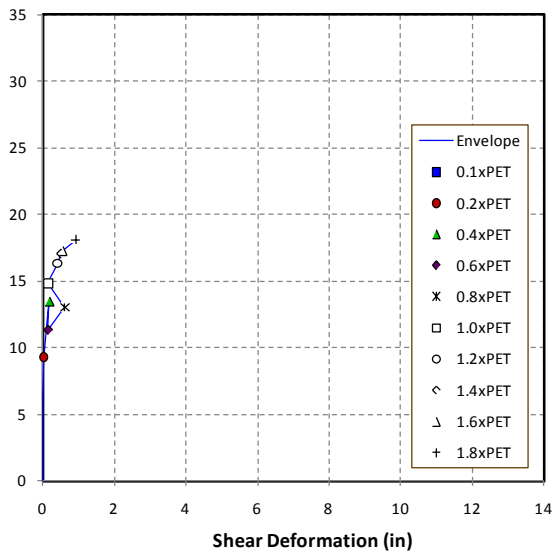


a) Longitudinal Direction

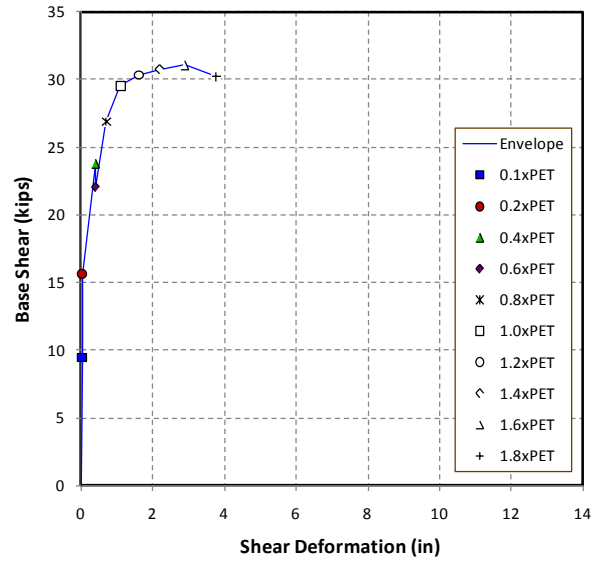


b) Transverse Direction

Figure 4-91 Flexural Deformation for Specimen C2

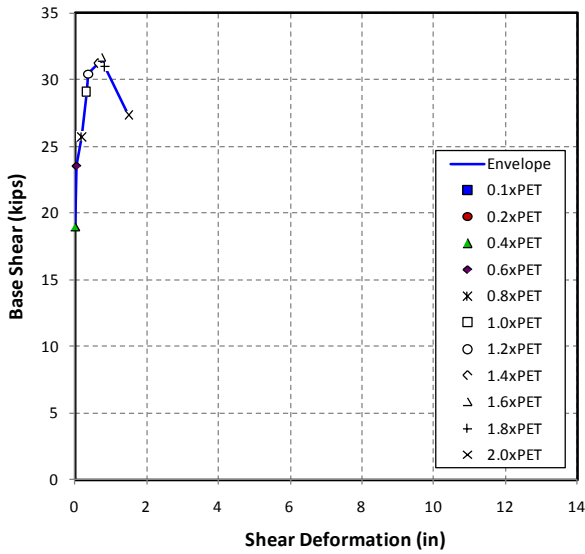


a) Longitudinal Direction

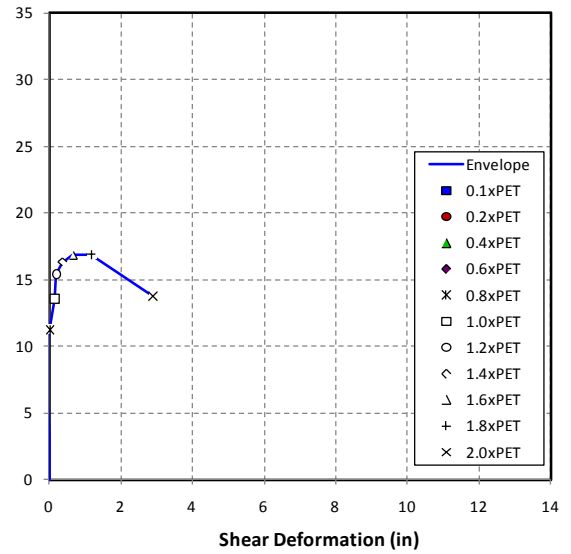


b) Transverse Direction

Figure 4-92 Shear Deformation for Specimen C1



a) Longitudinal Direction



b) Transverse Direction

Figure 4-93 Shear Deformation for Specimen C2

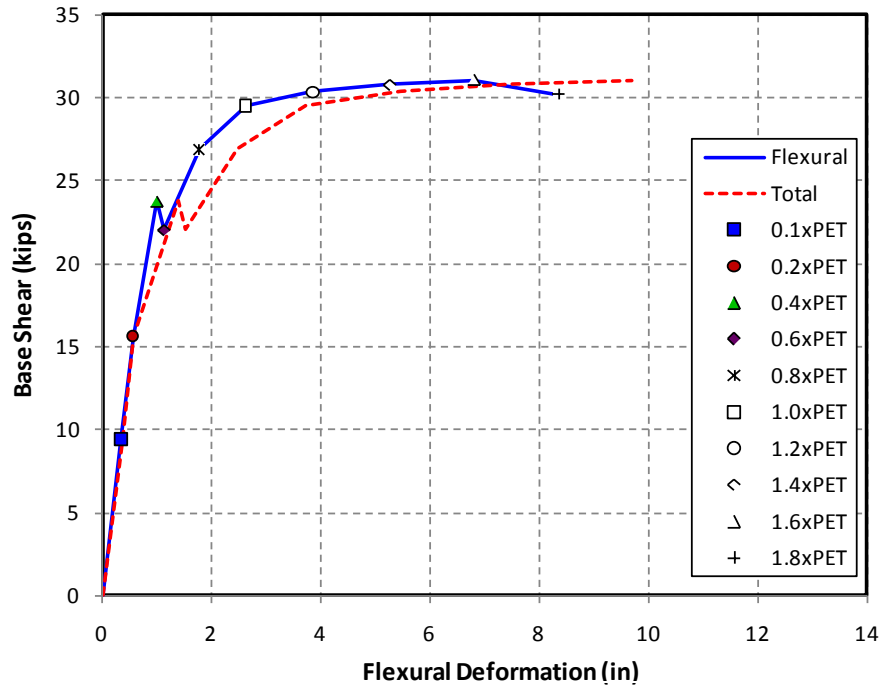


Figure 4-94 Contribution of Flexural Deformation to Total Deformation, Specimen C1

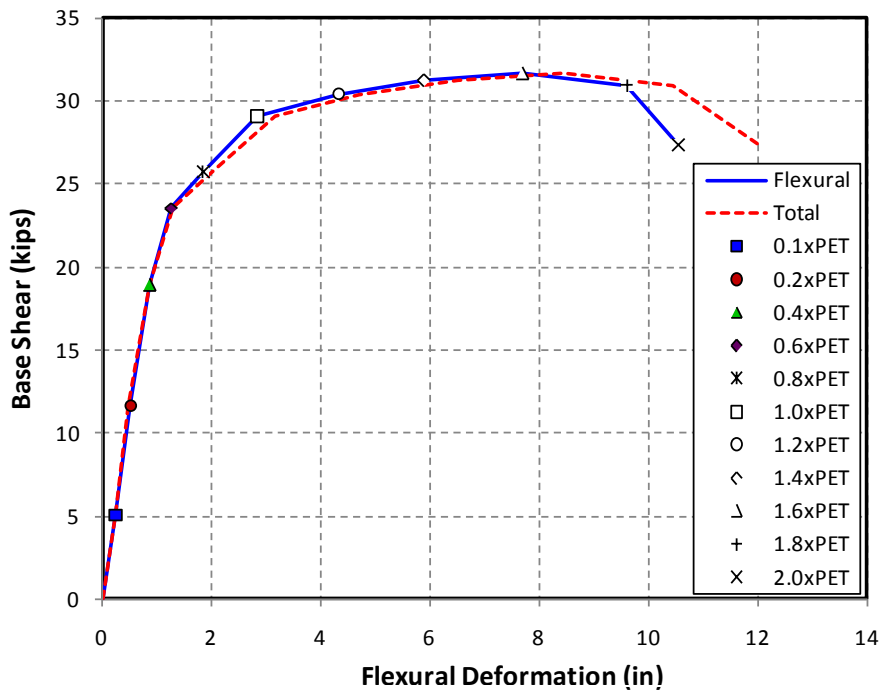


Figure 4-95 Contribution of Flexural Deformation to Total Deformation, Specimen C2



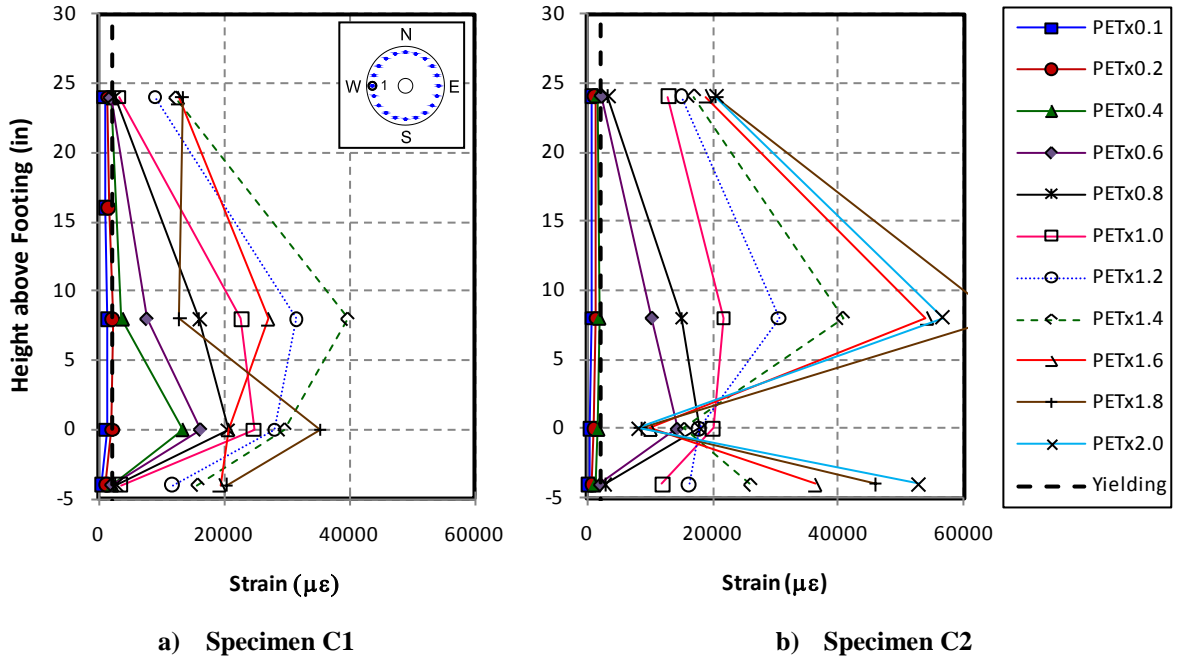


Figure 4-96 Longitudinal Bar Strain Distribution in Circular Specimens, Bar No.1

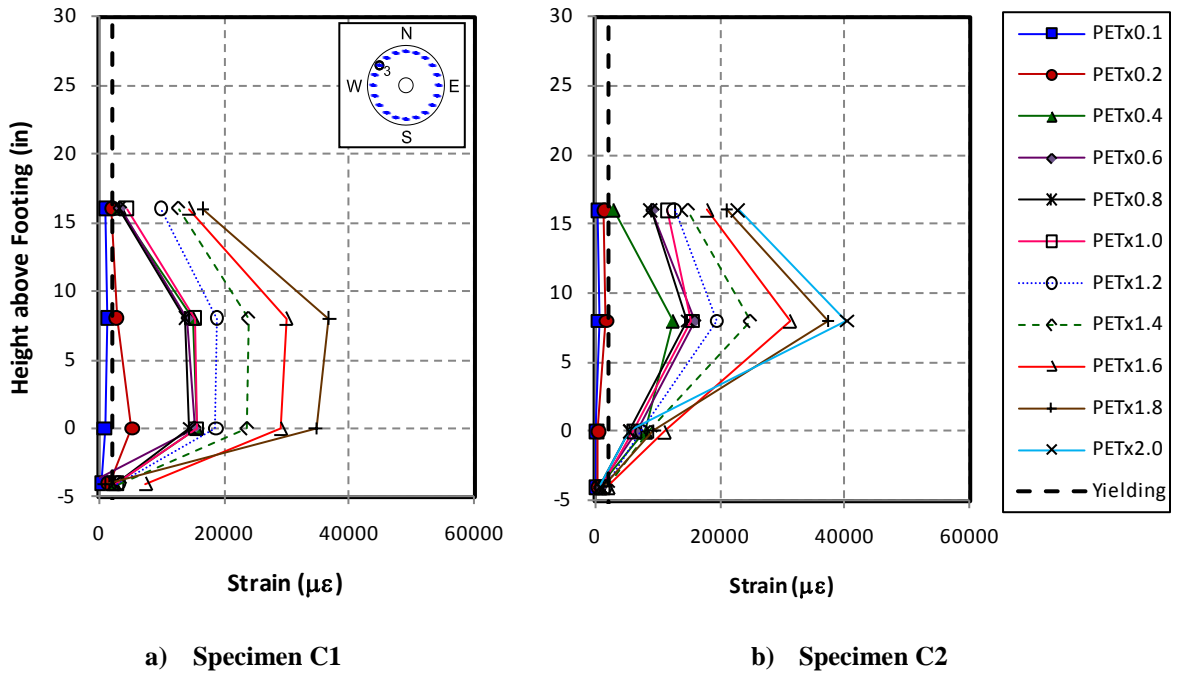


Figure 4-97 Longitudinal Bar Strain Distribution in Circular Specimens, Bar No.3

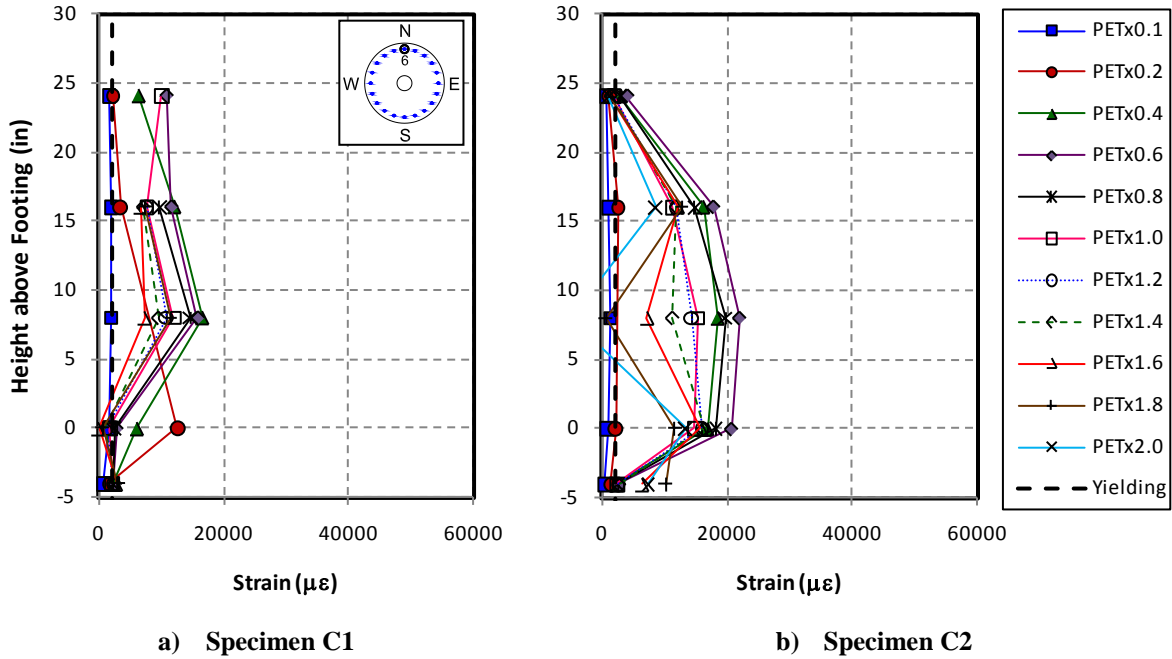


Figure 4-98 Longitudinal Bar Strain Distribution in Circular Specimens, Bar No.6

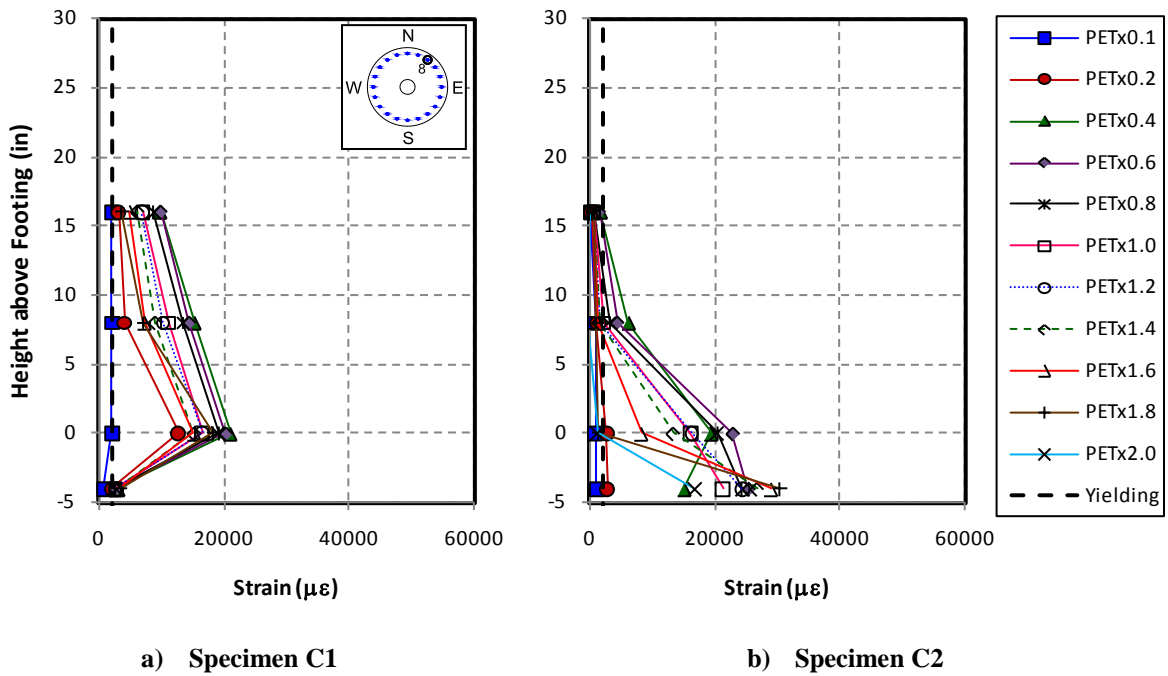


Figure 4-99 Longitudinal Bar Strain Distribution in Circular Specimens, Bar No.8

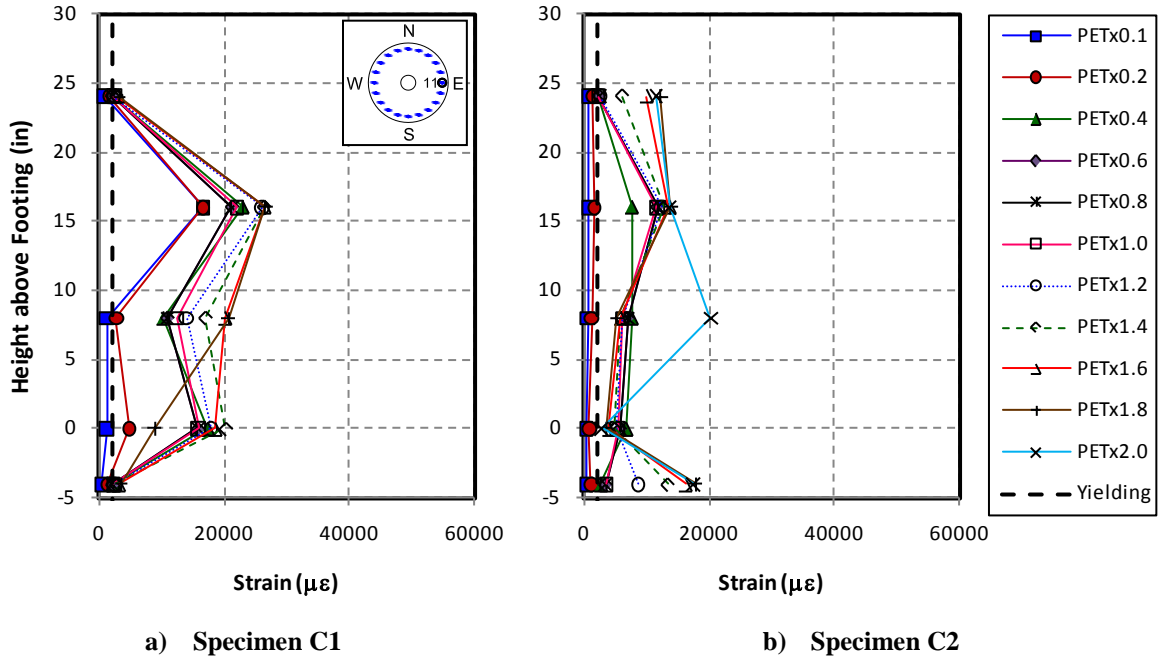


Figure 4-100 Longitudinal Bar Strain Distribution in Circular Specimens, Bar No.11

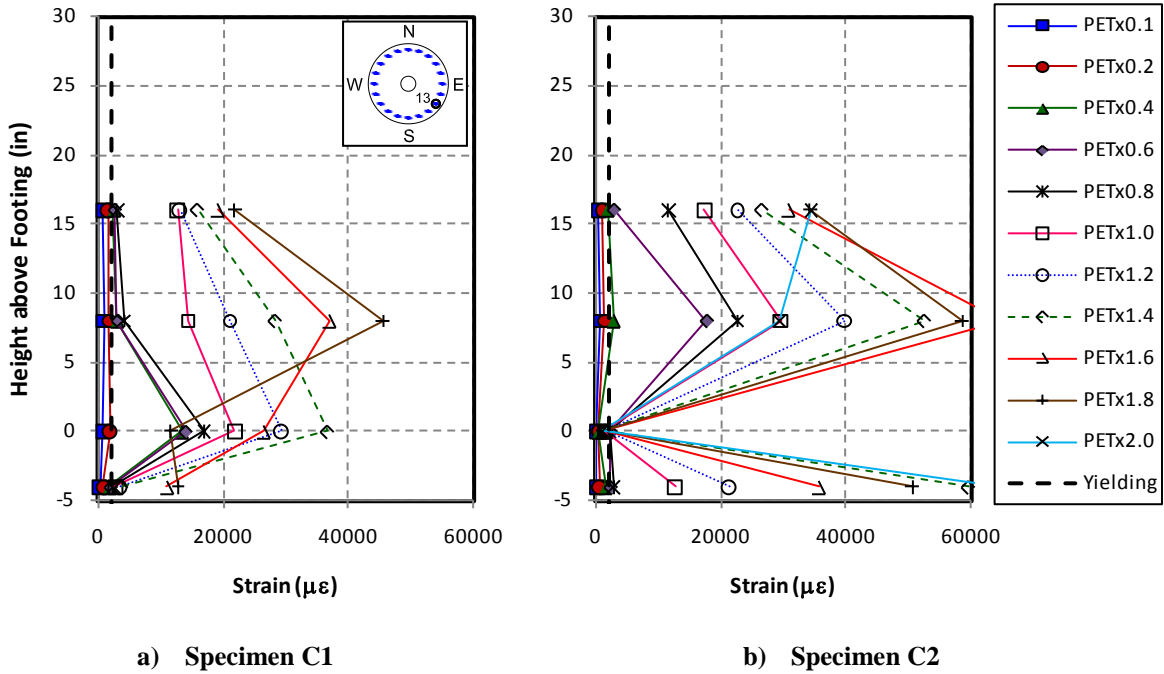


Figure 4-101 Longitudinal Bar Strain Distribution in Circular Specimens, Bar No.13

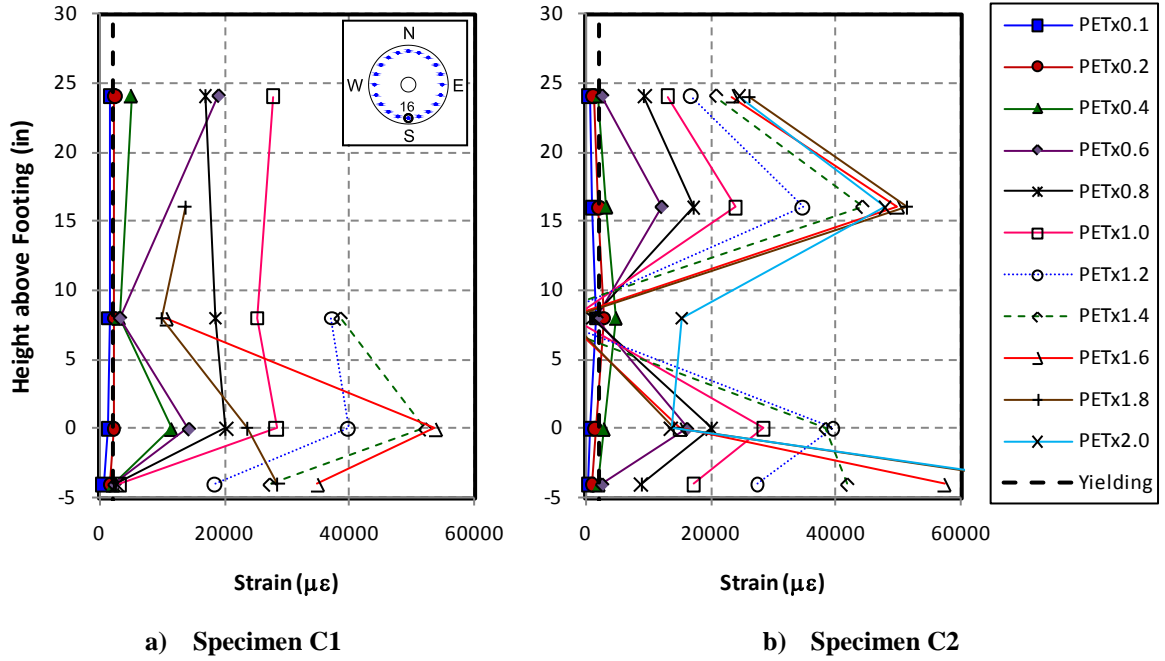


Figure 4-102 Longitudinal Bar Strain Distribution in Circular Specimens, Bar No.16

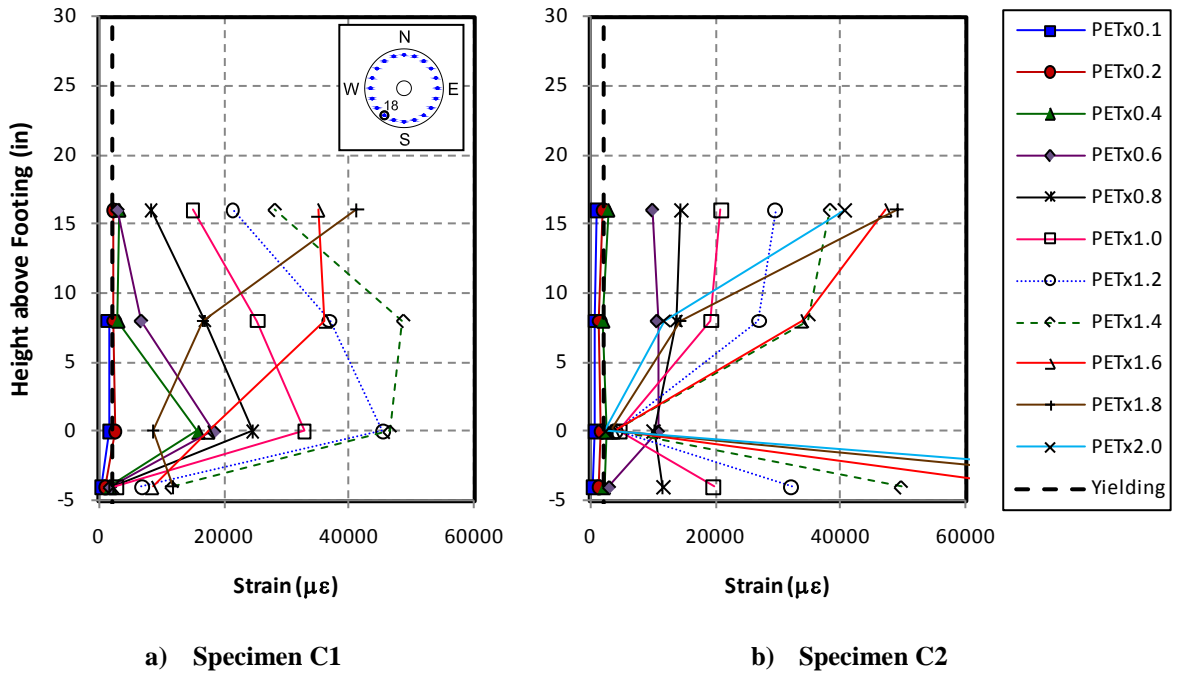


Figure 4-103 Longitudinal Bar Strain Distribution in Circular Specimens, Bar No.18

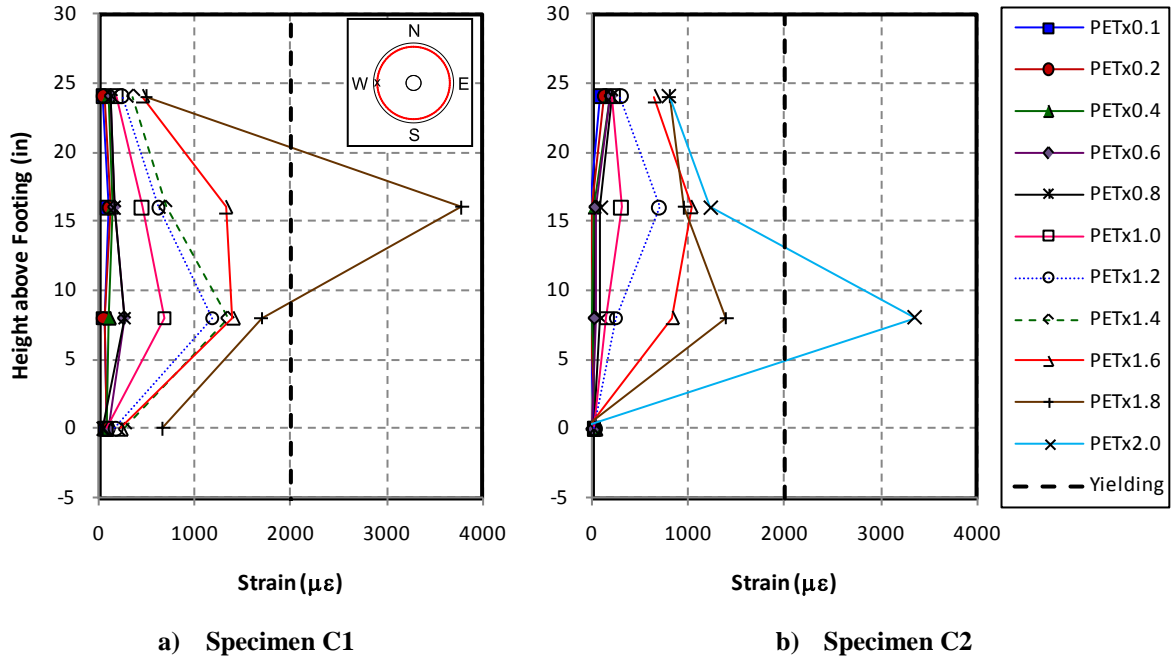


Figure 4-104 Spiral Strain Distribution in Circular Specimens, West Side

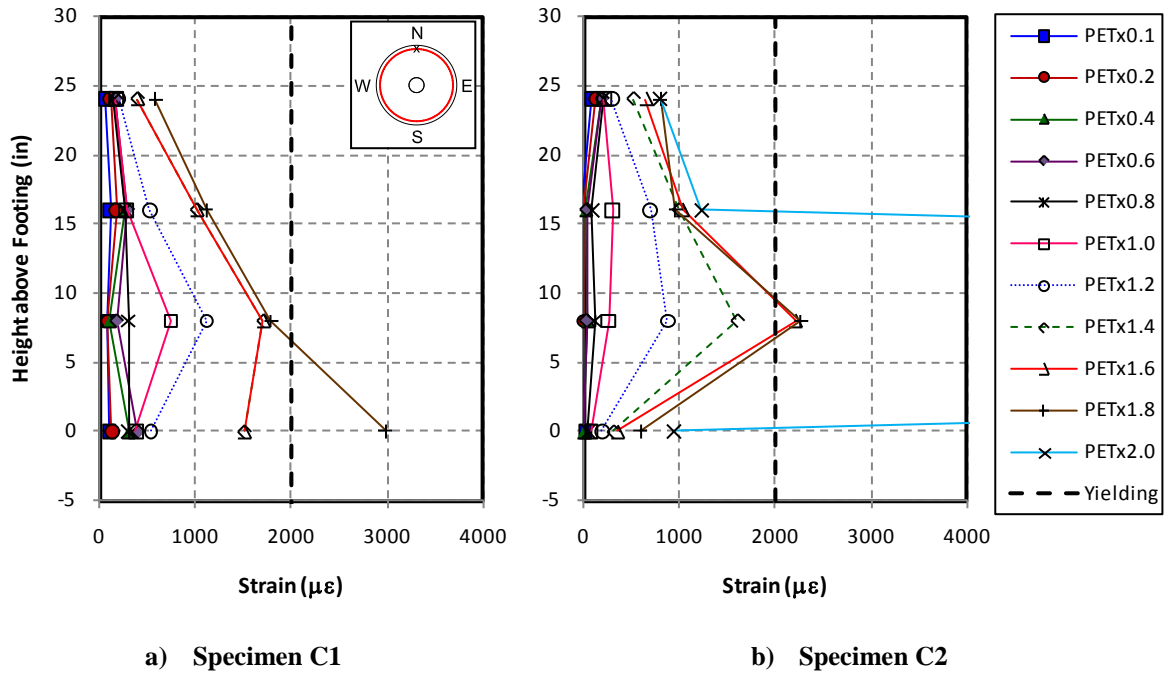


Figure 4-105 Spiral Strain Distribution in Circular Specimens, North Side

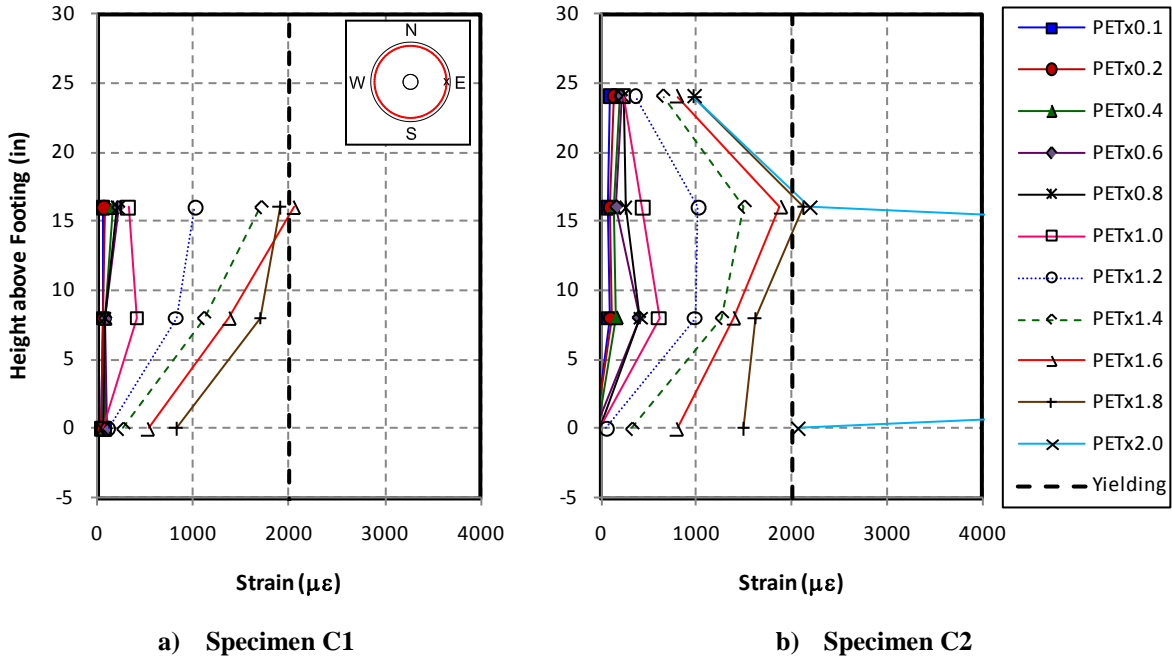


Figure 4-106 Spiral Strain Distribution in Circular Specimens, East Side

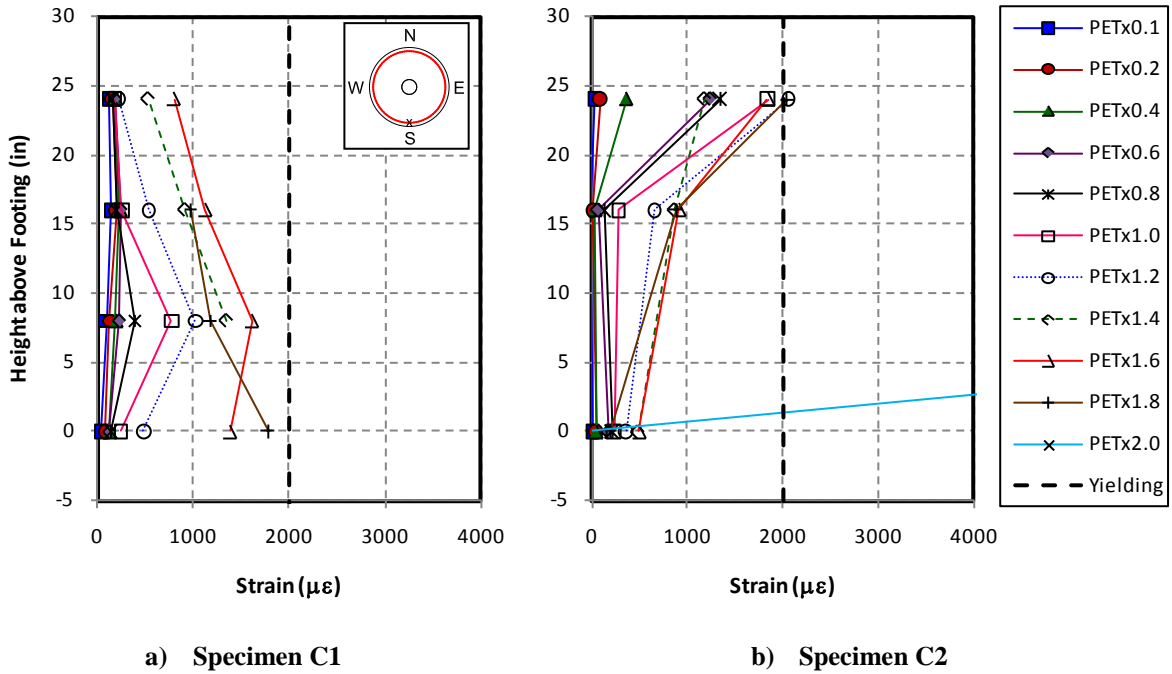
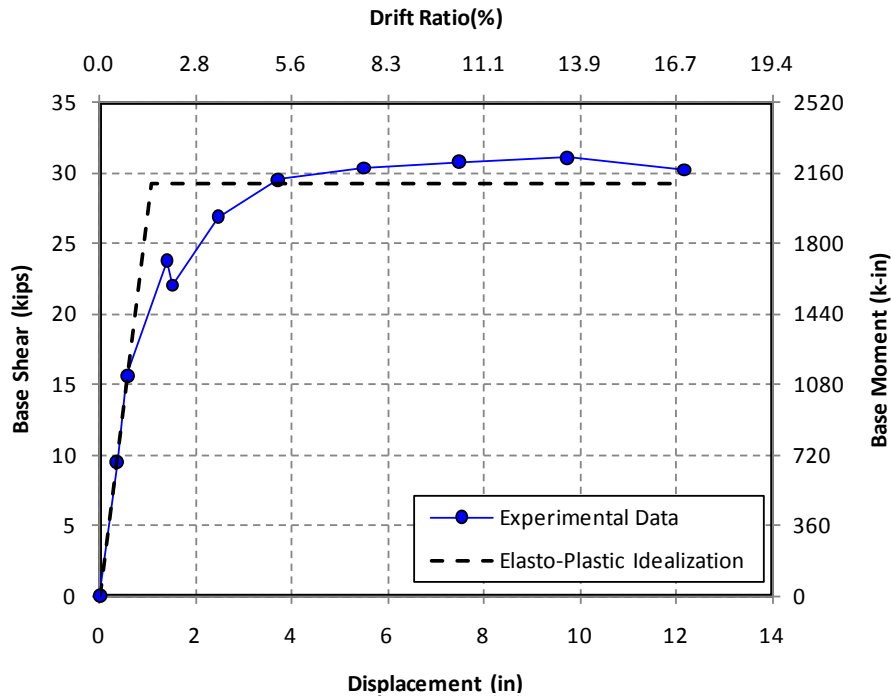
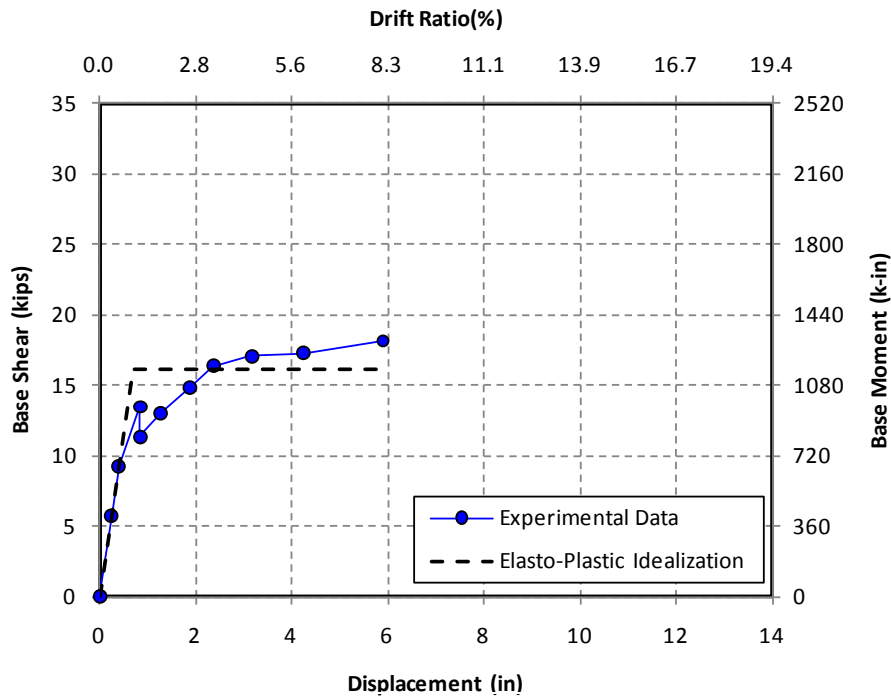


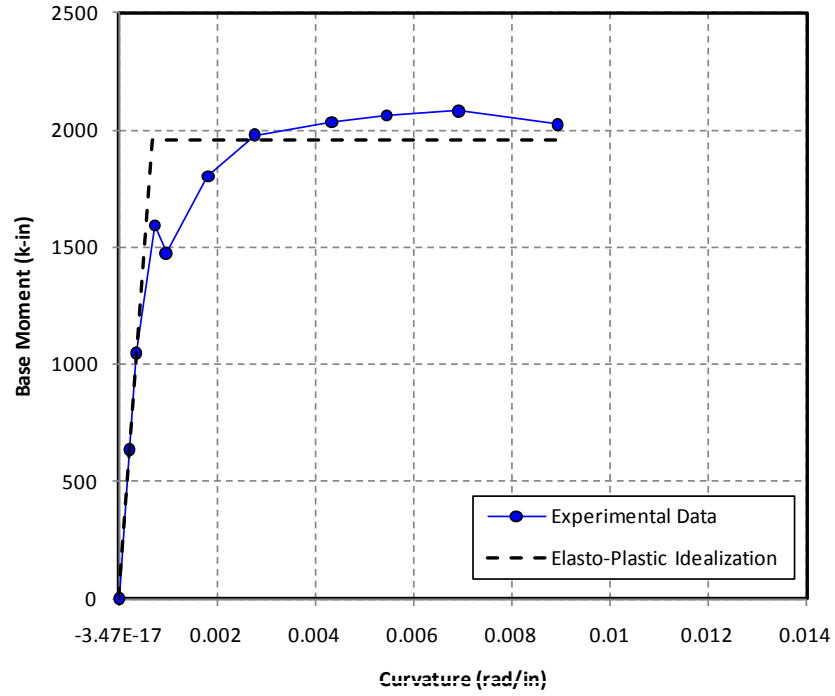
Figure 4-107 Spiral Strain Distribution in Circular Specimens, South Side



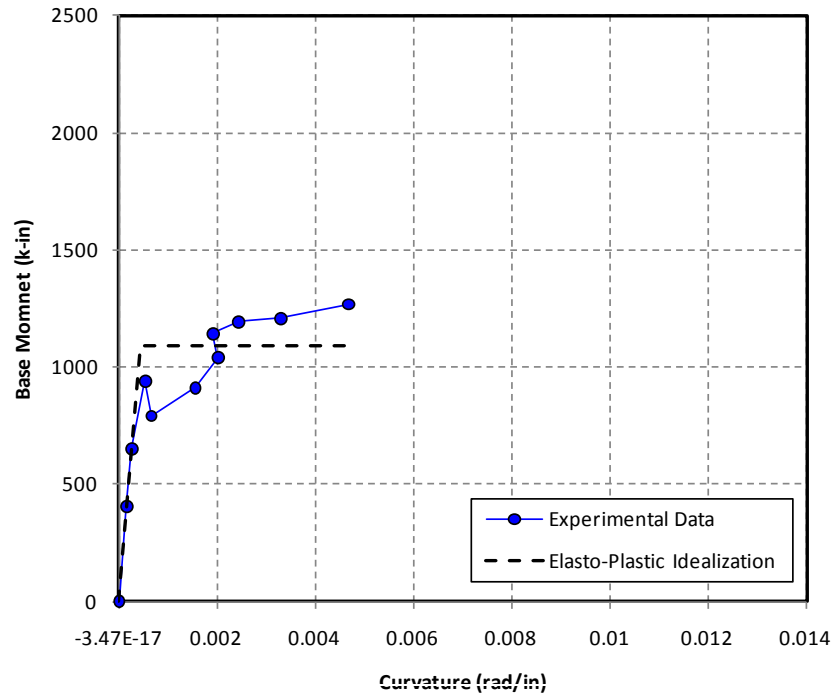
**Figure 4-108 Elasto-Plastic Idealization for Force-Displacement, Specimen C1 (Longitudinal)**



**Figure 4-109 Elasto-Plastic Idealization for Force-Displacement, Specimen C1 (Transverse)**



**Figure 4-110 Elasto-Plastic Idealization for Moment-Curvature, Specimen C1 (Longitudinal)**



**Figure 4-111 Elasto-Plastic Idealization for Moment-Curvature, Specimen C1 (Transverse)**



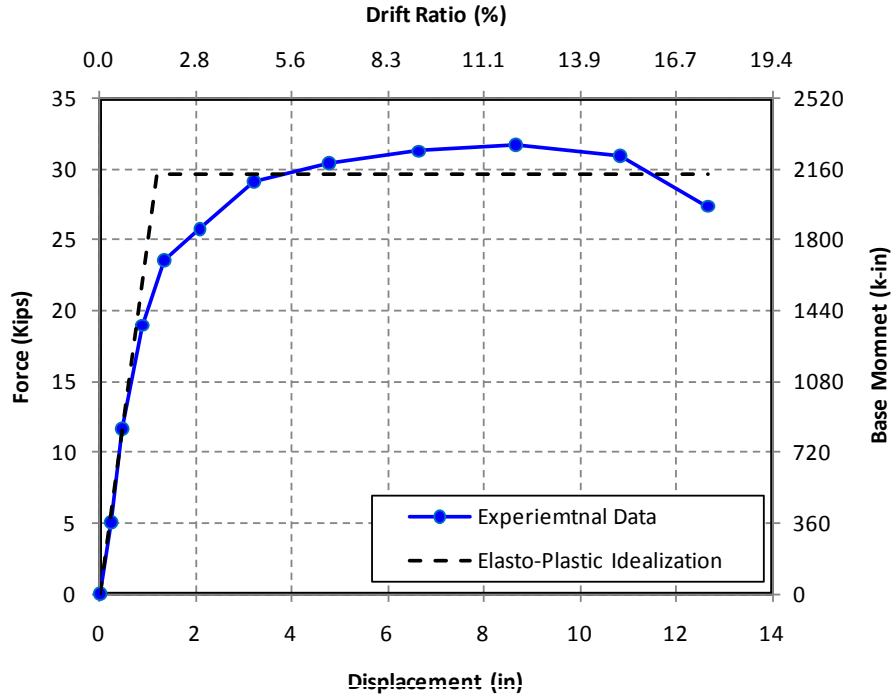


Figure 4-112 Elasto-Plastic Idealization for Force-Displacement, Specimen C2 (Longitudinal)

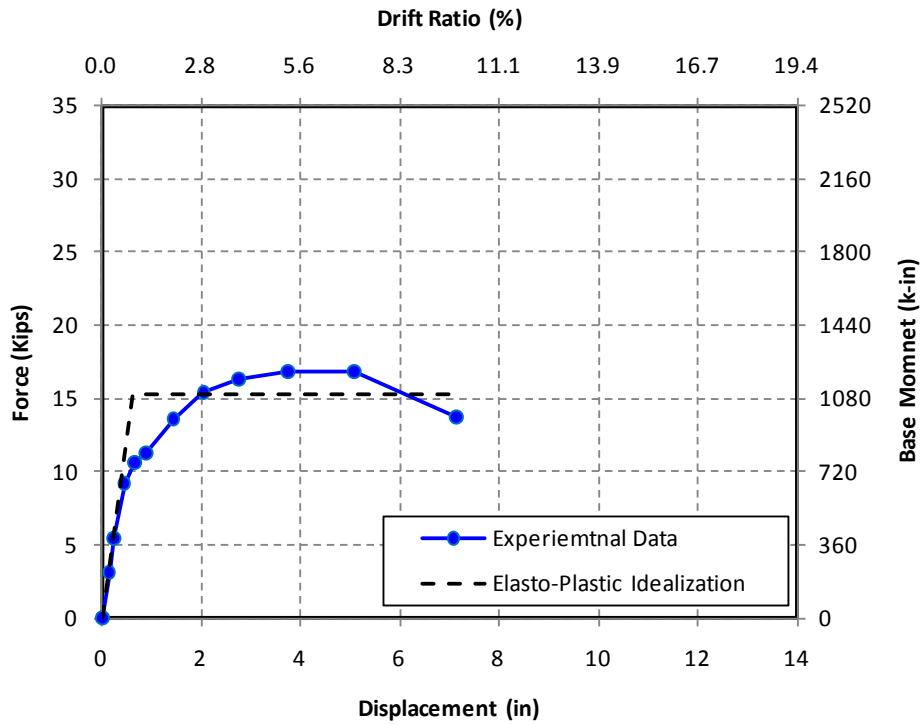
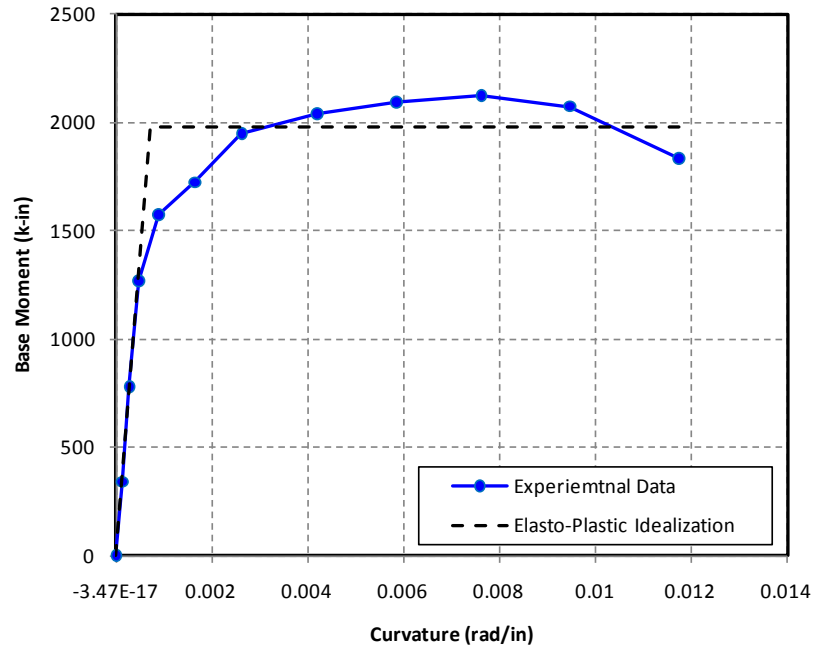
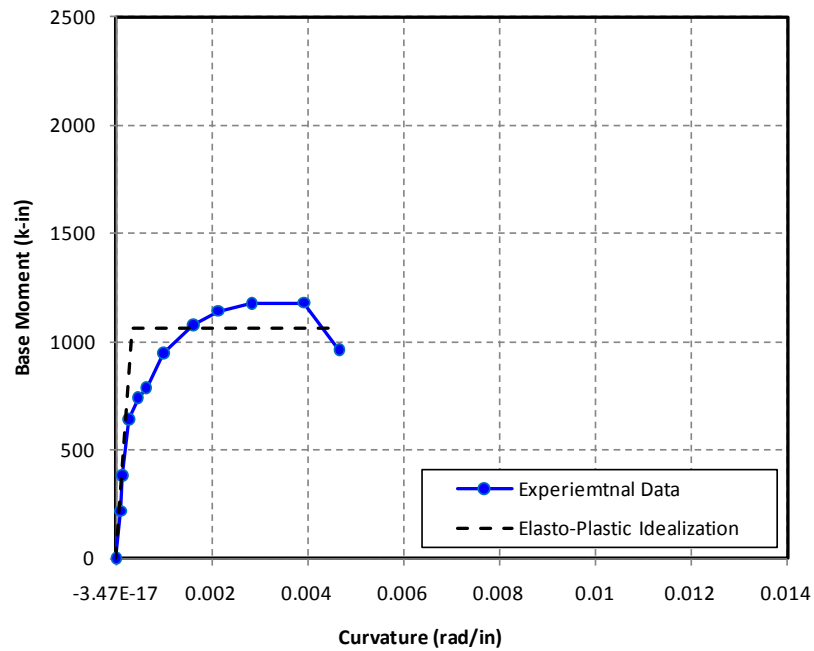


Figure 4-113 Elasto-Plastic Idealization for Force-Displacement, Specimen C2 (Transverse)



**Figure 4- 114 Elasto-Plastic Idealization for Moment-Curvature, Specimen C2 (Longitudinal)**



**Figure 4-115 Elasto-Plastic Idealization for Moment-Curvature, Specimen C2 (Transverse)**

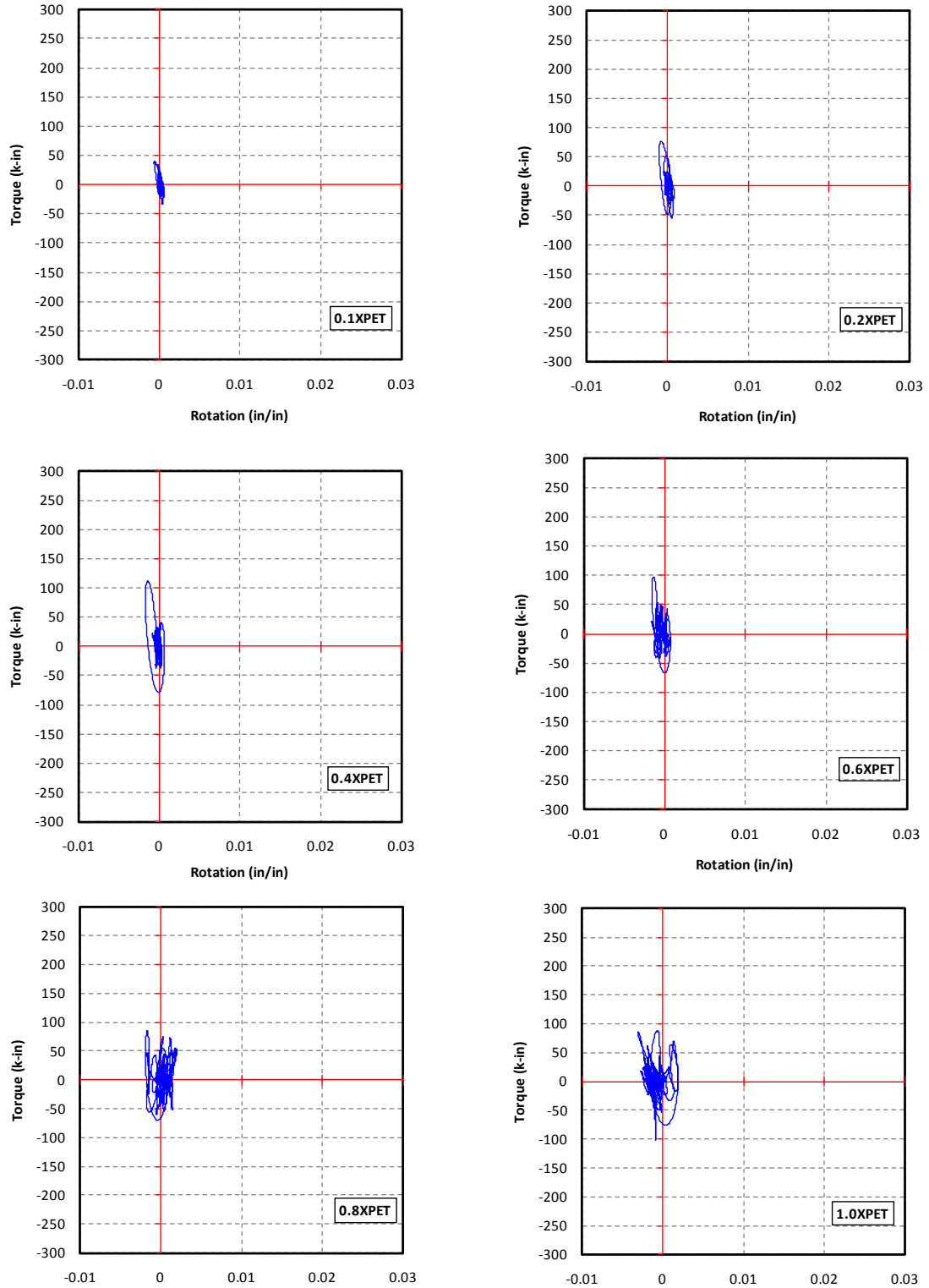


Figure 4-116 Torque-Rotation Hysteresis, Specimen C1

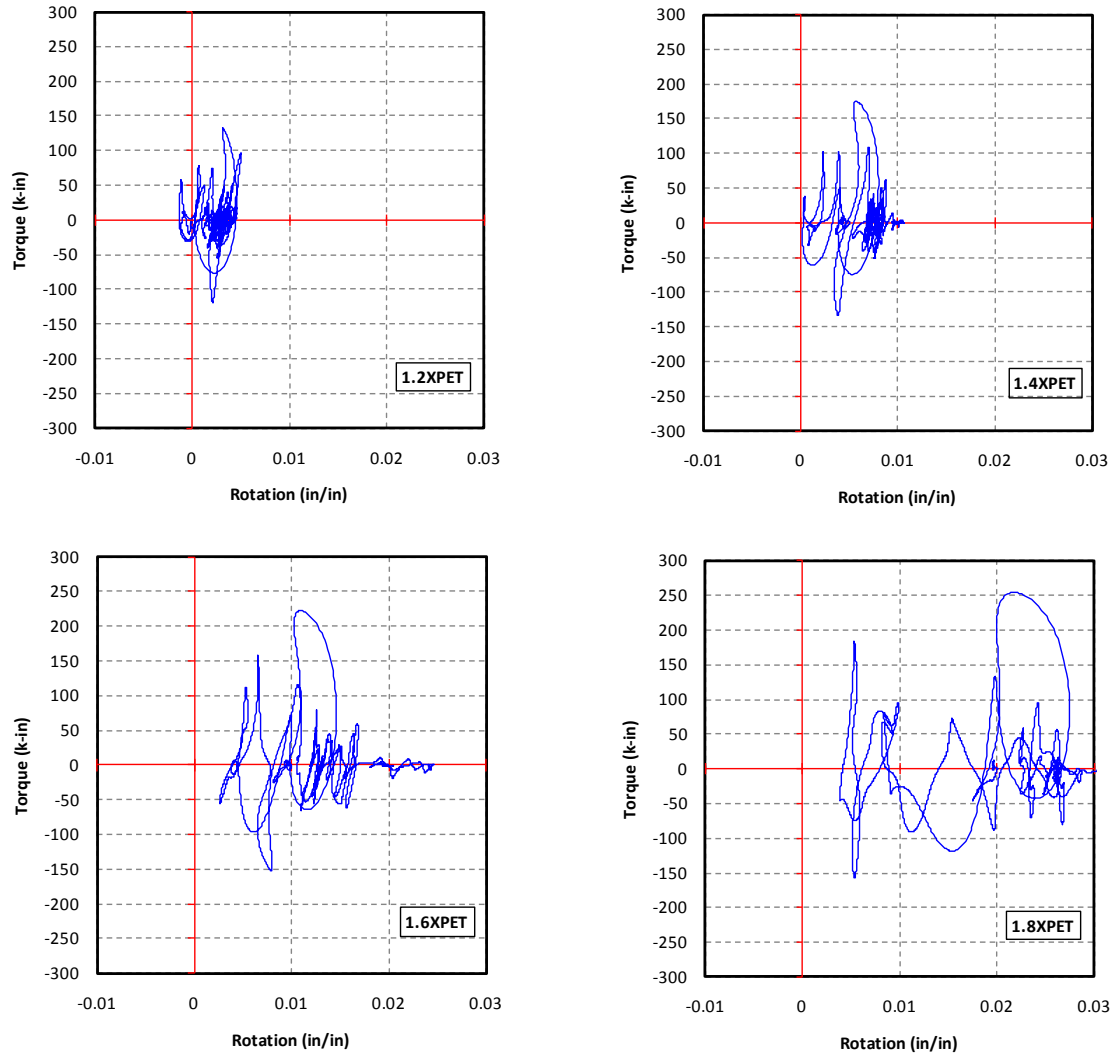


Figure 4-117 Torque-Rotation Hysteresis, Specimen C1

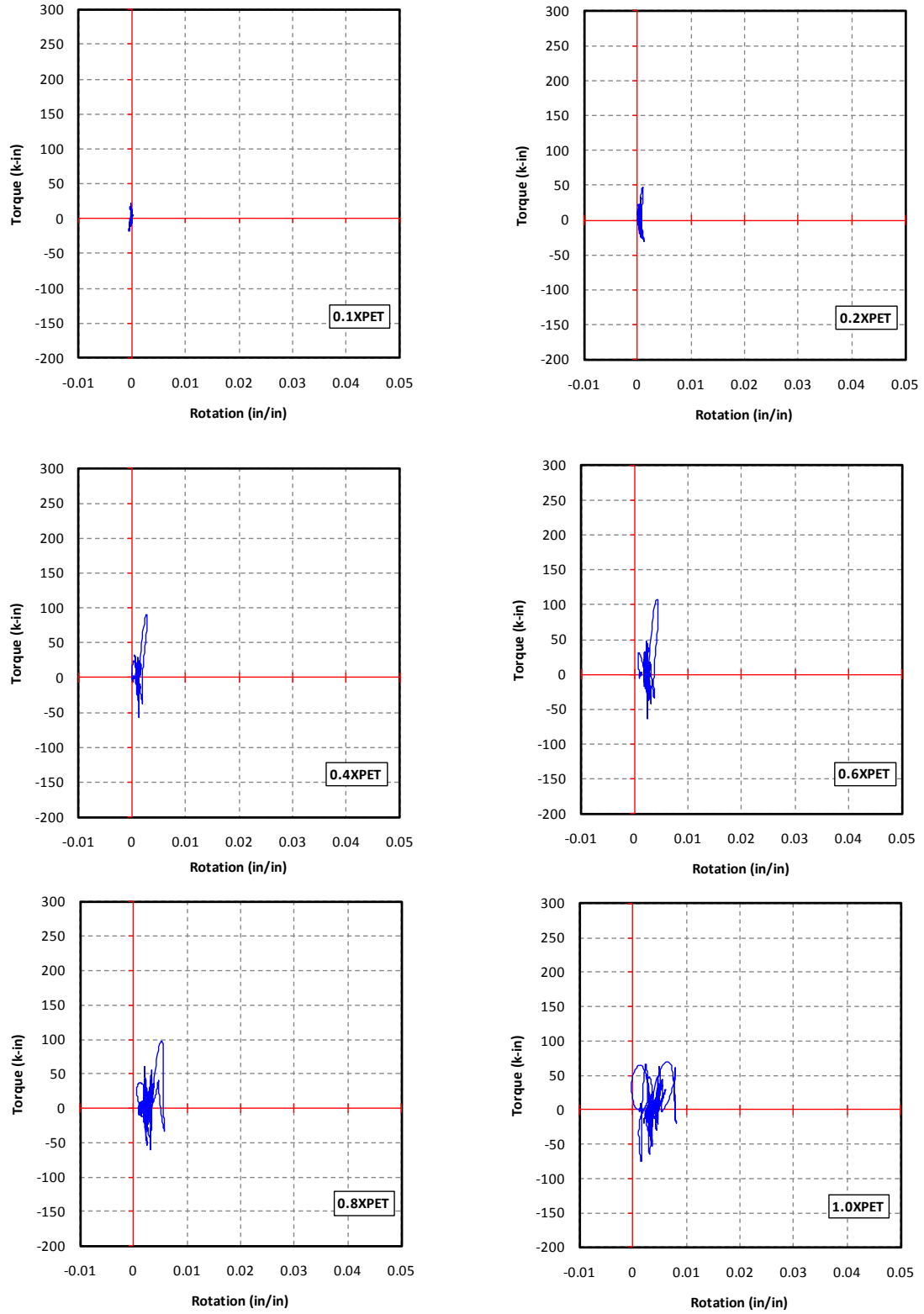


Figure 4-118 Torque-Rotation Hysteresis, Specimen C2

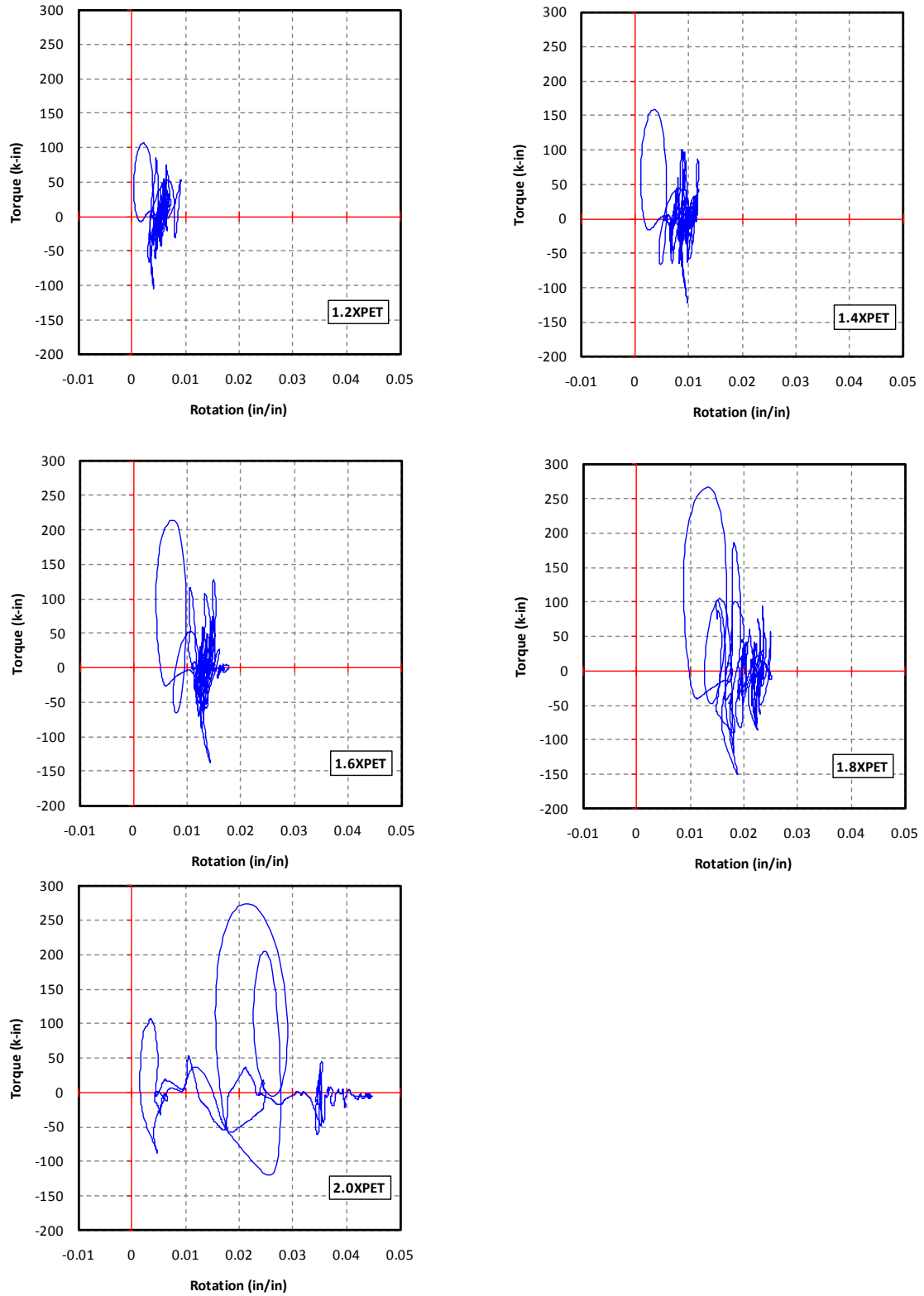
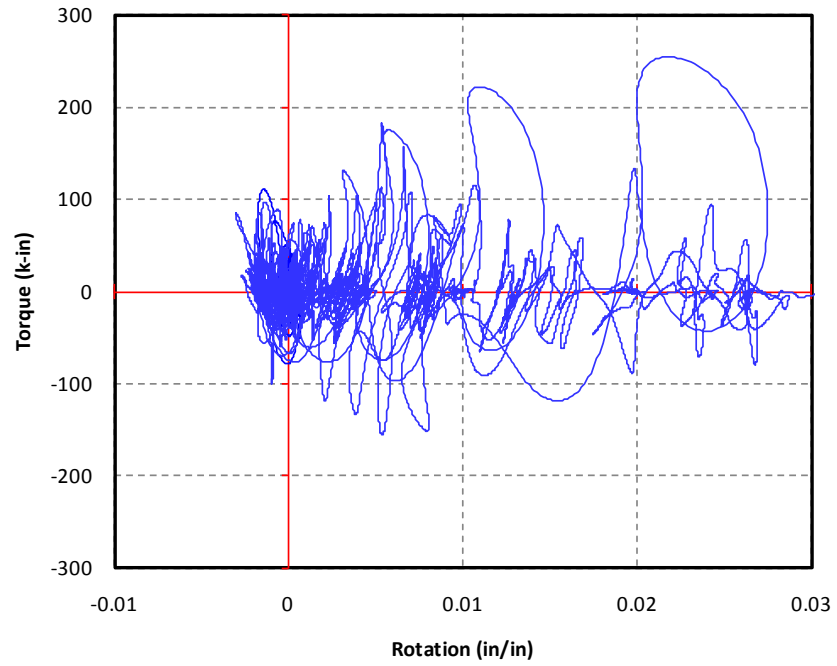
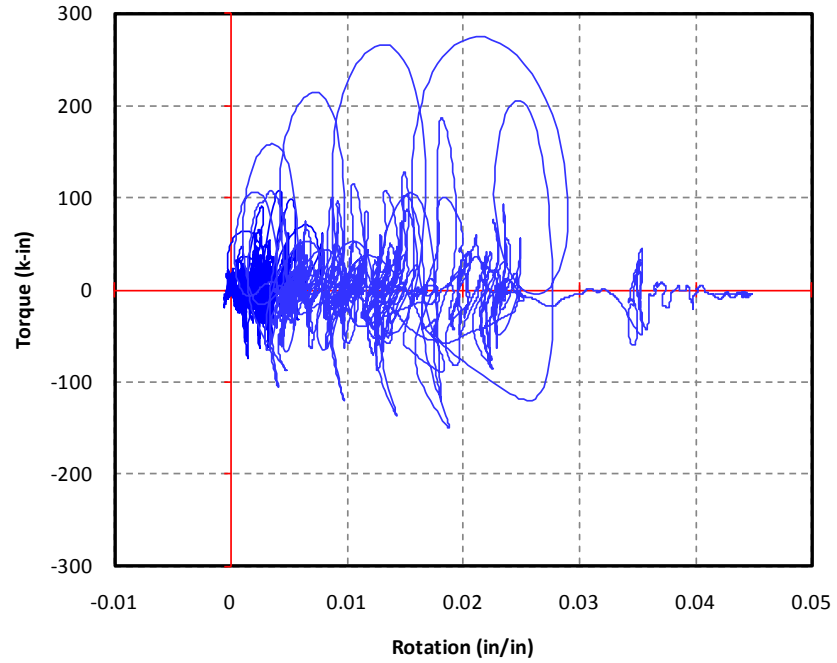


Figure 4-119 Torque-Rotation Hysteresis, Specimen C2



**Figure 4-120 Cumulative Torque-Rotation Hysteresis, Specimen C1**



**Figure 4-121 Cumulative Torque-Rotation Hysteresis, Specimen C2**

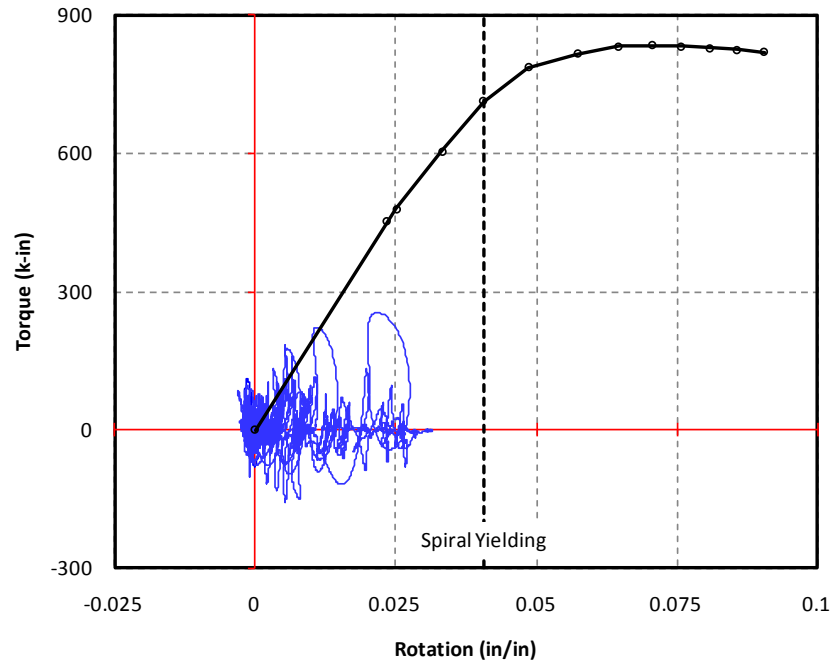


Figure 4-122 Torque-Rotation Hysteresis and Capacity, Specimen C1

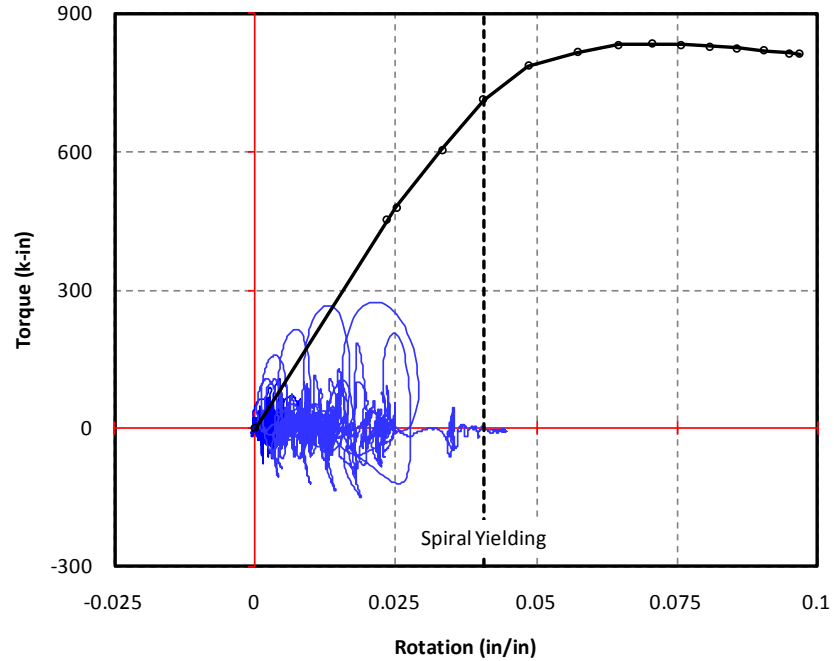


Figure 4-123 Torque-Rotation Hysteresis and Capacity, Specimen C2



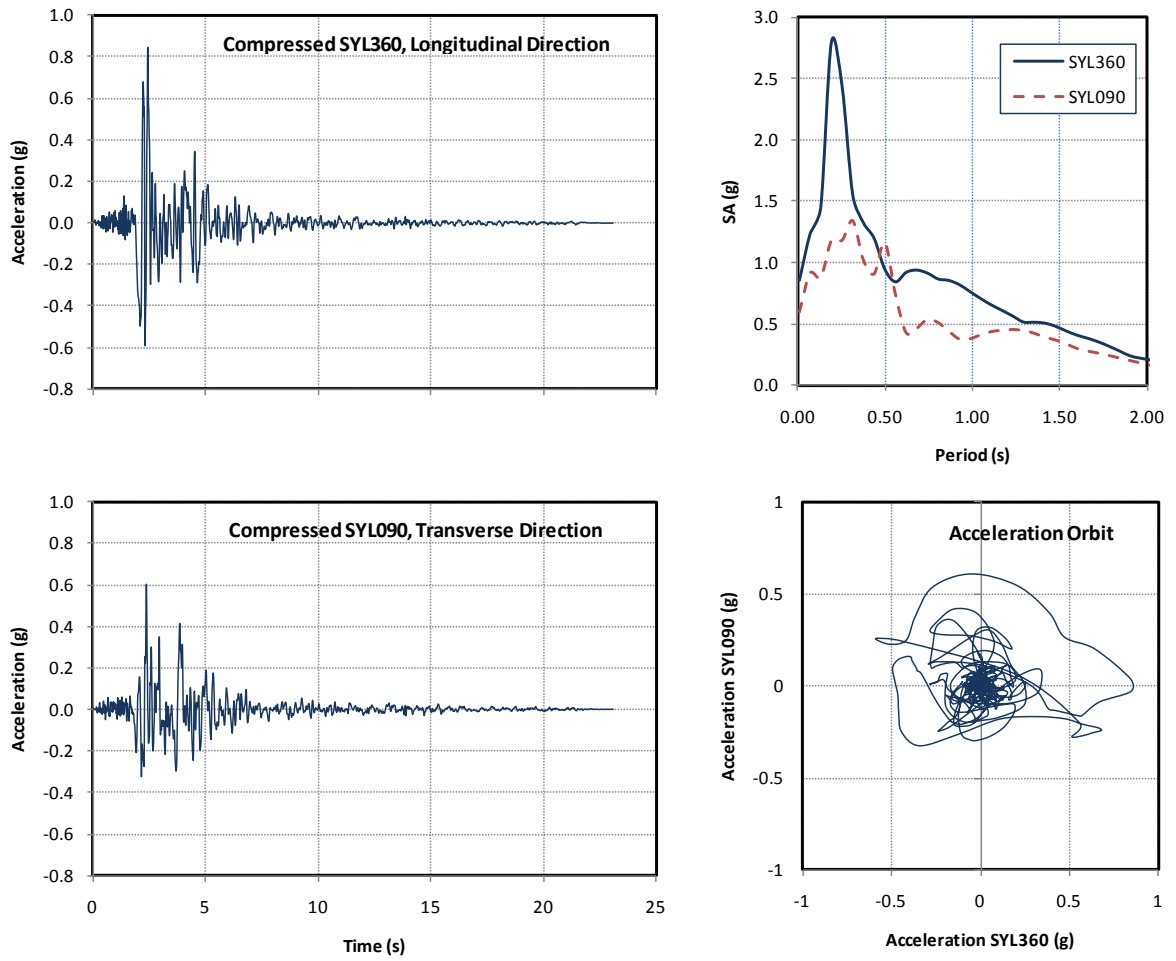


Figure 5-1 Compressed Sylmar Earthquake (Time History, Spectrum and Orbit)

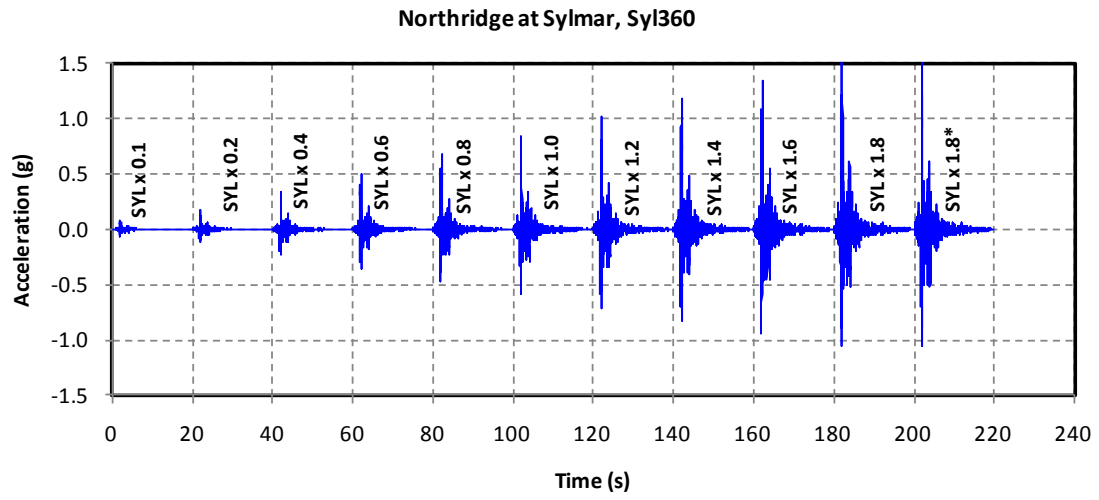


Figure 5-2 Time History Acceleration used for Specimens I2 (Long. Direction)

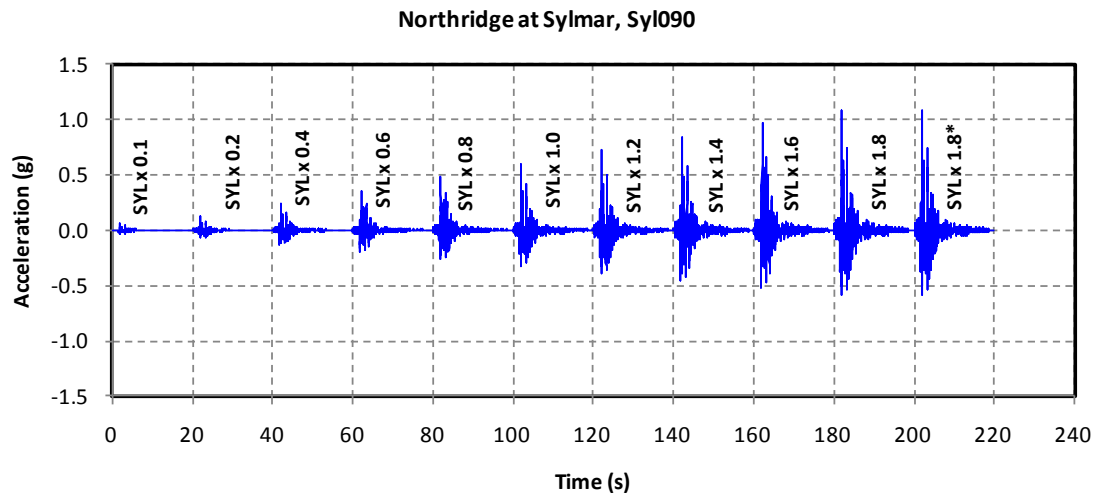
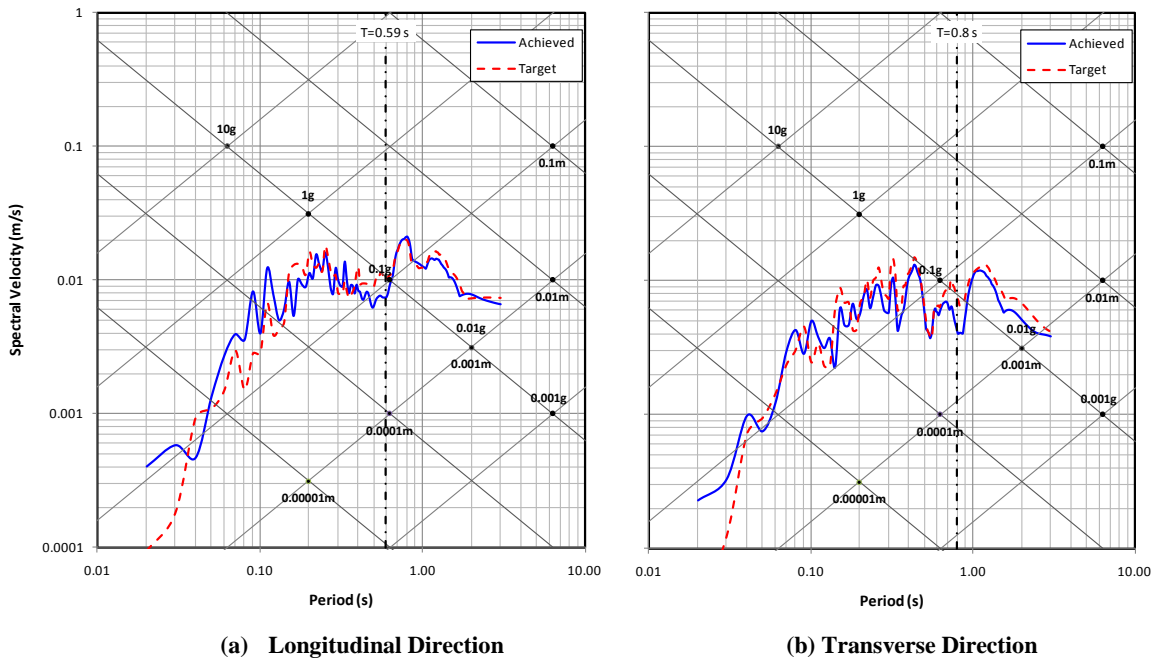
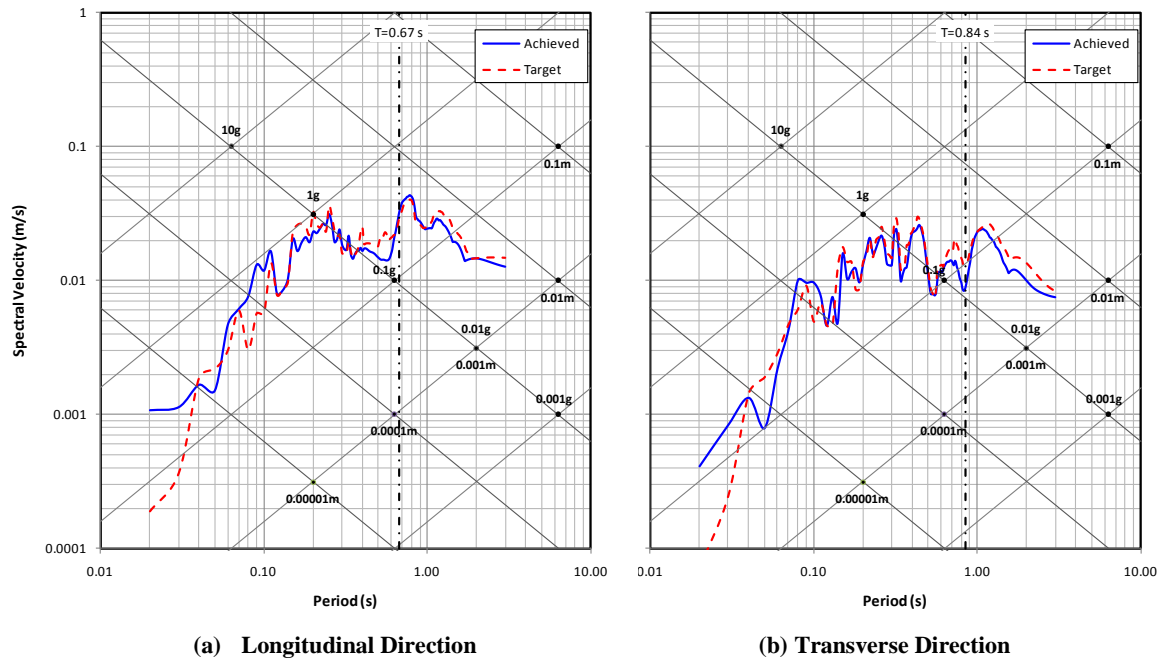


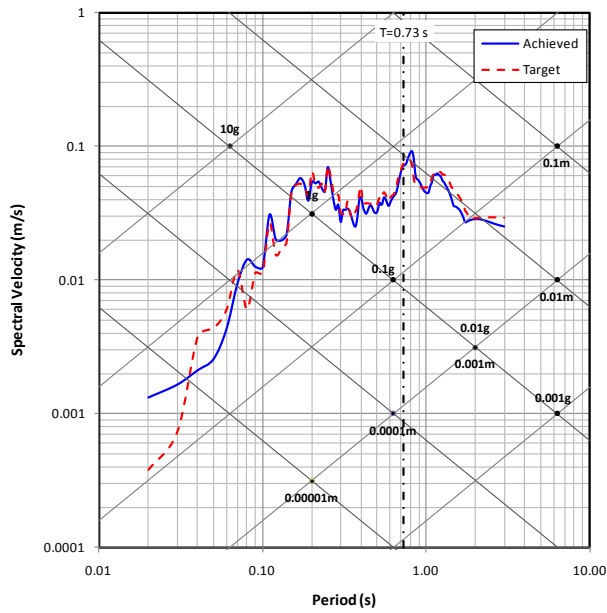
Figure 5-3 Time History Acceleration used for Specimens I2 (Trans. Direction)



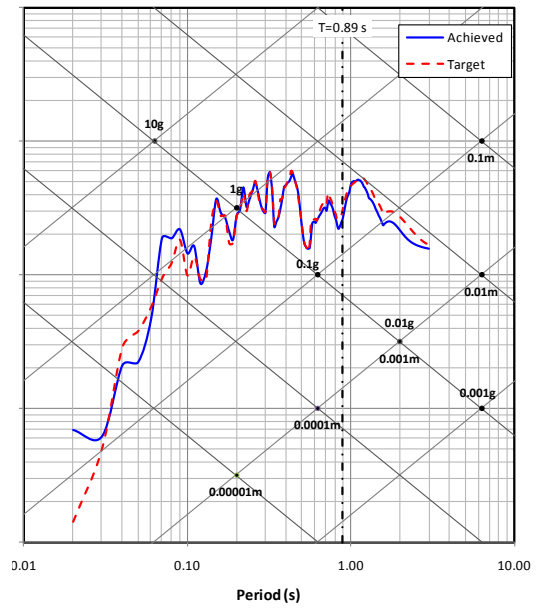
**Figure 5-4 Comparison of Target and Achieved Trilogarithmic Response Spectra  
0.1 x Sylmar Specimen I1**



**Figure 5-5 Comparison of Target and Achieved Trilogarithmic Response Spectra  
0.2 x Sylmar Specimen I1**

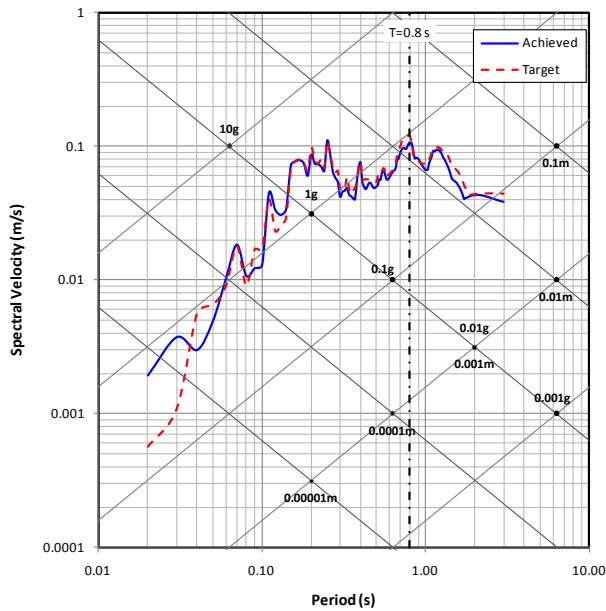


(a) Longitudinal Direction

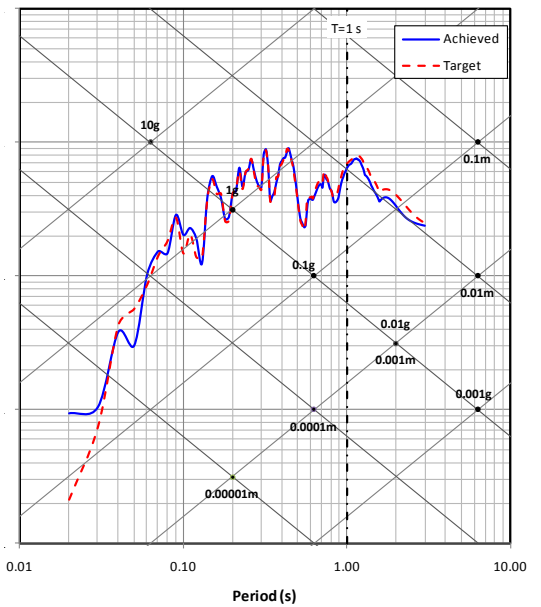


(b) Transverse Direction

**Figure 5-6 Comparison of Target and Achieved Trilogarithmic Response Spectra  
0.4x Sylmar Specimen I1**

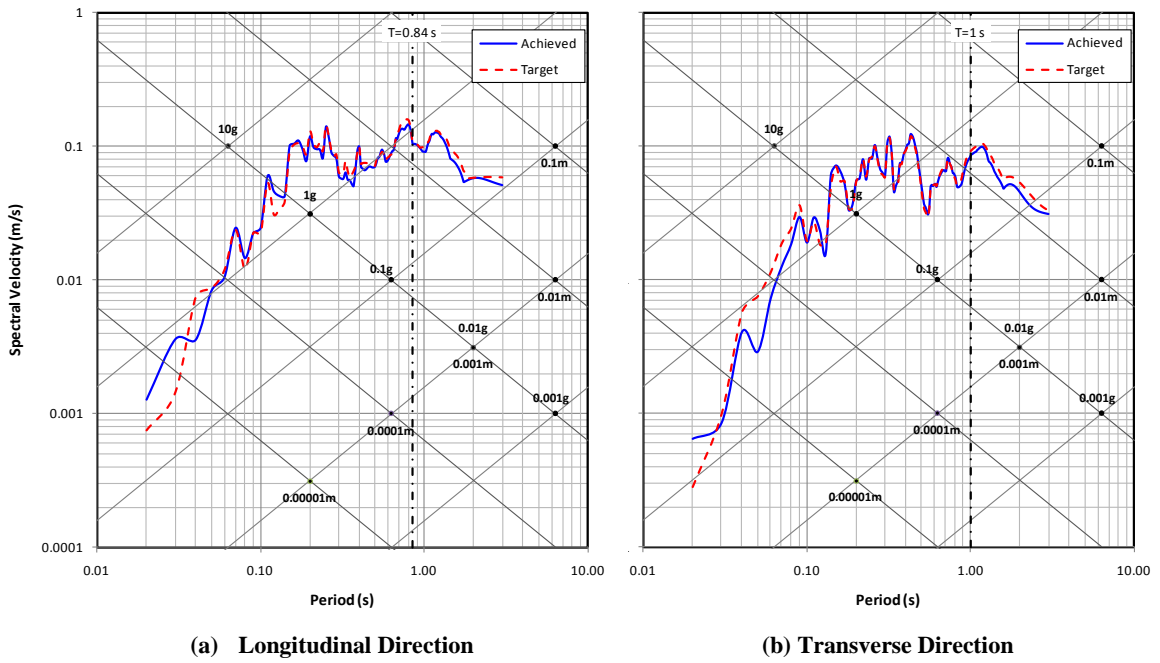


(a) Longitudinal Direction

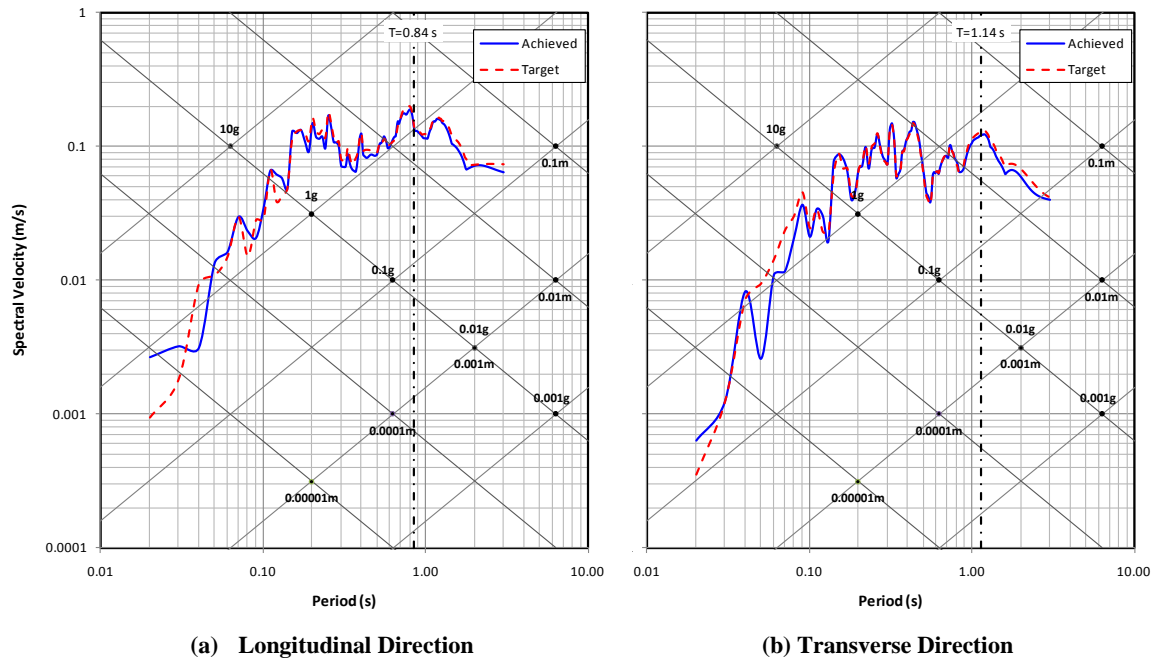


(b) Transverse Direction

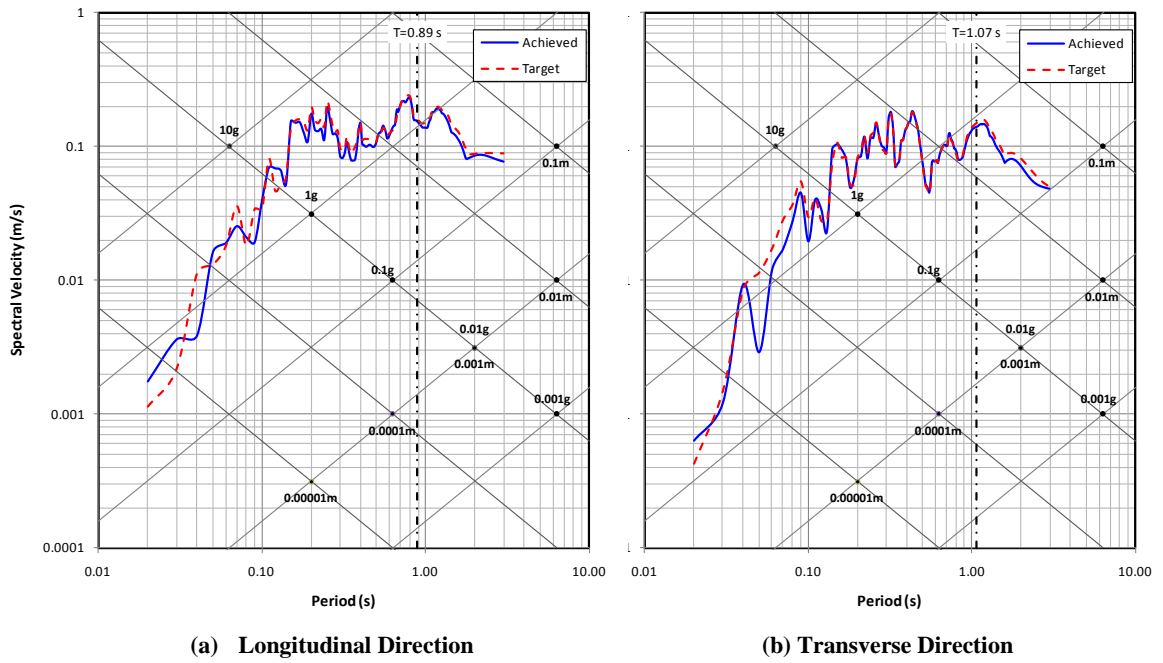
**Figure 5-7 Comparison of Target and Achieved Trilogarithmic Response Spectra  
0.6 x Sylmar Specimen I1**



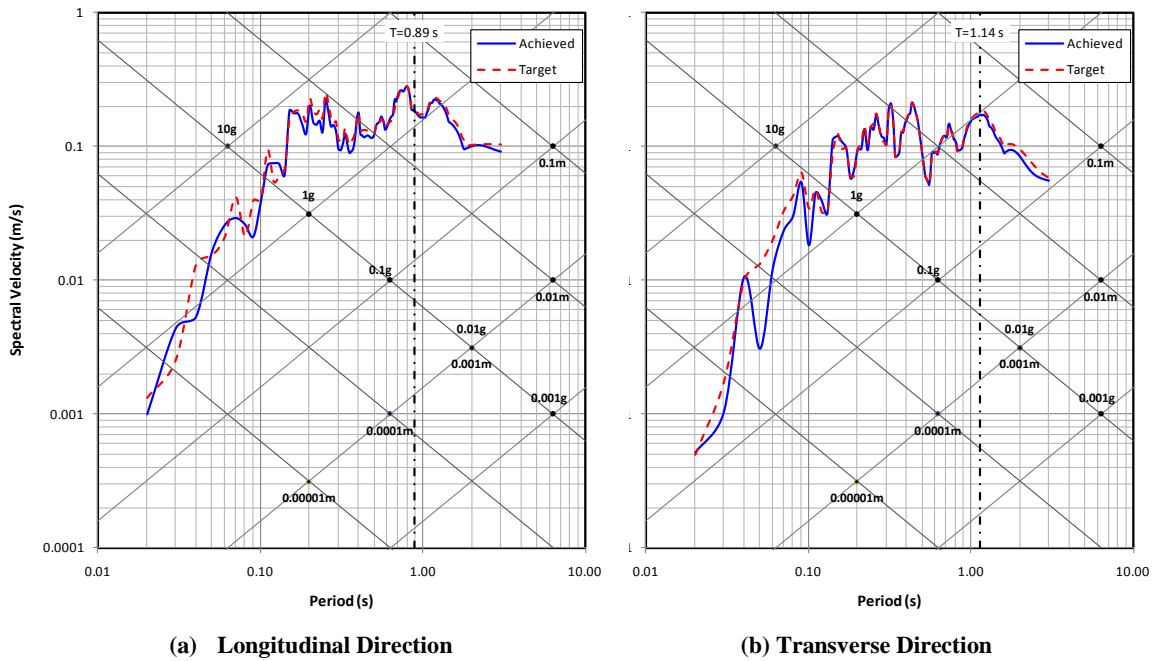
**Figure 5-8 Comparison of Target and Achieved Trilogarithmic Response Spectra  
0.8 x Sylmar Specimen I1**



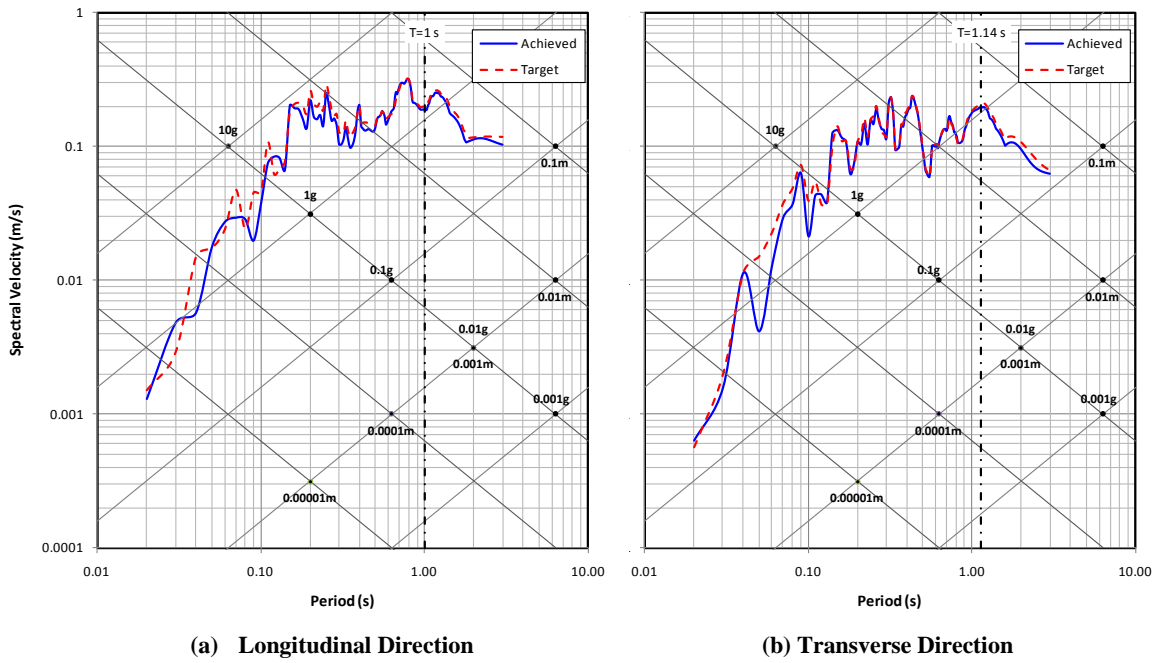
**Figure 5-9 Comparison of Target and Achieved Trilogarithmic Response Spectra  
1.0 x Sylmar Specimen I1**



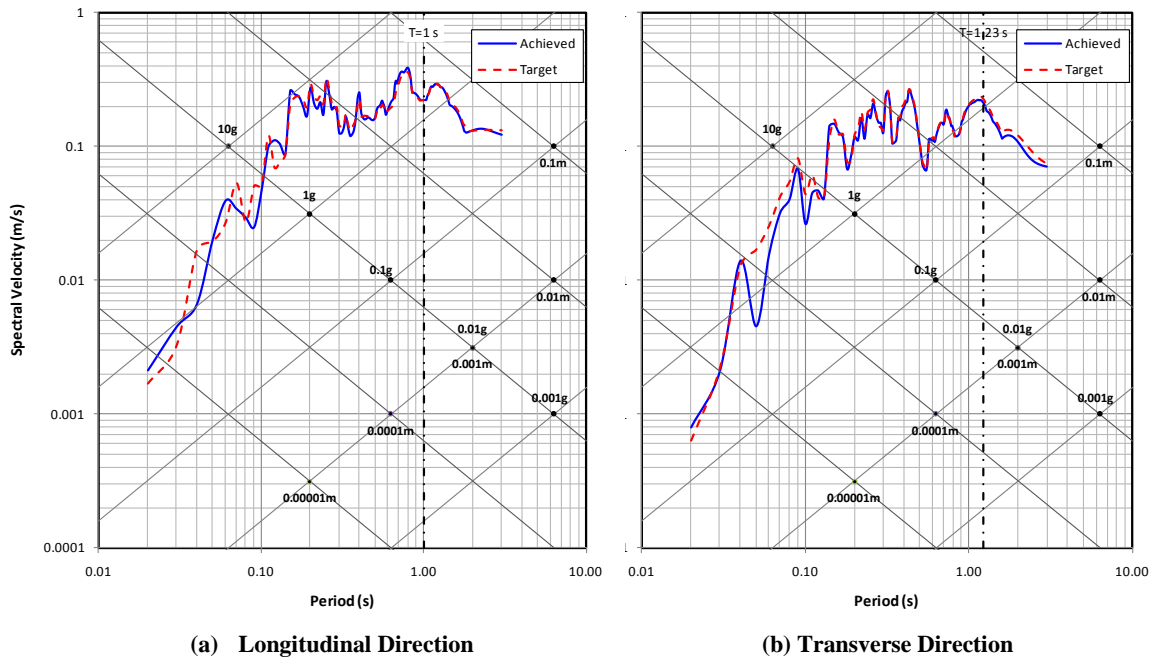
**Figure 5-10 Comparison of Target and Achieved Trilogarithmic Response Spectra  
1.2 x Sylmar Specimen I1**



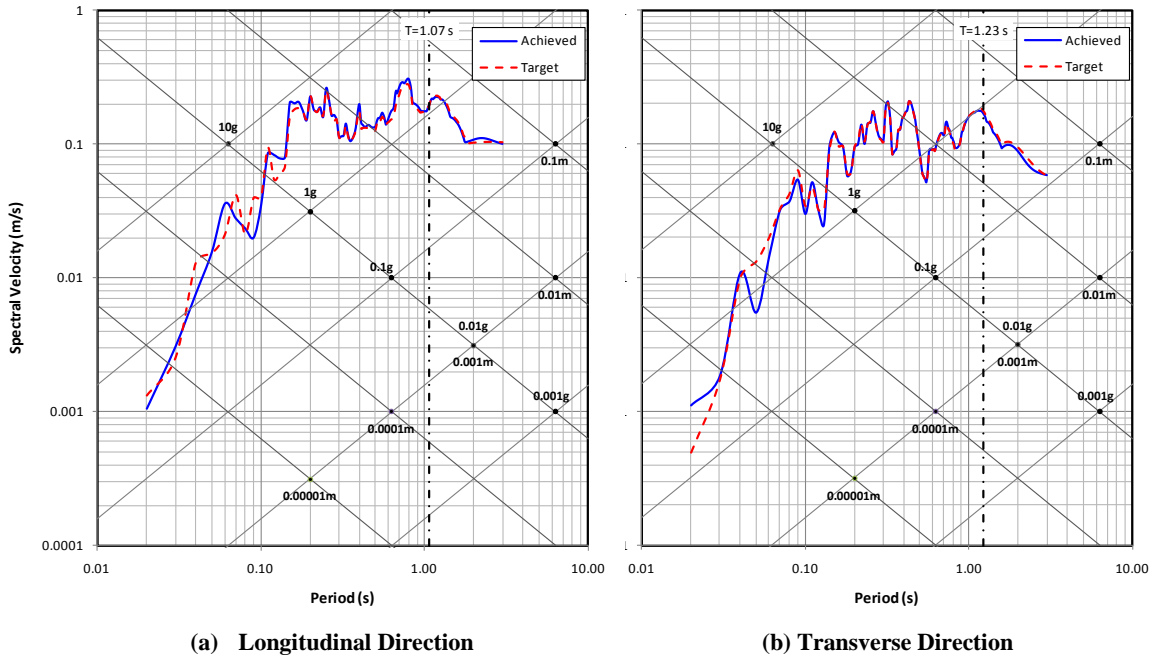
**Figure 5-11 Comparison of Target and Achieved Trilogarithmic Response Spectra  
1.4 x Sylmar Specimen I1**



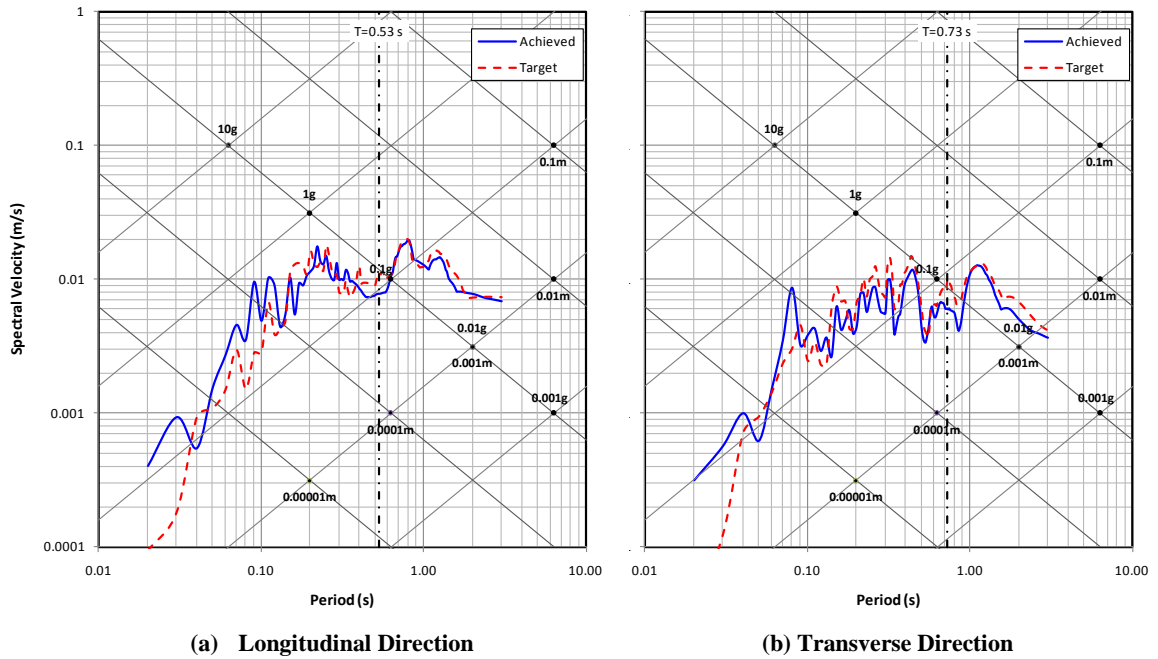
**Figure 5-12 Comparison of Target and Achieved Trilogarithmic Response Spectra  
1.6 x Sylmar Specimen I1**



**Figure 5-13 Comparison of Target and Achieved Trilogarithmic Response Spectra  
1.8 x Sylmar Specimen I1**

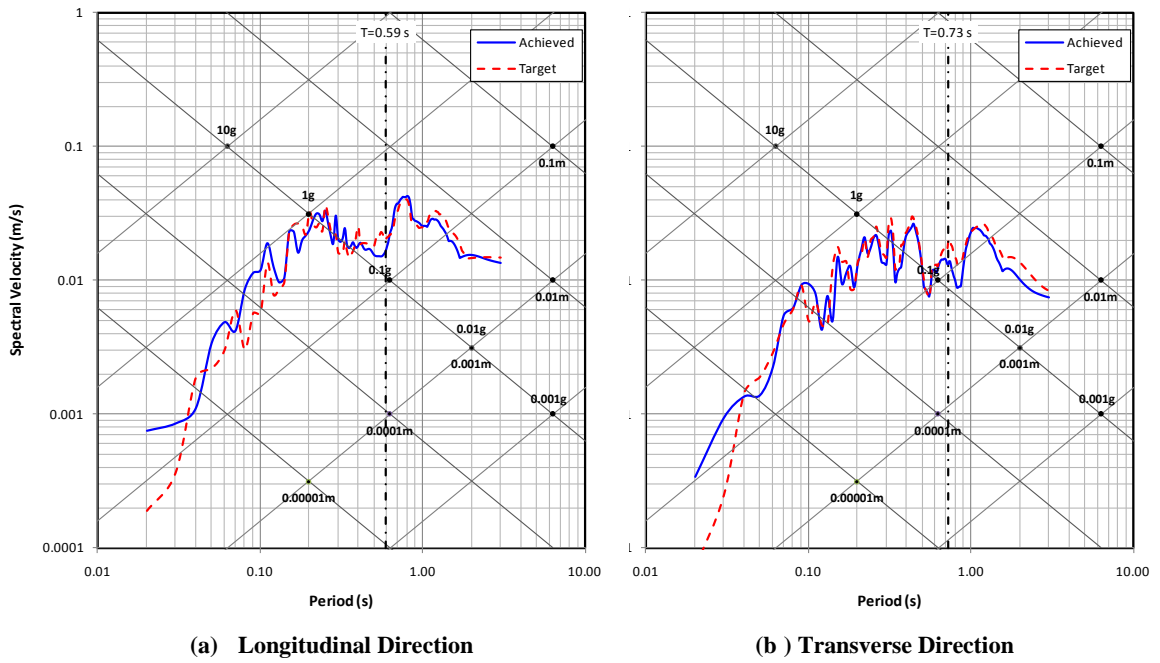


**Figure 5-14 Comparison of Target and Achieved Trilogarithmic Response Spectra  
1.4\* x Sylmar Specimen I1**

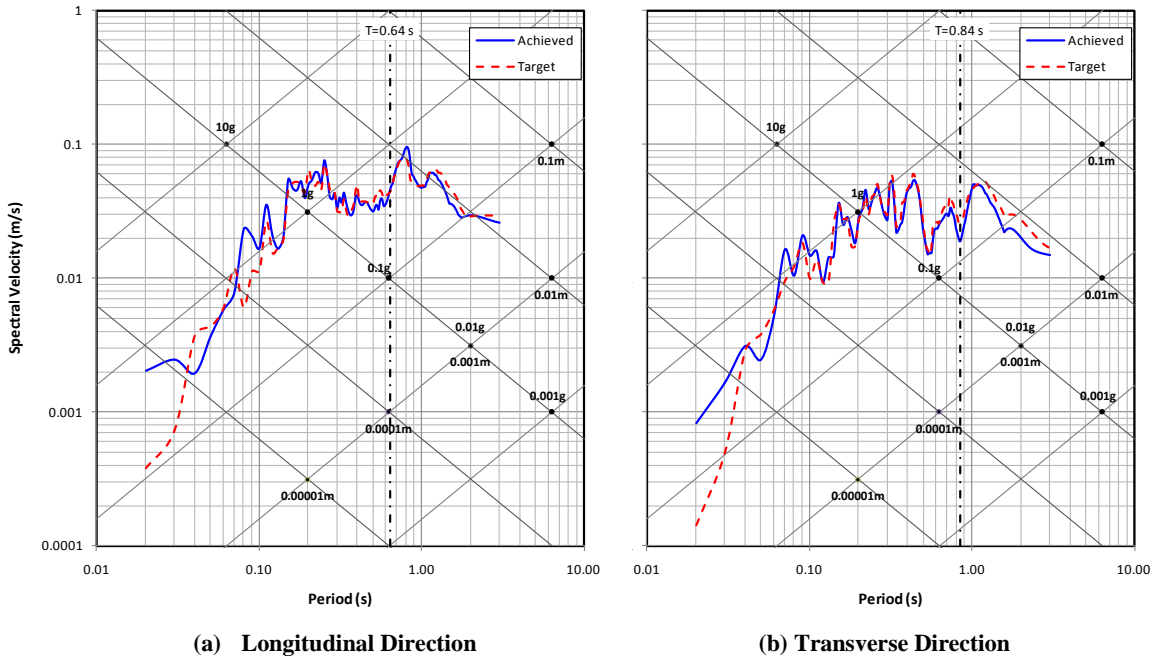


**Figure 5-15 Comparison of Target and Achieved Trilogarithmic Response Spectra  
0.1 x Sylmar Specimen I2**

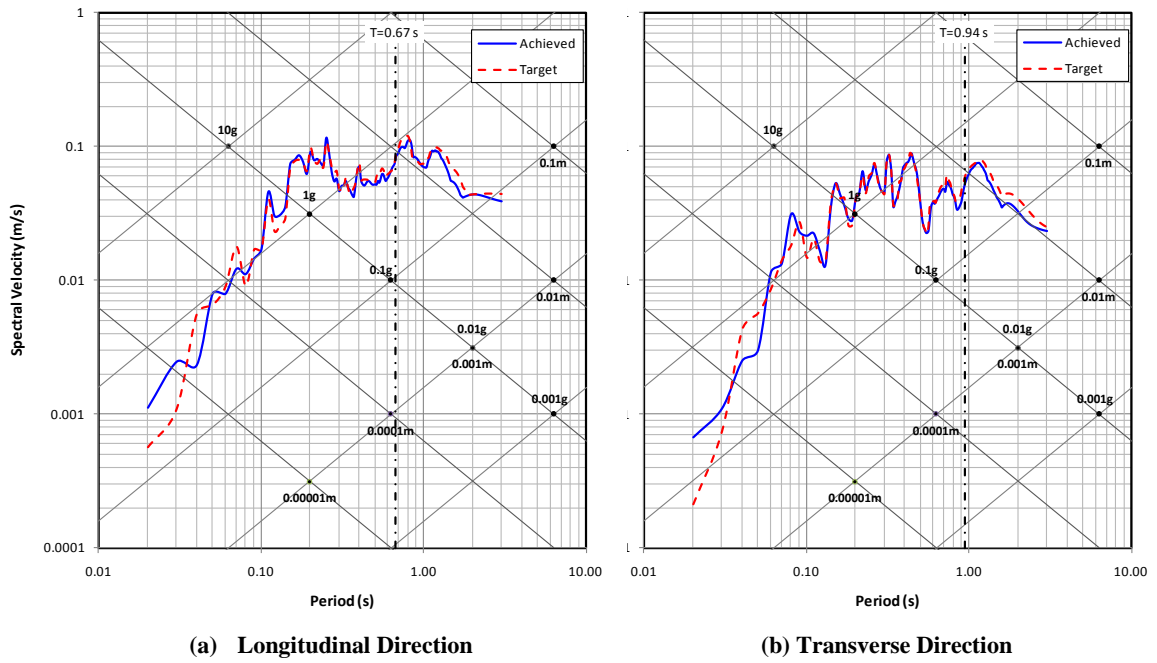




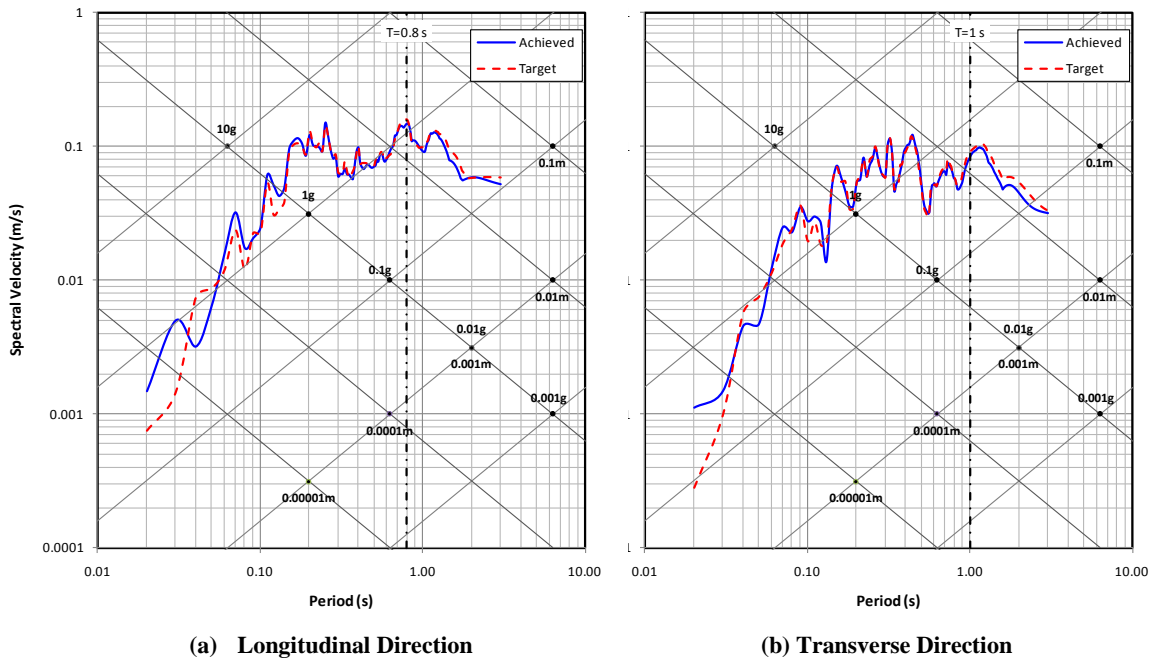
**Figure 5- 16 Comparison of Target and Achieved Trilogarithmic Response Spectra  
0.2 x Sylmar Specimen I2**



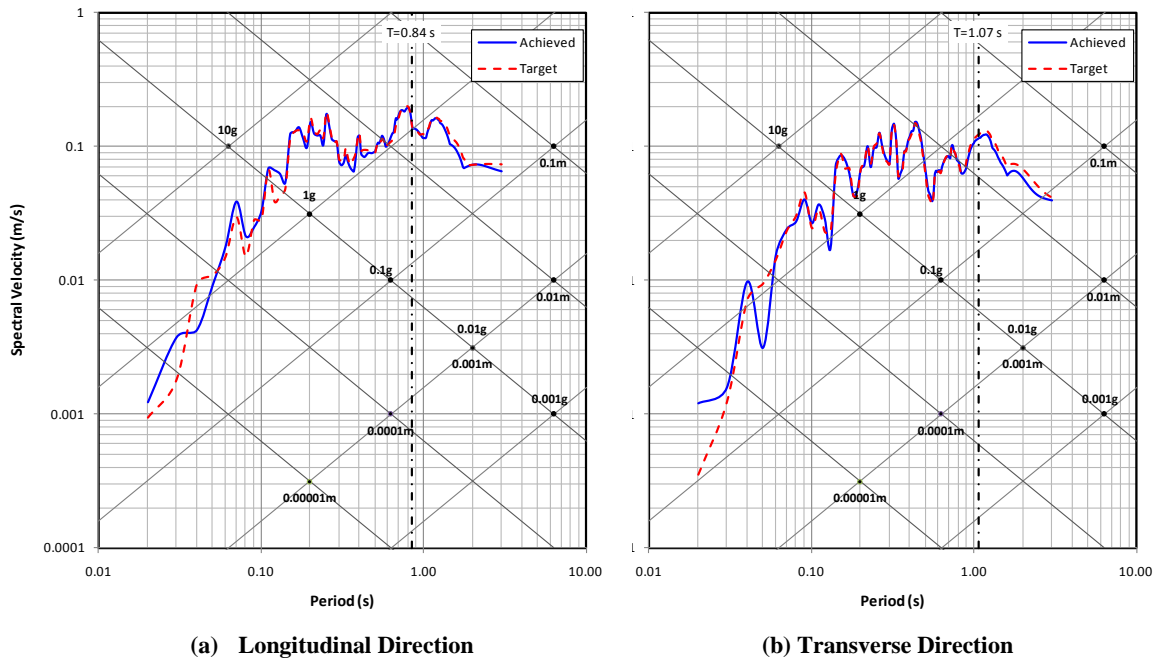
**Figure 5-17 Comparison of Target and Achieved Trilogarithmic Response Spectra  
0.4 x Sylmar Specimen I2**



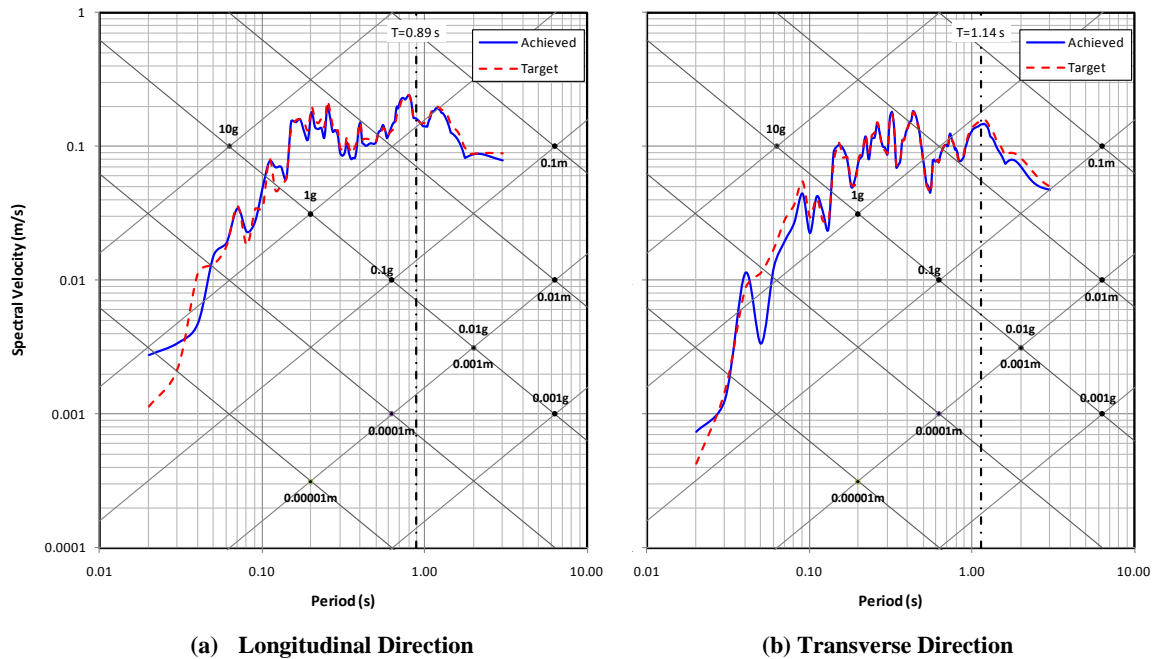
**Figure 5-18 Comparison of Target and Achieved Trilogarithmic Response Spectra  
0.6 x Sylmar Specimen I2**



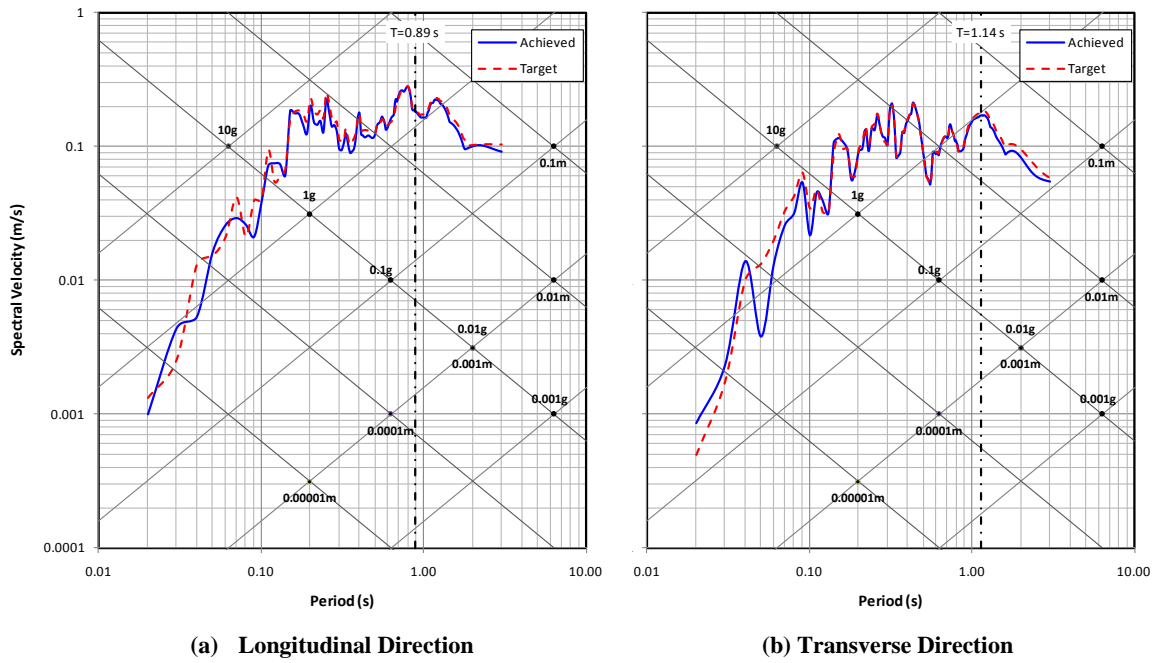
**Figure 5-19 Comparison of Target and Achieved Trilogarithmic Response Spectra  
0.8 x Sylmar Specimen I2**



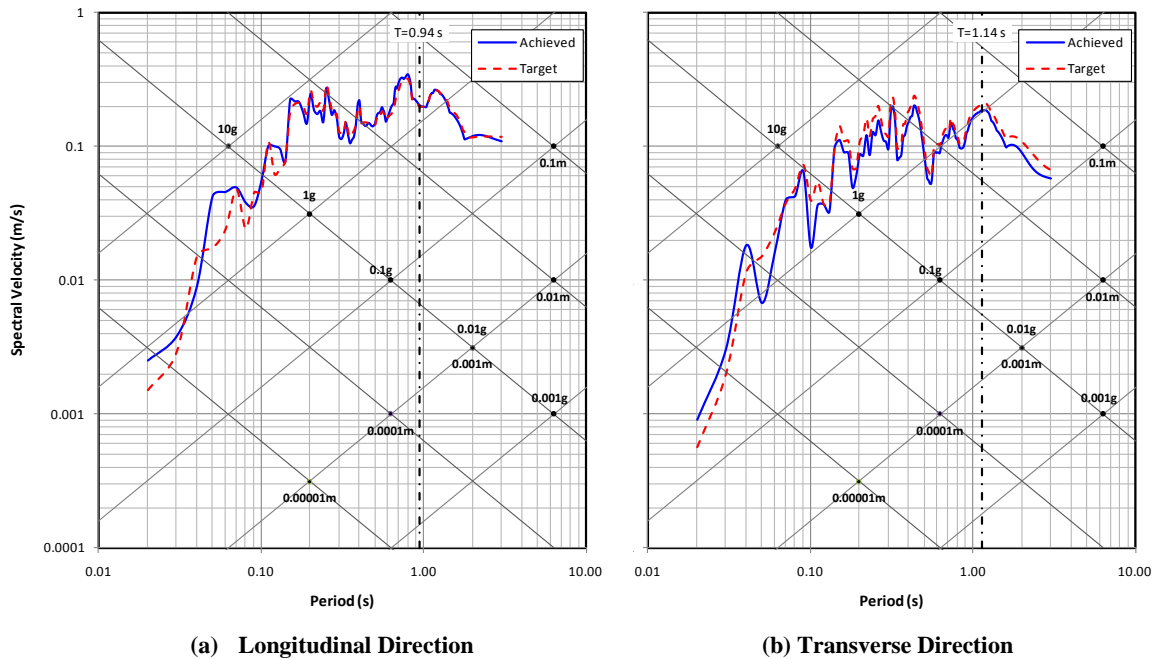
**Figure 5-20 Comparison of Target and Achieved Trilogarithmic Response Spectra  
1.0 x Sylmar Specimen I2**



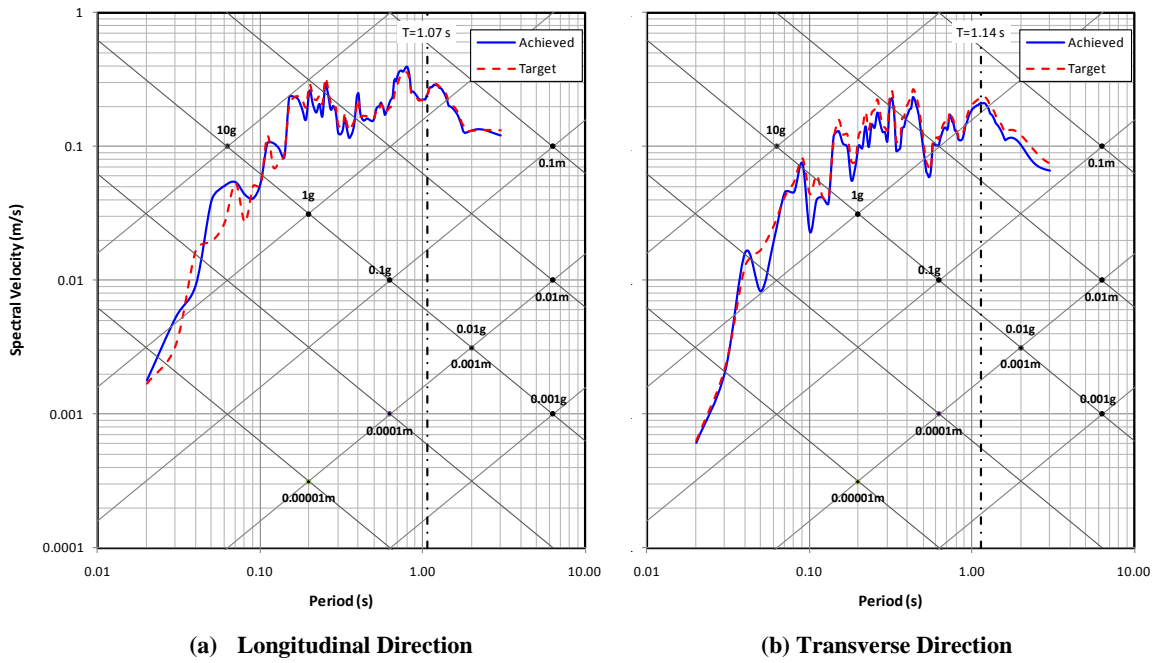
**Figure 5-21 Comparison of Target and Achieved Trilogarithmic Response Spectra  
1.2 x Sylmar Specimen I2**



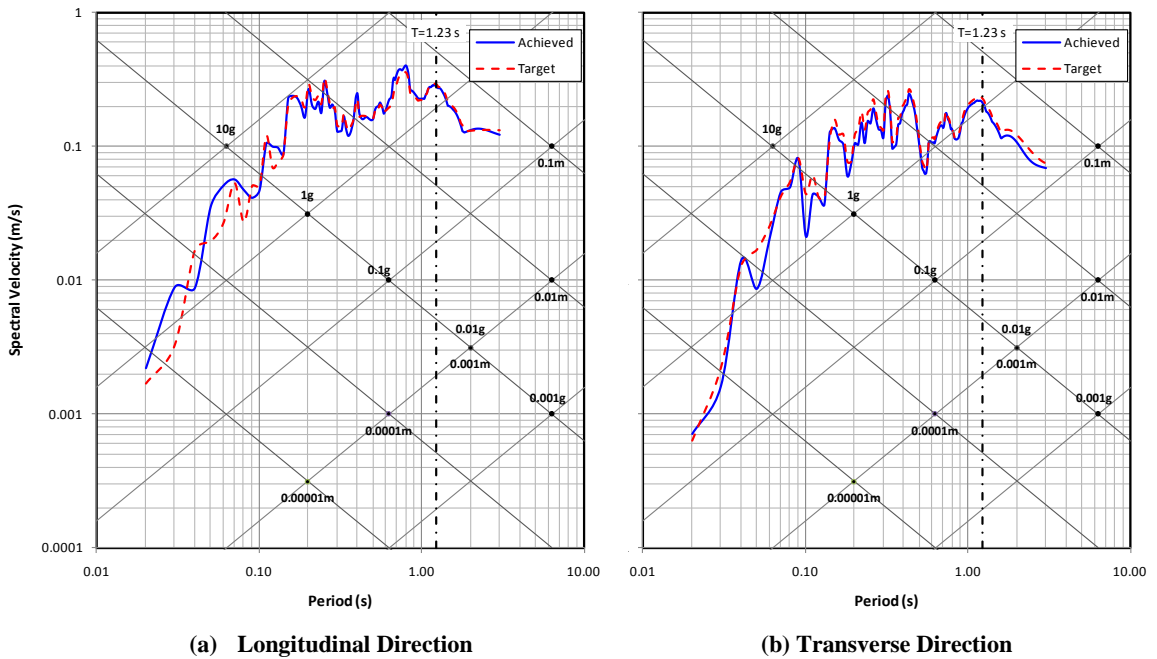
**Figure 5-22 Comparison of Target and Achieved Trilogarithmic Response Spectra  
1.4 x Sylmar Specimen I2**



**Figure 5-23 Comparison of Target and Achieved Trilogarithmic Response Spectra  
1.6 x Sylmar Specimen I2**



**Figure 5-24 Comparison of Target and Achieved Trilogarithmic Response Spectra  
1.8 x Sylmar Specimen I2**



**Figure 5-25 Comparison of Target and Achieved Trilogarithmic Response Spectra  
1.8\* x Sylmar Specimen I2**



Figure 5-26 Hairline Horizontal Cracks, Specimens I1 and I2 (SYLx0.1)



Figure 5-27 Cracks at First Longitudinal Bar Yielding, Specimens I1 and I2 (SYLx0.2)

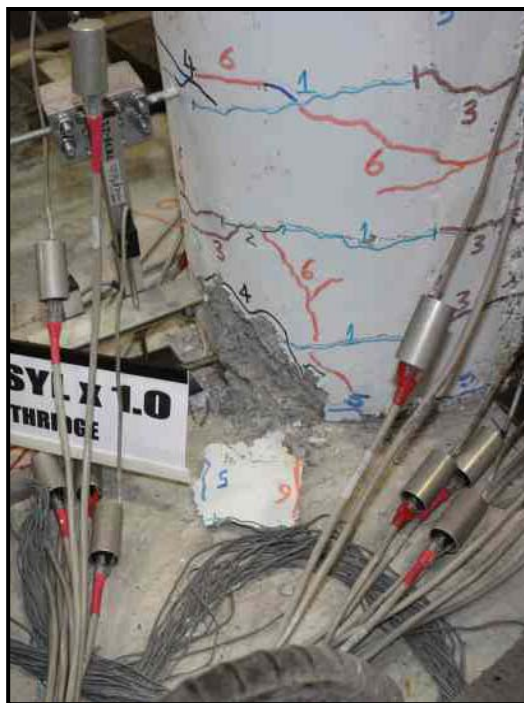
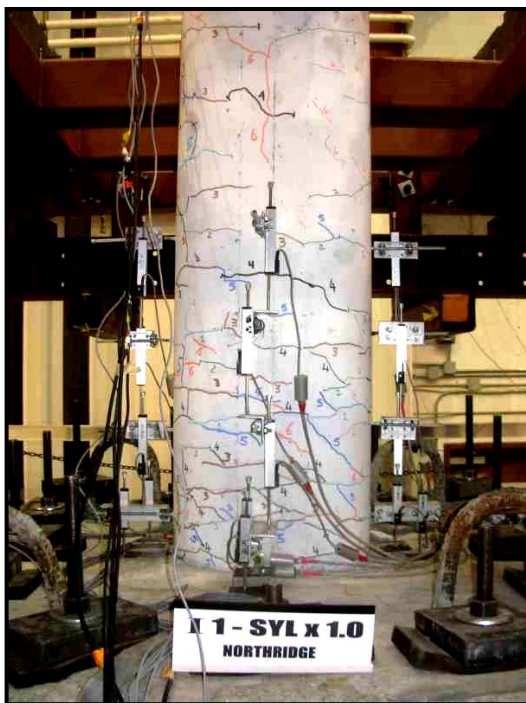


Figure 5-28 First Concrete Spalling Specimens I1 (SYLx1.0)

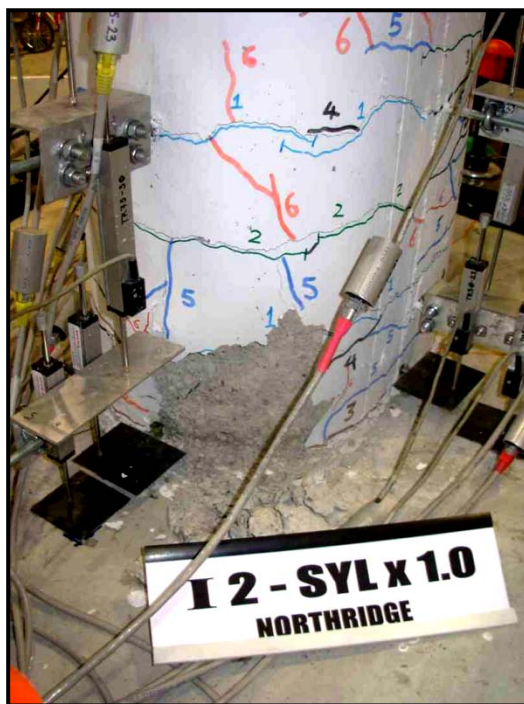
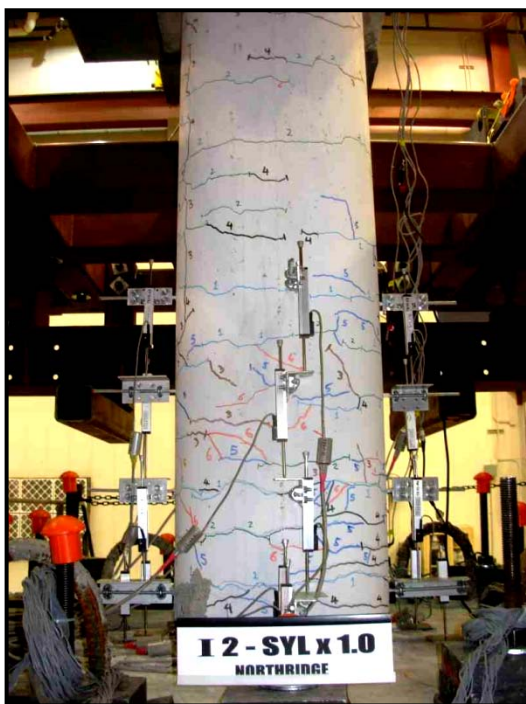


Figure 5-29 First Concrete Spalling Specimens I2 (SYLx1.0)

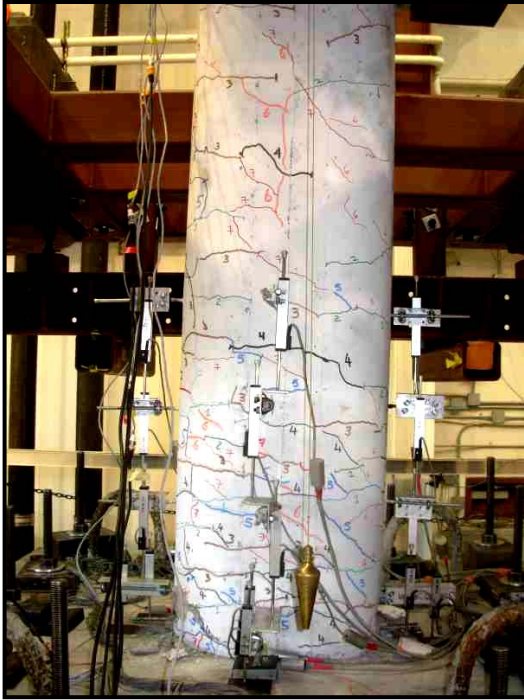


Figure 5-30 Specimen I1, Increasing of Cracks and Spalling (SYLx1.2)

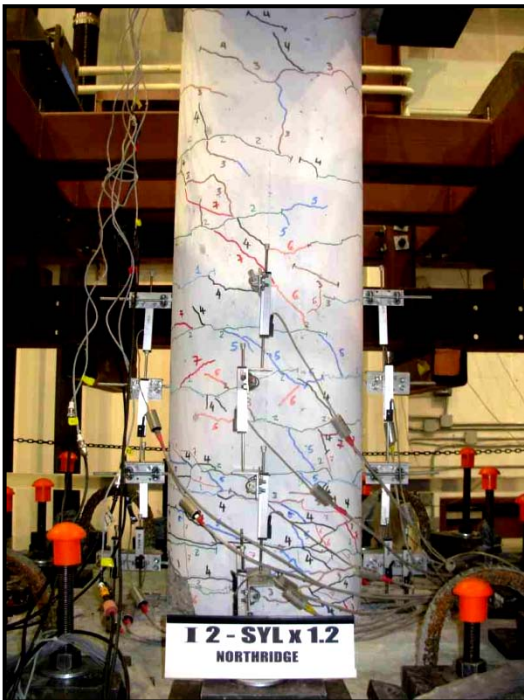


Figure 5-31 Specimen I2, Increasing of Cracks and Spalling (SYLx1.2)

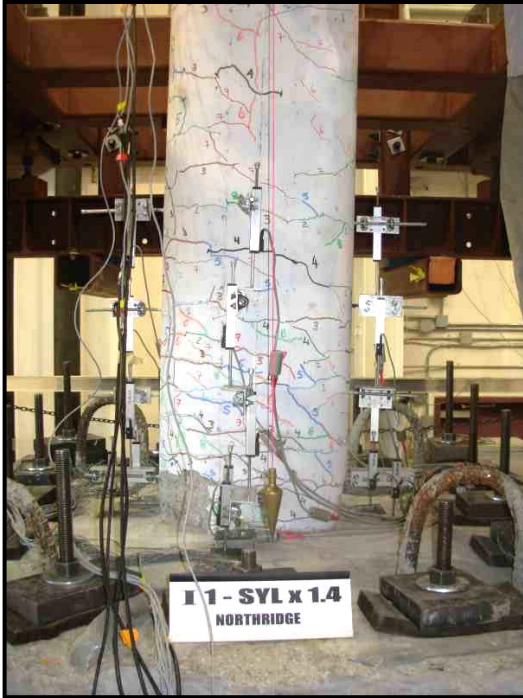




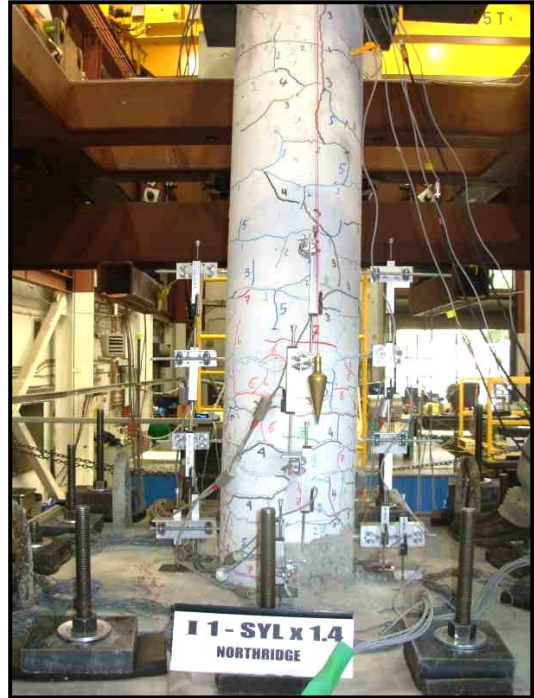
Figure 5-32 Spiral and Longitudinal Bars Visible, Specimen I1



Figure 5-33 Spiral and Longitudinal Bars Visible, Specimen I2



a) Long side View



b) Short Side View

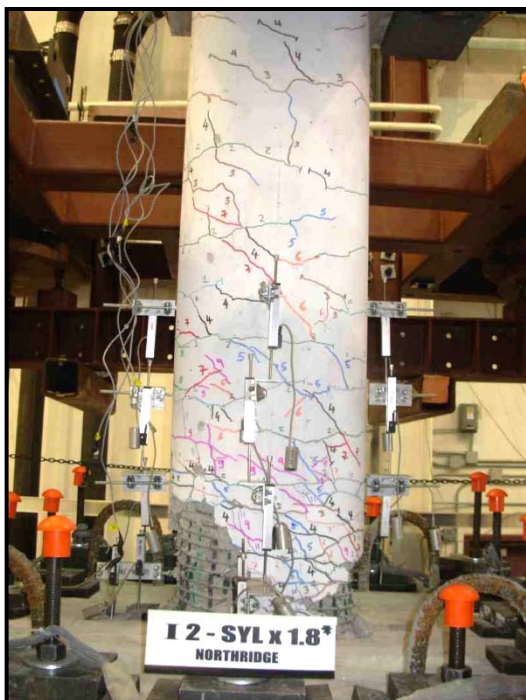


d) Long. Bars Buckling



e) Long. Bars Rupture

Figure 5-34 Specimen I1, Damage at Failure



a) Long side View



b) Short Side View



c) Long. Bars Buckling



d) Long. Bars and Spiral Rupture

Figure 5-35 Specimen I2, Damage at Failure



a) Specimen I1

b) Specimen I2

**Figure 5-36 Specimens I1 and I2, Damage Pattern after Testing**

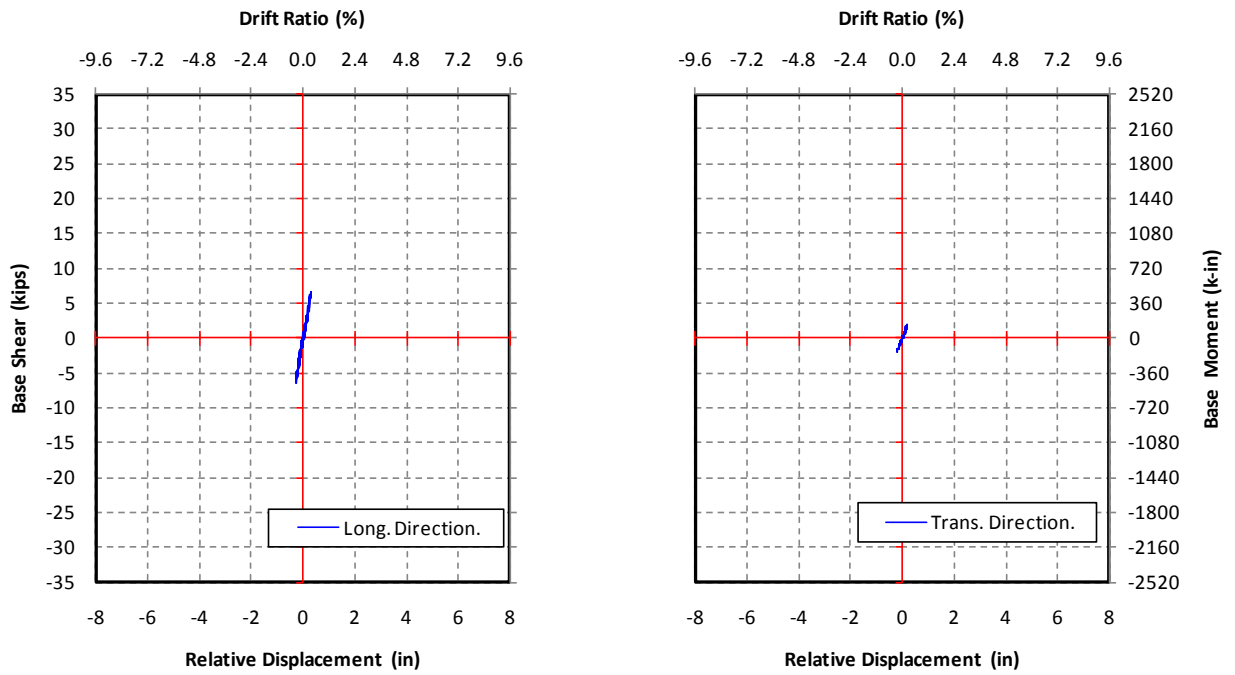


Figure 5-37 Base Shear-Displacement Hysteresis, Specimen I1 (0.1xSYL)

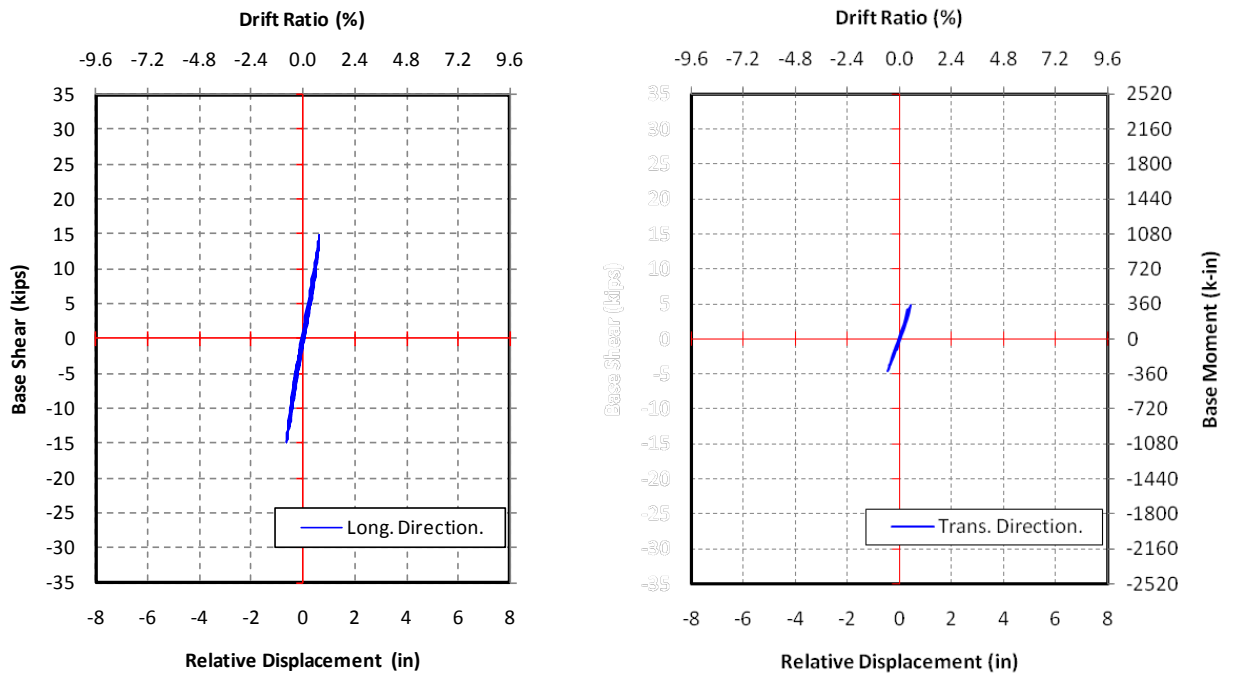


Figure 5-38 Base Shear-Displacement Hysteresis, Specimen I1 (0.2xSYL)

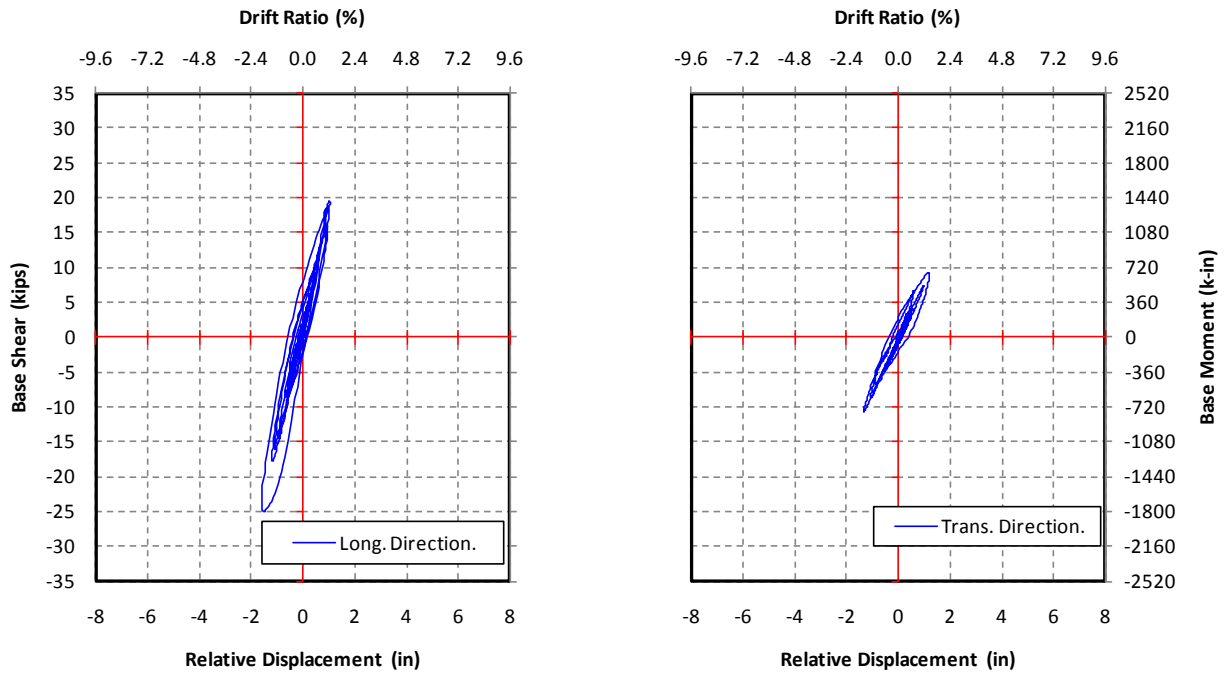


Figure 5-39 Base Shear-Displacement Hysteresis, Specimen I1 (0.4xSYL)

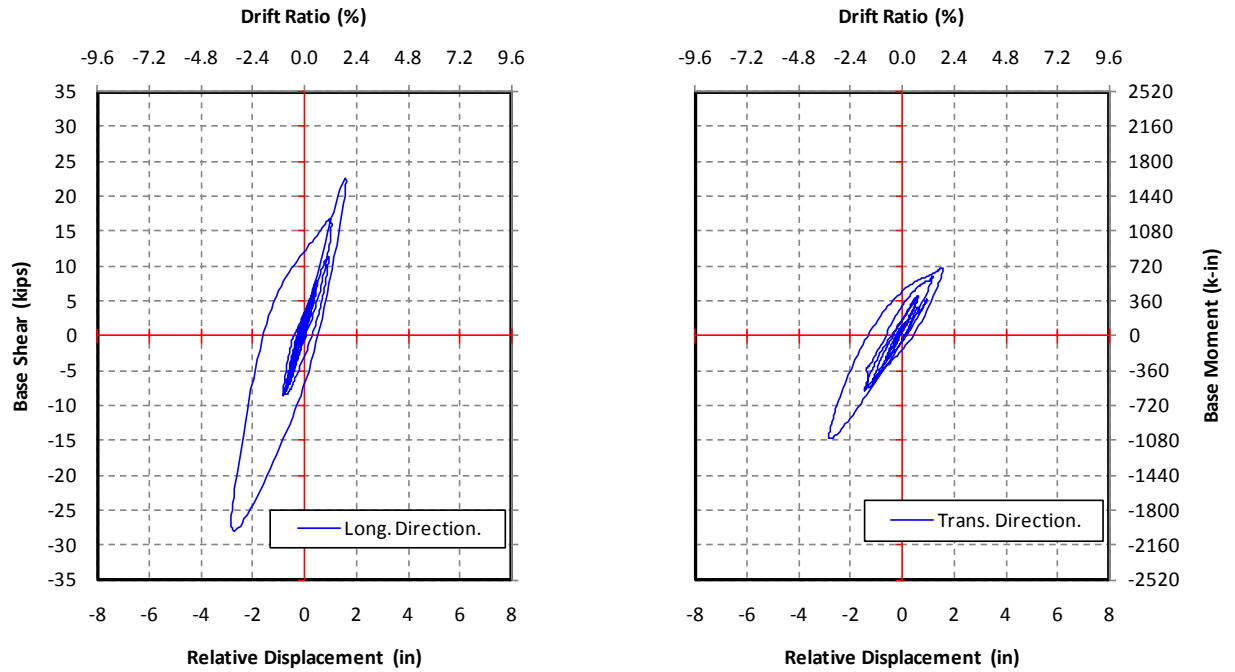


Figure 5-40 Base Shear-Displacement Hysteresis, Specimen I1 (0.6xSYL)

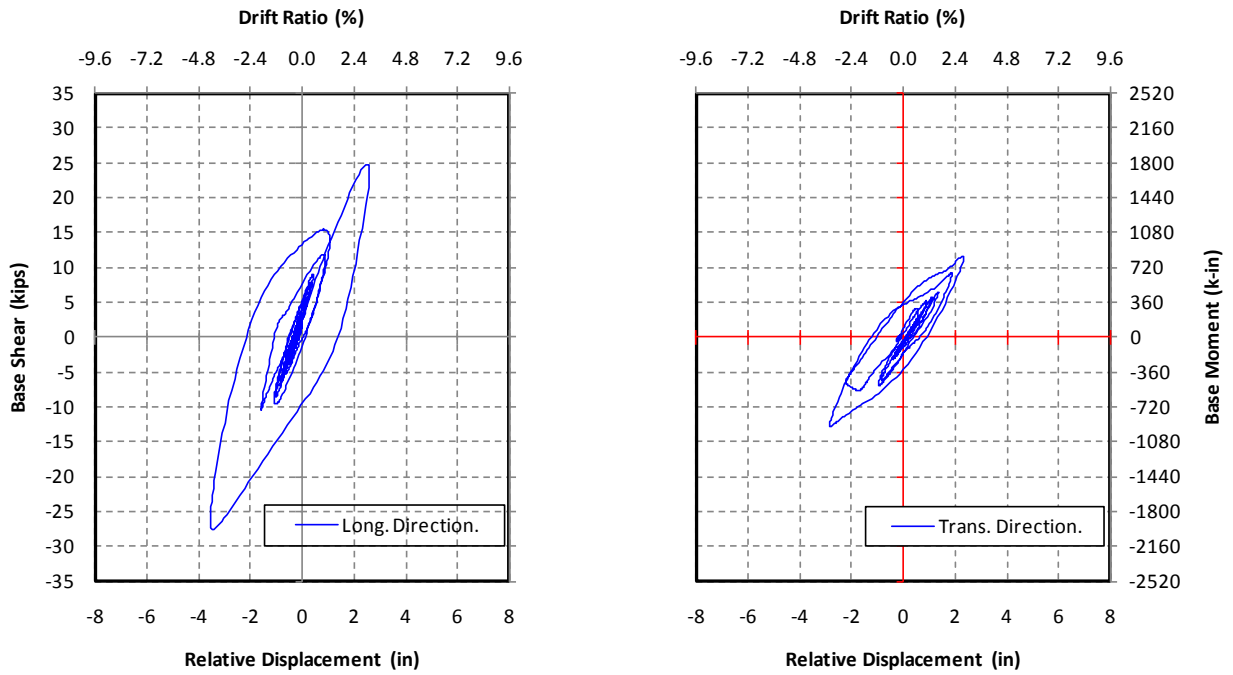


Figure 5-41 Base Shear-Displacement Hysteresis, Specimen I1 (0.8xSYL)

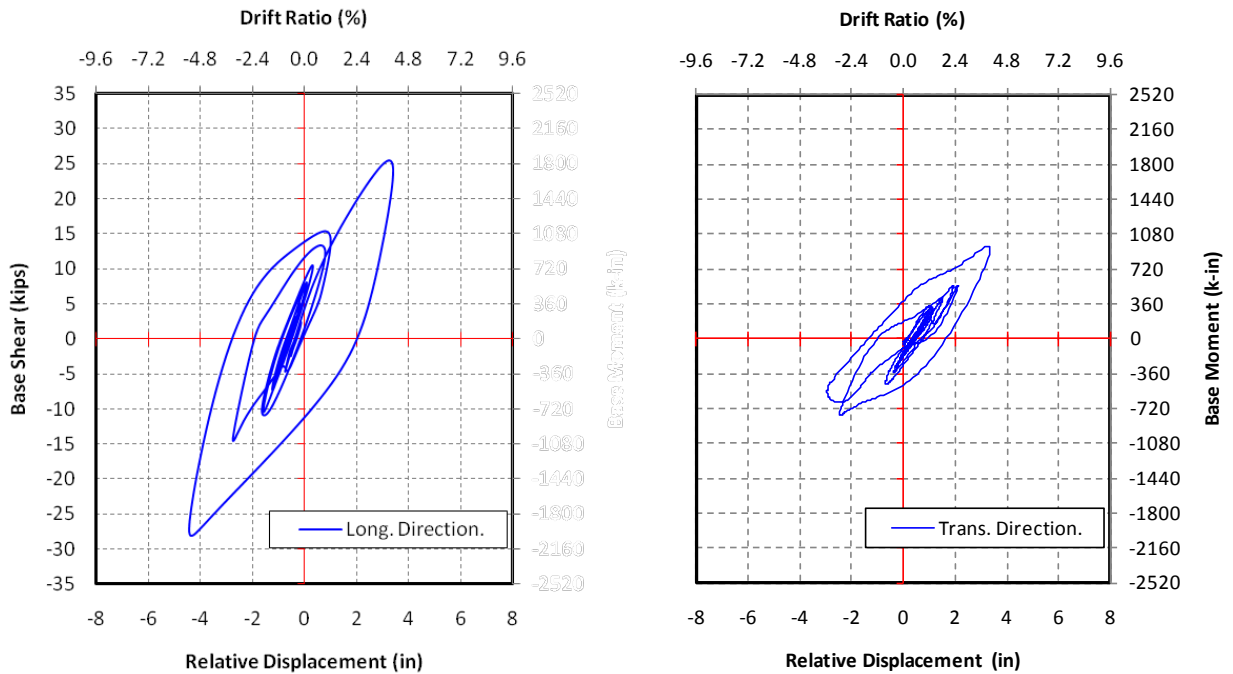


Figure 5-42 Base Shear-Displacement Hysteresis, Specimen I1 (1.0xSYL)

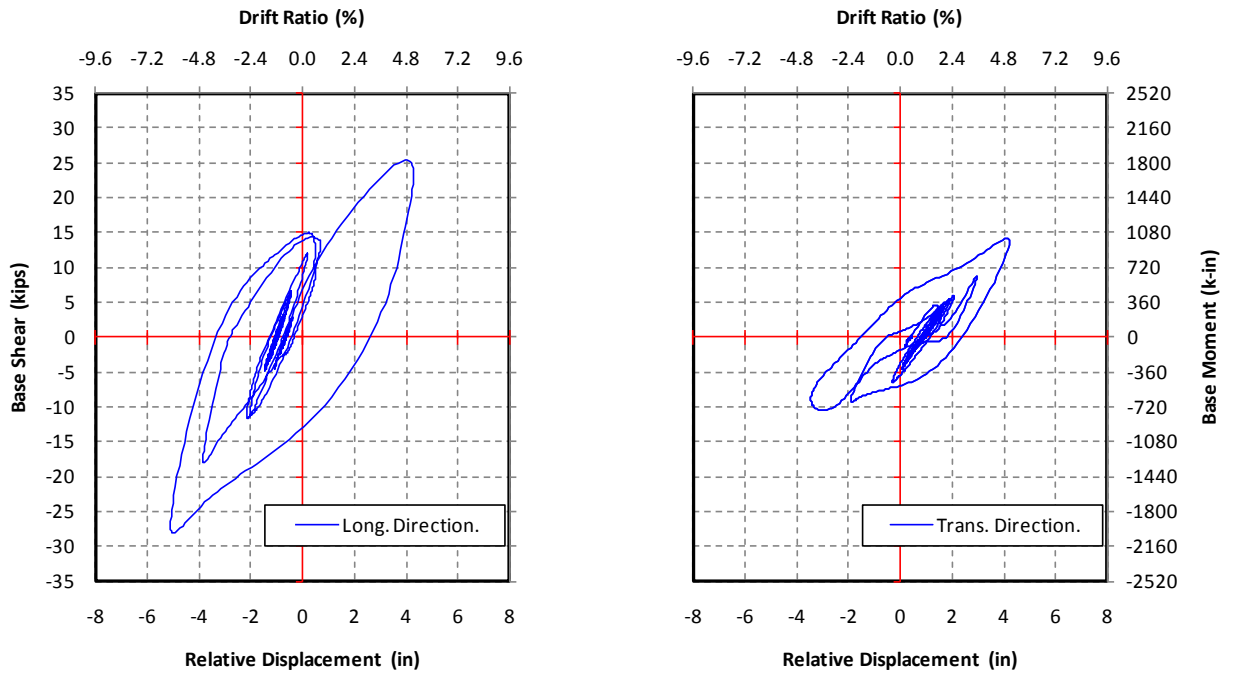


Figure 5-43 Base Shear-Displacement Hysteresis, Specimen I1 (1.2xSYL)

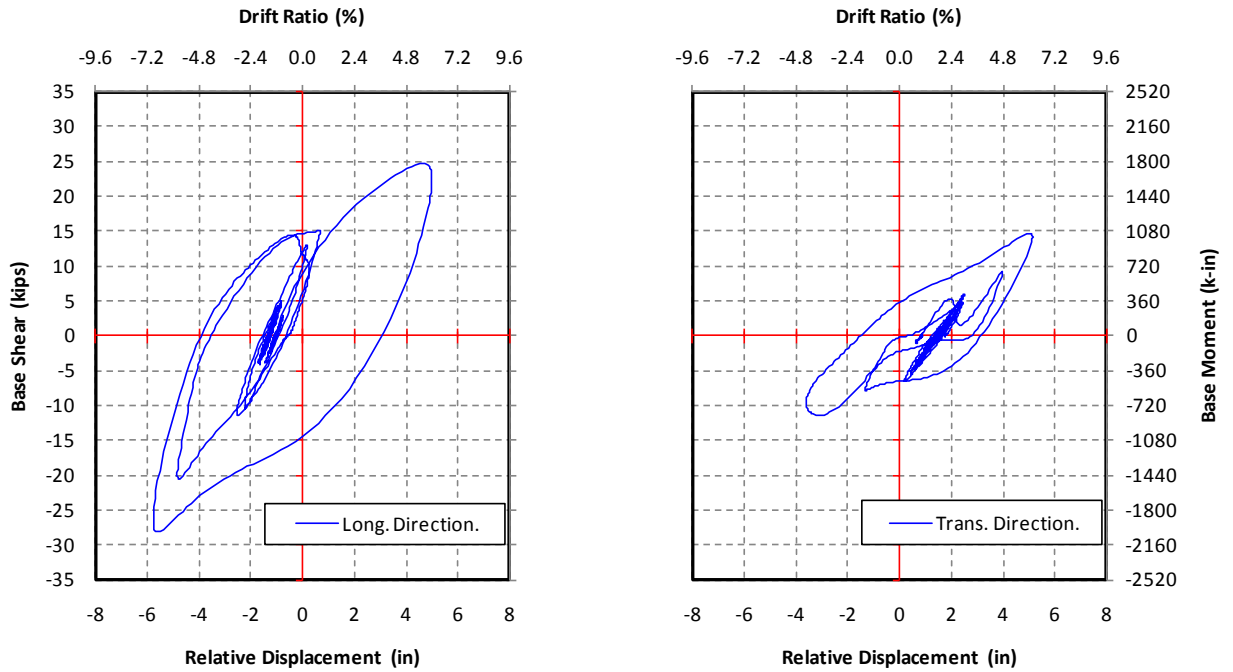


Figure 5-44 Base Shear-Displacement Hysteresis, Specimen I1 (1.4xSYL)



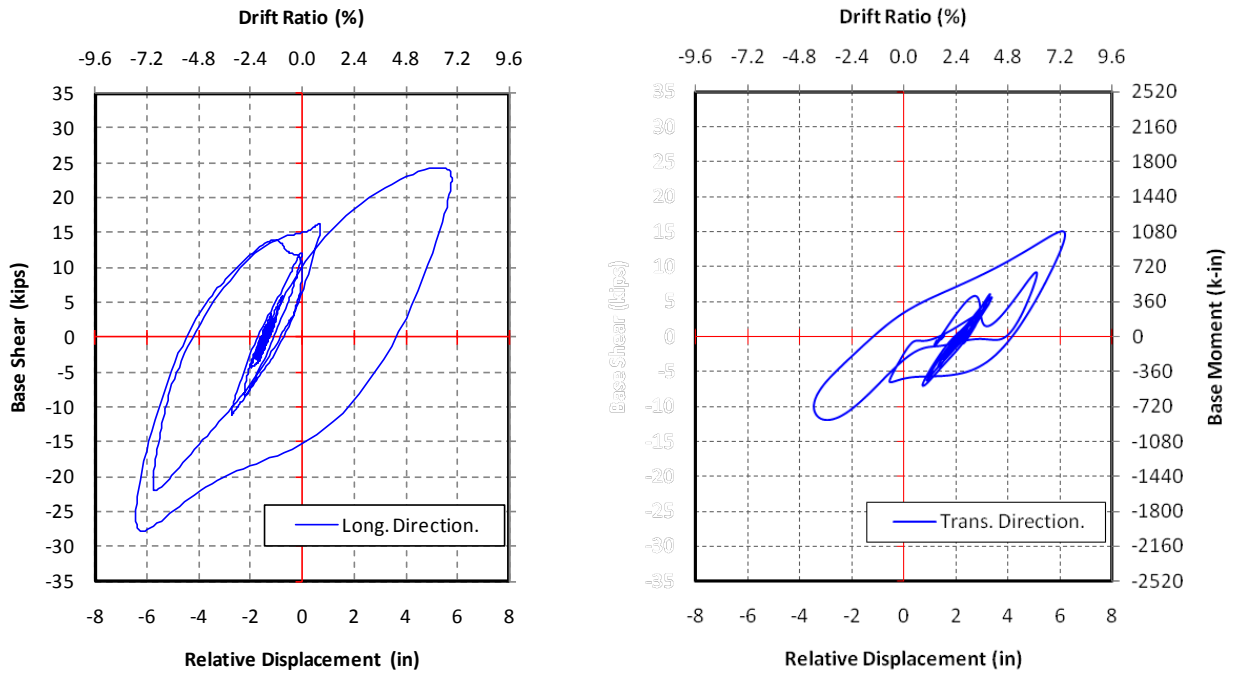


Figure 5-45 Base Shear-Displacement Hysteresis, Specimen I1 (1.6xSYL)

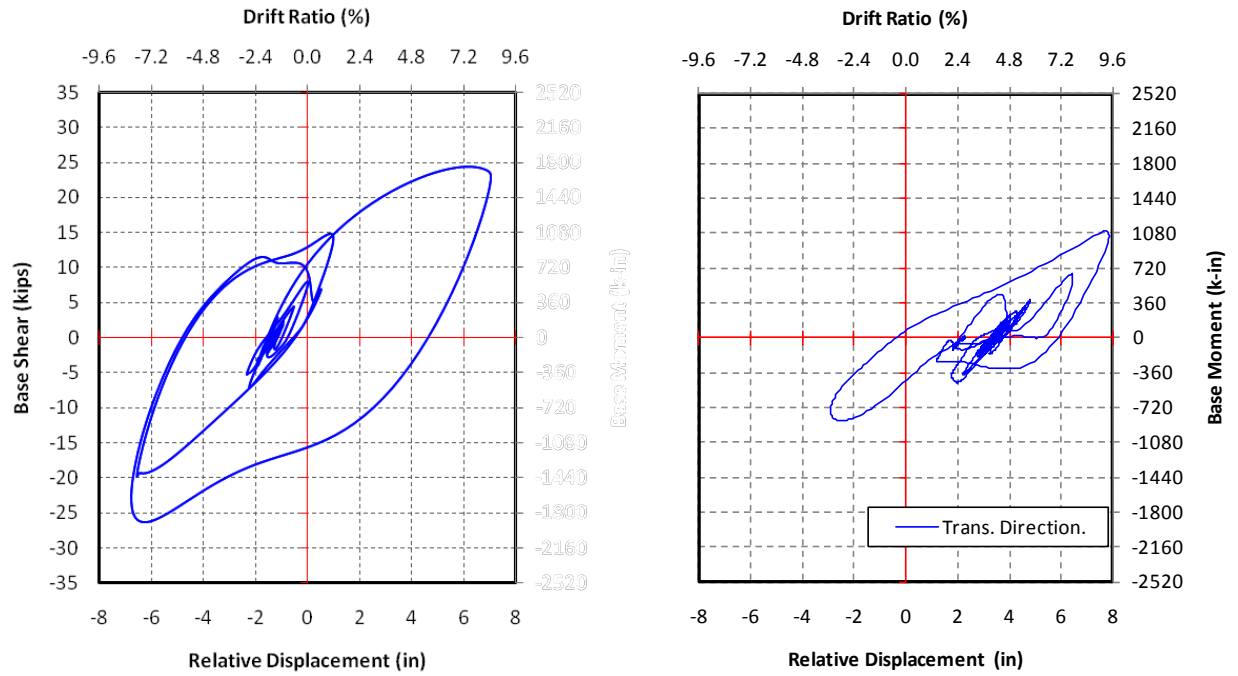


Figure 5-46 Base Shear-Displacement Hysteresis, Specimen I1 (1.8xSYL)

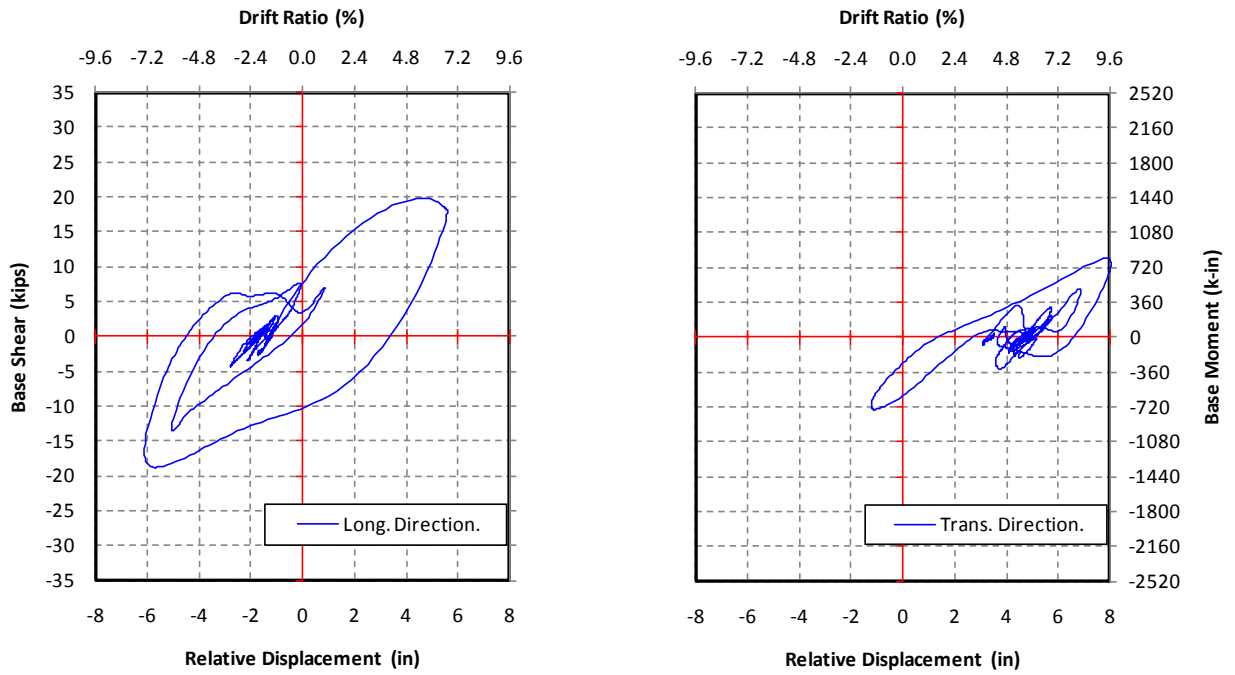


Figure 5-47 Base Shear-Displacement Hysteresis, Specimen I1 (1.4\*xSYL)

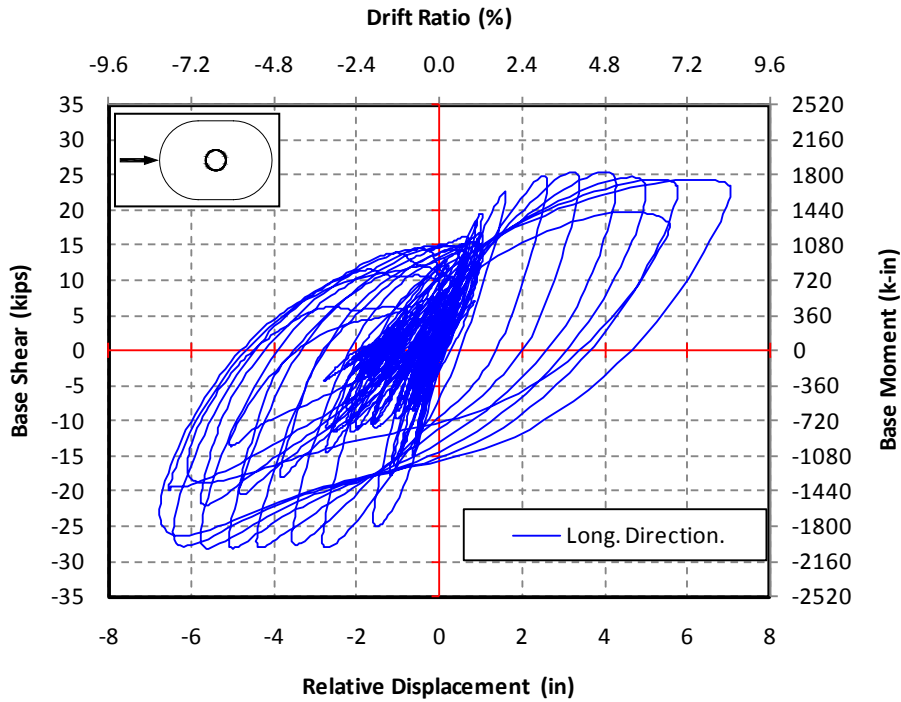


Figure 5-48 Cumulative Base Shear-Displacement Hysteresis, Specimen I1 (Longitudinal)

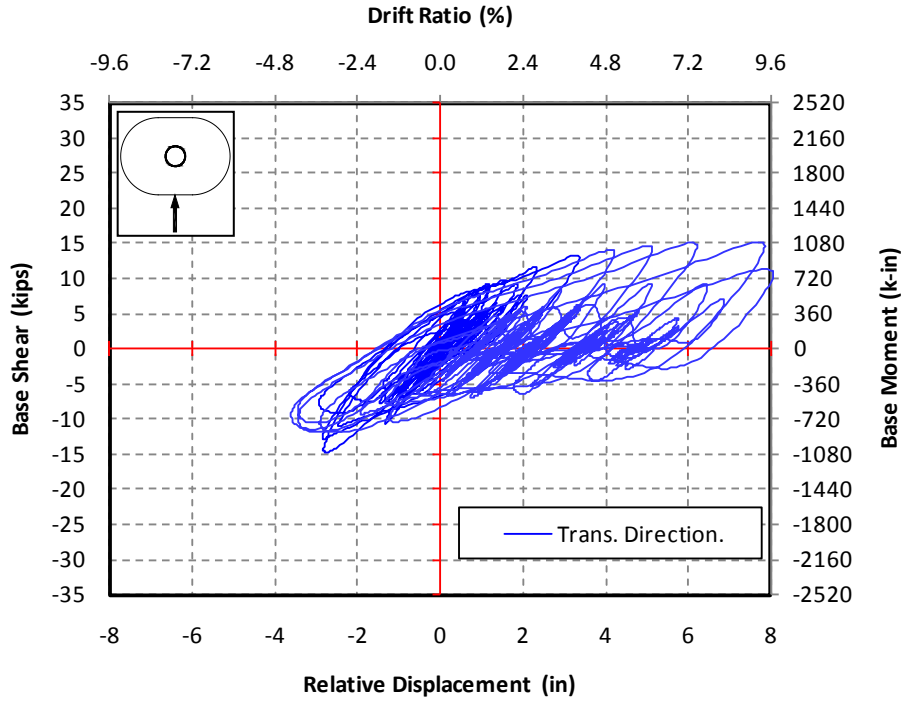


Figure 5-49 Cumulative Base Shear-Displacement Hysteresis, Specimen I1 (Transverse)

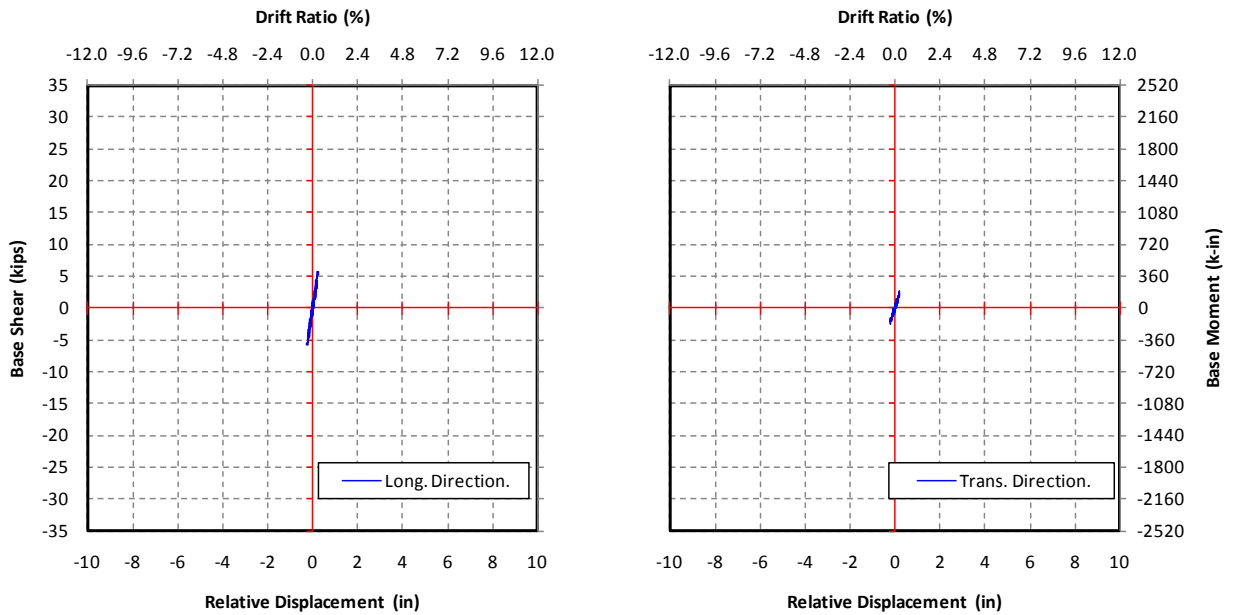


Figure 5-50 Base Shear-Displacement Hysteresis, Specimen I2 (0.1xSYL)

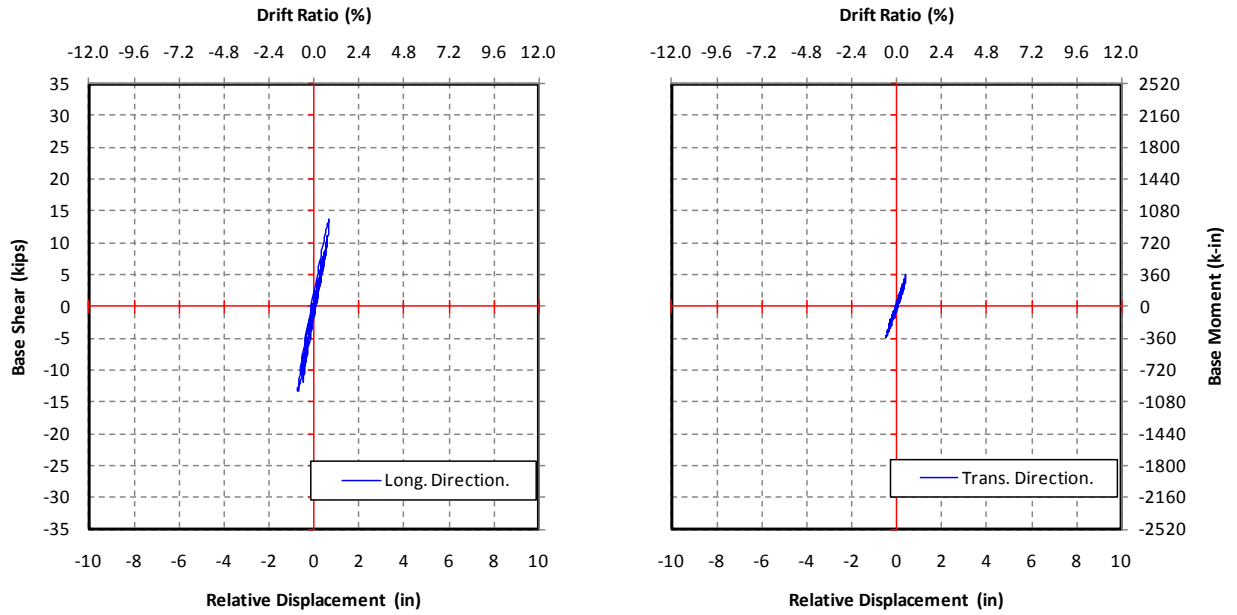


Figure 5-51 Base Shear-Displacement Hysteresis, Specimen I2 (0.2xSYL)

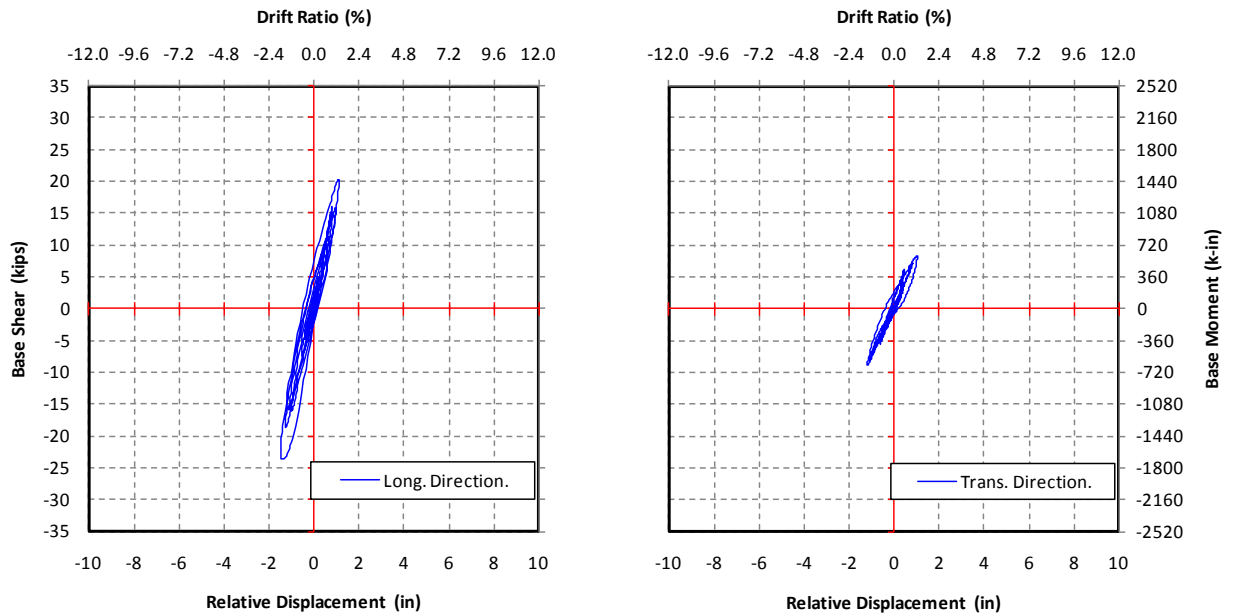


Figure 5-52 Base Shear-Displacement Hysteresis, Specimen I2 (0.4xSYL)

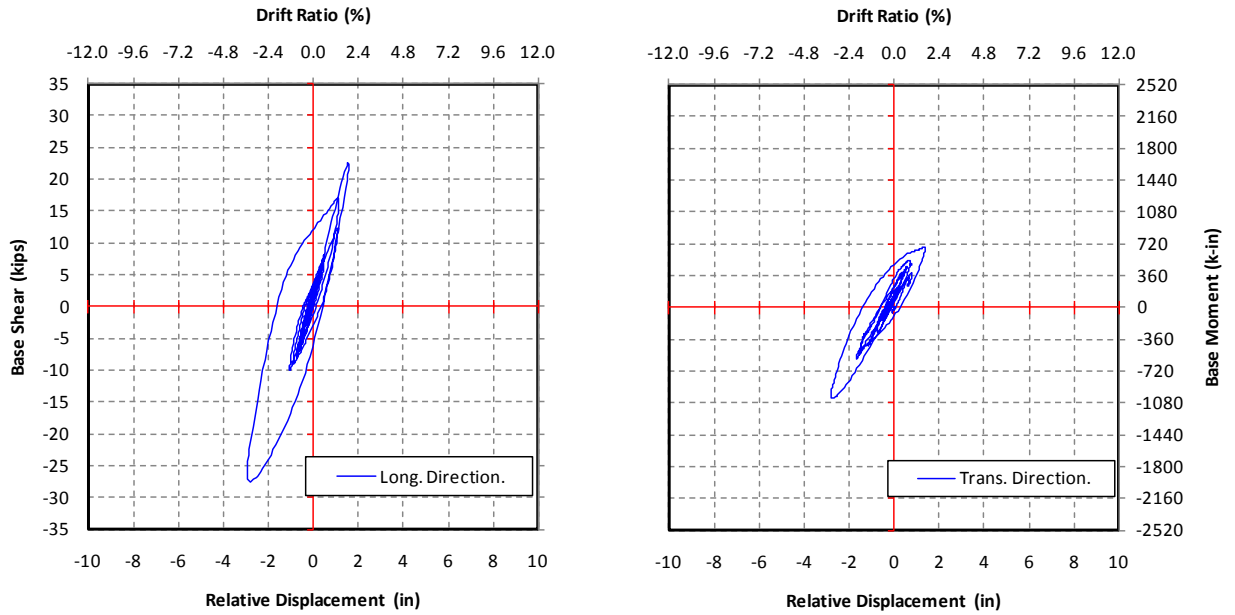


Figure 5-53 Base Shear-Displacement Hysteresis, Specimen I2 (0.6xSYL)

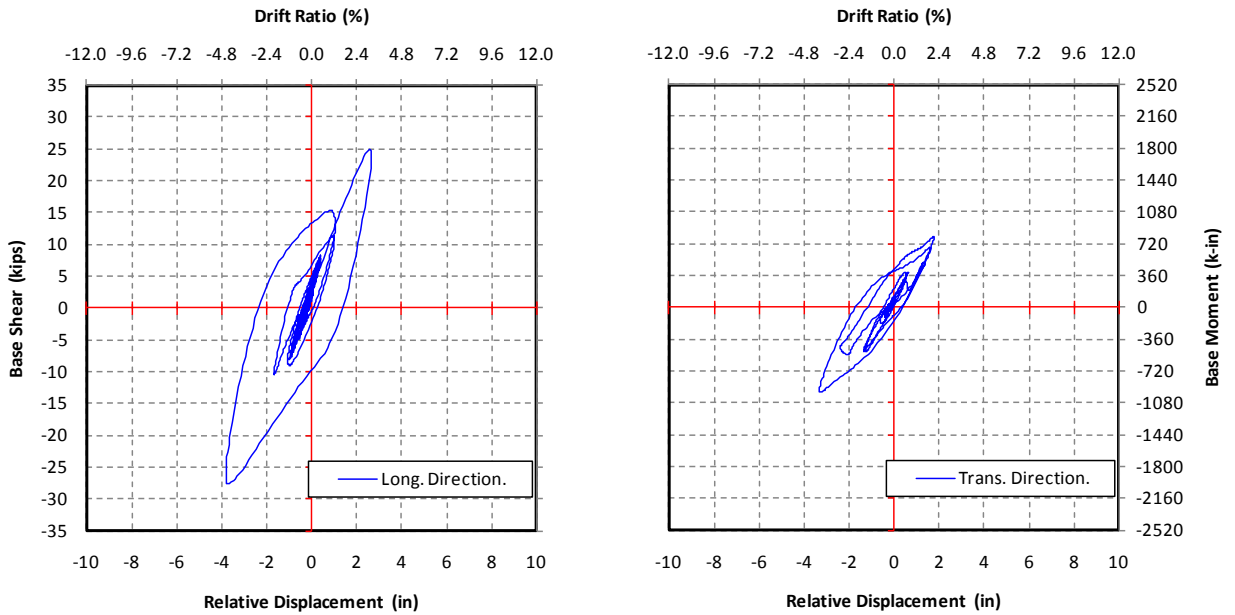


Figure 5-54 Base Shear-Displacement Hysteresis, Specimen I2 (0.8xSYL)

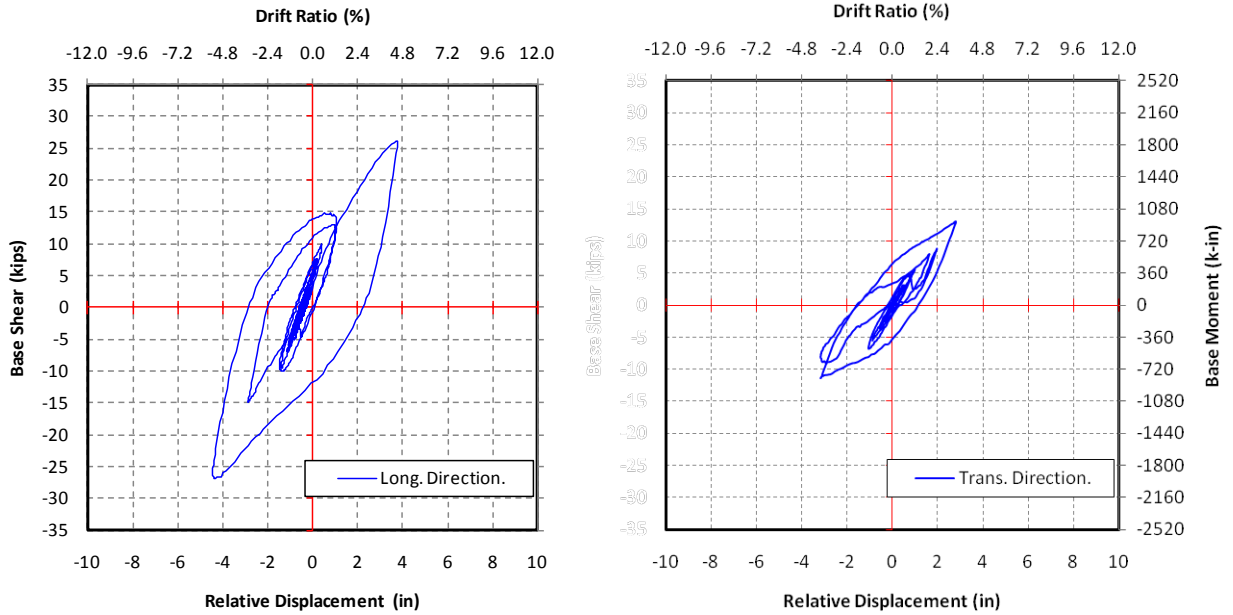


Figure 5-55 Base Shear-Displacement Hysteresis, Specimen I2 (1.0xSYL)

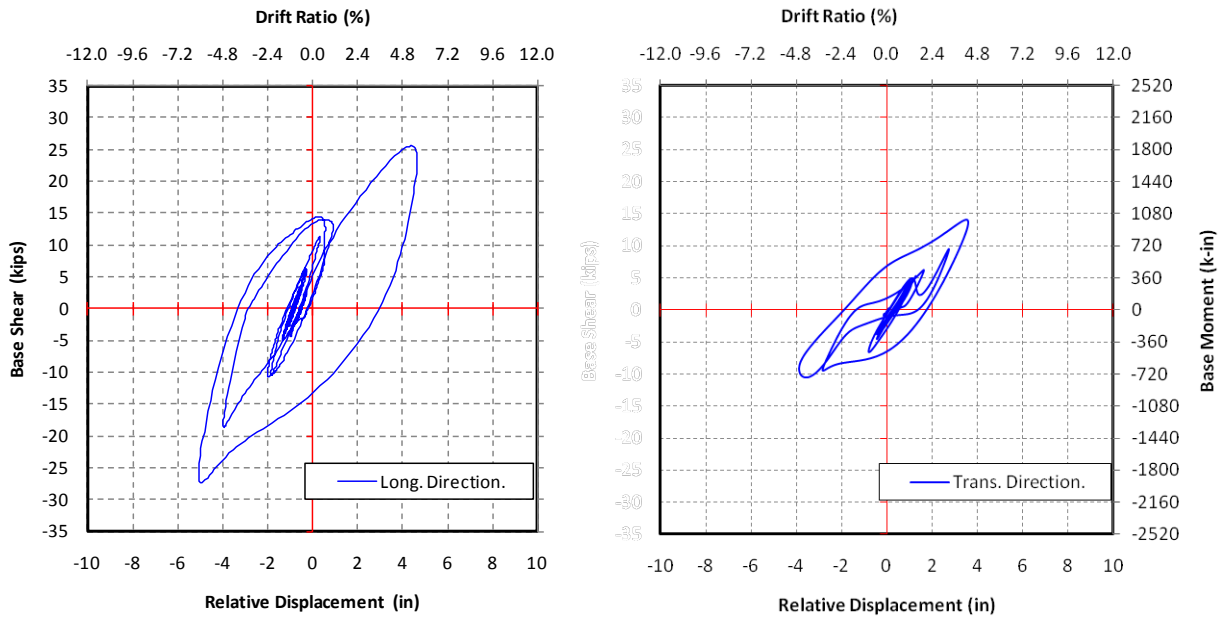
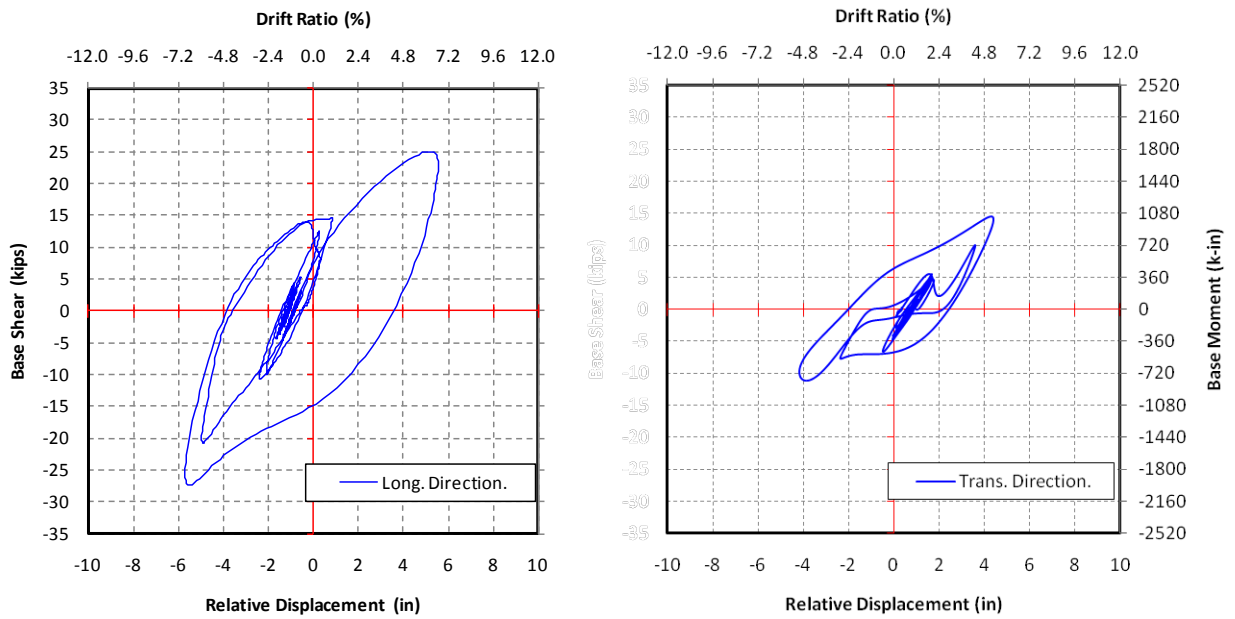
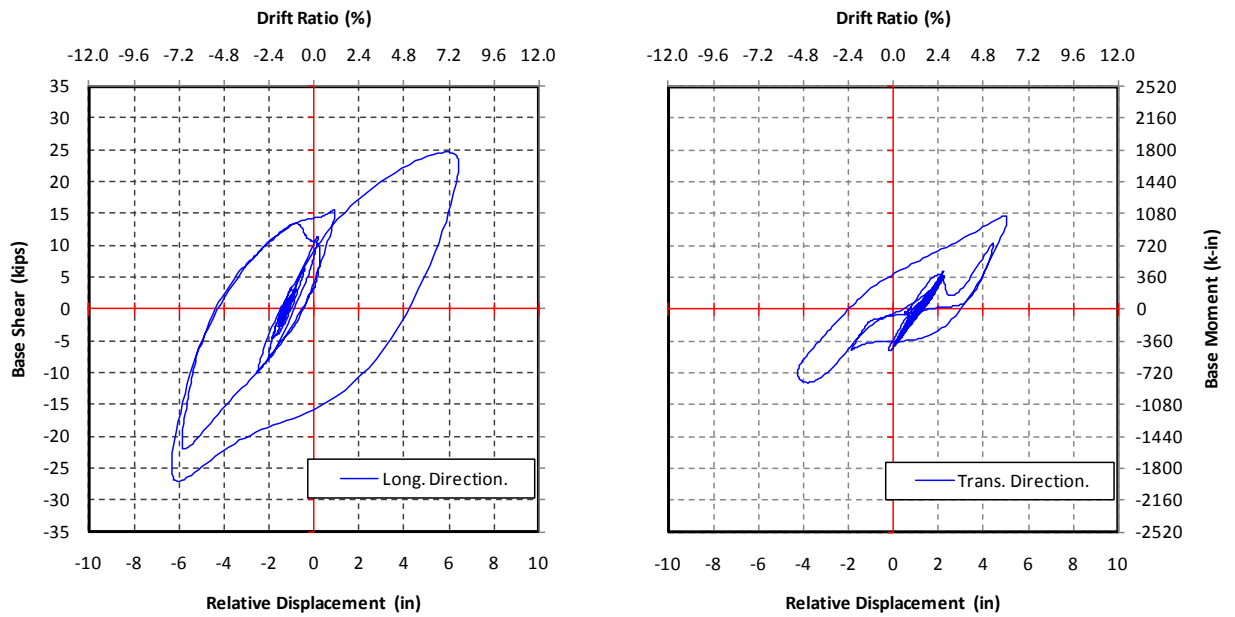


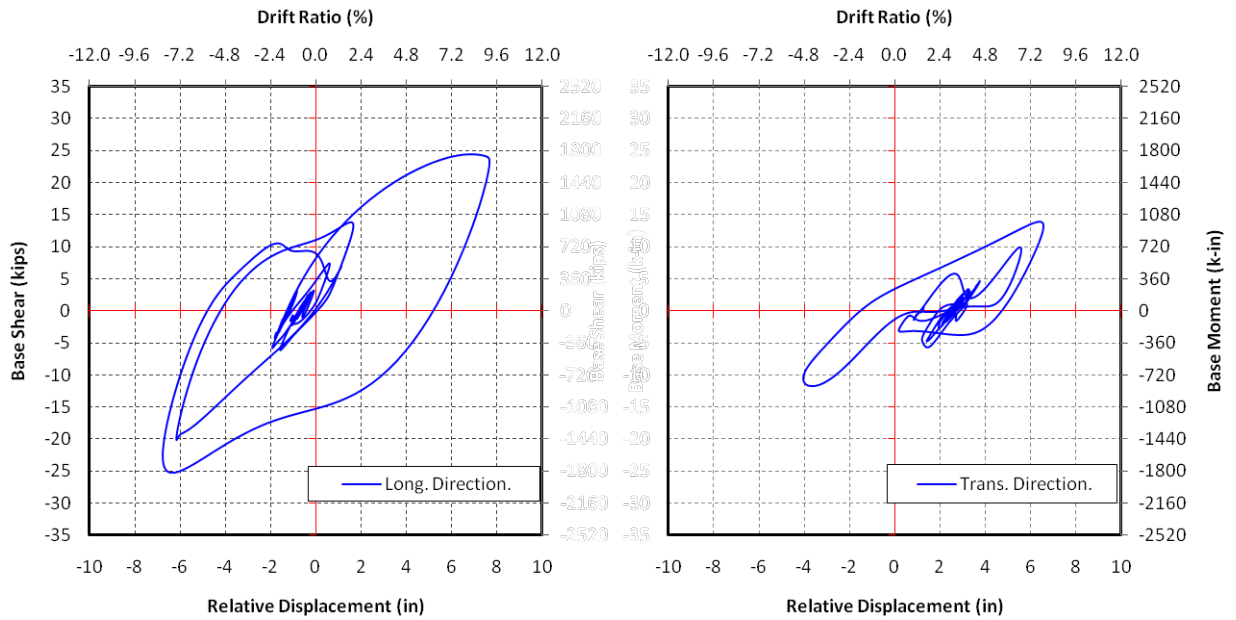
Figure 5-56 Base Shear-Displacement Hysteresis, Specimen I2 (1.2xSYL)



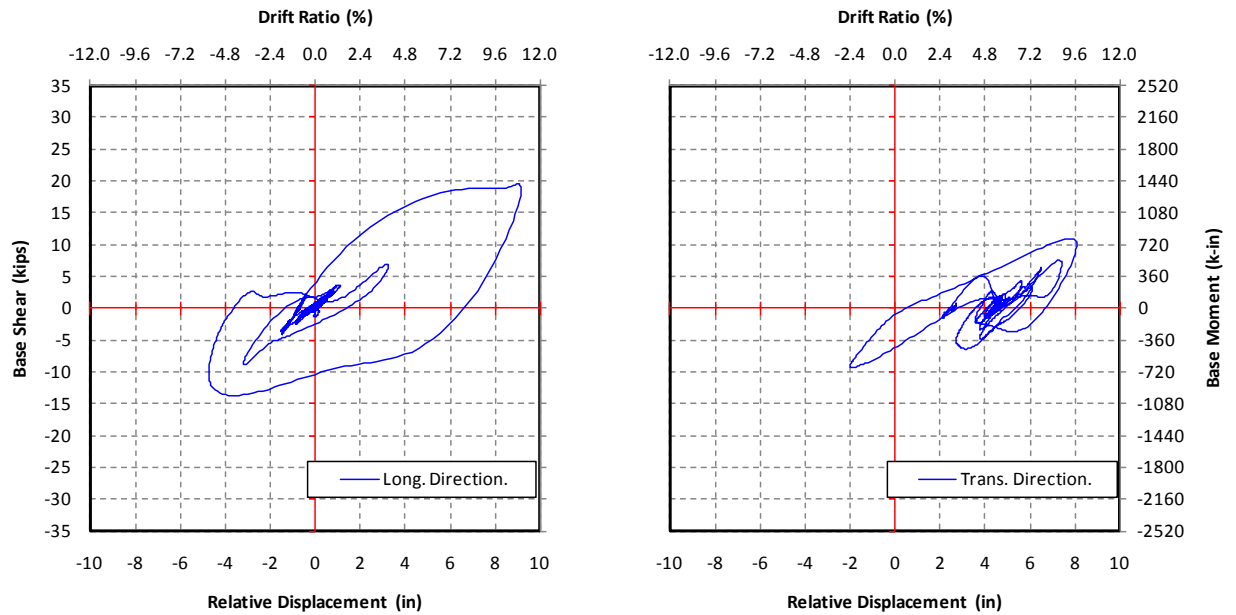
**Figure 5-57 Base Shear-Displacement Hysteresis, Specimen I2 (1.4xSYL)**



**Figure 5-58 Base Shear-Displacement Hysteresis, Specimen I2 (1.6xSYL)**



**Figure 5-59 Base Shear-Displacement Hysteresis, Specimen I2 (1.8xSYL)**



**Figure 5-60 Base Shear-Displacement Hysteresis, Specimen I2 (1.8\*xSYL)**



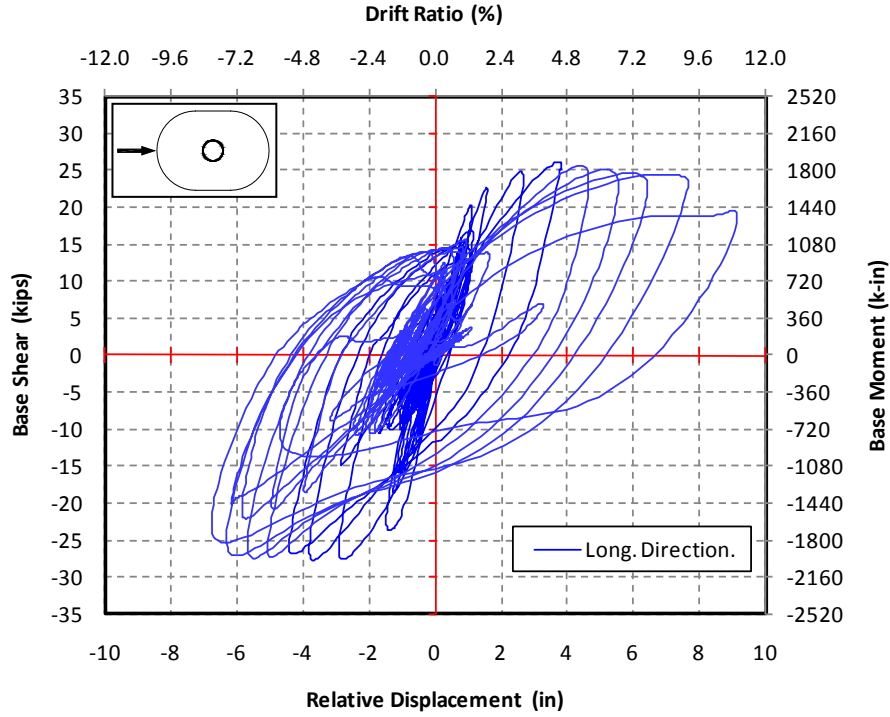


Figure 5-61 Cumulative Base Shear-Displacement Hysteresis, Specimen I2 (Longitudinal)

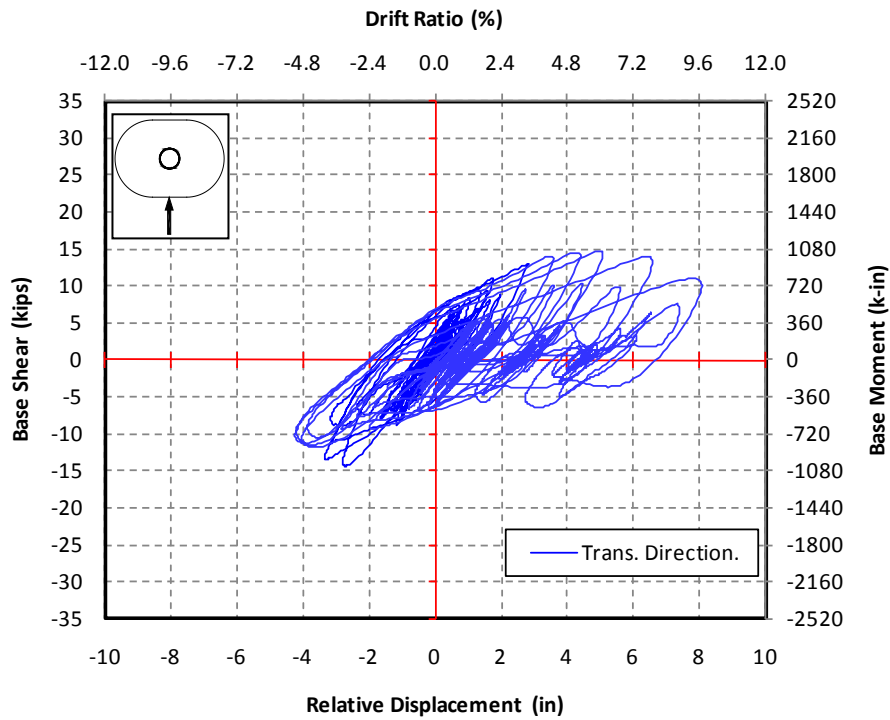


Figure 5-62 Cumulative Base Shear-Displacement Hysteresis, Specimen I2 (Transverse)

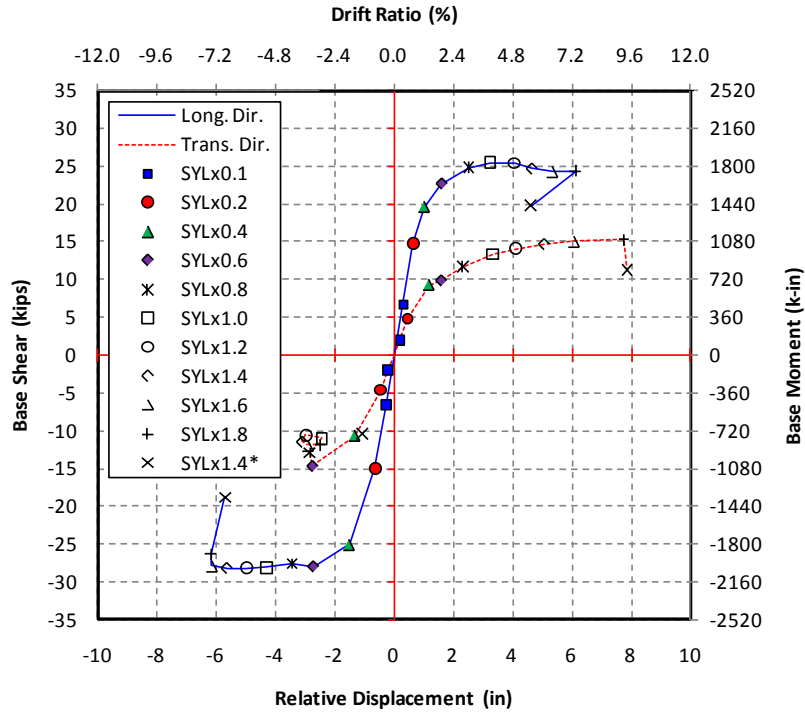


Figure 5-63 Envelope of Cumulative Base Shear-Displacement Hysteresis, Specimen I1

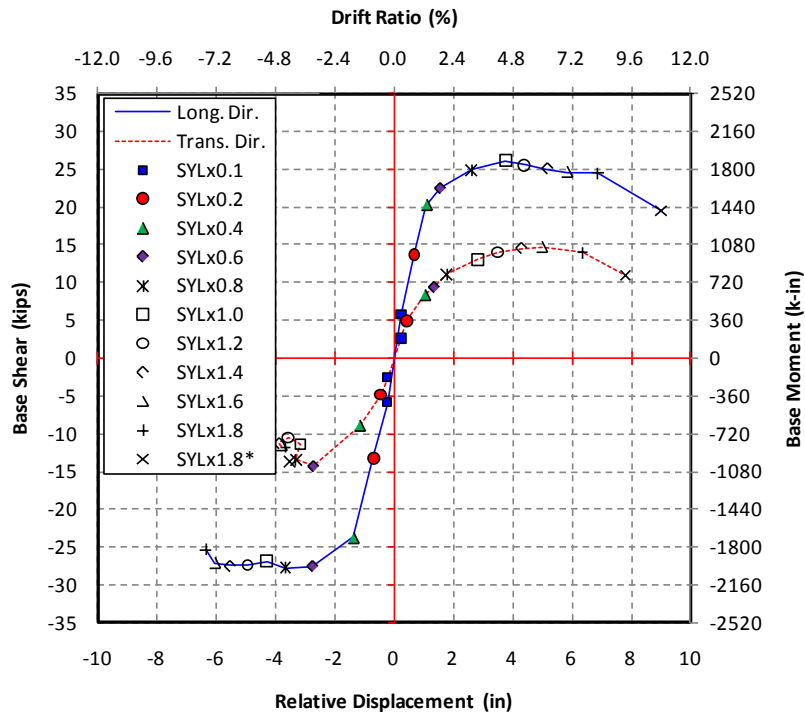
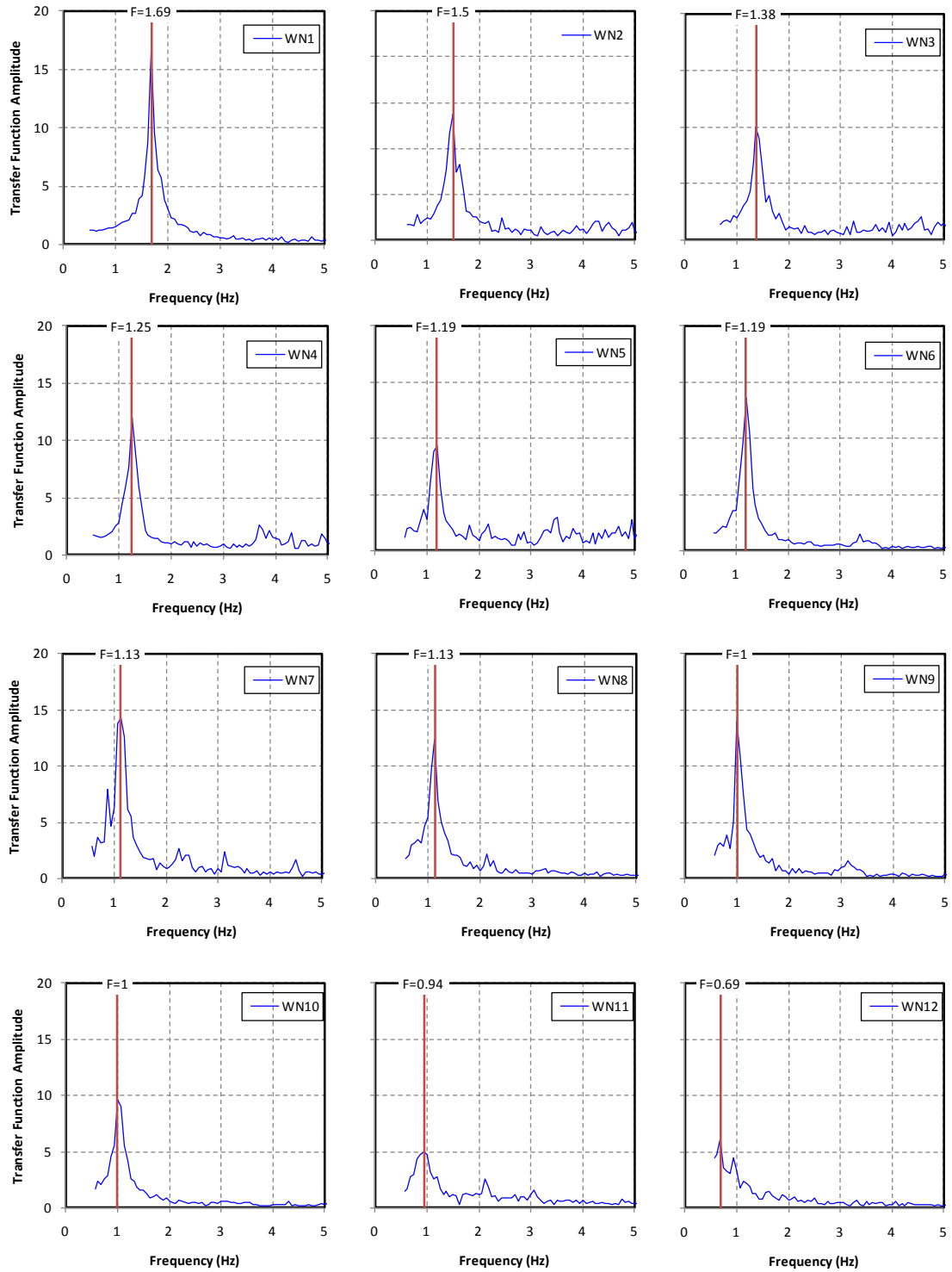
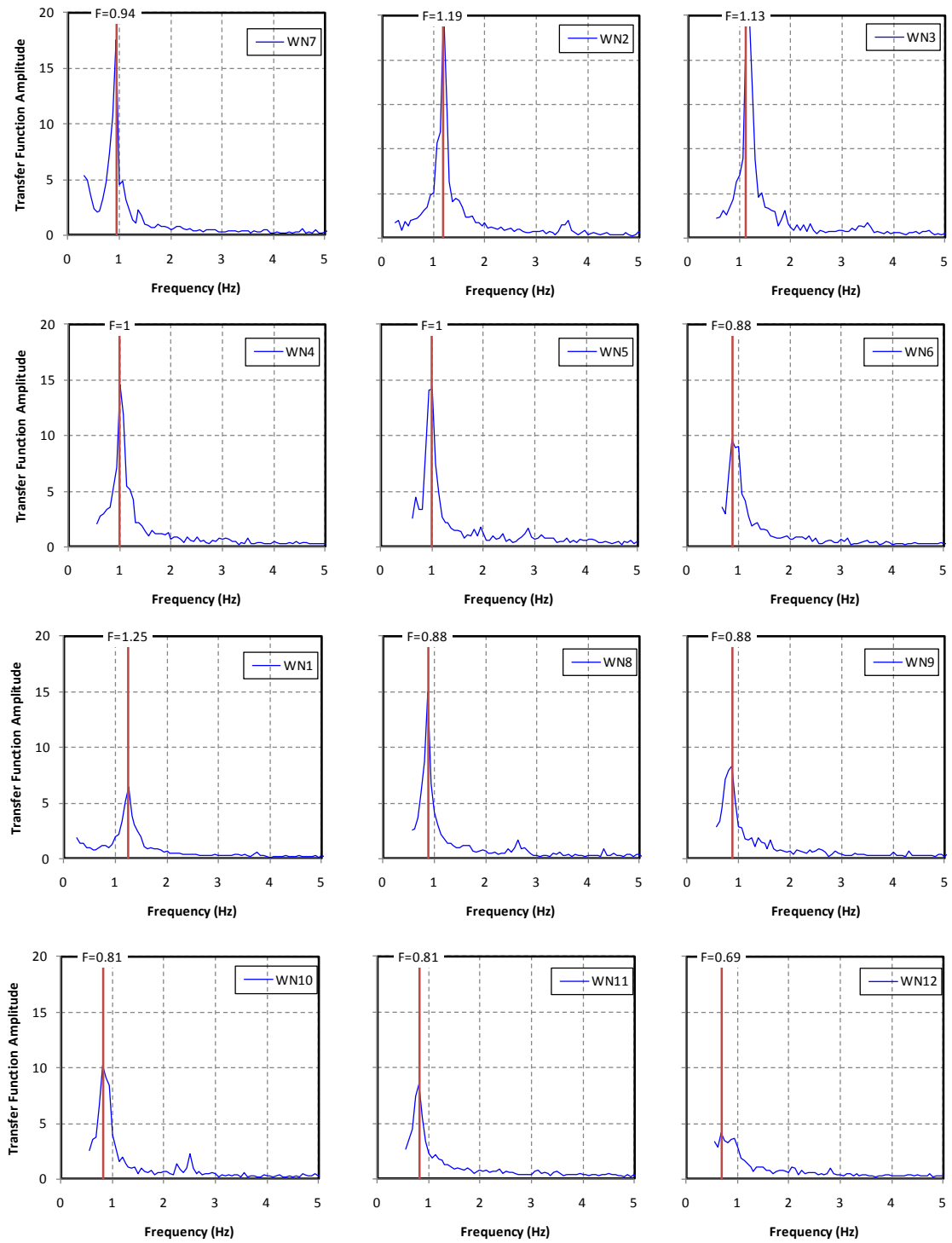


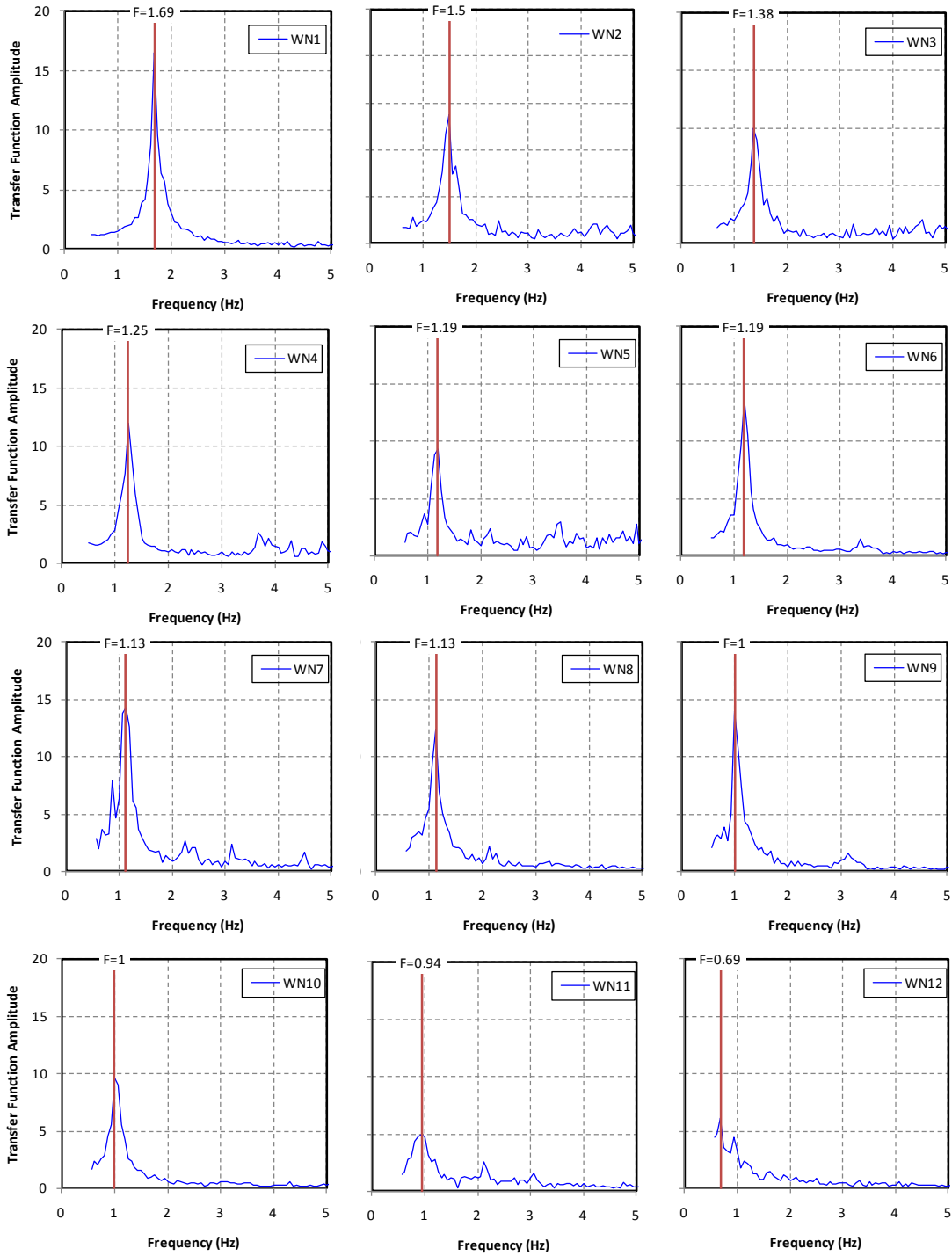
Figure 5-64 Envelope of Cumulative Base Shear-Displacement Hysteresis, Specimen I2



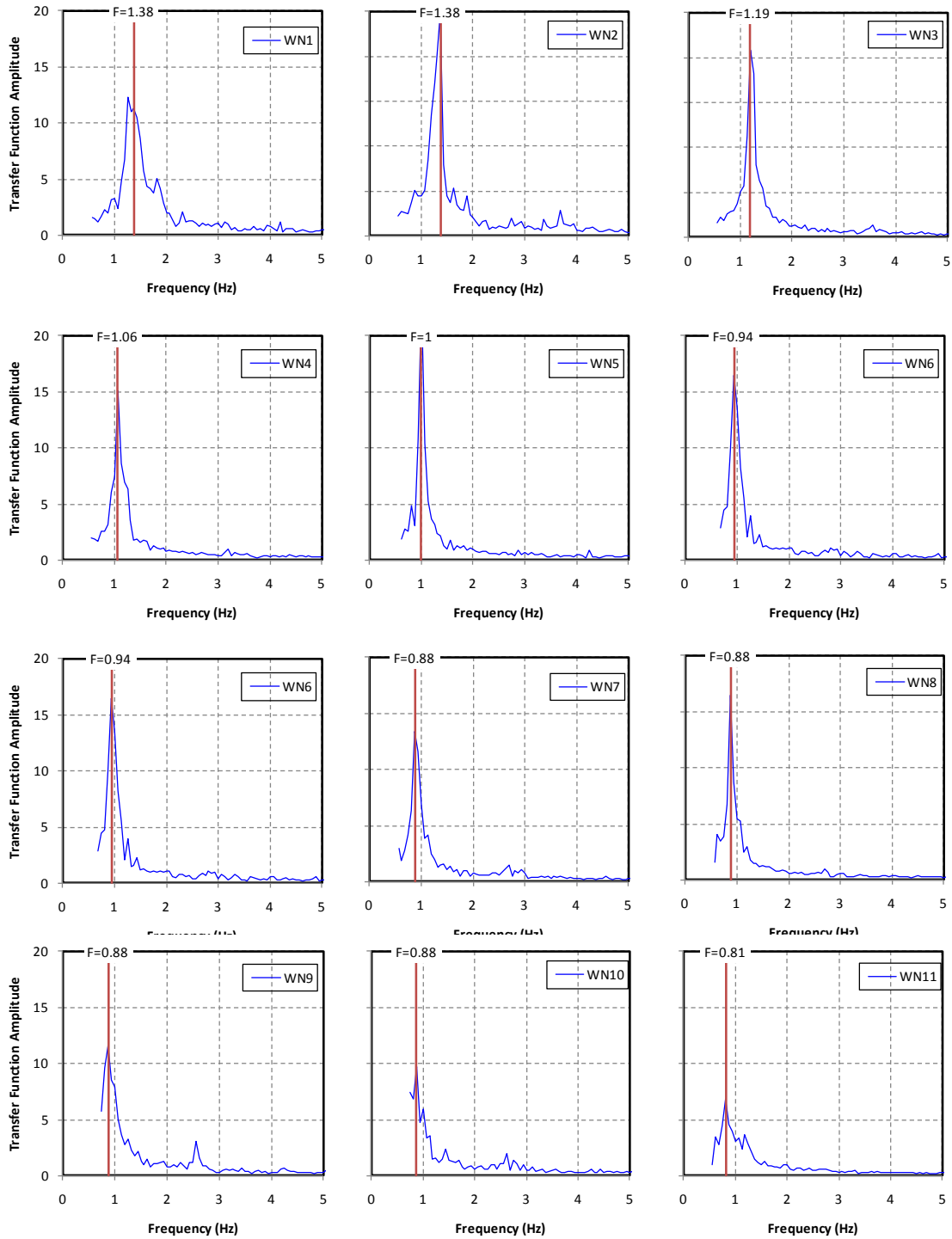
**Figure 5-65 Power Spectral Density and Natural Frequencies, Specimen I1 (Longitudinal Direction)**



**Figure 5-66 Power Spectral Density and Natural Frequencies, Specimen I1 (Transverse Direction)**



**Figure 5-67 Power Spectral Density and Natural Frequencies, Specimen I2 (Longitudinal Direction)**



**Figure 5-68 Power Spectral density and natural Frequencies, specimen I2 (Transverse Direction)**

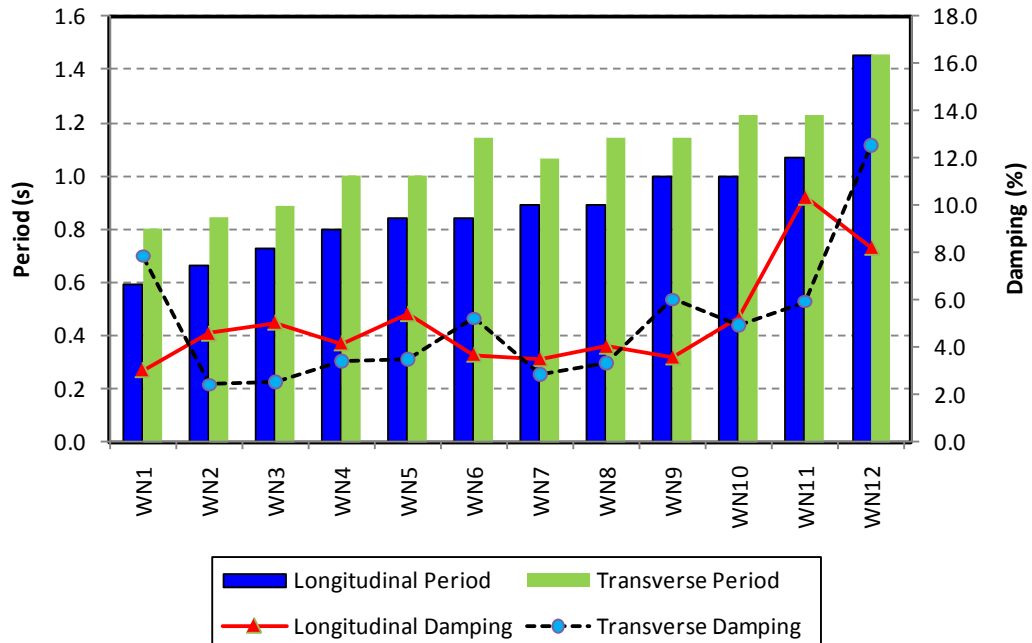


Figure 5-69 Variation in the Dynamic Properties Measured using Power Spectrum, Col. I1

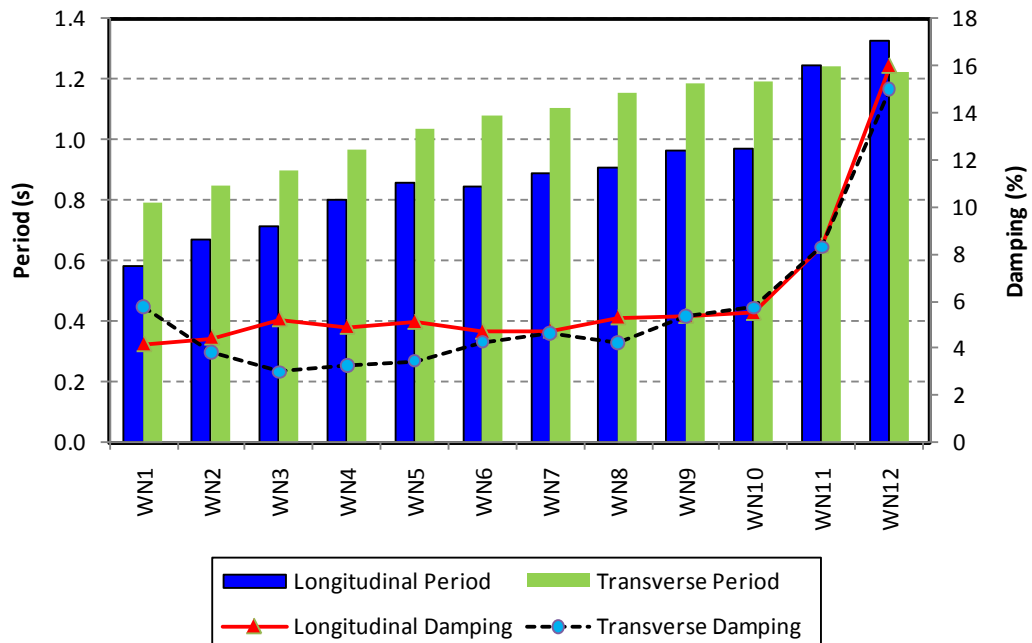


Figure 5-70 Variation in the Dynamic Properties Measured using MIMO, Col. I1

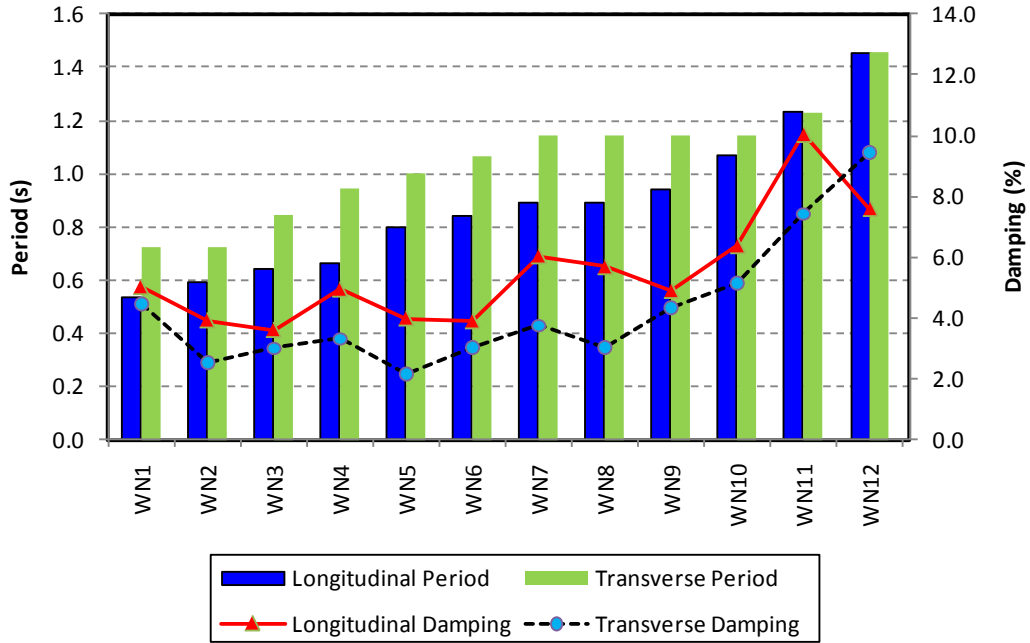


Figure 5-71 Variation in the Dynamic Properties Measured using Power Spectrum, Col. I2

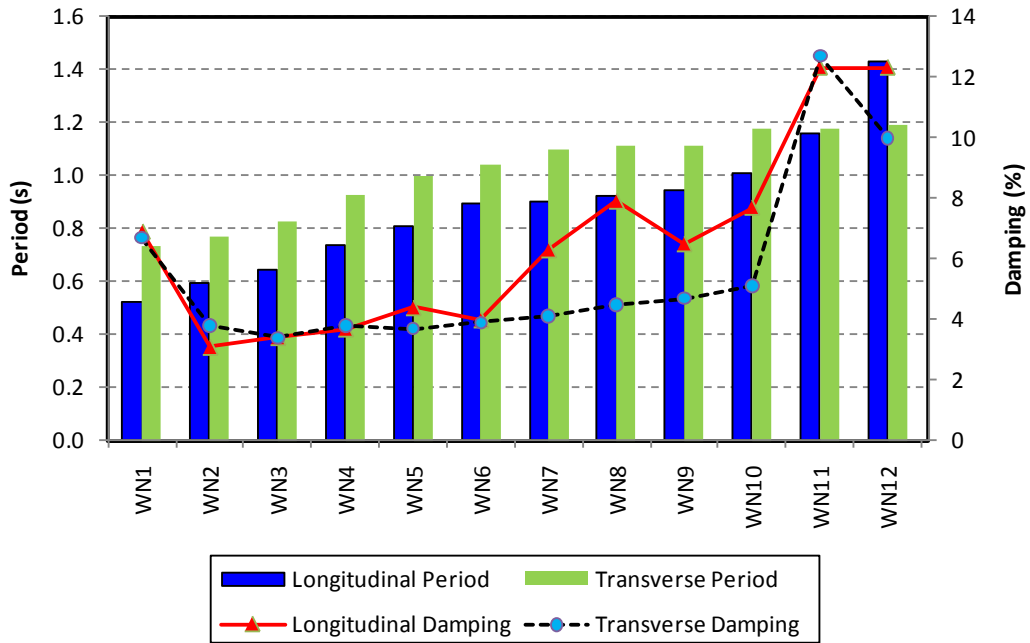


Figure 5-72 Variation in the Dynamic Properties Measured using MIMO, Col. I2



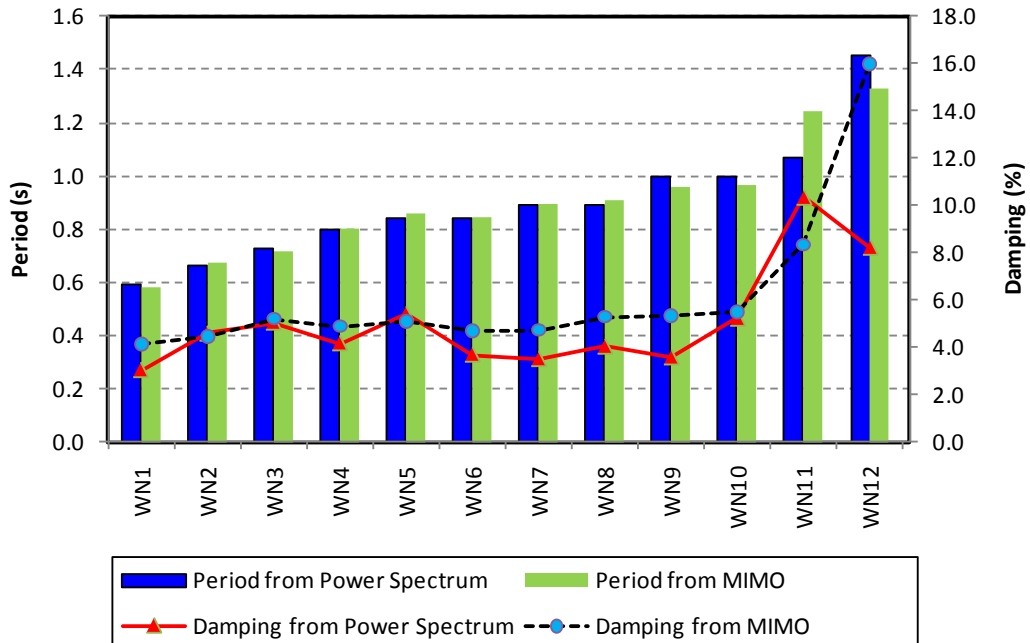


Figure 5-73 Comparison between the Dynamic Properties Measured using Power Spectrum and MIMO, Specimen I1 (Longitudinal Direction)

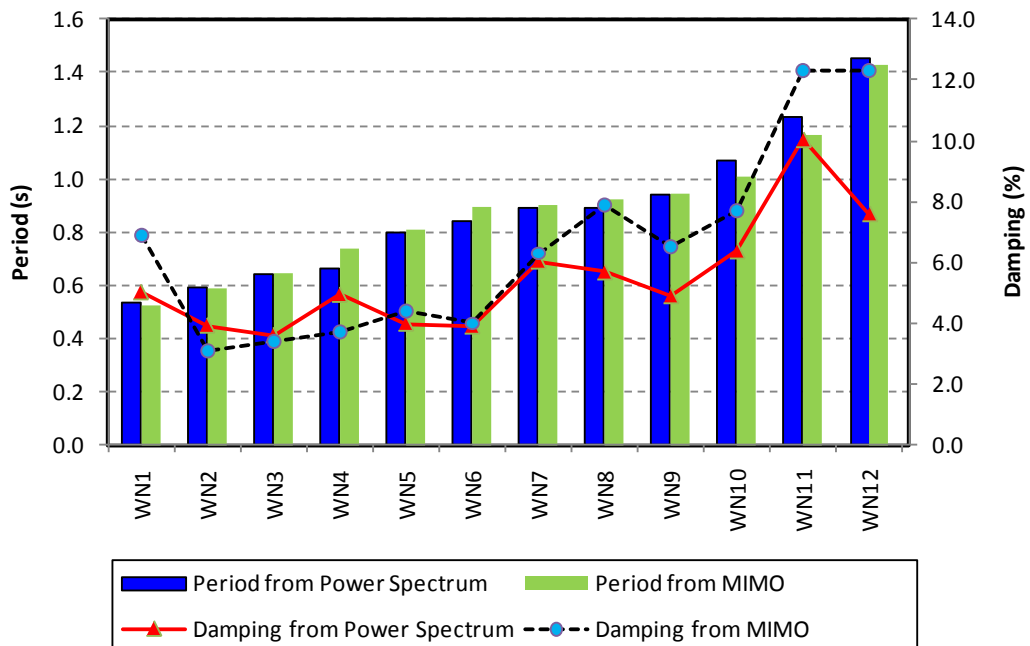


Figure 5-74 Comparison between the Dynamic Properties Measured using Power Spectrum and MIMO, Specimen I2 (Longitudinal Direction)

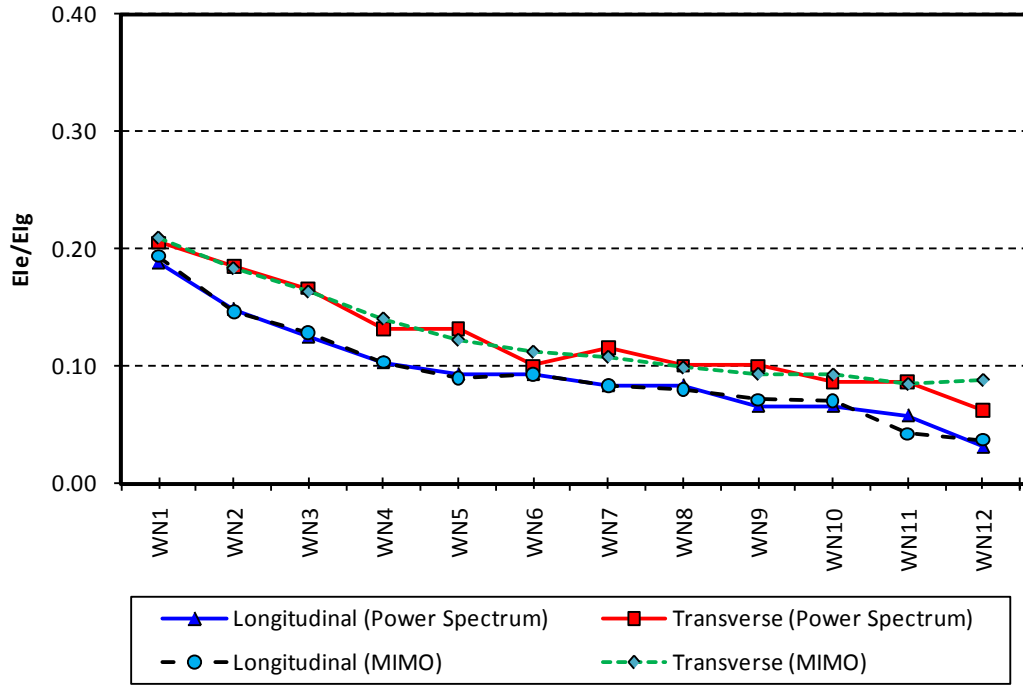


Figure 5-75 Variation in Effective Stiffness, Specimen I1

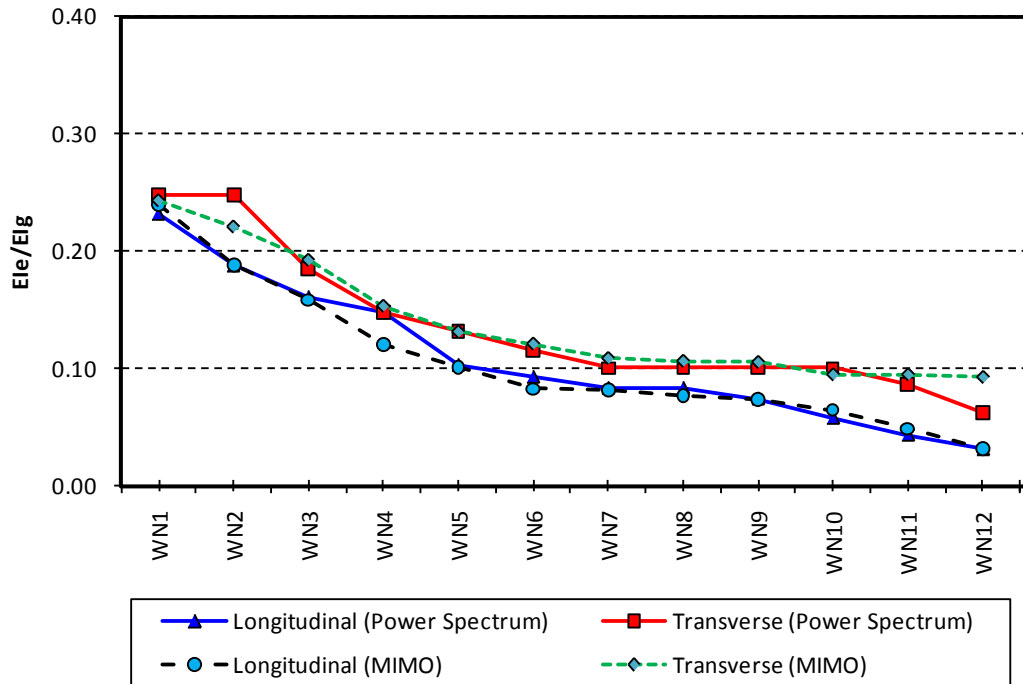


Figure 5-76 Variation in Effective Stiffness, Specimen I2

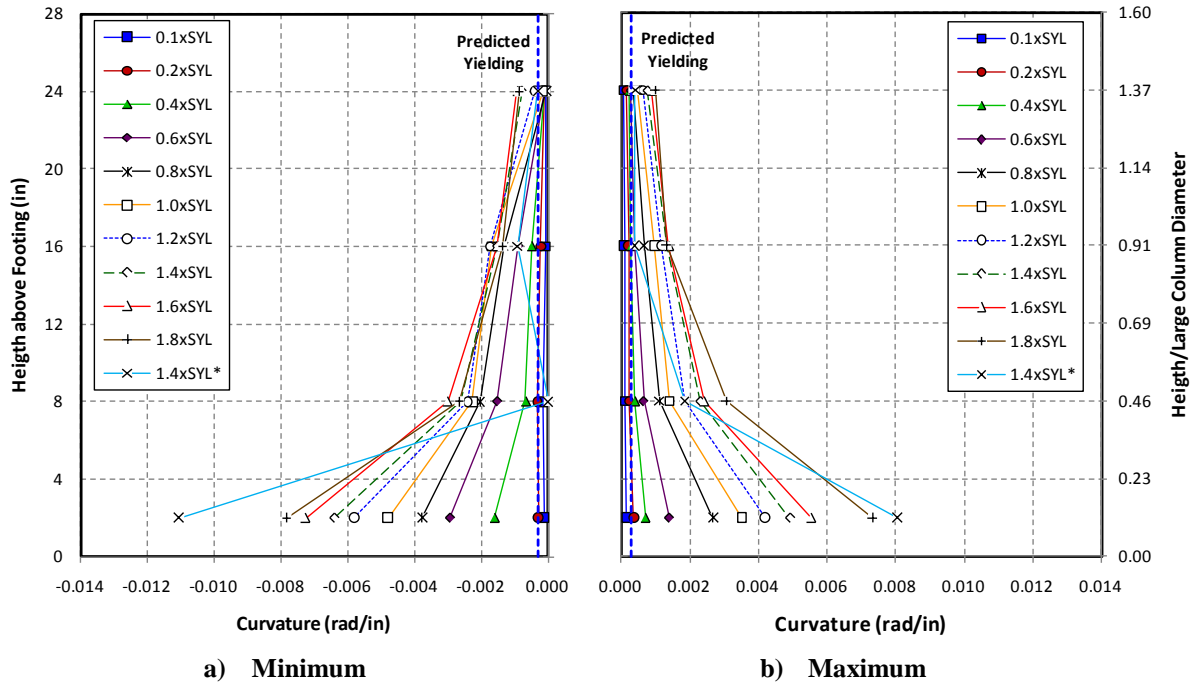


Figure 5-77 Curvature Profile along Longitudinal Direction, Specimen I1

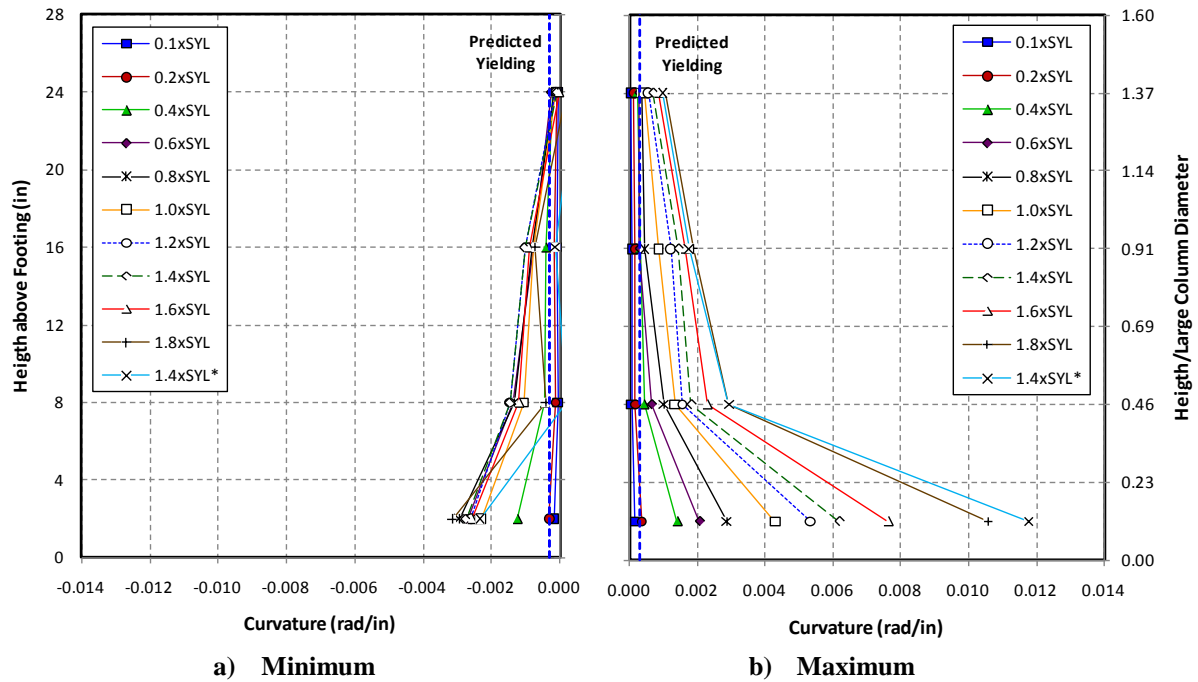


Figure 5-78 Curvature Profile along Transverse Direction, Specimen I1

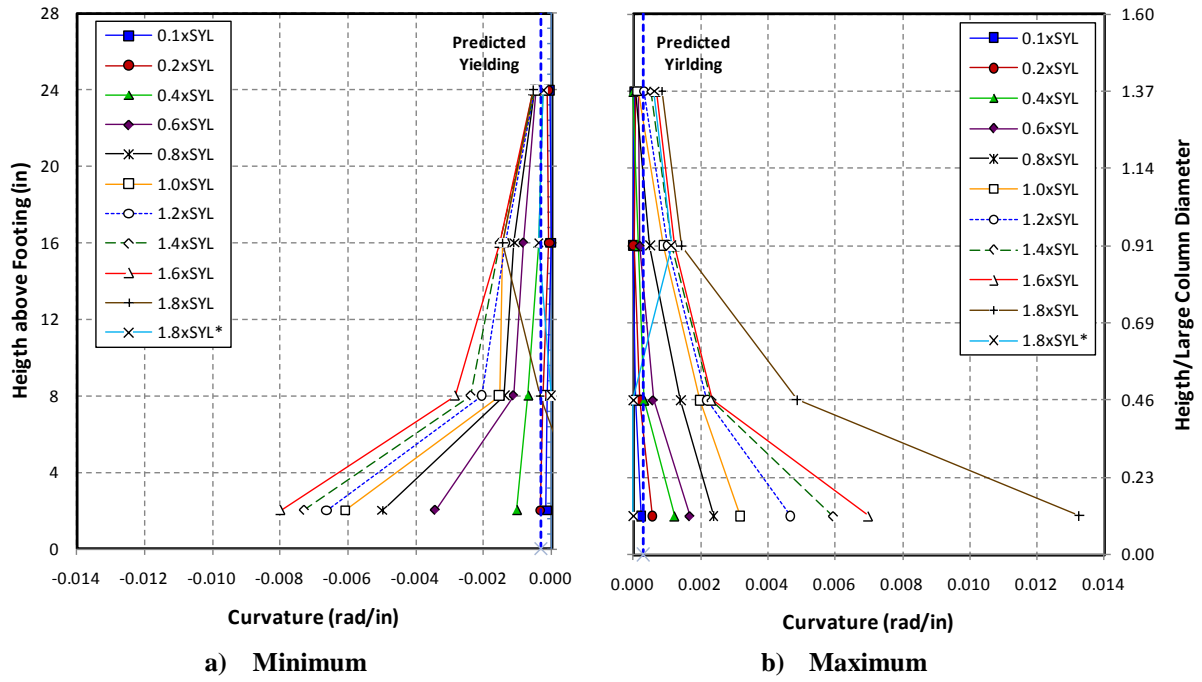


Figure 5-79 Curvature Profile along Longitudinal Direction, Specimen I2

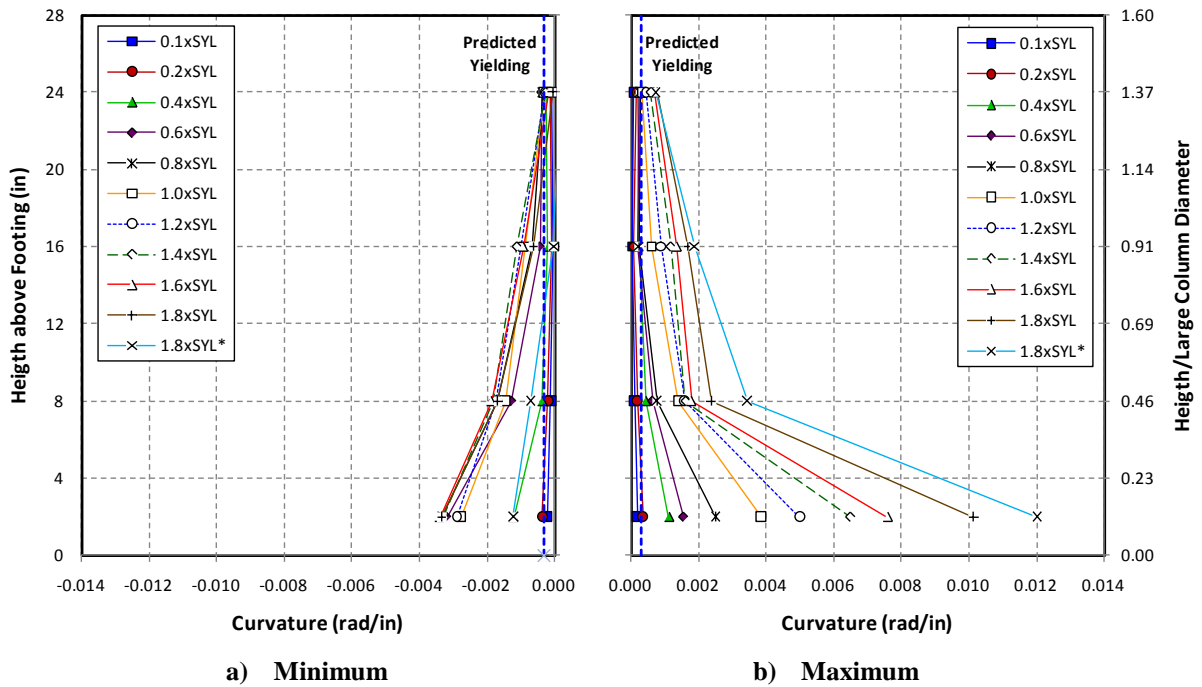
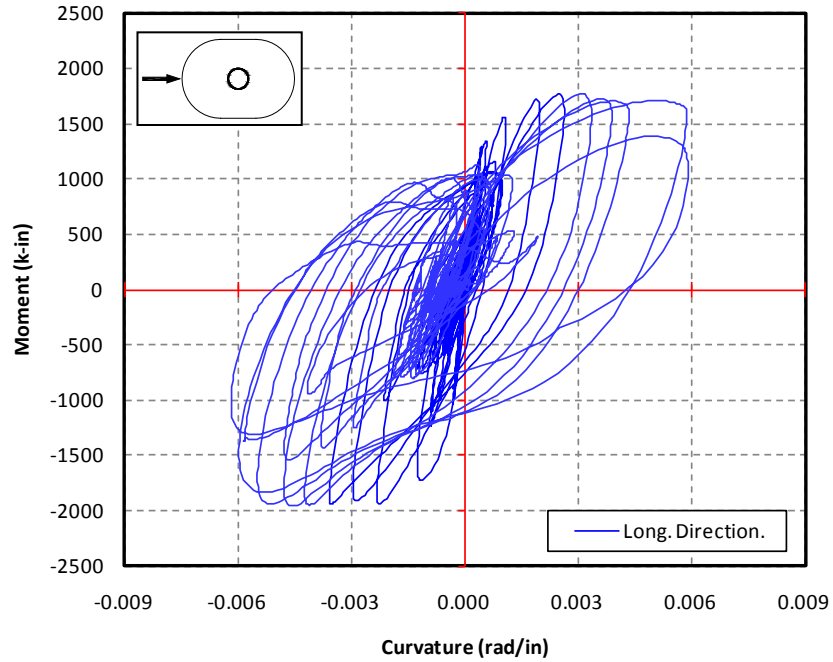
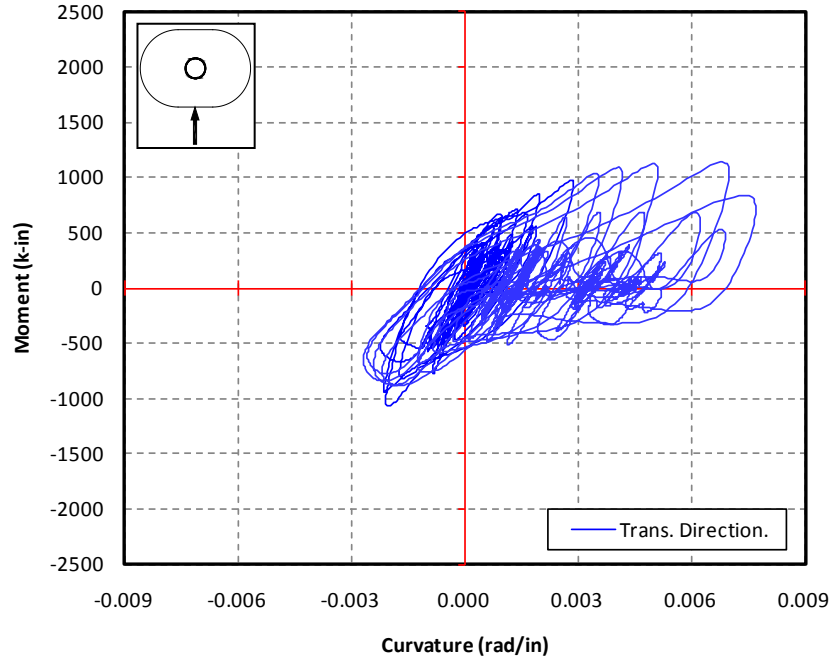


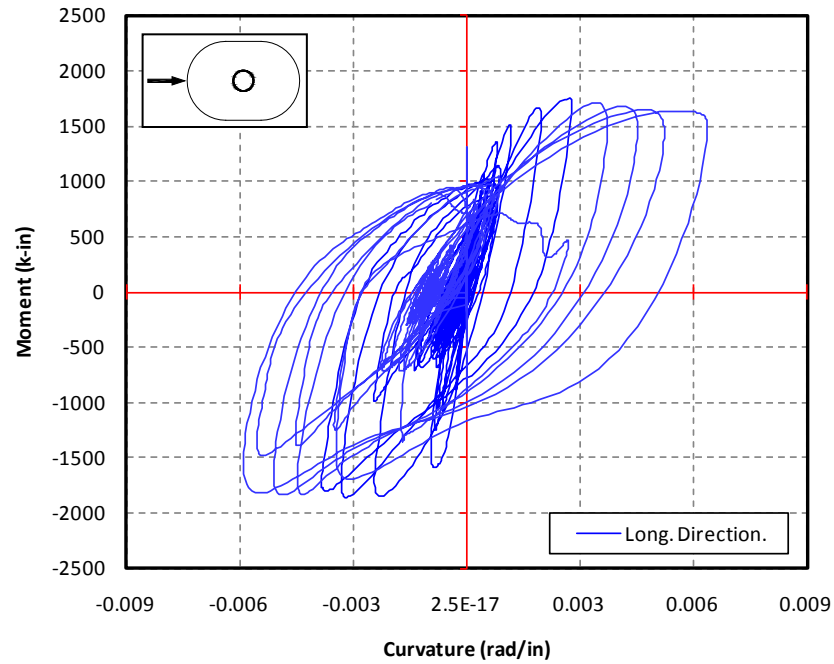
Figure 5-80 Curvature Profile along Transverse Direction, Specimen I2



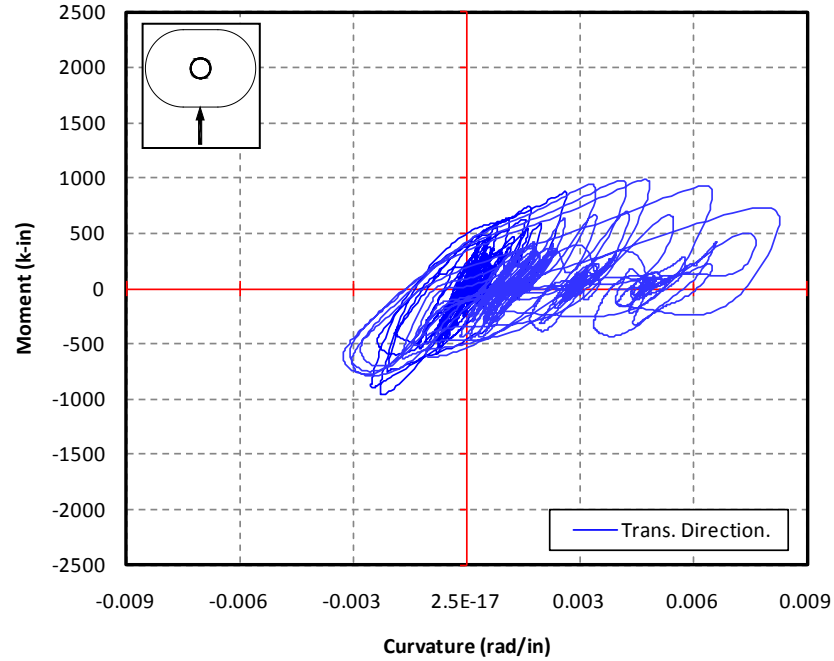
**Figure 5-81 Average Moment-Curvature Hysteresis Measured at 3 in. and 8 in., Specimen I1 (Longitudinal Direction)**



**Figure 5-82 Average Moment-Curvature Hysteresis Measured at 3 in. and 8 in., Specimen I1 (Transverse Direction)**



**Figure 5-83 Average Moment-Curvature Hysteresis Measured at 3 in. and 8 in., Specimen I2, (Longitudinal Direction)**



**Figure 5-84 Average Moment-Curvature Hysteresis Measured at 3 in. and 8 in., Specimen I2, (Transverse. Direction)**

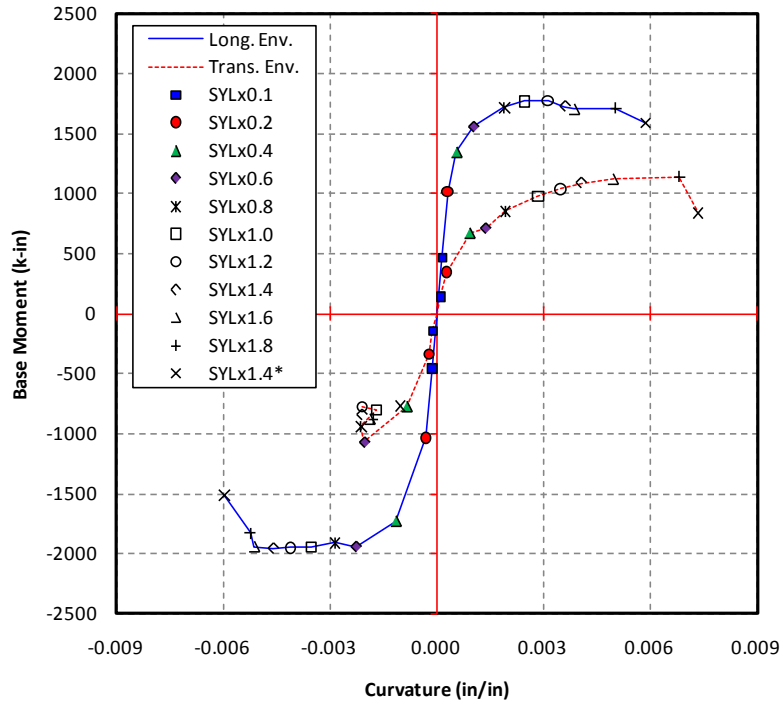


Figure 5-85 Average Moment-Curvature Envelope Measured at 3in. and 8 in., Specimen I1

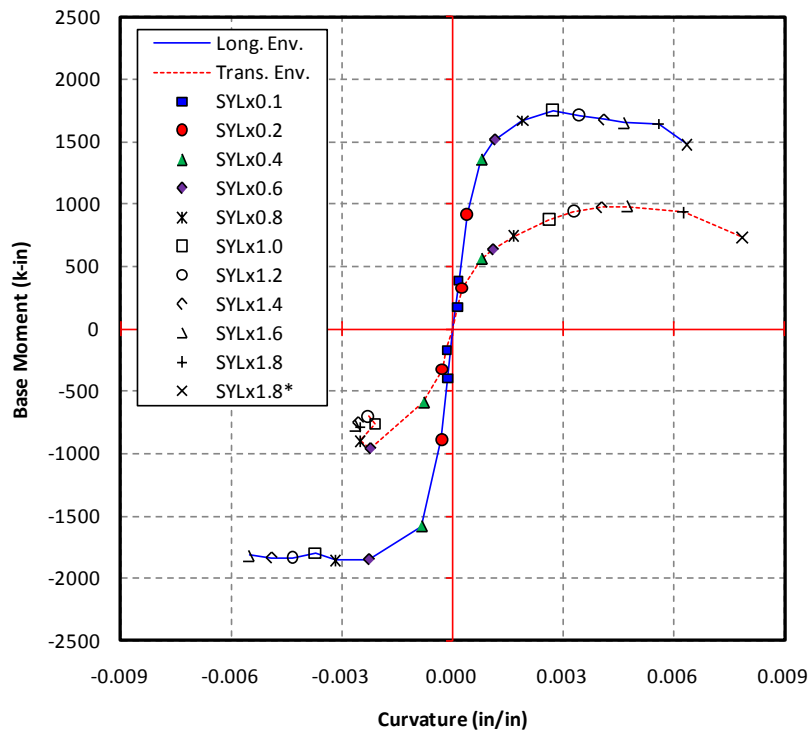
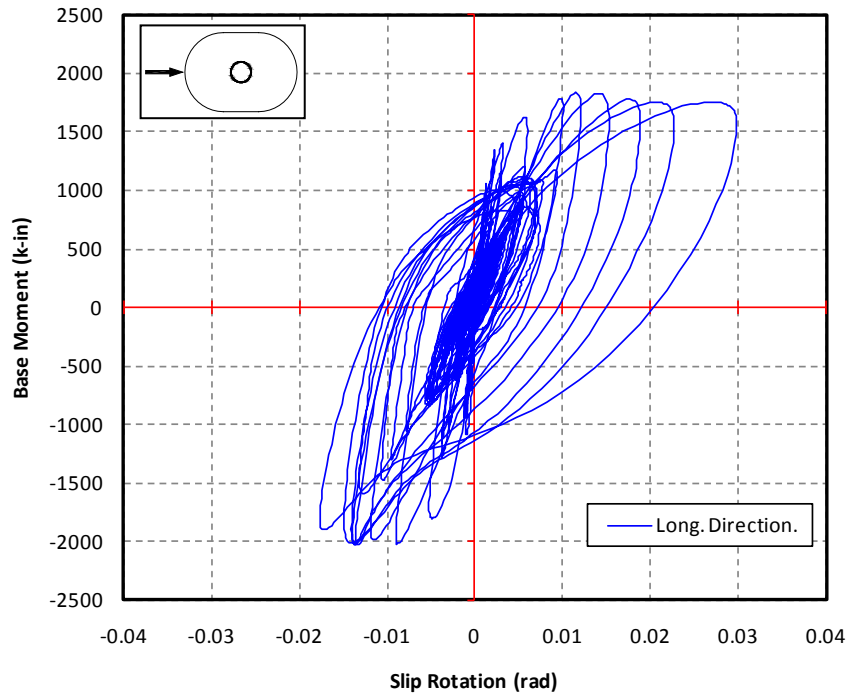
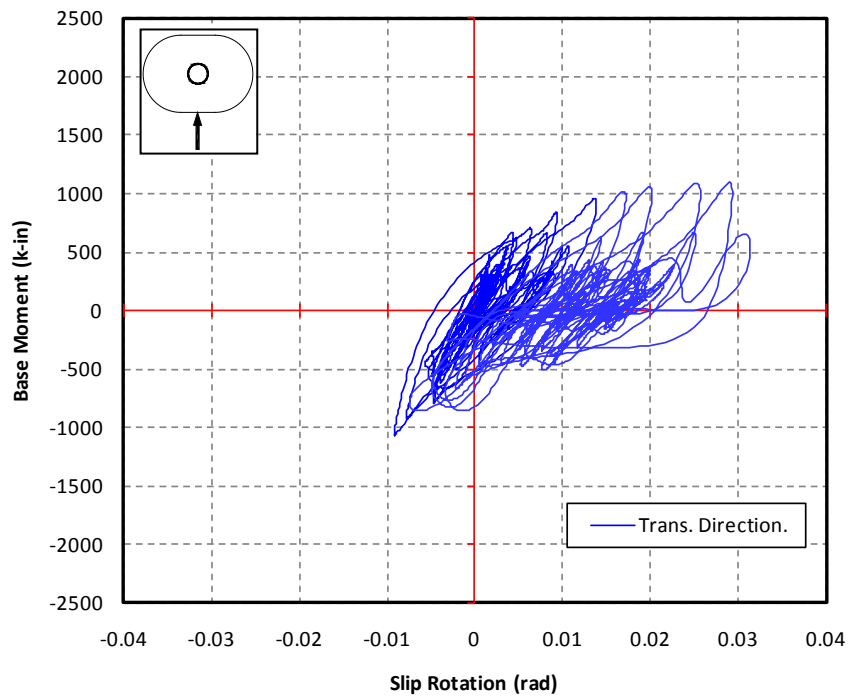


Figure 5-86 Average Moment-Curvature Envelope Measured at 3in. and 8 in., Specimen I2



**Figure 5-87 Base Moment – Bond Slip Rotation Hysteresis, I1 (Longitudinal Direction)**



**Figure 5-88 Base Moment – Bond Slip Rotation Hysteresis, I1 (Transverse Direction)**



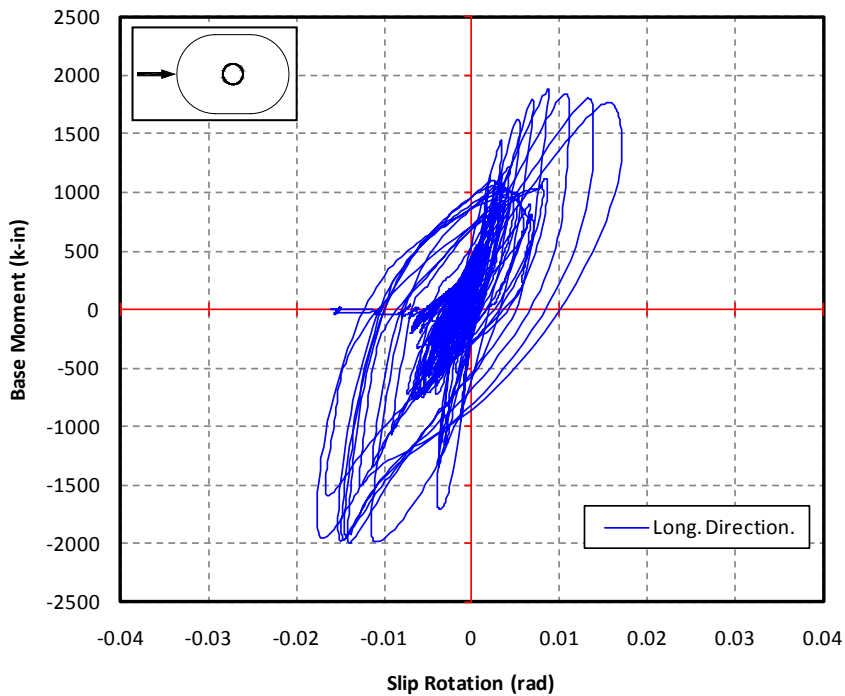


Figure 5-89 Base Moment – Bond Slip Hysteresis, I2 (Longitudinal Direction)

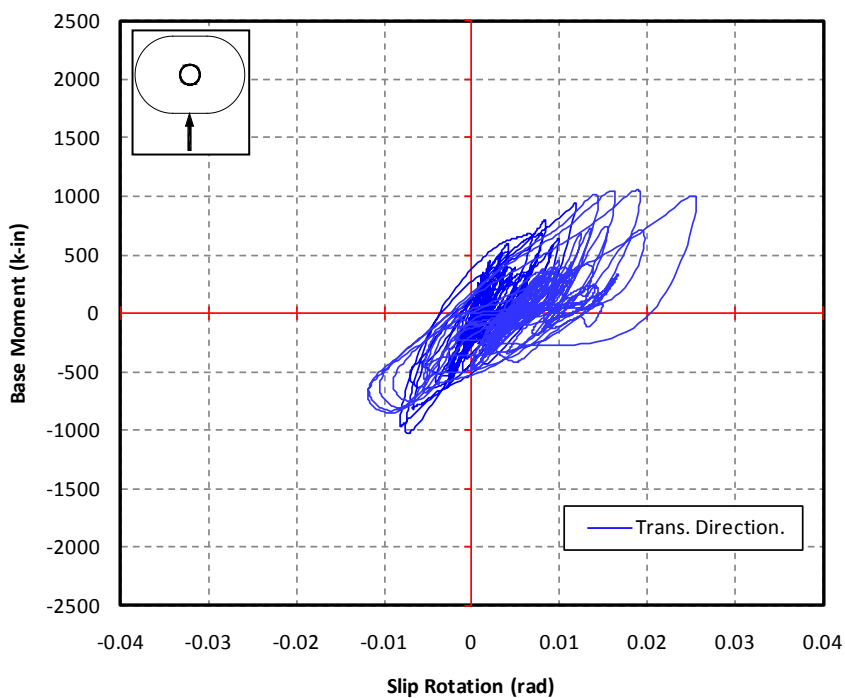


Figure 5-90 Base Moment – Bond Slip Hysteresis, I2 (Longitudinal Direction)

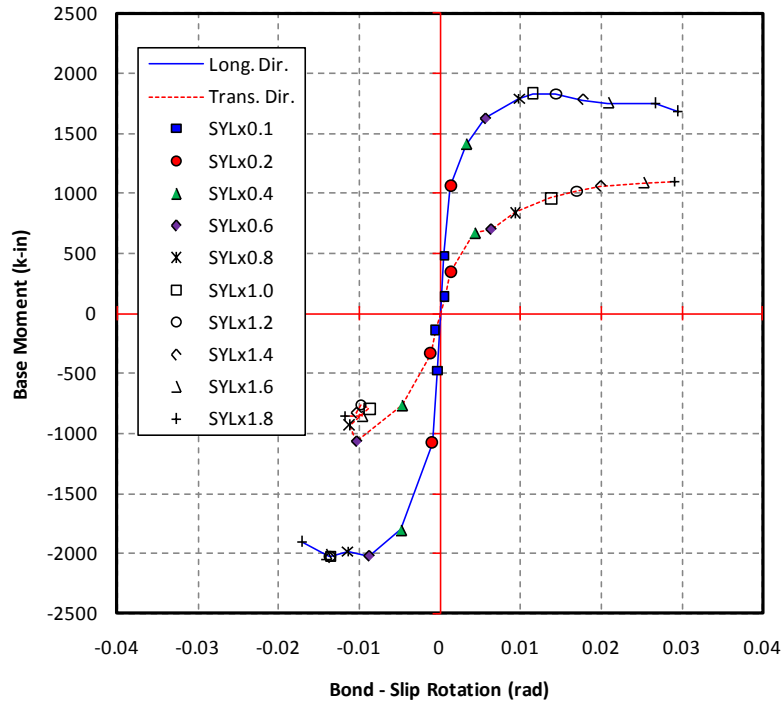


Figure 5-91 Base Moment – Bond Slip Rotation Backbone Envelope, I1

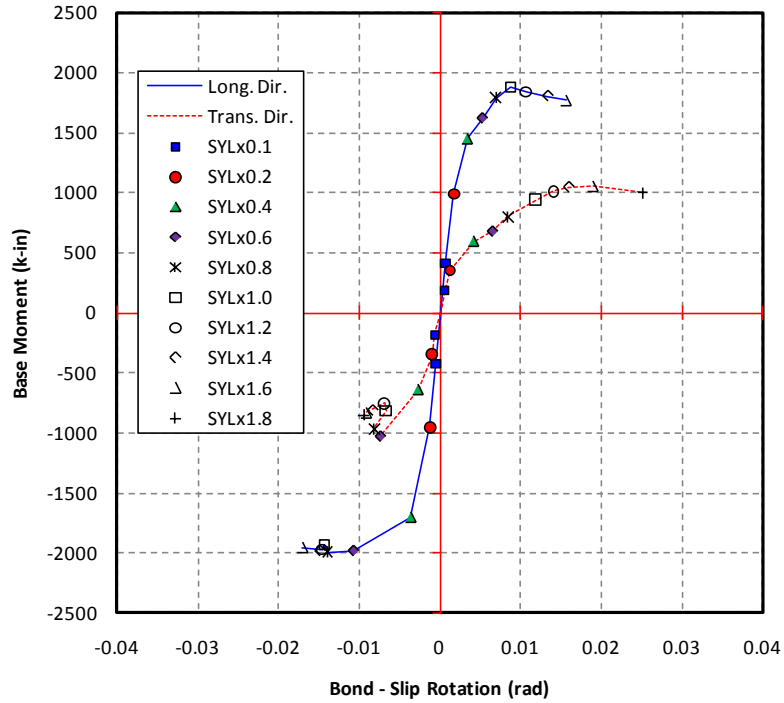
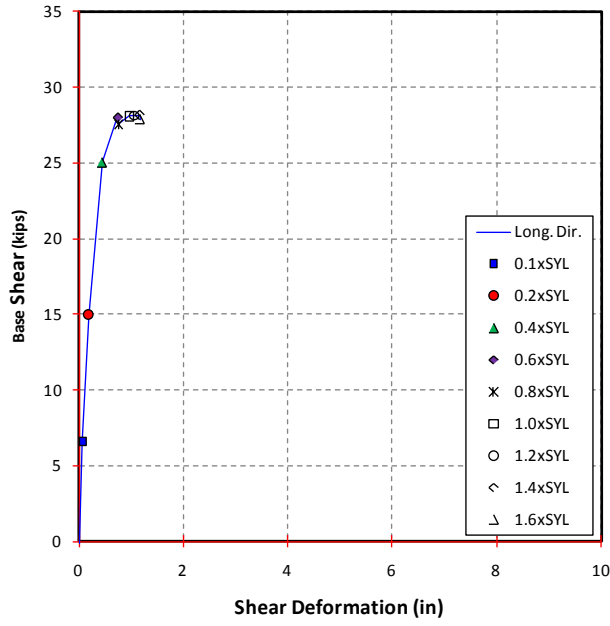
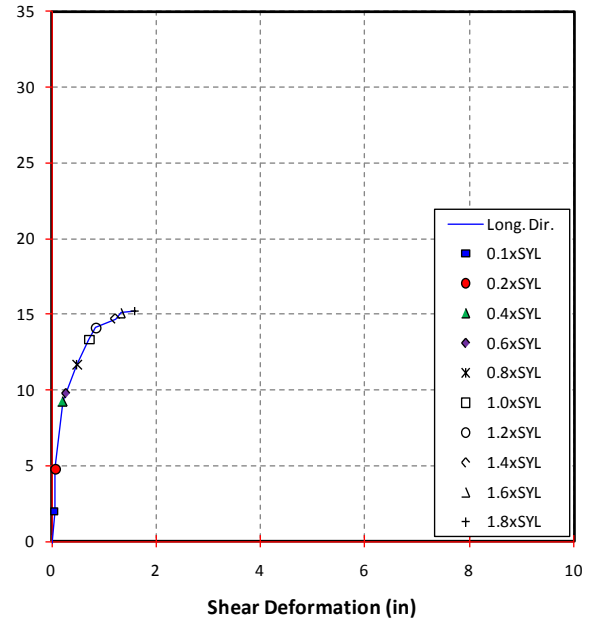


Figure 5-92 Base Moment – Bond Slip Rotation Backbone Envelope, I2

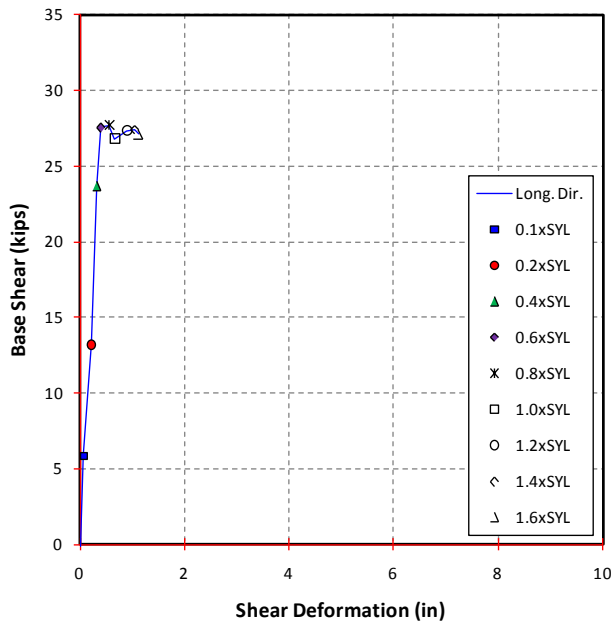


a) Longitudinal Direction

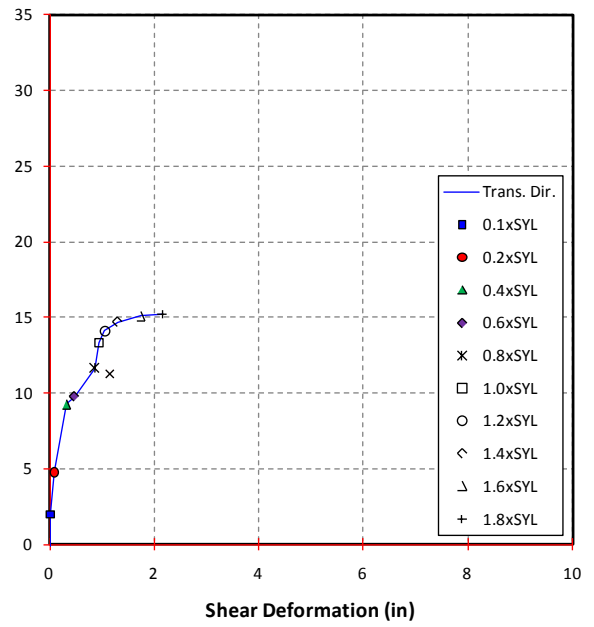


b) Transverse Direction

Figure 5-93 Shear Deformation for Specimen I1



a) Longitudinal Direction



b) Transverse Direction

Figure 5-94 Shear Deformation for Specimen I2

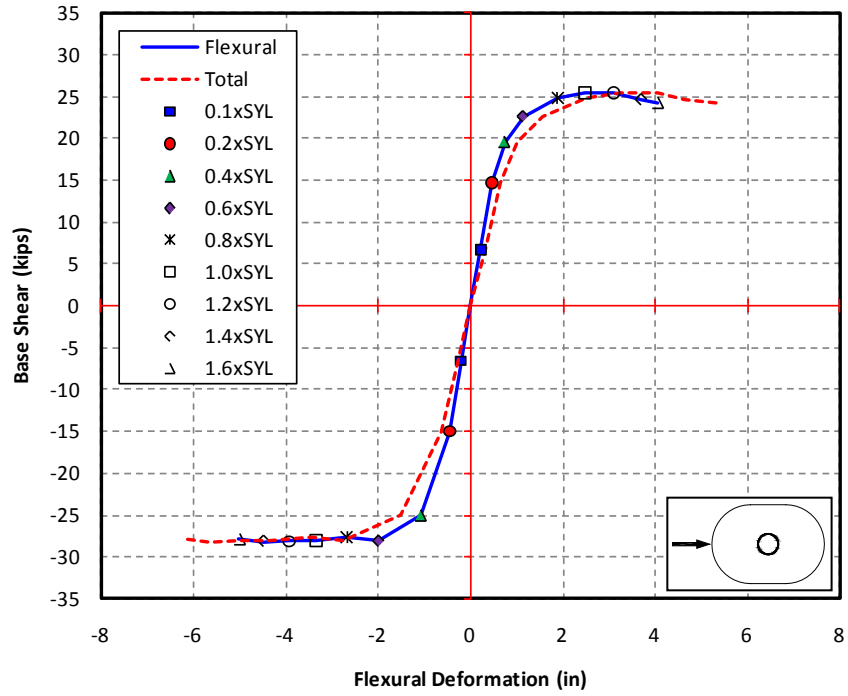


Figure 5-95 Contribution of Flexion to Total Deflexion, Specimen I1

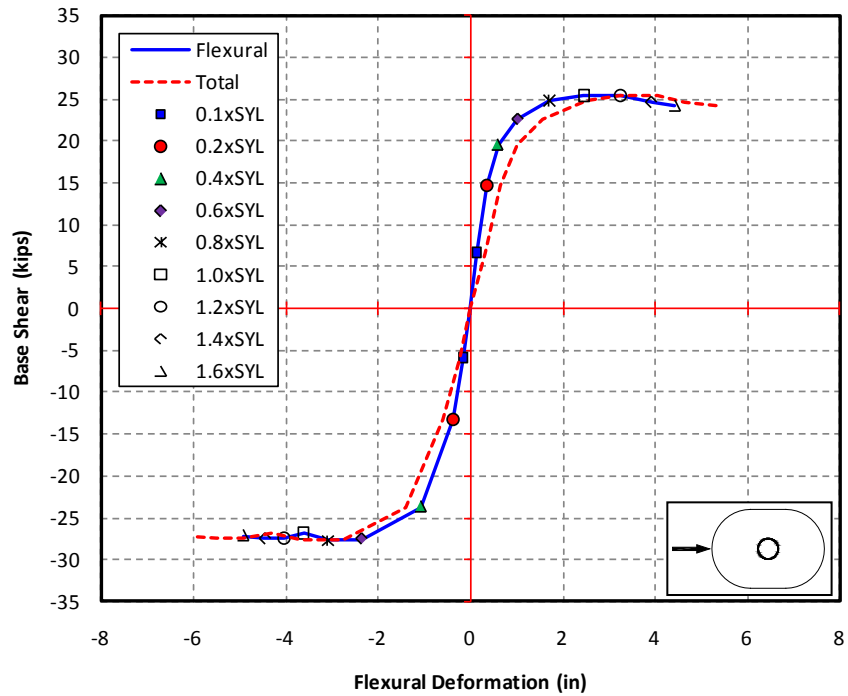


Figure 5-96 Contribution of Flexion to Total Deflexion, Specimen I2

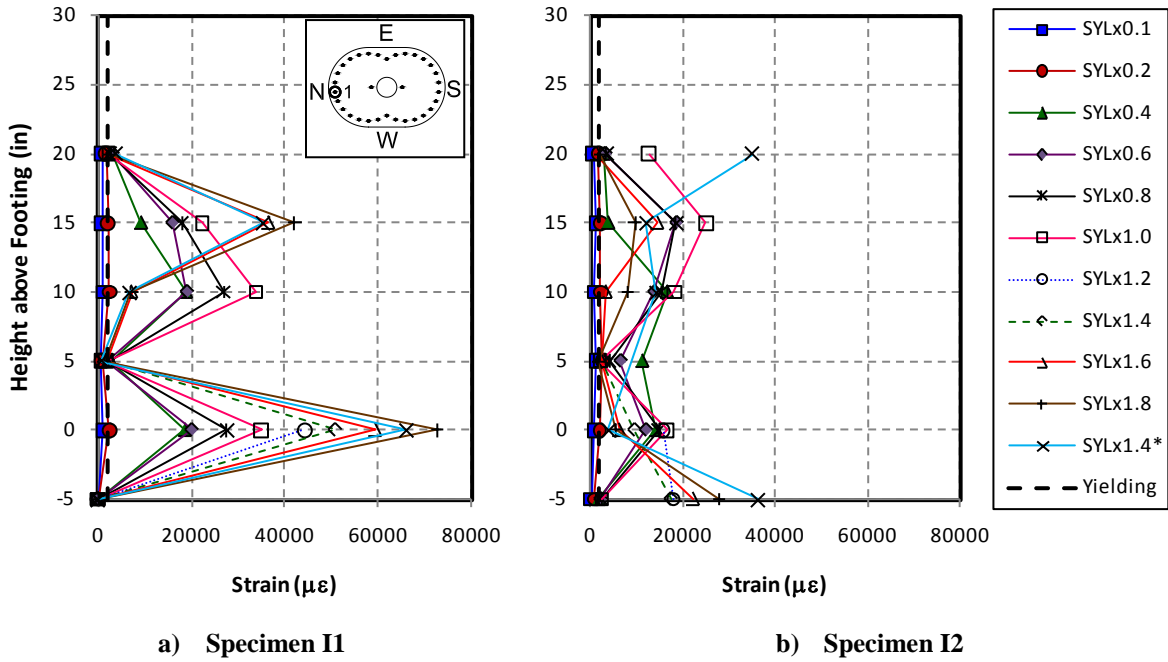


Figure 5-97 Longitudinal Bar Strain Distribution in Interlocking Specimens, Bar No.1

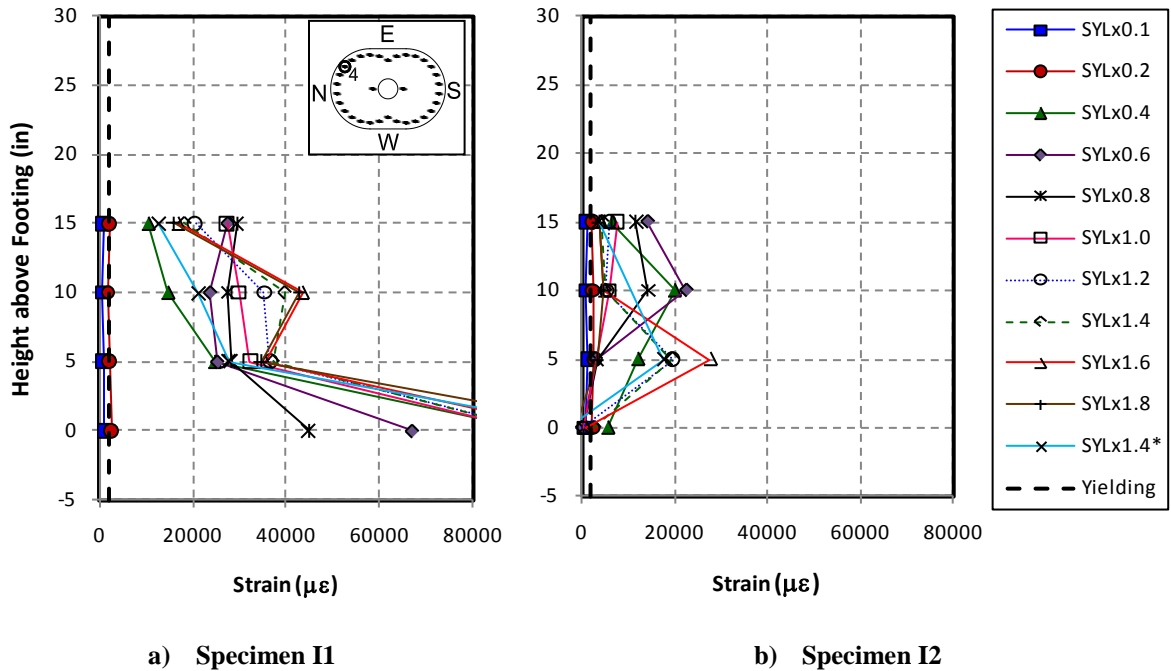


Figure 5-98 Longitudinal Bar Strain Distribution in Interlocking Specimens, Bar No.4

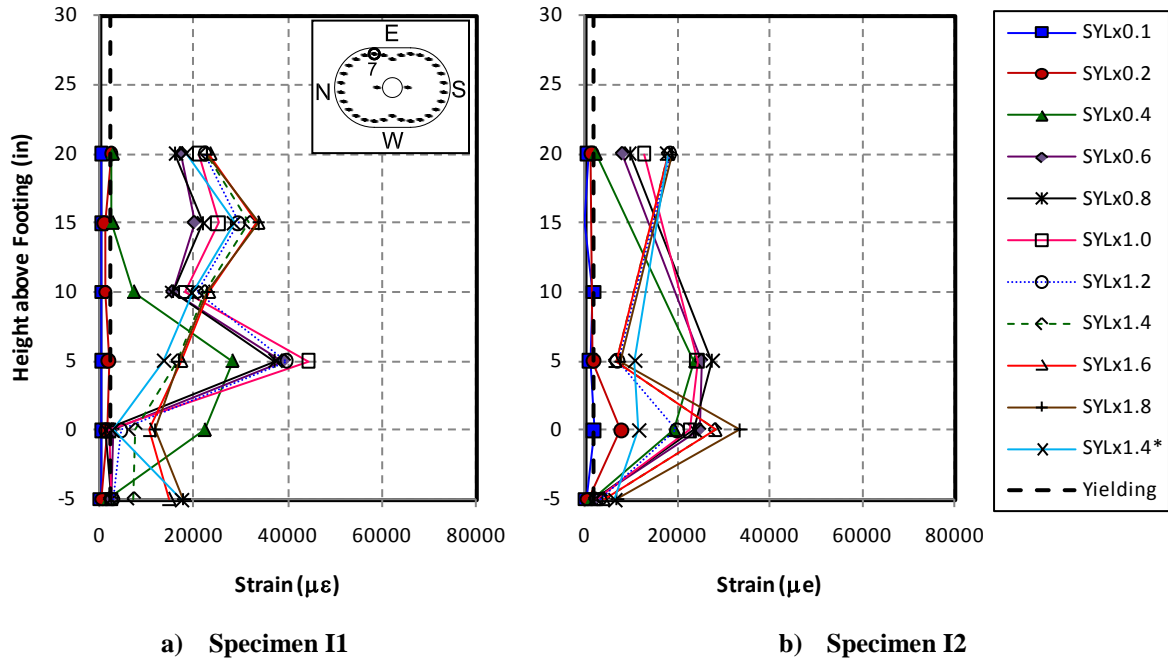


Figure 5-99 Longitudinal Bar Strain Distribution in Interlocking Specimens, Bar No.7

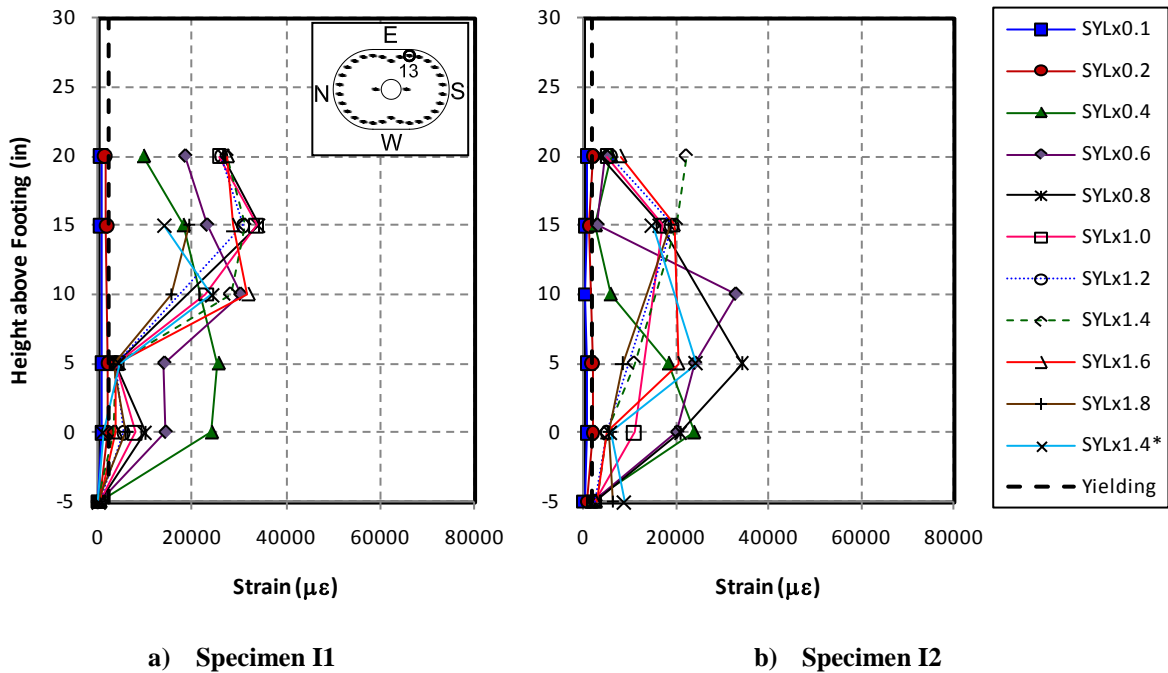


Figure 5-100 Longitudinal Bar Strain Distribution in Interlocking Specimens, Bar No.13

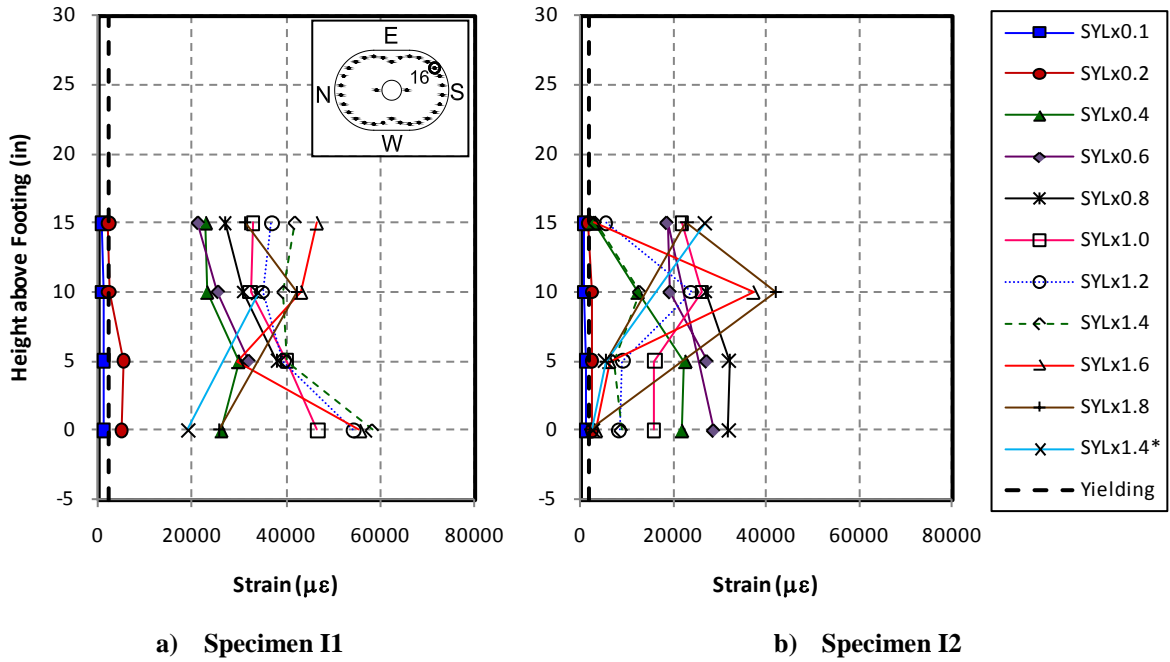


Figure 5-101 Longitudinal Bar Strain Distribution in Interlocking Specimens, Bar No.16

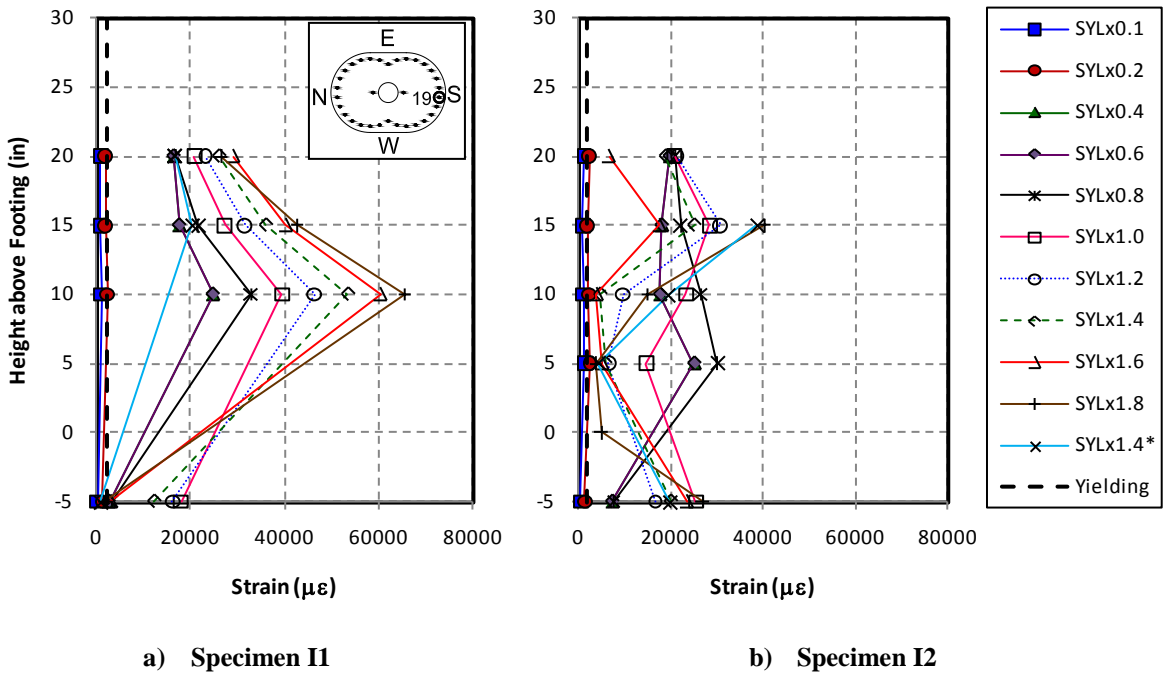
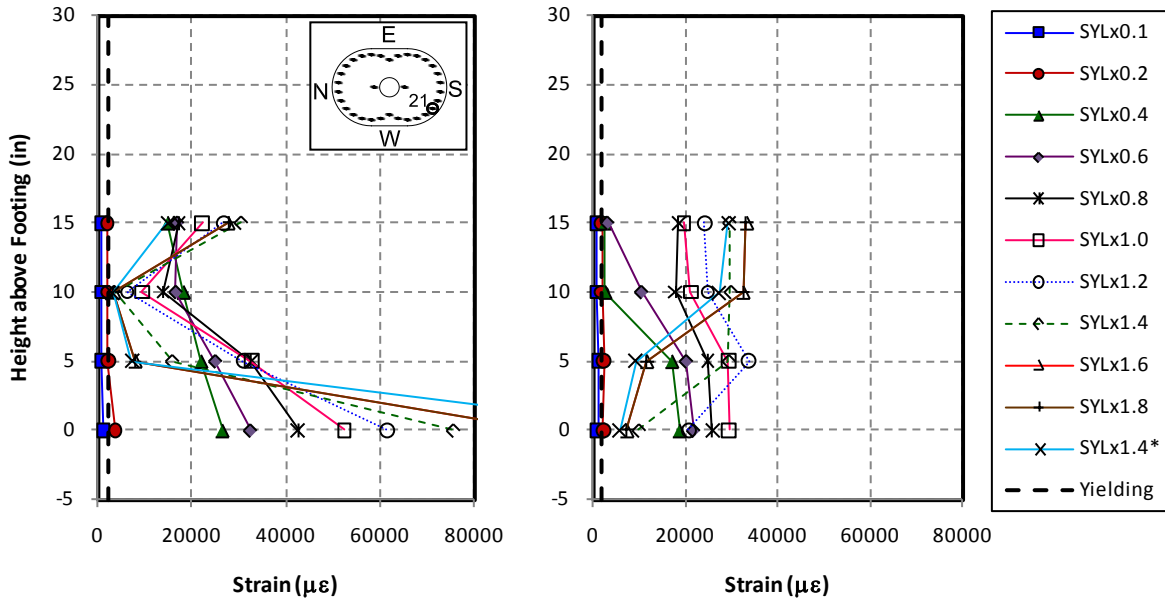


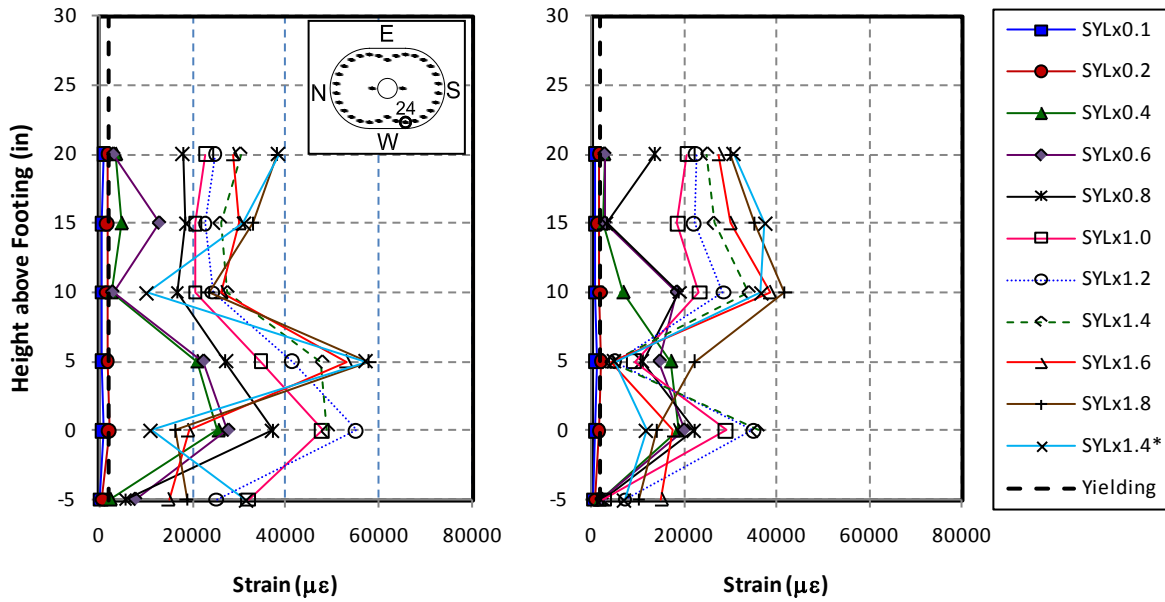
Figure 5-102 Longitudinal Bar Strain Distribution in Interlocking Specimens, Bar No.19



a) Specimen I1

b) Specimen I2

Figure 5-103 Longitudinal Bar Strain Distribution in Interlocking Specimens, Bar No.21

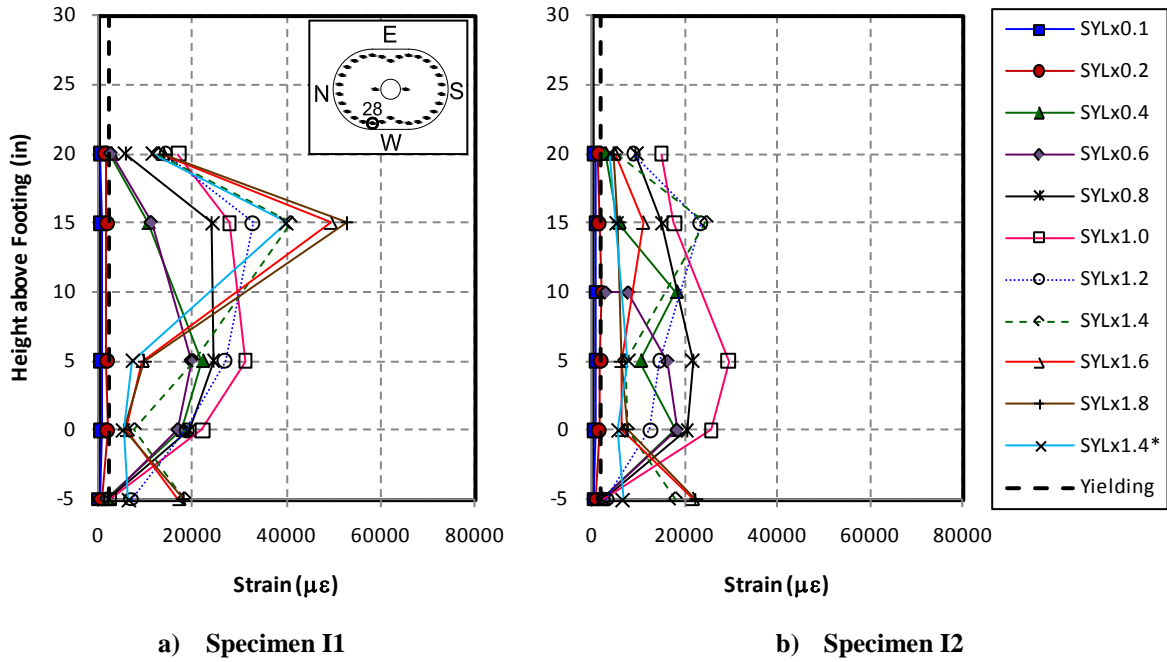


a) Specimen I1

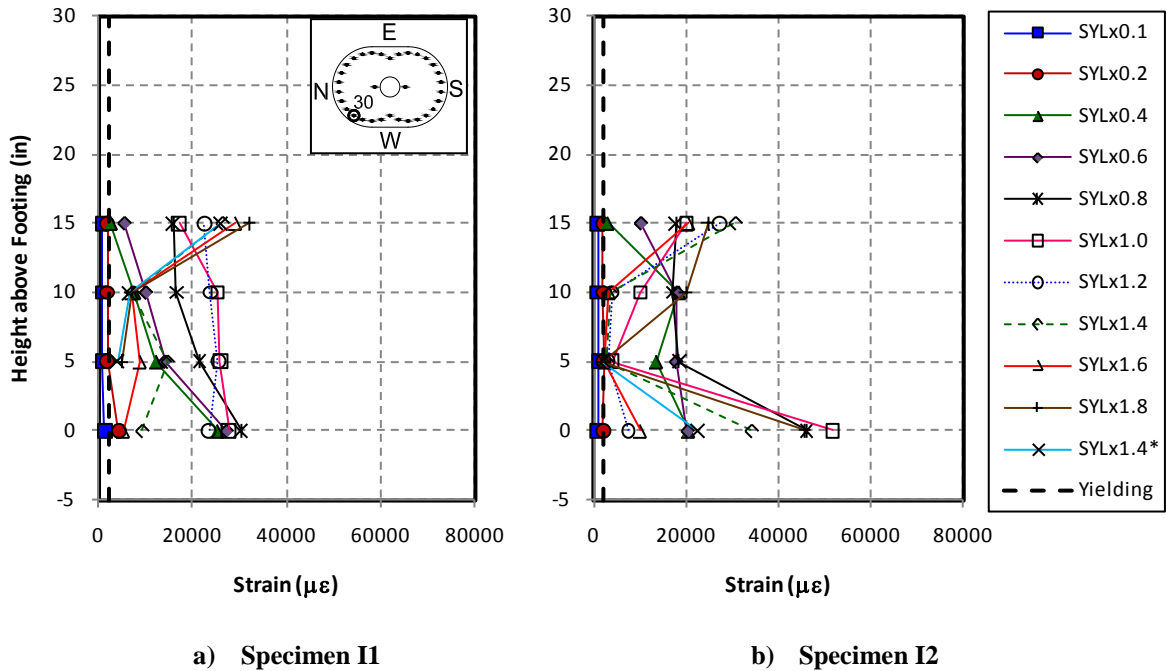
b) Specimen I2

Figure 5-104 Longitudinal Bar Strain Distribution in Interlocking Specimens, Bar No.24





**Figure 5-105 Longitudinal Bar Strain Distribution in Interlocking Specimens, Bar No.28**



**Figure 5-106 Longitudinal Bar Strain Distribution in Interlocking Specimens, Bar No.30**

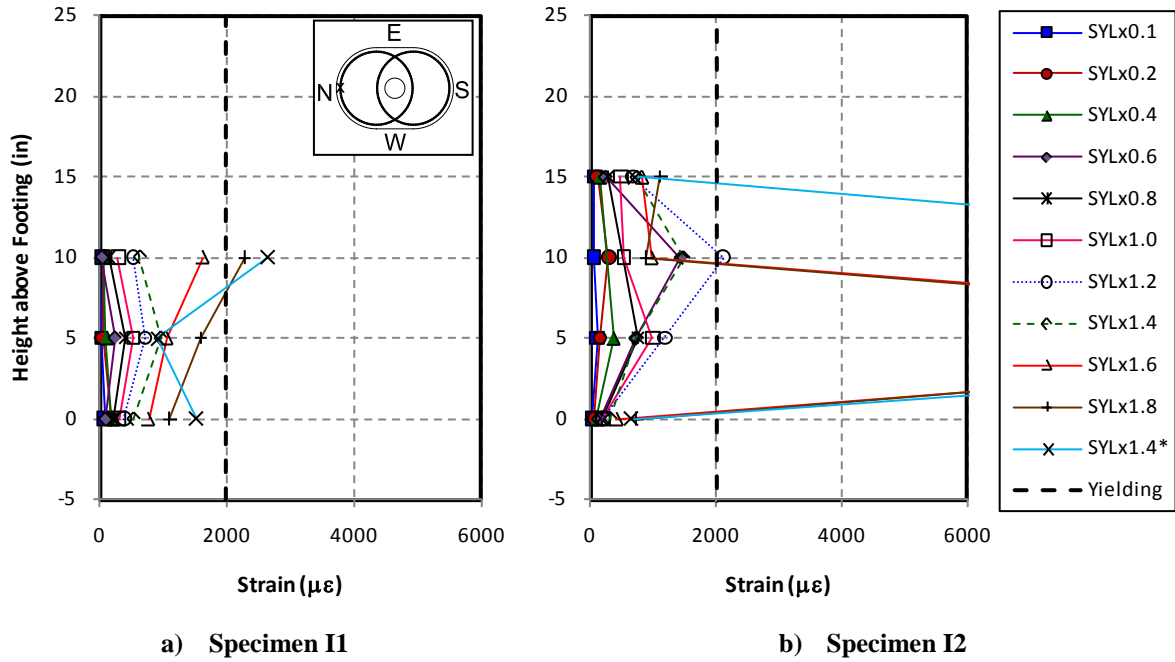


Figure 5-107 Spiral Strain Distribution in Interlocking Specimens, North

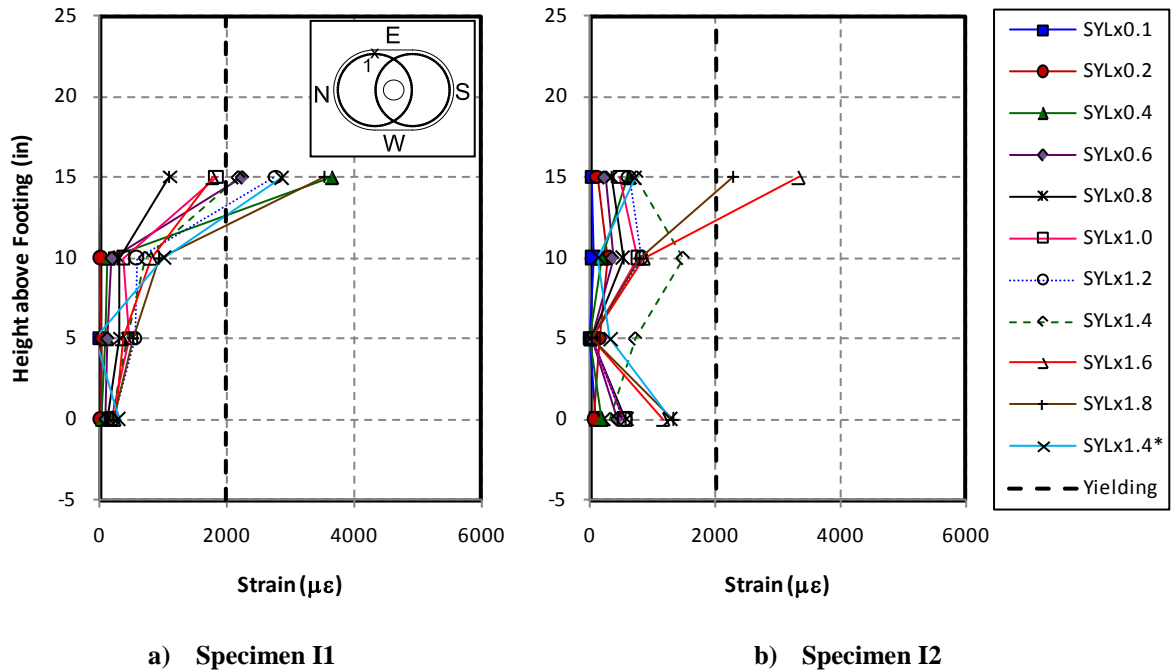


Figure 5-108 Spiral Strain Distribution in Interlocking Specimens, East 1

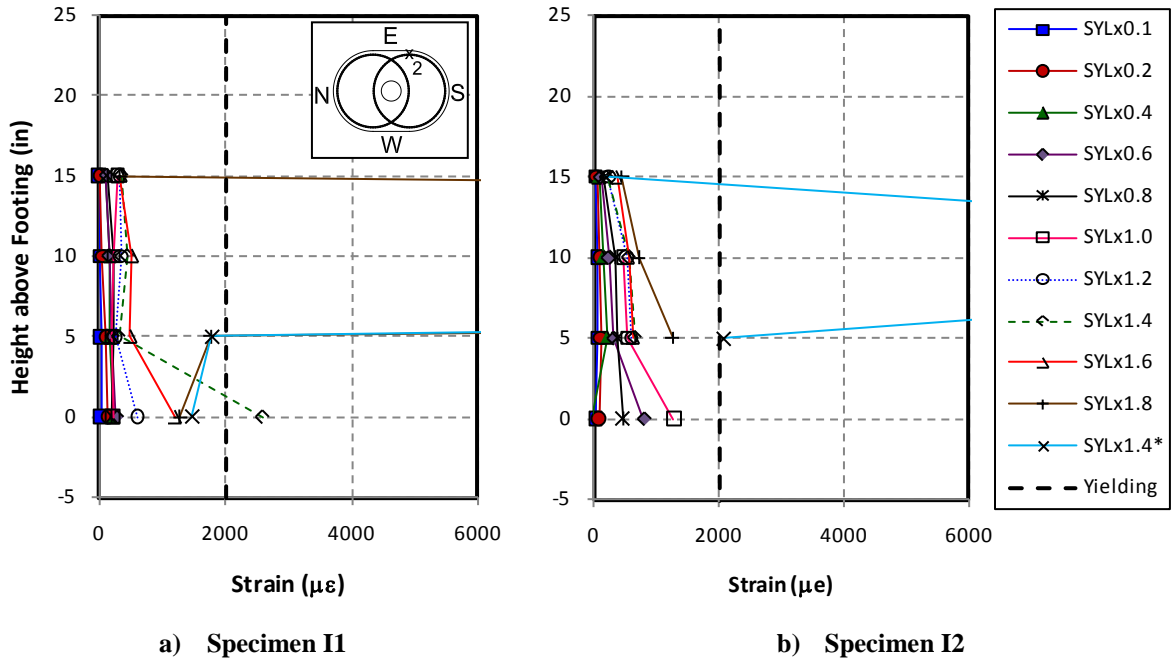


Figure 5-109 Spiral Strain Distribution in Interlocking Specimens, East 2

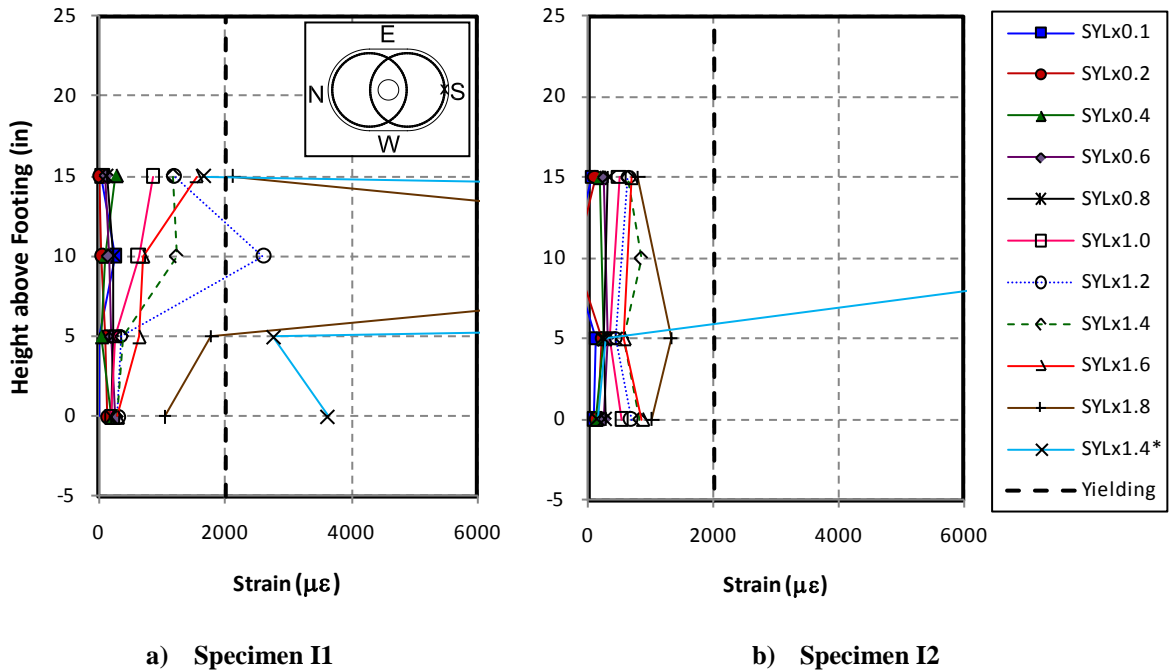


Figure 5-110 Spiral Strain Distribution in Interlocking Specimens, South



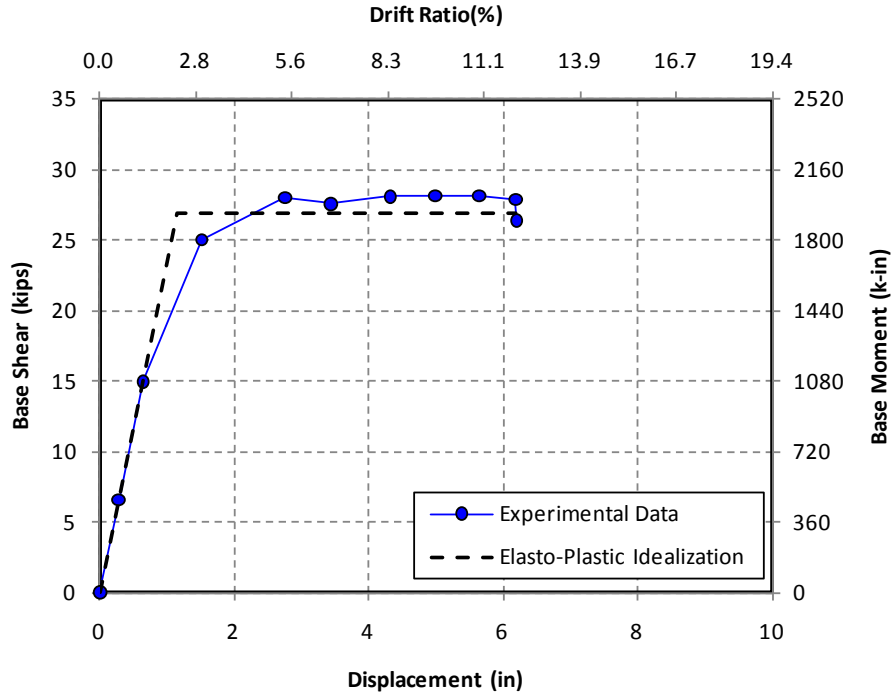


Figure 5-113 Elasto-Plastic Idealization for Force-Displacement, Specimen I1 (Longitudinal)

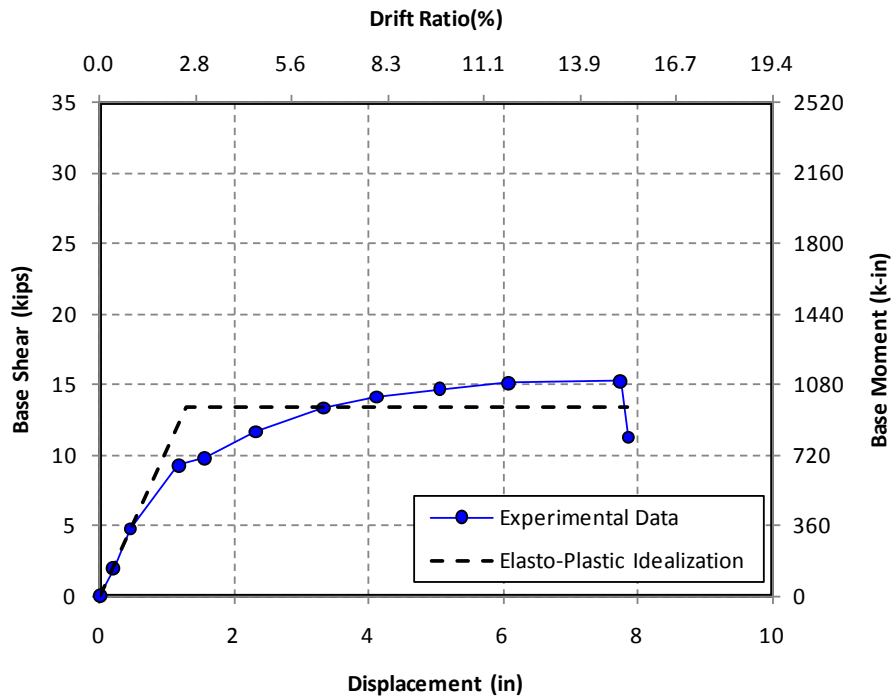


Figure 5-114 Elasto-Plastic Idealization for Force-Displacement, Specimen I1 (Transverse)

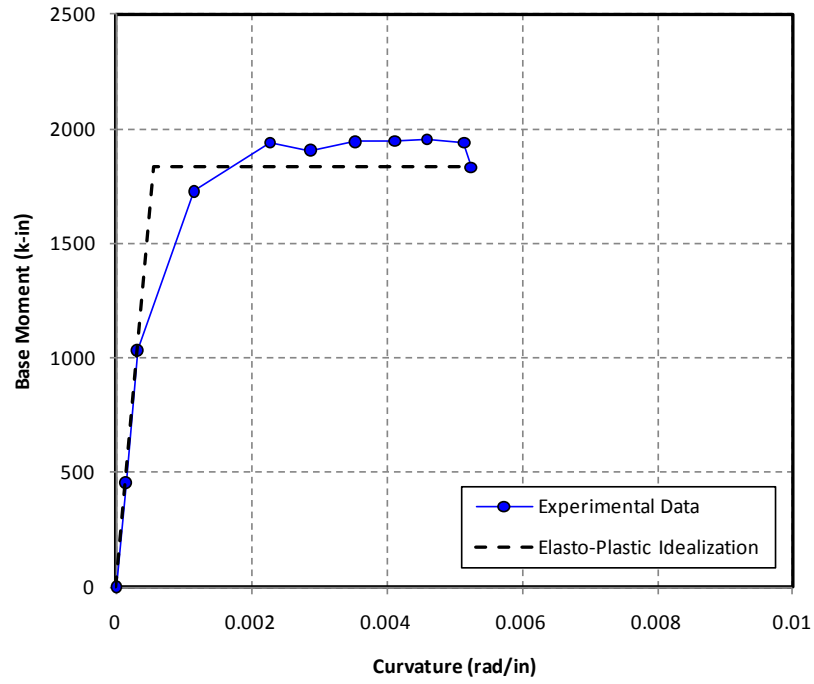


Figure 5-115 Elasto-Plastic Idealization for Moment-Curvature, Specimen I1 (Longitudinal)

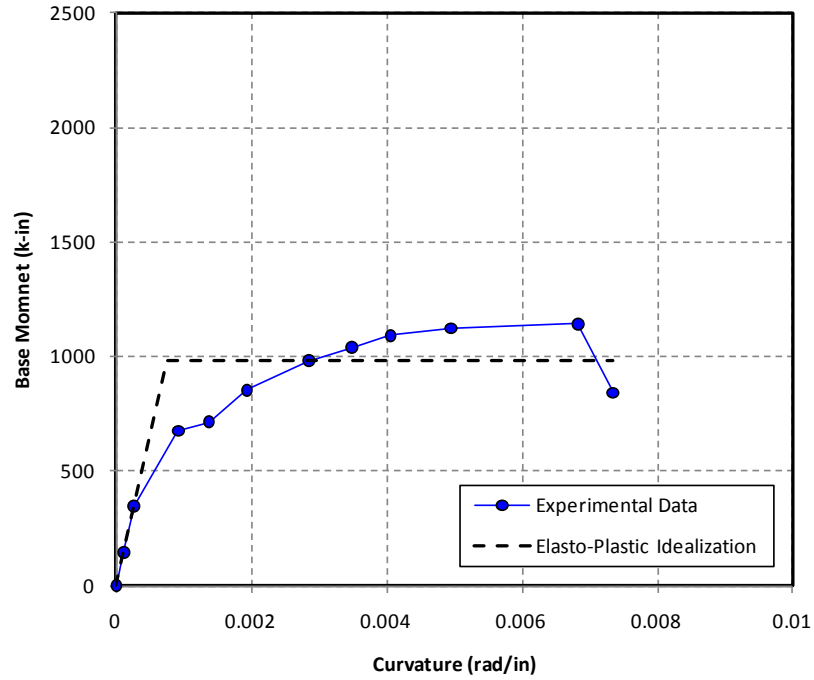


Figure 5-116 Elasto-Plastic Idealization for Moment-Curvature, Specimen I1 (Transverse)

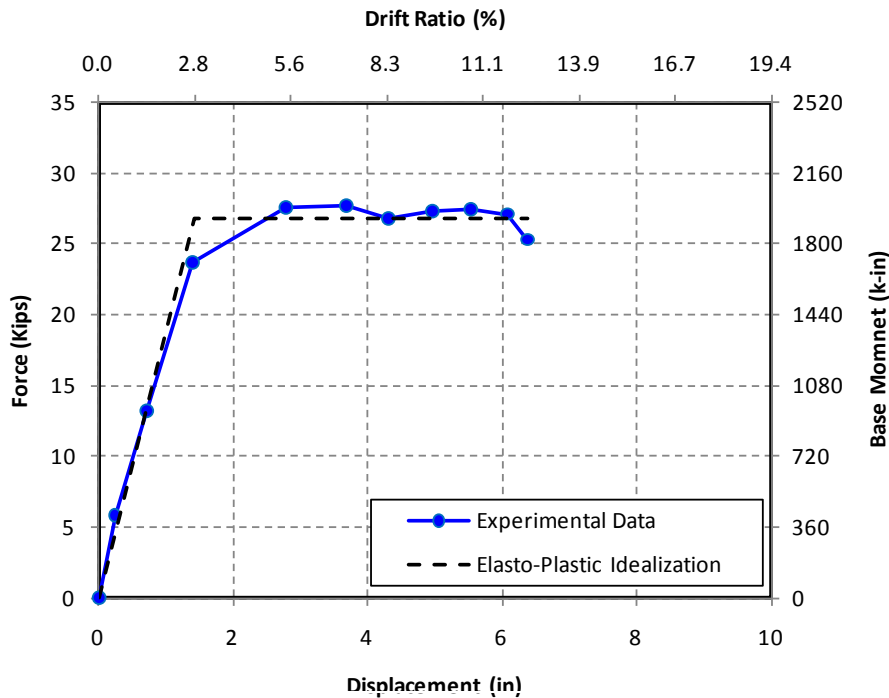


Figure 5-117 Elasto-Plastic Idealization for Force-Displacement, Specimen I2 (Longitudinal)

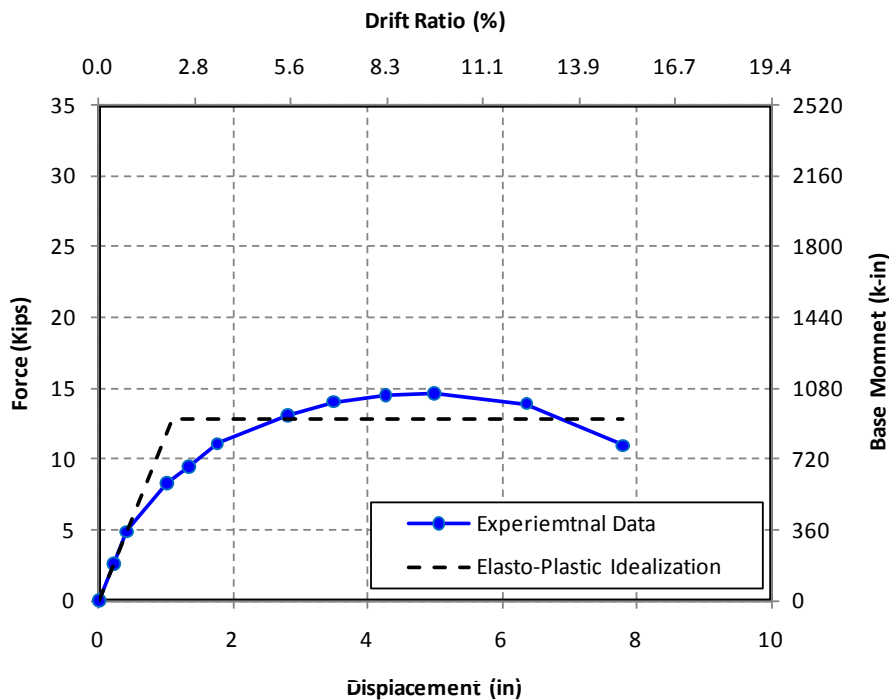


Figure 5-118 Elasto-Plastic Idealization for Force-Displacement, Specimen I2 (Transverse)

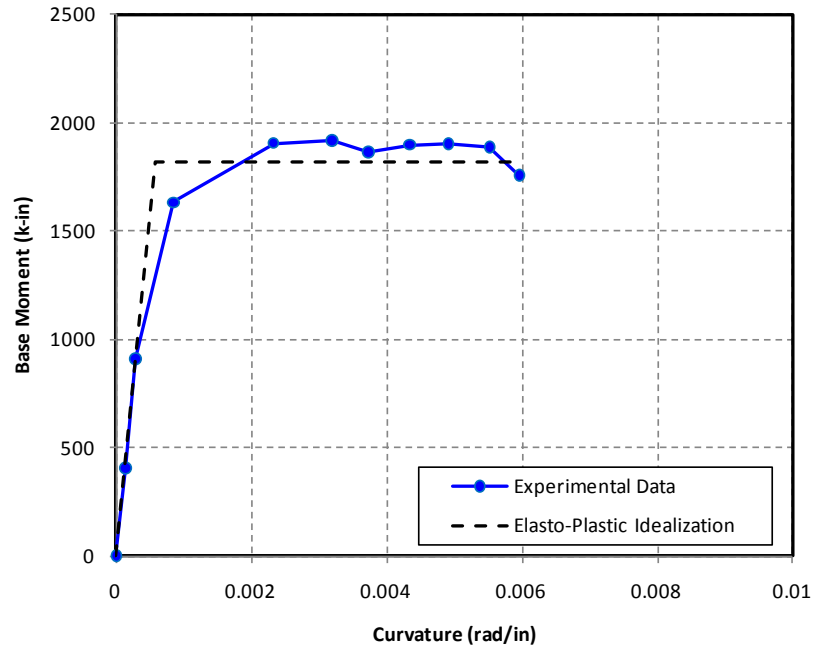


Figure 5-119 Elasto-Plastic Idealization for Moment-Curvature, Specimen I2 (Longitudinal)

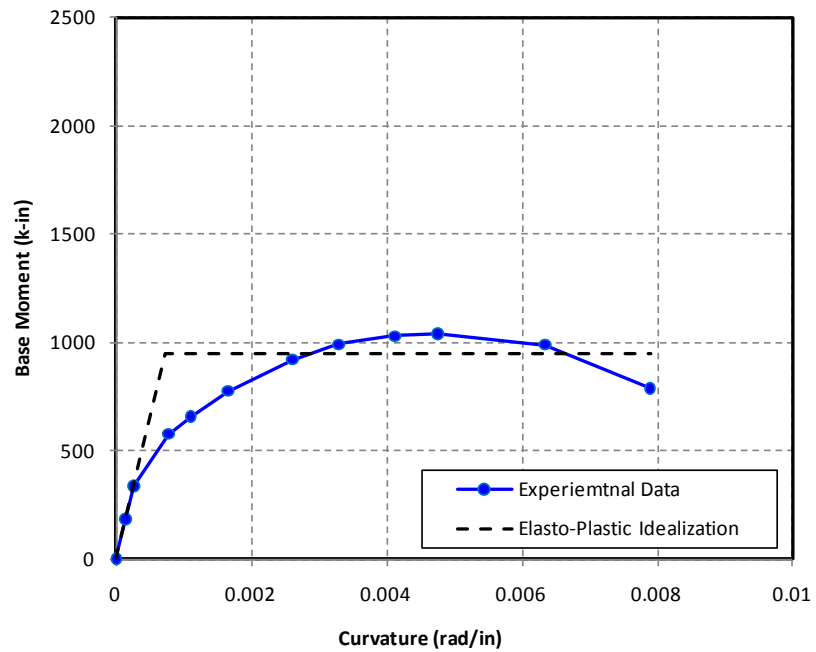


Figure 5-120 Elasto-Plastic Idealization for Moment-Curvature, Specimen I2 (Transverse)



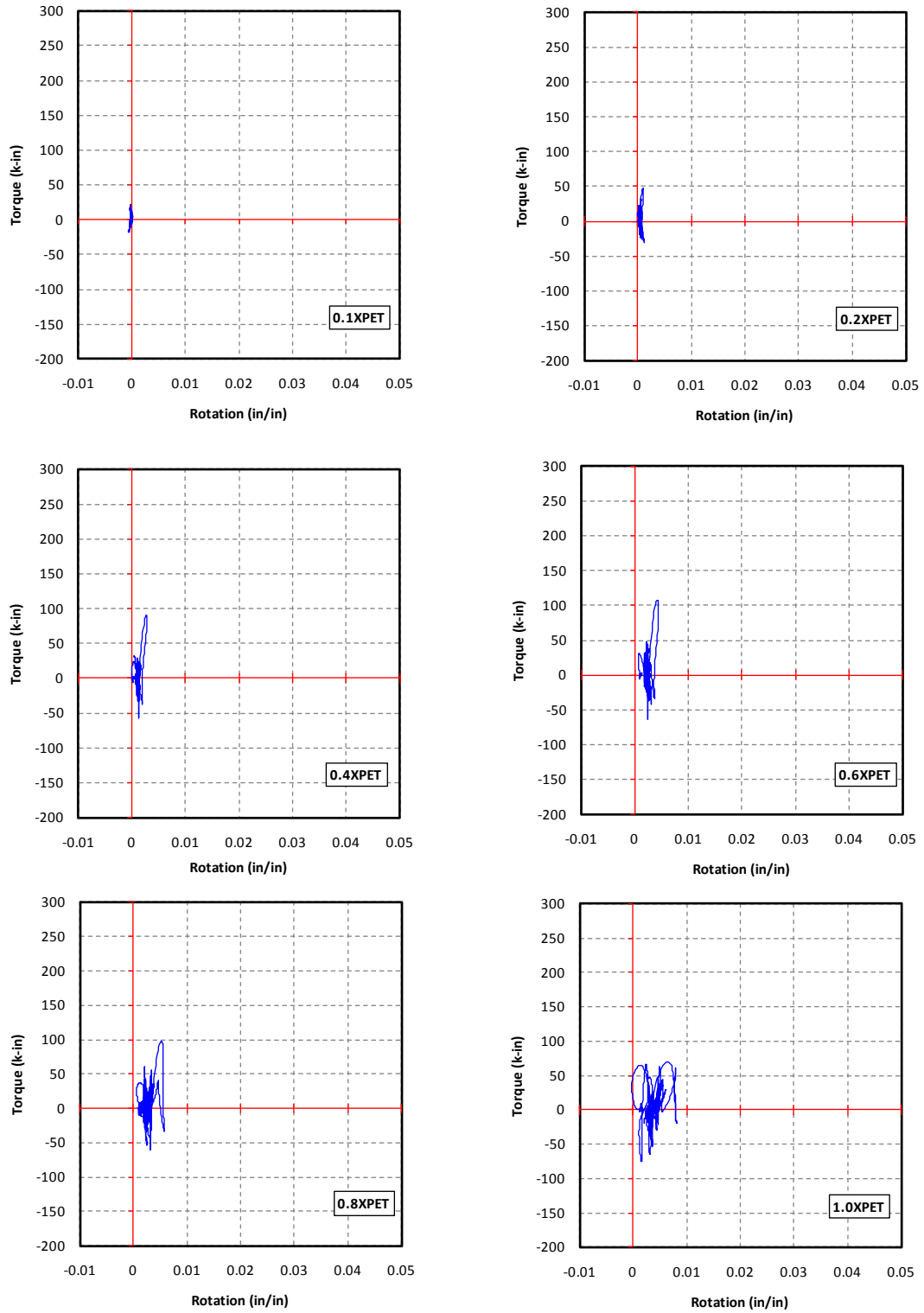


Figure 5-121 Torque-Rotation Hysteresis, Specimen I1

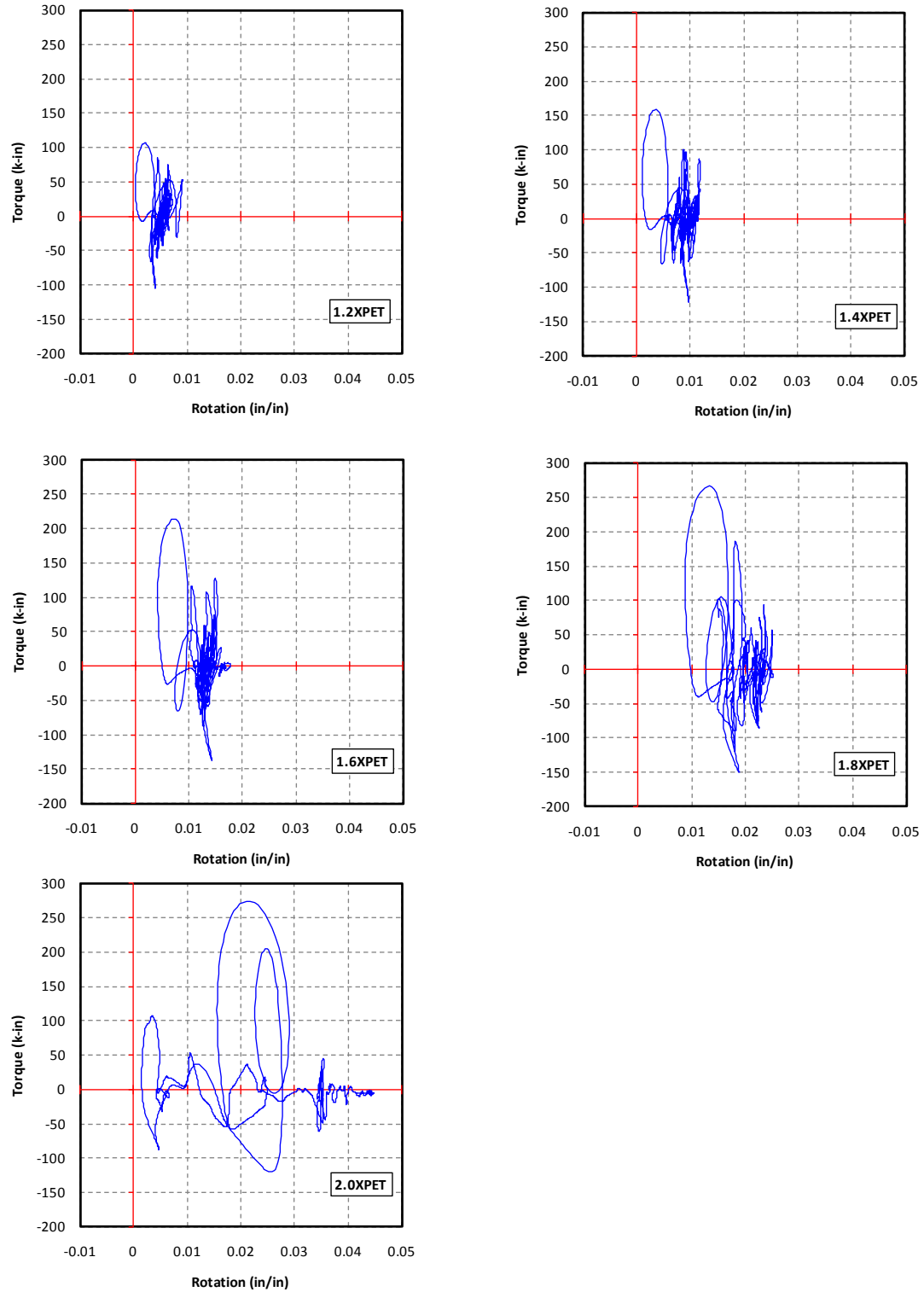


Figure 5-122 Torque-Rotation Hysteresis, Specimen I1

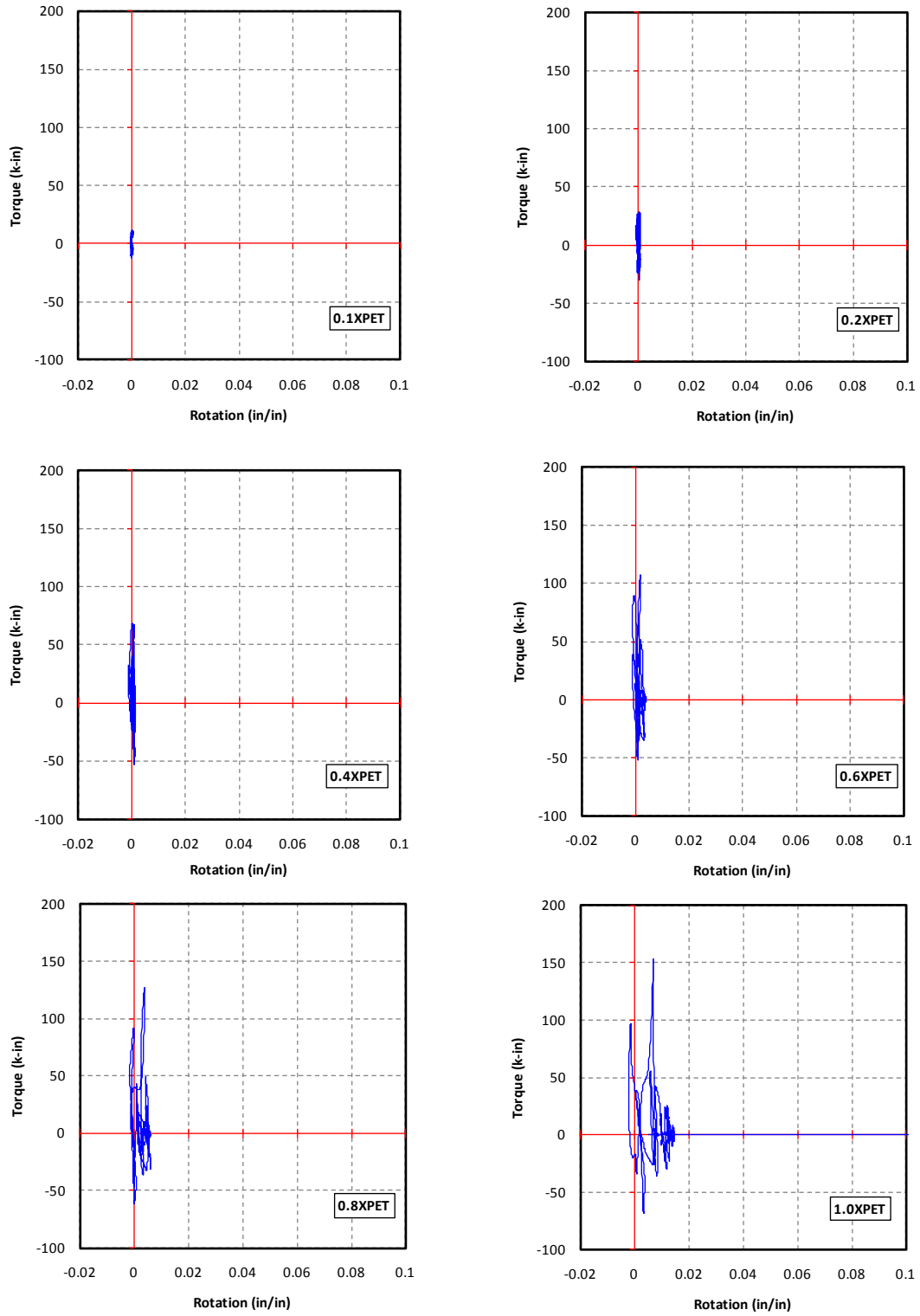


Figure 5-123 Torque-Rotation Hysteresis, Specimen I2

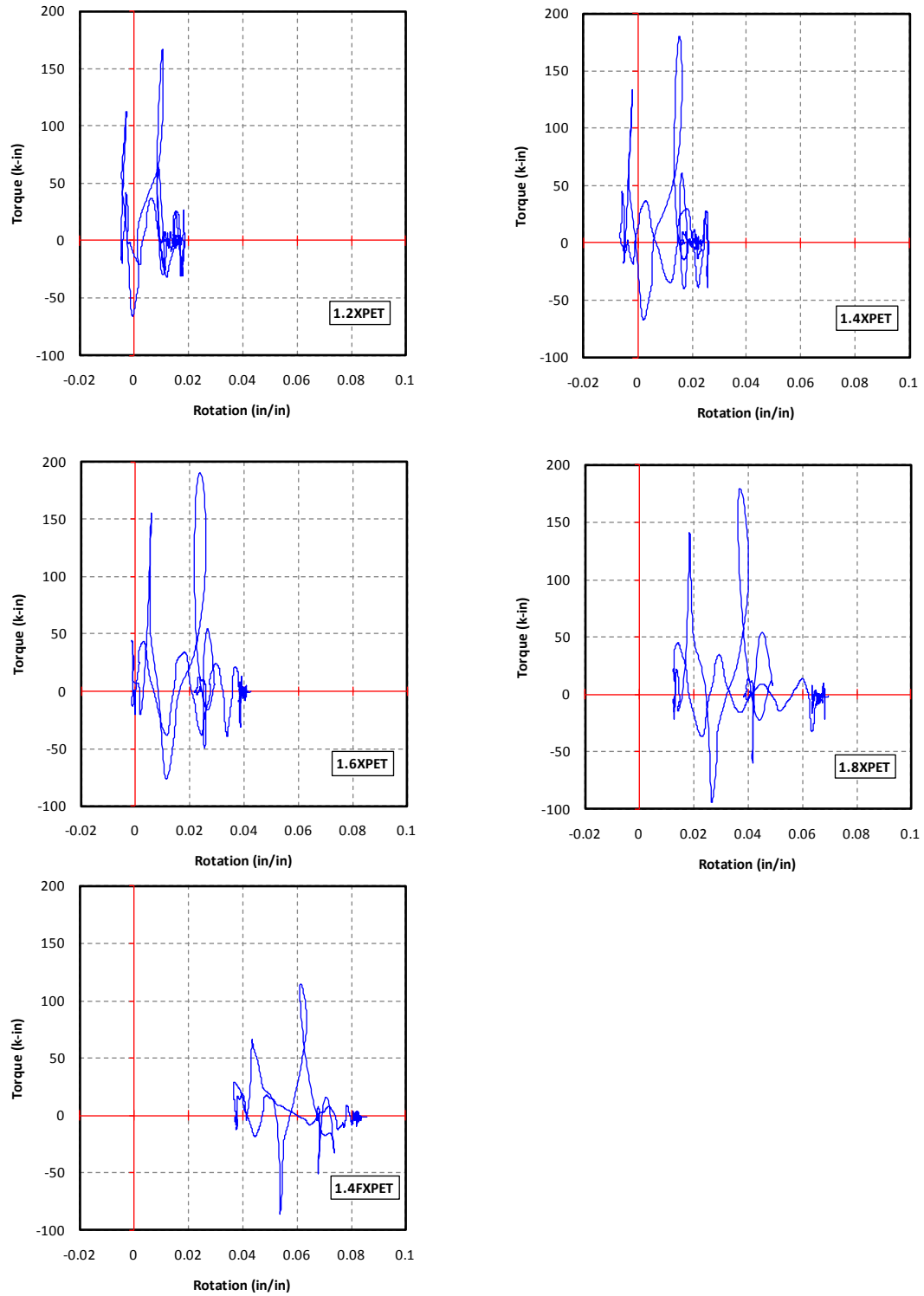
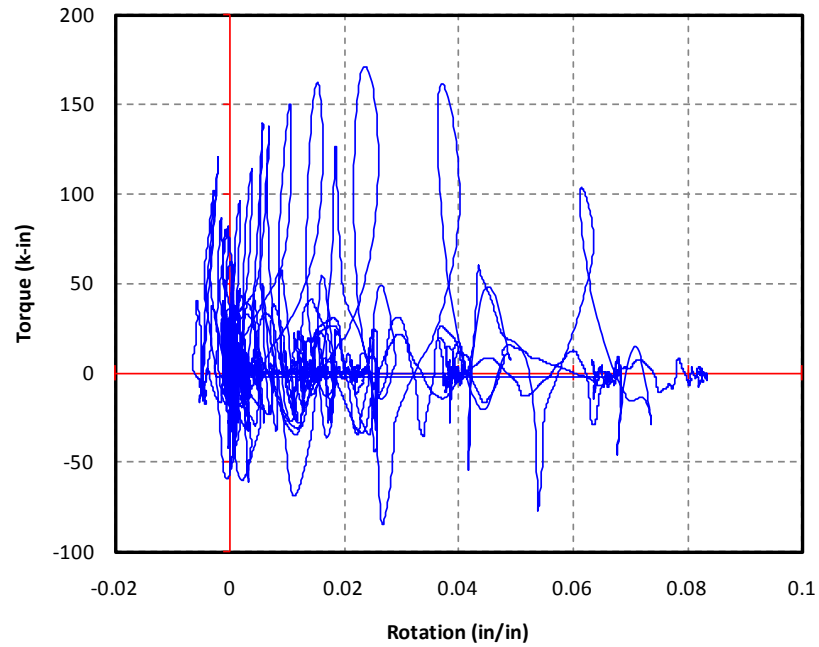
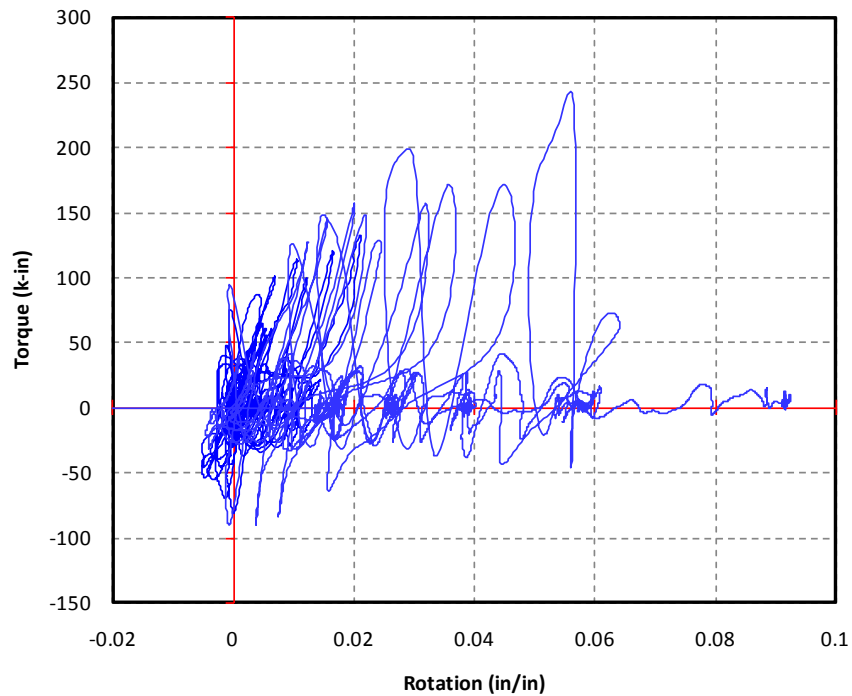


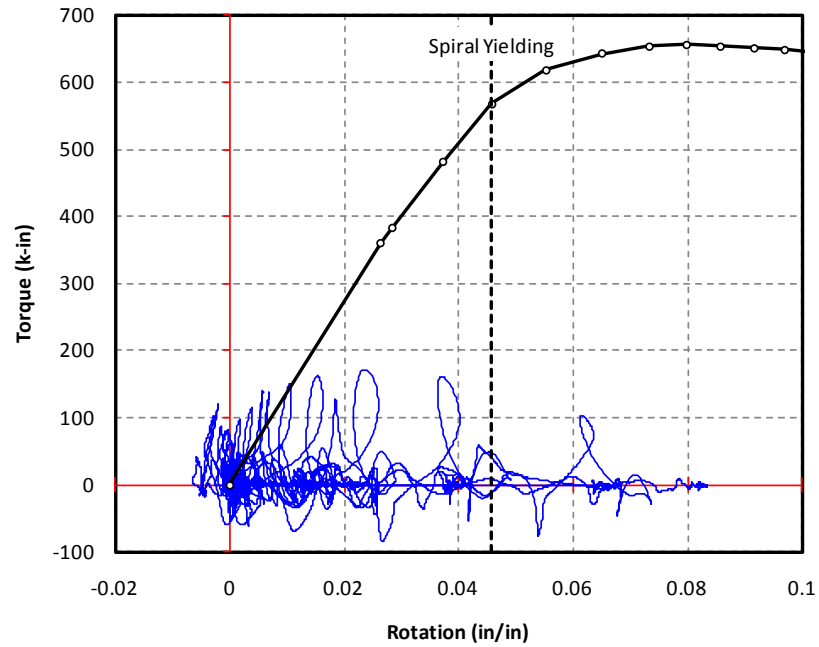
Figure 5-124 Torque-Rotation Hysteresis, Specimen I2



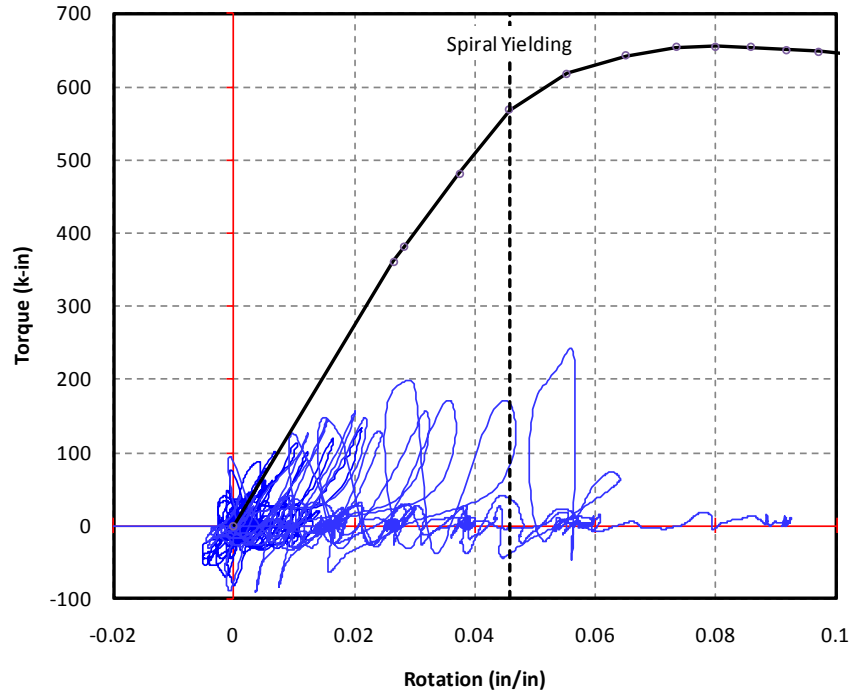
**Figure 5-125 Cumulative Torque-Rotation Hysteresis, Specimn I1**



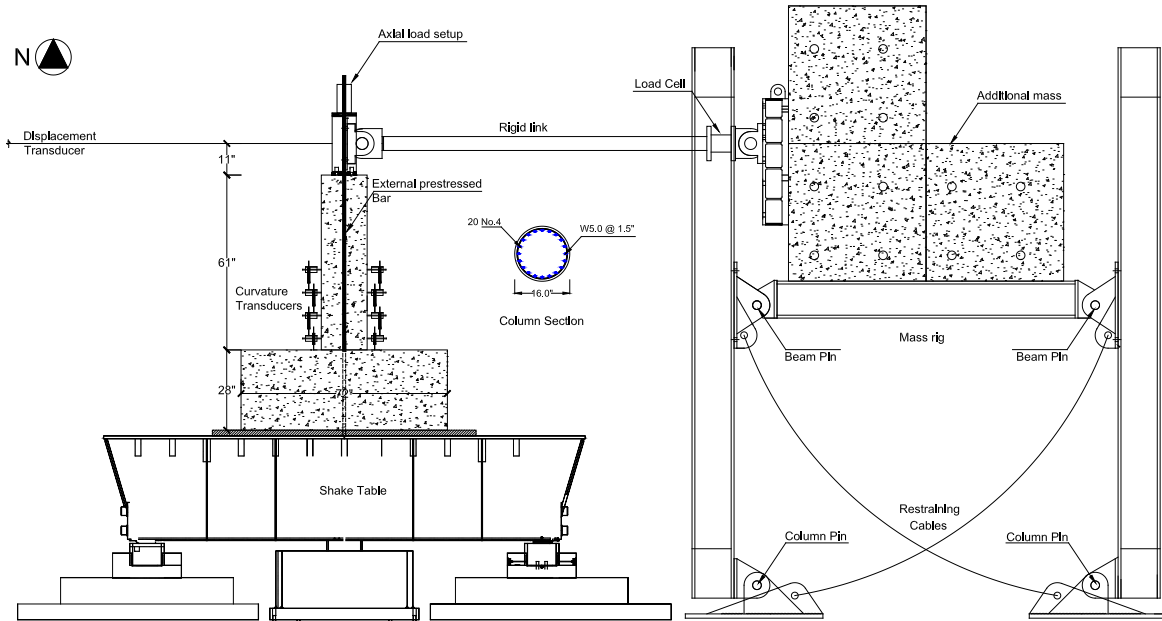
**Figure 5-126 Cumulative Torque-Rotation Hysteresis, Specimn I2**



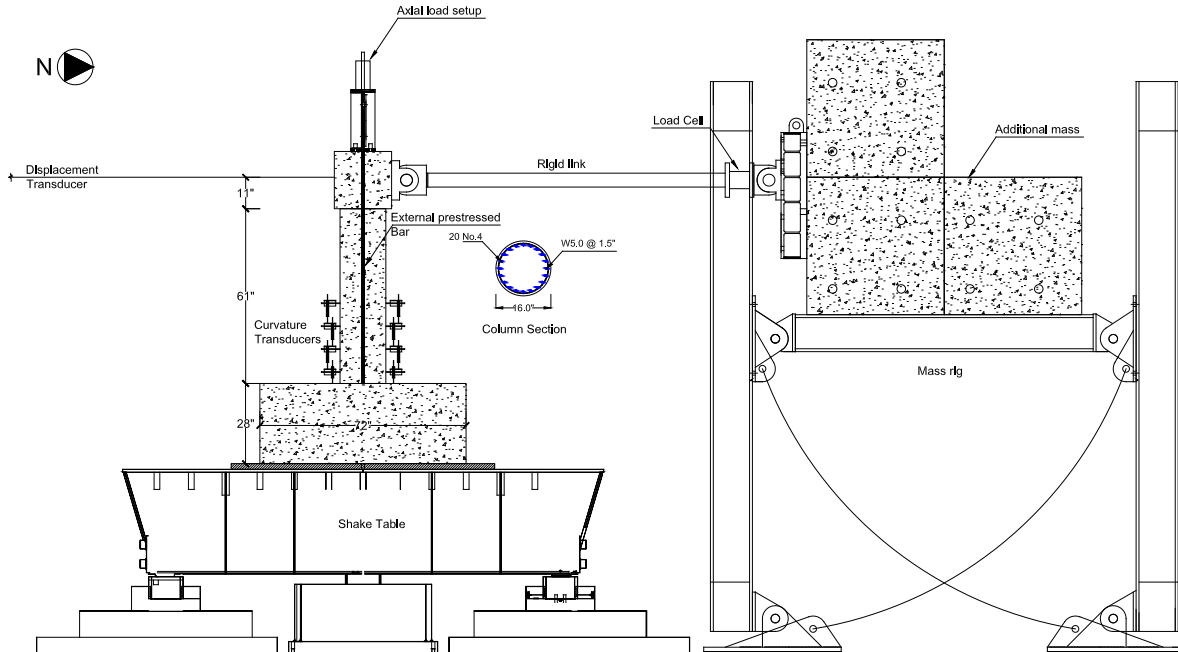
**Figure 5-127 Torque-Rotation Hysteresis and Capacity, Specimn I1**



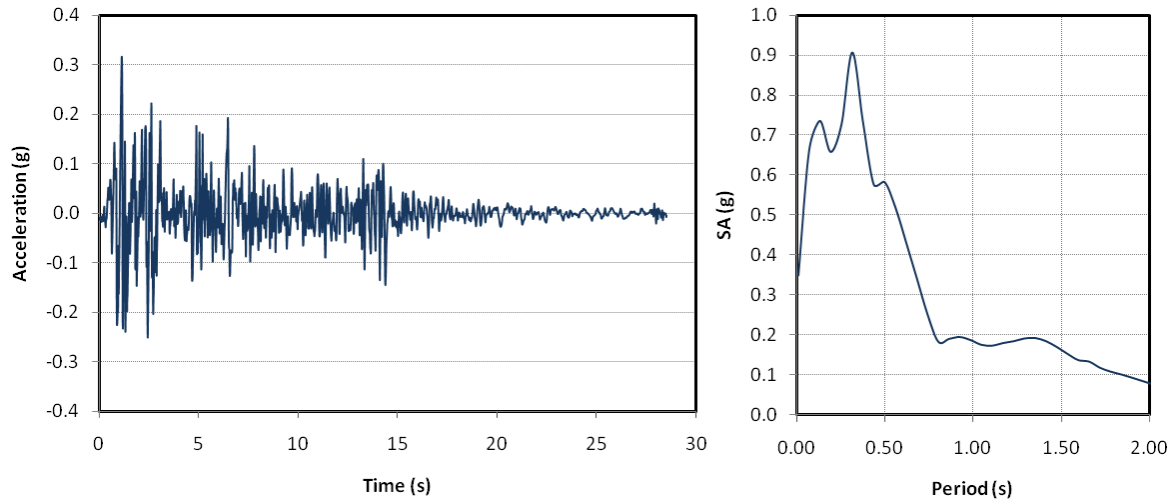
**Figure 5-128 Torque-Rotation Hysteresis and Capacity, Specimn I2**



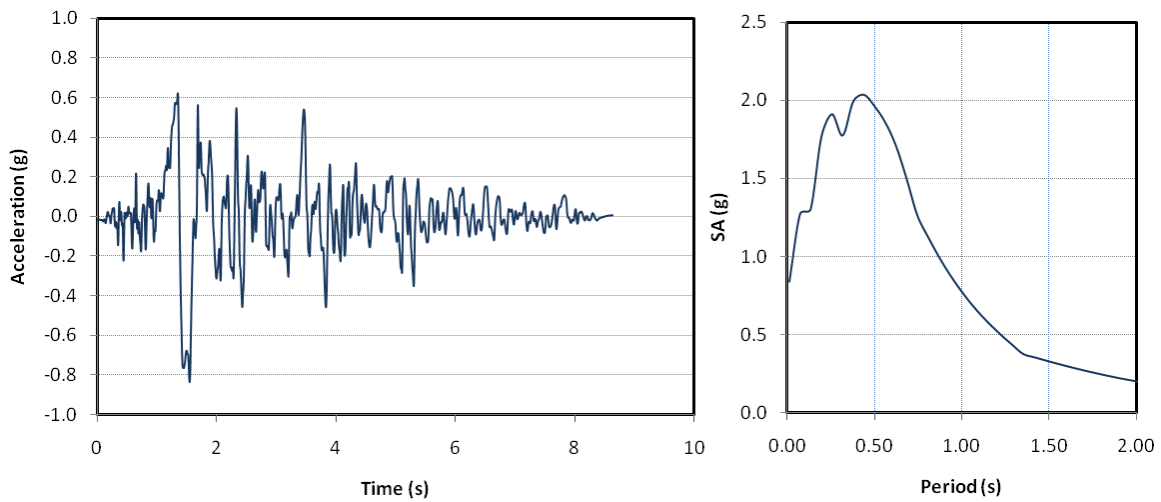
**Figure 6-1 Experimental Test Setup, Circular Specimen 9F1**



**Figure 6-2 Experimental Test Setup, Circular Specimen NF1**



**Figure 6-3 Compressed El Centro Ground Acceleration, Time History and SA Spectrum for Specimen 9F1**



**Figure 6-4 Compressed Rinaldi Ground Acceleration, Time History and SA Spectrum for Specimen NF1**



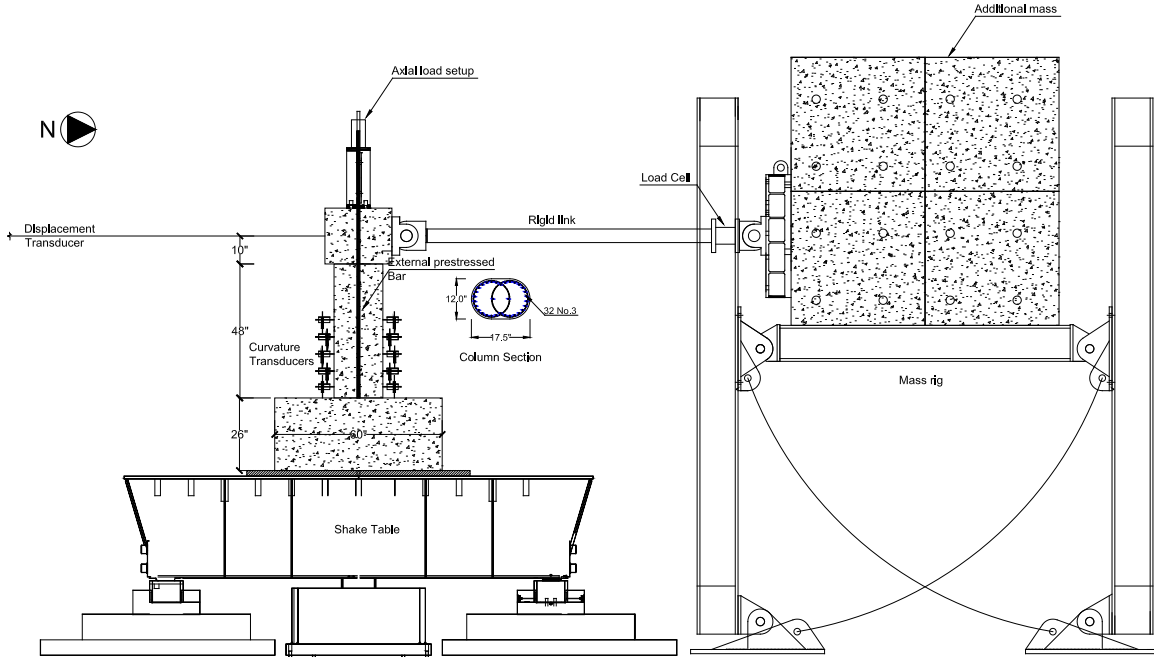


Figure 6-5 Experimental Test Setup, Interlocking Specimen ISL1.0

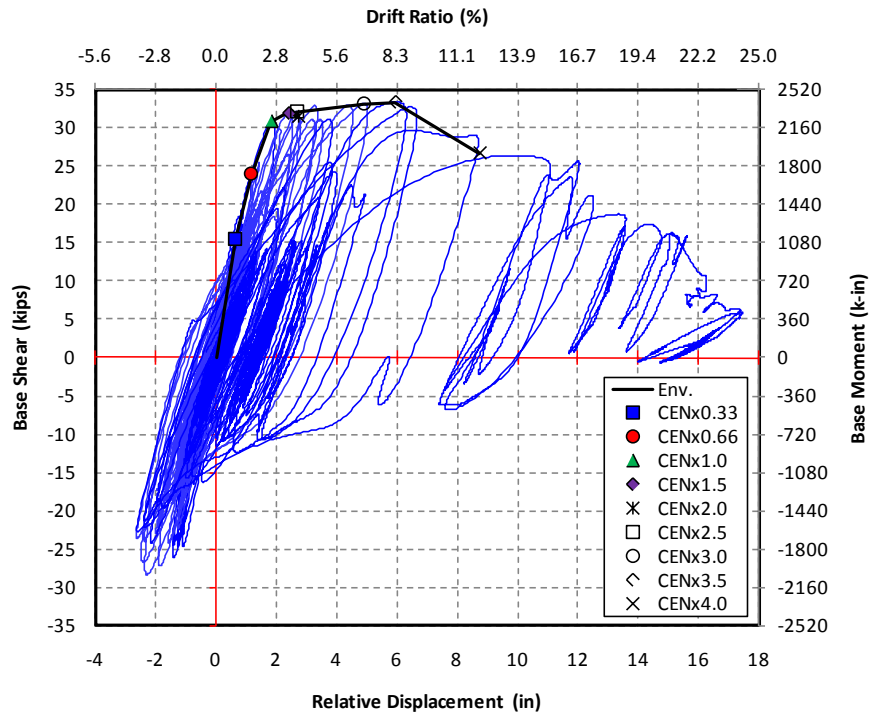


Figure 6-6 Cumulative Hysteresis and Envelope for Circular Specimen 9F1

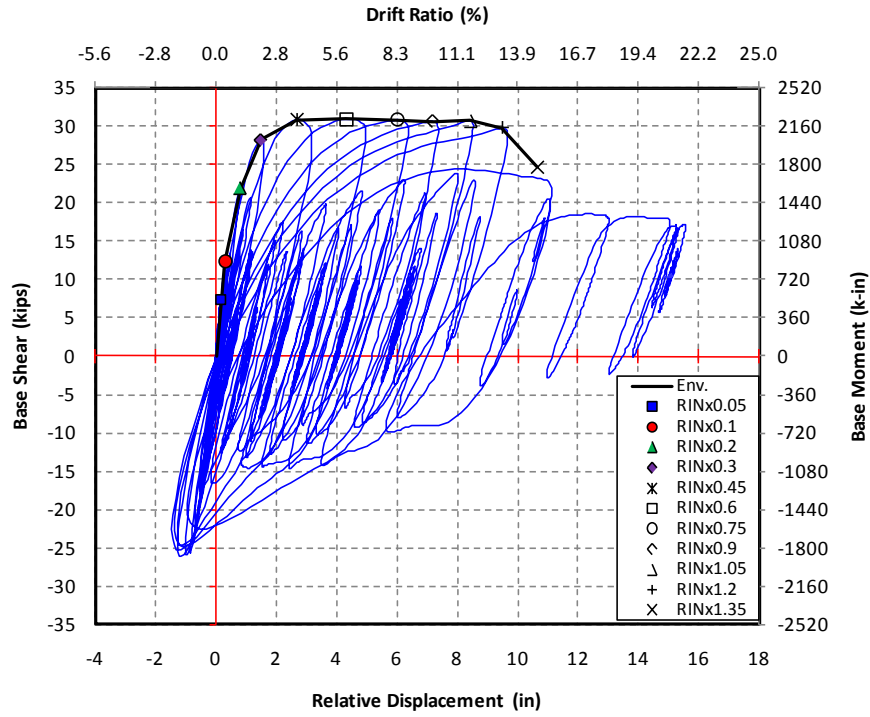


Figure 6-7 Cumulative Hysteresis and Envelope for Circular Specimen NF1

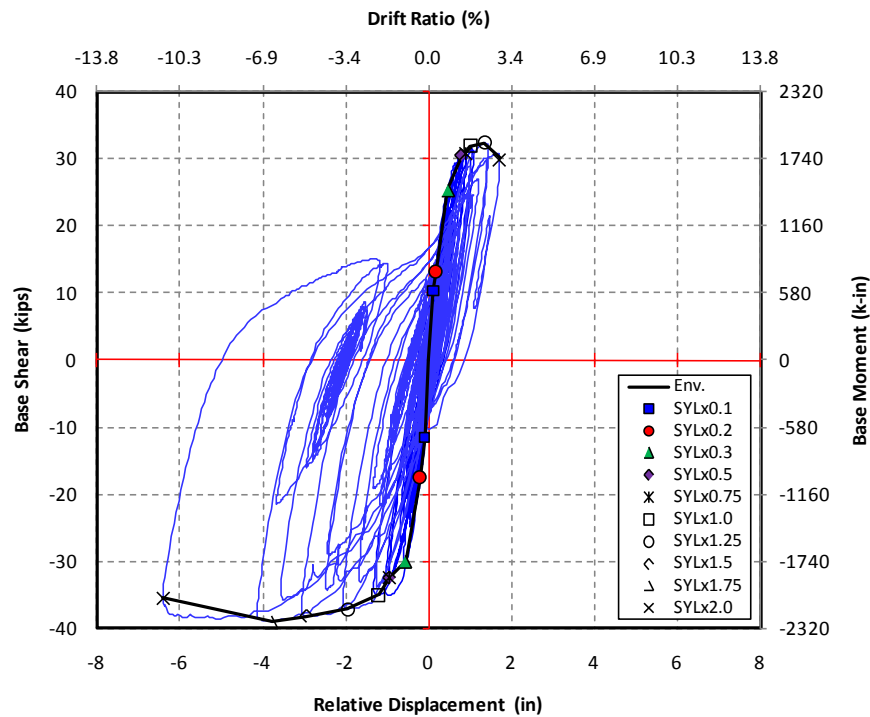


Figure 6-8 Cumulative Hysteresis and Envelope for Interlocking Specimen ISL1.0

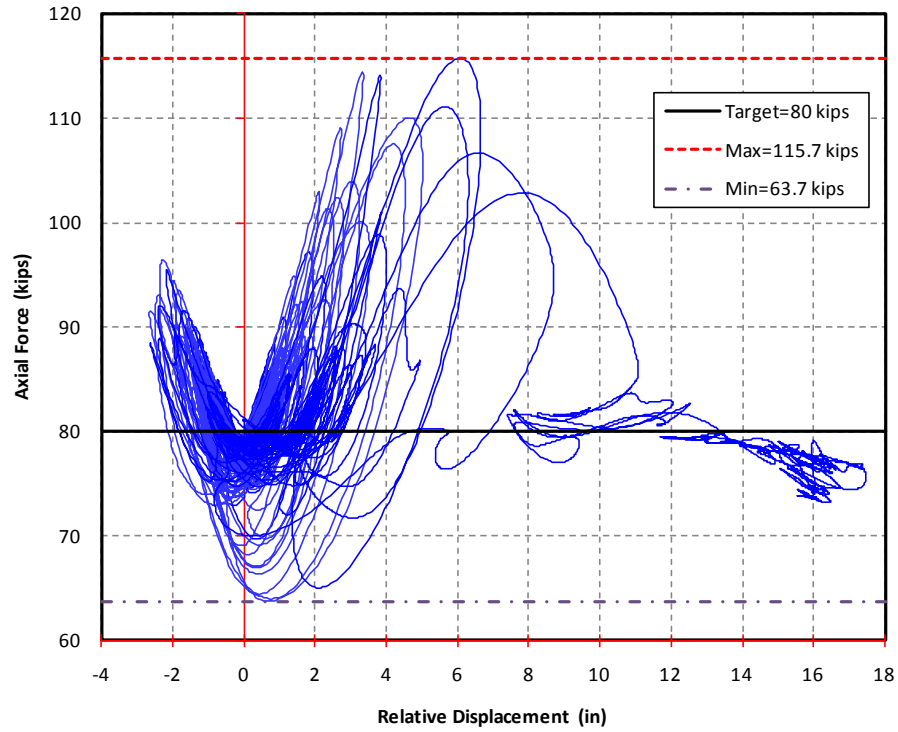


Figure 6-9 Axial Load - Displacement Accumulated Hysteresis for Specimen 9F1

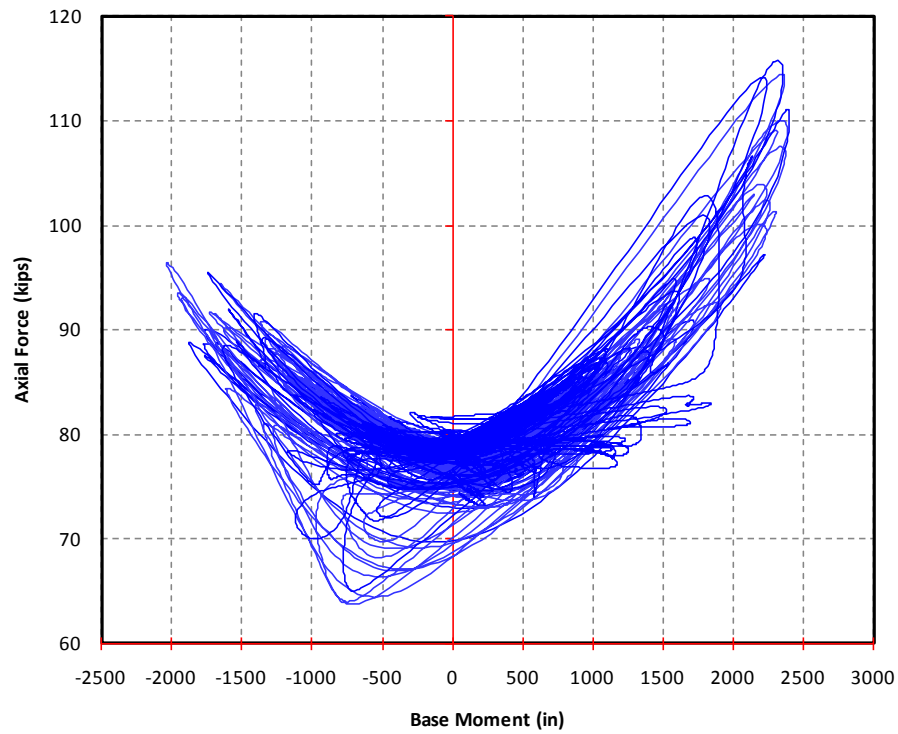
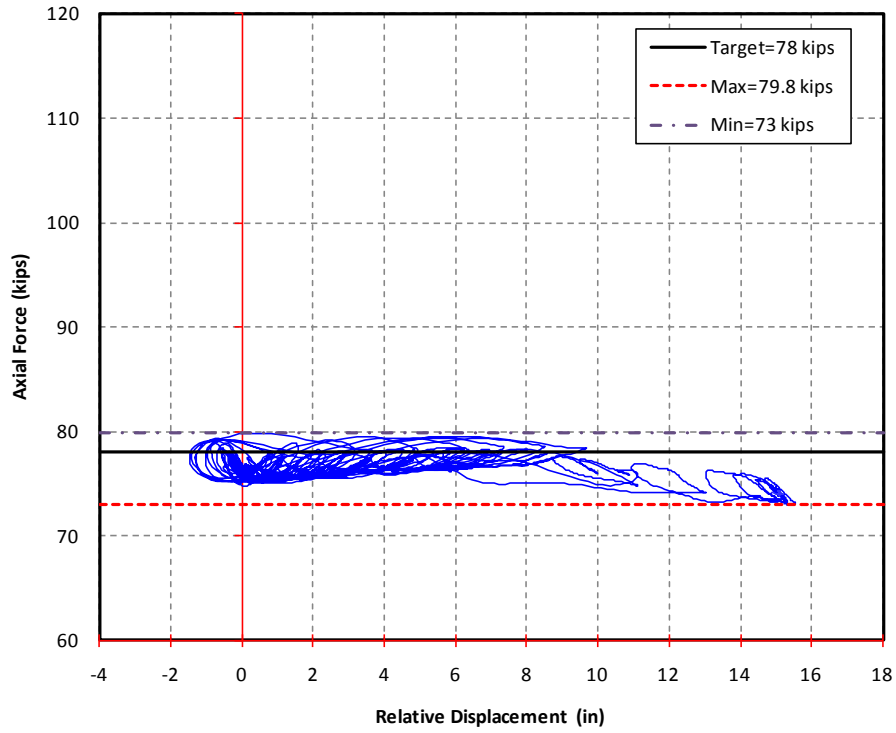
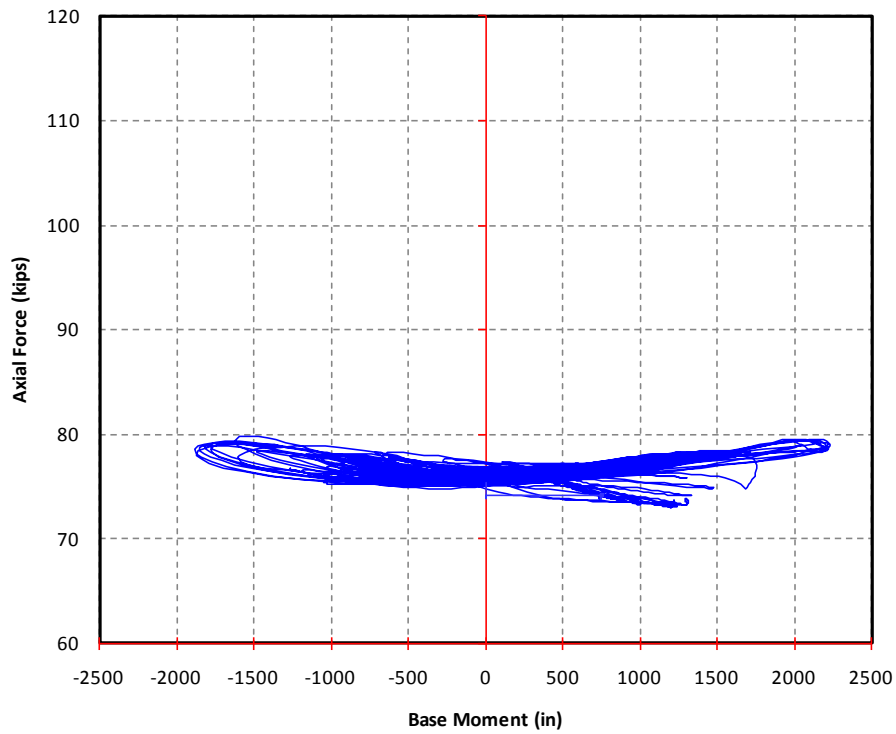


Figure 6-10 Axial Load - Base Moment Accumulated Hysteresis for Specimen 9F1



**Figure 6-11 Axial Load - Displacement Accumulated Hysteresis for Specimen NF1**



**Figure 6-12 Axial Load - Displacement Accumulated Hysteresis for Specimen NF1**

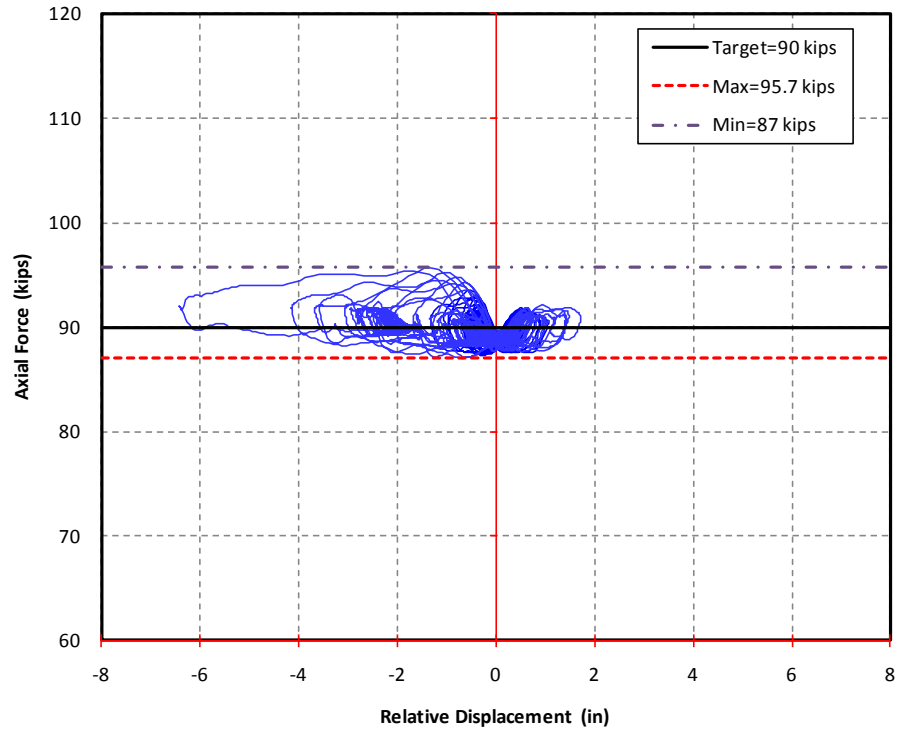


Figure 6-13 Axial Load - Displacement Accumulated Hysteresis for Specimen ISL1.0

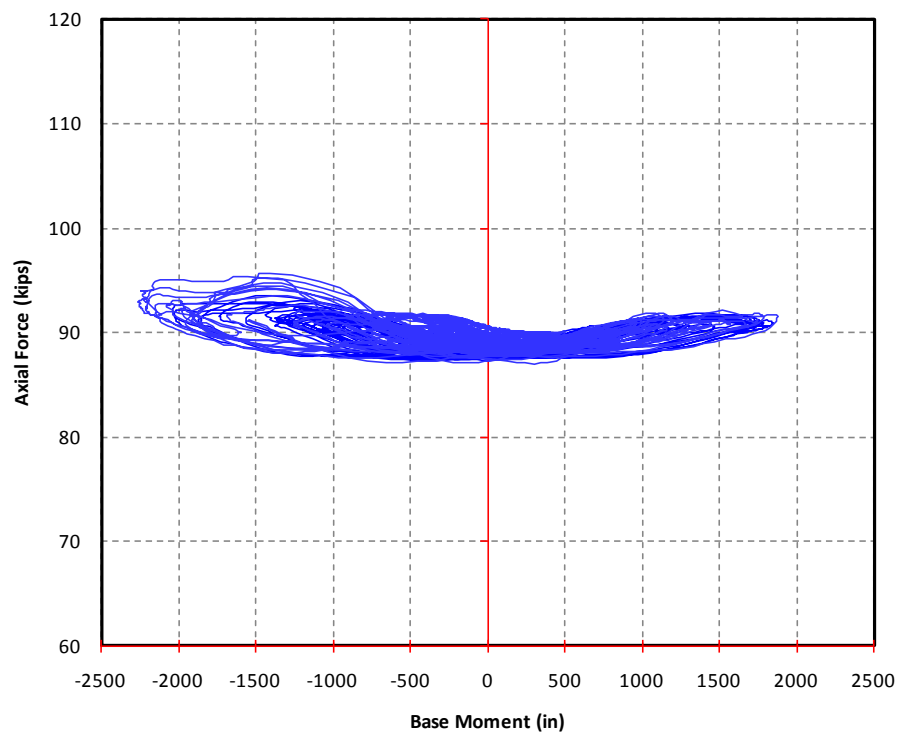


Figure 6-14 Axial Load - Base Moment Accumulated Hysteresis for Specimen ISL1.0

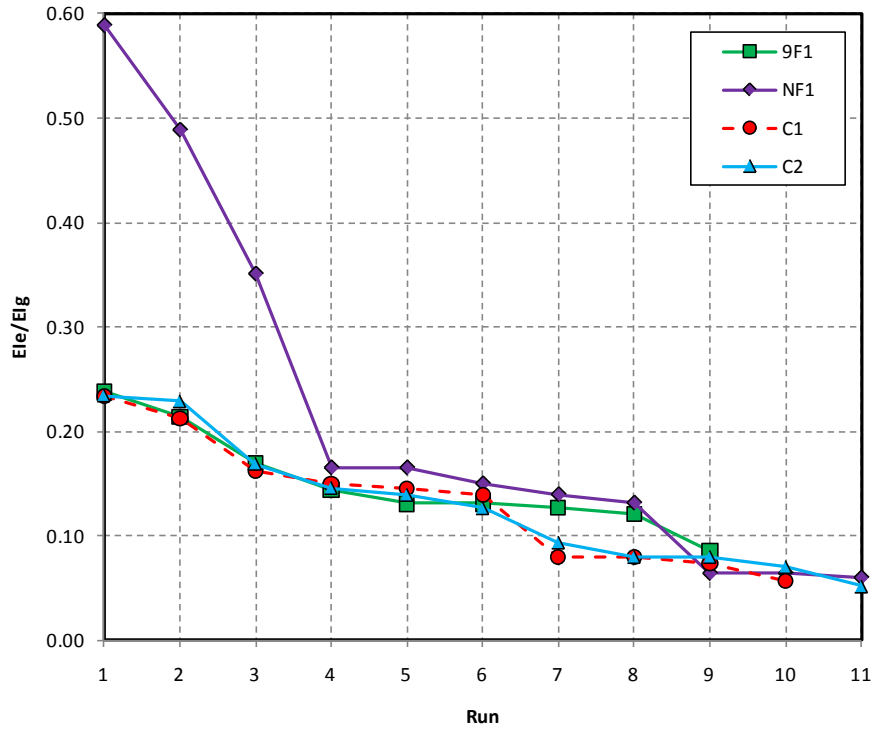


Figure 6-15 Variation in Effective Lateral Stiffness, Circular Specimens

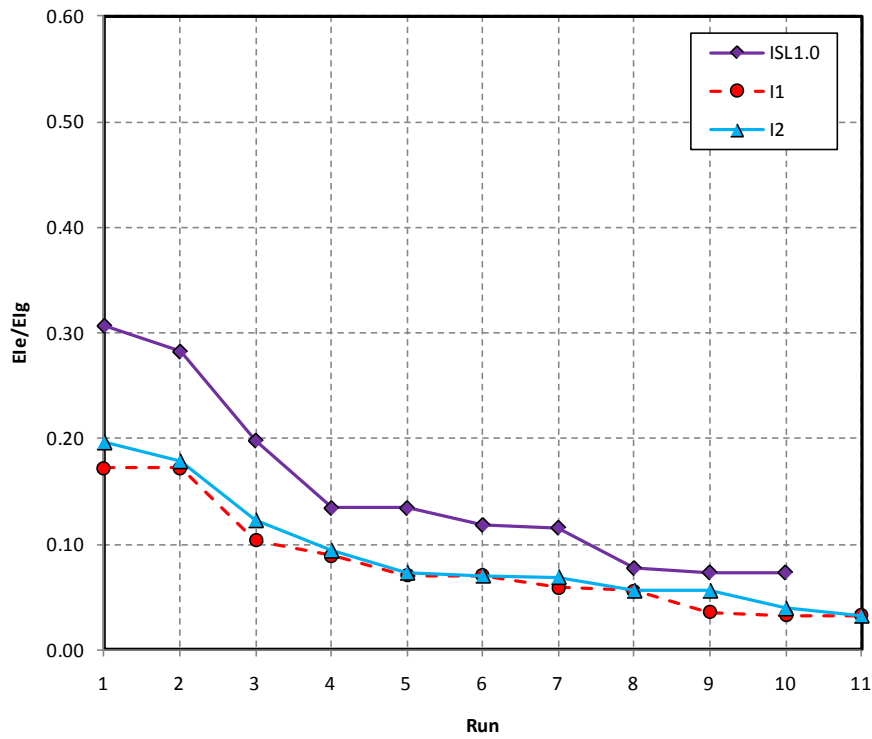


Figure 6-16 Variation in Effective Lateral Stiffness, Interlocking Specimens

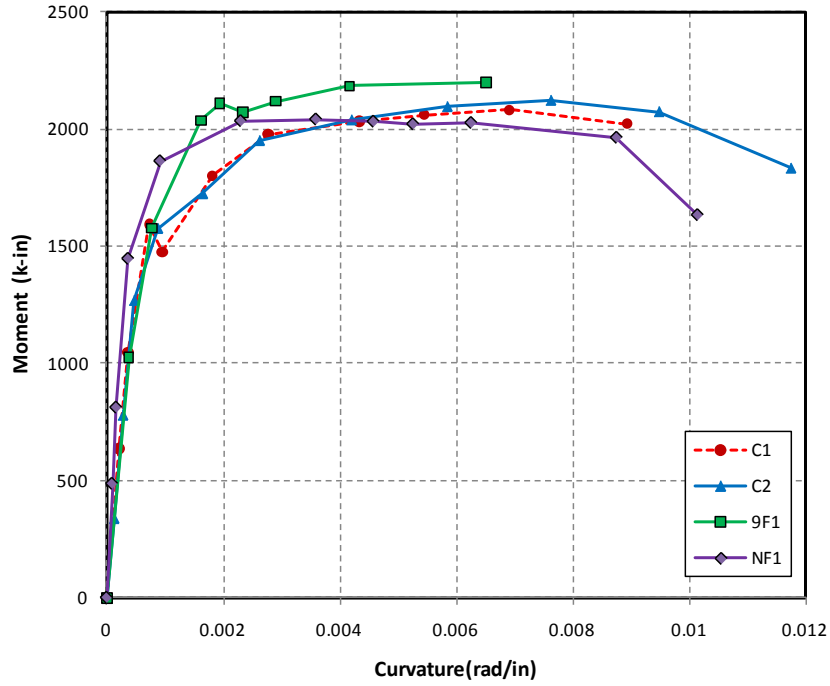


Figure 6-17 Comparison of Moment-Curvature (M-φ) Envelopes, Circular Specimens

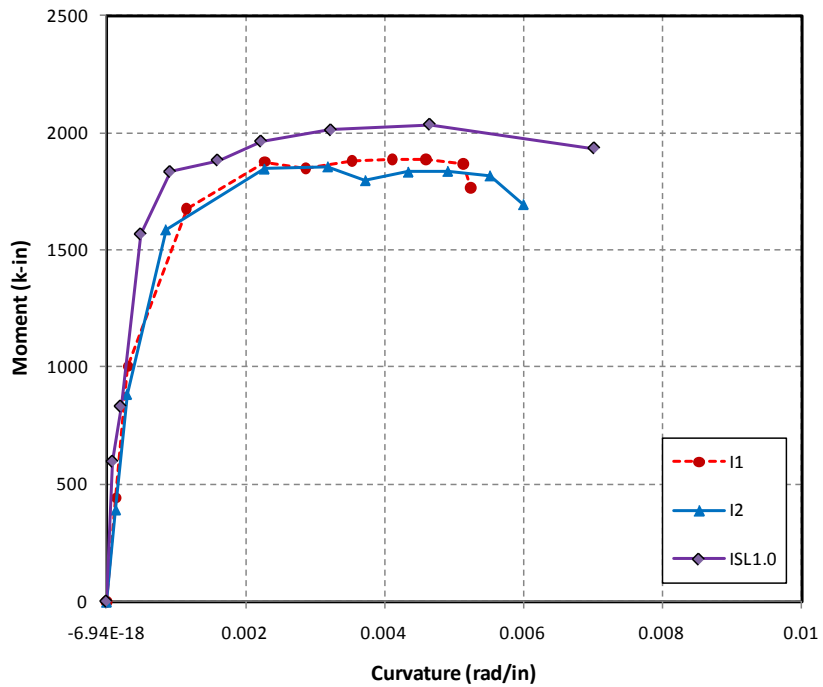


Figure 6-18 Comparison of Moment-Curvature (M-φ) Envelopes, Interlocking Specimens

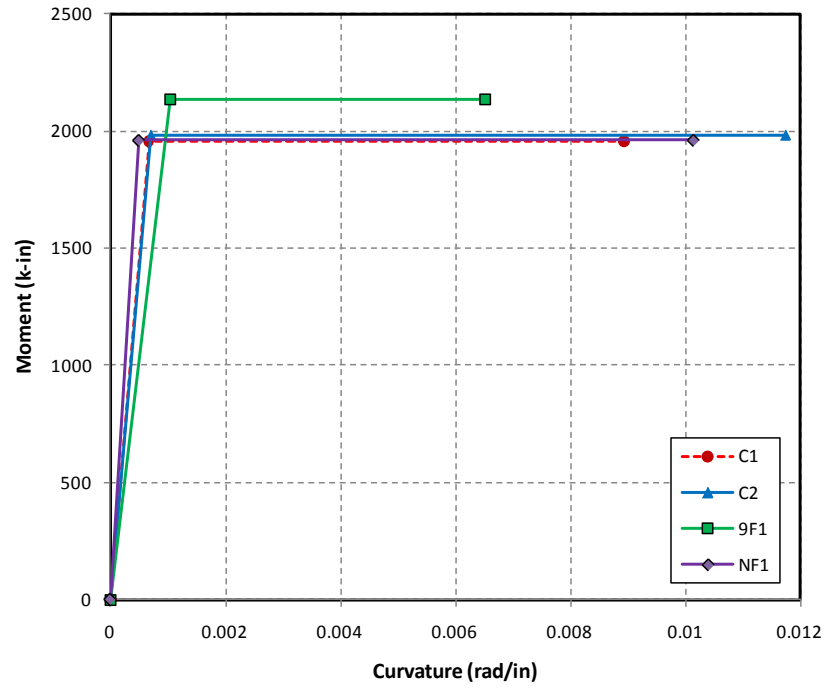


Figure 6-19 Comparison of Elasto-Plastic Envelopes (M- $\phi$ ), Circular Specimens

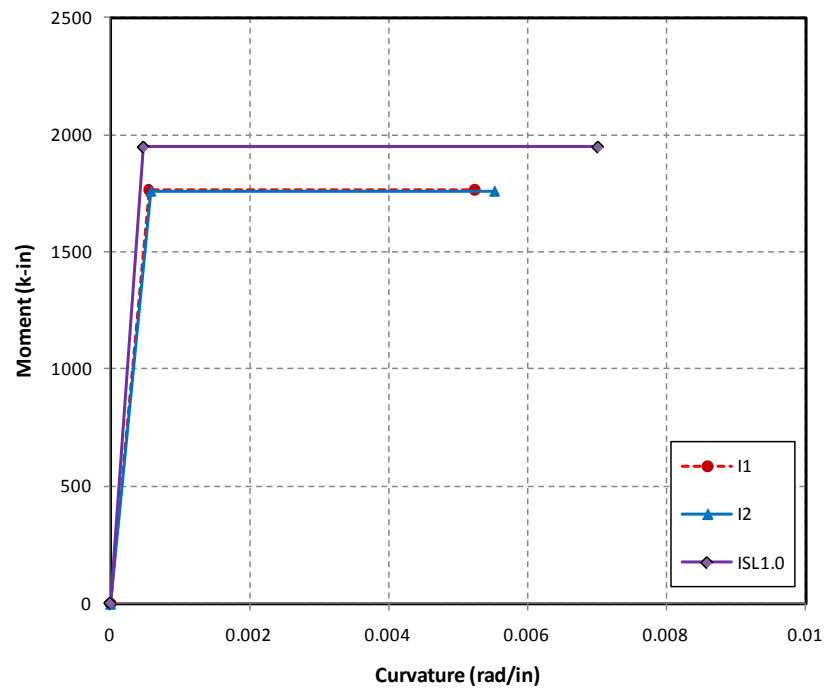


Figure 6-20 Comparison of Elasto-Plastic Envelopes (M- $\phi$ ), interlocking Specimens



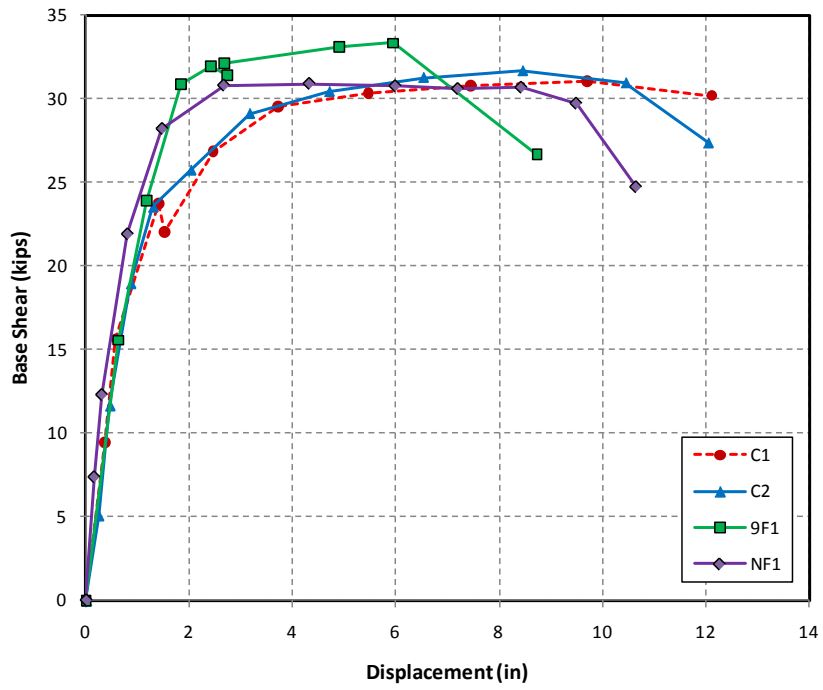


Figure 6-21 Comparison of Base Shear-Displacement Envelopes, Circular Specimens

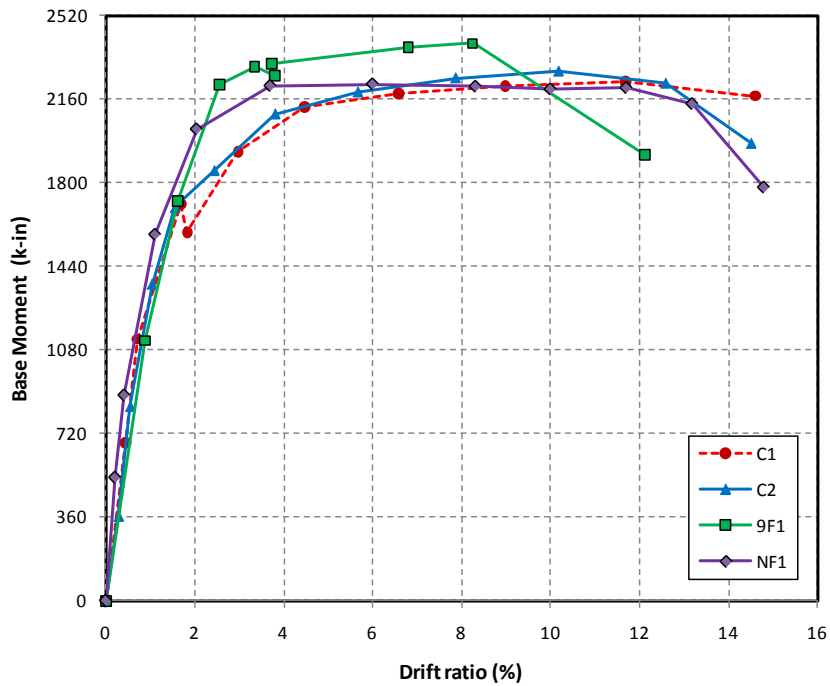


Figure 6-22 Comparison of Base Moment-Drift Ratio Envelopes, Circular Specimens

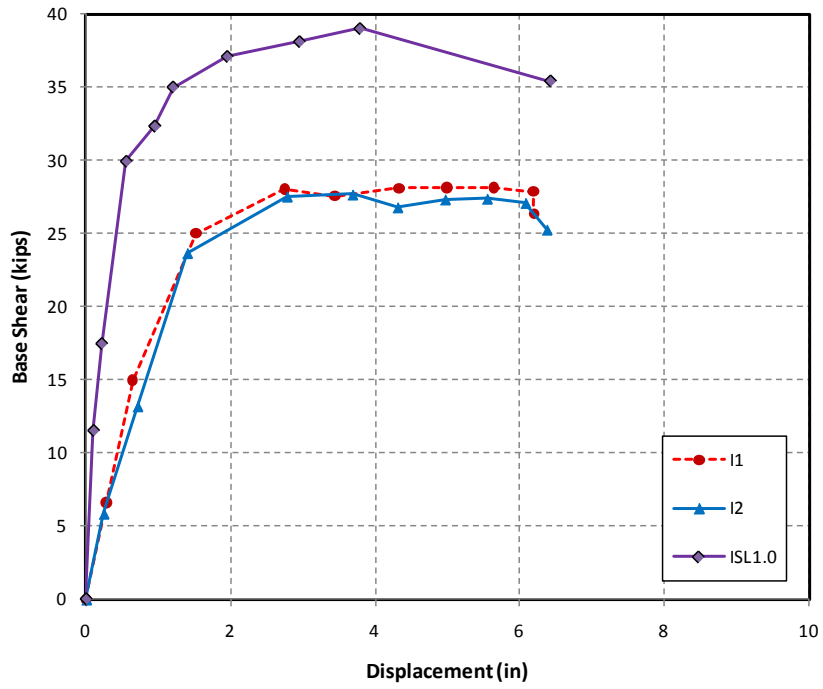


Figure 6-23 Comparison of Envelopes Base Shear-Displacement, Interlocking Specimens

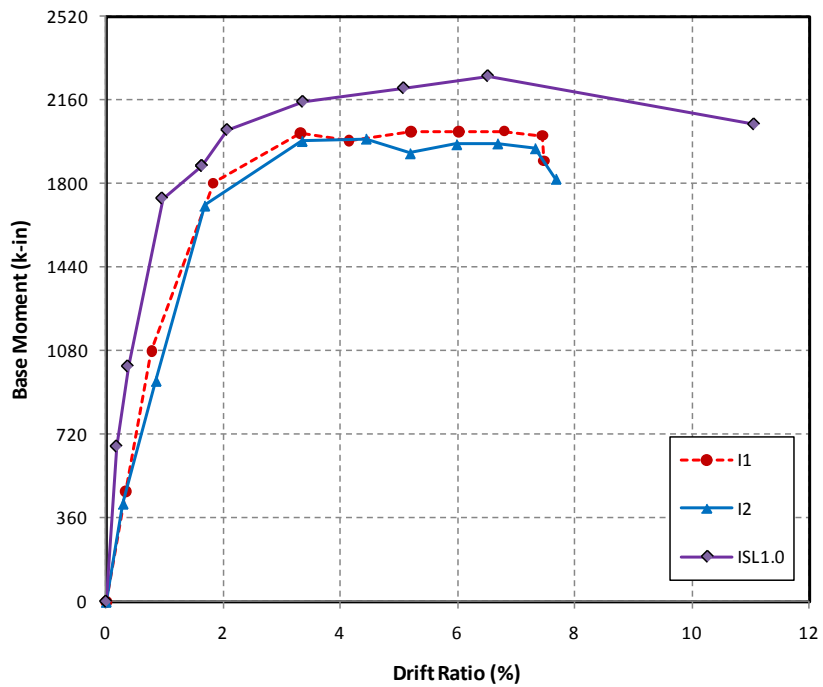


Figure 6-24 Comparison of Elasto-Plastic Envelopes (F-D) for Interlocking Specimens

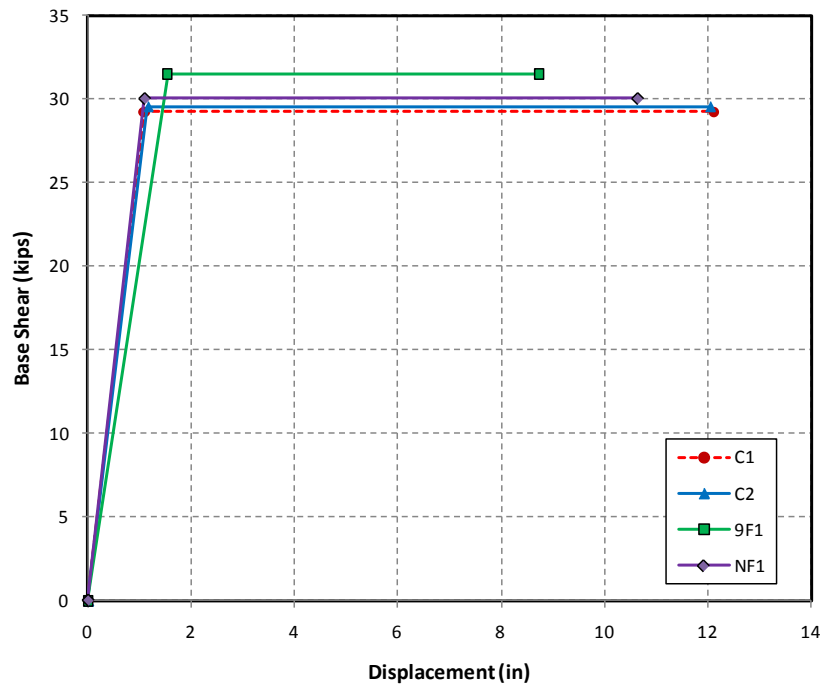


Figure 6-25 Comparison of Elasto-Plastic Envelopes (BS-D), Circular Specimens

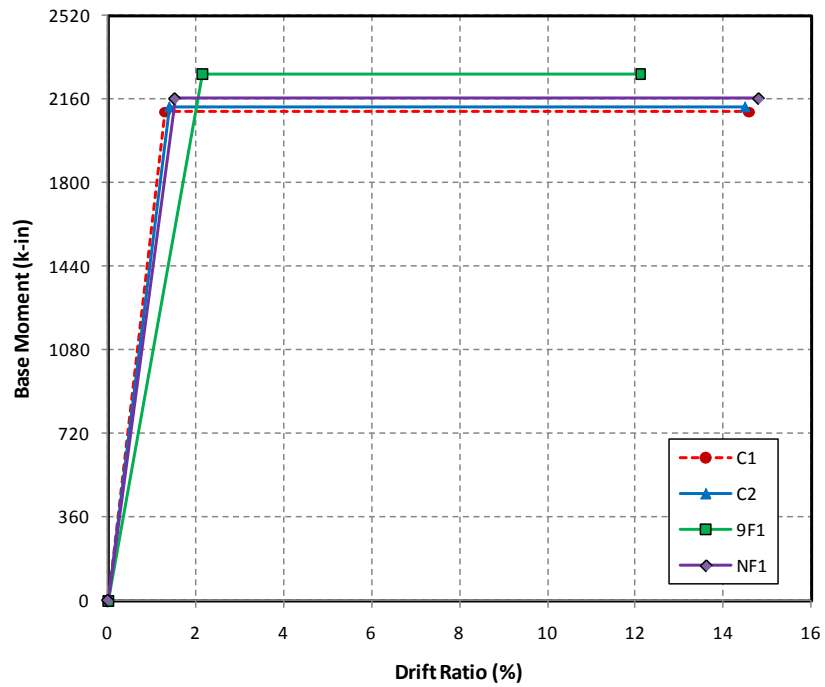


Figure 6-26 Comparison of Elasto-Plastic Envelopes (M- $\delta$ ), Circular Specimens

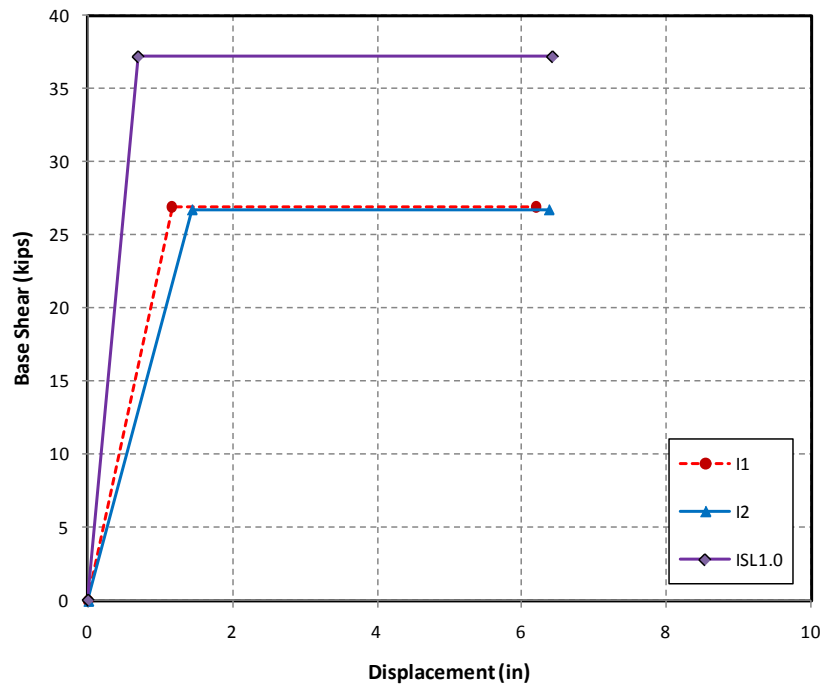


Figure 6-27 Comparison Between Elasto-Plastic Envelopes (BS-D), Interlocking Specimens

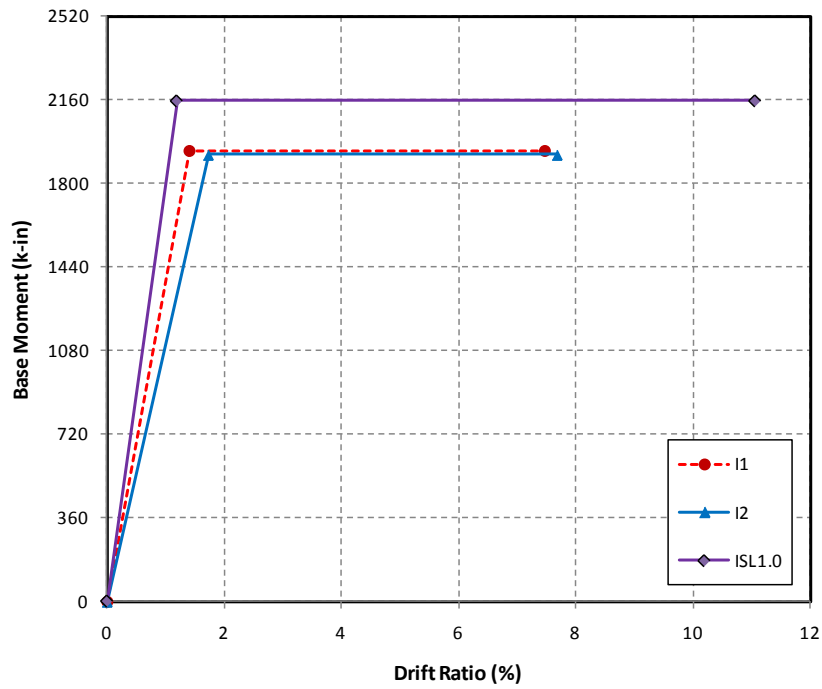
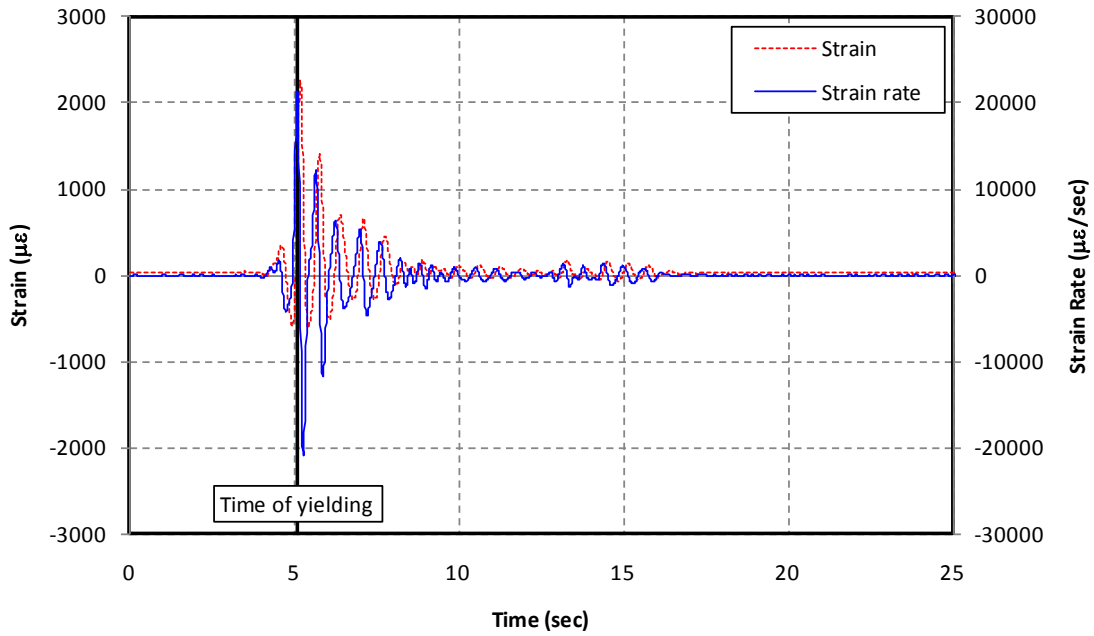
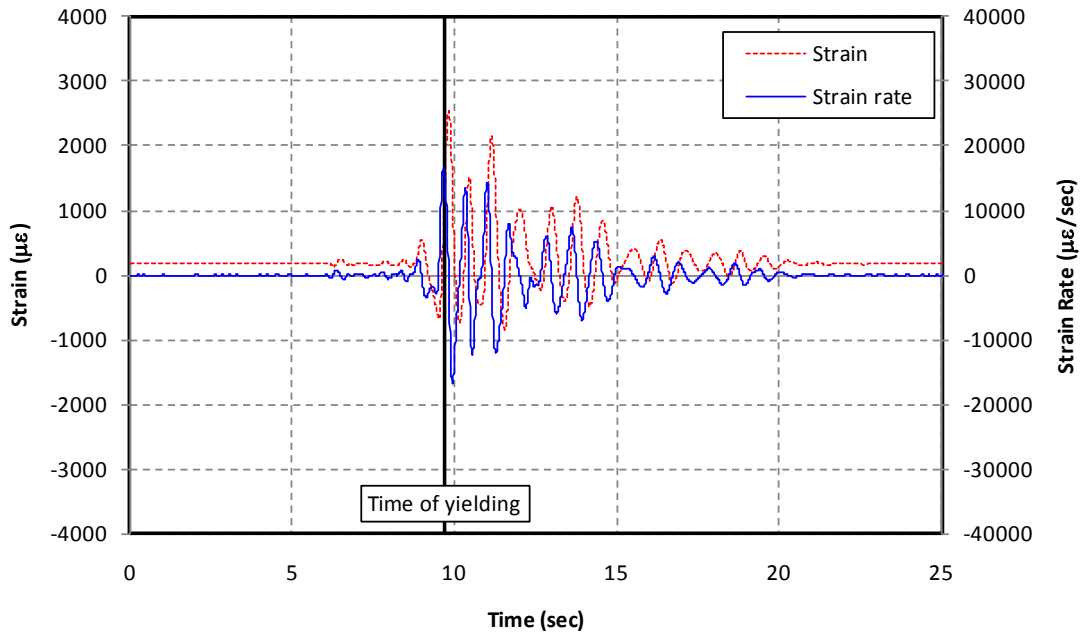


Figure 6-28 Comparison Between Elasto-Plastic Envelopes (M- $\delta$ ), Interlocking Specimens



**Figure 7-1 Typical Strain and Strain Rate Histories at First Yielding, Specimen C2**



**Figure 7-2 Typical Strain and Strain Rate Histories at First Yielding, Specimen I2**

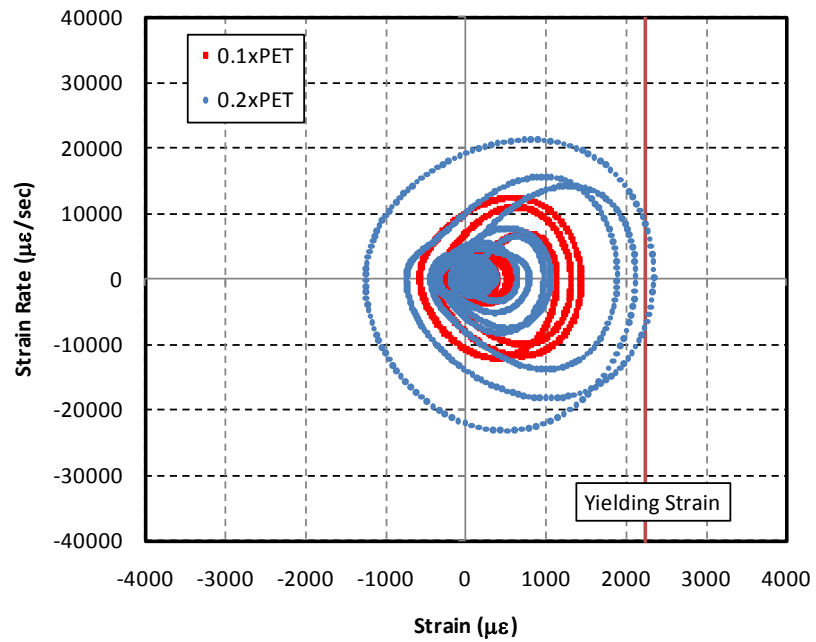


Figure 7-3 Measured Strain Rate versus Strain at Yielding, Specimen C1 (Sg 16)

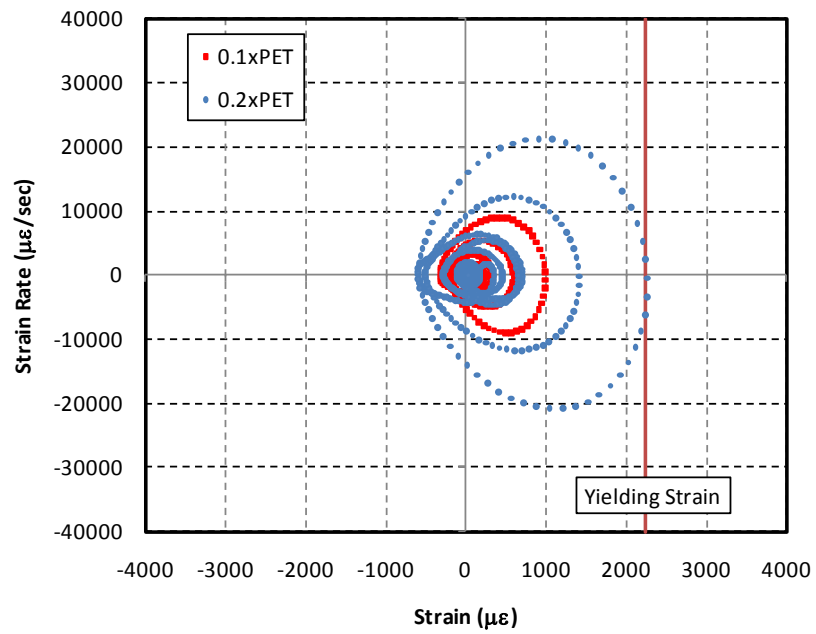


Figure 7-4 Measured Strain Rate versus Strain at Yielding, Specimen C2 (Sg 12)

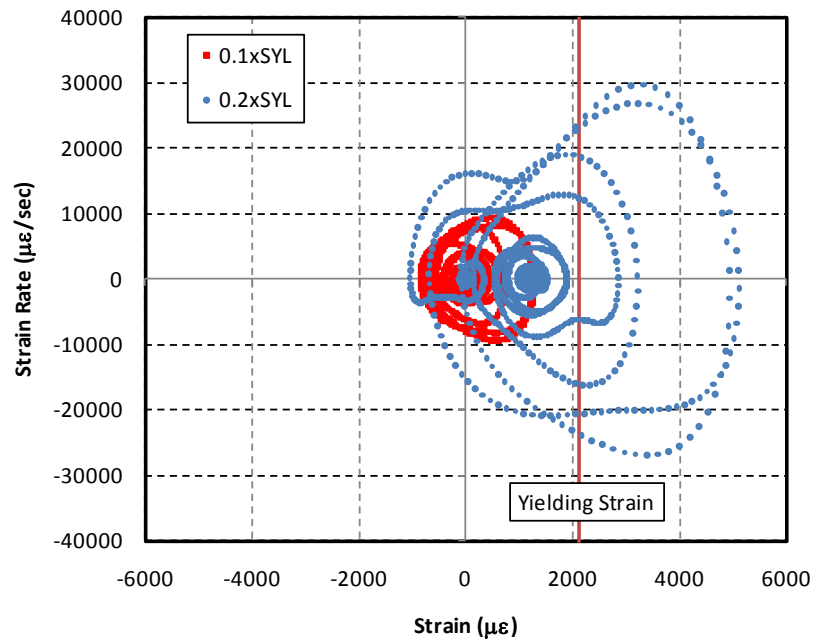


Figure 7-5 Measured Strain Rate versus Strain at Yielding, Specimen I1 (Sg 11)

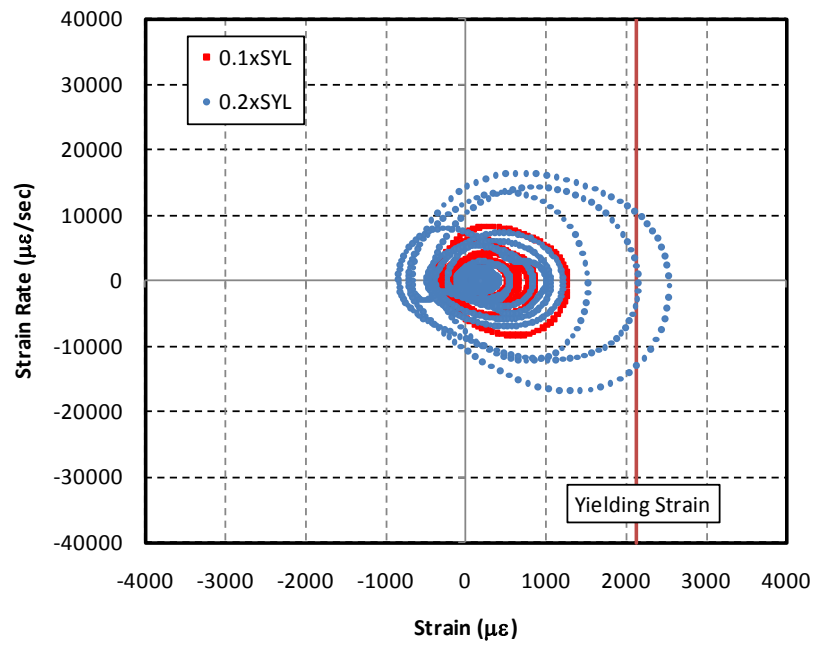


Figure 7-6 Measured Strain Rate versus Strain at Yielding, Specimen I2 (Sg 11)

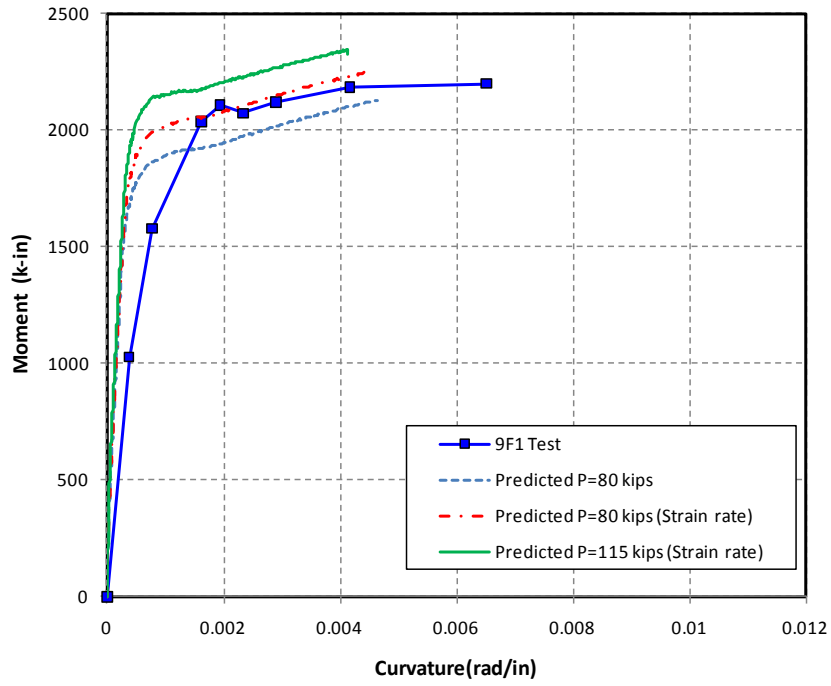


Figure 7-7 Measured and Calculated Moment-Curvature, 9F1

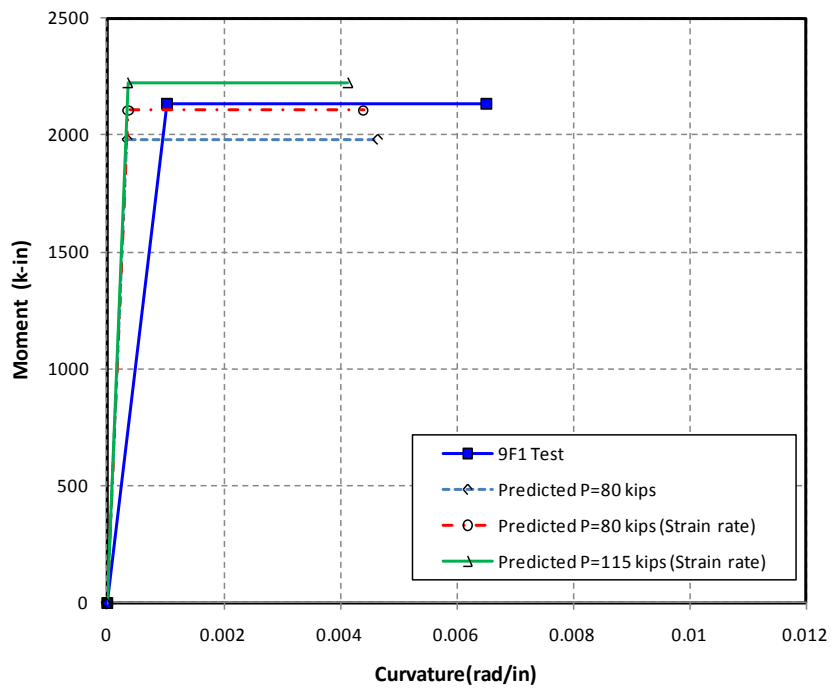


Figure 7-8 Measured and Calculated Elasto-Plastic  $M-\phi$ , 9F1



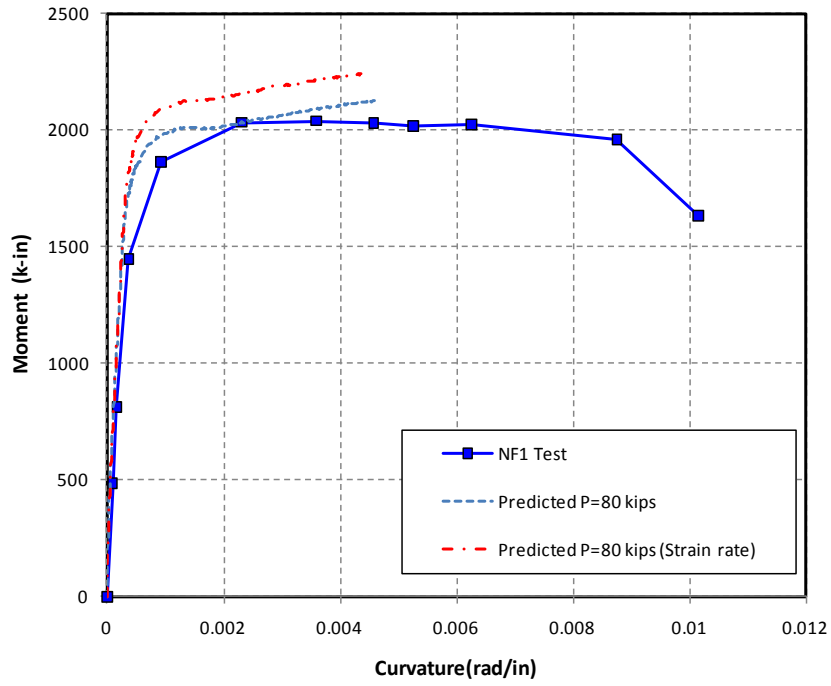


Figure 7-9 Measured and Calculated Moment-Curvature, NF1

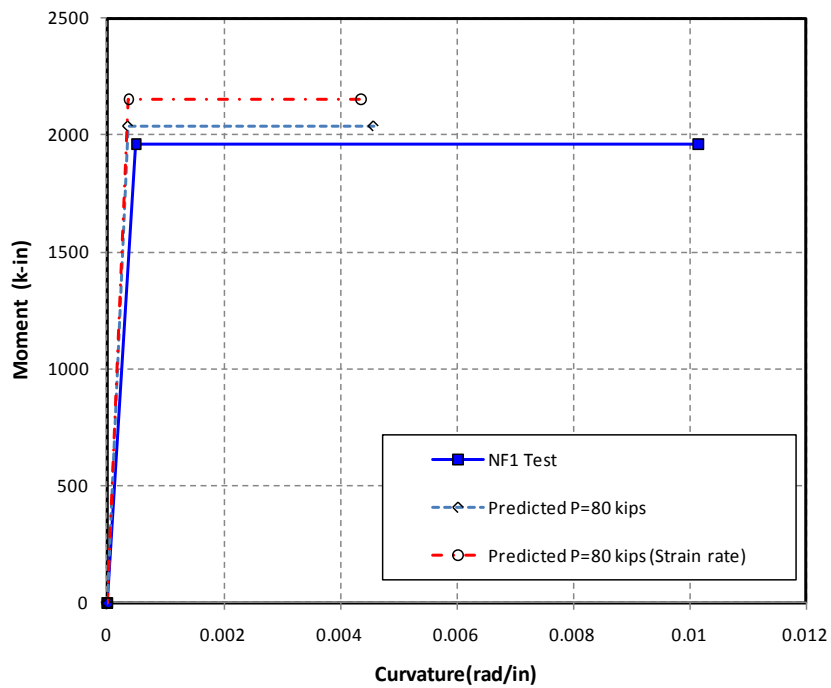


Figure 7-10 Measured and Calculated Elasto-Plastic M- $\phi$ , NF1

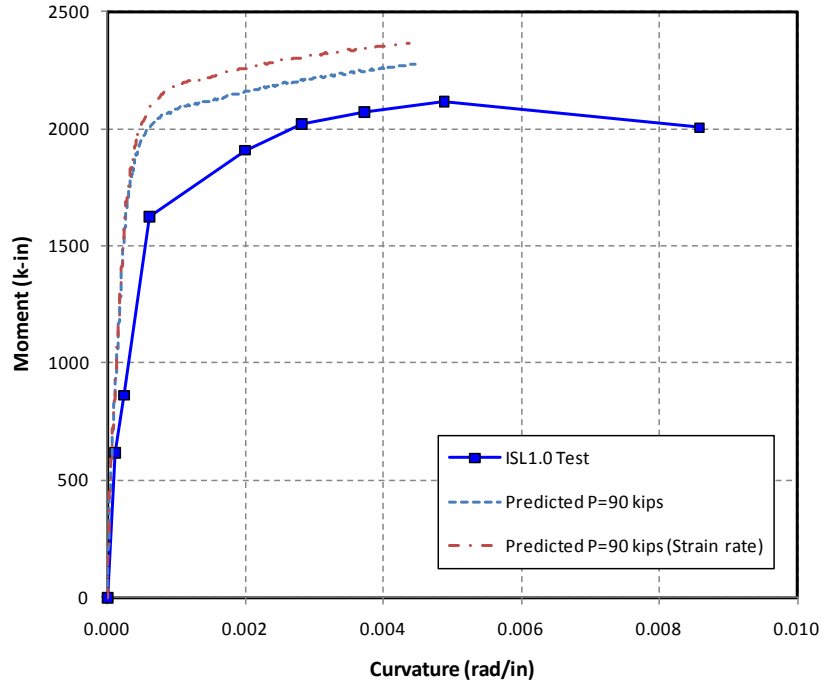


Figure 7-11 Measured and Calculated Moment-Curvature, ISL1.0

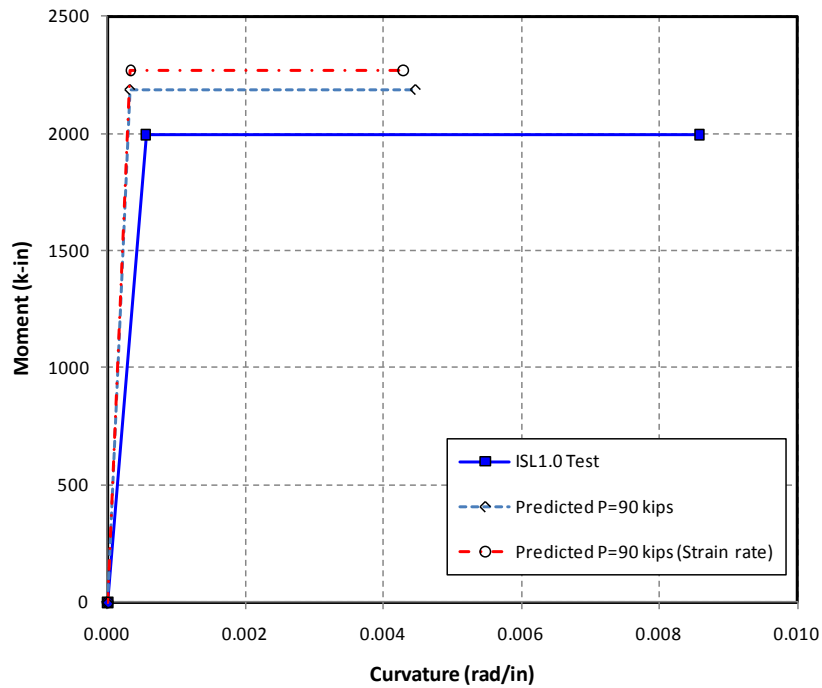


Figure 7-12 Measured and Calculated Elasto-Plastic M-φ, ISL1.0

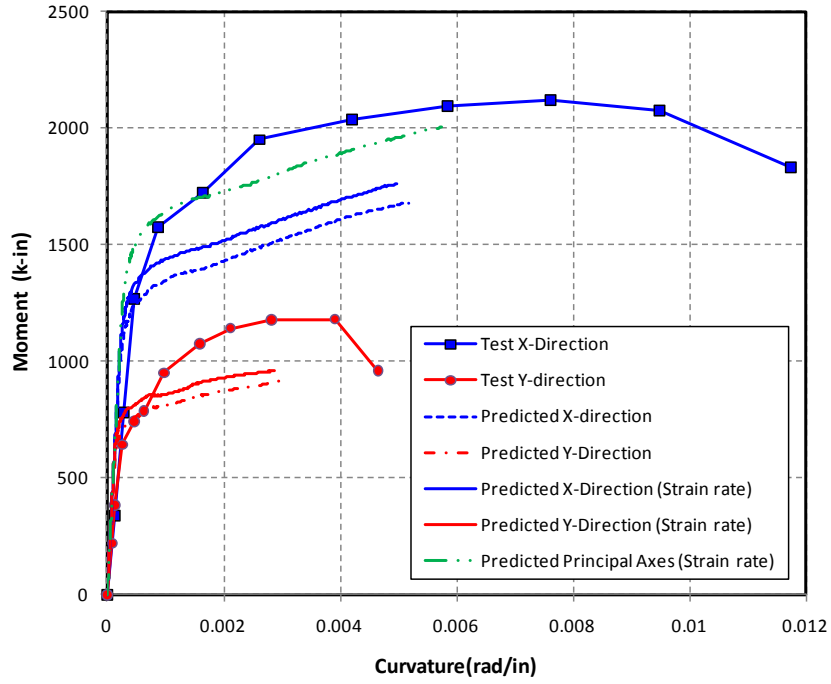


Figure 7-13 Measured and Calculated Moment-Curvature, C1 and C2 (NA=30°)

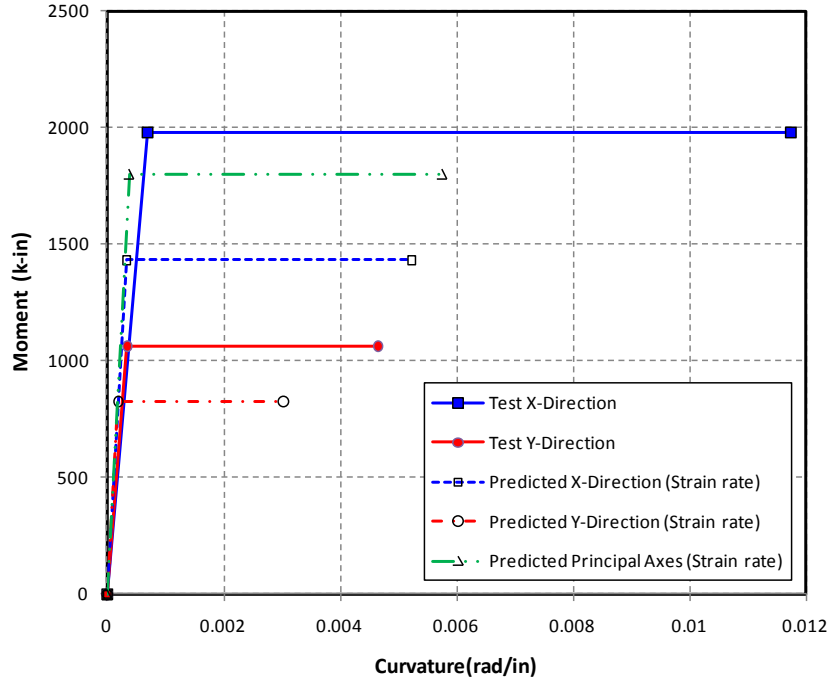


Figure 7-14 Measured and Calculated Elasto-Plastic M-φ, C1 and C2 (NA=30°)

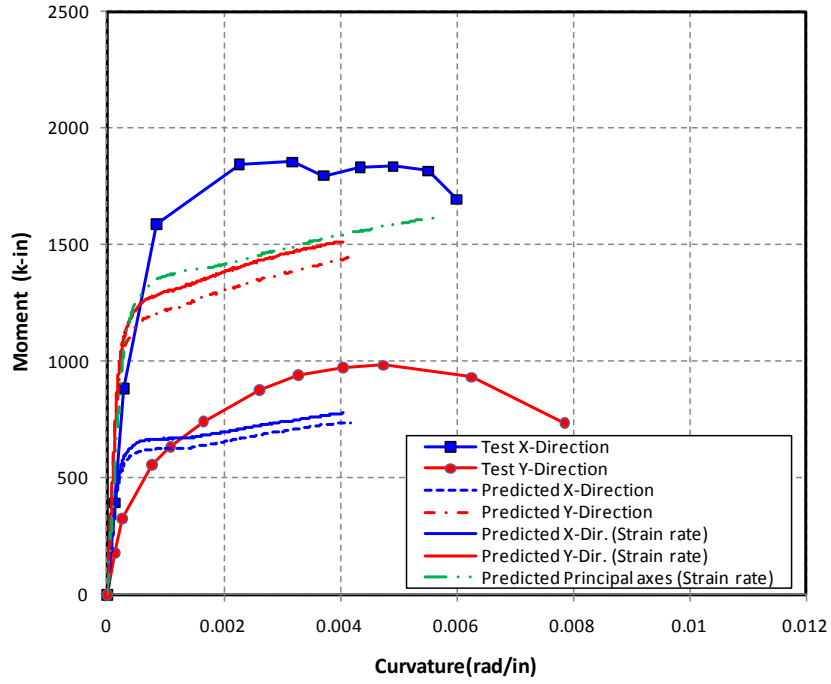


Figure 7-15 Measured and Calculated Moment-Curvature, I1 and I2 (NA=45°)

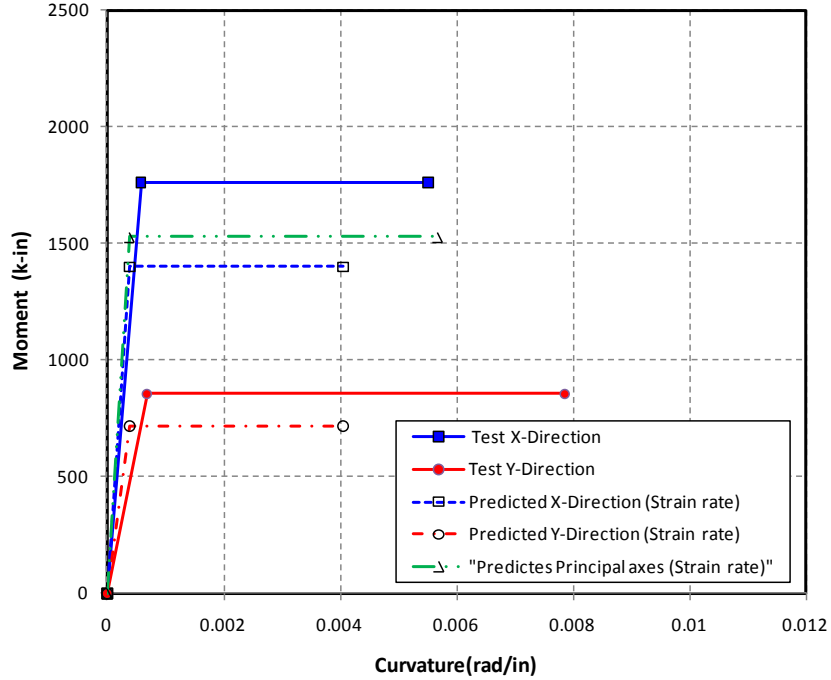


Figure 7-16 Measured and Calculated Elasto-Plastic M-φ, I1 and I2 (NA=45°)

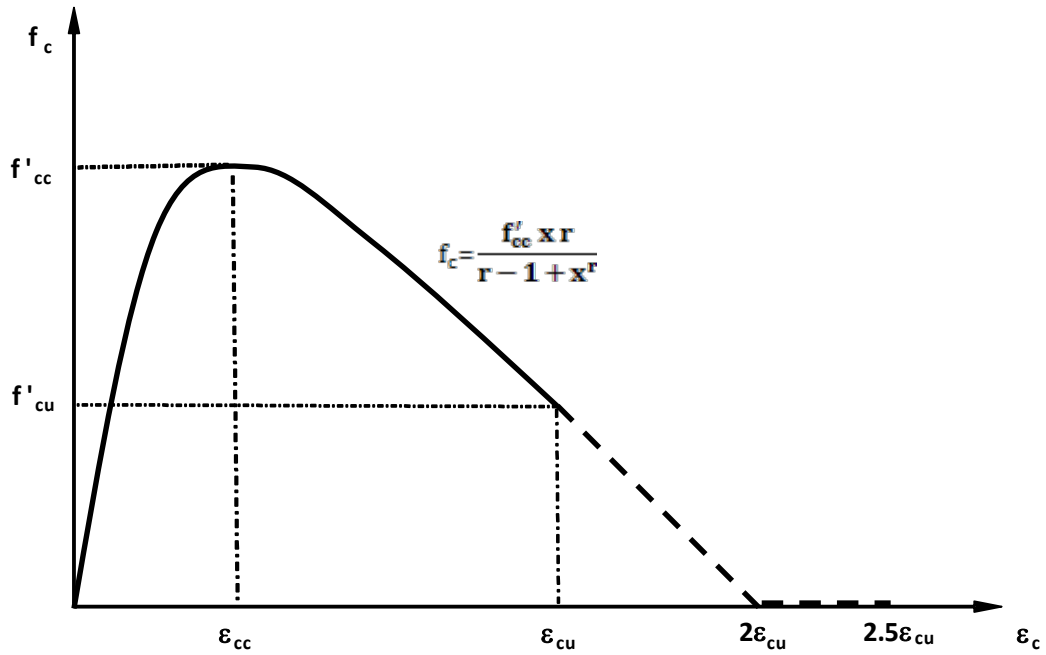


Figure 7-17 Modified Mander's Model for Confined Concrete, Used for M- $\phi$  Analysis

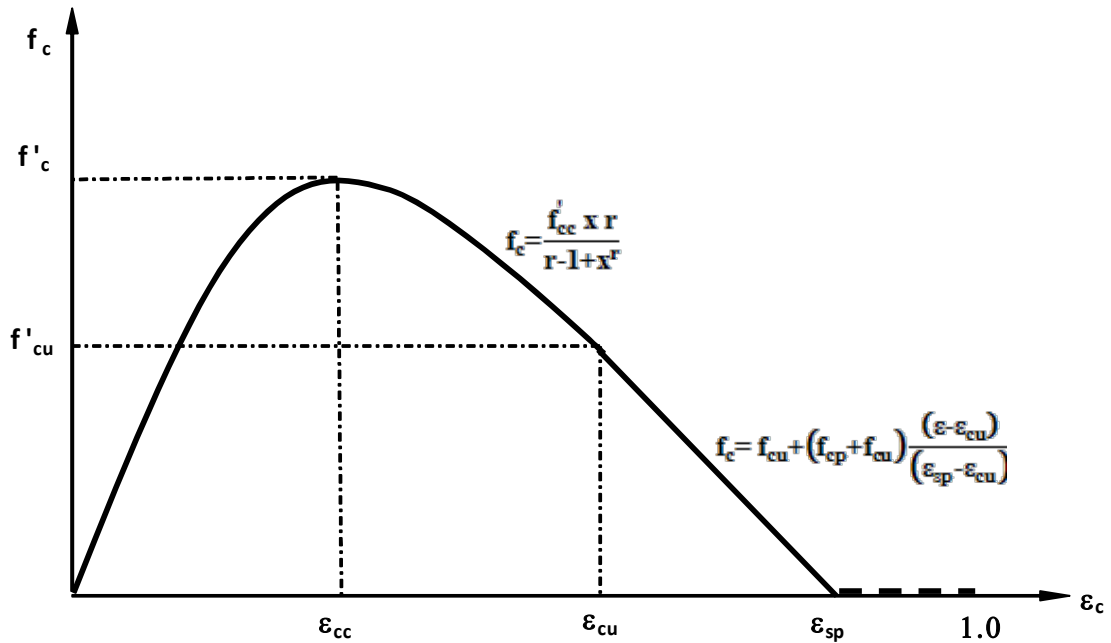


Figure 7-18 Modified Mander's Model for Unconfined Concrete, Used for M- $\phi$  Analysis

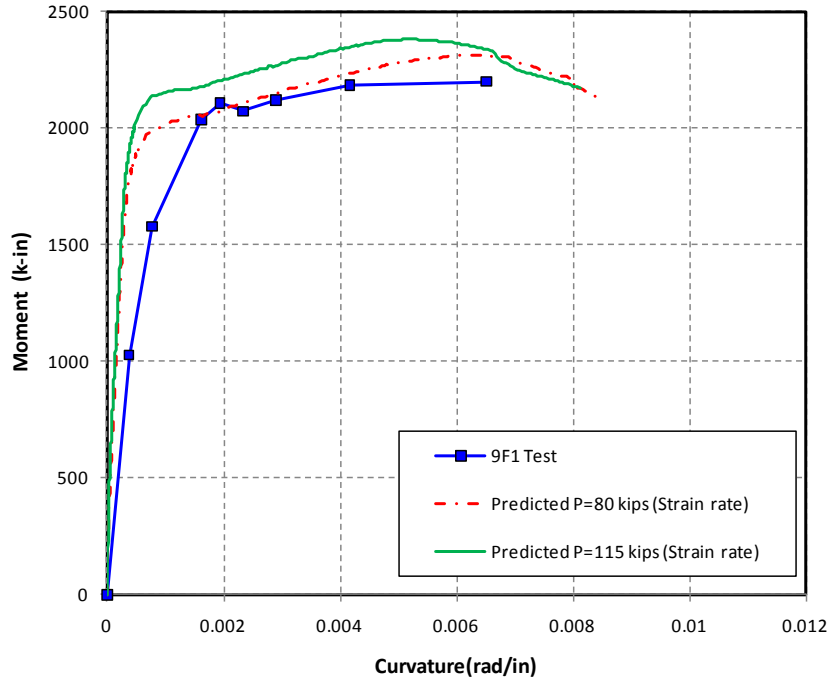


Figure 7-19 Measured and Calculated Moment-Curvature, 9F1 (Modified Model)

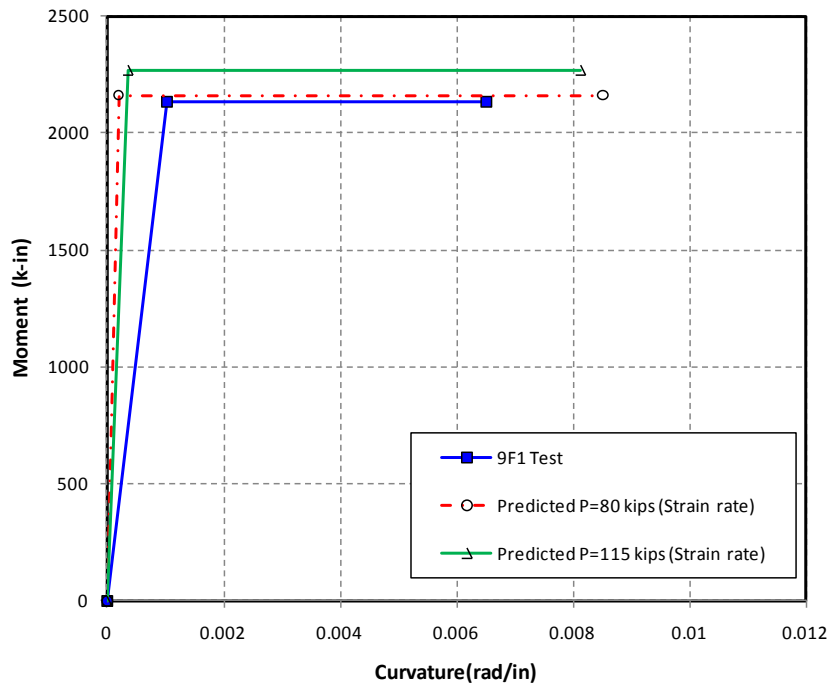


Figure 7-20 Measured and Calculated Elasto-Plastic  $M-\phi$ , 9F1 (Modified Model)

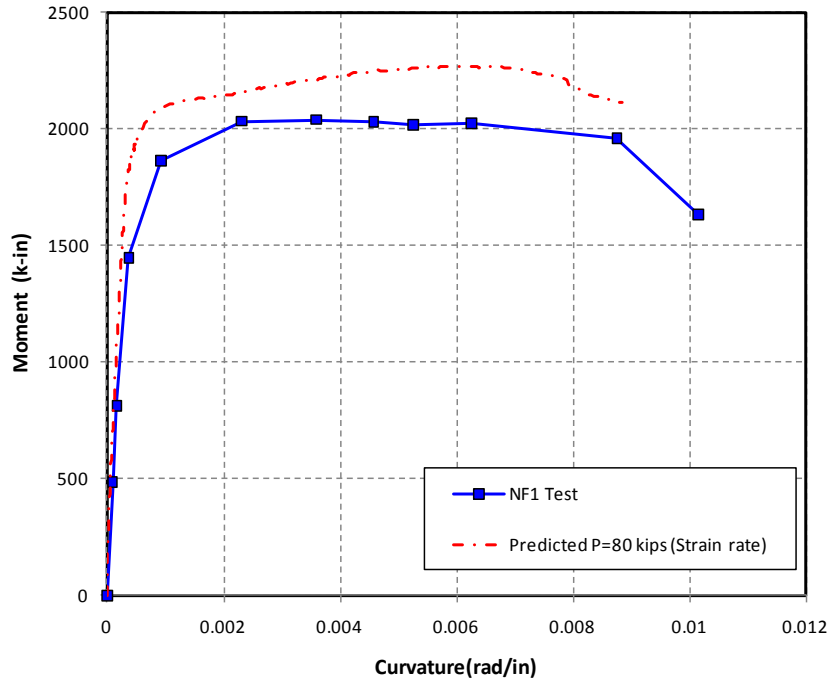


Figure 7-21 Measured and Calculated Moment-Curvature, NF1 (Modified Model)

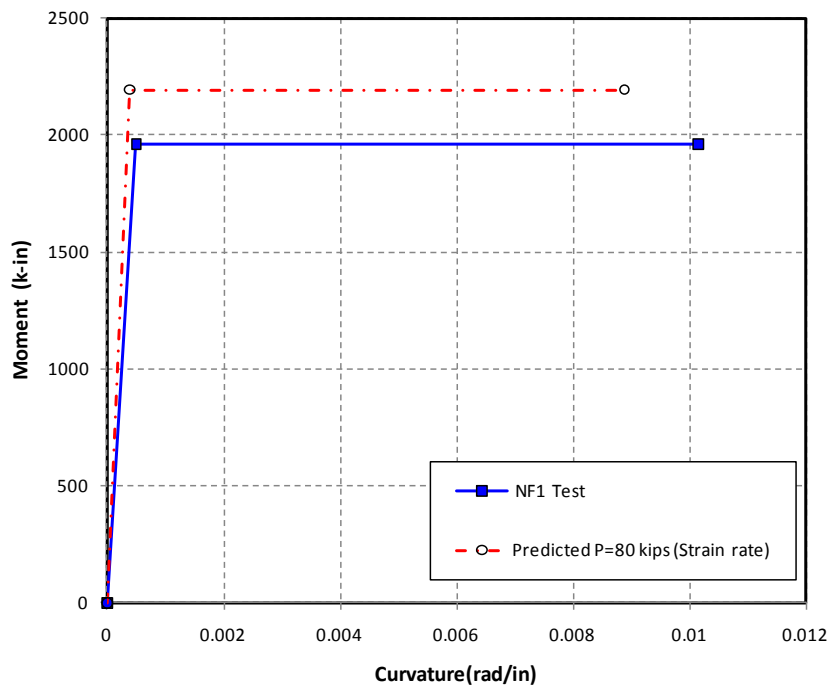


Figure 7-22 Measured and Calculated Elasto-Plastic M-φ, NF1 (Modified Model)

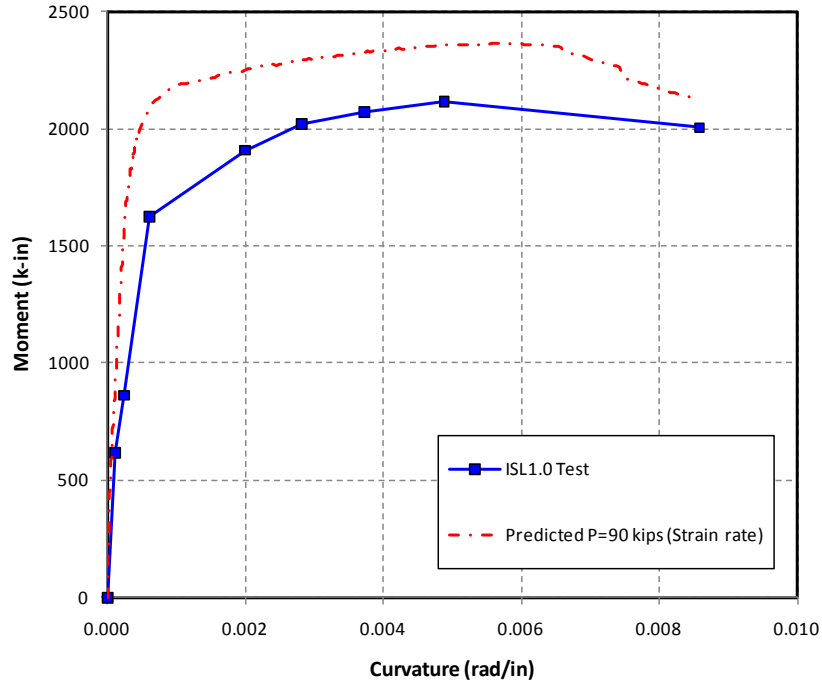


Figure 7-23 Measured and Calculated Moment-Curvature, ISL1.0 (Modified Model)

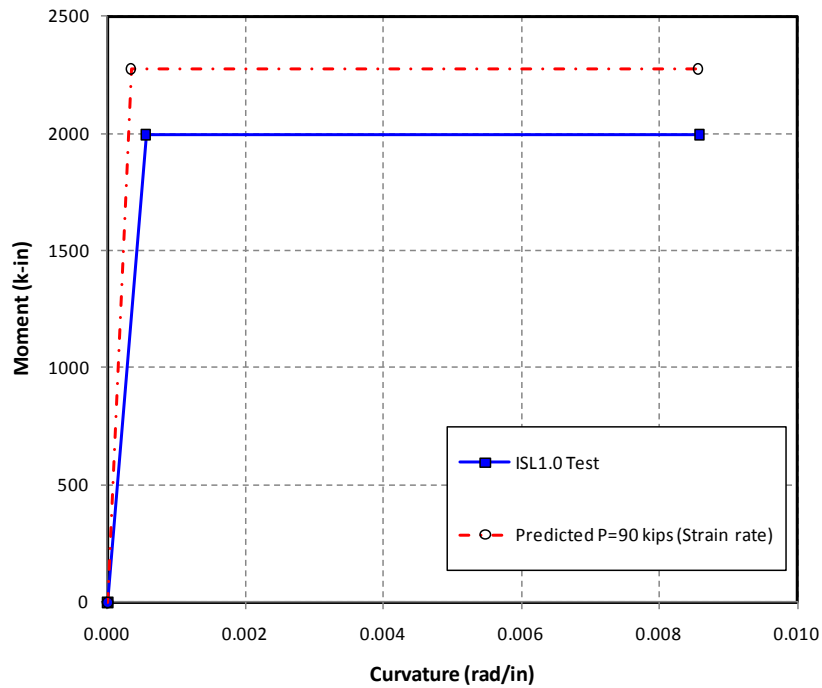


Figure 7-24 Measured and Calculated Elasto-Plastic M-phi, ISL1.0 (Modified Model)



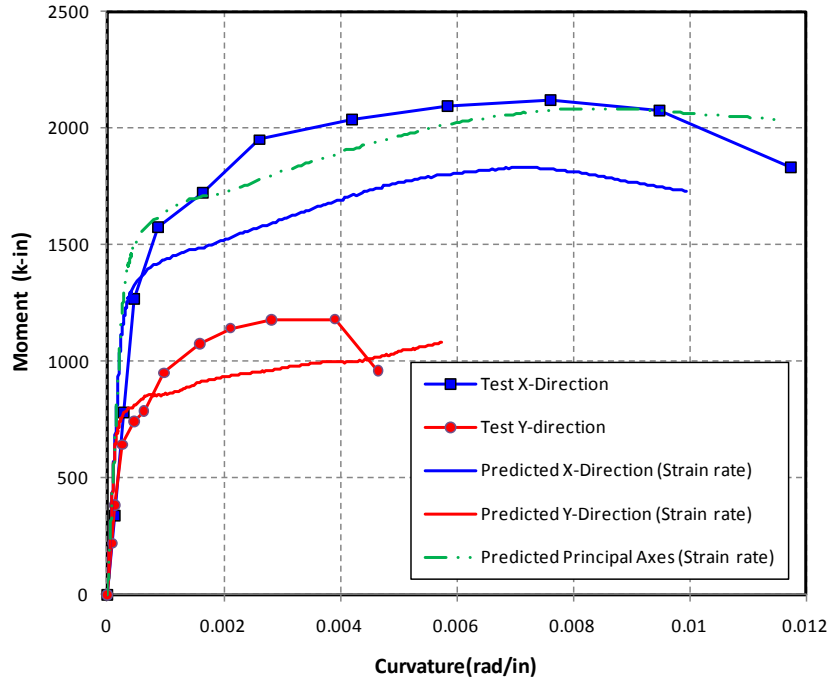


Figure 7-25 Measured and Calculated M- $\phi$ , C1 and C2 (NA=30°) (Modified Model)

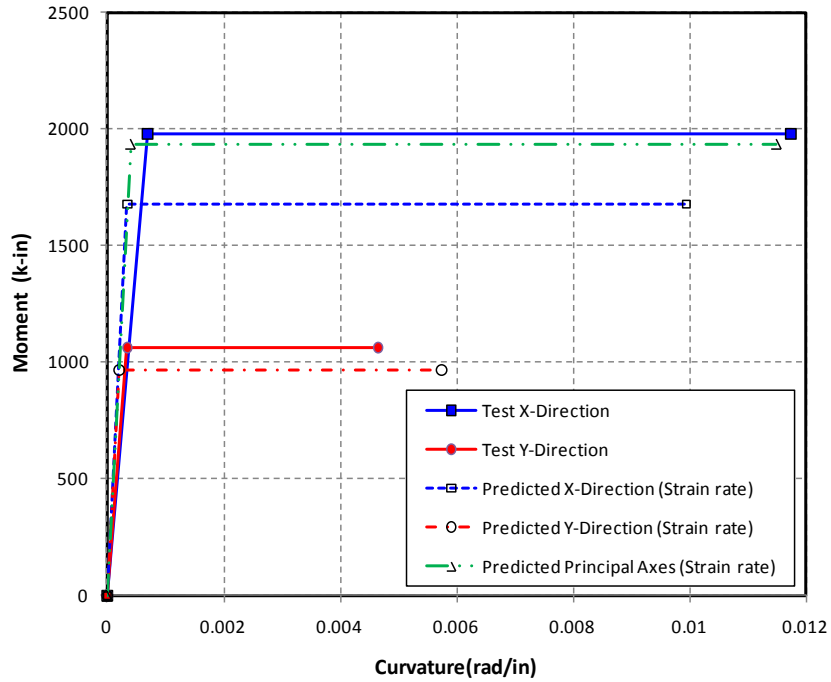


Figure 7-26 Measured and Calculated Elasto-Plastic M- $\phi$ , C1 and C2 (Modified Model)

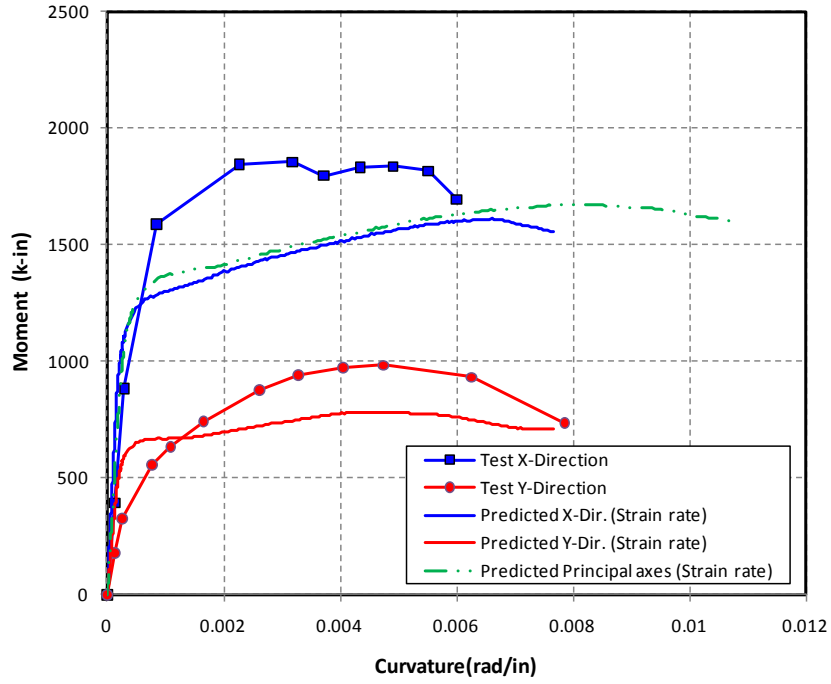


Figure 7-27 Measured and Calculated  $M-\phi$ ,  $I_1$  and  $I_2$  ( $NA=45^\circ$ ) (Modified Model)

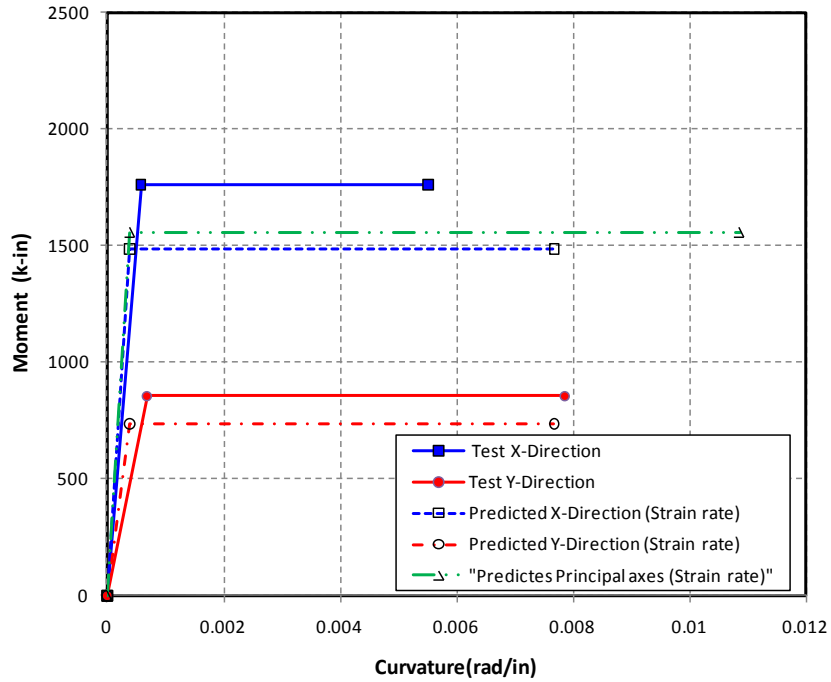


Figure 7-28 Measured and Calculated Elasto-Plastic  $M-\phi$ ,  $I_1$  and  $I_2$  (Modified Model)

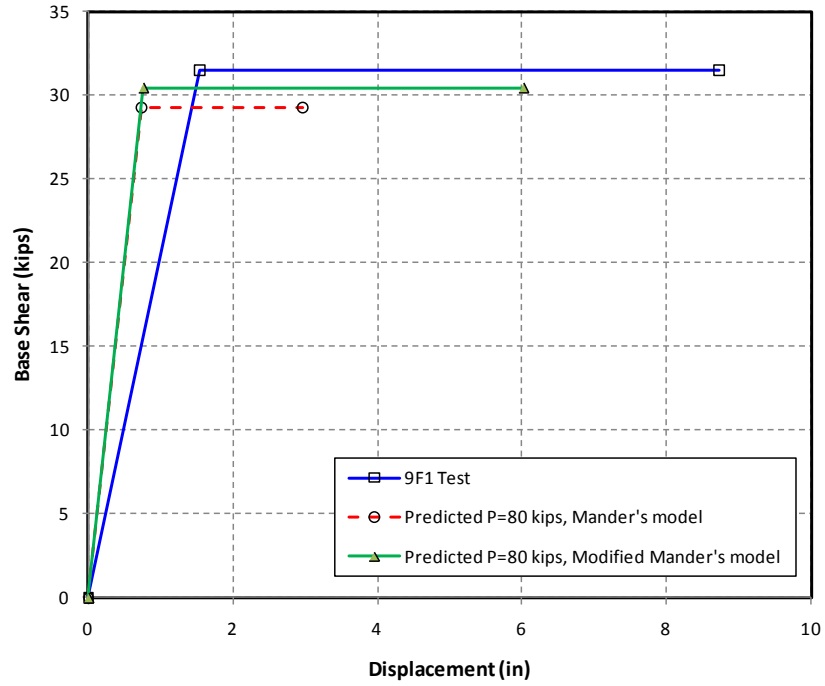


Figure 7-29 Measured and Calculated Force-Displacement, 9F1 (P=80 kips)

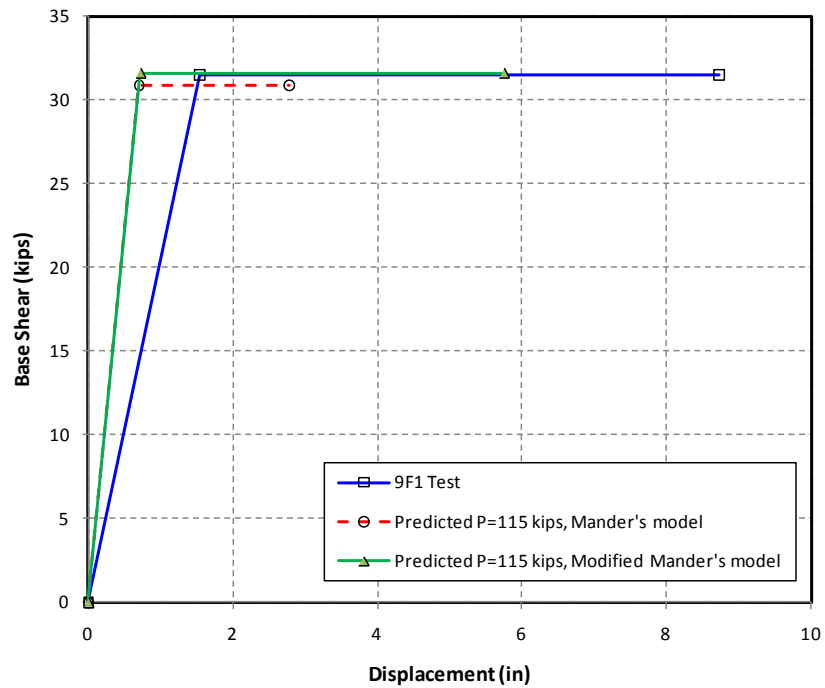


Figure 7-30 Measured and Calculated Force-Displacement, 9F1 (P=115 kips)

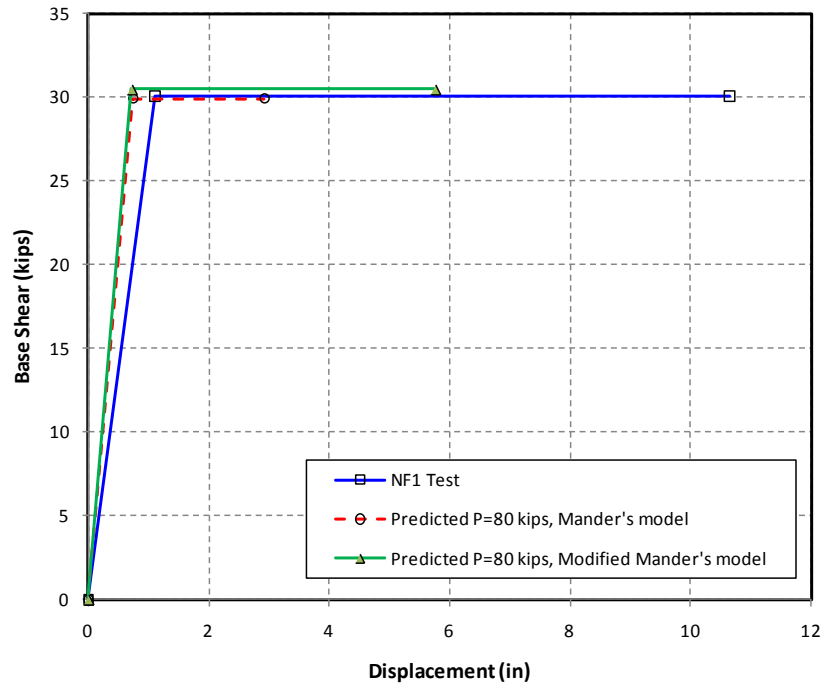


Figure 7-31 Measured and Calculated Force-Displacement, NF1

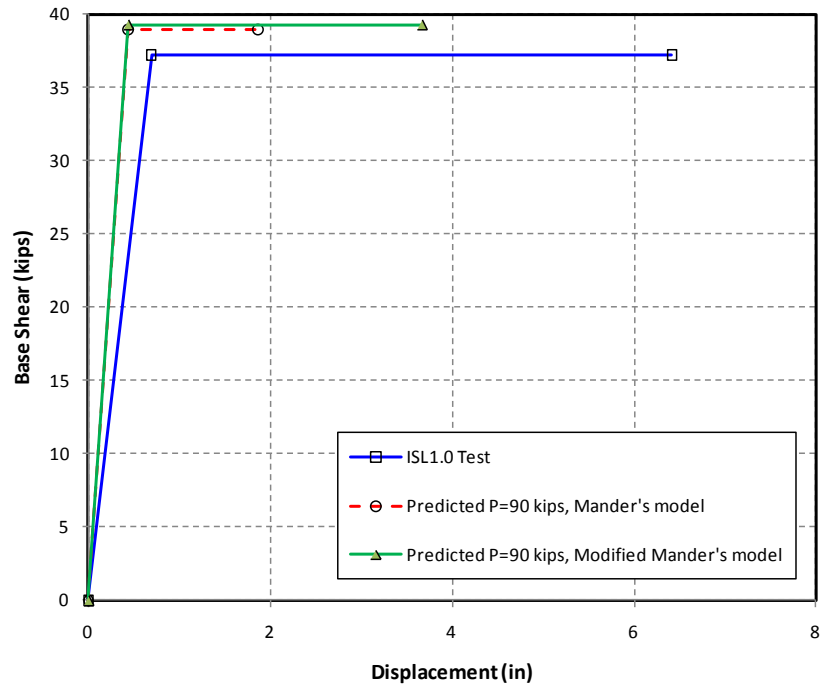


Figure 7-32 Measured and Calculated Force-Displacement, ISL1.0

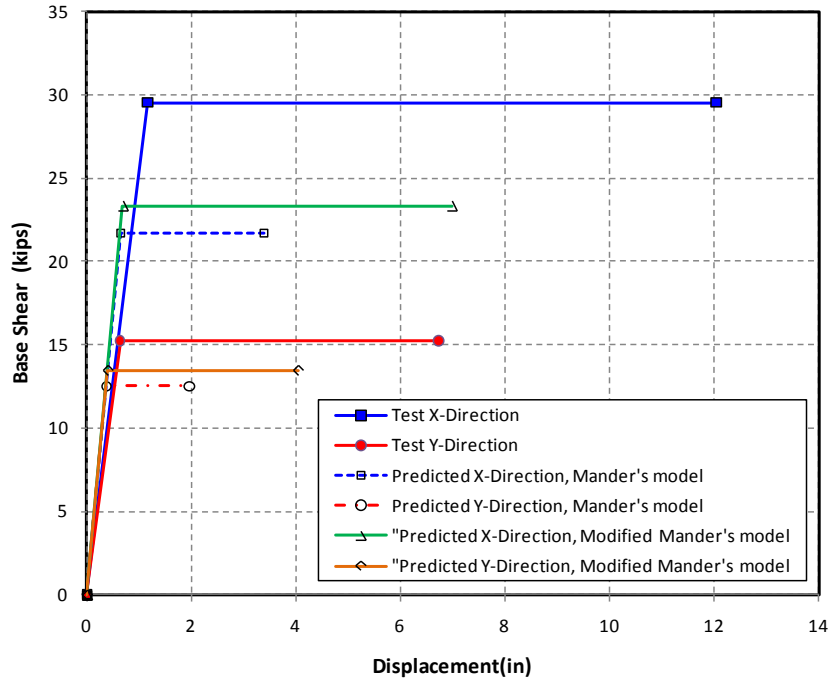


Figure 7-33 Measured and Calculated Force-Displacement, C1 and C2 (NA=30°)

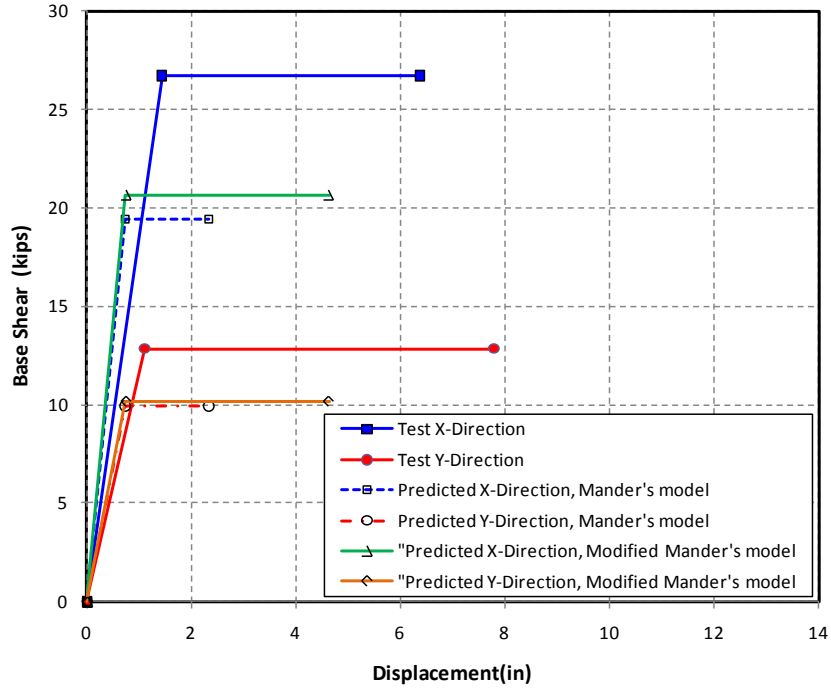
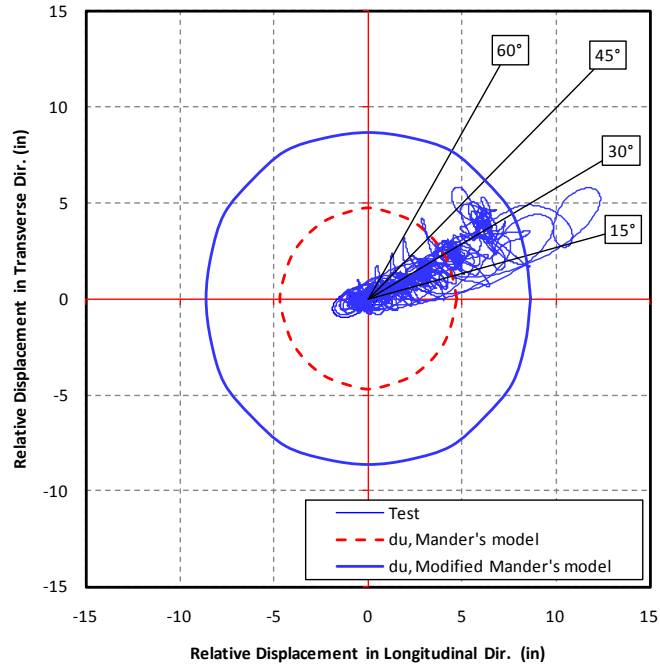
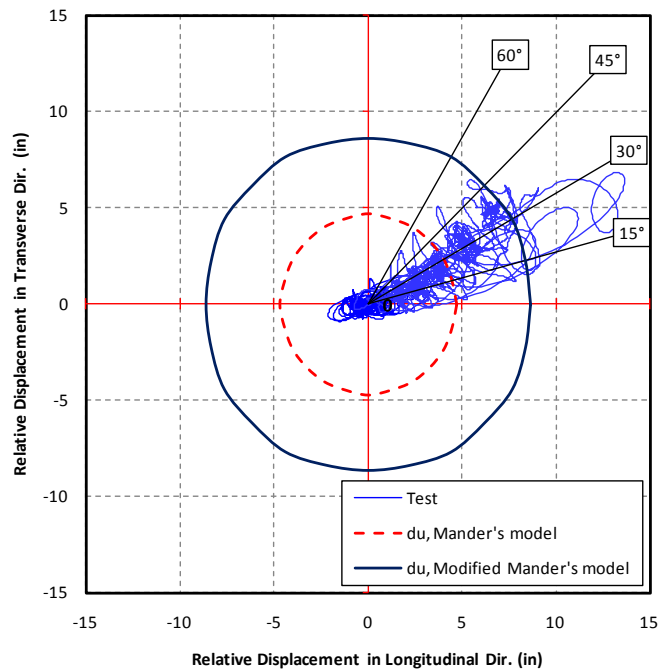


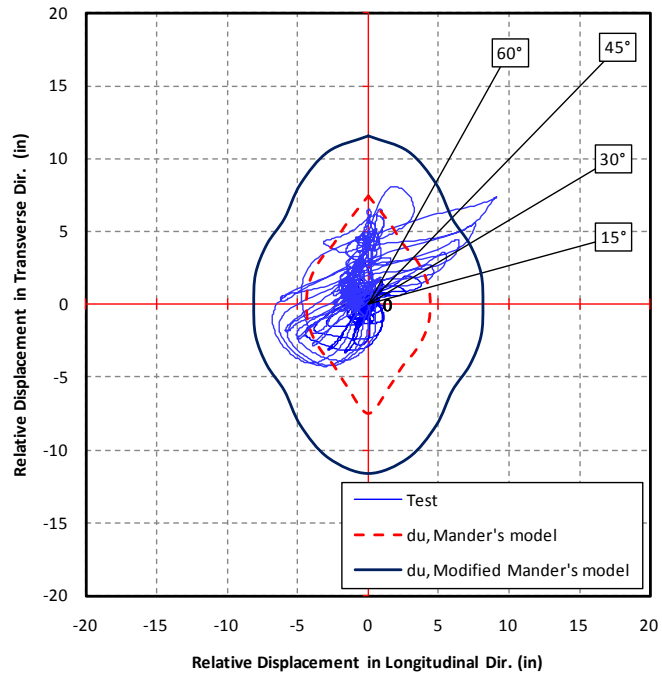
Figure 7-34 Measured and Calculated Force-Displacement, I1 and I2 (NA=45°)



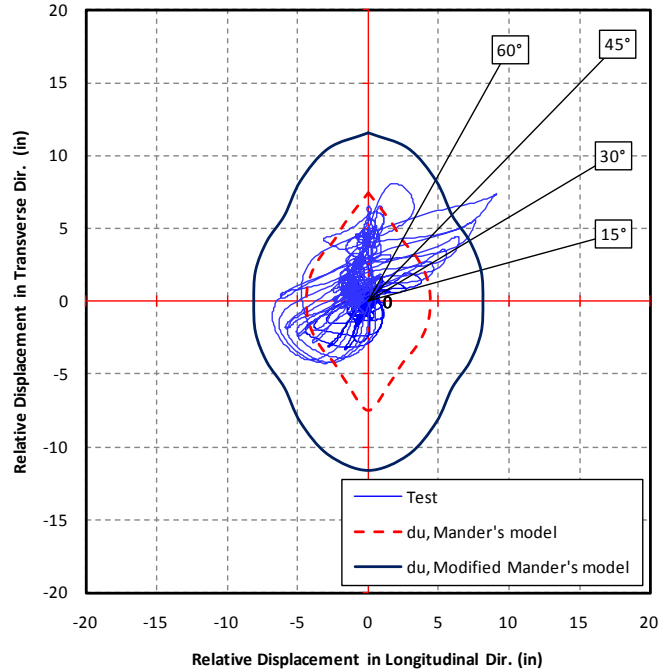
**Figure 7-35 Bidirectional Displacement Interaction Orbits, C1**



**Figure 7-36 Bidirectional Displacement Interaction Orbits, C2**



**Figure 7-37 Bidirectional Displacement Interaction Orbits, I1**



**Figure 7-38 Bidirectional Displacement Interaction Orbits, I2**

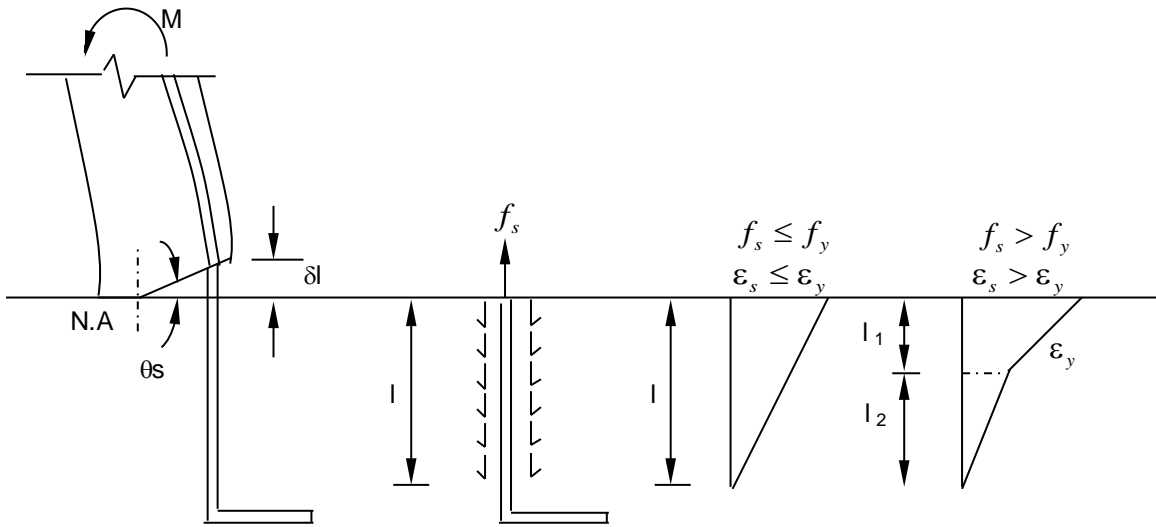


Figure 7-39 Bond-Slip Idealization, Wehbe Method

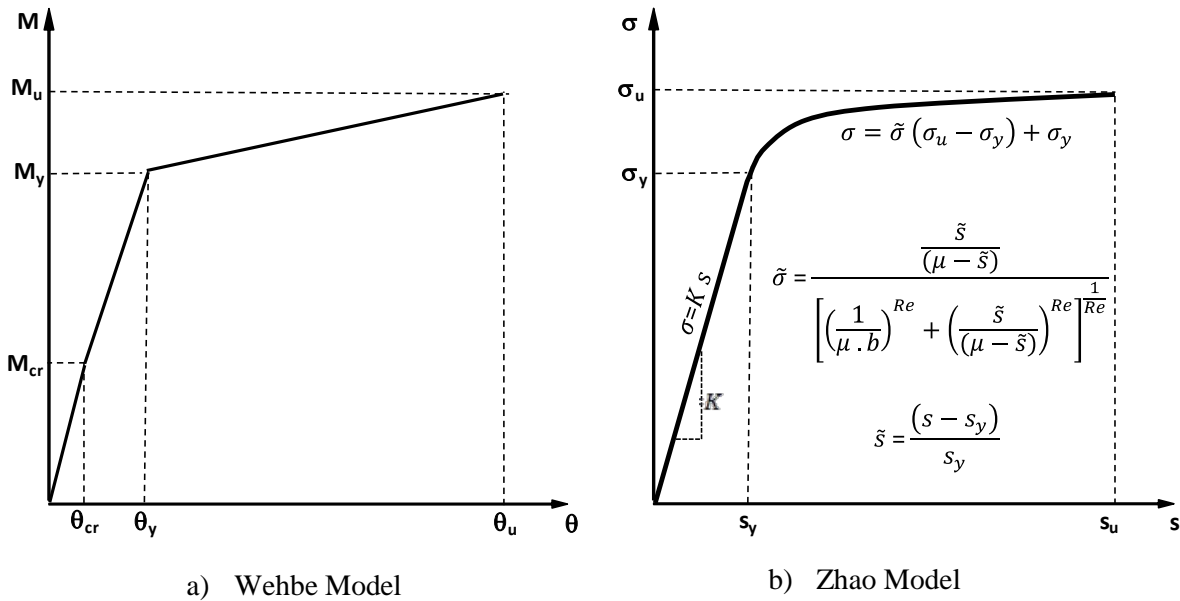
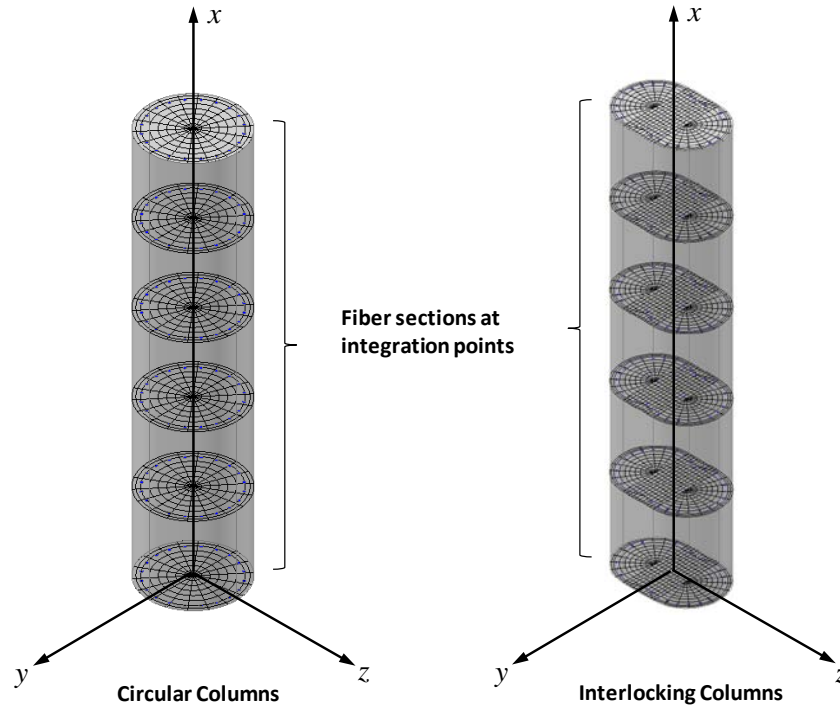
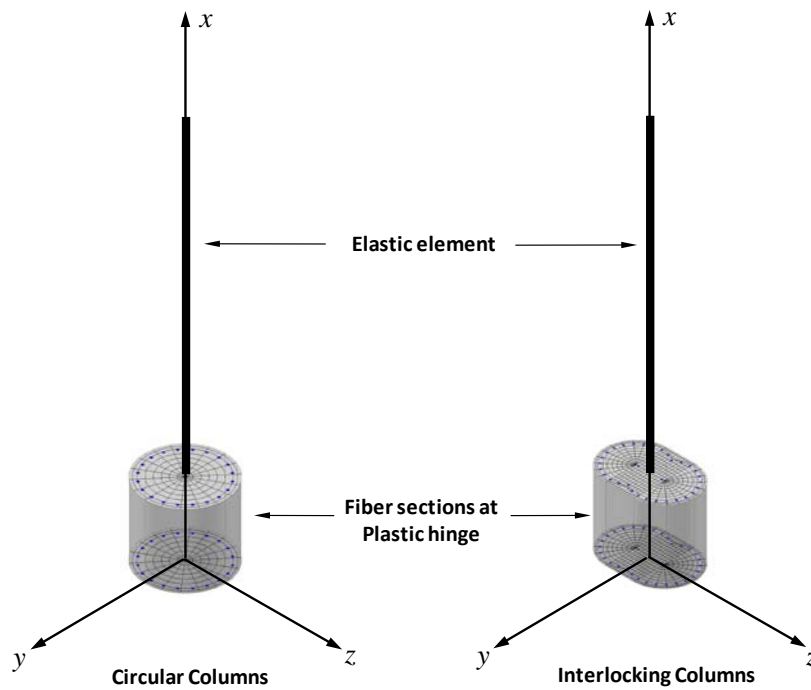


Figure 7-40 Bond-Slip Monotonic curves

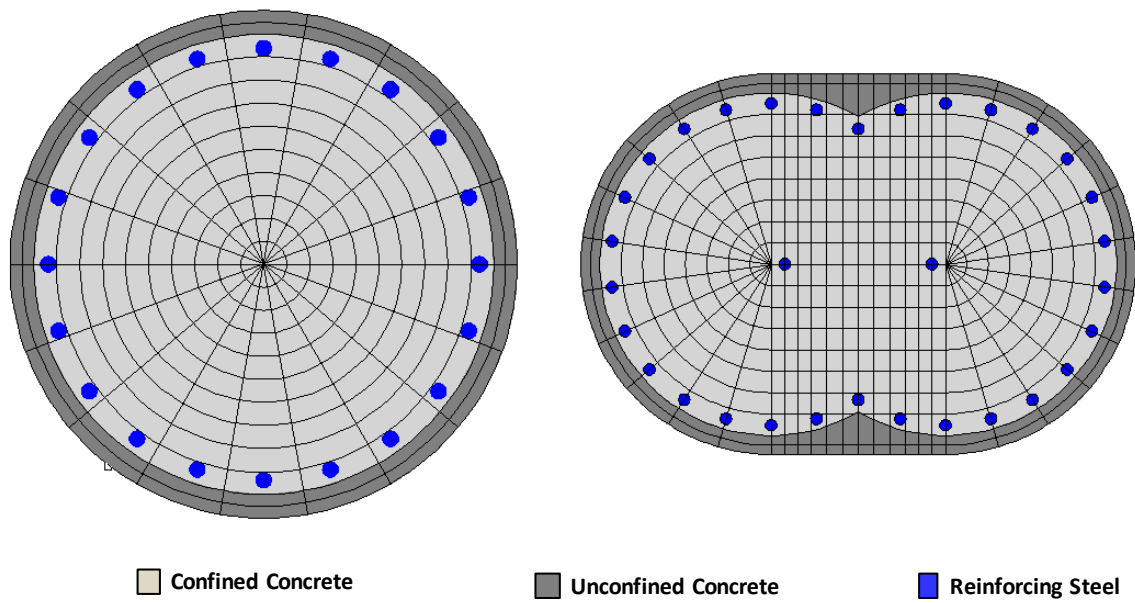




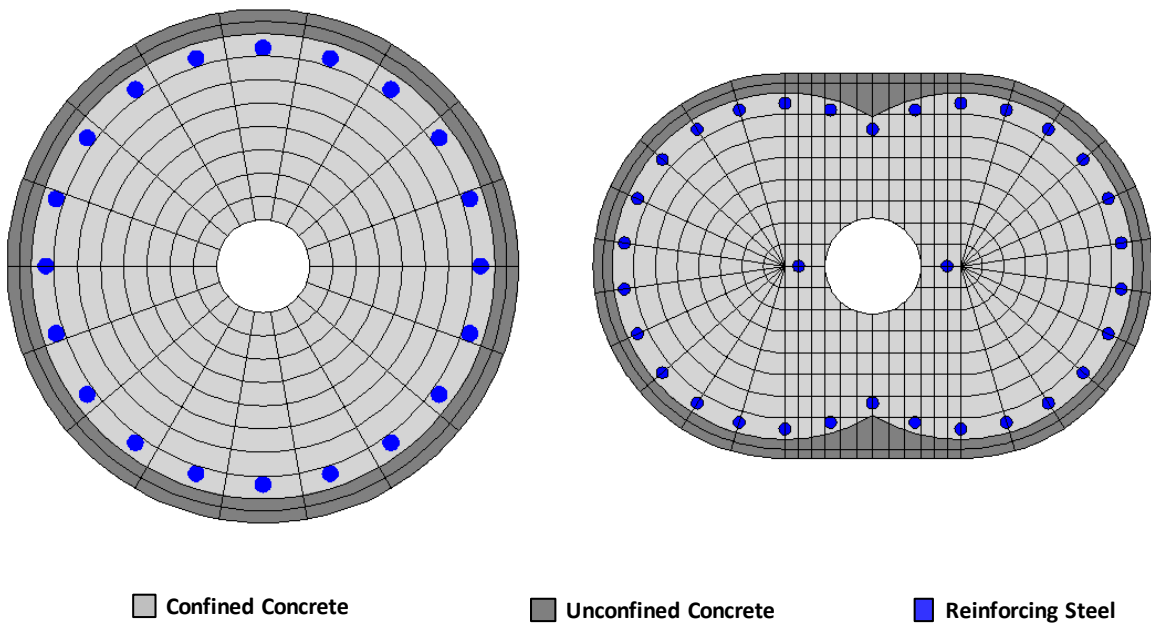
**Figure 7-41 Specimens Idealization Using Nonlinear Beam-Column Fiber Elements**



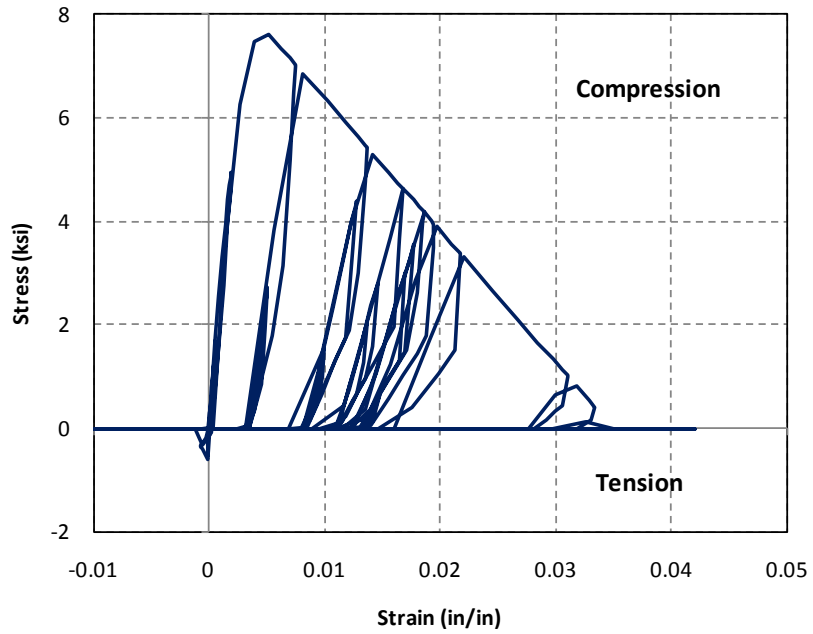
**Figure 7-42 Specimens Idealization Using Beam with Hinges Beam-Column Elements**



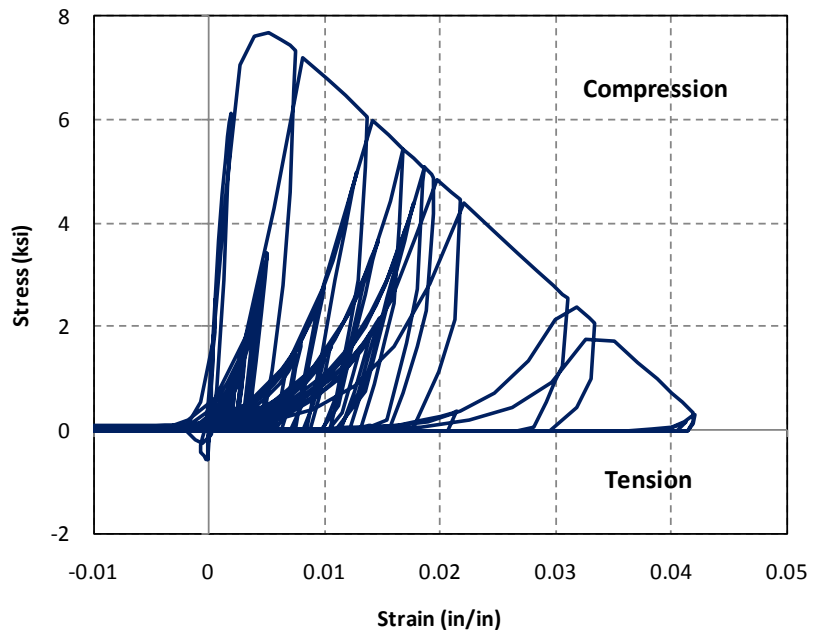
**Figure 7-43 Fiber Section Discretization in OpenSees, Unidirectionally Tested Specimens**



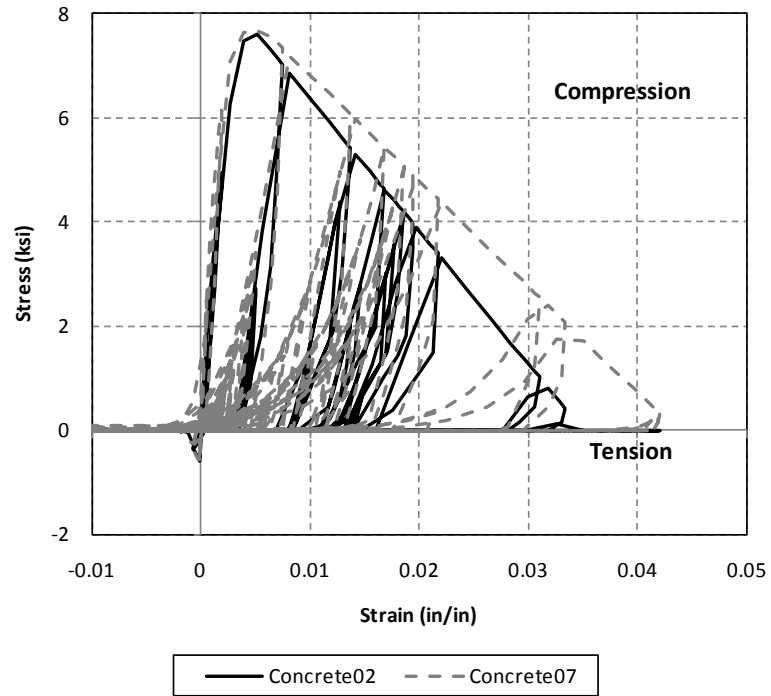
**Figure 7-44 Fiber Section Discretization in OpenSees, Bidirectionally Tested Specimens**



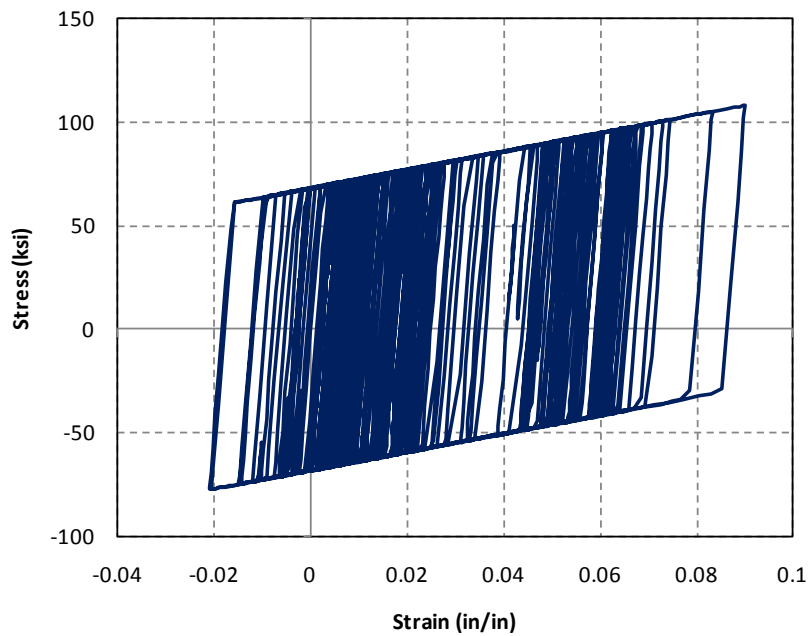
**Figure 7-45 Typical Hysteretic Stress-Strain Behavior in Concrete02**



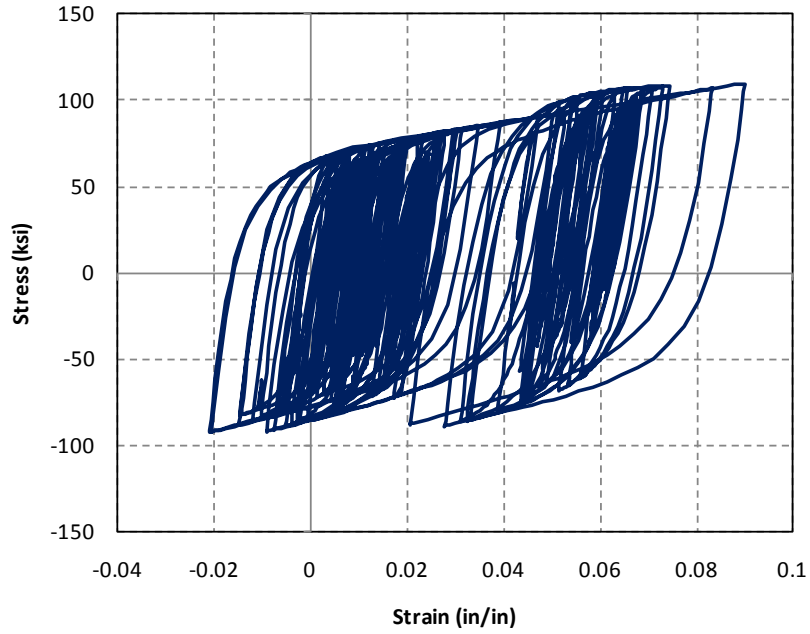
**Figure 7-46 Typical Hysteretic Stress-Strain Behavior in Concrete07**



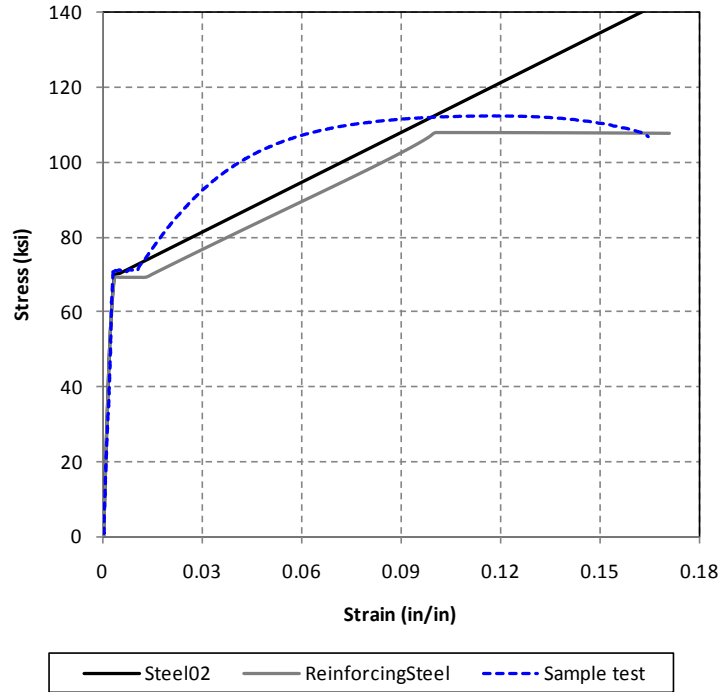
**Figure 7-47 Comparison of Hysteretic Stress-Strain for Different Concrete Models**



**Figure 7-48 Typical Hysteretic Stress-Strain Behavior in Steel02 Material**



**Figure 7-49 Typical Hysteretic Stress-Strain Behavior in ReinforcingSteel Material**



**Figure 7-50 Comparison of Tension Stress-Strain Envelopes for Different Reinforcement Models**

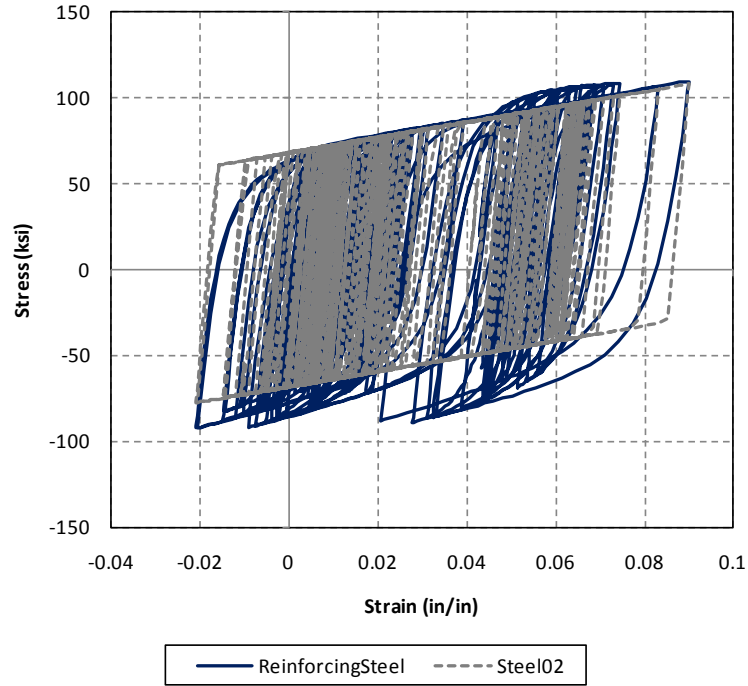


Figure 7-51 Comparison of Hysteretic Stress-strain for Different reinforcement Models

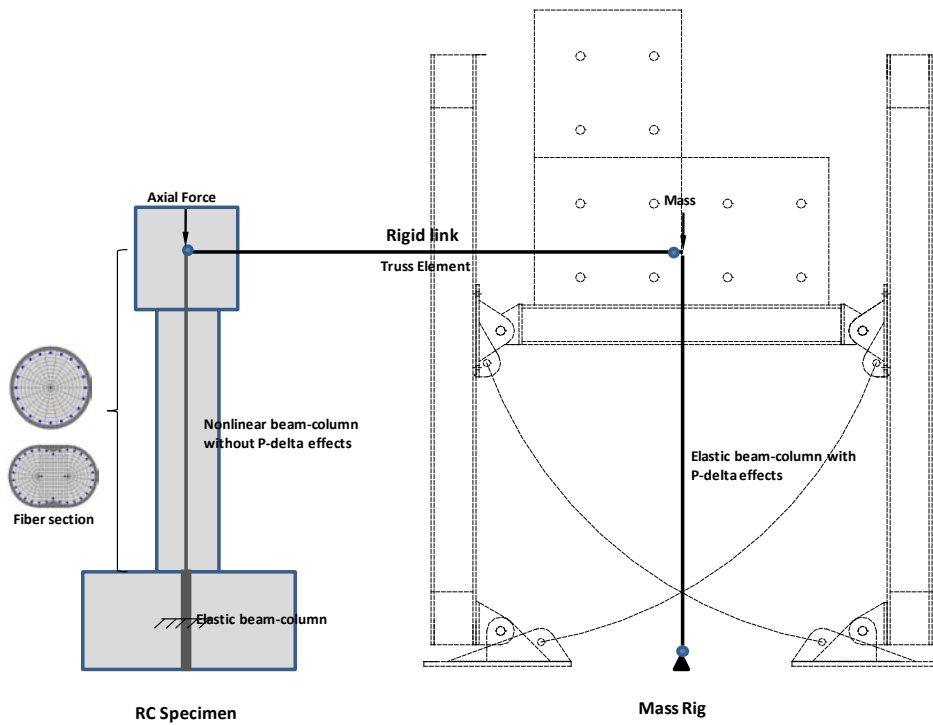


Figure 7-52 OpenSees Analytical Model for Unidirectionally Tested Columns (Pushover Analysis)

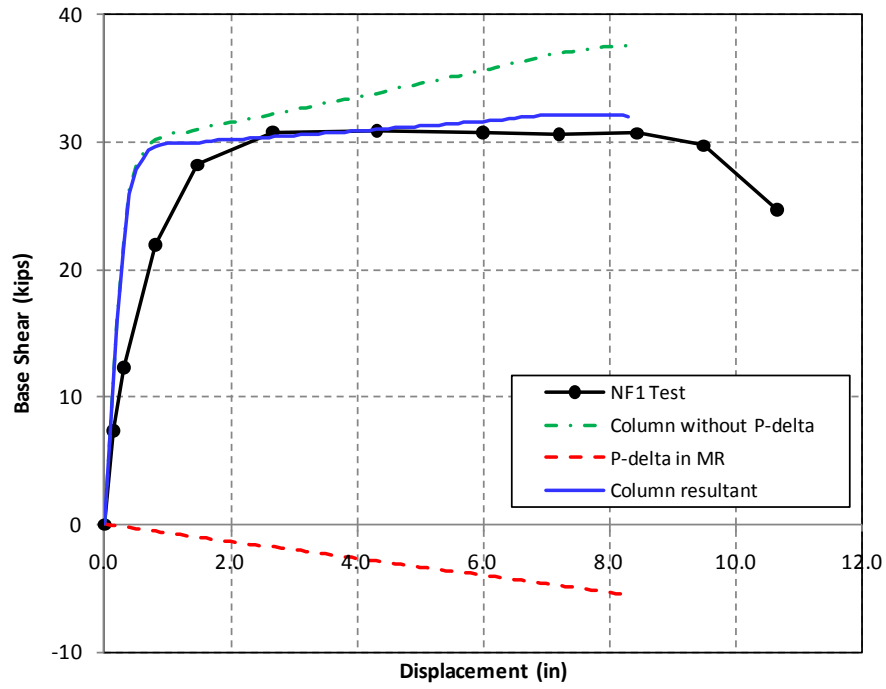


Figure 7-53 Measured and Predicted Force-Displacement Envelope, NF1 (Without Bondslip)

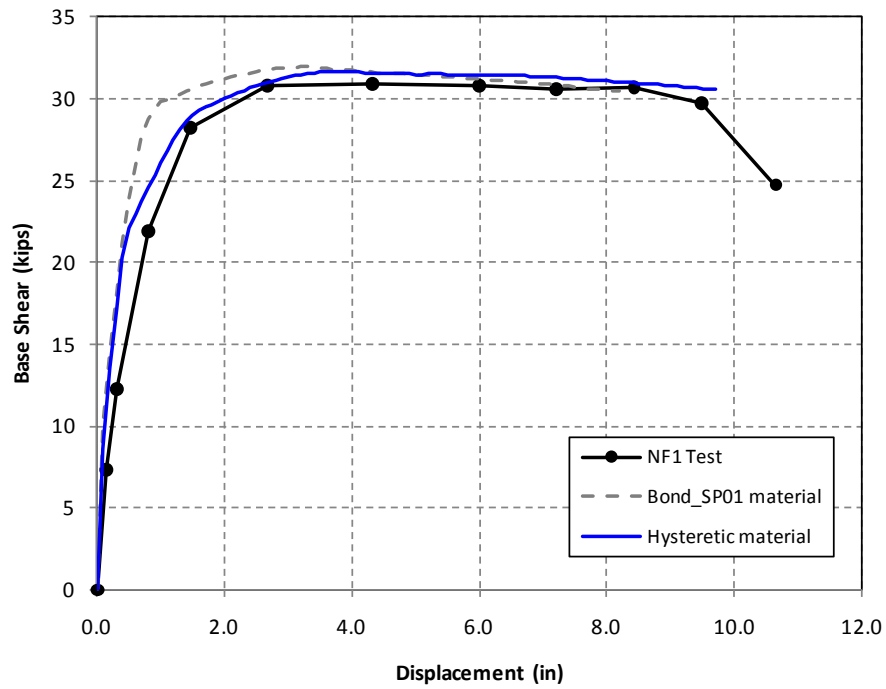


Figure 7-54 Measured and Predicted Force-Displacement Envelope, NF1 (With Bondslip)

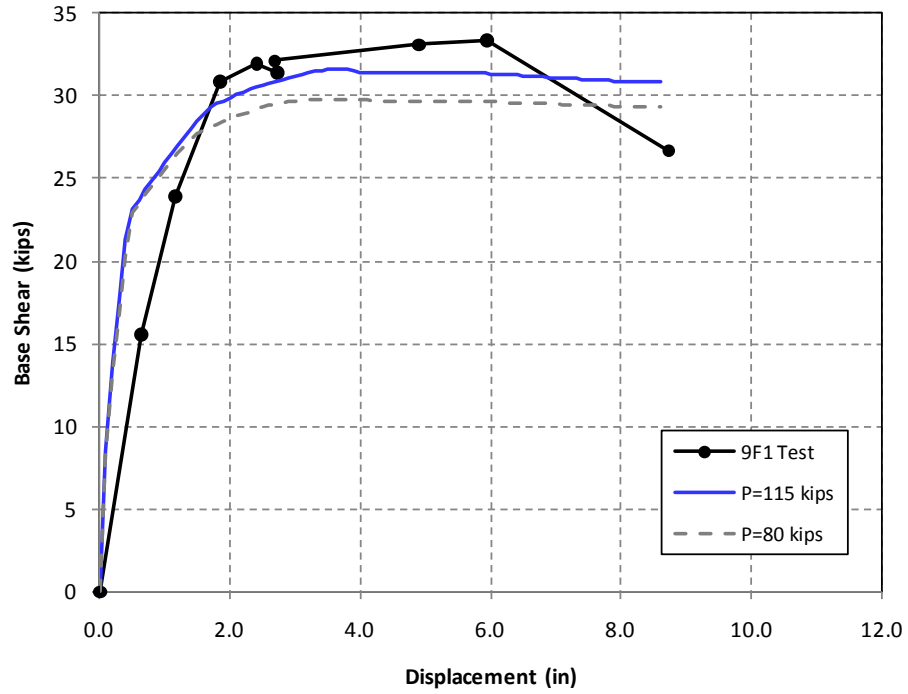


Figure 7-55 Measured and Predicted Force-Displacement Envelope, 9F1 (With Bondslip)

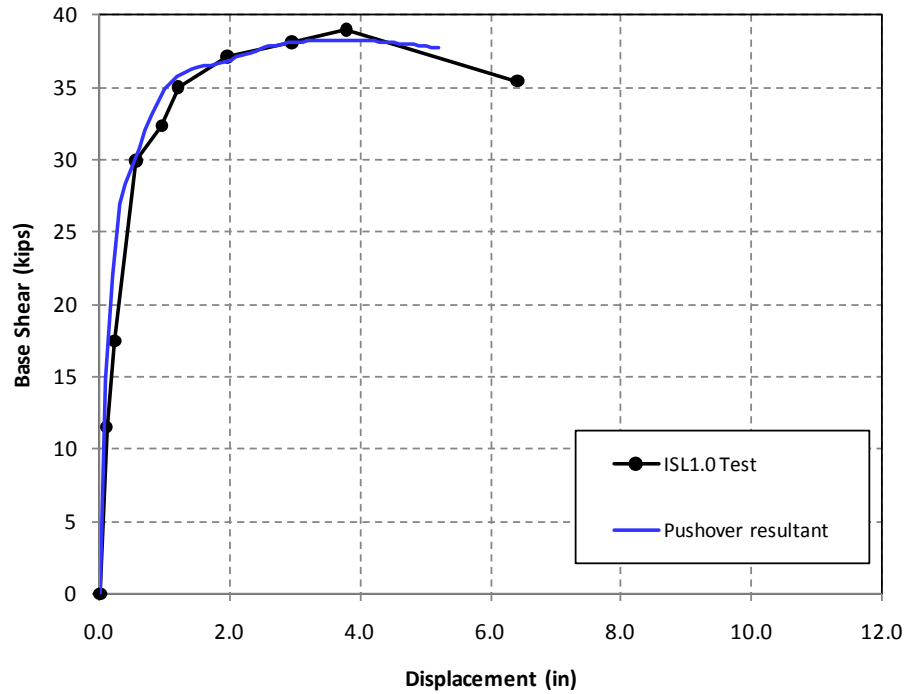


Figure 7-56 Measured and Predicted Force-Displacement Envelope, ISL1.0 (With Bondslip)



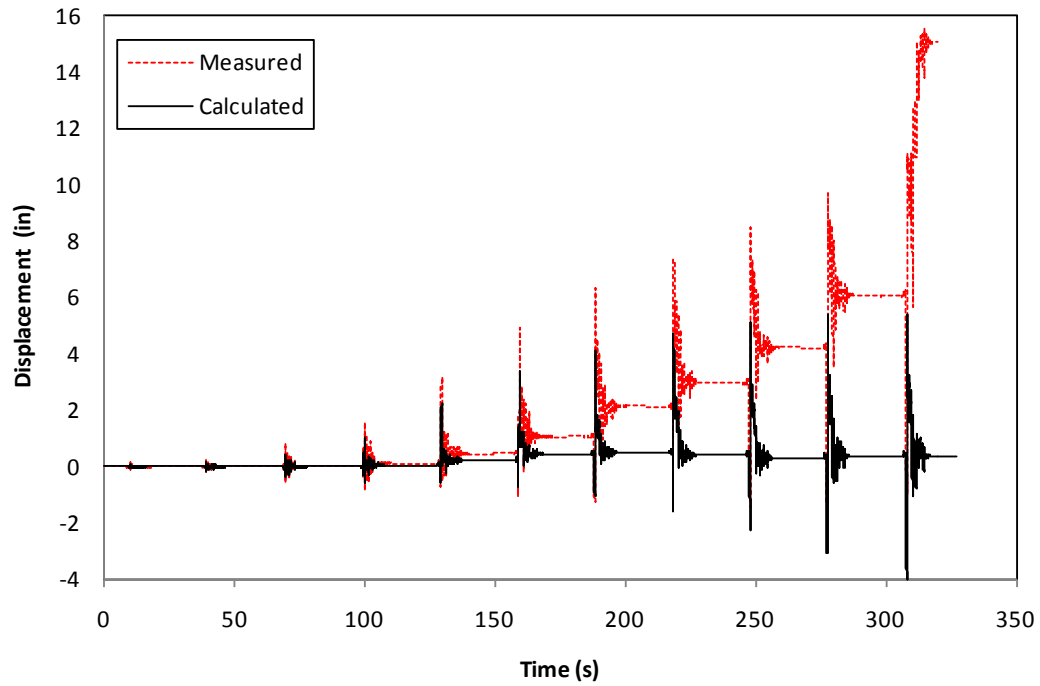


Figure 7-57 Measured and Calculated Displacement History, NF1-Model C02S02

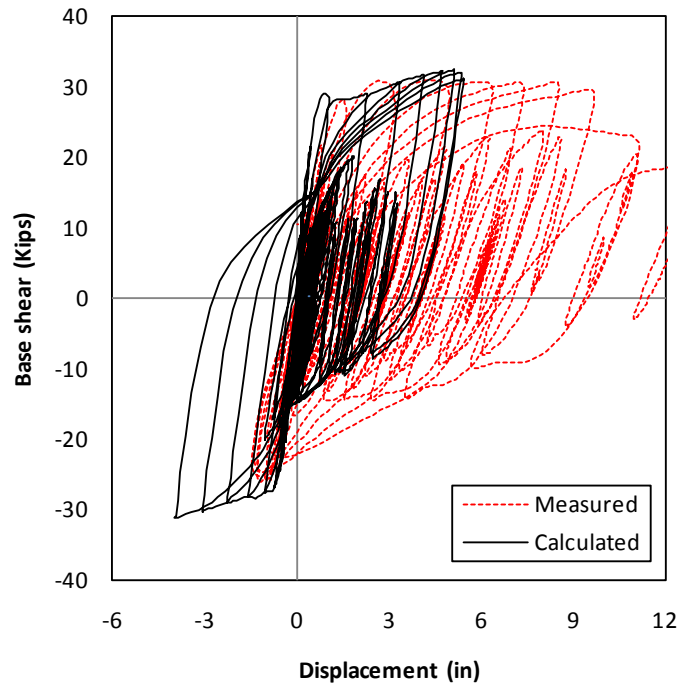


Figure 7-58 Measured and Calculated F-D Hysteresis, NF1-Model C02S02

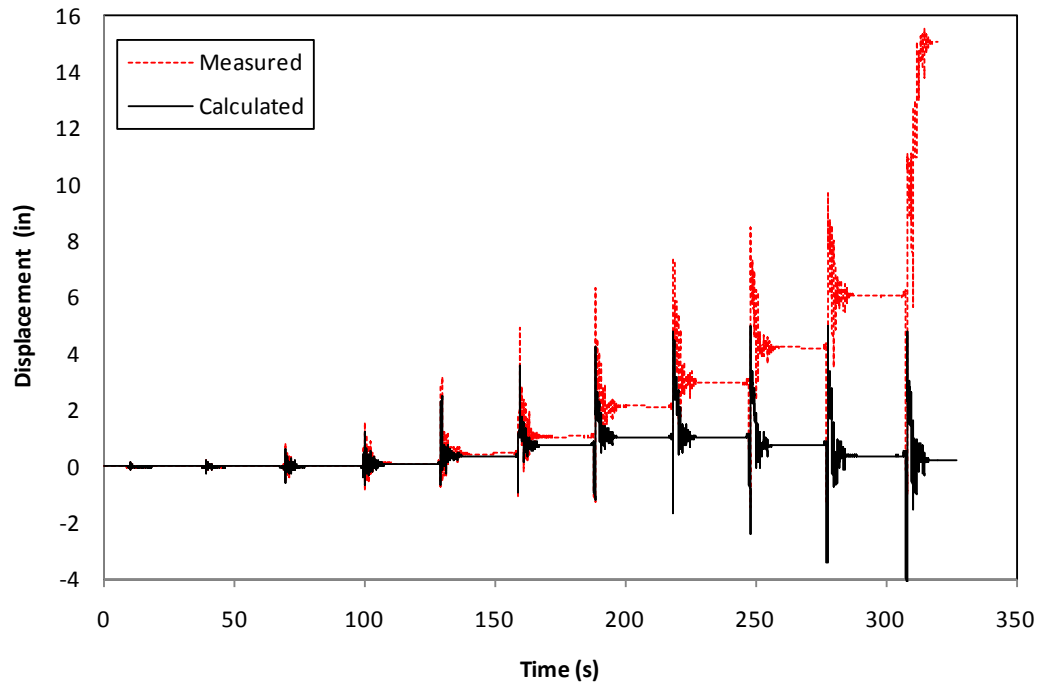


Figure 7-59 Measured and Calculated Displacement History, NF1-Model BWHC02S02

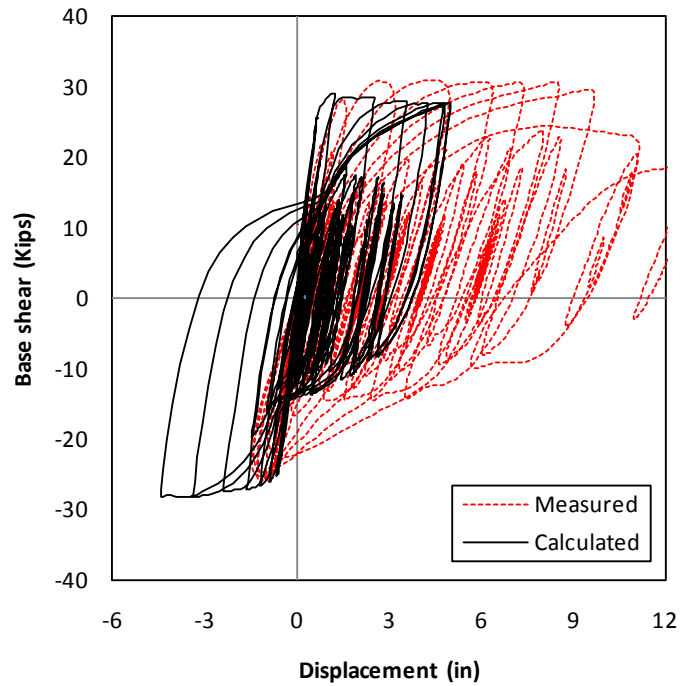


Figure 7-60 Measured and Calculated F-D Hysteresis, NF1-Model BWHC02S02

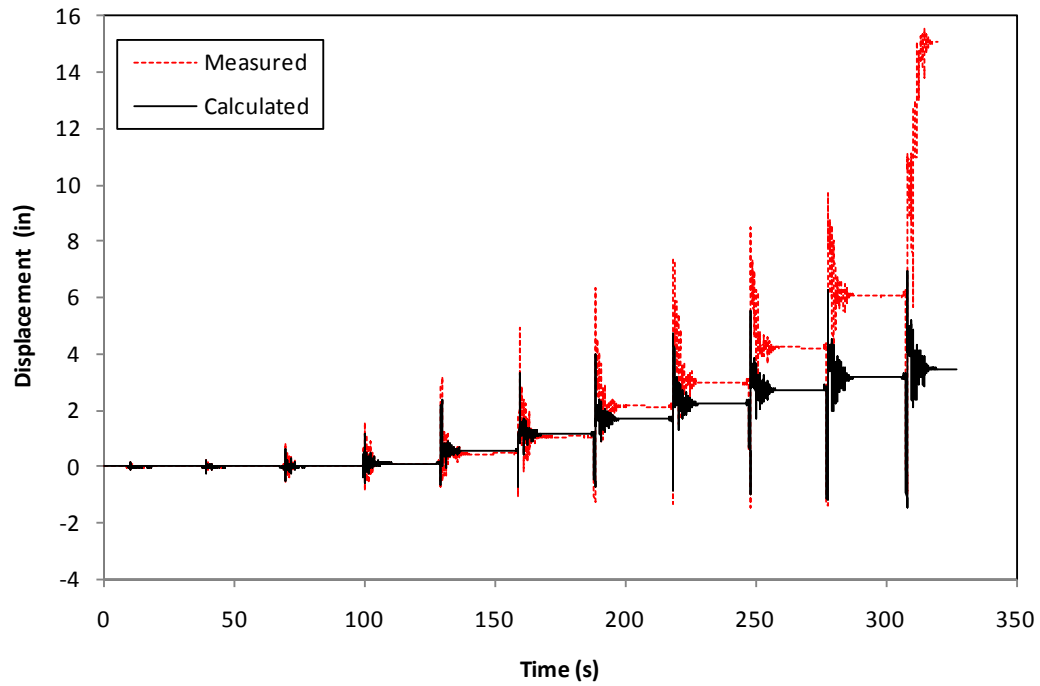


Figure 7-61 Measured and Calculated Displacement History, NF1-Model BWHC07RS

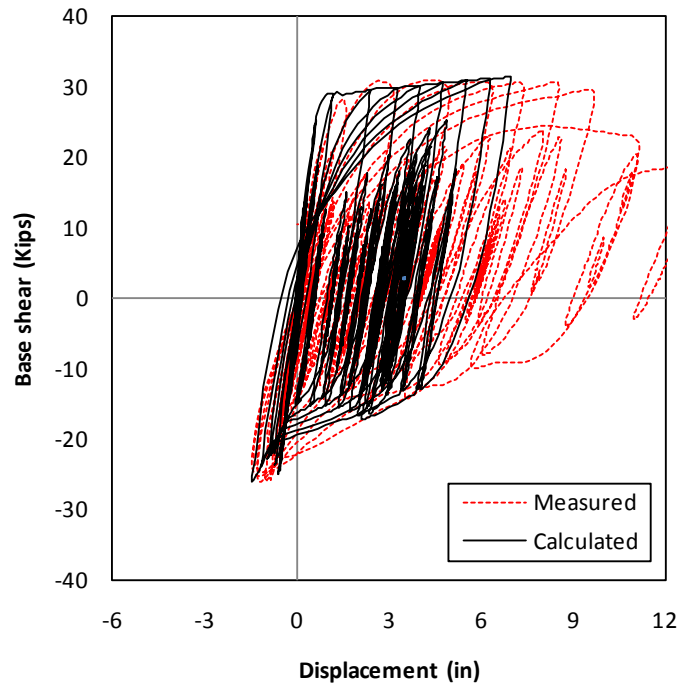


Figure 7-62 Measured and Calculated F-D Hysteresis, NF1-Model BWHC07RS

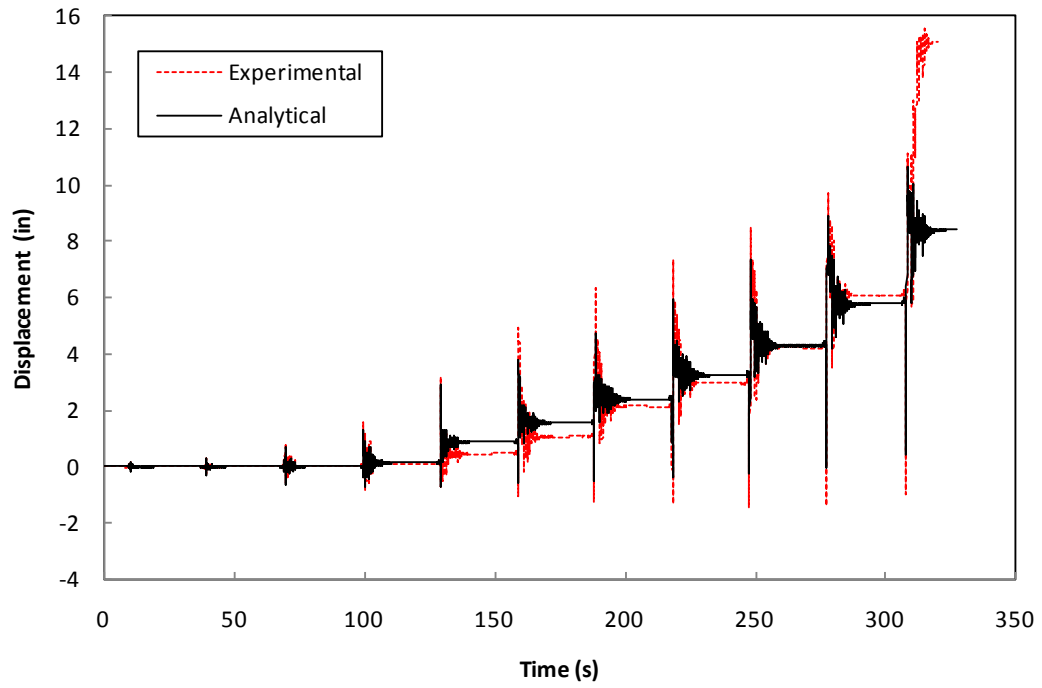


Figure 7-63 Measured and Calculated Displacement History, NF1-Best Model

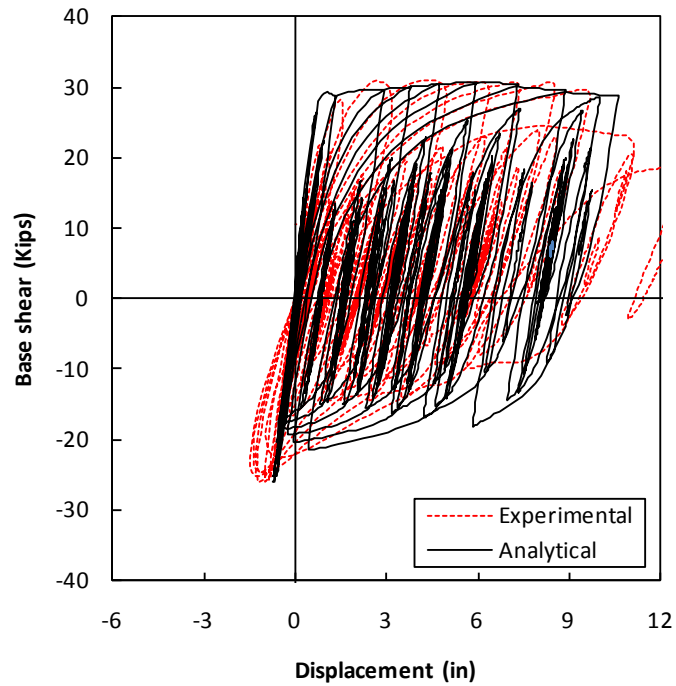


Figure 7-64 Measured and Calculated F-D Hysteresis, NF1-Best Model

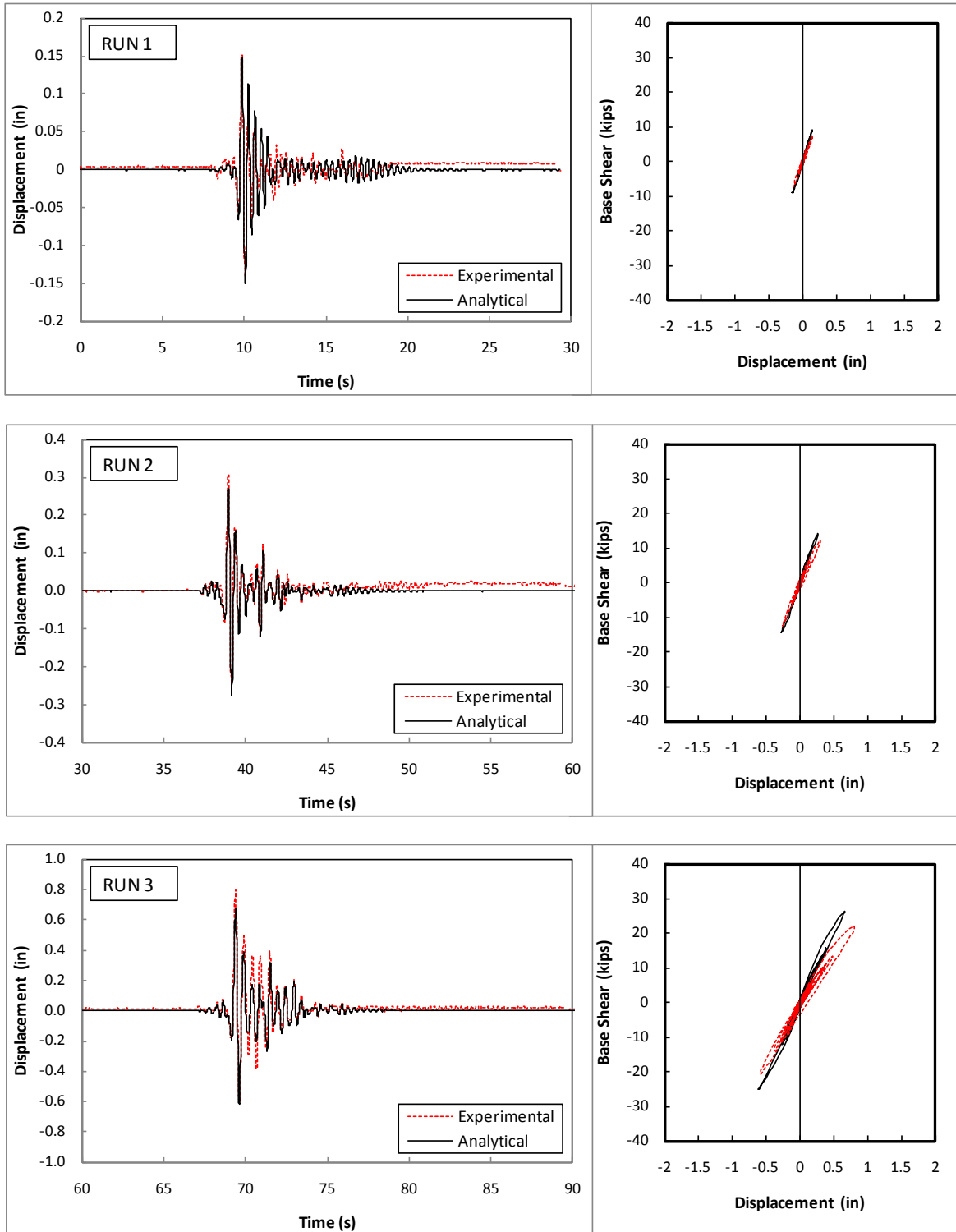


Figure 7-65 Measured and Calculated Displacement Hysteresis, NF1 (Runs 1 to 3)

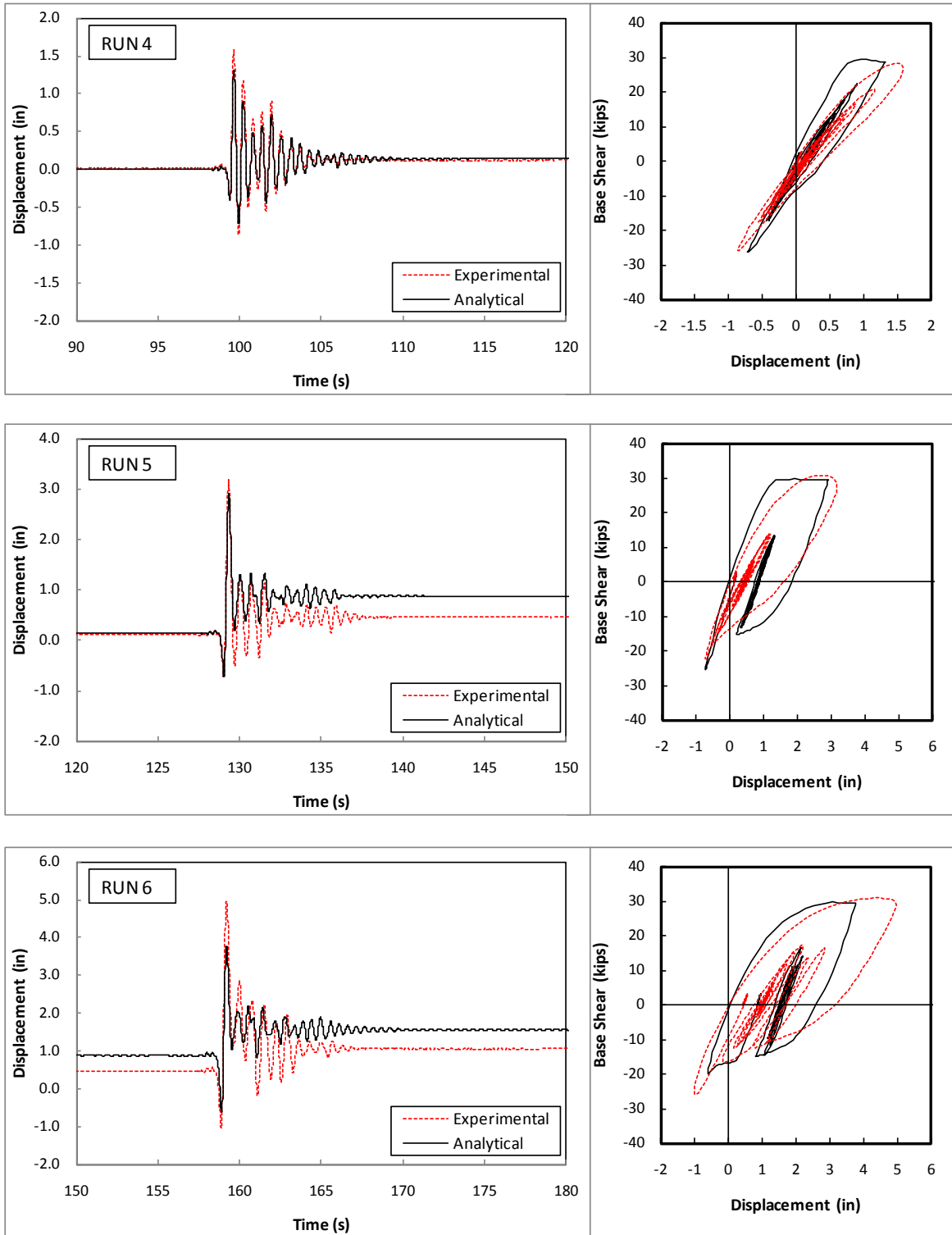


Figure 7-66 Measured and Calculated Displacement Hysteresis, NF1 (Runs 4 to 6)

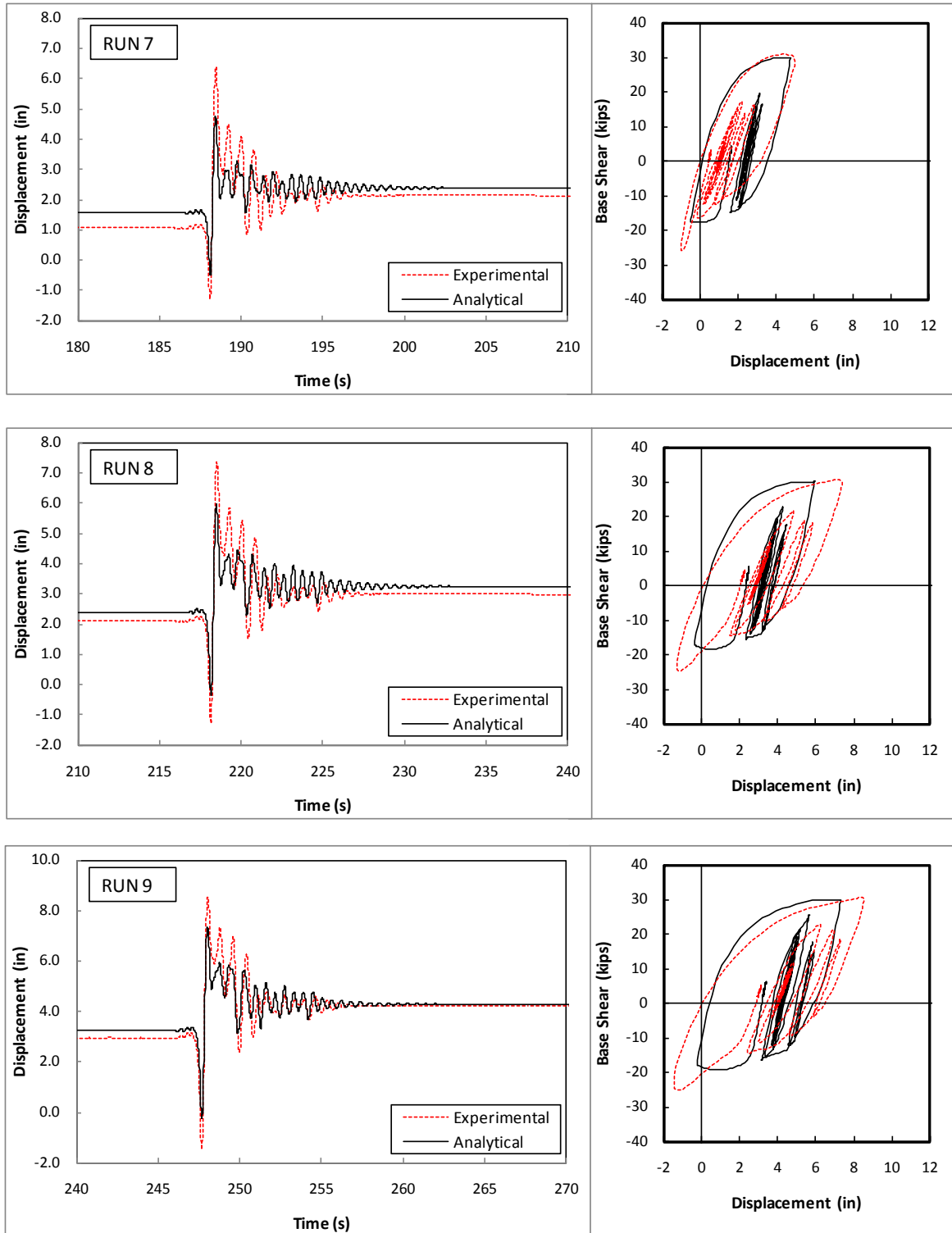


Figure 7-67 Measured and Calculated Displacement Hysteresis, NF1 (Runs 7 to 9)

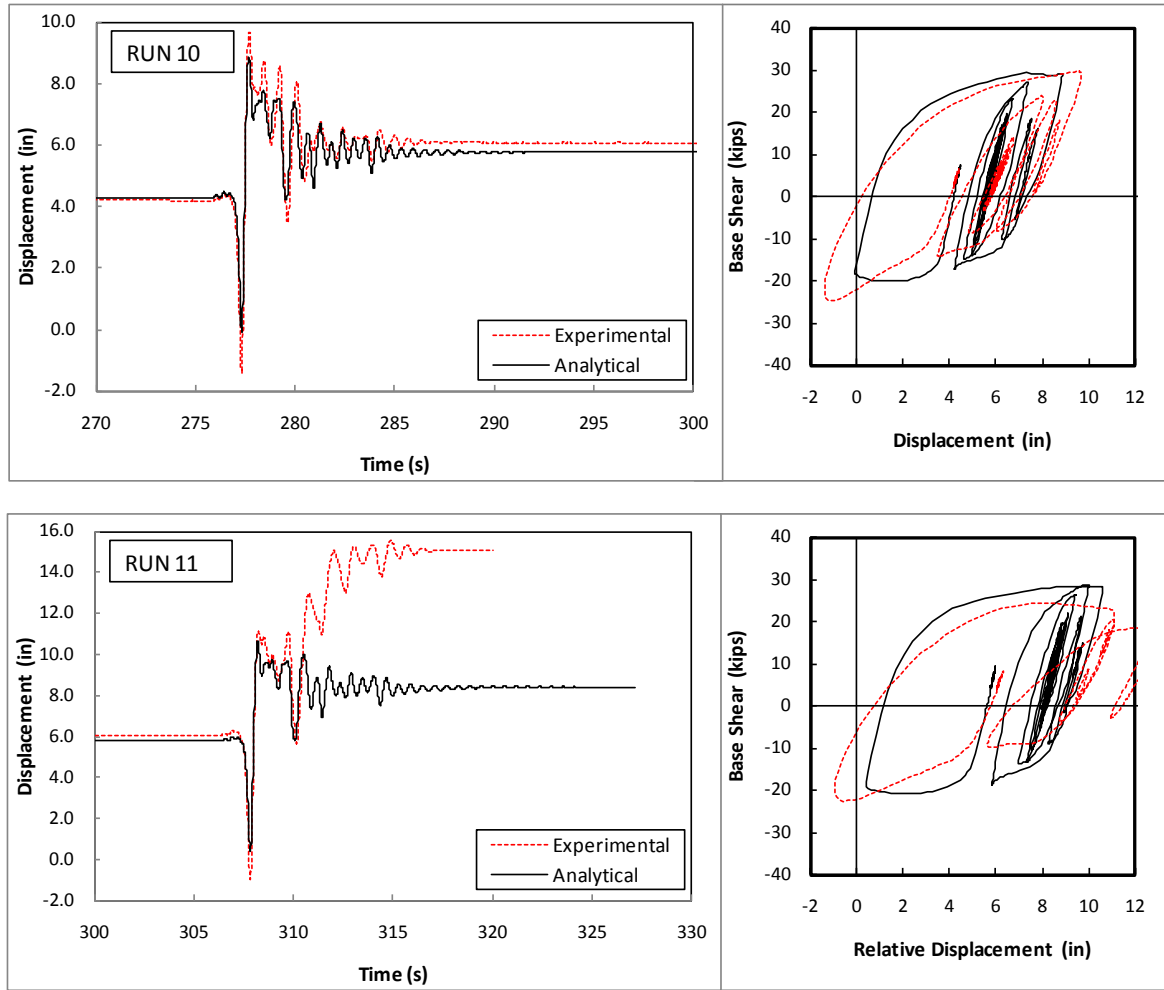


Figure 7-68 Measured and Calculated Displacement Hysteresis, NF1 (Runs 10 and 11)



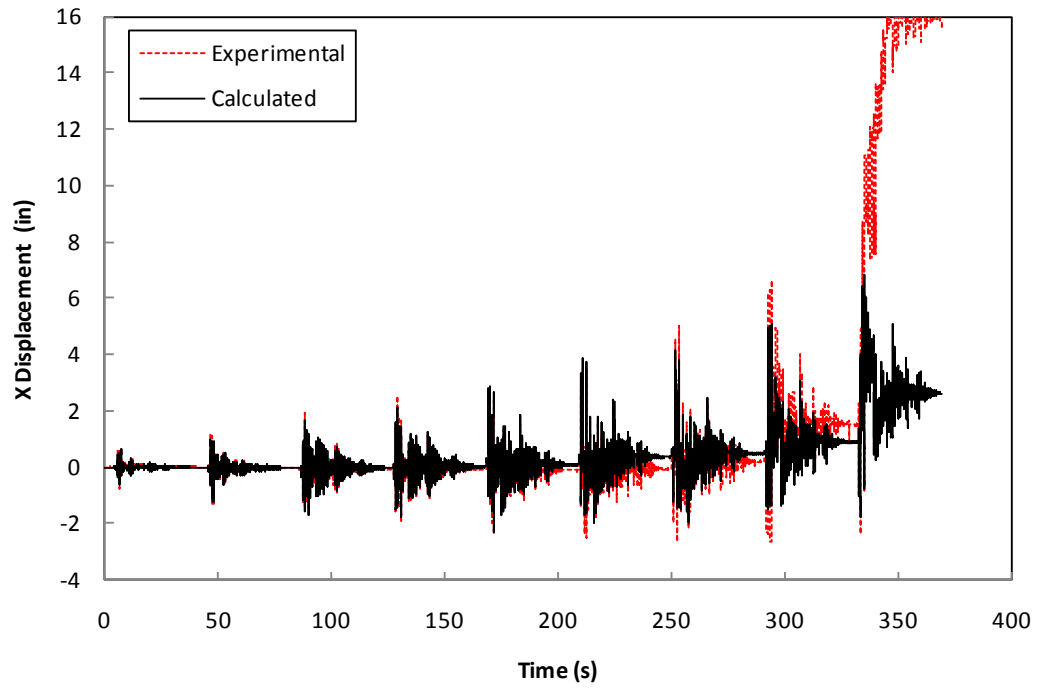


Figure 7-69 Measured and Calculated Displacement History, 9F1-Best Model

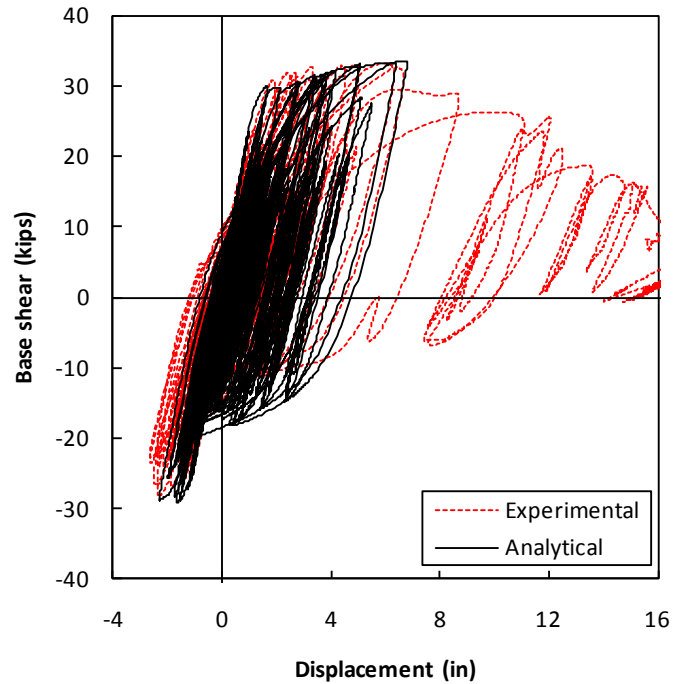


Figure 7-70 Measured and Calculated Displacement Hysteresis, 9F1-Best Model

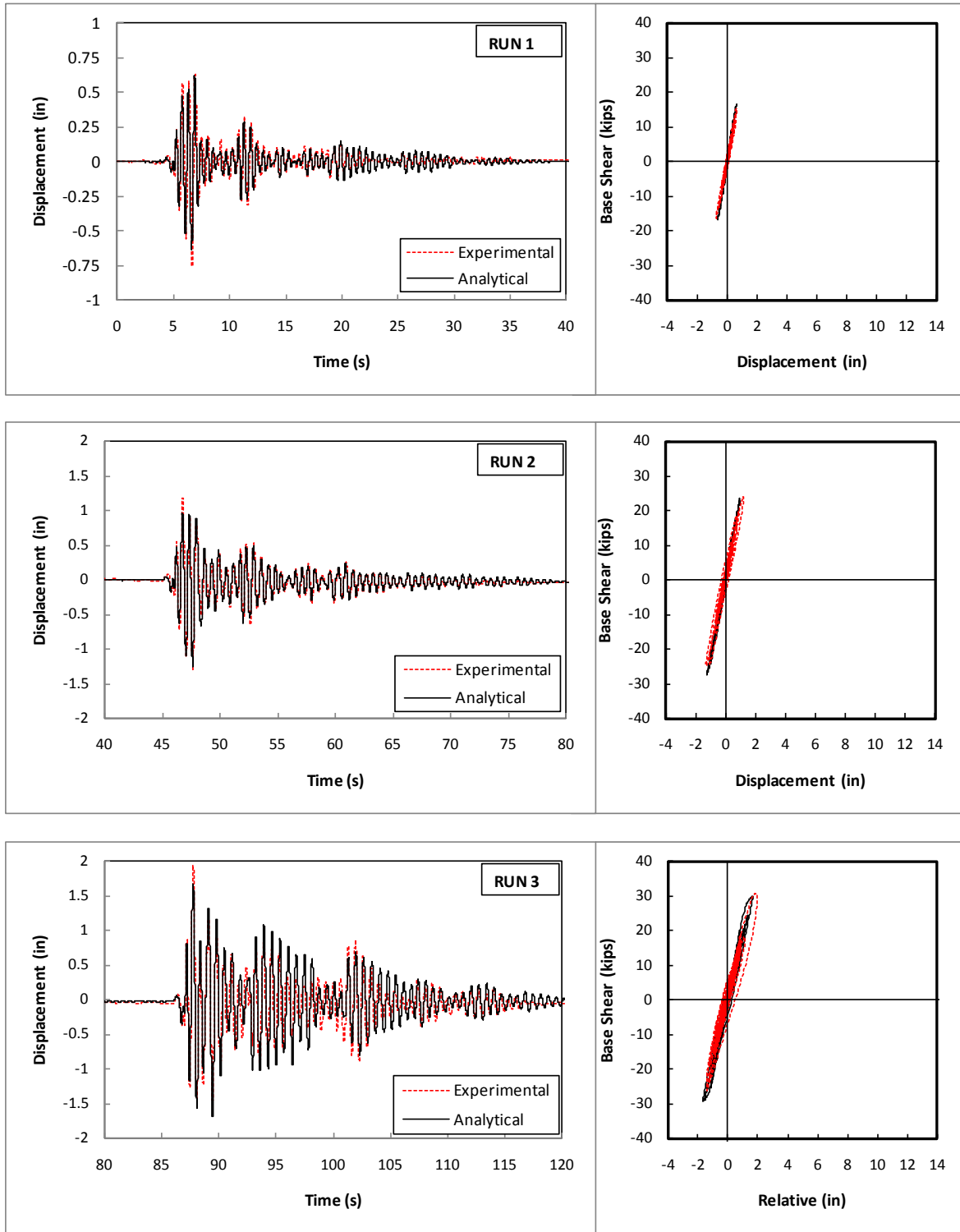


Figure 7-71 Measured and Calculated Displacement Hysteresis, 9F1 (Runs 1 to 3)

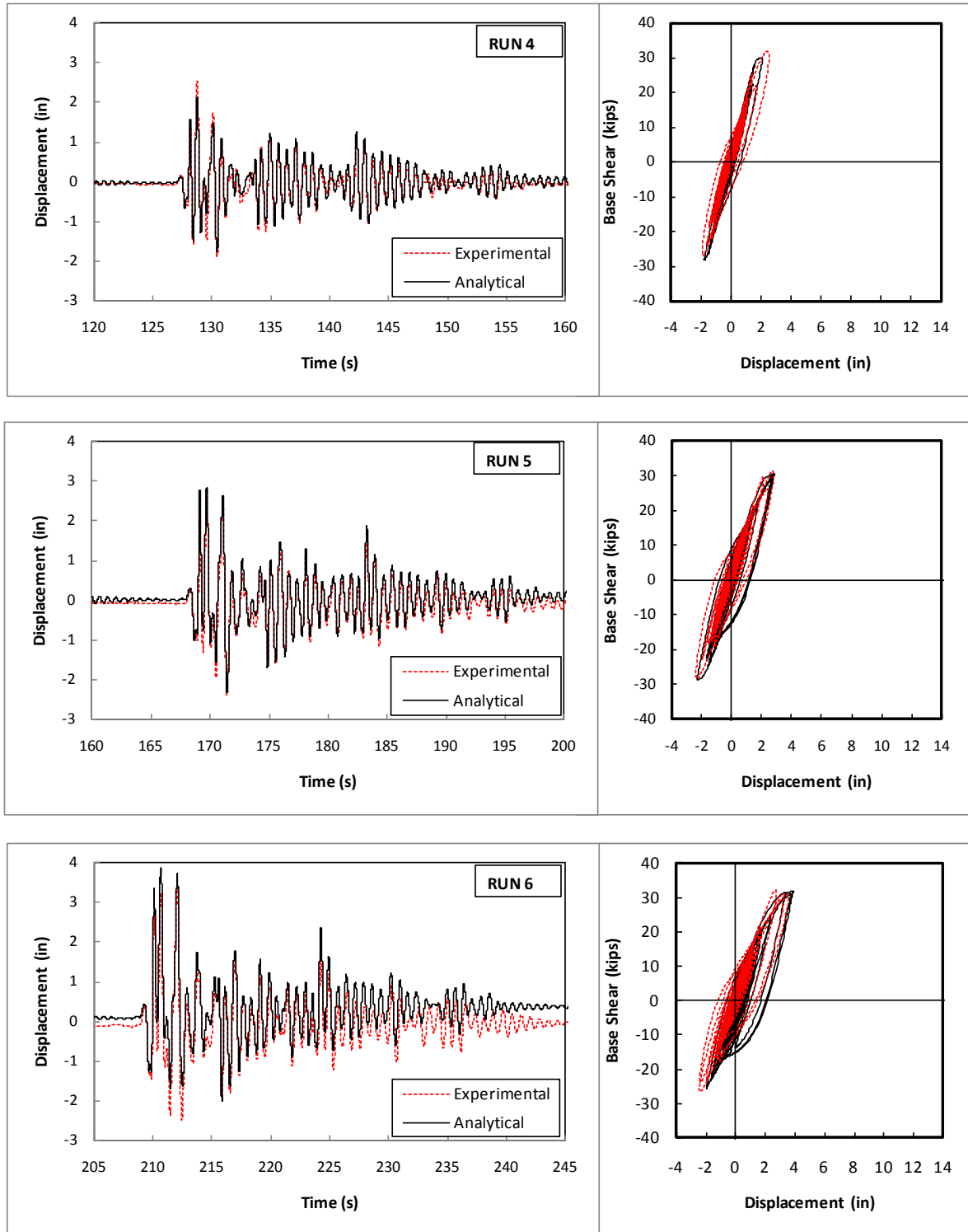


Figure 7-72 Measured and Calculated Displacement Hysteresis, 9F1 (Runs 4 to 6)

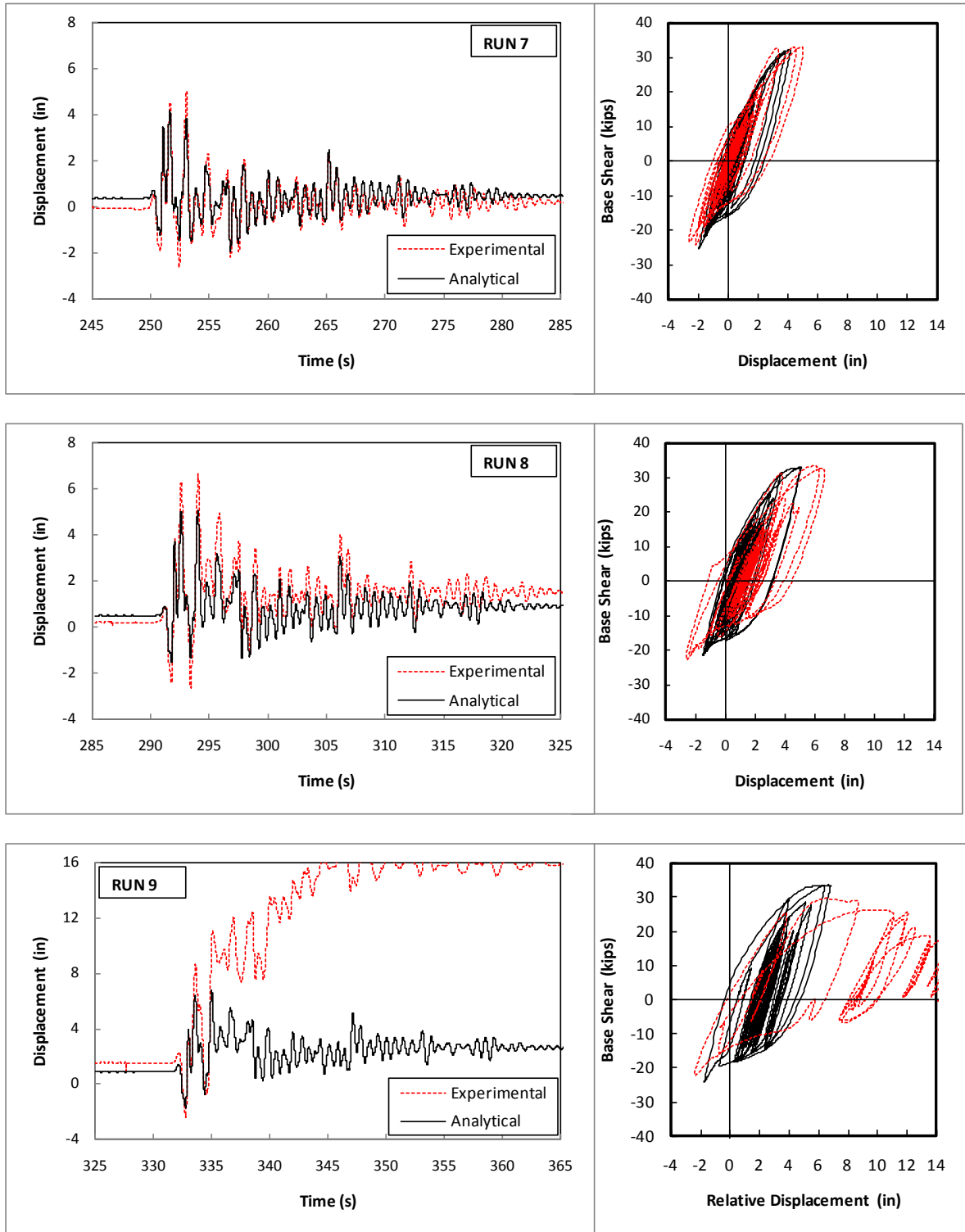


Figure 7-73 Measured and Calculated Displacement Hysteresis, 9F1 (Runs 7 to 9)

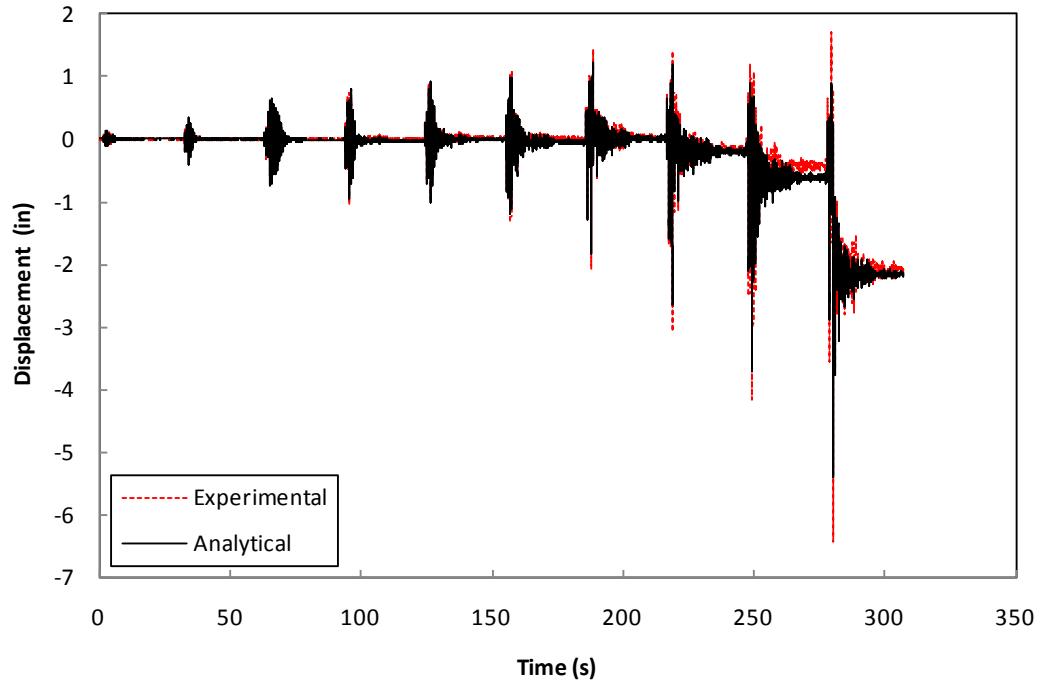


Figure 7-74 Measured and Calculated Displacement History, ISL1.0-Best Model

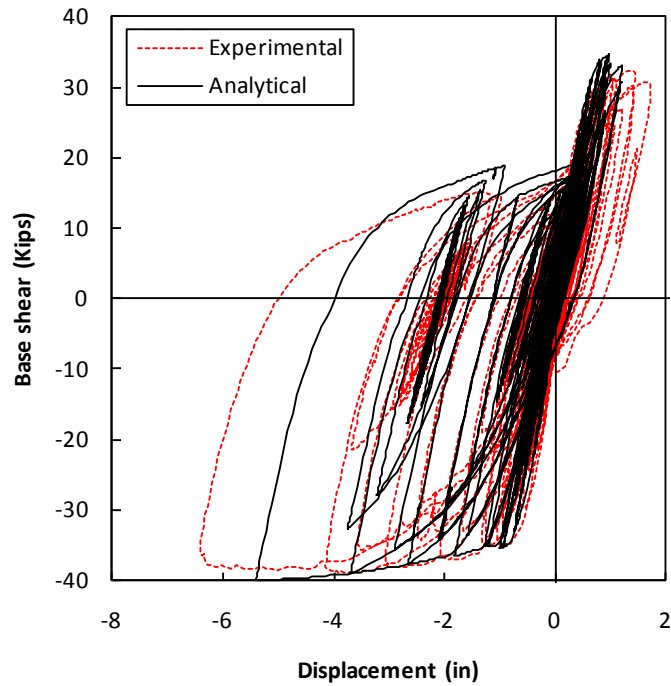


Figure 7-75 Measured and Calculated Cumulative F-D Hysteresis, ISL1.0-Best Model

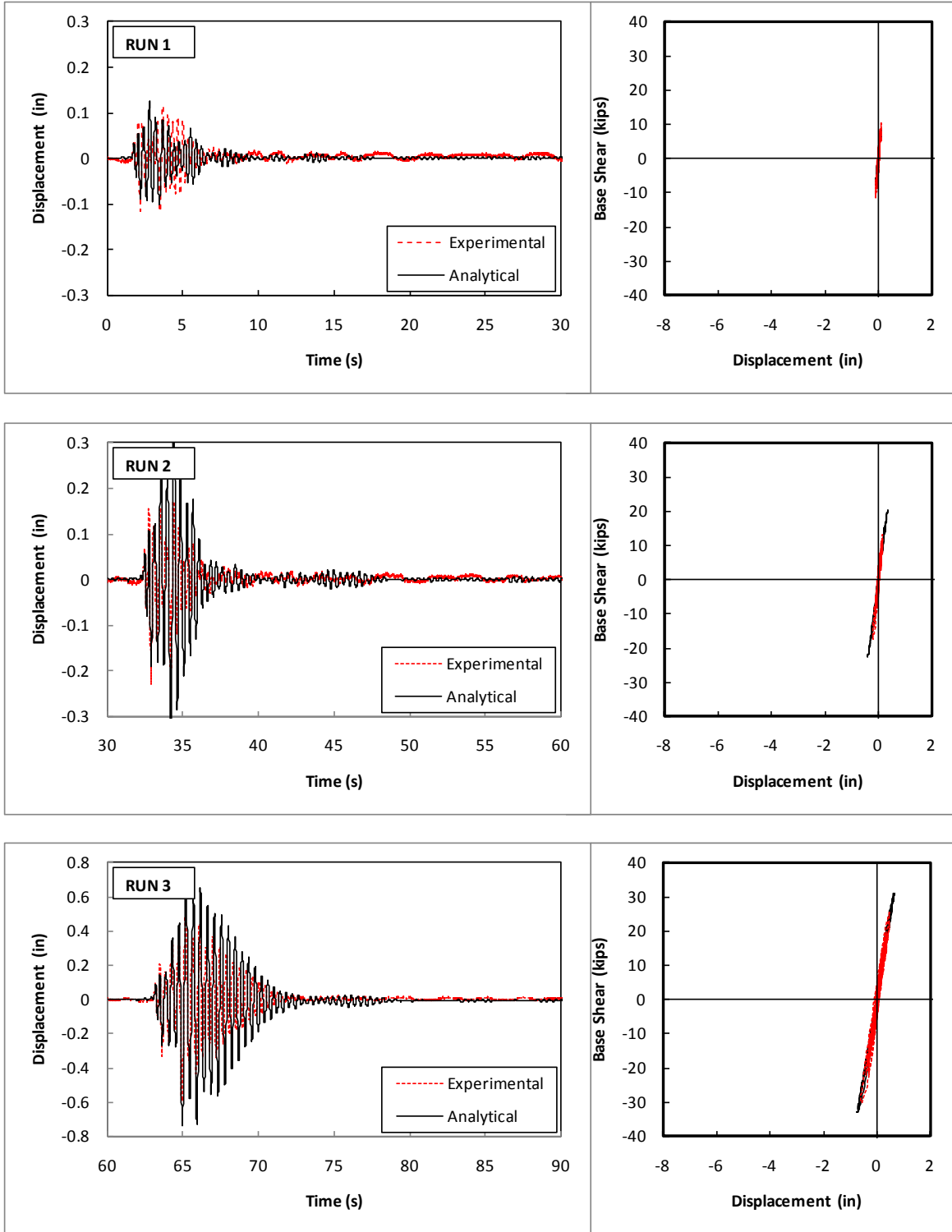
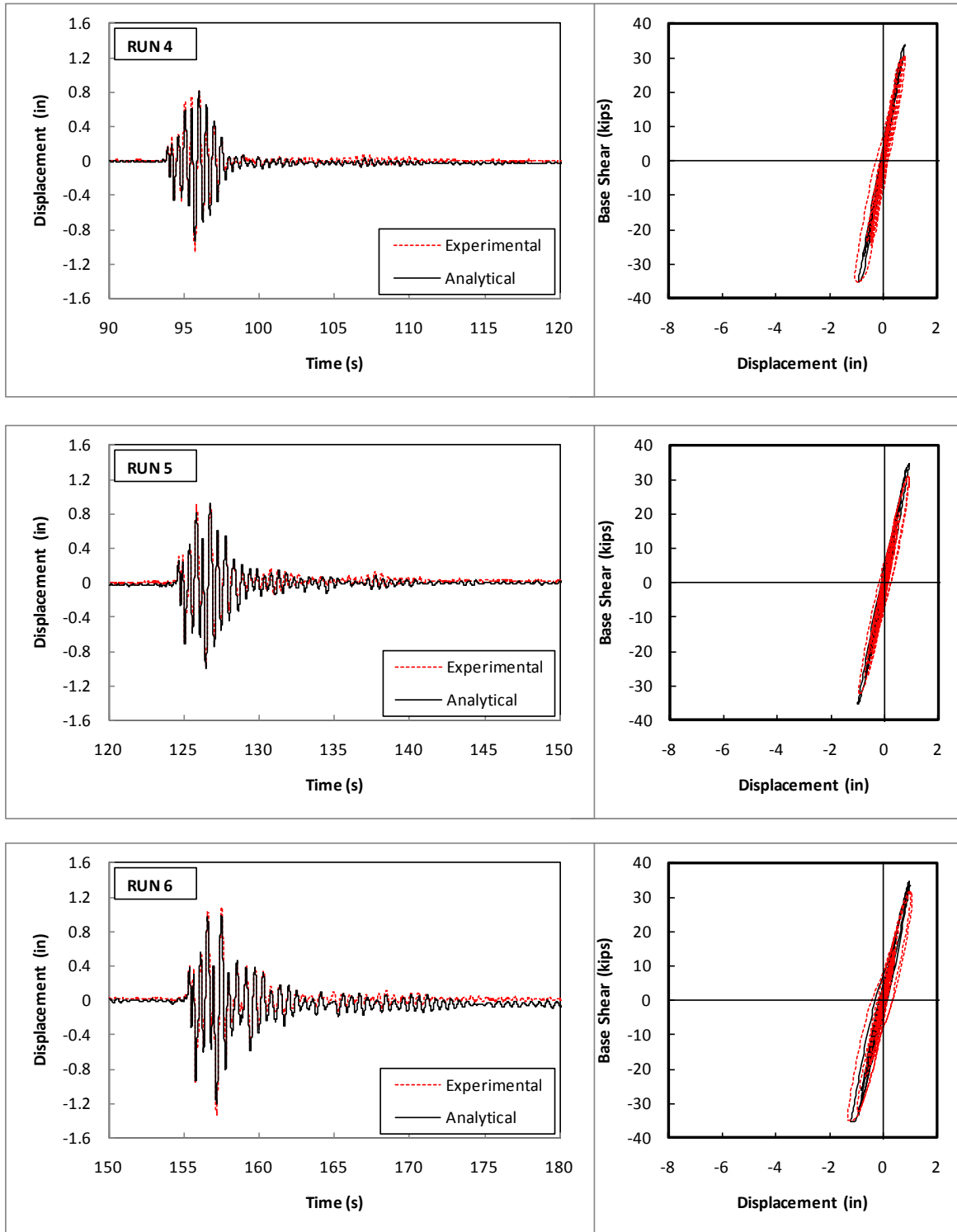


Figure 7-76 Measured and Calculated Displacement and Hysteresis, ISL1.0 (Runs 1 to 3)



**Figure 7-77 Measured and Calculated Displacement and Hysteresis, ISL1.0 (Runs 4 to 6)**

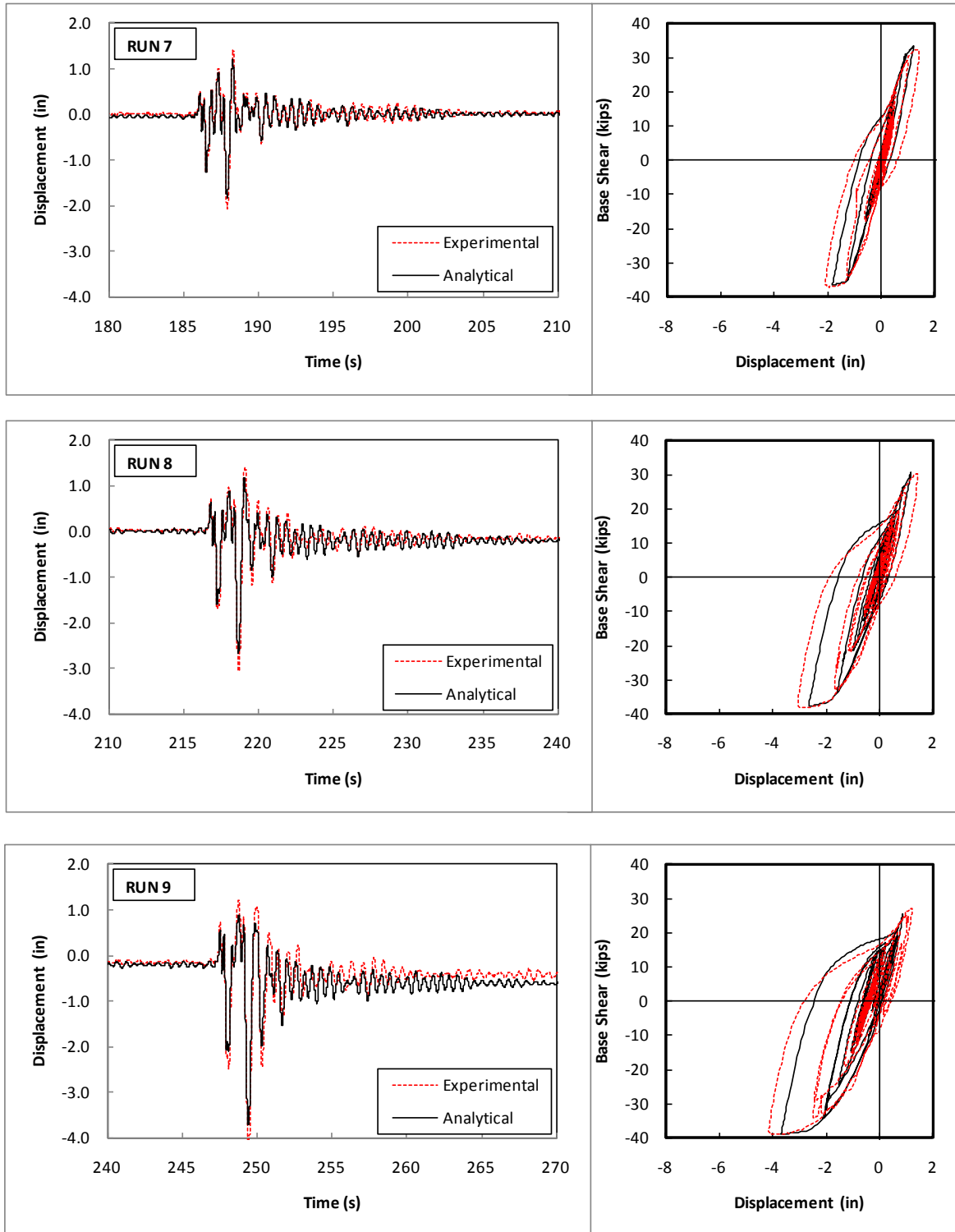


Figure 7-78 Measured and Calculated Displacement and Hysteresis, ISL1.0 (Runs 7 to 9)



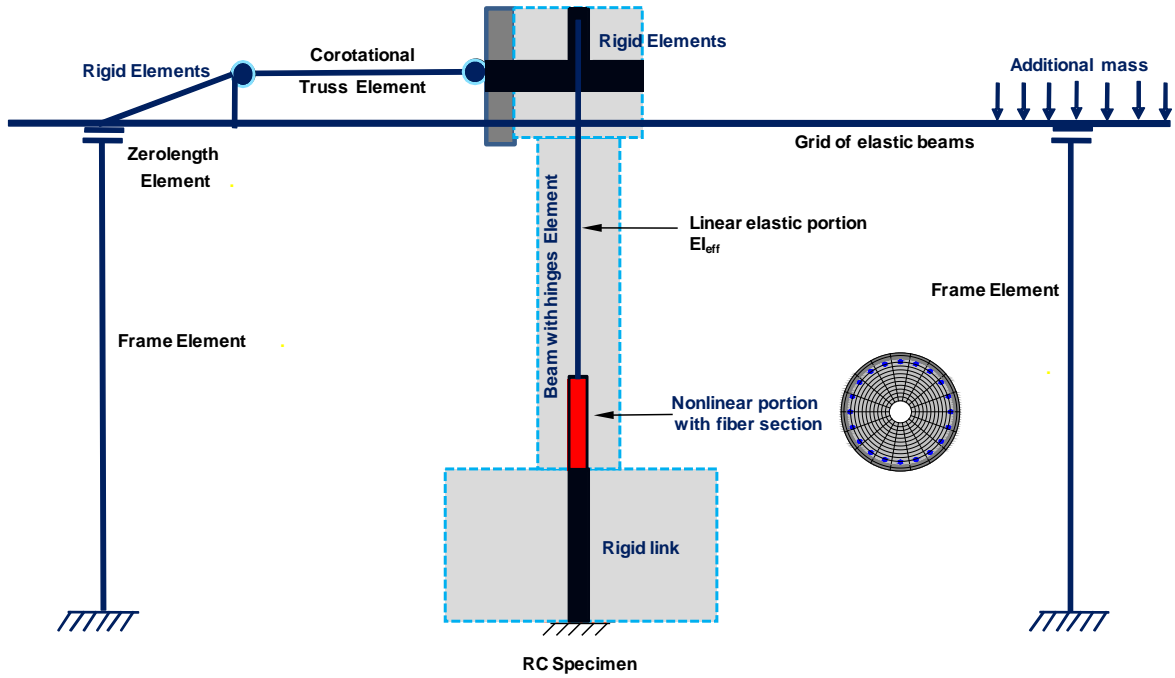


Figure 7-79 OpenSees Analytical Model for Bidirectionally Tested Circular Specimens

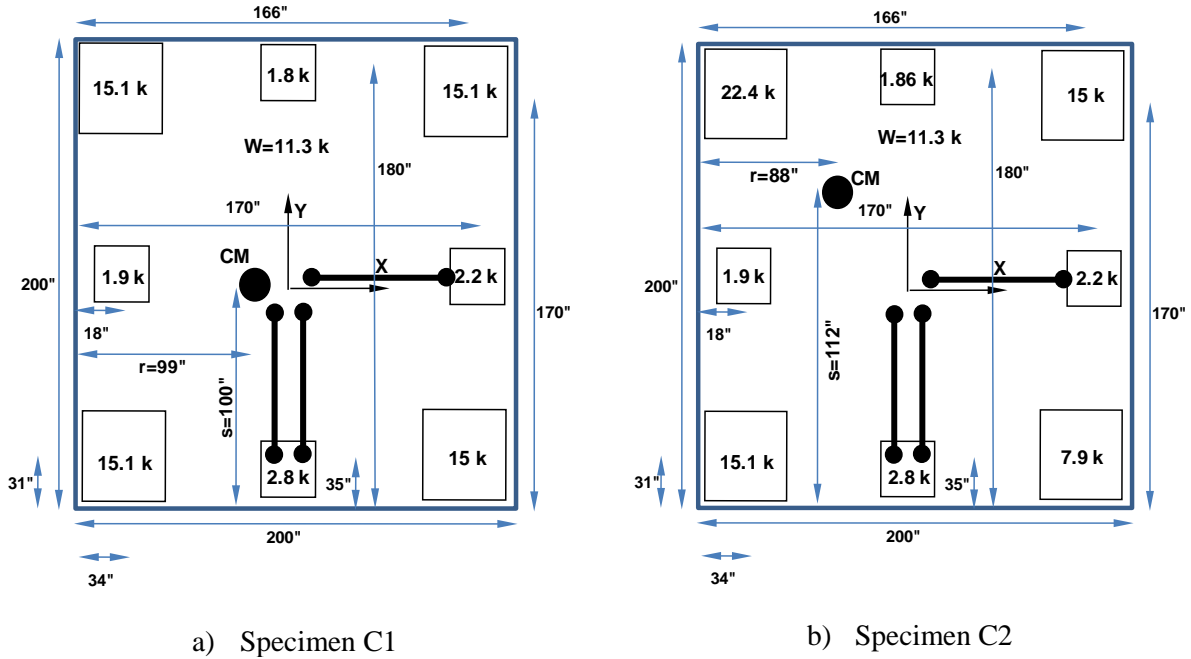
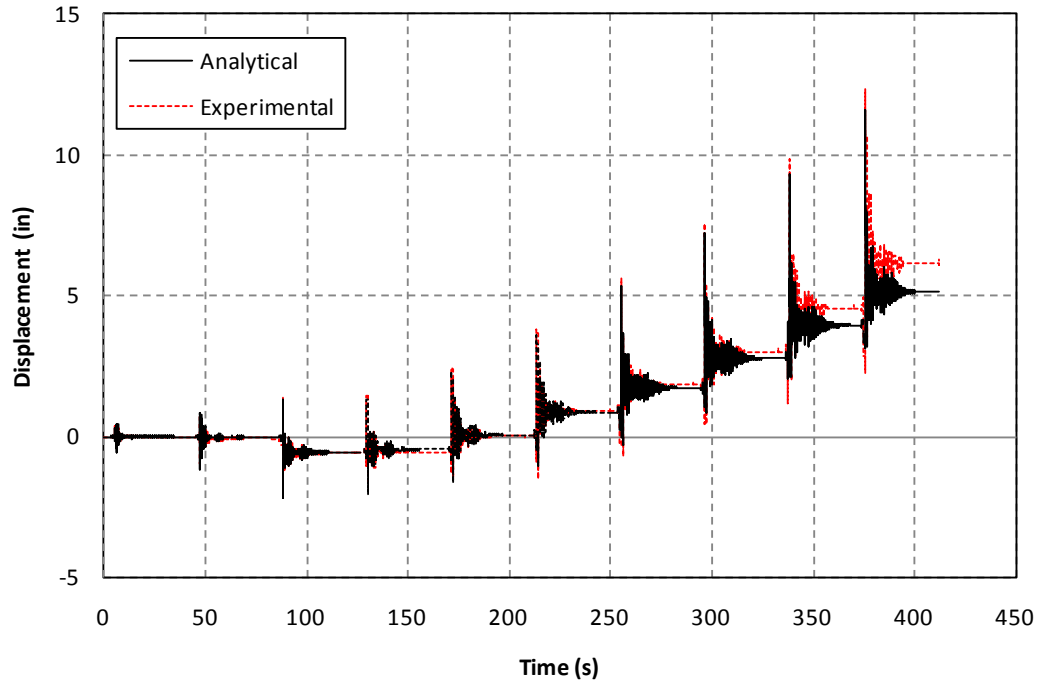
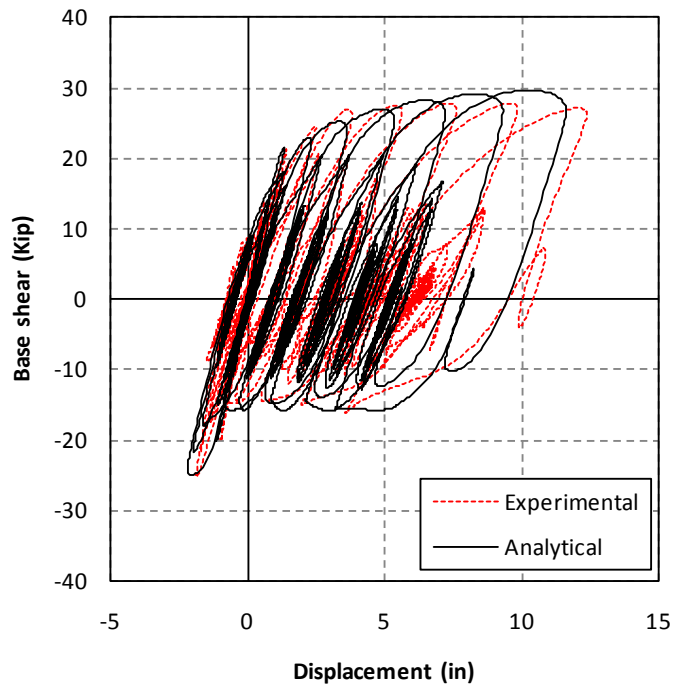


Figure 7-80 Mass Distribution and Mass Centroid for Circular Specimens



**Figure 7-81 Measured and Calculated Displacement History, C1-Long.**



**Figure 7-82 Measured and Calculated Cumulative F-D Hysteresis, C1-Long.**

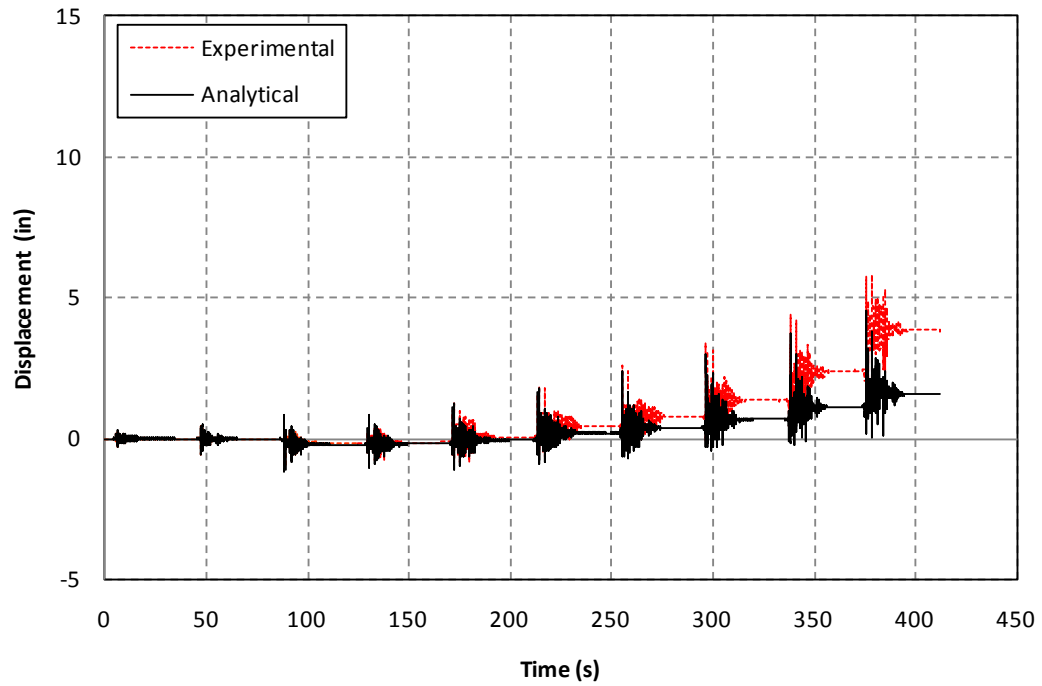


Figure 7-83 Measured and Calculated Displacement History, C1-Trans.

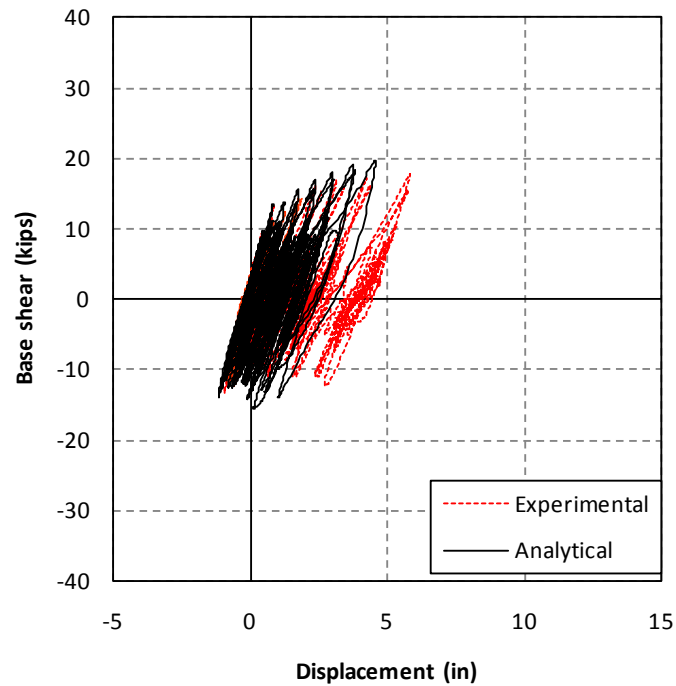
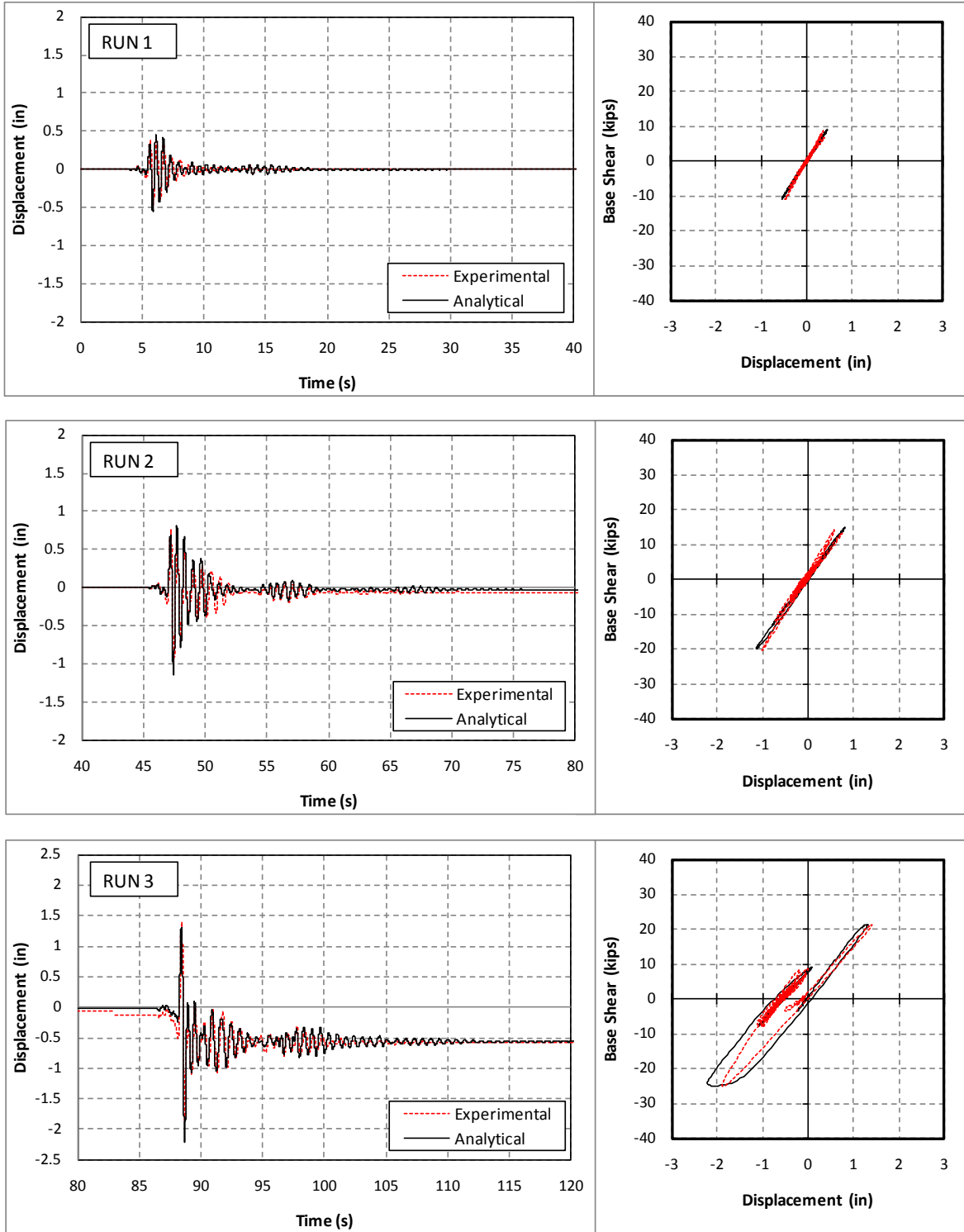
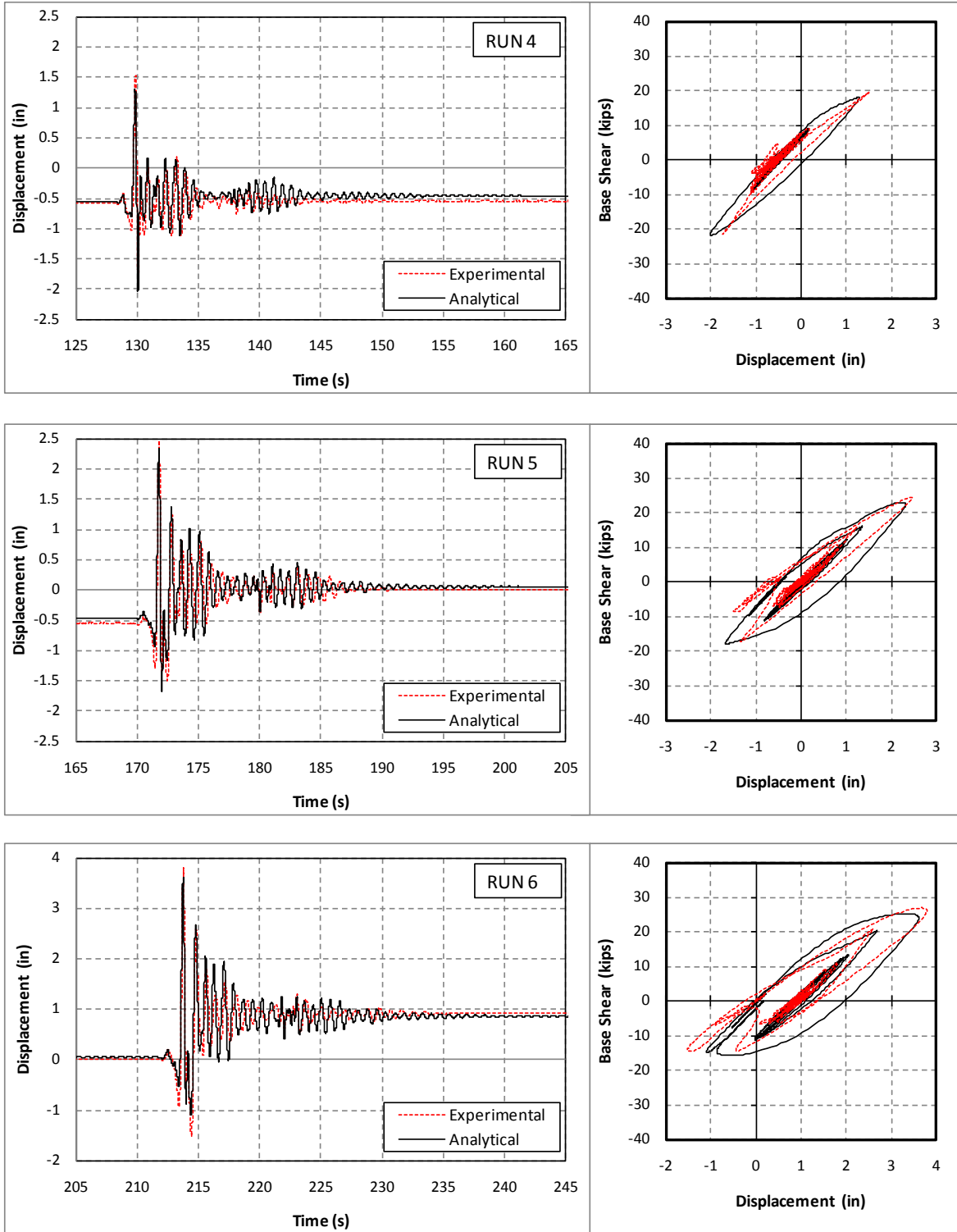


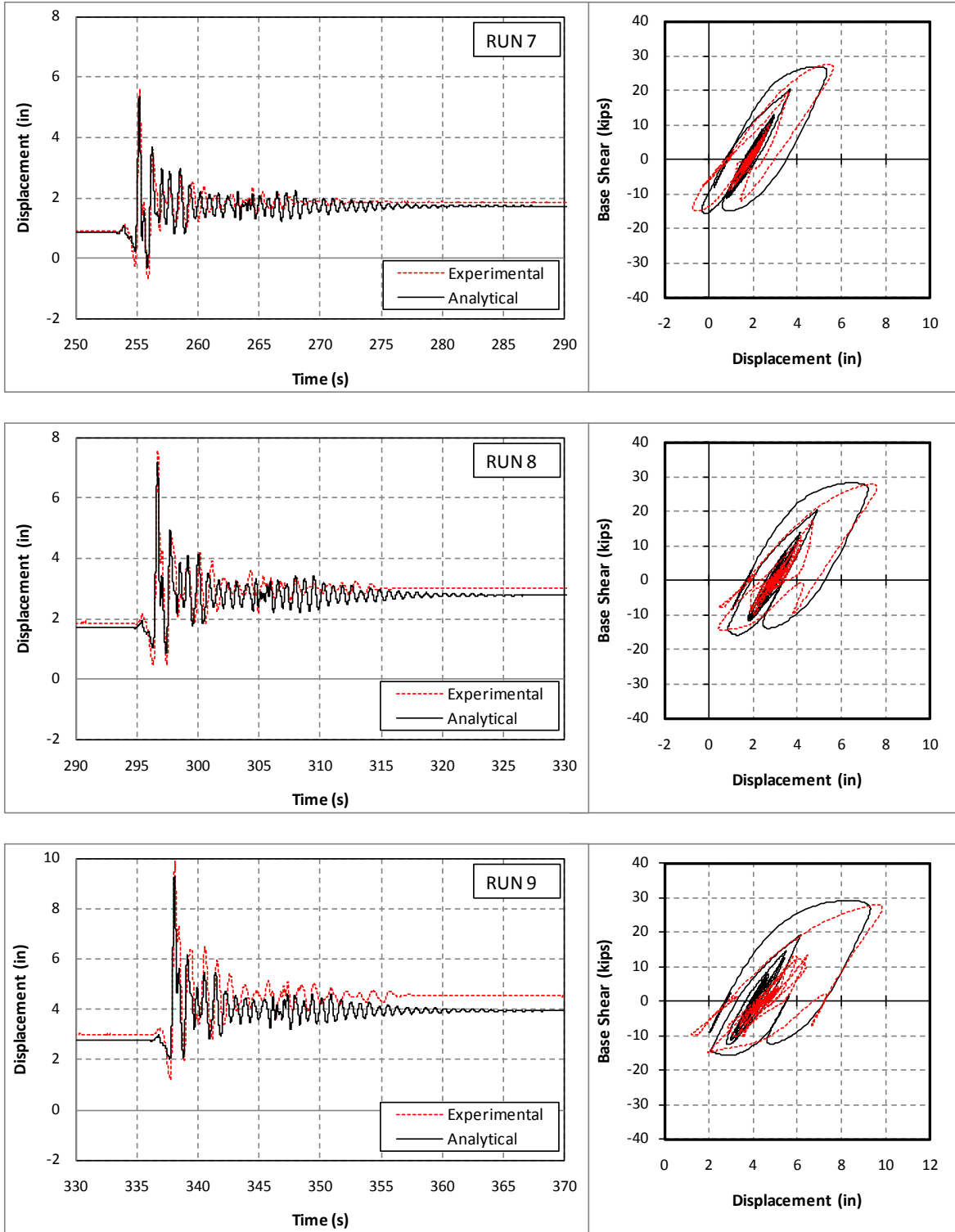
Figure 7-84 Measured and Calculated Cumulative F-D Hysteresis, C1-Trans.



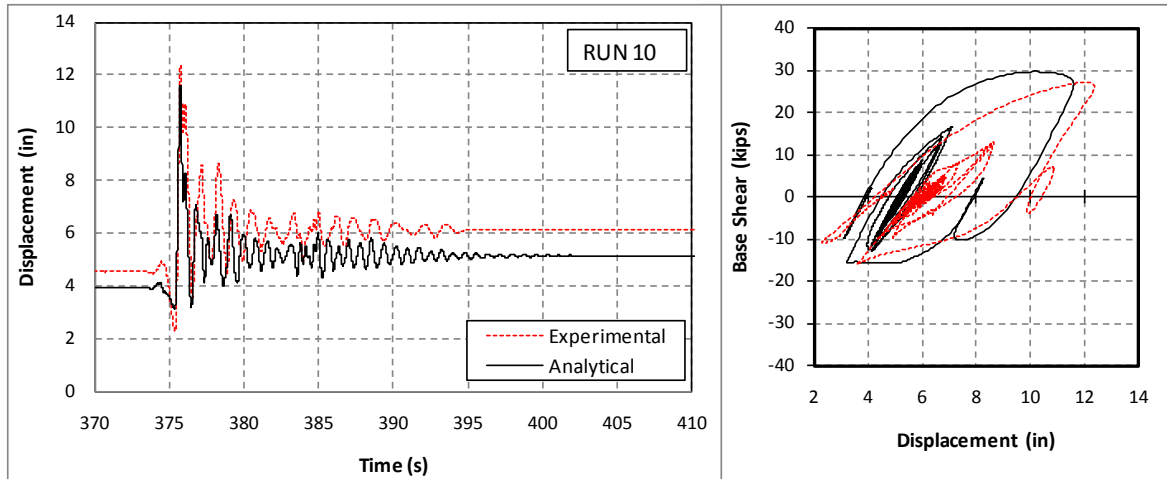
**Figure 7-85 Measured and Calculated Displacement and Hysteresis, C1-Long. (Runs 1 to 3)**



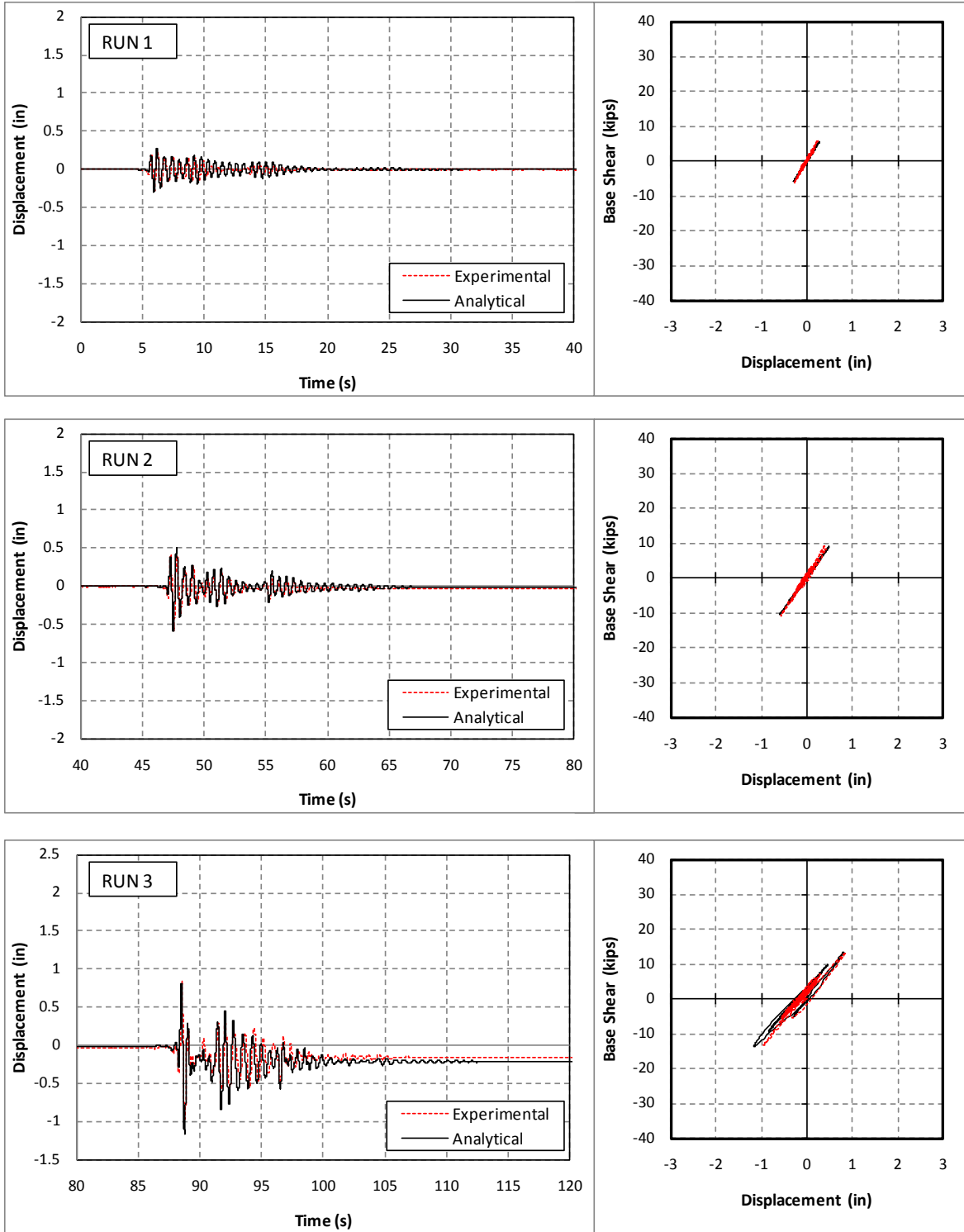
**Figure 7-86 Measured and Calculated Displacement and Hysteresis, C1-Long. (Runs 4 to 6)**



**Figure 7-87 Measured and Calculated Displacement and Hysteresis, C1-Long. (Runs 7 to 9)**

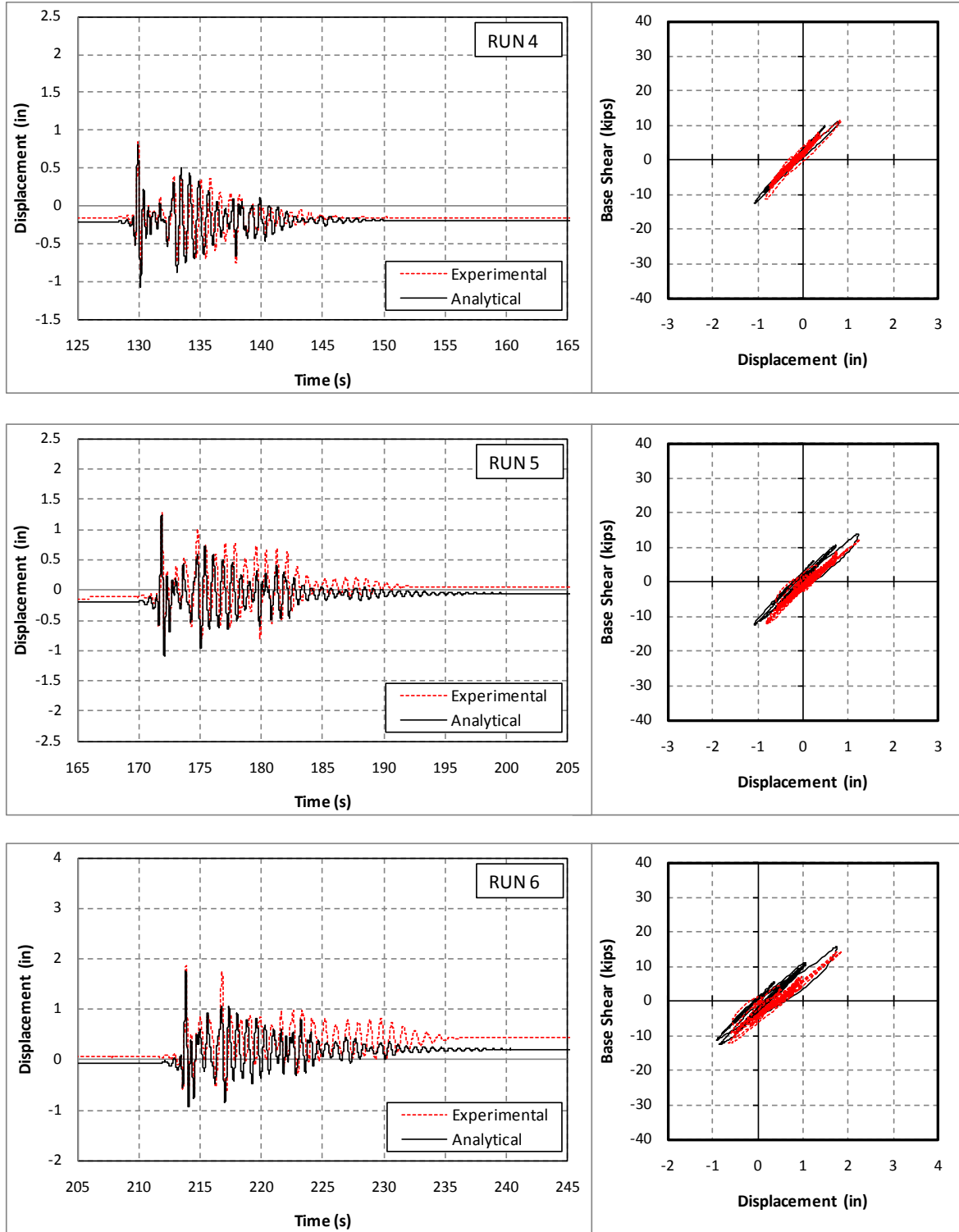


**Figure 7-88 Measured and Calculated Displacement and Hysteresis, C1-Long.  
(Run 10)**

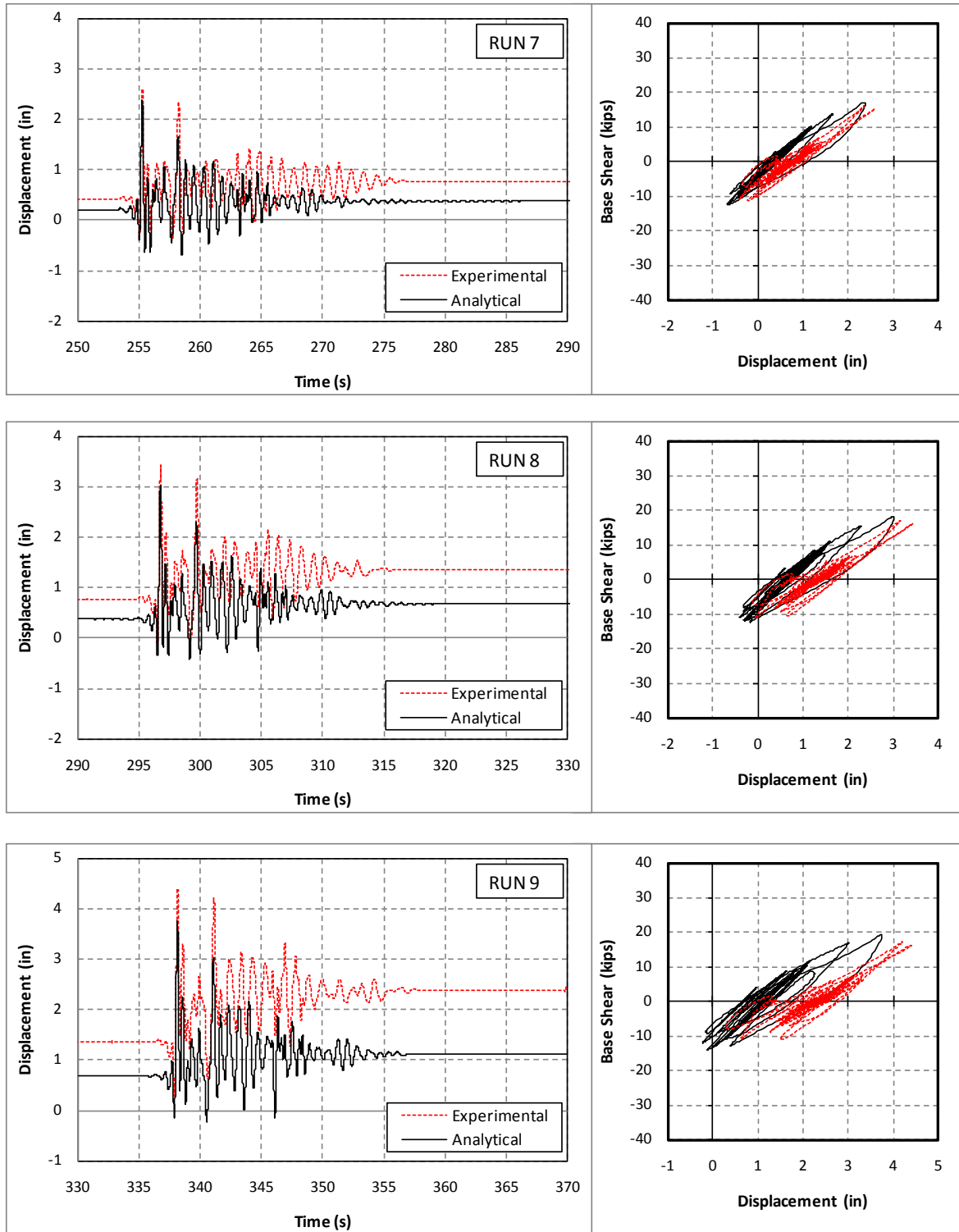


**Figure 7-89 Measured and Calculated Displacement and Hysteresis, C1-Trans. (Runs 1 to 3)**

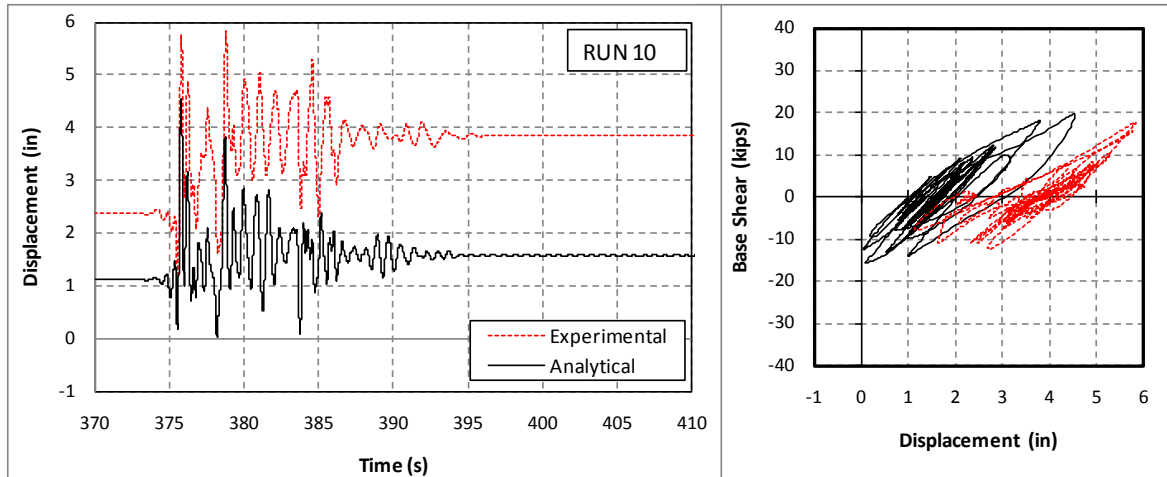




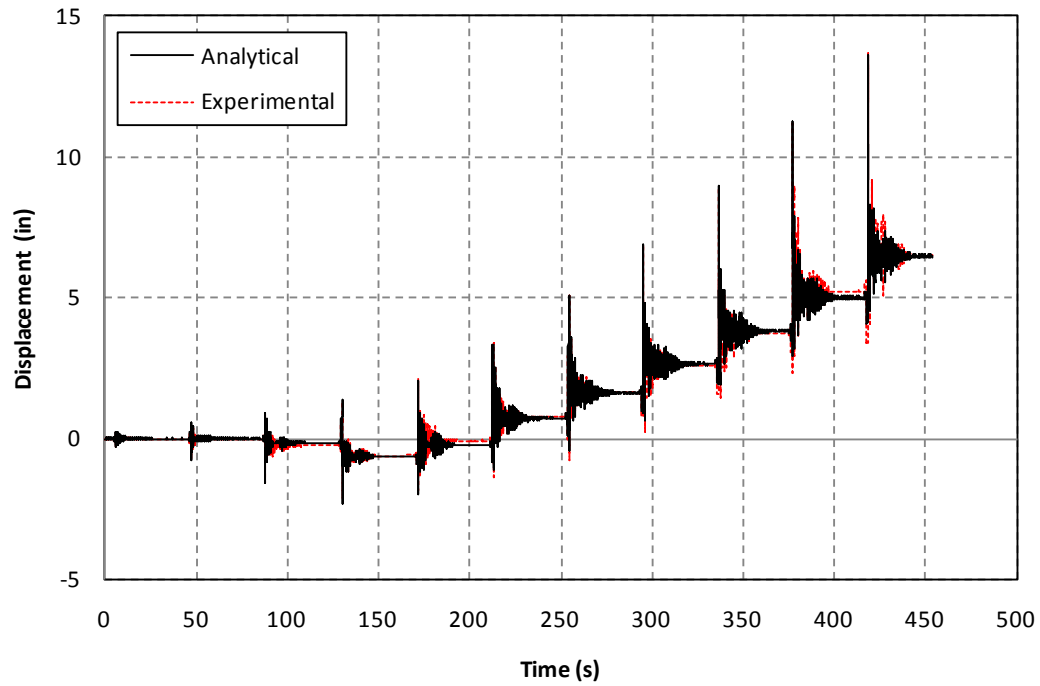
**Figure 7-90 Measured and Calculated Displacement and Hysteresis, C1-Trans. (Runs 4 to 6)**



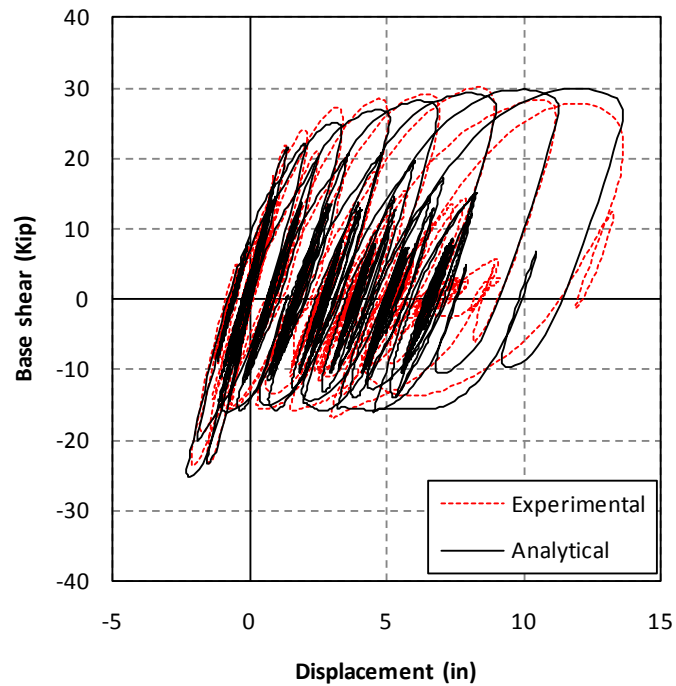
**Figure 7-91 Measured and Calculated Displacement and Hysteresis, C1-Trans. (Runs 7 to 9)**



**Figure 7-92 Measured and Calculated Displacement and Hysteresis, C1-Trans.  
(Run 10)**



**Figure 7-93 Measured and Calculated Displacement History, C2-Long.**



**Figure 7-94 Measured and Calculated Cumulative F-D Hysteresis, C2-Long.**

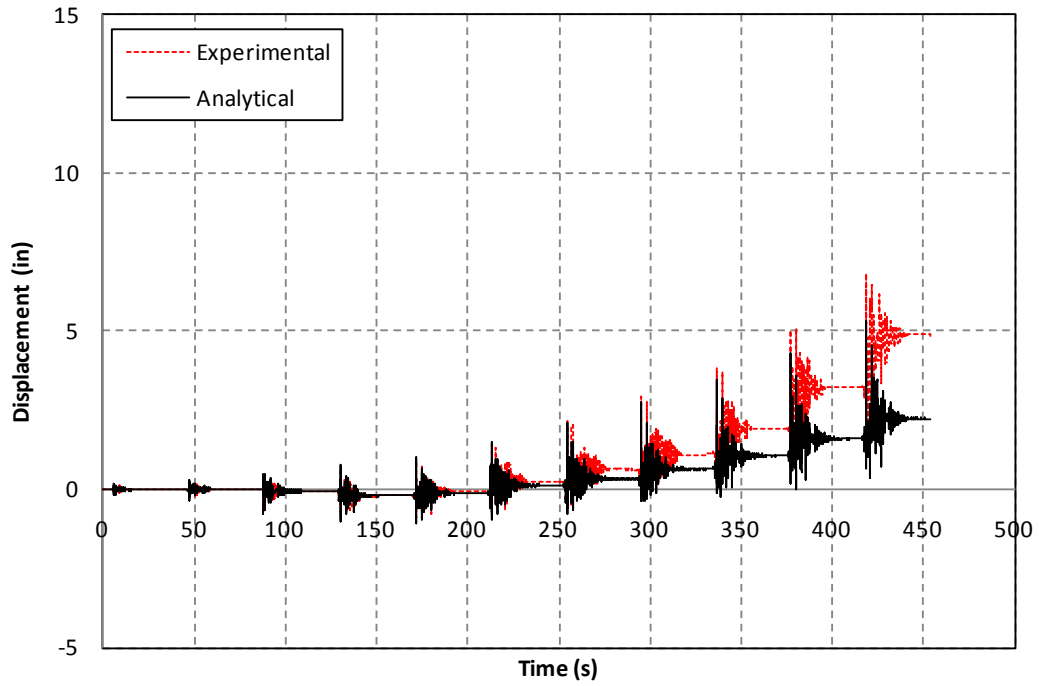


Figure 7-95 Measured and Calculated Displacement History, C2-Trans.

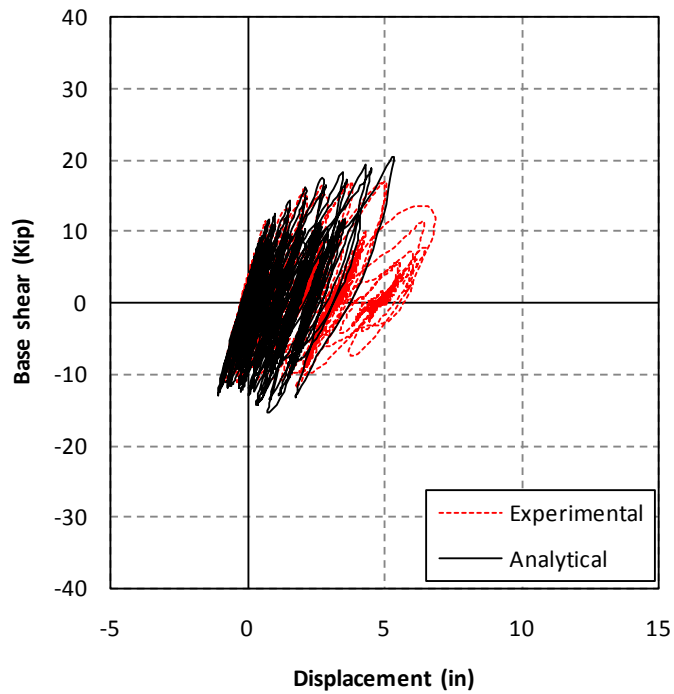
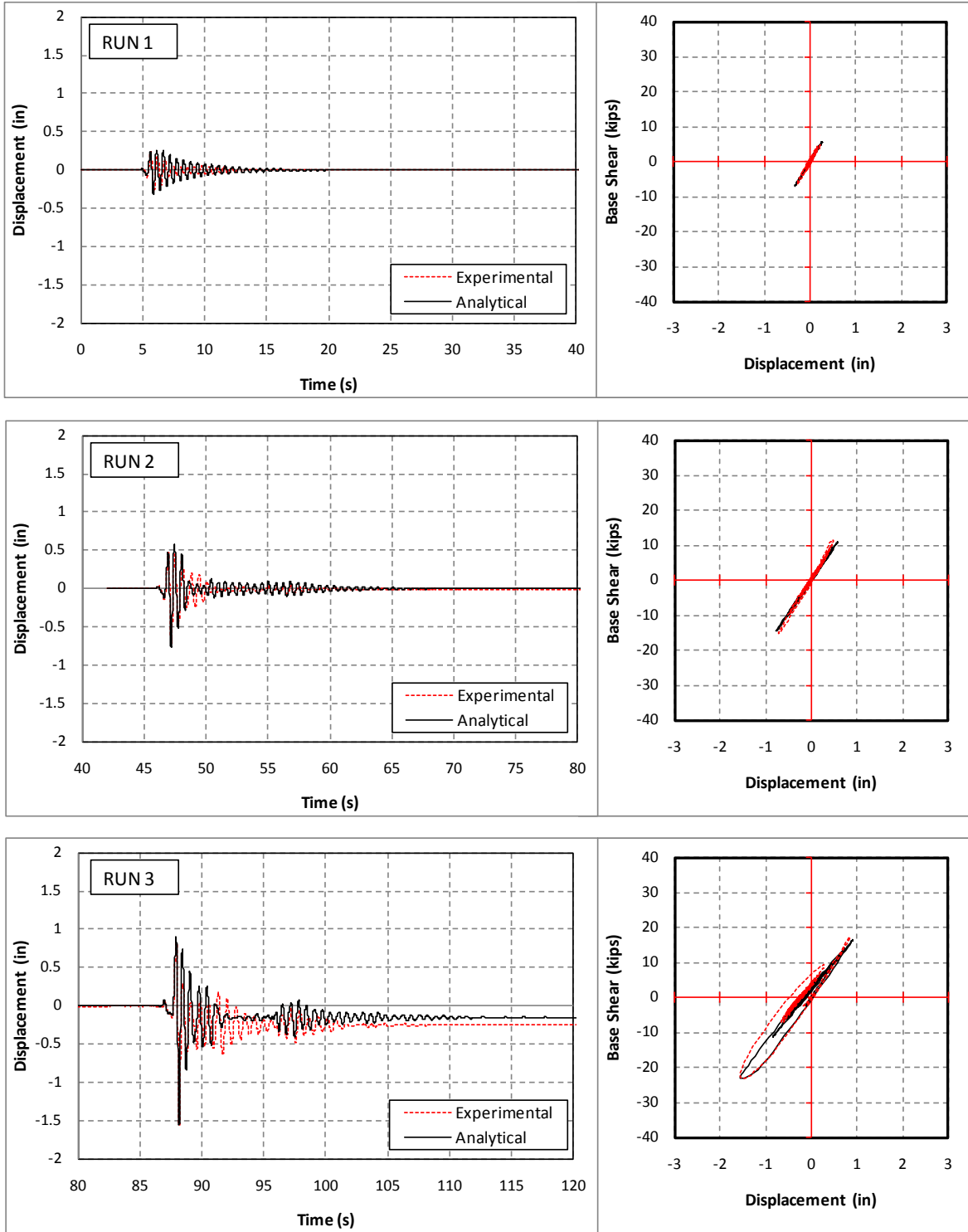
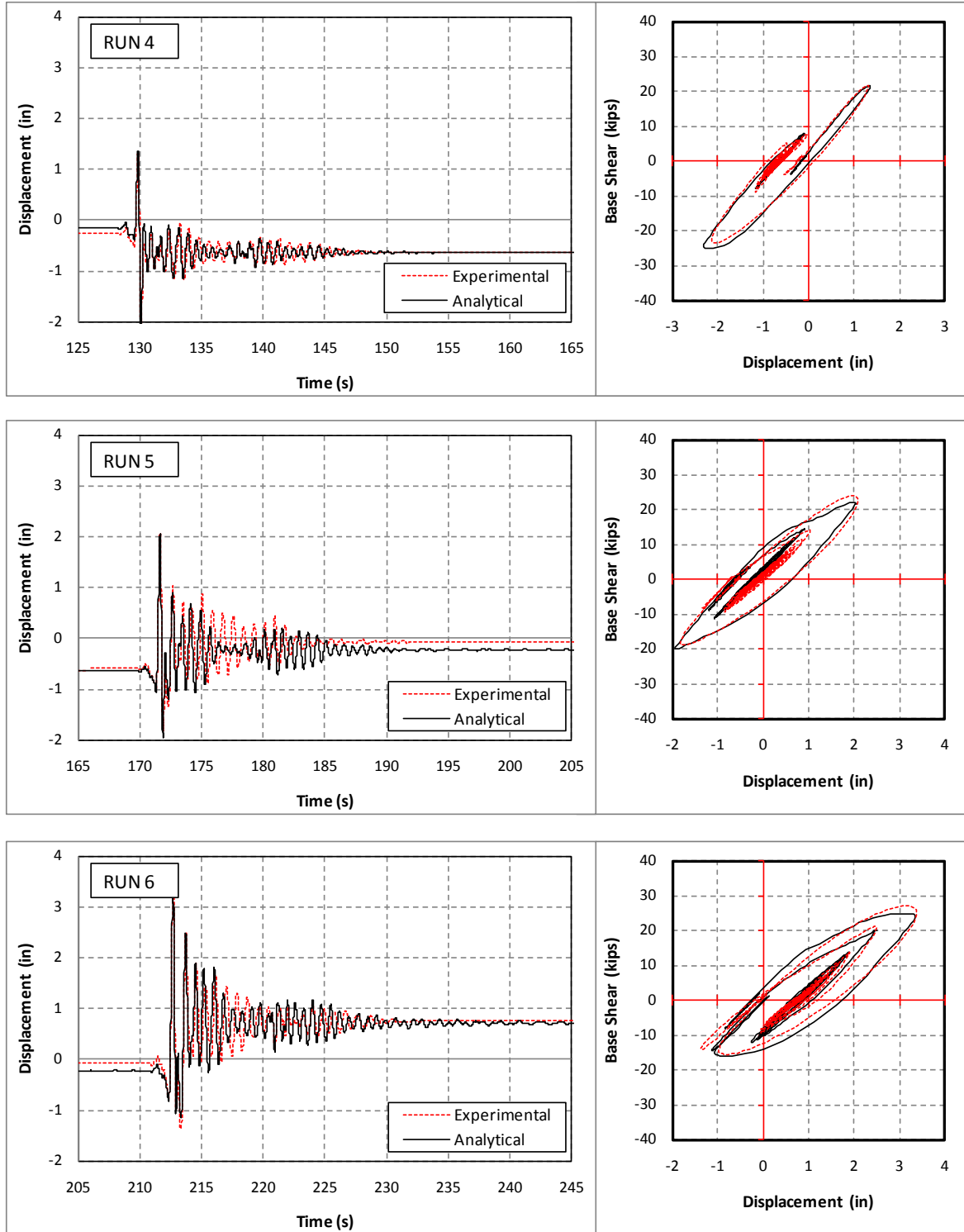


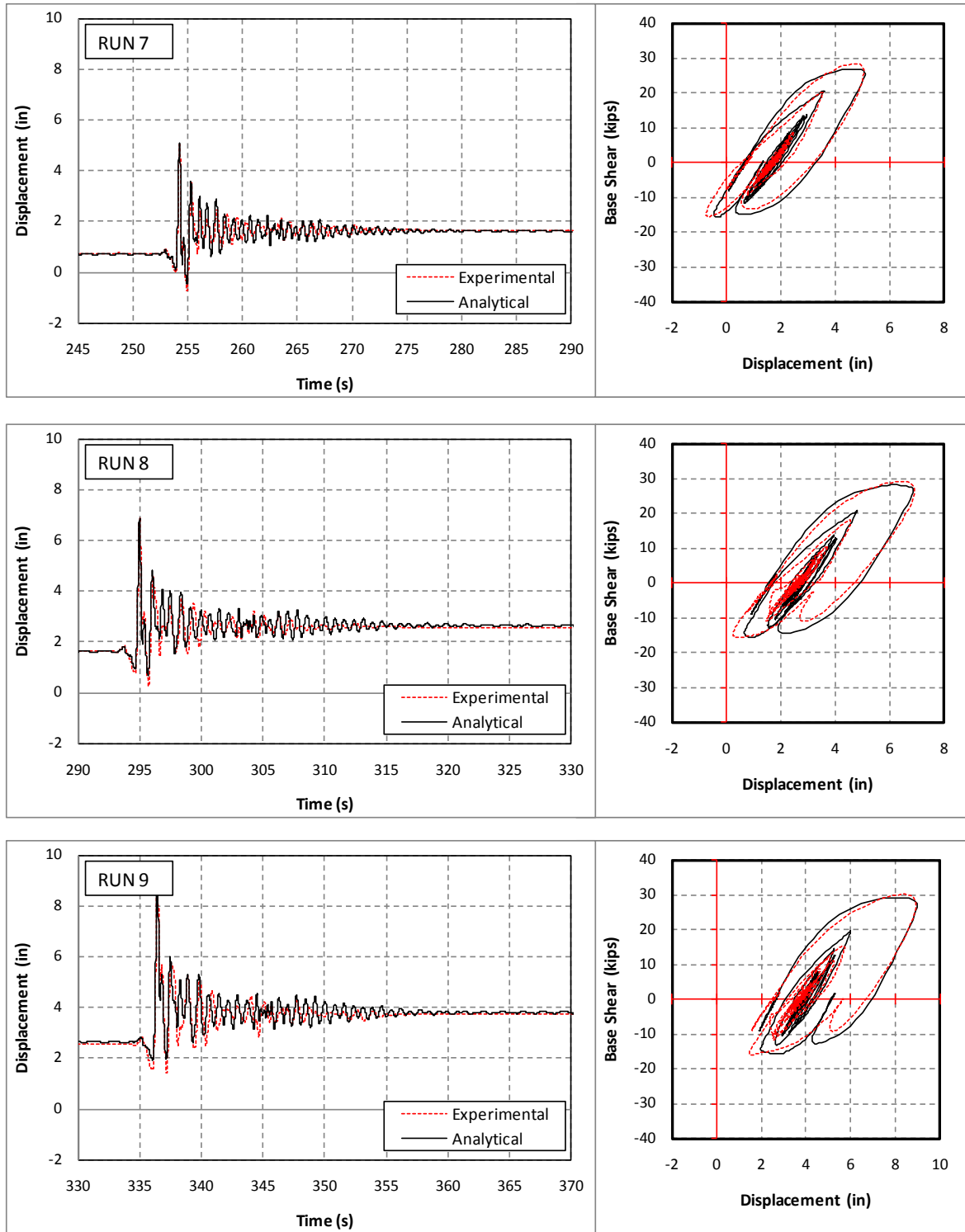
Figure 7-96 Measured and Calculated Cumulative F-D Hysteresis, C2-Trans.



**Figure 7-97 Measured and Calculated Displacement and Hysteresis, C2-Long. (Runs 1 to 3)**

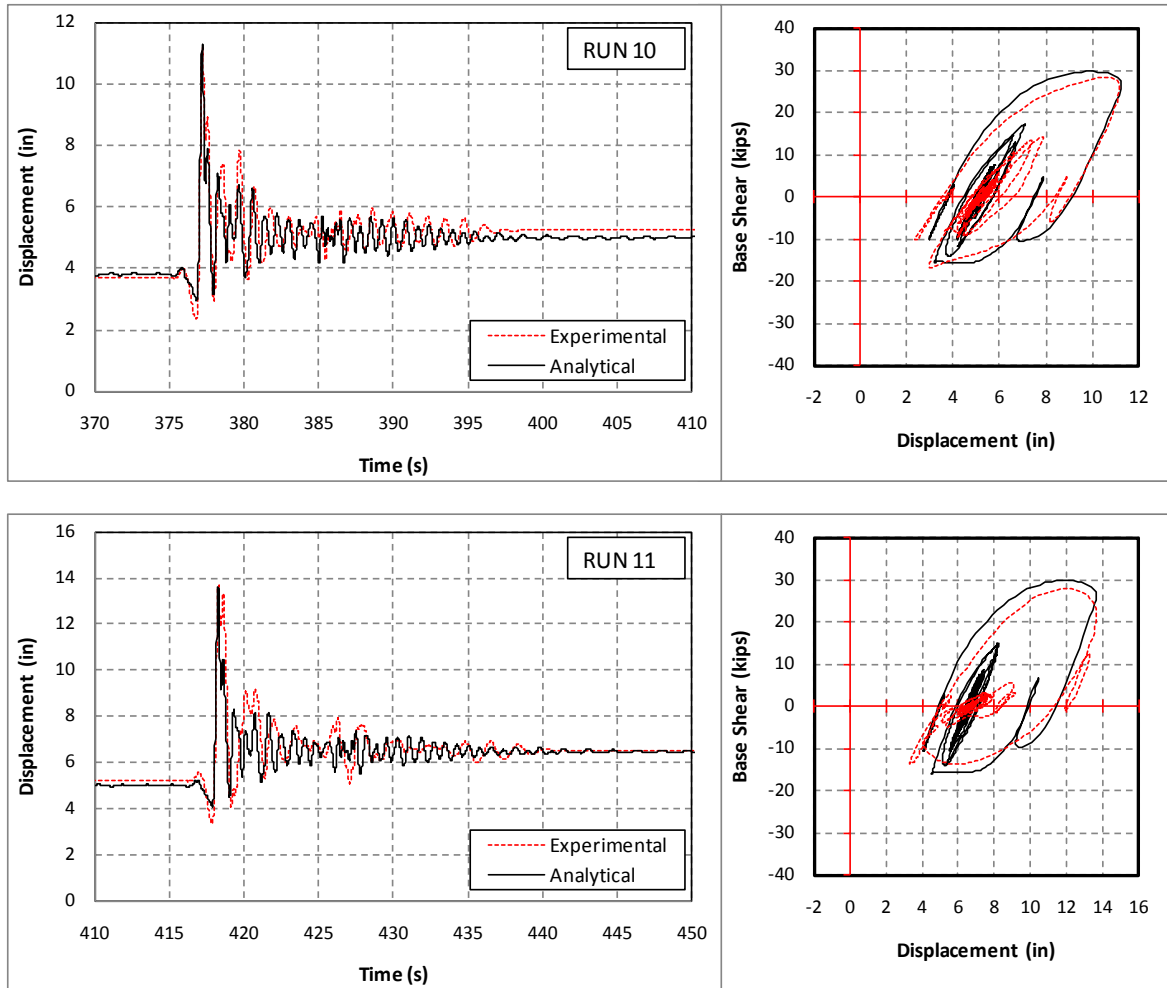


**Figure 7-98 Measured and Calculated Displacement and Hysteresis, C2-Long.  
(Runs 4 to 6)**

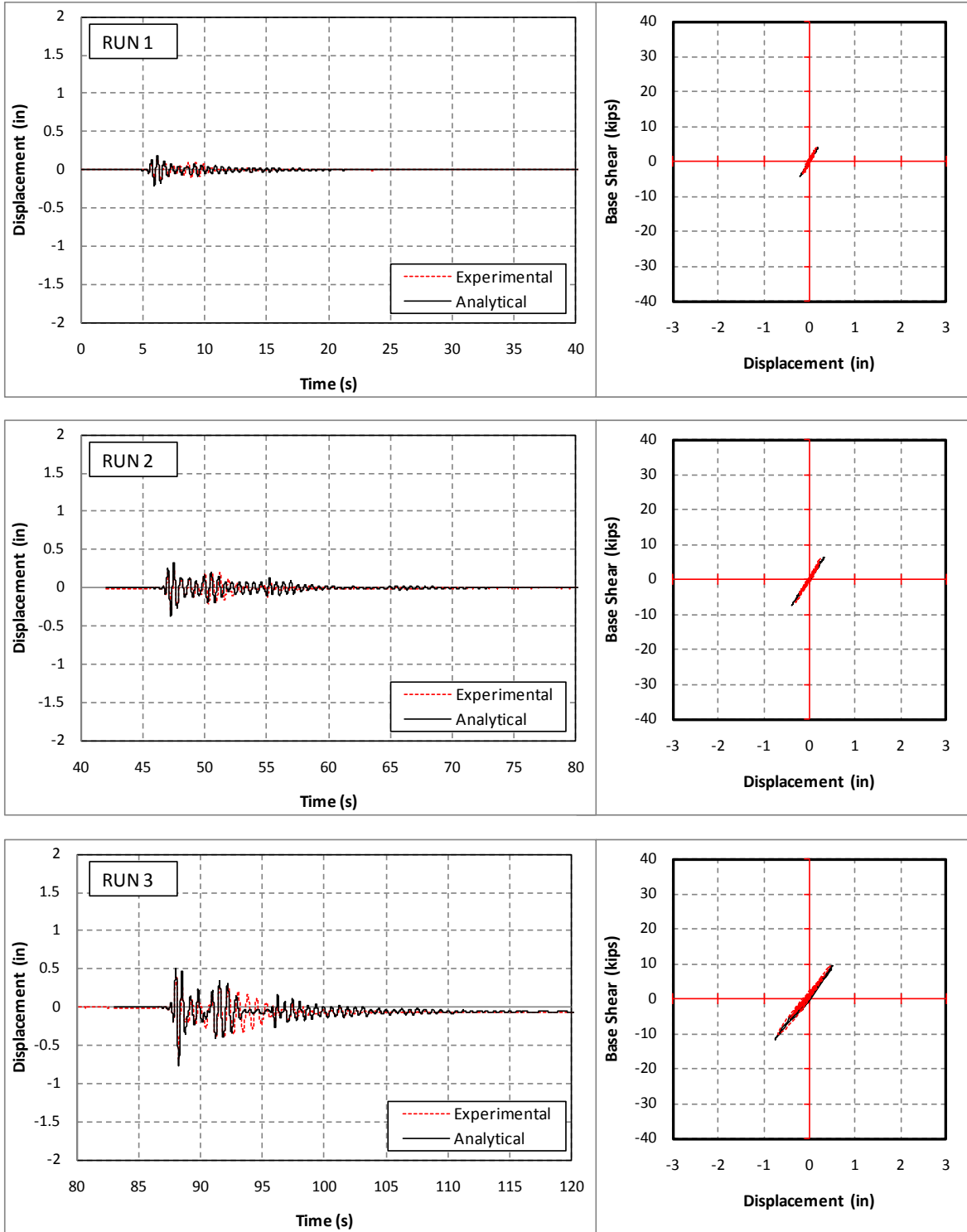


**Figure 7-99 Measured and Calculated Displacement and Hysteresis, C2-Long. (Runs 7 to 9)**

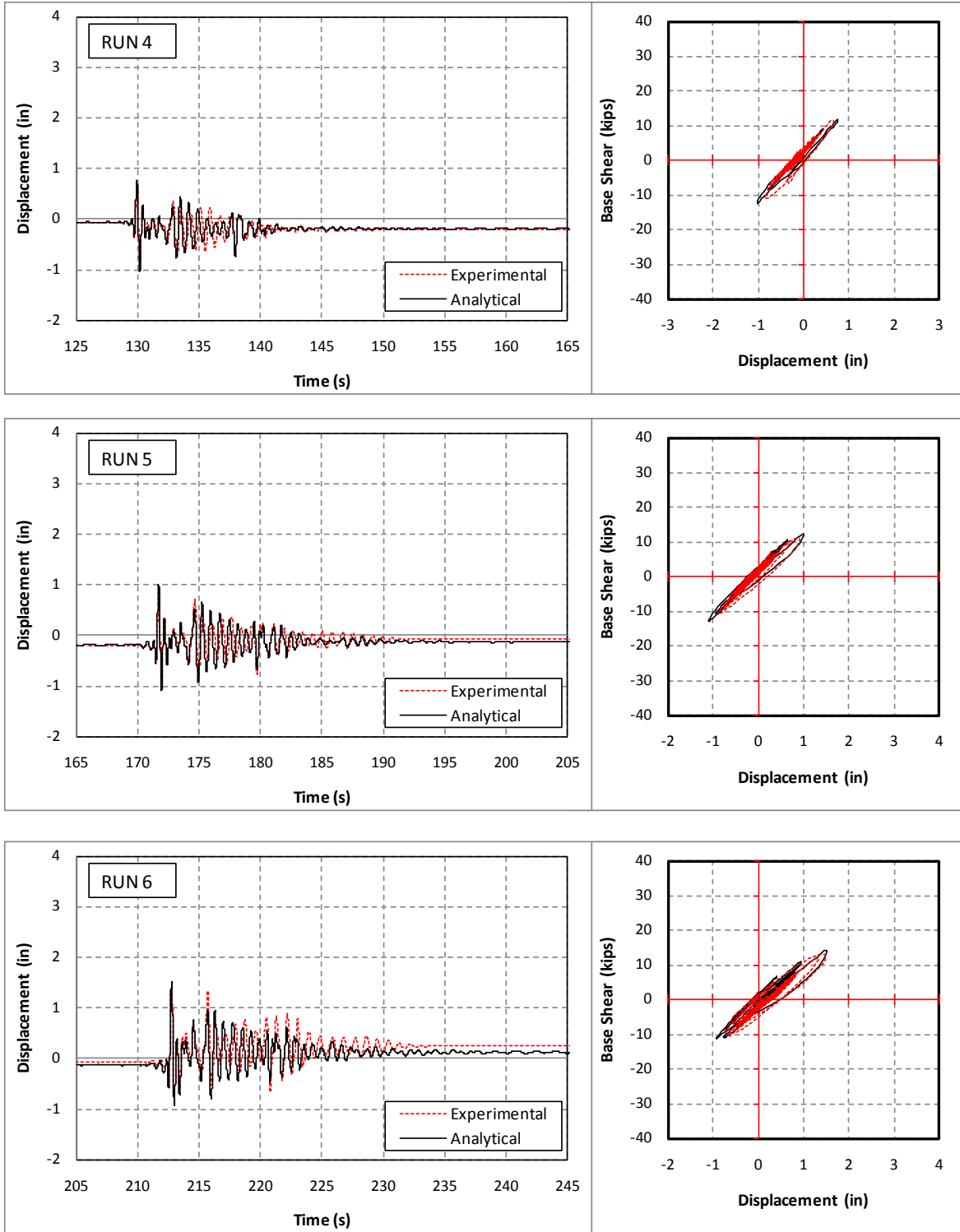




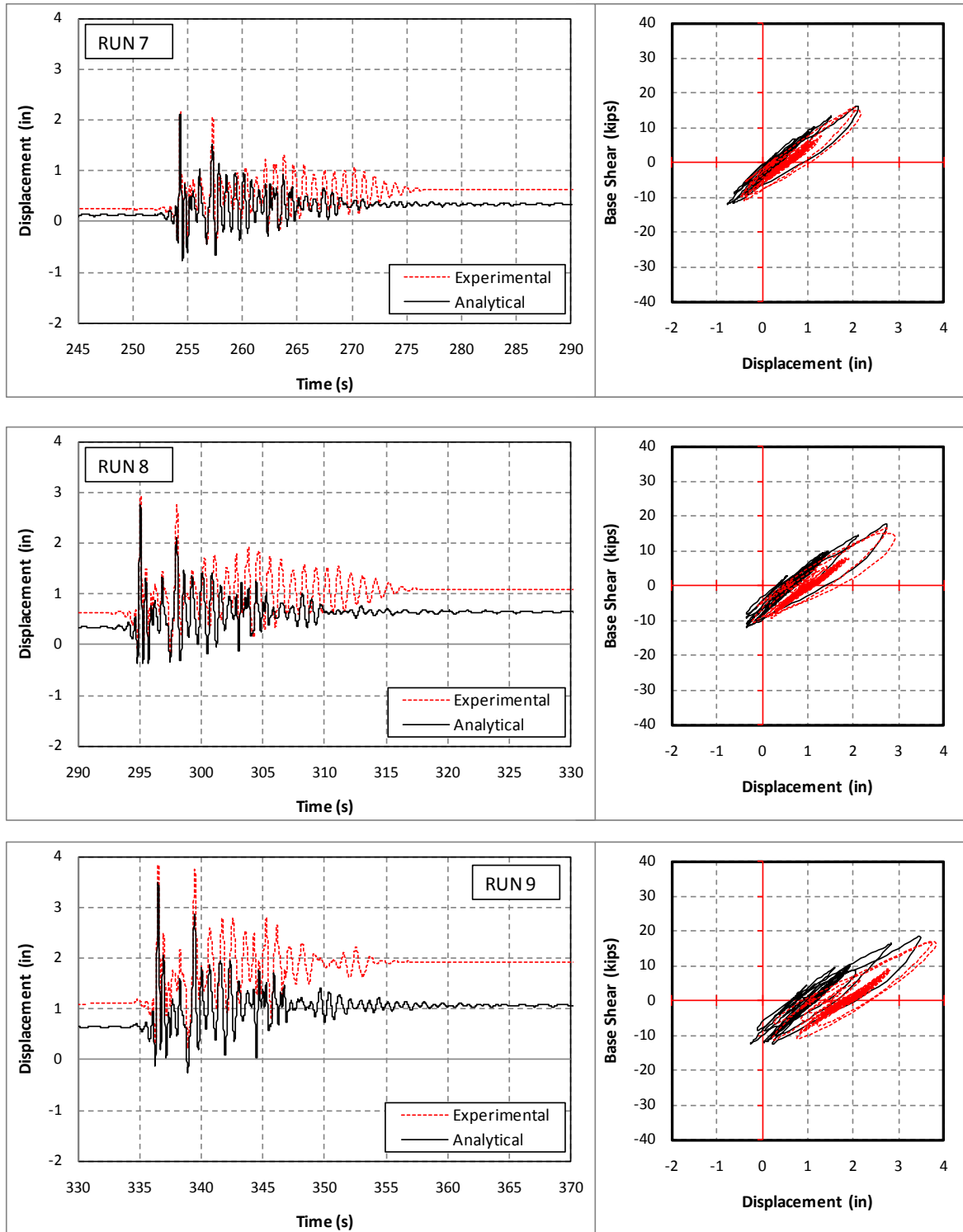
**Figure 7-100 Measured and Calculated Displacement and Hysteresis, C2-Long.  
(Runs 10 and 11)**



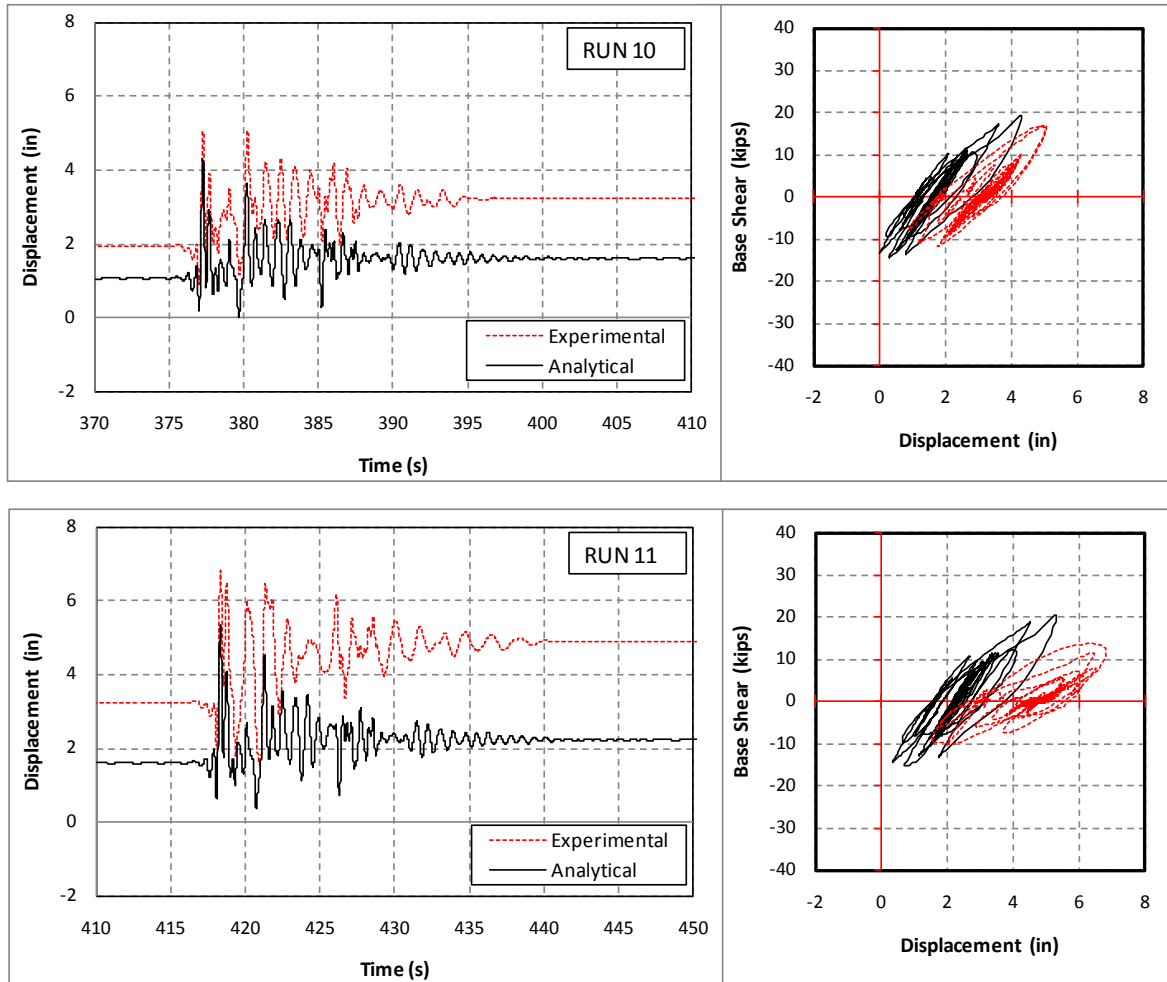
**Figure 7-101 Measured and Calculated Displacement and Hysteresis, C2-Trans. (Runs 1 to 3)**



**Figure 7-102 Measured and Calculated Displacement and Hysteresis, C2-Trans. (Runs 4 to 6)**



**Figure 7-103 Measured and Calculated Displacement and Hysteresis, C2-Trans.  
(Runs 7 to 9)**



**Figure 7-104 Measured and Calculated Displacement and Hysteresis, C2-Trans.  
(Runs 10 and 11)**

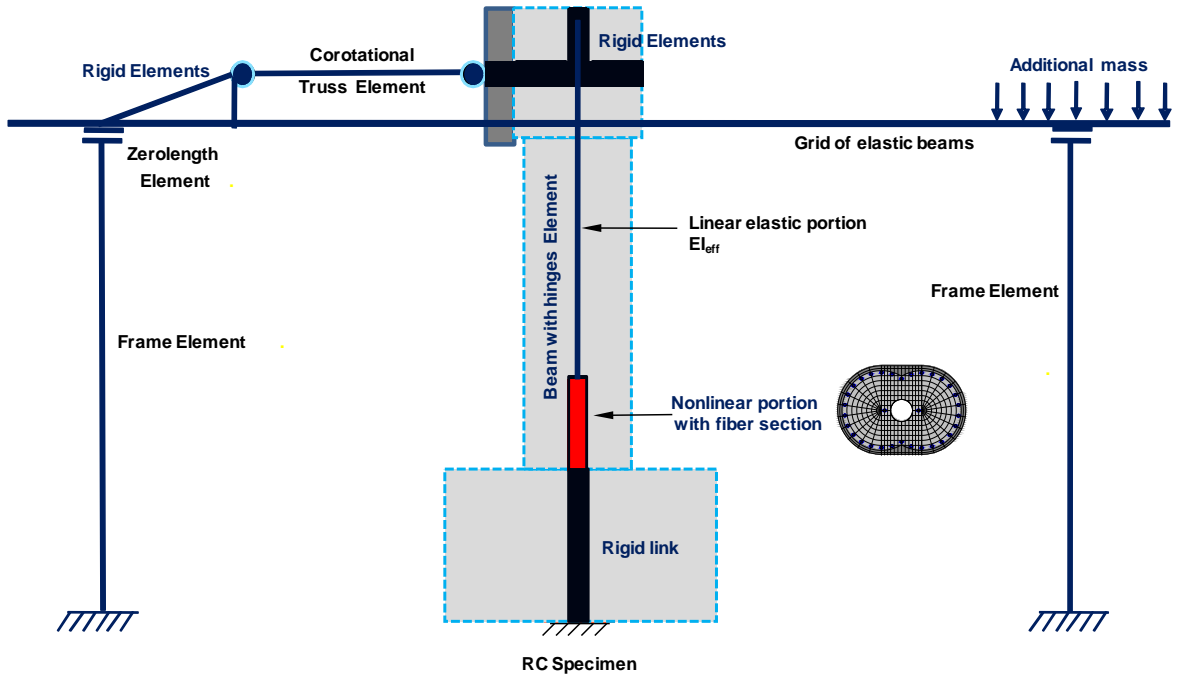


Figure 7-105 OpenSees Analytical Model for Bidirectionally Tested Interlocking Specimens

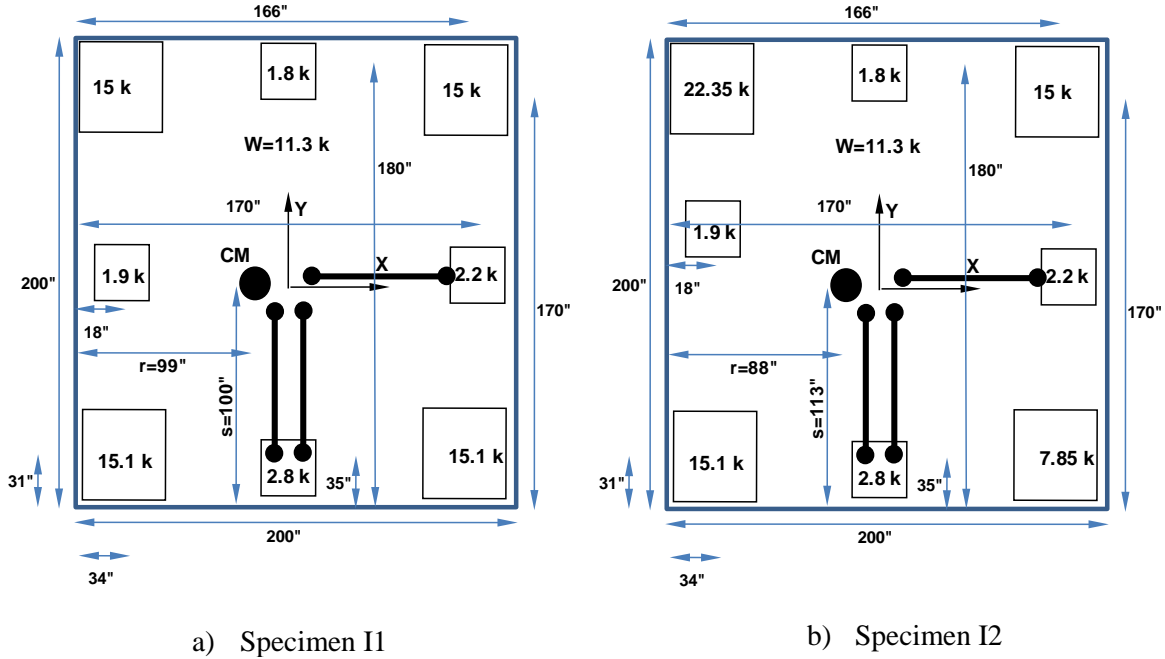


Figure 7-106 Mass Distribution and Mass Centroid for Interlocking Specimens

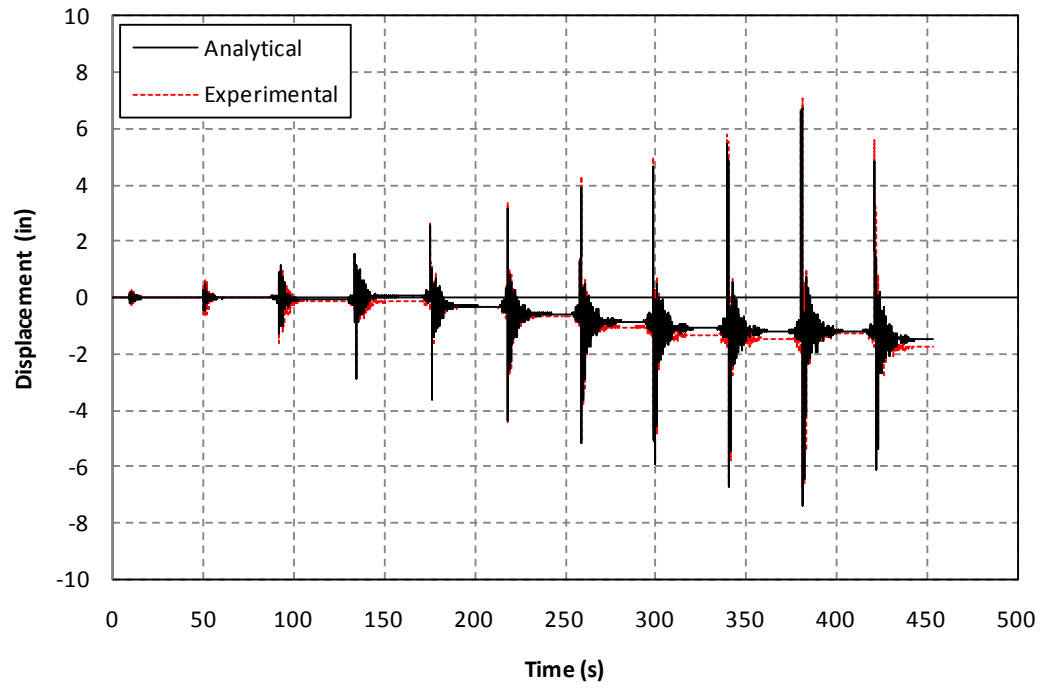


Figure 7-107 Measured and Calculated Displacement History, I1-Long.

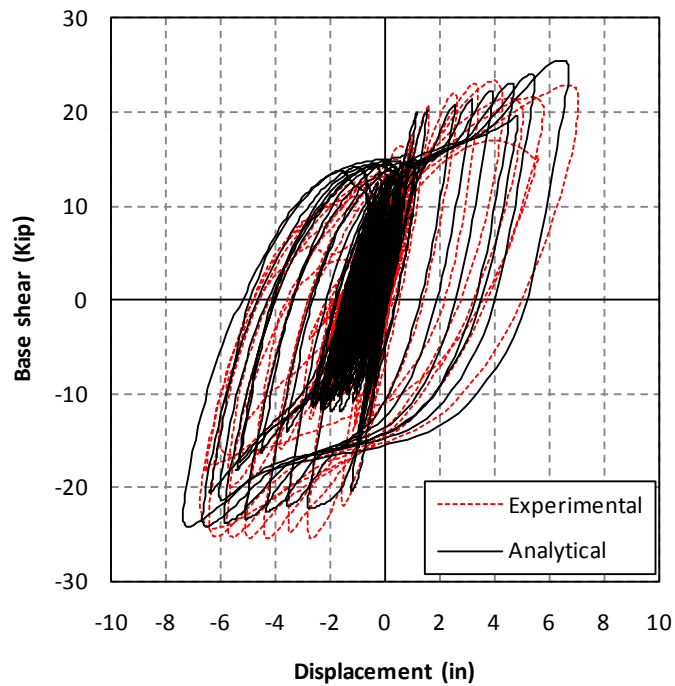


Figure 7-108 Measured and Calculated Cumulative F-D Hysteresis, I1-Long.

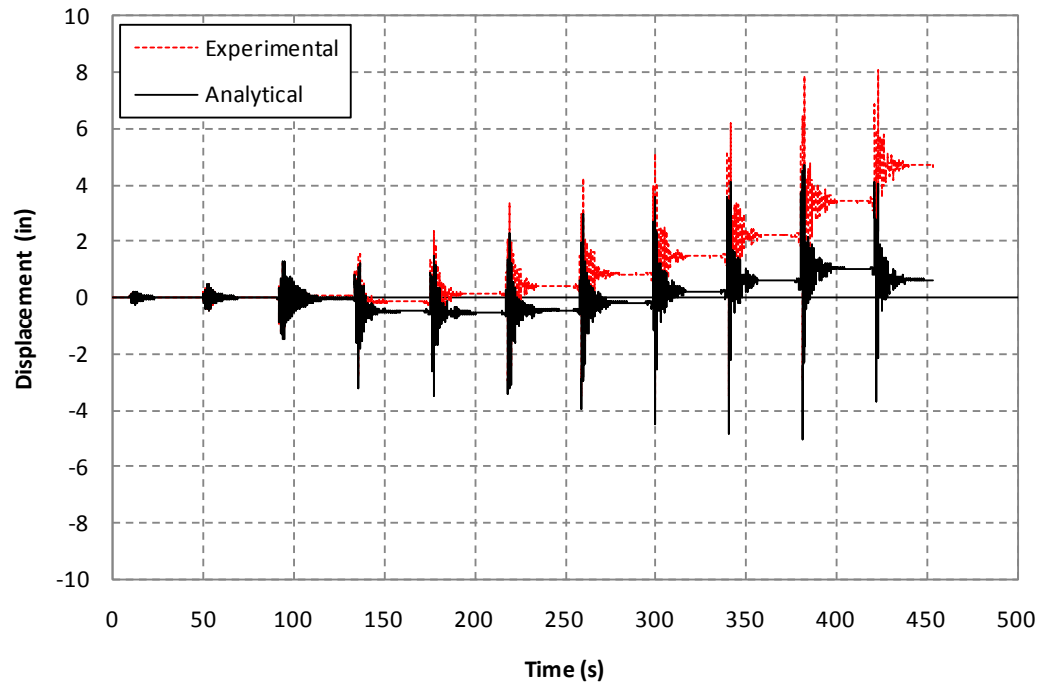


Figure 7-109 Measured and Calculated Displacement History, I1-Trans.

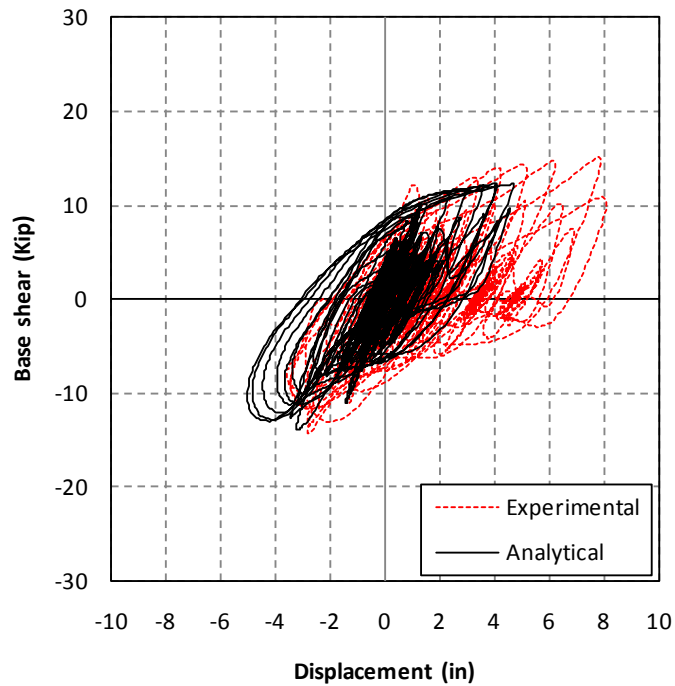
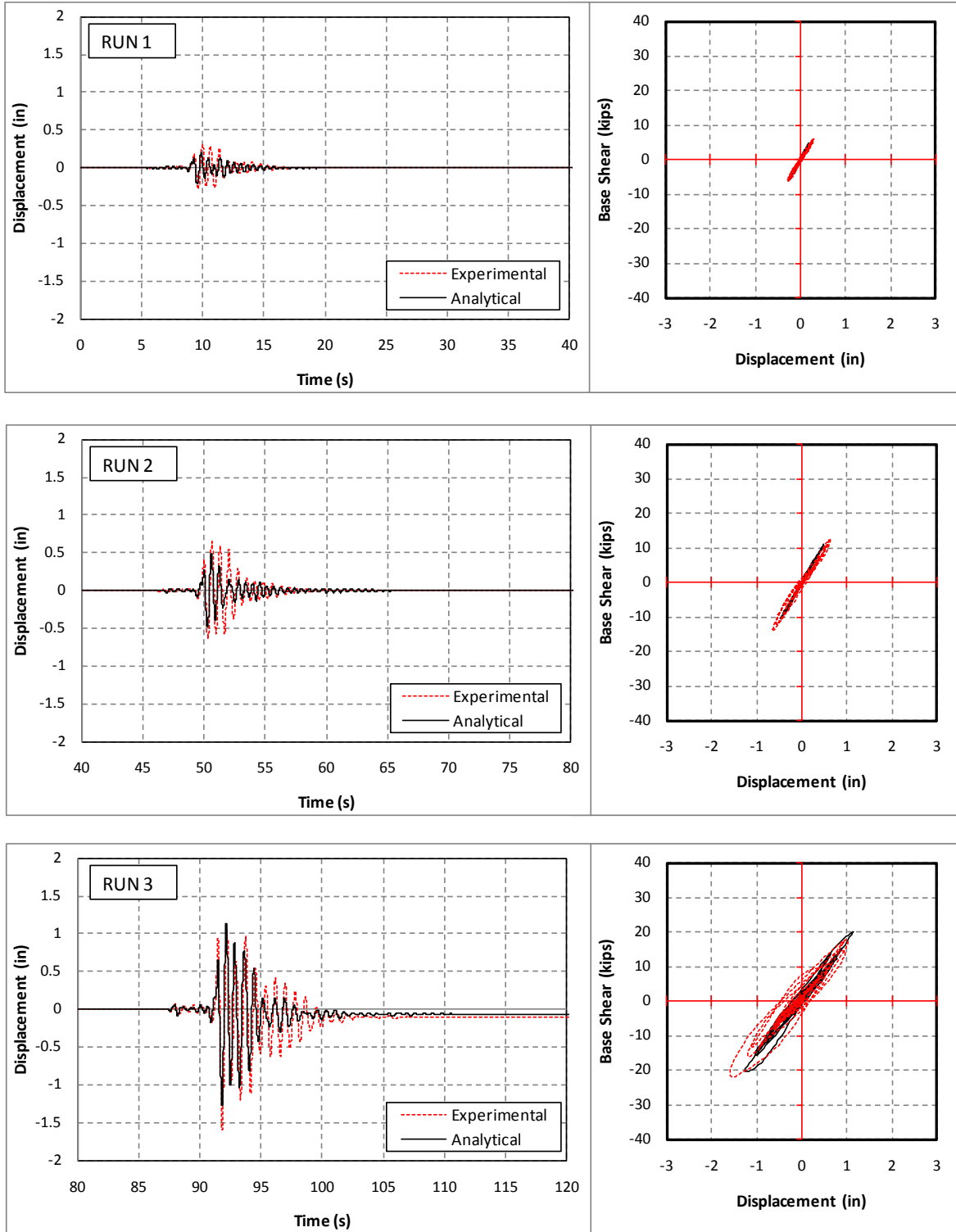


Figure 7-110 Measured and Calculated Cumulative F-D Hysteresis, I1-Trans.





**Figure 7-111 Measured and Calculated Displacement and Hysteresis, I1-Long. (Runs 1 to 3)**

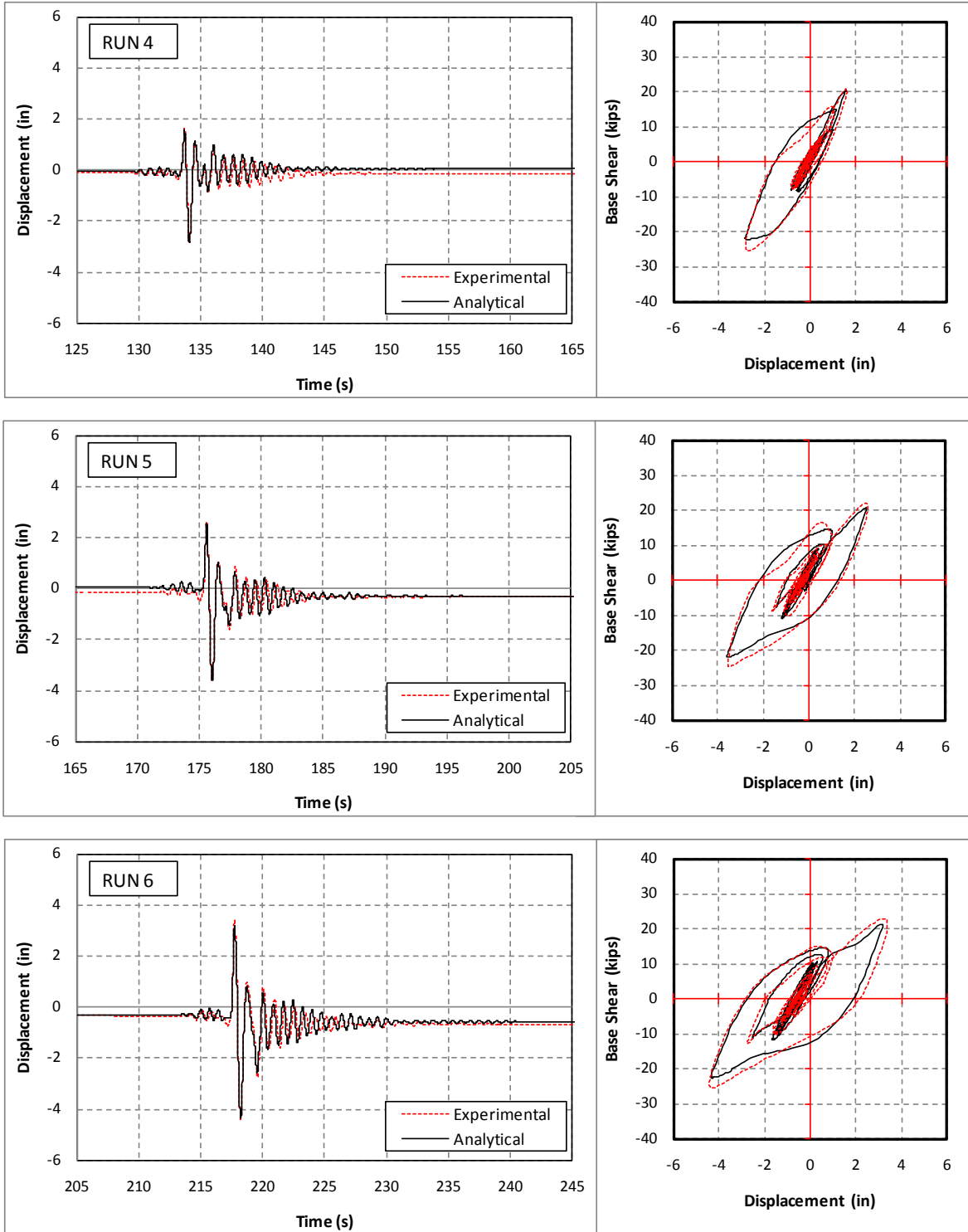
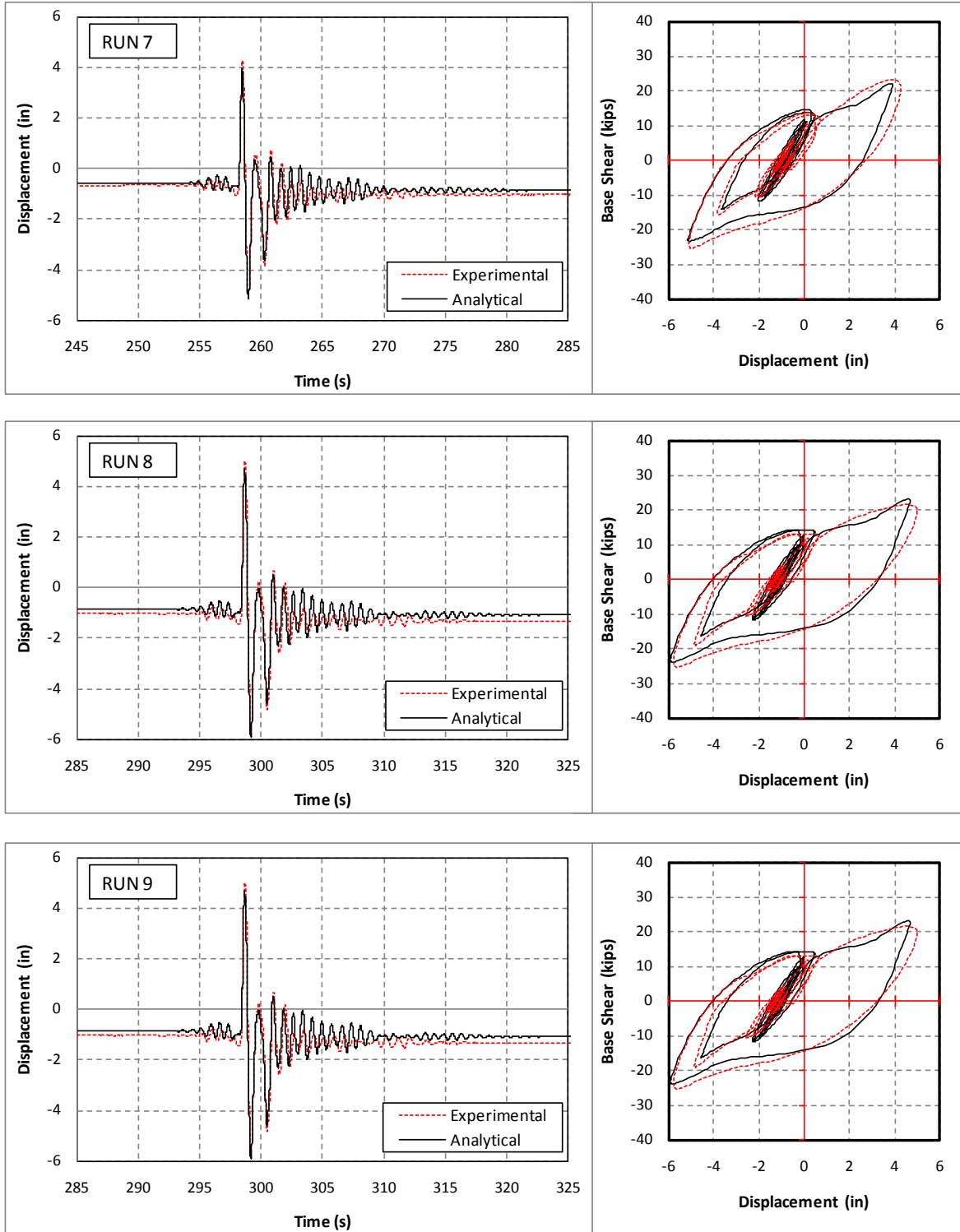
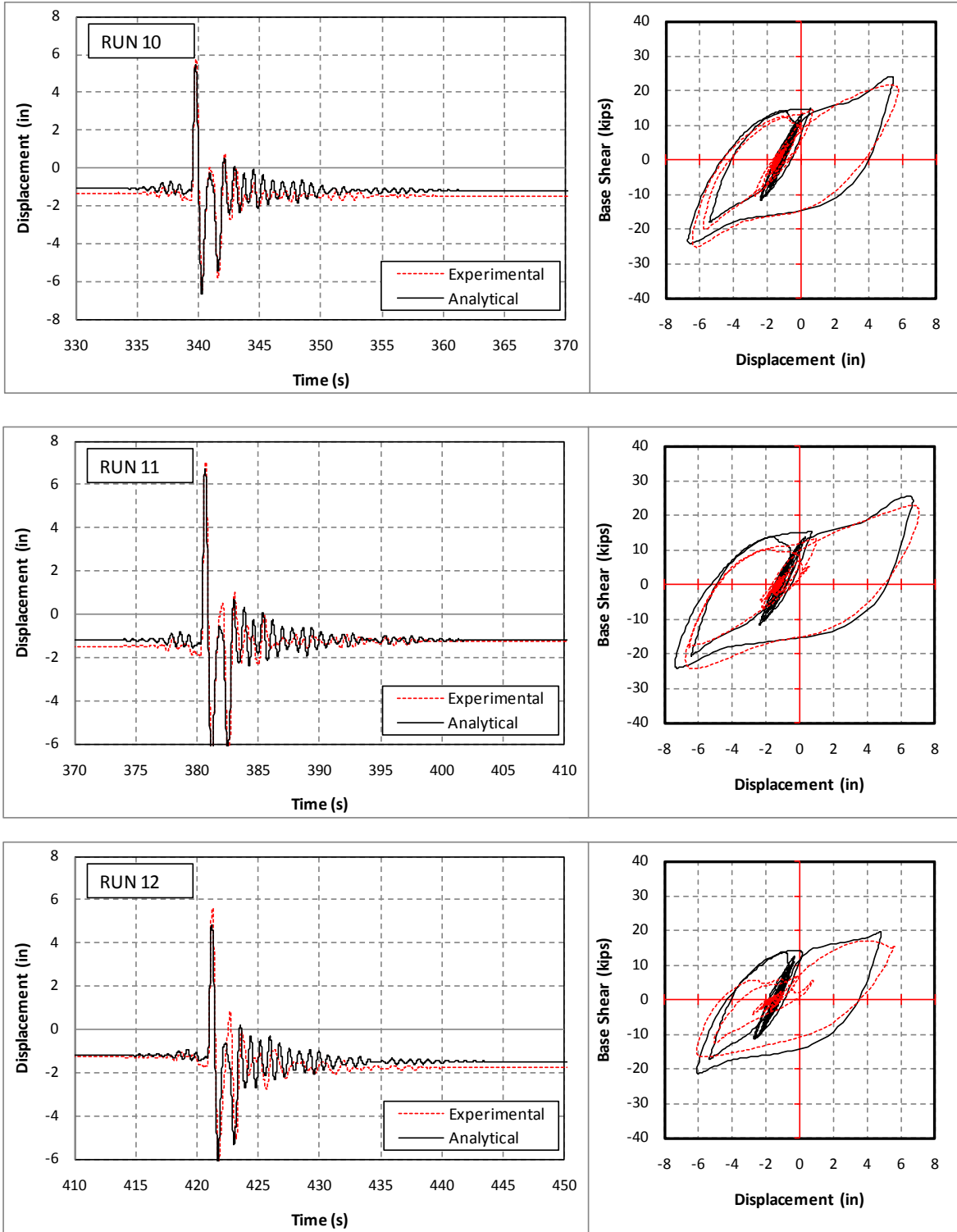


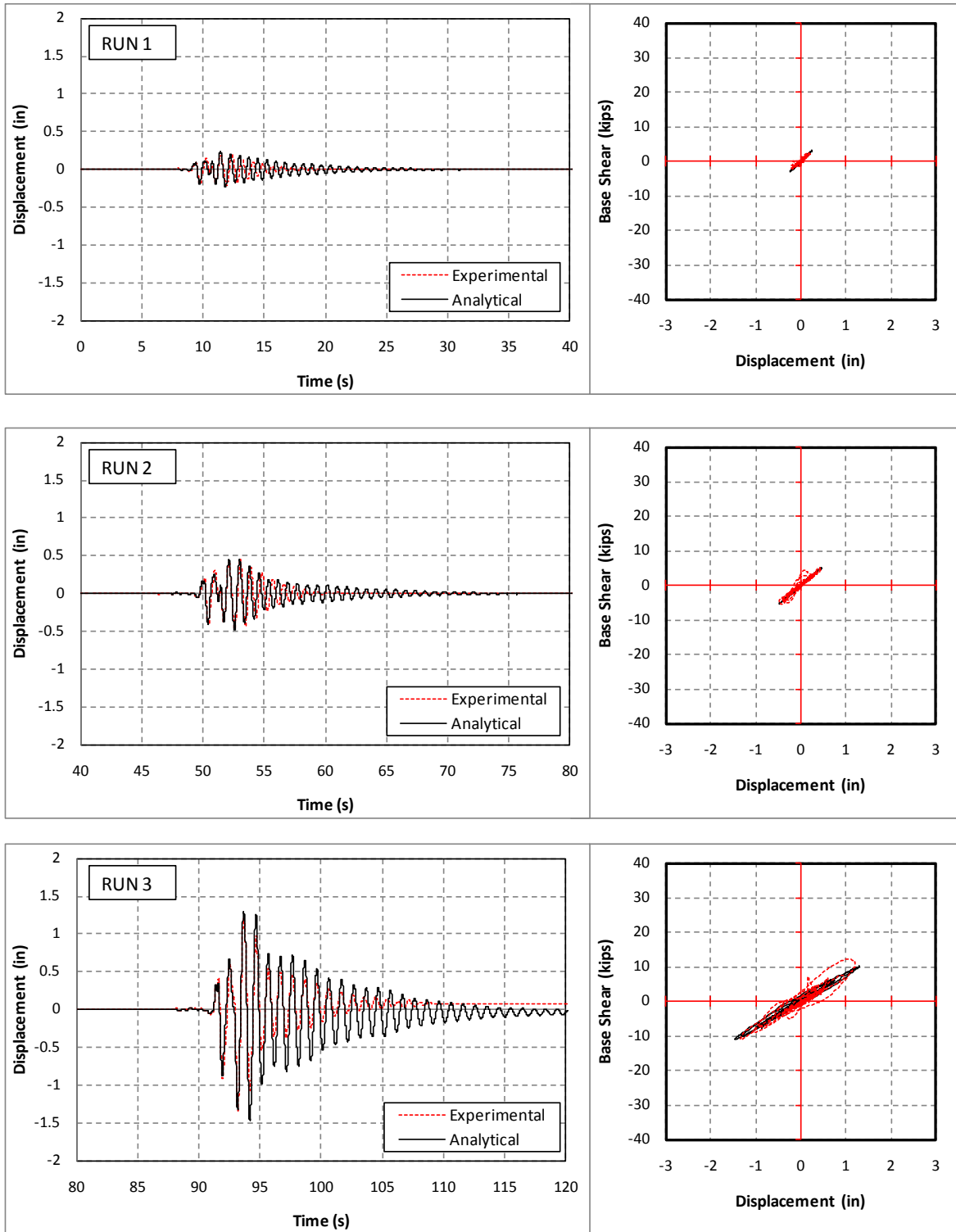
Figure 7-112 Measured and Calculated Displacement and Hysteresis, I1-Long.  
(Runs 4 to 6)



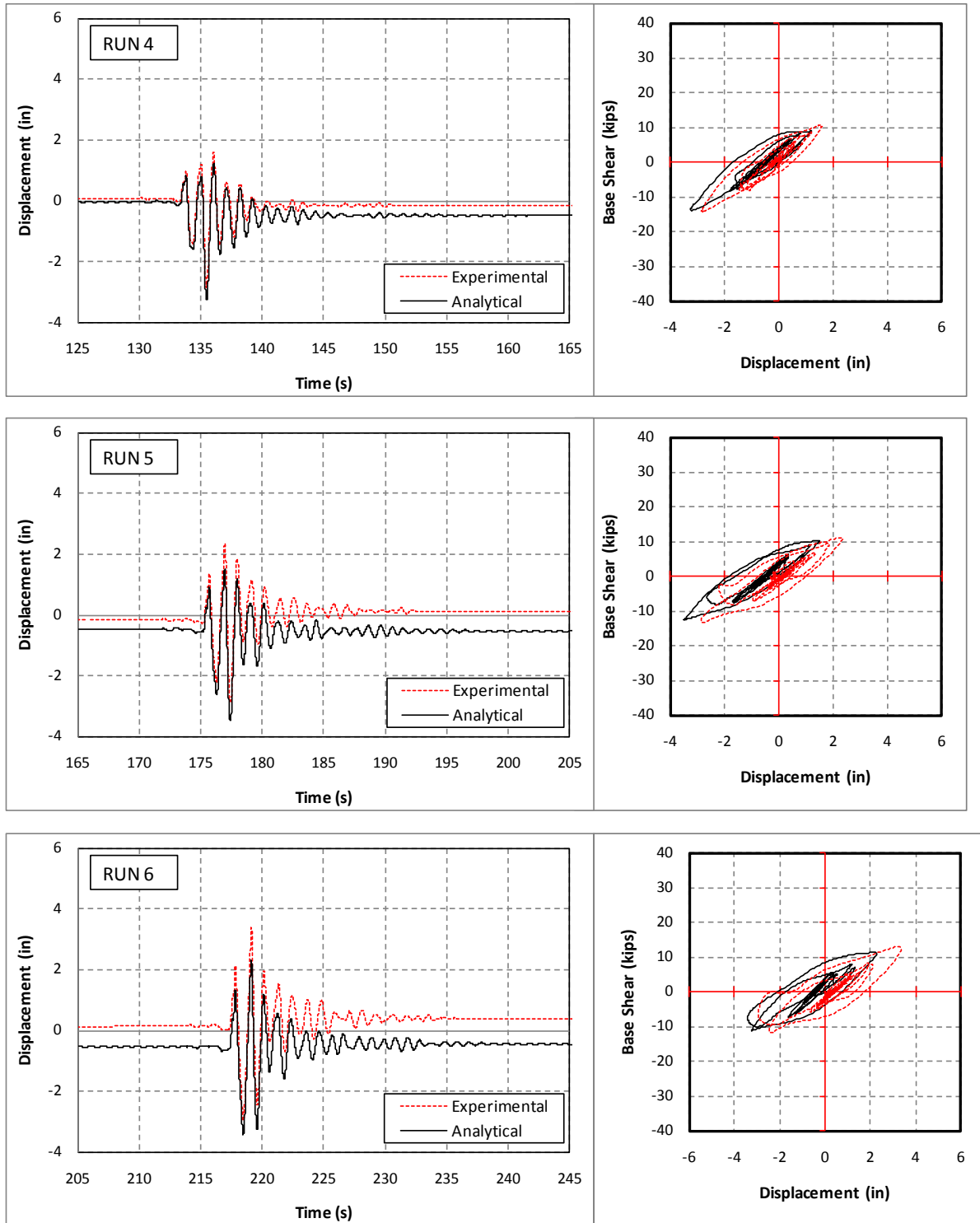
**Figure 7-113 Measured and Calculated Displacement and Hysteresis, I1-Long.  
(Runs 7 to 9)**



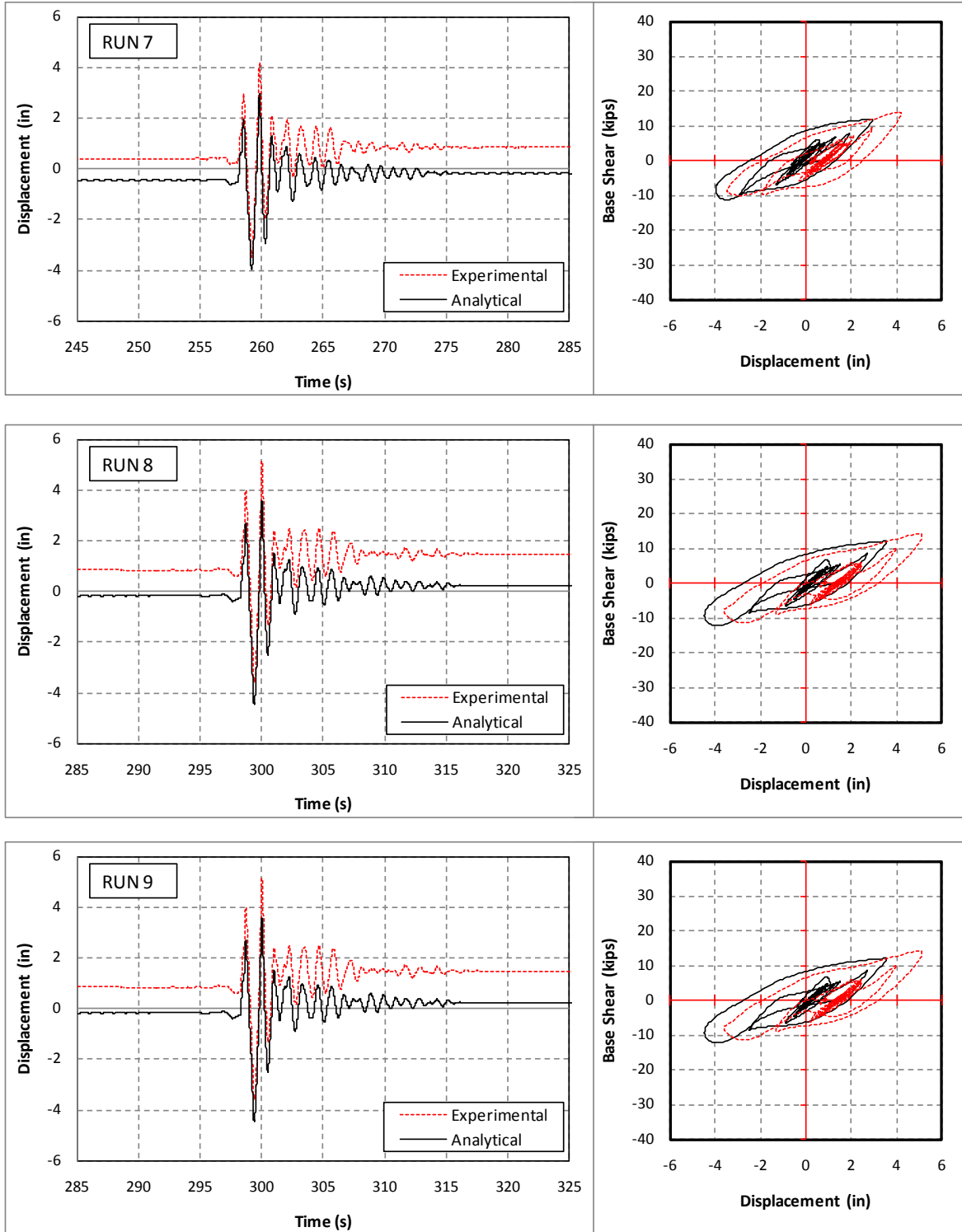
**Figure 7-114 Measured and Calculated Displacement and Hysteresis, I1-Long. (Runs 10 to 12)**



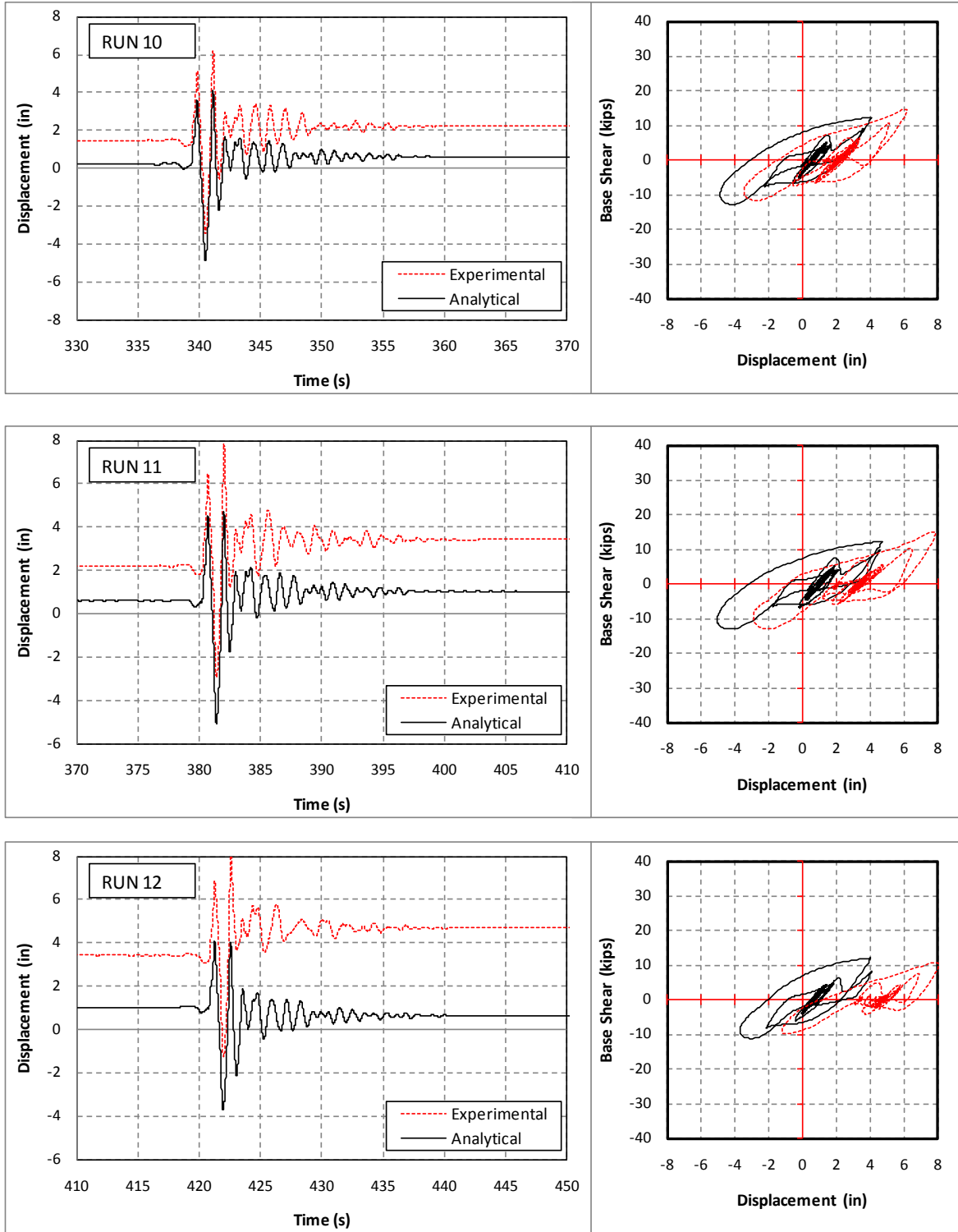
**Figure 7-115 Measured and Calculated Displacement and Hysteresis, I1-Trans. (Runs 1 to 3)**



**Figure 7-116 Measured and Calculated Displacement and Hysteresis, I1-Trans.  
(Runs 4 to 6)**



**Figure 7-117 Measured and Calculated Displacement and Hysteresis, I1-Trans. (Runs 7 to 9)**



**Figure 7-118 Measured and Calculated Displacement and Hysteresis, I1-Trans.  
(Runs 10 to 12)**



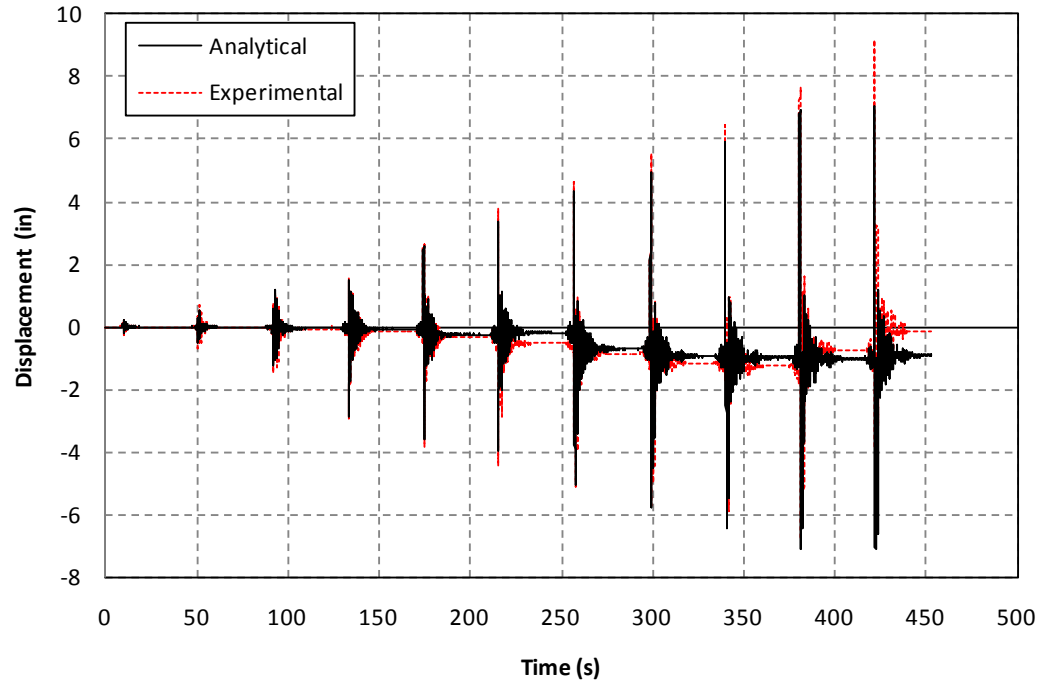


Figure 7-119 Measured and Calculated Displacement History, I2-Long.

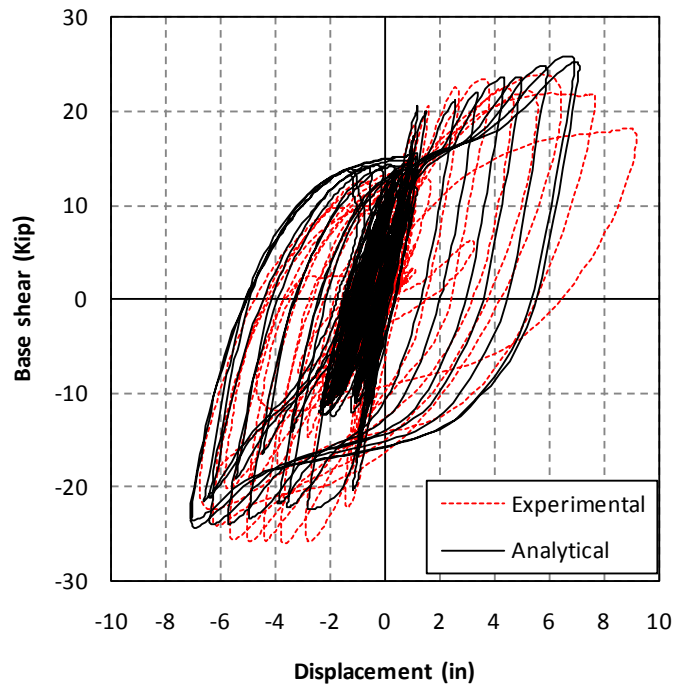


Figure 7-120 Measured and Calculated Cumulative F-D Hysteresis, I2-Long.

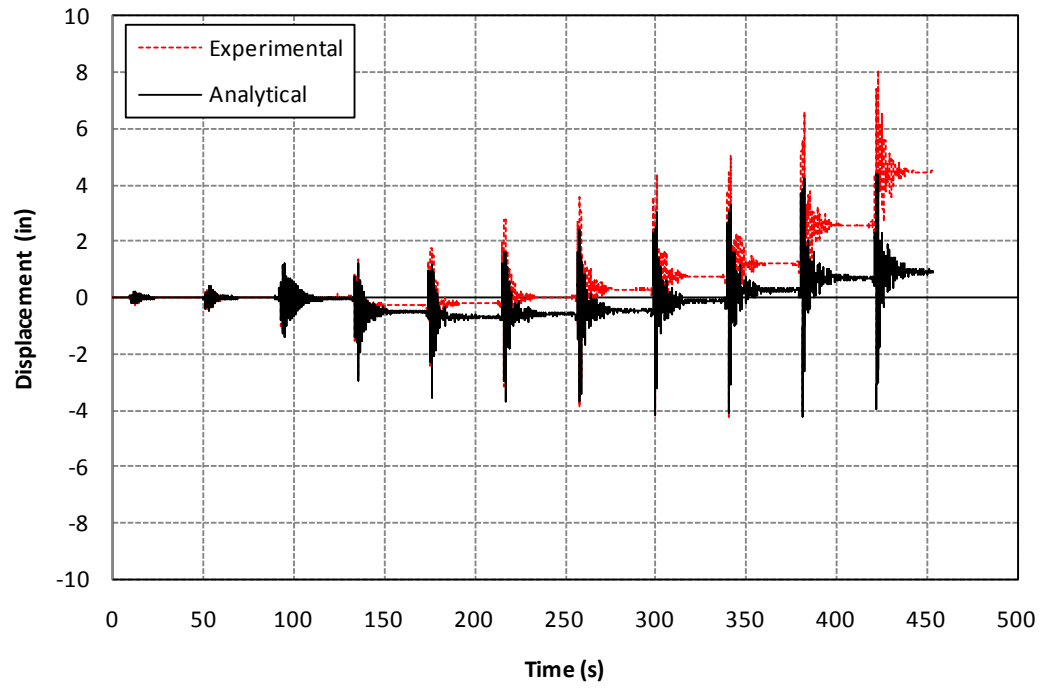


Figure 7-121 Measured and Calculated Displacement History, I2-Trans.

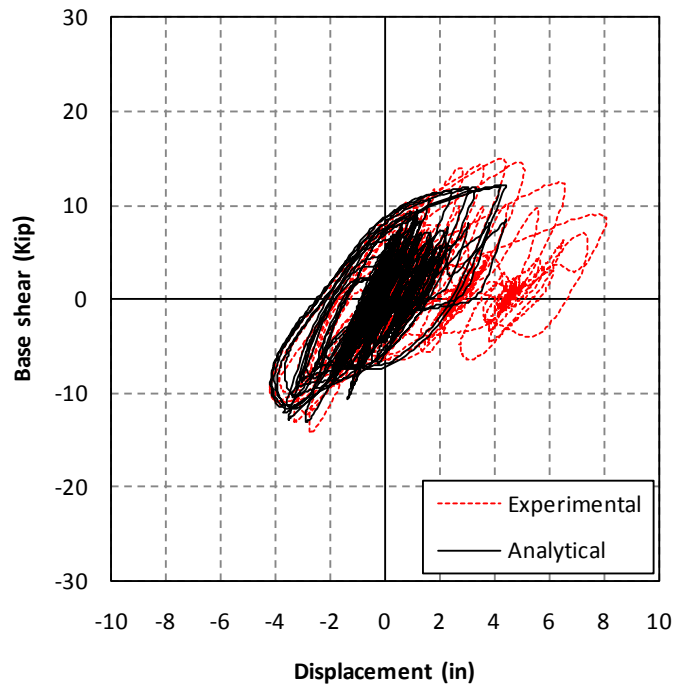


Figure 7-122 Measured and Calculated Cumulative F-D Hysteresis, I2-Trans.

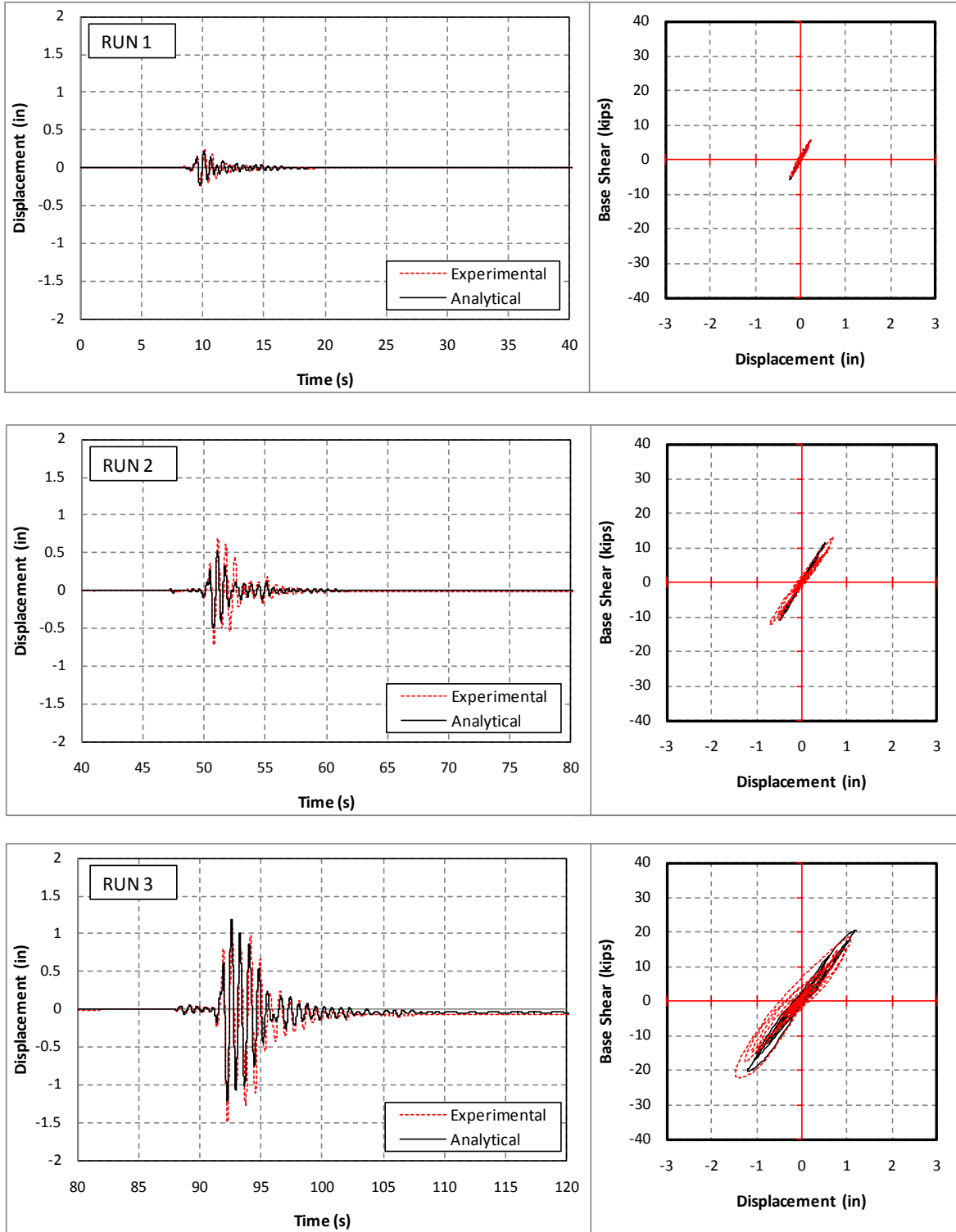
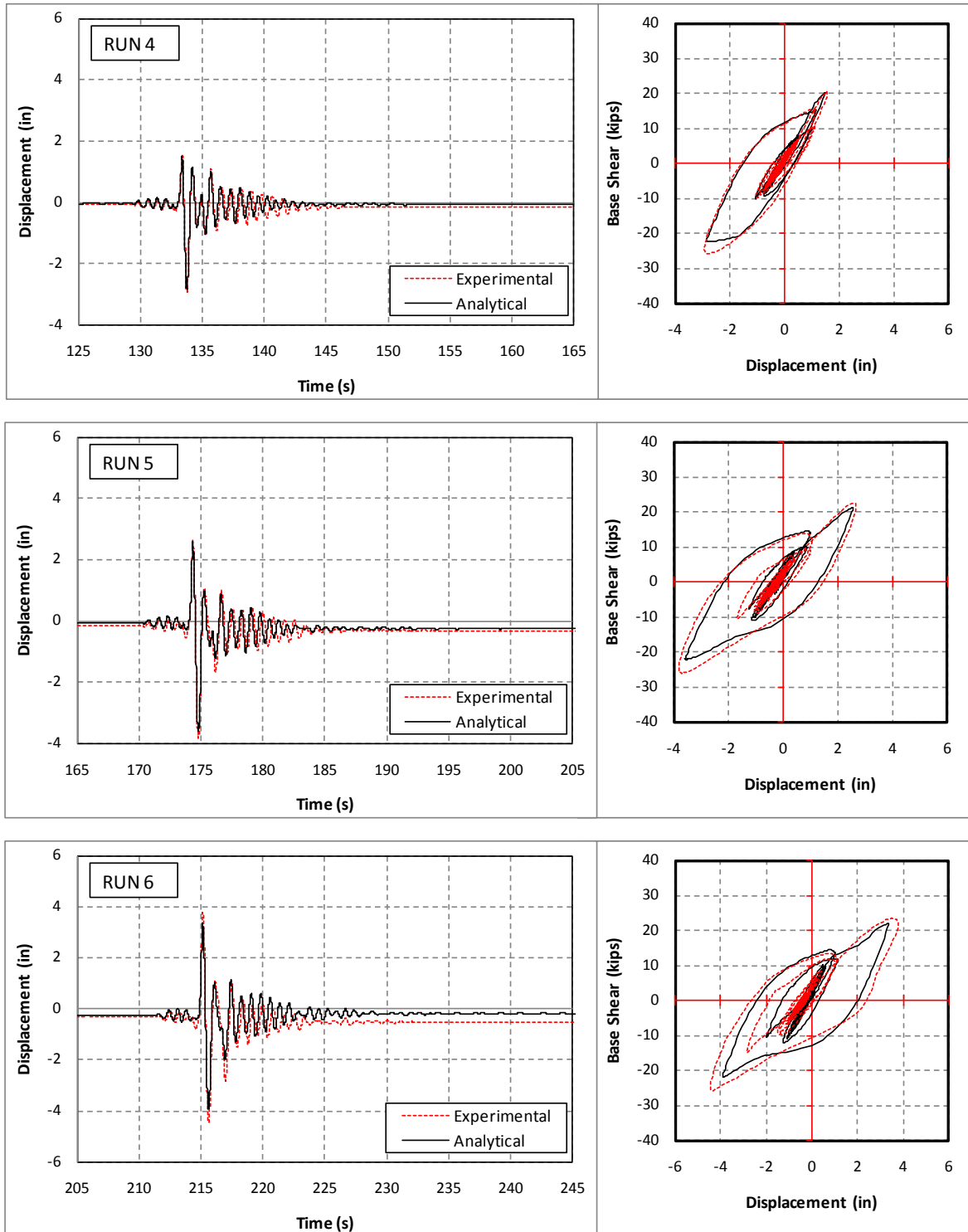
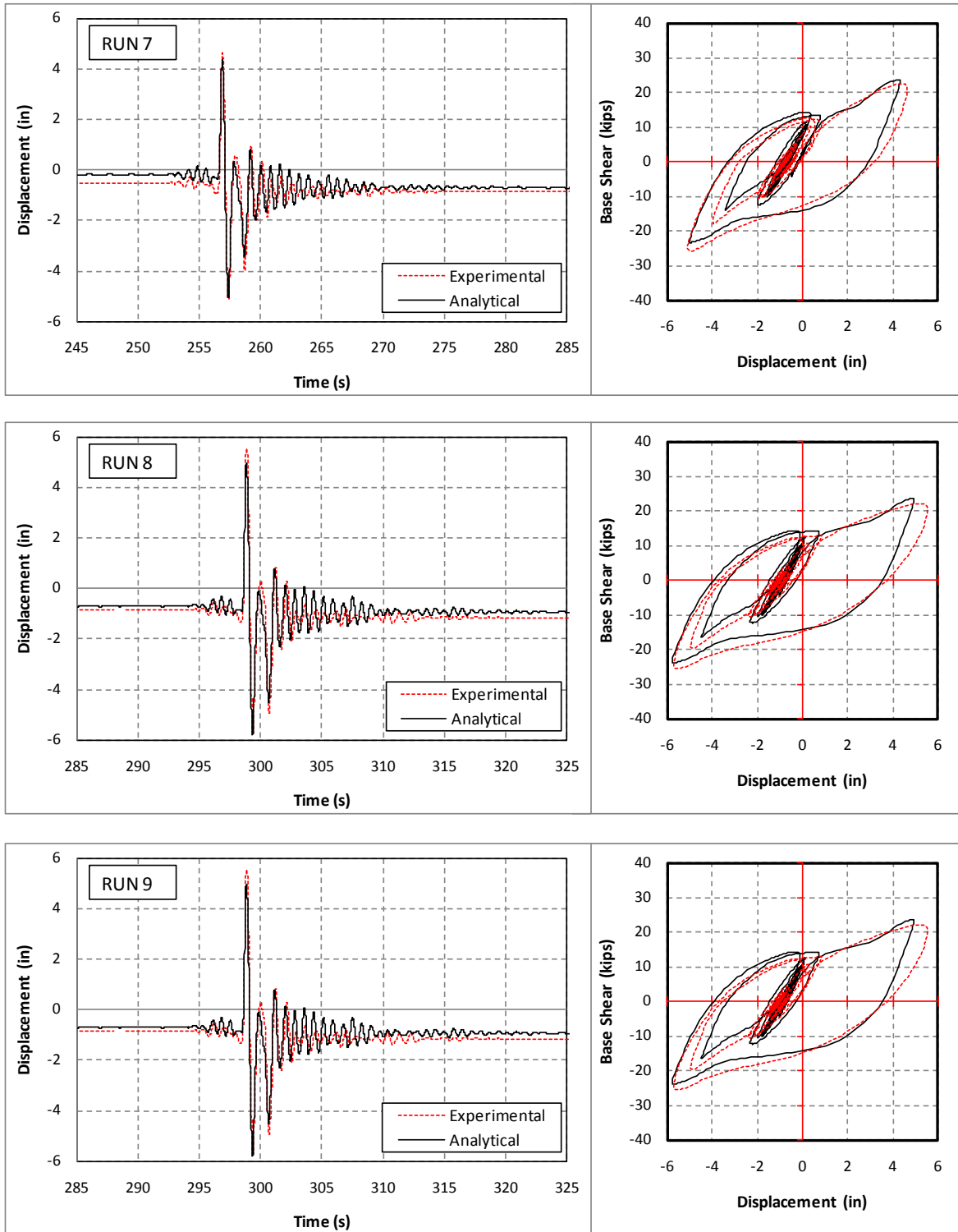


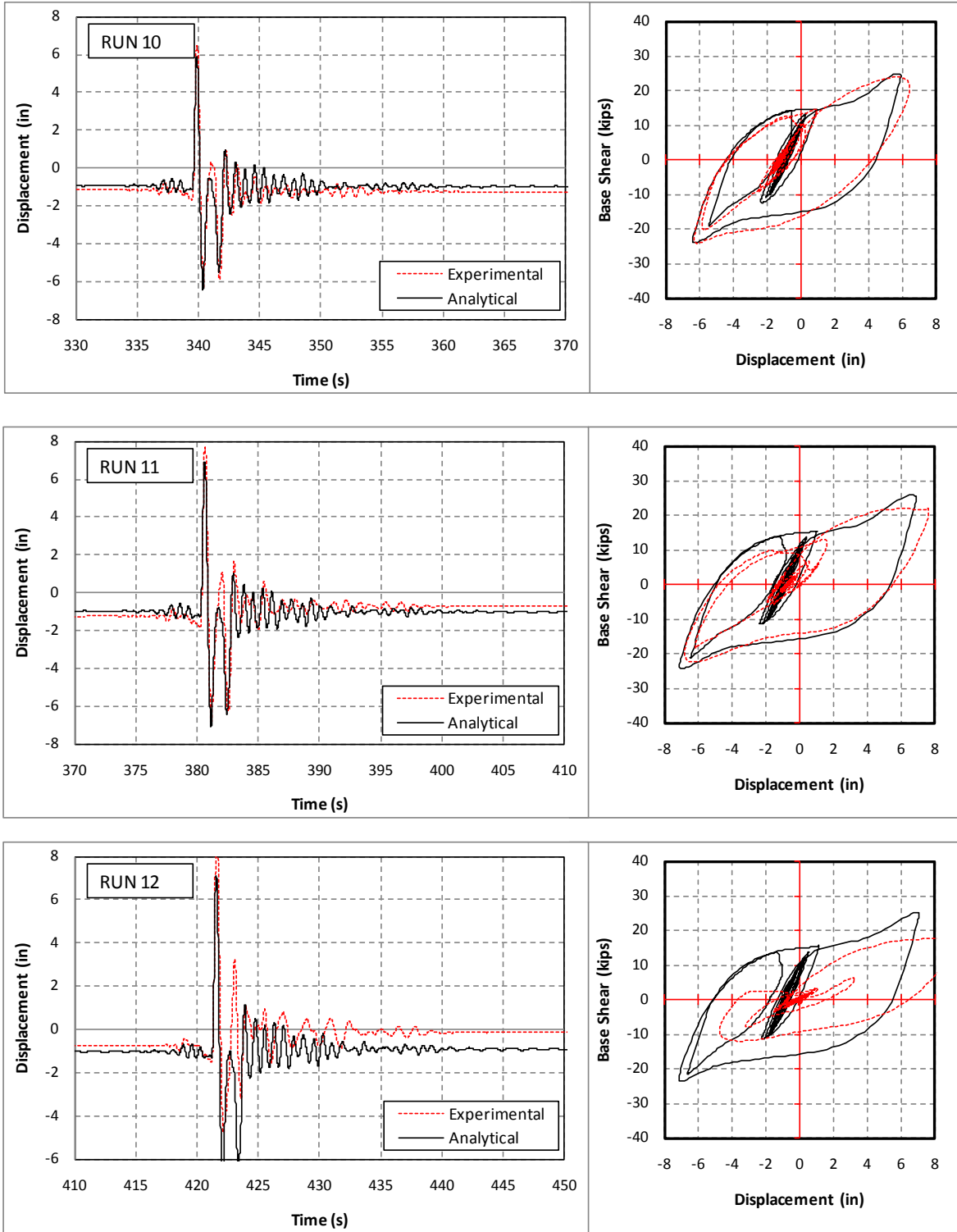
Figure 7-123 Measured and Calculated Displacement and Hysteresis, I2-Long. (Runs 1 to 3)



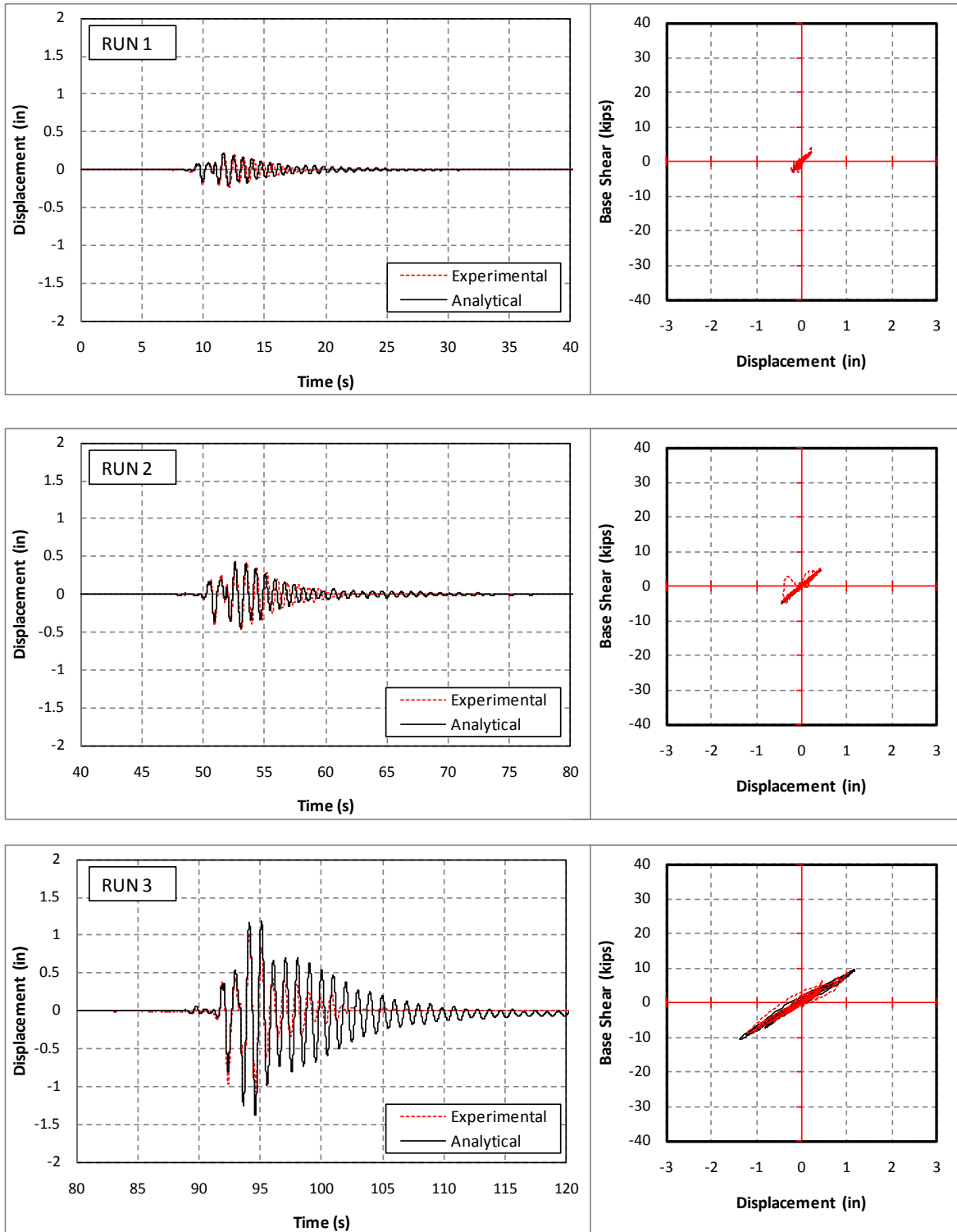
**Figure 7-124 Measured and Calculated Displacement and Hysteresis, I2-Long.  
(Runs 4 to 6)**



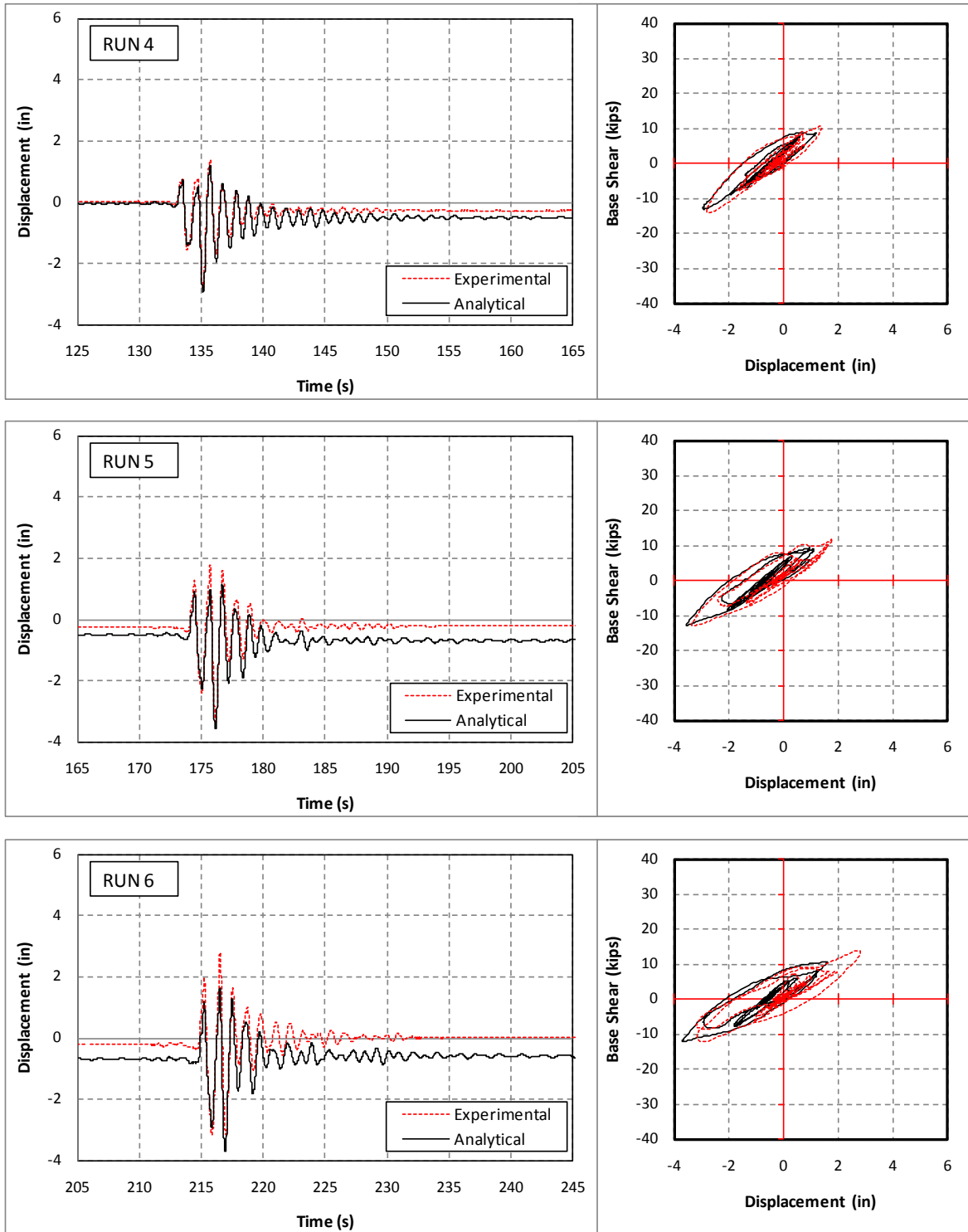
**Figure 7-125 Measured and Calculated Displacement and Hysteresis, I2-Long.  
(Runs 7 to 9)**



**Figure 7-126 Measured and Calculated Displacement and Hysteresis, I2-Long. (Runs 10 to 12)**

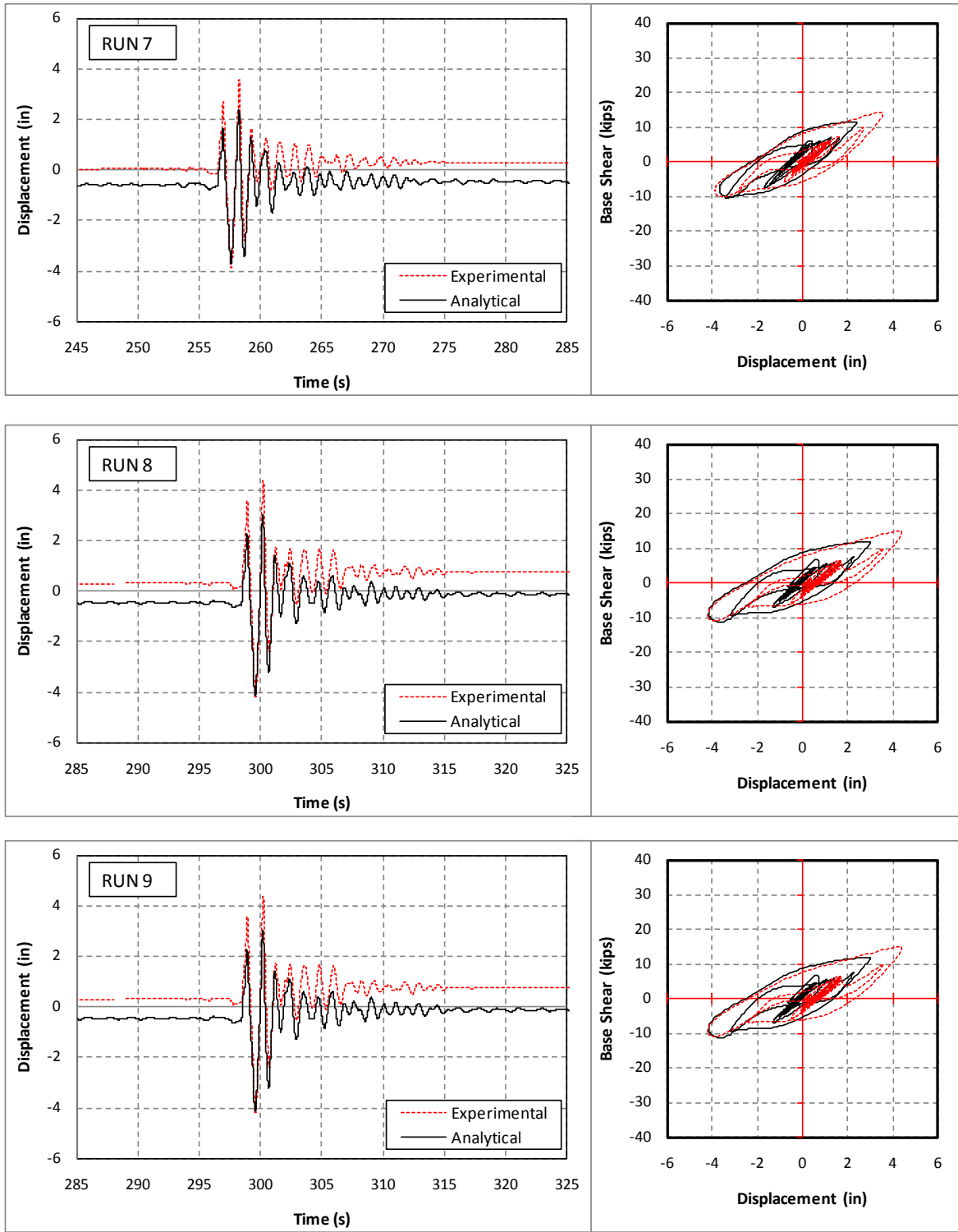


**Figure 7-127 Measured and Calculated Displacement and Hysteresis, I2-Trans.  
(Runs 1 to 3)**



**Figure 7-128 Measured and Calculated Displacement and Hysteresis, I2-Trans.  
(Runs 4 to 6)**





**Figure 7-129 Measured and Calculated Displacement and Hysteresis, I2-Trans. (Runs 7 to 9)**

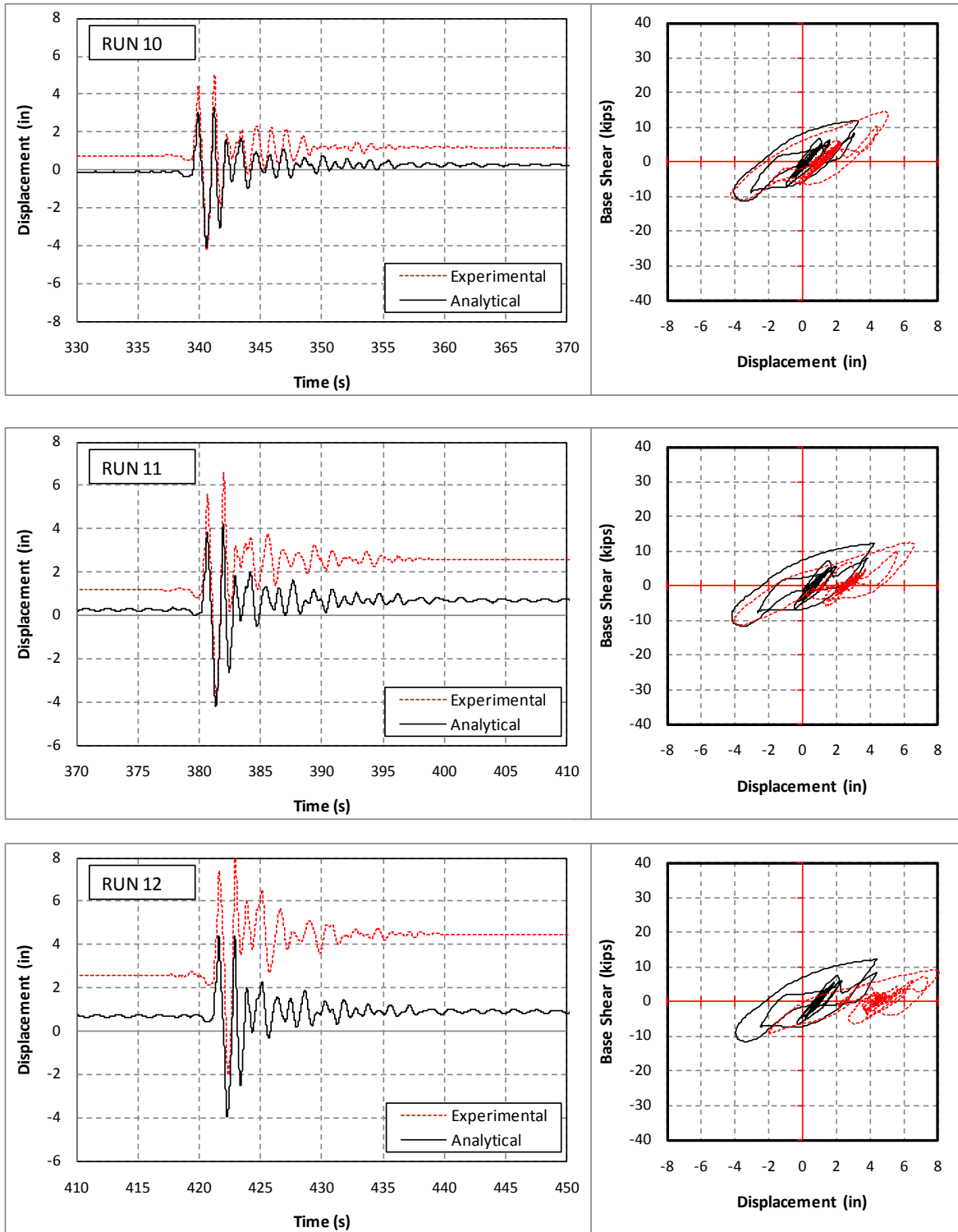
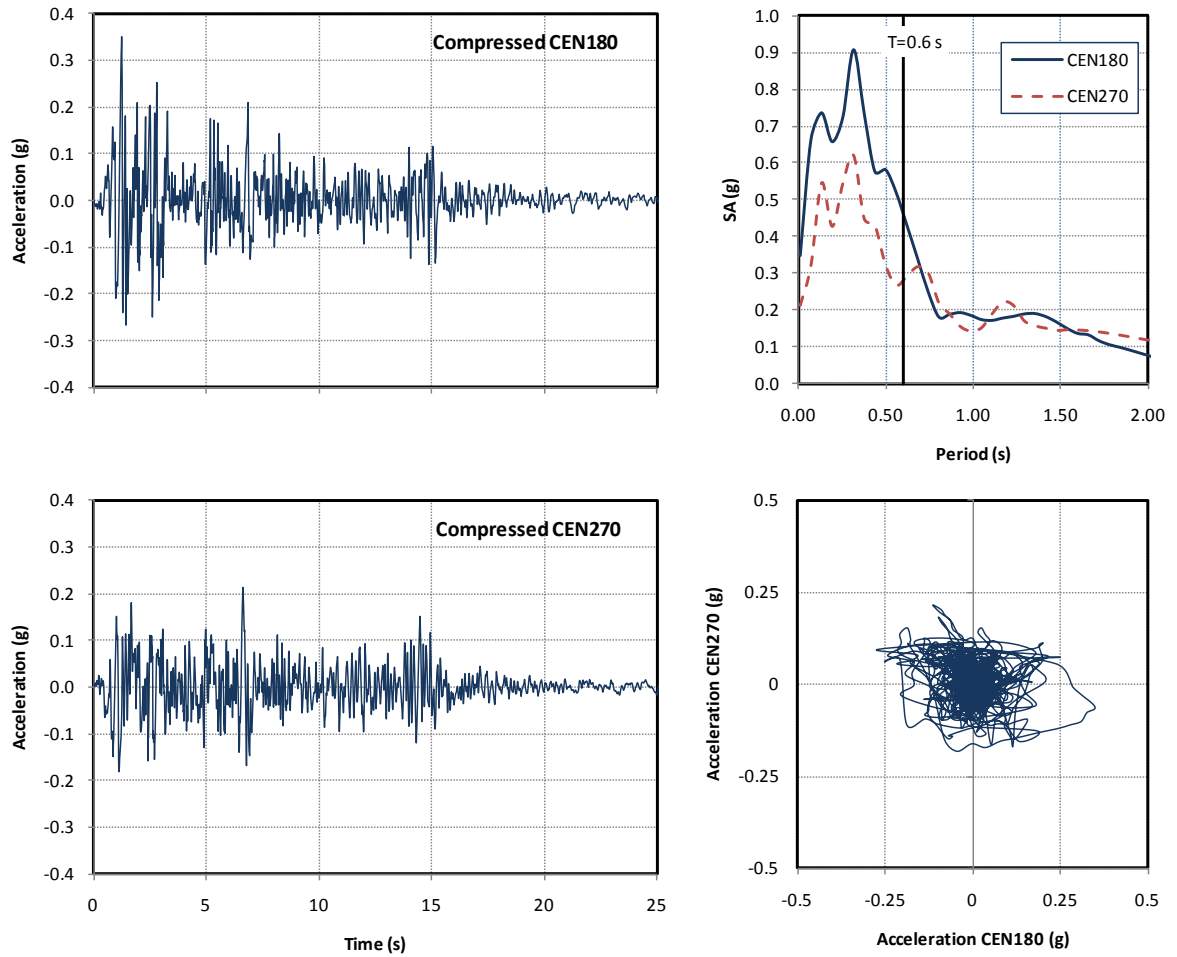
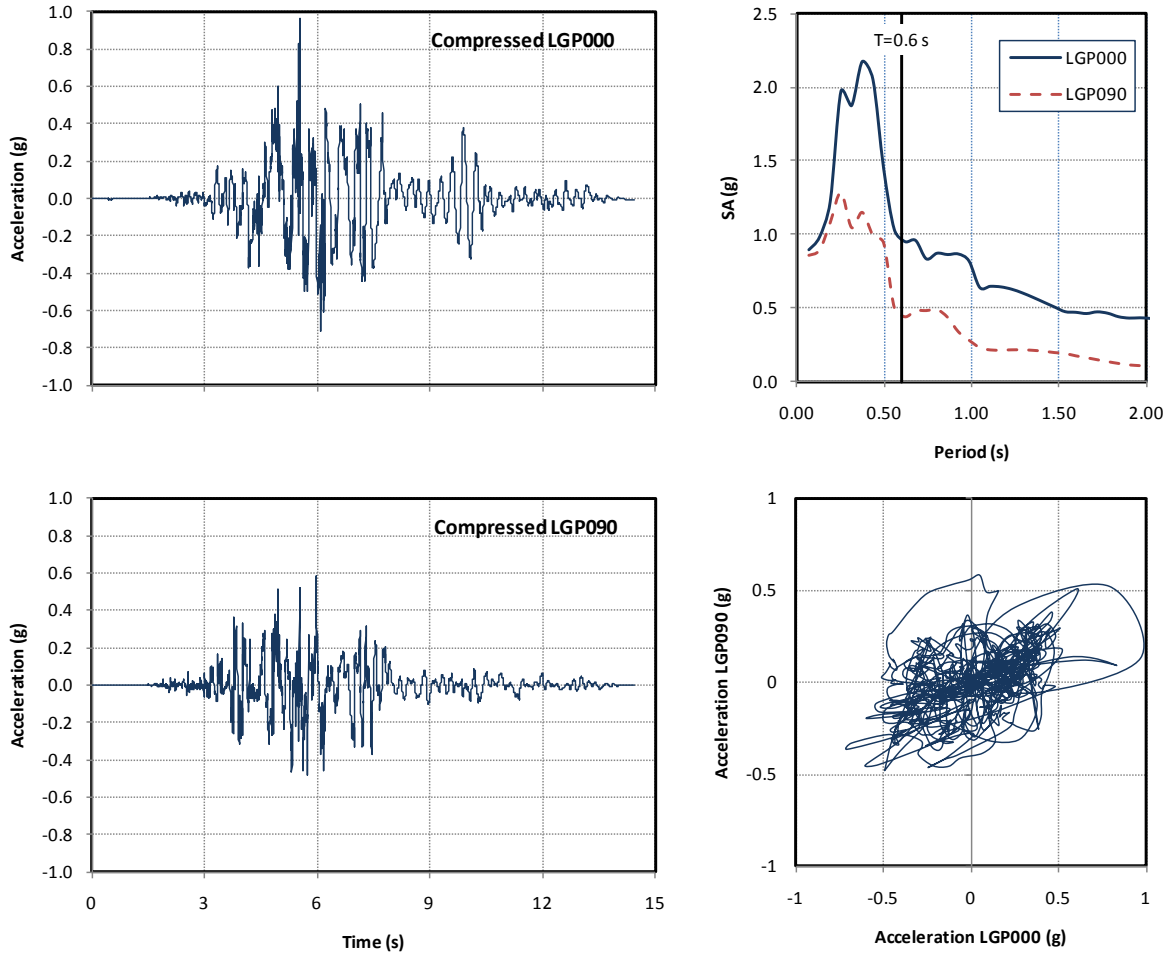


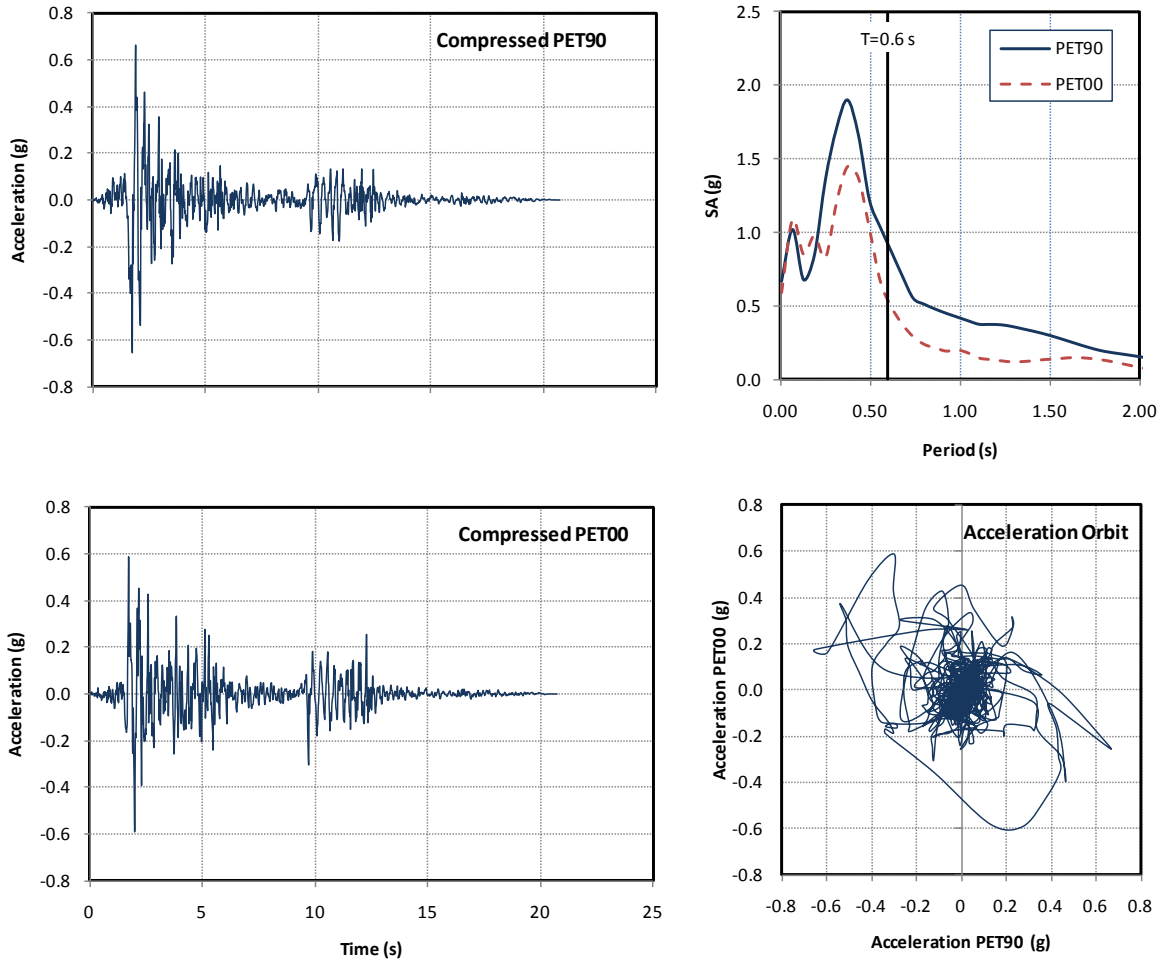
Figure 7-130 Measured and Calculated Displacement and Hysteresis, I2-Trans. (Runs 10 to 12)



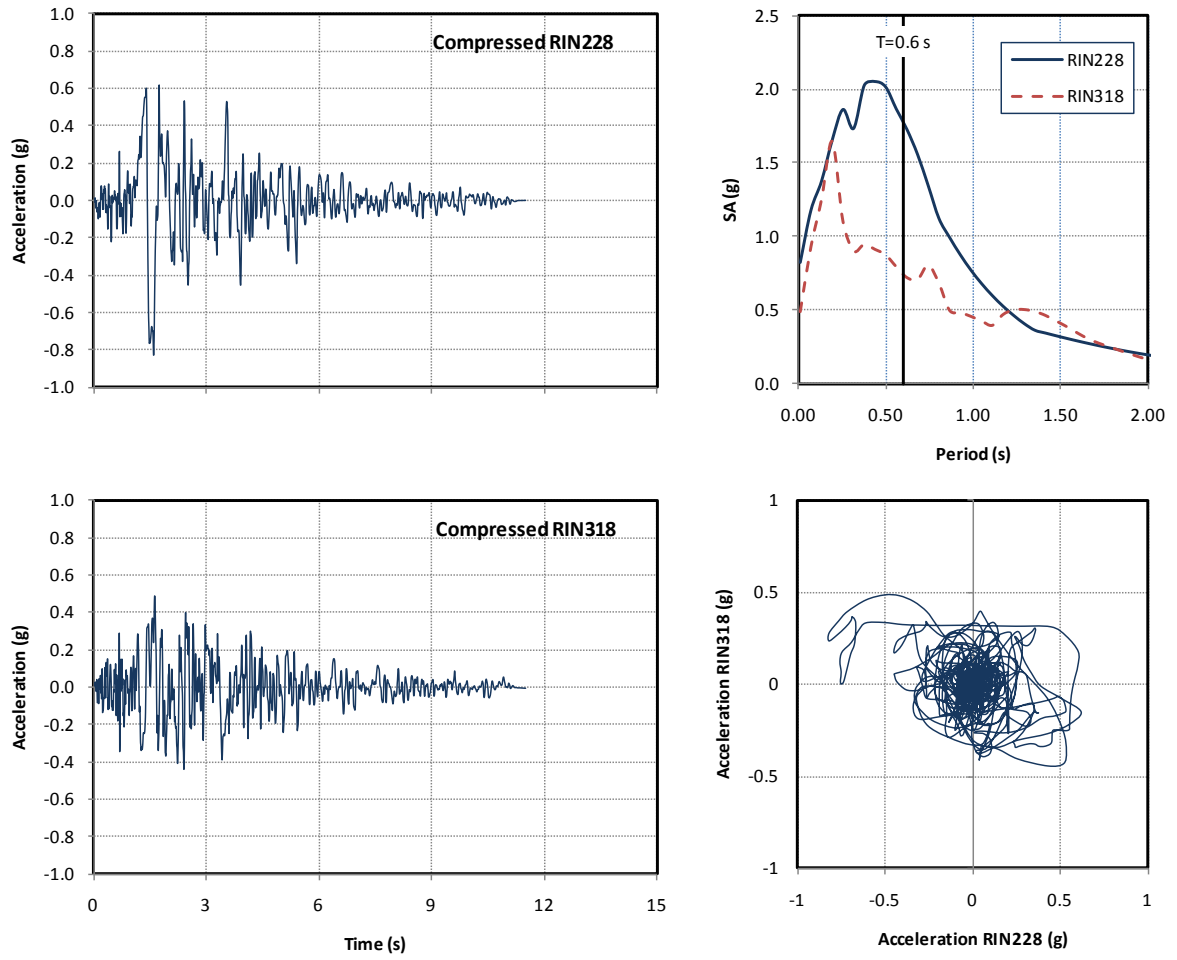
**Figure 8-1 Acceleration, Spectrum and Orbit of the El Centro Record (Circular Column)**



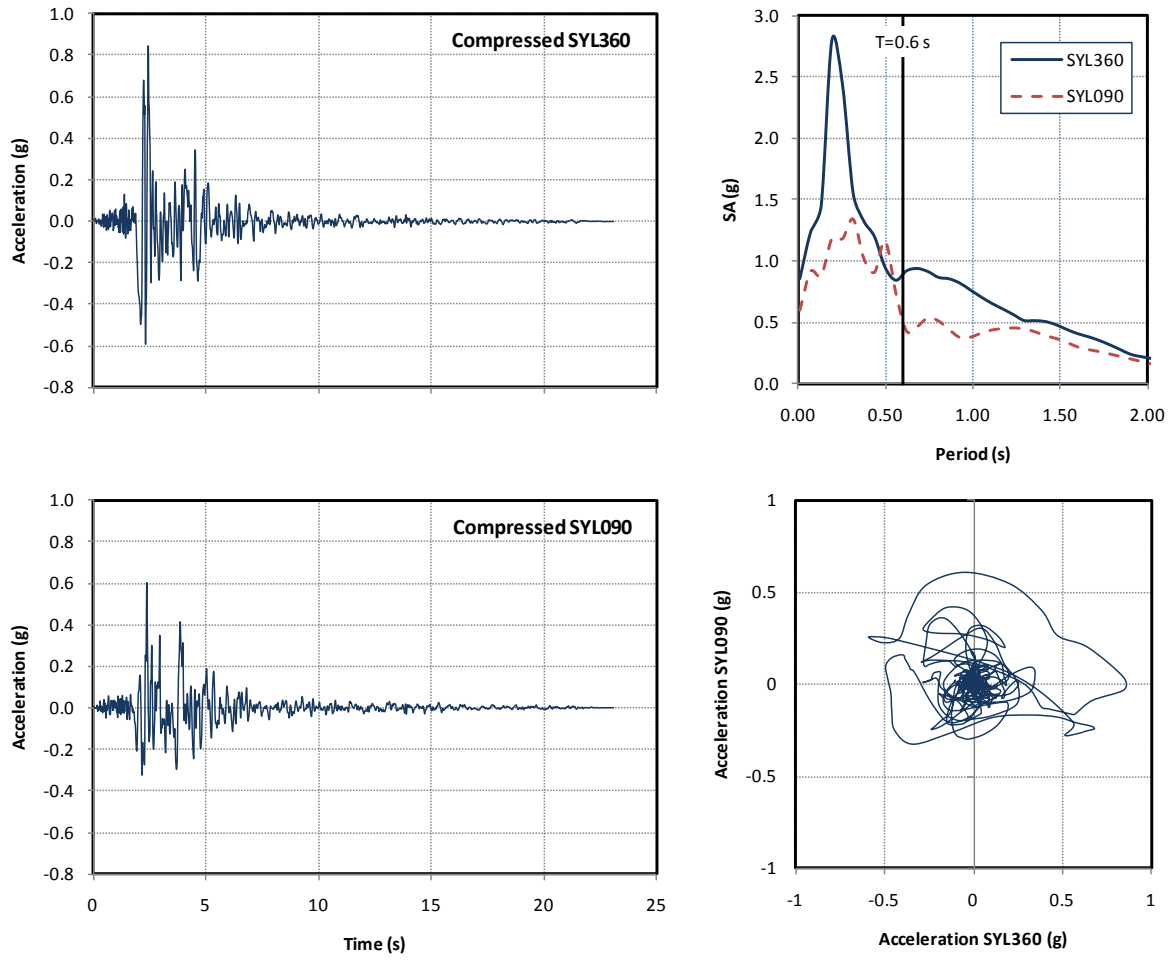
**Figure 8-2 Acceleration, Spectrum and Orbit of Los Gatos record (Circular Column)**



**Figure 8-3 Acceleration, Spectrum and Orbit of Petrolia Record (Circular Column)**



**Figure 8-4 Acceleration, Spectrum and Orbit of Rinaldi (Circular Column)**



**Figure 8-5 Acceleration, Spectrum and Orbit of Sylmar Record (Circular Column)**

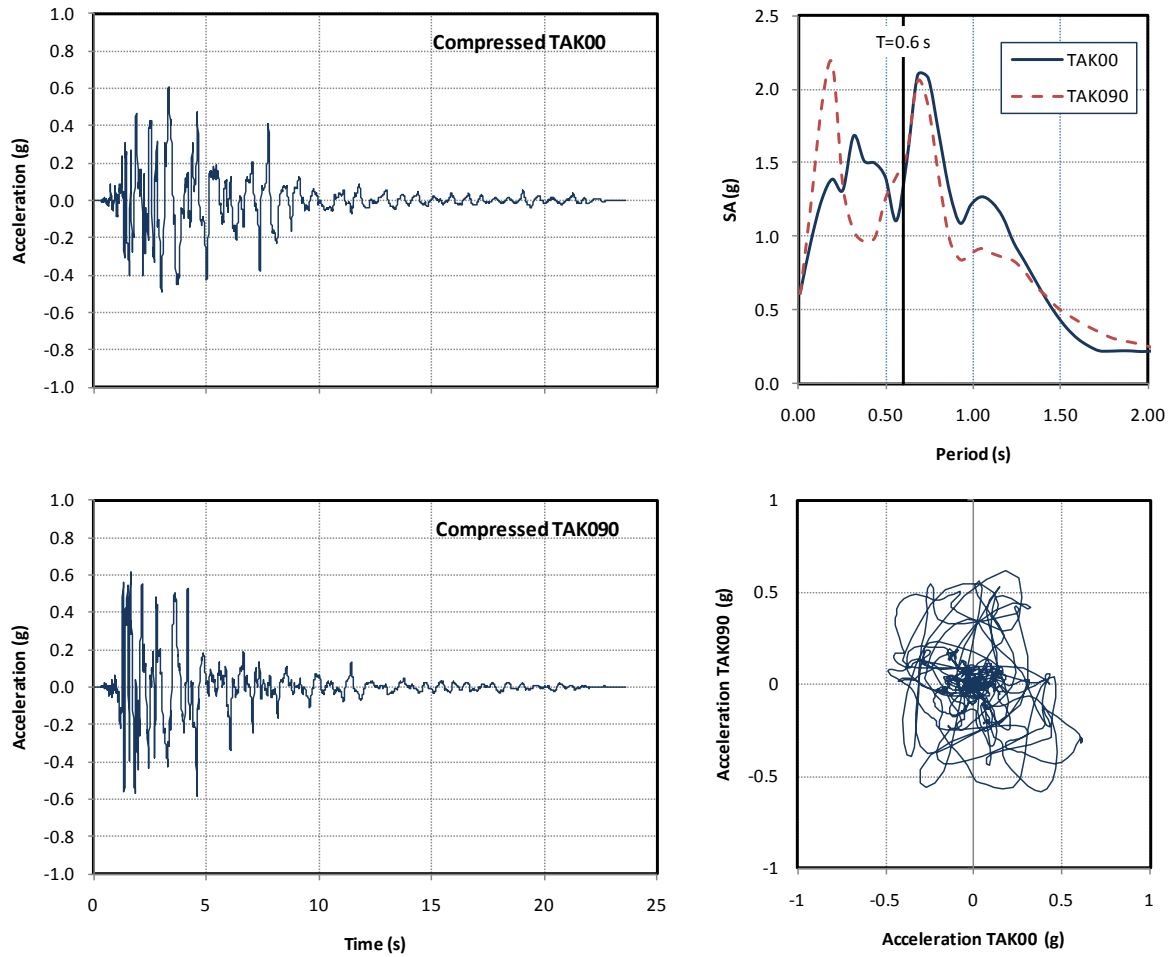
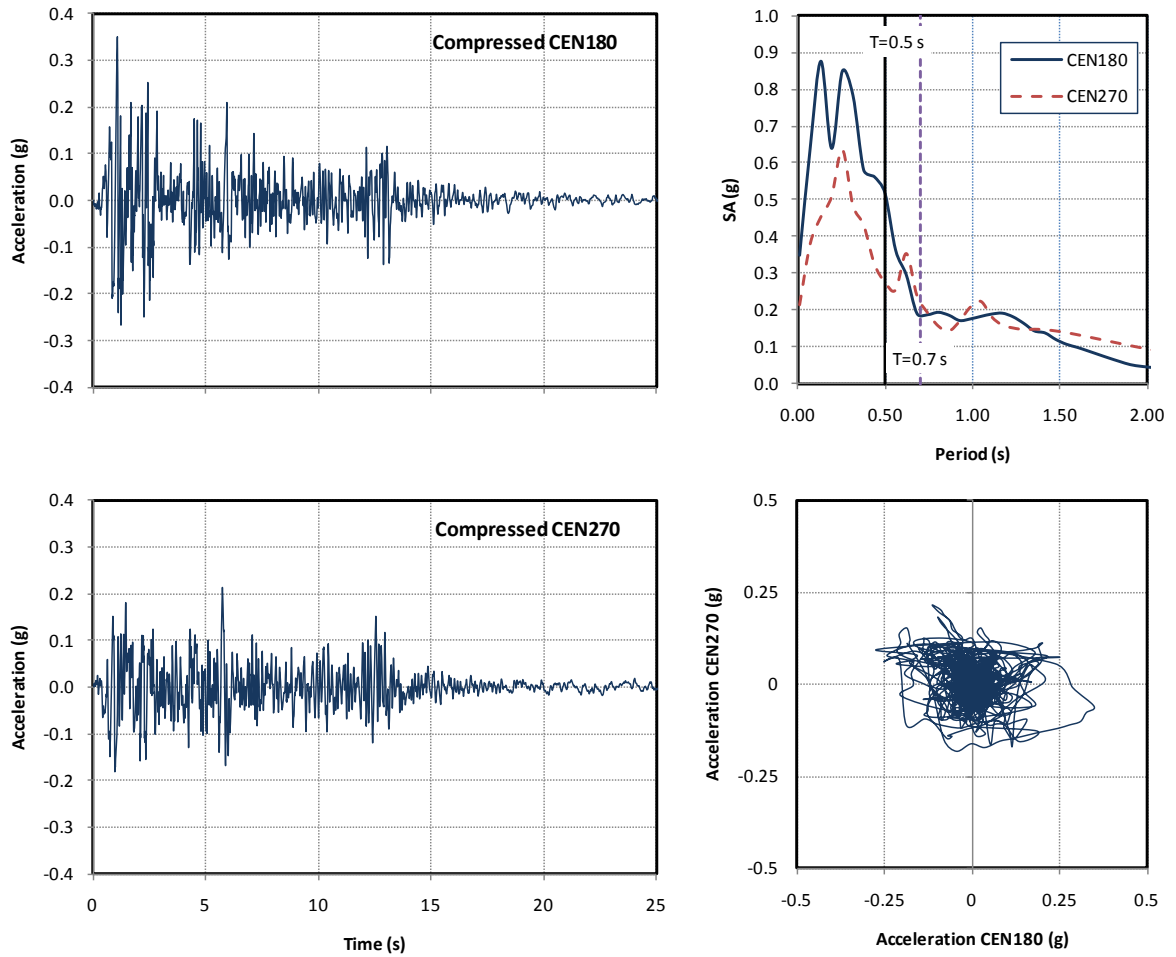
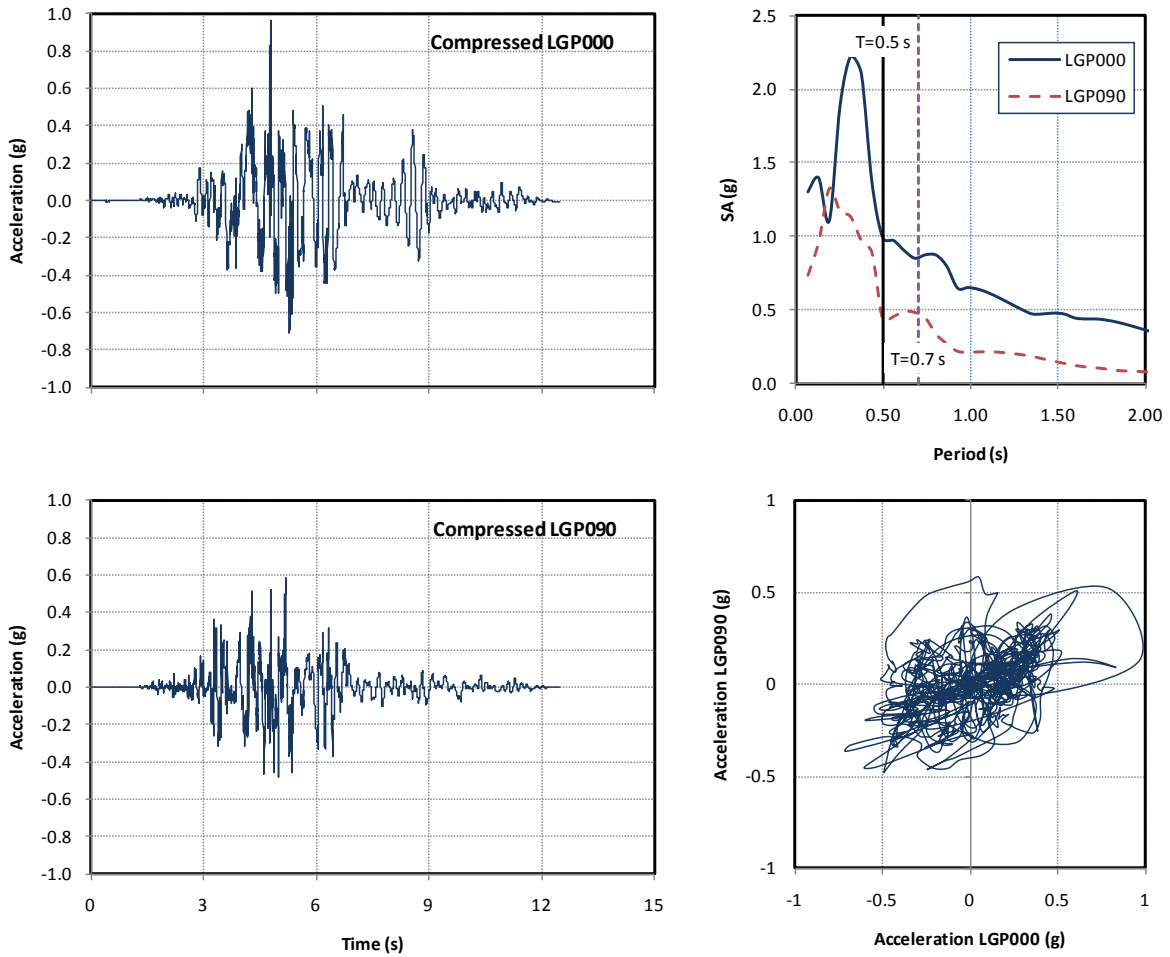


Figure 8-6 Acceleration, Spectrum and Orbit of Takatori Record (Circular Column)

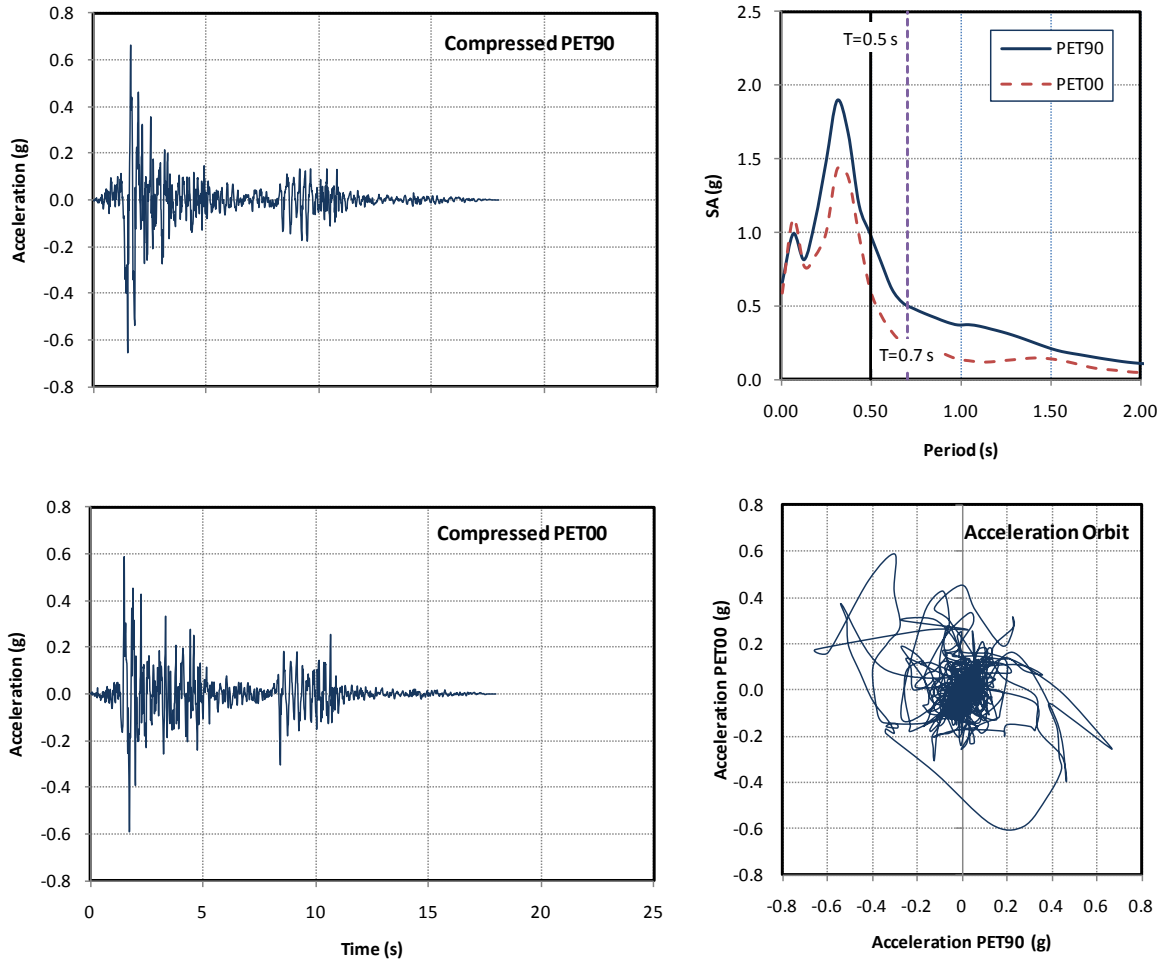




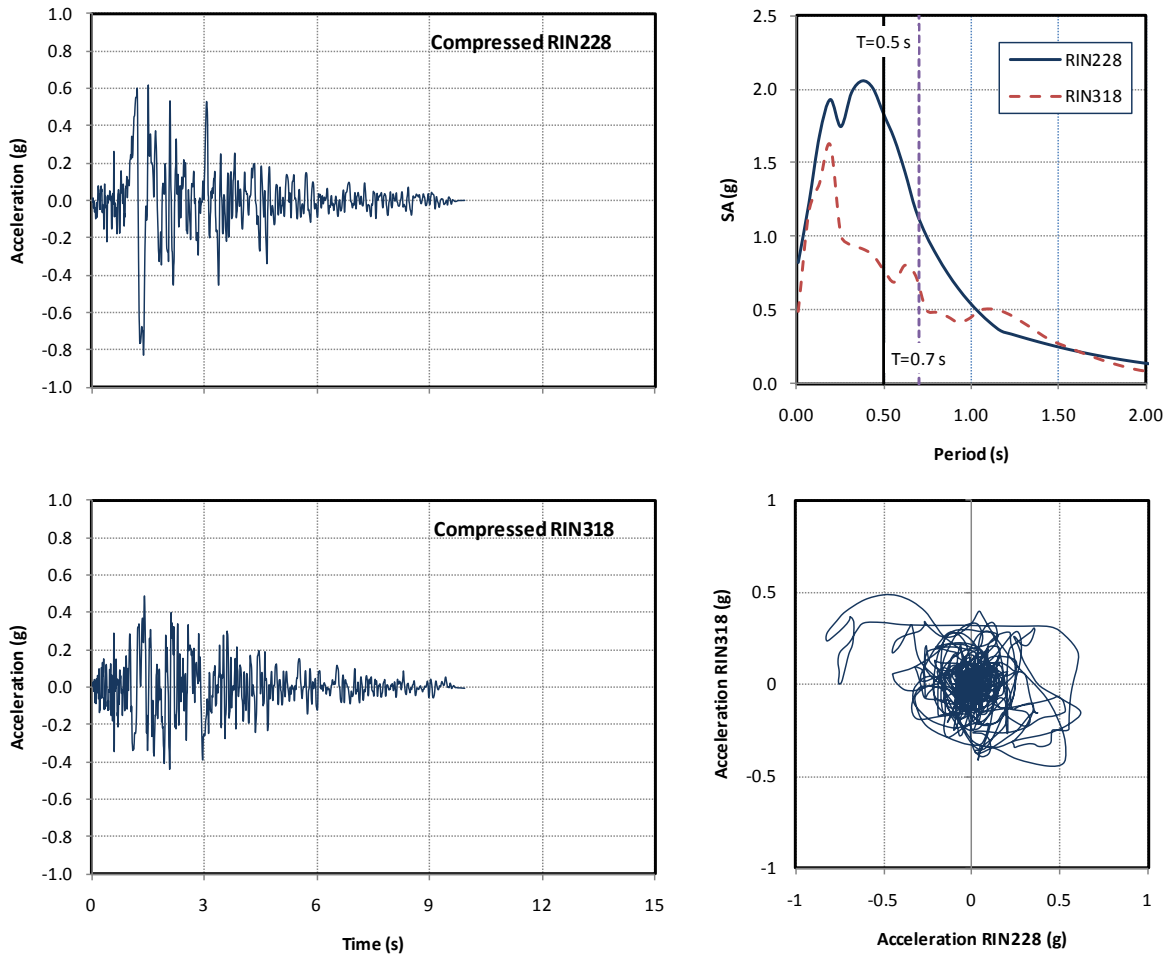
**Figure 8-7 Acceleration, Spectrum and Orbit of the El Centro Record (Interlockig Column)**



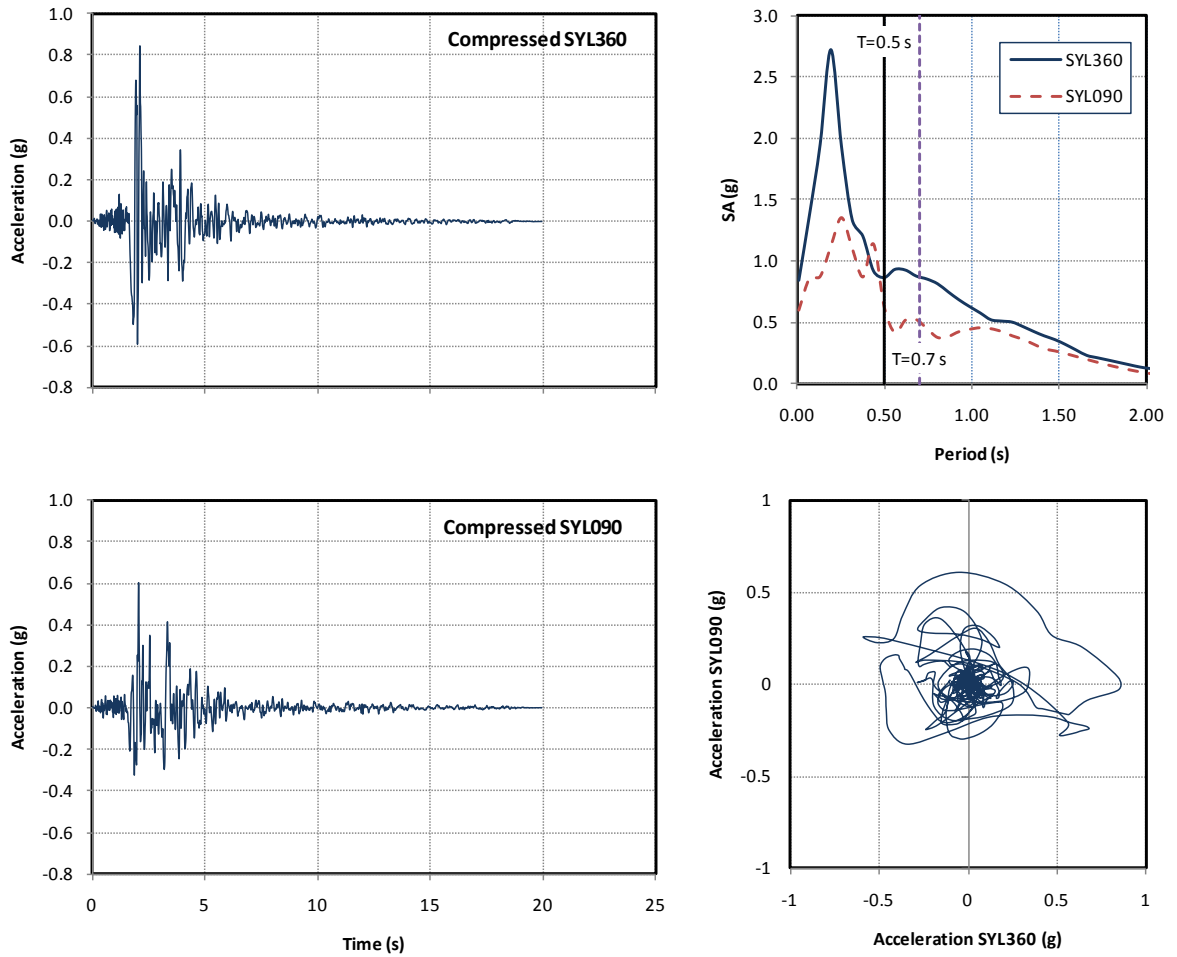
**Figure 8-8 Acceleration, Spectrum and Orbit of Los Gatos record (Interlocking Column)**



**Figure 8-9 Acceleration, Spectrum and Orbit of Petrolia Record (Interlockig Column)**



**Figure 8-10 Acceleration, Spectrum and Orbit of Rinaldi (Interlockig Column)**



**Figure 8-11 Acceleration, Spectrum and Orbit of Sylmar Record (Interlockig Column)**

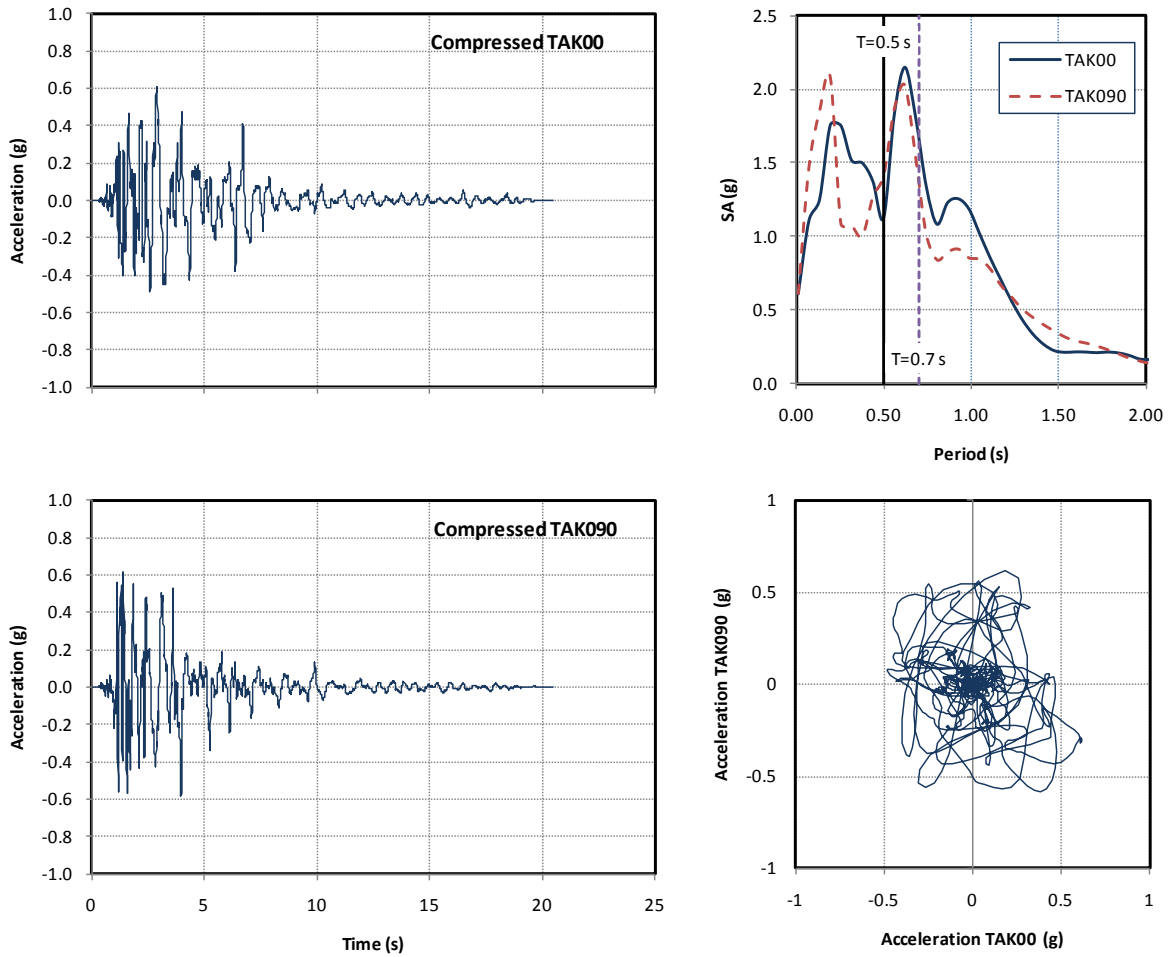
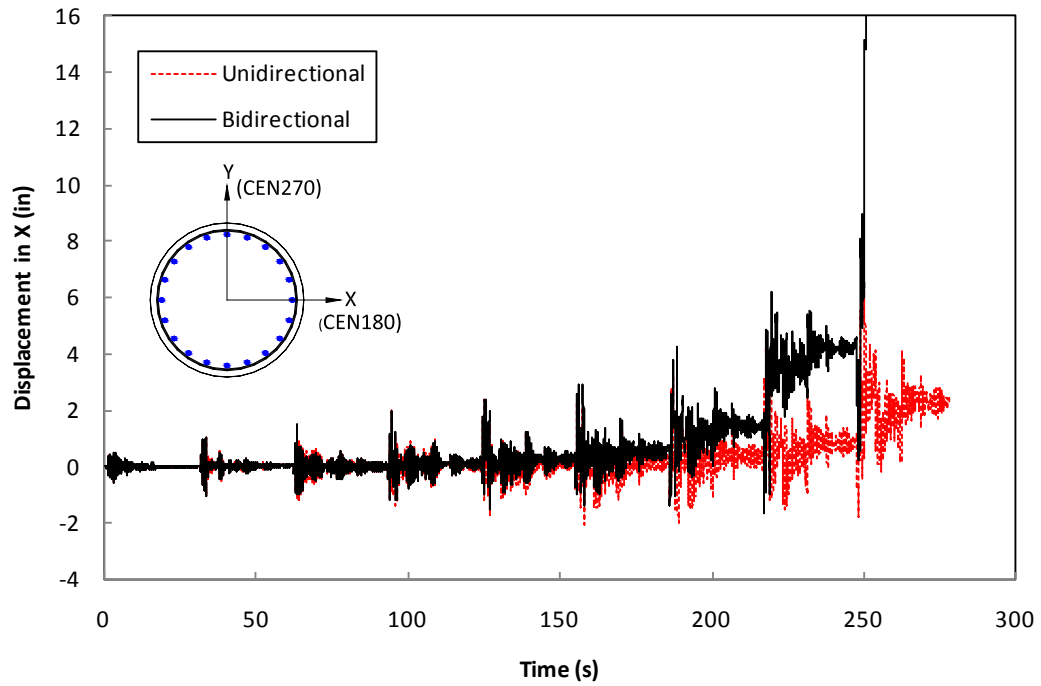
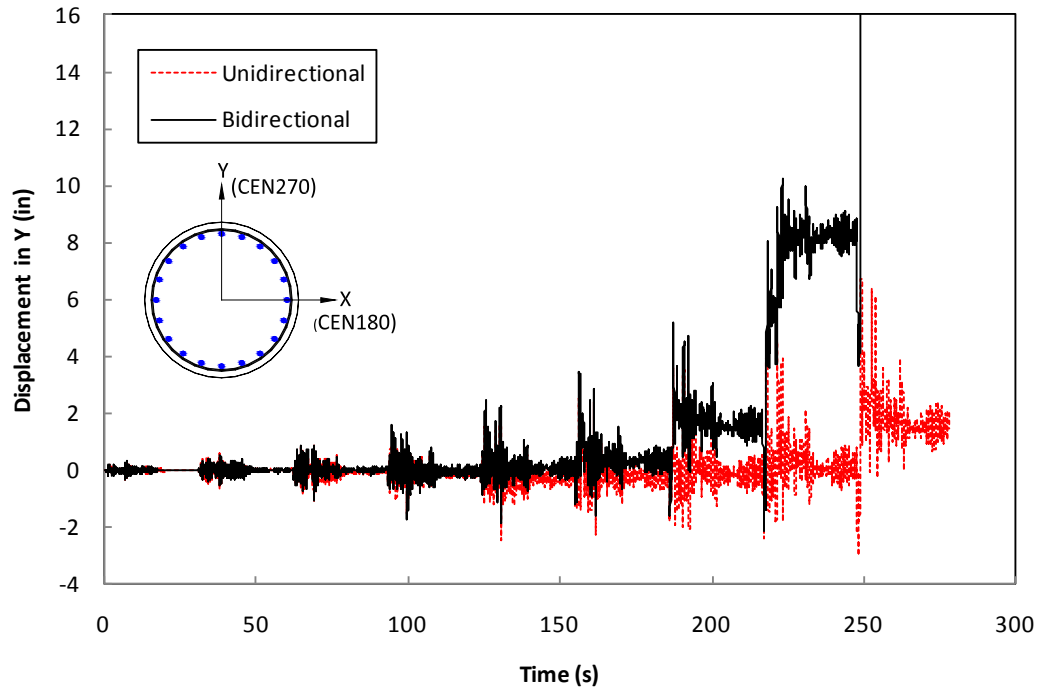


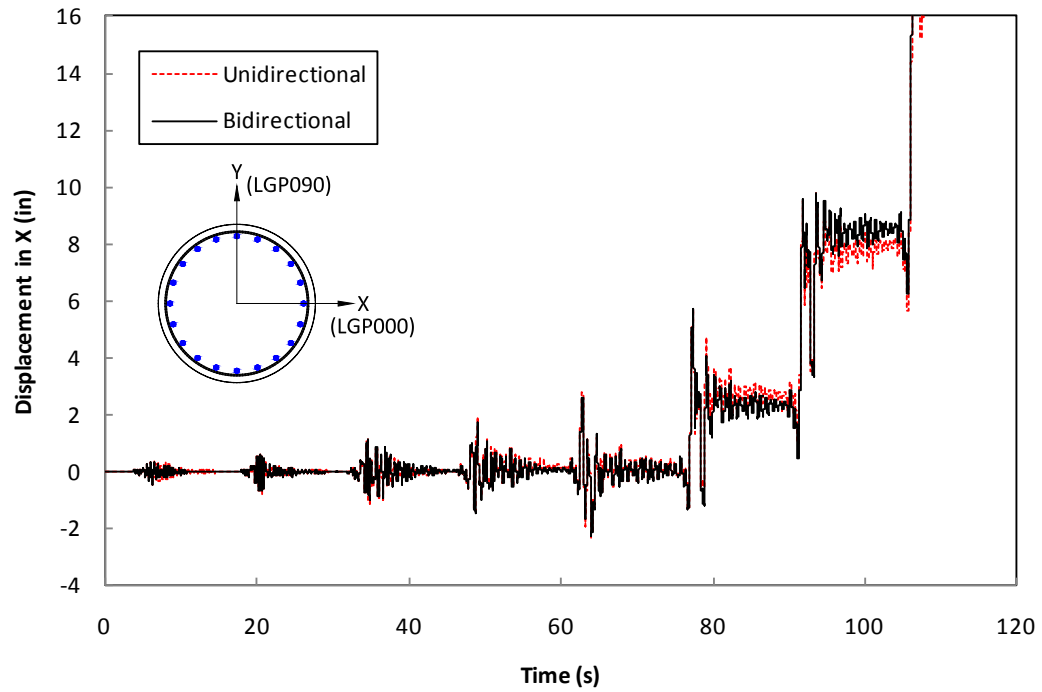
Figure 8-12 Acceleration, Spectrum and Orbit of Takatori Record (Interlockig Column)



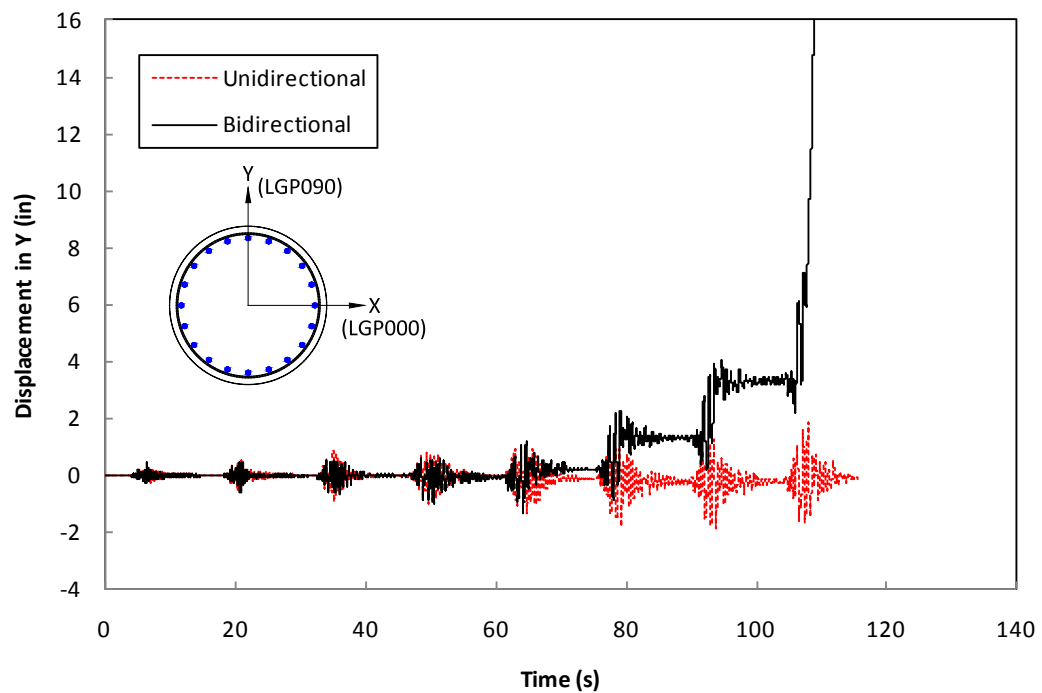
**Figure 8-13 Unidirectional vs. Bidirectional Displacement History, El Centro (Circular) Longitudinal Direction**



**Figure 8-14 Unidirectional vs. Bidirectional Displacement History, El Centro (Circular) Transverse Direction**

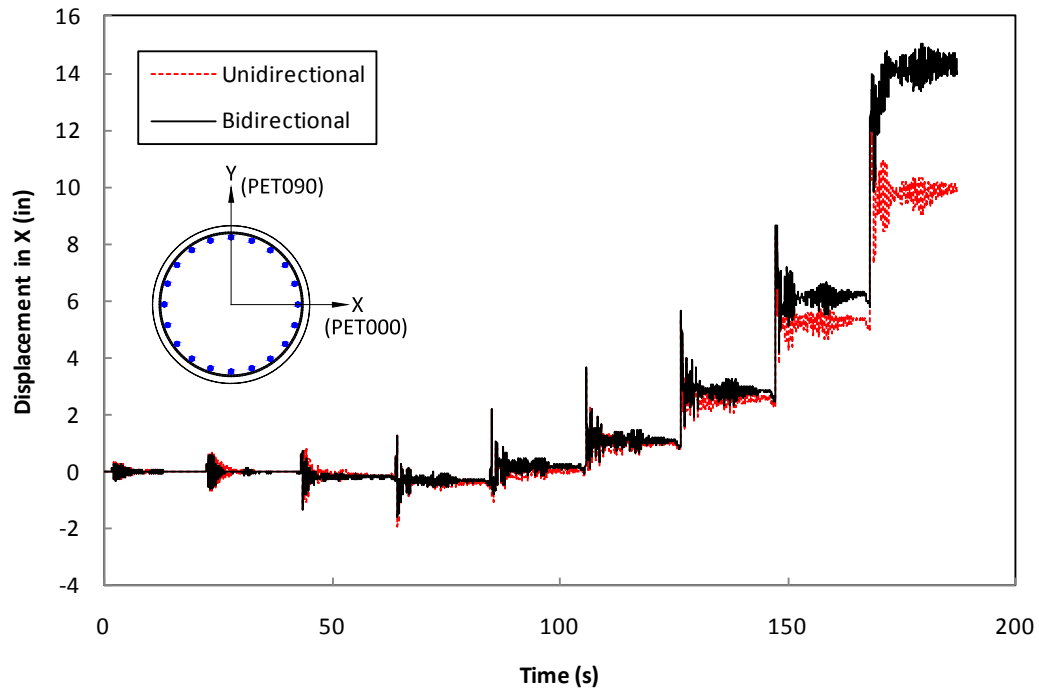


**Figure 8-15 Unidirectional vs. Bidirectional Displacement History, Los Gatos (Circular) Longitudinal Direction**

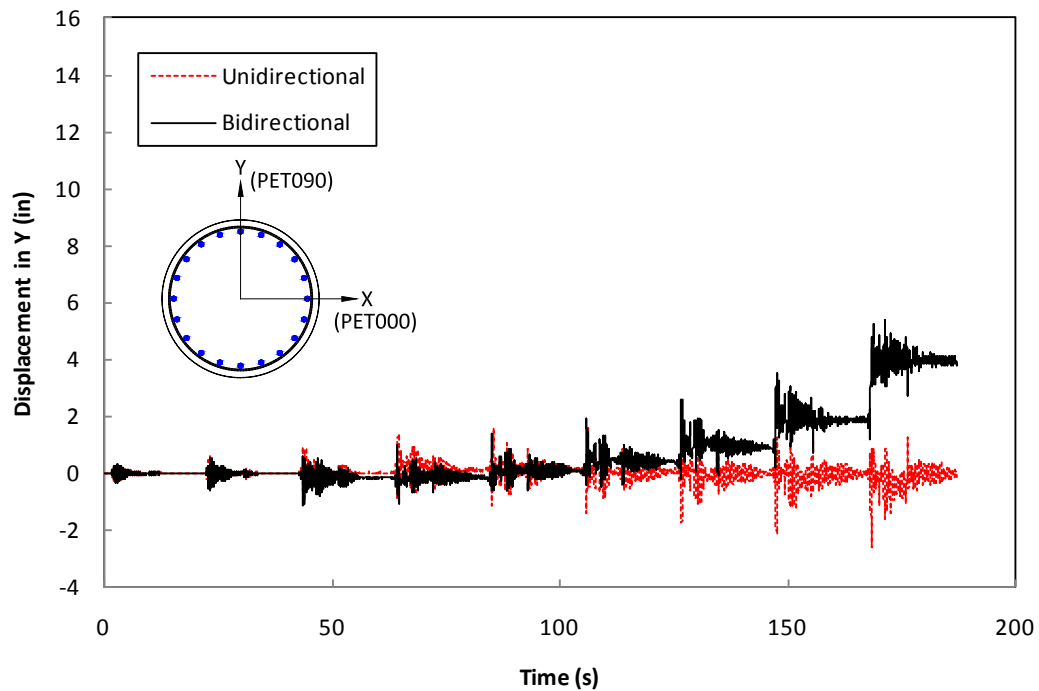


**Figure 8-16 Unidirectional vs. Bidirectional Displacement History, Los Gatos (Circular) Transverse Direction**

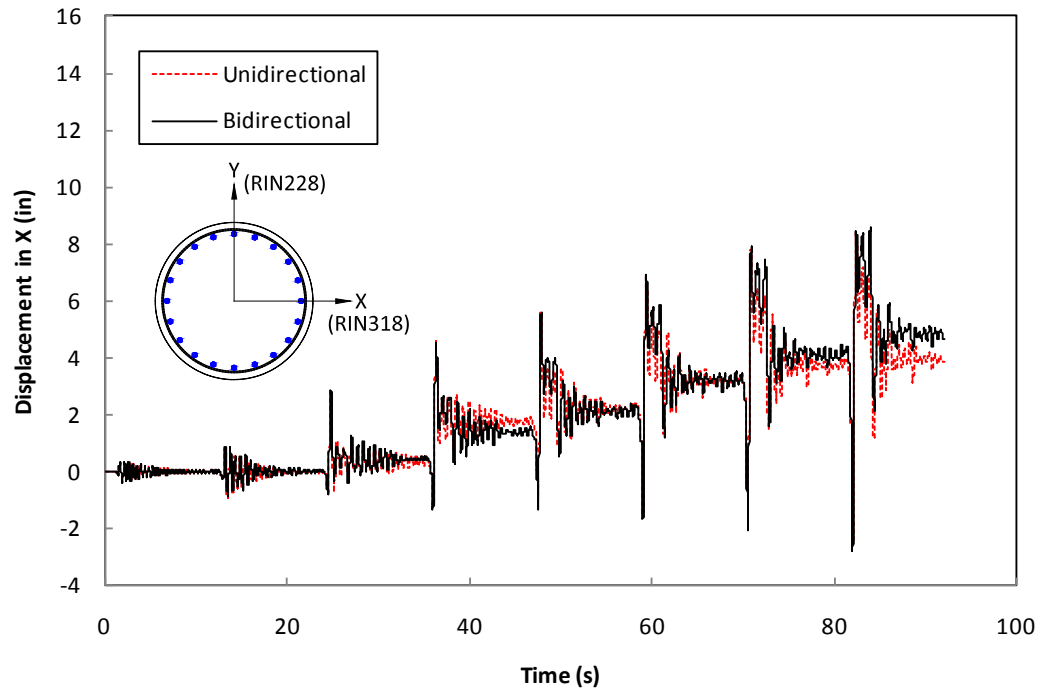




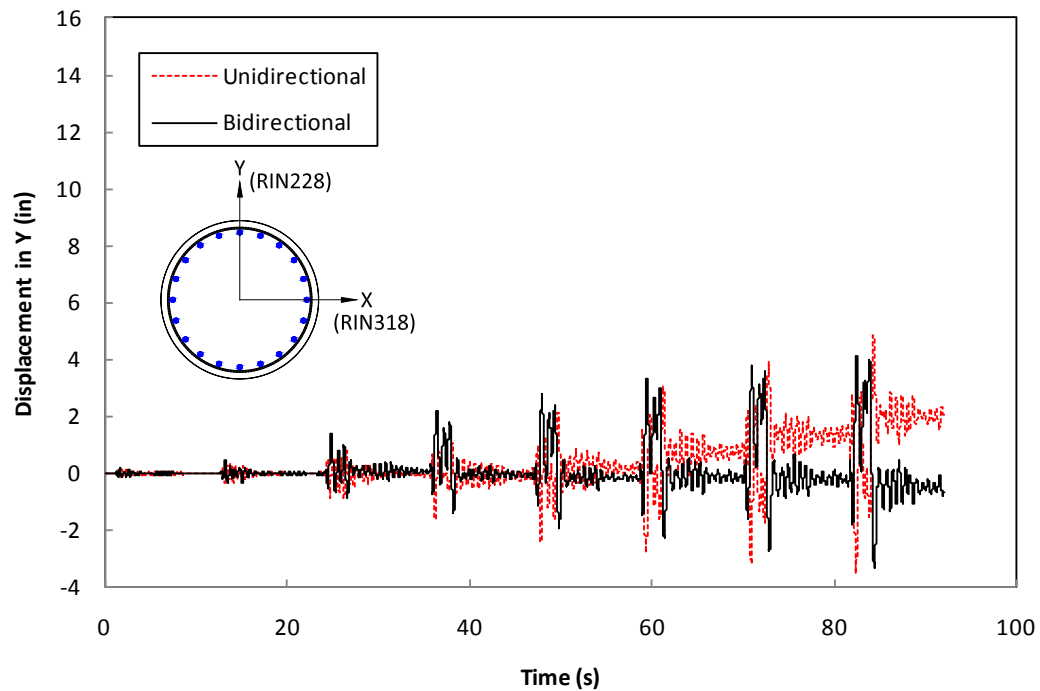
**Figure 8-17 Unidirectional vs. Bidirectional Displacement History, Petrolia (Circular) Longitudinal Direction**



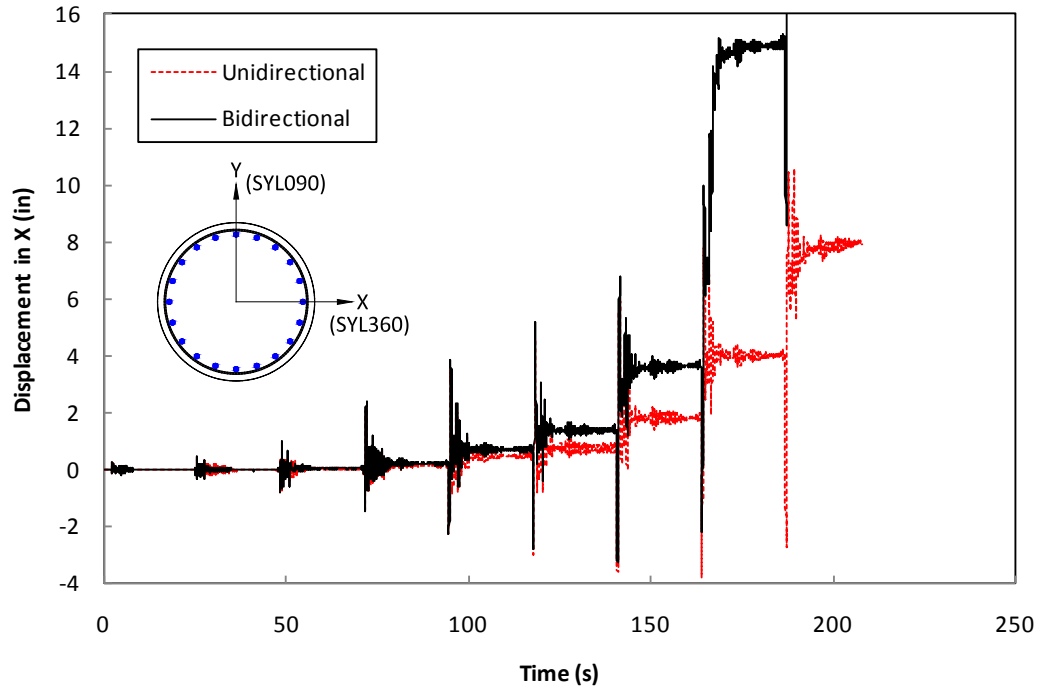
**Figure 8-18 Unidirectional vs. Bidirectional Displacement History, Petrolia (Circular) Transverse Direction**



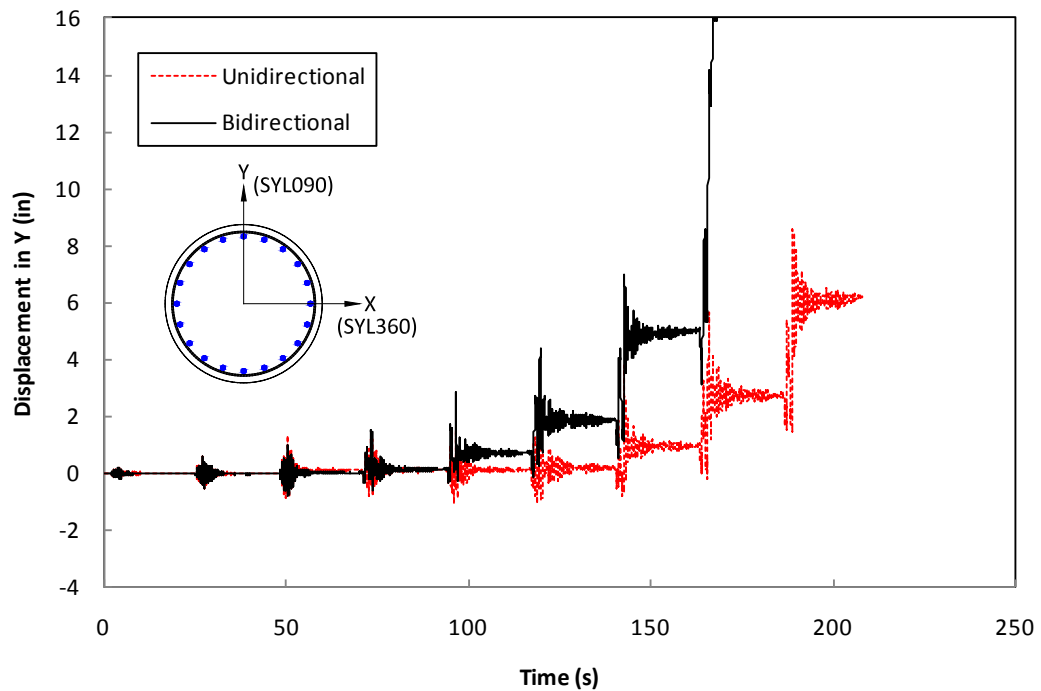
**Figure 8-19 Unidirectional vs. Bidirectional Displacement History, Rinaldi (Circular) Longitudinal Direction**



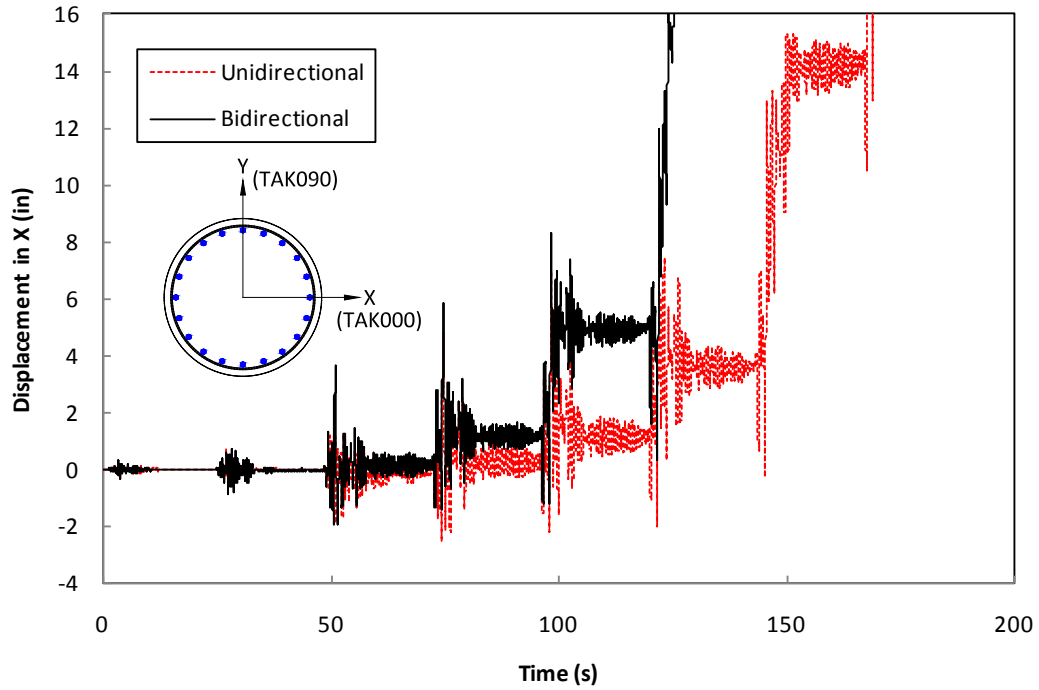
**Figure 8-20 Unidirectional vs. Bidirectional Displacement History, Rinaldi (Circular) Transverse Direction**



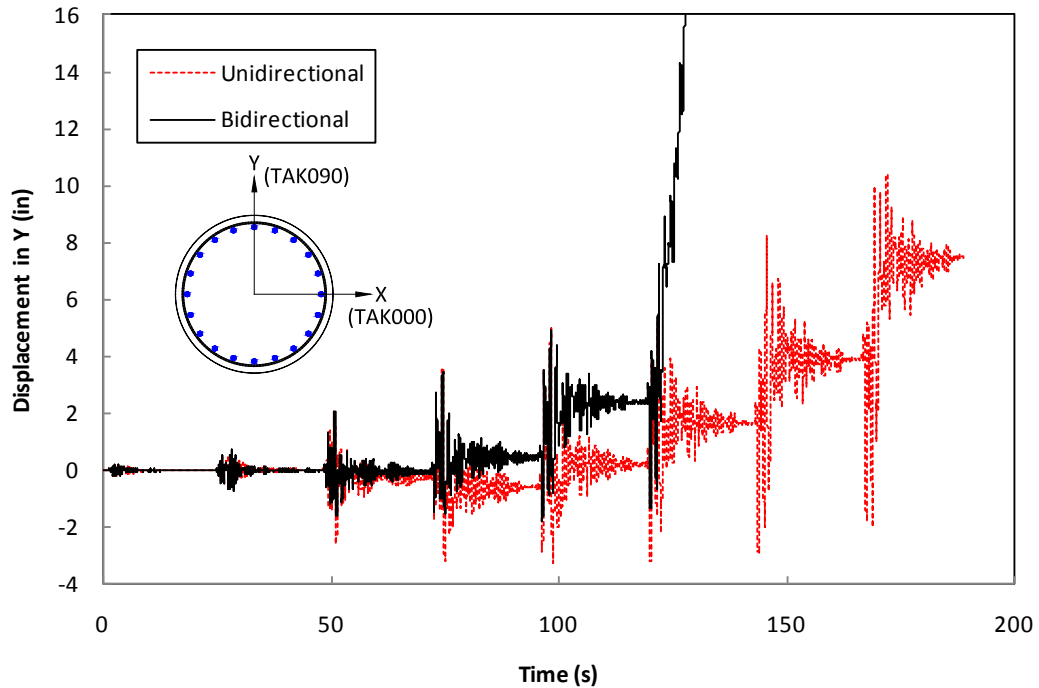
**Figure 8-21 Unidirectional vs. Bidirectional Displacement History, Sylmar (Circular) Longitudinal Direction**



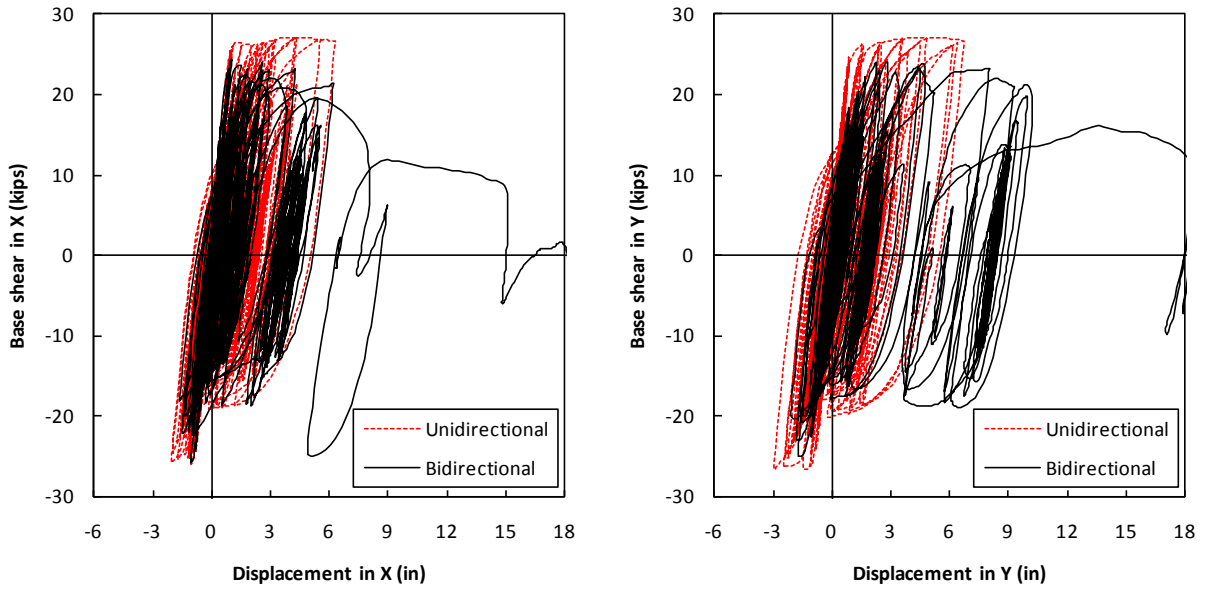
**Figure 8-22 Unidirectional vs. Bidirectional Displacement History, Sylmar (Circular) Transverse Direction**



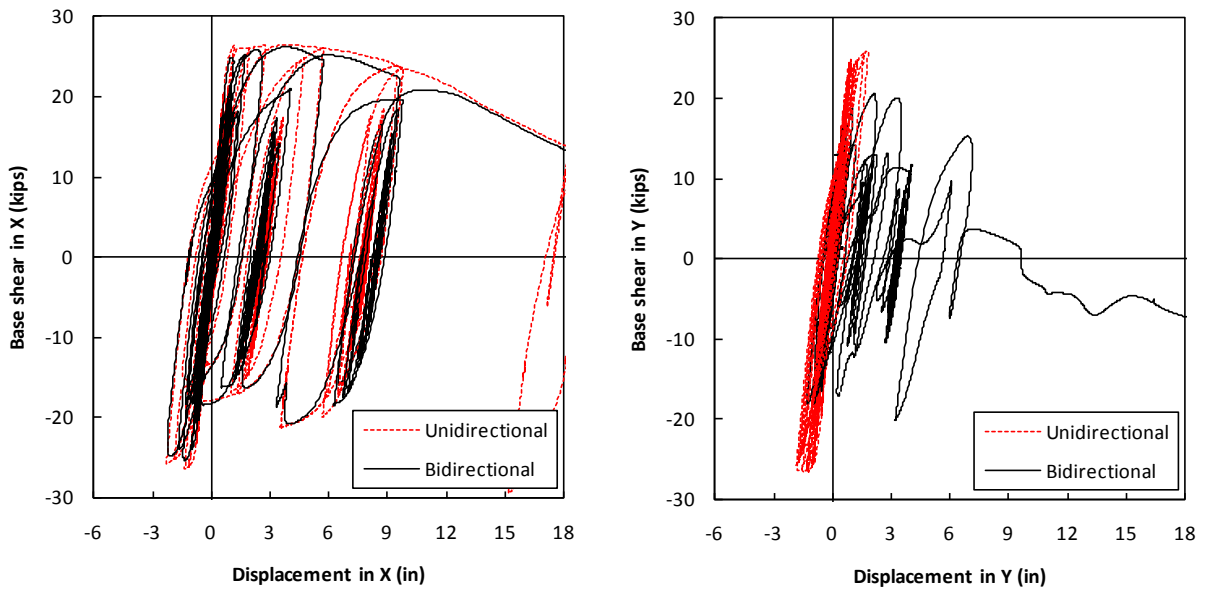
**Figure 8-23 Unidirectional vs. Bidirectional Displacement History, Takatori (Circular) Longitudinal Direction**



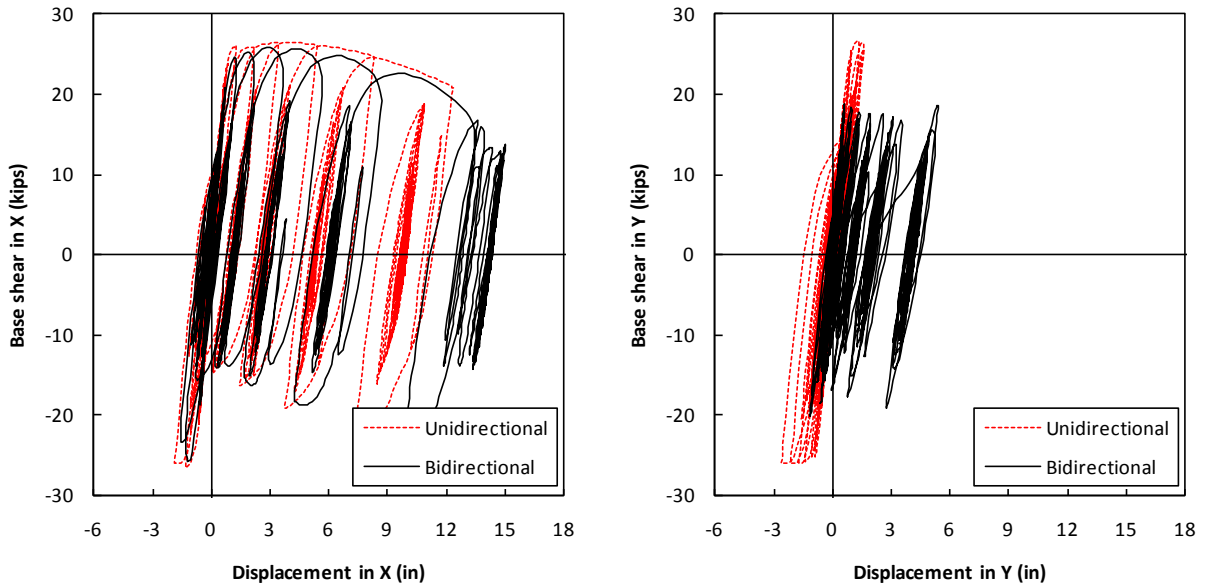
**Figure 8-24 Unidirectional vs. Bidirectional Displacement History, Takatori (Circular) Transverse Direction**



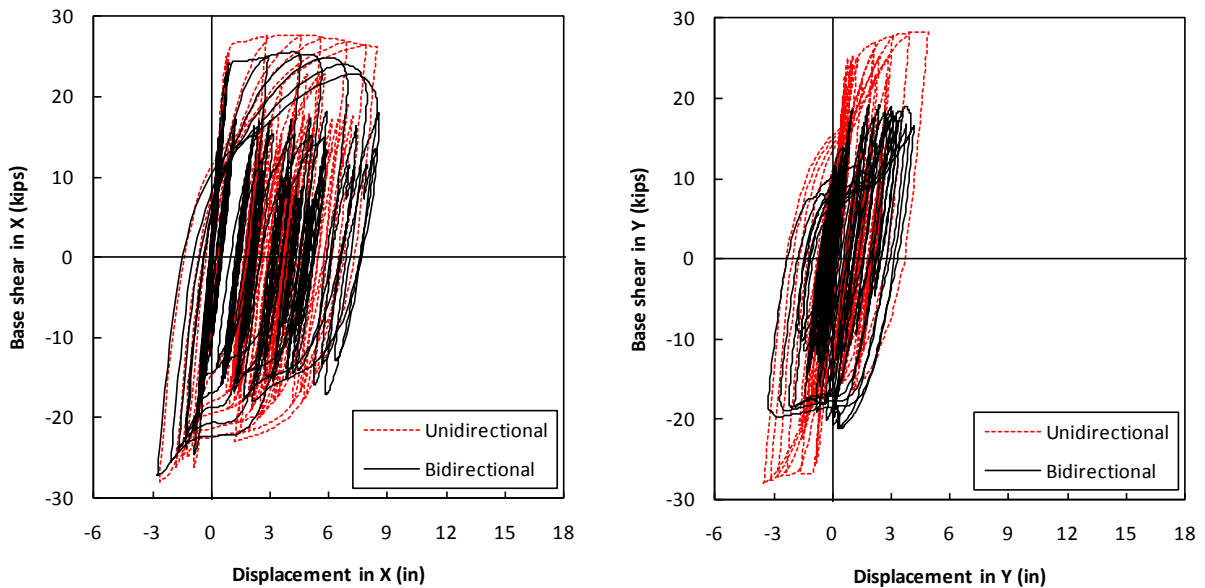
**Figure 8-25 Unidirectional vs. Bidirectional Force-Displacement Hysteresis, El Centro (Circular)**



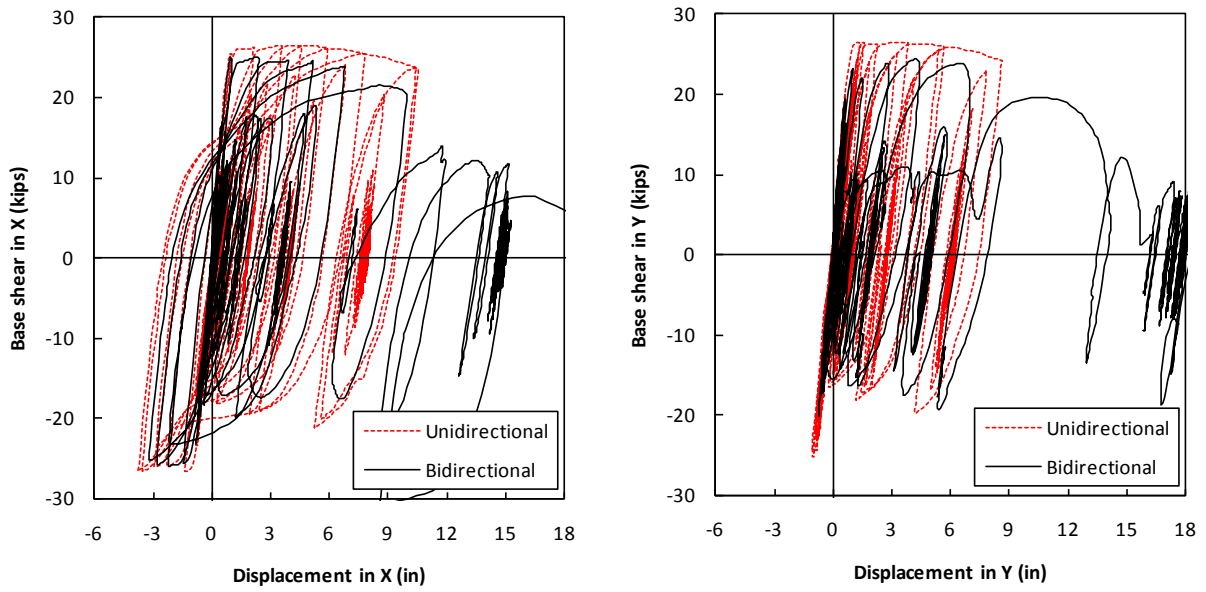
**Figure 8-26 Unidirectional vs. Bidirectional Force-Displacement Hysteresis, Los Gatos (Circular)**



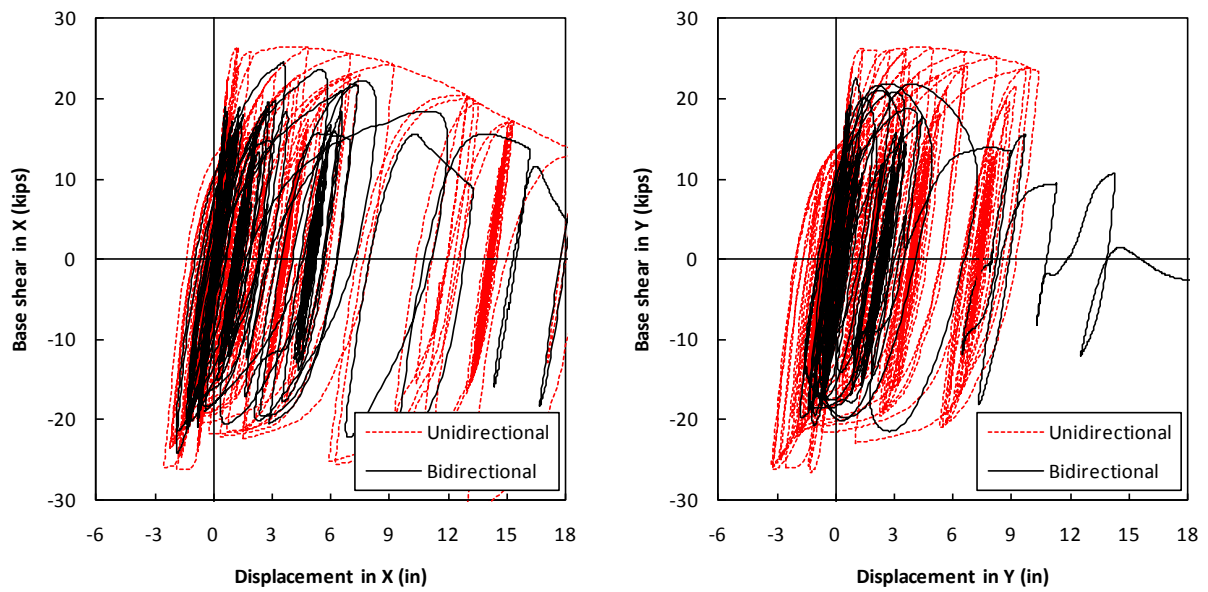
**Figure 8-27 Unidirectional vs. Bidirectional Force-Displacement Hysteresis, Petrolia (Circular)**



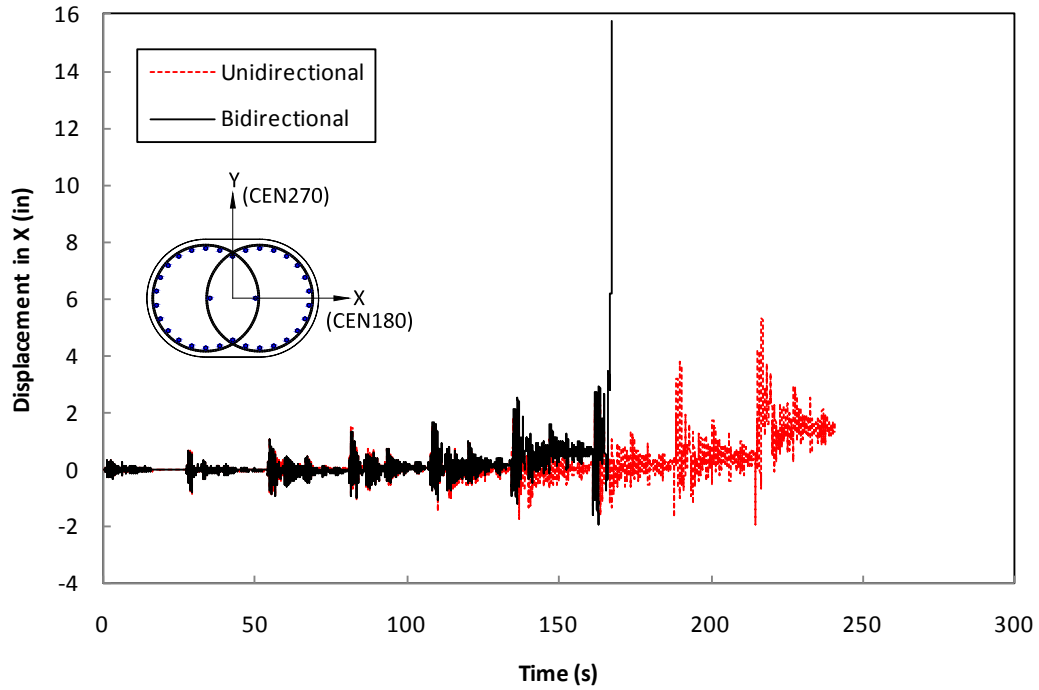
**Figure 8-28 Unidirectional vs. Bidirectional Force-Displacement Hysteresis, Rinaldi (Circular)**



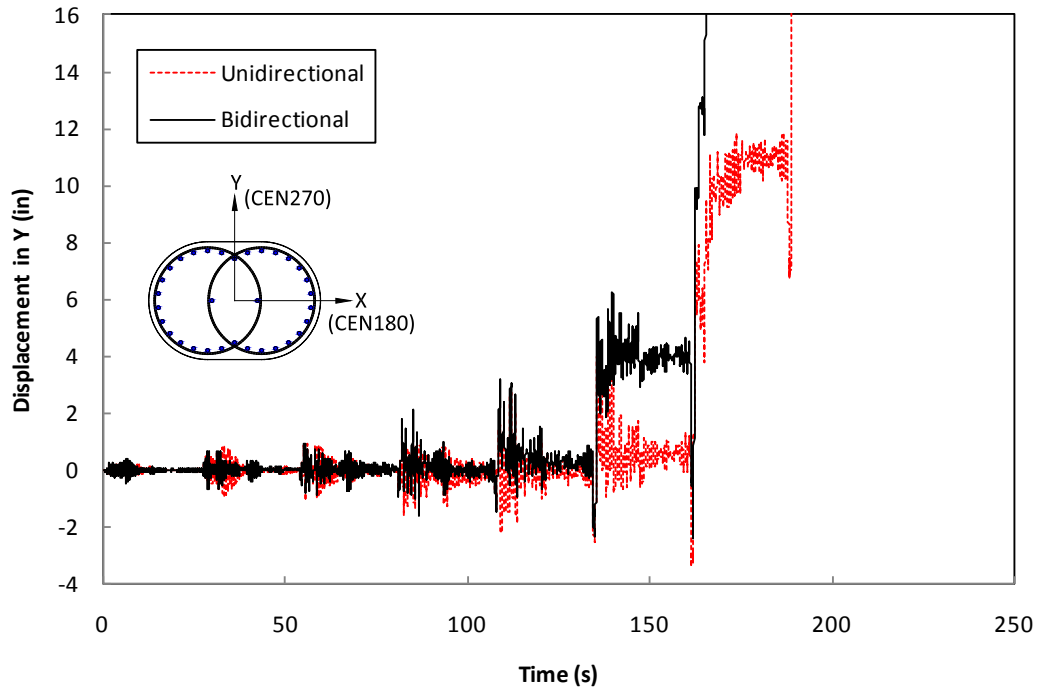
**Figure 8-29 Unidirectional vs. Bidirectional Force-Displacement Hysteresis, Sylmar (Circular)**



**Figure 8-30 Unidirectional vs. Bidirectional Force-Displacement Hysteresis, Takatori (Circular)**

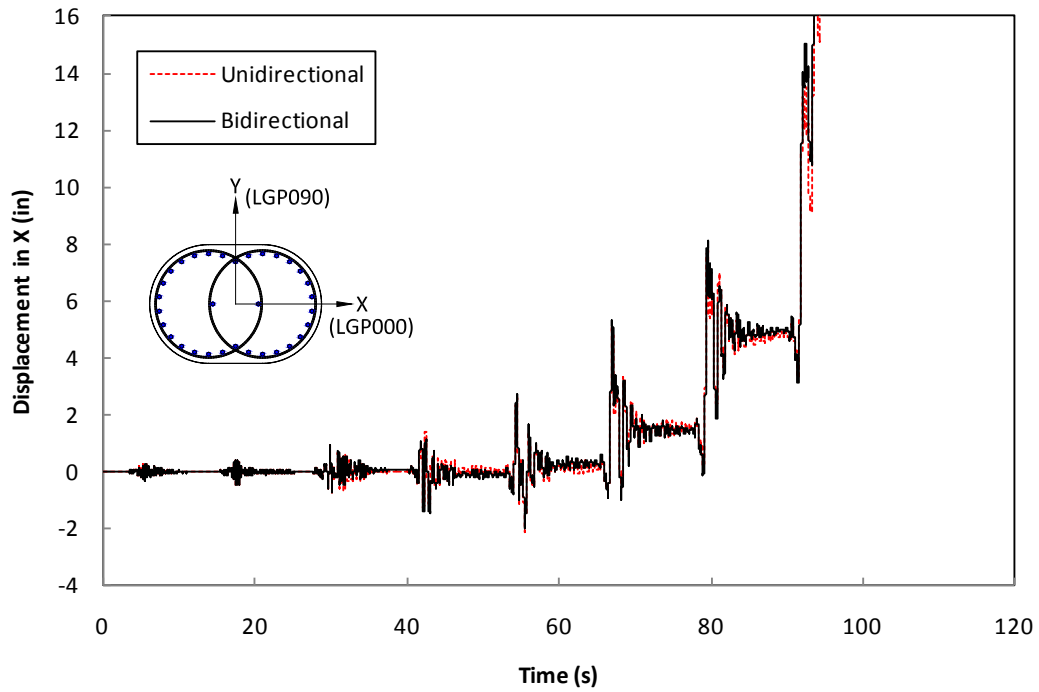


**Figure 8-31 Unidirectional vs. Bidirectional Displacement History, El Centro (Interlocking) Longitudinal Direction**

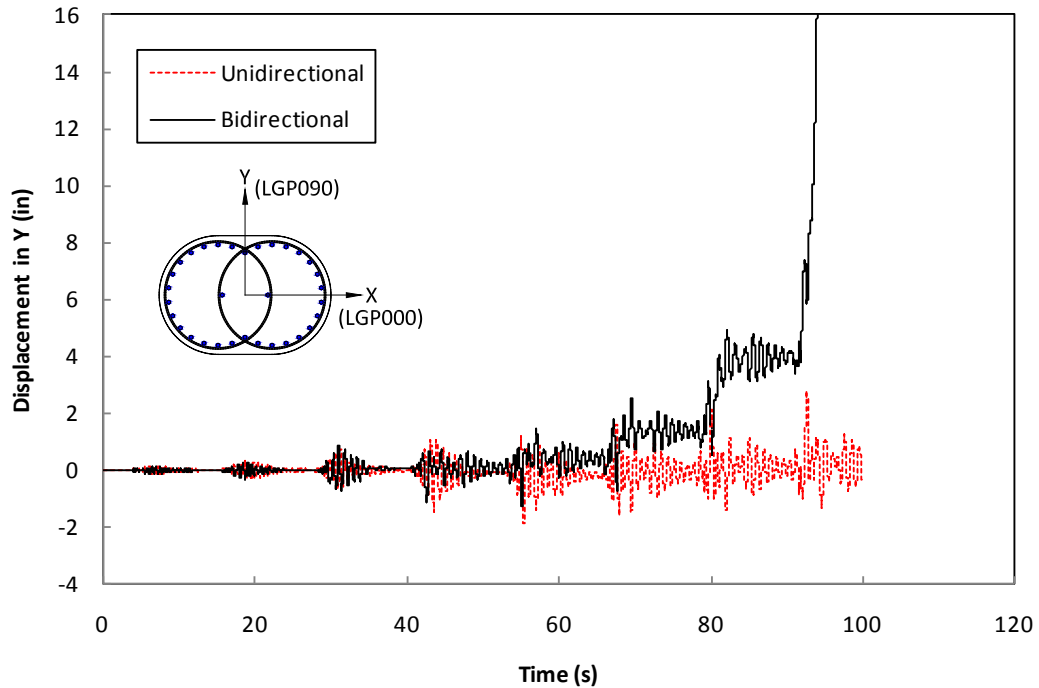


**Figure 8-32 Unidirectional vs. Bidirectional Displacement History, El Centro (Interlocking) Transverse Direction**

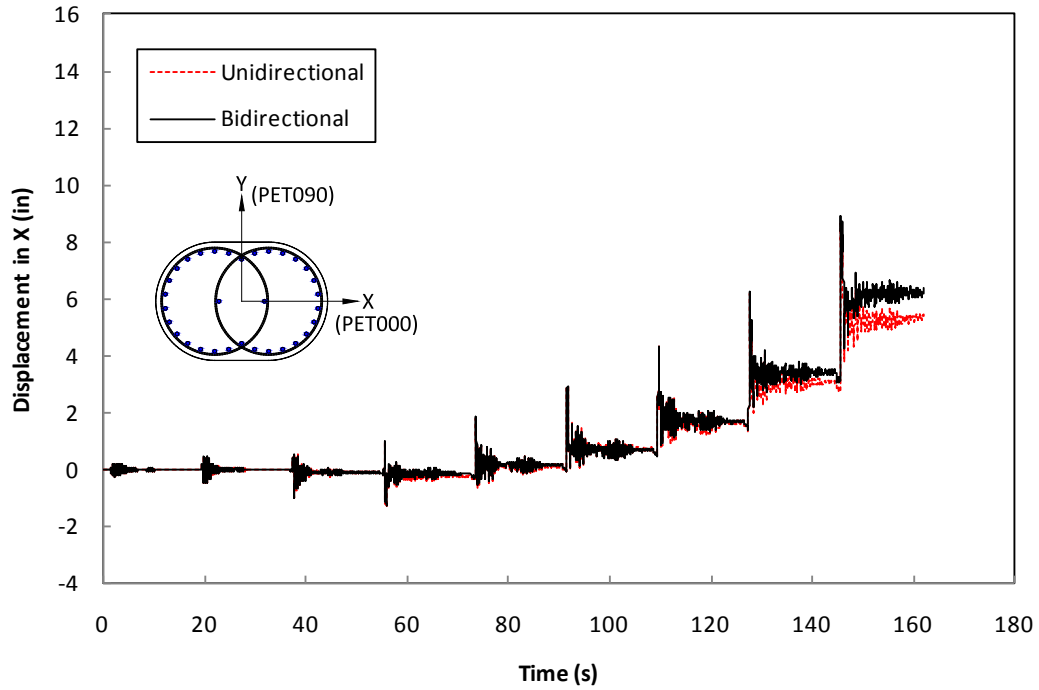




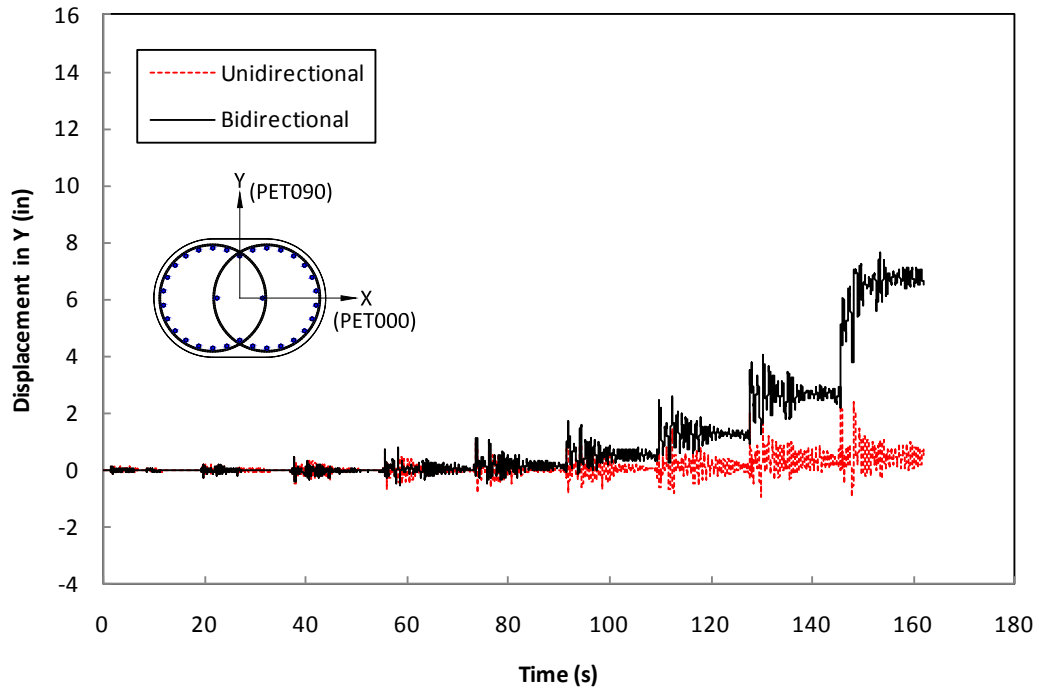
**Figure 8-33 Unidirectional vs. Bidirectional Displacement History, Los Gatos (Interlocking) Longitudinal Direction**



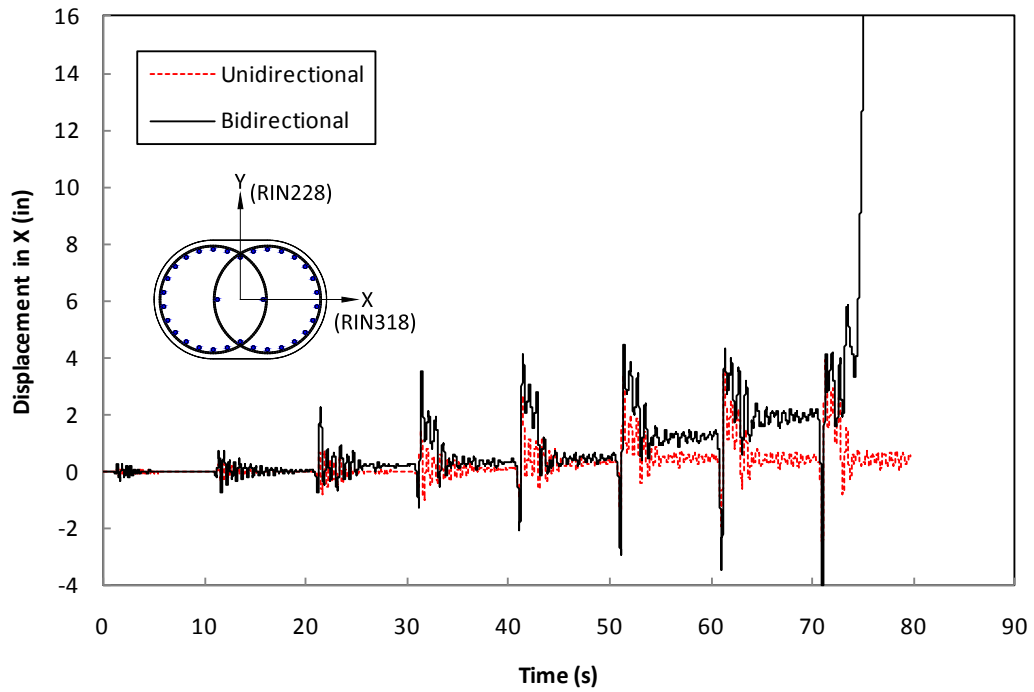
**Figure 8-34 Unidirectional vs. Bidirectional Displacement History, Los Gatos (Interlocking) Transverse Direction**



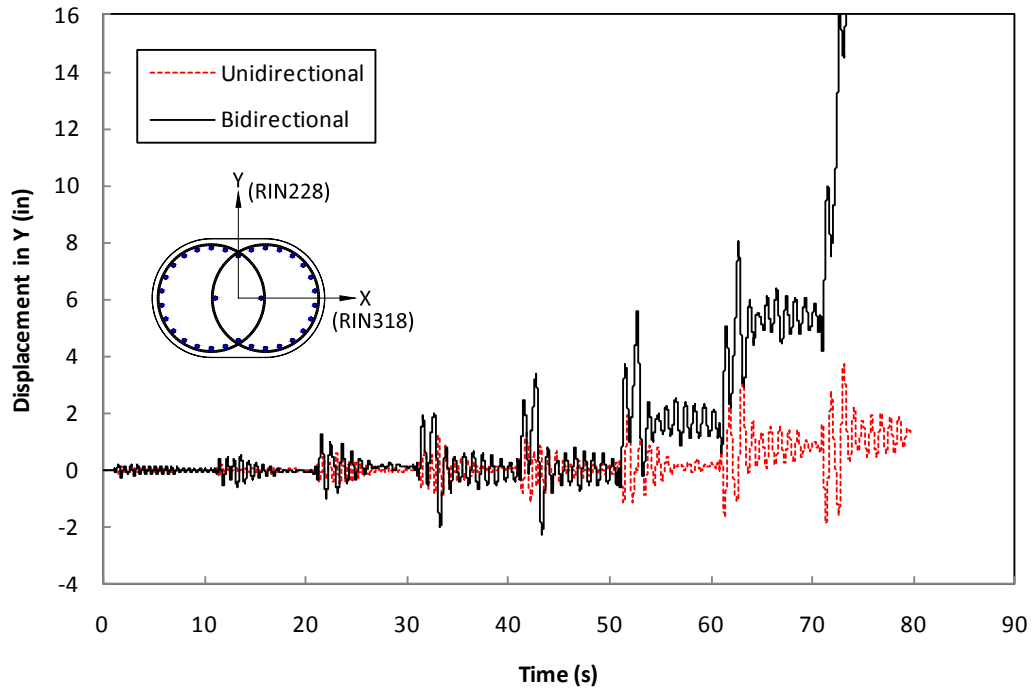
**Figure 8-35 Unidirectional vs. Bidirectional Displacement History, Petrolia (Interlocking) Longitudinal Direction**



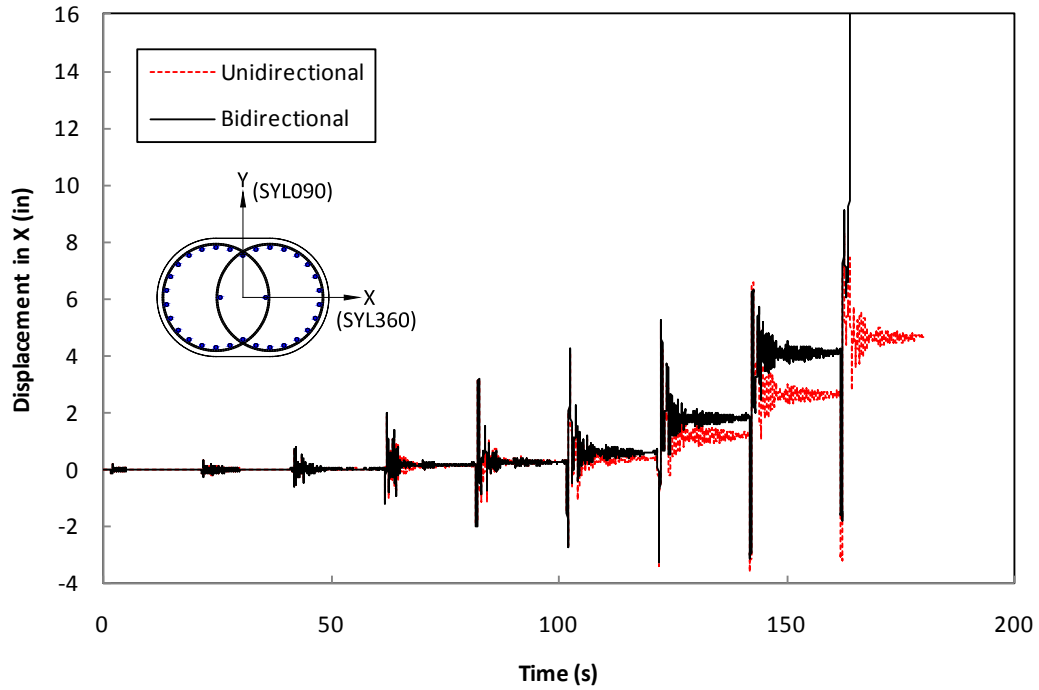
**Figure 8-36 Unidirectional vs. Bidirectional Displacement History, Petrolia (Interlocking) Transverse Direction**



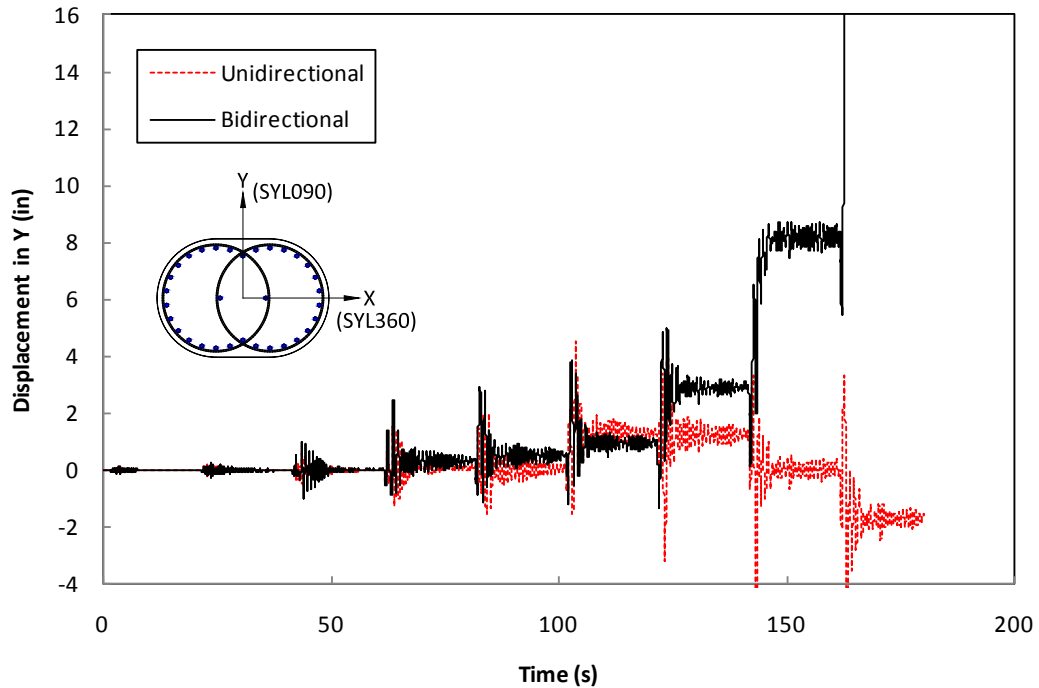
**Figure 8-37 Unidirectional vs. Bidirectional Displacement History, Rinaldi (Interlocking) Longitudinal Direction**



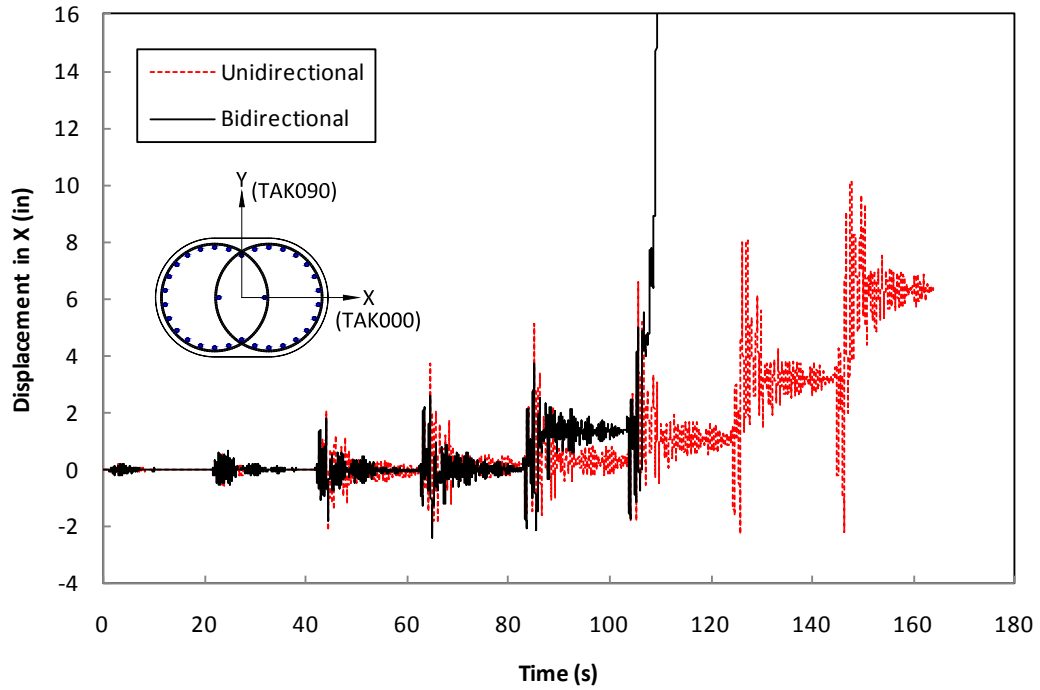
**Figure 8-38 Unidirectional vs. Bidirectional Displacement History, Rinaldi (Interlocking) Transverse Direction**



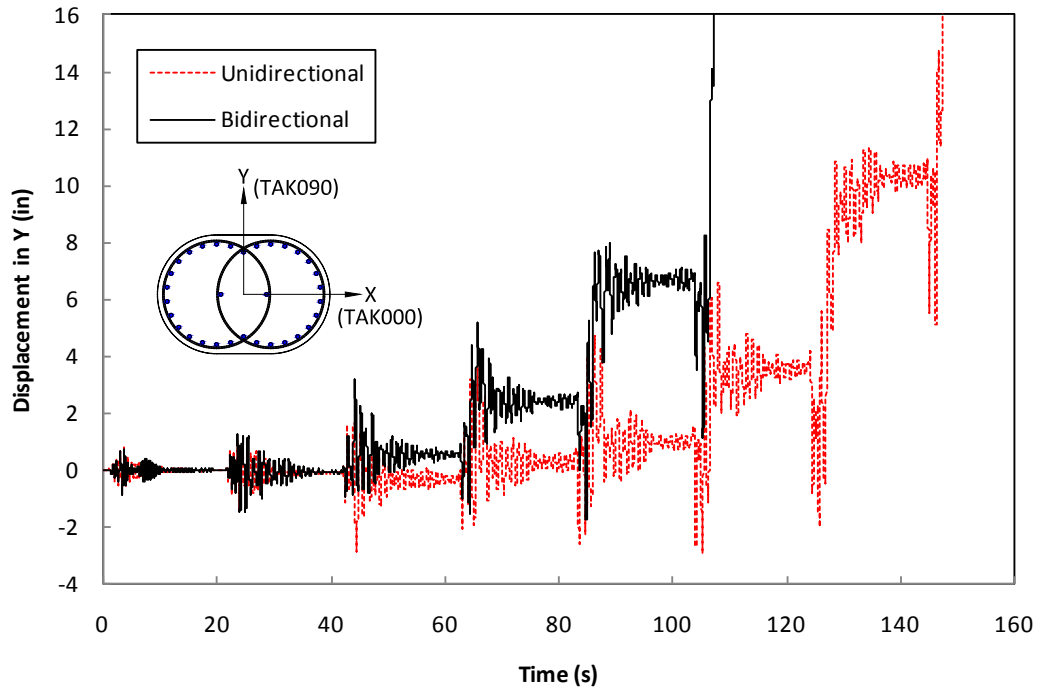
**Figure 8-39 Unidirectional vs. Bidirectional Displacement History, Sylmar (Interlocking) Longitudinal Direction**



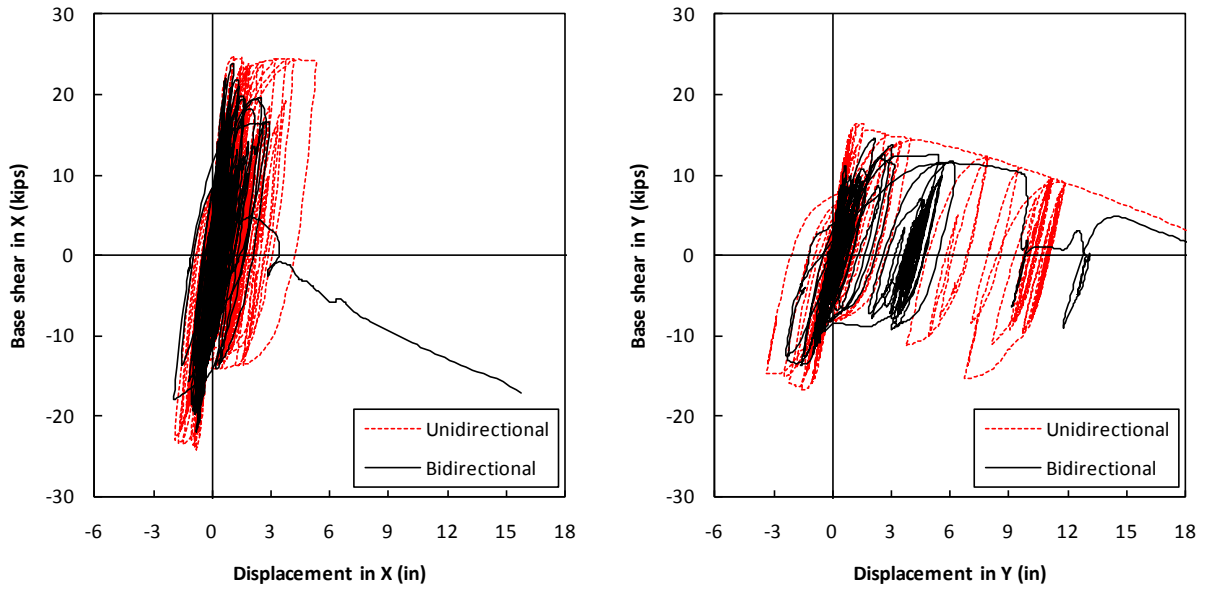
**Figure 8-40 Unidirectional vs. Bidirectional Displacement History, Sylmar (Interlocking) Transverse Direction**



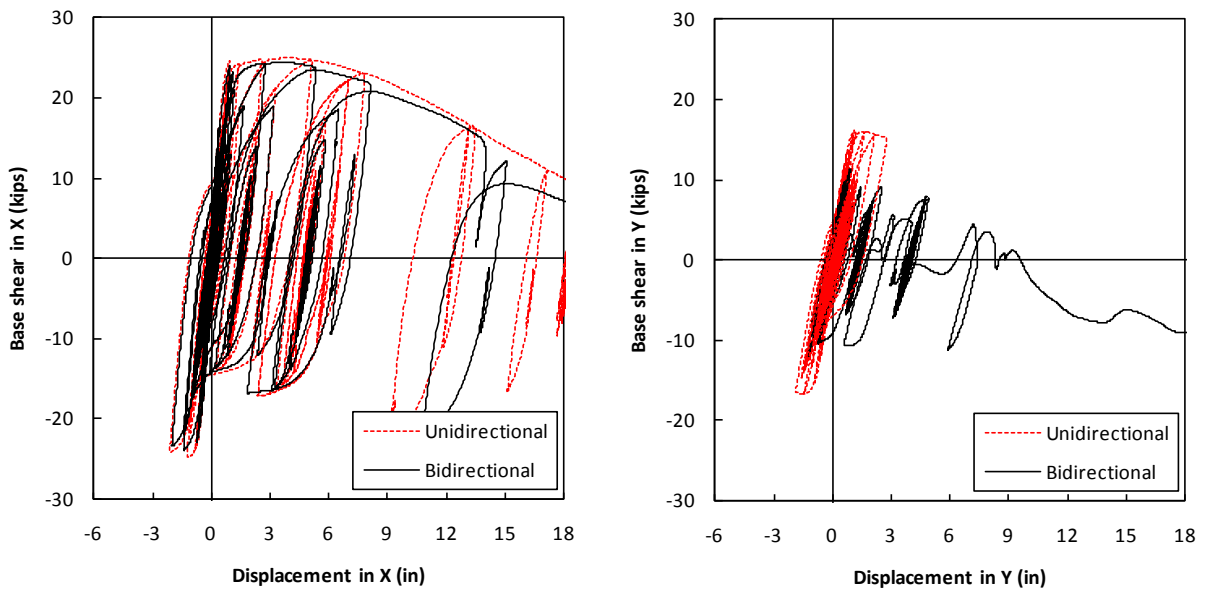
**Figure 8-41 Unidirectional vs. Bidirectional Displacement History, Takatori (Interlocking) Longitudinal Direction**



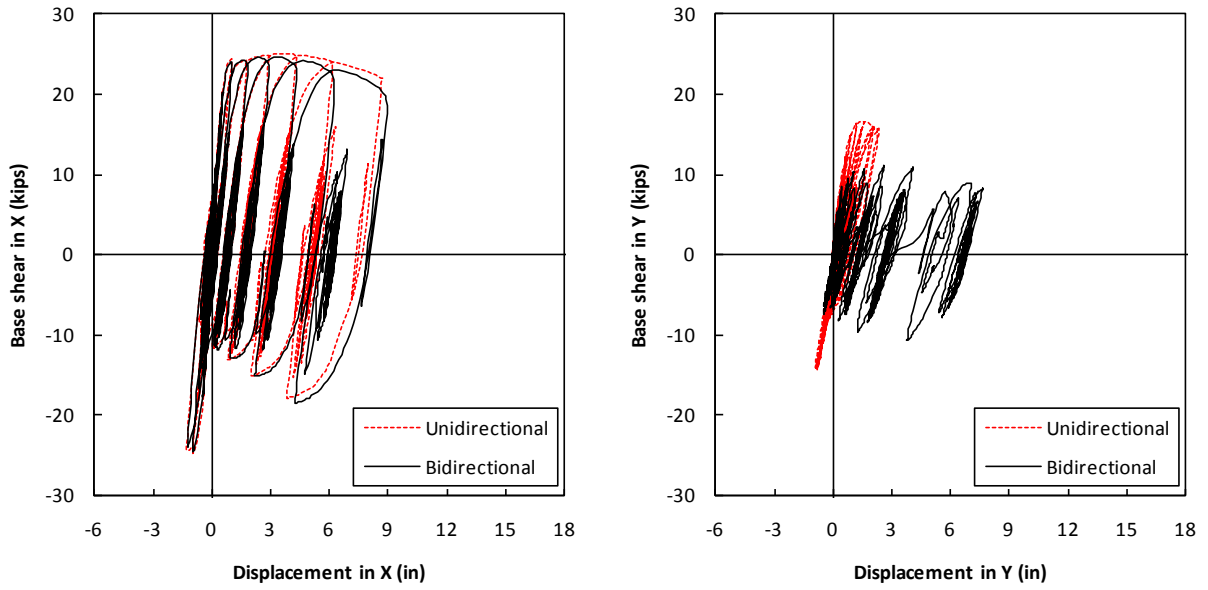
**Figure 8-42 Unidirectional vs. Bidirectional Displacement History, Takatori (Interlocking) Transverse Direction**



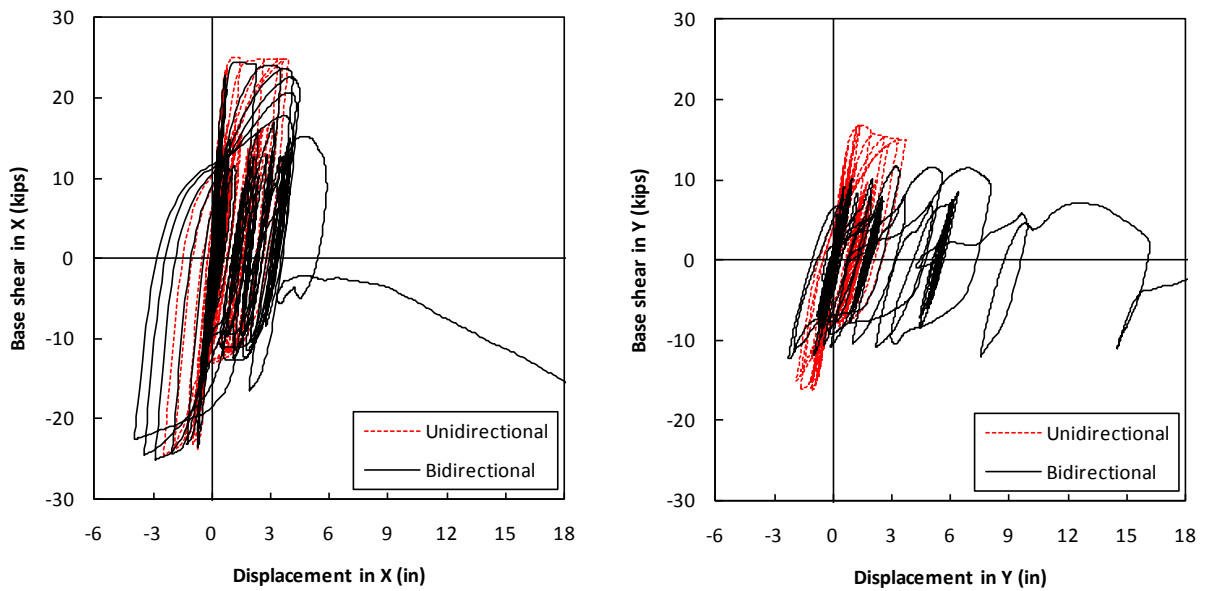
**Figure 8-43 Unidirectional vs. Bidirectional Force-Displacement Hysteresis, El Centro (Interlocking)**



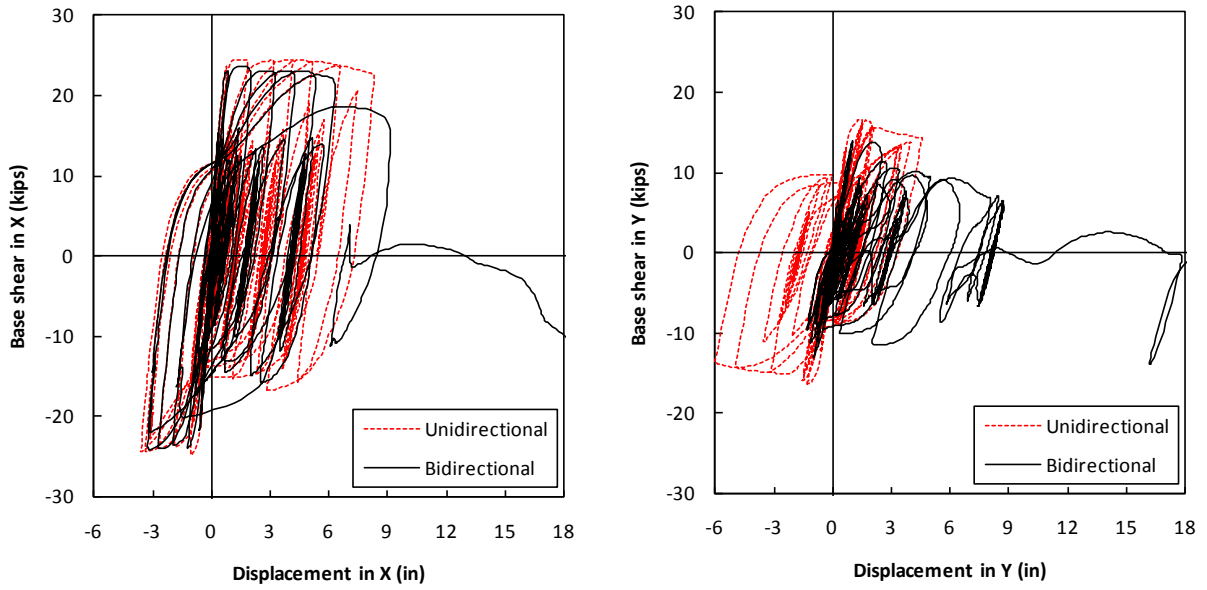
**Figure 8-44 Unidirectional vs. Bidirectional Force-Displacement Hysteresis, Los Gatos (Interlocking)**



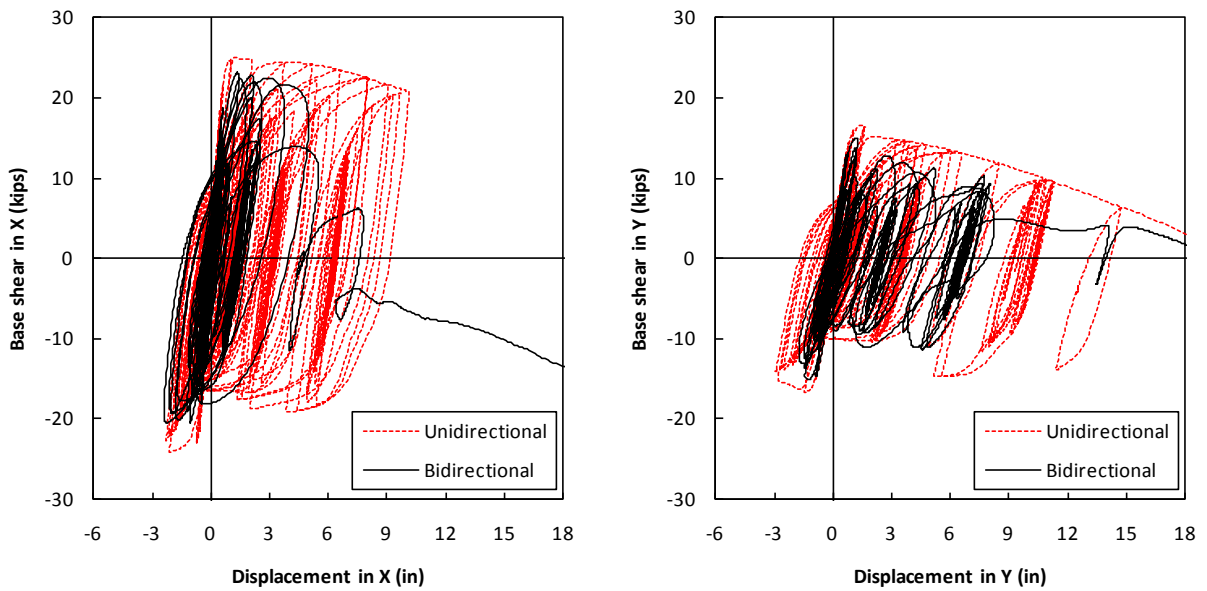
**Figure 8-45 Unidirectional vs. Bidirectional Force-Displacement Hysteresis, Petrolia (Interlocking)**



**Figure 8-46 Unidirectional vs. Bidirectional Force-Displacement Hysteresis, Rinaldi (Interlocking)**



**Figure 8-47 Unidirectional vs. Bidirectional Force-Displacement Hysteresis, Sylmar (Interlocking)**



**Figure 8-48 Unidirectional vs. Bidirectional Force-Displacement Hysteresis, Takatori (Interlocking)**



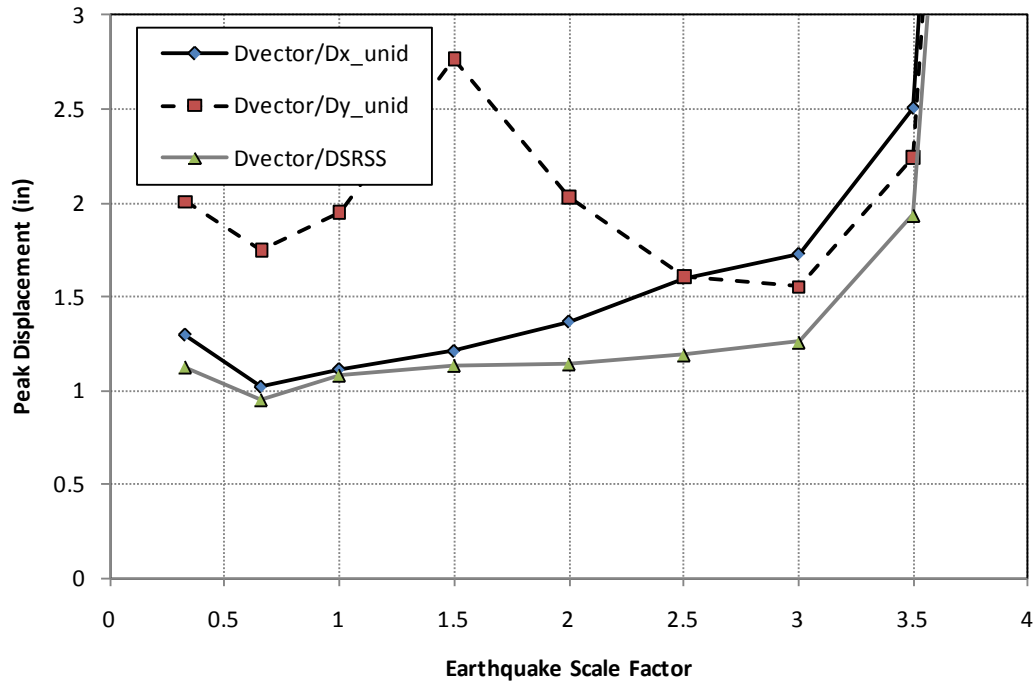
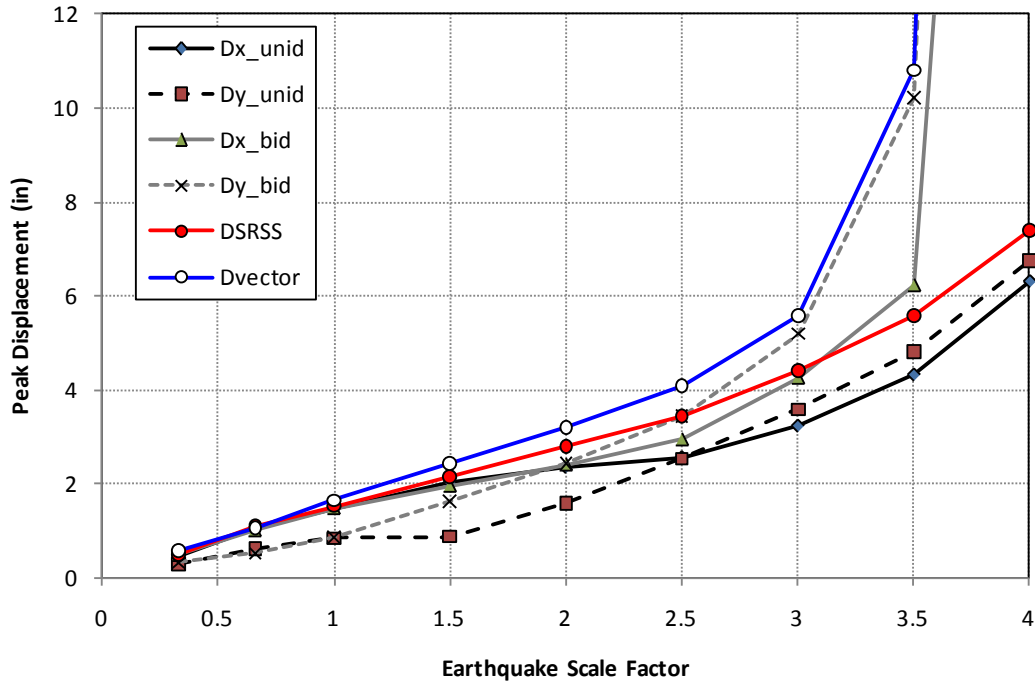


Figure 8-49 Unidirectional vs. Bidirectional at Maximum Displacement, El Centro(Circular)

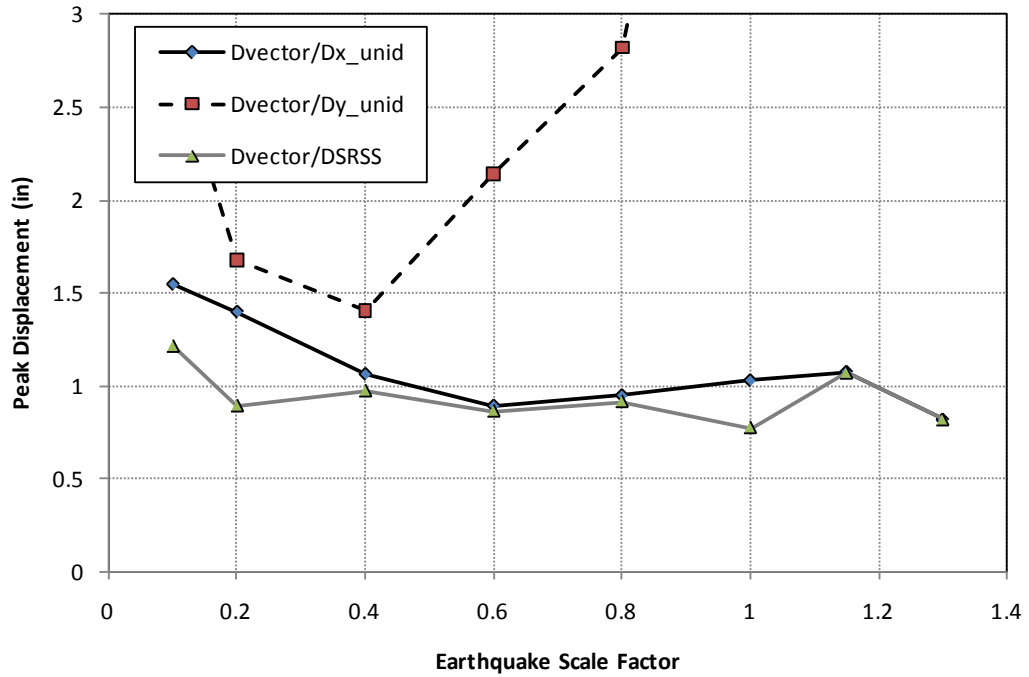
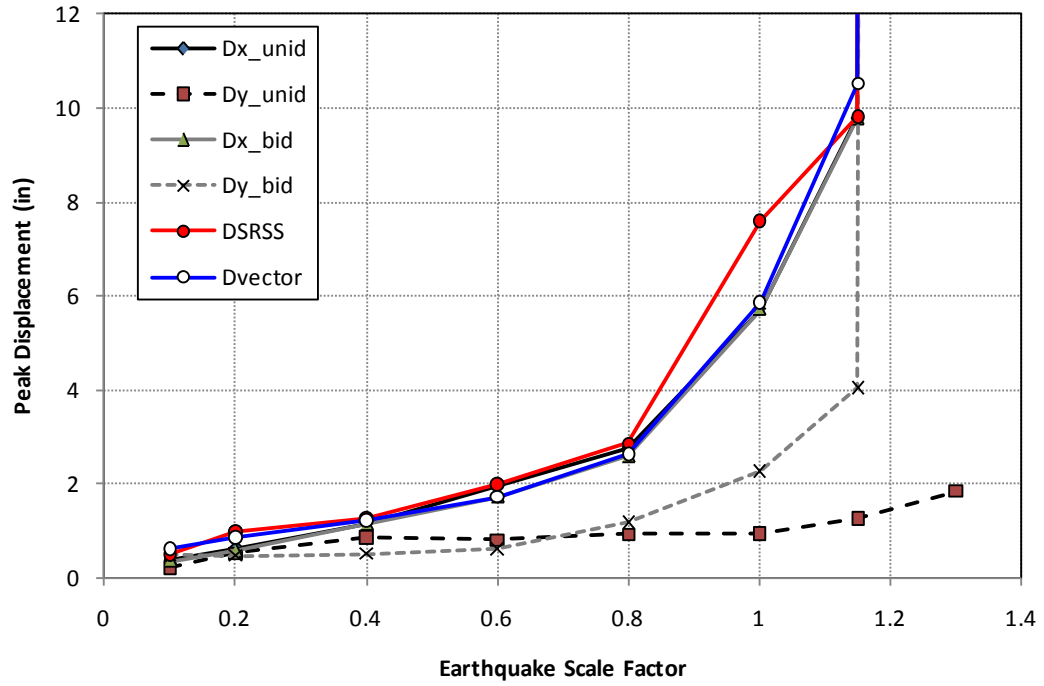


Figure 8-50 Unidirectional vs. Bidirectional at Maximum Displacement, Los Gatos (Circular)

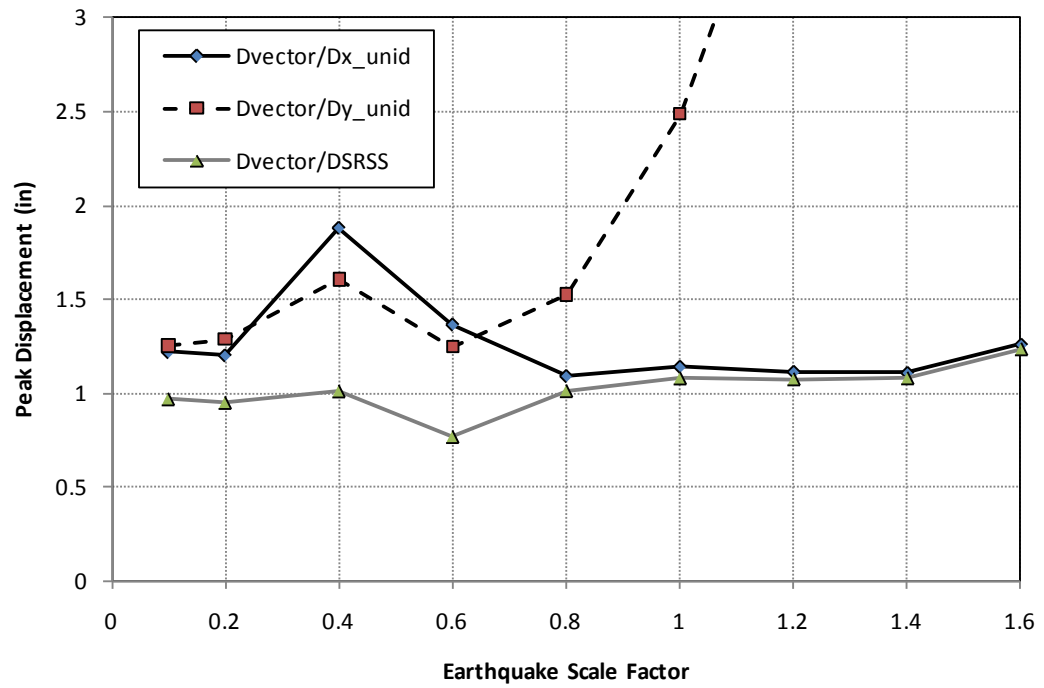
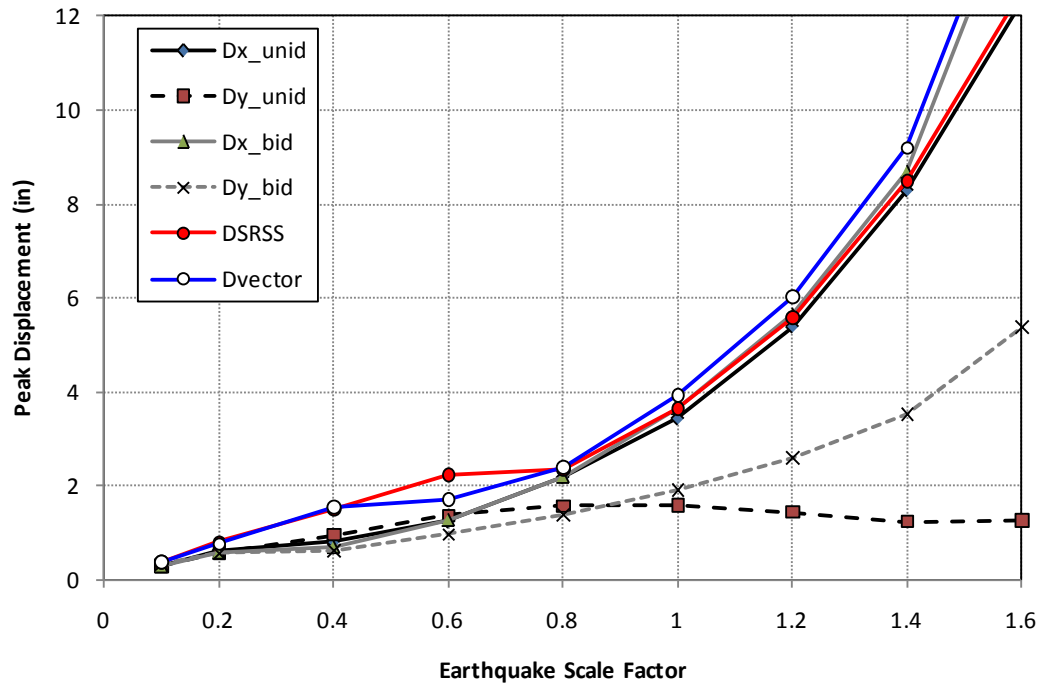


Figure 8-51 Unidirectional vs. Bidirectional at Maximum Displacement, Petrolia (Circular)

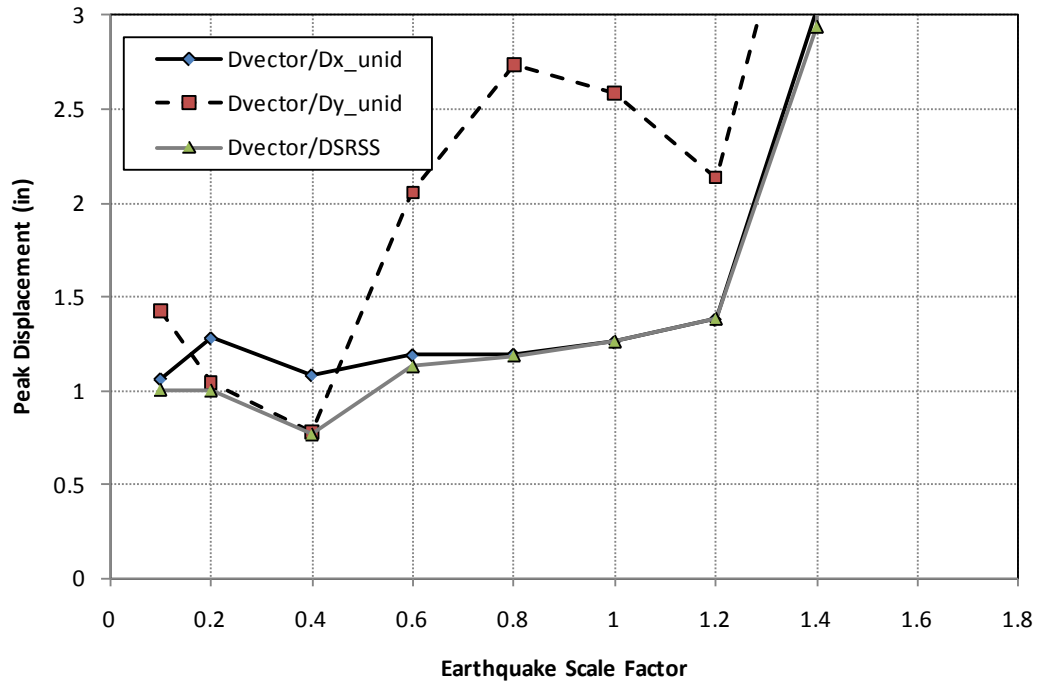
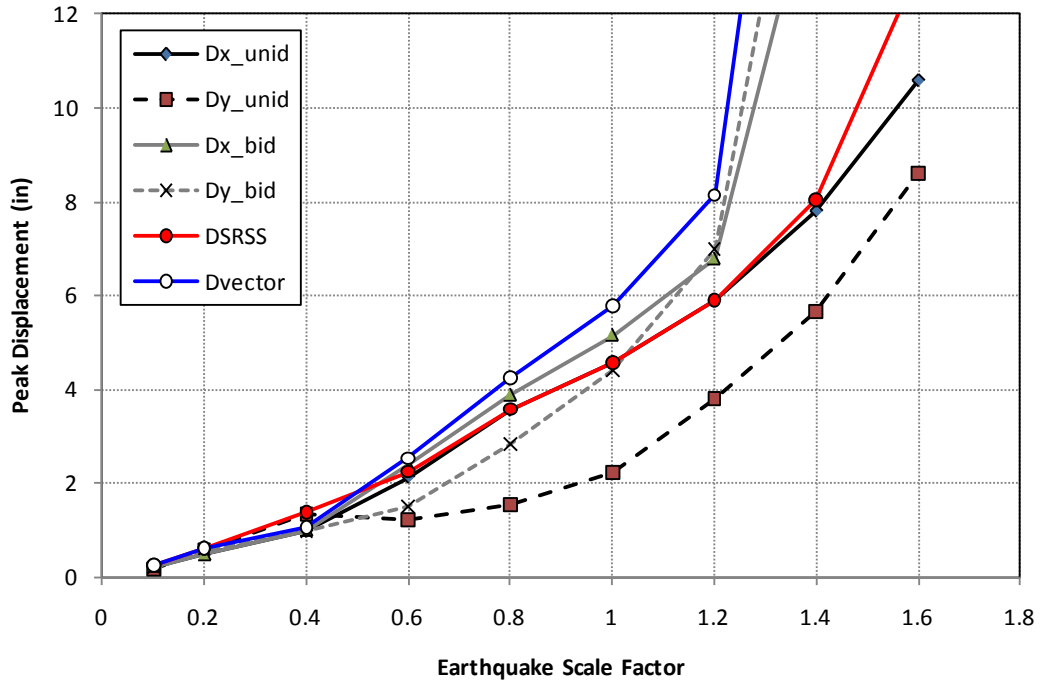


Figure 8-52 Unidirectional vs. Bidirectional at Maximum Displacement, Sylmar (Circular)

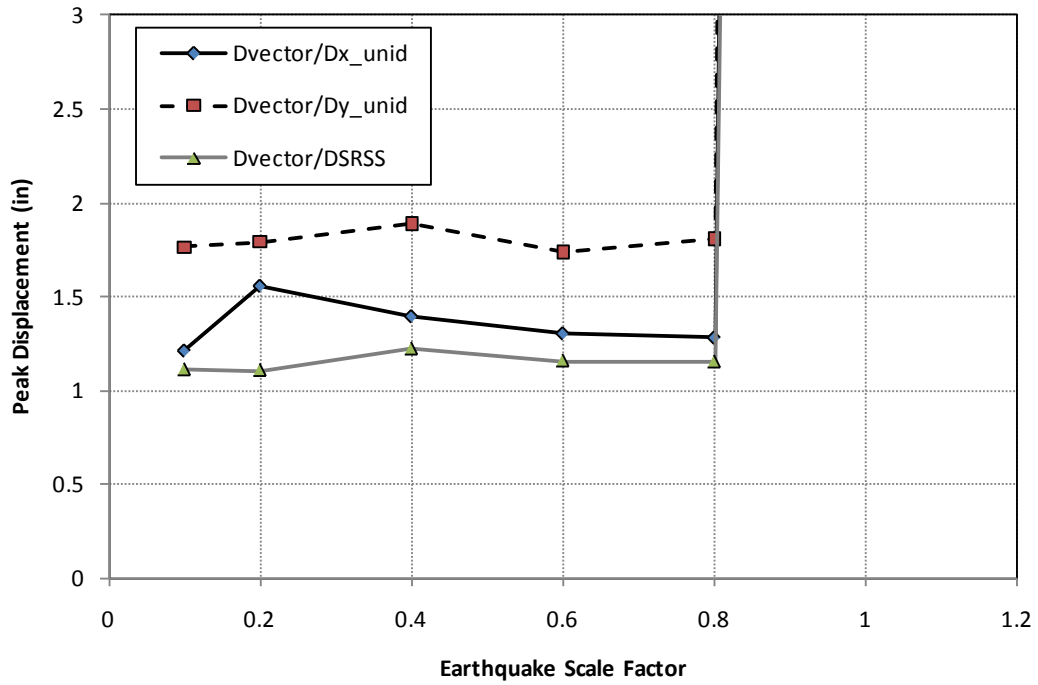
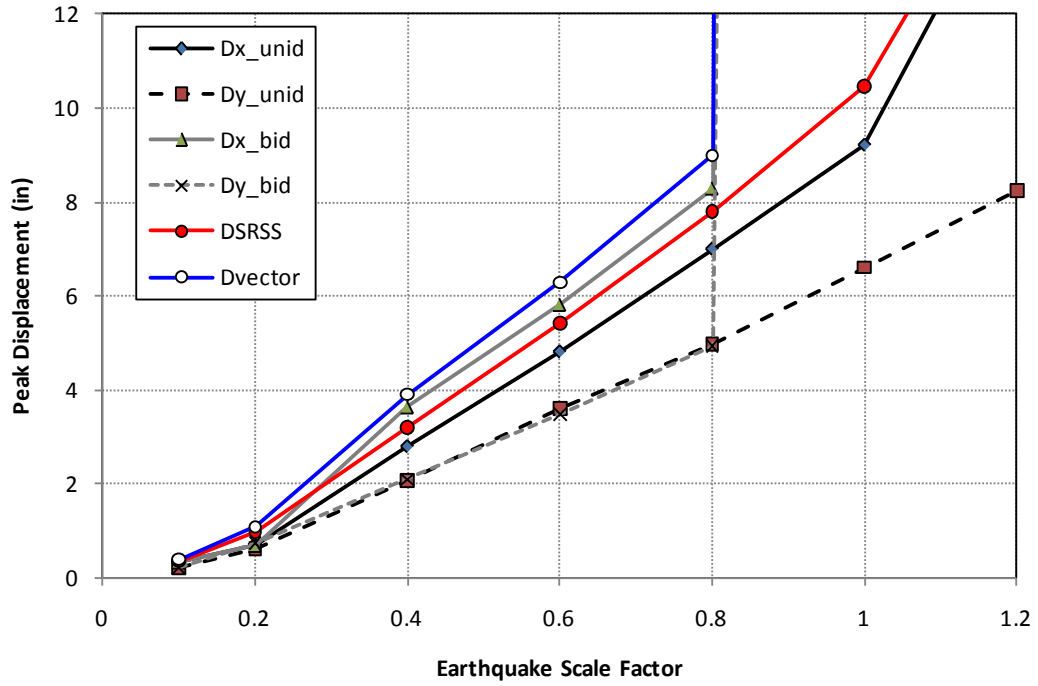


Figure 8-53 Unidirectional vs. Bidirectional at Maximum Displacement, Takatori (Circular)

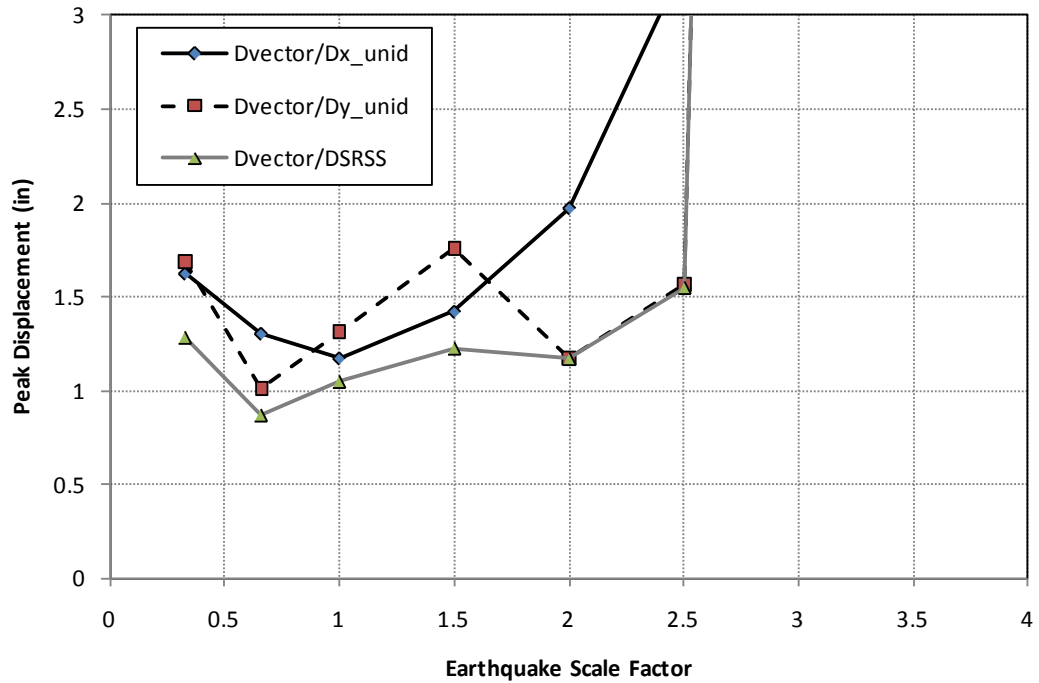
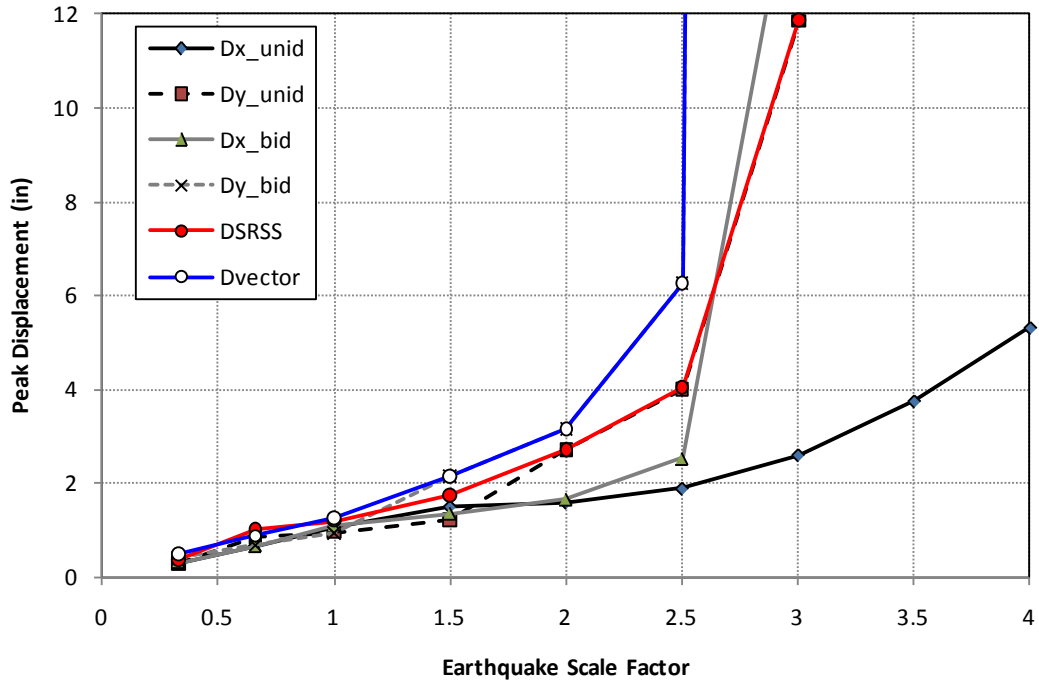
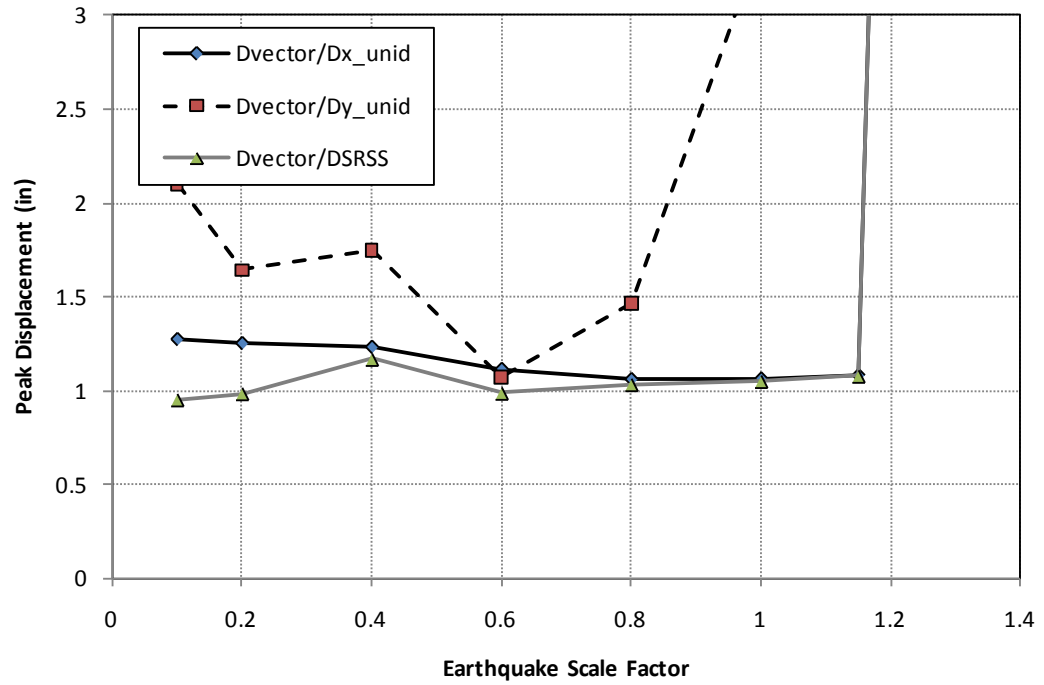
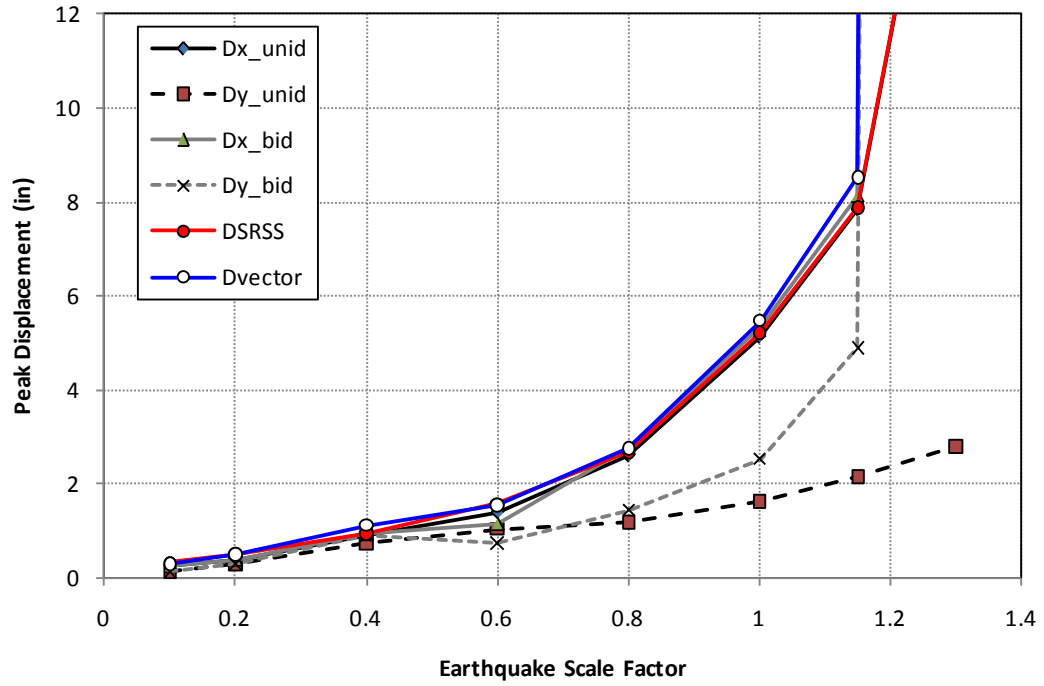


Figure 8-54 Unidirectional vs. Bidirectional at Maximum Displacement, El Centro (Interlocking)



**Figure 8-55 Unidirectional vs. Bidirectional at Maximum Displacement, Los Gatos (Interlocking)**

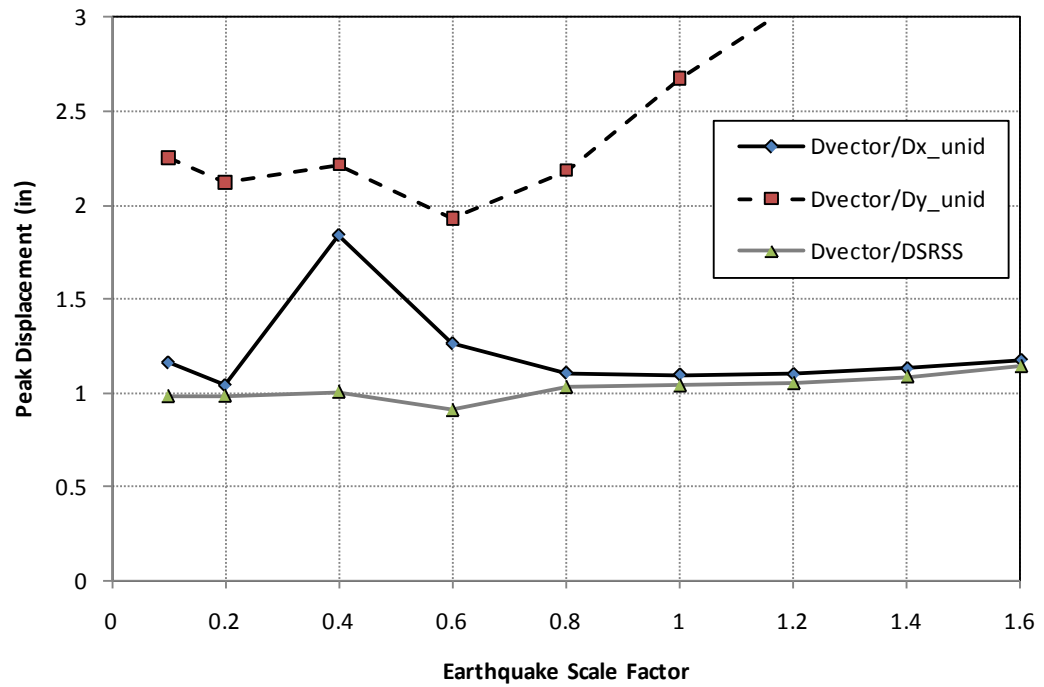
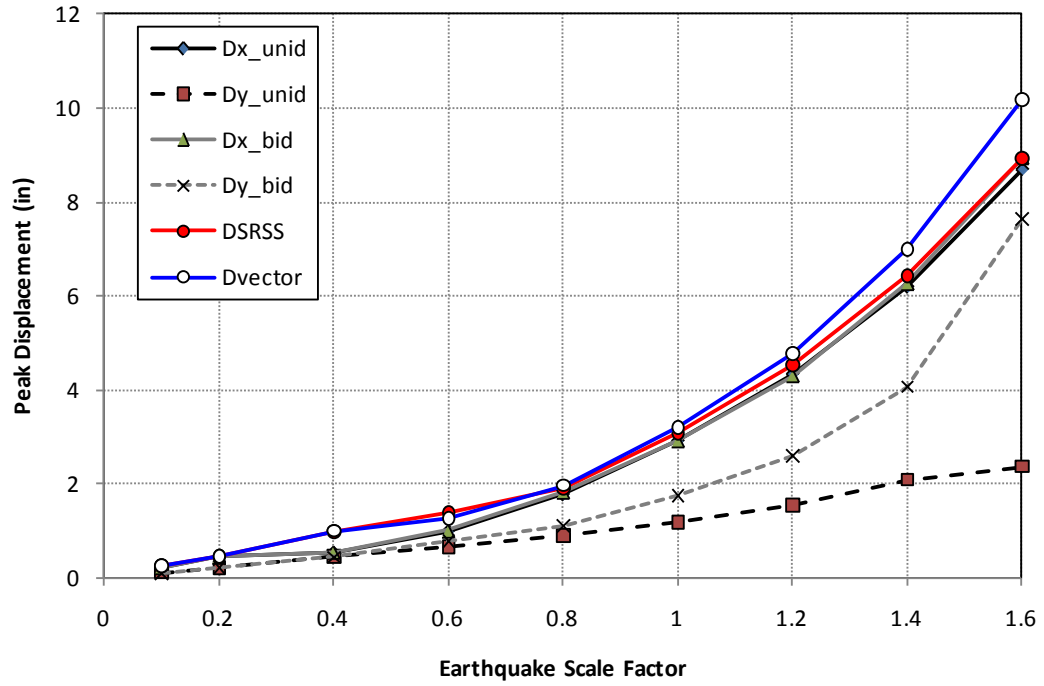


Figure 8-56 Unidirectional vs. Bidirectional at Maximum Displacement, Petrolia (Interlocking)



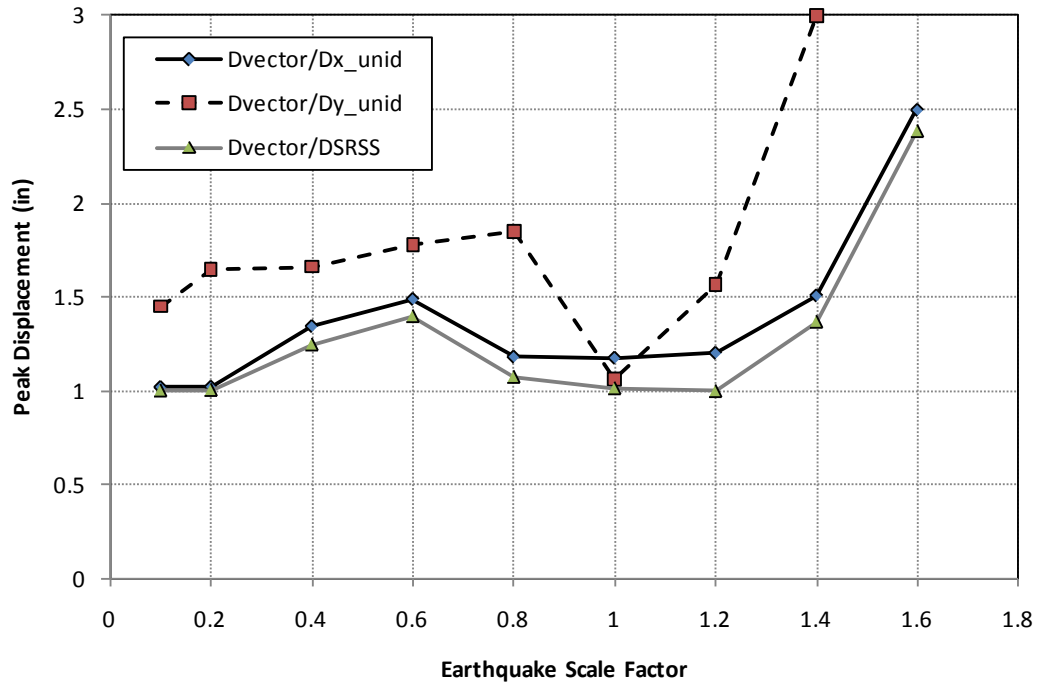
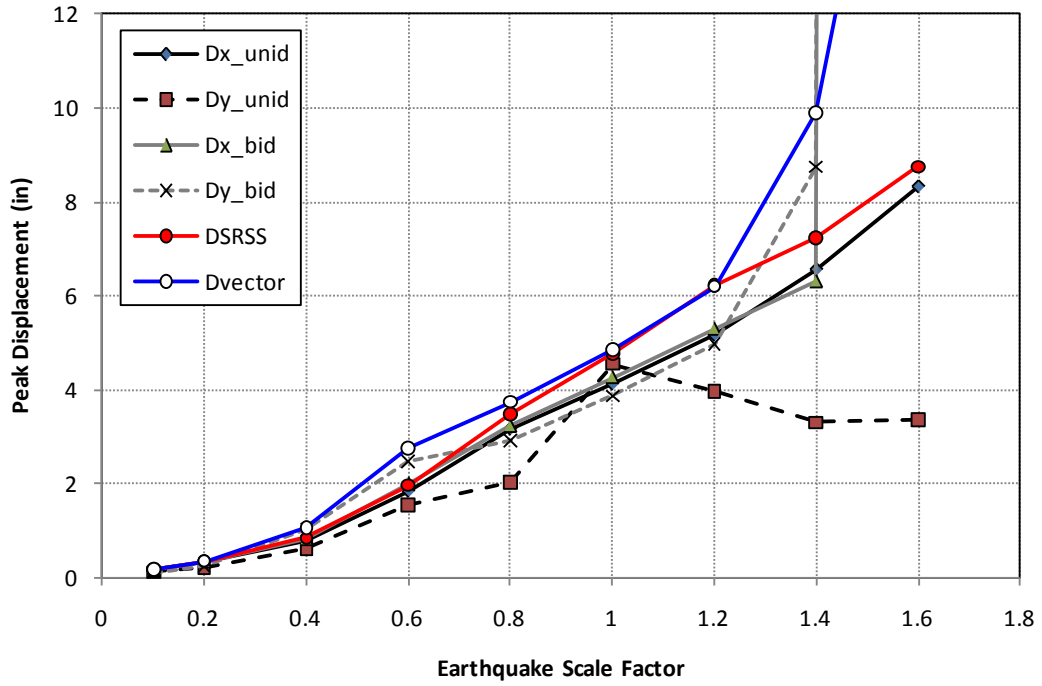


Figure 8-57 Unidirectional vs. Bidirectional at Maximum Displacement, Sylmar (Interlocking)

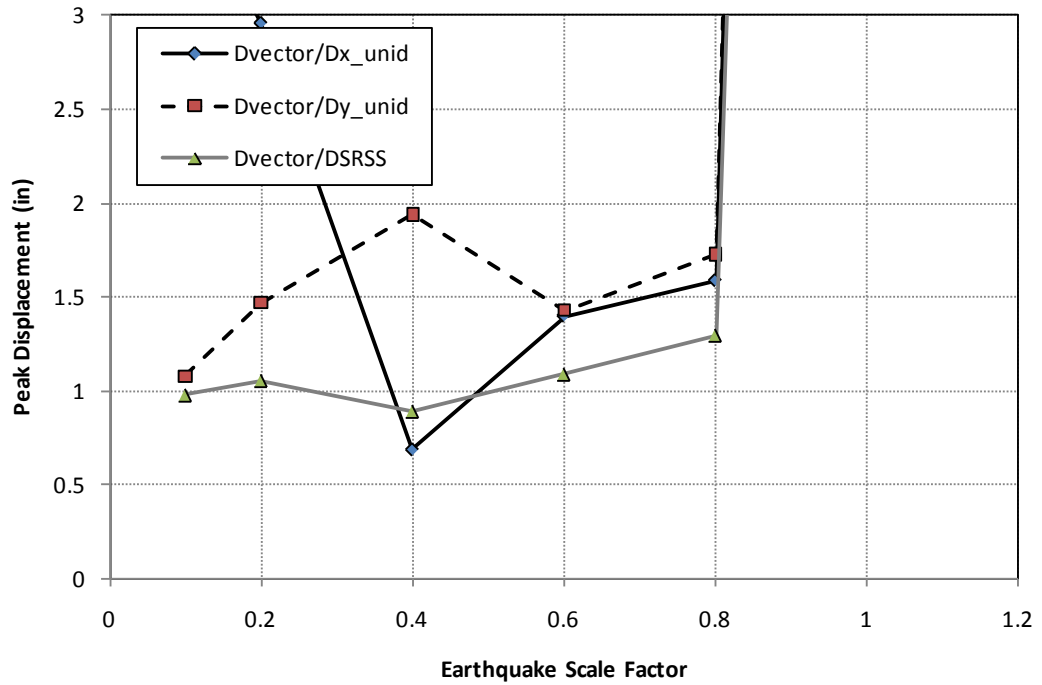
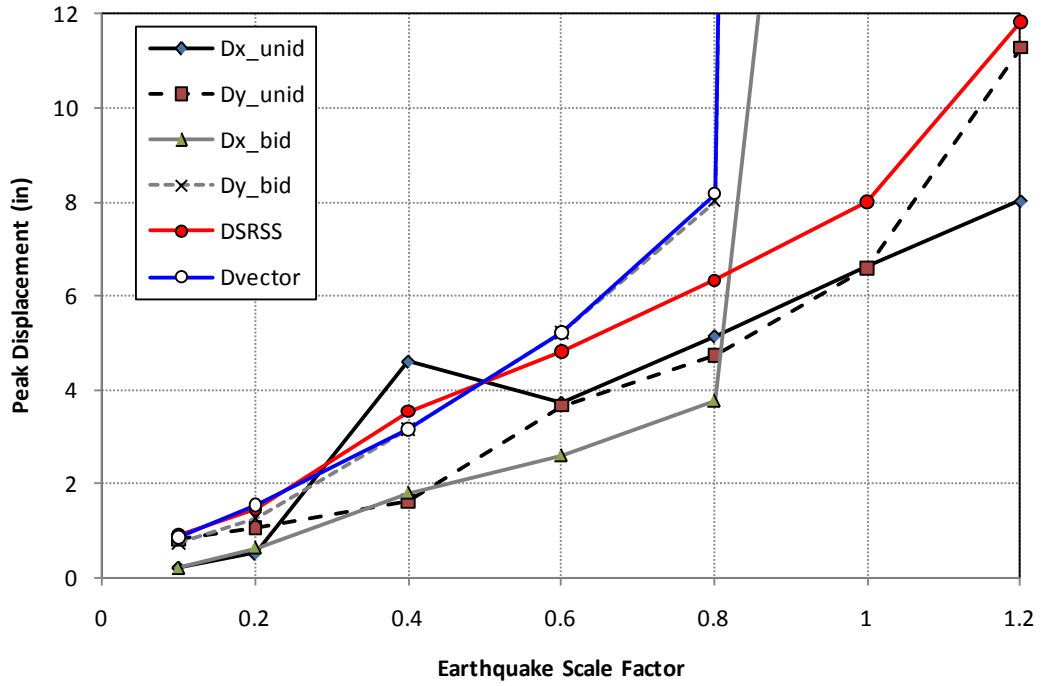





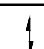

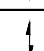

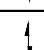

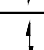




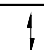
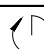
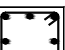



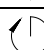

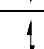
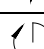



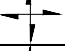
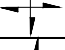
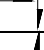
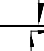






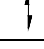

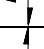
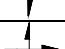
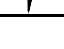



Figure 8-58 Unidirectional vs. Bidirectional at Maximum Displacement, Takatori (Interlocking)

**Table A-1 Summary of RC Columns Tested Using Quasi-static Tests**

Research	Specimen	Section	Scale	Dimensions mm (in)	Height mm (in)	L/d	Curvature path	Reinforcement				f <sub>c</sub> Mpa (psi)	Load path	Path	Axial load KN (Kips)	N/Agf <sub>c</sub>
								Long. (p)	f <sub>y</sub> Mpa (Ksi)	Transverse	f <sub>y</sub> Mpa (Ksi)					
Kalisson, Aoyama and Sozen 5 <sup>th</sup> WCEE, Vol 1. pp 803 - 806 Rome, Italy, 1973	1		1:2	330 x 330 (13 x 13)	1200 (44)	3.64	Single	8 No.7 (2.85)	414 (60)	No.3 @ 41 mm	414 (60)	39 (5660)	Uniaxial-cyclic		445 (100)	10.48
	2		1:2	330 x 330 (13 x 13)	1200 (44)	3.64	Single	8 No.7 (2.85)	414 (60)	No.3 @ 41 mm	414 (60)	37.3 (5410)	Uniaxial-cyclic		890 (200)	21.91
	3		1:2	330 x 330 (13 x 13)	1200 (44)	3.64	Single	8 No.7 (2.85)	414 (60)	No.3 @ 41 mm	414 (60)	36.9 (5350)	Uniaxial-cyclic		1335 (300)	33.22
	4		1:2	330 x 330 (13 x 13)	1200 (44)	3.64	Single	12 No.7 (4.27)	414 (60)	No.3 @ 41 mm 1 No.3 @ 230 mm	414 (60)	39.8 (5770)	Uniaxial-cyclic		890 (200)	20.53
	5		1:2	330 x 330 (13 x 13)	1200 (44)	3.64	Single	8 No.9 (4.74)	414 (60)	No.3 @ 41 mm	414 (60)	40.1 (5820)	Uniaxial-cyclic		890 (200)	20.38
	6		1:2	330 x 330 (13 x 13)	1200 (44)	3.64	Single	12 No.9 (7.10)	414 (60)	No.3 @ 41 mm 1 No.3 @ 230 mm	414 (60)	34.5 (5000)	Uniaxial-cyclic		890 (200)	23.69
Takiguchi, Kokusho Kobayashi, Kimura 7 <sup>th</sup> WCEE, Vol VI. pp 403 - 410 Istambul, Turkey 1980	1		-	150 x 150 (6 x 6)	1250 (50)	8.33	Double	8 No.3 (2.53)	378.5 (55)	1φ 6 mm @ 40 mm	436.9 (63)	26.6 (3867)	Uniaxial-cyclic		9 (2)	1.50
	2		-	150 x 150 (6 x 6)	1250 (50)	8.33	Double	8 No.3 (2.53)	378.5 (55)	1φ 6 mm @ 40 mm	436.9 (63)	26.6 (3867)	Biaxial-cyclic circular phat		9 (2)	1.50
	3		-	150 x 150 (6 x 6)	1250 (50)	8.33	Double	8 No.3 (2.53)	378.5 (55)	1φ 6 mm @ 40 mm	436.9 (63)	26.6 (3867)	Biaxial-cyclic Elliptical phat Diagonal		9 (2)	1.50
	4		-	150 x 150 (6 x 6)	1250 (50)	8.33	Double	8 No.3 (2.53)	378.5 (55)	1φ 6 mm @ 40 mm	436.9 (63)	26.6 (3867)	Uniaxial-cyclic		53 (12)	8.86
	5		-	150 x 150 (6 x 6)	1250 (50)	8.33	Double	8 No.3 (2.53)	378.5 (55)	1φ 6 mm @ 40 mm	436.9 (63)	26.6 (3867)	Biaxial-cyclic circular phat		53 (12)	8.86
	6		-	150 x 150 (6 x 6)	1250 (50)	8.33	Double	8 No.3 (2.53)	372.3 (54)	1φ 6 mm @ 35 mm	259.5 (37.6)	30.3 (4395)	Uniaxial-cyclic		53 (12)	7.77
	7		-	150 x 150 (6 x 6)	1250 (50)	8.33	Double	8 No.3 (2.53)	372.3 (54)	1φ 6 mm @ 35 mm	259.5 (37.6)	30.3 (4395)	Biaxial-cyclic circular phat		53 (12)	7.77
	8		-	150 x 150 (6 x 6)	1250 (50)	8.33	Double	8 No.3 (2.53)	372.3 (54)	1φ 6 mm @ 40 mm	444.7 (64.5)	30.3 (4395)	Uniaxial-cyclic		53 (12)	7.77
	9		-	150 x 150 (6 x 6)	1250 (50)	8.33	Double	8 No.3 (2.53)	372.3 (54)	1φ 6 mm @ 40 mm	444.7 (64.5)	30.3 (4395)	Biaxial-cyclic circular phat		53 (12)	7.77
	10		-	150 x 150 (6 x 6)	1250 (50)	8.33	Double	6 No.3 (1.90)	372.3 (54)	1φ 6 mm @ 35 mm	259.5 (37.6)	30.3 (4395)	Uniaxial-cyclic		53 (12)	7.77
	11		-	150 x 150 (6 x 6)	1250 (50)	8.33	Double	6 No.3 (1.90)	372.3 (54)	1φ 6 mm @ 35 mm	259.5 (37.6)	30.3 (4395)	Uniaxial-cyclic		53 (12)	7.77
	12		-	150 x 150 (6 x 6)	1250 (50)	8.33	Double	6 No.3 (1.90)	372.3 (54)	1φ 6 mm @ 35 mm	259.5 (37.6)	30.3 (4395)	Biaxial-cyclic circular phat		53 (12)	7.77

**Table A-2 Summary of RC Columns Tested Using Quasi-static Tests**

Research	Specimen	Section	Scale	Dimensions mm (in)	Height mm (in)	L/d	Curvature path	Reinforcement				f'c Mpa (psi)	Load path	Path	Axial load KN (Kips)	N/Agf'c
								Long. (p)	f <sub>y</sub> Mpa (Ksi)	Transverse	f <sub>y</sub> Mpa (Ksi)					
Maruyama, Ramirez and Jirsa Journal of Structural Engineering, Vol.110 No.1, pp 120-137 1984	O-U		2:3	305 x 305 (12 x 12)	910 (36)	2.98	Double	8 No.6 (2.44)	334 (54.2)	1φ 6 mm @ 65 mm	466 (68)	34.5 (5000)	Uniaxial-cyclic		0	0.00
	O-B2		2:3	305 x 305 (12 x 12)	910 (36)	2.98	Double	8 No.6 (2.44)	334 (54.2)	1φ 6 mm @ 65 mm	466 (68)	30.3 (4400)	Biaxial-cyclic Previous deform.		0	0.00
	O-B4		2:3	305 x 305 (12 x 12)	910 (36)	2.98	Double	8 No.6 (2.44)	334 (54.2)	1φ 6 mm @ 65 mm	466 (68)	30.3 (4400)	Biaxial-cyclic Previous def.		0	0.00
	O-B		2:3	305 x 305 (12 x 12)	910 (36)	2.98	Double	8 No.6 (2.44)	334 (54.2)	1φ 6 mm @ 65 mm	466 (68)	41.4 (6000)	Biaxial-cyclic Alternate		0	0.00
	O-U2		2:3	305 x 305 (12 x 12)	910 (36)	2.98	Double	8 No.6 (2.44)	450 (65.2)	1φ 6 mm @ 65 mm	466 (68)	37.9 (5500)	Uniaxial-cyclic Const. ortho Deformation		0	0.00
	O-U4		2:3	305 x 305 (12 x 12)	910 (36)	2.98	Double	8 No.6 (2.44)	334 (54.2)	1φ 6 mm @ 65 mm	466 (68)	34.5 (5000)	Uniaxial-cyclic Const. ortho Deformation		0	0.00
	O-Z		2:3	305 x 305 (12 x 12)	910 (36)	2.98	Double	8 No.6 (2.44)	334 (54.2)	1φ 6 mm @ 65 mm	466 (68)	38.6 (5600)	Biaxial-cyclic square in opposite quadrants		0	0.00
	O-S		2:3	305 x 305 (12 x 12)	910 (36)	2.98	Double	8 No.6 (2.44)	450 (65.2)	1φ 6 mm @ 65 mm	466 (68)	36.6 (5300)	Biaxial-cyclic square path		0	0.00
	O-UD		2:3	305 x 305 (12 x 12)	910 (36)	2.98	Double	8 No.6 (2.44)	450 (65.2)	1φ 6 mm @ 65 mm	466 (68)	34.5 (5000)	Uniaxial-cyclic Diagonal		0	0.00
	O-BD		2:3	305 x 305 (12 x 12)	910 (36)	2.98	Double	8 No.6 (2.44)	450 (65.2)	1φ 6 mm @ 65 mm	466 (68)	35.2 (5100)	Biaxial-cyclic Diagonal		0	0.00
	120C-U		2:3	305 x 305 (12 x 12)	910 (36)	2.98	Double	8 No.6 (2.44)	450 (65.2)	1φ 6 mm @ 65 mm	466 (68)	30.3 (4400)	Uniaxial-cyclic		534 (120) cons. comp.	18.95
	50T-U		2:3	305 x 305 (12 x 12)	910 (36)	2.98	Double	8 No.6 (2.44)	334 (54.2)	1φ 6 mm @ 65 mm	466 (68)	35.2 (5100)	Uniaxial-cyclic		223 (50) cons. tens.	6.81
	100T-U		2:3	305 x 305 (12 x 12)	910 (36)	2.98	Double	8 No.6 (2.44)	334 (54.2)	1φ 6 mm @ 65 mm	466 (68)	38.6 (5600)	Uniaxial-cyclic		445 (100) cons. tens.	12.39
	200T-U		2:3	305 x 305 (12 x 12)	910 (36)	2.98	Double	8 No.6 (2.44)	334 (54.2)	1φ 6 mm @ 65 mm	466 (68)	40 (5800)	Uniaxial-cyclic		890 (200) cons. tens.	23.92
	ATC-U		2:3	305 x 305 (12 x 12)	910 (36)	2.98	Double	8 No.6 (2.44)	450 (65.2)	1φ 6 mm @ 65 mm	466 (68)	32.4 (4700)	Uniaxial-cyclic		Alternated tens - comp.	-
	120C-B		2:3	305 x 305 (12 x 12)	910 (36)	2.98	Double	8 No.6 (2.44)	334 (54.2)	1φ 6 mm @ 65 mm	466 (68)	40.7 (5900)	Biaxial-cyclic		534 (120) cons. comp.	14.10
	50T-B		2:3	305 x 305 (12 x 12)	910 (36)	2.98	Double	8 No.6 (2.44)	450 (65.2)	1φ 6 mm @ 65 mm	466 (68)	31.7 (4600)	Biaxial-cyclic		223 (50) cons. comp.	7.56
ATC-B	2:3	305 x 305 (12 x 12)	910 (36)	2.98	Double	8 No.6 (2.44)	450 (65.2)	1φ 6 mm @ 65 mm	466 (68)	34.5 (5000)	Biaxial-cyclic		Alternated tens - comp.	-		

**Table A-3 Summary of RC Columns Tested Using Quasi-static Tests**

Research	Specimen	Section	Scale	Dimensions mm (in)	Height mm (in)	L/d	Curvature path	Reinforcement				f <sub>c</sub> Mpa (psi)	Load path	Path	Axial load KN (Kips)	N/Ag'c	
								Long. (ρ)	f <sub>y</sub> Mpa (Ksi)	Transverse	f <sub>y</sub> Mpa (Ksi)						
Umehara, Jirsa Journal of Structural Engineering, Vol.110 No.3, pp 605-618 1984	O-PM		2:3	305 x 305 (12 x 12)	910 (36)	2.98	Double	8 No.6 (2.44)	366 (53)	1φ 6 mm @ 65 mm	466 (68)	30.0 (4350)	Uniaxial Monotonic	↑	N.A	0.00	
	O-PU		2:3	305 x 305 (12 x 12)	910 (36)	2.98	Double	8 No.6 (2.44)	366 (53)	1φ 6 mm @ 65 mm	466 (68)	34.5 (5000)	Uniaxial-cyclic	↑ ↓	N.A	0.00	
	C-PU		2:3	305 x 305 (12 x 12)	910 (36)	2.98	Double	8 No.6 (2.44)	366 (53)	1φ 6 mm @ 65 mm	466 (68)	30.7 (4450)	Uniaxial-cyclic	↑ ↓	534 (120) cons. comp.	18.70	
	O-PB		2:3	229 x 410 (9 x 16)	910 (36)	3.97 2.22	Double	10 No.6 (3.06)	366 (53)	1φ 6 mm @ 89 mm	466 (68)	41.4 (6000)	Biaxial-cyclic	↕	N.A	0.00	
	C-PB		2:3	229 x 410 (9 x 16)	910 (36)	3.97 2.22	Double	10 No.6 (3.06)	366 (53)	1φ 6 mm @ 89 mm	466 (68)	41.0 (5950)	Biaxial-cyclic	↕	534 (120) cons. comp.	13.87	
	O-DM		2:3	305 x 305 (12 x 12)	910 (36)	2.98	Double	8 No.6 (2.44)	483 (70)	1φ 6 mm @ 65 mm	504 (73)	41.0 (5950)	Uniaxial-monotonic Diagonal	↗	N.A	0.00	
	C-DM		2:3	305 x 305 (12 x 12)	910 (36)	2.98	Double	8 No.6 (2.44)	455 (66)	1φ 6 mm @ 65 mm	511 (74)	36.2 (5250)	Uniaxial-monotonic Diagonal	↗	534 (120) cons. comp.	15.86	
	O-DU		2:3	305 x 305 (12 x 12)	910 (36)	2.98	Double	8 No.6 (2.44)	379 (55)	1φ 6 mm @ 65 mm	466 (68)	34.1 (4950)	Biaxial-cyclic Diagonal	↗ ↘	N.A	0.00	
	O-DB		2:3	229 x 410 (9 x 16)	910 (36)	3.97 2.22	Double	10 No.6 (3.06)	448 (65)	1φ 6 mm @ 89 mm	466 (68)	34.8 (5050)	Biaxial-cyclic Diagonal	↗ ↘	N.A	0.00	
	C-DB		2:3	229 x 410 (9 x 16)	910 (36)	3.97 2.22	Double	10 No.6 (3.06)	455 (66)	1φ 6 mm @ 89 mm	511 (74)	32.1 (4650)	Biaxial-cyclic Diagonal	↗ ↘	534 (120) cons. comp.	17.72	
	OUS		2:3	305 x 305 (12 x 12)	910 (36)	2.98	Double	8 No.6 (2.44)	441 (64)	1φ 6 mm @ 65 mm	414 (60)	40.1 (5810)	Uniaxial-cyclic Strong direction	↑	N.A	0.00	
	OJW		2:3	305 x 305 (12 x 12)	910 (36)	2.98	Double	8 No.6 (2.44)	441 (64)	1φ 6 mm @ 65 mm	414 (60)	40.1 (5820)	Uniaxial-cyclic Weak direction	→	N.A	0.00	
	CMS		2:3	305 x 305 (12 x 12)	910 (36)	2.98	Double	8 No.6 (2.44)	441 (64)	1φ 6 mm @ 65 mm	414 (60)	42 (6090)	Uniaxial-monotonic Strong direction	↑	534 (120) cons. comp.	13.67	
	CUS		2:3	305 x 305 (12 x 12)	910 (36)	2.98	Double	8 No.6 (2.44)	441 (64)	1φ 6 mm @ 65 mm	414 (60)	34.9 (5060)	Uniaxial-cyclic Strong direction	↑	534 (120) cons. comp.	16.45	
	CUW		2:3	305 x 305 (12 x 12)	910 (36)	2.98	Double	8 No.6 (2.44)	441 (64)	1φ 6 mm @ 65 mm	414 (60)	34.9 (5060)	Uniaxial-cyclic Weak direction	→	534 (120) cons. comp.	16.45	
	2CUS		2:3	305 x 305 (12 x 12)	910 (36)	2.98	Double	8 No.6 (2.44)	441 (64)	1φ 6 mm @ 65 mm	414 (60)	42 (6090)	Uniaxial-cyclic Strong direction	↑	1068 (240) cons. comp.	27.34	
	CDS30		2:3	305 x 305 (12 x 12)	910 (36)	2.98	Double	8 No.6 (2.44)	441 (64)	1φ 6 mm @ 65 mm	414 (60)	42.6 (6180)	Biaxial-cyclic Diagonal 30° of Strong direction	↗	534 (120) cons. comp.	13.48	
	CDW30		2:3	305 x 305 (12 x 12)	910 (36)	2.98	Double	8 No.6 (2.44)	441 (64)	1φ 6 mm @ 65 mm	414 (60)	42.2 (6120)	Biaxial-cyclic Diagonal 30° of weak direction	↗	534 (120) cons. comp.	13.60	
	CBSW			2:3	229 x 410 (9 x 16)	910 (36)	3.97 2.22	Double	10 No.6 (3.06)	441 (64)	1φ 6 mm @ 89 mm	414 (60)	35.1 (5090)	Biaxial-cyclic	↕	534 (120) cons. comp.	16.20
	CDSW30			2:3	229 x 410 (9 x 16)	910 (36)	3.97 2.22	Double	10 No.6 (3.06)	441 (64)	1φ 6 mm @ 89 mm	414 (60)	35.1 (5090)	Biaxial-cyclic Diagonal 30° of weak direction	↗	534 (120) cons. comp.	16.20




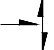





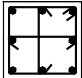
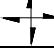

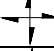
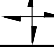


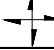


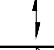

**Table A-4 Summary of RC Columns Tested Using Quasi-static Tests**

Research	Specimen	Section	Scale	Dimensions mm (in)	Height mm (in)	L/d	Curvature path	Reinforcement				f <sub>c</sub> Mpa (psi)	Load path	Path	Axial load KN (Kips)	N/Agf <sub>c</sub>	
								Long. (ρ)	f <sub>y</sub> Mpa (Ksi)	Transverse	f <sub>y</sub> Mpa (Ksi)						
Otani, Cheung and Lai 7 <sup>th</sup> WCEE, Vol X pp 525 - 532 Istanbul, Turkey 1980	SP-1		1:1	305 x 305 (12 x 12)	1524 (60)	5.00	Single	12 No.6 (3.67)	454 (65.83)	3 No.3 @ 127 mm	510 (73.95)	34.2 (4960)	Uniaxial-cyclic		0	0.00	
	SP-2		1:1	305 x 305 (12 x 12)	1524 (60)	5.00	Single	12 No.6 (3.67)	454 (65.83)	3 No.3 @ 127 mm	510 (73.95)	34.2 (4960)	Biaxial-cyclic		0	0.00	
	SP-3		1:1	305 x 305 (12 x 12)	1524 (60)	5.00	Single	8 No.7 (4.39)	441 (63.95)	1 No.3 @ 53 mm	501 (72.65)	33.7 (4890)	Uniaxial-cyclic		0	0.00	
	SP-4		1:1	305 x 305 (12 x 12)	1524 (60)	5.00	Single	8 No.7 (4.39)	441 (63.95)	1 No.3 @ 53 mm	501 (72.65)	33.7 (4890)	Biaxial-cyclic		0	0.00	
	SP-5		1:1	305 x 305 (12 x 12)	1524 (60)	5.00	Single	8 No.7 (4.39)	441 (63.95)	1 No.2 @ 51 mm	236 (34.22)	22.6 (3280)	Uniaxial-cyclic		0	0.00	
	SP-6		1:1	305 x 305 (12 x 12)	1524 (60)	5.00	Single	8 No.7 (4.39)	441 (63.95)	1 No.2 @ 51 mm	236 (34.22)	22.6 (3280)	Biaxial-cyclic		0	0.00	
	SP-7&8		1:1	305 x 305 (12 x 12)	1524 (60)	5.00	Single	8 No.7 (4.39)	466 (67.57)	1 No.2 @ 44 mm 2 types alternately	302 (43.79)	26.7 (3870)	Biaxial-cyclic square path		0	0.00	
Low, Moeble UCB/EERC-87/14 University of California Berkeley, 1987	1		1:4	127 x 165 (5 x 6.5)	545 (21.5)	4.29	Single	4 No.3 6 No.2 (2.26)	448 (64.9) 444 (64.4)	No.1 @ 25 mm (C.Z) No.1 @ 38 mm	414 (60)	36.7 (5318)	Uniaxial-cyclic Weak direction		44.5 (10)	5.79	
	3.30																
	2		1:4	127 x 165 (5 x 6.5)	545 (21.5)	4.29	Single	4 No.3 6 No.2 (2.26)	448 (64.9) 444 (64.4)	No.1 @ 25 mm (C.Z) No.1 @ 38 mm	414 (60)	36.7 (5318)	Biaxial-cyclic Diagonal		44.5 (10)	5.79	
	3.30																
	3		1:4	127 x 165 (5 x 6.5)	545 (21.5)	4.29	Single	4 No.3 6 No.2 (2.26)	448 (64.9) 444 (64.4)	No.1 @ 25 mm (C.Z) No.1 @ 38 mm	414 (60)	36.7 (5318)	Biaxial-cyclic		44.5 (10)	5.79	
3.30																	
4	1:4	127 x 165 (5 x 6.5)	545 (21.5)	4.29	Single	4 No.3 6 No.2 (2.26)	448 (64.9) 444 (64.4)	No.1 @ 25 mm (C.Z) No.1 @ 38 mm	414 (60)	35 (5071)	Biaxial-cyclic Diagonal		2.2 - 89 (0.5 - 20) Variable	0.03 - 12			
3.30																	
5	1:4	127 x 165 (5 x 6.5)	545 (21.5)	4.29	Single	4 No.3 6 No.2 (2.26)	448 (64.9) 444 (64.4)	No.1 @ 25 mm (C.Z) No.1 @ 38 mm	414 (60)	35 (5071)	Biaxial-cyclic		2.2 - 89 (0.5 - 20) Variable	0.3 - 12			
3.30																	
Li, Aoyama, Otani 9 <sup>th</sup> WCEE, Vol III. pp 537 - 542 Tokyo - Japan 1988	U8-0		1:4	200 x 200 (8 x 8)	570 (22.5)	2.85	Single	8 No.3 (1.43)	418 (64.3)	1 No.2 @ 50 mm	386 (56)	27.1 (3930)	Uniaxial-cyclic		76 (17)	7.01	
	U8-1		1:4	200 x 200 (8 x 8)	570 (22.5)	2.85	Single	8 No.3 (1.43)	418 (64.3)	1 No.2 @ 50 mm	386 (56)	27.1 (3930)	Uniaxial-cyclic axial variable		0.0 - 140 (0.0 - 31.5)	0.0 - 13	
	B8-0		1:4	200 x 200 (8 x 8)	570 (22.5)	2.85	Single	8 No.3 (1.43)	418 (64.3)	1 No.2 @ 50 mm	386 (56)	27.1 (3930)	Biaxial-cyclic		76 (17)	7.01	
	B8-1		1:4	200 x 200 (8 x 8)	570 (22.5)	2.85	Single	8 No.3 (1.43)	418 (64.3)	1 No.2 @ 50 mm	386 (56)	27.1 (3930)	Biaxial-cyclic axial variable		0.0 - 140 (0.0 - 31.5)	0.0 - 13	
	B8-2		1:4	200 x 200 (8 x 8)	570 (22.5)	2.85	Single	8 No.3 (1.43)	418 (64.3)	1 No.2 @ 50 mm	386 (56)	30.8 (4470)	30.8 (4470)	Biaxial-cyclic axial variable		-74 - 160 (-16.5 - 36)	-6 - 13
	B40-1		1:4	200 x 200 (8 x 8)	570 (22.5)	2.85	Single	8 No.3 (1.43)	418 (64.3)	1 No.2 @ 50 mm	386 (56)	30.8 (4470)	30.8 (4470)	Biaxial-cyclic axial variable		235 - 550 (53 - 125)	19 - 45
	B40-2		1:4	200 x 200 (8 x 8)	570 (22.5)	2.85	Single	8 No.3 (1.43)	418 (64.3)	1 No.2 @ 50 mm	386 (56)	30.8 (4470)	30.8 (4470)	Biaxial-cyclic axial variable		160 - 640 (36 - 145)	13 - 52

**Table A-5 Summary of RC Columns Tested Using Quasi-static Tests**


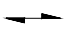

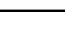
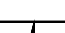



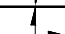

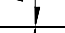



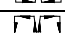


Research	Specimen	Section	Scale	Dimensions mm (in)	Height mm (in)	L/d	Curvature path	Reinforcement				f <sub>c</sub> Mpa (psi)	Load path	Path	Axial load KN (Kips)	N/Agf <sub>c</sub>
								Long. (ρ)	f <sub>y</sub> Mpa (Ksi)	Transverse	f <sub>y</sub> Mpa (Ksi)					
Saaticioglu, Ozcebe ACI Structural Journal Vol.86 No.1, pp 3-12 Jan-Feb, 1989	U1		1:1	350 x 350 (14 x 14)	1000 (40)	2.86	Single	8 No.8 (3.27)	430 (62.4)	1No.3 @ 150 mm	470 (68.1)	43.6 (6310)	Uniaxial-cyclic		N.A	0.00
	U2		1:1	350 x 350 (14 x 14)	1000 (40)	2.86	Single	8 No.8 (3.27)	453 (65.7)	1No.3 @ 150 mm	470 (68.1)	30.2 (4380)	Uniaxial-cyclic		600 (135)	16.22
	U3		1:1	350 x 350 (14 x 14)	1000 (40)	2.86	Single	8 No.8 (3.27)	430 (62.4)	1No.3 @ 75 mm	470 (68.1)	34.8 (5045)	Uniaxial-cyclic		600 (135)	14.07
	U4		1:1	350 x 350 (14 x 14)	1000 (40)	2.86	Single	8 No.8 (3.27)	438 (63.5)	1No.3 @ 50 mm	470 (68.1)	32.0 (4640)	Uniaxial-cyclic		600 (135)	15.31
	U5		1:1	350 x 350 (14 x 14)	1000 (40)	2.86	Single	8 No.8 (3.27)	430 (62.4)	1No.3 @ 150 mm	470 (68.1)	49.3 (7150)	Uniaxial-cyclic		Variable	-
	U6		1:1	350 x 350 (14 x 14)	1000 (40)	2.86	Single	8 No.8 (3.27)	437 (63.4)	1No.2 @ 65 mm Ties No.2 @ 65 mm	425 (61.6)	37.3 (5410)	Uniaxial-cyclic		600 (135)	13.13
	U7		1:1	350 x 350 (14 x 14)	1000 (40)	2.86	Single	8 No.8 (3.27)	437 (63.4)	1No.2 @ 65 mm Ties No.2 @ 65 mm	425 (61.6)	39.0 (5655)	Uniaxial-cyclic		600 (135)	12.56
	D1		1:1	350 x 350 (14 x 14)	1000 (40)	2.86	Single	8 No.8 (3.27)	453 (65.7)	1No.3 @ 150 mm	470 (68.1)	40.3 (5845)	Biaxial-cyclic Diagonal		N.A	0.00
	D2		1:1	350 x 350 (14 x 14)	1000 (40)	2.86	Single	8 No.8 (3.27)	453 (65.7)	1No.3 @ 150 mm	470 (68.1)	30.2 (4380)	Biaxial-cyclic Diagonal		600 (135)	16.22
	D3		1:1	350 x 350 (14 x 14)	1000 (40)	2.86	Single	8 No.8 (3.27)	430 (62.4)	1No.3 @ 75 mm	470 (68.1)	34.8 (5045)	Biaxial-cyclic Diagonal		600 (135)	14.07
	D4		1:1	350 x 350 (14 x 14)	1000 (40)	2.86	Single	8 No.8 (3.27)	430 (62.4)	1No.3 @ 50 mm	470 (68.1)	43.6 (6320)	Biaxial-cyclic Diagonal		600 (135)	11.23
	D5		1:1	350 x 350 (14 x 14)	1000 (40)	2.86	Single	8 No.8 (3.27)	430 (62.4)	1No.3 @ 150 mm	470 (68.1)	49.3 (7150)	Biaxial-cyclic Diagonal		Variable	-
	B1		1:1	350 x 350 (14 x 14)	1000 (40)	2.86	Single	8 No.8 (3.27)	438 (63.5)	1No.3 @ 50 mm	470 (68.1)	32.0 (4640)	Biaxial-cyclic		600 (135)	15.31
	B2		1:1	350 x 350 (14 x 14)	1000 (40)	2.86	Single	8 No.8 (3.27)	437 (63.4)	1No.3 @ 75 mm	470 (68.1)	39.5 (5730)	Biaxial-cyclic		600 (135)	12.40
Zahn, Park and Priestley ACI Structural Journal Vol.56 No.2, pp 123-131 Mar-Apr, 1989	1		1:1	400 x 400 (15.7 x 15.7)	2000 (78.7)	5.00	Double	12 No.5 (1.48)	423 (61.3)	1No.3 @ 84 mm	318 (46.1)	32.0 (5245)	Uniaxial-cyclic Diagonal		1200	23.44
	2		1:1	400 x 400 (15.7 x 15.7)	2000 (78.7)	5.00	Double	12 No.5 (1.48)	423 (61.3)	1No.3 @ 65 mm	318 (46.1)	28.8 (4175)	Uniaxial-cyclic Diagonal		2000	43.40
	3		1:1	400 x 400 (15.7 x 15.7)	2000 (78.7)	5.00	Double	12 No.5 (1.48)	423 (61.3)	1No.3 @ 72 mm	318 (46.1)	32.3 (4680)	Uniaxial-cyclic Diagonal		1200	23.22
	4		1:1	400 x 400 (15.7 x 15.7)	2000 (78.7)	5.00	Double	12 No.5 (1.48)	423 (61.3)	1No.3 @ 55 mm	318 (46.1)	27.0 (3915)	Uniaxial-cyclic Diagonal		1800	41.67

**Table A-6 Summary of RC Columns Tested Using Quasi-static Tests**














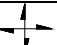


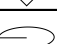






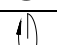
Research	Specimen	Section	Scale	Dimensions mm (in)	Height mm (in)	L/d	Curvature path	Reinforcement				f'c Mpa (psi)	Load path	Path	Axial load KN (Kips)	N/Agf'c
								Long. (p)	f <sub>y</sub> Mpa (Ksi)	Transverse	f <sub>y</sub> Mpa (Ksi)					
Bousias, Verzeletti Magonette, Fardis 10 <sup>th</sup> WCEE Madrid, Spain 1992	1			250 x 250 (10 x 10)	1500 (60)	6.00	Single	8 No.5 (2.53)	440 (63.8)	φ 8 mm @ 70 mm	660 (95.7)	31 (4495)	Biaxial Monotonic in X Cyclic in Y		291 (65.4)	15.02
	2			250 x 250 (10 x 10)	1500 (60)	6.00	Single	8 No.5 (2.53)	440 (63.8)	φ 8 mm @ 70 mm	660 (95.7)	28 (4060)	Biaxial-cyclic circular path		52.5 - 291 (11.8 - 65.4) Variable	3 to 17
	3			250 x 250 (10 x 10)	1500 (60)	6.00	Single	8 No.5 (2.53)	440 (63.8)	φ 8 mm @ 70 mm	660 (95.7)	30 (4350)	Biaxial Monotonic in Y Cyclic in X		319 (71.8)	17.01
	4			250 x 250 (10 x 10)	1500 (60)	6.00	Single	8 No.5 (2.53)	440 (63.8)	φ 8 mm @ 70 mm	660 (95.7)	28 (4060)	Biaxial Monotonic in Y Cyclic in X		263 (59)	15.03
	5			250 x 250 (10 x 10)	1500 (60)	6.00	Single	8 No.5 (2.53)	440 (63.8)	φ 8 mm @ 70 mm	660 (95.7)	26 (3770)	Biaxial-cyclic Triangular path in opposit quadrants		195 (43.8)	12.00
	6			250 x 250 (10 x 10)	1500 (60)	6.00	Single	8 No.5 (2.53)	440 (63.8)	φ 8 mm @ 70 mm	660 (95.7)	33 (4785)	Biaxial-cyclic Triangular path in opposit quadrants		206 (46.4)	9.99
	7			250 x 250 (10 x 10)	1500 (60)	6.00	Single	8 No.5 (2.53)	440 (63.8)	φ 8 mm @ 70 mm	660 (95.7)	25.5 (4700)	Biaxial-cyclic Square path		191 (43)	11.98
	8			250 x 250 (10 x 10)	1500 (60)	6.00	Single	8 No.5 (2.53)	440 (63.8)	φ 8 mm @ 70 mm	660 (95.7)	28 (4060)	Biaxial-cyclic Square path		193 (43.3)	11.03
Ogawa, Shibucha and Moshi 10 <sup>th</sup> WCEE Madrid, Spain 1992	BC-1		1:1	500 x 500 (20 x 20)	1100 (44)	2.20	Single	8 No.6 (0.92)	371.7 (54)	No.3 @ 100 mm	384.5 (56)	24.9 (3610)	Biaxial-cyclic		1542 (347)	24.77
	BC-2		1:1	500 x 500 (20 x 20)	1100 (44)	2.20	Single	8 No.6 (0.92)	371.7 (54)	No.3 @ 100 mm	384.5 (56)	28 (4060)	Biaxial-cyclic Square path		1570 (353)	22.43
	BC-3		1:1	500 x 500 (20 x 20)	1100 (44)	2.20	Single	8 No.6 (0.92)	364.7 (53)	No.3 @ 100 mm	347.4 (50)	24.8 (3595)	Biaxial-cyclic		1713 (385)	27.63
	BC-4		1:1	500 x 500 (20 x 20)	1100 (44)	2.20	Single	8 No.6 (0.92)	364.7 (53)	No.3 @ 100 mm	347.4 (50)	24.9 (3610)	Biaxial-cyclic		1731 (389)	27.81
	BC-5		1:1	500 x 500 (20 x 20)	1100 (44)	2.20	Single	8 No.6 (0.92)	364.7 (53)	No.3 @ 100 mm	347.4 (50)	25.4 (3685)	Biaxial-cyclic Diagonal		1718 (387)	27.06
	BC-6		1:1	500 x 500 (20 x 20)	1100 (44)	2.20	Single	8 No.6 (0.92)	364.7 (53)	No.3 @ 100 mm	347.4 (50)	32.2 (4670)	Biaxial-cyclic circular path		1717 (386)	21.33
	BC-7		1:1	500 x 500 (20 x 20)	1100 (44)	2.20	Single	8 No.6 (0.92)	364.7 (53)	No.3 @ 100 mm	347.4 (50)	28.2 (40.90)	Biaxial-cyclic		1687 (380)	23.93
	BC-8		1:1	500 x 500 (20 x 20)	1100 (44)	2.20	Single	8 No.6 (0.92)	364.7 (53)	No.3 @ 100 mm	347.4 (50)	28.6 (4150)	Biaxial-cyclic Elliptical path		1720 (387)	24.06
	BC-9		1:1	500 x 500 (20 x 20)	1100 (44)	2.20	Single	8 No.6 (0.92)	366.8 (53)	No.3 @ 100 mm	344.9 (50)	20.3 (2945)	Biaxial-cyclic circular path		1571 (353)	30.96
	BC-10		1:1	500 x 500 (20 x 20)	1100 (44)	2.20	Single	8 No.6 (0.92)	366.8 (53)	No.3 @ 100 mm	344.9 (50)	19.2 (2785)	Uniaxial-cyclic		1575 (354)	32.81
	BC-11		1:1	500 x 500 (20 x 20)	1100 (44)	2.20	Single	8 No.6 (0.92)	366.8 (53)	No.3 @ 100 mm	344.9 (50)	20.7 (3000)	Biaxial-cyclic Elliptical path		1543 (347)	29.82



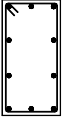

**Table A-7 Summary of RC Columns Tested Using Quasi-static Tests**

Research	Specimen	Section	Scale	Dimensions mm (in)	Height mm (in)	L/d	Curvature path	Reinforcement				f <sub>c</sub> Mpa (psi)	Load path	Path	Axial load KN (Kips)	N/Agf <sub>c</sub>
								Long. (ρ)	f <sub>y</sub> Mpa (Ksi)	Transverse	f <sub>y</sub> Mpa (Ksi)					
Wong, Paulay and Priestley ACI Structural Journal Vol.90 No.2, pp 180-191 Mar-Apr, 1993	1		1:1	400 (15.7)	800 (31.5)	2.00	Single	20 No.5 (3.15)	423 (61.3)	φ 10 mm @ 60 mm Spiral	300 (43.5)	38 (5510)	Uniaxial-cyclic		925 (208)	19.37
	2		1:1	400 (15.7)	800 (31.5)	2.00	Single	20 No.5 (3.15)	475 (68.8)	φ 6 mm @ 65 mm Spiral	340 (49.3)	37 (5360)	Uniaxial-cyclic		1830 (411)	39.36
	3		1:1	400 (15.7)	800 (31.5)	2.00	Single	20 No.5 (3.15)	475 (68.8)	φ 10 mm @ 60 mm Spiral	300 (43.5)	37 (5360)	Uniaxial-cyclic		1830 (411)	39.36
	4		1:1	400 (15.7)	800 (31.5)	2.00	Single	20 No.5 (3.15)	475 (68.8)	φ 6 mm @ 80 mm Spiral	340 (49.3)	42 (6085)	Biaxial-cyclic		0 (0)	0.00
	5		1:1	400 (15.7)	800 (31.5)	2.00	Single	20 No.5 (3.15)	475 (68.8)	φ 6 mm @ 50 mm Spiral	340 (49.3)	41 (5940)	Biaxial-cyclic		0 (0)	0.00
	6		1:1	400 (15.7)	800 (31.5)	2.00	Single	20 No.5 (3.15)	475 (68.8)	φ 6 mm @ 30 mm Spiral	340 (49.3)	42 (6085)	Biaxial-cyclic		0 (0)	0.00
	7		1:1	400 (15.7)	800 (31.5)	2.00	Single	20 No.5 (3.15)	475 (68.8)	φ 6 mm @ 60 mm Spiral	340 (49.3)	39.0 (5655)	Biaxial-cyclic		935 (210)	19.08
	8		1:1	400 (15.7)	800 (31.5)	2.00	Single	20 No.5 (3.15)	475 (68.8)	φ 6 mm @ 30 mm Spiral	340 (49.3)	39 (5655)	Biaxial-cyclic		935 (210)	19.08
	9		1:1	400 (15.7)	800 (31.5)	2.00	Single	20 No.5 (3.15)	475 (68.8)	φ 6 mm @ 40 mm Spiral	340 (49.3)	27 (3915)	Biaxial-cyclic		1287 (289)	37.93
	10		1:1	400 (15.7)	1000 (40)	2.50	Single	20 No.5 (3.15)	475 (68.8)	φ 10 mm @ 65 mm Spiral	300 (43.5)	37 (5360)	Biaxial-cyclic		1815 (408)	39.04
	11		1:1	400 (15.7)	1000 (40)	2.50	Single	20 No.5 (3.15)	475 (68.8)	φ 6 mm @ 30 mm Spiral	340 (49.3)	42 (6085)	Biaxial-cyclic square in opposite quadrants		0 (0)	0.00
	12		1:1	400 (15.7)	1000 (40)	2.50	Single	20 No.5 (3.15)	475 (68.8)	φ 10 mm @ 35 mm Spiral	300 (43.5)	27 (3915)	Biaxial-cyclic square in opposite quadrants		0 (0)	0.00
	13		1:1	400 (15.7)	1000 (40)	2.50	Single	20 No.5 (3.15)	475 (68.8)	φ 6 mm @ 30 mm Spiral	340 (49.3)	39 (5650)	Biaxial-cyclic square in opposite quadrants		935 (210)	19.08
	14		1:1	400 (15.7)	1000 (40)	2.50	Single	20 No.5 (3.15)	475 (68.8)	φ 10 mm @ 60 mm Spiral	300 (43.5)	38 (5510)	Biaxial-cyclic square in opposite quadrants		910 (205)	19.06
	15		1:1	400 (15.7)	1000 (40)	2.50	Single	20 No.5 (3.15)	475 (68.8)	φ 10 mm @ 60 mm Spiral	300 (43.5)	27 (3915)	Biaxial-cyclic square in opposite quadrants		1287 (289)	37.93
	16		1:1	400 (15.7)	1000 (40)	2.50	Single	20 No.5 (3.15)	475 (68.8)	φ 6 mm @ 30 mm Spiral	340 (49.3)	38 (5510)	Multidirectional		910 (205)	19.06

**Table A-8 Summary of RC Columns Tested Using Quasi-static Tests**

Research	Specimen	Section	Scale	Dimensions mm (in)	Height mm (in)	L/d	Curvature path	Reinforcement				f <sub>c</sub> Mpa (psi)	Load path	Path	Axial load KN (Kips)	N/Ag'c
								Long. (ρ)	f <sub>y</sub> Mpa (Ksi)	Transverse	f <sub>y</sub> Mpa (Ksi)					
Kuramoto, Kabeyasawa and Shen ACI Structural Journal Vol.92 No.5, pp 610-618 Sep-Oct, 1995	N-1		1:3	250 x 250 (10 x 10)	1000 (40)	4.00	Double	12 No.4 (2.44)	717 (103.9)	φ 5 mm @ 40 mm	1380 (200)	65.4 (9485)	Biaxial-cyclic square in opposite quadrants		1500 (337.5)	36.70
	N-2		1:3	250 x 250 (10 x 10)	1000 (40)	4.00	Double	12 No.4 (2.44)	717 (103.9)	φ 5 mm @ 40 mm	1380 (200)	65.4 (9485)	Biaxial-cyclic square in opposite quadrants		-500 to 2500 (-113 to 563)	-12 to 62
	N-3		1:3	250 x 250 (10 x 10)	1000 (40)	4.00	Double	12 No.4 (2.44)	717 (103.9)	φ 5 mm @ 60 mm	1380 (200)	60.3 (8745)	Biaxial-cyclic square in opposite quadrants		-400 to 2300 (-90 to 518)	-10 to 61
	N-4		1:3	250 x 250 (10 x 10)	1000 (40)	4.00	Double	12 No.4 (2.44)	717 (103.9)	φ 5 mm @ 60 mm	1380 (200)	60.3 (8745)	Biaxial-cyclic square in opposite quadrants		250 to 2250 (56 to 506)	-6 to 59
Yoshimura, Tsumura 11 <sup>th</sup> WCEE Mexico 1996	S205		1:1	400 x 400 (16 x 16)	1200 (48)	3.00	Single	12 No.6 (2.14)	375 (54.4)	No.4 @ 60 mm	347 (50.3)	25.2 (3655)	Biaxial Monotonic in Y Cyclic in X		785 (177)	19.47
	S405		1:1	400 x 400 (16 x 16)	1200 (48)	3.00	Single	12 No.6 (2.14)	375 (54.4)	No.4 @ 60 mm	347 (50.3)	25.2 (3655)	Biaxial Monotonic in Y Cyclic in X		1570 (353)	38.94
	S210		1:1	400 x 400 (16 x 16)	1200 (48)	3.00	Single	12 No.6 (2.14)	375 (54.4)	No.4 @ 60 mm	347 (50.3)	25.2 (3655)	Biaxial Monotonic in Y Cyclic in X		785 (177)	19.47
	S410		1:1	400 x 400 (16 x 16)	1200 (48)	3.00	Single	12 No.6 (2.14)	375 (54.4)	No.4 @ 60 mm	347 (50.3)	25.2 (3655)	Biaxial Monotonic in Y Cyclic in X		1570 (353)	38.94
Qiu, Li, Pang, Qian Engineering Structures V.24 2002	1			200 x 200 (7.9 x 7.9)	760 (30)	3.80	Single	8 No.4 (2.53)	-	φ 6 mm @ 500 mm	-	39.6 (5742)	Uniaxial-cyclic		350 (78.8)	22.10
	2			200 x 200 (7.9 x 7.9)	760 (30)	3.80	Single	8 No.4 (2.53)	-	φ 6 mm @ 500 mm	-	40.9 (5930)	Uniaxial-cyclic Diagonal		350 (78.8)	21.39
	3			200 x 200 (7.9 x 7.9)	760 (30)	3.80	Single	8 No.4 (2.53)	-	φ 6 mm @ 500 mm	-	37.7 (5467)	Biaxial-cyclic		350 (78.8)	23.21
	4			200 x 200 (7.9 x 7.9)	760 (30)	3.80	Single	8 No.4 (2.53)	-	φ 6 mm @ 500 mm	-	37.5 (5467)	Biaxial-cyclic Square path		350 (78.8)	23.33
	5			200 x 200 (7.9 x 7.9)	760 (30)	3.80	Single	8 No.4 (2.53)	-	φ 6 mm @ 500 mm	-	38.9 (5640)	Biaxial-cyclic Square path		350 (78.8)	22.49
	6			200 x 200 (7.9 x 7.9)	760 (30)	3.80	Single	8 No.4 (2.53)	-	φ 6 mm @ 500 mm	-	38.2 (5540)	Biaxial-cyclic Elliptical path		360 (81)	23.56
	7			200 x 200 (7.9 x 7.9)	760 (30)	3.80	Single	8 No.4 (2.53)	-	φ 6 mm @ 500 mm	-	34.8 (5046)	Biaxial-cyclic square in opposite quadrants		300 (68)	21.55
Kawashima et al. 8 <sup>th</sup> US National Conf. on Earthquake Eng. California, US 2006	C-1		1:1	400 x 400 (16 x 16)	1350 (55)	3.38	Single	16 No.4 (1.27)	295 (42.8)	φ 6 mm @ 500 mm	295 (42.8)	28.2 (4089)	Uniaxial-cyclic		160 (36)	3.55
	C-2		1:1	400 x 400 (16 x 16)	1350 (55)	3.38	Single	16 No.4 (1.27)	295 (42.8)	φ 6 mm @ 500 mm	295 (42.8)	28.0 (4060)	Biaxial-cyclic Diagonal		160 (36)	3.57
	C-3		1:1	400 x 400 (16 x 16)	1350 (55)	3.38	Single	16 No.4 (1.27)	295 (42.8)	φ 6 mm @ 500 mm	295 (42.8)	28.6 (4147)	Biaxial-cyclic square in opposite quadrants		160 (36)	3.50
	C-4		1:1	400 x 400 (16 x 16)	1350 (55)	3.38	Single	16 No.4 (1.27)	295 (42.8)	φ 6 mm @ 500 mm	295 (42.8)	26.4 (3828)	Biaxial-cyclic Circular path		160 (36)	3.79
	C-5		1:1	400 x 400 (16 x 16)	1350 (55)	3.38	Single	16 No.4 (1.27)	295 (42.8)	φ 6 mm @ 500 mm	295 (42.8)	26.7 (3872)	Biaxial-cyclic Elliptical path		160 (36)	3.75


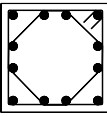
**Table A-9 Summary of RC Columns Tested Using Quasi-static Tests under Lateral Loading and Torsion**

Research	Specimen	Section	Scale	Dimensions mm (in)	Height mm (in)	L/d	Curvature path	Reinforcement			f <sub>c</sub> Mpa (psi)	Load path	Path	Axial load KN (Kips)	N/Agf <sub>c</sub> %	
								Long. (ρ%)	f <sub>y</sub> Mpa (Ksi)	Transverse						f <sub>y</sub> Mpa (Ksi)
Nguyen and Irawan FIB Symposium on Concrete Structures in Seismic regions Athens, Greece 2003	U0		-	200 x 400 (8 x 16)	1200 (48)	3.00	Double	10 No.6 (4.1)	540 (78.4)	φ 8 mm @ 100 mm Hops (ρ <sub>v</sub> =0.88)	300 (43.5)	61.2 (8882)	Uniaxial-cyclic Shear	↑↓	2010 (452)	41.05
	U90		-	200 x 400 (8 x 16)	1200 (48)	3.00	Double	10 No.6 (4.1)	540 (78.4)	φ 8 mm @ 100 mm Hops (ρ <sub>v</sub> =0.88)	300 (43.5)	61.2 (8882)	Uniaxial-cyclic Shear	←→	2010 (452)	41.05
	B30		-	200 x 400 (8 x 16)	1200 (48)	3.00	Double	10 No.6 (4.1)	540 (78.4)	φ 8 mm @ 100 mm Hops (ρ <sub>v</sub> =0.88)	300 (43.5)	61.2 (8882)	Biaxial-cyclic Shear @ 30°	↗↘	2010 (452)	41.05
	B60		-	200 x 400 (8 x 16)	1200 (48)	3.00	Double	10 No.6 (4.1)	540 (78.4)	φ 8 mm @ 100 mm Hops (ρ <sub>v</sub> =0.88)	300 (43.5)	61.2 (8882)	Biaxial-cyclic Shear @ 60°	↗↘	2010 (452)	41.05
	UT0		-	200 x 400 (8 x 16)	1200 (48)	3.00	Double	10 No.6 (4.1)	540 (78.4)	φ 8 mm @ 100 mm Hops (ρ <sub>v</sub> =0.88)	300 (43.5)	64.1 (9303)	Uniaxial-cyclic Shear-Torsion	↑↓	2010 (452)	39.20
	UT90		-	200 x 400 (8 x 16)	1200 (48)	3.00	Double	10 No.6 (4.1)	540 (78.4)	φ 8 mm @ 100 mm Hops (ρ <sub>v</sub> =0.88)	300 (43.5)	64.1 (9303)	Uniaxial-cyclic Shear-Torsion	←→	2010 (452)	39.20
	BT30		-	200 x 400 (8 x 16)	1200 (48)	3.00	Double	10 No.6 (4.1)	540 (78.4)	φ 8 mm @ 100 mm Hops (ρ <sub>v</sub> =0.88)	300 (43.5)	64.1 (9303)	Biaxial-cyclic Shear-Torsion	↗↘	2010 (452)	39.20
	BT60		-	200 x 400 (8 x 16)	1200 (48)	3.00	Double	10 No.6 (4.1)	540 (78.4)	φ 8 mm @ 100 mm Hops (ρ <sub>v</sub> =0.88)	300 (43.5)	64.1 (9303)	Biaxial-cyclic Shear-Torsion	↗↘	2010 (452)	39.20
	T		-	200 x 400 (8 x 16)	1200 (48)	3.00	Single	10 No.6 (4.1)	540 (78.4)	φ 8 mm @ 100 mm Hops (ρ <sub>v</sub> =0.88)	300 (43.5)	64.1 (9303)	Cyclic Torsion	↻	2010 (452)	39.20
Otzuka et al. Proceedings 13th WCEE Vancouver, Canada 2004 Paper No. 393	1		-	400 x 400 (16 x 16)	1600 (64)	4.00	Single	16 No.4 (1.48)	360 (52)	φ 6 mm @ 30 mm Hops	340 (49)	35.3 (5120)	Cyclic Torsion (T/M=∞)	↻	640 (1440)	11.33
	2		-	400 x 400 (16 x 16)	1600 (64)	4.00	Single	16 No.4 (1.48)	360 (52)	φ 6 mm @ 30 mm Hops	340 (49)	49.3 (7155)	Cyclic Bending + Torsion (T/M=1.73)	↑↓	640 (1440)	8.11
	3		-	400 x 400 (16 x 16)	1600 (64)	4.00	Single	16 No.4 (1.48)	360 (52)	φ 6 mm @ 30 mm Hops	340 (49)	47.5 (6895)	Cyclic Bending + Torsion (T/M=0.58)	↑↓	640 (1440)	8.42
	4		-	400 x 400 (16 x 16)	1600 (64)	4.00	Single	16 No.4 (1.48)	360 (52)	φ 6 mm @ 30 mm Hops	340 (49)	40.6 (5890)	Cyclic Bending (T/M=0)	↑↓	640 (1440)	9.85
	5		-	400 x 400 (16 x 16)	1600 (64)	4.00	Single	16 No.4 (1.48)	360 (52)	φ 6 mm @ 60 mm Hops	340 (49)	45.7 (6630)	Cyclic Torsion (T/M=∞)	↻	640 (1440)	8.75
	6		-	400 x 400 (16 x 16)	1600 (64)	4.00	Single	16 No.4 (1.48)	360 (52)	φ 6 mm @ 60 mm Hops	340 (49)	60.4 (9290)	Cyclic Bending + Torsion (T/M=1.73)	↑↓	640 (1440)	6.62
	7		-	400 x 400 (16 x 16)	1600 (64)	4.00	Single	16 No.4 (1.48)	360 (52)	φ 6 mm @ 60 mm Hops	340 (49)	35.2 (5110)	Cyclic Bending + Torsion (T/M=1.0)	↑↓	640 (1440)	11.36
	8		-	400 x 400 (16 x 16)	1600 (64)	4.00	Single	16 No.4 (1.48)	360 (52)	φ 6 mm @ 60 mm Hops	340 (49)	51.6 (7490)	Cyclic Bending + Torsion (T/M=0.58)	↑↓	640 (1440)	7.75
	9		-	400 x 400 (16 x 16)	1600 (64)	4.00	Single	16 No.4 (1.48)	360 (52)	φ 6 mm @ 60 mm Hops	340 (49)	41.1 (5970)	Cyclic Bending (T/M=0)	↑↓	640 (1440)	9.73


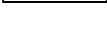




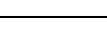




**Table A-10 Summary of RC Columns Tested Using Quasi-static Tests under Lateral Loading and Torsion**

Research	Specimen	Section	Scale	Dimensions mm (in)	Height mm (in)	L/d	Curvature path	Reinforcement				f <sub>c</sub> Mpa (psi)	Load path	Path	Axial load KN (Kips)	N/Agf <sub>c</sub> %
								Long. (ρ%)	f <sub>y</sub> Mpa (Ksi)	Transverse	f <sub>y</sub> Mpa (Ksi)					
Tirasit, Kawashima and Watanabe 8th US National Conf. on Earthquake Eng. San Francisco, USA 2006 Paper No. 431	P1		-	400 x 400 (16 x 16)	1350 (54)	3.38	Single	16 No.4 (1.48)	354 (52)	φ 6 mm @ 50 mm Hops	328 (48)	28.6 (4150)	Cyclic Bending (θ/Δ=0)	↑	160 (36)	3.50
	P2		-	400 x 400 (16 x 16)	1350 (54)	3.38	Single	16 No.4 (1.48)	354 (52)	φ 6 mm @ 50 mm Hops	328 (48)	28.3 (4110)	Cyclic Torsion (θ/Δ=∞)		0 (0)	0.00
	P3		-	400 x 400 (16 x 16)	1350 (54)	3.38	Single	16 No.4 (1.48)	354 (52)	φ 6 mm @ 50 mm Hops	328 (48)	28.4 (4120)	Cyclic Torsion (θ/Δ=∞)		160 (36)	3.52
	P4		-	400 x 400 (16 x 16)	1350 (54)	3.38	Single	16 No.4 (1.48)	354 (52)	φ 6 mm @ 50 mm Hops	328 (48)	32.2 (4670)	Cyclic Bending + Torsion (θ/Δ=0.5)		160 (36)	3.11
	P5		-	400 x 400 (16 x 16)	1350 (54)	3.38	Single	16 No.4 (1.48)	354 (52)	φ 6 mm @ 50 mm Hops	328 (48)	28.4 (4120)	Cyclic Bending + Torsion (θ/Δ=1.0)		160 (36)	3.52
	P6		-	400 x 400 (16 x 16)	1350 (54)	3.38	Single	16 No.4 (1.48)	354 (52)	φ 6 mm @ 50 mm Hops	328 (48)	32.8 (4760)	Cyclic Bending + Torsion (θ/Δ=2.0)		160 (36)	3.05
	P7		-	400 x 400 (16 x 16)	1350 (54)	3.38	Single	16 No.4 (1.48)	354 (52)	φ 6 mm @ 50 mm Hops	328 (48)	33.1 (4800)	Cyclic Bending + Torsion (θ/Δ=4.0)		160 (36)	3.02
Nagata, Kawashima and Watanabe 8th US National Conf. on Earthquake Eng. San Francisco, USA 2006 Paper No. 422	H-1		-	400 x 400 (16 x 16)	1350 (54)	3.38	Single	16 No.4 (1.27)	349 (50.6)	φ 6 mm @ 50 mm Hops (ρ <sub>v</sub> =0.79)	329 (48)	28.7 (4165)	Cyclic Uniaxial Eccentricity=0	↑	160 (36)	3.48
	H-4		-	400 x 400 (16 x 16)	1350 (54)	3.38	Single	16 No.4 (1.27)	349 (50.6)	φ 6 mm @ 50 mm Hops (ρ <sub>v</sub> =0.79)	329 (48)	31.2 (4530)	Cyclic Biaxial Eccentricity=0		160 (36)	3.21
	H-2		-	400 x 400 (16 x 16)	1350 (54)	3.38	Single	17 No.4 (1.35)	349 (50.6)	φ 6 mm @ 50 mm Hops (ρ <sub>v</sub> =0.99)	329 (48)	32.1 (4165)	Cyclic Uniaxial Eccentricity=0.5B	↑	160 (36)	3.12
	H-5		-	400 x 400 (16 x 16)	1350 (54)	3.38	Single	17 No.4 (1.35)	349 (50.6)	φ 6 mm @ 50 mm Hops (ρ <sub>v</sub> =0.99)	329 (48)	29.1 (4225)	Cyclic Biaxial Eccentricity=0.5B		160 (36)	3.44
	H-3		-	400 x 400 (16 x 16)	1350 (54)	3.38	Single	24 No.4 (1.9)	349 (50.6)	φ 6 mm @ 50 mm Hops (ρ <sub>v</sub> =1.19)	329 (48)	31.3 (4540)	Cyclic Uniaxial Eccentricity=1.0B	↑	160 (36)	3.19
	H-6		-	400 x 400 (16 x 16)	1350 (54)	3.38	Single	24 No.4 (1.9)	349 (50.6)	φ 6 mm @ 50 mm Hops (ρ <sub>v</sub> =1.19)	329 (48)	28.6 (4150)	Cyclic Biaxial Eccentricity=1.0B		160 (36)	3.50

**Table A-11 Summary of RC Columns Tested Using Quasi-static Tests under Lateral Loading and Torsion**

Research	Specimen	Section	Scale	Dimensions mm (in)	Height mm (in)	L/d	Curvature path	Reinforcement				f <sub>c</sub> Mpa (psi)	Load path	Path	Axial load KN (Kips)	N/Agf' <sub>c</sub> %
								Long. (ρ%)	f <sub>y</sub> Mpa (Ksi)	Transverse ρ <sub>v</sub>	f <sub>y</sub> Mpa (Ksi)					
Belarbi, Qi and Prakash 25th US-Japan Bridge Engineering Workshop Tsukuba, Japan 2009	H/D(6)- T/M(0)		1:2	610 (24)	3660 (146)	6.00	Single	12 No.8 (2.1)	457 (66.3)	φ 13 mm @ 70 mm Spiral (ρ <sub>v</sub> =1.32)	450 (65.3)	33.4 (4850)	Cyclic Bending (T/M=0)	↑↓	700 (158)	7.17
	H/D(6)- T/M(∞)		1:2	610 (24)	3660 (146)	6.00	Single	12 No.8 (2.1)	457 (66.3)	φ 13 mm @ 70 mm Spiral (ρ <sub>v</sub> =1.32)	450 (65.3)	28 (4065)	Cyclic Torsion (T/M=∞)	↷	580 (130)	7.09
	H/D(6)- T/M(0.2)		1:2	610 (24)	3660 (146)	6.00	Single	12 No.8 (2.1)	457 (66.3)	φ 13 mm @ 70 mm Spiral (ρ <sub>v</sub> =1.32)	450 (65.3)	41.2 (5980)	Cyclic Bending + Torsion (T/M=0.2)	↷↑↓	850 (190)	7.06
	H/D(6)- T/M(0.4)		1:2	610 (24)	3660 (146)	6.00	Single	12 No.8 (2.1)	457 (66.3)	φ 13 mm @ 70 mm Spiral (ρ <sub>v</sub> =1.32)	450 (65.3)	41.2 (5980)	Cyclic Bending + Torsion (T/M=0.4)	↷↑↓	850 (190)	7.06
	H/B(6)- T/M(0)		1:2	550 x 550 (22 x 22)	3350 (134)	6.09	Single	4 No.9 + 8 No.8 (2.13)	512 (74.3)	φ 10 mm @ 83 mm Square + Octagonal Hoops (ρ <sub>v</sub> =1.32)	454 (66)	36.27 (5265)	Cyclic Torsion (T/M=0)	↑↓	770 (175)	7.02
	H/B(6)- T/M(∞)		1:2	550 x 550 (22 x 22)	3350 (134)	6.09	Single	4 No.9 + 8 No.8 (2.13)	512 (74.3)	φ 10 mm @ 83 mm Square + Octagonal Hoops (ρ <sub>v</sub> =1.32)	454 (66)	34.63 (5025)	Cyclic Torsion (T/M=∞)	↷	730 (165)	6.97
	H/B(6)- T/M(0.2)		1:2	550 x 550 (22 x 22)	3350 (134)	6.09	Single	4 No.9 + 8 No.8 (2.13)	512 (74.3)	φ 10 mm @ 83 mm Square + Octagonal Hoops (ρ <sub>v</sub> =1.32)	454 (66)	40.5 (5880)	Cyclic Bending + Torsion (T/M=0.2)	↷↑↓	860 (195)	7.02
	H/B(6)- T/M(0.4)		1:2	550 x 550 (22 x 22)	3350 (134)	6.09	Single	4 No.9 + 8 No.8 (2.13)	512 (74.3)	φ 10 mm @ 83 mm Square + Octagonal Hoops (ρ <sub>v</sub> =1.32)	454 (66)	40.43 (5870)	Cyclic Bending + Torsion (T/M=0.4)	↷↑↓	850 (190)	6.95

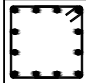



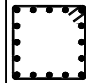


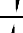









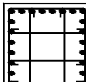





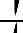
**Table A-12 Summary of RC Columns Tested Using Dynamic Testing (Unidirectional Shake Table)**

Research	Specimen	Section	Scale	Dimensions mm (in)	Height mm (in)	L/d	Curvature path	Reinforcement			f <sub>c</sub> Mpa (psi)	Load path	Axial load KN (Kips)	N/Agf <sub>c</sub> %	
								Long. (ρ %)	f <sub>y</sub> Mpa (Ksi)	Transverse					f <sub>y</sub> Mpa (Ksi)
Shiying and Zhenchang 4 <sup>th</sup> US National Conf. on Earthquake Eng. California, USA 1990 pp 717-725	DZ1		-	180 x 600 (7.09 x 23.6)	1660 (65.35)	9.22 2.77	Single	12 ϕ 14 mm (1.71)	280 (40.6)	ϕ 4 mm @ 10 mm	280 (40.6)	31.8 (4611)	Uniaxial-dynamic Harmonic	171 (38.5)	4.98
	DZ2		-	180 x 600 (7.09 x 23.6)	1660 (65.35)	9.22 2.77	Single	12 ϕ 14 mm (1.41)	430 (62.4)	ϕ 4 mm @ 10 mm	280 (40.6)	31.8 (4611)	Uniaxial-dynamic Harmonic	171 (38.5)	4.98
	DZS-1		-	185 x 217 (7.28 x 8.54)	2740 (107.9)	14.81 12.63	Single	8 ϕ 18 mm (5.0)	412 (59.7)	ϕ 6 mm @ 10 mm	280 (40.6)	26 (3770)	Uniaxial-dynamic Harmonic	110 (24.75)	10.54
	DZS-2		-	185 x 217 (7.28 x 8.54)	2740 (107.9)	14.81 12.63	Single	8 ϕ 18 mm (5.0)	412 (59.7)	ϕ 6 mm @ 10 mm	280 (40.6)	26 (3770)	Uniaxial-dynamic Harmonic	110 (24.75)	10.54
	SZS-3		-	181 x 221 (7.13 x 8.7)	2740 (107.9)	15.14 12.40	Single	8 ϕ 16 mm (4.02)	375 (54.4)	ϕ 6 mm @ 10 mm	280 (40.6)	30.2 (4380)	Uniaxial-dynamic Harmonic	110 (24.75)	9.11
	DZS-4		-	181 x 221 (7.13 x 8.7)	2740 (107.9)	15.14 12.40	Single	8 ϕ 16 mm (4.02)	375 (54.4)	ϕ 6 mm @ 10 mm	280 (40.6)	30.2 (4380)	Uniaxial-dynamic Harmonic	110 (24.75)	9.11
	SZS-5		-	187 x 270 (7.36 x 10.6)	2740 (107.9)	14.65 10.15	Single	8 ϕ 14 mm (2.44)	430 (62.4)	ϕ 6 mm @ 10 mm	280 (40.6)	25.1 (3640)	Uniaxial-dynamic Harmonic	110 (24.75)	8.68
	DZS-6		-	187 x 270 (7.36 x 10.6)	2740 (107.9)	14.65 10.15	Single	8 ϕ 14 mm (2.44)	430 (62.4)	ϕ 6 mm @ 10 mm	280 (40.6)	25.1 (3640)	Uniaxial-dynamic Harmonic	110 (24.75)	8.68
Kogoma, Hayashida and Minowa 10 <sup>th</sup> WCEE Madrid, Spain 1992 pp 3013-3017	CT1		1:3	130 x 130 (5.12 x 5.12)	850 (33.5)	6.54	Double	4 ϕ 16 mm (4.75)	362.2 (52.5)	ϕ 6 mm @ 285 mm (ρ <sub>v</sub> =0.17)	270 (39.15)	27 (3915)	Uniaxial-dynamic Takachi-Oki (1968)	69.46 (15.63)	15.22
	CT2		1:3	130 x 130 (5.12 x 5.12)	850 (33.5)	6.54	Double	4 ϕ 16 mm (4.75)	362.2 (52.5)	ϕ 6 mm @ 170 mm (ρ <sub>v</sub> =0.29)	258 (37.41)	25.8 (3741)	Uniaxial-dynamic Takachi-Oki (1968)	69.46 (15.63)	15.93
	CT3		1:3	130 x 130 (5.12 x 5.12)	850 (33.5)	6.54	Double	4 ϕ 16 mm (4.75)	362.2 (52.5)	ϕ 6 mm @ 110 mm (ρ <sub>v</sub> =0.45)	289 (41.9)	28.9 (4191)	Uniaxial-dynamic Takachi-Oki (1968)	69.46 (15.63)	14.22
	CT4		1:3	130 x 130 (5.12 x 5.12)	850 (33.5)	6.54	Double	4 ϕ 16 mm (4.75)	362.2 (52.5)	ϕ 6 mm @ 50 mm (ρ <sub>v</sub> =0.98)	299 (43.4)	29.9 (4336)	Uniaxial-dynamic Takachi-Oki (1968)	69.46 (15.63)	13.75
MacRae, Hodge Priestley and Saible Report SSRP 94/18 UCSD - 1994	Column bent Route 5/405		1:6	203 x 254 (8 x 10)	1070 (42)	5.27 4.21	Double	28 No.3 (4.16)	444 (64.3)	ϕ 2.7 mm @ 50 mm (ρ <sub>v</sub> =0.14)	221 (32.1)	35.2 (5120)	Uniaxial-dynamic EI Centro	169 (38)	9.80
Laplace, Sanders and Saiidi CCEER 99-13 1999	9F1		1:3	405 (16)	1828 (72)	4.51	Single	20 No.4 (1.97)	448.5 (65)	No.2 @ 38 mm (ρ <sub>v</sub> =1.1)	398 (57.64)	37.4 (5428)	Uniaxial-dynamic EI Centro Low strain rate	356 (80) (65 - 116)	7.39
	9F2		1:3	405 (16)	1828 (72)	4.51	Single	20 No.4 (1.97)	448.5 (65)	No.2 @ 38 mm (ρ <sub>v</sub> =1.1)	398 (89.9)	38.1 (5523)	Biaxial-dynamic Systetic High strain rate	356 (80) (65 - 116)	7.25

**Table A-13 Summary of RC Interlocking Columns Tested Using Quasi-static Tests**


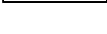




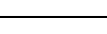




Research	Specimen	Section	Scale	Dimensions mm (in)	Height mm (in)	L/d	Curvature path	Reinforcement				f <sub>c</sub> Mpa (psi)	Load path	Path	Axial load KN (Kips)	N/Agf'c %
								Long. (p)	f <sub>y</sub> Mpa (Ksi)	Transverse	f <sub>y</sub> Mpa (Ksi)					
Tanaka and Park ACI Structural Jour. Vol.90 No.2, pp 192-203 Mar-Apr, 1993	9		1:1	400 x 600 (16 x 24)	1784 (70.24)	4.46	Single	10 No.7 (1.88)	432 (63.5)	φ 12 mm @ 80 mm	305 (44.2)	26.9 (3900)	Uniaxial-cyclic	↕	650 (146)	10.07
	10		1:1	400 x 600 (16 x 24)	1784 (70.24)	4.46	Single	16 No.8 (2.14)	485 (70.3)	φ 10 mm @ 80 mm Spiral	308 (44.7)	21.2 (3060)	Uniaxial-cyclic	↔	780 (176)	10.06
	11		1:1	400 x 600 (16 x 24)	1784 (70.24)	4.46	Single	16 No.8 (2.14)	485 (70.3)	φ 10 mm @ 100 mm Spiral	308 (44.7)	29.7 (4306)	Uniaxial-cyclic	↔	3260 (734)	30.02
	12		1:1	400 x 600 (16 x 24)	1784 (70.24)	4.46	Single	16 No.8 (2.14)	485 (70.3)	φ 10 mm @ 75 mm Spiral	308 (44.7)	24.6 (3567)	Uniaxial-cyclic	↔	4500 (1012)	50.03
Tsitotas and Tegos Advances in EE Vol.2, Oct-Nov, 1996 Grece	2		1:8	205 x 300 (8 x 11.8)	1000 (78.7)	4.88 3.33	Single	14 No.5 (3.69)	485 (70.3)	φ 5.5 mm @ 35 mm Spiral	465 (67.4)	24 (3480)	Uniaxial-monotonic	↔	0	0.00
	3		1:8	205 x 300 (8 x 11.8)	650 (26)	3.17 2.17	Single	14 No.5 (3.69)	480 (69.6)	φ 5.5 mm @ 35 mm Spiral	465 (67.4)	22.5 (3263)	Uniaxial-cyclic	↔	170 (38.3)	7.99
Benzoni, Priestley and Seible 12 <sup>th</sup> WCEE, 2000 Paper 1532	9		1:4	400 x 600 (16 x 24)	2440 (96)	6.10	Double	30 No.5 (2.6)	442 (64.1)	φ 6 mm @ 89 mm Spiral	448.2 (65)	35.17 (5100)	Uniaxial-cyclic	↔	180 (42)	2.20
	10		1:4	400 x 600 (16 x 24)	2440 (96)	6.10	Double	30 No.5 (2.6)	442 (64.1)	φ 6 mm @ 89 mm Spiral	448.2 (65)	34.48 (5000)	Uniaxial-cyclic	↔	-801 (187)	-10.00
	11		1:4	400 x 600 (16 x 24)	2440 (96)	6.10	Double	30 No.5 (2.6)	442 (64.1)	φ 6 mm @ 89 mm Spiral	448.2 (65)	35.17 (5100)	Uniaxial-cyclic	↔	2960 (666)	35.00
	12		1:4	400 x 600 (16 x 24)	2440 (96)	6.10	Double	30 No.5 (2.6)	442 (64.1)	φ 6 mm @ 89 mm Spiral	448.2 (65)	36.55 (5300)	Uniaxial-cyclic	↔	3000 (187 - 666)	-10 - 35
Mizugami 16 <sup>th</sup> US-Japan Bridge Engineering Workshop 2000	0		1:5	900 x 600 (36 x 24)	3000 (120)	5	Single	32 No.5 (1.18)	399 (57.9)	φ 6 mm @ 80 mm hoop/tie (ρ <sub>v</sub> =0.88)	345 (50)	39.8 (5776)	Uniaxial-cyclic	↔	432 (97)	0.92
	1		1:5	900 x 600 (36 x 24)	3000 (120)	5.00	Single	38 No.5 (1.63)	409 (59.4)	φ 6 mm @ 120 mm Spiral (ρ <sub>v</sub> =0.19)	359 (52.1)	28.1 (4080)	Uniaxial-cyclic	↔	370 (83)	1.12
	2		1:5	900 x 600 (36 x 24)	3000 (120)	5.00	Single	38 No.5 (1.63)	399 (57.9)	φ 6 mm @ 80 mm Spiral (ρ <sub>v</sub> =0.29)	345 (50)	39.7 (5760)	Uniaxial-cyclic	↔	370 (83)	0.79
	3		1:5	900 x 600 (36 x 24)	3000 (120)	5.00	Single	38 No.5 (1.63)	409 (59.4)	φ 10 mm @ 100 mm Spiral (ρ <sub>v</sub> =0.52)	337 (48.9)	29.2 (3840)	Uniaxial-cyclic	↔	370 (83)	1.08
	4		1:5	850 x 600 (34 x 24)	1620 (65)	2.70	Single	36 No.4 (1.05)	386 (56)	φ 6 mm @ 50 mm Hoop (ρ <sub>v</sub> =0.46)	364 (52.8)	30.9 (4485)	Uniaxial-cyclic	↕	650 (146)	1.95
	5		1:5	850 x 600 (34 x 24)	1620 (65)	2.70	Single	36 No.4 (1.05)	386 (56)	φ 6 mm @ 100 mm Hoop (ρ <sub>v</sub> =0.23)	364 (52.8)	29.3 (4250)	Uniaxial-cyclic	↕	650 (146)	2.06
	6		1:5	850 x 600 (34 x 24)	1620 (65)	2.70	Single	36 No.4 (1.05)	386 (56)	φ 6 mm @ 200 mm Hoop (ρ <sub>v</sub> =0.12)	364 (52.8)	31.4 (4560)	Uniaxial-cyclic	↕	650 (146)	1.92

**Table A-14 Summary of RC Columns Tested Using Pseudo-dynamic Tests**


Research	Specimen	Section	Scale	Dimensions mm (in)	Height mm (in)	H/d	Curvature path	Reinforcement				f <sub>c</sub> Mpa (psi)	Load path	Path	Axial load KN (Kips)	N/Agf <sub>c</sub>
								Long. (ρ %)	f <sub>y</sub> Mpa (Ksi)	Transverse	f <sub>y</sub> Mpa (Ksi)					
Cuadra, Ogawa and Inoue Risk Analysis II U.K 2000	PSD-R1		1:1	400 x 400 (16 x 16)	1000 (40.8)	2.50	Single	12 No.4 (1.27)	380 (55)	No.3 @ 600 mm	380 (55)	24 (3625)	Uniaxial-cyclic EI Centro N-S Modify		960 (36)	25.00
	PSD-R2		1:1	400 x 400 (16 x 16)	1000 (40.8)	2.50	Single	12 No.4 (1.27)	380 (55)	No.3 @ 600 mm	380 (55)	24 (3625)	Biaxial-cyclic EI Centro N-S EI Centro E-W		960 (36)	25.00
	PSD-R2		1:1	400 x 400 (16 x 16)	1000 (40.8)	2.50	Single	12 No.4 (1.27)	380 (55)	No.3 @ 600 mm	380 (55)	24 (3625)	Biaxial-cyclic Kobe N-S Kobe E-W		960 (36)	25.00
Kawashima et al. 8 <sup>th</sup> US National Conf. on Earthquake Eng. California, US 2006	P1		1:1	400 x 400 (16 x 16)	1350 (55)	3.38	Single	16 No.4 (1.27)	295 (42.8)	φ 6 mm @ 500 mm	295 (42.8)	28.68 (3869)	Uniaxial-cyclic 30% Kobe N-S		160 (36)	3.49
	P2		1:1	400 x 400 (16 x 16)	1350 (55)	3.38	Single	16 No.4 (1.27)	295 (42.8)	φ 6 mm @ 500 mm	295 (42.8)	25.43 (3687)	Biaxial-cyclic 30% Kobe N-S 30% Kobe E-W		160 (36)	3.93
	P3		1:1	400 x 400 (16 x 16)	1350 (55)	3.38	Single	16 No.4 (1.27)	295 (42.8)	φ 6 mm @ 500 mm	295 (42.8)	27.16 (3938)	Uniaxial-cyclic 40% Kobe N-S		160 (36)	3.68
	P4		1:1	400 x 400 (16 x 16)	1350 (55)	3.38	Single	16 No.4 (1.27)	295 (42.8)	φ 6 mm @ 500 mm	295 (42.8)	26.93 (3905)	Biaxial-cyclic 40% Kobe N-S 40% Kobe E-W		160 (36)	3.71
	P5		1:1	400 x 400 (16 x 16)	1350 (55)	3.38	Single	16 No.4 (1.27)	295 (42.8)	φ 6 mm @ 500 mm	295 (42.8)	31.77 (4607)	Uniaxial-cyclic 50% Sylmar N-S		160 (36)	3.15
	P6		1:1	400 x 400 (16 x 16)	1350 (55)	3.38	Single	16 No.4 (1.27)	295 (42.8)	φ 6 mm @ 500 mm	295 (42.8)	34.23 (4963)	Biaxial-cyclic 50% Sylmar N-S 50% Sylmar E-W		160 (36)	2.92
Dhakal, Mander and Mashiko 8 <sup>th</sup> US National Conf. on Earthquake Eng. California, US 2006	1 Caltrans		1:3	600 (25)	2000 (40.8)	3.33	Single	32 No.4 (1.27)	528 (76.6)	φ 6 mm @ 25 mm	461 (66.8)	40.7 (5900)	Imperial Valley, 1979 Loma Prieta, 1989		630 (142)	5.47
	2 NZ		1:3	500 (20.4)	2000 (40.8)	4.00	Single	24 No.3 (1.27)	539 (78.2)	φ 6 mm @ 50 mm	461 (66.8)	41.2 (5975)	Superstition Hills, 1987		630 (142)	7.79
	3 Japan		1:3	600 (25)	2000 (40.8)	3.33	Single	24 No.5 (1.27)	517 (75)	φ 6 mm @ 35 mm	461 (66.8)	38.5 (5585)	N-S and E-W		630 (142)	5.79
Chang. ASCE Journal of Struct. Engineer Vol 136, No.1, pp 12-25 Jan, 2010	A*		2:5	750 x 600 (30 x 24)	3250 (130)	4.33 =H39/G39	Single	32 No.6 (1.95)	500 (72.5)	No.3 @ 100 mm	350 (51)	23 (3340)	Uniaxial-cyclic Chi-Chi earthquake		680 (153)	6.57
	B*		2:5	750 x 600 (30 x 24)	3250 (130)	4.33 5.42	Single	32 No.6 (1.95)	500 (72.5)	No.3 @ 100 mm	350 (51)	23 (3340)	Uniaxial-cyclic Chi-Chi earthquake		680 (153)	6.57
	C*		2:5	750 x 600 (30 x 24)	3250 (130)	4.33 5.42	Single	32 No.6 (1.95)	500 (72.5)	No.3 @ 100 mm	350 (51)	23 (3340)	Uniaxial-cyclic Chi-Chi earthquake		680 (153)	6.57
	A		2:5	750 x 600 (30 x 24)	3250 (130)	4.33 5.42	Single	32 No.6 (1.95)	520 (75.5)	No.3 @ 100 mm	400 (58)	25 (3630)	Biaxial-cyclic Chi-Chi earthquake		680 (153)	6.04
	B		2:5	750 x 600 (30 x 24)	3250 (130)	4.33 5.42	Single	32 No.6 (1.95)	520 (75.5)	No.3 @ 100 mm	400 (58)	25 (3630)	Biaxial-cyclic Chi-Chi earthquake		680 (153)	6.04
	C		2:5	750 x 600 (30 x 24)	3250 (130)	4.33 5.42	Single	32 No.6 (1.95)	520 (75.5)	No.3 @ 100 mm	400 (58)	25 (3630)	Biaxial-cyclic Chi-Chi earthquake		680 (153)	6.04



**Table A-15 Summary of RC Columns Tested Using Dynamic Testing (Unidirectional Shake Table)**

Research	Specimen	Section	Scale	Dimensions mm (in)	Height mm (in)	L/d	Curvature path	Reinforcement			f <sub>c</sub> Mpa (psi)	Load path	Axial load KN (Kips)	N/Agf <sub>c</sub> %	
								Long. (ρ %)	f <sub>y</sub> Mpa (Ksi)	Transverse					f <sub>y</sub> Mpa (Ksi)
Shiying and Zhenchang 4 <sup>th</sup> US National Conf. on Earthquake Eng. California, USA 1990 pp 717-725	DZ1		-	180 x 600 (7.09 x 23.6)	1660 (65.35)	9.22 2.77	Single	12 ϕ 14 mm (1.71)	280 (40.6)	ϕ 4 mm @ 10 mm	280 (40.6)	31.8 (4611)	Uniaxial-dynamic Harmonic	171 (38.5)	4.98
	DZ2		-	180 x 600 (7.09 x 23.6)	1660 (65.35)	9.22 2.77	Single	12 ϕ 14 mm (1.41)	430 (62.4)	ϕ 4 mm @ 10 mm	280 (40.6)	31.8 (4611)	Uniaxial-dynamic Harmonic	171 (38.5)	4.98
	DZS-1		-	185 x 217 (7.28 x 8.54)	2740 (107.9)	14.81 12.63	Single	8 ϕ 18 mm (5.0)	412 (59.7)	ϕ 6 mm @ 10 mm	280 (40.6)	26 (3770)	Uniaxial-dynamic Harmonic	110 (24.75)	10.54
	DZS-2		-	185 x 217 (7.28 x 8.54)	2740 (107.9)	14.81 12.63	Single	8 ϕ 18 mm (5.0)	412 (59.7)	ϕ 6 mm @ 10 mm	280 (40.6)	26 (3770)	Uniaxial-dynamic Harmonic	110 (24.75)	10.54
	SZS-3		-	181 x 221 (7.13 x 8.7)	2740 (107.9)	15.14 12.40	Single	8 ϕ 16 mm (4.02)	375 (54.4)	ϕ 6 mm @ 10 mm	280 (40.6)	30.2 (4380)	Uniaxial-dynamic Harmonic	110 (24.75)	9.11
	DZS-4		-	181 x 221 (7.13 x 8.7)	2740 (107.9)	15.14 12.40	Single	8 ϕ 16 mm (4.02)	375 (54.4)	ϕ 6 mm @ 10 mm	280 (40.6)	30.2 (4380)	Uniaxial-dynamic Harmonic	110 (24.75)	9.11
	SZS-5		-	187 x 270 (7.36 x 10.6)	2740 (107.9)	14.65 10.15	Single	8 ϕ 14 mm (2.44)	430 (62.4)	ϕ 6 mm @ 10 mm	280 (40.6)	25.1 (3640)	Uniaxial-dynamic Harmonic	110 (24.75)	8.68
	DZS-6		-	187 x 270 (7.36 x 10.6)	2740 (107.9)	14.65 10.15	Single	8 ϕ 14 mm (2.44)	430 (62.4)	ϕ 6 mm @ 10 mm	280 (40.6)	25.1 (3640)	Uniaxial-dynamic Harmonic	110 (24.75)	8.68
Kogoma, Hayashida and Minowa 10 <sup>th</sup> WCEE Madrid, Spain 1992 pp 3013-3017	CT1		1:3	130 x 130 (5.12 x 5.12)	850 (33.5)	6.54	Double	4 ϕ 16 mm (4.75)	362.2 (52.5)	ϕ 6 mm @ 285 mm (ρ <sub>v</sub> =0.17)	270 (39.15)	27 (3915)	Uniaxial-dynamic Takachi-Oki (1968)	69.46 (15.63)	15.22
	CT2		1:3	130 x 130 (5.12 x 5.12)	850 (33.5)	6.54	Double	4 ϕ 16 mm (4.75)	362.2 (52.5)	ϕ 6 mm @ 170 mm (ρ <sub>v</sub> =0.29)	258 (37.41)	25.8 (3741)	Uniaxial-dynamic Takachi-Oki (1968)	69.46 (15.63)	15.93
	CT3		1:3	130 x 130 (5.12 x 5.12)	850 (33.5)	6.54	Double	4 ϕ 16 mm (4.75)	362.2 (52.5)	ϕ 6 mm @ 110 mm (ρ <sub>v</sub> =0.45)	289 (41.9)	28.9 (4191)	Uniaxial-dynamic Takachi-Oki (1968)	69.46 (15.63)	14.22
	CT4		1:3	130 x 130 (5.12 x 5.12)	850 (33.5)	6.54	Double	4 ϕ 16 mm (4.75)	362.2 (52.5)	ϕ 6 mm @ 50 mm (ρ <sub>v</sub> =0.98)	299 (43.4)	29.9 (4336)	Uniaxial-dynamic Takachi-Oki (1968)	69.46 (15.63)	13.75
MacRae, Hodge Priestley and Saible Report SSRP 94/18 UCSD - 1994	Column bent Route 5/405		1:6	203 x 254 (8 x 10)	1070 (42)	5.27 4.21	Double	28 No.3 (4.16)	444 (64.3)	ϕ 2.7 mm @ 50 mm (ρ <sub>v</sub> =0.14)	221 (32.1)	35.2 (5120)	Uniaxial-dynamic EI Centro	169 (38)	9.80
Laplace, Sanders and Saiidi CCEER 99-13 1999	9F1		1:3	405 (16)	1828 (72)	4.51	Single	20 No.4 (1.97)	448.5 (65)	No.2 @ 38 mm (ρ <sub>v</sub> =1.1)	398 (57.64)	37.4 (5428)	Uniaxial-dynamic EI Centro Low strain rate	356 (80) (65 - 116)	7.39
	9F2		1:3	405 (16)	1828 (72)	4.51	Single	20 No.4 (1.97)	448.5 (65)	No.2 @ 38 mm (ρ <sub>v</sub> =1.1)	398 (89.9)	38.1 (5523)	Biaxial-dynamic Systetic High strain rate	356 (80) (65 - 116)	7.25







**Table A-16 Summary of RC Columns Tested Using Dynamic Testing (Unidirectional Shake Table)**

Research	Specimen	Section	Scale	Dimensions mm (in)	Height mm (in)	L/d	Curvature path	Reinforcement			f <sub>c</sub> Mpa (psi)	Load path	Axial load KN (Kips)	N/Agf <sub>c</sub> %	
								Long. (ρ %)	f <sub>y</sub> Mpa (Ksi)	Transverse fy Mpa (Ksi)					
Dodd and Cooke 10 <sup>th</sup> WCEE Madrid, Spain 1992 pp 3035-3039	1a		1:6	200 (8)	800 (32)	4.00	Single	16 ϕ 6 mm (1.44)	450 (65.25)	ϕ 4 mm @ 30 mm spiral (ρ <sub>v</sub> =0.88)	260 (37.7)	40.7 (5900)	Uniaxial-dynamic Sinusoidal EI Centro	51.5 (11.6)	4.03
	1b		1:6	200 (8)	800 (32)	4.00	Single	16 ϕ 6 mm (1.44)	450 (65.25)	ϕ 4 mm @ 30 mm spiral (ρ <sub>v</sub> =0.88)	260 (37.7)	32 (4640)	Uniaxial-dynamic Sinusoidal EI Centro	51.5 (11.6)	5.12
	2a		1:6	200 (8)	1400 (56)	7.00	Single	16 ϕ 6 mm (1.44)	450 (65.25)	ϕ 4 mm @ 25 mm spiral (ρ <sub>v</sub> =1.05)	260 (37.7)	34.5 (5000)	Uniaxial-dynamic Sinusoidal EI Centro	51.5 (11.6)	4.75
	2b		1:6	200 (8)	1400 (56)	7.00	Single	16 ϕ 6 mm (1.44)	450 (65.25)	ϕ 4 mm @ 25 mm spiral (ρ <sub>v</sub> =1.05)	260 (37.7)	30.3 (4395)	Uniaxial-dynamic EI Centro	51.5 (11.6)	5.41
	3a		1:6	200 (8)	2000 (80)	10.00	Single	16 ϕ 6 mm (1.44)	450 (65.25)	ϕ 3.15 mm @ 25 mm spiral (ρ <sub>v</sub> =0.67)	260 (37.7)	37.4 (5425)	Uniaxial-dynamic EI Centro	51.5 (11.6)	4.38
	3b		1:6	200 (8)	2000 (80)	10.00	Single	16 ϕ 6 mm (1.44)	450 (65.25)	ϕ 3.15 mm @ 25 mm spiral (ρ <sub>v</sub> =0.67)	260 (37.7)	29.1 (4220)	Uniaxial-dynamic EI Centro	51.5 (11.6)	5.63
	4		1:6	200 (8)	800 (32)	4.00	Single	16 ϕ 6 mm (1.44)	450 (65.25)	ϕ 4 mm @ 28 mm spiral (ρ <sub>v</sub> =0.94)	260 (37.7)	39.4 (4715)	Uniaxial-dynamic EI Centro	484 (109)	39.10
	5		1:6	200 (8)	1400 (56)	7.00	Single	16 ϕ 6 mm (1.44)	450 (65.25)	ϕ 4 mm @ 26 mm spiral (ρ <sub>v</sub> =1.02)	260 (37.7)	37.2 (4395)	Uniaxial-dynamic EI Centro	454 (102)	38.85
	6		1:6	200 (8)	2000 (80)	10.00	Single	16 ϕ 6 mm (1.44)	450 (65.25)	ϕ 3.15 mm @ 21 mm spiral (ρ <sub>v</sub> =0.79)	260 (37.7)	38.6 (5600)	Uniaxial-dynamic EI Centro	469 (106)	38.68
	7		1:6	200 (8)	800 (32)	4.00	Single	16 ϕ 6 mm (1.44)	450 (65.25)	ϕ 3.15 mm @ 36 mm spiral (ρ <sub>v</sub> =0.46)	260 (37.7)	41.3 (5990)	Uniaxial-dynamic EI Centro	51.5 (11.6)	3.97
	8		1:6	200 (8)	800 (32)	4.00	Single	16 ϕ 6 mm (1.44)	450 (65.25)	ϕ 4 mm @ 28 mm spiral (ρ <sub>v</sub> =0.94)	260 (37.7)	40.1 (5815)	Uniaxial-dynamic EI Centro	494 (111)	39.21
ACI Structural Jour. Vol.97 No.2, pp 297-307 Mar-Apr, 2000	9	1:6	200 (8)	1400 (56)	7.00	Single	16 ϕ 6 mm (1.44)	450 (65.25)	ϕ 3.15 mm @ 36 mm spiral (ρ <sub>v</sub> =0.46)	260 (37.7)	40.4 (5860)	Uniaxial-dynamic EI Centro	51.5 (11.6)	4.06	
	10	1:6	200 (8)	800 (32)	4.00	Single	16 ϕ 6 mm (1.44)	450 (65.25)	ϕ 4 mm @ 30 mm spiral (ρ <sub>v</sub> =0.88)	260 (37.7)	36.9 (5350)	Uniaxial-dynamic EI Centro	51.5 (11.6)	4.44	
	11	1:6	200 (8)	800 (32)	4.00	Single	16 ϕ 6 mm (1.44)	450 (65.25)	ϕ 4 mm @ 28 mm spiral (ρ <sub>v</sub> =0.94)	260 (37.7)	43 (6235)	Uniaxial-dynamic EI Centro	484 (109)	35.83	

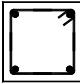



**Table A-17 Summary of RC Columns Tested Using Dynamic Testing (Unidirectional Shake Table)**

Research	Specimen	Section	Scale	Dimensions mm (in)	Height mm (in)	L/d	Curvature path	Reinforcement			f <sub>c</sub> Mpa (psi)	Load path	Axial load KN (Kips)	N/Agf <sub>c</sub> %	
								Long. (ρ %)	f <sub>y</sub> Mpa (Ksi)	Transverse f <sub>y</sub> Mpa (Ksi)					
Kowalsky, Priestley and Seible ACI Structural Jour. Vol.97 No.4, pp 602-618 Jul-Aug, 2000	MC1 Bent Columns		1:6	203 (8)	1524 (60)	7.51	Double	12 No.3 (2.64)	455 (65.98)	φ 5 mm @ 32 mm spiral (ρ <sub>v</sub> =1.22)	210 (30.45)	19.7 (2857)	Uniaxial-dynamic Tabas (1978)	59.32 (13.35)	9.30
	MC2 Bent Columns		1:6	203 (8)	1524 (60)	7.51	Double	12 No.3 (2.64)	455 (65.98)	φ 5 mm @ 32 mm spiral (ρ <sub>v</sub> =1.22)	210 (30.45)	35.5 (5148)	Uniaxial-dynamic Tabas (1978)	59.32 (13.35)	5.16
Inoue, Weniuhuan Kanno, Hori & Ogawa 12WCEE, 2000 Paper 1734	Bent Columns Case 1		-	100 x 120 (3.94 x 4.7)	600 (26.6)	6.00 5.00	Single	6 φ 6 mm (0.8)	419 (60.8)	φ 4 mm @ 30 mm Hoops (ρ <sub>v</sub> =0.7)	214.3 (31.1)	30.8 (4466)	Uniaxial-static Simulated	22.2 (5)	6.01
	Bent Columns Case 2		-	100 x 120 (3.94 x 4.7)	600 (26.6)	6.00 5.00	Single	6 φ 6 mm (0.8)	419 (60.8)	φ 4 mm @ 30 mm Hoops (ρ <sub>v</sub> =0.7)	214.3 (31.1)	33.1 (4800)	Uniaxial-dynamic Simulated long duration	22.2 (5)	5.59
	Bent Columns Case 2		-	100 x 120 (3.94 x 4.7)	600 (26.6)	6.00 5.00	Single	6 φ 6 mm (0.8)	419 (60.8)	φ 4 mm @ 30 mm Hoops (ρ <sub>v</sub> =0.7)	214.3 (31.1)	36 (5220)	Uniaxial-dynamic Simulated short duration	22.2 (5)	5.14
Laplace, Sanders and Saiidi CCEER 01-6 2001	6F		1:3	405 (16)	1828 (72)	4.51	Single	20 No.4 (1.97)	351 (50.9)	φ 4.5 mm @ 114 mm Hoops (ρ <sub>v</sub> =0.15)	319.5 (46.3)	40.7 (5903)	Uniaxial-dynamic EI Centro	356 (65)	6.79
	9S1		1:3	405 (16)	1220 (48)	3.01	Single	16 No.6 (3.5)	448.5 (65)	φ 6.3 mm @ 38 mm Spiral (ρ <sub>v</sub> =0.92)	398 (57.64)	36.9 (5360)	Uniaxial-dynamic EI Centro	356 (65)	7.49
	9S2		1:3	405 (16)	1220 (48)	3.01	Single	16 No.6 (3.5)	448.5 (65)	φ 6.3 mm @ 38 mm Spiral (ρ <sub>v</sub> =0.92)	398 (57.64)	36.7 (5325)	Biaxial-dynamic EI Centro	356 (65)	7.53
Park et al. Earthquake spectra V.19, No.4 2003	C356 AASHTO		1:6	356 (14)	2445 (96.26)	6.87	Single	14 No.6 (4.03)	375.3 (54.4)	φ 6.0 mm @ 40 mm Spiral (ρ <sub>v</sub> =1.02)	346.7 (50.3)	33.4 (4843)	Uniaxial-dynamic Kaihohoku-bashi	356 (65)	10.71
	C450		1:6	450 (17.7)	2445 (96.26)	5.43	Single	48 No.4 (3.8)	377.3 (54.7)	φ 6.0 mm @ 85 mm Double hoop (ρ <sub>v</sub> =0.84)	346.7 (50.3)	29.3 (4248)	Uniaxial-dynamic Kaihohoku-bashi	356 (65)	7.64
	C533		1:6	533 (21)	2445 (96.26)	4.59	Single	50 No.8 (1.6)	366.1 (53.1)	φ 6.0 mm @ 110 mm Double hoop (ρ <sub>v</sub> =0.52)	346.7 (50.3)	33.3 (4829)	Biaxial-dynamic Kaihohoku-bashi	356 (65)	4.79
Moustafa, Sanders and Saiidi CCEER 04-3 2004	Column bent Tall		1:3	350 (14)	2325 (91.5)	6.64	Double	15 No.4 (1.98)	448 (65)	φ 4.0 mm @ 56 mm Spiral (ρ <sub>v</sub> =0.27)	414 (60)	28.3 (4110)	Uniaxial-dynamic Northridge (1994) Sylmar	166 (37.35)	6.10
	Column bent Medium		1:3	350 (14)	1575 (62)	4.50	Double	15 No.4 (1.98)	448 (65)	φ 4.0 mm @ 56 mm Spiral (ρ <sub>v</sub> =0.27)	414 (60)	28.3 (4100)	Uniaxial-dynamic Northridge (1994) Sylmar	166 (37.35)	6.10
	Column bent Short		1:3	350 (14)	875 (34.5)	2.50	Double	15 No.8 (1.98)	448 (65)	φ 4.0 mm @ 56 mm Spiral (ρ <sub>v</sub> =0.27)	414 (60)	41 (5860)	Biaxial-dynamic Northridge (1994) Sylmar	166 (37.35)	4.21

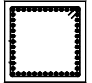






**Table A-18 Summary of RC Columns Tested Using Dynamic Testing (Unidirectional Shake Table)**

Research	Specimen	Section	Scale	Dimensions mm (in)	Height mm (in)	L/d	Curvature path	Reinforcement				F <sub>c</sub> Mpa (psi)	Load path	Axial load KN (Kips)	N/Agf' <sub>c</sub> %
								Long. (ρ %)	f <sub>y</sub> Mpa (Ksi)	Transverse	f <sub>y</sub> Mpa (Ksi)				
Phan, Saiidi, Anderson and Ghasemi  8 <sup>th</sup> USNCEE California, US 2006	NF-1		1:3	405 (16)	1829 (74.7)	4.52	Single	20 No.4 (1.97)	469 (68)	φ 6.3 mm @ 38 mm Spiral (ρ <sub>v</sub> =1.1)	396.4 (585)	41.3 (5990)	Uniaxial-dynamic Northridge (1994) Rinaldi	356 (80)	6.69
	NF-2		1:3	405 (16)	1829 (74.7)	4.52	Single	22 No.4 (1.97)	469 (68)	φ 6.3 mm @ 38 mm Spiral (ρ <sub>v</sub> =0.92)	396.4 (58)	42.4 (6150)	Uniaxial-dynamic Northridge (1994) Rinaldi	356 (80)	6.52
Choi, Saiidi, Somerville CCEER 01-6 2006	MN		1:3	355 (14)	1600 (63)	4.51	Single	22 No.4 (2.9)	486 (71)	φ 6.3 mm @ 28.6 mm Spiral (ρ <sub>v</sub> =1.37)	428 (62)	43.8 (6350)	Uniaxial-dynamic Northridge (1994) Rinaldi	276 (62)	6.37
	ETN		1:3	355 (14)	2750 (108.5)	7.75	Single	22 No.4 (2.9)	486 (71)	φ 6.3 mm @ 25 mm Spiral (ρ <sub>v</sub> =1.54)	428 (62)	44 (6365)	Uniaxial-dynamic Northridge (1994) Rinaldi	276 (62)	6.34
	SETN		1:3	355 (14)	2750 (108.5)	7.75	Single	18 No.5 (3.6)	441 (64)	φ 6.3 mm @ 19 mm Spiral (ρ <sub>v</sub> =2.05)	400 (58)	46.8 (6790)	Uniaxial-dynamic Northridge (1994) Rinaldi	276 (62)	5.96
	SVTN		1:3	305 (12)	2500 (98.5)	8.20	Single	17 No.4 (3.0)	475 (69)	φ 6.3 mm @ 25 mm Spiral (ρ <sub>v</sub> =1.82)	400 (58)	47.1 (6835)	Uniaxial-dynamic Northridge (1994) Rinaldi	200 (45)	5.81



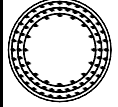

**Table A-19 Summary of RC Columns Tested Using Dynamic Testing (Bidirectional Shake Table)**

Research	Specimen	Section	Scale	Dimensions mm (in)	Height mm (in)	L/d	Curvature path	Reinforcement				f <sub>c</sub> Mpa (psi)	Load path	Axial load KN (Kips)	N/Agf <sub>c</sub> %
								Long. (ρ %)	f <sub>y</sub> Mpa (Ksi)	Transverse	f <sub>y</sub> Mpa (Ksi)				
Kitajima et al. 10 <sup>th</sup> WCEE Madrid, Spain 1992 pp 3019-3024	EDX		1:9	80 x 80 (3.15 x 3.15)	480 (18.9)	6.00	Double	4 ϕ 6 mm (2.0)	425 (61.6)	ϕ 2.6 mm @ 30 mm (ρ <sub>v</sub> =0.44%)	-	26 (3770)	Uniaxial-dynamic Takachi-Oki (1968) NS	18 (4.0)	10.82
	EDY		1:9	80 x 80 (3.15 x 3.15)	480 (18.9)	6.00	Double	4 ϕ 6 mm (2.0)	425 (61.6)	ϕ 2.6 mm @ 30 mm (ρ <sub>v</sub> =0.44%)	-	26 (3770)	Uniaxial-dynamic Takachi-Oki (1968) EW	18 (4.0)	10.82
	EDXY		1:9	80 x 80 (3.15 x 3.15)	480 (18.9)	6.00	Double	4 ϕ 6 mm (2.0)	425 (61.6)	ϕ 2.6 mm @ 30 mm (ρ <sub>v</sub> =0.44%)	-	26 (3770)	Biaxial-dynamic Takachi-Oki (1968) NS - EW	18 (4.0)	10.82
	DX		1:9	80 x 80 (3.15 x 3.15)	480 (18.9)	6.00	Double	4 ϕ 6 mm (2.0)	425 (61.6)	ϕ 2.6 mm @ 30 mm (ρ <sub>v</sub> =0.44%)	-	26 (3770)	Uniaxial-dynamic Takachi-Oki (1968) NS	18 (4.0)	10.82
	DY		1:9	80 x 80 (3.15 x 3.15)	480 (18.9)	6.00	Double	4 ϕ 6 mm (2.0)	425 (61.6)	ϕ 2.6 mm @ 30 mm (ρ <sub>v</sub> =0.44%)	-	26 (3770)	Uniaxial-dynamic Takachi-Oki (1968) EW	18 (4.0)	10.82
	DXY		1:9	80 x 80 (3.15 x 3.15)	480 (18.9)	6.00	Double	4 ϕ 6 mm (2.0)	425 (61.6)	ϕ 2.6 mm @ 30 mm (ρ <sub>v</sub> =0.44%)	-	26 (3770)	Biaxial-dynamic Takachi-Oki (1968) NS - EW	18 (4.0)	10.82
Kitajima, Adachi and Nakanishi 11 <sup>th</sup> WCEE 1996 Paper No.566	1		1:9	80 x 80 (3.15 x 3.15)	320 (12.6)	4.00	Single	12 ϕ 3 mm (1.33)	291.1 (42.2)	ϕ 1.3 mm @ 10 mm (ρ <sub>v</sub> =0.4%)	344 (49.9)	23 (3335)	Biaxial-dynamic Takachi-Oki (1968) NS-EW	23.3 (5.24)	15.83
	2		1:9	80 x 80 (3.15 x 3.15)	480 (18.9)	6.00	Single	12 ϕ 3 mm (1.33)	280.6 (40.7)	ϕ 1.4 mm @ 10 mm (ρ <sub>v</sub> =0.4%)	437 (63.4)	26 (3770)	Biaxial-dynamic Takachi-Oki (1968) NS-EW	23.3 (5.24)	14.00
Nakayama et al. 11 <sup>th</sup> WCEE 1996 Paper No.1001	5 columns connected with plate			100 x 100 (3.94 x 3.94)	600 (23.6)	6.00	Single	4 ϕ 6 mm (1.13)	383 (55.5)	ϕ 3.1 mm @ 10 mm	225 (32.6)	29.3 (4248)	Uniaxial-dynamic Synthetic NS	40 (9)	13.65
	5 columns connected with plate			100 x 100 (3.94 x 3.94)	600 (23.6)	6.00	Single	4 ϕ 6 mm (1.13)	383 (55.5)	ϕ 3.1 mm @ 10 mm	225 (32.6)	29.3 (4248)	Biaxial-dynamic Synthetic NS - EW	40 (9)	13.65
Hachem, Mahin and Moehle PEER 2003/06 2003	A1		1:4.5	405 (16)	1625 (64)	4.01	Single	12 No.4 (1.17)	520 (75.4)	ϕ 4.5 mm @ 32 mm Spiral (ρ <sub>v</sub> =0.54%)	620 (89.9)	39.3 (5707)	Uniaxial-dynamic Northridge (1994)	290 (65)	5.73
	A2		1:4.5	405 (16)	1625 (64)	4.01	Single	12 No.4 (1.17)	520 (75.4)	ϕ 4.5 mm @ 32 mm Spiral (ρ <sub>v</sub> =0.54%)	620 (89.9)	39.3 (5707)	Biaxial-dynamic Llollo-Chile (1985)	290 (65)	5.73
	B1		1:4.5	405 (16)	1625 (64)	4.01	Single	12 No.4 (1.17)	520 (75.4)	ϕ 4.5 mm @ 32 mm Spiral (ρ <sub>v</sub> =0.54%)	620 (89.9)	39.1 (5664)	Uniaxial-dynamic Northridge (1994)	290 (65)	5.76
	B2		1:4.5	405 (16)	1625 (64)	4.01	Single	12 No.4 (1.17)	520 (75.4)	ϕ 4.5 mm @ 32 mm Spiral (ρ <sub>v</sub> =0.54%)	620 (89.9)	39.1 (5664)	Biaxial-dynamic Llollo-Chile (1985)	290 (65)	5.76











**Table A-20 Summary of RC Columns Tested Using Dynamic Testing (Bidirectional Shake Table)**

Research	Specimen	Section	Scale	Dimensions mm (in)	Height mm (in)	L/d	Curvature path	Reinforcement				f <sub>c</sub> Mpa (psi)	Load path	Axial load KN (Kips)	N/Agf <sub>c</sub> %
								Long. (ρ %)	f <sub>y</sub> Mpa (Ksi)	Transverse	f <sub>y</sub> Mpa (Ksi)				
Nichida and Unjoh 13 <sup>th</sup> WCEE Vancouver, Canada 2004 Paper 576	Square		1:4	600 x 600 (23.6 x 23.6)	2500 (102)	4.17	Single	48 No.3 (0.95)	384 (55.7)	φ 6.0 mm @ 75 mm Hoops	350 (50.75)	34.1 (4945)	Biaxial-dynamic Kobe - 1995 N-S + E-W + Up	360 (81)	2.93
	Circular		1:4	600 (23.6)	2640 (104)	4.40	Single	40 No.3 (1.01)	372 (53.9)	φ 6.0 mm @ 75 mm Hoops (ρ <sub>v</sub> =0.31%)	340 (49.3)	33.7 (4885)	Biaxial-dynamic Kobe - 1995 N-S + E-W + Up	280 (63)	2.94
	Rectangular		1:4	450 x 800 (17.7 x 34.5)	2500 (102)	5.56 3.125	Single	48 No.3 (0.95)	373 (54)	φ 6.0 mm @ 75 mm Hoops	316 (45.8)	30.4 (4408)	Biaxial-dynamic Kobe - 1995 N-S + E-W + Up	360 (81)	3.29
Sakai, Jeong and Mahin 8 <sup>th</sup> USNCEE California, US 2006	RC		1:4.5	406 (16)	2030 (80)	5.00	Single	12 No.4 (1.19)	491 (71.3)	φ 6.0 mm @ 32 mm Spiral (ρ <sub>v</sub> =0.76%)	607 (88)	41.7 (6050)	Biaxial-dynamic Northridge (1994) Los Gatos N-S, E-W, Up	290 (65)	5.37
	PRC		1:4.5	406 (16)	2030 (80)	5.00	Single	12 No. 3 (0.66) Tendon φ 32 mm	488 (71)	φ 6.0 mm @ 32 mm Spiral (ρ <sub>v</sub> =0.76%)	607 (88)	41.7 (6050)	Biaxial-dynamic Northridge (1994) N-S, E-W, Up	644 (145)	12.41
	PRC-2		1:4.5	406 (16)	2030 (80)	5.00	Single	12 No. 3 (0.66) Tendon φ 36 mm	488 (71)	φ 6.0 mm @ 32 mm Spiral (ρ <sub>v</sub> =0.76%)	607 (88)	32.6 (4760)	Biaxial-dynamic Northridge (1994) N-S, E-W, Up	450 (100)	11.09
	PRC-U		1:4.5	406 (16)	2030 (80)	5.00	Single	12 No. 3 (0.66) Tendon φ 36 mm	488 (71)	φ 6.0 mm @ 127 mm Spiral (ρ <sub>v</sub> =0.76%)	607 (88)	32.2 (4675)	Biaxial-dynamic Northridge (1994) N-S, E-W, Up	433 (97)	10.81
	PRC-U2		1:4.5	406 (16)	2030 (80)	5.00	Single	12 No. 3 (0.66) Tendon φ 36 mm	488 (71)	φ 6.0 mm @ 127 mm Spiral (ρ <sub>v</sub> =0.76%)	607 (88)	32.5 (4675)	Biaxial-dynamic Northridge (1994) N-S, E-W, Up	570 (128)	14.09
	PRC-UJ Steel Jacket		1:4.5	406 (16)	2030 (80)	5.00	Single	12 No. 3 (0.66) Tendon φ 36 mm	488 (71)	φ 6.0 mm @ 127 mm Spiral (ρ <sub>v</sub> =0.19%)	607 (88)	32.1 (4675)	Biaxial-dynamic Northridge (1994) N-S, E-W, Up	445 (100)	11.14
Sakai and Unjoh Earthquake Eng. And Engineering vibrations Vol. 5. No.1	Circular		1:4	600 (23.6)	2640 (104)	4.40	Single	40 No.3 (1.01)	351 (50.9)	φ 6.0 mm @ 75 mm Hoops (ρ <sub>v</sub> =0.31%)	340 (49.3)	41.7 (6050)	Biaxial-dynamic Nihonkai (1983) N-S + E-W + Up	280 (63)	2.37
Johnson, Saiidi and Sanders CCEER 06-02 2006	Bent 1		1:4	305 (12)	1520 (60)	4.98	Double	16 No.3 (0.88)	468.2 (68)	φ 4.9 mm @ 19 mm Spiral (ρ <sub>v</sub> =0.88%)	385 (55.8)	40.8 (5920)	Biaxial-dynamic Northridge (1994) Century City	250 (56)	8.39
	Bent 2		1:4	305 (12)	2440 (96)	8.00	Double	16 No.3 (0.88)	468.2 (68)	φ 4.9 mm @ 19 mm Spiral (ρ <sub>v</sub> =0.88%)	385 (55.8)	40.8 (5920)	Biaxial-dynamic Northridge (1994) Century City	218 (50)	7.31
	Bent 3		1:4	305 (12)	1830 (72)	6.00	Double	16 No.3 (0.88)	468.2 (68)	φ 4.9 mm @ 19 mm Spiral (ρ <sub>v</sub> =0.88%)	385 (55.8)	40.8 (5920)	Biaxial-dynamic Northridge (1994) Century City	250 (56)	8.39

**Table A-21 Summary of RC Columns Tested Using Dynamic Testing (Bidirectional Shake Table)**

Research	Specimen	Section	Scale	Dimensions mm (in)	Height mm (in)	L/d	Curvature path	Reinforcement				f <sub>c</sub> Mpa (psi)	Load path	Axial load KN (Kips)	N/Agf <sub>c</sub> %
								Long. (ρ %)	f <sub>y</sub> Mpa (Ksi)	Transverse	f <sub>y</sub> Mpa (Ksi)				
Nelson, Saiidi and Zadeh CCEER 07-04 2007	Bent 1		1:4	305 (12)	1525 (60)	5.00	Double	16 No.3 (0.88)	-	φ 4.9 mm @ 19 mm Spiral (ρ <sub>v</sub> =0.88%)	-	-	Biaxial-dynamic Northridge (1994) Century City	183 (41.1)	7.00
	Bent 2		1:4	305 (12)	2134 (84)	7.00	Double	16 No.3 (0.88)	-	φ 4.9 mm @ 19 mm Spiral (ρ <sub>v</sub> =0.88%)	-	-	Biaxial-dynamic Northridge (1994) Century City	175 (39.4)	7.30
	Bent 3		1:4	305 (12)	1830 (72)	6.00	Double	16 No.3 (0.88)	-	φ 4.9 mm @ 19 mm Spiral (ρ <sub>v</sub> =0.88%)	-	-	Biaxial-dynamic Northridge (1994) Century City	183 (41.1)	7.00
Choi, Saiidi and Somerville CCEER 07-06 2007	Bent 1		1:4	305 (12)	1520 (60)	4.98	Double	16 No.3 (0.88)	468.2 (68)	φ 4.9 mm @ 19 mm Spiral (ρ <sub>v</sub> =0.88%)	385 (55.8)	44.6 (6470)	Biaxial-dynamic Synthetic	250 (56)	7.67
	Bent 2		1:4	305 (12)	2440 (96)	8.00	Double	16 No.3 (0.88)	468.2 (68)	φ 4.9 mm @ 19 mm Spiral (ρ <sub>v</sub> =0.88%)	385 (55.8)	44.6 (6470)	Biaxial-dynamic Synthetic	218 (50)	6.69
	Bent 3		1:4	305 (12)	1830 (72)	6.00	Double	16 No.3 (0.88)	468.2 (68)	φ 4.9 mm @ 19 mm Spiral (ρ <sub>v</sub> =0.88%)	385 (55.8)	44.6 (6470)	Biaxial-dynamic Synthetic	250 (56)	7.67
Kawashima, Sasaki and Kajiwara 25th US-Japan Bridge Engineering Workshop Tsukuba, Japan 2009	C1-1		Full size	1800 (70)	7500 (295)	4.17	Single	32 No.9 32 No.9 16 No.9	345 (50)	No.4 @ 150 mm Hoops, lap splice (ρ <sub>v</sub> =0.88%)	345 (50)	27 (3920)	Biaxial-dynamic 1995 JR Takatori N-S, E-W, Up	3070 (690)	4.47
	C1-2		Full size	1800 (70)	7500 (295)	4.17	Single	32 No.9 cut @ 4.8m 16 No.9 cut @ 3m (2.02)	345 (50)	No.4 @ 150 mm Hoops, lap splice (ρ <sub>v</sub> =0.88%)	345 (50)	30.8 (4470)	Biaxial-dynamic 1995 JR Takatori N-S, E-W, Up	3070 (690)	3.92
	C1-5		Full size	1800 (70)	7500 (295)	4.17	Single	36 No.11 36 No.11 (2.19)	345 (50)	No.4 @ 150 mm Hoops, 135° hooks (ρ <sub>v</sub> =0.92%)	345 (50)	27 (3920)	Biaxial-dynamic 1995 JR Takatori N-S, E-W, Up	3720 (836)	5.41

**Table A-22 Summary of Interlocking Columns Tested Using Dynamic Testing (Shake Table)**

Research	Specimen	Section	Scale	Dimensions mm (in)	Height mm (in)	L/d	Curvature path	Reinforcement			f <sub>c</sub> Mpa (psi)	Load path	Axial load KN (Kips)	N/Agf <sub>c</sub> %	
								Long. (ρ %)	f <sub>y</sub> Mpa (Ksi)	Transverse f <sub>y</sub> Mpa (Ksi)					
Correal, Saiidi and Sanders CCEER 04- 2004	ISL1		1:4	305 x 445 (12 x 17.5)	1473 (58)	4.83 3.31	Single	32 No.3 (2.0)	520 (75.4)	φ 4.9 mm @ 25 mm Spirals (ρ <sub>v</sub> =1.1)	620 (89.9)	39.3 (5707)	Uniaxial-dynamic Northridge (1994)	400 (90)	8.79
	ISL1.5		1:4	305 x 521 (12 x 20.5)	1829 (72)	6.00 3.51	Single	38 No.3 (2.0)	520 (75.4)	φ 4.9 mm @ 25 mm Spirals (ρ <sub>v</sub> =1.1)	620 (89.9)	39.3 (5707)	Uniaxial-dynamic Northridge (1994)	471 (106)	8.63
	ISH1.0		1:5	254 x 368 (10 x 14.5)	1473 (58)	5.80 4.00	Double	32 No.3 (2.9)	520 (75.4)	φ 4.0 mm @ 38 mm Spirals (ρ <sub>v</sub> =0.6)	620 (89.9)	39.1 (5664)	Uniaxial-dynamic Northridge (1994)	276 (62)	8.86
	ISH1.25		1:5	254 x 397 (10 x 15.6)	1600 (63)	6.30 4.03	Double	34 No.3 (2.8)	520 (75.4)	φ 4.0 mm @ 25 mm Spirals (ρ <sub>v</sub> =0.9)	620 (89.9)	39.3 (5707)	Uniaxial-dynamic Northridge (1994)	298 (67)	8.72
	ISH1.5		1:5	254 x 425 (10 x 16.75)	1753 (69)	6.90 4.12	Double	38 No.3 (2.9)	520 (75.4)	φ 4.0 mm @ 25 mm Spirals (ρ <sub>v</sub> =0.9)	620 (89.9)	39.1 (5664)	Uniaxial-dynamic Northridge (1994)	258 (58)	7.01
	ISH1.5T		1:5	254 x 425 (10 x 16.75)	1753 (69)	6.90 4.12	Double	38 No.3 (2.9)	520 (75.4)	φ 4.0 mm @ 25 mm and cross ties φ 4.0 mm @ 58 mm	620 (89.9)	39.1 (5664)	Uniaxial-dynamic Northridge (1994)	356 (80)	9.68
Tatsumoto, Oskad Kawashima and Mahin 14 <sup>th</sup> WCEE Beijing, China 2010	I1		1:6	280 x 400 (11 x 15.7)	1100 (43)	3.93 2.75	Single	30 No.3 (2.16)	398 (57.7)	φ 6 mm @ 37 mm (ρ <sub>v</sub> =1.30)	363.2 (52.7)	32 (4645)	Triaxial-dynamic TR Takatori station Kobe - 1995	231 (52)	8.36
	I2		1:6	280 x 440 (11 x 17.3)	1100 (43)	3.93 2.5	Single	30 No.3 (1.94)	398 (57.7)	φ 6 mm @ 37 mm (ρ <sub>v</sub> =1.17)	363.2 (52.7)	32 (4645)	Triaxial-dynamic TR Takatori station Kobe - 1995	231 (52)	7.40
	R1		1:6	280 x 400 (11 x 15.7)	1100 (43)	3.93 2.75	Single	30 No.3 (1.66)	398 (57.7)	φ 6 mm @ 37 mm (ρ <sub>v</sub> =1.15)	363.2 (52.7)	32.2 (4675)	Triaxial-dynamic TR Takatori station Kobe - 1995	231 (52)	6.41
	R2		1:6	280 x 440 (11 x 17.3)	1100 (43)	3.93 2.5	Single	30 No.3 (1.51)	398 (57.7)	φ 6 mm @ 37 mm (ρ <sub>v</sub> =1.05)	363.2 (52.7)	32.2 (4675)	Triaxial-dynamic TR Takatori station Kobe - 1995	231 (52)	5.82



## **Appendix B. Columns Design According to the 2006 Caltrans SDC**

### **B.1 Introduction**

As it was stated in Chapter 2, the specimens used in this study were selected to have similar geometry, reinforcement details and materials than previous columns tested under unidirectional excitations on the shake table at the University of Nevada, Reno (Laplace *et al.*, 1999 and Correal *et al.*, 2005). The unidirectional tested specimens were designed using details typical of bridges in California and in accordance with the Caltrans Seismic Design Criteria (SDC) and Bridge Design Specifications (BDS). The circular column was designed according to the 1992 SDC (CALTRANS, 1992) whereas the double interlocking column was designed according to the 2001 SDC (CALTRANS, 2001). Since at the time of designing the columns of this study a new version of the SDC was published by Caltrans (CALTRANS, 2006), the capacity of the reinforced concrete columns was verified in order to fulfill the new capacity requirements. The capacity of the scaled models was verified instead the prototype; when required, the scale factors were used. The main calculation of the flexural and shear capacity of the columns is presented in this appendix.

### **B.2 Circular Columns**

The geometry, reinforcement and material properties of the unidirectionally tested specimen 9F1 (Laplace *et al.*, 1999) were used to verify the capacity of the section

**B.2.1 Section Properties**

Diameter of the section;  $D=20$  in

Height of column;  $H=72$  in

Clear cover to the spirals;  $cc=0.75$  in

Cross sectional area;  $A_g=\pi D^2/4= 201$  in<sup>2</sup>

Aspect ratio;  $H/D=4.5$

Core diameter;  $D_c=14.25$  in

Confined core area;  $A_c=\pi D_c^2/4= 159.5$  in<sup>2</sup>

Axial load;  $P=80$  kips

Column displacement ductility;  $\mu_d=5$

**B.2.2 Material Properties**

Longitudinal reinforcement; 20 No.4

Longitudinal bar diameter;  $d_b=0.5$  in

Longitudinal bar area;  $A_b=0.20$  in<sup>2</sup> ( $A_s=4$  in<sup>2</sup>)

Transverse reinforcement (smooth wire); W5.0

Transverse wire diameter;  $d_s=0.252$  in

Transverse wire area;  $A_s=0.05$  in<sup>2</sup>

Spiral pitch;  $s=1.5$  in

Concrete strength;  $f'_c=4.5$  ksi

Longitudinal reinforcement yielding stress;  $f_y=65$  ksi

Transverse reinforcement yielding stress;  $f_y=58$  ksi

Reinforcement elastic modulus;  $E_s=29000$  ksi

### B.2.3 Maximum and Minimum Longitudinal Reinforcement

According to Caltrans SDC section 3.7.1 and 3.7.2 the longitudinal steel ratio need to satisfy the limits:

$$1\% < \rho_l = \frac{A_s}{A_g} = \frac{4}{201} = 1.99\% < 4\% \quad \text{OK!}$$

### B.2.4 Confinement Reinforcement

According to Caltrans SDC section 3.8.1 the volumetric steel ratio need to satisfy the limits on BDS section 8.18.2.2:

$$\rho_{smin} = 0.45 \left( \frac{A_g}{A_c} - 1 \right) \frac{f'_c}{f_y} = 0.45 \left( \frac{201}{159.5} - 1 \right) \frac{4.5}{58} = 0.91\%$$

$$\rho_{smin} = 0.12 \frac{f'_c}{f_y} \left( 0.5 + \frac{1.25 P}{f'_c A_g} \right) = 0.12 \frac{4.5}{58} \left( 0.5 + \frac{1.25(80)}{4.5(201)} \right) = 0.56\% \quad (D > 3ft)$$

$$\rho_s = \frac{4A_s}{D_c S} = \frac{4(0.05)}{14.25(1.5)} = 0.94\% > \rho_{smin} \quad \text{OK!}$$

In addition, from SDC section 8.2.5, it is required that the maximum spacing of transverse reinforcement in the plastic hinge zone be the less of:

$$D/5 = 16/5 = 3.2 \text{ in}$$

$$6 d_b = 6(0.5) = 3 \text{ in}$$

$$8 \text{ in (scale factor } 1/3) = 2.67 \text{ in} > \mathbf{1.5 \text{ in}} \quad \text{OK!}$$

### B.2.5 Flexural Capacity

By using the method described in section 2.4.1 and program XTRACT (TRC/Imbsen, 2007) it was possible to calculate the plastic moment of the column as

$M_p = 1950$  k/in.; for  $P = 80$  kips

$M_p = 1678$  k/in.; for  $P = 0$  kips

### B.2.6 Shear Capacity

According to Caltrans SDC section 3.6.2 the shear capacity provided by the concrete need to be:

For axial force **P=80** kips

$$0.3 \geq F1 = \frac{\rho_s f_y h}{0.15} + 3.67 - \mu_d = \frac{0.0091 (58)}{0.15} + 3.67 - 5 = 2.18 < 3.0$$

$$F2 = 1 + \frac{P}{2000 A_g} = 1 + \frac{80000}{2000 (201)} = 1.19 < 1.5$$

$$v_c = F1 F2 \sqrt{f'_c} = 2.18 (1.19) \sqrt{4500} = 174 \text{ psi} \leq 4 \sqrt{4500} = 268.3 \text{ psi}$$

$$V_c = v_c (0.8 A_g) = 174 (0.8 \times 201) = 27.9 \text{ kip}$$

For axial force **P=0** kips

$$F2 = 1 + \frac{P}{2000 A_g} = 1 + \frac{0}{2000 (201)} = 1.0 < 1.5$$

$$v_c = F1 F2 \sqrt{f'_c} = 2.18 (1.0) \sqrt{4500} = 146 \text{ psi} \leq 4 \sqrt{4500} = 268.3 \text{ psi}$$

$$V_c = v_c A_e = v_c (0.8 A_g) = 146 (0.8 \times 201) = 23.5 \text{ kip}$$

The shear capacity provided by the spiral according to Caltrans SDC section 3.6.3 and 3.6.5 is:

$$A_v = n \frac{\pi}{2} A_s = 1 \frac{\pi}{2} 0.05 = 0.078 \geq 0.025 \frac{D_c s}{f_{yh}} = 0.025 \frac{14.25(1.5)}{58} = 0.09$$

$$V_s = \frac{A_v f_{yh} D_c}{s} = \frac{0.09(58)(14.25)}{1.5} = 49.6 \text{ kip} \leq 8\sqrt{f'_c} (0.8 A_g) = 86.29 \text{ kip}$$

The nominal shear capacity according to Caltrans SDC section 3.6.1 is:

$$V_n = V_c + V_s = 27.9 + 49.6 = 77.5 \text{ kip} \quad \text{For P=80 kips}$$

$$\phi V_n = 0.85 V_n = 0.85(77.5) = 65.9 \text{ kip} \quad \text{For P=80 kips}$$

$$V_n = V_c + V_s = 23.5 + 49.6 = 73.1 \text{ kip} \quad \text{For P=0 kips}$$

$$\phi V_n = 0.85 V_n = 0.85(73.1) = 62.1 \text{ kip} \quad \text{For P=0 kips}$$

Based on the calculated plastic moment, the maximum shear demand is:

$$V_p = \frac{M_p}{H} = \frac{1945}{72} = 27 \text{ kip} < \phi V_n = 65.9 \text{ kip} \quad \text{P=80 kips} \quad \text{OK!}$$

$$V_p = \frac{M_p}{H} = \frac{1678}{72} = 23 \text{ kip} < \phi V_n = 62.1 \text{ kip} \quad \text{P=0 kips} \quad \text{OK!}$$

Therefore the circular column satisfies the requirements of the 2006 Caltrans seismic design specification.

### B.3 Interlocking Column

The geometry, reinforcement and material properties of the unidirectionally tested specimen ISL1.0 (Correal *et al.*, 2005) were used to verify the capacity of the section

#### B.3.1 Section Properties

Long side of the section;  $D_x=17.5$  in

Short side of the section;  $D_y=12$  in

Height of column;  $H=72$  in

Clear cover to the spirals;  $cc=0.5$  in

Cross sectional area;  $A_g=\pi D^2/4+ A_{interlocking} = \pi(12)^2/4+5.5(12)= 179 \text{ in}^2$

Aspect ratio;  $H/D_x=4.1$  and  $H/D_y =6$

Core diameter;  $D_c=10.8$  in

Confined core area;  $A_c=\pi D_c^2/4+A_{interlocking}= \pi(10.8)^2/4+5.5(10.8)= 151 \text{ in}^2$

Axial load;  $P=90$  kips

Column displacement ductility;  $\mu_d=5$

#### B.3.2 Material Properties

Longitudinal reinforcement; 32 No.3

Longitudinal bar diameter;  $d_b=0.375$  in

Longitudinal bar area;  $A_b=0.11 \text{ in}^2$  ( $A_s=3.52 \text{ in}^2$ )

Transverse reinforcement (smooth wire); W2.9

Transverse wire diameter;  $d_s=0.192$  in

Transverse wire area;  $A_s=0.029 \text{ in}^2$

Spiral pitch;  $s=1.0$  in

Concrete strength;  $f'_c=4.5$  ksi

Longitudinal reinforcement yielding stress;  $f_y=65$  ksi

Transverse reinforcement yielding stress;  $f_y=58$  ksi

Reinforcement elastic modulus;  $E_s=29000$  ksi

### B.3.3 Maximum and Minimum Longitudinal Reinforcement

According to Caltrans SDC section 3.7.1 and 3.7.2 the longitudinal steel ratio need to satisfy the limits:

$$1\% < \rho_l = \frac{A_s}{A_g} = \frac{3.52}{179} = 1.97\% < 4\% \quad \text{OK!}$$

According to Caltrans BDS section 8.18.1.4 the maximum spacing between centers of the spirals need to be:

$$d_i = 10.8 \text{ in} < 1.5D_c = 1.5(10.8) = 16.2 \quad \text{OK!}$$

### B.3.4 Confinement Reinforcement

According to Caltrans SDC section 3.8.1 the volumetric steel ratio need to satisfy the limits on BDS section 8.18.2.2:

$$\rho_{smin} = 0.45 \left( \frac{A_g}{A_c} - 1 \right) \frac{f'_c}{f_y} = 0.45 \left( \frac{179}{151} - 1 \right) \frac{4.5}{58} = 0.65\%$$

$$\rho_{smin} = 0.12 \frac{f'_c}{f_y} \left( 0.5 + \frac{1.25 P}{f'_c A_g} \right) = 0.12 \frac{4.5}{58} \left( 0.5 + \frac{1.25(90)}{4.5(179)} \right) = 0.6\% \quad (D>3\text{ft})$$

$$\rho_s = \frac{4A_s}{D_c s} = \frac{4(0.029)}{10.8(1.0)} = 1.07\% > \rho_{smin} \quad \text{OK!}$$

In addition, from SDC section 8.2.5, it is required that the maximum spacing of transverse reinforcement in the plastic hinge zone be the less of:

$$D/5 = 12/5 = 2.4 \text{ in}$$

$$6 d_b = 6 (0.375) = 2.25 \text{ in}$$

$$8 \text{ in (scale factor } 1/4) = 2.0 \text{ in} > \mathbf{1.0 \text{ in}} \quad \mathbf{OK!}$$

### B.3.5 Flexural Capacity

By using the method described in section 2.4.1 and the program XTRACT (TRC/Imbsen, 2007) it was possible to calculate the plastic moment of the column as  
 $(Mp)_x=2056 \text{ k/in.}$  and  $(Mp)_y=1436 \text{ k/in.}$ ; for  $P=80 \text{ kips}$   
 $(Mp)_x=1738 \text{ k/in.}$  and  $(Mp)_y=1236 \text{ k/in.}$ ; for  $P=0 \text{ kips}$

### B.3.6 Shear Capacity

According to Caltrans SDC section 3.6.2 the shear capacity provided by the concrete need to be:

For axial force  $P=90 \text{ kips}$

$$0.3 \geq F1 = \frac{\rho_s f_{yh}}{0.15} + 3.67 - \mu_d = \frac{0.0107 (58)}{0.15} + 3.67 - 5 = 2.81 < 3.0$$

$$F2 = 1 + \frac{P}{2000 A_g} = 1 + \frac{90000}{2000 (179)} = 1.25 < 1.5$$

$$v_c = F1 F2 \sqrt{f'_c} = 2.81 (1.25) \sqrt{4500} = 235.6 \text{ psi} \leq 4 \sqrt{4500} = 268.3 \text{ psi}$$

$$V_c = v_c (0.8 A_g) = 235.6 (0.8 \times 179) = 33.7 \text{ kip}$$



For axial force  $P=0$  kips

$$F2 = 1 + \frac{P}{2000 A_g} = 1 + \frac{0}{2000 (179)} = 1.0 < 1.5$$

$$v_c = F1F2\sqrt{f'_c} = 2.81 (1.0)\sqrt{4500} = 188.5 \text{ psi} \leq 4\sqrt{4500} = 268.3 \text{ psi}$$

$$V_c = v_c(0.8 A_g) = 188.5 (0.8 \times 179) = 27 \text{ kip}$$

The shear capacity provided by the spiral according to Caltrans SDC section 3.6.3 and 3.6.5 is:

$$A_v = n \frac{\pi}{2} A_s = 2 \frac{\pi}{2} 0.029 = 0.091 \geq 0.025 \frac{D_c s}{f_{yh}} = 0.025 \frac{10.8(1.0)}{58} = 0.05$$

$$V_s = \frac{A_v f_{yh} D_c}{s} = \frac{0.091(58)(10.8)}{1.0} = 57 \text{ kip} \leq 8\sqrt{f'_c} (0.8 A_g) = 76.8 \text{ kip}$$

The nominal shear capacity according to Caltrans SDC section 3.6.1 is:

$$V_n = V_c + V_s = 33.7 + 57 = 90.7 \text{ kip} \quad \text{For } P=90 \text{ kips}$$

$$\phi V_n = 0.85 V_n = 0.85(90.7) = 77.1 \text{ kip} \quad \text{For } P=90 \text{ kips}$$

$$V_n = V_c + V_s = 27 + 57 = 84 \text{ kip} \quad \text{For } P=0 \text{ kips}$$

$$\phi V_n = 0.85 V_n = 0.85(84) = 71.4 \text{ kip} \quad \text{For } P=0 \text{ kips}$$

Based on the calculated plastic moment, the maximum shear demand is:

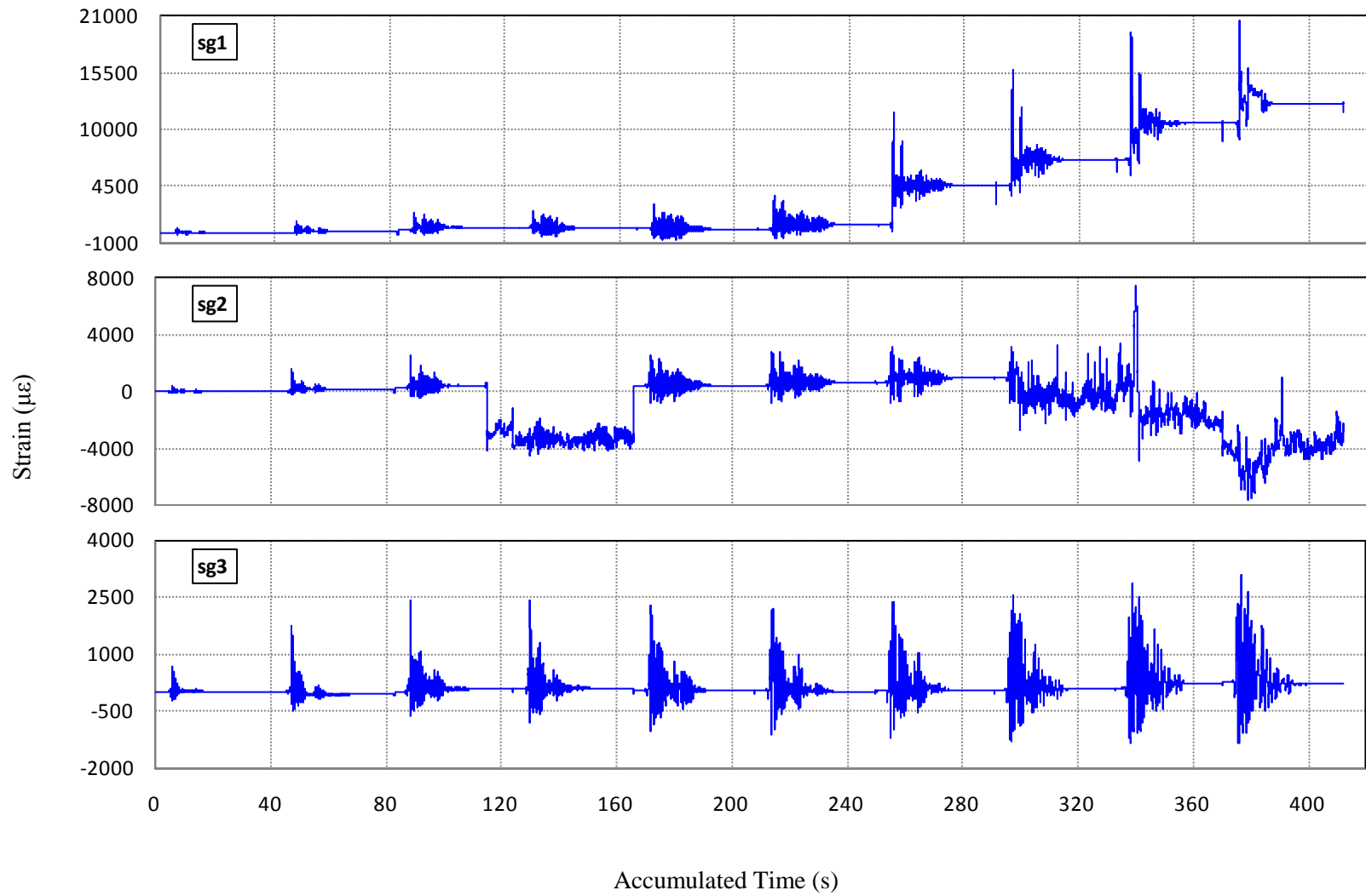
$$V_p = \frac{(M_p)_x}{H} = \frac{2056}{72} = 28.6 \text{ kip} < \phi V_n = 77.1 \text{ kip} \quad P=80 \text{ kips} \quad \text{OK!}$$

$$V_p = \frac{(M_p)_y}{H} = \frac{1436}{72} = 19.9 \text{ kip} < \phi V_n = 77.1 \text{ kip} \quad P=80 \text{ kips} \quad \mathbf{OK!}$$

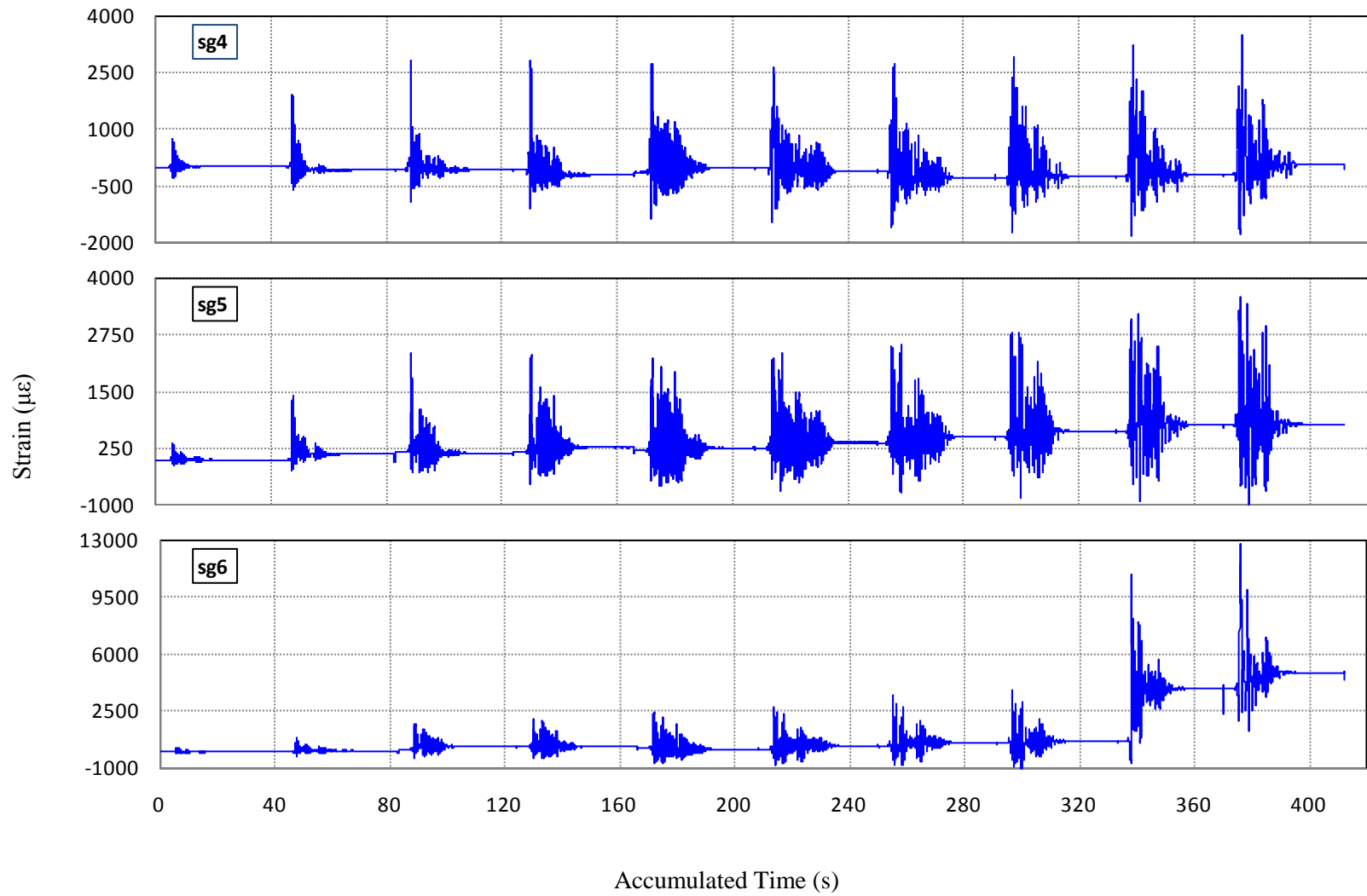
$$V_p = \frac{(M_p)_x}{H} = \frac{1738}{72} = 24.1 \text{ kip} < \phi V_n = 71.4 \text{ kip} \quad P=0 \text{ kips} \quad \mathbf{OK!}$$

$$V_p = \frac{M_p}{H} = \frac{1236}{72} = 17.2 \text{ kip} < \phi V_n = 71.4 \text{ kip} \quad P=0 \text{ kips} \quad \mathbf{OK!}$$

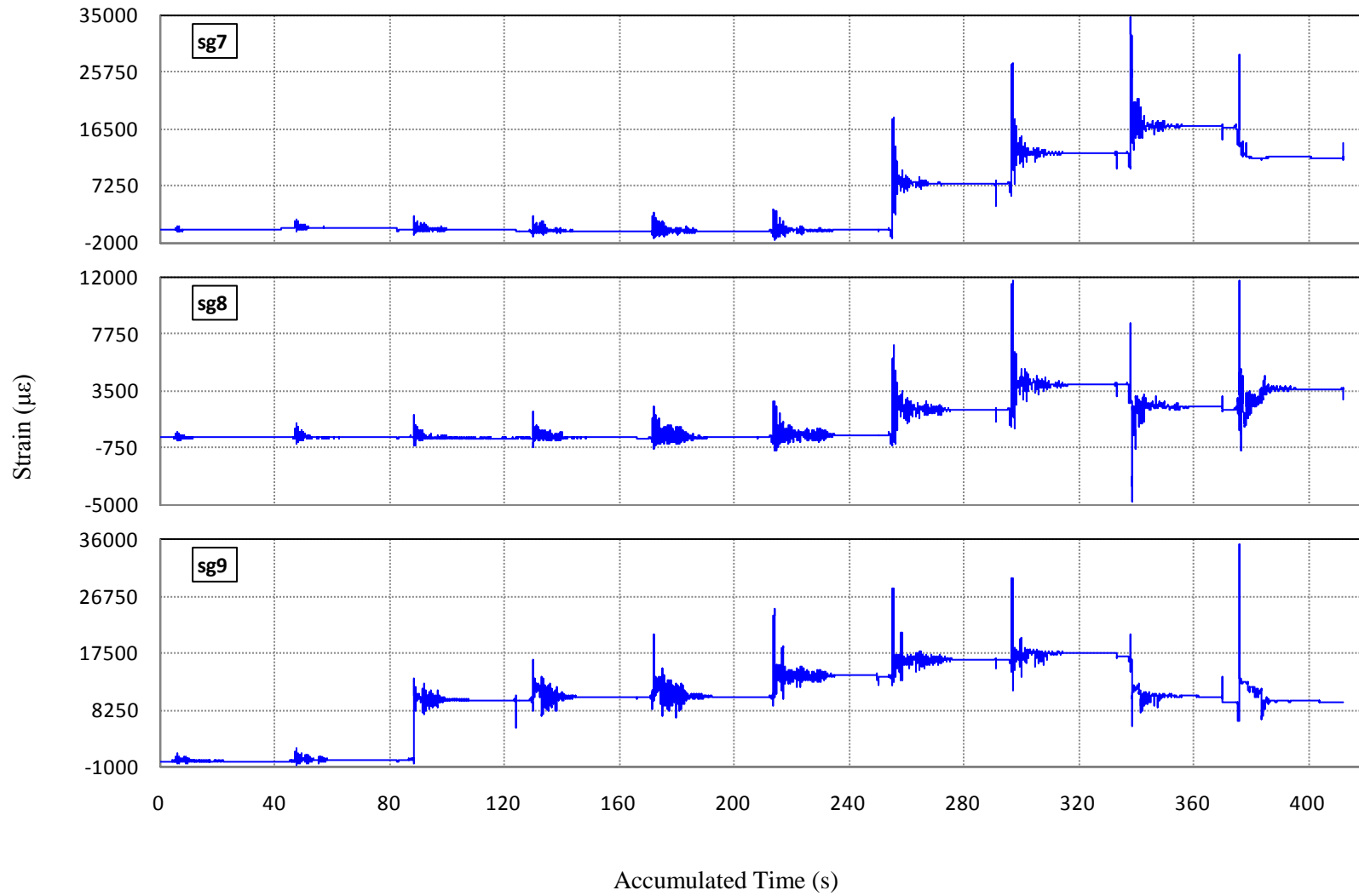
Therefore the interlocking column satisfies the requirements of the 2006 Caltrans seismic design specifications.



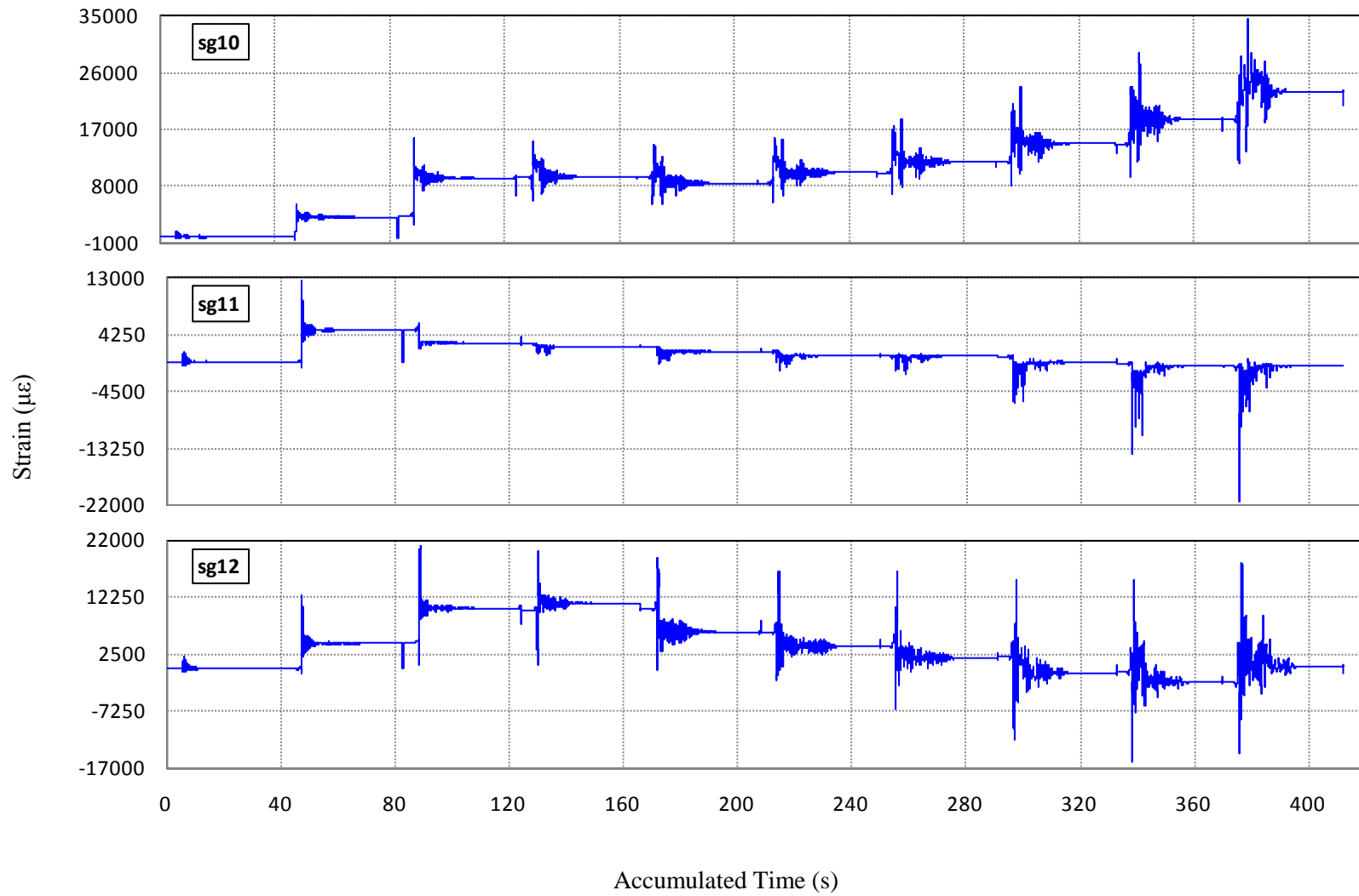
**Figure C-1 Strain History of Gauges 1, 2 and 3 in Specimen C1**



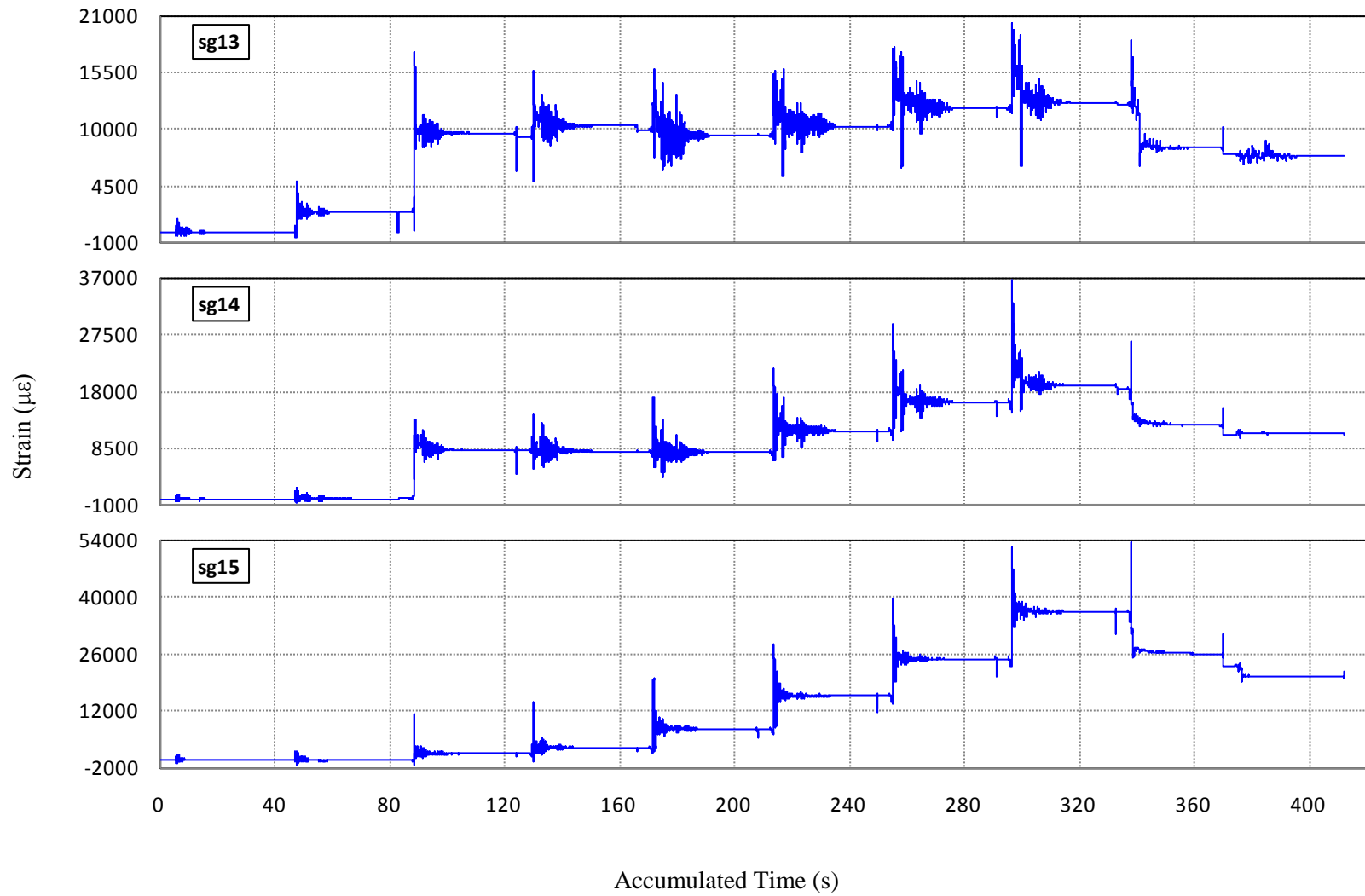
**Figure C-2 Strain History of Gauges 4, 5 and 6 in Specimen C1**



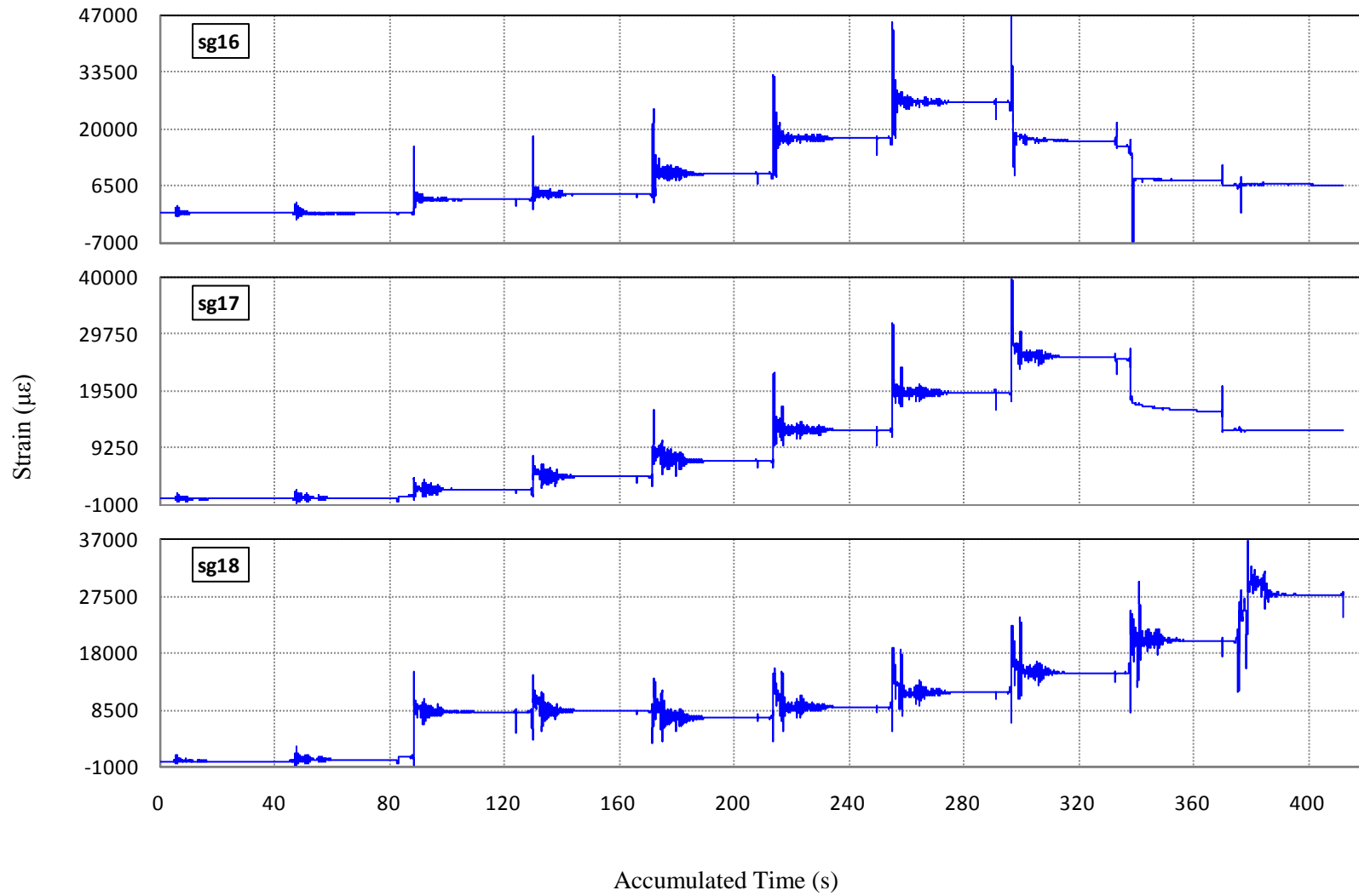
**Figure C-3 Strain History of Gauges 7, 8 and 9 in Specimen C1**



**Figure C-4 Strain History of Gauges 10, 11 and 12 in Specimen C1**

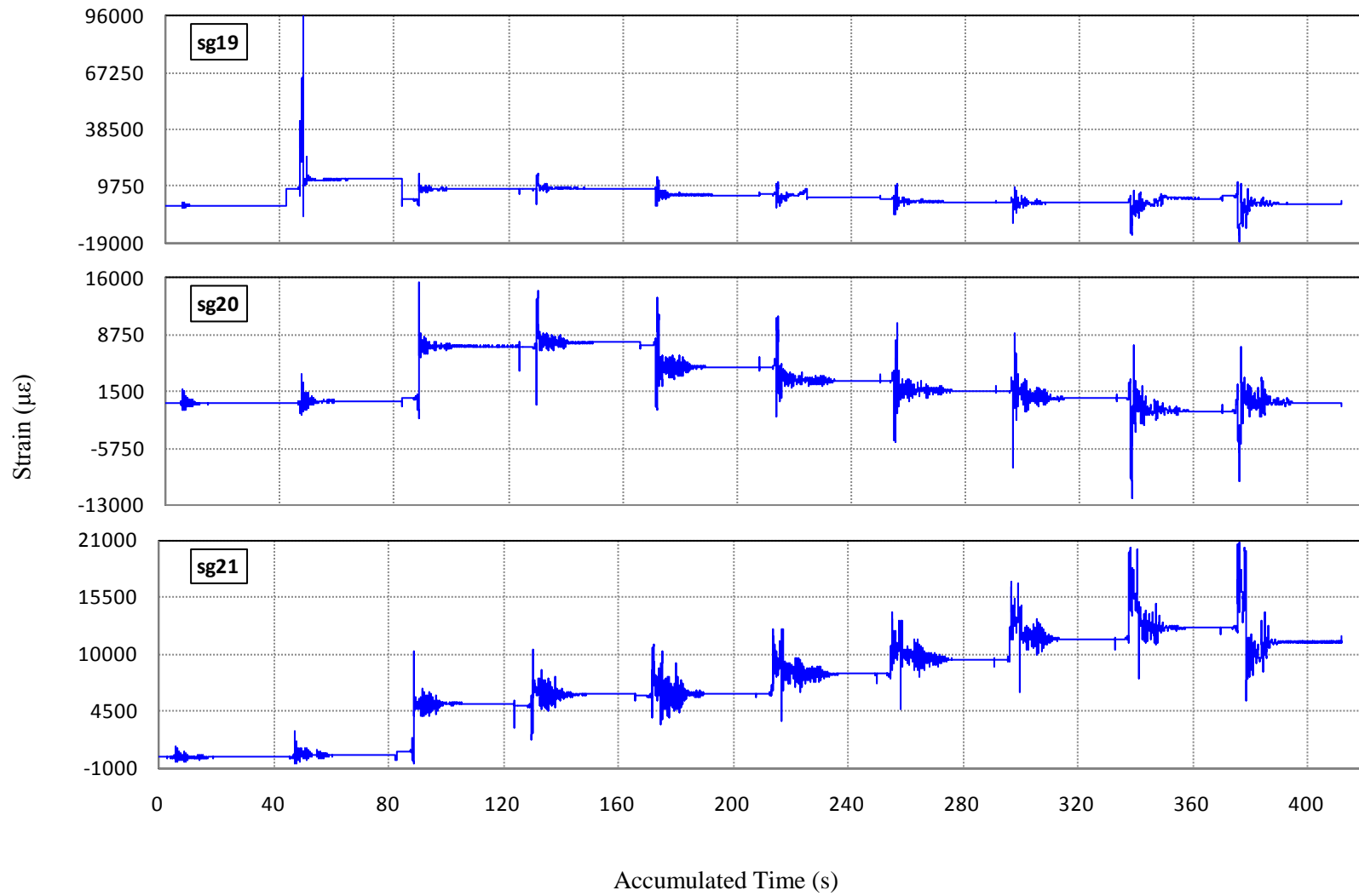


**Figure C-5 Strain History of Gauges 13, 14 and 15 in Specimen C1**

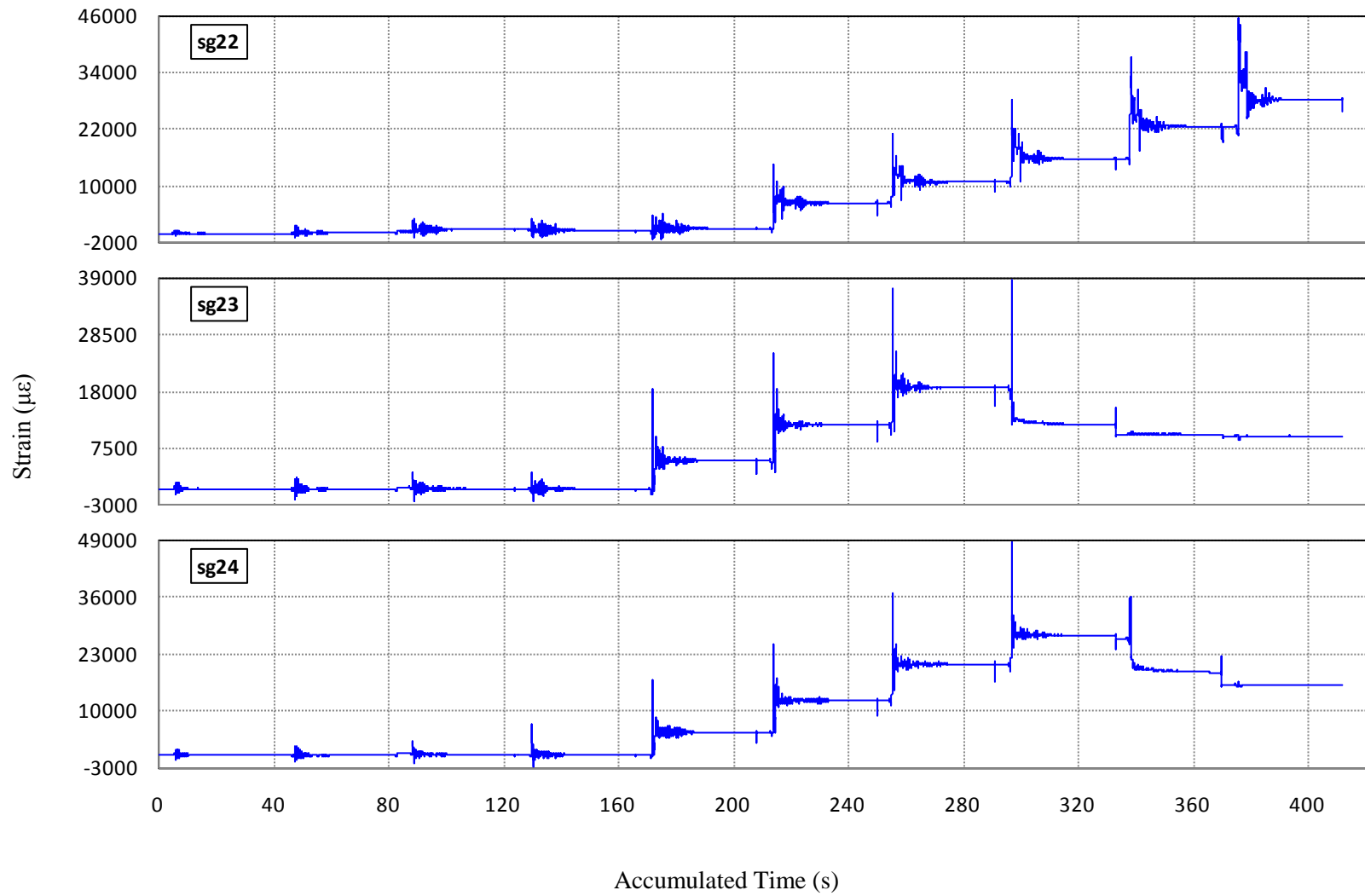


**Figure C-6 Strain History of Gauges 16, 17 and 18 in Specimen C1**

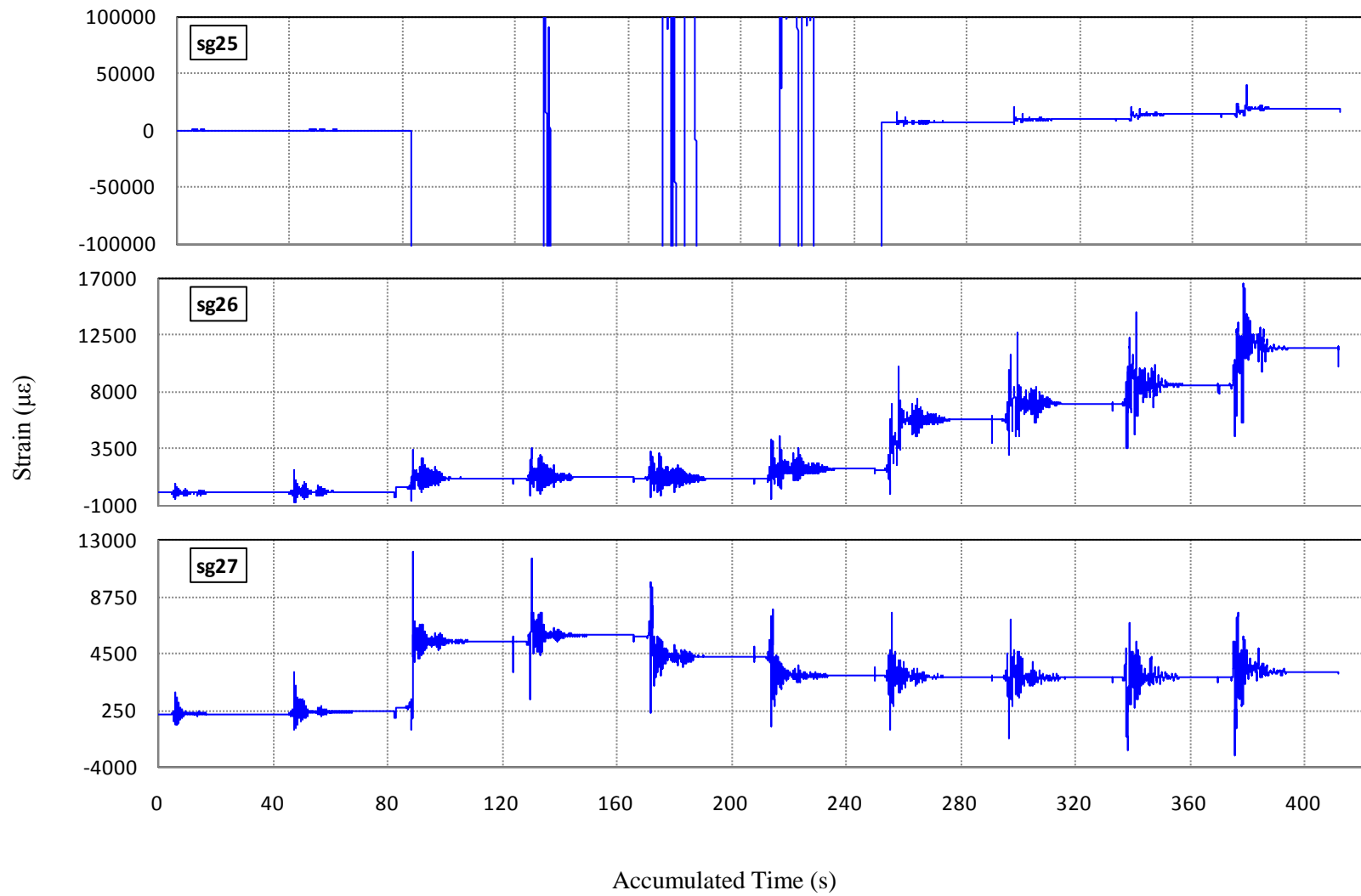




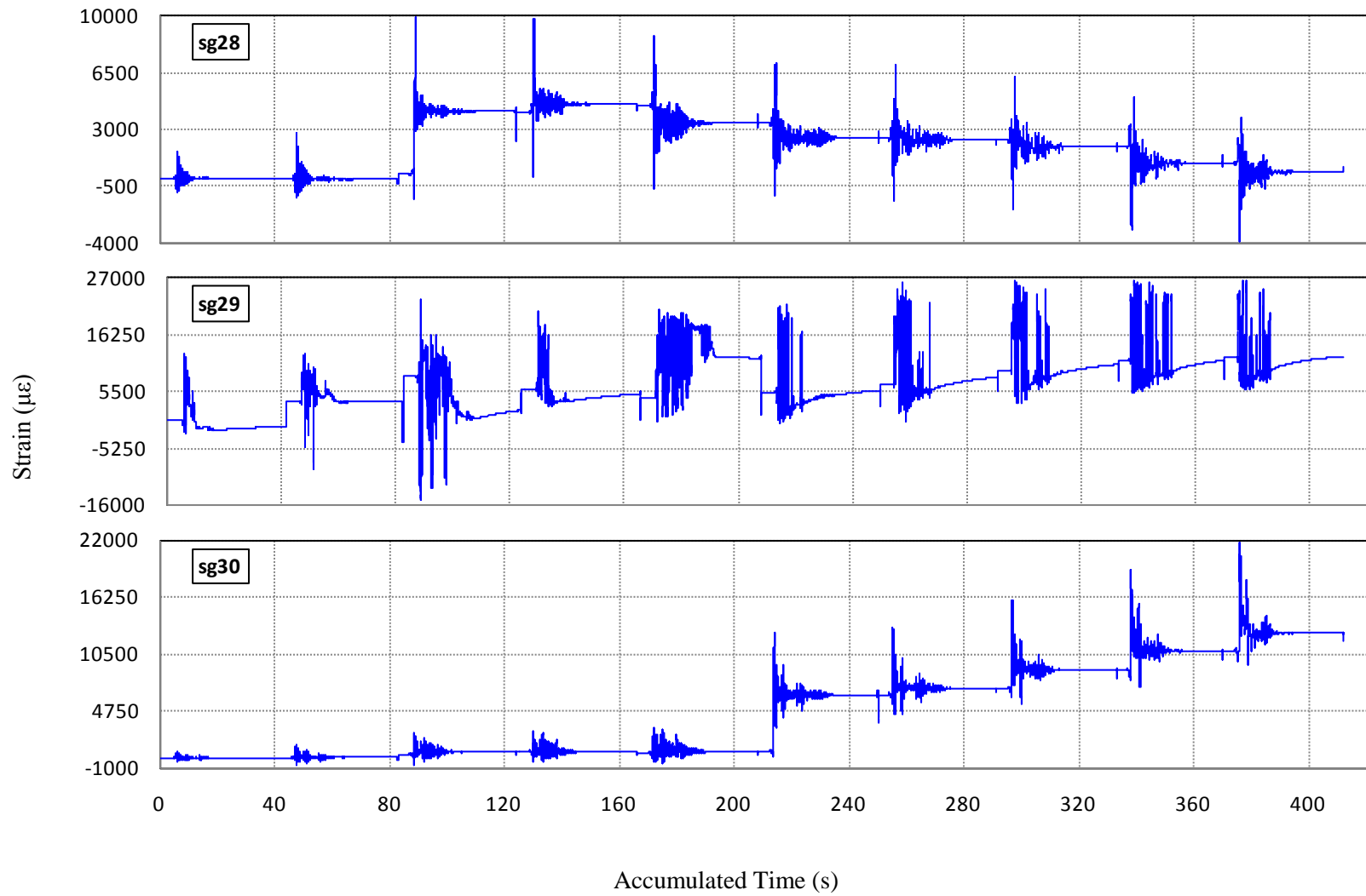
**Figure C-7 Strain History of Gauges 19, 20 and 21 in Specimen C1**



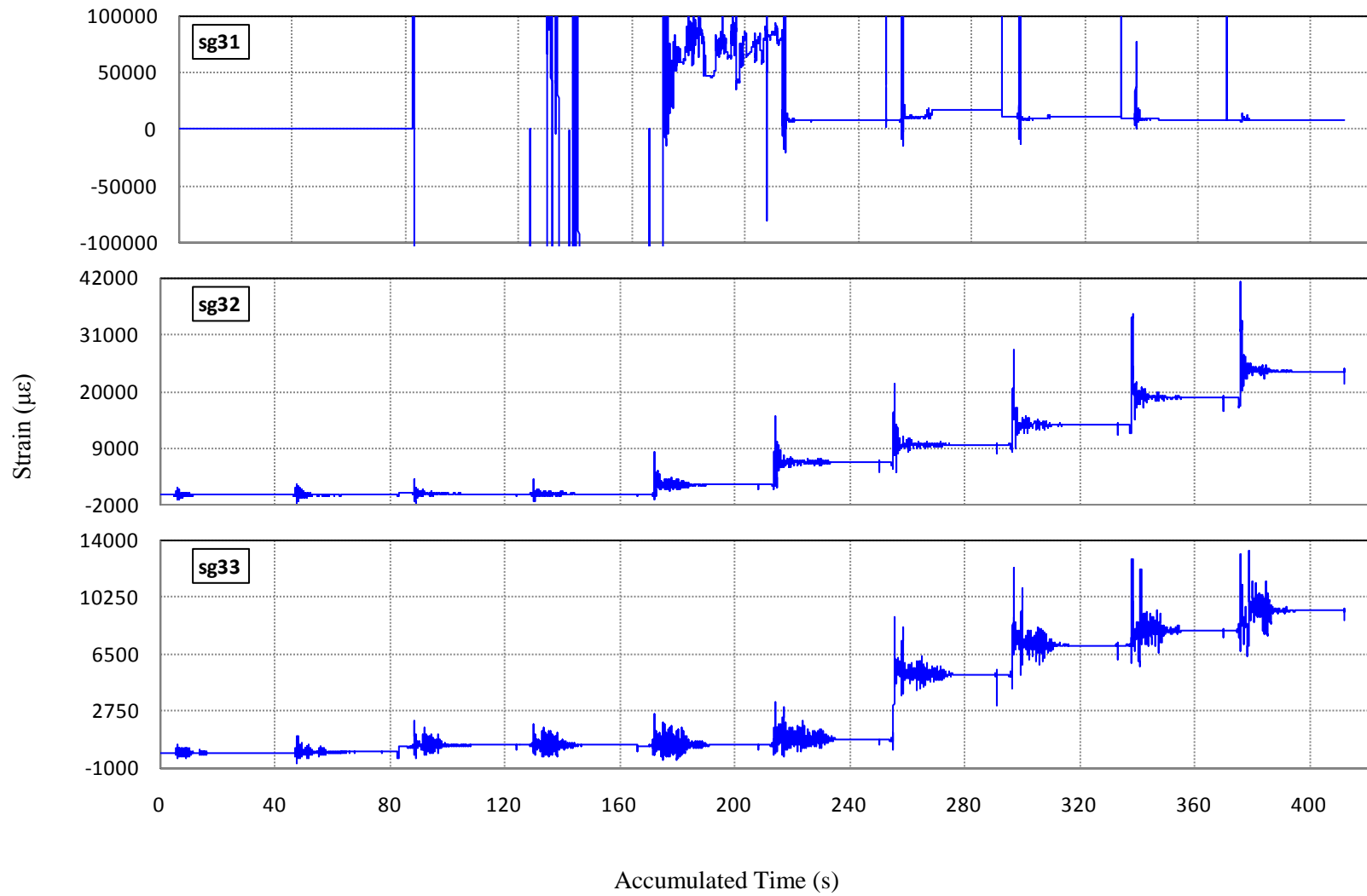
**Figure C-8 Strain History of Gauges 22, 23 and 24 in Specimen C1**



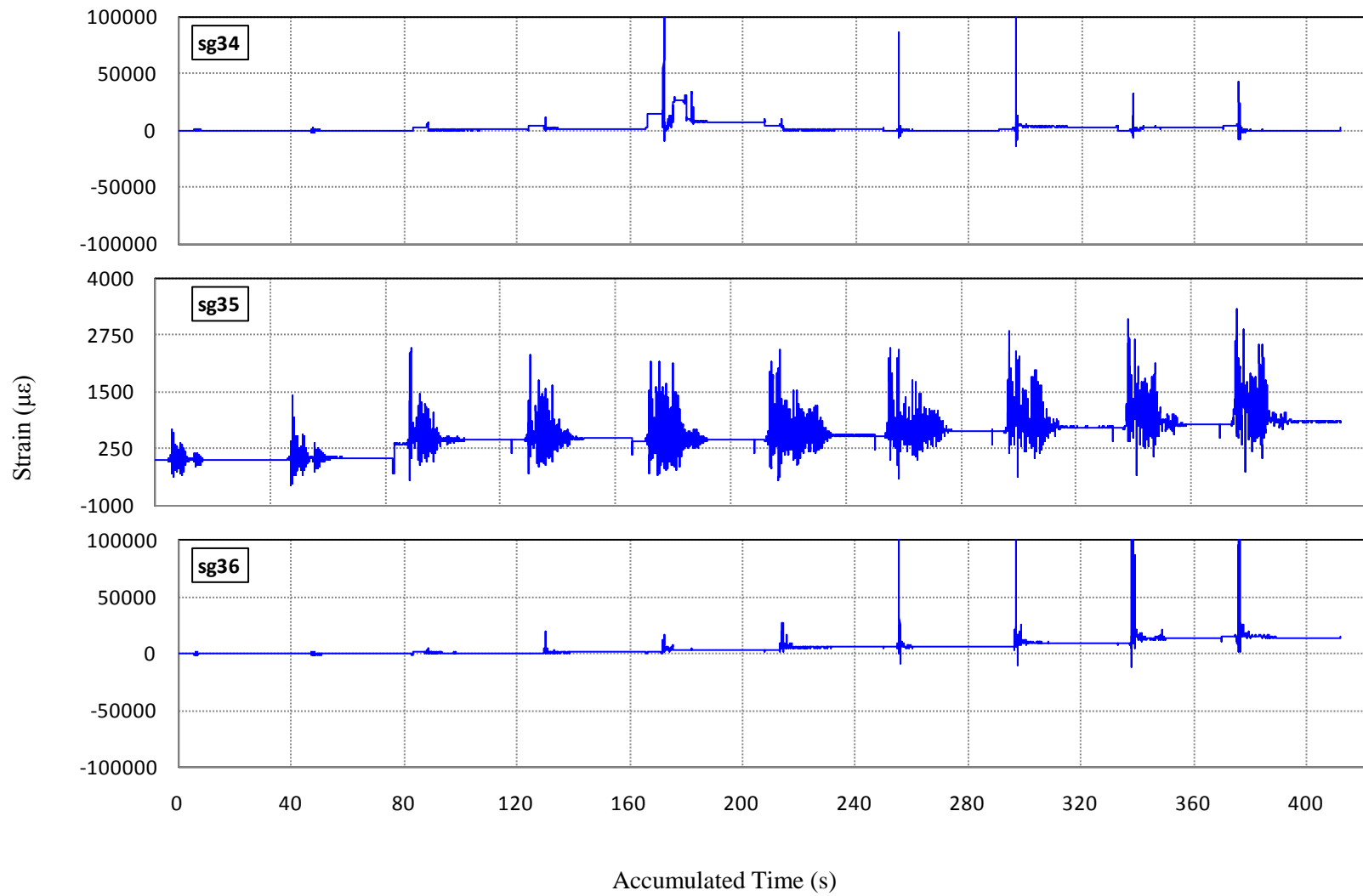
**Figure C-9 Strain History of Gauges 25, 26 and 27 in Specimen C1**



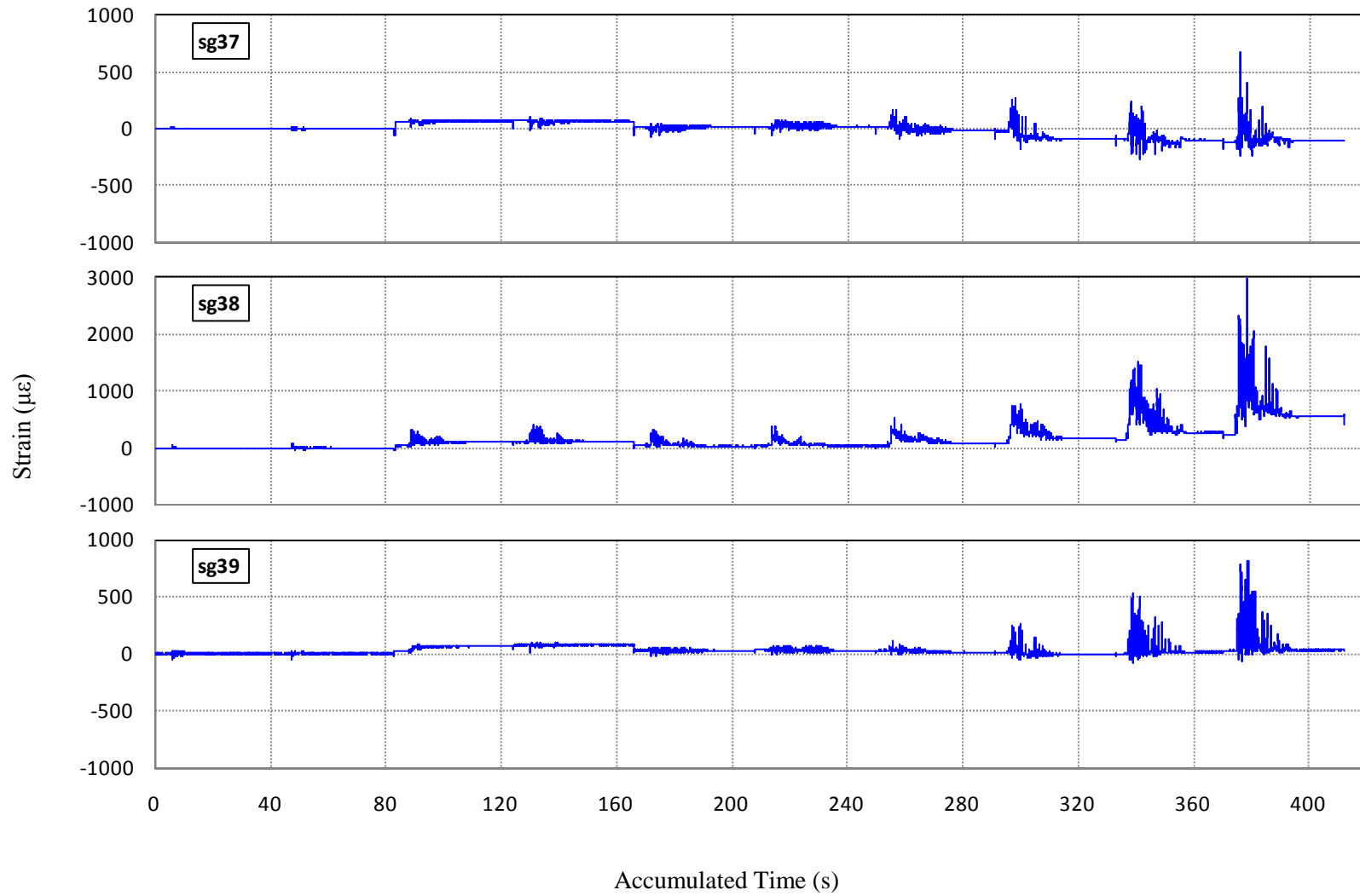
**Figure C-10 StrainHistory of Gauges 28, 29 and 30 in Specimen C1**



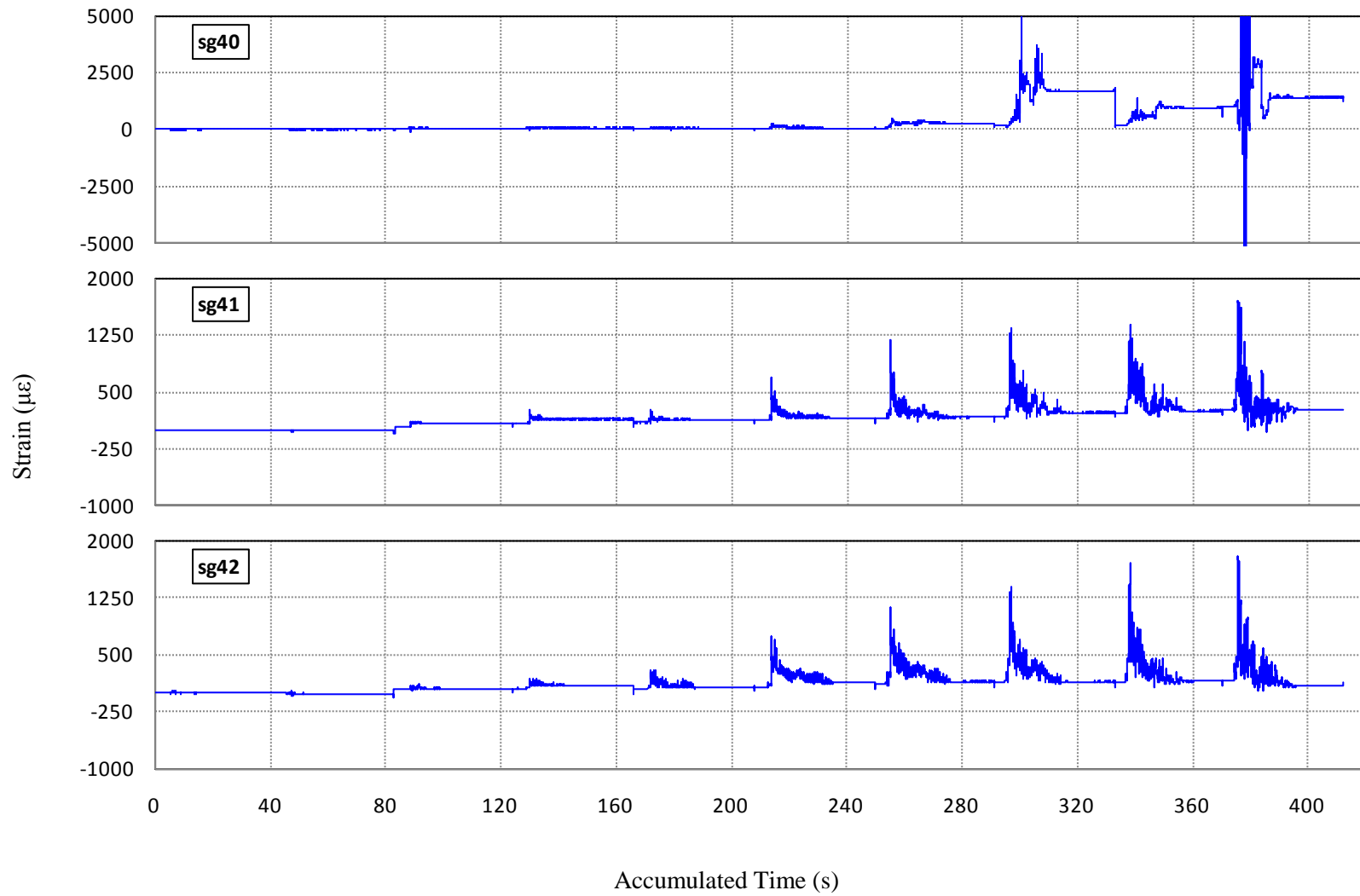
**Figure C-11 Strain History of Gauges 31, 32 and 33 in Specimen C1**



**Figure C-12 Strain History of Gauges 34, 35 and 36 in Specimen C1**

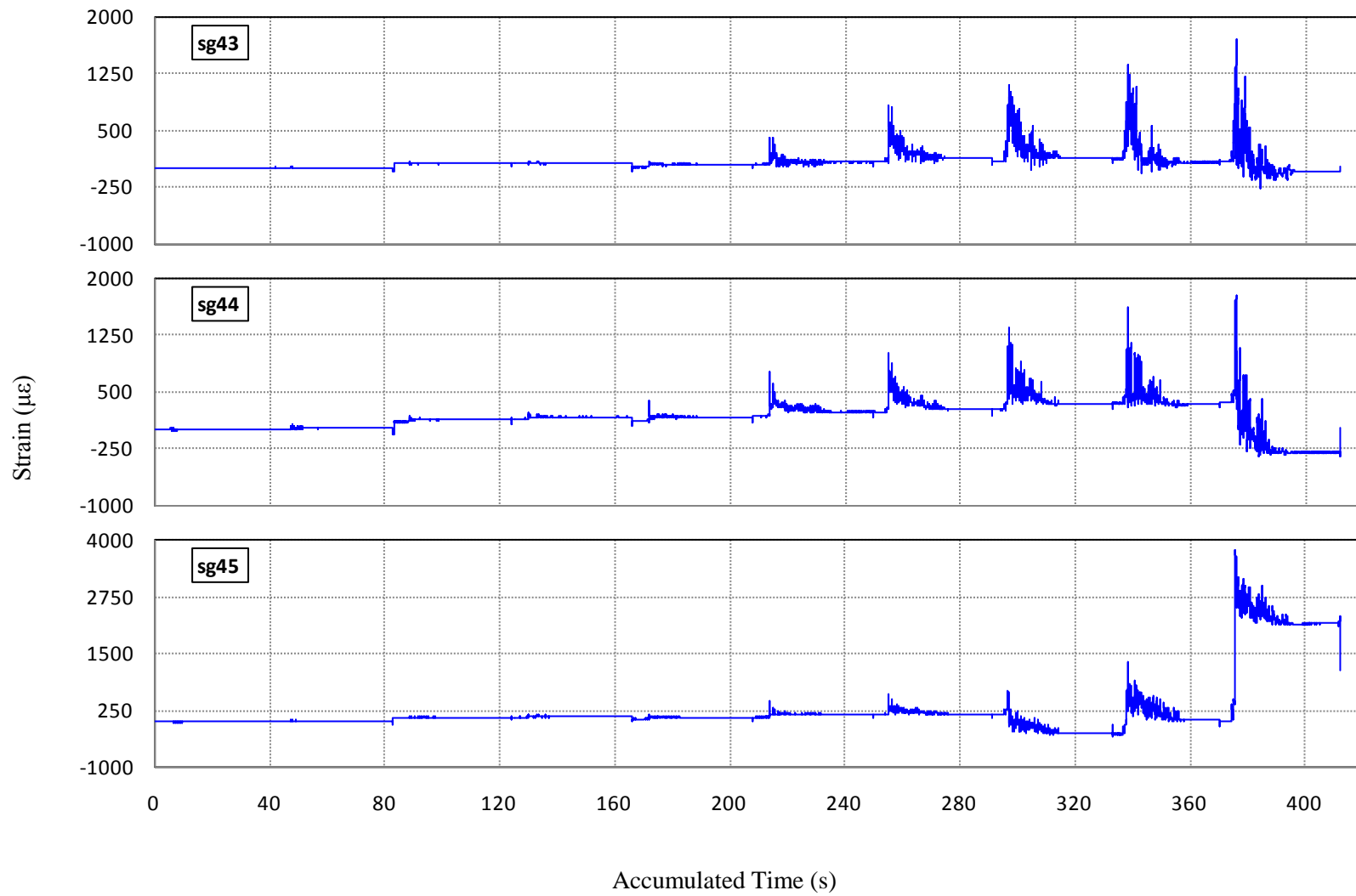


**Figure C-13 Strain History of Gauges 37, 38 and 39 in Specimen C1**

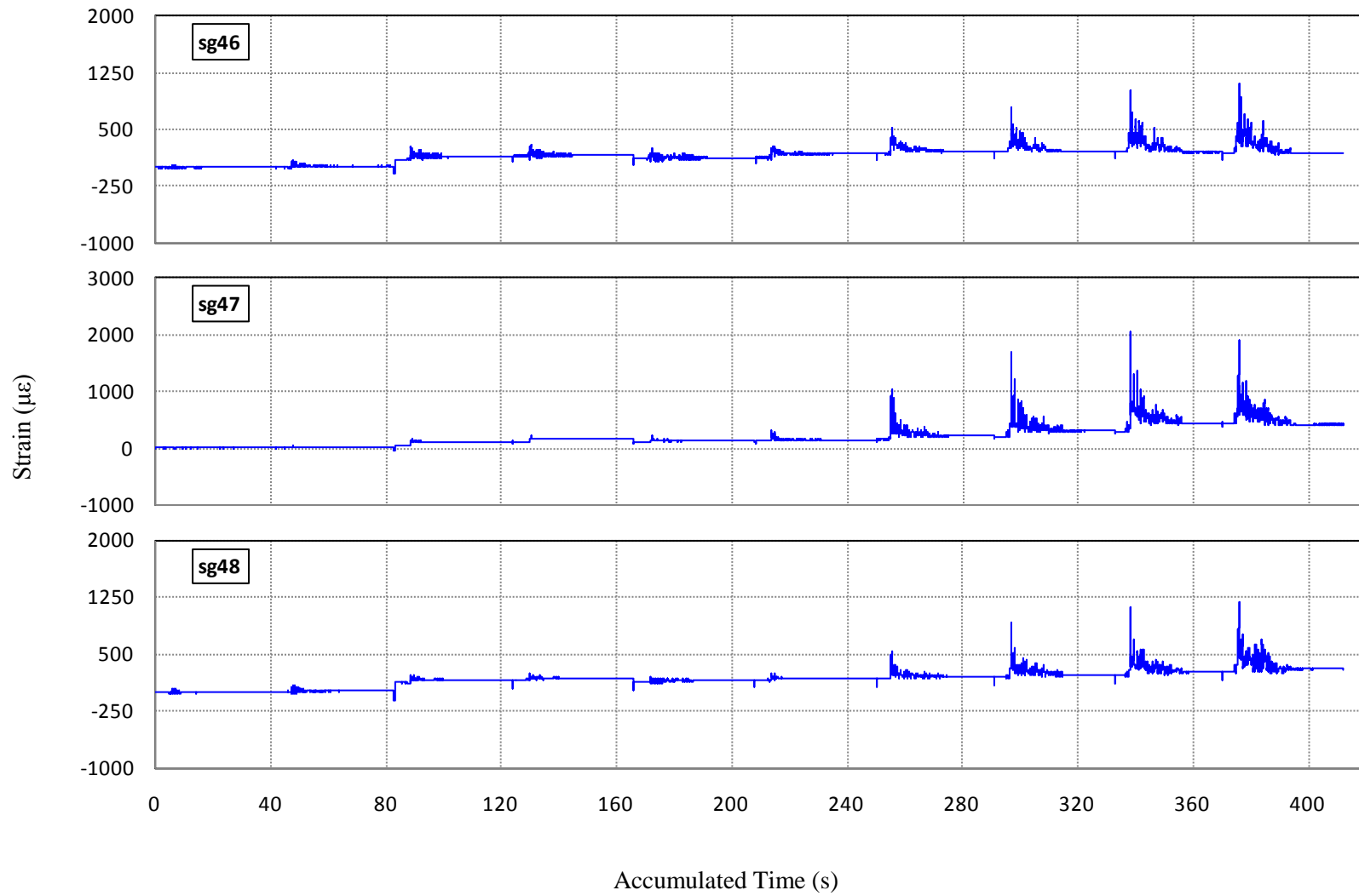


**Figure C-14 Strain History of Gauges 40, 41 and 42 in Specimen C1**

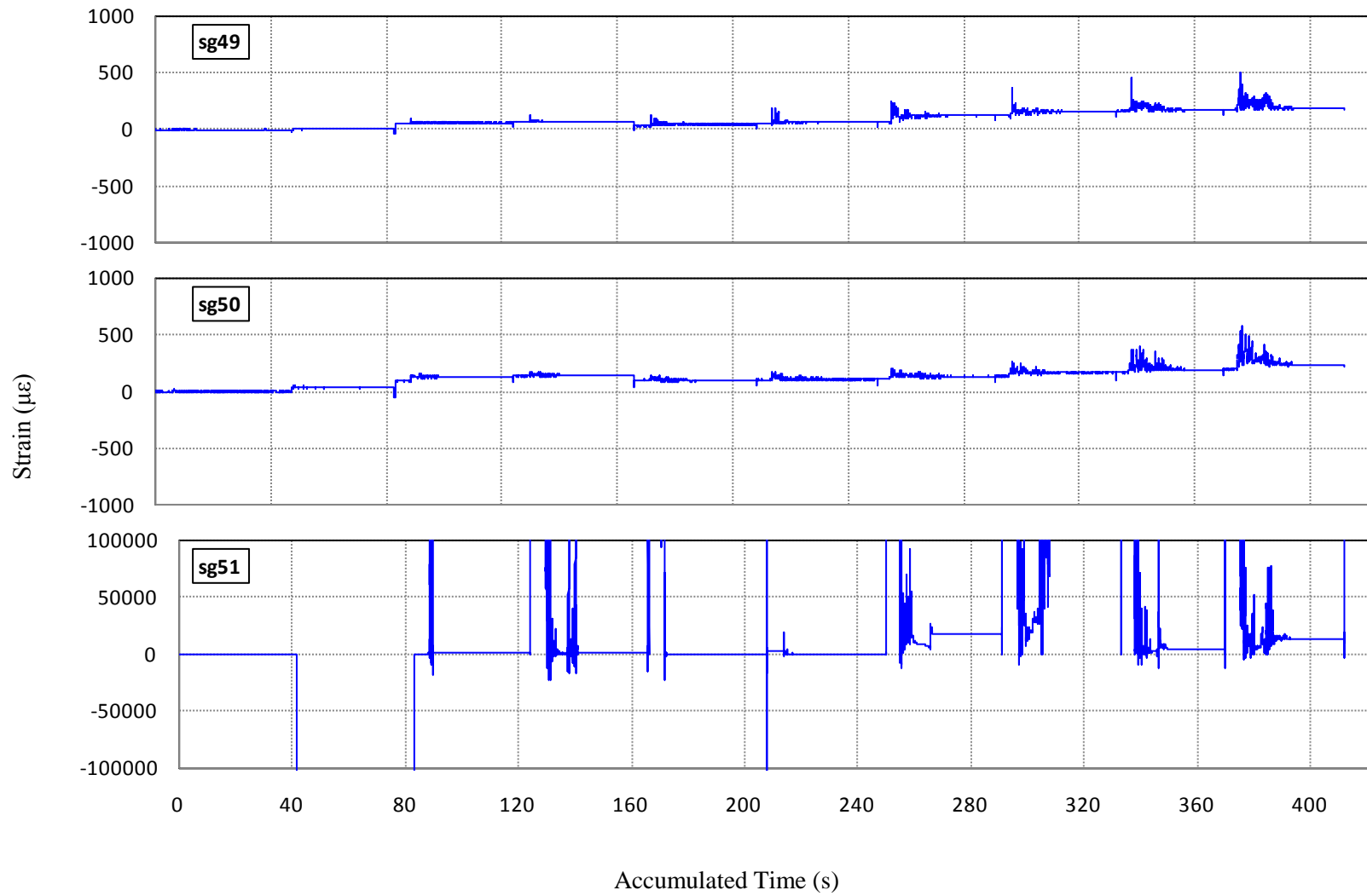




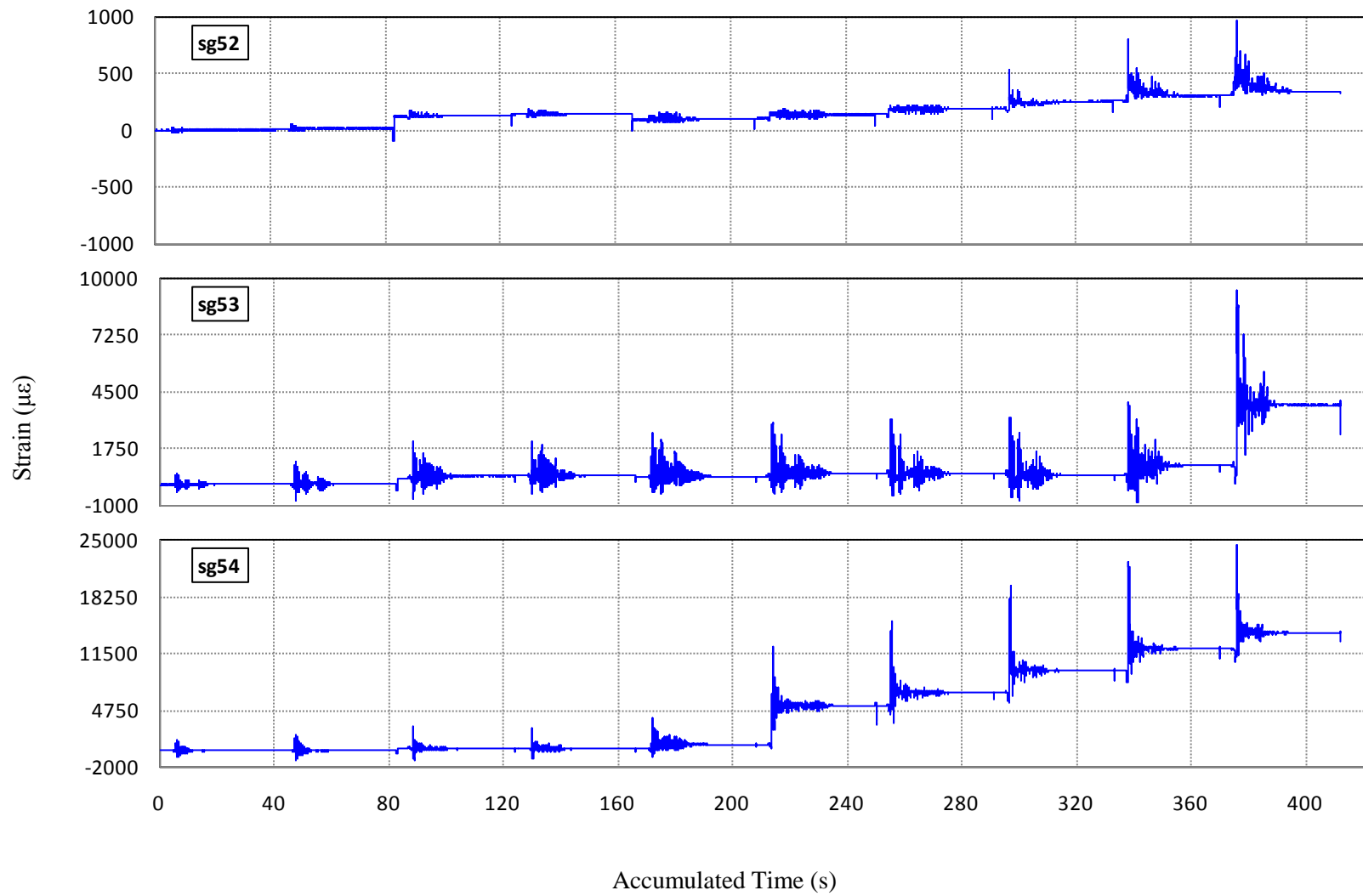
**Figure C-15 Strain History of Gauges 43, 44 and 45 in Specimen C1**



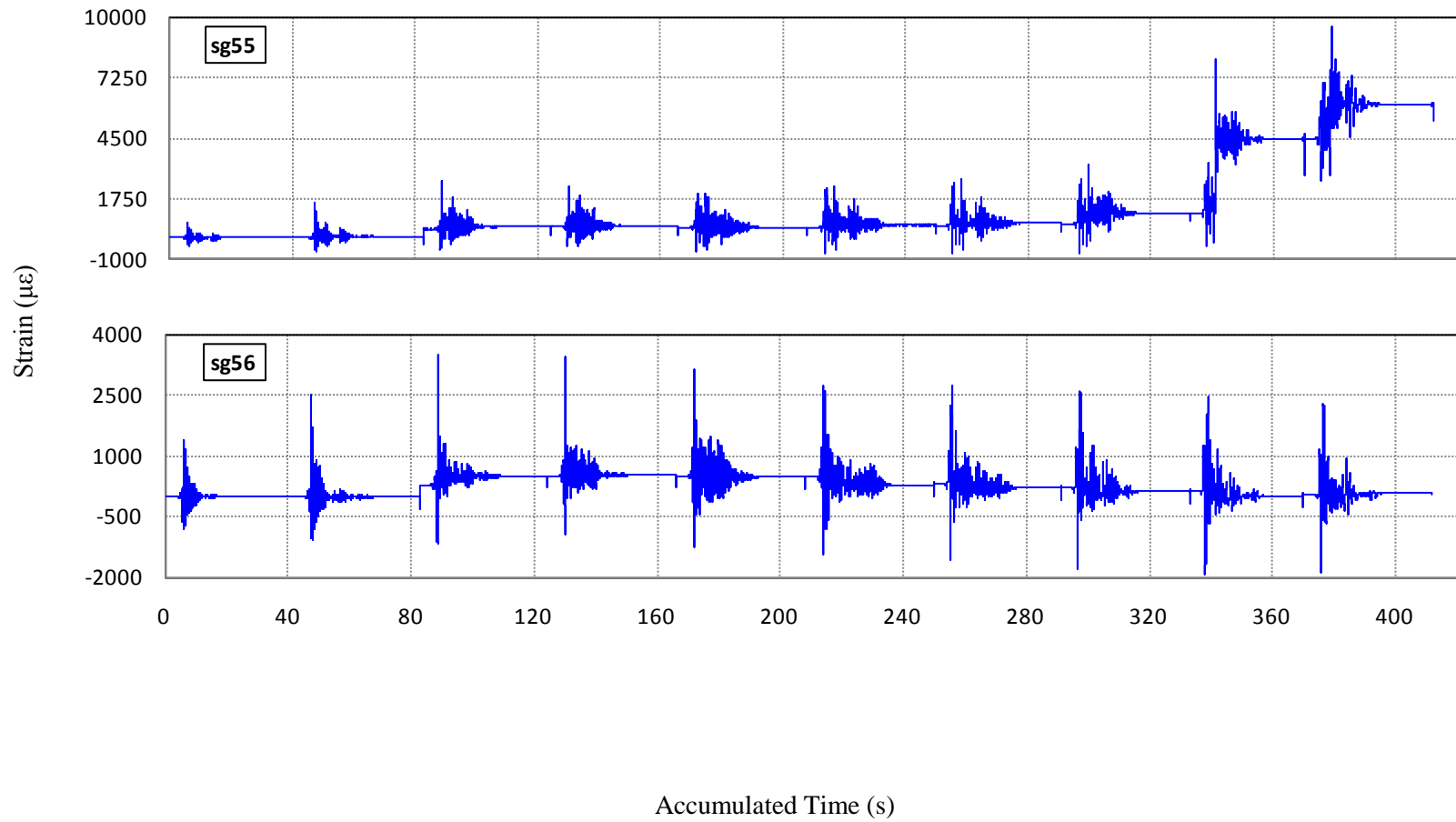
**Figure C-16 Strain History of Gauges 46, 47 and 48 in Specimen C1**



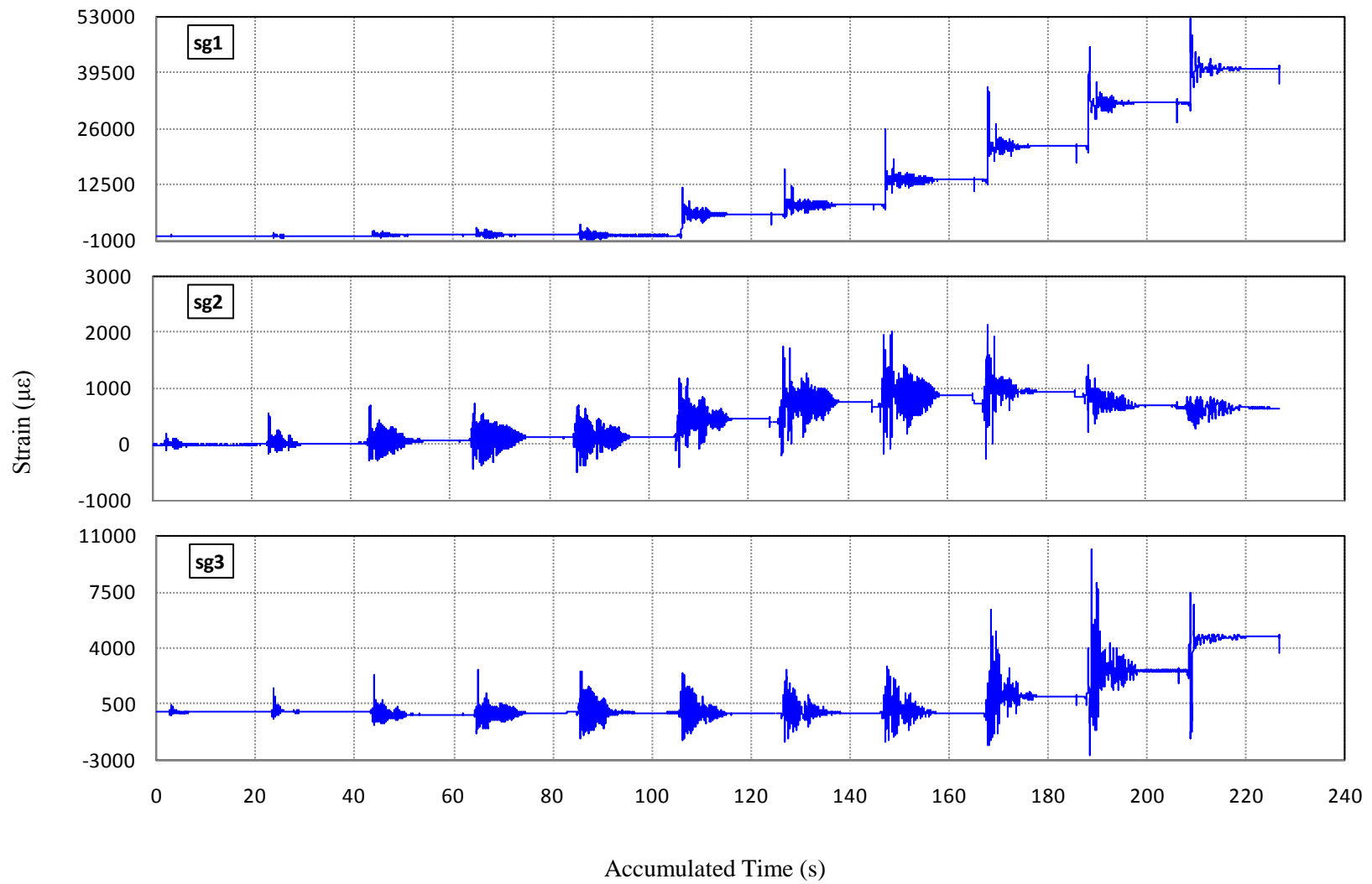
**Figure C-17 Strain History of Gauges 49, 50 and 51 in Specimen C1**



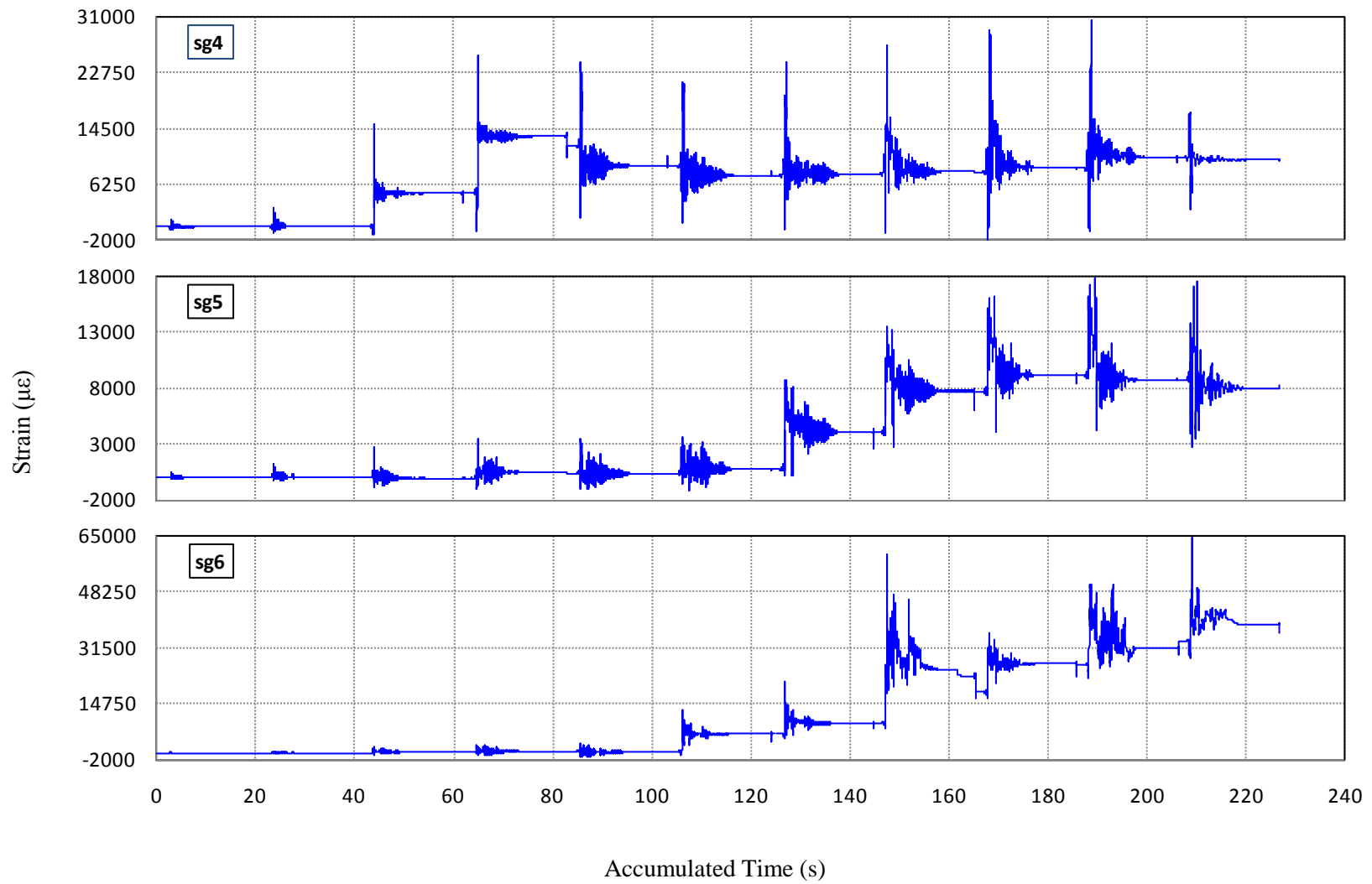
**Figure C-18 Strain History of Gauges 52, 53 and 54 in Specimen C1**



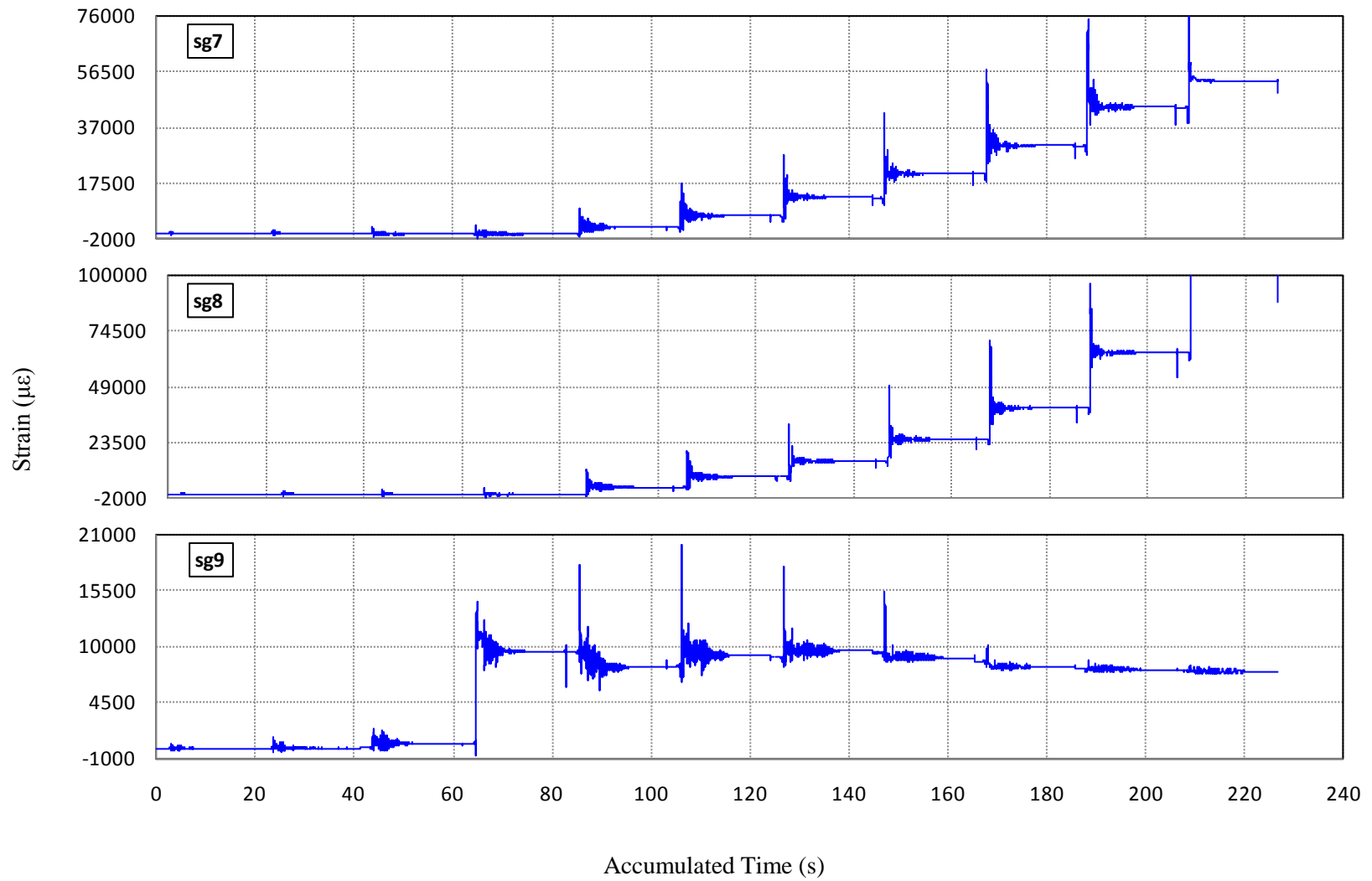
**Figure C-19 Strain History of Gauges 55 and 56 in Specimen C1**



**Figure C-20 Strain History of Gauges 1, 2 and 3 in Specimen C2**

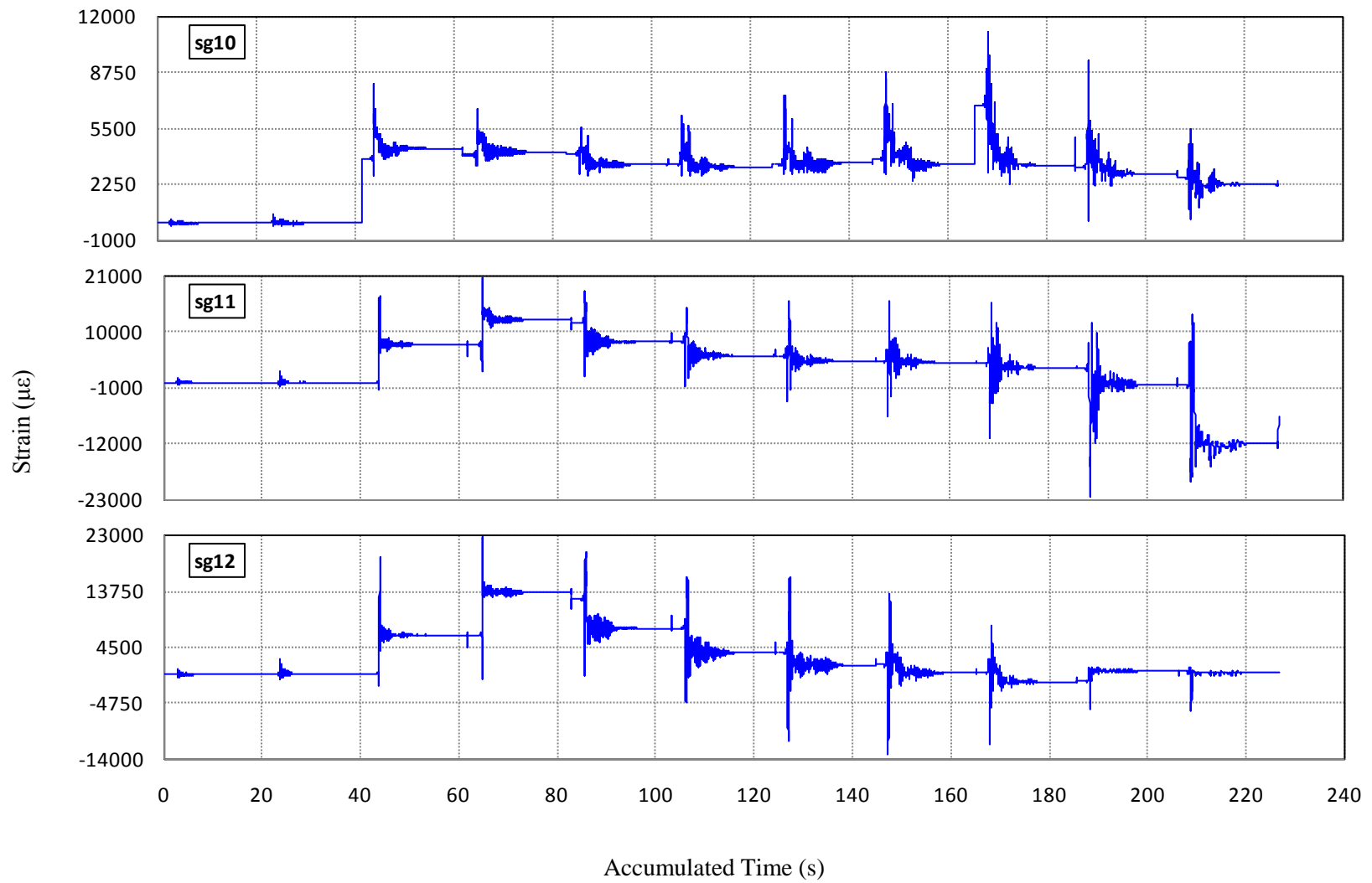


**Figure C-21 Strain History of Gauges 4, 5 and 6 in Specimen C2**

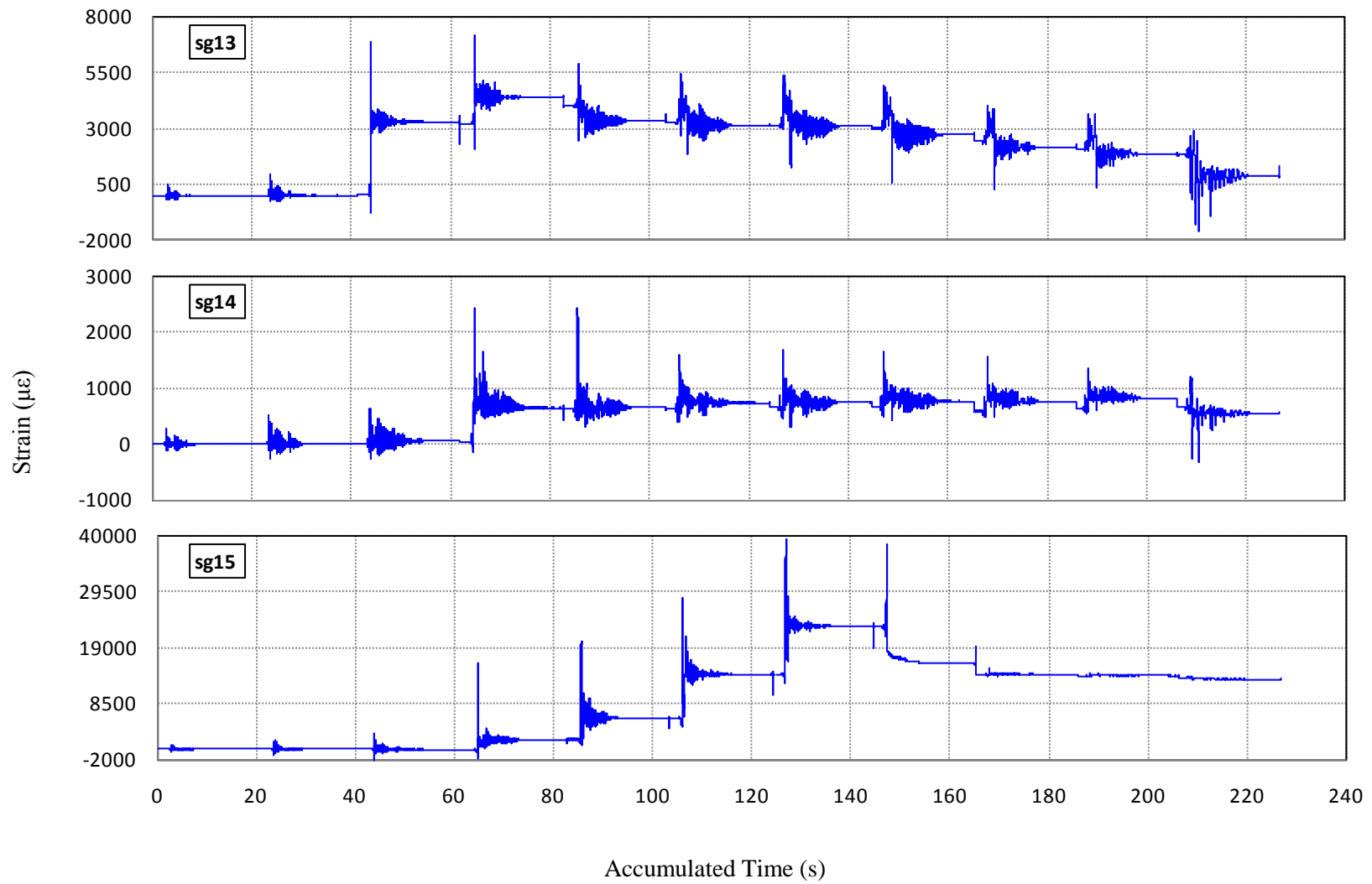


**Figure C-22 Strain History of Gauges 7, 8 and 9 in Specimen C2**

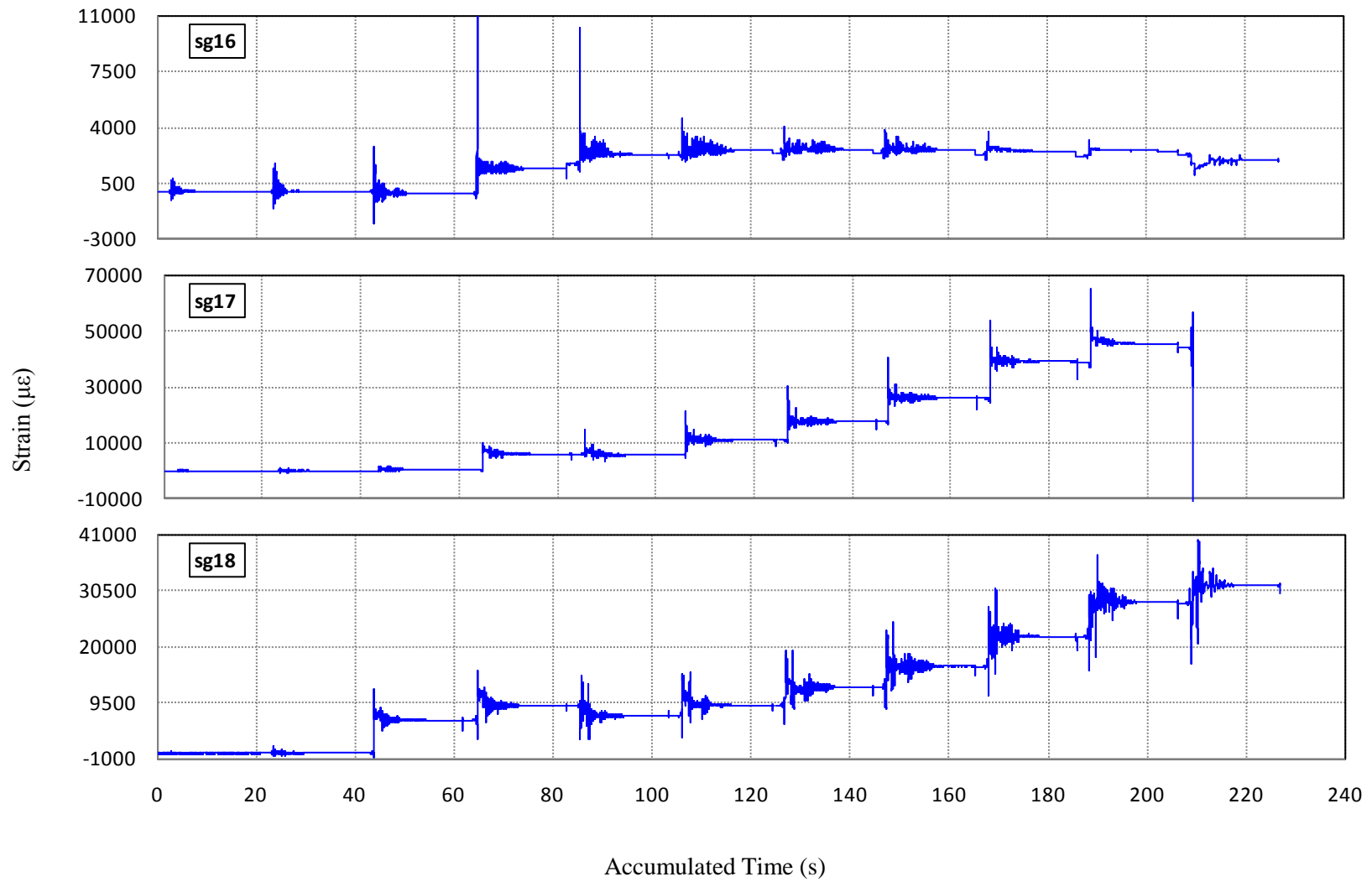




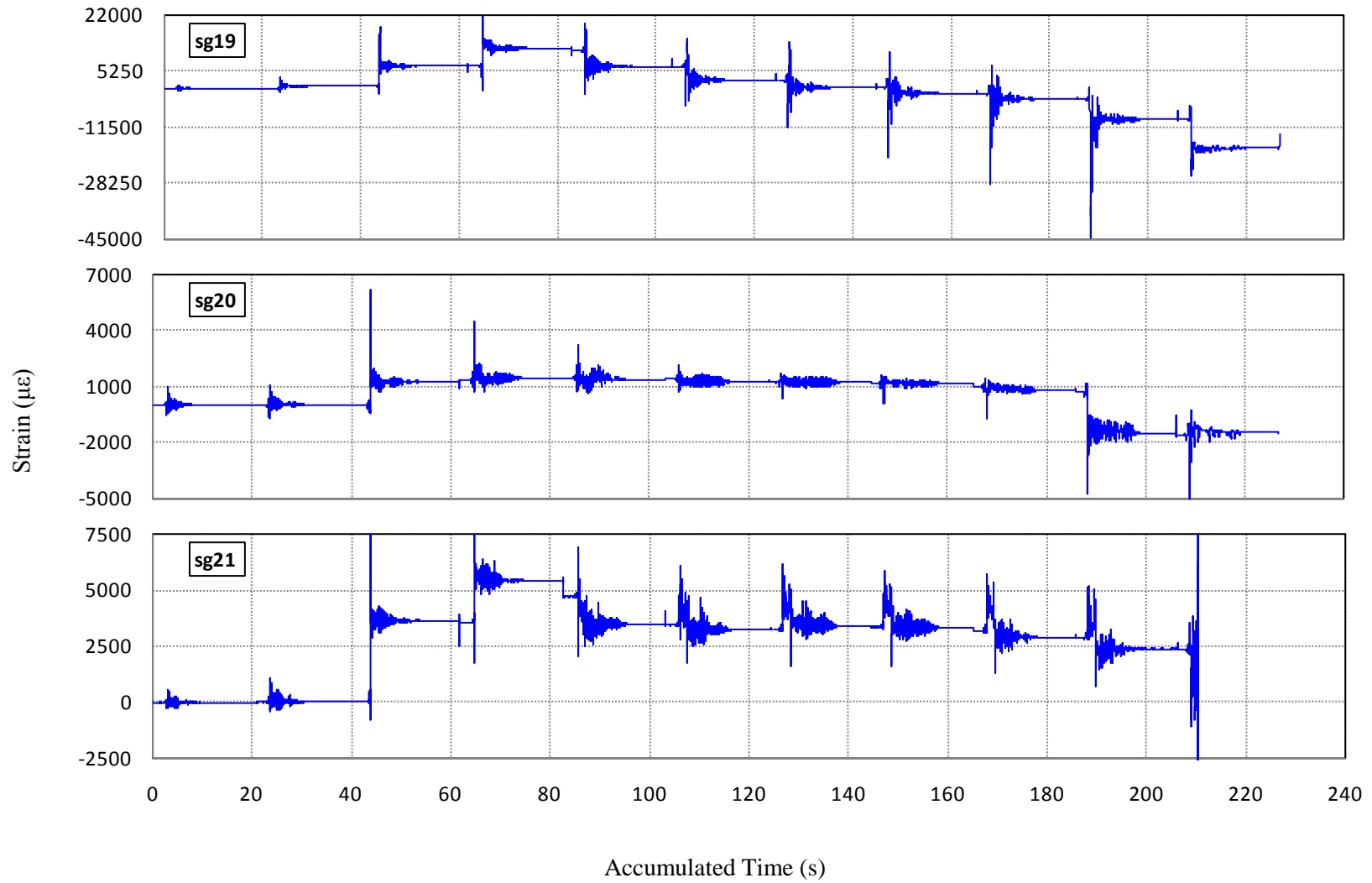
**Figure C-23 Strain History of Gauges 10, 11 and 12 in Specimen C2**



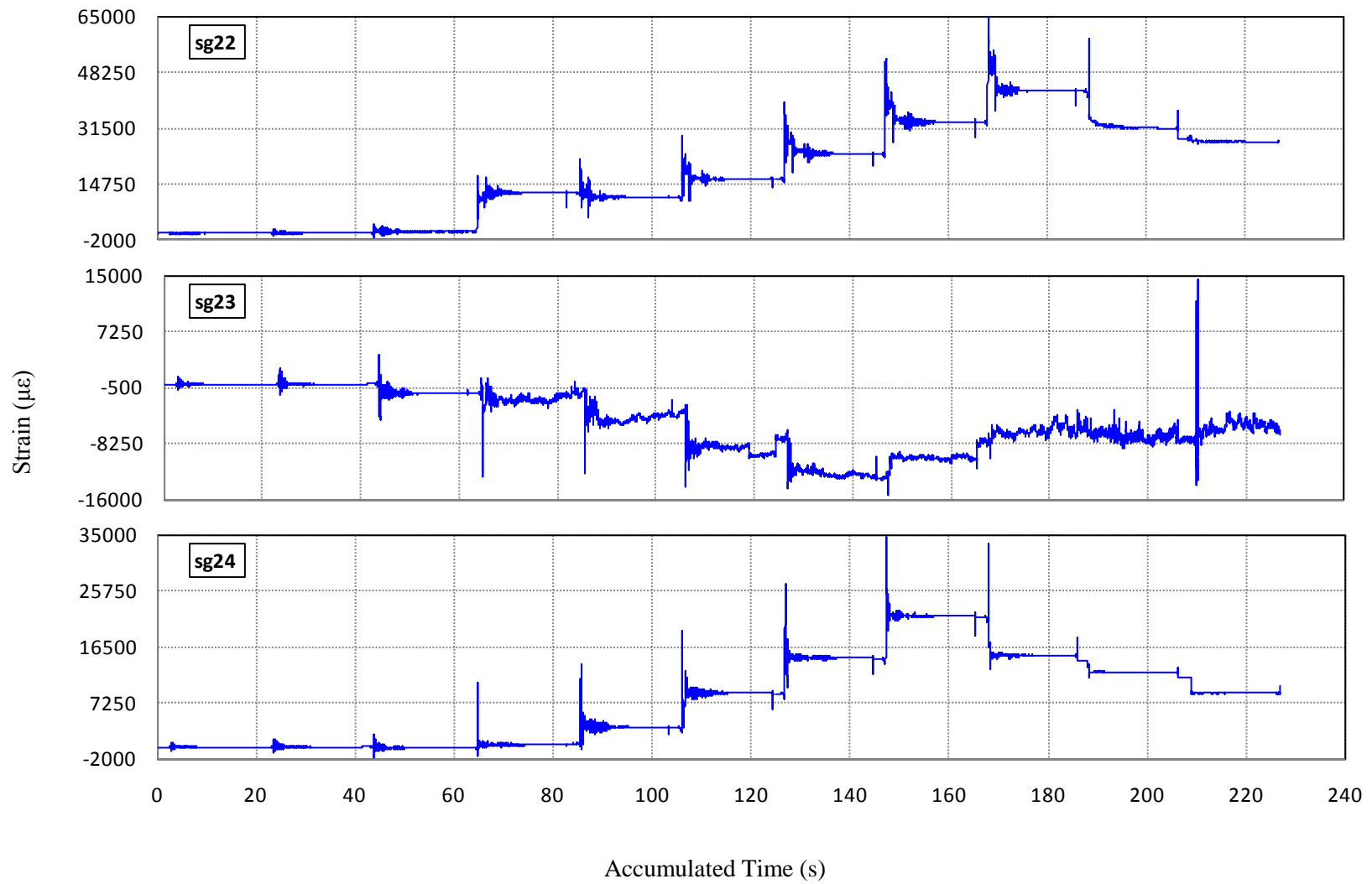
**Figure C-24 Strain History of Gauges 13, 14 and 15 in Specimen C2**



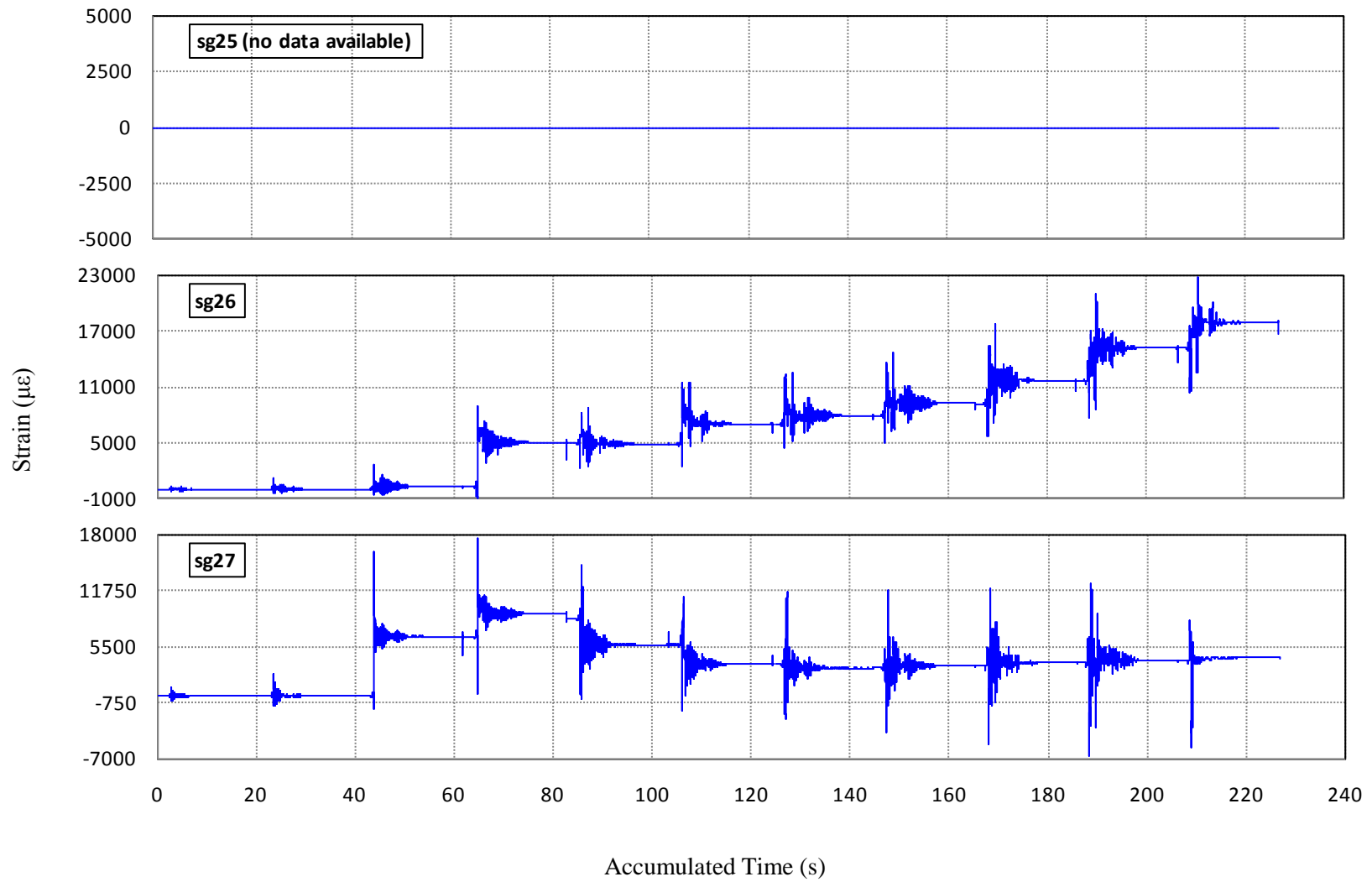
**Figure C-25 Strain History of Gauges 16, 17 and 18 in Specimen C2**



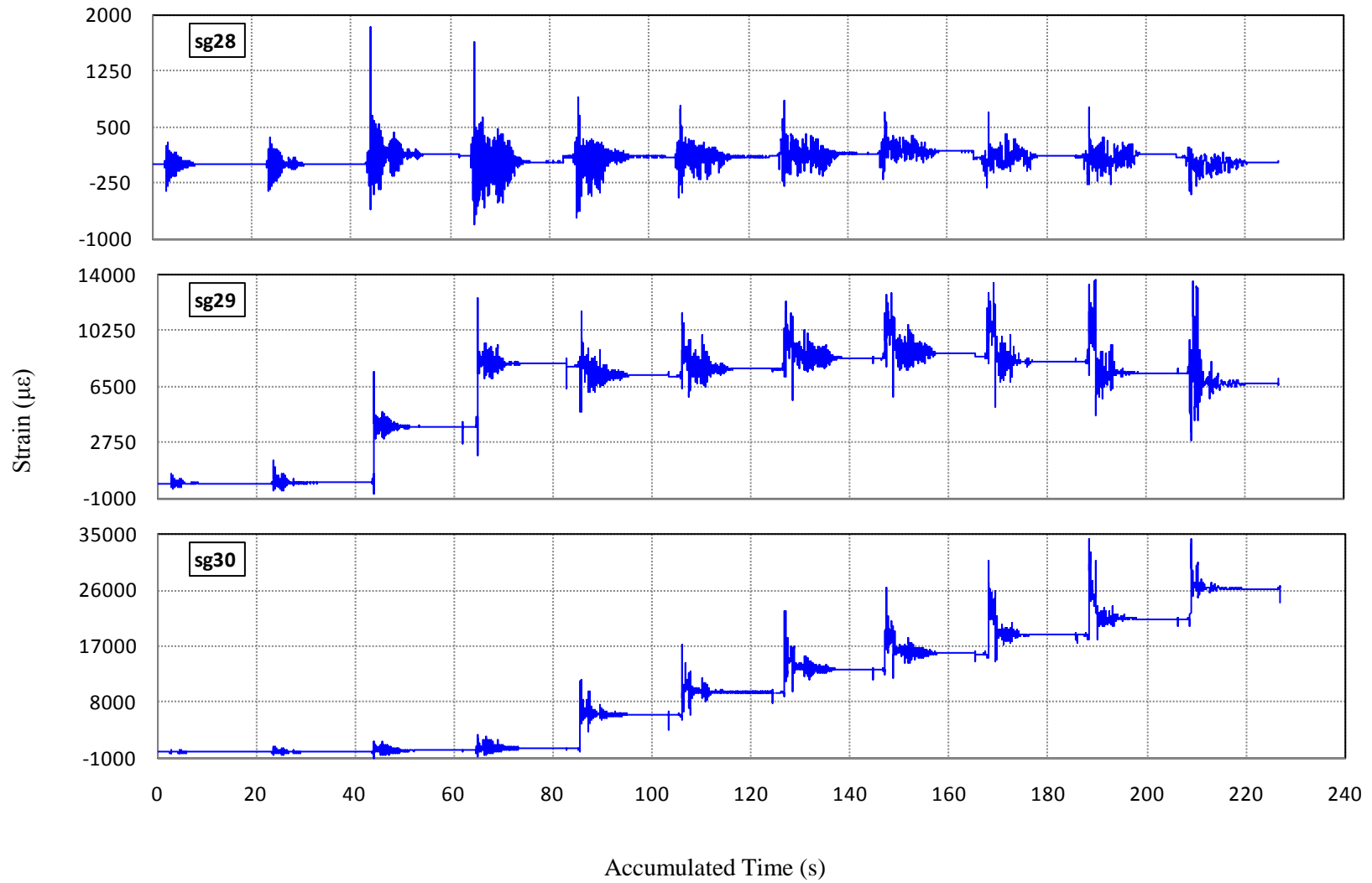
**Figure C-26 Strain History of Gauges 19, 20 and 21 in Specimen C2**



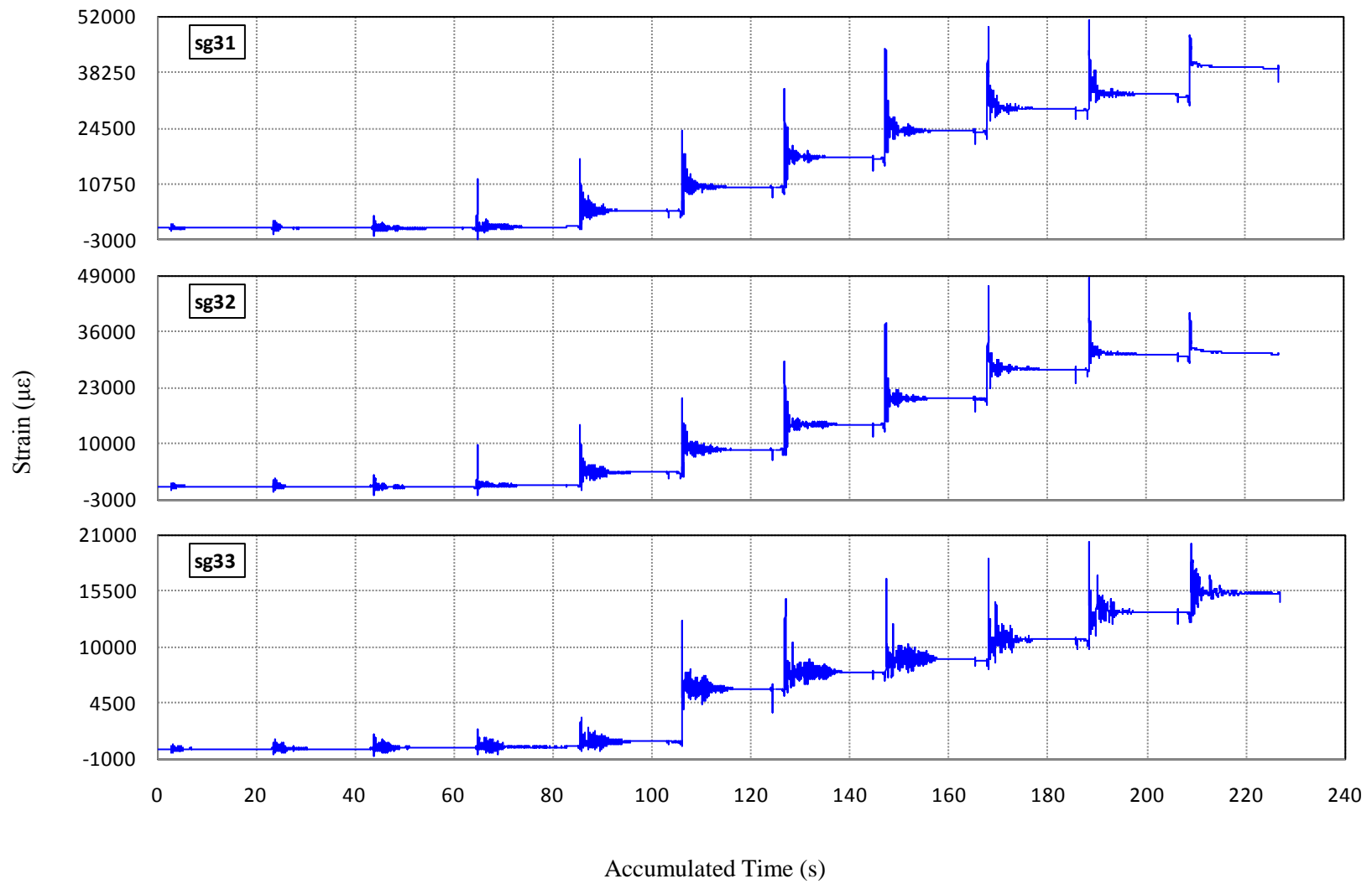
**Figure C-27 Strain History of Gauges 22, 23 and 24 in Specimen C2**



**Figure C-28 Strain History of Gauges 25, 26 and 27 in Specimen C2**

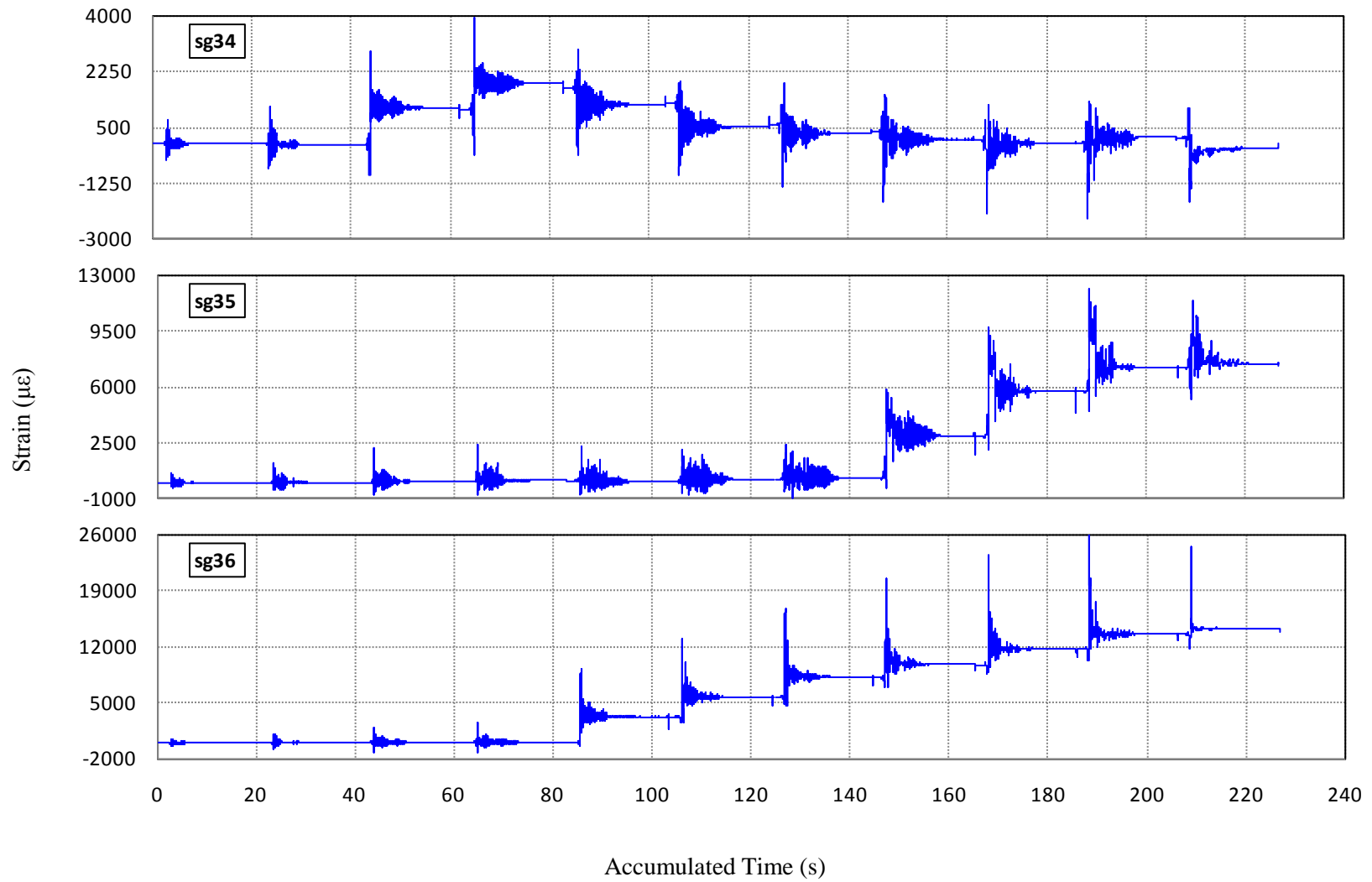


**Figure C-29 Strain History of Gauges 28, 29 and 30 in Specimen C2**

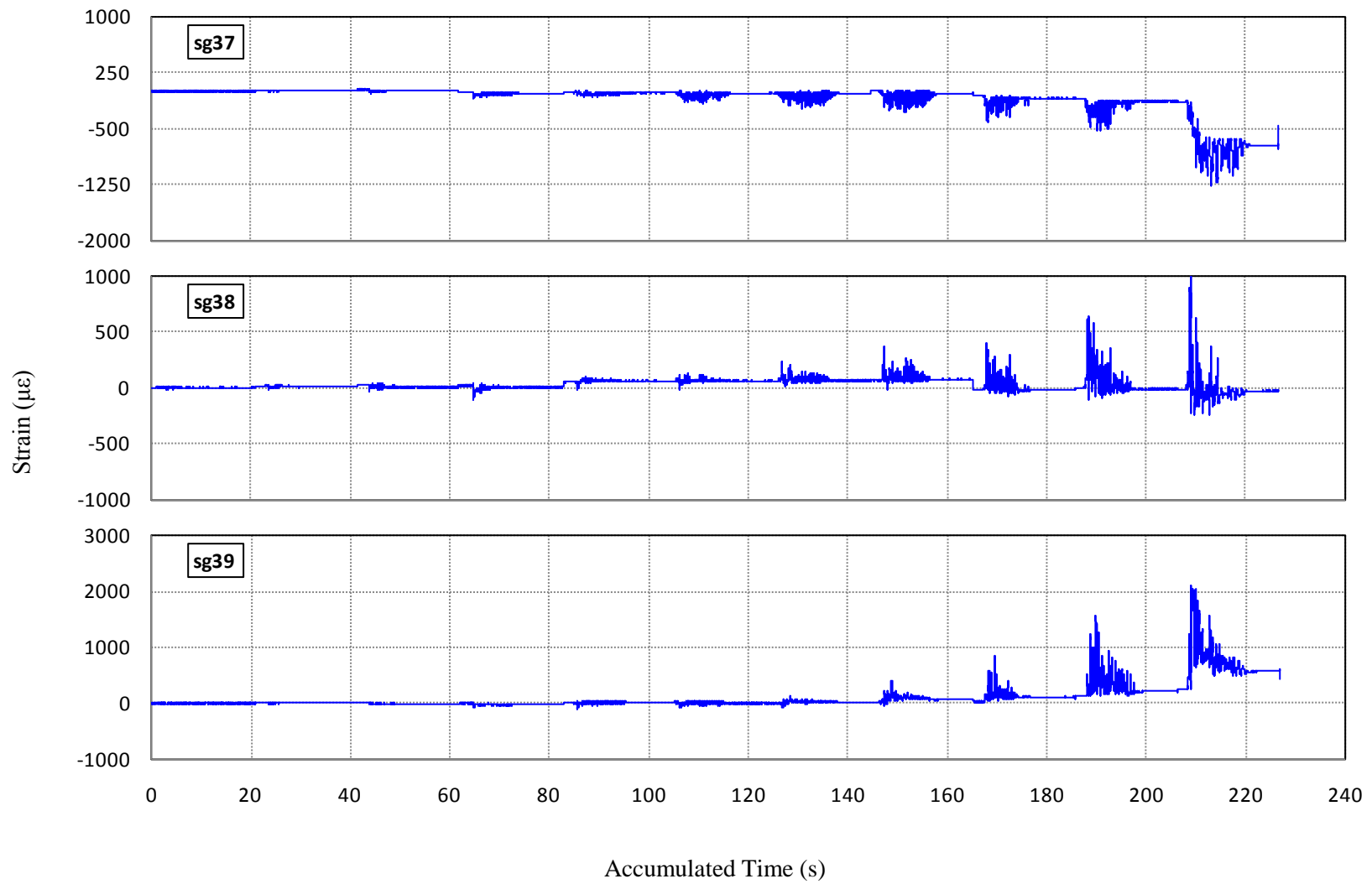


**Figure C-30 Strain History of Gauges 31, 32 and 33 in Specimen C2**

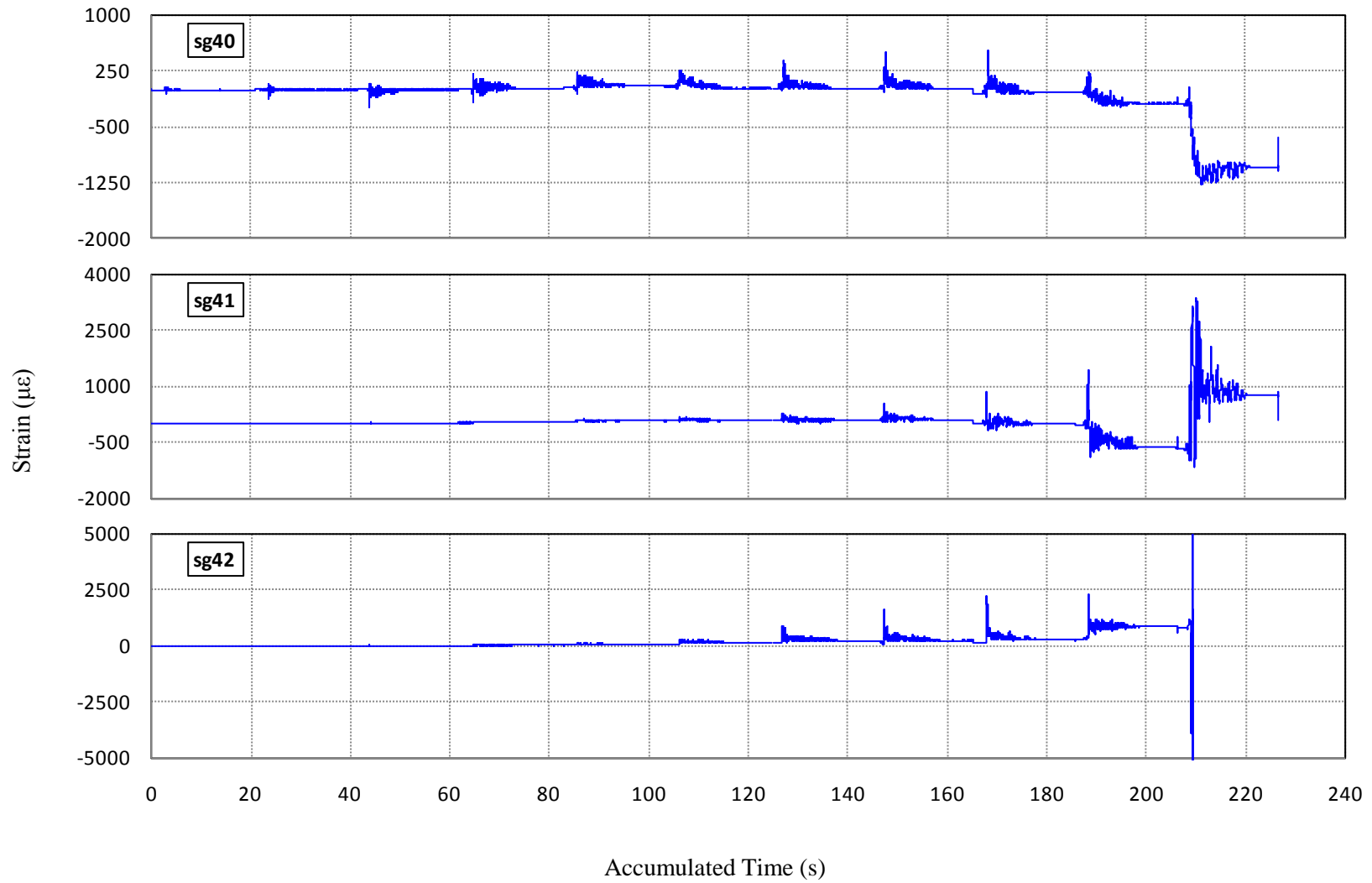




**Figure C-31 Strain History of Gauges 34, 35 and 36 in Specimen C2**



**Figure C-32 Strain History of Gauges 37, 38 and 39 in Specimen C2**



**Figure C-33 Strain History of Gauges 40, 41 and 42 in Specimen C2**

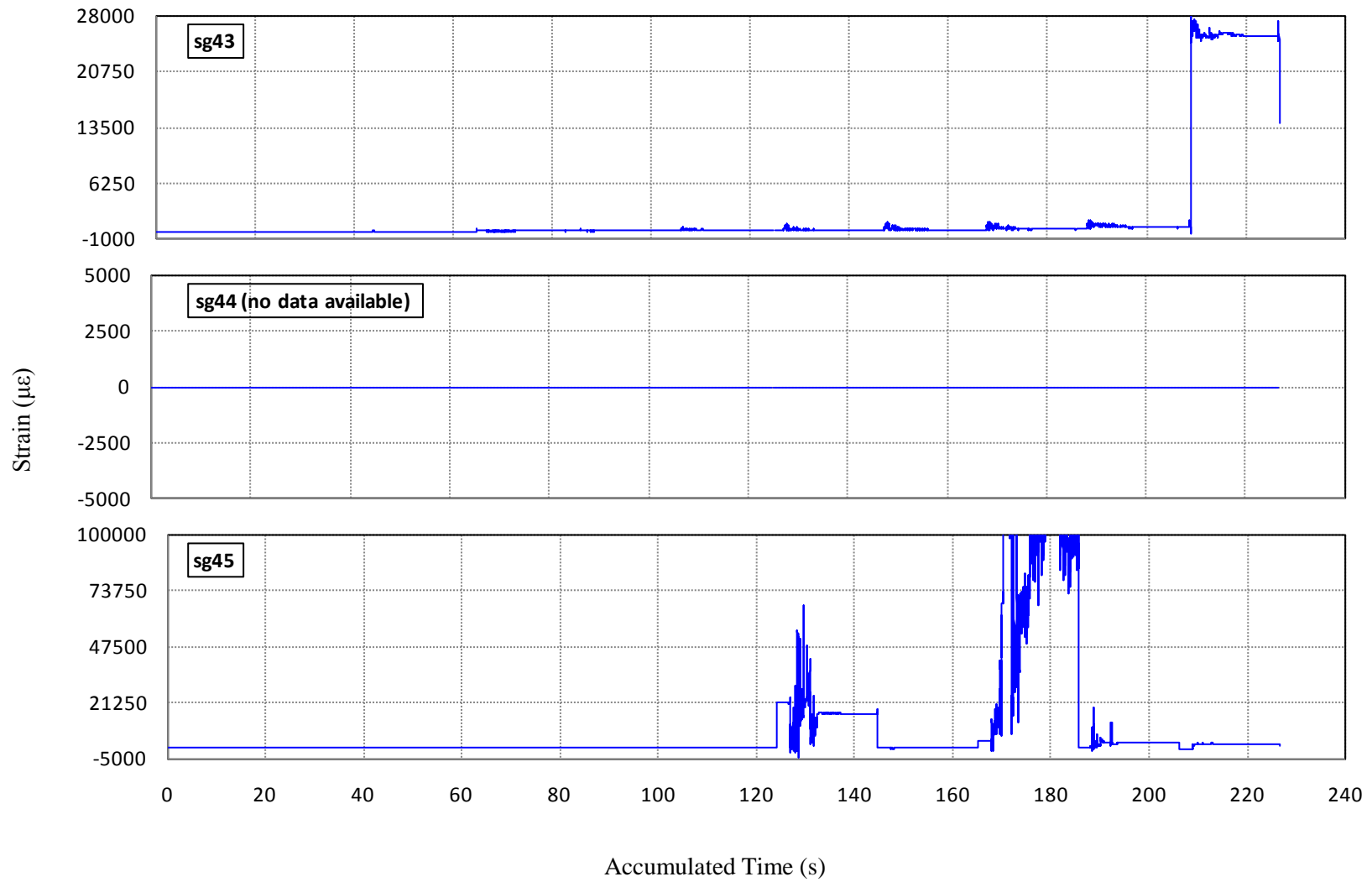
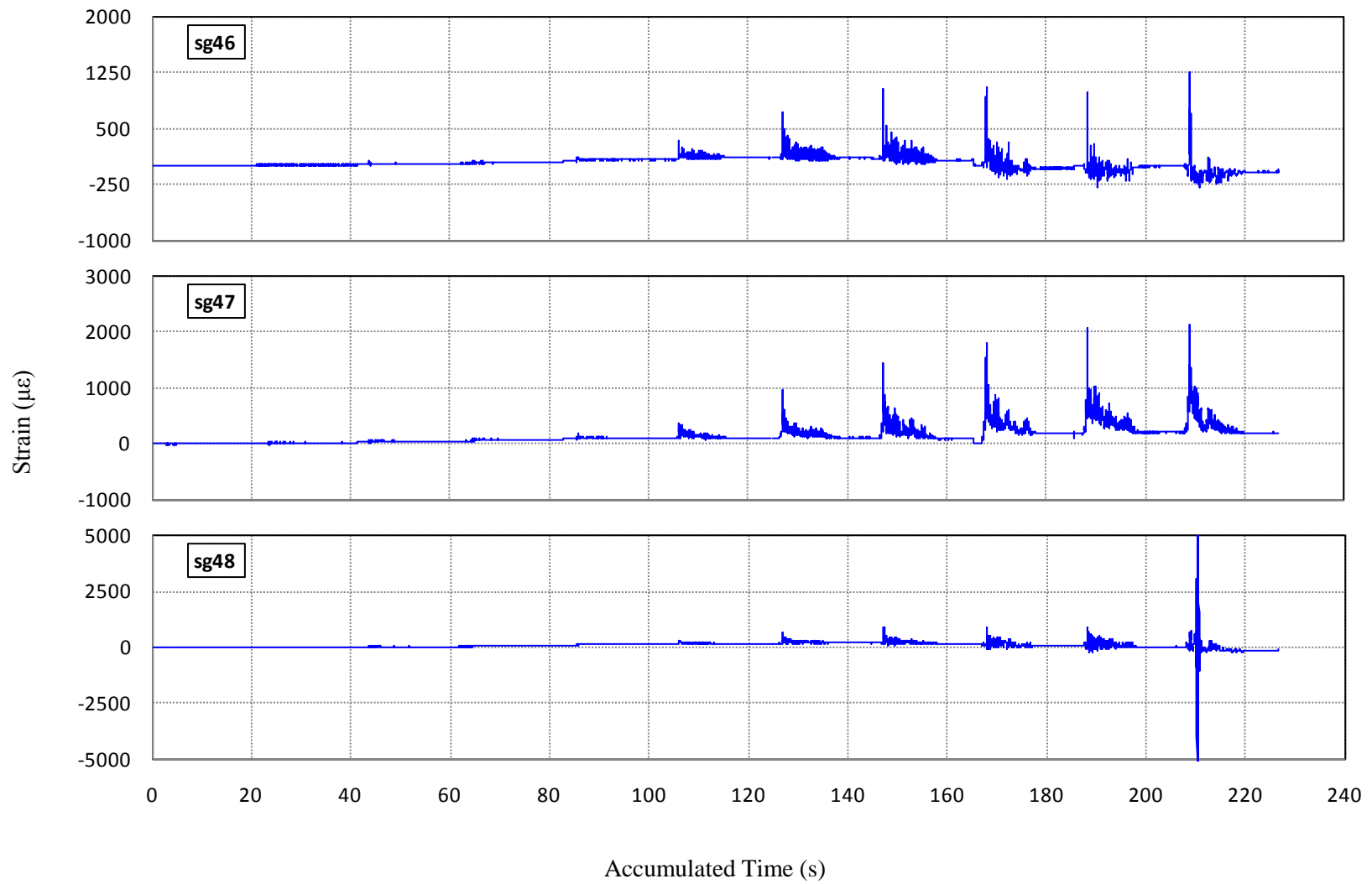
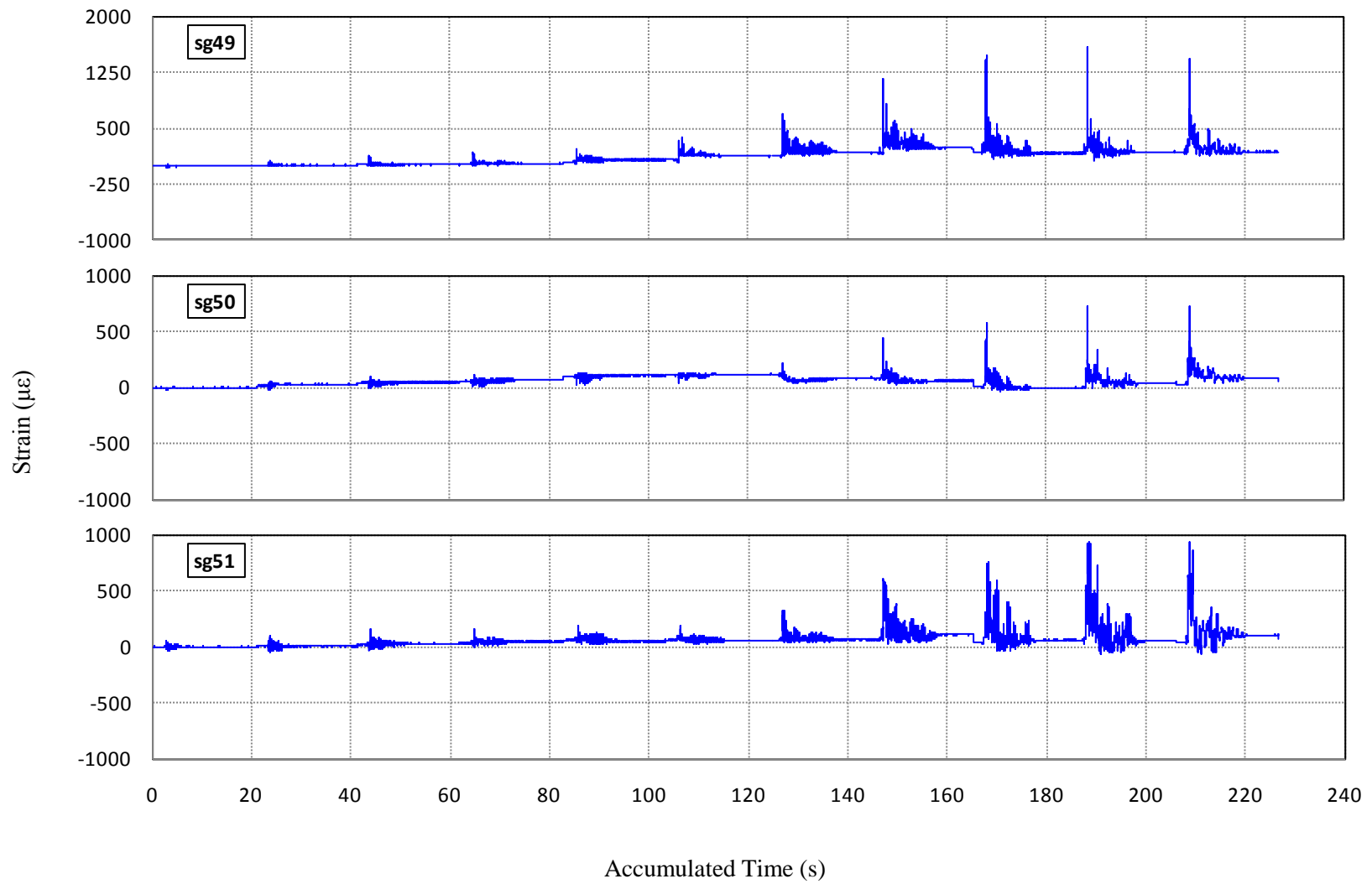


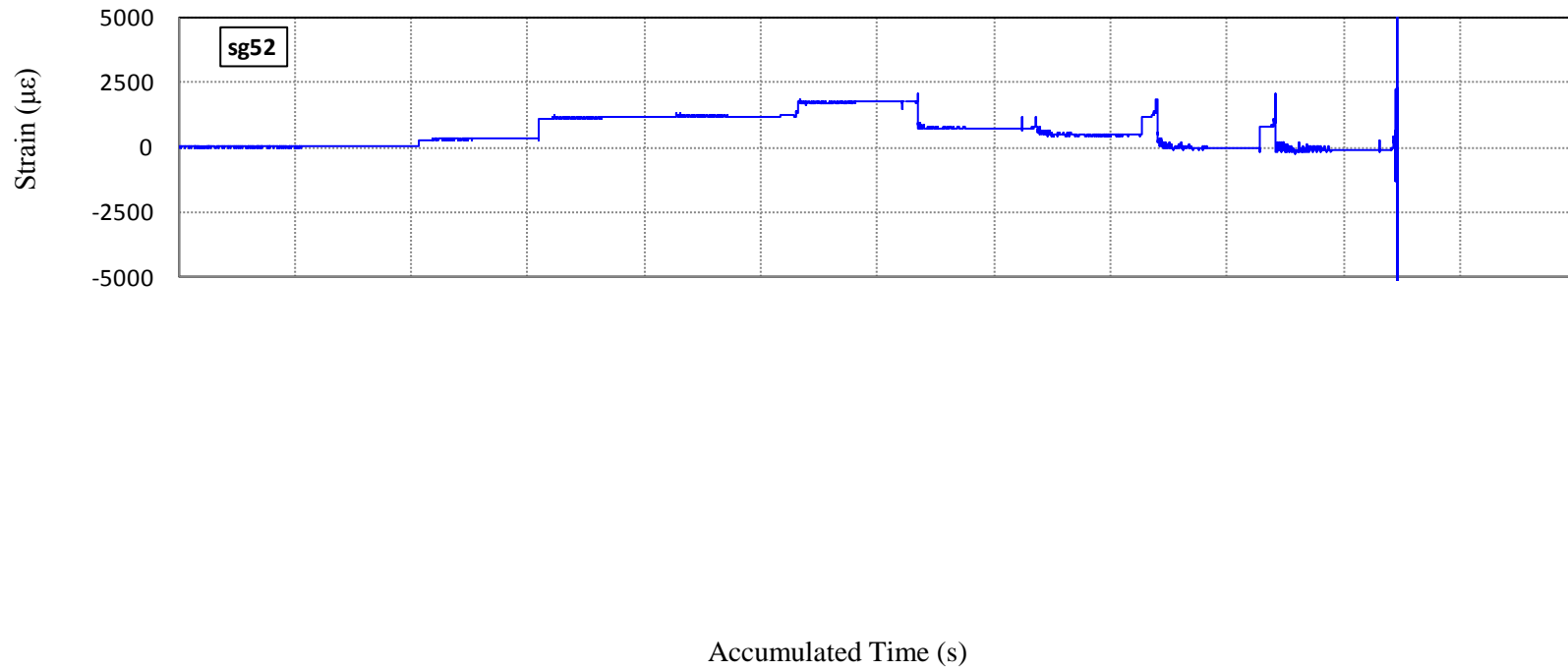
Figure C-34 Strain History of Gauges 43, 44 and 45 in Specimen C2



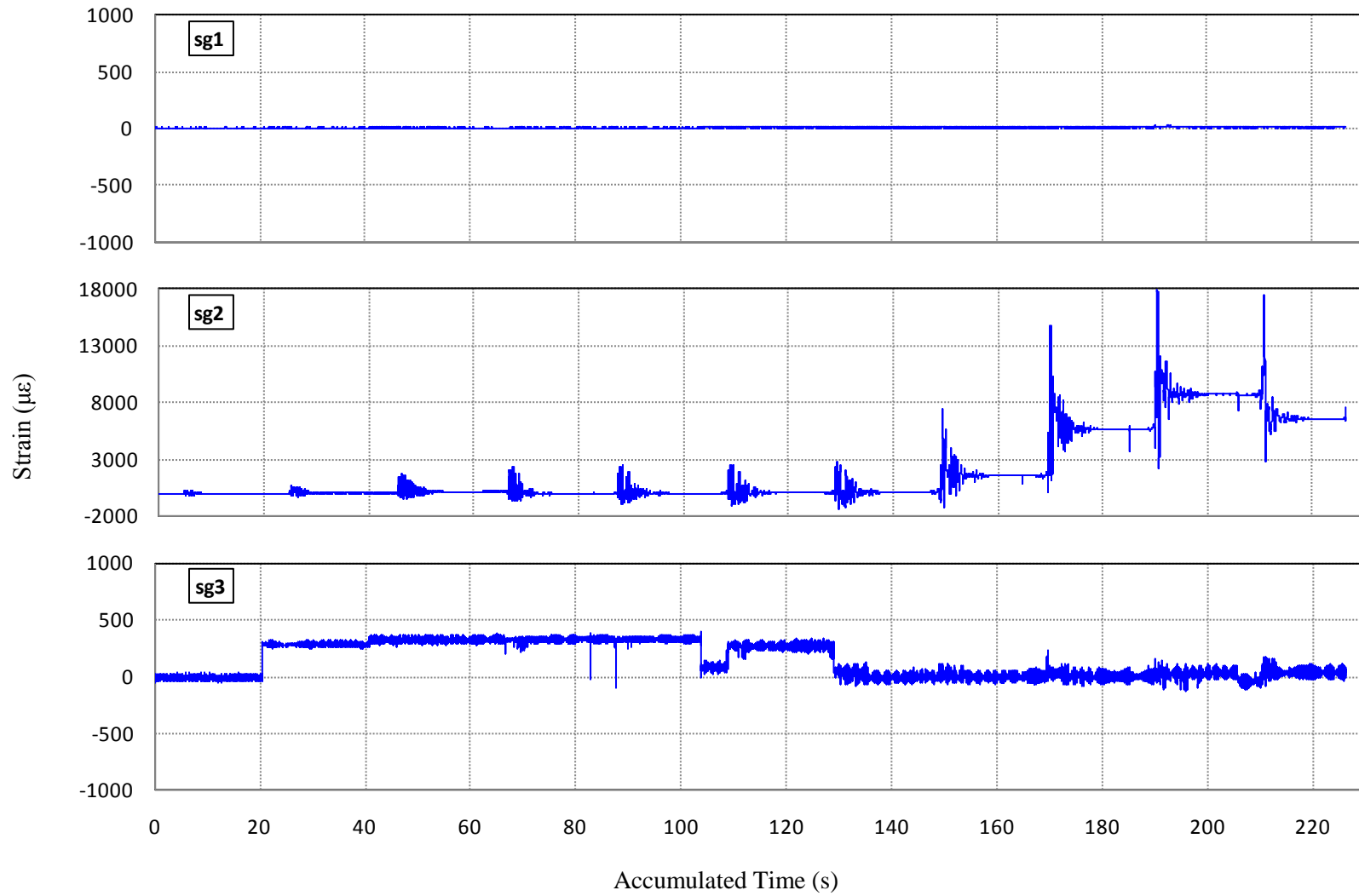
**Figure C-35 Strain History of Gauges 46, 47 and 48 in Specimen C2**



**Figure C-36 Strain History of Gauges 49, 50 and 51 in Specimen C2**

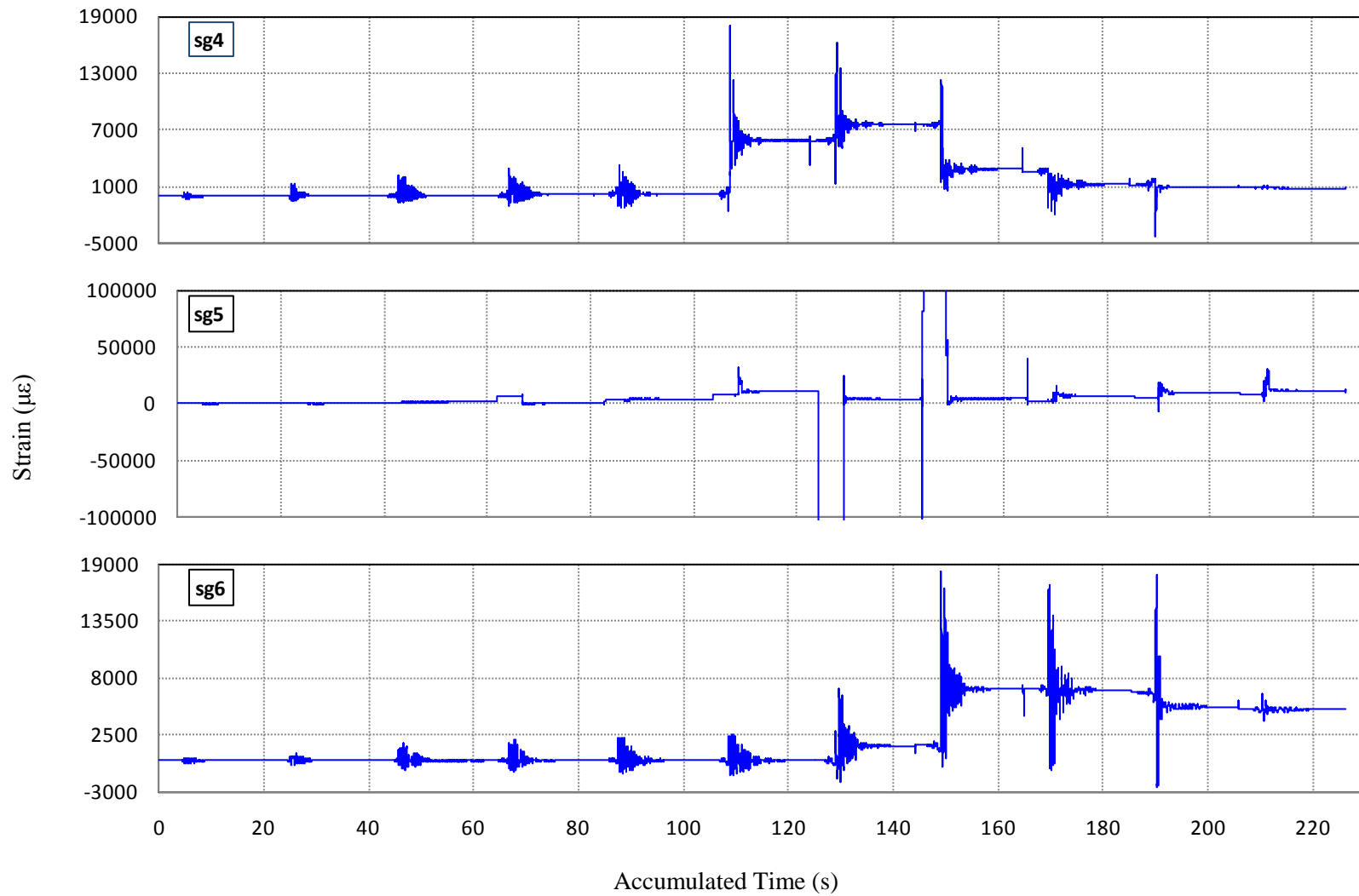


**Figure C-37 Strain History of Gauge 52 in Specimen C2**

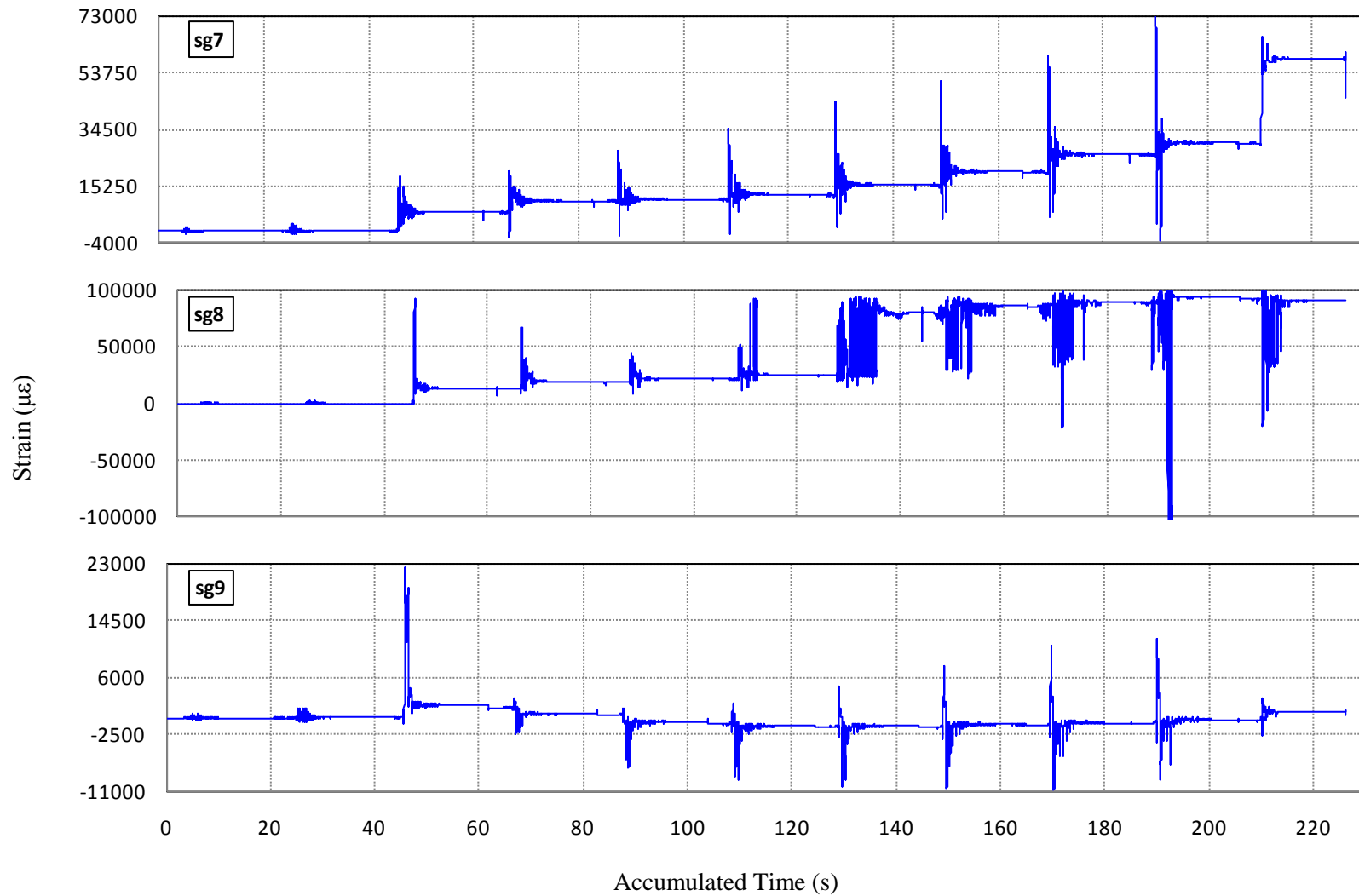


**Figure C-38 Strain History of Gauges 1, 2 and 3 in Specimen II**

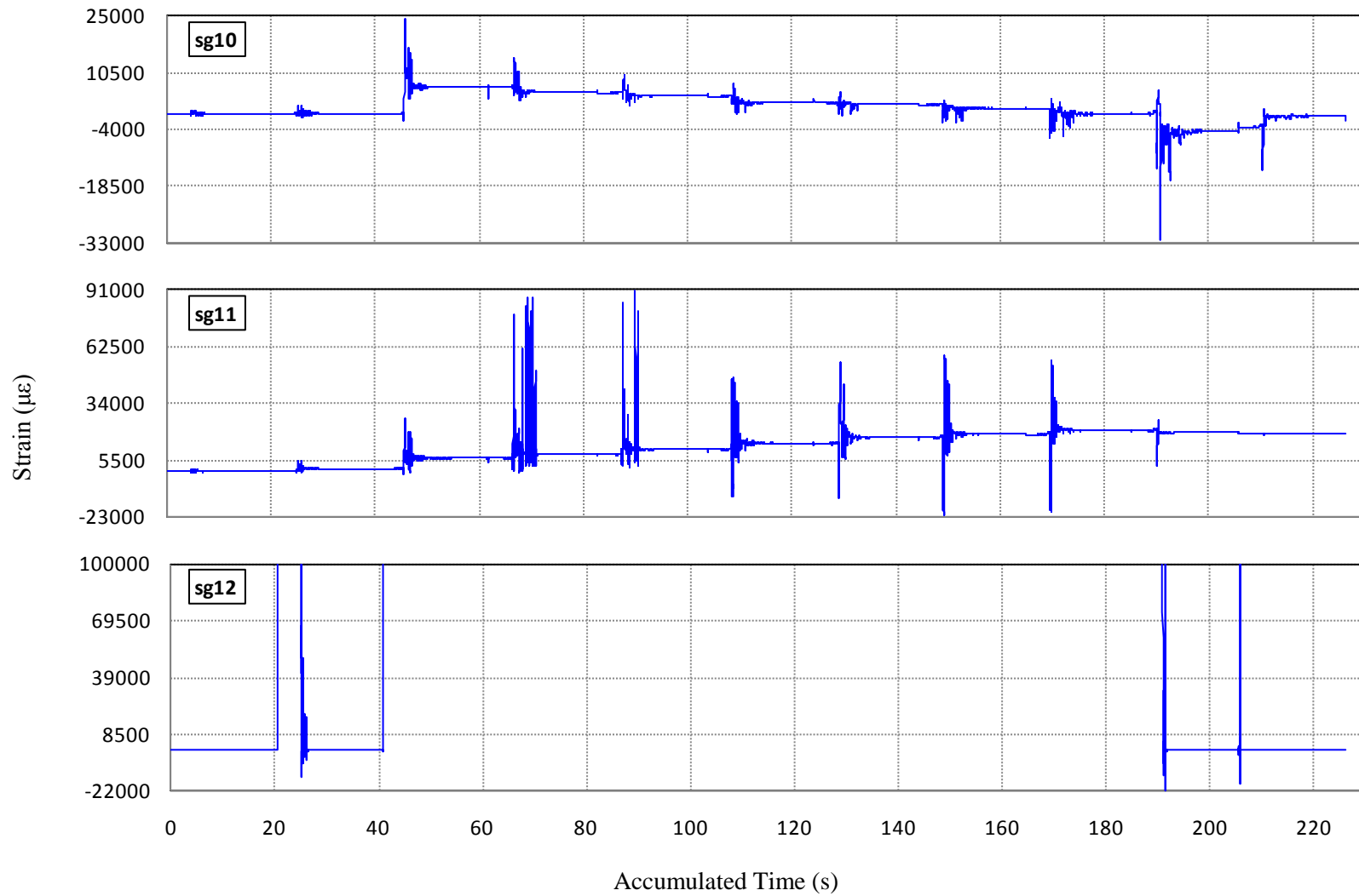




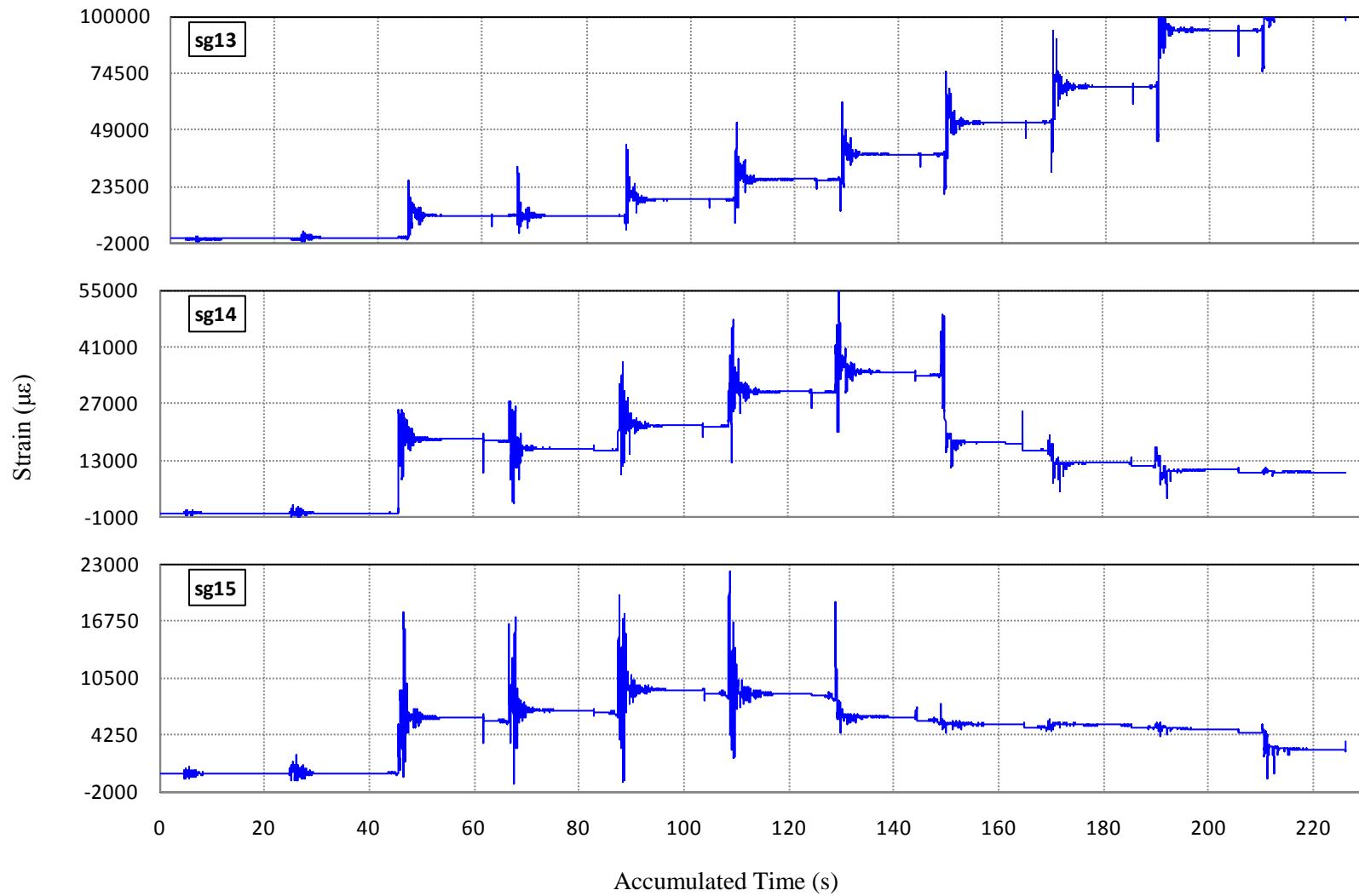
**Figure C-39 Strain History of Gauges 4, 5 and 6 in Specimen II**



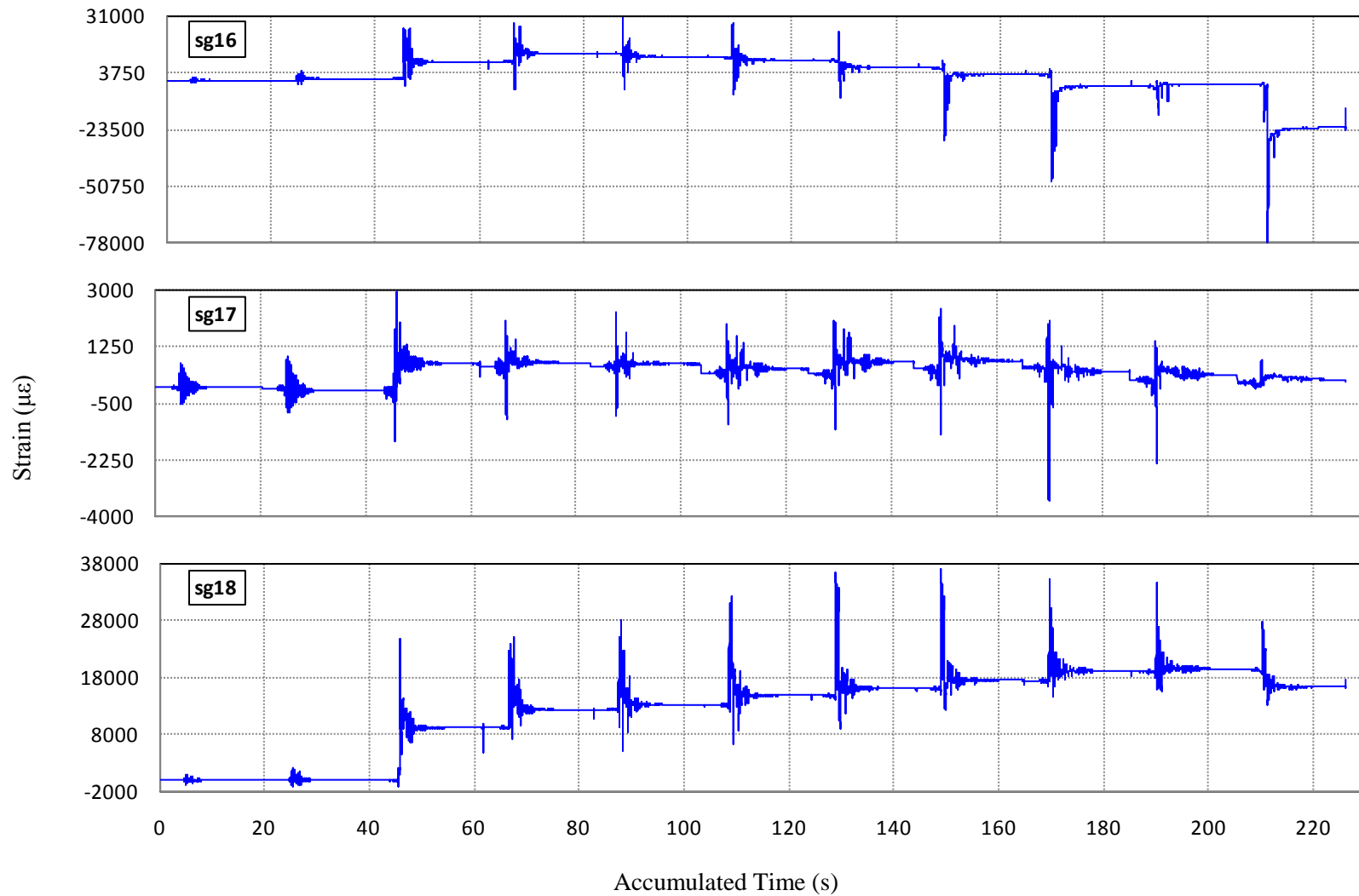
**Figure C-40 Strain History of Gauges 7, 8 and 9 in Specimen I1**



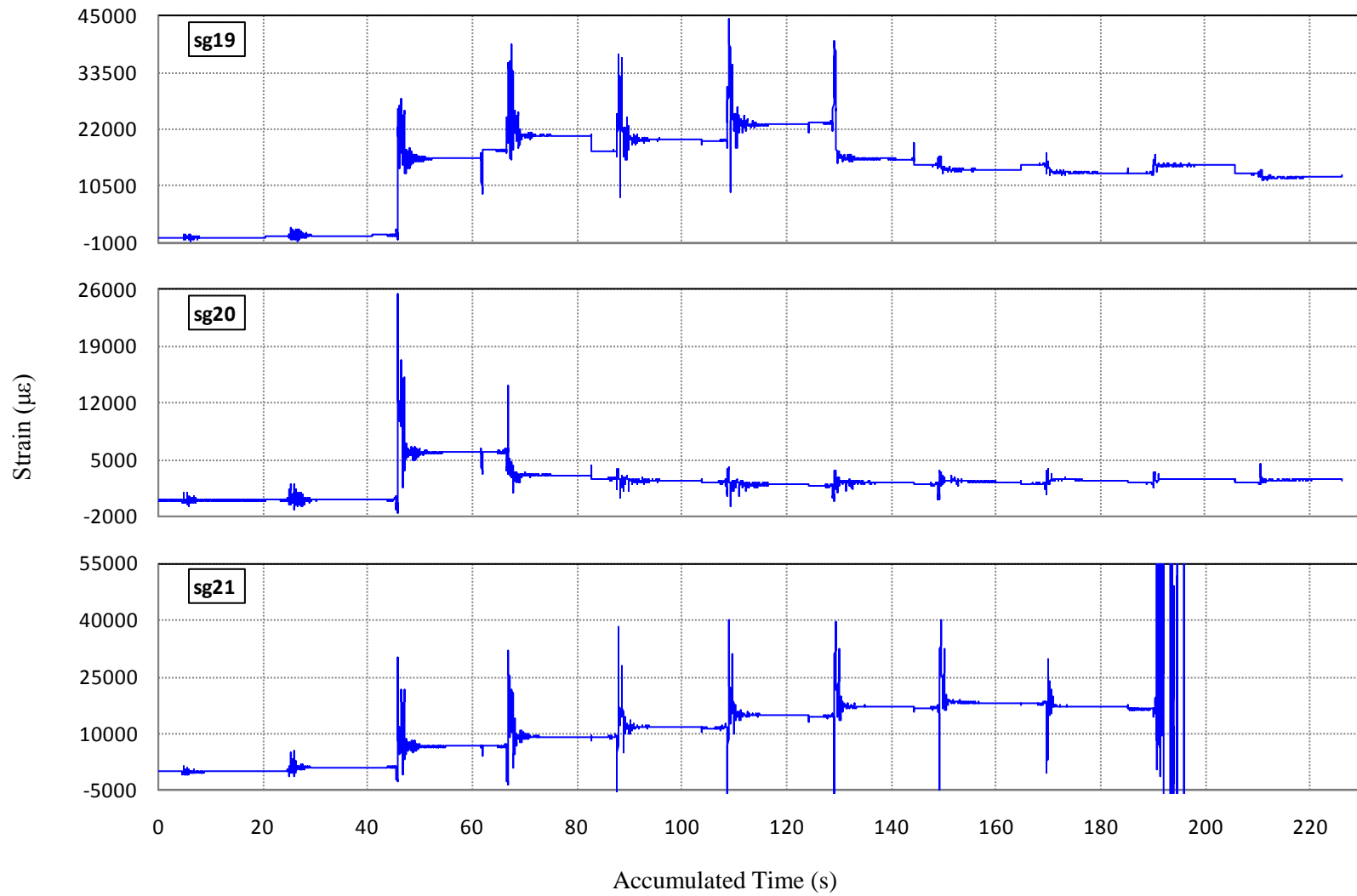
**Figure C-41 Strain History of Gauges 10, 11 and 12 in Specimen I1**



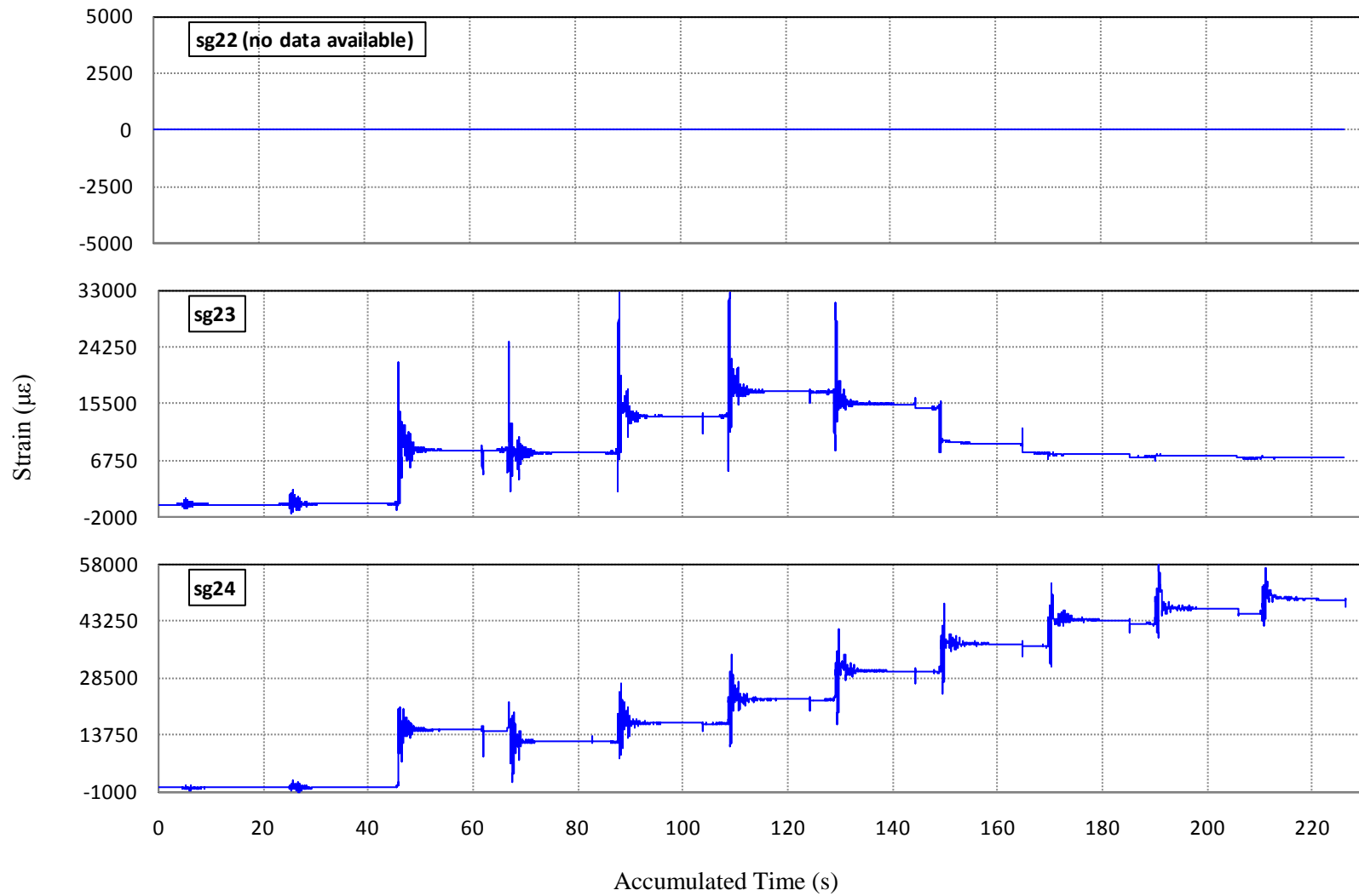
**Figure C-42 Strain History of Gauges 13, 14 and 15 in Specimen I1**



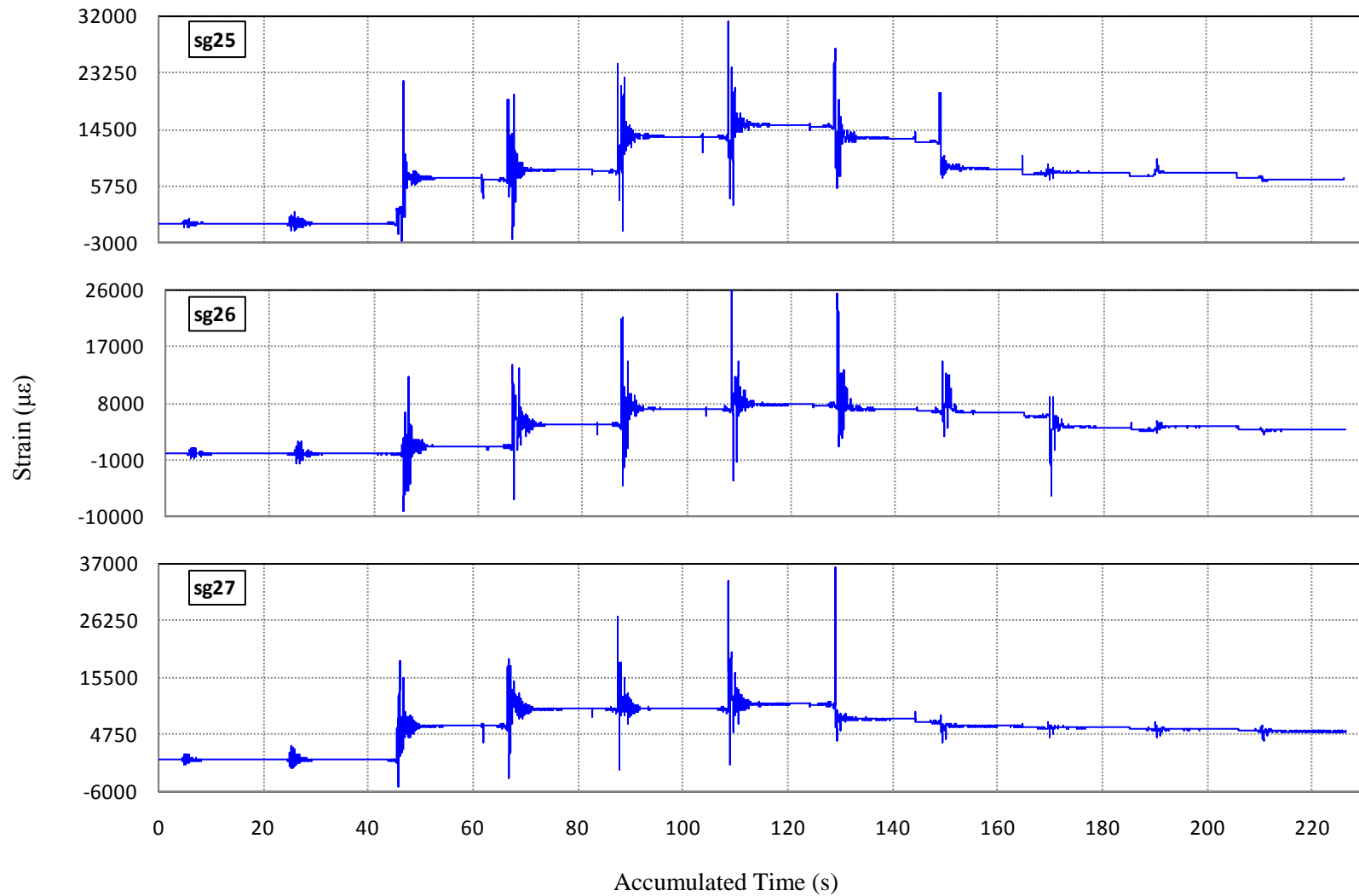
**Figure C-43 Strain History of Gauges 16, 17 and 18 in Specimen I1**



**Figure C-44 Strain History of Gauges 19, 20 and 21 in Specimen I1**

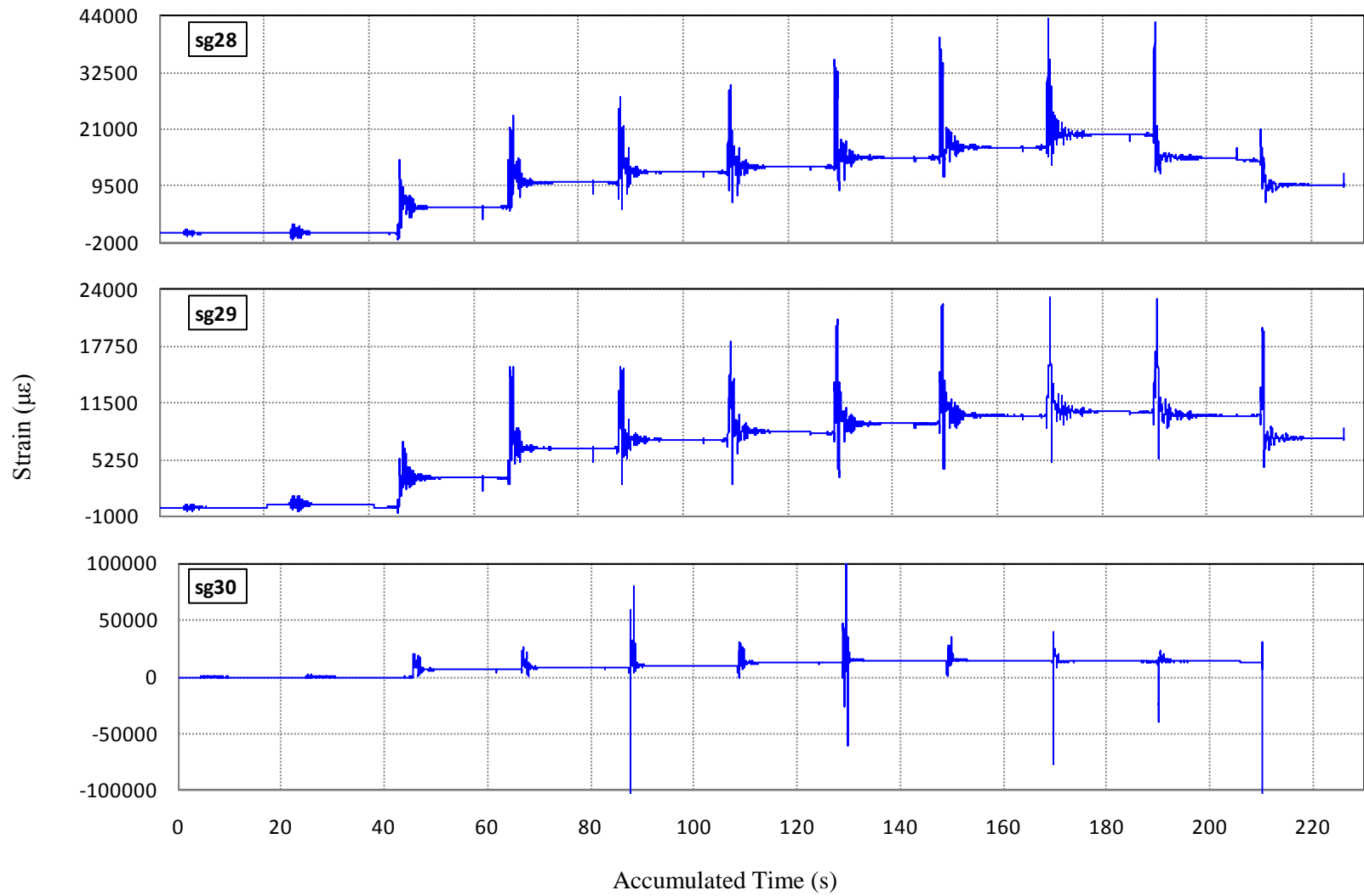


**Figure C-45 Strain History of Gauges 22, 23 and 24 in Specimen I1**

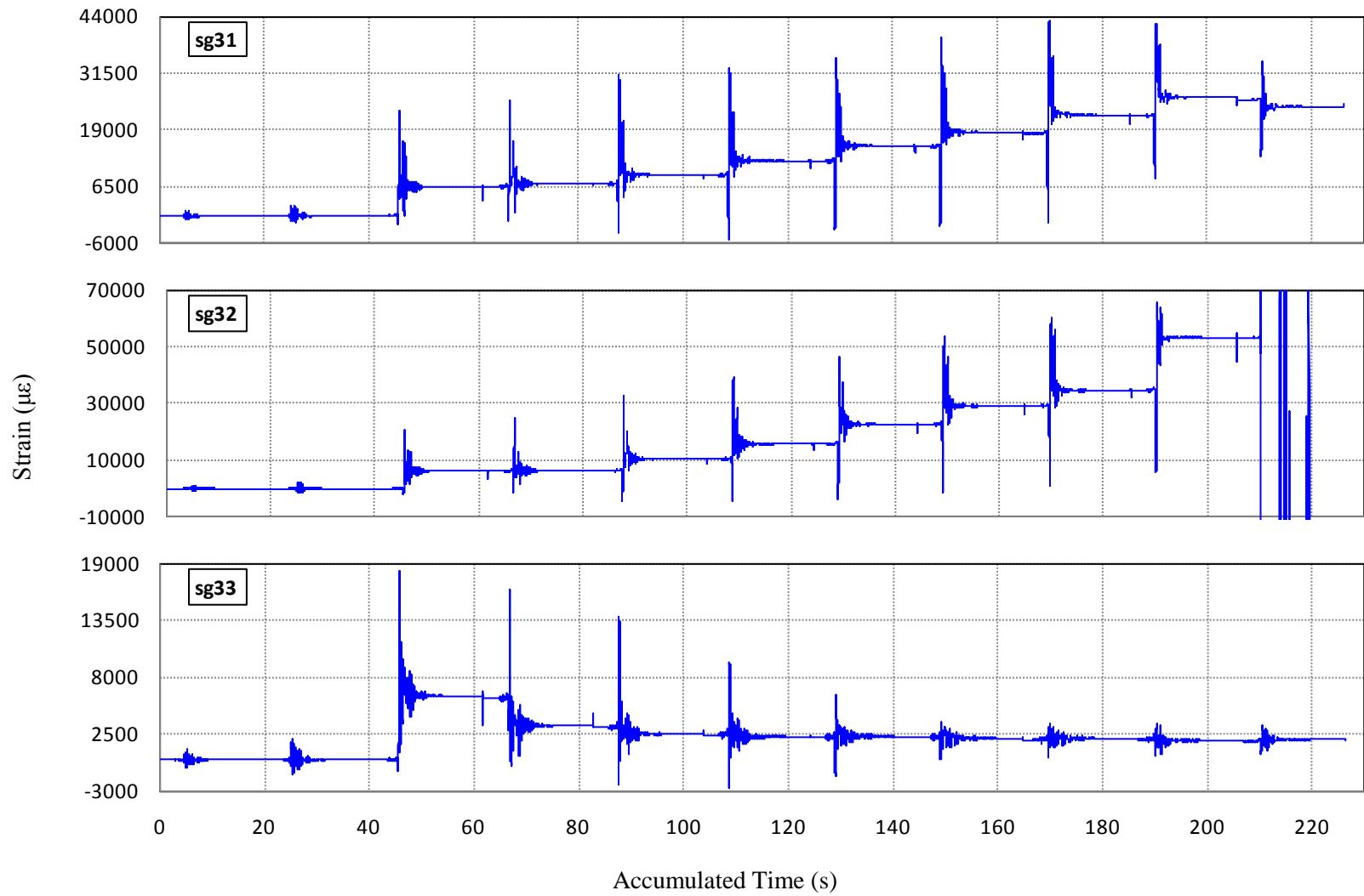


**Figure C-46 Strain History of Gauges 25, 26 and 27 in Specimen I1**

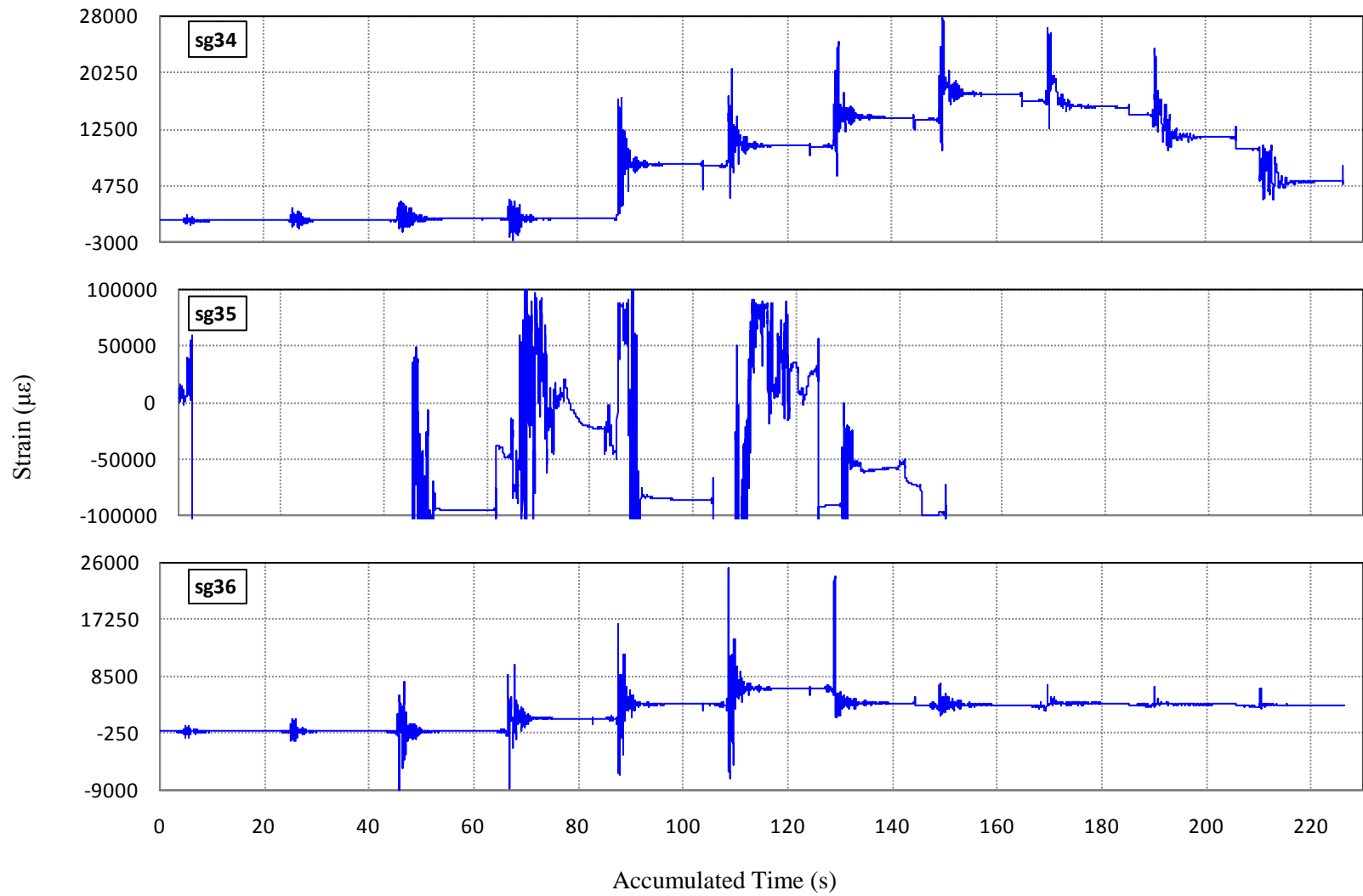




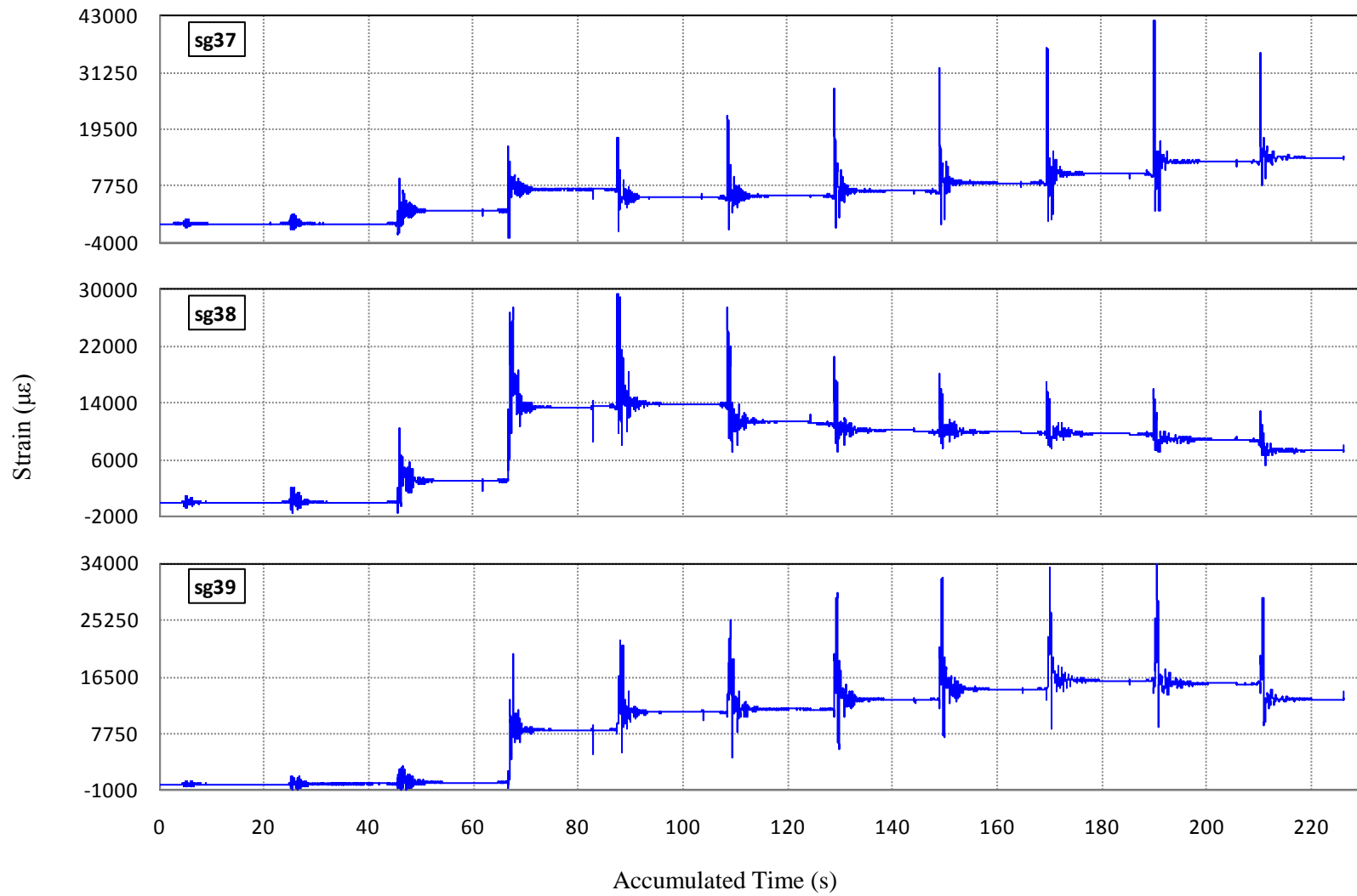
**Figure C-47 Strain History of Gauges 28, 29 and 30 in Specimen I1**



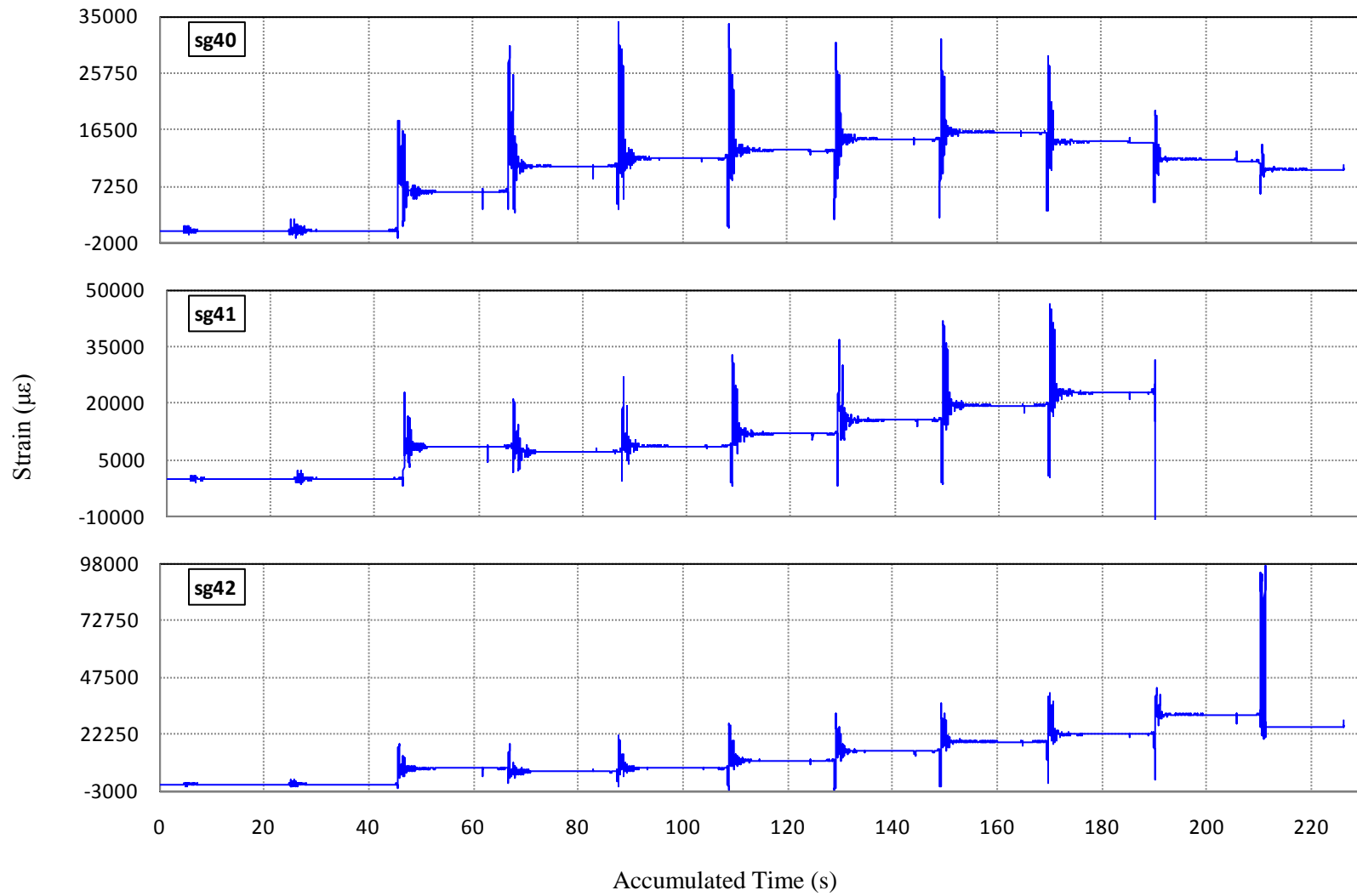
**Figure C-48 Strain History of Gauges 31, 32 and 33 in Specimen I1**



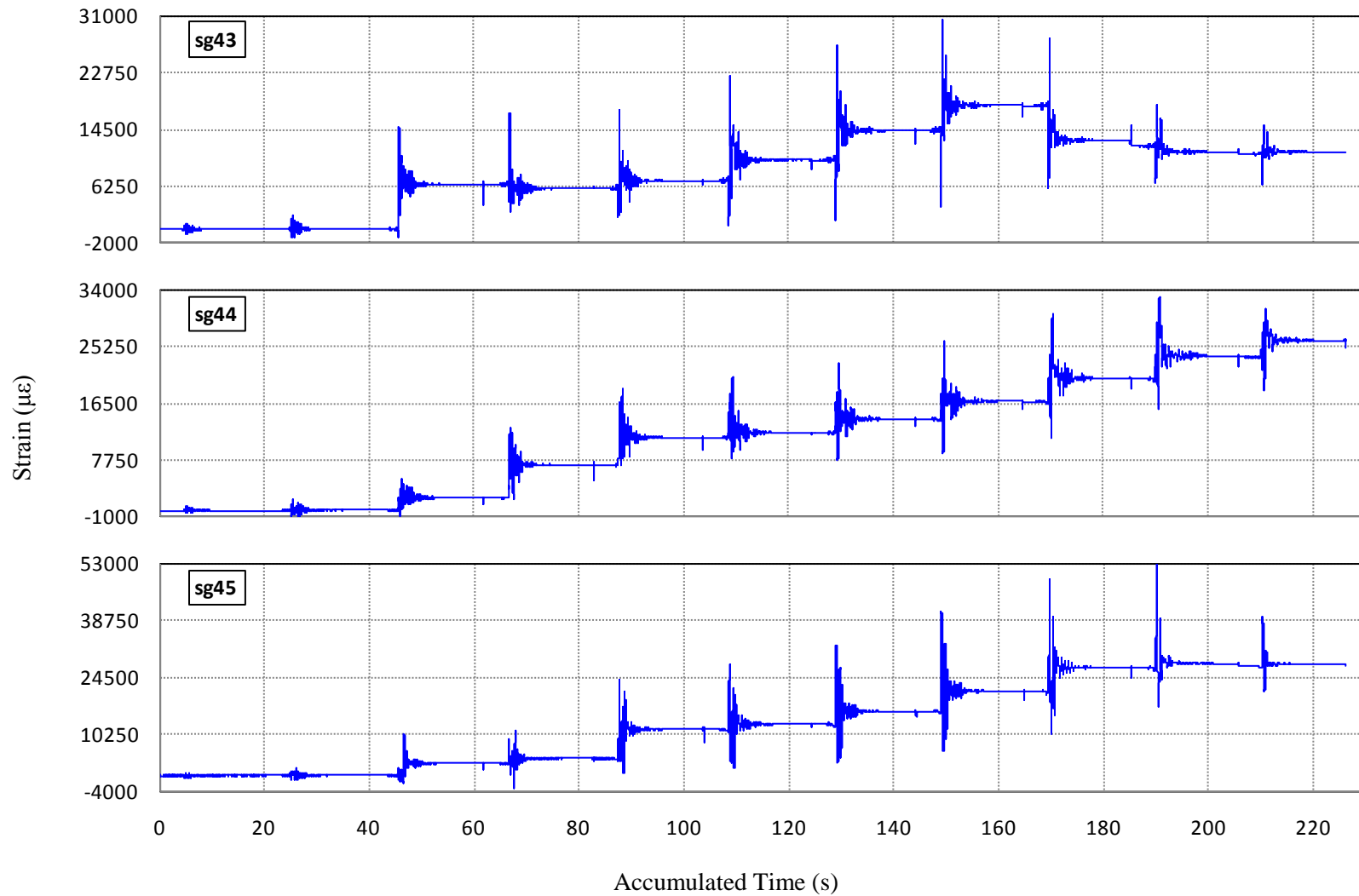
**Figure C-49 Strain History of Gauges 34, 35 and 36 in Specimen I1**



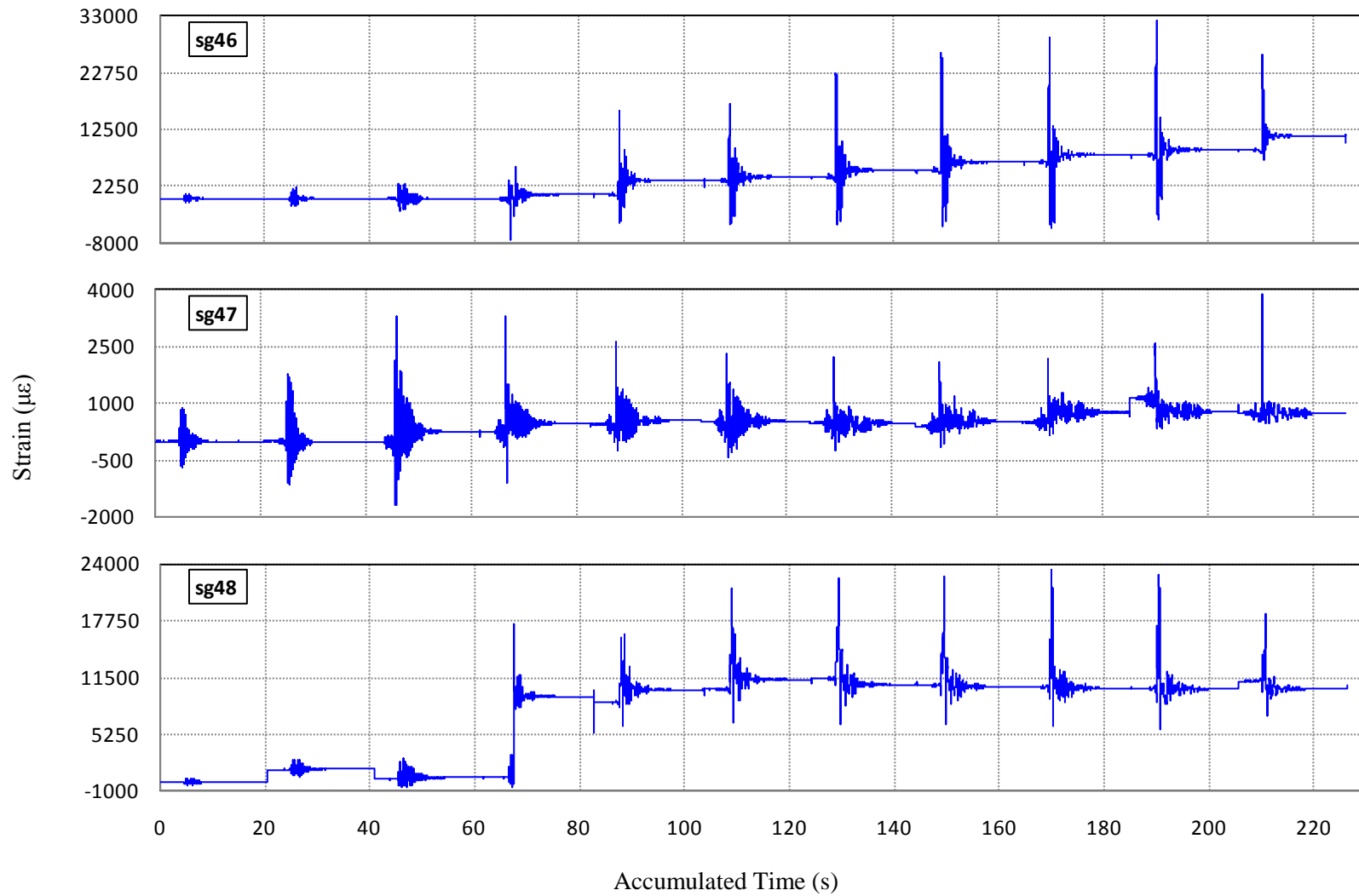
**Figure C-50 Strain History of Gauges 37, 38 and 39 in Specimen I1**



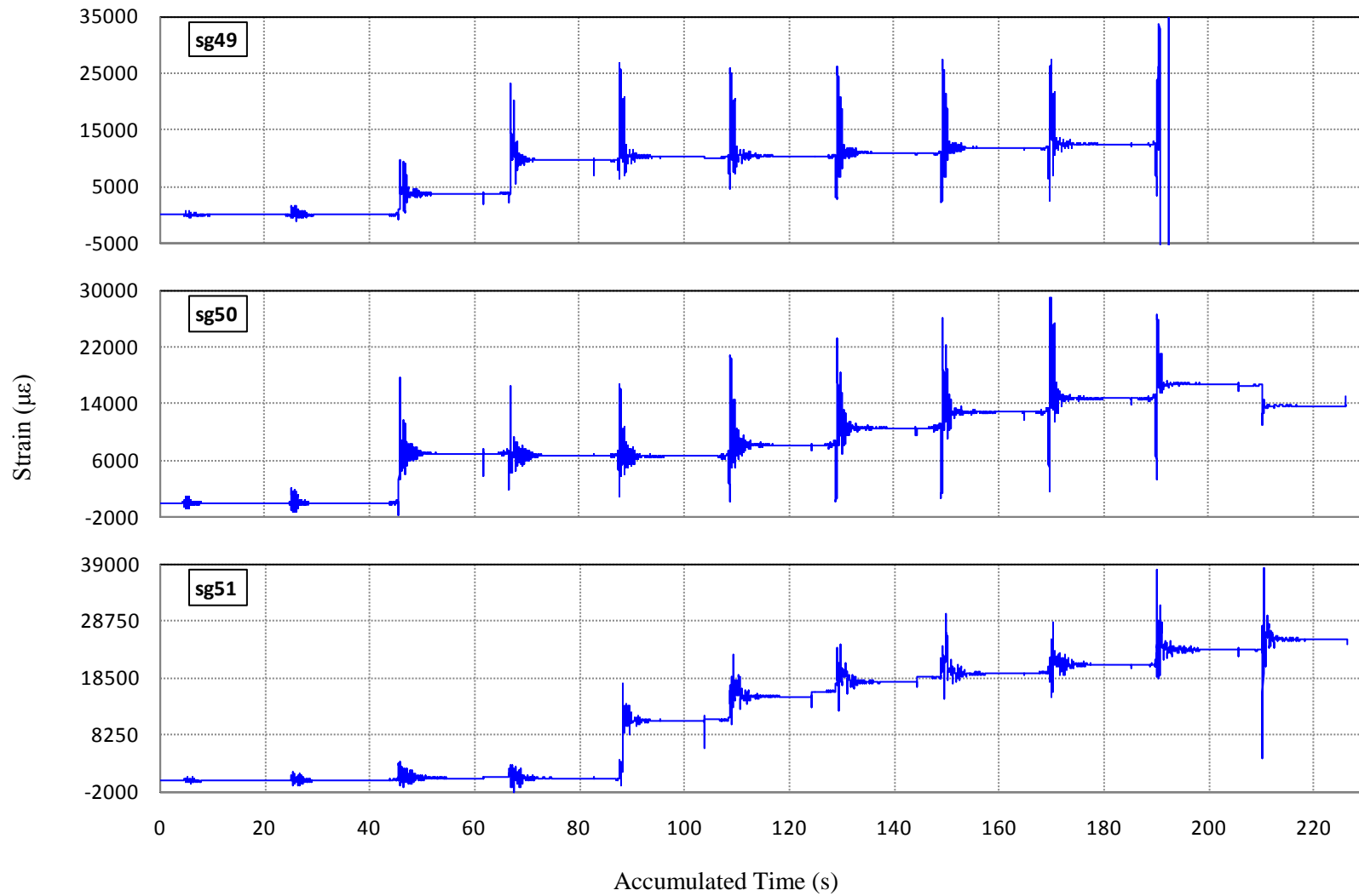
**Figure C-51 Strain History of Gauges 40, 41 and 42 in Specimen I1**



**Figure C-52 Strain History of Gauges 43, 44 and 45 in Specimen I1**

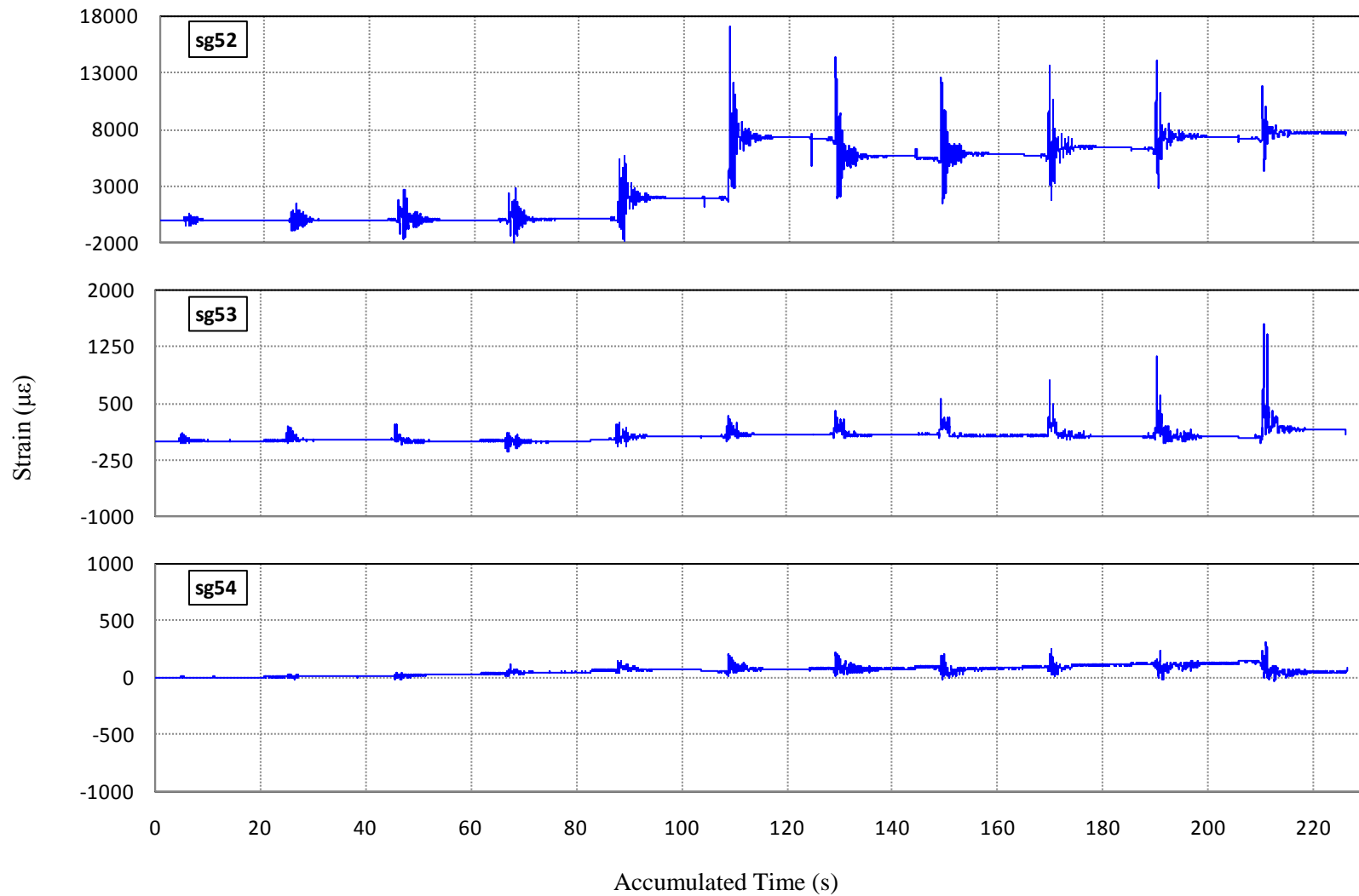


**Figure C-53 Strain History of Gauges 46, 47 and 48 in Specimen I1**

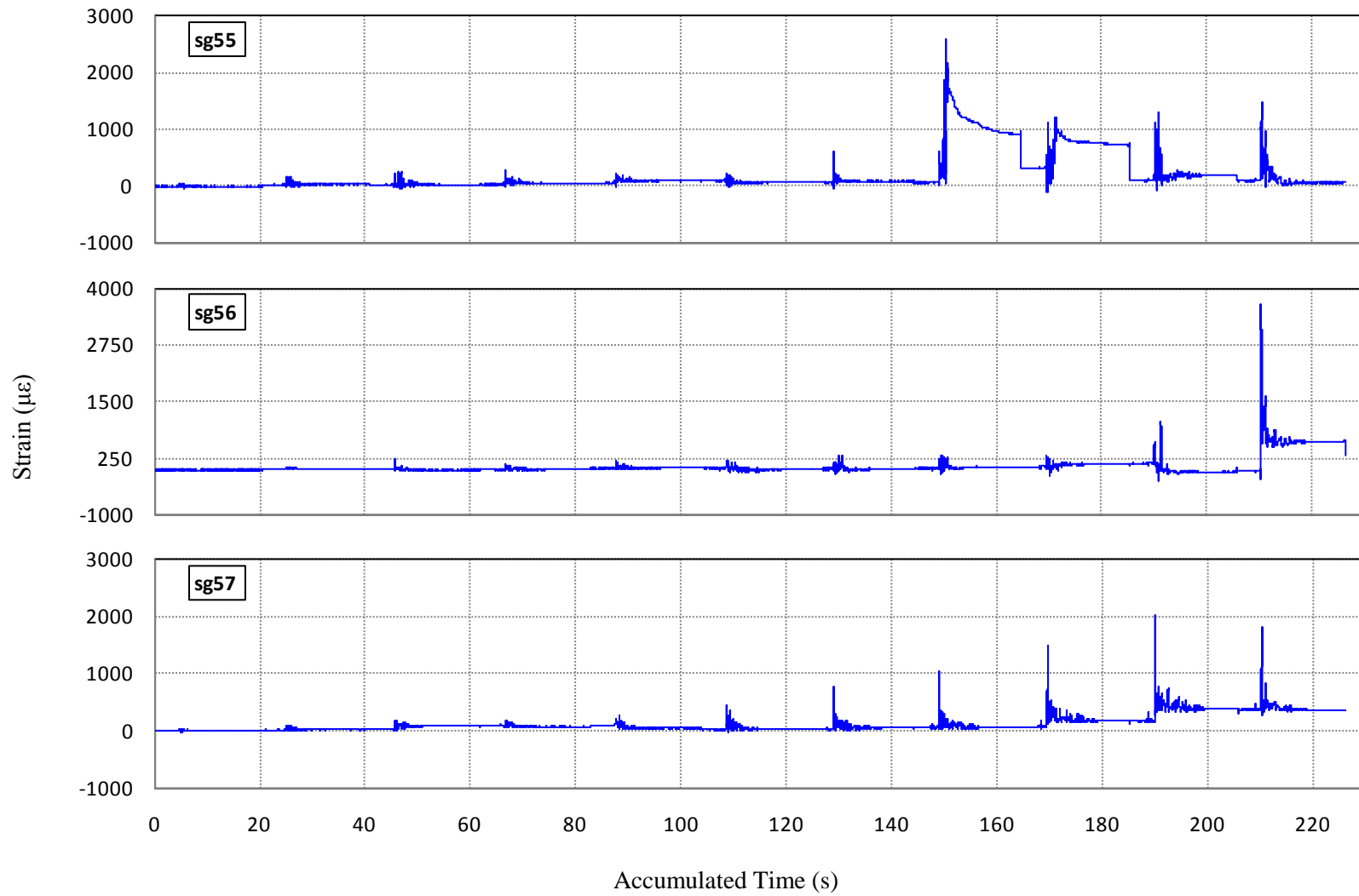


**Figure C-54 Strain History of Gauges 49, 50 and 51 in Specimen I1**

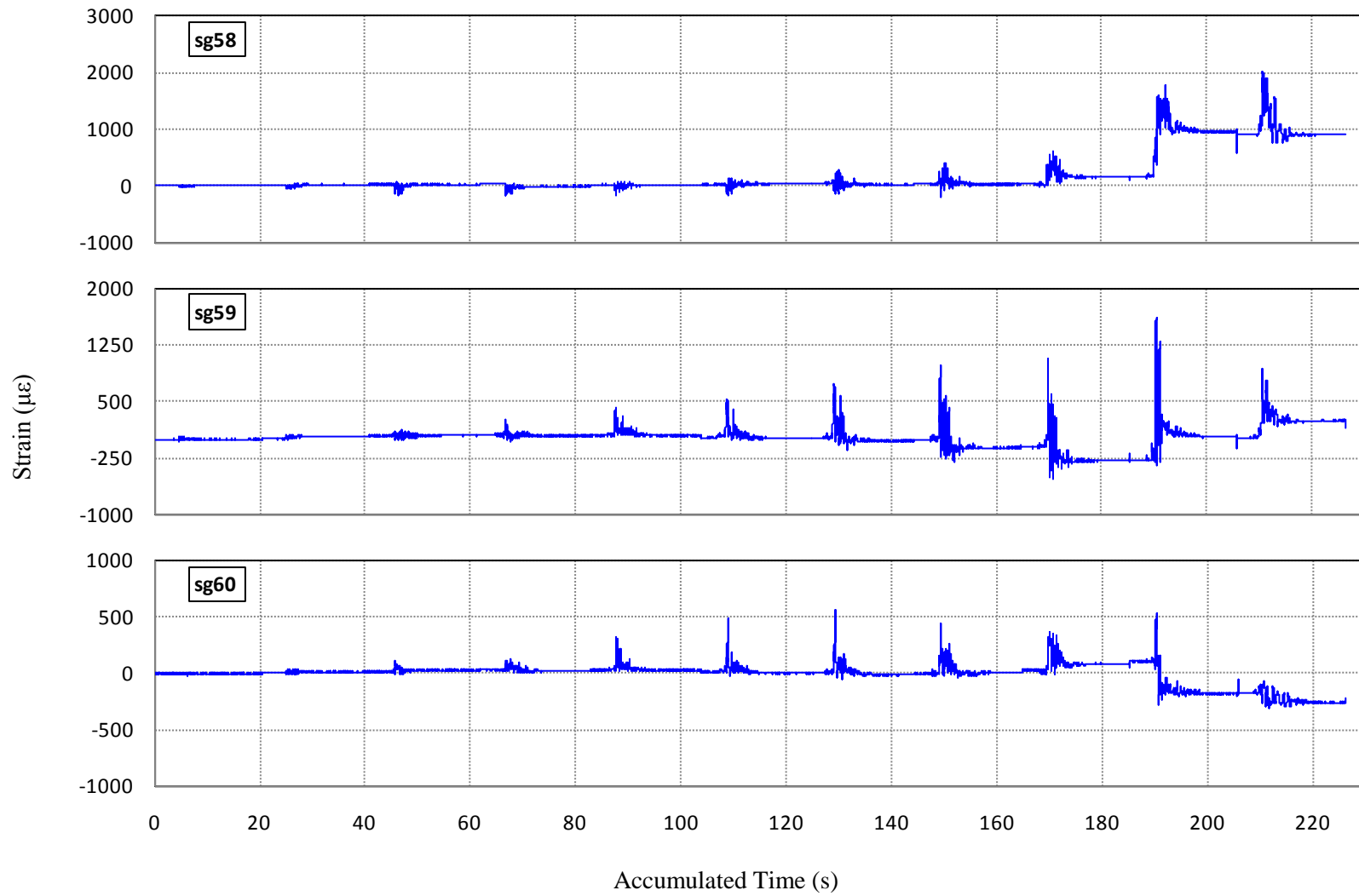




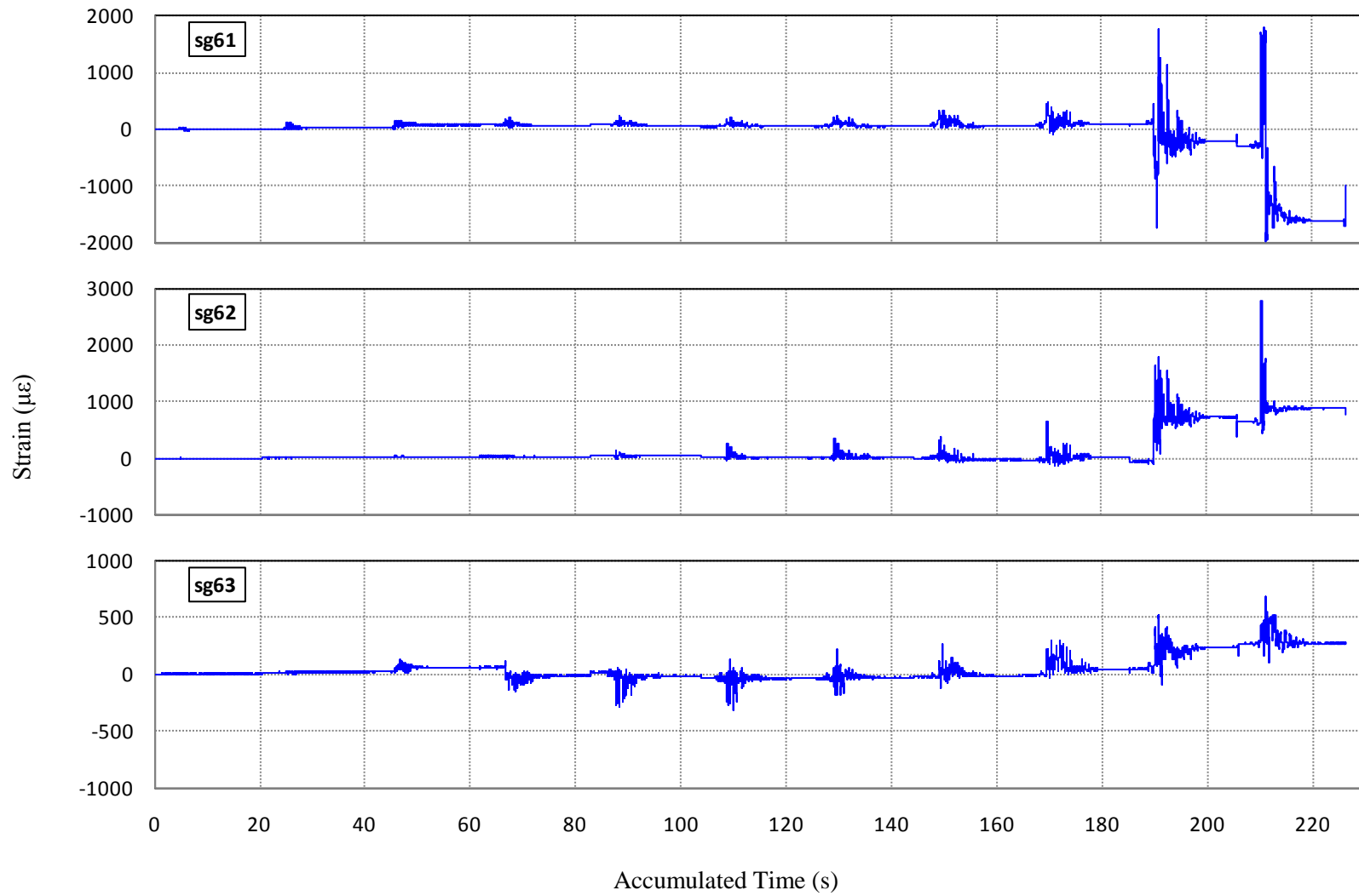
**Figure C-55 Strain History of Gauges 52, 53 and 54 in Specimen I1**



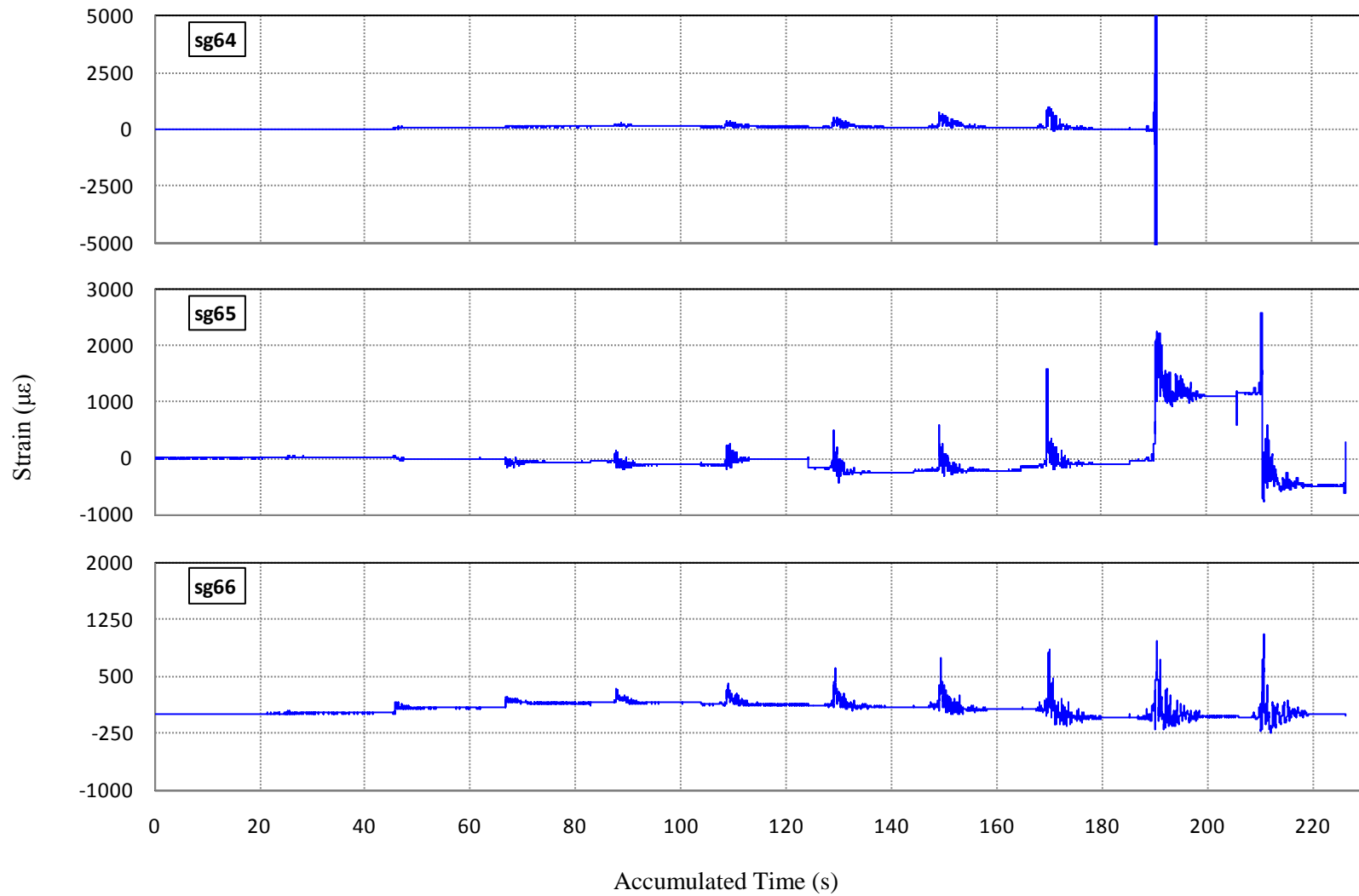
**Figure C-56 Strain History of Gauges 55, 56 and 57 in Specimen I1**



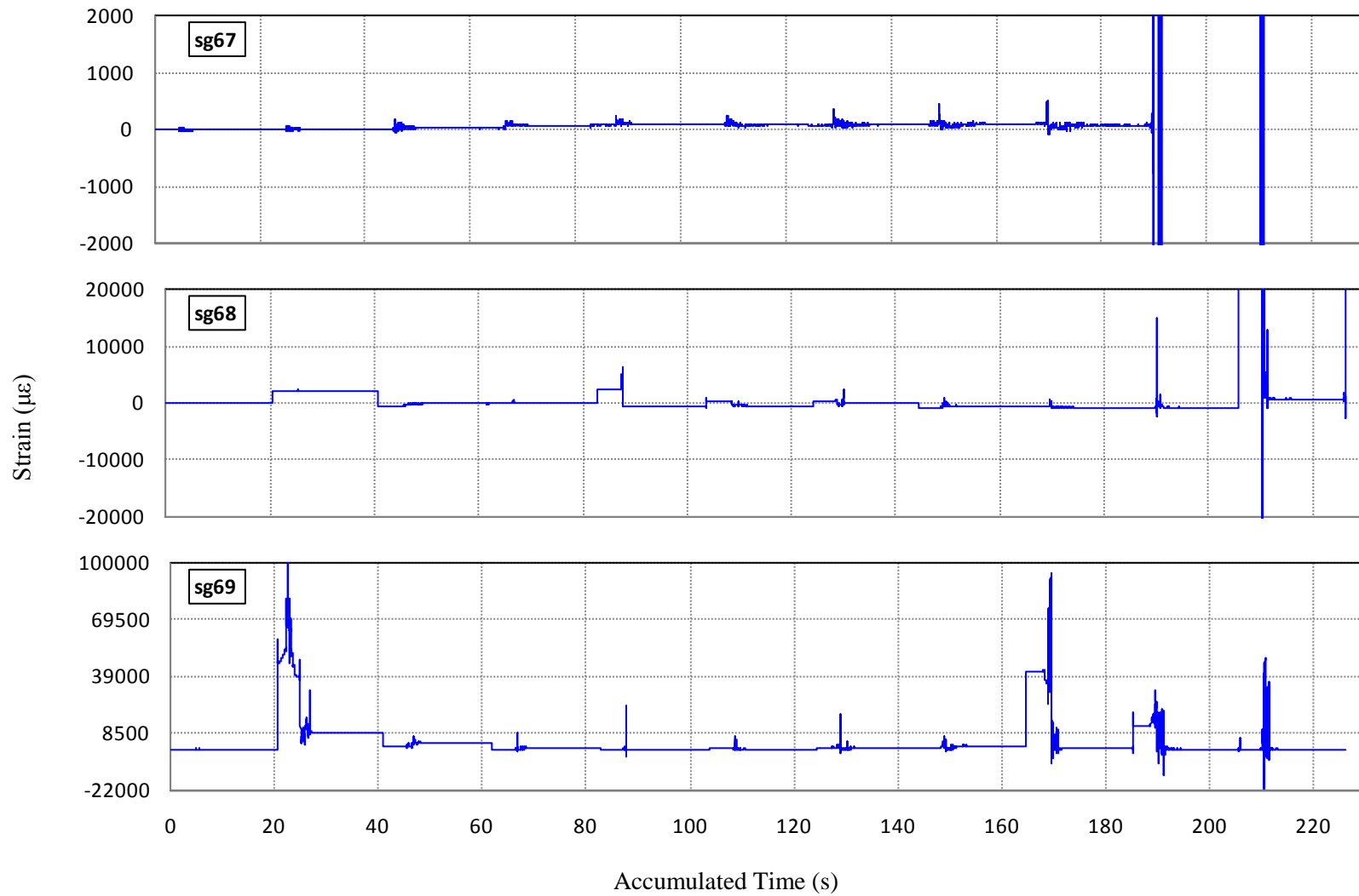
**Figure C-57 Strain History of Gauges 58, 59 and 60 in Specimen I1**



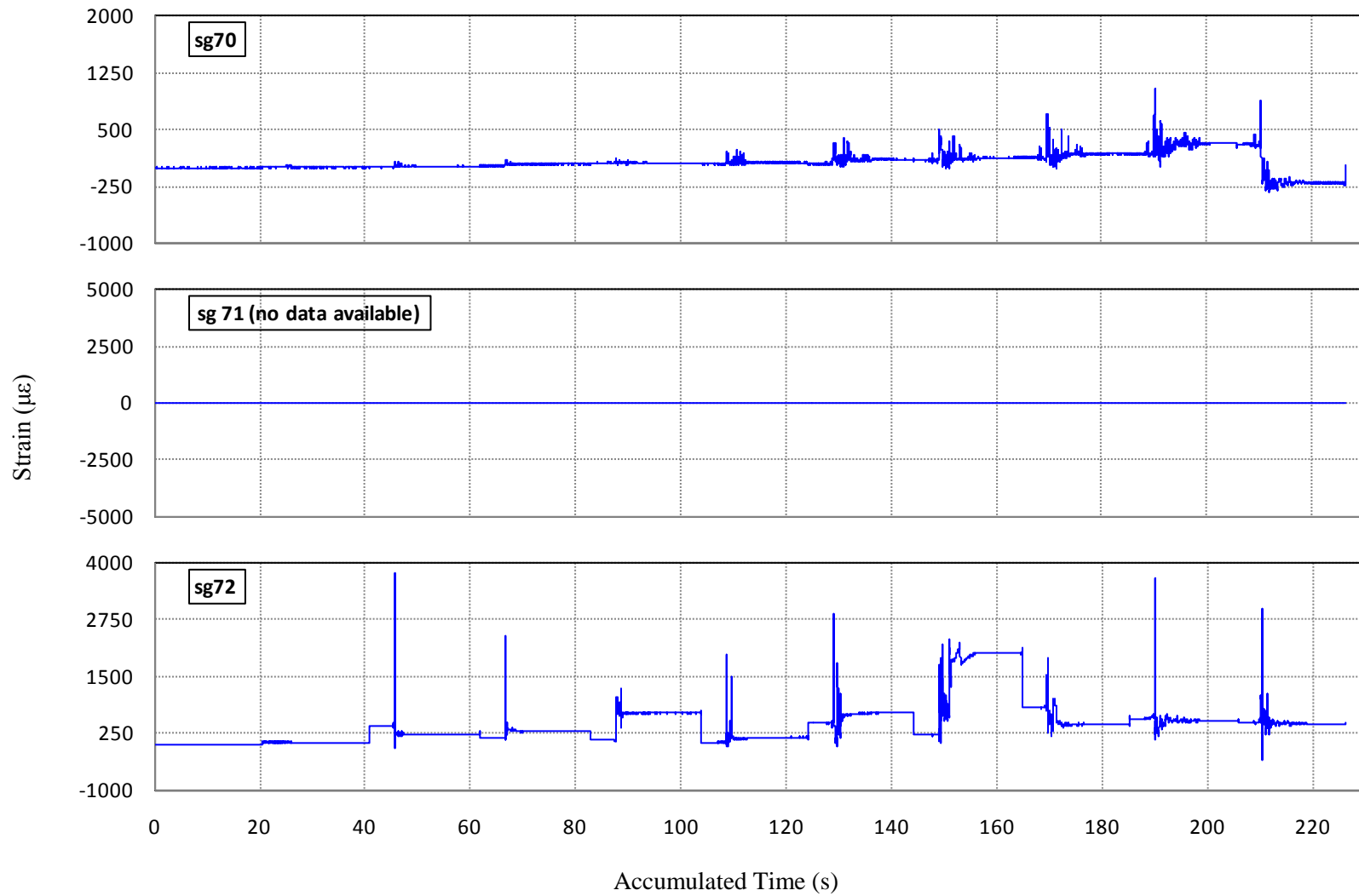
**Figure C-58 Strain History of Gauges 61, 62 and 63 in Specimen I1**



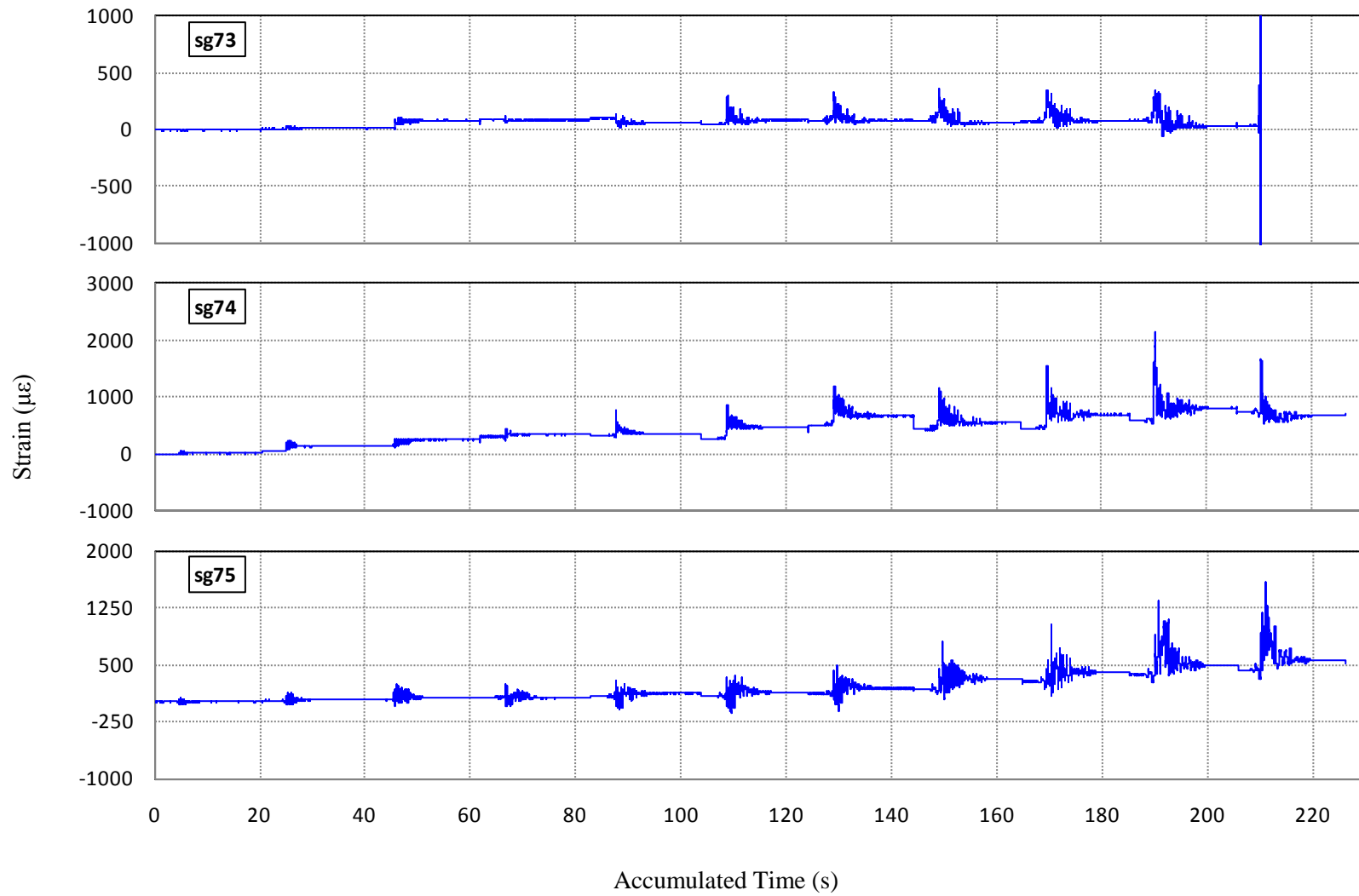
**Figure C-59 Strain History of Gauges 64, 65 and 66 in Specimen I1**



**Figure C-60 Strain History of Gauges 67, 68 and 69 in Specimen I1**

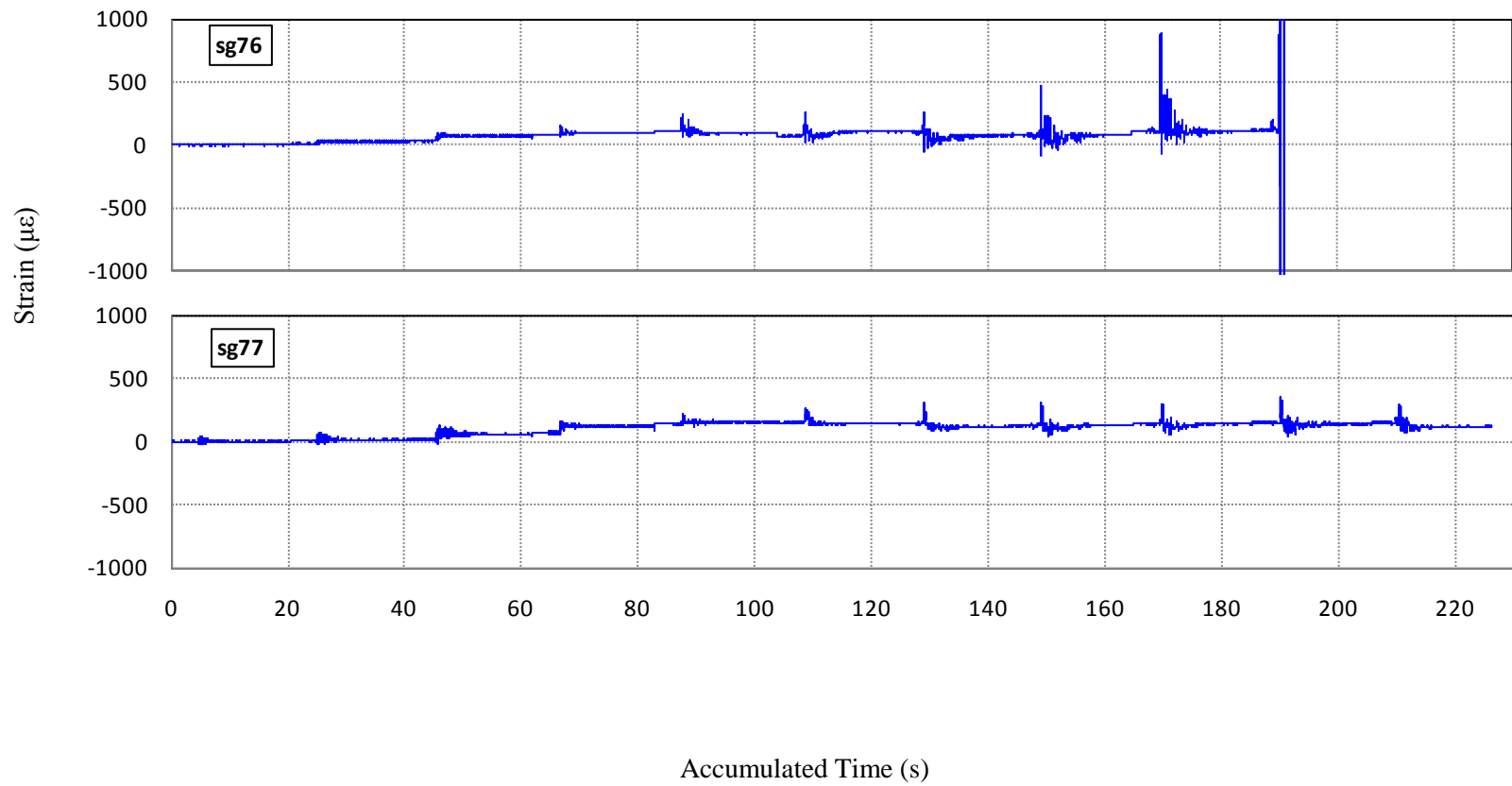


**Figure C-61 Strain History of Gauges 70, 71 and 72 in Specimen I1**

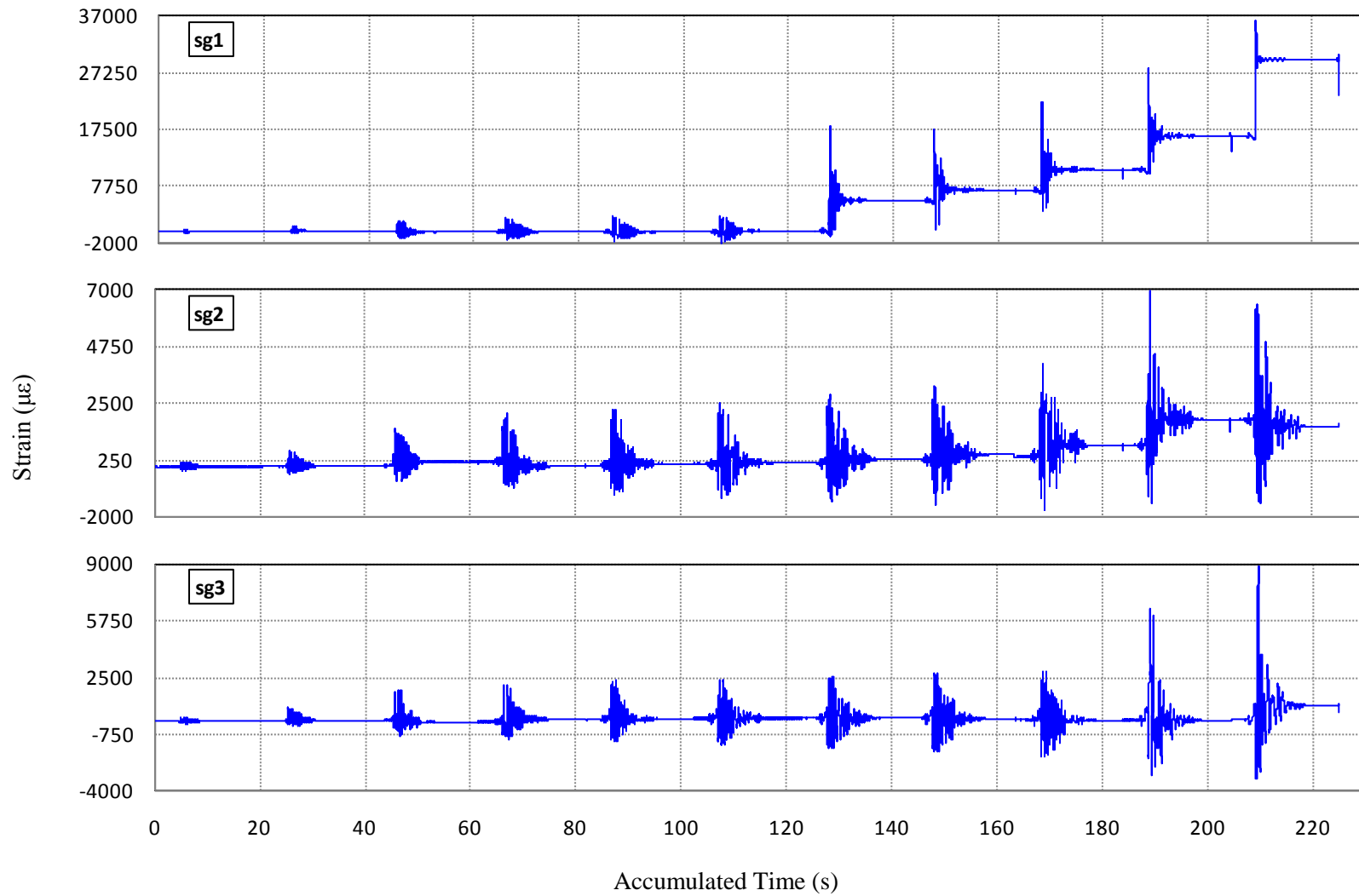


**Figure C-62 Strain History of Gauges 73, 74 and 75 in Specimen I1**





**Figure C-63 Strain History of Gauges 76 and 77 in Specimen I1**



**Figure C-64 Strain History of Gauges 1, 2 and 3 in Specimen I2**

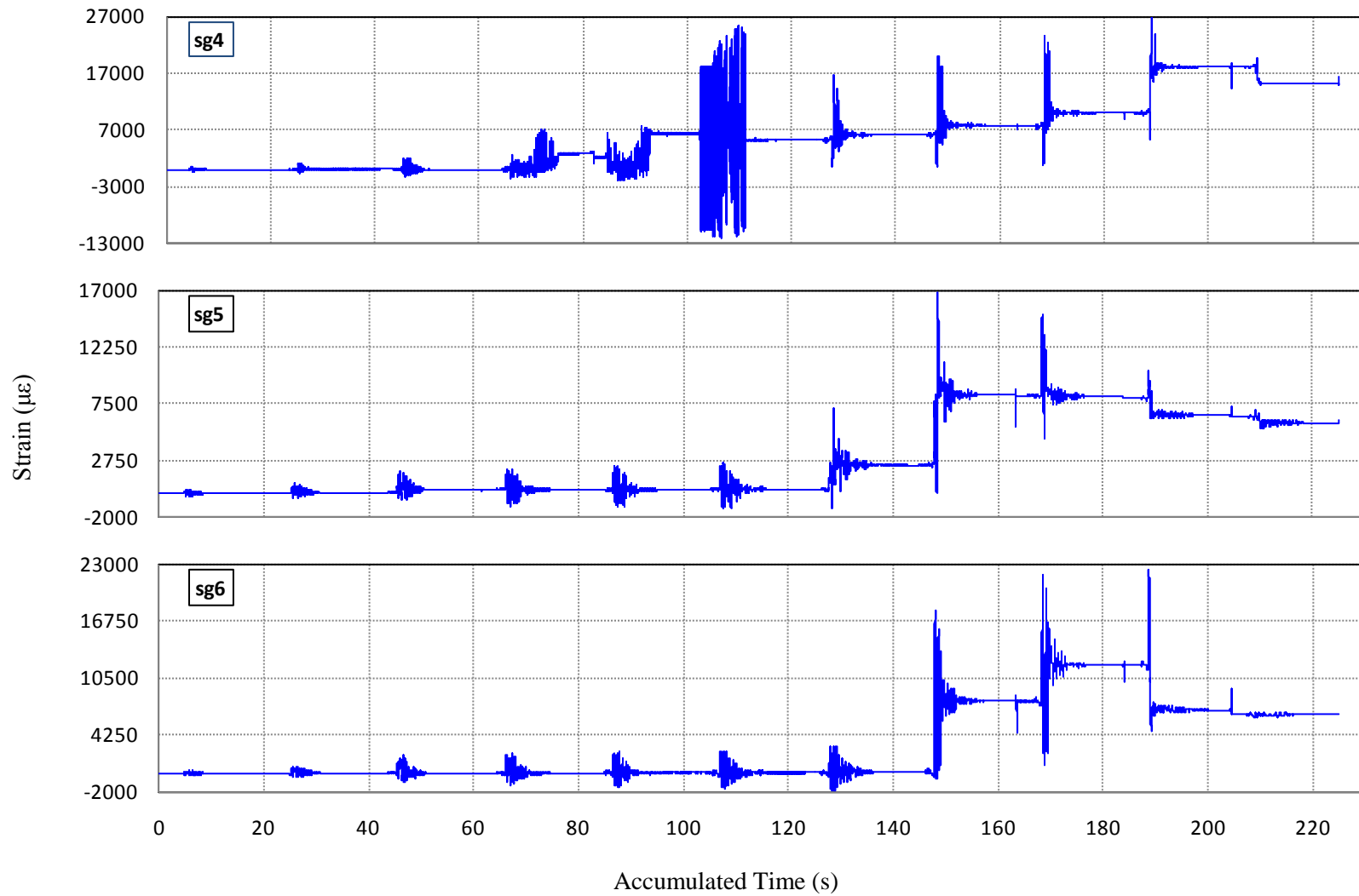
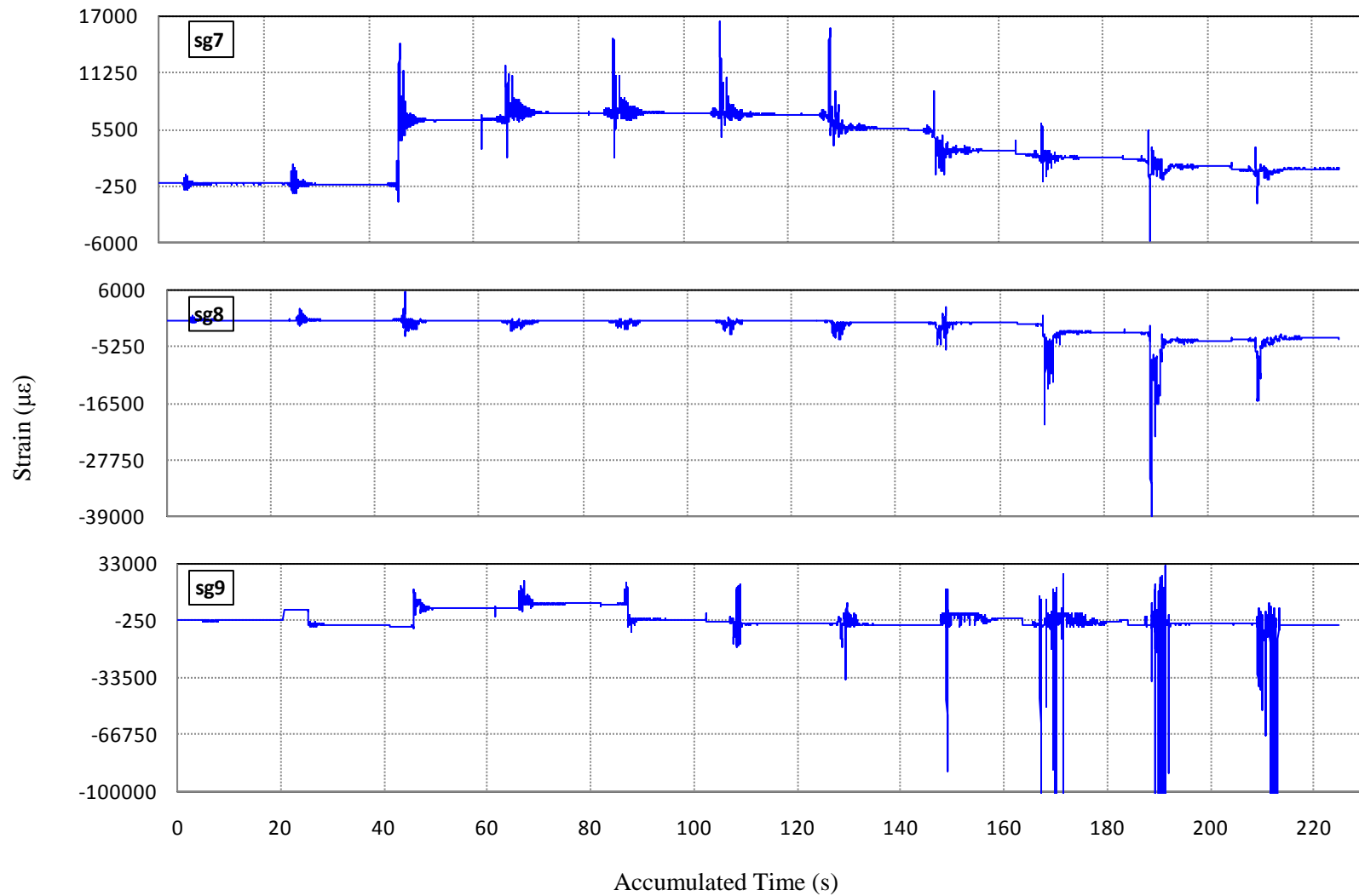
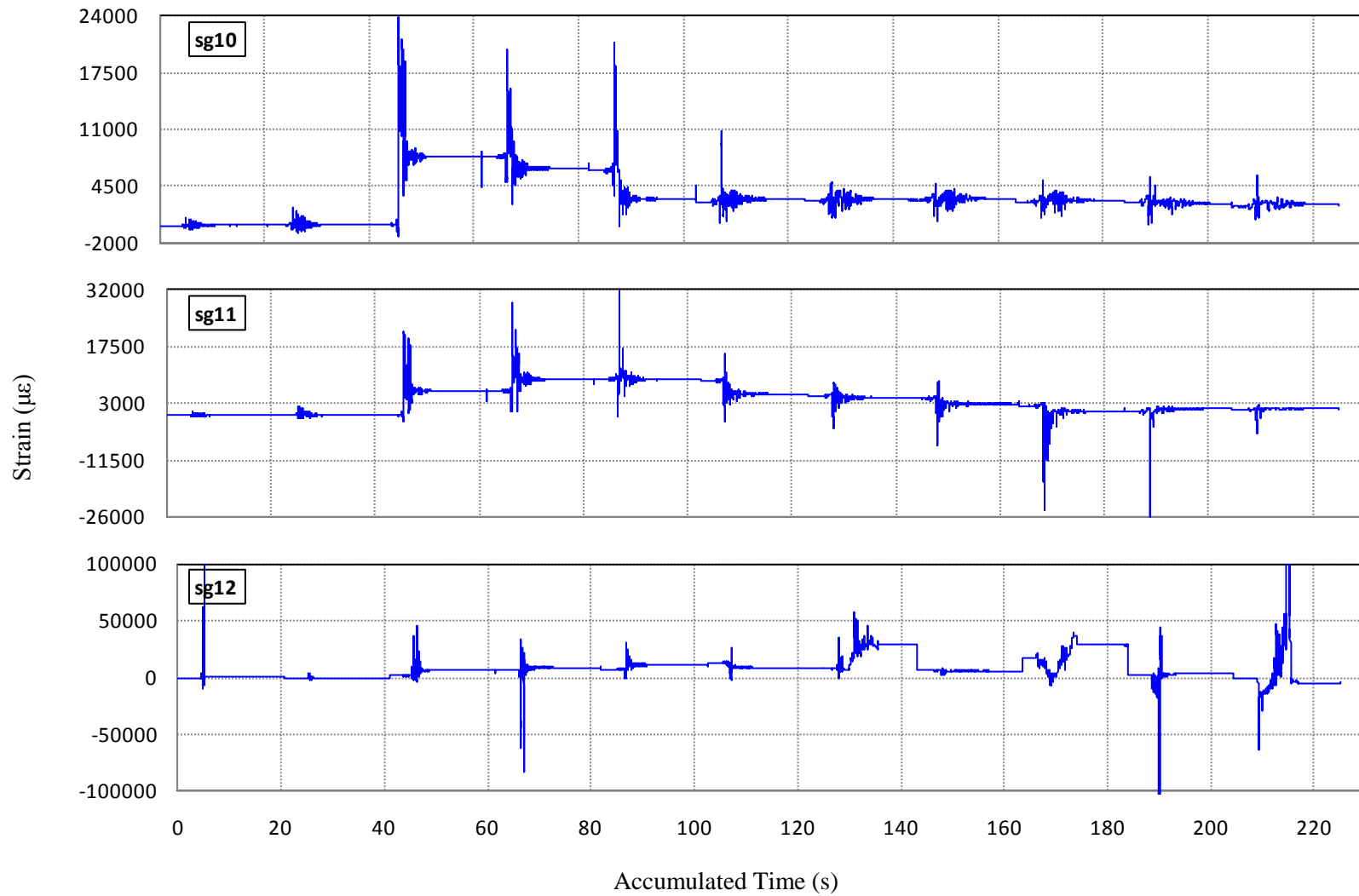


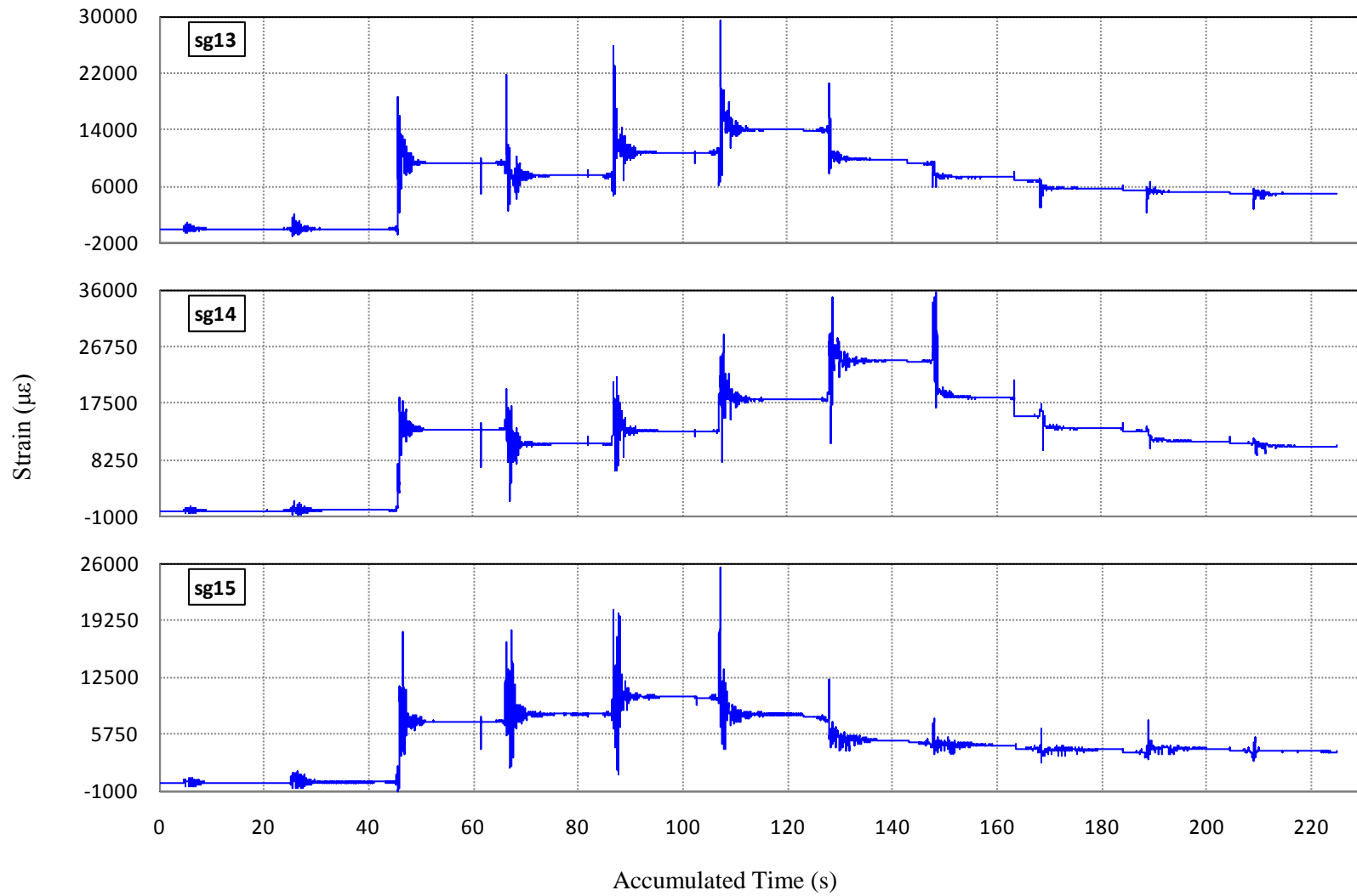
Figure C-65 Strain History of Gauges 4, 5 and 6 in Specimen I2



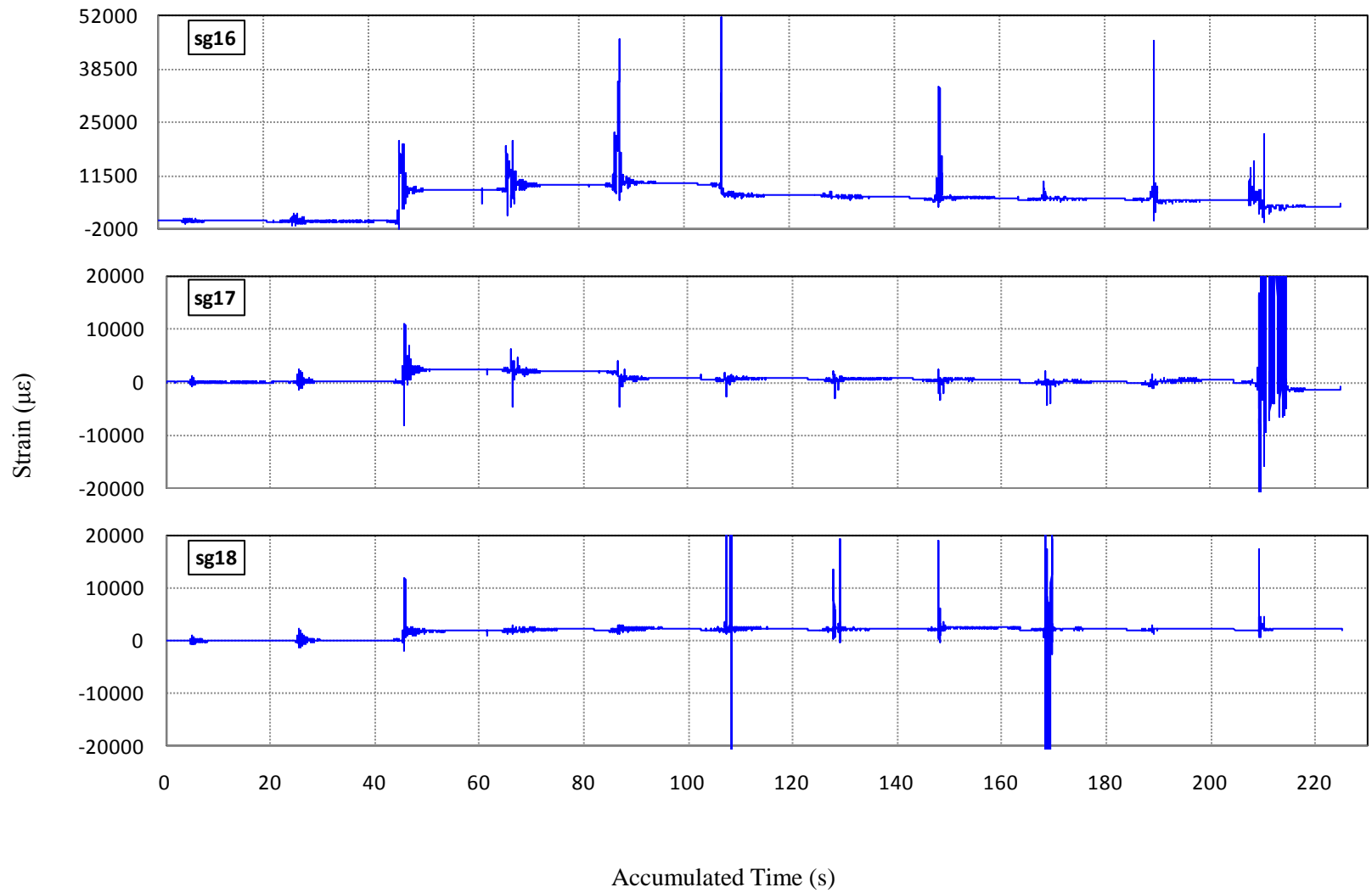
**Figure C-66 Strain History of Gauges 7, 8 and 9 in Specimen I2**



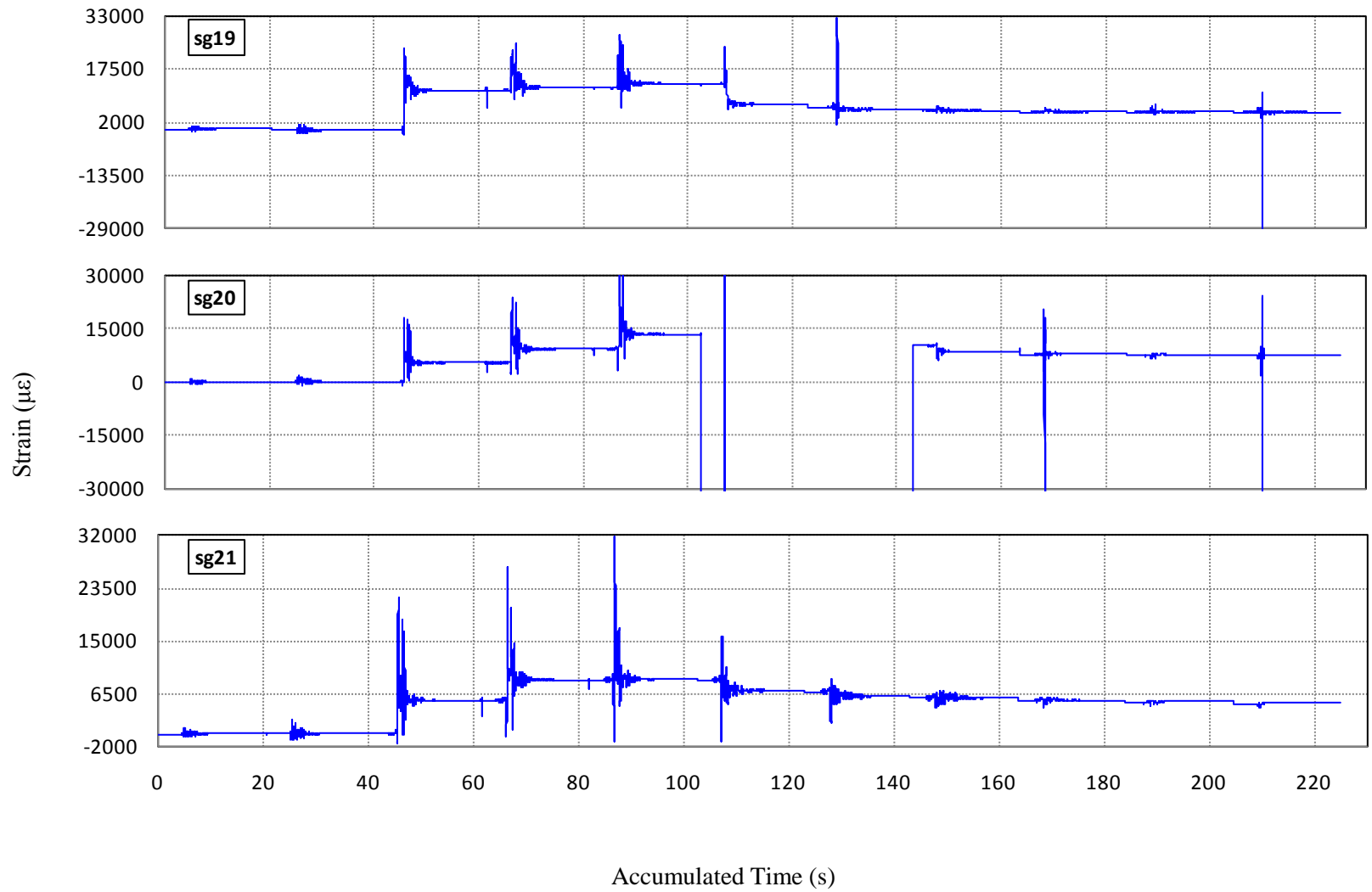
**Figure C-67 Strain History of Gauges 10, 11 and 12 in Specimen I2**



**Figure C-68 Strain History of Gauges 13, 14 and 15 in Specimen I2**

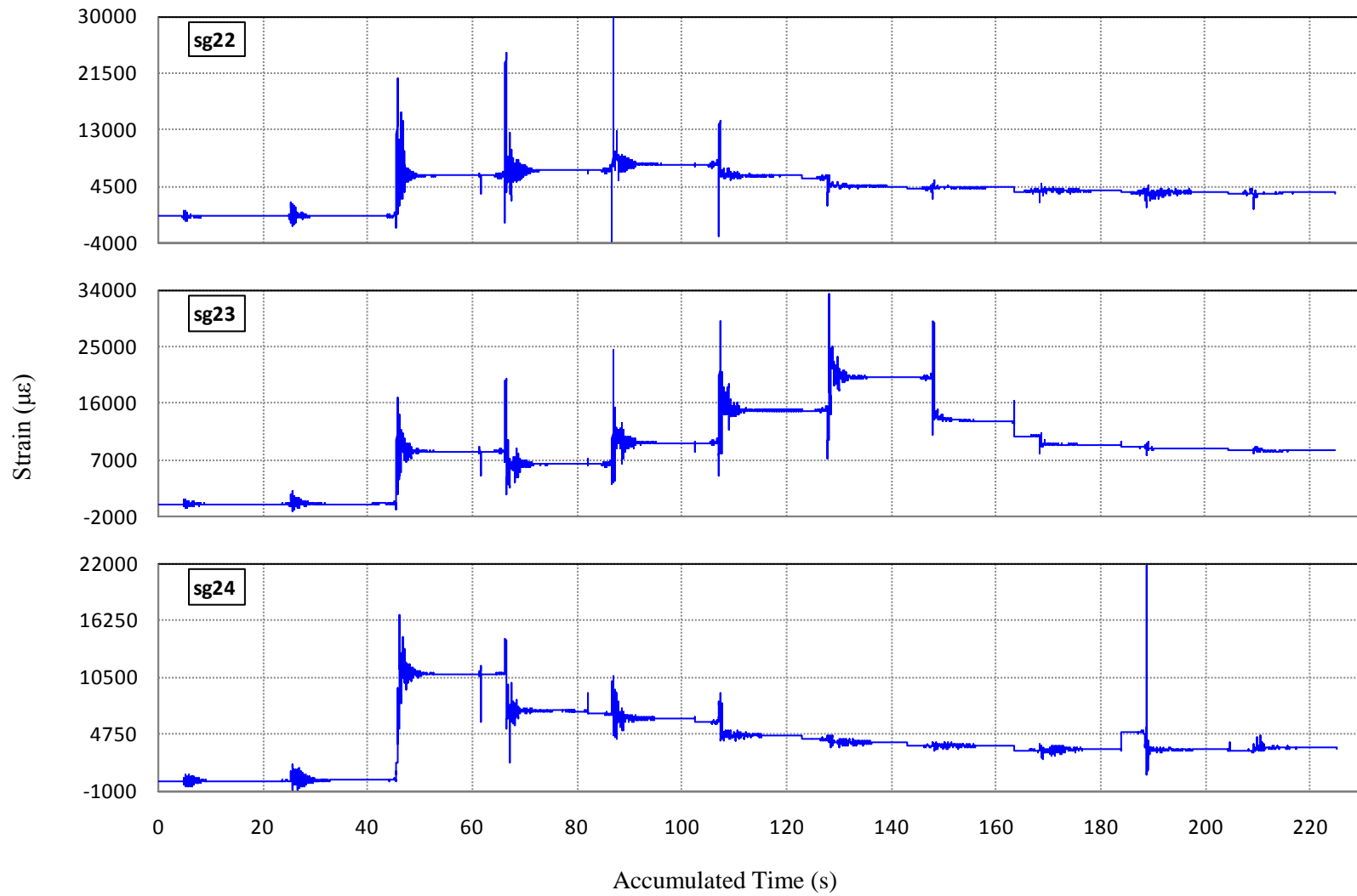


**Figure C-69 Strain History of Gauges 16, 17 and 18 in Specimen I2**

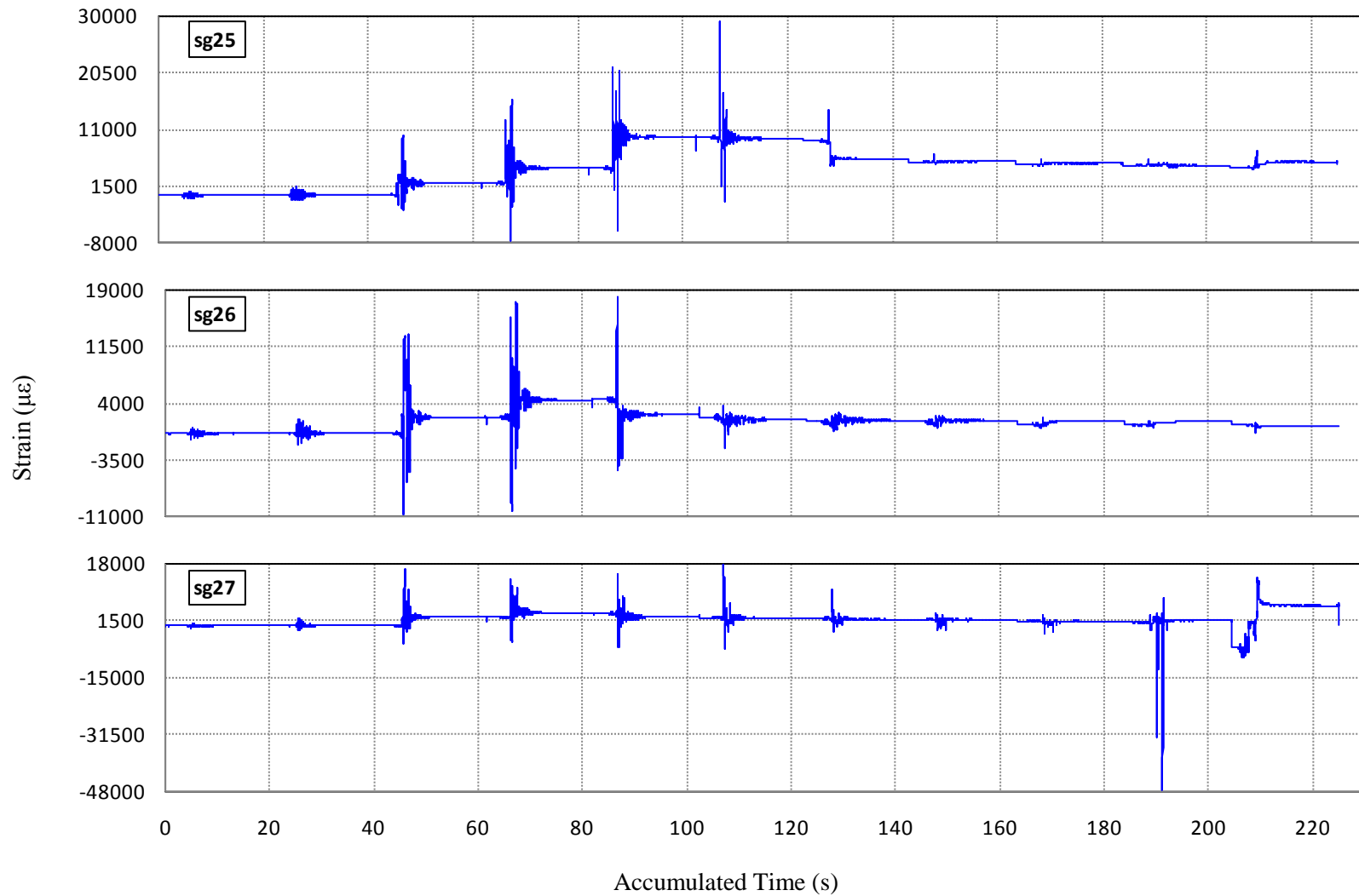


**Figure C-70 Strain History of Gauges 19, 20 and 21 in Specimen I2**

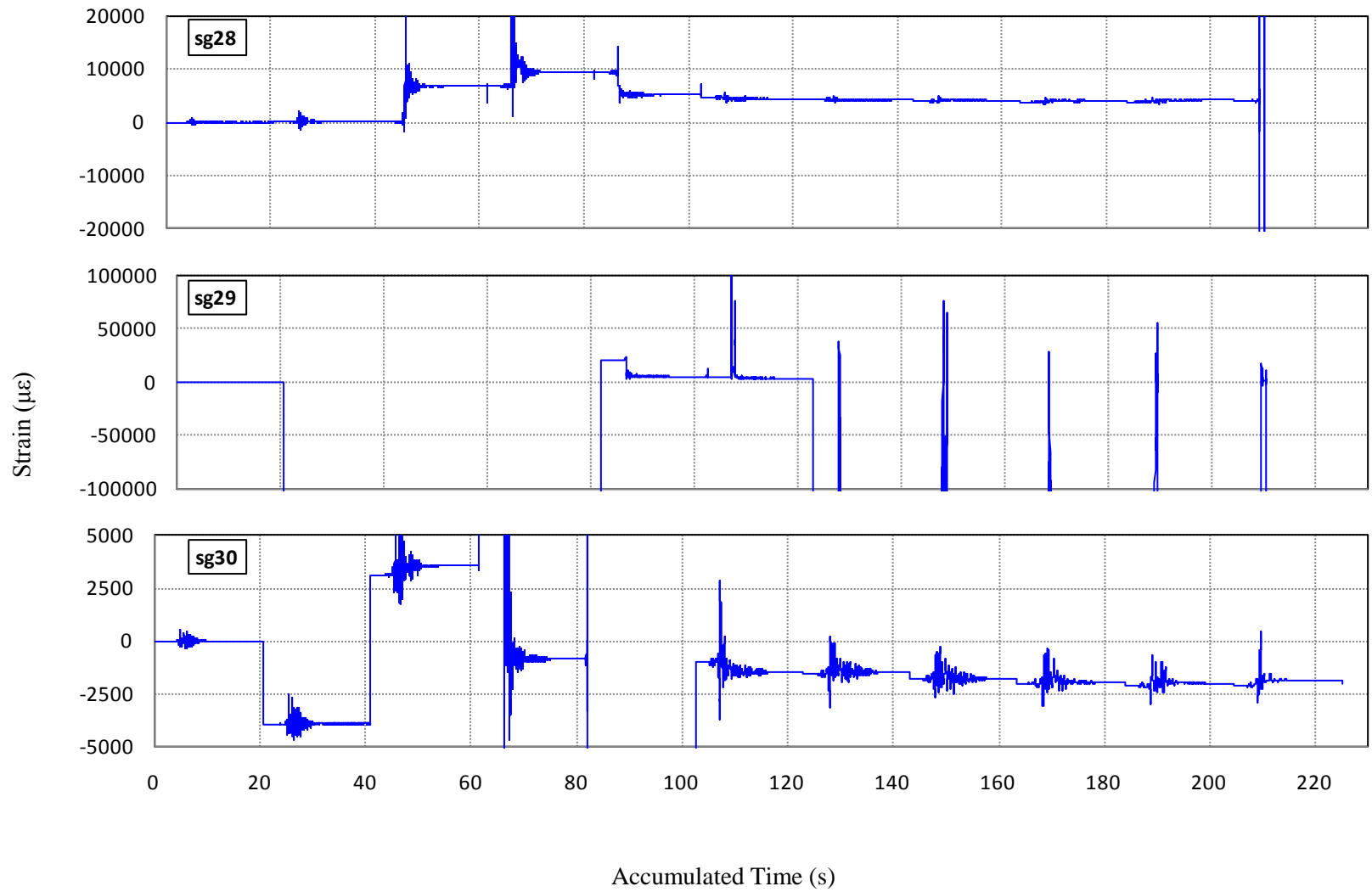




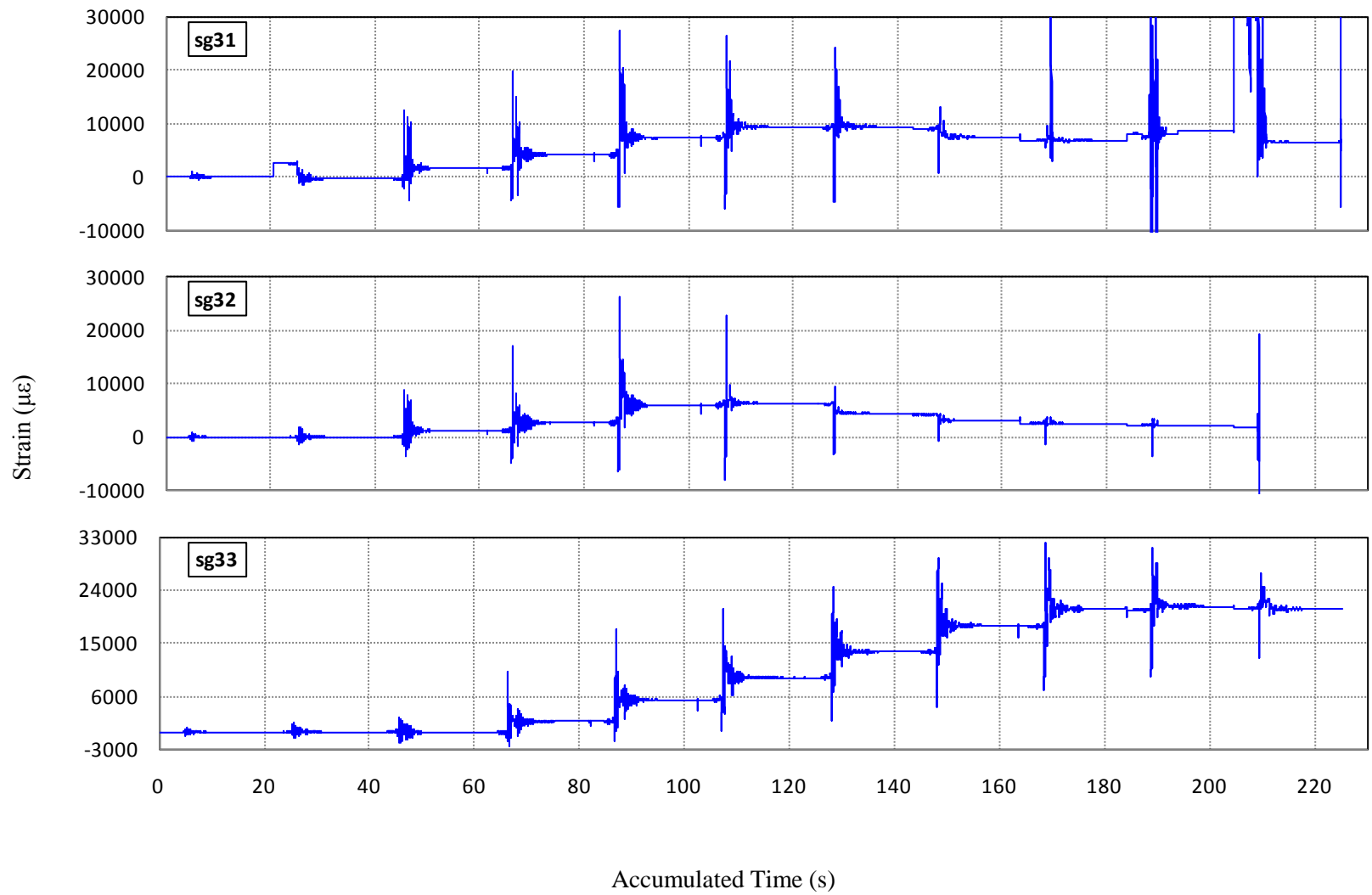
**Figure C-71 Strain History of Gauges 22, 23 and 24 in Specimen I2**



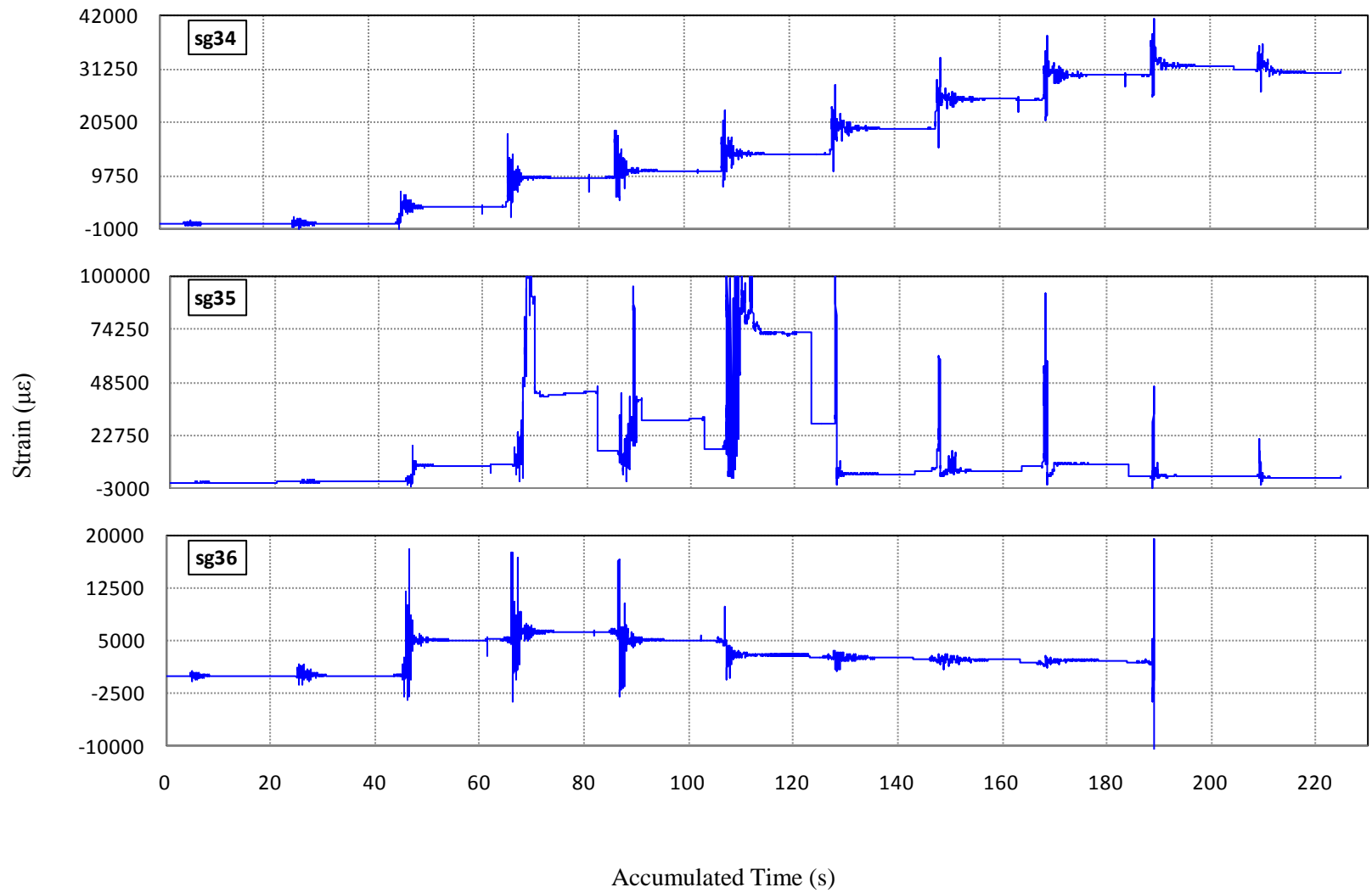
**Figure C-72 Strain History of Gauges 25, 26 and 27 in Specimen I2**



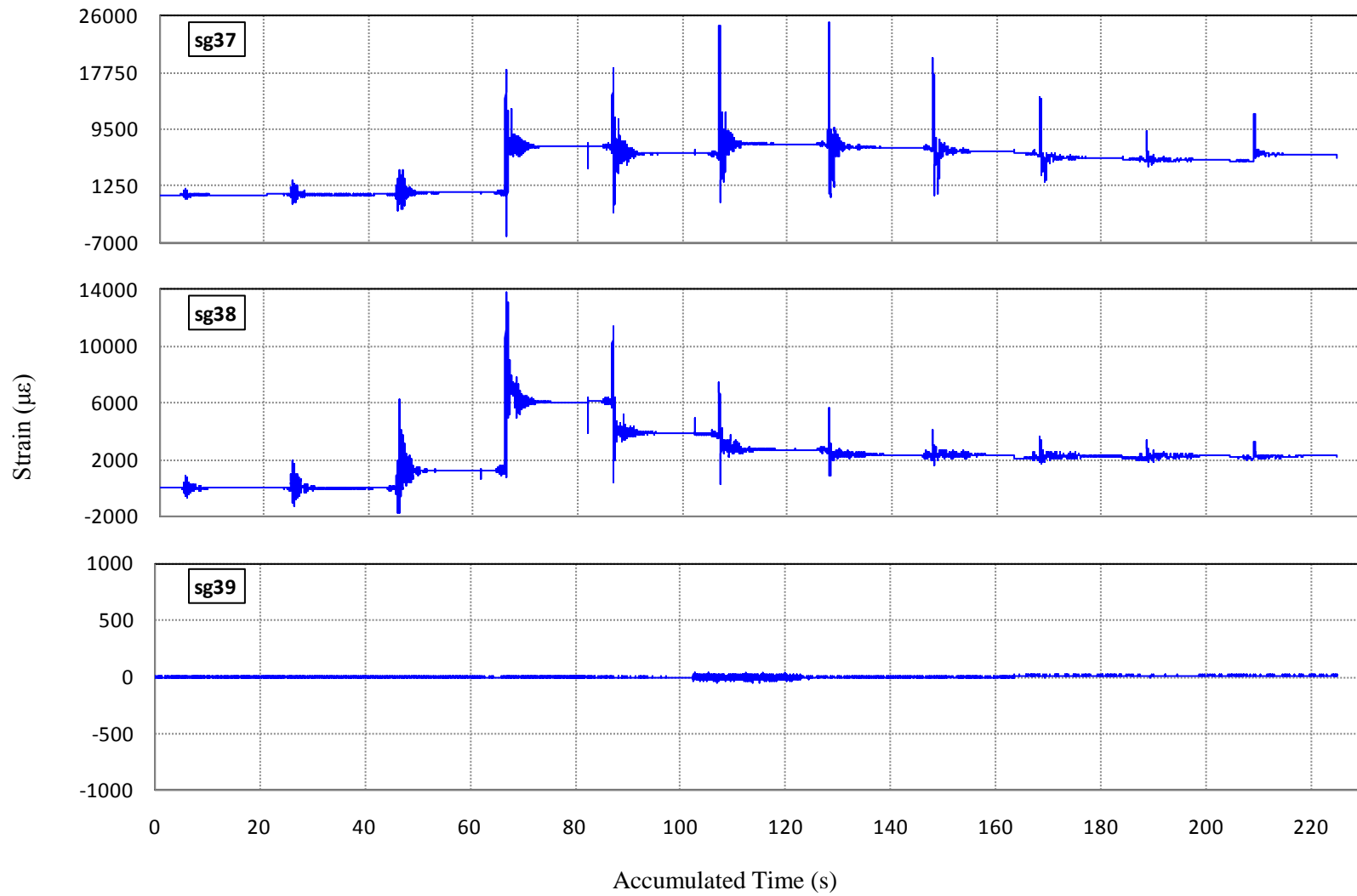
**Figure C-73 Strain History of Gauges 28, 29 and 30 in Specimen I2**



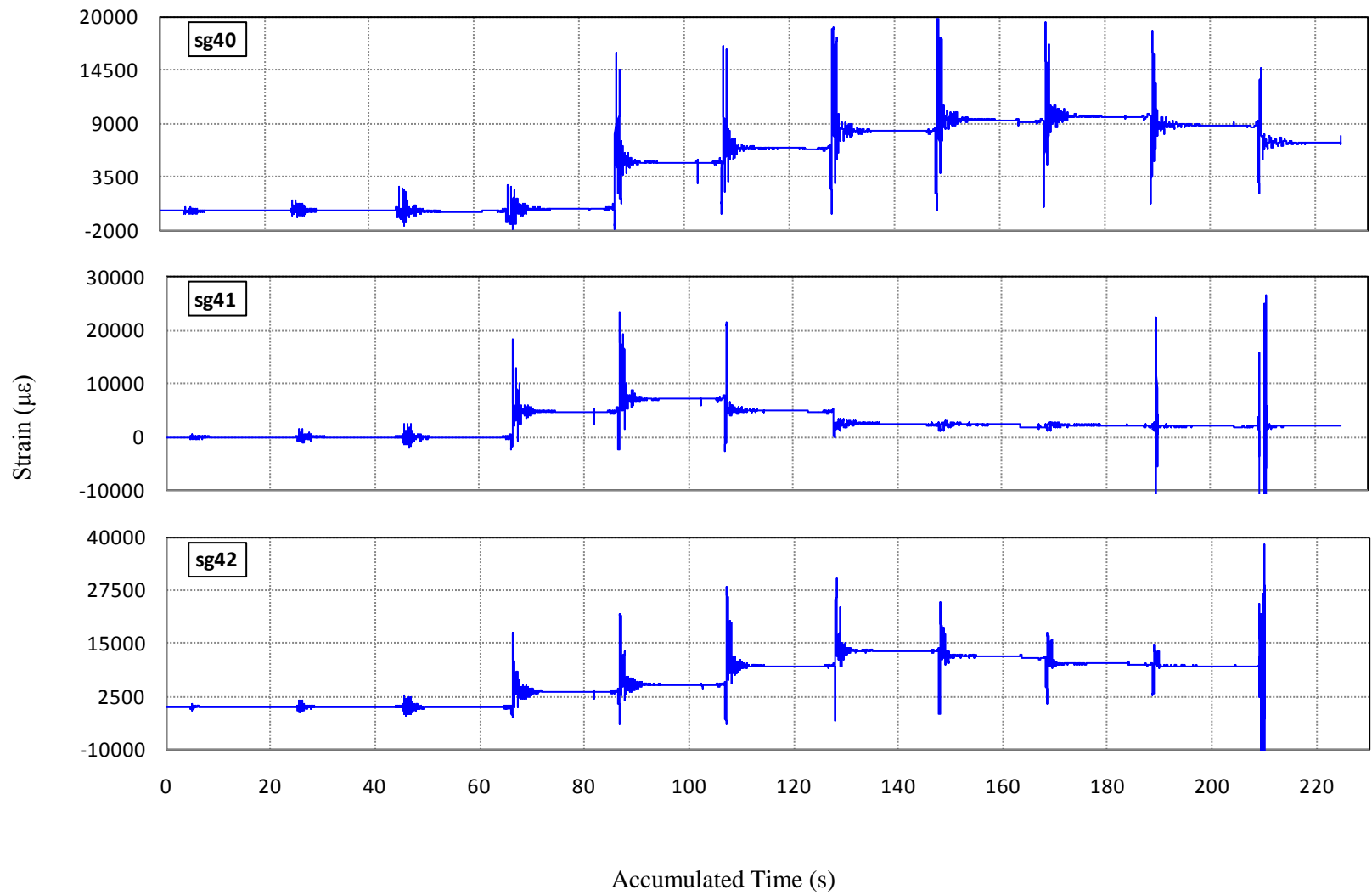
**Figure C-74 Strain History of Gauges 31, 32 and 33 in Specimen I2**



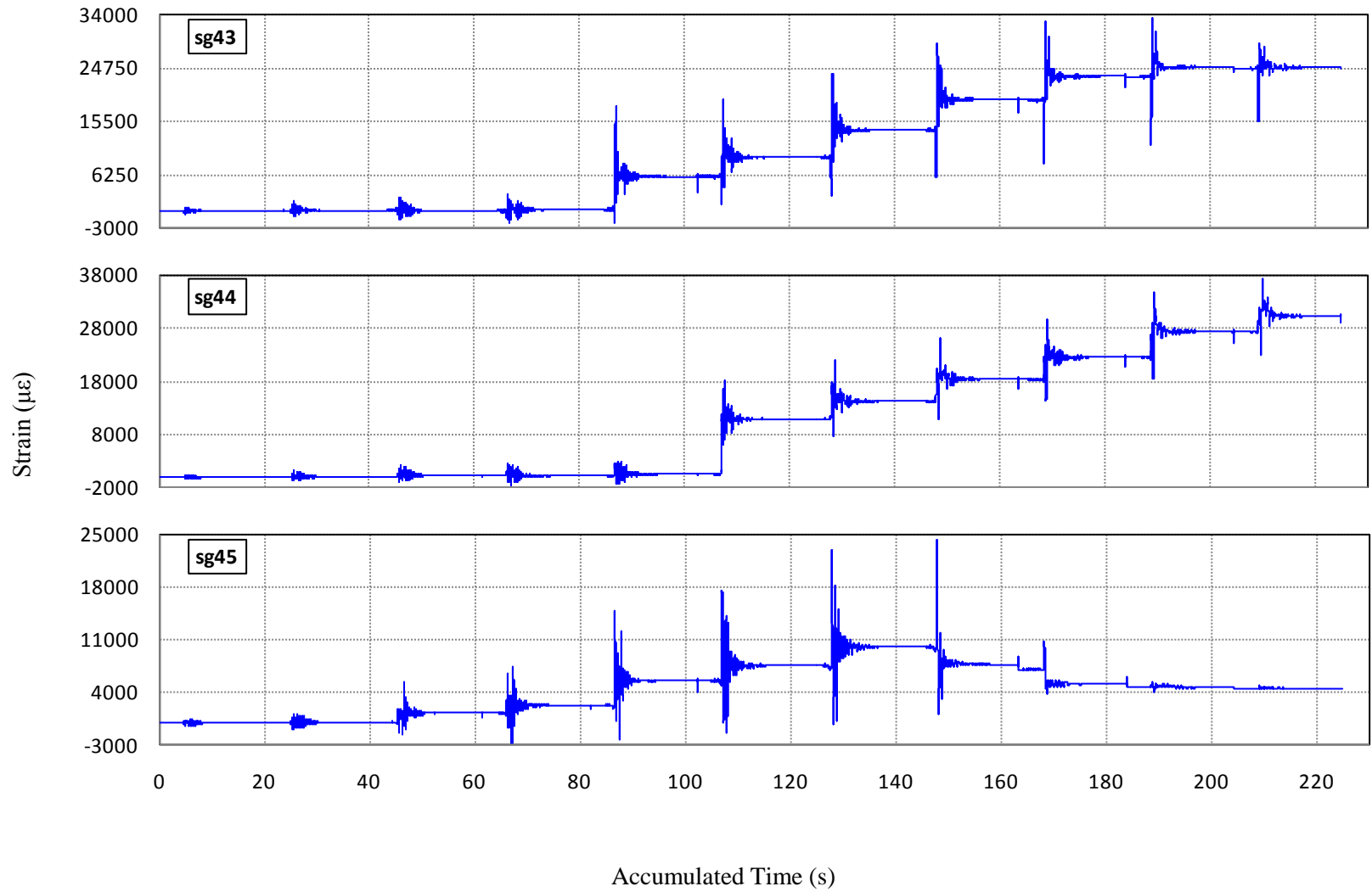
**Figure C-75 Strain History of Gauges 34, 35 and 36 in Specimen I2**



**Figure C-76 Strain History of Gauges 37, 38 and 39 in Specimen I2**

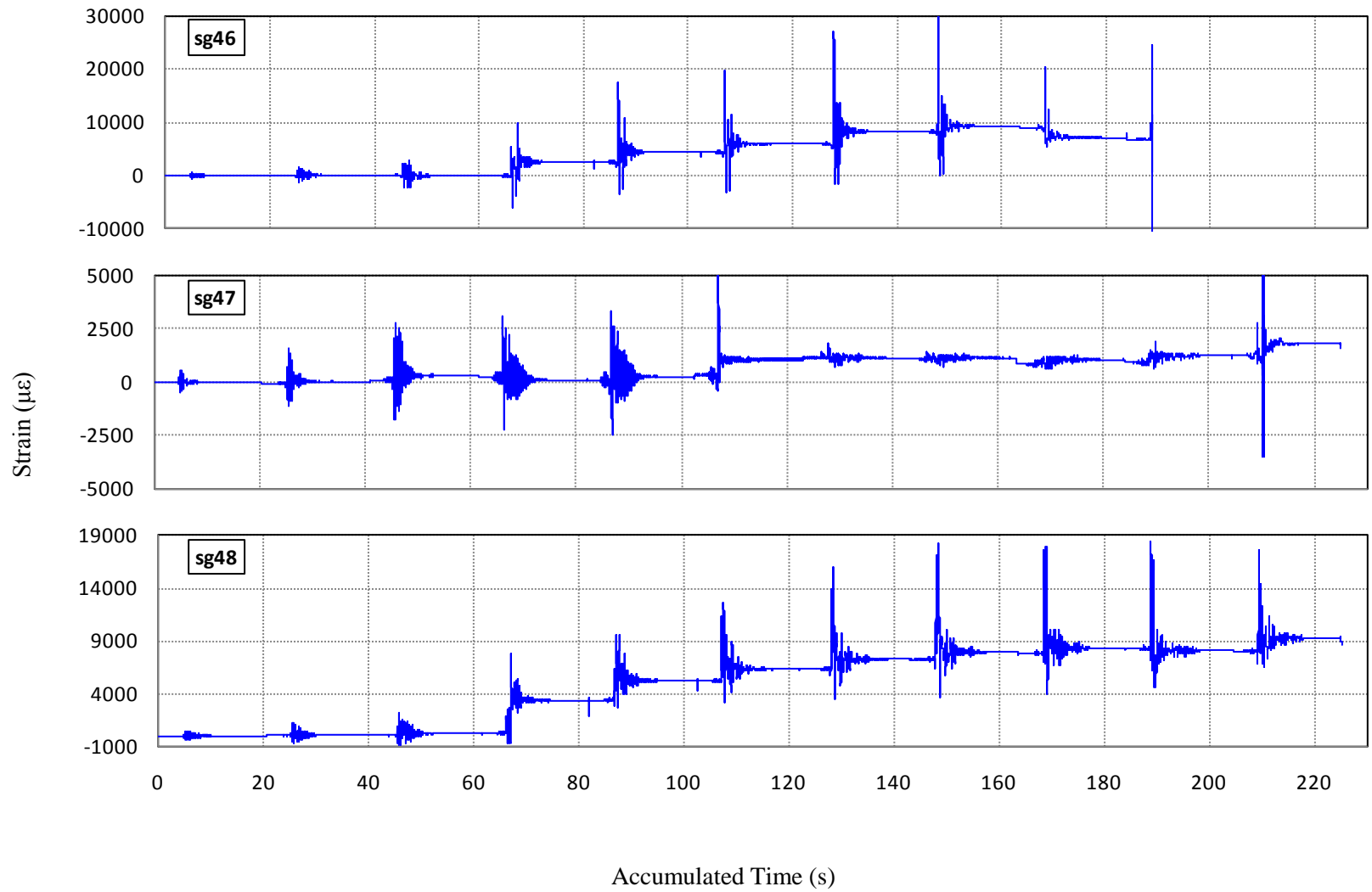


**Figure C-77 Strain History of Gauges 40, 41 and 42 in Specimen I2**

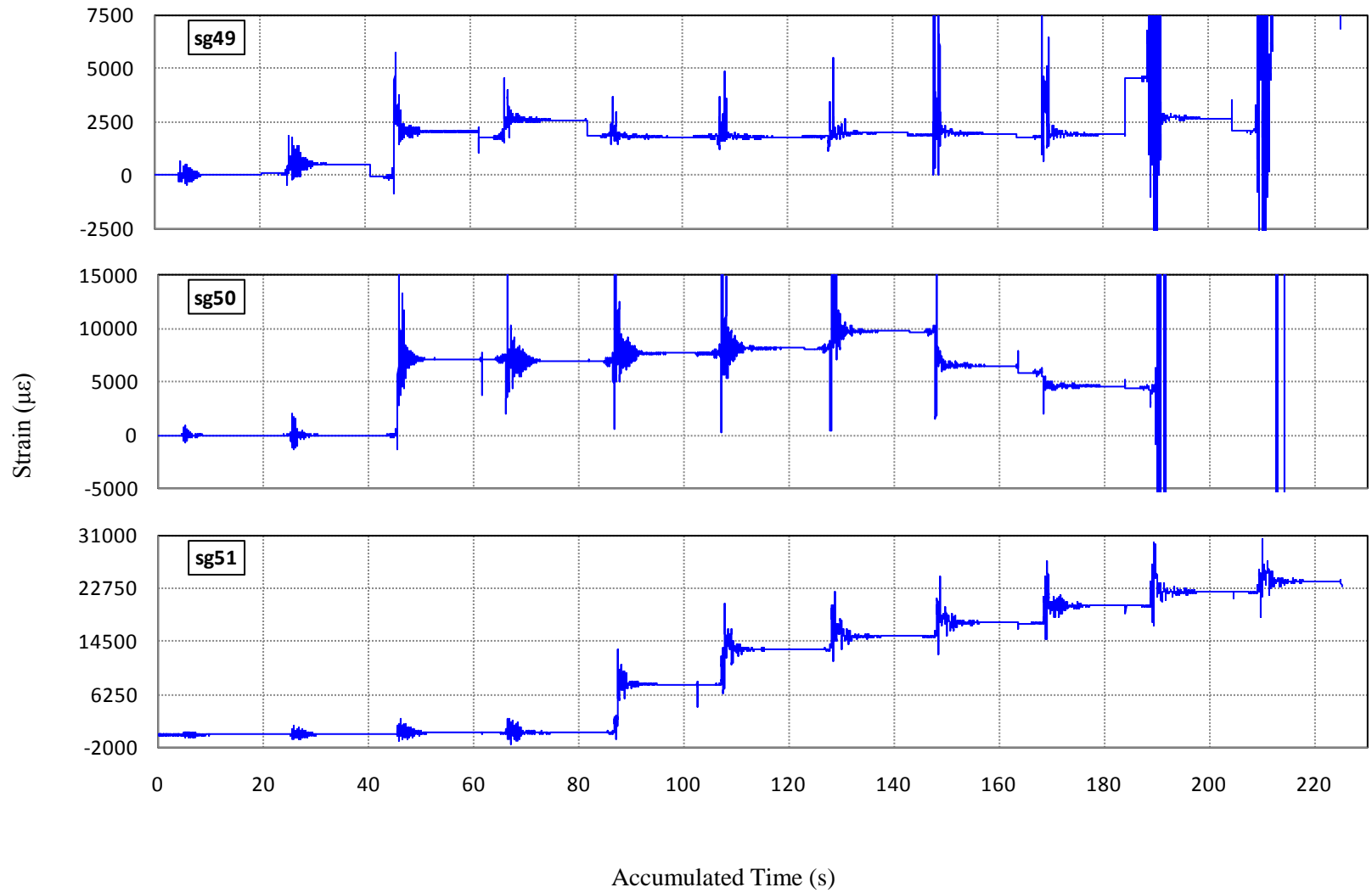


**Figure C-78 Strain History of Gauges 43, 44 and 45 in Specimen I2**

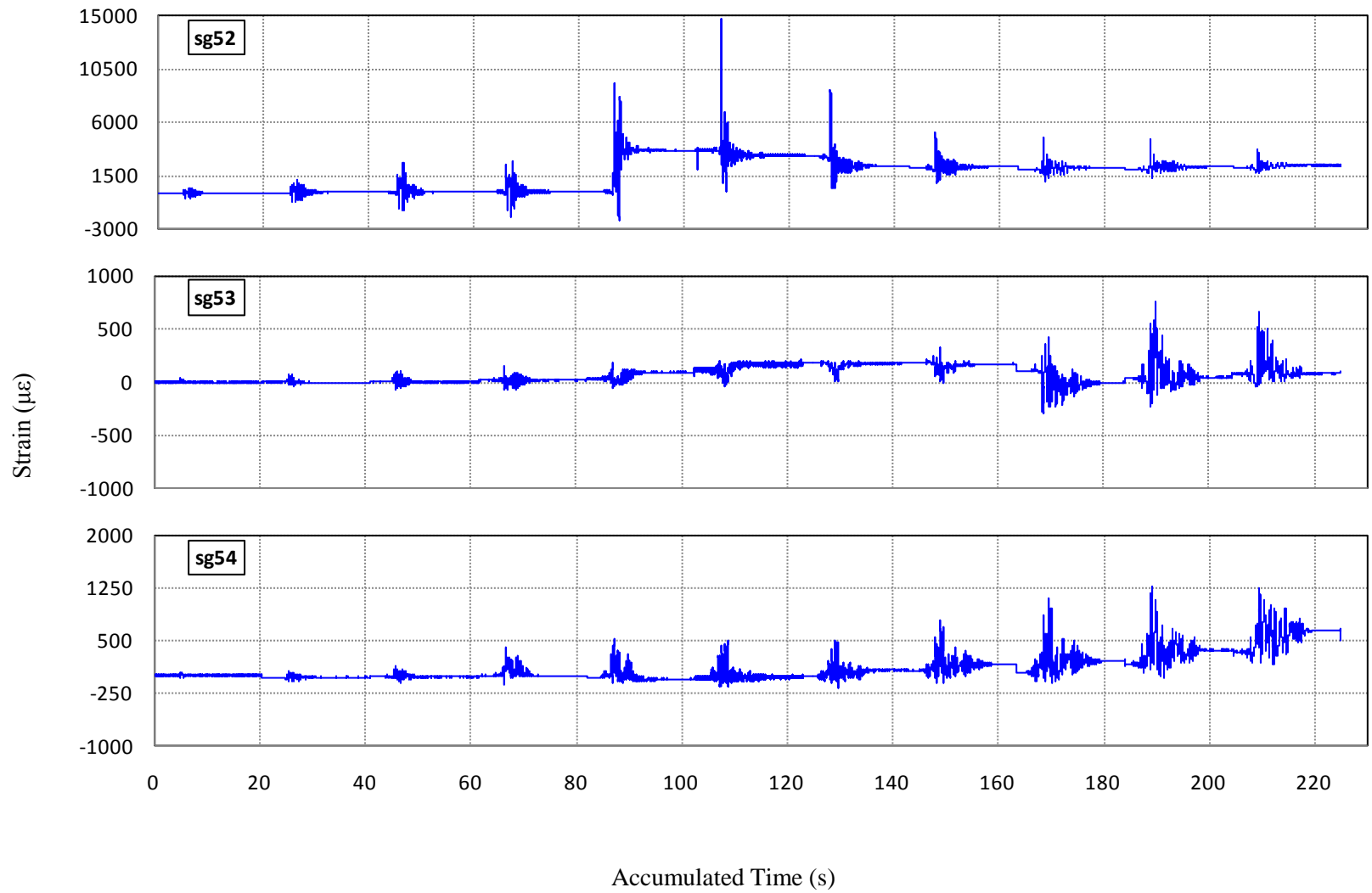




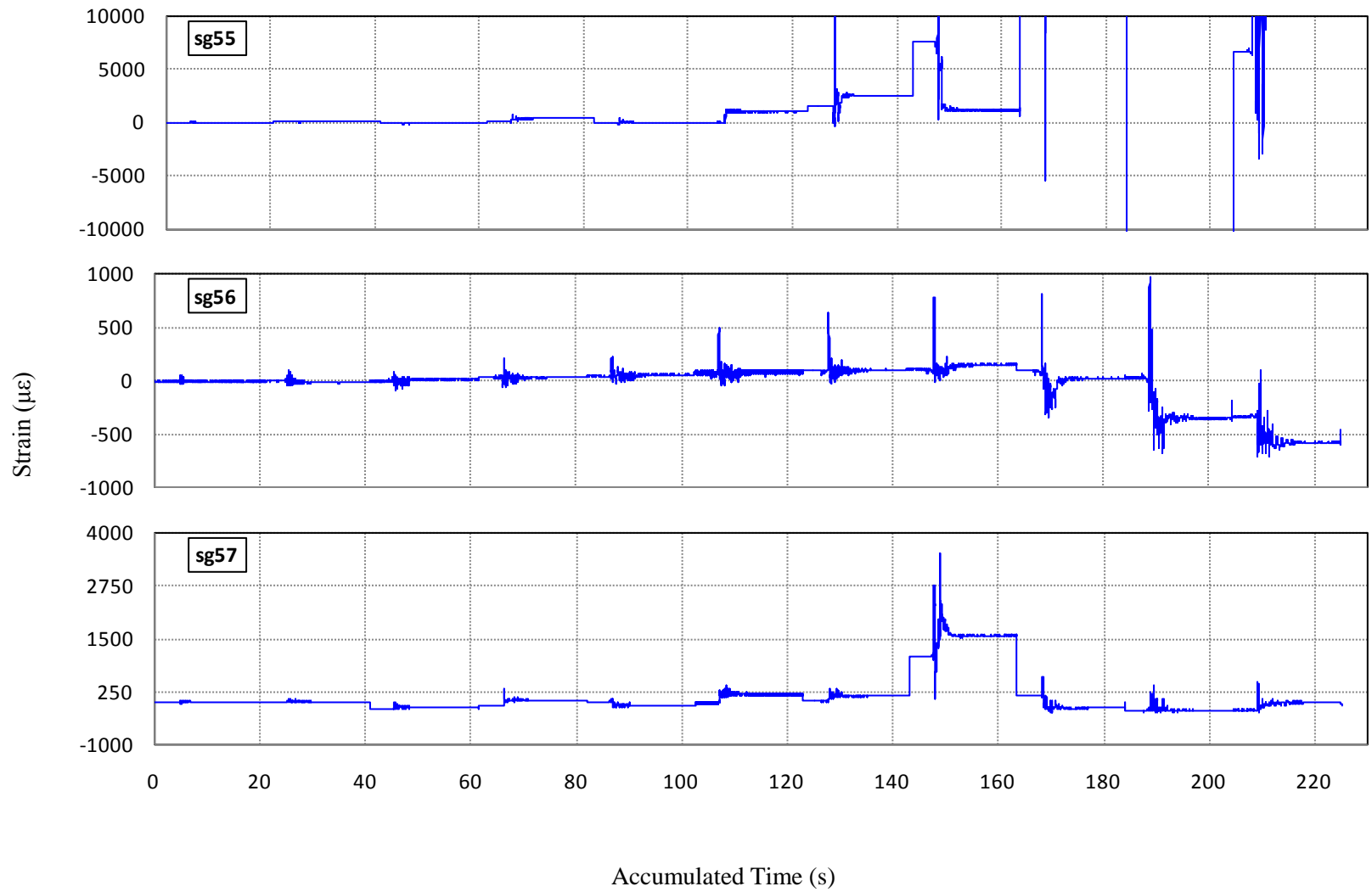
**Figure C-79 Strain History of Gauges 46, 47 and 48 in Specimen I2**



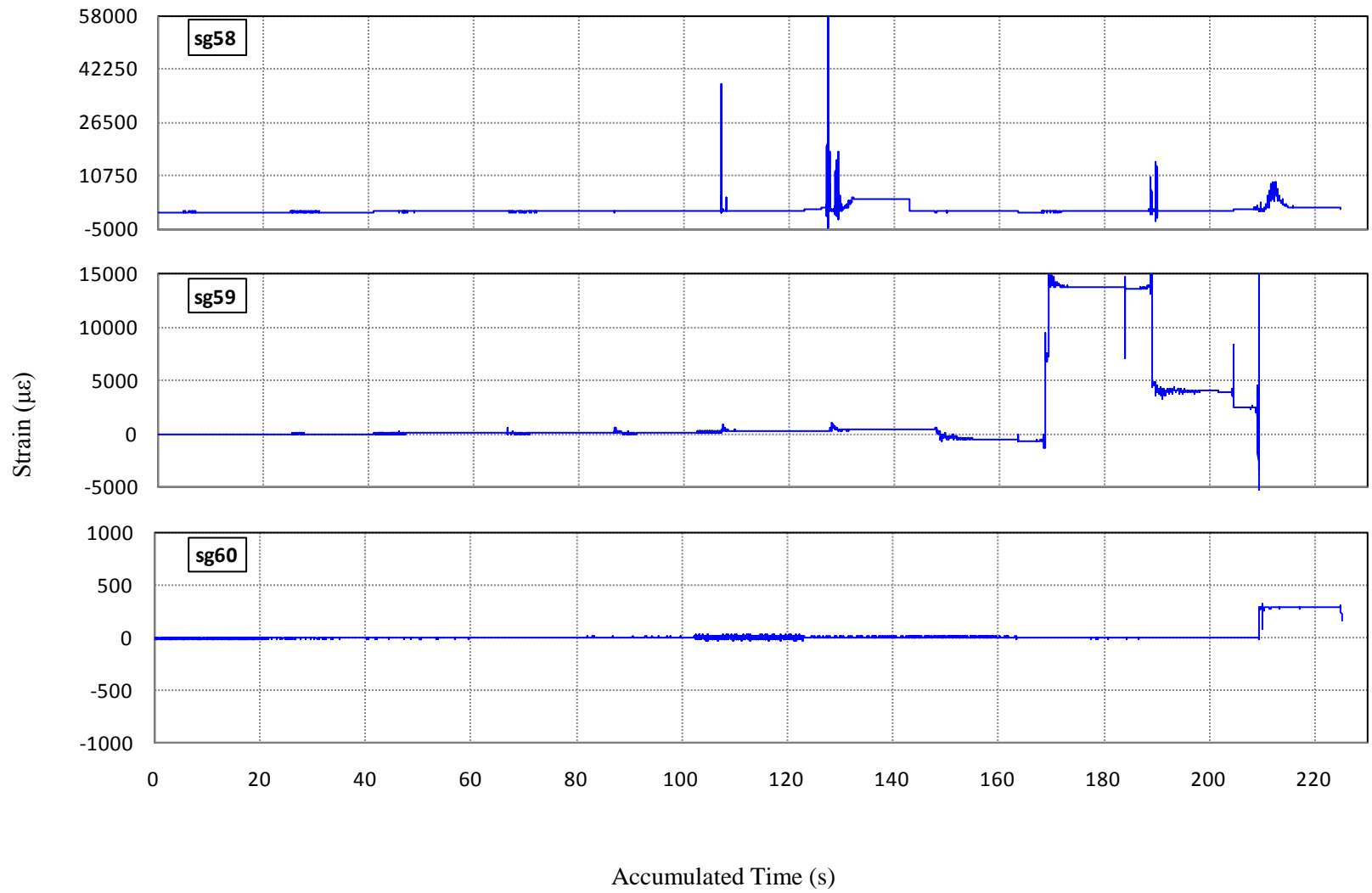
**Figure C-80 Strain History of Gauges 49, 50 and 51 in Specimen I2**



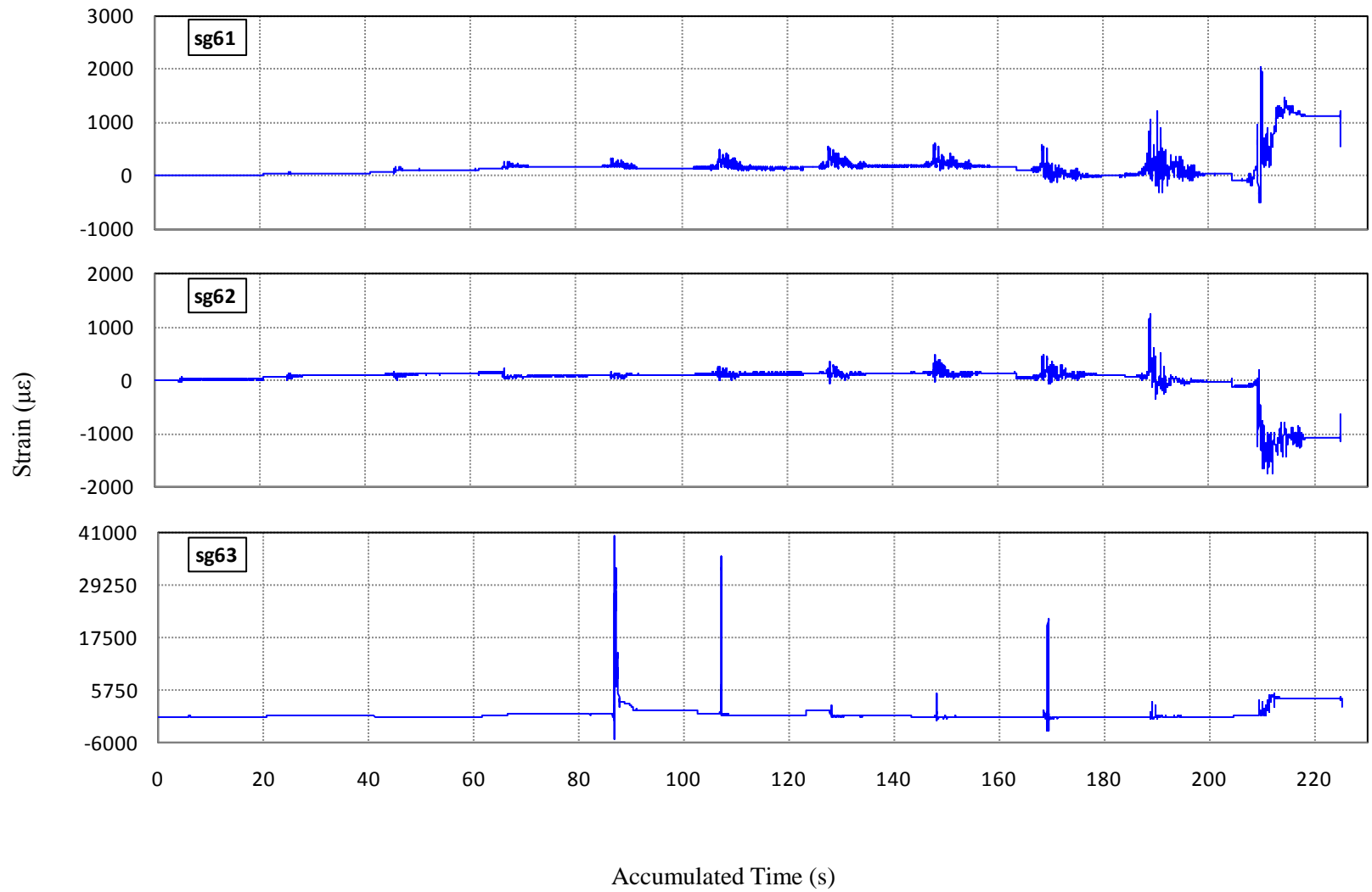
**Figure C-81 Strain History of Gauges 52, 53 and 54 in Specimen I2**



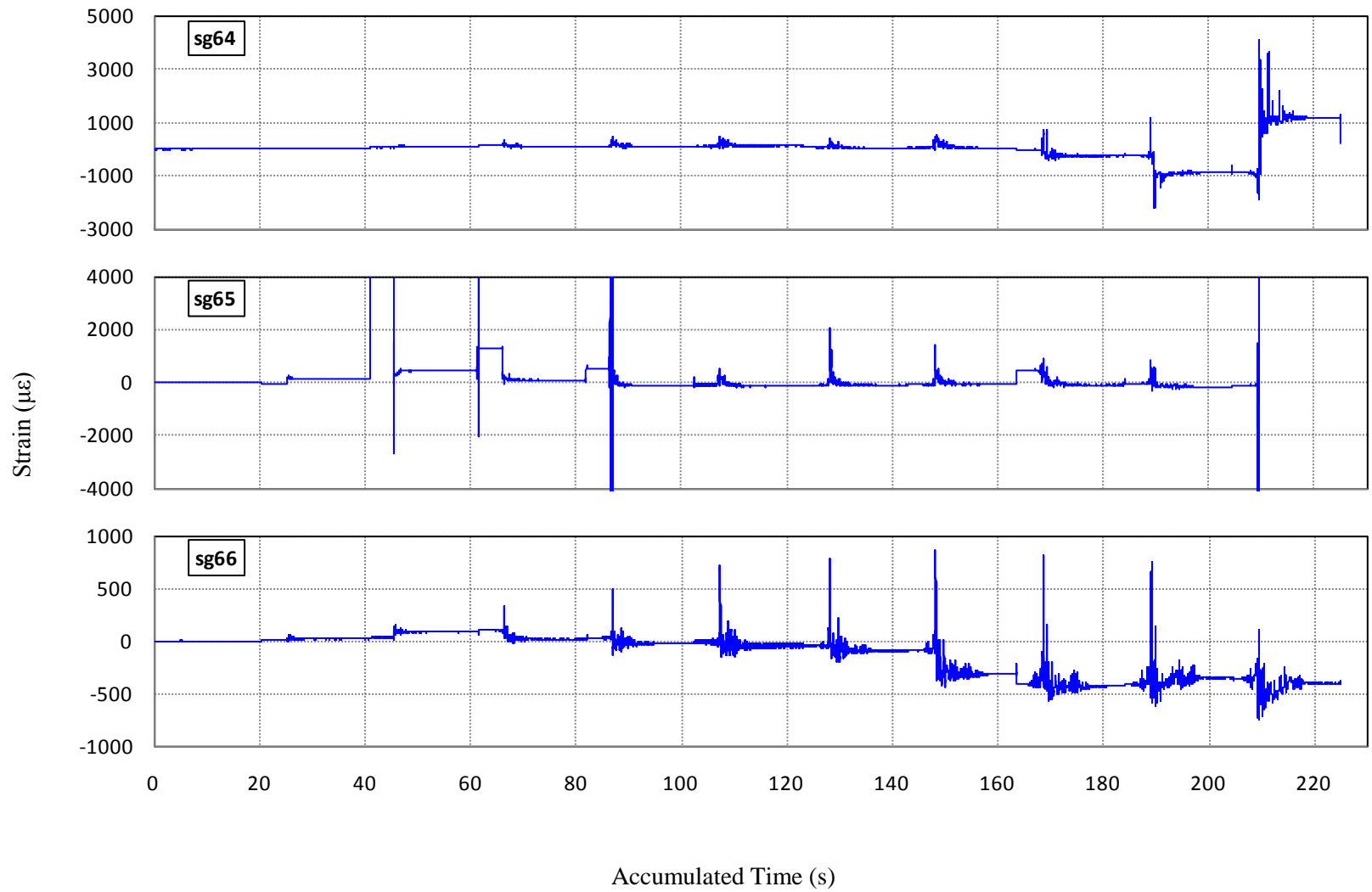
**Figure C-82 Strain History of Gauges 55, 56 and 57 in Specimen I2**



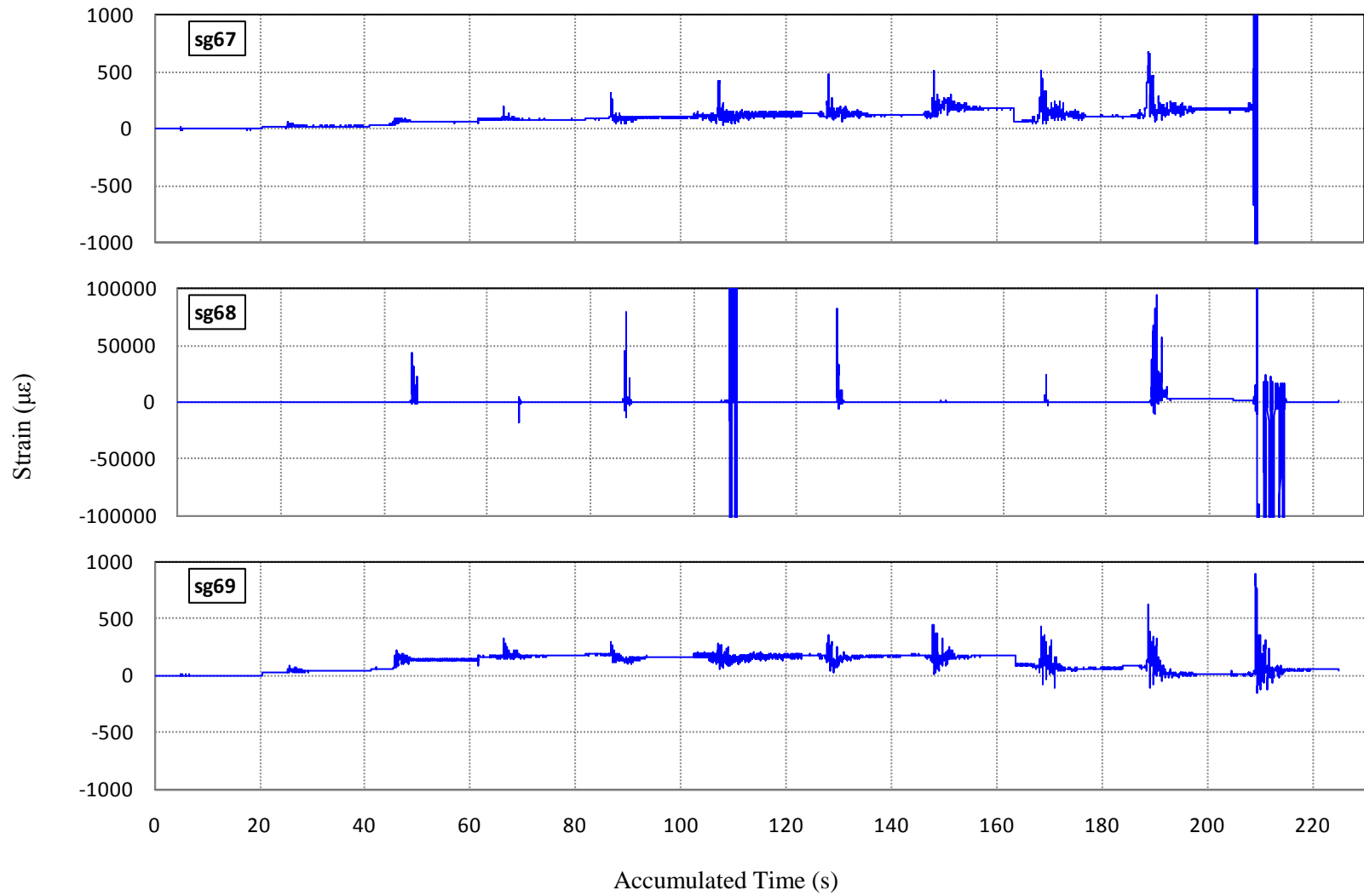
**Figure C-83 Strain History of Gauges 58, 59 and 60 in Specimen I2**



**Figure C-84 Strain History of Gauges 61, 62 and 63 in Specimen I2**

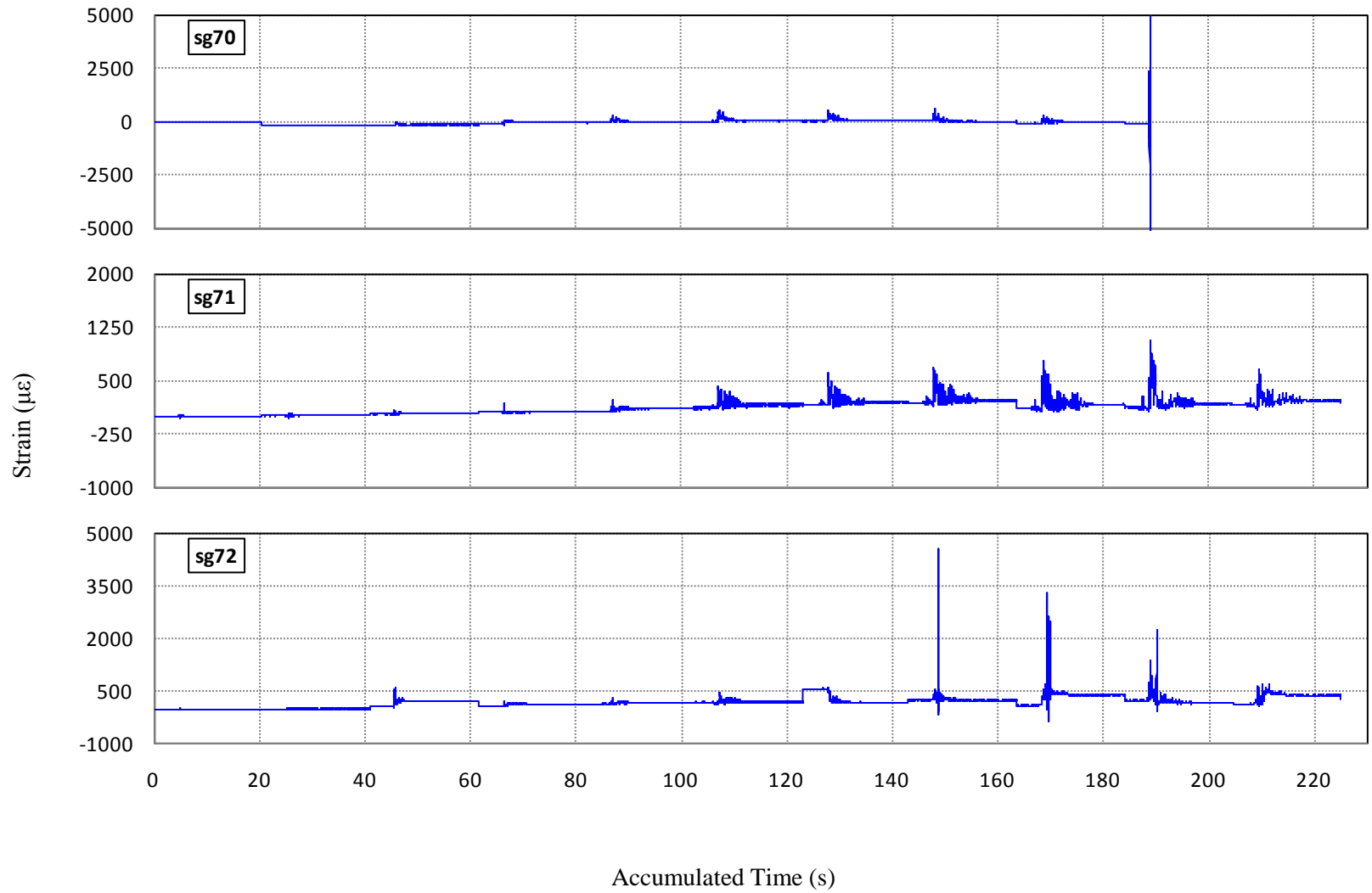


**Figure C-85 Strain History of Gauges 64, 65 and 66 in Specimen I2**

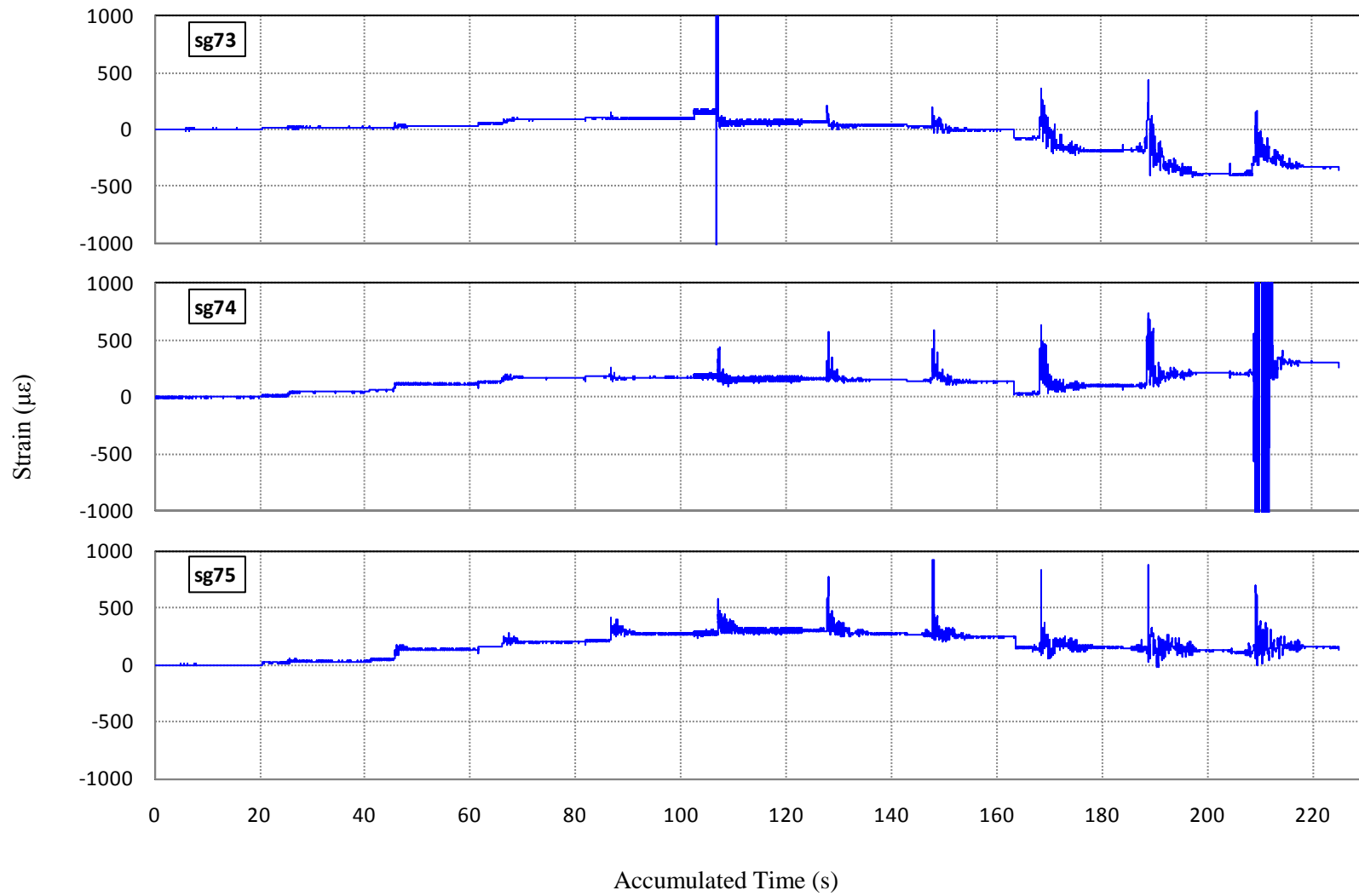


**Figure C-86 Strain History of Gauges 67, 68 and 69 in Specimen I2**

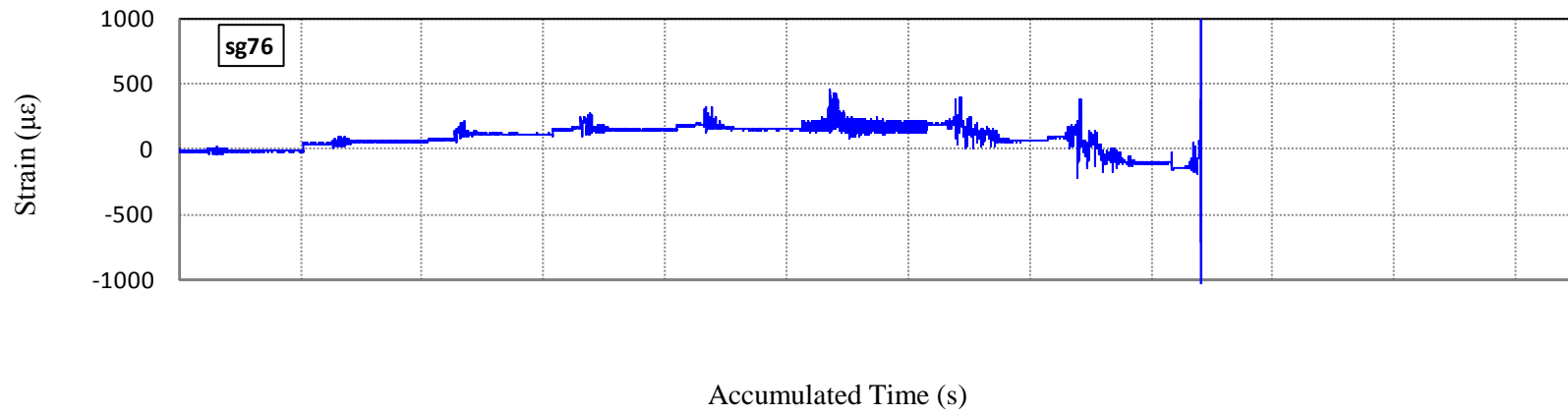




**Figure C-87 Strain History of Gauges 70, 71 and 72 in Specimen I2**



**Figure C-88 Strain History of Gauges 73, 74 and 75 in Specimen I2**



**Figure C-89 Strain History of Gauge 76 in Specimen I2**